8th Spacecraft Charging Technology Conference

J.L. Minor, Compiler
Marshall Space Flight Center, Marshall Space Flight Center, Alabama

Proceedings of a conference co-sponsored
by the Air Force Research Laboratory (AFRL)
and the European Space Agency (ESA) and hosted
by NASA's Space Environments and Effects (SEE) Program
held in Huntsville, Alabama, October 20–24, 2003

National Aeronautics and
Space Administration

Marshall Space Flight Center • MSFC, Alabama 35812

The NASA STI Program Office…in Profile

Since its founding, NASA has been dedicated to the advancement of aeronautics and space science. The NASA Scientific and Technical Information (STI) Program Office plays a key part in helping NASA maintain this important role.

The NASA STI Program Office is operated by Langley Research Center, the lead center for NASA's scientific and technical information. The NASA STI Program Office provides access to the NASA STI Database, the largest collection of aeronautical and space science STI in the world. The Program Office is also NASA's institutional mechanism for disseminating the results of its research and development activities. These results are published by NASA in the NASA STI Report Series, which includes the following report types:

- TECHNICAL PUBLICATION. Reports of completed research or a major significant phase of research that present the results of NASA programs and include extensive data or theoretical analysis. Includes compilations of significant scientific and technical data and information deemed to be of continuing reference value. NASA's counterpart of peer-reviewed formal professional papers but has less stringent limitations on manuscript length and extent of graphic presentations.

- TECHNICAL MEMORANDUM. Scientific and technical findings that are preliminary or of specialized interest, e.g., quick release reports, working papers, and bibliographies that contain minimal annotation. Does not contain extensive analysis.

- CONTRACTOR REPORT. Scientific and technical findings by NASA-sponsored contractors and grantees.

- CONFERENCE PUBLICATION. Collected papers from scientific and technical conferences, symposia, seminars, or other meetings sponsored or cosponsored by NASA.

- SPECIAL PUBLICATION. Scientific, technical, or historical information from NASA programs, projects, and mission, often concerned with subjects having substantial public interest.

- TECHNICAL TRANSLATION. English-language translations of foreign scientific and technical material pertinent to NASA's mission.

Specialized services that complement the STI Program Office's diverse offerings include creating custom thesauri, building customized databases, organizing and publishing research results…even providing videos.

For more information about the NASA STI Program Office, see the following:

- Access the NASA STI Program Home Page at http://www.sti.nasa.gov

- E-mail your question via the Internet to help@sti.nasa.gov

- Fax your question to the NASA Access Help Desk at (301) 621–0134

- Telephone the NASA Access Help Desk at (301) 621–0390

- Write to:
  NASA Access Help Desk
  NASA Center for AeroSpace Information
  7121 Standard Drive
  Hanover, MD 21076–1320
  (301) 621–0390

Available from:

NASA Center for AeroSpace Information
7121 Standard Drive
Hanover, MD 21076–1320
(301) 621–0390

National Technical Information Service
5285 Port Royal Road
Springfield, VA 22161
(703) 487–4650

INTRODUCTION

The 8th Spacecraft Charging Technology Conference was held in Huntsville, Alabama, October 20–24, 2003. Hosted by NASA's Space Environments and Effects (SEE) Program and co-sponsored by the Air Force Research Laboratory (AFRL) and the European Space Agency (ESA), the 2003 conference saw attendance from eleven countries with over 65 oral papers and 18 poster papers.

Presentation topics highlighted the latest in spacecraft charging mitigation techniques and on-orbit investigations, including:

- Plasma Propulsion and Tethers
- Ground Testing Techniques
- Interactions of Spacecraft and Systems With the Natural and Induced Plasma Environment
- Materials Characterizations
- Models and Computer Simulations
- Environment Specifications
- Current Collection and Plasma Probes in Space Plasmas
- On-Orbit Investigations.

A round-table discussion of international standards regarding electrostatic discharge (ESD) testing was also held with the promise of continued discussions in the off years and an official continuation at the next conference.

The Japanese Aerospace Exploration Agency (JAXA) offered to host the 9th Spacecraft Charging Technology Conference in Tsukuba, Japan, in the spring of 2005. (A separate presentation regarding the next conference is also included in these proceedings.) The Centre National d'Etudes Spatiales (CNES) will host the 10th Spacecraft Charging Technology Conference in Toulouse, France, in the fall of 2006.

Every effort has been made to provide the most accurate conversion into pdf format within a timely manner. However, some fonts do not easily convert and conversion errors may have been missed during the review process. If an error is found, simply contact the author of the paper to obtain the correct information.

It is our hope that these proceedings will be of great benefit to you. In addition to the presentation papers, we have included a photographic history of the conference, comprised of a group photo, silhouette* of the attendees, and photos of the more casual, light-hearted moments.

We thank you for the opportunity to host this conference and look forward to seeing everyone again in Tsukuba in 2005.

Cordially,

The Staff of NASA's Space Environments and Effects (SEE) Program

* Special thanks to DPL Science, Inc., for their help in processing the photos and providing the silhouette.

TABLE OF CONTENTS

Characteristic of Charge Accumulation in Glass Materials Under Electron Beam Irradiation
Hiroaki Miyake – Mushashi Institute of Technology

Measurement of Bulk Charge in Dielectric Materials Irradiated by Electron Beam in Vacuum Environment
Noriyuki Osawa – Mushashi Institute of Technology

Improved Demonstration of Internal Charging Hazards Using the 'Realistic Electron Environment Facility' (REEF)
Keith Ryden – QinetiQ

High Voltage Solar Array Arc Testing for a Direct Drive Hall Effect Thruster System
Todd Schneider – NASA Marshall Space Flight Center (MSFC)

Measurement of Charge Distribution in Electron Beam Irradiated PMMA Using Electro-Optical Effect
Yusuke Usui – Mushashi Institute of Technology

Plasma Phenomena Associated With Solar Array Discharges and Their Role in Scaling Coupon Test Results to a Full Panel
Philip Leung – The Boeing Company

POSTER SESSION I

Materials Characterization at Utah State University: Facilities and Knowledgebase of Electronic Properties of Materials Applicable to Spacecraft Charging
John Robert Dennison – Utah State University

Feedback on the Picup3d Experience and the Open Source Strategy Applied to a Spacecraft-Plasma Interaction Simulation Code
Julien Forest – Swedish Institute of Space Physics & CETP

On-Orbit Daytime Solar Heating Effects: A Comparison of Ground Chamber Arcing Results
Joel Galofaro – NASA Glenn Research Center (GRC)

SEE Program: Spacecraft Charging Technology Development Activities
Billy Kauffman – NASA Space Environments and Effects (SEE) Program

Secondary Electron Emission Causing Potential Barriers Around Negatively Charged Spacecraft
Eloy Sasot Samplon – European Space Agency (ESA)

Investigation of Electrostatic Potential Barrier Near an Electron-Emitting Body
Benoit Thiebault – European Space Agency (ESA)

Instrumentation for Studies of Electron Emission and Charging From Insulators
Clint Thomson – Utah State University

AF-Geospace 2.0
Robert Hilmer – Air Force Research Laboratory (AFRL)

**INTERACTIONS OF SPACECRAFT AND SYSTEMS WITH THE NATURAL
AND INDUCED PLASMA ENVIRONMENT SESSION**

A Review of Spacecraft Effects on Plasma Measurements
Alain Hilgers – European Space Agency (ESA)

Observations of Vehicle Surface Charging in Dusty Plasma
Aroh Barjatya – Utah State University

**Spacecraft Charging in a Quasi-Static and Dynamic Plasma Environment and the Scaling
Laws for ESD-Induced Current Transients**
Richard Briët – The Aerospace Corporation

Modeling of the Plasma Thruster Impact on Spacecraft Charging
Sylvie Brosse – Alcatel Space Industries

**The Viability of Using Weight-Saving Material for Future Long-Term Space Vehicles
(i.e., Satellites)**
Nicola Burgess – Raytheon

Simulations of Solar Wind Plasma Flow Around a Simple Solar Sail
Henry Garrett – NASA Jet Propulsion Laboratory (JPL)

High Voltage Solar Array for 400V Operation in LEO Plasma Environment
Satoshi Hosoda – Kyushu Institute of Technology

High-Level Spacecraft Charging at Geosynchronous Altitudes: A Statistical Study
Shu Lai – Air Force Research Laboratory (AFRL)

Degradation of High Voltage Solar Array Due to Arching in LEO Plasma Environment
Teppei Okumura – Kyushu Institute of Technology

**ECSS-E-20-06 Draft Standard on Spacecraft Charging: Environment-Induced Effects
on the Electrostatic Behaviour of Space Systems**
David Rodgers – QinetiQ

Modeling of the Photoelectron Sheath Around an Active Magnetospheric Spacecraft With PicUp3D
Benoit Thiebault – European Space Agency (ESA)

Feasibility Study of an Experimental Platform With Active Plasma Emission for Japan Experimental Module Onboard *ISS*
Hideyuki Usui – Kyoto University

Onset of Spacecraft Charging in Single and Double Maxwellian Plasmas in Space: A Pedagogical Review
Shu Lai – Air Force Research Laboratory (AFRL)

Solar Array in Simulated Leo Plasma Environment
Dr. Boris Vayner – NASA Glenn Research Center (GRC)

MATERIAL CHARACTERIZATIONS SESSION

Charge Storage, Conductivity and Charge Profiles of Insulators as Related to Spacecraft Charging
J.R. Dennison – Utah State University

Electron Emission Properties of Insulator Materials Pertinent to the *International Space Station*
Clint Thomson – Utah State University

European Approach to Material Characterization for Plasma Interaction Analysis
Marc Van Eesbeek – European Space Agency (ESA)

An Improved Method for Simulating the Charge of Dielectrics in a Charging Electron Environment
Denis Payan – Centre National d'Etudes Spatiales (CNES)

Clear, Conductive, Transparent, Flexible Space Durable Composite Films for Electrostatic Charge Mitigation
Kent Watson – National Institute of Aerospace

MODELS AND COMPUTER SIMULATIONS SESSION

An Educational Multimedia Presentation on the Introduction to Spacecraft Charging
Elise Lin – DPL Science, Incorporated

NASCAP-2K – An Overview
Myron Mandell – Science Applications International Corporation (SAIC)

Validation of NASCAP-2K Spacecraft-Environment Interactions Calculations
Victoria Davis – Science Applications International Corporation (SAIC)

NASCAP-2K As a PIC Code
Myron Mandell – Science Applications International Corporation (SAIC)

Assessment and Control of Spacecraft Charging Risks on the *International Space Station*
Steve Koontz – NASA Johnson Space Center (JSC)

***ISS* Plasma Interaction: Measurements and Modeling**
Hagop Barsamian – The Boeing Company

Specification of *ISS* Plasma Environment Variability
Joseph Minow – Jacobs Sverdrup

Electron Collection by *International Space Station* Solar Arrays
Barbara Gardner – Science Applications International Corporation (SAIC)

The Electric Propulsion Interactions Code (EPIC)
Yiangos Mikellides – Science Applications International Corporation (SAIC)

Effects of Large-Amplitude RF Emissions on OEDIPUS-C Floating Voltages
James Laframboise – York University

SPARCS: An Advanced Software for Spacecraft Charging Analyses
Sebastian Clerc – Alcatel Space Industries

Computer Simulation of Radiation Charging Processes in Spacecraft Materials
Valery Mileev – Moscow State University

Design of a New Modular Spacecraft Plasma Interaction Modeling Software (SPIS)
Jean-Francois Roussel – ONERA / DESP

Development of a Virtual Testing Laboratory for Spacecraft-Plasma Interactions
Joseph Wang – Virginia Polytechnic Institute and State University

Features of Charging of Composite Configuration Spacecraft Charging in High Orbits
Valery Mileev – Moscow State University

ENVIRONMENT SPECIFICATIONS SESSION

Representation of the Geosynchronous Plasma Environment for Spacecraft Charging Calculations
Victoria Davis – Science Applications International Corporation (SAIC)

An Empirical Low-Energy Ion Model of the Inner Magnetosphere
James Roeder – The Aerospace Corporation

Inner Radiation Belt Representation of the Energetic Electron Environment: Model and Data Synthesis Using the Salammbo Radiation Belt Transport Code and Los Alamos Geosynchronous and GPS Energetic Particle Data
Reiner Friedel – Los Alamos National Laboratory (LANL)

Assimilative Forecasting of the Energetic Particle Environment
Steve Naehr – Rice University

Operational Prediction and Specification of the Spacecraft Charging Environment
Terrance Onsager – National Oceanic and Atmospheric Administration (NOAA)

The Flumic Electron Environment Model
David Rodgers – QinetiQ

New NASA SEE LEO Spacecraft Charging Design Guidelines – How to Survive in LEO Rather than GEO
Dale Ferguson – NASA Glenn Research Center (GRC)

POSTER SESSION II

Embedded-Probe Floating Potential Charge-Discharge Monitor
Keith Balmain – University of Toronto

Wake Effects on Positively Charged Spacecraft in Flowing Tenuous Plasmas: Cluster Observations and Modeling
Erik Engwall – Swedish Institute of Space Physics

Modeling of the Plasma Environment of a FEEP Micro Thruster with PICUP3D Simulation Code: Sample Results
Julien Forest – European Space Research and Technology Center (ESA-ESTEC)

Carbon Nanofiber-Filled Materials for Charge Dissipation
Ronald Jacobsen – Applied Sciences Incorporated

Comparison of Classical and Charge Storage Methods for Determining Conductivity of Thin Film Insulators
Prasanna Swaminathan – Utah State University

Particle-In-Cell Simulations on Antenna Characteristics in Magnetized Plasma
Hideyuki Usui – Kyoto University

An Educational Multimedia Presentation on the Introduction to Spacecraft Charging
Elise Lin – DPL Science, Incorporated

CURRENT COLLECTION AND PLASMA PROBES IN SPACE PLASMAS SESSION

Current Collection by a Segmented Langmuir Probe in the Ionosphere Plasma
Elena Seran – CETP

Calibrating the Floating Potential Measurement Unit
Charles Swenson – Utah State University

The Deflection Plate Analyzer: A Technique for Space Plasma Measurements Under Highly Disturbed Conditions
Ken Wright – NASA MSFC National Space & Science Technology Center (NSSTC)

ON-ORBIT INVESTIGATIONS SESSION

Nearly Eighty Years of SOHO Observations – Some Highlights
Paal Brekke – European Space Agency (ESA)

Space Weather Effects on SOHO and its Role as a Space Weather Watchdog
Paal Brekke – European Space Agency (ESA)

In-Flight Anomalies Attributed to ESD's. Recent Cases and Trends
Jean-Pierre Catani – Centre National d'Etudes Spatiales (CNES)

A Novel Spacecraft Charge Monitor for LEO
Luke Goembel – Goembel Instruments

Active Spacecraft Potential Control for Cluster Results from Three Years in Orbit
Klaus Torkar – Austrian Academy of Sciences

On-Orbit Experiments and Research on Measuring the Spacecraft Charging
Nikolski Evgeny – Russian Aviation-Space Agency, Lavochkin Association

CONFERENCE PHOTOS
Group photo, silhouette of the attendees, and casual photos

9th SPACECRAFT CHARGING TECHNOLOGY CONFERENCE
The Japanese Aerospace Exploration Agency (JAXA) will host the 9th Spacecraft Charging Technology Conference in Tsukuba, Japan, in the spring of 2005

Brekke, Paal
European Space Agency
NASA/GSFC Mailcode 682.3
Bldg 26, Room G-1
Greenbelt, MD 20817
USA
301-286-6983
pbrekke@esa.nascom.nasa.gov

Brickhouse, Kyle
Universities Space Research Association
108 Gray Run
Huntsville, AL 35824
USA
256-544-4193
kyle.brickhouse@msfc.nasa.gov

Briet, Richard
The Aerospace Corporation
2350 E El Segundo Blvd
El Segundo, CA 90245-4691
USA
310-366-1912
Richard.Briet@aero.org

Brown, Gayle
Universities Space Research Association
108 Gray Run
Huntsville, AL 35824
USA
256-544-2104
gayle.brown@msfc.nasa.gov

Burch, Jackie
Teledyne Solutions, Inc.
5000 Bradford Drive, Suite 200
Huntsville, AL 35805
USA
256-726-3505
jackie.burch@tdytsi.com

Burgess, Nicola
Raytheon
7401 E. Speedway, #12206
Tuscon, AZ 85710
USA
520-794-0845
nicola_burgess@raytheon.com

Catani, Jean-Pierre
Centre National d'Etudes Spatiales
(CNES)
18, Avenue Edouard-Belin – 31401
Toulouse Cedex 9
France
05.61.27.36.77
jean-pierre.catani@cnes.fr

Cho, Mengu
Kyushu Institute of Technology
1-1 Sensui Tobata-ku
Kitakyushu, Fukuoka 8048550
Japan
+81-93-884-3228
cho@ele.kyutech.ac.jp

Clark, Tony
NASA Marshall Space Flight Center
Mail Code ED44/4708
Huntsville, AL 35812
USA
256-544-2394
tony.clark@nasa.gov

Cooke, David
AFRL/VSBX – Hanscom AFB
Bedford, MA 01731-3010
USA
781-377-2931
david.cooke@hanscom.af.mil

PHYSICAL PROBLEMS OF ARTIFICIAL MAGNETOSPHERIC PROPULSION

J.T. Mendonça
GoLP, Instituto Superior Técnico, 1049-001 Lisboa, Portugal
E-mail: titomend@ist.utl.pt

A.L. Brinca
R. Fonseca
J. Loureiro
L.O. Silva and I. Vieira
GoLP, Instituto Superior Técnico

We discuss here some physical problems related to the recently proposed scheme for solar sailing, using an artificial magnetosphere. We will concentrate on the forces acting on the plasma bubble, and their transfer to the spacecraft. Upper and lower limits of the force acting on the bubble are established. The results of test particle dynamics are presented, concerning the interaction of the solar wind with the modified magnetic dipole resulting from the spacecraft coils and the plasma expansion. Propagation of the forces along the magnetic flux tubes, from the bubble magnetopause down to the spacecraft vicinity, is discussed by using a simple MHD theoretical model. Emphasis is made on the distribution of currents flowing in the immediate vicinity of the spacecraft. Finally, results of PIC code simulations of the magnetized plasma expansion are presented and an overall qualitative picture of the physical processes is given, with a discussion of the strategy for obtaining more quantitative estimates of the magnetospheric propulsion efficiency.

Introduction

We discuss here some of physical problems related to the Mini-Magnetosphere Plasma Propulsion (M2P2) scheme for solar sailing and outer planet exploration. This scheme was recently proposed by Winglee el al. [1], and assumes that a large plasma bubble is formed and expands around the spacecraft (s/c), taking the size of several kilometers, and is forced to move due to the solar wind pressure. The proposed artificial magnetosphere could be created by a helicon plasma source, and confined by the magnetic dipole generated by a coil, also installed at the s/c. The plasma particles could stay attached to the s/c due to magnetization.

The plasma produced by the plasma source should be dense and warm (n and T of the order of 5×10^{13} cm^{-3} and 5 eV, so that a discharge of the helicon type fulfills, in principle, these requirements. Most probably, the helicon produces a weekly ionized, collisional gas with $T_e > T_i$ that is injected into the magnetic field generated by the coil.

The success of the mini-magnetospheric plasma propulsion (M2P2) idea hinges on the value of the force that acts upon the spacecraft (S/C). We also discuss here several aspects that might intervene in its estimate. Upper and lower limits of the force acting on the bubble are established. The results of test particle dynamics are presented, concerning the interaction of the solar wind with the modified magnetic dipole resulting from the spacecraft coils and the plasma expansion. Propagation of the forces along the magnetic flux tubes, from the bubble magnetopause down to the spacecraft vicinity, is discussed by using a simple MHD theoretical model. Emphasis is made on the distribution of currents flowing in the immediate vicinity of the spacecraft. Finally, results of PIC code simulations of the magnetized plasma expansion are presented and an overall qualitative picture of the physical processes is given,

with a discussion of the strategy for obtaining more quantitative estimates of the magnetospheric propulsion efficiency.
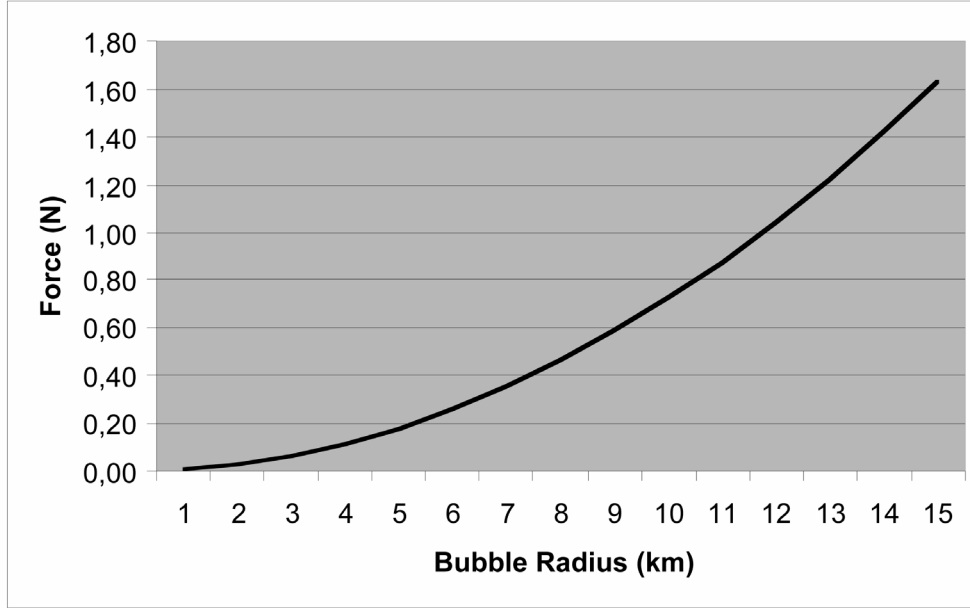
Forces Acting on the Bubble

While analyzing the complex interaction between the solar wind (SW) and the artificial mini-magnetosphere, perhaps the first attempt at estimating the force on the spacecraft comes from the realization that the momentum of the SW particles changes and its conservation requires that it should be picked up by the S/C. However, leaving aside the difficulties associated with a realistic calculation of the variation in the SW particle momentum, one cannot conclude that this change is totally absorbed by the S/C: the momentum of the artificially injected plasma particles is also modified during the interaction with the SW. An alternative way of addressing the calculation of the force on the spacecraft relies on the consideration of the coil in the S/C.

First, we should notice that the gravitational attraction of the Sun at 1 A.U. is of the order of F_S/kg = G M m(= 1 kg) (1 A.U.)$^{-2}$ = 5.93 mN/Kg. For a s/c prototype with 100 kg this corresponds to F_S = 0.6 N. This value gives an estimate of the force necessary for the M2P2 method to work.

Let us now make an upper estimate of the force acting on the plasma bubble. For simplicity, we can define the boundary of the plasma bubble created around the spacecraft as the region where the solar wind pressure equals the magnetic pressure of the artificial magnetic dipole. We can call it the magnetopause of the artificial magnetosphere. The number of particles hitting the surface of the magnetopause, per unit time and per unit surface is $N = N_0 v \cos(\phi)$, where N_0 is the density of solar wind protons ($\sim$ 5/cc near the Earth), v is the velocity of the solar wind ($\sim$ 400 km/s), and ϕ is the angle of incidence. If we assume specular reflection of the protons on the magnetopause, they will suffer a change of momentum equal to $2 m_p v \cos(\phi)$, where m_p is the proton mass. So, the pressure of the solar wind will be $p = 2 N0 m_p . v^2 \cos^2(\phi)$. We can then calculate the force of the solar wind on the magnetopause, by assuming that this surface is approximately spherical with a radius R. The result is:

$$F = \int pdS = \pi R^2 N_0 m_p v^2 \qquad (1)$$

This expression gives the upper limit of the force acting on the plasma bubble, and this result is illustrated in Figure 1.

Figure 1. Solar attraction as a function of bubble radius

Let us now look at the force acting on the s/c itself. The spacecraft creates its own magnetic dipole, which will eventually confine the plasma produced by a helicon source. The expected characteristics of the coil are: number of turns: $n_c = 1000$, current in the coil: $I_c = 10$ A, and coil radius: $a_c = 10$ cm. The resulting value for the magnetic dipolar momentum is: $m_c = \pi\, a_c^2\, n_c\, I_c = 300$ A m^2 and, assuming that the axis Oz coincides with the direction of the magnetic dipolar momentum, we can write $\vec{m}_c = m_c \vec{e}_z$.

The interaction of the solar wind with the plasma bubble will lead to the formation of induced currents, which will be responsible for the deformation of the magnetic dipolar configuration. The magnetic force acting on the s/c will then be due to the magnetic field $\vec{B}$ created by these induced currents:

$$\vec{F} = \nabla\left(\vec{m}_c \cdot \vec{B}\right) = m_c \nabla B_z \qquad (2)$$

Or, assuming that the gradient is directed along the axis Ox:

$$\vec{F} = m_c \frac{\partial B_z}{\partial x}\vec{e}_x \qquad (3)$$

As a simple model for the currents induced in the plasma in the immediate vicinity of the spacecraft, we consider a linear current I aligned with the axis Oy, flowing at a distance x from the spacecraft. The resulting magnetic field at the spacecraft position will be written as: $\vec{B} = \mu_0 I (2\pi x)^{-1} \vec{e}_z$. The resulting magnetic force acting on the spacecraft will then be determined by

$$F = m_c \left|\frac{dB_z}{dx}\right| = 6 \times \frac{I}{x^2} \quad N \qquad (4)$$

This means that, in order to obtain a force similar to attractive force from the Sun, $F \approx F_S \approx 1$ N, we need to have a current I such that $I > 10^4 x^{-2}$ A/m². For a linear current located at a distance x = 1 m from the s/c, we would need a current larger than ten kilo-Ampere: $I > 10^4$A. This is an extremely large value of induced currents near the s/c, but the actual plasma currents are induced over a large volume inside the magnetic bubble and are not concentrated as assumed in the present model. The interest of the model is that, whatever the actual volume distribution of currents is, it will have to be responsible for the same value of the magnetic field gradient.

Let us now look at the force propagation along field lines. The solar wind, moving with a velocity $\vec{v}_0 = v_0 \vec{e}_x$, perturbs the magnetic flux tubes of the magnetic dipole created by the s/c coils. This perturbation can is described by the MHD equations. These equations relate the velocity of the medium $\dot{v}$ with the pressure p, the current density $\vec{J}$ and the magnetic field $\vec{B}$

$$\rho\left(\frac{\partial \vec{v}}{\partial t} + \vec{v} \cdot \nabla \vec{v}\right) = -\nabla p + \vec{J} \times \vec{B} \tag{5}$$

where ρ is the plasma density, and

$$\frac{\partial \vec{B}}{\partial t} = \nabla \times \left(\vec{v} \times \vec{B}\right) \tag{6}$$

If we assume a simple geometry such that: $\vec{v} = (v_x, 0, 0)$ and $\vec{B} = (B_x, 0, B_0)$, and use the constancy of the total plasma pressure: $p + \mu_0 B_x^2 / 2 = p_0$ we can obtain the propagation equation for the magnetic field perturbation B_x:

$$\frac{\partial^2 B_x}{\partial t^2} = v_A^2 \frac{\partial^2 B_x}{\partial z^2} \tag{7}$$

where v_A is the Alfven velocity, $v_A = B_0 / \sqrt{\mu_0 \rho}$. This shows that the perturbations induced by the solar wind propagate without significant losses along the magnetic flux tube, with the Alfven velocity, from the magnetopause down to the spacecraft. Particular solutions for this model were discussed long time ago by Scholer [2]. The collisional plasma located in the near vicinity of the spacecraft will eventually introduce some dissipation. But, apart from that, the force is transmitted without attenuation along the magnetic flux tubes.

In order to complete this qualitative discussion let us now use a test particle approach to establish a lower limit for the force produced by the solar wind over an artificial magnetosphere. We assumed that the magnetic field existing inside the plasma bubble is that of a modified magnetic dipole:

$$\vec{B} = \vec{b} K r^{-\alpha} \tag{8}$$

where α is the decay factor (the usual magnetic dipole would be $\alpha = 3$), K is the magnetic field amplitude that depends of the current and dimensions of the coil installed inside the s/c, $\vec{b}$ is a unit vector giving the orientation of the magnetic dipole, and r is the distance of the particle to the spacecraft. A simple simulation code has been developed to solve the test particle trajectory in such a modified magnetic dipole. This allows us to determine the momentum transfer to the particle due to its collision with the magnetic field as a function of

its impact parameter and initial velocity, and thus by momentum conservation, and after averaging over the particle population of the solar wind, to obtain the force acting on the magnetic dipole. Here we neglect the possible collisions with the particles of the plasma bubble, which means that we can only get a lower limit to the force acting on the dipole. The area of simulation is a cube of 30 km x 30 km x 30 km. A uniform flux of protons from the solar wind is introduced along the positive Ox direction. The magnetic dipole is oriented along the Oz direction, $\vec{b} = \vec{e}_z$. Both the magnetic field and particle position-velocity are simulated in three dimensions. Using the Runge-Kutta method, the particles are moved during a step of time, named dt. The velocity of the particles is updated assuming the presence of the magnetic field created by the modified dipole, which is not considered self-consistent.
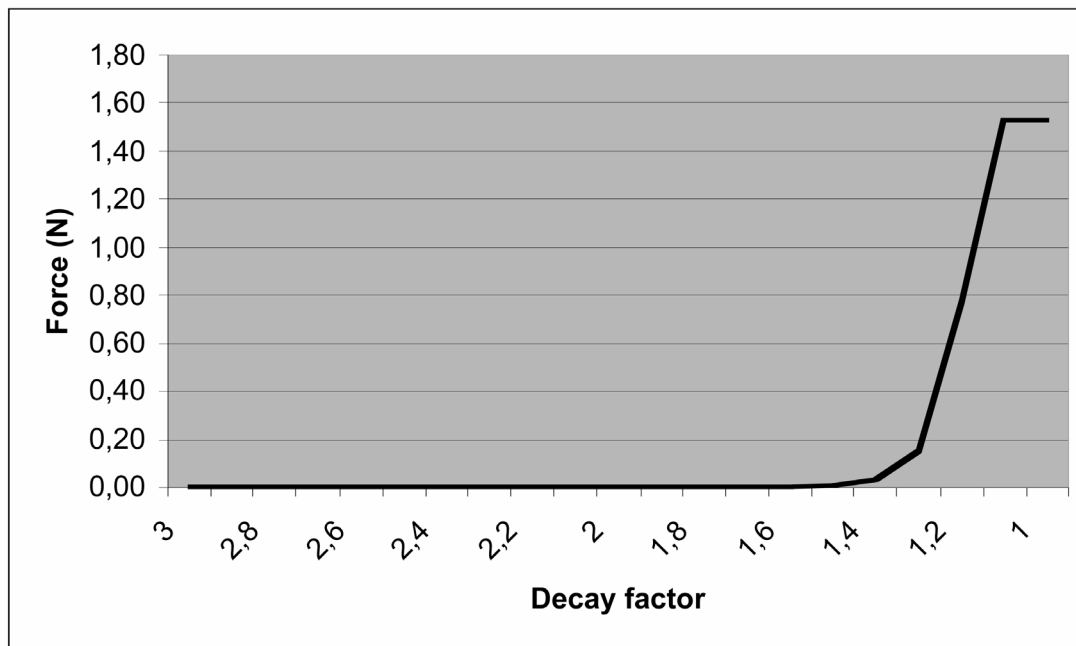
**Figure 2. Total force versus magnetic decay factor**

Several values of the decay factor α (between 3 and 1) were used and the results are shown in Figure 2. We conclude from here that a significant value for the force can only be attained for α , 1.2, which means that the plasma expansion mechanism and the subsequent action of the solar wind on the expanded bubble have to be effective. For even smaller values, it is possible to observe a saturation on the force created. This is due to the limited volume of simulation used in our code, and has no physical relevance.

Kinetic Modeling

Previous studies employed MHD models to validate the assumptions of the magnetic field configuration after the mini-magnetosphere formation. However, as also mentioned in the original paper [1], kinetic effects can play an important role in the dynamics of the plasma-magnetic sail unfolding, in particular, associated with instabilities and wave excitation, that might damp some of the kinetic energy release in the plasma, and can give rise to a foamy sail.

Due to the non-trivial magnetic field configuration arising in a mini-magnetosphere,

kinetic simulations are required to understand the plasma sail expansion into a dipole magnetic field configuration. The interaction of the solar wind with this plasma sail also plays a crucial role in the whole mechanism, and needs to be taken into account. It is clear that an electrostatic particle-in-cell simulation cannot model such a system. Only a full electromagnetic PIC code can deal with the currents generated in the plasma that lead to conversion of the plasma kinetic energy into magnetic fields. We have used a modified version of the object-oriented parallel particle-in-cell code OSIRIS [3], in order to include cathodes and externally applied fields. The full problem can be split in two different aspects: (i) plasma expansion into a dipole magnetic field configuration, (ii) interaction of the solar wind with a plasma immersed in a modified magnetic dipole field.
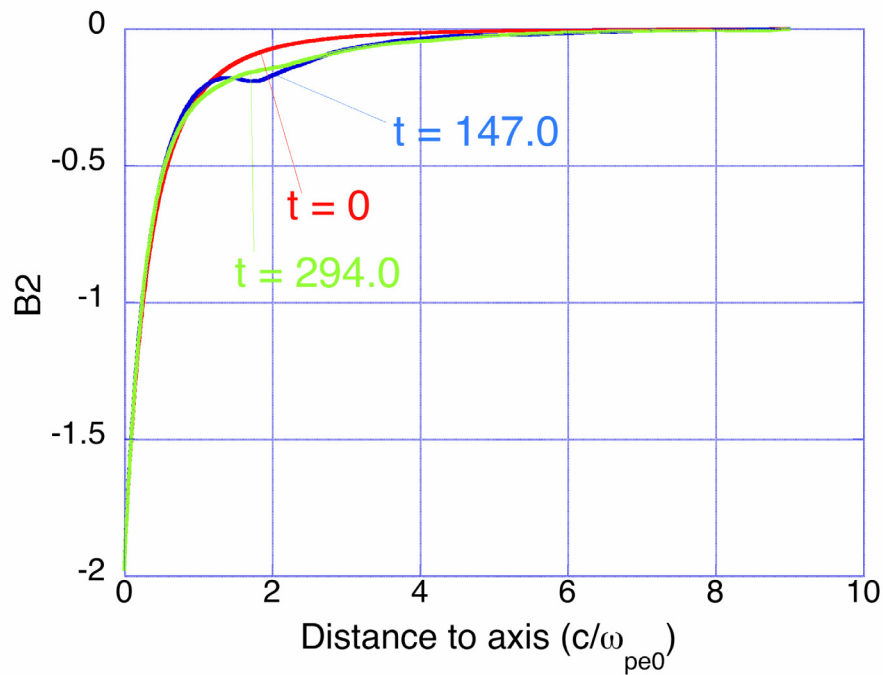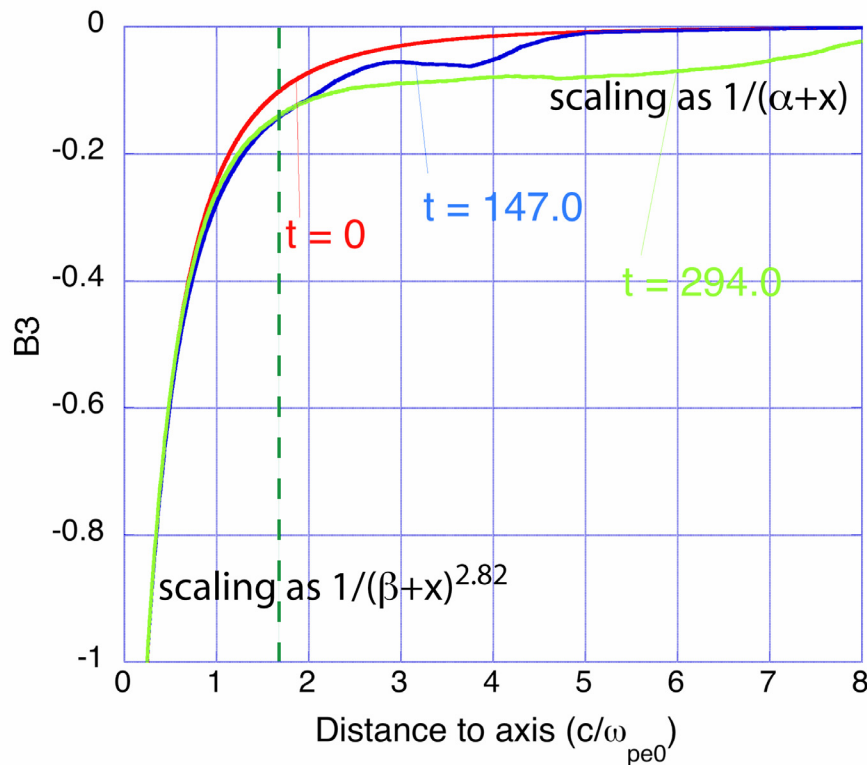

Figure 3. Radial decay of the magnetic field for initial, mid and final times of plasma expansion in the polar plane of the magnetic dipole

Here we show results of 2D PIC code simulations, performed in two complementary versions of the first problem configurations. The simulations were done with a modified version of the code OSIRIS [3]. We have used a mass ratio of $m_p/m_e = 400$, an injection velocity of 3×10^{-2} c, thermal velocity of 3×10^{-3} c, and we have continuous injection of plasma with density n_0 and a Gaussian profile of width 5.0 c/ω_{pe0}. The β parameter (defined as usual by the ratio of the plasma pressure over the magnetic pressure) was taken as 10 % at maximum of the B-field. We have assumed a dipole strength equal to 2.0 m_e c^4/e ω_{pe0}^2. We have used normalized units, with space normalized to c/ω_{pe0}, time to $1/\omega_{pe0}$, charge to the electron charge e, mass to the electron mass m_e, and magnetic field to me c ω_{pe0}/e. The duration of the runs corresponds to $300/\omega_{pe0}$ with time steps $\Delta t = 4.9 \times 10^{-3}/\omega_{pe0}$, and the number of macro-particles was 20×10^6. The data generated in each run is larger than 125 GB.

The first configuration corresponds to a plasma expansion in the polar plane, or the plane Oxy which contains the two poles of the magnetic field. The magnetic field lines are here parallel to the computational plane. The other configuration corresponds to the equatorial

plane Oxz, perpendicular to the magnetic field lines. The results of the total magnetic field spatial decay, for these two configurations are shown on Figures 3 and 4. for the initial, intermediate and final times of the runs. We can clearly observe the drag of the magnetic field lines due to the plasma expansion, especially in the equatorial plane where a decay of 1/r is observed.

Figure 4. Radial decay of the magnetic field for initial, mid and final times of plasma expansion in the equatorial plane of the magnetic dipole

Conclusions

Several physical problems relevant to the M2P2 propulsion scheme were discussed here. In particular, upper and lower limits of the force acting on the magnetic bubble were established. The upper limit is based on specular reflection at the artificial magnetopause, considered as a kind of opaque and totally reflecting barrier. The lower limit was based on the dynamic reflection of solar wind particles by the modified magnetic dipole field. We have also briefly mentioned how the perturbed currents, originating near the artificial magnetopause, can propagate down to the vicinity of the spacecraft, with the Alfven speed and with negligible losses. The resulting magnetic force on the spacecraft is due to large local currents. In order to determine the local current distribution and to establish a convincing value for the magnetic force acting on the spacecraft, we have used PIC code simulations. The first results of these calculations show that the plasma ejected from the spacecraft can indeed drag the magnetic field lines. Expansion of the magnetic field radial decay, from the initial $1/r^3$ down to 1/r was observed, thus confirming previous results based on MHD simulations. PIC code simulations of the solar wing interaction with the magnetized plasma bubble will be presented somewhere. A coherent qualitative picture of the process was established. A more quantitative view (of the current distributions) will imply the use of PIC

and hybrid code simulations. Another important aspect of M2P2 is related with the plasma formation, which as also been analyzed by us and will be presented in a future publication.

Acknowledgements

References

1. R.M. Winglee, J. Slough, T. Ziemba and A. Goodson, J. Geophys. Res, , 067-21.077 (2000).

2. M. Scholer, Planet. Space Sci., , 977 (1970).

3. R. Fonseca et al., Lecture Notes in Computer Science, 2329, III-342, Springer-Verlag, Heidelberg (2002).

ASSESSMENT OF HIGH-VOLTAGE PHOTOVOLTAIC TECHNOLOGIES FOR THE DESIGN OF A DIRECT DRIVE HALL EFFECT THRUSTER SOLAR ARRAY[*]

I.G. Mikellides
G.A. Jongeward
Science Applications International Corporation
10260 Campus Point Drive, San Diego, CA 92121

T. Schneider
M.R. Carruth
NASA Marshall Space Flight Center

T. Peterson
T.W. Kerslake
D. Snyder
D. Ferguson
NASA Glenn Research Center at Lewis Field

A. Hoskins
Aerojet Corporation

Abstract

A three-year program to develop a Direct Drive Hall-Effect Thruster system (D2HET) begun in 2001 as part of the NASA Advanced Cross-Enterprise Technology Development initiative. The system, which is expected to reduce significantly the power processing, complexity, weight, and cost over conventional low-voltage systems, will employ solar arrays that operate at voltages higher than (or equal to) 300 V. The lessons learned from the development of the technology also promise to become a stepping-stone for the production of the next generation of power systems employing high voltage solar arrays. This paper summarizes the results from experiments conducted mainly at the NASA Marshal Space Flight Center with two main solar array technologies. The experiments focused on electron collection and arcing studies, when the solar cells operated at high voltages. The tests utilized small coupons representative of each solar array technology. A hollow cathode was used to emulate parts of the induced environment on the solar arrays, mostly the low-energy charge-exchange plasma (10^{12}-10^{13} m^{-3} and 0.5-1 eV). Results and conclusions from modeling of electron collection are also summarized. The observations from the total effort are used to propose a preliminary, new solar array design for 2 kW and 30-40 kW class, deep space missions that may employ a single or a cluster of Hall-Effect thrusters.

Introduction

Electric propulsion, with its highly efficient use of propellant, has long been recognized as the technology of choice for a number of space missions. These include long duration deep space

---

[*] Major portions of this paper have been presented at the AIAA 39th Joint Propulsion Conference (Paper no. 2003-4725)

missions as well as station keeping for geostationary satellites. Since its conception over three decades ago the Hall thruster's unique combination of high specific impulse and thrust-to-power ratio established it as a favored propulsion system for a variety of such missions. Employment of these thrusters continues to be evaluated, worldwide, for orbit insertion to LEO,[1] GEO station-keeping,[2] and in more ambitious missions for the human exploration and development of space.[3] A promising systems approach that may significantly reduce cost and weight associated with the employment of these thrusters onboard both deep space and near-Earth spacecraft is the use of direct drive. A joined NASA/Naval Research Laboratory effort conducted in the late 90s demonstrated that direct drive operation with a Hall thruster is indeed a viable option.[4]

In a conventional electric propulsion system, power is supplied by low voltage solar arrays (usually <150 V). The high voltages needed to operate the electric thruster are provided by the (propulsion) power processing unit (PPU). If the array could provide the required voltage directly, the power processing electronics and heat rejection system would be smaller and lighter. The reductions would translate directly into cost savings and/or allow for additional payload. The effort presented here is part of a NASA program that aims to demonstrate this promise for HET applications.

A main focus in the D2HET program has been the assessment of the interactions between high-voltage solar array technologies and the HET-induced environment. Such tests are expected to benefit not only direct drive systems but other high-voltage space applications as well, such as MW-level electric propulsion power systems[5] and the Space Solar Power (SSP) satellite technology.[6] For D2HET, the assessments have been carried out largely through experiments at the NASA Marshal Space Flight Center (MSFC). Wherever possible the experiments have also been supported by modeling and simulation. The plasma environment under which representative solar array coupons have been tested emulates typical conditions under which the flight D2HET solar arrays would be exposed during thruster operation. Such conditions were defined by modeling and simulation calculations that were carried out early in the program.[7] The calculations assumed a representative 2x2 matrix of thrusters and mission scenarios. Specifically the matrix consisted of the 4-kW class Busek-Primex Thruster (BPT4000) and the 1.4-kW Stationary Plasma Thruster (SPT-100), onboard the DS-1 and EXPRESS spacecraft. As an example of the calculations performed to define the induced environment around the solar arrays, Figure 1 shows the computed plume from the BPT-4000. A system study was also conducted by Aerojet to quantify the potential savings of a direct drive system over conventional technologies, and to identify trends that may offer additional benefits at power levels and/or mission scenarios other than the representative 2x2 matrix considered in the D2HET program.[8,9]

The high-voltage assessment tests have been driven by two main plasma interactions concerns: leakage (or "parasitic") currents and arcing. The first will reduce solar array performance, which can in turn affect the overall S/C design if the collected electron current is a significant fraction (more than a few percent) of the current generated by the array. At the higher operating voltages enhanced parasitic currents can easily occur when dielectric surfaces "snap over". Commonly termed "snapover," the phenomenon is the "shift" in the mechanism by which a dielectric achieves current balance, from repelling most of the incoming electrons to emitting secondary electrons. These secondary electrons are emitted as a result of primary electron bombardment of the dielectric surface and get collected by the nearby conductor (which is

usually positively biased), leading to a sudden increase in both current collection and dielectric potential.

Arcing is most prominent when the conducting surfaces, such as exposed interconnects or semiconductor edges, are at a negative potential with respect to nearby insulating surfaces (e.g. when the HET is not operating). If sustained for long periods of time, arcs can lead to permanent electrical shorts. Most of the efforts to investigate the causes of these and other array failures[10,11] have concentrated at voltages greater than -300 V (i.e. lower in magnitude than |-300 V|).
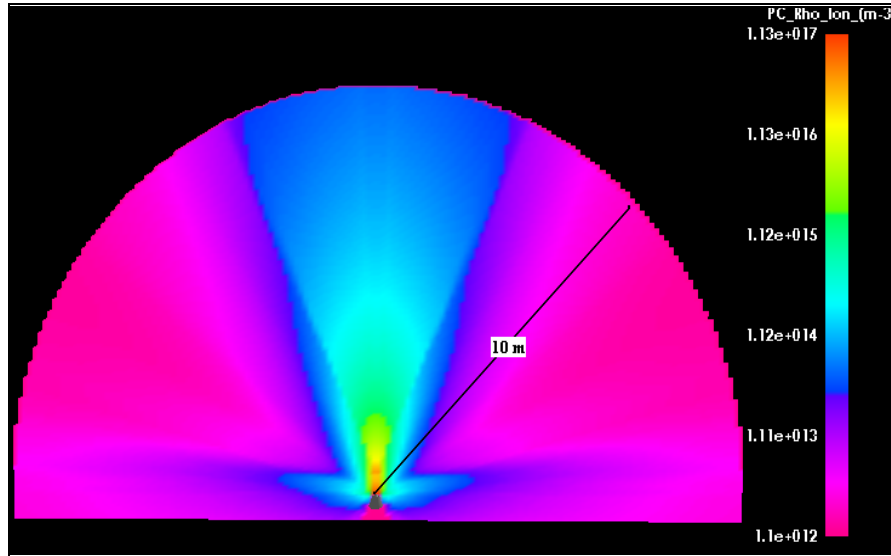
Figure 1. Simulated plume of the BPT-4000 operating at 3 kW showing ion particle density(m^{-3}) within a 10-m radius of the thruster exit.

Solar Array Photovoltaic Technologies

A variety of solar array technologies have been considered some of which employ interconnect shielding from the plasma, array string layout patterns, spacing and grouting, isolation diodes, substrate structural makeup and multi-layer insulation (MLI). We describe below the two main technologies that have been tested at NASA MSFC.

International Space Station (ISS) sample coupon

Several of the technology characteristics mentioned above apply to the ISS solar array. Despite its lower efficiency compared to newer, multi-junction designs such as that by TECSTAR, the ISS design was chosen as a D2HET candidate due to its relative maturity and demonstrated operation in space. Moreover, both on orbit observations and modeling of ISS cells operating at voltages less than 150 V, suggested that the gap geometry shields the exposed semiconductor edges from the plasma and may therefore offer a natural isolation from the environment. No such shielding however has been confirmed at the higher voltages (>300 V) of interest here, where snapover of insulating surfaces is expected to in fact suppress any electric potential barriers and enhance electron current collection.

Two ISS coupons were tested at NASA MSFC one of which is shown in Figure 2. The 15-cell coupon was part of an 80-cell panel (16 x 5 cells) fabricated in 1994 by Lockheed-Martin (Sunnyvale, CA) for the International Space Station Phase 01 Mir Cooperative Solar Array Program. The solar cells were fabricated by SpectroLab, Inc. (Sylmar, CA). The second coupon, cut out of the same 80-cell panel, was identical in geometry to the first coupon. The panel design, materials and fabrication techniques are also identical to those used in the International Space Station Photovoltaic Power Module with two exceptions: (1) the solar cell submodule is 2 x 5 cells (instead of 2 x 4) and (2) the introduction of a pair of small diameter "button holes" in the substrate between solar cells. The latter feature was used to attach the solar cell panels to Russian-built solar array frames. The coupon positive polarity tab (shown to come off cell 56 in Figure 2,a) is connected to the cell p contacts while the negative polarity tab (off of cell 70 in Figure 2,a) is connected to the cell n contacts. A by-pass diode is connected between cells 70 and 61. Figure 2,b shows a top view photograph of the coupon.
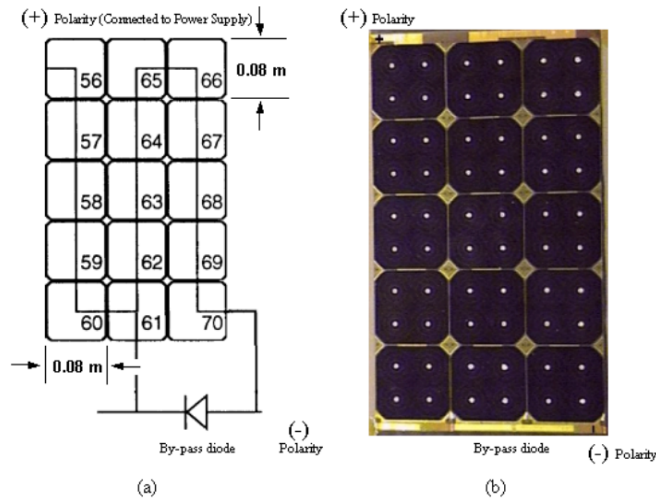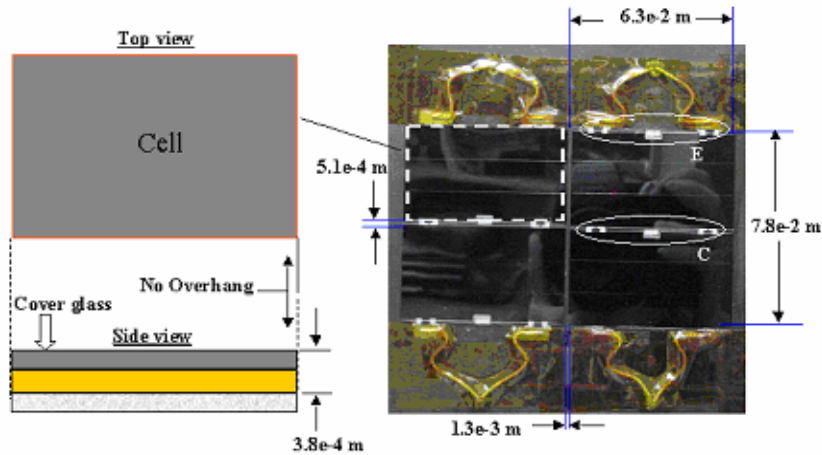

Figure 2. The ISS sample coupon used for the high-voltage D2HET tests.

TECSTAR sample coupon

The TECSTAR coupon is shown in Figure 3. It is comprised of two Solar Power Modules (SPM), each containing two solar cells as shown on the right of Figure 3. The TECSTAR cell is made of Gallium Indium Phosphide/Gallium Arsenide (GaInP/GaAs) on a Germanium (Ge) substrate (active junction). This technology was chosen primarily due to its higher efficiency (GaInP/GaAs/Ge cells have reportedly demonstrated >30% efficiency under concentrated light[12]). In contrast to the ISS coupon the TECSTAR coupon utilizes conventional interconnects that may lead to greater electron collection. The exposed interconnects also increase the possibility of arcing. However, a SPM covers multiple cells with a coverglass. The coverglass isolates interior interconnects from the plasma almost completely but leaves some of the ones that lie around edges partially exposed. To emulate this arrangement in the laboratory Kapton tape was placed on top of part of the edge interconnects (circled as "E" in Figure 3) leaving approximately half of their area exposed. Also in contrast to the ISS coupon, the coverglass does not extend over the solar cell in the direction of the adjacent SPM thus leaving no "overhang".

The coverglass material is made of silica micro sheet and is bonded to the cell with silicon adhesive. The substrate materials consist of Kapton tape laid on top of graphite layer.


Figure 3. The TECSTAR sample coupon used for the high-voltage D2HET tests.

Facilities

Two vacuum chambers at MSFC were utilized for the tests. Chamber 4605 depicting the ISS solar array sample coupon is shown in Figure 4, left. Chamber 4711 with the TECSTAR coupon is shown in Figure 4, right. The first chamber is approximately 1 meter in diameter and 2 meters long. Two liquid nitrogen trapped diffusion pumps provide the vacuum. A hollow cathode with an annular keeper electrode has been used to simulate the HET plasma conditions in the vacuum chamber. The source was constructed was operated with Argon. The second chamber is of similar dimensions and capabilities, and was used later in the D2HET program for both electron collection and arcing tests.

Plasma particle densities in the range of high 10^{11} to low 10^{13} m^{-3}, and electron temperatures on the order of 0.5-1 eV (eV=11604 ^{o}K) were produced in the vacuum chambers. With the plasma source off the chamber pressure was about 5×10^{-7} Torr. During the operation of the source the background pressure was in the high 10^{-5} to low 10^{-4} Torr. Various diagnostics were used to determine the plasma conditions around the array segments, which are described in greater detail in Jongeward, G. *et al*.[7]
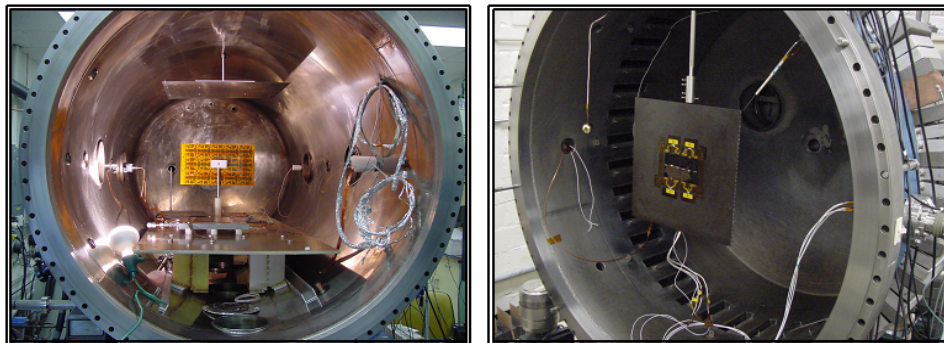
Figure 4. The ISS and TECSTAR coupon setups in the NASA MSFC vacuum chambers.

Summary of Results From Experiments and Modeling

Electron collection experiments

Electron collection measurements were performed in both vacuum chambers. Only one coupon was tested each time in the chamber. All solar cells on each coupon were positively biased (at the same voltage) with respect to ground. Current collection measurements were obtained for the applied voltage range 200-500 V.

The data reveal two main trends for the ISS coupons: (a) relaxation time is in the order of tens to hundreds of seconds. Figure 5 shows representative signals collected during the period 9/5-11, 2002 using the original coupon, dubbed "ISS-A." (b) The variability (standard deviation divided by the mean value) of collected current after exposure to the plasma for 300 seconds generally increases with bias voltage, ranging 13-27% for ISS-A and 26-71% for the second ISS coupon tested, the "ISS-B." ISS-B also collected higher currents the longer the coupon was tested (Figure 6, left). Similarly to the ISS coupons, the TECSTAR sample also exhibited large variability at each bias voltage, as shown in Figure 6, right. However, in contrast to ISS the variability generally decreased with increasing bias voltage, from 43% (at 300 V) to 18% (at 500 V). Table 1 lists average values of electron current collection after 300 seconds, scaled to nominal plasma density of 10^{13} m^{-3} and electron temperature of 0.55 eV. The scaled values were used to determine the variability of the measurements at each bias voltage.

Table 1. Average electron current collected by ISS and TECSTAR coupons (after 300 sec) at j_{th}=200 mA/m^2. Coupon collecting areas: $A_{ISS}\approx$9.75e-4m^2 (ISS), $A_{TEC} \approx$ 2.07e-4 m^2 (TECSTAR).

Applied Voltage (V)	ISS-A Avg. I (mA)	ISS-B Avg. I (mA)	TECSTAR Avg. I (mA)	TECSTAR (xA_{ISS}/A_{TEC}) Avg. I (mA)
200	2.038	0.407	0.055	0.233
300	5.538	1.201	0.180	0.776
400	10.31	2.687	0.405	1.745
500	16.88	5.974	0.661	2.875

Dynamical effects due to dielectric charging during electron collection were determined to be negligible under the conditions of the experiments.[13] In the absence of charging effects other mechanisms that may possibly lead to the prolonged times observed during current collection must be considered. For example, it is possible that the high electron fluxes and energies bombarding the dielectrics at these high voltages may alter the materials' secondary electron yield (SEY) properties. There have been numerous studies on the adverse effects of "electron-clouds" on high-energy particle accelerator facilities that involved measurements of the change in secondary electron yield (SEY) properties with charged-particle dose (in units of charge per unit area) for various metals.[14,15] These efforts were primarily motivated by the need to reduce the electron cloud generated by secondary electron emission of metal surfaces. One proposed way to reduce this effect has in fact been to condition the emitting surface, by exposing it to electron doses that are sufficiently high to permanently reduce its secondary electron yield

characteristics. The results from one such study on copper is reported by Baglin, I., *et al.*[15] Recent modeling work has also suggested that changing SEY material properties may indeed be a driving mechanism for the observed current collection trends.[13] However, both the lack of SEY measurements for the dielectric material on the ISS coupons, and the significant variability in current collection observed during the tests, do not allow for a conclusive assessment based on the comparisons made between theory and experiment.
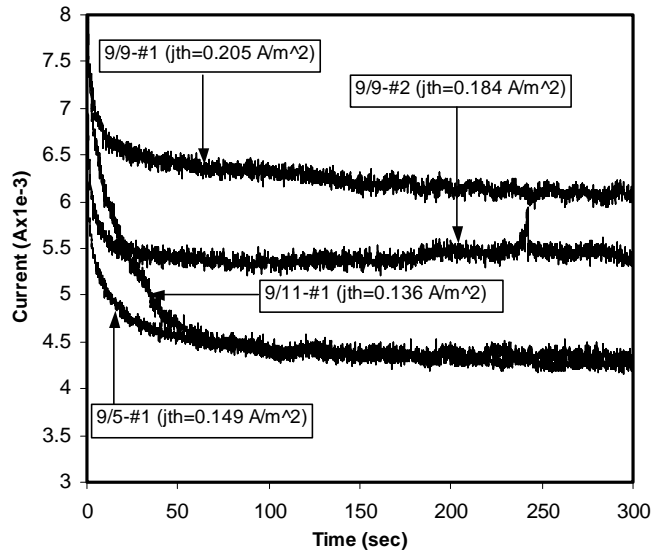
Figure 5. Representative transient data for the ISS-A coupon biased to 300 Volts.
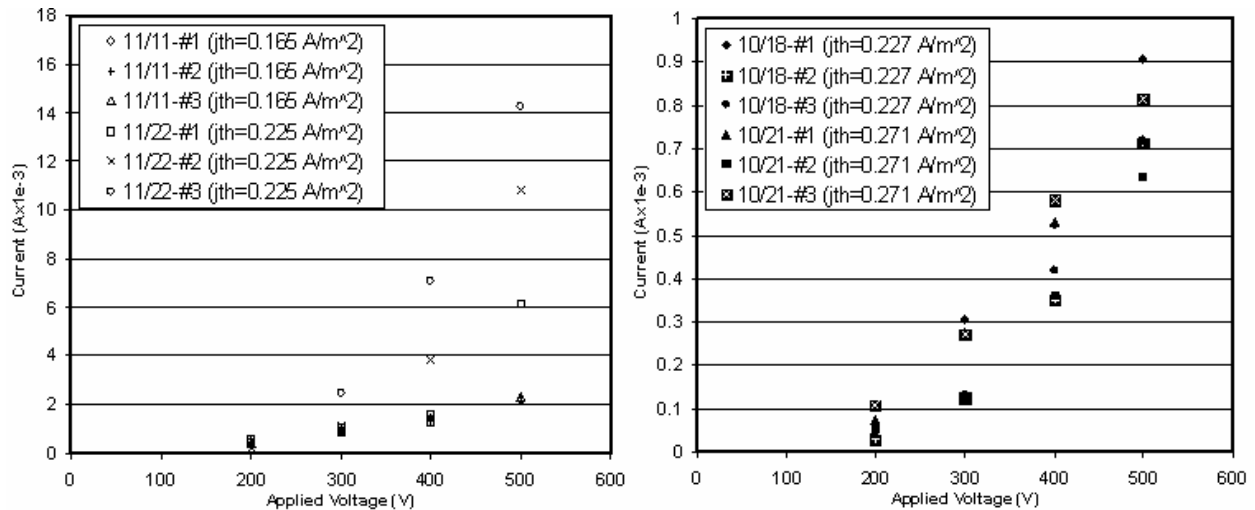

Figure 6. Left: Electron current collected by the ISS-B coupon, after 300 sec, on various days during the 11/2002 tests. Right: Electron current collected by the TECSTAR coupon, after 300 sec, on various days during the 10/2002 tests.

Experiments to determine arcing thresholds

We present here a summary of results from tests during which the coupons were biased negatively with respect to the plasma. The electrical circuits, setups and assessments of arc discharge initiation and coupon damage that occurred during these tests are described in greater detail by Schneider, T. *et al.*[16] The ultimate goal of the experiments was to define operating limits for the D2HET array below which the possibility of damage from sustained arcs would be minimized if not completely eliminated. These limits or "thresholds" would in turn guide the design of the solar array, specifically in regards to the maximum potential difference that would be allowed between adjacent solar cells.

The results from the sustained arc tests are shown in Figure 7. Figure 7, left provides threshold values in terms of power in the arc, sustained current and voltage drop across those ISS cells that supported the arc. The TECSTAR results are shown in Figure 7, right. The red-circled points in Figure 7, right are first-time occurrences, i.e. the recorded values were obtained only the first time the case was performed. Subsequent runs of the same cases yielded different values that, in most cases, were more consistent with each other.
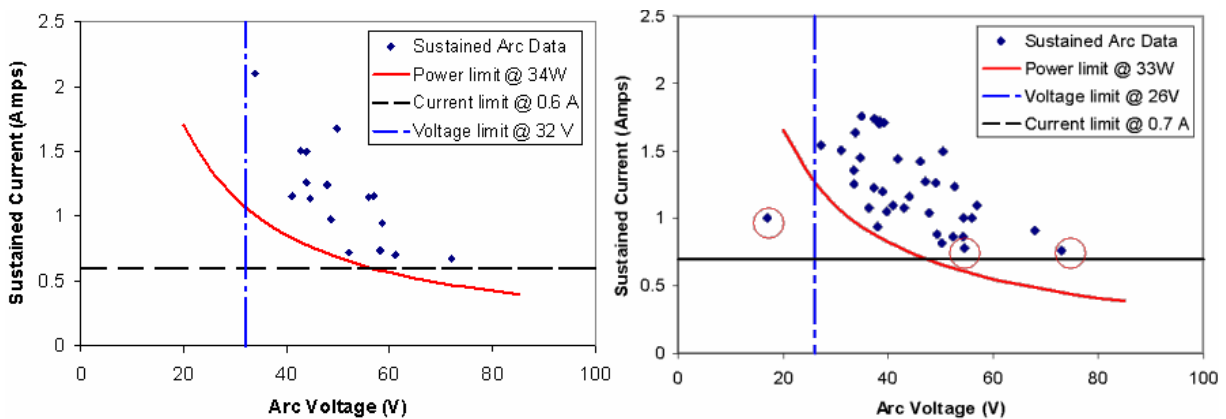
Figure 7. Left: Sustained arc thresholds for ISS design. Right: Sustained arc thresholds for TECSTAR (planar) design.

D2HET Solar Array Design

The test results above suggest both high electron collection and low arcing thresholds. The first would lead to degradation of the array performance if not taken into account in the design. If adjacent cells are not designed to operate below the sustained-arcing threshold then arcs may lead to permanent damage of the array.

A design approach is followed here that reduces inefficiencies by electron collection, allows a maximum differential voltage at about the observed arc voltage threshold between cells while providing additional security against sustained arcing. Specifically, the design employs coverglass sheets that cover more than one cell thus reducing the number of cell sides that can collect electrons. The design also arranges strings (of in-series cells) such that the maximum voltage difference between two cells is approximately equal to the measured arc voltage threshold. Additional security against arcs is implemented by organizing coverglass sheets in an

alternating manner such that the plasma expelled during trigger arcs, which can lead to sustained arcs, is partially blocked from reaching those adjacent cells that are at the highest potential difference. We also arrange strings in a manner that reduces induced torques with the ambient magnetic field.

Based on the electron collection tests, the TECSTAR technology is used as the basis for the D2HET array. As shown in Table 1, at 300 V the TECSTAR coupon collected about 1.5 times less current than ISS-B. Both the lower performance of the ISS cells and the large differences in collected current observed between "identical" coupons make it a less favorable technology compared to TECSTAR.

Solar cell performance

For the design the solar cell performance parameters listed in equation (1) are assumed,[17] where V_{mp}, i_{mp} and P_{mp} are the cell voltage, current and power at the optimum power output point.

$$V_{mp} = 2.29\,V$$
$$i_{mp} = 0.445\,A\ (j_{mp} = 158.4\,A/m^2\ for\ 37mm\,x\,76mm\,cell) \tag{1}$$
$$P_{mp} = 1.02\,W$$

The cell type and size are very similar to the original TECSTAR coupon (Figure 3). From Table 1 and the TECSTAR coupon geometry the following empirical relationship are deduced for the non-dimensional electron current density collected, $\bar{j}_{ec}$:

$$\chi \equiv \frac{eV}{kT_e},\ \ \bar{j}_{ec} \equiv \frac{j_{ec}}{j_{e,th}} = c_1\chi^{c_2}$$
$$c_1 = 6.495x10^{-7},\ \ c_2 = 2.5 \tag{2}$$

where $j_{e,th}$ is the electron thermal current density, e is the electron charge, V is the cell voltage, k is the Boltmann factor and T_e is the electron temperature. The fitting constants are c_1 and c_2. The following nominal conditions were used to deduce equation (2) above (which is also plotted in Figure 8 below): $j_{e,th} = 200$ mA/m^2, V = 200-500 volts, $T_e = 0.55$ electronvolts.

With A_c being the collecting area, the current collected per cell i_{ec} may then be expressed as,

$$i_{ec} = \bar{j}_{ec}\,j_{e,th}\,A_c = c_1\chi^{c_2}\,j_{e,th}\,A_c \tag{3}$$
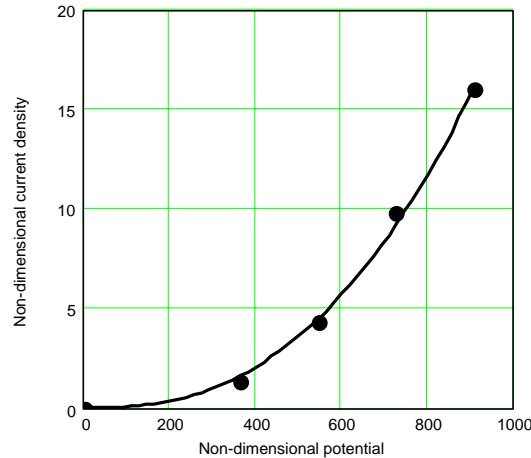
Figure 8. Empirically-reduced dependence of non-dimensional electron collection $\bar{\mathrm{j}}_{ec}$ on the non-dimensional collection potential χ, based on averaged data from the TECSTAR coupon tests.

The design approach presented here provides additional security against arcing that can be sustained between cells. It also improves the electron collection current ratio η_{ec}, defined by equation (4) below, where, I_{ec} is the total electron current collected and I_o is the total operating current.

$$\eta_{ec} \equiv \frac{I_{ec}}{I_o} \tag{4}$$

A modified arrangement of the TECSTAR sample coupon in regards to the coverglass is proposed. Specifically, the coverglass sheet is placed to cover more than one cell thus shielding some of the exposed cell sides from collecting electrons. The solar cell size is similar to the original TECSTAR cell tested at NASA MSFC (Figure 3): t = 6.1 mil, Lc= 37 mm, Wc= 76 mm, where, t is the cell thickness, Lc is the cell length (taken here as the short side of the cell) and Wc is the cell width (taken here as the long side of the cell).

Solar array for low-power deep space mission

A design that is based on the Deep Space-1 (DS-1) spacecraft power requirement is presented in this section. In a subsequent section all pertinent parameters are re-computed to produce a design for a higher power spacecraft. The power requirements are comparable to those specified by NASA in a recent Design Reference Mission (DRM) that was part of an NASA Research Announcement (NRA) solicitation (http://www.spacetransportation.com/code_s/ AdvancedSEP.pdf). The DRM required solar arrays capable of providing a total of 30 kW, and solicited component and subsystem development of Solar Electric Propulsion (SEP) technologies that have the potential to provide benefits beyond those provided by Ion propulsion.

DS-1 operated the NASA Solar Electric Propulsion Technology Applications Readiness (NSTAR) ion engine,[18] which required a maximum power of about 2.1 kW. The solar arrays

produced a maximum of 2.5 kW.[19] A recent calculation to estimate the mass benefits from direct-drive drive compared specifically the DS-1 NSTAR conventional system and the same type of spacecraft and mission requirement using a D2SPT-100. The results from that comparison were favorable for the D2SPT-100 in that it reduced the total launch mass by 4%.[20] A similar DS-1 type of spacecraft, with a total power capability of 2.25 kW is therefore chosen here, as a representative low-power mission on which to base the design of the solar array. The spacecraft is assumed to employ a single SPT-100 (requiring about 1.5 kW of power) for primary propulsion, operating in direct drive mode.

The strings are designed to produce a voltage of V_o=316 V. Thus, the number of cells in series N_s must be,

$$N_s = \frac{V_o}{V_{mp}} = \frac{316}{2.29} = 138 \tag{5}$$

For a total power requirement of P_o=2.25 kW we must have,

$$N_t = \frac{P_o}{P_{mp}} = \frac{2252}{1.02} = 2208 \rightarrow N_p = \frac{N_t}{N_s} = \frac{2208}{138} = 16 \tag{6}$$

where, N_t is the total number of cells, N_p is the number of cells in parallel.

Cell arrangement and array size. The proposed solar array arrangement is shown in Figure **9**. The arrangement minimizes torques that may be induced by the interaction of solar array currents and the ambient magnetic field, and ensures no more than $V_{arc} = 27.5$ V differential between adjacent cells.

From $V_{mp} = 2.29$ V the number of cells in each row of a single string $N_{s,row}$ is computed as,

$$N_{s,row} = \frac{V_{arc}}{2V_{mp}} = 6 \tag{7}$$

Then the width of each 6-cell row in a string (and therefore the width of each string) w_{row} is approximately

$$w_{row} \approx N_{s,row} Lc = 0.22\,m \tag{8}$$

If the two strings are united into one submodule (as shown in Figure 9 top) then the
- submodule would produce $2i_{mp}$=0.89 A and $2N_s V_{mp} i_{mp} = 0.282$ kW
- number of submodules required would be $N_t/N_s/2 = 8$ submodules (4 on each side of the spacecraft bus)
- approximate width of the submodule would be $2w_{row} \approx 0.44$ m
- approximate array width on each side of the spacecraft bus would be $W_{SA} \approx 4w_{row} = 0.88$ m.

- approximate length of the array on each side of the spacecraft bus would be $L_{SA} \approx 2[N_s/N_{s,row}]Wc = 3.5$ m.

A summary of the proposed array design parameters is provided in Table 3.

Coverglass arrangement and η_{ec}. Using equation (3) the total collection current by the solar array may be estimated by summing up the collection by each cell as shown in equation (9),

$$I_{ec} \approx c_1 j_{e,th} A_c N_p \sum_{n=0}^{N_s-1} \chi_n^{c_2}$$

$$\chi_n = \frac{e\phi_n}{kT_e}, \quad \phi_n \equiv \frac{2n+1}{2}V_{mp}$$

$$(9)$$

where it is assumed that each cell is collecting at an effective potential of ϕ_n.
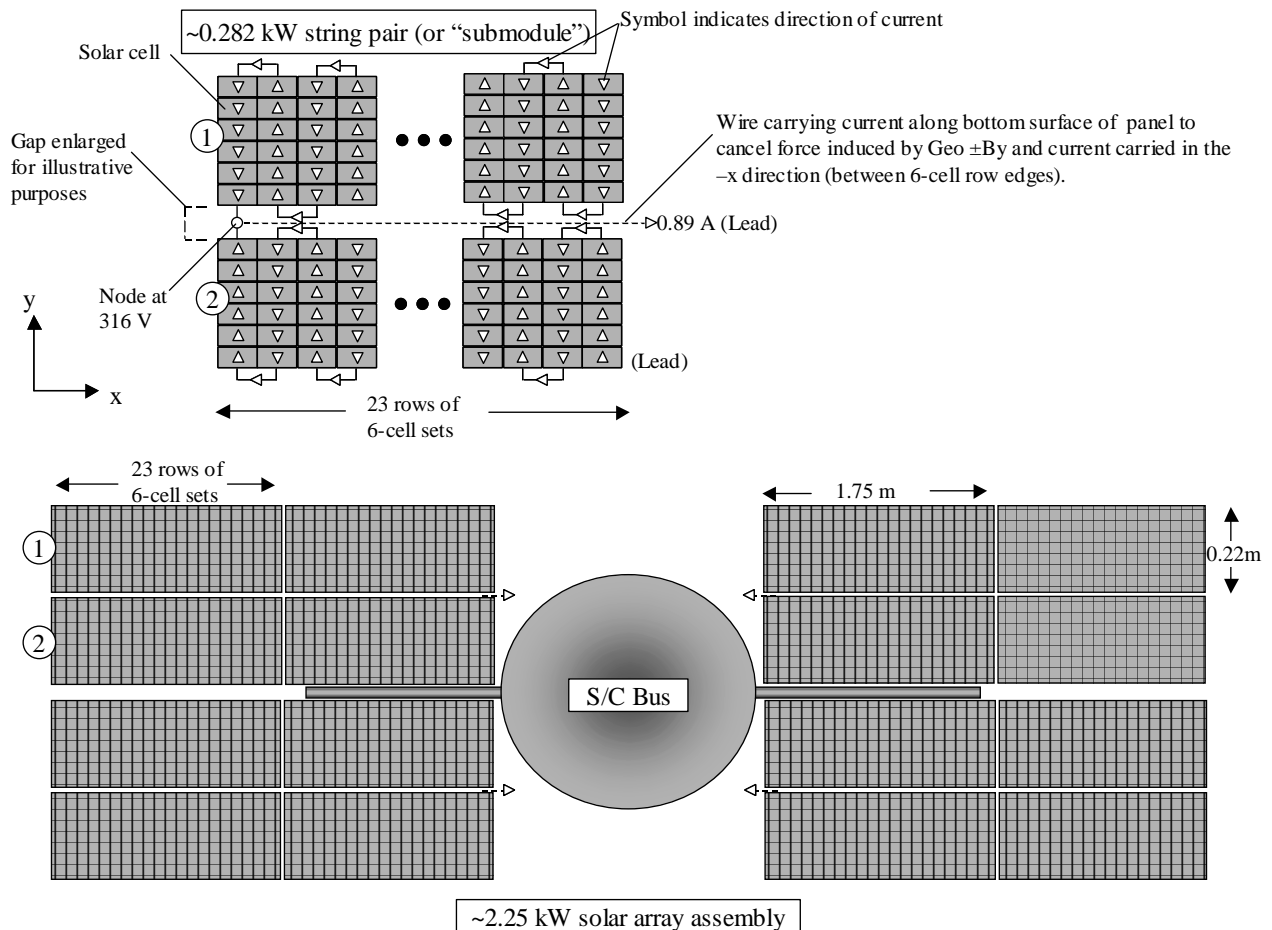
Figure 9. Arrangement of panels in a proposed design of a 2.25 kW D2HET solar array. The design is based on a DS-1 type of spacecraft and mission that would operate a single SPT-100 in direct drive mode.
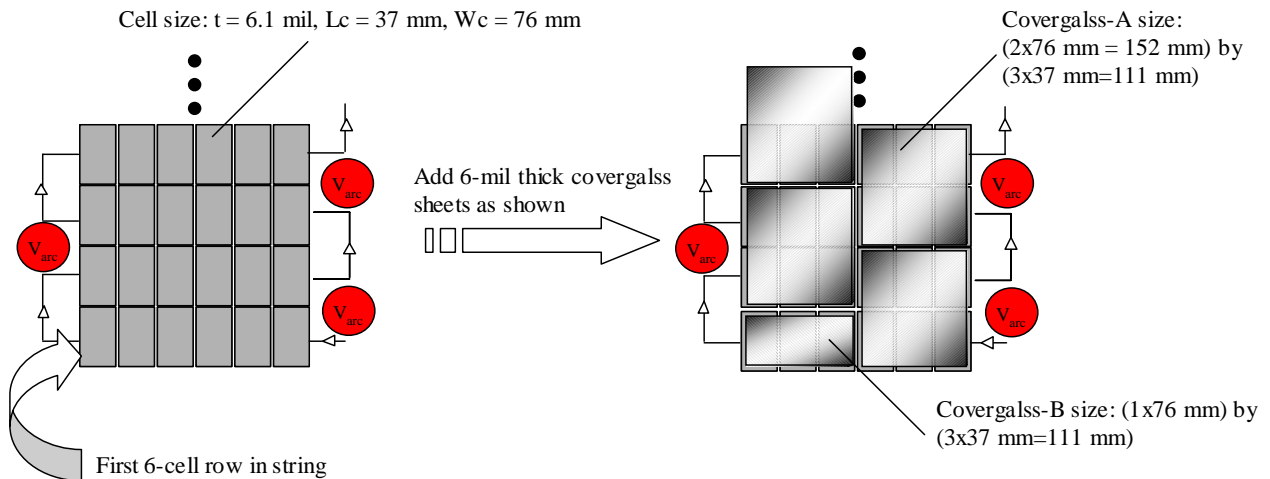
For the design shown in Figure 9, assuming that all four sides of each cell are exposed and therefore allowed to collect (i.e. $A_c = 2t(Lc+Wc)$), η_{ec} is approximated as follows:

$$\eta_{ec} \approx \frac{c_1 j_{e,th} A_c \sum_{n=0}^{N_s-1} \chi_n^{c_2}}{i_{mp}} = 3.17 \times 10^{-3} \tag{10}$$

It is noted that the result of equation (10) is for a thermal electron current of 200 mA/m^2 (based on a plasma density of $n=10^7$/cc and temperature of Te=0.55 eV). Table 2 illustrates the range of values η_{ec} may acquire if no measures are taken to cover part or all of the exposed cell areas that may collect electrons. To account for the higher plasma densities that may be present (e.g. see Figure 1), which is strongly dependent upon mission, spacecraft configuration, thruster position relative to arrays, etc., and to reduce even further the possibility of arcing across those cells that are at the maximum potential difference of 27.5 V, the alternating coverglass arrangement shown in Figure 10 is proposed. The design in Figure 10 would require 22 sheets of Coverglass-A size and 2 sheets of Coverglass-B size, per string. Another option would be to cover 2x2 cells (instead of 2x3).

Table 2. Approximate changes in η_{ec} with various plasma conditions attainable in the plume of an HET.

	$n_e = 10^{12}$ m^{-3}		$n_e = 10^{13}$ m^{-3}		$n_e = 10^{14}$ m^{-3}	
Te	$j_{e,th}$ (mA/m^2)	% η_{ec}	$j_{e,th}$ (mA/m^2)	% η_{ec}	$j_{e,th}$ (mA/m^2)	% η_{ec}
0.1	8.48	1	84.8	10	848	100
1	26.8	10^{-2}	268	10^{-1}	2680	1
10	84.8	10^{-4}	848	10^{-3}	8476	10^{-2}

Cell size: t = 6.1 mil, Lc = 37 mm, Wc = 76 mm

Covergalss-A size: (2x76 mm = 152 mm) by (3x37 mm=111 mm)

Add 6-mil thick covergalss sheets as shown

Covergalss-B size: (1x76 mm) by (3x37 mm=111 mm)

First 6-cell row in string

Figure 10. Proposed covergalss arrangement on a solar array string with V_{arc}=27.5 V.

Solar array for high-power deep space mission

The approach outlined above is applied to design a solar array for a total power requirement of 30 kW. The power level is chosen based on a recent NASA DRM (http://www.spacetransportation.com/code_s/AdvancedSEP.pdf). Such power levels may be used to operate Hall propulsion at tens of kilowatts. One example of a potential thruster candidate is the NASA GRC 50-kW class 457 M operated at lower than nominal powers (which has already been demonstrated at GRC),[21,22] or two BPT-4000 engines requiring a total of ~8 kW. We recognize that the plasma conditions generated by these higher-power propulsion systems may differ drastically from the nominal conditions emulated in the laboratory during the D2HET program (which were based an a specific 2x2 spacecraft-thruster matrix). Therefore, as suggested by Table 2, the proposed design may not sufficiently minimize electron collection and/or arcing. The advantages of the design would be heavily dependent upon spacecraft geometry, thruster location relative to the arrays, and of course the type of thruster.

The solar array design parameters are re-computed for two maximum operating voltages, 300 V and 500 V. The results are summarized in Table 3.

Table 3. Summary of direct drive solar array design parameters for different S/C requirements.

Sol. Array parameter	300-V solar array for low-power spacecraft	300-V solar array for high-power spacecraft	500-V solar array for high-power spacecraft
Cell size	Lc=37 mm, Wc= 76 mm $t = 6.1$ mil	Lc=37 mm, Wc= 76 mm $t = 6.1$ mil	Lc=37 mm, Wc= 76 mm $t = 6.1$ mil
P_o	2.25 kW	36.035 kW	33.195 kW
V_{max}	316.1 V	316.1 V	517.54 V
I_o	7.12 A	113.9 A	64.1 A
$\eta_{ec}\,(max^\S)$	0.317%	0.317%	1.78%
N_s	138	138	226
N_t	2208	35328	32544
N_p	16	256	144
$N_{s,row}$	6	6	6
w_{row}	0.22 m	0.22 m	0.22 m
$N_t/N_s/2$	8 submdls (4 on each side of S/C in 2x2 setup)	128 submdls (64 on each S/C side in a 8x8 setup)	72 submdls (36 on each S/C side in a 6x6 setup)
$2i_{mp}$	0.89 A	0.89 A	0.89 A
$2N_sV_{mp}i_{mp}$	0.2815 kW	0.2815 kW	0.461 kW
W_{SA}	0.88 m	3.55 m	2.66 m
L_{SA}	3.5 m	13.97 m	17.164 m

§Assumes all cells collect electrons and therefore the actual value will be reduced with the proposed coverglass arrangements. The precise reduction would depend on the specific coverglass arrangement.

Summary and Conclusions

Two solar array technologies have been tested for electron current collection at voltages in the range 0-500 V, as part of a program sponsored by NASA to develop a Direct Drive Hall Effect Thruster system. The first technology sample was a coupon containing (3x5), single-junction silicon cells that are almost identical to those used onboard ISS, and thus have no exposed interconnects. The second coupon was a Solar Power Module designed by TECSTAR (now part of EMCORE Corp.) that utilizes multi-junction cells with conventional interconnects. Both coupons exhibited transient variations in current collection with characteristic times greatly exceeding dielectric charging times. After many hours of exposure to the plasma the first of two 3x5 coupons, ISS-A, cut from the same 80-cell PPM at NASA GRC, collected 2-5 times more current than its counterpart did, ISS-B, when it was first tested at NASA MSFC. ISS-B exhibited increased current collection with increasing exposure to the plasma. TECSTAR also displayed transient collection. All coupons showed large variability from the mean value. For ISS the variability increased with bias voltage; for TECSTAR it decreased. Combined with results from electron collection modeling, and from experiments at negative applied voltages (ion collection) that determined arcing thresholds for the two technologies, the observations have allowed for a preliminary design of a low-power (~2 kW) and higher power D2HET solar arrays.

Acknowledgments

References

[1] Oleson, S.R., "Electric Propulsion for Low Earth Orbit Communications Satellites," IEPC paper 97-102, Aug. 1997.

[2] Oleson, S.R., Myers, R.M., "Advanced Propulsion for Geostationary Orbit Insertion and North-South Station Keeping," J. of Spacecraft and Rockets, Vol. 34, No. 1, pp. 22-28, Jan-Feb 1997.

[3] Oleson, S.R. and Sankovic, J.M., "Advanced Hall Electric Propulsion for Future In-Space Transportation," NASA TM-2001-210676, April 2001.

[4] Hamley, J.A., et al., "Hall Thruster Direct Drive Demonstration," AIAA-97-2787, July 1997.

[5] Kerslake, T.W., and Gefert, L.P., "Solar Power System Analyses for Electric Propulsion Missions," NASA/TM-1999-209289, July 1999.

[6] Dudenhoefer, J.E., and George, P.J., "Space Solar Satellite Technology Development at the Glenn Research Center – An Overview," NASA/TM-2000-210210, July 2000.

[7] Jongeward, G.A., et al., " Development of a Direct Drive Hall Effect Thruster System," Society of Automotive Eng. (SAE), Power Systems Conference, Paper 02PSC-77, Oct. 2002.

[8] Hoskins, A., et al., "Direct Drive Hall Thruster System Development," AIAA-03-4726, July 2003.

[9] Kerslake, T.W., "Effect of Voltage Level on Power System Design for Solar Electric Propulsion Missions," ISEC Paper 2003-44008, March 2003.

[10] Katz, I., Davis, V.A., and Snyder, D.B., "Mechanism For Spacecraft Charging Initiated Destruction of Solar Arrays in GEO," AIAA-98-1002, Jan. 1998.

[11] Jongeward, G. A., et al., "The Role Of Unneutralized Surface Ions In Negative Potential Arcing," IEEE Trans. Nucl. Sci., 32, p. 4087, 1985.

[12] http://www.nrel.gov/ncpv/higheff.html

[13] Mikellides, I.G., et al., "Assessment of High-Voltage Solar Array Concepts for a Direct Drive Hall Effect Thruster System," AIAA-03-4725, July 2003.

[14] Kirby, R.E., et al., "Secondary Electron Emission Yields From PEP-II Accelerator Materials," SLAC-PUB-8212, Oct. 2000.

[15] Baglin, I., et al., "The Secondary Electron Yield of Technical Materials and its Variation with Surface Treatments," Proceedings of EPAC, p. 217, Vienna, Austria, 2000.

[16] Schneider, T., et al., "Experimental Investigation of Plasma Interactions with Candidate Solar Array Technologies for a Direct Drive Hall Thruster System," AIAA-03-5017, July 2003.

[17] Conversations with solar array manufacturers from EMCORE Corporation.

[18] Polk, J.E., et al., "Validation of the NSTAR Ion Propulsion System on the Deep Space One Mission: Overview and Initial Results," AIAA-99-2274, June 1999.

[19] http://nmp.jpl.nasa.gov/ds1/quick_facts.html

[20] Jongeward, G.A., et al., " Development of a Direct Drive Hall Effect Thruster System," NRA Review Presentation for the Enabling Concepts and Technologies Program at NASA GRC, Jan. 2003, SAIC Quarterly Report no. 03/2019.

[21] Jankovsky, R.S., Jacobson, D.T., Pinero, L.R., Sarmiento, C.J., "NASA's Hall Thruster Program 2002," AIAA-02-3675, July 2002.

[22] Manzella, D., Jankovsky, R., and Hofer, R., "Laboratory Model 50 kW Hall Thruster," AIAA-02-3676, July 2002.

PLASMA INTERACTIONS WITH A NEGATIVE BIASED
ELECTRODYNAMIC TETHER

Jason A. Vaughn
George C. Marshall Space Flight Center
Environmental Effects Group
Mail Code: ED31
MSFC, AL 35812
Phone: (256) 544-9347
Fax: (256) 544-5103
Email: jason.a.vaughn@nasa.gov

Leslie Curtis
Ken J. Welzyn
Space Transportation Directorate, MSFC

Abstract

The ProSEDS conductive tether design incorporates two distinct types of tethers from a plasma interaction viewpoint. The 200 m closest to the Delta II spacecraft is insulated from the plasma, and the remaining 4800 m is semi-bare. This latter portion is considered semi-bare because a conductive coating, which is designed to collect electrons from the plasma, was applied to the wires to regulate the overall tether temperature. Because the tether has both insulating and conductive tether sections, a transition point exists between the two that forms a triple point with the space plasma. Also, insulated tethers can arc to the space plasma if the insulation is weakened or breached by pinholes caused by either improper handling or small meteoroid and orbital debris strikes. Because electrodynamic tethers are typically long, they have a high probability of these impacts. The particles, which strike the tether, may not have sufficient size to severe the tether, but they can easily penetrate the tether insulation producing a plasma discharge to the ambient plasma.

Samples of both the ProSEDS tether transition region and the insulated tether section with various size of pinholes were placed into the MSFC plasma chamber and biased to typical ProSEDS open circuit tether potentials (-500 V to −1600 V). The results of the testing showed that the transition region of the tether (i.e. the triple point) arced to the ambient plasma at −900 V, and the tethers damaged by a pinhole or simulated debris strike arced to the plasma between −700 V and −900 V. Specific design steps were taken to eliminate the triple point issue in the ProSEDS tether design and make it ready for flight. To reduce the pinhole arcing risk, ProSEDS mission operations were changed to eliminate the high negative potential on the insulated tether. The results of the testing campaign and the design changes implemented to ensure a successful flight are described.

Introduction

ProSEDS is an electrodynamic (ED) tether mission designed to fly as a secondary payload on a DELTA II Global Positioning System (GPS) satellite, and demonstrate electrodynamic thrust

as a potential propellant less propulsion application. After the primary GPS payload is placed in its orbit, the Delta II second stage fires to place ProSEDS in a near circular orbit with an altitude of about 275 km. The Delta II will then begin the ProSEDS mission by turning on the ProSEDS computer, which will control the payload for the remainder of the mission. The signal to release the endmass and deploy the tether comes from the Delta II once the stage has established the correct orientation. After the tether has been deployed ProSEDS will begin what is expected to be approximately a 1-day mission.

ProSEDS consists of two separate hardware platforms, the Instrument Panel (IP) hardware and the Deployer side hardware. Both of these platforms are diametrically opposing each other around the Delta II bellyband. The IP hardware consists of a 10 A rated hollow cathode plasma contactor, primary battery, secondary battery, Power Distribution Box (PDB), a Langmuir Probe Spacecraft Potential (LPSP) electronics box, Differential Ion Flux Probe with Mass (DIFP/M) electronics box, and transmitter. The LPSP and DIFP/M probes are mounted on the Delta II struts[1]. The Deployer side hardware consists of an on-board computer called the Data System Electronic Box (DSEB), tether and deployer hardware, both a GPS receiver and antenna, and a student built endmass. The deployer hardware includes the tether canister, which housed the tether, brake mechanism, and the High Voltage Control and Monitor (HVCM) box to switch the tether in and out of the electrical circuit. The deployer side hardware closely resembles the design of the old Small Expendable Deployer System (SEDS)[2].

ProSEDS on orbit operation is to begin with the tether deployment and slowly bring the instruments on-line after tether deployment. Once the entire payload is operating, the primary mission would begin and last about five orbits due to primary battery life. These first five orbits ensure ProSEDS of at least five orbits of data, which is sufficient to meet all primary objectives established for the experiment. After the five orbits, the extended phase begins. The extended mission phase operates off the secondary battery, and during this time ProSEDS attempts to regulate the charge of the secondary battery using the current collected by the tether. During normal operation, the system is designed to both open and close the tether circuit to collect background plasma data. This data is needed for further model development of ED tether propulsion.

The ProSEDS tether, shown in Figure 1, is a 15 km long tether, and consists of a non-conductive ballast tether and a conductive ED tether. The ballast tether is attached to the endmass using a 20 m Kevlar leader designed to withstand the exhaust plume of the Delta II motor firing. The Kevlar leader is attached to the 10 km non-conductive Dyneema section, which is designed with sufficient length to overcome the friction force generated by the ED tether as it exits the deployer canister. The non-conductive tether is attached to the conductive tether using a special Kevlar to Dyneema splice. This splice is designed to prevent the metallic wire of the conductive tether from coming in contact with the Dyneema due to its low melting point.

The conductive tether has two distinct sections that have unique purposes during the mission. The conductive tether is designed to collect the ionospheric electrons on the semi-bare portion of the tether to evaluate the effectiveness of the bare tether current collection, which was proposed by Sanmartin[3]. The insulating tether enables the ProSEDS scientists to open circuit the tether

and measure the tether open circuit tether voltage. Computer simulations of the 5000 m ED tether, which include its late mission dynamics, have predicted the maximum open circuit tether voltage to be almost −1400 V.[4] This prediction is to be verified using on orbit data.
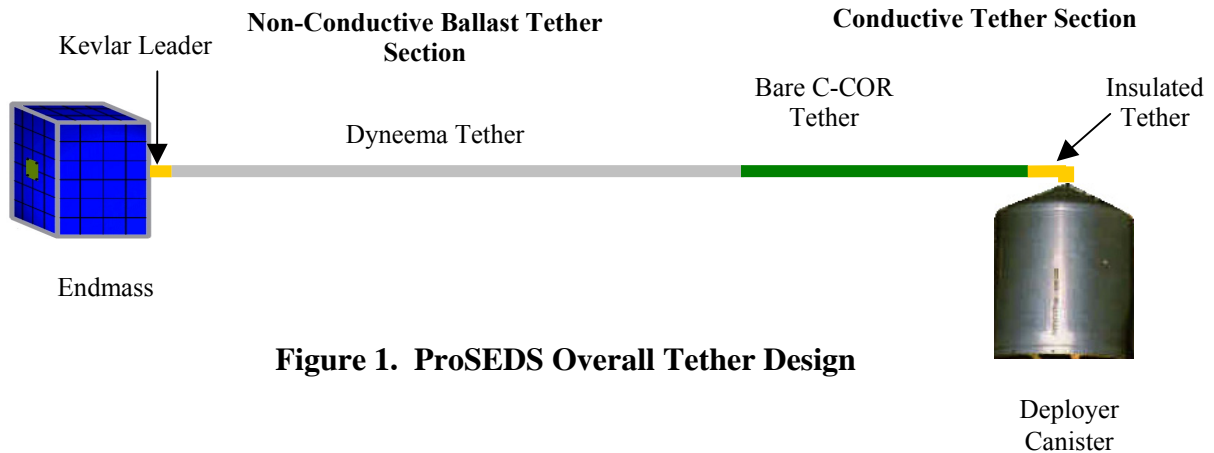
Figure 1. ProSEDS Overall Tether Design

The conductive tether consists of a 4800 m semi-bare tether and a 200 m insulated section. The entire conductive tether is made up of seven individually coated 28 AWG aluminum wires. The coating used for the semi-bare tether is an electrically conductive atomic oxygen resistant polymer, conductive colorless oxygen resistant (C-COR), specifically designed for the ProSEDS mission. The insulating coating consists of two distinct layers, triton oxygen resistant (TOR) and polyimide.[5,6] TOR is an atomic oxygen resistant polymer, which protects the main dielectric layer, the polyimide. Finally, the insulated tether is then over braided with Kevlar for abrasion protection during tether deployment.

An independent high voltage assessment of the entire ProSEDS system was performed early on in the program.[7] In that assessment two items of concern specifically related to the tether were identified. The items were: 1) The triple point at the junction between the bare and insulated tether, and 2) The triple point produced at the junction between the bare and the non-conducting tether interface. Also, early on in the ProSEDS tether design, the importance of maintaining the integrity of the insulating coating was recognized based on past history with TSS-1R where a breach in the insulation led to an electrical discharge event which severed the tether.[8] During all testing and handling with the flight tethers every effort was taken to maintain and verify the insulation integrity using a spark test. The two triple points identified in the high voltage assessment are located at two very different points on the tethers both physically and electrically. The first triple point, which is at the transition between the semi-bare tether and the insulated tether, is located very close to the Delta II, and it will see very high negative potentials during tether open circuit. Whereas the second triple point is located at the end farthest from the Delta II stage, and during open circuit it will experience mostly high positive voltages.

The three potential tether interactions with the LEO plasma were investigated in plasma chamber testing at MSFC, and where problems existed design changes were implemented. The

plasma chamber tests focused on the transition between the semi-bare conductive tether and the insulated tether and on the effects of pinholes in the insulated tether. The transition between the conductive tether and non-conductive tether does not experience negative potentials, so it was not tested at these potentials. However, a single test was done at positive potentials on the transition between the conductive and non-conductive tethers. The results of these investigations are discussed, and the required design changes described.
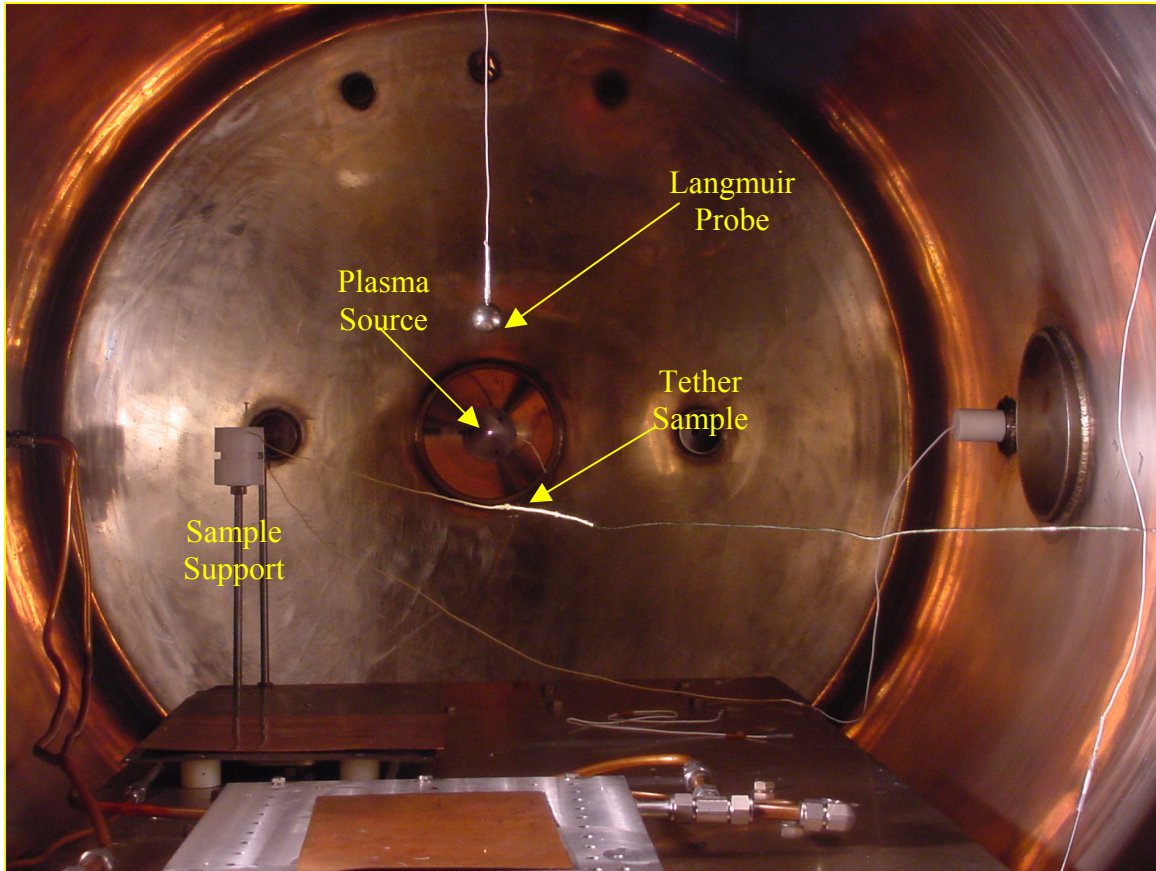
Plasma Test Chamber Set-Up

The ProSEDS tether sections were placed in a 1.2 m diameter and 3 m long cryo-pumped vacuum system. The chamber was capable of a base pressure in the low 10^{-6} Torr, and mid 10^{-5} Torr with the hollow cathode plasma source running. A photograph of the internal chamber set-up for these tests is shown in Figure 2. The hollow cathode source can operate on any noble gas, but for these tests argon was used except for one test that utilized nitrogen. The plasma source is designed to deliver cool diffuse plasma to the sample location with an electron temperature of 0.5 to 2 eV and plasma density of $5x10^5$ to $2x10^6$ cm^{-3}. The plasma chamber contained a spherical Langmuir probe with an overall diameter of 2.5 cm to verify plasma conditions before and after testing.

A 2 m long tether sample was placed in the plasma chamber diagonally across the vessel so that the center of the sample under test was directly in line with the hollow cathode plasma source about a meter away. Later a second sample was added to the setup by placing one sample eight inches below the other sample. In this case, both samples were equally spaced from the centerline of the hollow cathode source. One sample was allowed to float while not under test eliminating it from interacting with the other sample during testing. The 2 m long tether sample was supported by a specially designed sample holder, which was insulated from ground and allowed the tether to make electrical contact to a high voltage power supply. The electrical contact required a Faraday cage to prevent plasma from coming in contact with the connection because the electrical connection produced its own triple point with the plasma.

The overall electrical circuit for studying the effects of the tether in a plasma is shown in Figure 3. The tether sample was connected to the high voltage power supply through a high power 250 Ω load resistor. The load resistor was used to simulate the resistance of the tether. However, the load resistor was divided into five resistive segments of 50 Ω each in an attempt to more closely simulate the distributed tether resistance. The power supply was controlled manually from the front panel, and a separate data acquisition computer recorded both tether current and voltage data during the test via the analog output on the back of the power supply.

The procedure for testing each tether sample was the same with the ultimate goal of meeting the design requirement of -1800 V. The -1800 V limit was determined based on the worst case open circuit tether voltage (~ -1400 V) and providing a small 30% factor of safety.

Figure 2. ProSEDS High Voltage Plasma Interactions Internal Chamber Set-Up

The sample or samples were placed in the plasma chamber and pumped down overnight to ensure a good hard vacuum. Starting chamber pressures were typically around 1-2 x10^{-6} Torr. Each test was started by turning on the plasma source and allowing it to come to thermal equilibrium. The voltage was set at -100 V and held for at least two minutes. The tether voltage was decreased in -100 V increments until the sample either arced to the plasma or passed the – 1800 V limit.

Triple Point at The Semi-Bare Conductive Tether and Insulated Tether Transition

The most volatile triple point condition was found to be at the transition between the semi-bare (C-COR coated) conductive tether and insulated tether transition splice because this tranisition will experience the highest negtaive potentials. That particular transition is shown in the schematic in Figure 4. At this transition the tether is being transitioned from the conductive C-COR coated wire to the insulated wire by cold welding or butt welding the two diffent coated wires together and the central Kevlar core is changing size. The butt welding process is a process that joins two aluminum wires together without any heating. This is accomplished by using an off-the-shelf product that cold flows the aluminum wire together. This process worked extremely well because the coatings were relatively thin (~0.01 mm to 0.03 mm) compared to the wire diameter (0.32 mm), and the butt weld joints turned out to be stronger than the virgin

aluminum wire. The butt welds were staggered over 7-10 cm to ensure that the butt welds would lay nicely in the tether volume. However, a by product of the cold welding process were sharp aluminum flanges that circled the butt welds. Every attempt was made to remove these flanges using a special cutting tool. Yet it was still difficult to make sure the joint was perfectly smooth. Also, a transition in the Kevlar core was necessitated by differences in the diameters of the two wire types (.i.e. 0.34 mm for the bare conductive wire and 0.39 mm for the insulated wire). This required a Kevlar coresplice which took place about 60-80 cm from the location of the butt welds. In order to protect the entire transition region the Kevlar overbraid, which was initally designed to protect the insulated wire, was extended over the region containing both the butt welds and the coresplice.
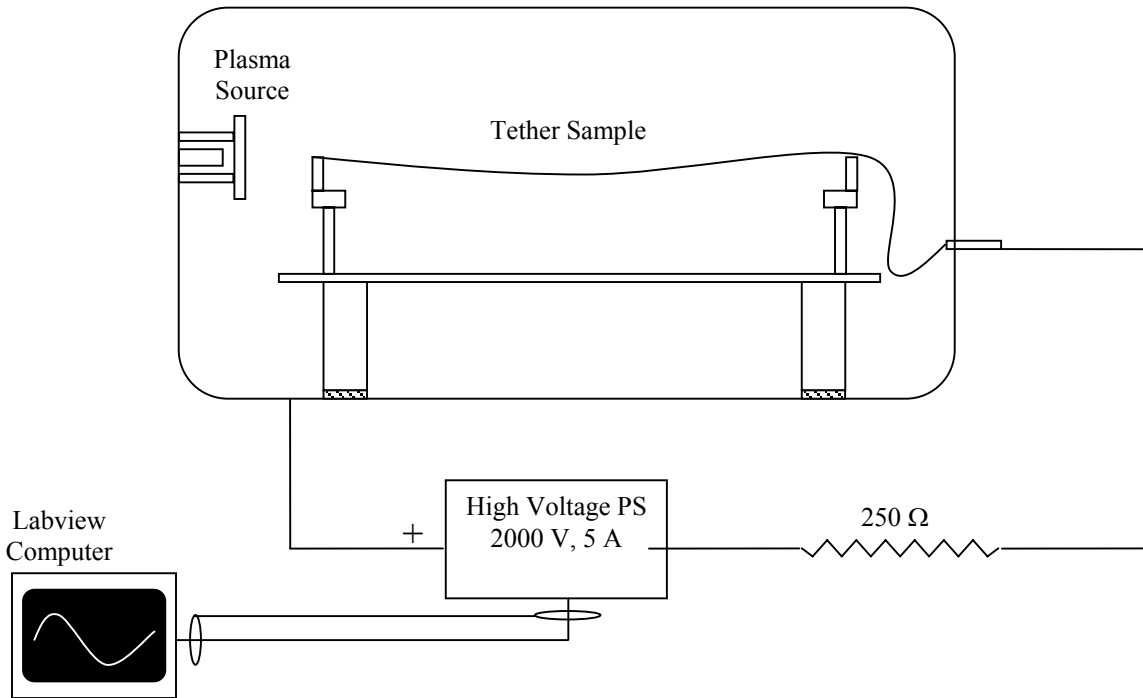
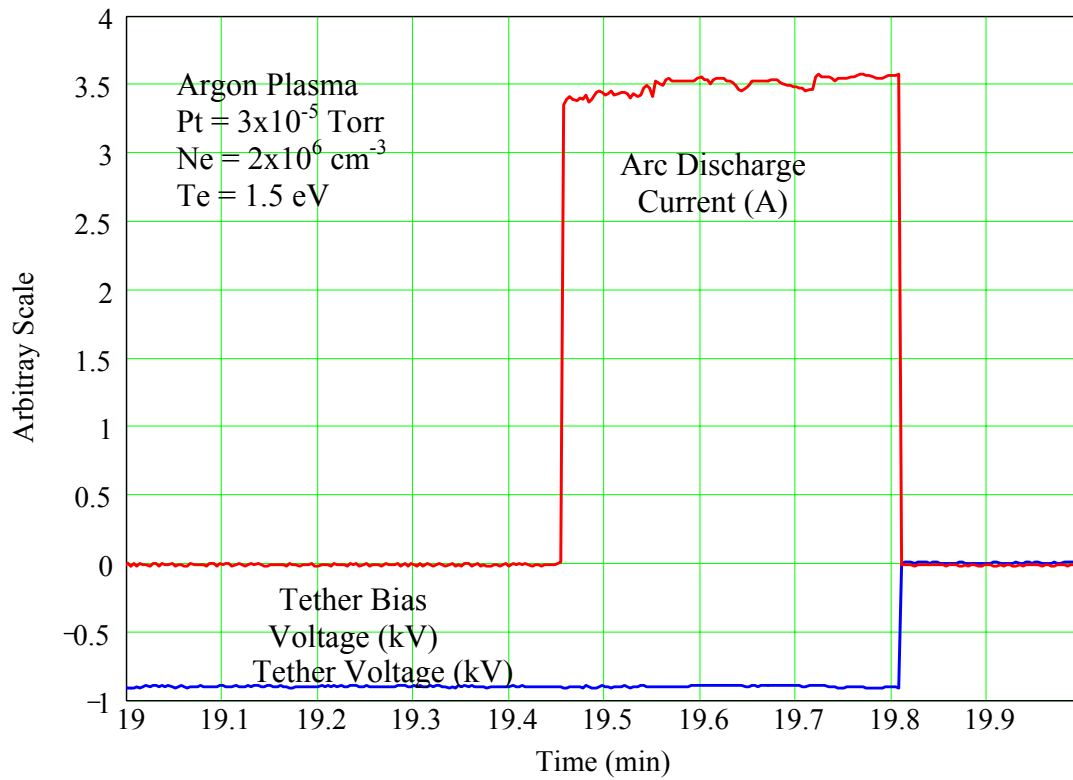**Figure 3. Tether High Voltage Test Schematic**
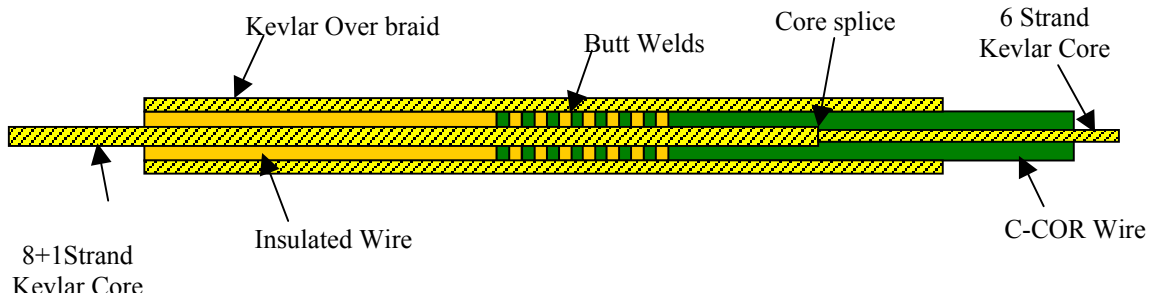
Figure 4. ProSEDS as Designed Conductive Tether to Insulated Transition

During the fabrication of the three ProSEDS flight tethers (F1, F2, and F3) extra conductive to insulated tether splices were made for post process testing. Some were used for strength testing while others were used for plasma testing. One of the samples created during the F2 processing was specifically used for triple point evaluation. The F2 transition sample was placed into the plasma chamber and the standard procedure followed. At −900 V bias the sample initiated ~3.5 A discharge which sustained for about 20 s. At that point the tether separated and the charged end landed against the chamber wall and continued to discharge until the power supply was turned off. Figure 5 shows the data collected during this test. The blue circle data points represent the power supply voltage in kilovolts and the square red data points represent the current draw from the power supply. It is believe that the large current from the arc is being fed from the power supply in the lab, but is being limited by the power resistor in line with the supply. However, the electrical circuit as close to reality as possible and on-orbit currents of this magnitude with an operating plasma contactor were predicted. Post-test evaluation showed that the arc was initiated at the triple point caused by the plasma interface with the conductive tether transition region. Figure 6 is a photograph of the intense plasma discharge started and sustained when the triple point ignited in the plasma chamber.
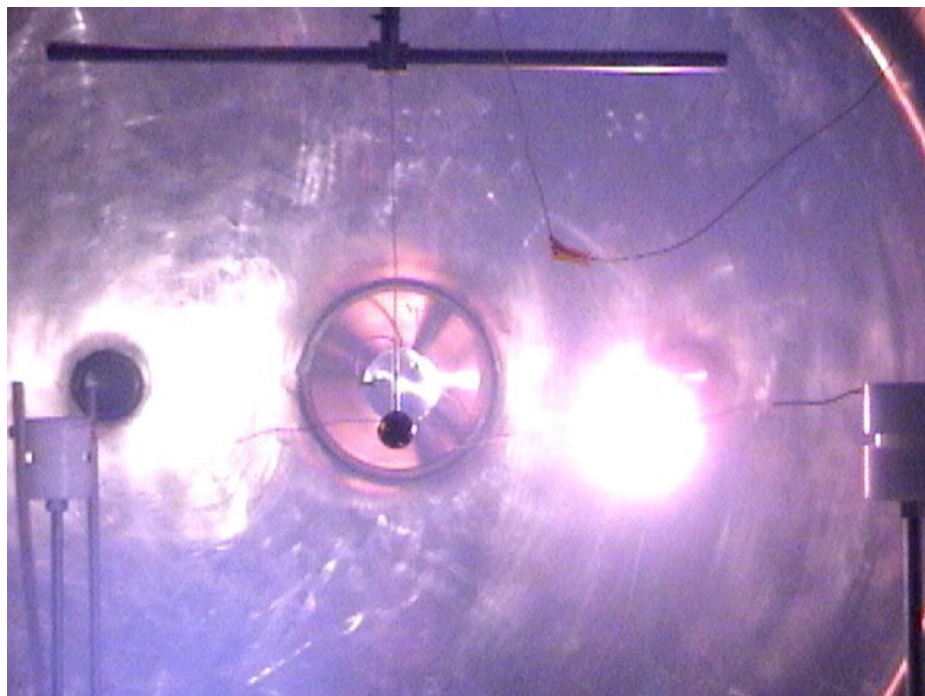
Once it was demonstrated the ProSEDS tether design had a triple point design problem, several materials and potential solutions were tested to find a solution that eliminated the problem.   The solutions focused on two particular areas. The first area of concern was to eliminate the sharp electric field change at the triple point by adding semi-conductive materials over that transition region, and the second area of concern was to focus on the sharp butt weld flanges. Four different materials, Aracon (i.e. nickel plated Kevlar), carbon loaded Kapton®, carbon loaded cotton, and Aerodag-G graphite spray, were tested as potential semiconductor material candidates. These materials were chosen because they met the basic requirements which were the material had to be easy to apply to the tethers, it had to be conductive, and it could not react adversely with the existing tether materials.

The results of the plasma chamber tests on the material design changes on the ProSEDS conductive tether triple point are detailed in Table 1. Of the materials detailed in Table 1 only one material, Aerodag-G, successfully passed the plasma chamber test at -1800 V. Aracon® did show surprising improvement over the initial transition design. The other materials did not show significant improvement or even made the situation worse.

The second problem of softening the butt weld flanges was done by attempting to wrap Teflon tape around the butt welds then over wrapping the entire 7-10 cm long transition with a contiguous Teflon tape wrap. This type of design successfully passed initial plasma chamber testing. However, when the transition region was put through a simulated deployment test, the cold weld flanges punctured through the Teflon exacerbating the problem (see Table 1). The final solution was to add the Aerodag-G spray to both underneath and on top of the over braid and to shorten the length of the over braid. Then Aerodag-G was applied from the over braid beyond the butt welds into the C-COR region. Figure 7 depicts the new conductive tether transition region, which eliminated the triple point from the tether design. The integrity of the transition was verified by completing both five simulated tether deployments and exposure to 6 days of on orbit atomic oxygen. Each of these samples was then subjected to a successful plasma chamber tests.

The graph shows:
- Argon Plasma
  - $Pt = 3 \times 10^{-5}$ Torr
  - $Ne = 2 \times 10^{6}$ cm^{-3}
  - $Te = 1.5$ eV
- Arc Discharge Current (A)
- Tether Bias Voltage (kV)
- Tether Voltage (kV)

Axis labels: Arbitray Scale (y-axis), Time (min) (x-axis)

Figure 5. Current and Voltage Data Due to ProSEDS Conductive Tether Triple Point Discharge

Figure 6. Photograph of ProSEDS Conductive Tether Undergoing Plasma Discharge

Table 1. ProSEDS Tether Triple Point Test Summary

Sample Description	Breakdown Voltage (V)	Chamber Pressure (Torr)	Test Summary
F2 Sample Transition	-900 V	4×10^{-5}	The failure occurred at the intersection of the conductive C-COR and Kevlar over braid.
F2 Simulated Tether Transition w/ Aracon®	-1500 V	5×10^{-5}	The sampled failed at -1500 V, about 1" from the end of the Metal clad Kevlar.
F2 Simulated Tether Transition w/ carbon loaded cotton fibers	-1000 V	4×10^{-5}	The sample failed at -1000 V, but began arcing at -700 V.
F2 Simulated Tether Transition w/ Teflon tape wrap on butt-welds	-1400	5×10^{-5}	The sample failed at -1400 V
F2 Simulated Tether Transition w/ carbon loaded Kapton (resistance of 18 kΩ).	-500	5×10^{-5}	The sample failed at -500 V
F2 Simulated Tether Transition w/ Aerodag-G and Teflon Tape on Butt-Welds	-1800+	6×10^{-5}	The sample passed the design voltage at -1800 V
F2 Simulated Tether Transition w/ Aerodag-G and Teflon Tape on Butt-Welds After simulated tether deployment	-1000	6×10^{-5}	The sample began arcing as early as -1000V.
F2 Simulated Tether Transition w/Aerodag-G	-1800+	6×10^{-5}	The sample passed the design voltage at -1800 V
F2 Simulated Tether Transition w/Aerodag-G which had undergone 5 simulated deployments	-1800+	6×10^{-5}	The sample passed the design voltage at -1800 V
F2 Simulated Tether Transition w/Aerodag-G which had been exposed to 6 days atomic oxygen exposure	-1800+	6×10^{-5}	The sample passed the design voltage at -1800 V
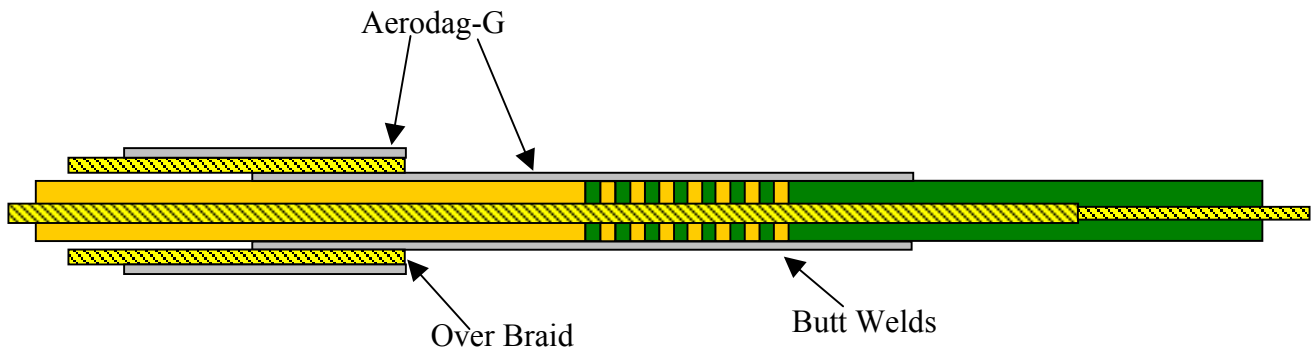
Figure 7. ProSEDS Tether Triple Point Mitigation Design

Plasma Interactions with Pinholes in ProSEDS Insulated Tether

Several tests were conducted on the insulated ED tether to investigate the interactions between small nicks in the tether caused by either ground handling or micrometeoroid and orbital debris impacts and the ambient plasma. Various methods were used to try and simulate the damage caused by either ground handling or debris impacts. It was recognized from the start that if damage was caused on the ground, it would manifest itself as a tiny insulation nick either caused by a cut or cracking of the insulation. However, an orbital debris impact could potentially do more damage by exposing completely severed wire strands. Every attempt was made to quantify the effects of these two different scenarios. Plasma chamber testing was done on both samples with small cuts and samples with wires that have been intentionally cut. This range of damage should bound the potential problem for ProSEDS. During the plasma chamber testing only negative bias potentials were applied, because the insulated section is located in a region where high negative potentials are expected.

The results of this investigation are detailed in Table 2. The main objective was to determine if the ProSEDS tether was at risk to an arcing event. A small cut was made in the insulation of a tether sample, which was verified with a digital multi meter (DMM) during the procedure. The sample was placed in the plasma chamber and biased using the standard procedure. The initial test did not show a problem, but there was some question as to weather the cut closed after the knife was removed, so a spark test at 3000 V was performed. The spark test is a standard test found in all electric cable manufacturers to look for holes in the insulation before shipping the product. During a spark test the wire is passed through a bead electrode, which is biased at the corresponding voltage. When a fault is present, an arc is produced. Because of the arc generated, the spark test is a destructive type test. The spark test verified the cut in the insulation. This sample was tested in the plasma chamber and a breakdown threshold of -900 V was measured. The difference between these two test results is likely the damage done by the spark test which likely enlarged the nick. The results of this tested verified that a nick in the tether insulation could cause a problem, but it did depend on the size of the nick.

Several methods were attempted to simulate the effects of orbital debris impacts short of having an actual impact test done. The method that was repeated on various samples was simply

cutting the wires and either leaving the wire inside the over braid or pulling the cut end outside. It was thought that during a debris strike the wire outside the over braid was a more plausible scenario as the over braid would likely be damaged during the impact. All simulated orbital debris tests where at least one wire was cut experienced electrical breakdown between -700 V and -1300 V. Because the insulated tether is expected to be at this potential during most open circuit periods, the ProSEDS tether has a design problem. Solutions to this problems could be design changes or to eliminate the open circuit period. Before any changes were made to either the tether design or ProSEDS operation, one last test was done to see if the chamber pressure of mid 10^{-5} Torr had a significant effect on the voltage breakdown thresholds. A test at mid 10^{-6} Torr pressures was proposed to determine the overall effect.

Table 2. ProSEDS Insulated Tether Pinhole Test Summary

Sample Description	Breakdown Voltage (V)	Chamber Pressure (Torr)	Test Summary
Small Pinhole in Insulated Tether, verified with DMM.	-1800+	5×10^{-5}	Sample passed the design voltage of –1800 V.
Insulated tether with Small pinhole arced at 3000 V in the spark tester several times.	-900 V	5×10^{-5}	At –900 V the sample broke down and burned the tether in half.
Insulated tether with knife cut; Aerodag applied along the length of the sample.	-700 V	5×10^{-5}	At –700 V the sample broke down and burned the tether in half.
Simulated debris hit; two wires intentionally cut.	-700 V	5×10^{-5}	At –700 V the sample failed.
A piece of insulated tether with two of the seven strands of wires intentionally cut.	-800 V	6×10^{-6}	The sample discharged at –800 V drawing a current of 1.5 A based on the supply current limit.

A titanium sublimation pump was added to the chamber to add extra pumping capacity of the neutral gas. In order to make the most efficient use of the titanium pump, the plasma source working gas was switched to nitrogen. When a piece of insulated tether, which had two of the seven strands cut, was placed in the plasma chamber and tested, the sample broke down at -800 V. When compared to the previous sample which had two wires cut yet the chamber pressure was mid 10^{-5} Torr, the breakdown voltage was only –100 V better. The results of this test indicated that a potential failure mode existed when an orbital debris hit the tether cutting at least one wire. A calculation of the probability that an orbital debris particle large enough to sever a single wire in the short 200 m insulated tether was done, and the probability that the insulated tether could sustain an arc inducing debris impact was about 13% per day[9]. This probability was higher than the accepted probability of 4 % per day that the entire tether will sustain a debris impact to sever the tether.

The potential corrections to the insulated tether centered on either changing the overall tether design or the ProSEDS operational scenario. Because the changes to the tether design were

going to be extremely costly in terms of cost and schedule, the operational timeline was changed. Initially, the tether was going to be in open circuit mode every 30 s the entire mission. Due to the potential debris induced arc event, the operational timeline was changed to allow open circuit mode every 30 s for only the first five orbits. After that point in time, the tether would no longer be allowed to enter the open circuit mode. The proposed operational change allowed scientists some time to collect needed data, though it reduced the total data set. The operational change reduced the probability of a debris particle impact large enough to cause an electrical breakdown to about 4% per day. This level of risk was equivalent to the risk accepted by the project early in the design phase.

ProSEDS Conductive Tether to Non-Conductive Tether Transition

The ProSEDS conductive tether to non-conductive tether transition did not show as volatile nature as the other transition. This is because this transition is biased at high positive potentials during open circuit. Because of the negative voltage potential did not exist, only a high positive potential was considered. The transition was placed into the plasma chamber and tested following the standard procedure, and it did not demonstrate any problems from 0 to +1500 V.

Summary

The ProSEDS tether design includes an insulated tether and a semi-bare conductive tether. The transition between the two creates a triple point with the ambient plasma. Plasma chamber testing of this transition region demonstrated electrical breakdown of -900 V, which was below the -1400 V design potential. Four semi-conductive materials were evaluated for use in reducing the electric field change at this point. Once the Aerodag-G spray was incorporated into the tether design, the tether passed all plasma chamber tests eliminating the triple point concern. The new tether design also passed both simulated deployment tests and six days on orbit of simulated atomic oxygen exposure. The ProSEDS insulated tether samples, which contained simulated orbital debris damage experienced plasma discharge between -700 V and -800 V. The cost of changing the tether design forced an operational change that eliminated the tether open circuit mode after the first five orbits. Finally, no plasma effects were measured at the remaining triple point at the conductive tether to non-conductive tether transition because it will only experience high positive tether potentials.

References

[1]Leslie Curtis and Les Johnson, "Propulsive Small Expendable Deployer System (ProSEDS)", Space Technology Applications International Forum (STAIF) 2002, February 3-6, 2002.

[2]Joseph A. Carroll, "SEDS Deployer Design and Flight Performance", Proceedings of the 4th International Conference on Tethers in Space, April 10, 1995, Washington, D.C.

[3]Leslie Curtis, Jason Vaughn, Ken Welzyn, and Joe Carroll, "Development of the Flight Tether for ProSEDS", Space Technology Applications International Forum (STAIF) 2002, February 3-6, 2002.

[4]J. A. Vaughn, M.M. Finckenor, R.R. Kamenetzky, Todd Schneider, and Pete Schuler, "Polymeric Coatings for Electrodynamic Tethers", AIAA 2000-3614, 36th AIAA/ASME/SAE/ASEE Joint Propulsion Conference, Hunstville, AL, July 2000.

[5] J.R. Sanmartin, M. Martinez-Sanchez and E. Ahedo, "Bare Wire Anodes for Electrodynamic Tethers." Journal of Propulsion and Power, Vol. 9, No. 3, pp. 353-360, May-June 1993.

[6]Les Johnson, R.D. Estes, E. Lorenzini, M. Martinez, J. Sanmartin, "Propulsive Small Expendable Deployer System Experiment," J. Spacecraft and Rockets 37(2), 173-176 (2000).

[7]A.B.White, "ProSEDS High Voltage Assessment", SDL/99-004, Feb. 1, 1999.

[8] Kenneth J Szalai, "TSS-1R Mission Failure Investigation Board, Final Report", 5/31/96.

[9]Bill Cook and Heather Lewis, ProSEDS Project Orbital Debris Assessment, Feb. 2002.

A 'FREE-LUNCH' TOUR OF THE JOVIAN SYSTEM

J. R. Sanmartín
E.T.S.I. Aeronáuticos/Universidad Politécnica de Madrid
Pza. C. Cisneros 3, Madrid 28040, Spain
Phone: 34/91/33663-02
Fax: 34/91/33663-03
Email: jrs@faia.upm.es

E. C. Lorenzini
Harvard-Smithsonian Center for Astrophysics

Abstract

An ED-tether mission to Jupiter is presented. A bare tether carrying cathodic devices at both ends but no power supply, and using no propellant, could move 'freely' among Jupiter's 4 great moons. The tour scheme would have current naturally driven throughout by the motional electric field, the Lorentz force switching direction with current around a 'drag' radius of 160,00 kms, where the speed of the jovian ionosphere equals the speed of a spacecraft in circular orbit. With plasma density and magnetic field decreasing rapidly with distance from Jupiter, drag/thrust would only be operated in the inner plasmasphere, current being near shut off conveniently in orbit by disconnecting cathodes or plugging in a very large resistance; the tether could serve as its own power supply by plugging in an electric load where convenient, with just some reduction in thrust or drag. The periapsis of the spacecraft in a heliocentric transfer orbit from Earth would lie inside the drag sphere; with tether deployed and current on around periapsis, magnetic drag allows Jupiter to capture the spacecraft into an elliptic orbit of high eccentricity. Current would be on at succesive perijove passes and off elsewhere, reducing the eccentricity by lowering the apoapsis progressively to allow visits of the giant moons. In a second phase, current is on around apoapsis outside the drag sphere, rising the periapsis until the full orbit lies outside that sphere. In a third phase, current is on at periapsis, increasing the eccentricity until a last push makes the orbit hyperbolic to escape Jupiter. Dynamical issues such as low gravity-gradient at Jupiter and tether orientation in elliptic orbits of high eccentricity are discussed.

Introduction

The present work is motivated by the challenges facing the exploration of the outer planets. A recent editorial in *Aerospace America* pointed at the basic difficulties [1]. Solar Power is insufficient at Jupiter and beyond. Radioisotope Generators are weak power sources (and they are heavy, and a source of heat and a danger to the electronics).

Propellant mass is the main issue, however. Just allowing capture by their planetary targets has placed a heavy toll on both the Galileo and Cassini missions, reducing scientific payload to a few percent of the respective 3-ton and 6-ton masses, and limiting mission lifetime. Getting a spacecraft into low, near-circular orbit appears beyond the reach of gravity assists.

The *Aerospace America* editorial advocated NASA's *Project Prometheus* on the use of nuclear reactors for outer-planet missions. Nuclear reactors would be directly used for electric power, and indirectly used for propulsion, as power source of electrical thrusters. The

1-order of magnitude gain in specific impulse as compared to chemical propulsion would greatly extend mission lifetime.

In the present work, electrodynamic (ED) tethers are discussed as providing both power and propulsion in an extremely efficient way for outer-planet missions. A seemingly paradoxical tour of the Jovian system is proposed. Some characteristic features of the thermodynamics of gravitation, which underlies that tour concept [2] - [3], and the relevant basics of ED-tethers, are first recalled.

Thermodynamics and Gravitation

Consider an isolated system conserving momentum, angular momentum, and energy, but exhibiting macroscopic motion. Thermodynamic equilibrium requires that entropy and thus internal energy be maximum. To conserve total energy, macroscopic energy (which need not be purely kinetic) must reach a minimum value compatible with the overall magnitudes conserved. Such minimum corresponds to rigid-body motion.

Different kinetic mechanisms are responsible for the dissipation of macroscopic energy in the approach to that equilibrium. In the trivial case of two blocks sliding on each other upon a frictionless floor, dry friction is involved in getting the blocks to finally move jointly as a rigid body. Air drag is determinant in making atmospheres corotate with their planets. Tidal forces are determinant in the equilibrium of planet-moon systems.

In a planet-moon system, both moon and planet rotations and the relative orbital revolution contribute to the angular momentum, H_0. The macroscopic energy ε_{Macro} involves, in addition, the gravitational interaction. In the simplest case, all three angular velocities for the two spins and the orbital revolution, ω_m, ω_p, and Ω_{orb}, are parallel, and the orbit is equatorial and circular. The condition $H_0 = const$ allows writing the macroscopic energy as $\varepsilon_{Macro}(\omega_p, \Omega_{orb})$, with semiaxis (radius) a related to Ω_{orb} by Kepler's law.

The condition for minimum $\varepsilon_{Macro}(\omega_p, \Omega_{orb})$ yields two relations leading to rigid-body motion,

$$\omega_m = \omega_p = \Omega_{orb}.$$

A spectacular example of this type of equilibrium is the *Pluto/Charon* system: the spins of both planet and moon, and the relative orbital revolution, all three have periods of 6.39 days... The *Earth/Moon* system, not quite fitting the simple-case conditions, has only achieved yet the locking of *Moon*'s spin with its orbital revolution.

Whenever a moon, say a satellite in general, makes a negligible contribution to both H_0 and ε_{Macro}, the condition $H_0 = const$ allows writing $\varepsilon_{Macro}(\Omega_{orb})$, or $\varepsilon_{Macro}(a)$. If Ω_{orb} is opposite H_0 (case of *Earth*'s westward satellites, and *Neptune*'s moon *Triton*), then $\varepsilon_{Macro}(a)$ decreases monotonically with decreasing a; any dissipation will make the satellite fall into the planet. If, however, Ω_{orb} and H_0 have the same direction (as with *Earth*'s eastward satellites) <u>and</u> $H_0 > 4 \times [(GM_p)^2 M_m^3 I_p/27]^{1/4}$, then a graph ε_{Macro} versus a exhibits extrema at two distances, where $\Omega_{orb} = \omega_p$: a maximum, and a minimum farther from the planet.

The (relative) minimum is a metastable thermodynamical equilibrium (it corresponds to a *relative* maximum of entropy), while <u>the maximum is thermodynamically unstable under</u>

dissipation; this is a case of rigid-body motion being unstable. For man-made satellites a_{max} is the geostationary radius, $r_{gE} \approx 42,200$ km (with dissipation times unphysically large, however). For $a < a_{max}$ we have $\Omega_{orb} > \omega_p$, as in the case of satellites at LEO altitudes, which decay from air friction with the slow corotating atmosphere.

ED Tethers

Deploying a conductive tether orbiting a planet that has ionosphere and magnetic field introduces a new kinetic mechanism for dissipation. Consider the Lorentz transformation of any electric and magnetic fields $\overline{E}$ and $\overline{B}$ in going from a frame moving with the local ionospheric plasma to a frame orbiting with the tether, the relative velocity being non-relativistic,

$$\overline{E}\,(tether\ frame) = \overline{E}\,(plasma\ frame) + \overline{E}_m. \tag{1}$$

Here $\overline{E}_m$ is the so-called induced electric field,

$$\overline{E}_m \equiv (\overline{v}_{orb} - \overline{v}_{pl}) \wedge \overline{B}, \tag{2}$$

and $\overline{B}$ is the same in both frames.

Far from the tether (meters away, typically) the electric field in the highly conductive plasma is zero (or just negligible when compared with $\overline{E}_m$), yielding

$$\overline{E}\,(tether\ frame) = \overline{E}_m \qquad (outside). \tag{3}$$

Equation (1) also holds inside the tether, where it provides no useful information however. On the other hand, if current flows along the tether, Ohm's law holds inside, in the tether's own frame,

$$\overline{E}\,(tether\ frame) = \overline{J}_e / \sigma_{cond} \qquad (inside). \tag{4}$$

For the simplest circular, equatorial orbit of Sec.2, and a centered, no-tilt dipole field, $\overline{B}$ is horizontal and lies in the meridian plane, and $\overline{E}$ is parallel to the tether, assumed vertical (a non-parallel component will in general produce a negligible potential difference accross the thin cross section of the tether). For an insulated tether making electric contact with the plasma through devices at both ends, the fields given by Eqs. (3) and (4) would be equal in the limit case of vanishing contact impedances. In general, $\overline{E}_m$ and $\overline{J}_e$ will have the same direction. The Lorentz force on the current I along the tether will be

$$L_t\,\overline{I} \wedge \overline{B} \qquad\qquad (\overline{I} \bullet \overline{E}_m > 0)$$

We then have

$$(L_t\,\overline{I} \wedge \overline{B}) \bullet (\overline{v}_{orb} - \overline{v}_{pl}) = -\,L_t\,\overline{I} \bullet \overline{E}_m\ < 0,$$

the negative sign meaning that electrical power is produced in the tether.

Whether $(L_t\,\overline{I} \wedge \overline{B}) \bullet \overline{v}_{orb}$ is positive (implying thrust) or negative (implying drag) depends on $\overline{v}_{orb}$ being opposite or having the same direction of the relative velocity

$\bar{v}_{orb} - \bar{v}_{pl}$. Going back to the case of Earth satellites, with $\bar{v}_{pl}$ pointing eastward, one can readily check that drag applies to westward orbits always, whereas, for eastward orbits, there is thrust beyond the geostationary radius r_{gE} where $\bar{v}_{orb} - \bar{v}_{pl}$ changes direction, and drag for $a < r_{gE}$. Note that these results from an analysis of the dissipative mechanism introduced by the tether are in agreement with the purely thermodynamic analysis of Sec.2, which applies to any kinetic mechanism.

(Note also that the example of a centered, no-tilt dipole magnetic field - Saturn's field being quite close to that limit model - shows clearly that tether thrust or drag does <u>not</u> result from *the magnetic field* moving faster or slower than the tether, an erroneous statement seen frequently.)

The Lorentz force, whether thrust or drag, is not related to high-velocity ejection of propellant. A tether therefore imposes no toll on a spacecraft, ensuing from a requirement of propellant mass. Devices (Hollow Cathodes) used <u>at present</u> with EDTs do eject some expellant with the electron current ejected at the cathodic end, but, typically, the (Xenon) mass expelled is about <u>1000</u> times smaller than the propellant mass consumed by an equal-thrust rocket. For the rocket one has

$$\frac{Thrust}{\dot{m}_{prop}} = v_{exh} \approx 3 \frac{km}{s}.$$

An Ion thruster has an exhaust velocity (*specific impulse × aceleration of gravity*) about 10 times greater, thus consuming only <u>10</u> times less mass for given thrust.

In the case of a tether, one can define an equivalent 'exhaust' velocity based on the ratio *current*-to-*expellant mass flow rate* at the Hollow Cathode, which has the same dimension of the *charge*-to-*mass* ratio of a particle (for state-of-the-art Hollow Cathodes, this is the ratio of an ion of atomic number 6-10), and leads to a 'gyrofrequency' when multiplied by the magnetic field [4]. One finds

$$\frac{Lorentz\ force}{\dot{m}_{hc}} \approx L_t \times \frac{I_{hc}}{\dot{m}_{hc}} B \approx 7000 \frac{km}{s},$$

$$(B \approx 0.3\ gauss, \qquad \frac{I_{hc}}{\dot{m}_{hc}} \times B \approx 350 \frac{1}{s}, \qquad L_t \approx 20\ km.)$$

At the anodic end, passive collection is used. The tether itself, left bare of insulation, collects electrons over a segment coming out positively. The collecting area is large because the anodic segment is kilometers long. For some operating regimes that segment comes out longer the lower the density of ionospheric electrons: bare-tether current can self-adapt to electron-density drops occurring in orbit [5].

As opposite collection by a large sphere, collection by a typically thin (radius up to 1 Debye length) bare tether is not reduced by space-charge shielding, because the two-dimensional electric potential it sets up dies off gradually with distance. Also, the planetary magnetic field that guides electrons along thin helices, may greatly reduce collection by a large sphere but hardly affect collection by a thin tether. Note that a tape would collect as

much current as a round wire with equal perimeter of cross section (and would be much lighter), if its width does not exceed 4 Debye lengths [6].

A 'Free-Lunch' Tour of the Jovian System

The equivalent of the geostationary radius for Jupiter, r_{gJ}, is about 2.24 R_J, where $R_J \approx$ 71,400 km is Jupiter's radius. This stationary distance lies well within Jupiter's plasmasphere, its complex magnetosphere extending much farther out. (For Earth, one has $r_{gE} \approx 6.6\ R_E$, plasma density and magnetic field being already extremely weak at the geostationary distance.) We may talk of a 'drag sphere', defined by condition $r < r_{gJ}$. As seen in Secs.2 and 3, the current 'naturally' driven along a tether in circular orbit by the induced electric field will result in drag for $a < r_{gJ}$ and thrust for $a > r_{gJ}$. This also applies approximately at $r < r_{gJ}$ and $r > r_{gJ}$, respectively, for elliptical orbits.

A paradoxical use of an ED bare tether for a tour of the Jovian system would follow this conceptual scheme: The tether would have Hollow Cathodes at both ends, each end allowed acting as cathodic or anodic. Current could be practically shut off at convenient points, by switching off the Hollow Cathodes/plugging in a very large resistance; since both plasma density and magnetic field decrease rapidly with increasing distance from Jupiter, tether drag or thrust would only operate near Jupiter, well within its plasmasphere. The tether could be used as its own power source by plugging in an electric load, again where convenient, the induced electric field generating useful power (to be stored) with just some reduction on drag or thrust as the case might be.

The tour would involve a capture phase and three additional phases, the capture phase being critical: the tether orbit, once closed, can be made to evolve dramatically by repeatedly applying the Lorentz force, even if weak. The spacecraft is assumed to approach Jupiter with the relative velocity resulting from a minimum-energy transfer from Earth, about 6 kilometers per second. The periapsis of this open (relative to Jupiter) orbit would lie inside the drag sphere, say at 1.5 R_J. Limited propellant mass would be needed for any required Trajectory Correction Maneuvers during the Earth-Jupiter trip, when the Lorentz force is not available.

The tether is deployed when entering the 'drag sphere', Jupiter's magnetic field braking the spacecraft continuously to barely close the orbit before leaving that sphere. At 1.5 R_J the velocity to escape Jupiter is about 48.5 km/s, the minimum Δv required being only 0.33 km/s. Taking $\Delta v = 0.67$ km/s leads to a highly elongated ellipse of 50-days period, and an apoapsis at 107.9 R_J. (Capture into a ellipse of greater period would be, of course, less requiring. Galileo had a first perijove at 4 R_J and was captured into a closed orbit of 198-days period, the Δv applied being only slightly greater than the minimum Δv required.)

Using electron density $N_\infty = 10^3 \text{cm}^{-3}$, $B = 1.6$ gauss, $E_m = 4.8$ V/m at 1.5 R_J and taking a total spacecraft mass $M_{S/C} = \alpha_t$ times the mass of the tether (an Al tape of width w_t and thickness h_t) we find that ohmic effects are negligible. A condition on the average Lorentz force to produce $\Delta v = 0.67$ km/s, setting $h_t = 0.05$ mm, $\alpha_t = 4$ requires a tether length $L_t \approx$ 34.8 km. Taking $w_t = 6$ cm leads to $M_{S/C} \approx 1124$ kg (including tether mass ≈ 281 kg).

A simple estimate of heating effects shows that it is possible to keep the tape at a working temperature. On the other hand, because of the low gravity gradient at 1.5 R_J, and the large

magnetic force the tether may support, some scheme to provide tension and dynamic stability is required. One way is setting the tether into a slow spin of period about 30 minutes (before the orbit is closed and orbital/attitude coupling itself could get the tether spining). This can be done with thrusters at the tether tips, requiring about 10 kg of propellant left over from the trip from Earth. With the direction of current always resulting in drag, that slow spin could allow each Hollow Cathode act as needed at the proper phase in rotation.

In a second phase, tether current will be off all along the elongated ellipse of capture until the spacecraft reenters the drag sphere, when again it is switched on. A second $\Delta v = 0.67$ km/s velocity reduction would lead to a 35 R_J apoapsis. This scheme is repeated in following passes: current on around periapsis, inside the drag sphere, and off elsewhere, to produce drag. This reduces the semi-major axis of the elliptic orbit, progressively making the apoapsis reach in succesion each one of the 4 big moons of Jupiter: *Callisto* at 11.8r_{gJ}, *Ganymedes* at 6.7r_{gJ}, *Europa* at 4.2r_{gJ}, and *Io* at 2.6r_{gJ}.

The third phase begins once magnetic drag brings down the apoapsis close to the drag sphere. Now tether current is kept on around apoapsis, where thrust rather than drag applies, and off around periapsis. This reduces the eccentricity, until the entire orbit lies outside the drag sphere and is not far from a circle.

In a last phase tether current is again on during periapsis, where thrust, rather than drag, still applies and off elsewhere, the evolution being the opposite of the second phase. Semi-major axis keeps increasing, reaching eccentricities very near unity, until a final push makes the orbit open for a transfer back to Earth.

Conclusions

ED bare tethers may represent a powerful alternative to the use of nuclear reactors for outer-planet missions, although careful tradeoff analyses are required to go beyond the conceptual scheme and simple calculations presented here.

References

1. E. Camhi and J. Grey, <u>Aerospace America</u> **41**, Editorial (2003).

2. J.R. Sanmartin, <u>Eur. J. Phys.</u> **16**, 8 (1995).

3. D.P. Sheehan, J. Glick, T. Duncan, J. A. Langton, M. J. Gagliardi, and R. Tobe, <u>Found. Phys.</u> **32**, 441 (2002).

4. J.R. Sanmartin, R. D. Estes, and E. C. Lorenzini, in <u>Space Technology and Applications International Forum 2001</u> (ed. M.S.El-Genk, Am. Ins. Phys., New York, 2002), pp. 479-487.

5. R.D. Estes, E. C. Lorenzini, J. R. Sanmartin, J. Pelaez, M. Martinez-Sanchez, C. L. Jonhson, and I. E. Vas, <u>J. Space. Rockets</u> **37**, 205 (2000).

6. J.R. Sanmartin, in <u>Space Environment: Prevention of Risks Related to Spacecraft Charging</u> (eds. J-P. Catani and M.Romero, CNES/ONERA, Toulouse, 2002), pp.515-533.

ISSUES CONCERNING THE INTERNATIONAL STANDARD OF ESD GROUND TEST FOR GEO SATELLITE SOLAR ARRAY

Mengu Cho
Kyushu Institute of Technology
1-1 Sensui Kitakyushu, Japan 804-855
Phone: +81-93-884-3228
Fax: +81-93-884-3228
E-mail: cho@ele.kyutech.ac.jp

Yoshio Shikata
Satoshi Hosoda
Kazuhiro Toyoda
Emanuel Amorim
Kyushu Institute of Technology

Tateo Goka
Japan Aerospace Exploration Agency

Leon Levy
Rene Reulet
Office National d'Etudes et de Recherches Aerospatiales

Denis Payan
Centre National d'Etudes Spatiales

Abstract

As the power level of Geostationary satellites increases, there is more demand of careful ground test on solar array insulation strength. International atmosphere surrounding commercial telecommunication satellites calls for common international standard on test conditions. The issues regarding test environment, test circuit, test duration and external capacitance are reviewed. Results of experiment on the influence of external capacitance on secondary arc formation are presented.

Introduction

Since the last decade, the power level of a geostationary satellite has increased dramatically to nearly 10 kW or even higher. To manage the large amount of power efficiently, nowadays

many commercial telecommunication satellites employ solar array that generates the electricity at 100V.

As the voltage of solar array increases to 100V, arcing during substorm has been recognized as serious hazard that sometimes threatens the stable supply of the solar array power. In Geosynchronous Orbit (GEO), when a satellite receives the sunlight, its charging is dominated by photoelectrons. As long as the satellite surface is well illuminated under the quiet condition, photoelectrons keep the satellite potential within a few electron volts from the plasma potential. Insulator surface such as coverglass has similar potential. When a satellite encounters substorm, the current due to high-energy electrons increases and sometimes exceeds the current due to photoelectrons. Then the potentials of the satellite body and the insulator surface can become negative. Due to the difference of the secondary electron emission coefficients, the insulator potential may drop slower than the satellite body. During that process, the coverglass potential can be more positive than the nearby conductor, e.g. interconnector. This situation is called "inverted potential gradient". In the present paper we call the potential difference between the coverglass and the satellite body *differential voltage*. The differential voltage, ΔV, is defined in the following equation;

$$\Delta V = \phi_{cg} - \phi_{sat} \quad (1)$$

where the satellite potential is equal to the interconnector potential at the negative end of the solar array circuit. As the differential voltage builds up between coverglass and interconnector, an arc may occur. It is well known that an arc occurs once the differential voltage reaches 100 or 200V in LEO plasma condition[1,2]. Cho et al[3] found that an arc may occur with the differential voltage of as low as 400V under simulated GEO plasma conditions during a ground experiment.

In Fig.1 we illustrate the definitions of arc phenomena discussed in this paper. If an arc occurs as a single pulse, we call it a *trigger arc*, a *primary electrostatic discharge* (ESD) or a *primary arc*. For the rest of present paper, we call it primary arc. There are two current paths of a primary arc. One is current 1 in Fig.1 that flows between spacecraft and the ambient plasma, where a capacitance of satellite body, typically of the order of 100pF provides energy. The other is current 2 in Fig.1 that flows between the arc point and insulator surface on spacecraft, where a capacitance of coverglass, at maximum more than 10μF, mostly provides energy.

If an arc occurs at a gap of two solar array strings or near defect of the insulator layer between cells and conductive substrate, there is a risk of one primary arc growing to a catastrophic arc receiving energy from the array itself. The risk has increased recently as the power level of solar array has increased. When an arc occurs, the arc plasma may short-circuit two points on solar array panel with different potentials, that is called *secondary arc*. The secondary arc has three stages as shown in Fig.2. The first stage is *non-sustained arc* that

continues only while the primary arc current flows. The second stage is *non-permanent sustained arc* that has a current pulse longer than that of the primary arc. The third stage is *permanent sustained arc* where the current is maintained by the solar array string circuit and keeps flowing until the solar array string circuit is disconnected. The sustained arc gives excessive heat to underlying insulation substrate. Thermal breakdown of the insulation substrate leads to permanent short-circuit of solar array strings. Several satellites[4,5] lost a part of solar array output power due to the sustained arc. The risk of sustained arc increases as output voltage of solar array increases, because the potential difference between two points short-circuited by the arc plasma becomes higher.

As size and price of GEO satellites become larger, there is more demand for careful ground test before launch. Ground tests are being carried out to confirm whether a given design of solar array can withstand the sustained arc. In Fig.2 we schematically illustrate experimental layout of a typical ground test. We place a solar array coupon inside a vacuum chamber. The coverglass surface is charged more positively than the solar cells either by an energetic electron beam or by positive ions. One string of solar cells is biased to a positive potential with respect to the conductive substrate, simulating the positive end of solar array. Another string is grounded (or sometimes connected through a resistance) to the conductive substrate, simulating the negative end of solar array. The positive potential given to the first string, V_{gap}, should be equivalent to solar array output voltage, V_{out}. The floating power supply simulates the solar array string circuit. The power supply should act as a constant voltage source before an arc and should act as a constant current source once the arc plasma short-circuits the strings or the string and the substrate. The maximum current provided by the power supply should be equivalent to the solar array short-circuit current, I_{sc}.

When we carry out an ESD test of solar array, proper test conditions that simulate the conditions in orbit are necessary. Inadequate testing conditions lead to unexpected failure in space. Increasing the level of harshness beyond a reasonable limit is not always a good solution. There is not yet any standard on how we carry out the ESD test on solar array. There are currently four major issues regarding the ESD test method.

(1) How do we charge the coverglass to produce the inverted potential gradient?
(2) What type of power supply do we use to simulate the solar aray string circuit?
(3) How long do we carry out the test?
(4) How do we implement the role of capacitance associated with coverglass of solar array panel that cannot be accommodated into the vacuum chamber?

As manufacturers, subcontractors, launchers, users and insurers of GEO telecommunication satellites have become international, there is more need of international standard on the ESD test

method. The purpose of the present paper is to describe the four issues in detail to stimulate the discussion to establish the common standard. There are many aspects in ESD test. In this paper we focus on the test that investigates the insulation strength of a given solar array design against the sustained arc phenomena.

Test Environment

Because a secondary arc occurs only when a primary arc occurs on a solar array coupon, to investigate the insulation strength against the sustained arc, we want primary arcs as many as possible. Table 1 lists the summary of three typical environment where ESD tests are carried out. The electron beam environment uses an energetic electron beam whose energy is typically of the order of keV. The electron beam charges the coverglass surface more positive than the solar array circuit by inducing secondary electron emission. Typical background pressure is of the order of 10^{-6} Torr or less. The plasma environment uses plasma as dense as Low Earth Orbit (LEO), such as $10^{10} \sim 10^{12} m^{-3}$ to charge the coverglass surface. The plasma is usually produced via a diffusion type glow discharge device and its temperature is of the order of 1eV. The background pressure during the test is of the order of 10^{-5} Torr or more. The ion beam environment uses an ion beam whose energy is 1keV or less. The background pressure is similar to the plasma environment because the ions are extracted from the glow discharge device.

Usually the plasma environment gives the highest rate of primary arcs (arc rate), because recharging of coverglass via the dense plasma is fast and the background pressure is high. Figure 2 shows a picture of solar array coupon used for the ESD test of ETS8 solar array [3,6]. Two identical coupons were tested in the same vacuum chamber for different environments, the electron beam environment and the plasma environment. In the electron beam environment where the electron current density was between $30\mu A/m^2$ and $3mA/m^2$ the arc rate was only 10 to 20 arcs per hour. On the other hand, in the plasma environment, the arc rate was more than 10 arcs per minute. Thermal ion current density in the plasma environment is of the order of $10\mu A/m^2$. Although this number is comparable to the electron beam current density, the solar array coverglass can collect ions crossing the sheath boundary surrounding the solar array coupon with much larger surface area than the coupon itself. Therefore, the actual current density charging the coverglass is much higher than the simple one-dimensional thermal current density.

There is no doubt that the electron beam environment provides the best simulation of inverted potential gradient in GEO that is caused by energetic electrons generated by susbstorm. Because we want the arc rate as high as possible, however, we are tempted to use the plasma environment to test a solar array coupon against sustained arc. Because the sustained arc phenomena is usually short-circuit of two points that are separated only by one millimeter or less, the phenomena may not depend on the nature of background conditions as long as a primary arc occurs. To make sure that the ESD tests carried out under the plasma or ion beam environments

are representative of GEO conditions, the effects of background plasma density and neutral density on the sustained arc formation must be studied. The best way is to confirm the sustained arc thresholds for string voltage, string current and cell gap distance are independent of the background parameters via experiments using the same test coupons in different environments. At least we should verify that the results in the plasma environment are scalable to the results in the electron beam environment.

Test circuit

To study sustained arc phenomena, we have at least two DC power supplies. One is a power supply to bias the solar array coupon negatively with respect to the chamber ground, which is shown as V_b in Fig.3. DC negative voltage given by this power supply simulates the satellite potential with respect to the space plasma when a satellite is severely charged by energetic electrons. We can charge the solar array coupon negatively by an electron beam alone. But, it is very difficult to control the coupon potential. Stable DC output voltage is required for the first power supply but not much capacity of current.

Another power supply simulates the solar array string output power that provides energy to the arc plasma once a secondary arc occurs, which is shown as I_{sc} in Fig.3. We call this power supply *string power supply* in this paper. The requirement for the string power supply was described by Payan *et al.*[7]. Basically the string power supply must behave in a very similar way to the real solar array circuit. Two strings on the test coupon are insulated before the primary arc inception. Therefore the power supply should provide a constant voltage, V_{gap}, between the two strings. Once the secondary arc plasma short-circuits the two strings, the voltage collapses and a constant current is provided. After the secondary arc inception, the second power supply must act as a constant current source that can provide the solar array short circuit current at maximum. Figure 5 shows a schematic picture of string power supply[7]. Three diodes ensure that a voltage determined by $V_{gap}=I_sR_L$ is kept before secondary arc inception and all of I_s can flow between the strings once the string gap is short-circuited by plasma. The DC power supply V_L keeps the voltage across the load R_L that simulates the satellite load even after the secondary arc, which is true for a real satellite as the bus voltage is maintained by other strings.

Transient current that flows at the transition from a primary arc to a secondary arc heavily affects the outcome of the secondary arc. Figure 6 schematically shows a waveform of secondary arc current. There is an overshoot at the beginning that is caused by capacitances parallel to the string gap. The current also shows oscillation after the initial overshoot that is caused by inductance associated with the string circuit.

There are three types of capacitance, capacitance of polyimide insulator and adhesive

between cells and conductive substrate, capacitance of cell PN junction and output capacitance of power supply. The first two capacitances exist in a real satellite, but not the third one. The combination of the first two capacitances is represented by C_1 and C_2 in Fig.5. These values of capacitance can be calculated regarding the solar array circuit as a distributed parameter circuit. The output capacitance of power supply varies depending on its type. When we use a conventional DC power supply that acts either as a constant voltage source or a constant current source, the output capacitance is even larger than 100μF. Therefore if we use a conventional DC power supply to give V_{gap}, the overshoot is very large and it takes a relatively long time, sometimes even longer than 1ms, to reach the steady state value, I_s. The energy supplied by the output capacitance does not exist in reality. Therefore, if we use a conventional power supply, we give a significant amount of overstress to the gap. It is recommended that we use a solar array simulator that has a small output capacitance of 100nF or less. Also, if we operate the solar array simulator in a constant current mode before the arc inception, the effect of output capacitance becomes even smaller.

The oscillation caused by inductance may lower the probability of secondary arc occurrence. If there is too much inductance, the secondary arc current becomes negative crossing zero. As it crosses zero, it might be terminated. Therefore, cable length must be as short as possible to avoid the unnecessary oscillation. In real solar array circuit, however, there is also inductance. We need a good estimate on the value of inductance to make the experimental circuit as realistic as possible.

Test duration

Inverted potential gradient that is responsible for primary arcs occurs only occasionally in orbit. Another paper presented in this conference[8] describes statistical analysis of GEO plasma environment and estimate on total number of primary arcs. For a given set of satellite geometry and surface material property, potentials of satellite body and insulator surface are determined by the combination of solar incident angle and plasma parameters such as electron temperature, electron density, ion temperature and ion density [2,8,9]. Once these parameters are known, it is possible to calculate the potentials for each case within certain accuracy using commercial software such as NASCAP/GEO[10].

From the statistical analysis, we can calculate expected duration of any combination of the plasma parameters. From the numerical simulation we can calculate the differential voltage, ΔV, for each case of the plasma parameters. If we know the threshold of primary arc inception in terms of differential voltage, we can calculate how long a satellite goes through the inverted potential gradient exceeding the threshold by combining the statistical analysis and the numerical simulation. If the numerical simulation code can properly calculate the temporal profile of the

potentials, we can deduce the number of primary arc by dividing the duration exceeding the threshold by the time for ΔV to reach the threshold.

From the total number of expected arcs in orbit, we can set a number of primary arcs that a test solar array coupon must endure to prove that it has sufficient insulation strength against the sustained arc. The insulation strength may degrade over time in orbit as solar array surface is exposed to ultra-violet (UV) ray, radiation or thermal cycles. The effect of these environmental factors on the insulation strength is still unknown. If the effect is negligible and test results in the plasma environment discussed in Sec.II are scalable to the GEO environment, we can finish the ESD test quickly by using the plasma environment.

External Capacitance

As shown in Fig.1, capacitance of satellite body with respect to space, C_{sat}, and capacitance across coverglass, C_{cg}, provide energy to a primary arc. The coverglass capacitance has been a subject of controversy. As a primary arc occurs, it quickly discharges the satellite capacitance via the current path 1 in Fig.1. Then the satellite body potential that is very negative before the arc inception jumps to near zero. The coverglass potential then becomes positive by ΔV with respect to the plasma. If the satellite were in LEO-like dense plasma, the positive coverglass surface would attract electrons and a large amount of electrostatic energy could be provided to the primary arc plasma as the coverglass charge is neutralized [10,11,12]. In tenuous plasma like GEO, the conductivity of ambient plasma is so low that the arc plasma itself has to neutralize the coverglass charge. Therefore, there is no guarantee the mechanisms of coverglass charge neutralization in LEO environment and GEO environment are same. Leung *et al.* [13] carried out an experiment using a large solar array coupon and showed that the plasma extends itself as far as 0.7m with a speed of 9×10^3m/s in GEO-like environment.

Because we cannot place the whole solar array panel in a vacuum chamber, the majority of the coverglass capacitance is usually simulated by a capacitor connected to the external circuit, C_{ext}, shown in Fig.3. The external capacitance represents both C_{sat} and C_{cg}, but the satellite capacitance is so small that even the capacitance of circuit cable, typically 100pF/m, might exceed the value. Therefore, the external capacitance C_{ext} is determined by how we implement the role of coverglass capacitance that is missing from a test coupon. Typical $7cm \times 3.5cm \times 100\mu m$ size coverglass has about 700pF each. For a 10kW-class satellite the total capacitance coverglass may exceed 10μF.

The amount of external capacitor currently employed differs among research institutions, ranging from 100pF (i.e. C_{sat} only) to 1μF. Because the electrostatic energy is given by

$\frac{1}{2}C_{ext}V_b^2$, not $\frac{1}{2}C_{cg}\Delta V^2$ and $|V_b| >> \Delta V$, employing 1μF is equivalent to employing C_{cg} of entire solar array paddles. The effect of external capacitance on a primary arc is significant. The larger the external capacitance, the higher and longer current flows in the primary arc. In this paper we call the primary arc current provided by C_{ext} *blow-off current*. Solar cells are sometimes damaged and suffer contamination when too much energy is injected from the external capacitance [14,15].

How much of charge from coverglass flow as the blow-off current and how fast primary arc plasma becomes a secondary arc could be the different problems, though. Once a primary arc becomes a secondary arc, the solar array strings provide energy to the arc plasma and the coverglass capacitance might affect little. If we focus only on the transition from the primary arc to the secondary arc, we might not need to consider the entire solar array paddle as the source of capacitance. We have carried out an experiment to study the properties of primary arc and secondary arc plasmas while varying the value of C_{ext}. The specific purpose of the experiment is to find the value of external capacitance beyond that the transition process from a primary arc to a secondary arc differs little. If we find such an upper bound, we have the appropriate value as the coverglass capacitance for the ESD test on the secondary arc. If the value is reasonably small, we can represent the coverglass capacitance only by the solar array coupon panel and avoid the controversial external capacitance. Even if the value is so big that we need the external capacitance, we can limit the value of external capacitance and avoid unnecessary overestimate on the damage caused by primary arc.

In Fig.7 we show the experimental circuit layout. Figure 8 shows photograph of test coupons used for the experiment. The experimental circuit and test coupons are kept as similar as possible to the earlier works carried out at ONERA[16]. The present experiment is carried out in a vacuum chamber at KIT. The purpose of using the same setup is to share the experimental results carried out at two different institutions by keeping consistency. One of the authors (E. Amorim) stayed at KIT for four months to participate in the initial phase of experiment. The string power supply in the experimental circuit is the same as the one shown in Fig.5. Once a primary arc occurs, the coupon potential rises and the detector sends a signal to the delay pulse generator. After a preset time delay, the pulse generator sends a gate signal to the spectrometer (Hamamatsu Photonix C8808) that is equipped with an image intensifier. The gate width for the present experiment is kept to 1μs. By varying the time delay, we can study the plasma properties at the moment of transition from a primary arc to a secondary arc. We also use the quadruple mass spectrometer to identify species of gas ejected at arc inception. We irradiate the test coupon biased to -5kV by an electron beam of 5.2kV energy. The test coupon is made of two plates of copper glued on insulating substrate. The copper plates simulate solar cells. They are separated by 0.9mm. In order to simulate coverglass, PET film and SSM Teflon film are placed on top of

the copper plate. Because we want a primary arc occur at the focus of spectrometer, we put scars at one side of copper plate. Only a part of metallic edge of copper plate is exposed and the other part is insulated by narrow polyimide film. The video camera records flashes associated with primary arcs. We identify the arc position by identifying the positions of primary arcs and disregard the spectrometer data if the primary arc does not occur within the focus of spectrometer.

Table 2 summarizes the experimental results. We have tested three types of coupons varying their sizes. We judged whether a given arc current was a secondary arc current or not based on the three criteria; (1) the current exceeded 1.3A (2) the current pulse width was longer than 10μs (3) the current continued even after the end of blow-off current pulse. The number of secondary arcs was much less than the number of primary arcs. It should be noted that secondary arcs occurred even for zero external capacitance, $C_{ext}=0$. In Fig.9 we show current waveforms of secondary arcs for $C_{ext}=0$. For this particular case, the secondary arc current continued up to 90μs. There were several other cases of secondary arc though they didn't last as long as the case shown in Fig.9. In Fig.10 we show a current waveform of secondary arcs for $C_{ext}=100nF$. For this case the secondary arc current continued 12μs. Figure 11 plots duration of secondary arcs for different values of C_{ext}. In the figure the results of sample 2 and 3 are combined. In order to increase the number of data points, we have added the data taken in a different series of experiment, though the experimental setting was the same, to the data listed in Table.2. There seems no dependence of the secondary arc duration on the value of external capacitance.

Figure 12 shows a typical spectrum observed for the sample No.2 with $C_{ext}=12.5nF$. At this time, only the blow-off current was flowing and the amplitude was 3.6A. We have identified strong lines of copper (324.7nm and 327.4nm), C_2 swan band and hydrogen (656.3nm). Copper atoms come from the metallic electrode. Carbon molecules probably come from insulator near the electrode or adsorbed molecules. Hydrogen atoms come from adsorbed water molecules. In Fig. 13 we plot a temporal profile of total pressure inside the vacuum chamber and partial pressure of copper measured by the mass spectrometer. The spikes in the total pressure indicate that primary arcs occur and adsorbed molecules are desorbed due to heat. Although very weak, we see spikes in the copper signal that result from vaporization due to the primary arcs.

Figure 14 shows the strongest lines in each spectrum taken at various values of blow-off current. The horizontal axis is the blow-off current that was flowing when the gate of spectrometer was open. The peak values of blow-off current are proportional to the external capacitance. When the blow-off current is higher than 8A, the copper line of 324.7nm dominates for most of the cases. The result is reasonable if the current at the arc spot is maintained by metallic vapor plasma evaporated from the electrode surface. The ratio of the two strong copper lines is relatively constant once the copper lines dominate over other lines. Figure 14 also shows

the ratio of the intensity of 327.4nm to the intensity of 324.7nm. They show little scatter for the blow-off current higher than 8A. If we derive electron temperature from this ratio assuming that the arc plasma is in local thermodynamic equilibrium, the temperature is about 1000K. This temperature is a little too low for typical vacuum arc plasma. These two lines originate from two energy states separated only by 0.03eV. Therefore, it is very difficult to derive accurate temperature with the resolution of the spectrometer used in the experiment (±1.5nm). Nevertheless, the fact that the dominant spectrum lines and their ratio stay relatively same once the blow-off current exceeds a certain value, 8A, suggests that there is an upper limit on plasma property such as temperature even if we increase the blow-off current by increasing the external capacitance, C_{ext}. To find the upper limit on the plasma property, especially electron temperature because arc plasma conductivity depends on the temperature not on the density, we need either finer resolution of the optical spectrum or multiple sets of lines used for the temperature derivation.

The present experimental results favor the use of external capacitance, C_{ext}, as small as satellite capacitance, C_{sat}, only. Secondary arc occurs even for C_{ext}=0 and the spectrum differs little beyond 8A of the blow-off current. The experimental results presented in this paper are still preliminary, however. We need more detailed picture of how the primary arc plasma becomes a secondary arc by following the temporal variation of arc plasma properties. The final answer to the problem of the external capacitance will be obtained only after we know coupling mechanism of coverglass charge and primary arc current. To do so, we need to study arc plasma expansion with a large solar array coupon such as the one carried out by Leung *et al.* [13] in tenuous GEO-like plasma. The results will be used to determine the external capacitance for the test purposes other than insulation strength against sustained arc, such as contamination or power degradation due to repeated primary arcs[14].

Conclusion

In this paper we have discussed the state of our knowledge regarding the four issues concerning conditions of ESD test of GEO satellite solar arrays. The followings are the conclusions and proposed research topics necessary to improve the credibility of test results.

(1) Because the plasma environment gives the highest arc rate, we want to use the plasma environment if possible. To do so, however, we have to make sure that the test results in the plasma environment is the same as or at least scalable to the test results in the electron beam environment.

(2) The power supply that simulates the solar array string circuit should have output capacitance as small as possible. We need good estimates on capacitance and inductance of solar array string.

(3) It is possible to estimate the number of primary arcs during operational lifetime of a given satellite. To test the insulation strength against sustained arc we should verify that no sustained arc occur even after the same number of arcs occurs on a solar array coupon. The effect of long duration degradation of insulation material due to exposure to space environment needs to be clarified.

(4) Even if there is no external capacitance connected to a solar array coupon, a primary arc can become a secondary arc. Beyond a certain value of arc current, the metallic vapor becomes the dominant species of arc plasma. These preliminary results suggest that, if the test purpose is only to know whether sustained arc occurs or not, the satellite capacitance and only a fraction of total coverglass capacitance are sufficient as the external capacitance. We need to study temporal variation of arc plasma properties to verify this finding.

Environment	Electron beam	Plasma	Ion beam
Energy of charged particles	> 1 keV	~1eV	$\leq$ 1 keV
Background pressure	$\leq 10^{-6}$ Torr	$\geq 10^{-5}$ Torr	$\geq 10^{-5}$ Torr
Primary arc rate	low	very high	high
Plasma density	low	high	

Table 1:   Comparison of three environments of ESD tests used to produce inverted potential gradient on a solar array coupon

Sample number	C_{ext} (nF)	number of primary arcs	number of secondary arcs
2	0	45	0
2	1.5	34	0
2	6.8	58	0
2	12.5	79	9
2	50	60	0
2	100	70	1
3	0	82	3
3	12.5	89	1
3	100	102	24

Table 2:   Number of secondary arcs observed for different values of C_{ext}.
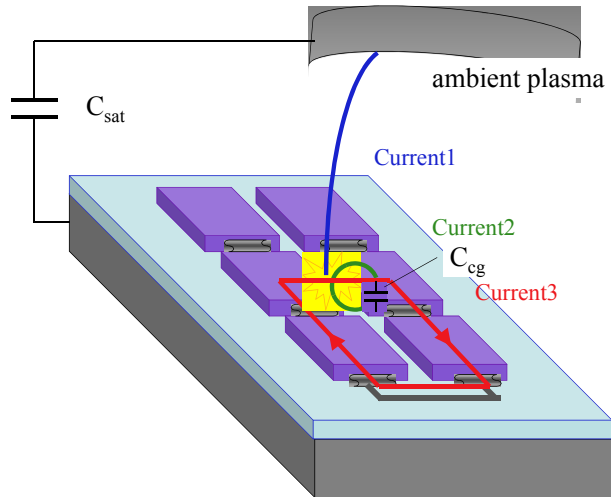
Figure 1. Schematic illustration of arc current paths.
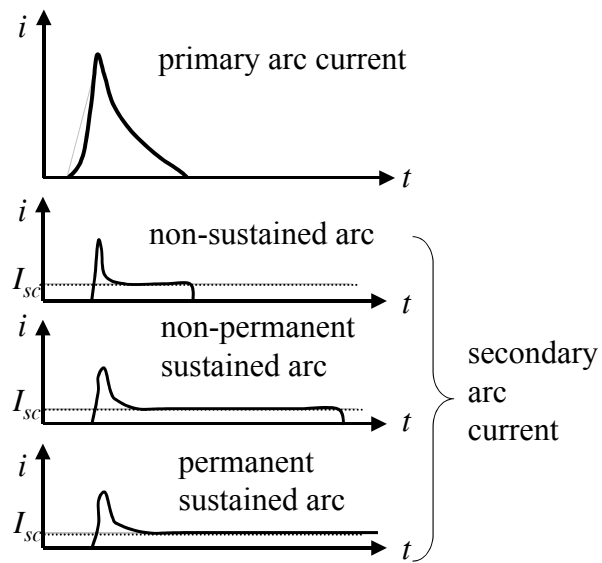
Figure 2. Definitions of various stages of secondary arc current.
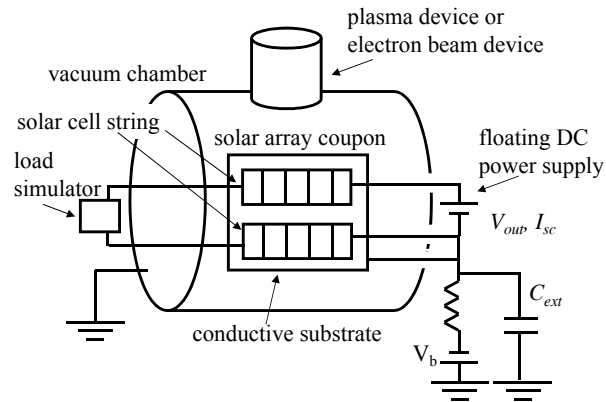
Figure 3.   Experimental layout of a typical ESD ground test with a solar array coupon.
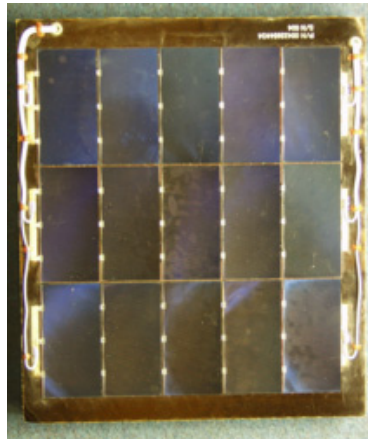
Figure 4.   Solar array coupon used for ETS8 solar array ESD test[2,6]
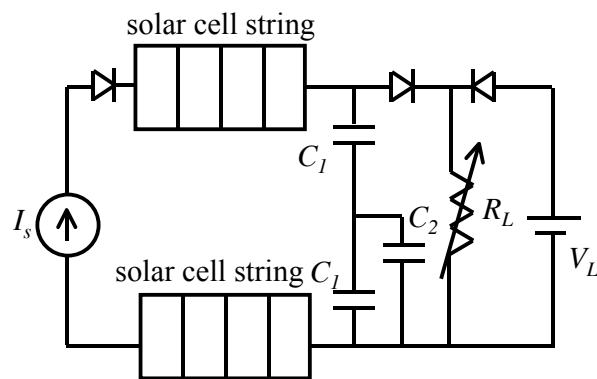
Figure 5.   Circuit layout of floating power supply described in Ref.7.
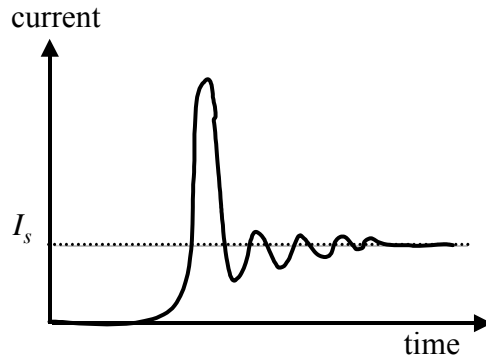
Figure 6. Schematic waveform of typical secondary arc current
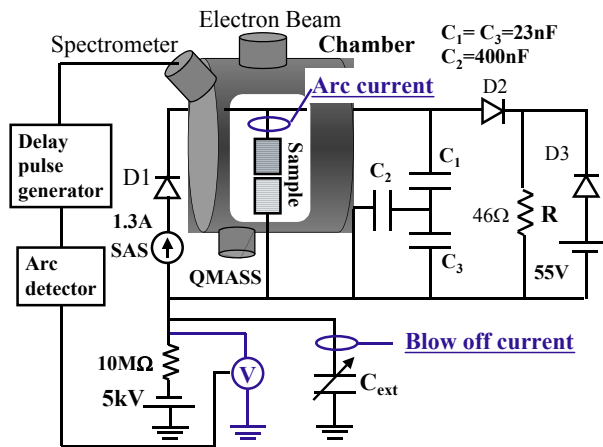
Figure 7. Schematic illustration of experimental circuit used to study the effects of external circuit
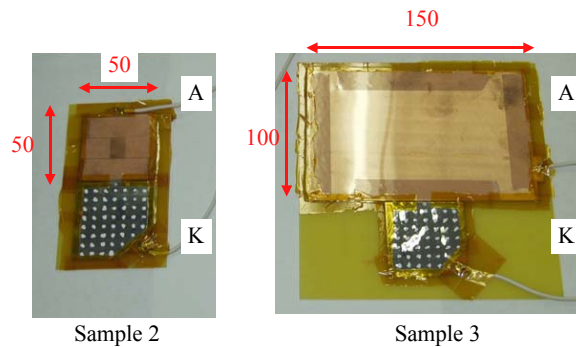
Figure 8. Photographs of test coupons used to study the effects of external circuit
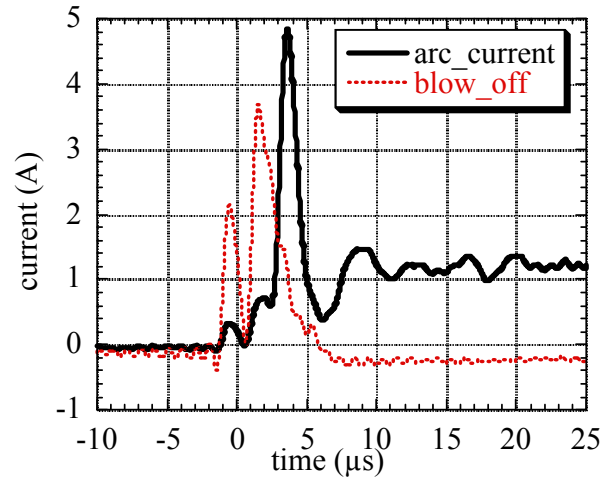
Figure 9. Example of waveforms of blow-off current and arc current with $C_{ext}=0$
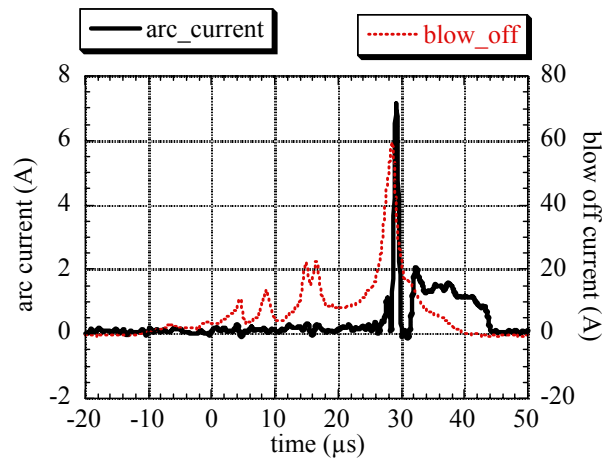
Figure 10. Example of waveforms of blow-off current and arc current with $C_{ext}=100nF$
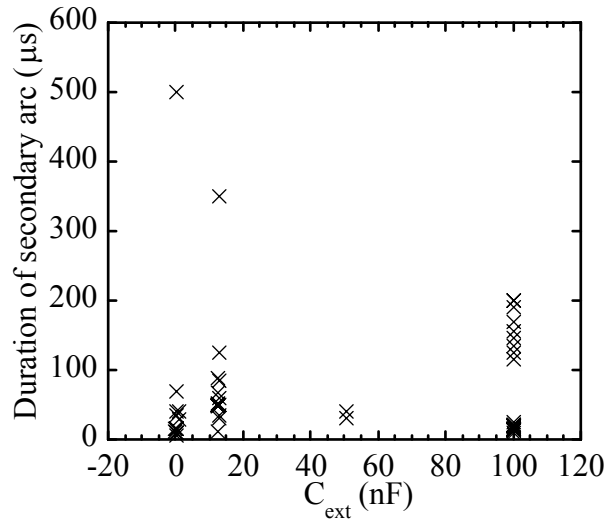
Figure 11.   Duration of secondary arc for different values of external capacitance, C_{ext}
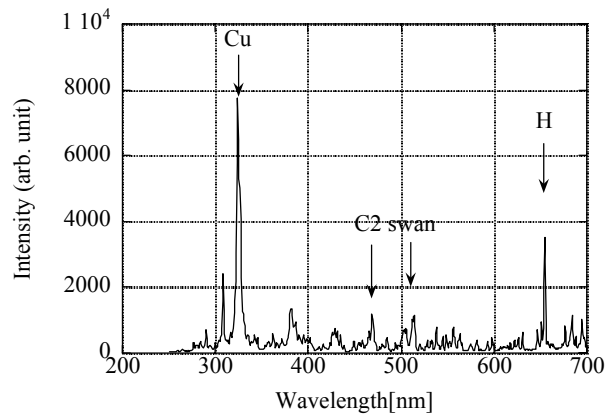
Figure 12.   Typical spectrum of arc plasma.
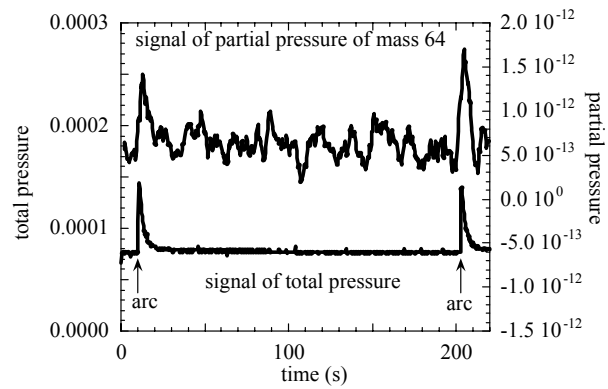
Figure 13.   Signals of mass spectrometer during experiment
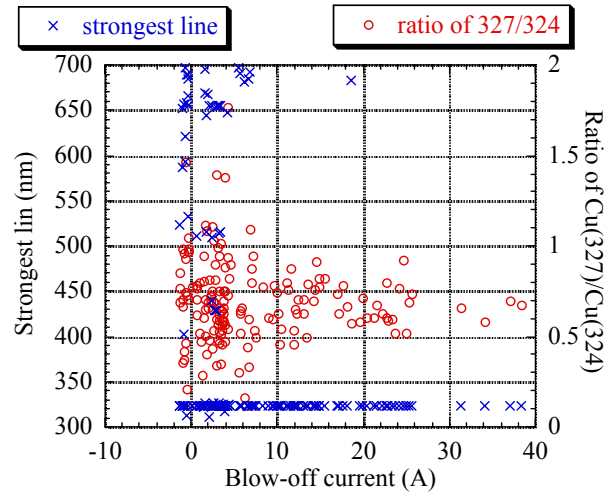
Figure 14. Strongest lines for different values of blow-off current. The ratio of two copper lines at each blow-off current is also shown.

References

1. Ferguson, D. C., Snyder, D. B., Vayner, B. V., and Galofaro, J. T., "Array Arcing in Orbit from LEO to GEO", AIAA paper 98-1002, January 1999.

2. Hastings,D.E., Garrett, H., "Spacecraft-Environmental Interactions", Cambridge Univ. Press, New York, 1996.

3. Cho, M., Ramasamy, R., Matsumoto, M., Toyoda, K., Nozaki, Y., and Takahashi, M., "Laboratory Tests on 110V Solar Arrays in a Simulated Geosynchronous Orbit Environment", Journal of Spacecraft and Rocket, Vol.40, No.2, pp.211-220, 2003.

4. Katz, I., Davis, V.A; and Snyder, D.B, "Mechanism for Spacecraft Charging Initiated Destruction of Solar Arrays in GEO", AIAA paper 98-1002, January 1998.

5. Bogus, K., Claassens, C., and Lechte, H., "Investigations & conclusions of the ECS-Solar-Array in-orbit Power Anomalies", Proceedings of 18th IEEE Photovoltaic Space Conference, October-1985, pp.368-375.

6. Cho, M., Ramasamy, M., Toyoda, K., Nozaki, Y., and Takahashi, M., "Laboratory Tests on 110-Volt Solar Arrays in Ion Thruster Plasma Environment", Journal of Spacecraft and Rocket, Vol.40, No.2, pp.221-229, 2003.

7. Payan, D., Schwander, D., Catani, J.P., "Risks of low voltage arcs sustained by the photovoltaic power of a satellite solar array during an electrostatic discharge. Solar Array Dynamic Simulator", Proceedings of 7th Spacecraft Charging Technology Conference, April-2001, ESA.

8. Satoh, T., Nakamura, M., Kawakita, S., Takahashi, M., Nozaki, Y., Toyoda, K., Cho, M., "Development of Solar Array for a Wideband Internetworking Engineering Test and Demonstration Satellite: System Design", 8th Spacecraft Charging Technology Conference, October-2003, Huntsville, USA.

9. Lai, S. T., Delia-Rose, D.J., "Spacecraft Charging at Geosynchronous Altitudes: New Evidence of Existence of Critical Temperature", J. Spacecraft and Rockets, 38, (2001), pp.922-928.

10. Rubin, A. G., Katz, I., Mandell, M., Schnuelle, G., Seen, P., Parks, D., Cassidy, J. and Roche, J. "A Three-dimensional Spacecraft-charging computer code in Space Systems and their interactions with Earth's Space Environment", in Progress in Astronautics and Aeronautics, Vol.71, H. Garret, C. Pike, Ed., pp.318-336. 1980

11. Cho, M., Ramasamy, R., Hikita, M., Tanaka, K., Sasaki, S., "Plasma Response to Arcing in Ionospheric Plasma Environment: Laboratory Experiment", J. Spacecraft and Rockets, May-June, pp.392-399, 2002.

12. Vaughn, J.A., Carruth Jr., M.R., Katz, I., Mandell M.J. and Jongeward, G.A., "Electrical Breakdown Currents on Large Spacecraft in Low Earth Orbit", J. Spacecraft and Rockets, Vol.31, pp.54-59, 1994.

13. Leung, P., "Plasma Phenomena Associated with Solar Array Discharge and Their Role in Scaling Coupon Test Results to a Full Panel", AIAA Paper 2002-0628, 40th Aerospace Sciences Meeting, January 2002.

14. Toyoda, K., Matsumoto, T., Cho, M., Nozaki, Y., Takahashi, M., "Power Reduction of Solar Arrays due to Arcing under Simulated GEO Environment", AIAA 2003-0682, 41st Aerospace Science Meeting, 6-9 January, Reno, USA, 2003

15. Toyoda, K., Cho, M., Satoh, T., Nakamura, M., Kawakita, S., Takahashi, M., Nozaki, "Development of Solar Array for a Wideband InterNetworking Satellite : ESD Test", 8th Spacecraft Charging Technology Conference, October-2003, Huntsville, USA

16. Levy, L., Sarrail, D., Viel, V., Amorim, E., Serrot, G., Bogus, K., "Secondary arcs on solar arrays: occurrence, thresholds, characteristics and induced damage", Proceedings of 7th Spacecraft Charging Technology Conference, April-2001, ESA

ELECTRON-BEAM-INDUCED ESD TRIGGERING DISCHARGE TESTS OF SOLAR ARRAYS FOR SPACE USE

Haruhisa Fujii

Department of Electrical Engineering, Nara National College of Technology
22, Yata-Cho, Yamatokoriyama, Nara, 639-1080 JAPAN
Phone: +81-743-55-6091
Fax: +81-743-55-6109
E-mail: fujii@elec.nara-k.ac.jp

Hideaki Koakutsu

Mitsubishi Electric Corporation, Japan

Abstract

This paper deals with the electron-beam irradiation experiments concerning the arcing discharge on the solar array.   It is very important to investigate this discharge phenomenon and offer a guideline to design solar arrays with high reliability.   We used a pair of real GaAs solar cells on a substrate as a sample.   The sample was biased to -9kV and the electron beam of the energy of 10keV was irradiated to the sample.   On that condition, the voltage from DC battery was applied to the gap between the cells.   The detrimental arcing did not occur even at the gap voltage of about 80V, although a few hundreds of ESD took place.

Therefore, the high voltage use of solar array, for example 100V, is thought not to cause sustained arcing discharge to destroy the satellite system if arrays are designed to lower the maximum voltage between cell strings with reasonable distance.

Introduction

Spacecraft charging problems appeared about 30 years ago [1].   After that, researches and developments for the spacecraft charging technology was conducted extensively [2, 3, 4].   As the results, satellite systems reliable to the spacecraft charging have been developed and operated in space.   In these R&D's for the spacecraft charging technology, the protection against the surface charging on satellites was the main subject.   However, in 1997 TEMPO-2 satellite was troubled on the geostationary orbit [5].   The electric power of the satellite was supplied in 100V.   From the investigation of the accident, the possibility of arcing discharge at the high voltage terminal between the solar cell strings was pointed out [6].   Since then investigations have been conducted in order to make the arcing discharge mechanism leading to detrimental failure of satellites clear [7].   However, it seems that the mechanism and the condition to cause arcing discharge are not yet clear.

From these viewpoints, we intended to make the mechanism clear by investigating discharge characteristics by means of the electron beam irradiation method and to reflect the results to the solar array design for future high-power satellites.   As a first step of our investigation, a pair of real GaAs cells for space use was used as a sample.   Inverted potential gradient as one condition causing discharges was formed on the sample by negatively biasing

the sample and by irradiating electron beam to it. By measuring transient currents and observing discharge lights induced at the time of the occurrence of electrostatic discharge (ESD) we carried out the experiments.

This paper describes the experimental results and the discussion.

Experimental Procedure

Figure 1 shows the sample configuration of a pair of real GaAs cells. The size of a GaAs cell was 76x37mm^2. The cells with cover glasses were bonded onto the 1mm-thick 100x100mm^2 aluminum plate (substrate) covered with 0.025mm-thick Kapton film. The long sides of the cells were opposed each other with the gap distance of d (mm). The three sides of the cell except for the gap side were covered with silicone adhesive in order to make discharges occur at the gap only.

Figure 2 shows the experimental setup to investigate the electron-beam induced discharge characteristics. After one sample was set in a vacuum chamber, the chamber was evacuated to the pressure of about 1.3x10^{-4}Pa by a rotary pump and a turbo-molecular pump.

The sample was biased to -9kV (V_b) by DC power supply. Then electron beam of the energy of 10keV was irradiated to the sample. And the beam current density (J_b) was about 0.1-0.3nA/cm^2 at the sample position. Due to this method the surfaces of the cell's cover glasses were irradiated with electrons of the energy of 1keV. Therefore the surfaces were expected to charge up positively against the cells and the substrate due to the secondary electron emission yield characteristics of the cover glass, that is, the inverted potential gradient was formed on the cover glasses. DC voltage V_a by connecting 9V batteries in series to suppress the influence of the capacitance of DC power supply was applied between the cell's gap to simulate the potential difference between cell strings on solar array.

Two current monitors (Pearson 411 and 4100) were used to measure transient currents at the time of the occurrence of discharge. One transient current, cell current I_c, flows the loop current path including the cell gap and the other, substrate current I_s, is the current flow between the sample and the earthed ground. The occurrence of the discharge was also detected from the abrupt change of the pressure which was always monitored by an ionization gauge in the chamber. Photographs were also taken out of the window of the chamber.

As shown in Fig.2, a capacitance C_a (=2x30.9nF) was inserted in parallel with the DC power supply (V_b). This capacitance simulates that of all cover glasses on the solar array panel wing of a typical real satellite.

All experiments were done at room temperature.

Experimental Results

We carried out the experiments according to the procedure described above under the several conditions as parameters of the cell's gap voltage V_a, the gap distance d between the

cells, and the existence of the scratched part in the cell's gap.

We first describe the results on the influence of the cell's gap voltage V_a in the case of the gap distance d=0.8mm.   Figure 3 (a) shows an example of the waveforms of the transient currents, I_c and I_s, observed in the case of a discharge occurred at V_a=77V.   And Fig.3 (b) shows the photograph of the light emission during about 2 minutes including the instant of the discharge occurrence. I_c in Fig.3 (a) continues for 25 microseconds after being triggered by ESD. I_s started to increase after the ESD, and at about 7 microseconds the current I_s reached the peak. Although the current I_s abruptly decreased after that, the cell current I_c continued to flow.   This discharge occurred near the center of the gap as seen in Fig.3 (b).   Also, straight and weak light emissions seen in this photograph continued until the occurrence of the main discharge.   Although the discharges like this occurred about 100 times, arcing discharge sustaining longer than 30 microseconds did not occur in this sample.   Therefore there was no detrimental damage on the cell's gap.

Next, an example of the waveform of the cell current I_c and the photograph of the discharge light occurred on the sample of d=0.8mm and V_a=30V are shown in Fig.4.   This is the 67th discharge shown in Fig.5.   The waveform of I_c shows that it continued for about 18 microseconds.   Weak light emission at the gap apart from the discharge point was also observed as shown in Fig.4 (a).   Although the sustaining time of the cell current changed with each discharge, as a whole, it had a tendency to become long with the applied voltage V_a. From Fig.5 we can also see that the time-to-discharge gradually became long with the number of discharge.

As the possibility, that the existence of the scratched part of the insulating film in the cell gap might cause the sustained arc, has been pointed out, we next investigated the influence by scratching the Kapton film in the cell gap.   Figure 6 shows the photograph of the scratched part.   This sample was subjected to the experiment under the condition of d=0.8mm and V_a=30V.   In this sample discharges occurred 190 times.   Figure 7 shows a typical example of the waveforms of I_c and I_s and the photograph of the light emissions including the instant of a discharge.   In this sample most of discharges occurred at the scratched part.   The waveforms of the transient currents at the discharge were similar to those of the other samples without the scratched part as shown in Fig.3 (a) and 4 (a).   That is, each waveform of the cell current has the two parts, the initial current triggered by ESD and the following secondary arc current. The peak of the secondary arc current is thought to be larger than the non-scratched samples.

We also carried out the experiment using the sample with the gap distance d=0.5mm at V_a=30V.   In this case, discharges occurred about 300 times in the cell gap.   Figure 8 shows a typical waveform of I_c and the photograph of the discharge light.   The value of the plateau of the secondary arc current is thought to be similar to the other cases.   No weak light emission before the discharge was, however, observed as shown in Fig.8 (b).

We measured the resistance of the cell gap on the sample after each experiment in the vacuum chamber.   The resistances in all samples were beyond 10Mohm.

Discussions

From the waveforms of I_c and I_s we speculate the discharge mechanism on solar array where the inverted potential gradient is formed.

Figure 9 shows the potential distribution in the neighborhood of the cell gap.   In this calculation, we assume that the surface potential of about +800V on the cover glass against the substrate [8] is formed by positive charging due to secondary electron emission and that the voltage between the cells is 50V and the negative terminal is grounded to the substrate as shown in Fig.2.   From Fig.9 we can see that both upper edges of the cells have higher electric field because of the dense concentration of the equi-potential lines and that the potential distribution over the cell gap expands to free space and the potential gradient exists on the cover glass.   Therefore the electron emission causing ESD starts at the triple junctions of the upper edges of the cells where the equi-potential lines concentrate.   The ESD generates locally dense plasma near the cell gap and induces current flow at the cell gap.   At the same time the plasma diffuses around the cell sample.   By the diffusing plasma the current through the sample substrate, substrate current I_s, increases gradually after the ESD.   This transient current is supplied from the capacitance C_a charged by the negative DC power supply.   In this stage, the main current channel changes to the substrate current.   Then the cell current I_c becomes unstable.   On the other hand, when the charges in the capacitor are almost lost to the grounded chamber wall, the plasma enhanced by the substrate current also diffuses to the cell gap.   The diffused plasma causes the increase of the current through the cell gap.   The cell current continues to sustain as secondary arc until the plasma declines to the chamber wall. The plasma density generated near the cell gap and the voltage V_a below about 80V are not enough to drive the secondary arc to sustained arc.

By the way, as seen in the photographs of the discharge light, Fig.3 (b), 4 (b) and 7 (b), straight and weak light emissions continuing for a few minutes on the cover glass were observed before the instant of discharge.   The light is assumed to be cathode-luminescence due to the impact of electrons emitted from the cell gap.   This weak light emission could not be always seen from the early stage of the experiment.   We could see such lights after the discharges occurred frequently.   Figure 10 shows the examples of the charts recording the pressures in the chamber during the experiments.   Figure 10 (a) is the pressure change near the time of the discharge shown in Fig.4.   In this Fig.10 (a) the pressure gradually increased before the discharge.   This shows that the gas was released by the continuous impact of electrons.   Therefore the cathode-luminescent light is seemed to be due to the impact of electrons emitted from some emission site generated by frequent discharges.   Because the discharge at the comparatively early stage was not accompanied with pre-discharge light as shown in Fig.8 (b), the gradual increase of the pressure was not recorded as seen in Fig.10 (b). These emitted low-energy electrons move along the line of the electric force generated by the potential distribution near the cell gap shown in Fig.9.

At last we discuss the influence of the damaged Kapton film between the cell gap.   We gave the Kapton film damage by scratching as shown in Fig.6.   In the sample, discharges were occurred well at the cell gap near the scratched part.   However, sustained arc did not occur similarly to the samples with the insulatingly sound cell gaps.   Therefore it is thought

that the secondary arc mainly flowed over the cell gap.   The value of the plateau of the secondary arc in the scratched sample was about twice larger than that in the non-scratched samples as shown Fig.7.   It is the reason why the cell current I_c is enhanced by the electron emission from the substrate through the scratched part.

Although the possibility of occurrence of the detrimental arcing discharges, sustained arcs, cannot be completely denied, it is thought to be very small from our experimental results.

Conclusion

In order to verify the possibility of the occurrence of the detrimental arcing discharge on the solar array where inverted potential gradient is formed, we carried out the model experiment using real GaAs solar cell samples by means of electron-beam irradiation. Obtained experimental results are as follows.

(1) In the cases of the cell gap distances of 0.5mm and 0.8mm, the voltage of the gap below 80V did not cause sustained arcing discharge, although the ESD-induced secondary arcs occurred a few hundreds times at the cell gap.
(2) The sustained arc did not occur even though there was scratched part in the Kapton film at the cell gap.

In the present study, the experimental parameters were not so many.   So, we will continue the experiments by changing parameters such as the capacitances or the cell gap.
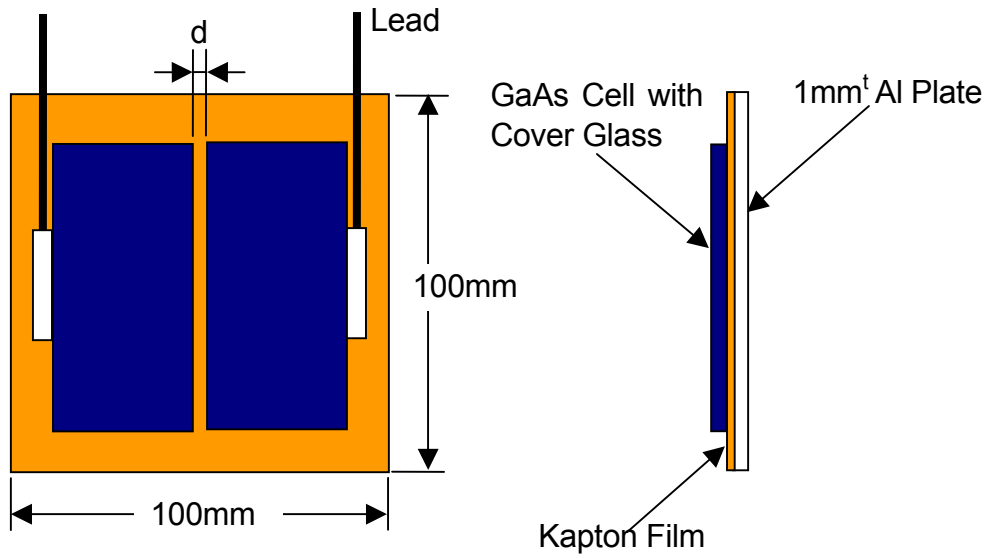
Figure 1.   Sample configuration
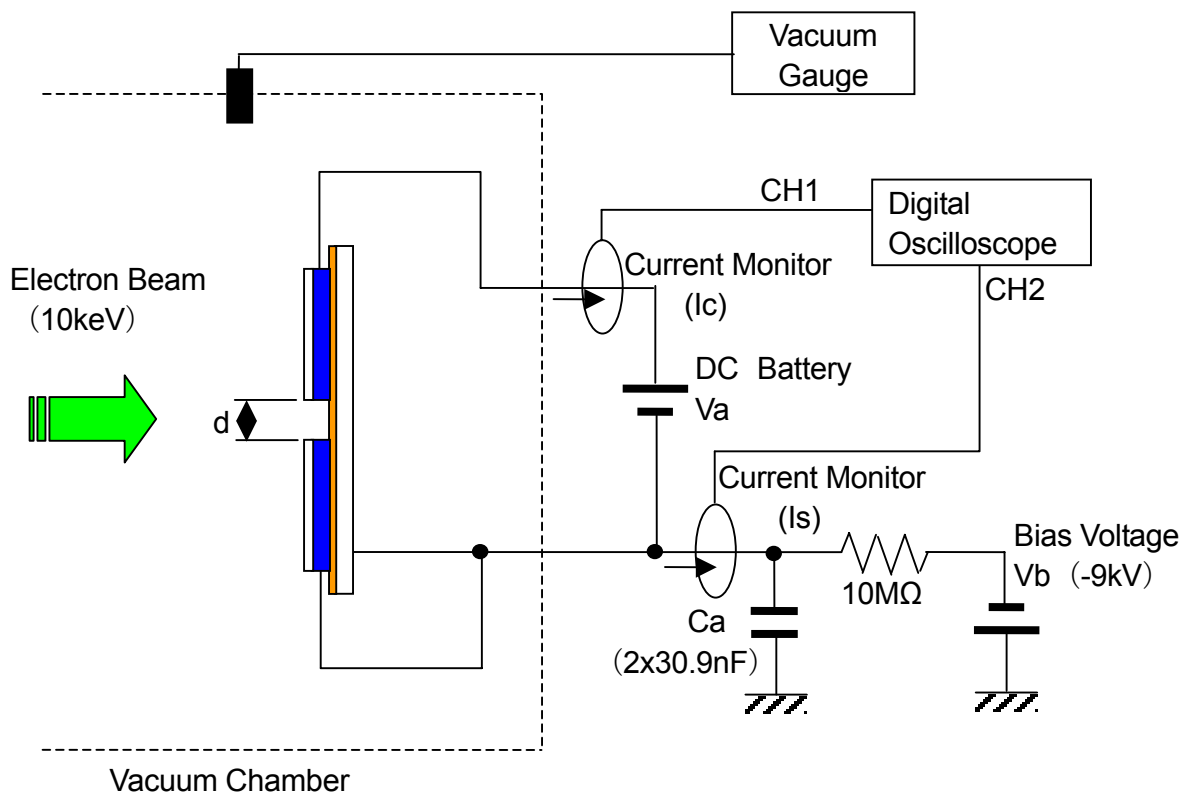
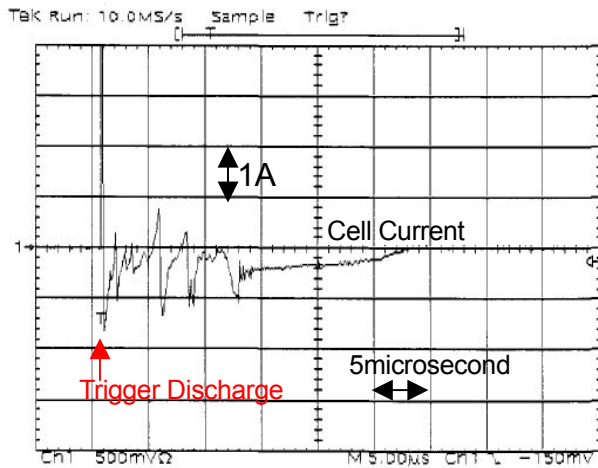**Figure 2.   Experimental setup**
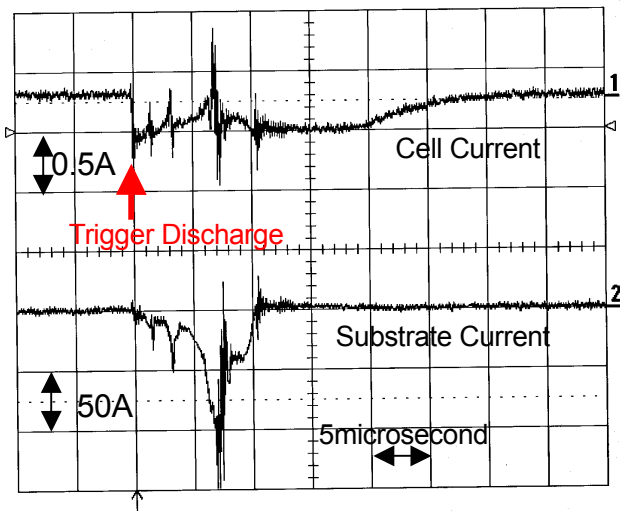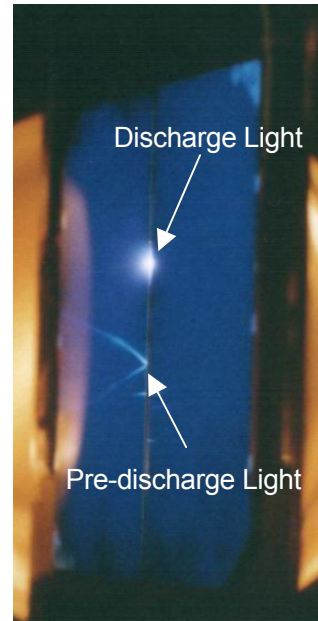
(a) Waveforms of transient currents　　　　(b) Photograph of light

Figure 3.　Example of the waveforms of transient currents and the discharge light in the case of d=0.8mm and V_a=77V.
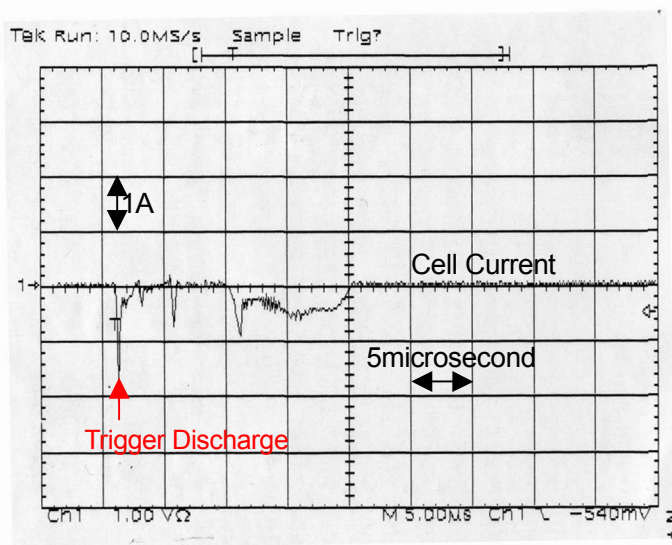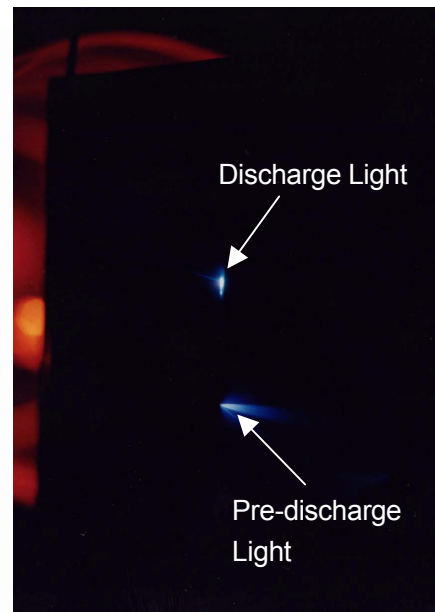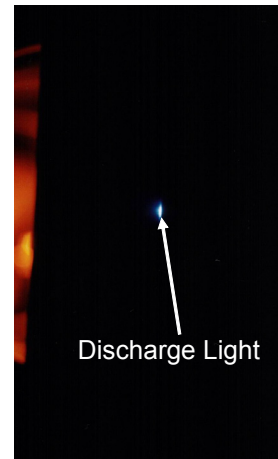

(a) Waveform of transient current　　　　(b) Photograph of light

Figure 4.　Example of the waveform of transient current and the discharge light in the case of d=0.8mm and V_a=30V.
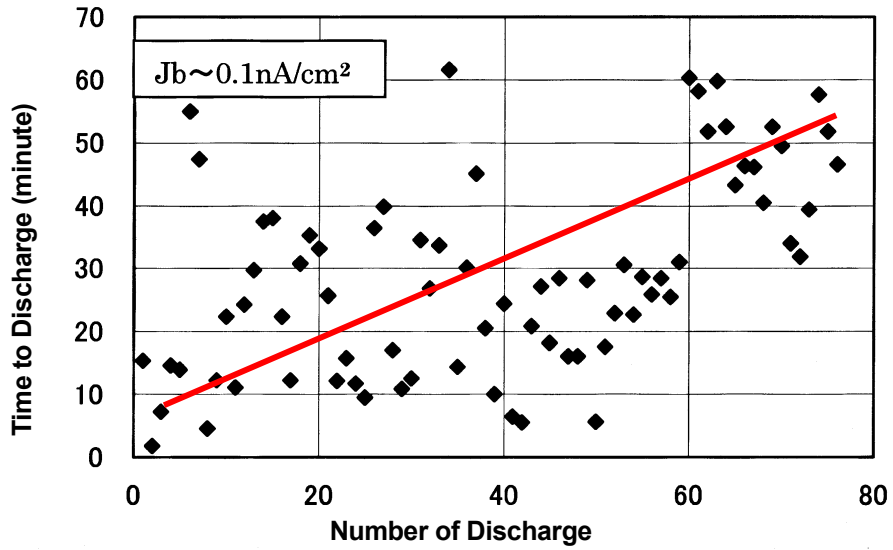
Figure 5. Dependence of the time-to-discharge on the number of discharge in the case of d=0.8mm and V_a=30V.
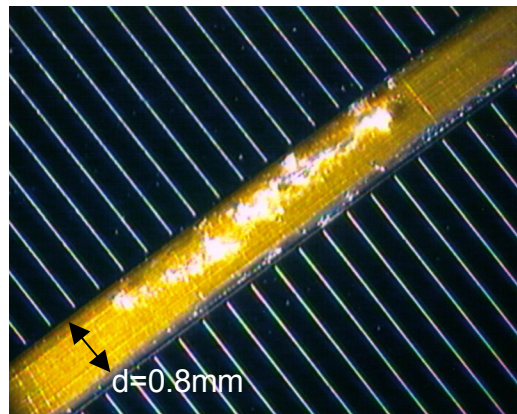
Figure 6. Photograph of scratched part of the cell gap.
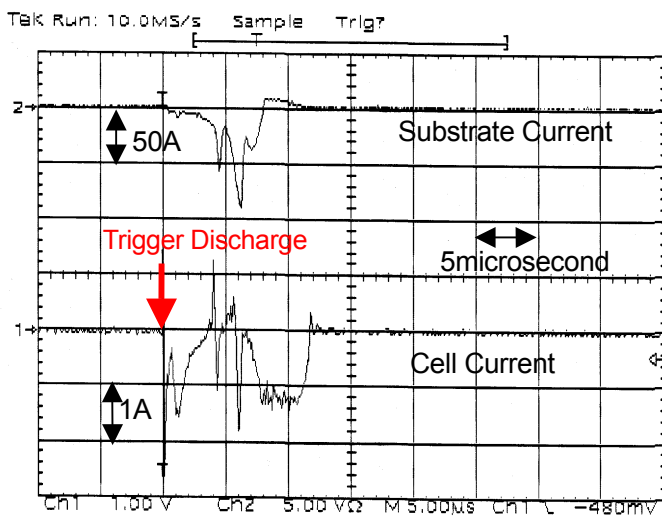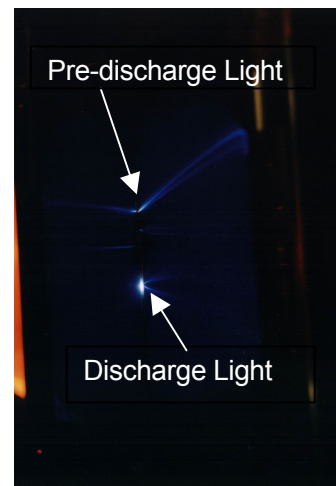
(a) Waveforms of transient currents   (b) Photograph of discharge light

Figure 7. Example of the waveforms of transient currents and the discharge light of the scratched sample at d=0.8mm and V_a=30V.
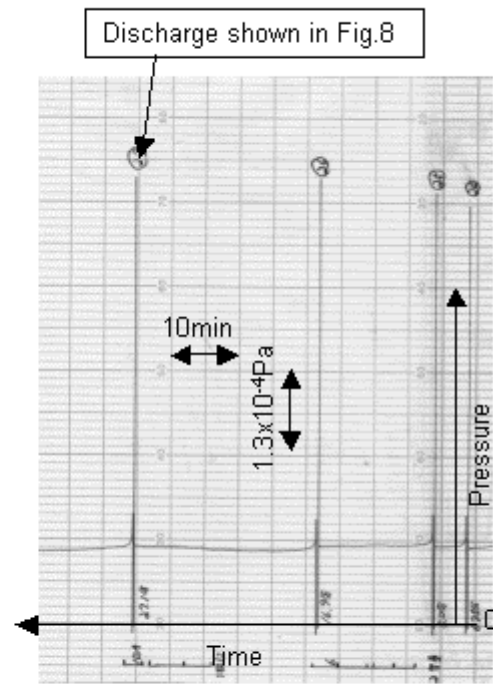
(a) Waveform of transient current

(b) Photograph of light

Figure 8.   Example of the waveform of the cell current and the discharge light in the case of d=0.5mm and Va=30V
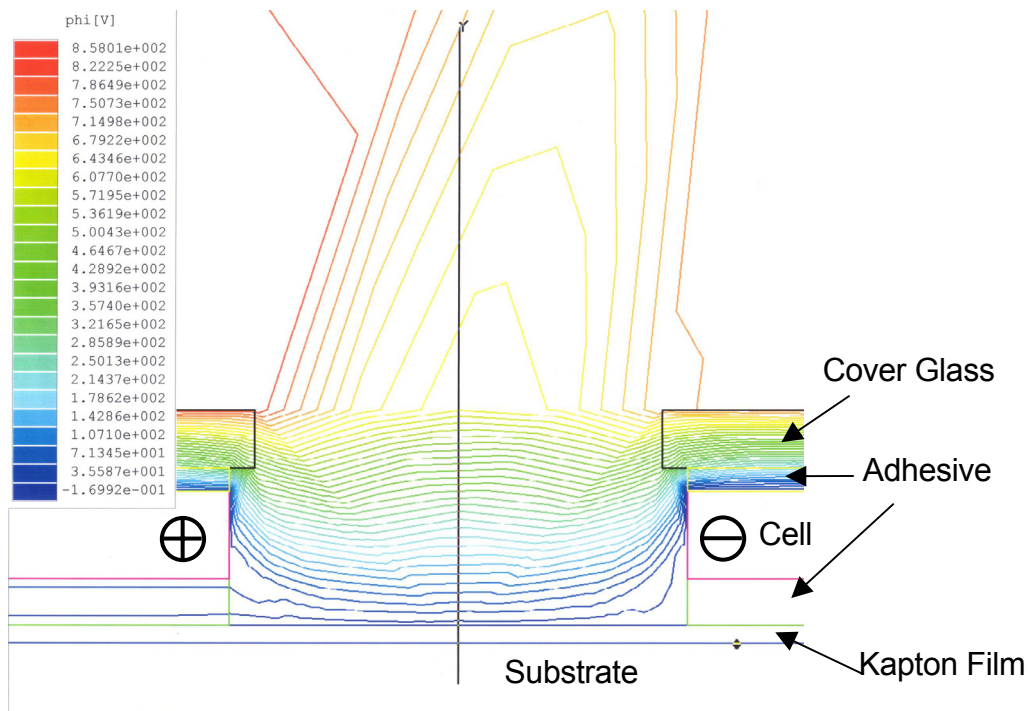
Figure 9.   Potential distribution near the cell gap.
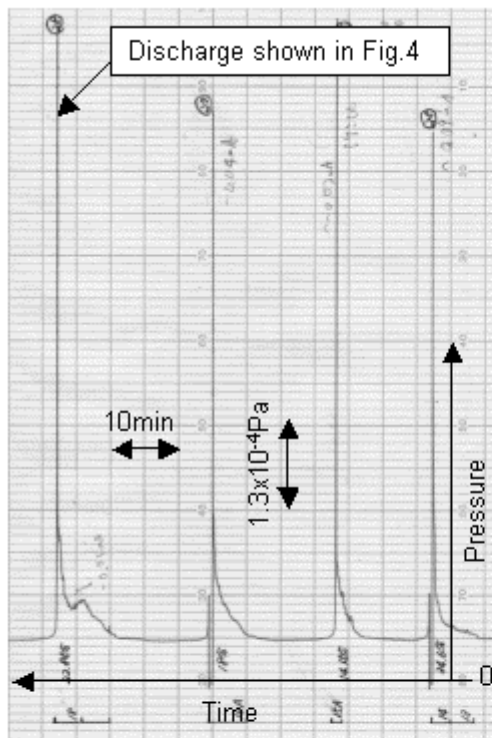
(a) d=0.8mm, V_a=30V

(b) d=0.5mm, V_a=30V

Figure 10.   Example of the pressure change during experiment

References

1. H. B. Garrett, "The charging of spacecraft surfaces", Rev. Geophys. Space Phys., Vol.19, pp.577-616 (1981)

2. Proc. Spacecraft Charging Technology, AFGL-TR-77-0051/NASA TMX-73537 (1977)

3. Spacecraft Charging Technology -1978, NASA CP-2071/AFGL-TR-79-0082 (1979)

4. Spacecraft Charging Technology 1980, NASA CP-2182/AFGL-TR-81-0270 (1981)

5. I. Katz, V. A. Davis, E. A. Robertson and D. B. Snyder, "ESD initiated failures on high voltage satellite", Space Environments and Effects, Flight Experiments Workshop, (1998)

6. I. Katz, V. A. Davis and D. B. Snyder, "Mechanism for spacecraft charging initiated destruction of solar arrays in GEO", 36th Aerospace Sci. Meeting, AIAA-98-1002 (1998)

7. For example, L. Leby, D. Sarrail, V. Viel, E. Amorim, G. Serrot and K. Bogus, "Secondary arcs on solar arrays: Occurrence, thresholds, characteristics and induced damage", Proc. 7th Spacecraft Charging Technology Conf., ESA SP-476, pp.377-382 (2001)

8. M. Cho, private communication

GROUND EXPERIMENT AND NUMRICAL SIMULATION OF SPACECRAFT ARCING IN AMBIENT PLASMA ENVIRONMENTS

Takahisa Masuyama
Department of Mechanical Science and Bioengineering
Graduate School of Engineering Science, Osaka University
1-3, Machikaneyama, Toyonaka, Osaka 560-8531, Japan
Phone: +81-6-6850-6178
Fax: +81-6-6850-6179
E-mail: tahara@me.es.osaka-u.ac.jp

Masato Nagata
Tatsuo Onishi
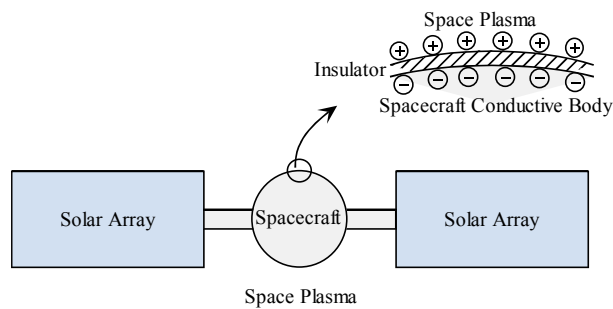**Hirokazu Tahara**
Takao Yoshikawa
Osaka University, Japan

Abstract

In the future, LEO spacecraft will be larger and higher powered.   Because of the balance of leakage currents through ambient space plasma, their main conductive body will have a higher negative potential without plasma contactor operation.   When spacecraft operate with a higher voltage, more intensive arcing is suspected to occur on the surface.   In this study, ground-based experiment and Direct-Simulation-Monte-Carlo Particle-In-Cell plasma simulation were carried out to understand the arcing phenomenon and to examine influences of ambient space plasma on the arcing process.   Simulating plasmas were generated by electron cyclotron resonance discharge.   When arcing occurred on negatively-biased anodized aluminum sample (AAS) plates in the plasma environment, the time variations in arc current and bias voltage were measured.   Arc spot diameter was also measured.   The experimental results showed that both the peak arc current and the total charge emitted by arcing increased with initial charging voltage and neutral particle number density. The diameter of arc spots increased with initial charging voltage although it was almost constant regardless of neutral particle density.   The calculated results showed that neutral particles in addition to charged particles around spacecraft played an important role in expansion of arc plasma causing the arcing characteristics.   Accordingly, high voltage operation of LEO spacecraft might bring drastic degradation of AAS by arcing depending on ambient plasma conditions.

Introduction

Spacecraft are in a severe environment in space.   Their surfaces are exposed to energetic and reactive particles, such as electrons, ions, protons and oxygen atoms and ultraviolet light, including particles exhausted from plasma thrusters, during space missions.   The environmental effect plays a crucial role in determining the spacecraft's reliability and lifetime [1].   Although the number density of ions such as oxygen and nitrogen is smaller than that of atomic oxygen in LEO, electrostatic interactions between the surface materials and the ambient plasma, such as negative or positive sheath creation, and charging and arcing phenomena, frequently occur.   The ions are accelerated in a negative potential sheath on a solar array, and the current generated by the solar array is leaked by impact of the ions; the solar array is still degraded by sputtering and arcing due to the collected ions [2],[3].   Accordingly, the environmental factors cause changes of chemical structures of spacecraft materials and their optical and/or electrical properties [4],[5].   In GEO satellites, it is well-known that the electrical breakdown of negative charging on their insulating surfaces causes intensive damages in

the systems.   In plasma contactor operations, the negative charging is expected to be mitigated by ions attracted from the plasma, resulting in surface degradation as well as in cases with high voltage solar arrays [6]-[8].   The mechanism of the material degradation, the structure of electrical sheaths, and the charging and arcing processes must be understood.

Figure 1.   Feature of charging on spacecraft surface insulators.

**(a) Spacecraft body.**

(b) Near arc spot.
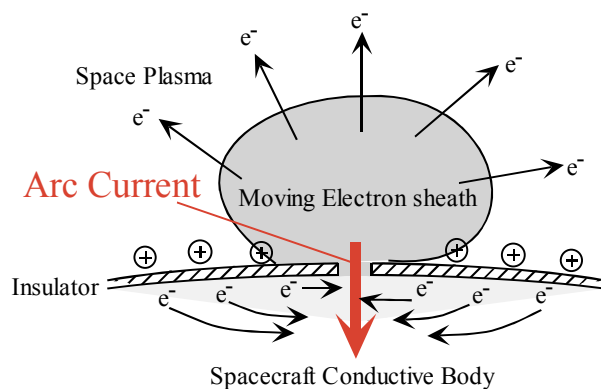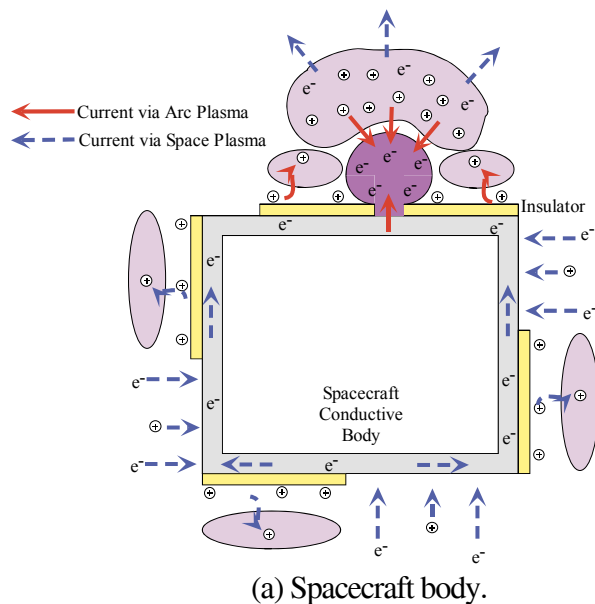
Figure 2.   Current paths for arcing on surface insulator between spacecraft conductive body and space plasma.

In Osaka University, the structure of an ion sheath created around a high voltage solar array and the degradation of surface materials near the array due to high energy ion bombardment have been investigated [2],[3],[5].   The mitigation of negative charging by plasma flow, i.e. the feature of plasma contactor operations, has also been studied [6]-[8].

In the future, LEO spacecraft will be larger and higher powered.   Because of the balance of leakage currents through ambient space plasma, their main conductive body will have a higher negative potential without plasma contactor operation.   When spacecraft operate with a higher voltage, more intensive arcing is suspected to occur on the spacecraft surface.   In this study, ground-based experiment is carried out to understand this phenomenon and to examine influences of ambient space plasma on the arcing process.   Simulating plasmas are generated by electron cyclotron resonance (ECR) discharge.   Arcing characteristics of negatively-biased anodized aluminum sample (AAS) plates in the plasma environment are investigated.   When arcing occurs on the plate, the time variations in arc current and bias voltage are measured.   Arc spot diameter is also measured. Furthermore, Direct-Simulation-Monte-Carlo Particle-In-Cell (DSMC-PIC) plasma simulation is conducted to understand features of plasma expanding from an arc spot on a spacecraft surface into the ambient plasma just after arcing.

Hazard of Drastic Destruction of Spacecraft Surface Materials by Arcing in Plasma Environment

In general, the spacecraft conductive body, as shown in Fig.1, has a negative potential, near solar array voltage, on potential of space plasma.   It is called absolute negative charging.   Then, positive charging occurs on an insulator of the spacecraft surface.   The large insulator works as a capacitor with a high capacitance.   As shown in Fig.2(a), if electric breakdown occurs between the spacecraft conductive body and space plasma, i.e. destruction of the insulator by arcing, arc currents flow through several paths until neutralization of charge is finished.   As a result, the arc current flowing from space plasma to the arc point of the spacecraft conductive body, as shown in Fig.2(b), is very high because of the high capacitance of the insulator.   The arcing is suspected to intensively degrade insulator materials of spacecraft surface, specially with a high voltage solar array.   Furthermore, the arcing characteristics are considered to depend on feature of space plasmas near spacecraft surface because interaction between electrons extracted from the arc spot and the ambient space plasma is expected to occur.   Intensive arcing is suspected to occur in some ambient plasma environment.
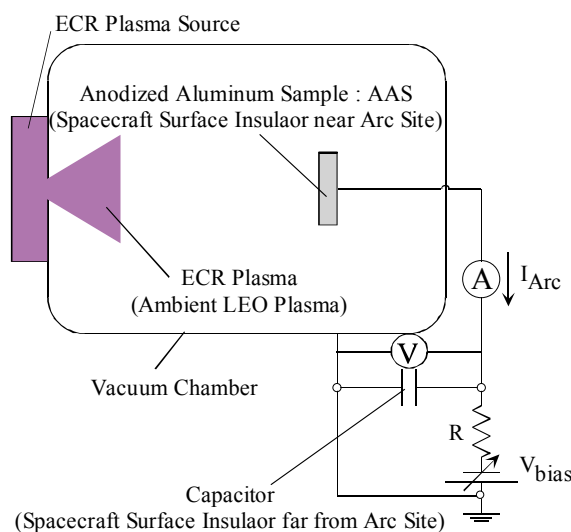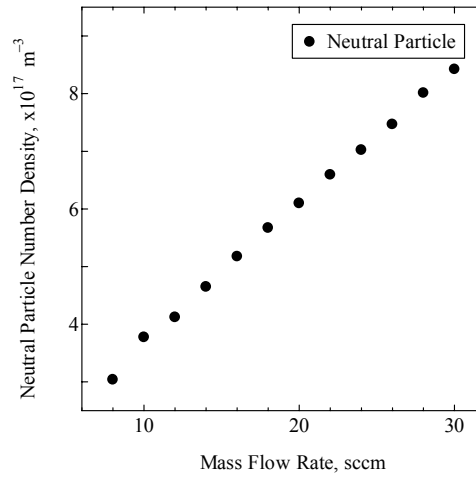

Figure 3.   Experimental system for arcing of negatively-biased anodized aluminum sample (AAS) plates in plasma environment.
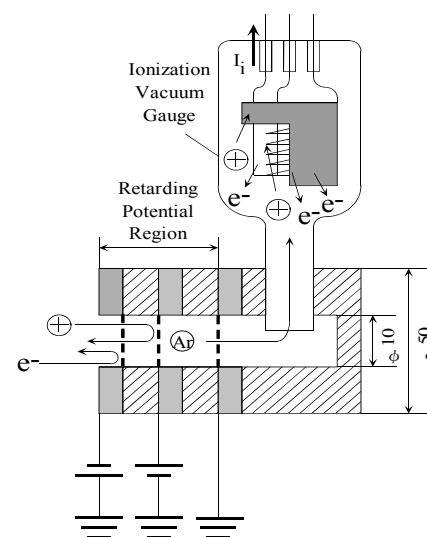
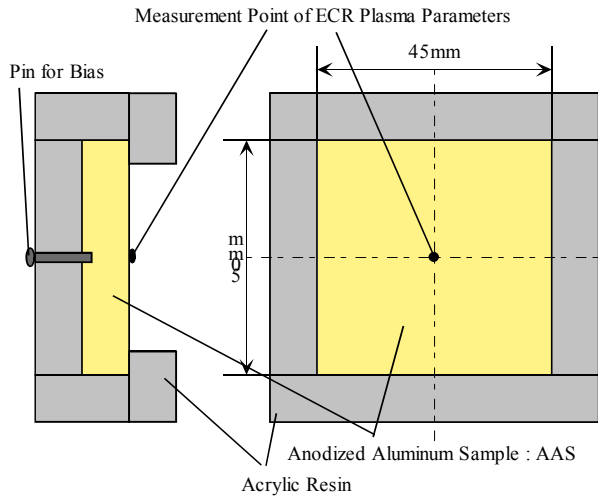**Figure 4.   Configuration of retarding-potential-type neutral particle probe.**
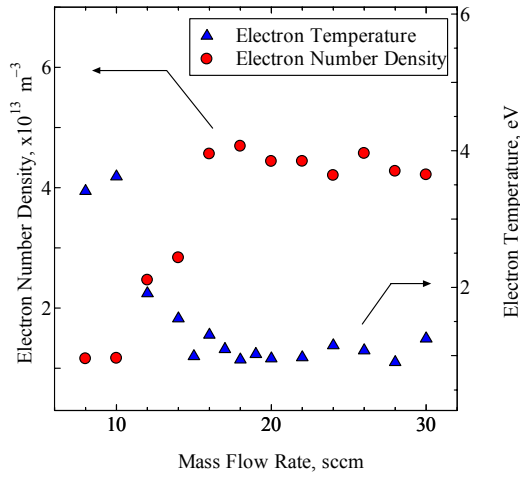
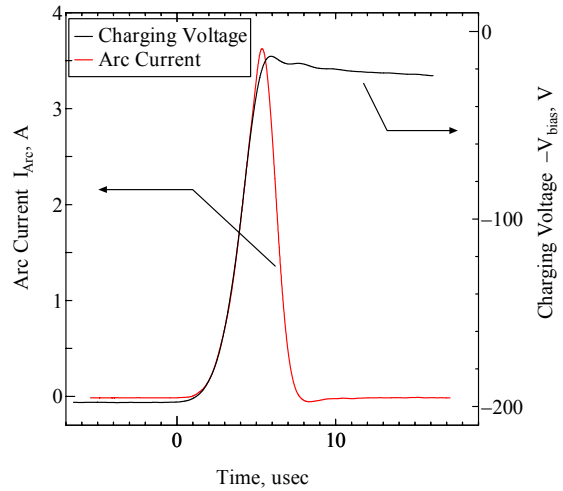(a) Electron number density and electron temperature.   (b) Neutral particle number density.

Figure 5.   Plasma properties measured at center of AAS plate located 660 mm downstream from plasma source exit.   The microwave input power is 300 W.

Figure 6.   Configuration of sample holder of negatively-biased AAS plates.

Figure 7.   Typical time variations in charging voltage and arc current for arcing of AAS plate in plasma environment.

Experimental Apparatus

Figure 3 shows the experimental system for arcing of negatively-biased anodized aluminum sample (AAS) plates in plasma environment.   The experimental facility developed in Osaka University mainly consists of a vacuum tank, a vacuum pump system, a plasma source and an AAS plate [9].   The electron cyclotron resonance (ECR) plasma source is set on a flange of the large stainless vacuum tank 0.7 m in diameter x 1.5 m long.   The main vacuum pump is an oil-free turbo-molecular pump with a high pumping speed of 5 m^3/s.   The tank pressure is kept some 10^{-3} Pa during all experiments.

Argon plasmas simulating spacecraft ambient plasma are produced by ECR discharge. Microwaves of maximum 1 kW and 2.45 GHz are introduced into the ECR discharge chamber.   An orifice is set to the downstream exit of the discharge chamber to produce a low-density plasma.

Electron number density and electron temperature are measured with a Langmuir probe. Neutral particle number density is also measured by a retarding-potential-type neutral particle probe shown in Fig.4.

Figure 5 shows the plasma properties measured at the center of the AAS plate located 660 mm downstream from the plasma source exit. The microwave input power is 300 W. When the argon flow rate increases from 8 sccm, the electron number density increases from $1.2 \times 10^{13} \text{m}^{-3}$ and the electron temperature decreases from 4.0 eV. Over a flow rate of 16 sccm, they saturate with 4.5×10^{13} m^{-3} and 1 eV, respectively. The neutral particle number density linearly increases from $3.0 \times 10^{17} \text{m}^{-3}$ with a flow rate of 8 sccm to $8.5 \times 10^{17} \text{m}^{-3}$ with 30 sccm.

As shown in Fig.6, an AAS plate 50 mm x 50 mm square is used in this experiment. The plate made from Al2017 is prepared with MIL-A-8625-TYPE I, and the anodized layer is 1.3 um thick as well as those of Japanese Experimental Module in International Space Station. To simulate large surface area of spacecraft, a capacitor is connected between the AAS and a vacuum chamber, i.e. the ground. When arcing occurs, the time variations in arc current and charging voltage are measured. The diameter of arc spots also is measured.

Experimental Results and Discussion

Figures 7 and 8 show typical time variations in charging voltage and arc current, and a photograph of arc spot, respectively, for arcing of an AAS plate. The charging voltage rapidly changes from an initial charging voltage to zero, and then the arc current also rapidly changes up and down. The peak arc current is the order of ampere. As shown in Fig.8, a large hole with some ten um is created by arcing. The anodized layer is eroded, and the main aluminum part appears. Accordingly, degradation of material properties by arcing is suspected.

Figure 9 shows the time variations in charging voltage and arc current, and the characteristics of peak arc current, arcing impedance, total emitted charge, total emitted charge ratio and arc spot diameter, dependent on initial charging voltage at constant plasma parameters of neutral particle density, plasma density and electron temperature of $3.0 \times 10^{17} \text{ m}^{-3}$, $1.2 \times 10^{13} \text{ m}^{-3}$ and 4 eV. The arc impedance is defined as a value of peak arc current divided into initial charging voltage. The total emitted charge is a value integrating arc current in time. Since the value does not equal the charge initially stored in the capacitor, the total emitted charge ratio can be defined as a ratio of total emitted charge to initial charge in the capacitor. The charging voltage, as shown in Fig.9(a), rapidly approaches zero from each initial charging voltage. At -400 and -500 V, the charging voltage transiently increases above zero. This is considered because a large amount of ions created by intensive ionization of an eroded and evaporated AAS, and/or neutral particles in the ambient plasma enters the arc spot. The arc current, as shown in Fig.9(b), rapidly increases and has a peak; then decreases. The peak arc current and the arc impedance, as shown in Figs.9(c) and 9(d), increases and decreases, respectively, with an increase in initial charging voltage from 100 to 500 V, and the duration time of arcing becomes short. A higher density plasma is considered to be created with increasing initial charging voltage. As a result, both the total emitted charge and the total emitted charge ratio, as shown in Fig.9(e), linearly increase with initial charging voltage. Because the total emitted charge ratio above 1.0 is achieved, an additional current flows from the ambient plasma. The additional current is considered to be an ion current created by intensive ionization in the ambient plasma as mentioned above. The diameter of arc spots, as shown in Fig.9(f), is almost constant at charging voltages up to 350 V and increases with above it. This shows that a large volume of the AAS is eroded and evaporated with a high initial charging voltage, resulting in creation of a dense plasma around the arc spot by intensive ionization.
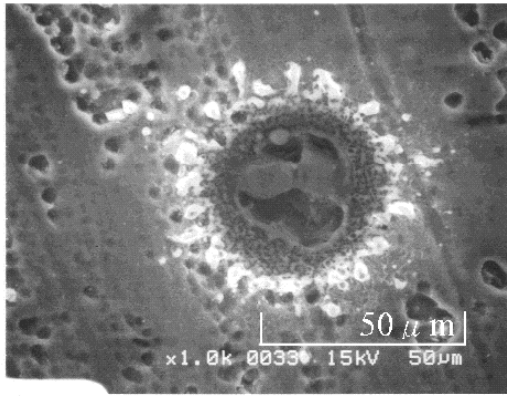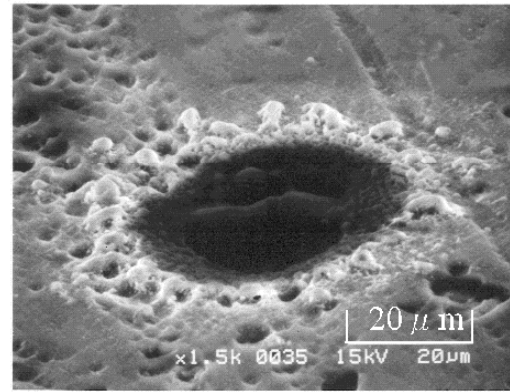
<div align="center">(a) Front.   (b) Sideways.</div>

Figure 8.   Typical photograph of arc spot for arcing of AAS plate.

Figure 10 shows the time variations in charging voltage and arc current, and the characteristics of peak arc current, arcing impedance, total emitted charge, total emitted charge ratio and arc spot diameter, dependent on neutral particle number density at plasma parameters of $1.2\text{-}4.5 \times 10^{13}$ m^{-3}, 1-4 eV and constant initial charging voltage of -200 V.   Both the charging voltage and the arc current, as shown in Figs.10(a) and 10(b), show rapider and more intensive changes with increasing neutral particle density.   This is considered because of ionization enhanced with high-density neutral particles as well as cases with high initial charging voltages shown in Fig.9.   The characteristics of peak arc current, arcing impedance, total emitted charge and total emitted charge ratio agree with those of charging voltage and arc current.   The total emitted charge ratio also reaches above 1.0 at high neutral particle densities.   On the other hand, the arc spot diameter, as shown in Fig.10(f), is almost constant regardless of neutral particle density because the energy stored in the capacitor is constant.

<div align="center">

Plasma Particle Simulation

</div>

DSMC-PIC simulation of electron-flow-induced plasma expandingfrom spacecraft surface into ambient plasma environment

Direct-Simulation-Monte-Carlo Particle-In-Cell (DSMC-PIC) plasma simulation is carried out to understand features of plasma expanding from an arc spot on a spacecraft surface into the ambient plasma just after arcing.   Figure 11 shows the two-dimensional calculation model.   Electrons are injected from an arc spot on Y-axis corresponding to a spacecraft insulator surface.   The width of the arc spot is assumed to be 2.36×10^{-5} m from the experimental data.   As shown in Fig.11(b), the electrical potential of the arc spot is linearly applied in time, and then the constant electron charge, which is the charge initially stored in the capacitor divided by the arc duration time of about 10 us, is introduced in time from the arc spot.   In the ambient plasma environment, there exist electrons, ions and neutrals.   Both elastic and ionization collisions between electrons and neutrals are considered. Both electrons and ions move electrostatically.   The kinetic equations of electron and ion, and Poisson's equation are governing ones, and Leap Flog scheme and Successive-Over-Relaxation method are used for their integrations.
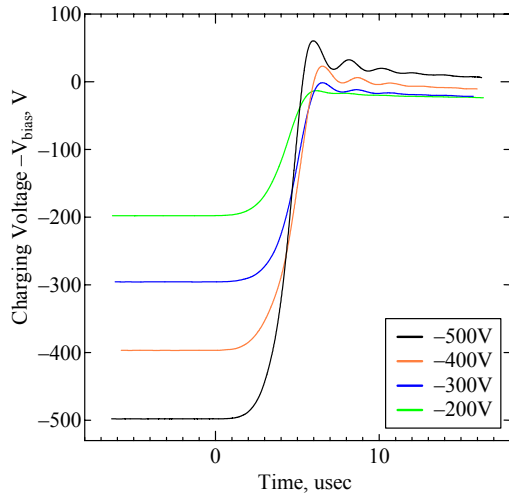
(a) Time variation in charging voltage.
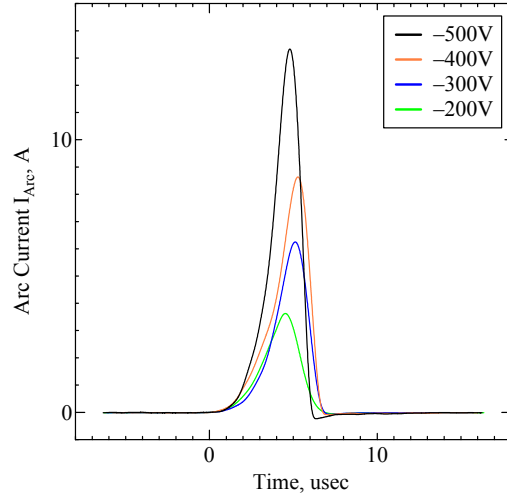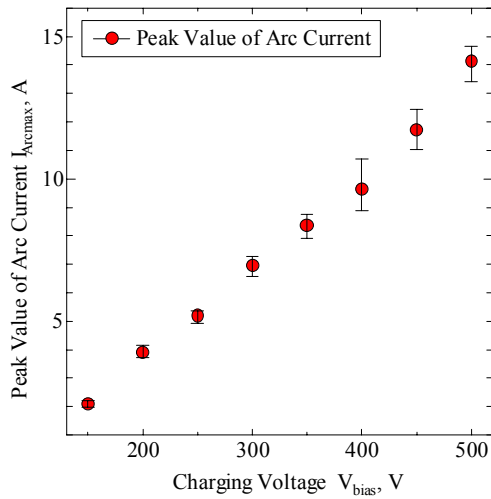
(b) Time variation in arc current.

(c) Peak arc current.

(d) Arcing impedance.

(e) Total emitted charge and total emitted charge ratio.

(f) Arc spot diameter.

Figure 9.   Arcing characteristics dependent on initial charging voltage at constant plasma parameters of neutral particle density, plasma density and electron temperature of 3.0×10^{17} m^{-3}, 1.2×10^{13} m^{-3} and 4 eV.
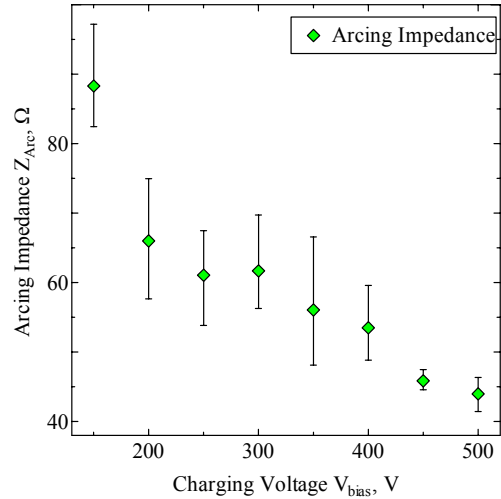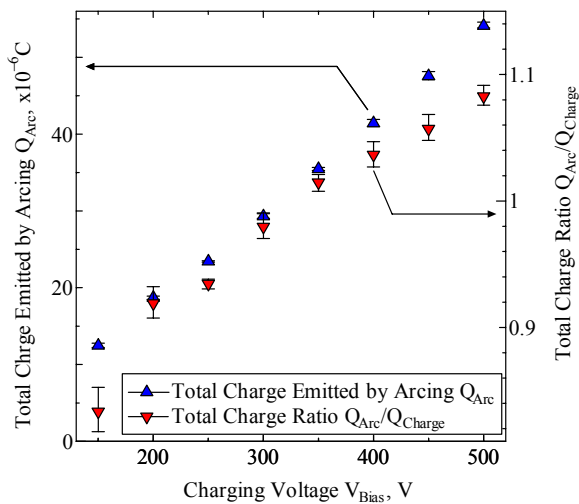
(a) Time variation in charging voltage.
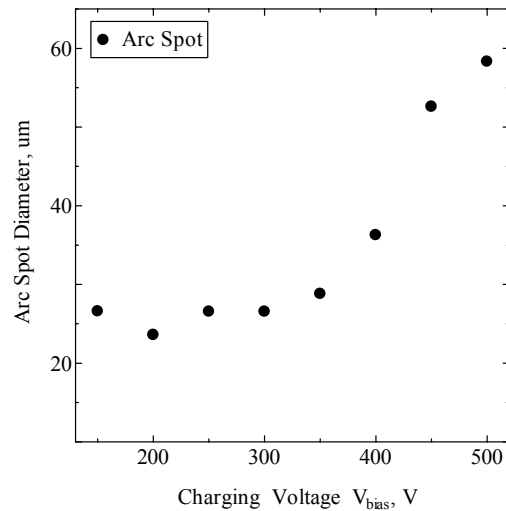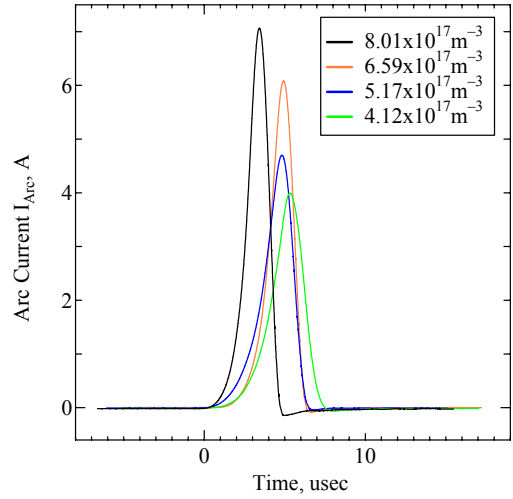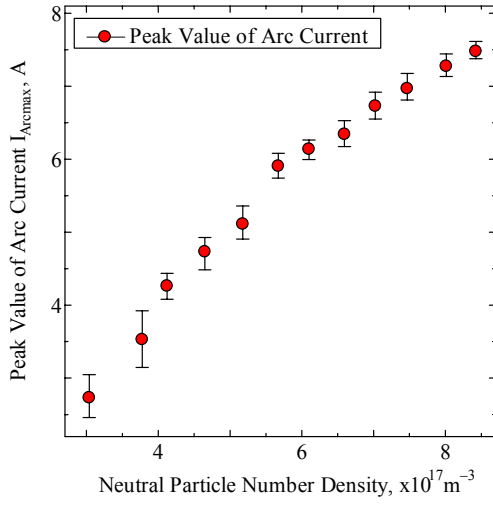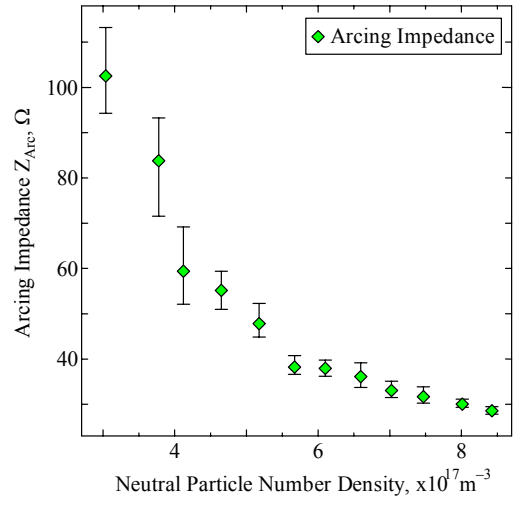
(b) Time variation in arc current.

(c) Peak arc current.

(d) Arcing impedance.
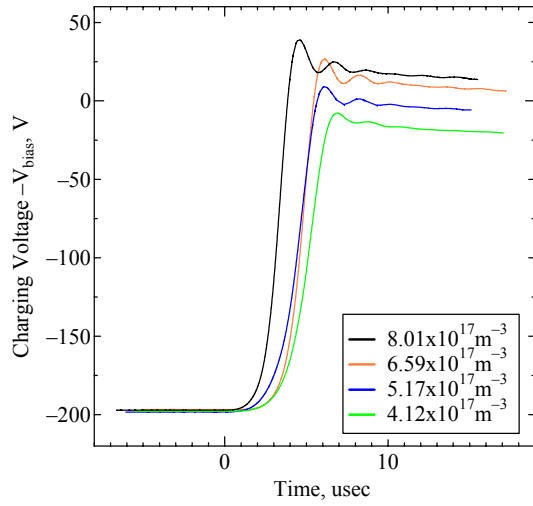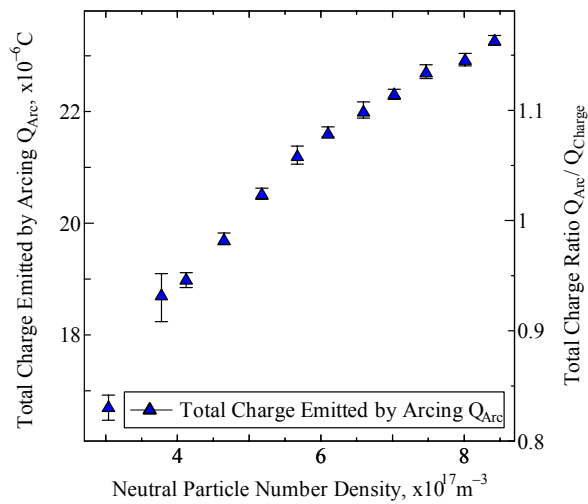
(e) Total emitted charge and total emitted charge ratio.
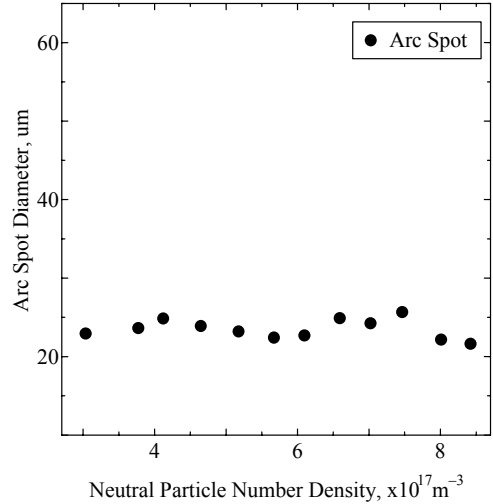
(f) Arc spot diameter.

Figure 10. **Arcing characteristics dependent on neutral particle number density at plasma parameters of 1.2-4.5x10^{13} m^{-3}, 1-4 eV and constant initial charging voltage of -200 V.**
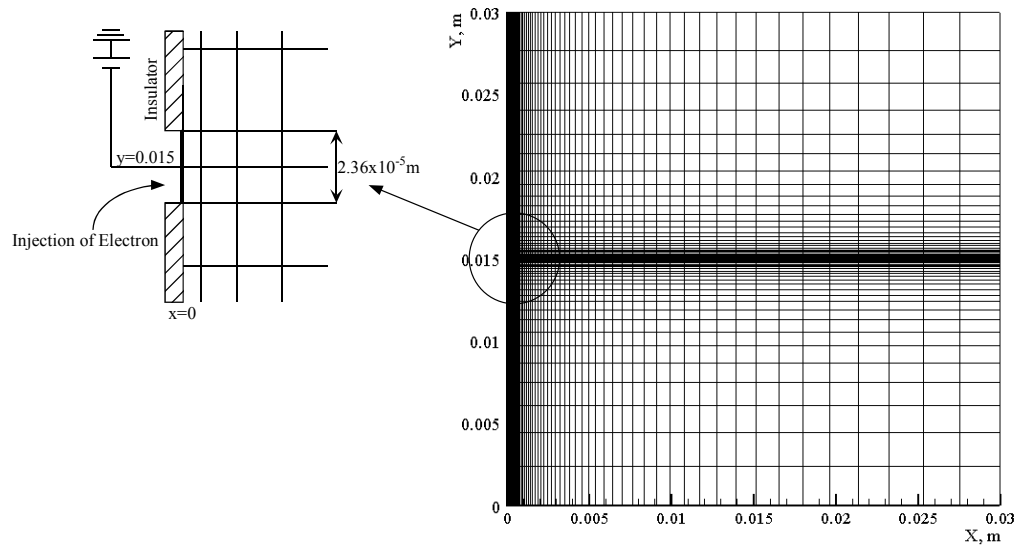
(a) Calculation domain.
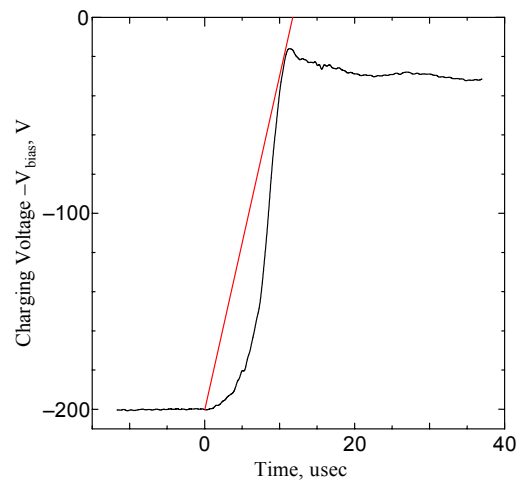
(b) Time variation in voltage applied at arc spot for calculation.

Figure 11. Two-dimensional calculation model of Direct-Simulation-Monte-Carlo Particle-In-Cell (DSMC-PIC) simulation of electron-flow-induced plasma expanding from spacecraft surface into ambient plasma environment
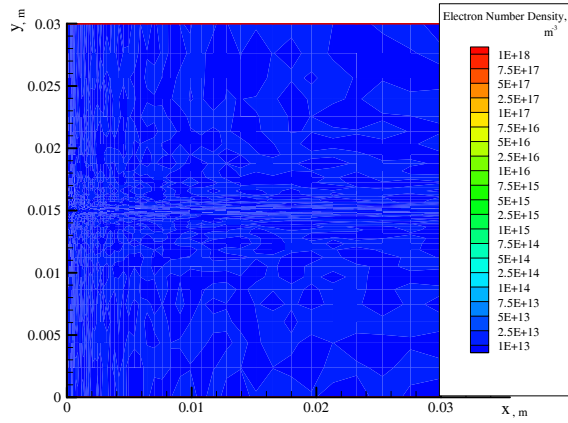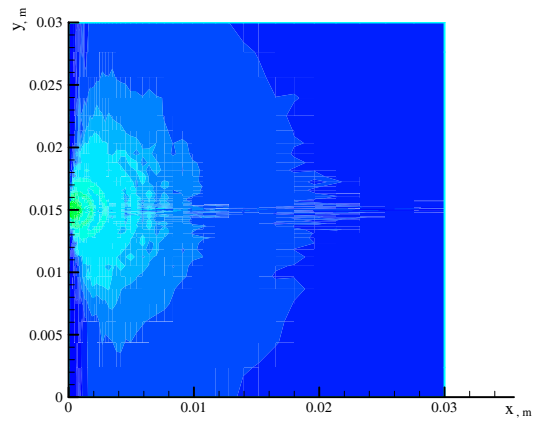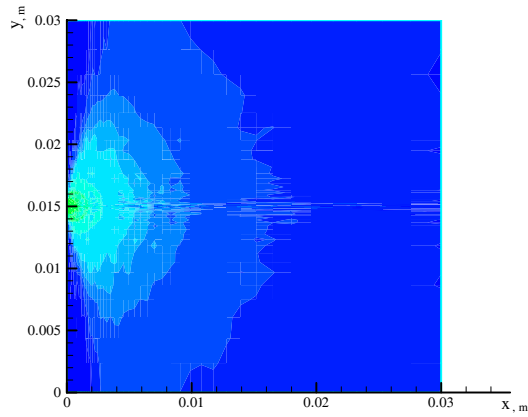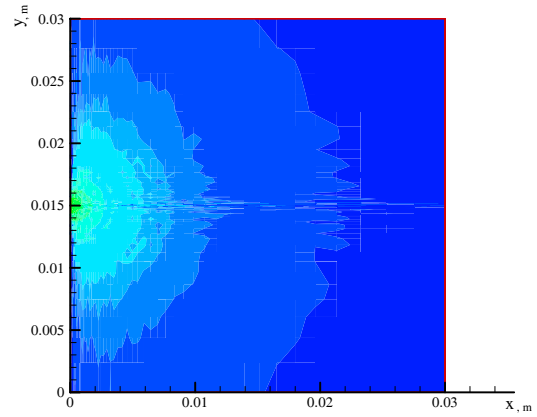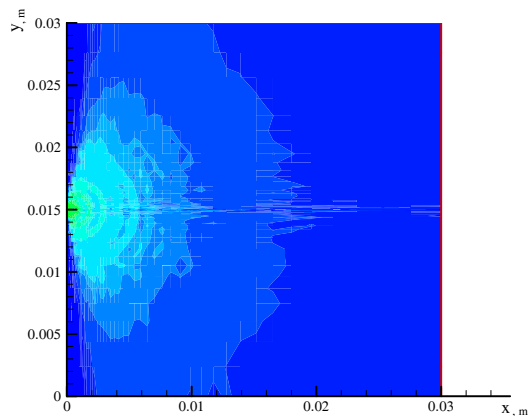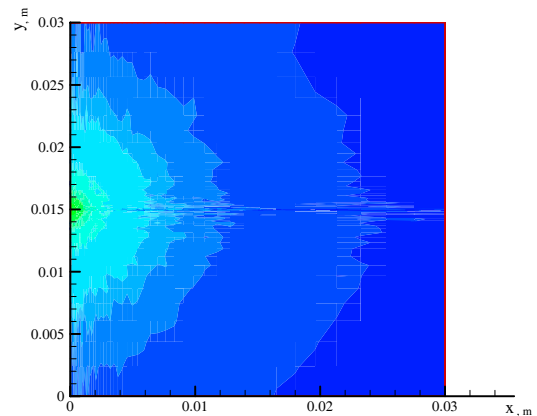
Figure 12. Time variation of pattern of electron number density at initial charging potential of -200 V with ambient plasma condition of plasma density 1.0×10^{13} m^{-3} and neutral particle density 1.0×10^{18} m^{-3}.
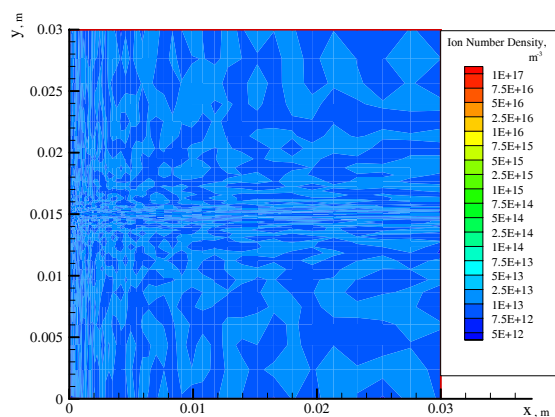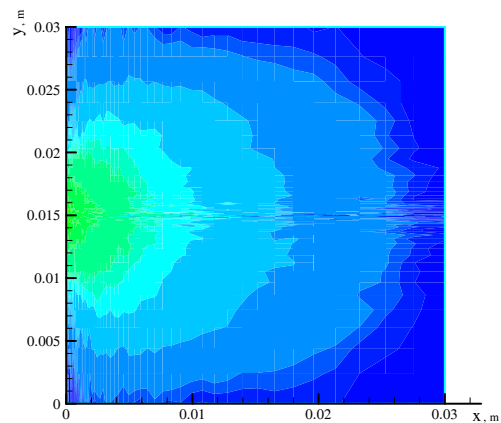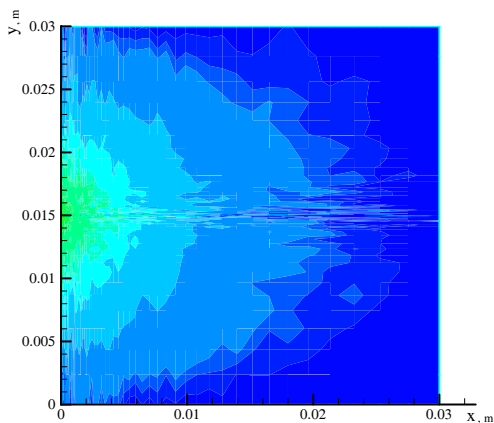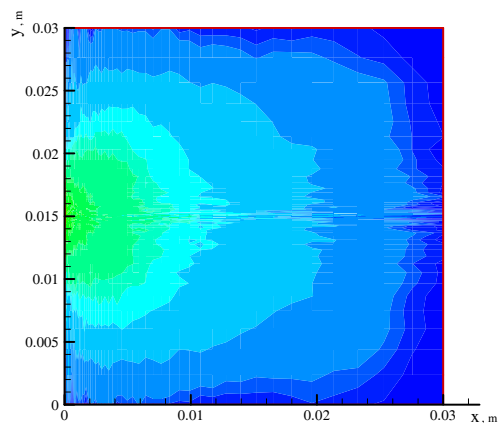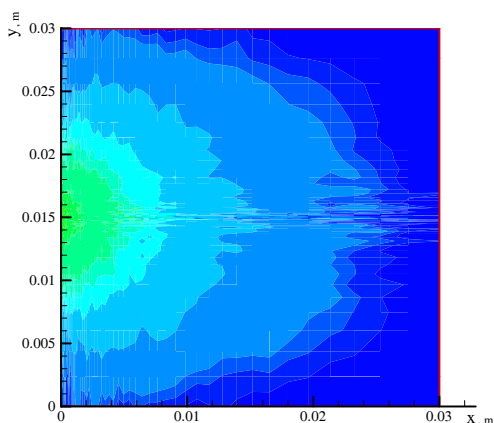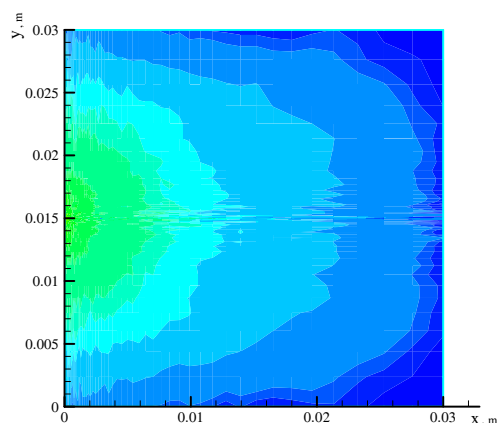
Figure 13. Time variation of pattern of ion number density at initial charging potential of -200 V with ambient plasma condition of plasma density 1.0×10^{13} m^{-3} and neutral particle density 1.0×10^{18} m^{-3}.
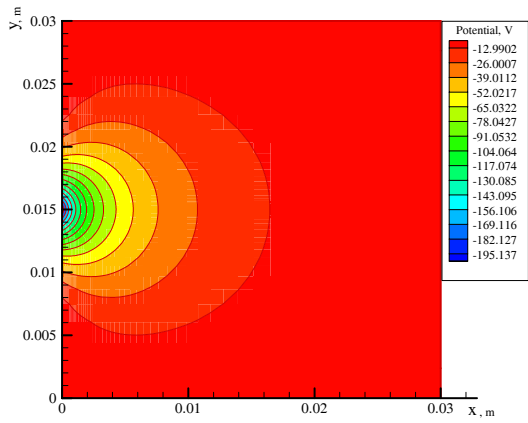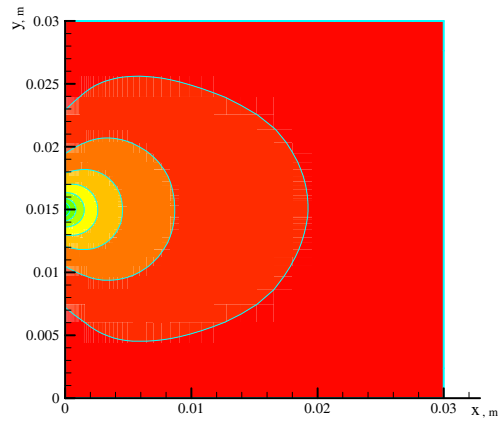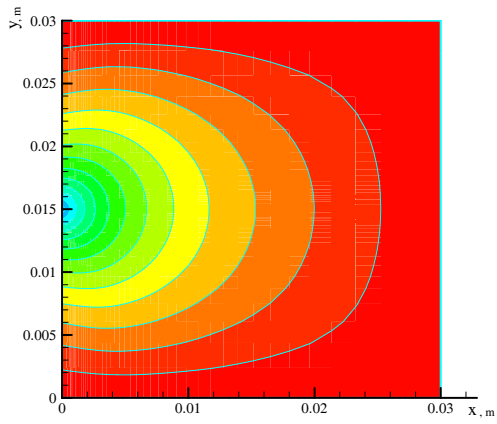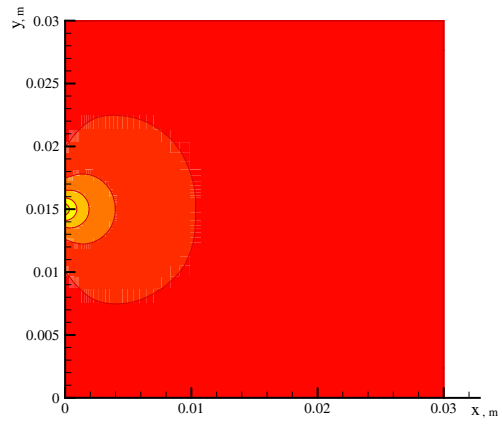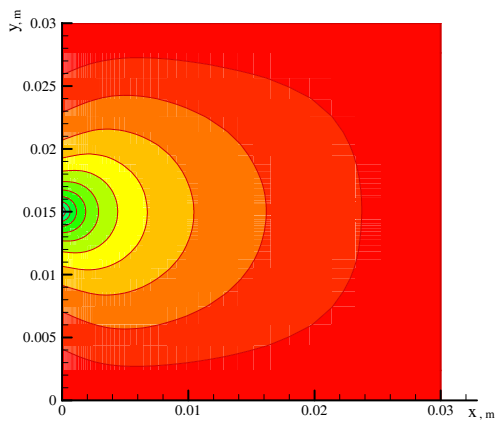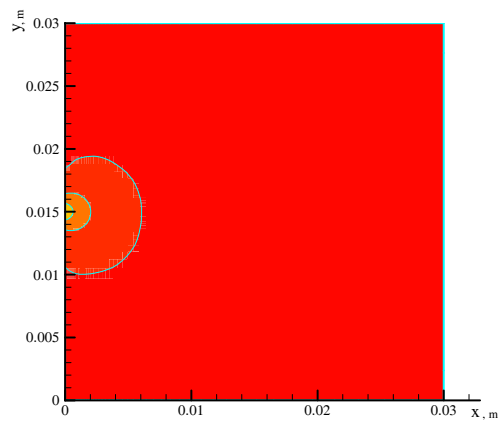
Figure 14.   Time variation of pattern of plasma potential at initial charging potential of -200 V with ambient plasma condition of plasma density 1.0×10^{13} m^{-3} and neutral particle density 1.0×10^{18} m^{-3}.

(a) Neutral density: 1.0×10^{17} m^{-3}. (b) Neutral density: 1.0×10^{19} m^{-3}.
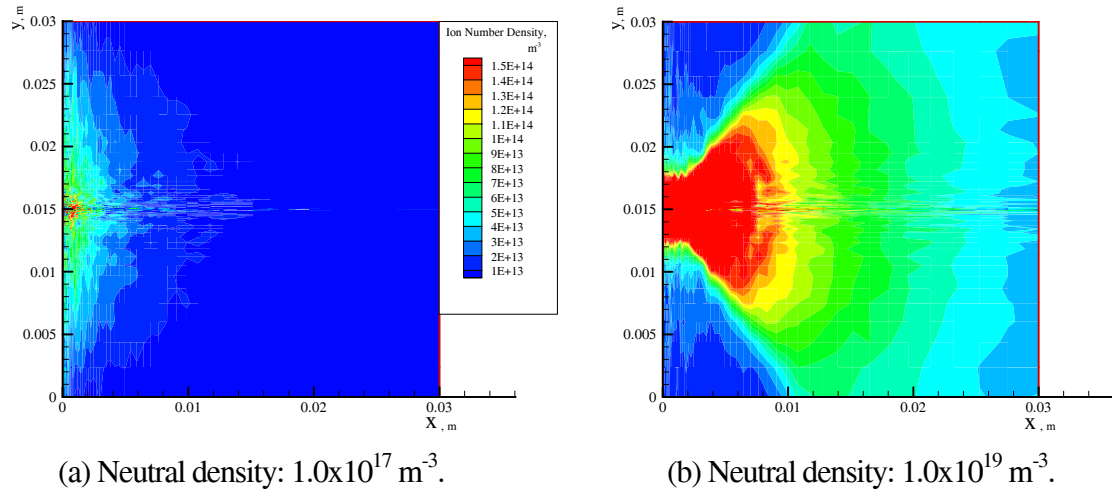
Figure 15.   Patterns of ion number density dependent on neutral particle number density at 8 us after start of arcing.

(a) Neutral density: 1.0×10^{17} m^{-3}. (b) Neutral density: 1.0×10^{19} m^{-3}.
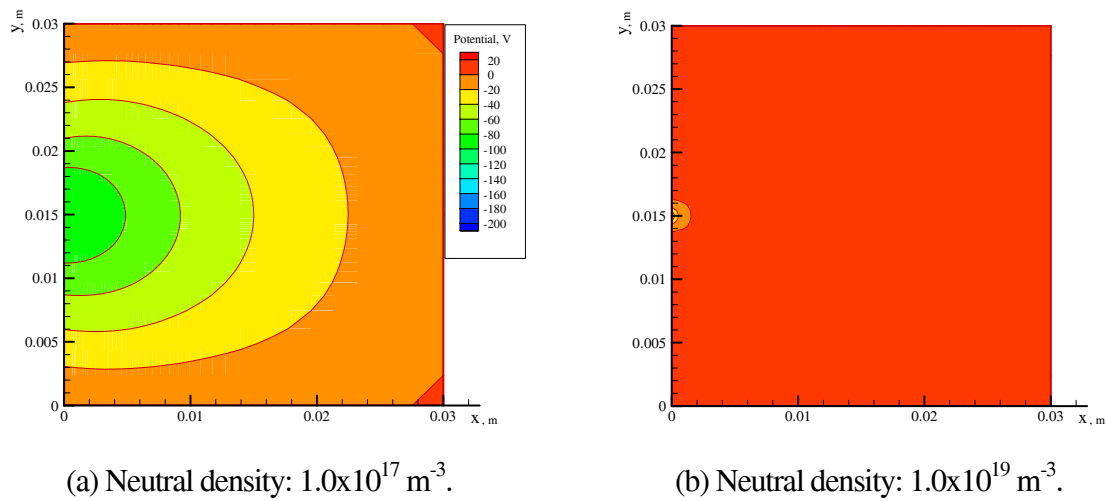
Figure 16.   Patterns of plasma potential dependent on neutral particle number density at 8 us after start of arcing.

Calculated results and discussion

Figures 12-14 show the time variations of patterns of electron number density, ion number density and plasma potential at an initial charging potential of -200 V with an ambient plasma condition of plasma density 1.0×10^{13} m^{-3} and neutral particle density 1.0×10^{18} m^{-3}.   Electrons injected from the arc spot are rapidly expanding.   The ion number density increases toward the arc spot.   This is mainly considered because of intensive ionization due to high-energy electrons near the arc spot and because of ions electrostatically attracted toward the arc spot.   The plasma potential pattern agrees with those of electron and ion densities.   From the plasma potential pattern shown in Fig.14, the electric field is very high near the arc spot and decreases outwards.   The spatial change in plasma potential expands up to 2 us because of drastic phenomena just after start of arcing, i.e. ionization, and rapid motions of electrons and ions, and after that the area becomes small.

Figures 15 and 16 show the patterns of ion density and plasma potential dependent on neutral particle number density at 8 us after start of arcing.   There exists a high ion density region in front of the arc spot.   When the neutral particle density increases, the area becomes large because of more intensive ionization.   Then, a higher electric field is created near the arc spot although the area intensively concentrates near the arc spot.

Accordingly, the experimental results shown in Section 4 can be explained from the calculated ones.   The arcing characteristics strongly depend on characteristics of ambient plasma, specially neutral particle number density.   Therefore, both the properties of spacecraft insulator materials and the characteristics of ambient plasmas around spacecraft are key factors to determine arcing phenomena on spacecraft surface insulators.

Conclusions

Ground-based experiment was carried out to understand discharge phenomena on spacecraft surface and to examine influences of ambient space plasma on the arcing process.   Simulating plasmas were generated by electron cyclotron resonance discharge.   The measured arcing characteristics for negatively-biased anodized aluminum sample (AAS) plates in the plasma environment showed that both the peak arc current and the total charge emitted by arcing increased with initial charging voltage and neutral particle number density.   The diameter of arc spots increased with initial charging voltage although it was almost constant regardless of neutral particle density. Furthermore, Direct-Simulation-Monte-Carlo Particle-In-Cell plasma simulation was conducted to understand features of plasma expanding from an arc spot on spacecraft surface into the ambient plasma just after arcing.   The calculated results showed that neutral particles in addition to charged particles around spacecraft played an important role in expansion of arc plasma causing the arcing characteristics.   Accordingly, high voltage operation of LEO spacecraft might bring drastic degradation of AAS by arcing; particularly with high neutral particle density, a high arc current is suspected to flow.

References

1. NASA/SDIO Space Environmental Effects on Material Workshop, NASA CP-3035, 1989.

2. H. Tahara, L. Zhang, M. Hiramatsu, T. Yasui, T. Yoshikawa, Y. Setsuhara and S. Miyake," Exposure of Space Material Insulators to Energetic Ions," J. Appl. Phys., Vol.78, No.6, pp.3719-3723, 1995.

3. L. Zhang, T. Yasui, H. Tahara and T. Yoshikawa," X-ray Photoelectron Spectroscopy Study of the Interactions of O^+ and N^+ Ions with Polyimide Films," Jpn. J. Appl. Phys., Vol.36, No.8, pp.5268-5274, 1997.

4. A.C. Tribble, R. Lukins, E. Watts, V.A. Borisov, S.A. Demidov, V.A. Denisenko, A.A. Gorodetskiy, V.K. Grishin, S.F. Nauma, V.K. Sergeev and S.P. Sokolova," United States and Russian Thermal Control Coating Results in Low Earth Orbit," J. Spacecraft & Rockets, Vol.33, No.1, pp.160-166, 1996.

5. H. Tahara, K. Kawabata, L. Zhang, T. Yasui and T. Yoshikawa," Exposure of Spacecraft Polymers to Energetic Ions, Electrons and Ultraviolet Light," Nucl. Instrum. & Methods, Vol.B121, pp.446-449, 1997.

6. D. Matsuyama, H. Tahara, T. Matsuda, T. Yasui and T. Yoshikawa," Ground Experiments of Interaction between Plasma Flow and Negatively Biased or Charged Materials," Proc. 26th Int. Electric Propulsion Conf., Kitakyushu, Japan, IEPC-99-224, pp.1314-1321, 1999.

7. H. Tahara, T. Yasui, D. Matsuyama and T. Yoshikawa," Laboratory Simulation of Charging Relaxation by Plasma Flow," Proc. 7th Spacecraft Charging Technology Conf., ESTEC, Noordwijk, The Netherlands, ESA SP-476, 2001.

8. H. Tahara, D. Matsuyama, T. Yasui and T. Yoshikawa," Mitigation Process of Spacecraft Negative Charging by Plasma Flow," 27th Int. Electric Propulsion Conf., Pasadena, CA, USA, IEPC-01-258, 2001.

9. H. Tahara, T. Yasui and T. Yoshikawa," Space Plasma Simulator Performance Using an Electron Cyclotron Resonance Plasma Accelerator," Trans. Japan Soc. Aero. Space Sci., Vol.40, No.127, pp.59-68, 1997.

DEVELOPMENT OF SOLAR ARRAY FOR A WIDEBAND INTERNETWORKING ENGINEERING TEST AND DEMONSTRATION SATELLITE: SYSTEM DESIGN

Tetsuo Sato
Masato Takahashi
Masao Nakamura
Shirou Kawakita
JAXA (Japan Aerospace Exploration Agency)

Mengu Cho
Kazuhiro Toyoda
Kyushu Institute of Technology

Yukishige Nozaki
NEC TOSHIBA Space System, Ltd.

Abstract

JAXA(Japan Aerospace Exploration Agency) is conducting the development of Wideband InterNetworking engineering test and Demonstration Satellite(WINDS), which aims at developing and verifying the main technologies for future ultra high speed satellite communications. WINDS has two solar array paddles laid down approximately 8,500 triple junction solar cells. From the point of view of certain and reliable development, ground based ESD test was carried out on 3 solar array coupons for WINDS. Although the power degradation caused by trigger arc was observed in all coupons, there was no sustained arc in any coupon. According to the test result, the power degradation by trigger arcs is estimated 1.4% for lifespan of 5 years

Outline

Table 1 and Figure 1 show major characteristics and overviews of WINDS respectively.

Table 1.   WINDS Major Characteristics

Item	Characteristics
Orbit	Geostationary Earth Orbit(GEO)
Mass	2,700kg at the beginning of mission life
Size	2m×3m×8m (tip to tip 21.5m including Solar Array Paddle), refer to Figure 1
Designated Lifespan	5 years (targeted life)
Attitude Control	3-axis-stabilized (zero-momentum)
Electricity	More than 5,200W
Launch	2005 fiscal year by H-IIA Launch Vehicle at Tanegashima Space Center)

Objectives of WINDS

WINDS has the following development objectives:

(1) Ultra fast communications
WINDS satellite communication system aims for a maximum speed of 155Mbps(receiving) / 6Mbps (transmitting) for home using 45-centimeter aperture antennas, which are as small as existing Communications Satellite antennas, and an ultra fast 1.2Gbps for office use.

(2) Broader communication area coverage
The technology for the Ka-band multi-beam antenna with a high-powered multi-port amplifier can achieve fixed ultra fast communications all over Japan and in major Asian cities, such as Seoul, Beijing, and Singapore. At the same time, flexible power distribution to each communication area can cope with the regional communication demand and the rain attenuation.

In addition, the Ka-band active phased array antenna technology makes it possible to control the antennas communications direction rapidly and electronically, thus communication can be carried out quickly to specific area with demand.

WINDS Solar Array Design

WINDS solar arrays, which adapt to DET (Direct Energy Transfer)/Shunt with 50V regulated Bus voltage, employ the following cell and cover glass:

- 3J GaAs/Ge solar cell(NASDA-QTS-2130/501)
    Thickness: 0.15mm / Size: 37mm X 76mm
- CMG-100-AR without conducting coating
    Thickness: 0.1mm

WINDS has two solar array paddles where 292 parallel strings of solar cells are mounted. Each string is made by the series connection of 30 triple-junction cells. Those parallel strings are divided into 2 charge-arrays for battery charging, and 6 main-arrays and 2 half-arrays for main power generation. The grouping of the solar array strings is the following;

- 20 strings for each charge-array, 1 charge array on each paddle.
- 36 strings for each main-array, 3 main-arrays on each paddle
- 18 strings for each half-array, 1 half-array on each paddle

Figure 2 shows the basic layout of the solar array strings. Although each string produces approximately 80V for open circuit, the spacecraft shunt regulator limits the string voltage to approximately 55V for non-shunted string and 0V for shunted string. The negative terminal of each string is arranged at center on the solar panel, while the positive one is arranged at the edge side.
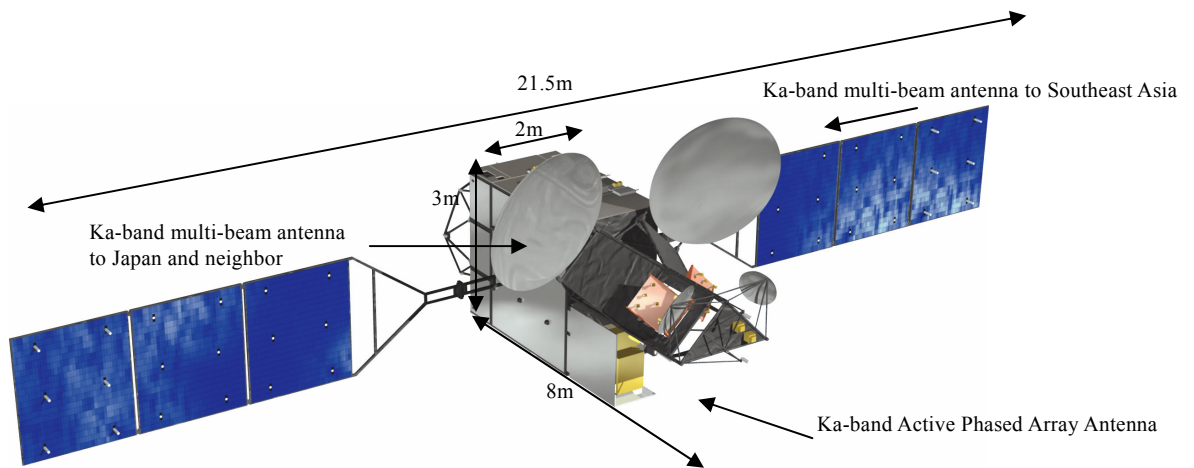
Figure 1. Overviews of WINDS on Orbit

Therefore a potential difference between adjacent strings is 0V, except 55V between the shunted string and non-shunted string. The gap between adjacent cells is potted with nonconductive adhesive, RTV, as same as previous JAXA's solar array design [1]. Also, because WINDS dose not carry ion thruster, there is no need to coat the bus bar with RTV to avoid the current leakage to the high density plasma generated by the backflow from the ion thruster plume [2].
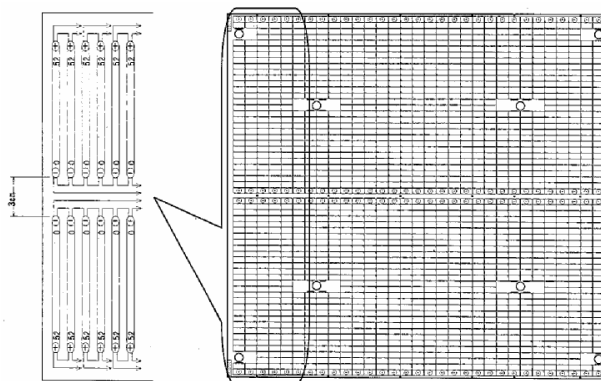
Figure 2. WINDS String Layout

ESD Test

The ground ESD test was performed by Kyushu Institute of Technology. The purposes of the test are the following.

- Confirm that the solar array suffers no sustained arc
- Study how the amount of RTV coating applied to the cell edge affects the power degradation due to trigger arcs
- Determine the flight design of solar array

The Outline of the test condition and result are described in this section. The detail explanation is presented in Ref. [3].

Test Condition and Test Configuration

Three test coupons were used for the ground ESD test. Photograph of a coupon is shown in Figure 3. The cross-sectional view of solar array coupon is shown in Figure 4 and 5. The summary of difference among the coupons are listed in Table 2. A coupon consists of 15 cells. Five cells are connected in series making three parallel strings. Each string was named as R, B and G string. All the three coupons has the same thickness of RTV layer between cells and Kapton sheet, approximately 100 μ m. The gap between strings are grouted by RTV. The coating of RTV at the cell edges of the coupon 1 is much thicker than the coupon 2 and 3. The bus bars of the coupon 3 is not coated with RTV to confirm whether the bus bars act as lighting rods where a trigger arc occurs before it occurs at more dangerous points such as the string-gaps or the cell edges.
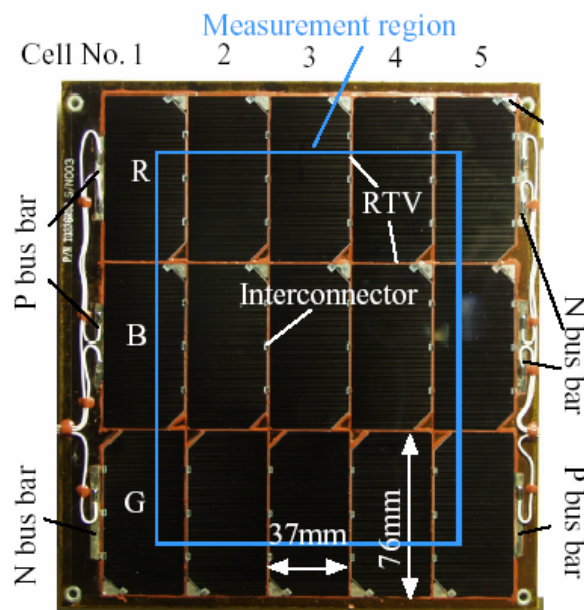
Figure 3.　Photograph of a test coupon

Table 2.　Difference of test coupons

Coupon No.	Amount of RTV	Bass bar coating
1	Large	Yes
2	Normal	Yes
3	Normal	No
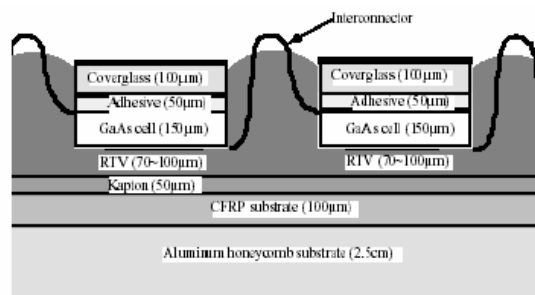
Figure 4.　Cross-Sectional view of coupon 1
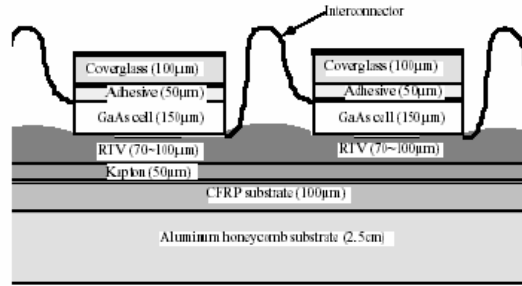
Figure 5.   Cross-sectional view of coupons 2 and 3

Figure 6 shows the set-up configuration of ESD test. A coupon panel was placed in a vacuum chamber. In the ESD test, the coupon panel was charged by the electron beam gun.
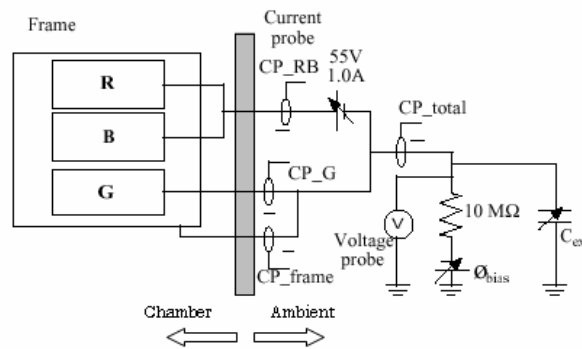
Figure 6.   ESD test circuit

WINDS test condition is defined as shown in Table 3. The bias voltage (ϕ_{bias}) and the emitted time (t_{exp}) were decided on NASCAP worst case analysis in next section. The coupons 1 and 2 were tested for 20 hours and the coupon 3 for 65 hours. From the case 1 to case 3, the beam center was aligned to the center of the coupons. For the cases 10 and 11, the beam center was set to the No.1 cell of the B string, because the test purpose was to see the trigger arcs at the bus bars.

At every 10 hours, the coupons were removed from the chamber. After the photographs of the cell edges were taken by the $60\times$ optical microscope, they were measured the output power. Each coupon was taken out form the vacuum chamber after the case 2, 3, 5, 6, 8, 9 and 11, it means every 10 hours emission. Once a coupon was put in the chamber, it was kept in vacuum for approximately three days. Every time the coupons were exposed to atmosphere, they were baked for 2 hours at 70℃ before the ESD test.

Table 3. WINDS test conditions

Case	Coupon	ϕ_{bias} -kV	C_{ext} nF	V_e kV	t_{exp} hour
1	1	3	400	2.8~4.0	6
2	1	4	200	3.0~4.0	4
3	1	6	100	3.0~6.0	10
4	2	3	400	2.8~4.0	6
5	2	4	200	3.0~4.0	4
6	2	6	100	3.0~6.0	10
7	3	3	400	2.8~4.0	6
8	3	4	400	3.0~4.0	4
9	3	6	100	3.0~6.0	10
10	3	3	400	2.8~4.0	6
11	3	4	200	3.0~4.0	4
12	3	3	400	3.0-4.0	35

Test Results

The number of arcs observed is listed in table 4. During the tests of 20 hours, the number of arcs is 288, 392 and 266, respectively for the coupons 1, 2 and 3. The coupon 2 had arcs more than the other two coupons. The cases 10 and 11 had 260 arcs in 10 hours. The cases with higher arc rates had higher chamber pressures. There is no significant difference for number of arcs depending on each coupon, according to this point. There was no sustained arc with so many trigger arcs, whether bass bar was coated or not. It was confirmed that the solar array design is very effective at suppressing the sustained arc occurrence.

Table 4. Number of arcs

Coupon	Difference of Coupon		N_{arc}	T_{exp}, h	Power Degradation	Failure Cell
	RTV	Bas bar				
1	Large	Coating	288	20	18%	2~3
2	Normal	Coating	392	20	32%	3
3	Normal	Non-Coating	266+260+84	20+10+35	36%	3~4*

*: T_{exp} =30h

The output power of each coupon was measured after the test. The ratio of degraded

power to the initial power is plotted in figure 7. The horizontal axis denotes the test time. The R and B strings were connected in parallel at the back side of the coupon, and were not separated as the output power was measured.
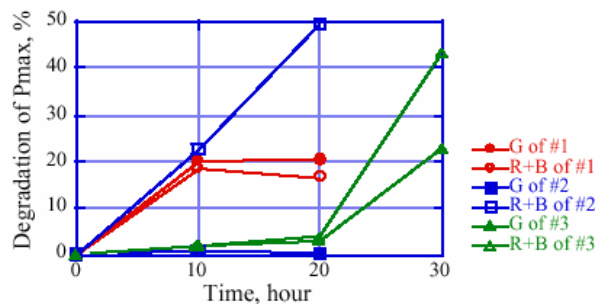
Figure 7.   Degradation of solar array output power

NASCAP Analysis

NASCAP Model

   The WINDS NASCAP model is shown in Figure 8. The major features are the following material.

 - Body: mostly covered with conducting thermal blankets and Optical Solar Reflector (OSR) with ITO (Indium-Tin- Oxide).
 - Solar Array: surface cover glass and backs of which are covered with a black conducting polymer.
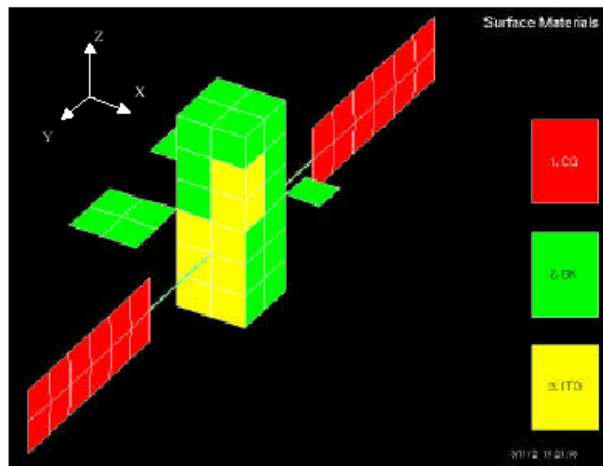
Figure 8.   NASCAP model of the WINDS

Worst Case Analysis

   Spacecraft charging analysis was carried out in order to clarify the spacecraft charging expected on the WINDS solar panel. The analysis defines bias voltage which simulated a relative voltage between cover glass and spacecraft ground for measurement of the threshold voltage for the trigger arc inception [4].

The calculation was performed under the condition of the charging environment as shown in Table 5 [5][6].

Table 5.   Charging Environment

	Electrons Density	Electrons Temp.	Ions Density	Ions Temp.
Population 1	1.2 (/cm^3)	27.5 (keV)	1.3 (/cm^3)	28.0 (keV)
Population 2	0.2 (/cm^3)	0.4 (keV)	0.6 (/cm^3)	0.2 (keV)

It was already known that the SEE (Second Electron Emission) coefficient of CMG-100-AR coated MgF2 is as Figure 9 [7][8].
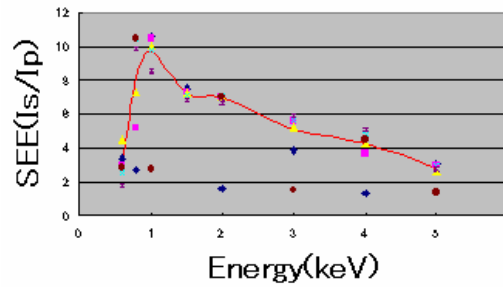
Figure 9.   SEE coefficient of CMG-100AR

The analytical result that was reflected the above -mentioned SEE coefficient is shown in Table 6, Figure 10 and Figure 11. The NASCAP calculation shows that maximum differential voltage observed at exit of eclipse, which reaches approximately 5.2kV.

Table 6.   Charging Analytical Result Summary

Case	Ground (V)	CG1 (V)	CG3 (V)	MaxDiff. (V)
Sun; +X	-1310	-893	-703	604
Sun; -Z	-1450	-1080	-798	652
Eclipse	-11300	-7810	-6110	5190
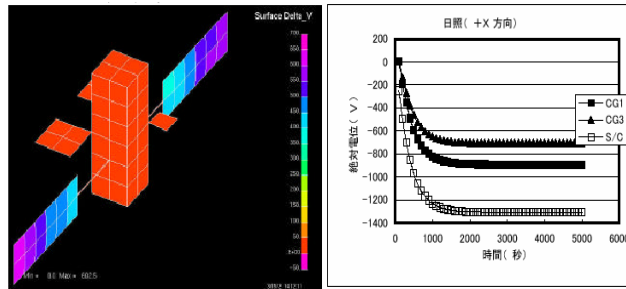
Figure 10.　Sun direction +X case
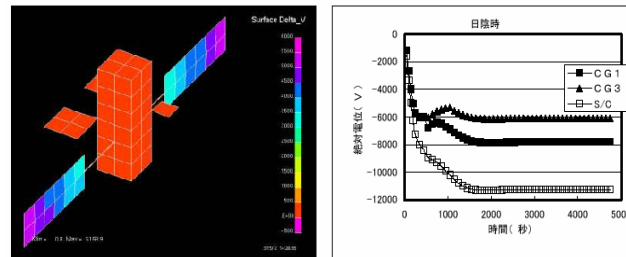
Figure 11.　Eclipse case

Static Analysis

Here, it should be considered that what is necessary to evaluate the result of ground ESD test. Namely the problems are following points.

(1) How many duration the satellite has critical charging in the orbit (exceeding 400V inverted potential gradient)?
(2) How many times the satellite has trigger arcs?

Therefore, the charging analysis was carried out based on statistics data.

Procedure:

(1) The $7.5*10^6$ GEO plasma environment data (equivalent to 21 years 5 month; 1993/03/15 ~ 2003/09/24) of LANL (Los Alamos National Laboratory) satellite were collected.

(2) The combination of parameters (Ne, Ni, Te, Ti) were divided to 556 cases and calculate the probability of each case at every 3 hours of local satellite time (LST) that the data point falls in a given box of parameters as shown Figure 12. Figure 13 shows accumulated probabilities of electron temperature distribution and ion temperature distribution.

(3) NASCAP/GEO simulation was carried out based on the Spacecraft Charging Analysis (mentioned-above 5.1) for all the combinations of plasma parameters and local time, and calculated the total duration when the differential charging between cover-glass and the satellite ground exceeds 400V. Total simulation cases are 5004 (=(eclipse　8LST zone)556 plasma parameters cases), but NASCAP/GEO cannot model the oblique solar incidence (e.g. LST=3, 9, 15, 21). Therefore NASCAP/GEO simulation was run for the 2780 cases identified.
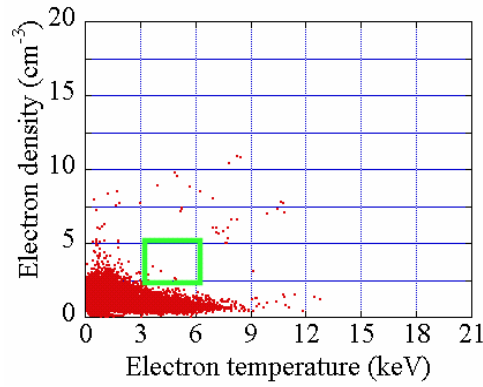
Figure 12.   Sample of parameters matrix box
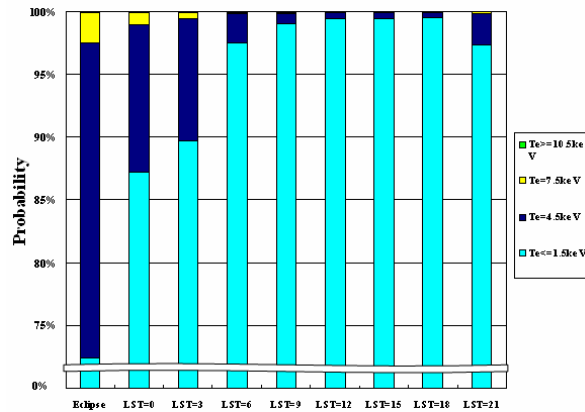
Figure 13.   Accumulated Probabilities (Electron temperature distribution)

Total Duration of Critical Charging:

The cases of exceeding 400V inverted potential gradient[8] was identified and the total critical charging duration was calculated. Table 7 shows sample of Maximum differential voltage (ΔV). Table 8 shows summary of critical charging duration in 1 year. The critical charging duration was estimated through multiplying by each combination of the parameters and each LST zone total hours or total eclipse hours a year. (e.g. one LST zone hours are 1095 hours a year.).

Table 7. Sample of Maximum ΔV

Te (keV)	Ne (cm-3)	Ti (keV)	Ni (cm-3)	LST=0 eclipse	LST=0 sunlit	LST=6 sunlit	LST=12 sunlit	LST=18 sunlit
4.5	10	5	0.25	6418	931	871	917	934
4.5	10	5	1	4324	883	827.8	870	888
4.5	10	10	0.25	6501	925	864	907	928
4.5	10	10	1	4270	856	800.2	844.9	860
4.5	15	5	0.25	7069	1290	1232	1275	1294
4.5	15	5	1	4927	1243	1188	1225	1246
4.5	15	10	0.25	7189	1286	1226	1265	1288
4.5	25	5	0.25	7901	1802	1752	1787	1810
4.5	25	10	0.25	8051	1802	1749	1787	1806
7.5	5	5	0.25	9480	1141	1064	1117	1145
7.5	5	5	1	6217	1084	1010	1059	1087
7.5	5	10	0.25	9760	1133	1056	1109	1136
7.5	5	10	1	6321	1054	980	1030	1057
7.5	10	5	0.25	11240	2015	1942	1987	2022
7.5	10	5	1	7831	1951	1882	1924	1957
7.5	10	10	0.25	11630	2012	1935	1976	2017
7.5	10	10	1	8070	1931	1857	1898	1937
7.5	15	10	1	9080	2549	2480	2521	2556
7.5	25	5	0.25	13660	3515	3450	3488	3524
10.5	5	0.2	0.25	8900	1712	1624	1677	1717
10.5	5	0.2	1	5367	1606	1535	1583	1616
10.5	5	5	0.25	13280	1723	1636	1685	1731

Table 8. Total duration of ΔV >400V in a year

	LST=0 eclipse	LST=0 sunlit	LST=6 sunlit	LST=12 sunlit	LST=18 sunlit
Total duration in 1 year(hour)	22.3	0.8	1.7	2.7	0.7

NASCAP/GEO cannot model the oblique solar- incidence, therefore it was estimated that total critical charging duration in sunlit as follow.

(0.8+1.7+2.7+0.7) * 2 = 11.8 hours/year

A possibility that sustained arc will occur is among sunlit. As a result, about 60 hours in mission life, the WINDS solar array generates the power under the inverted potential gradient. Figure 14 shows Te dependency of charging duration of each LST.
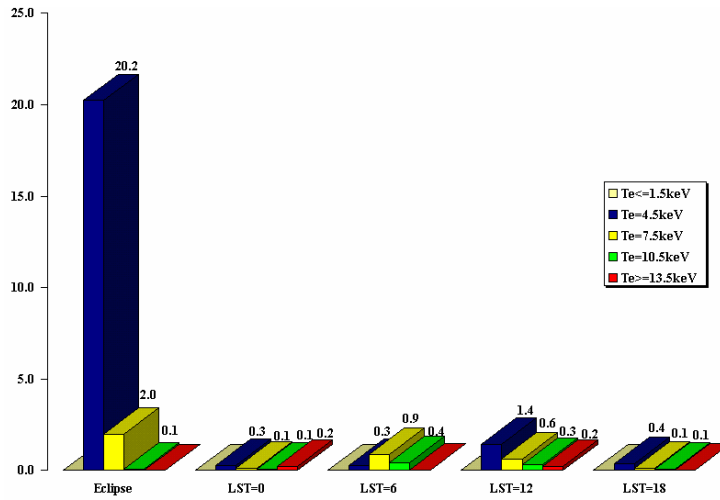
Figure 14.   Te dependency of Charging duration

Total Number of Trigger Arcs:

    The time (Tesd) to reach 400V differential voltage by NASCAP/GEO for the 2780 cases identified were calculated to estimate the total number of trigger arcs based on the charging duration result. Figure 15 shows calculation concept.
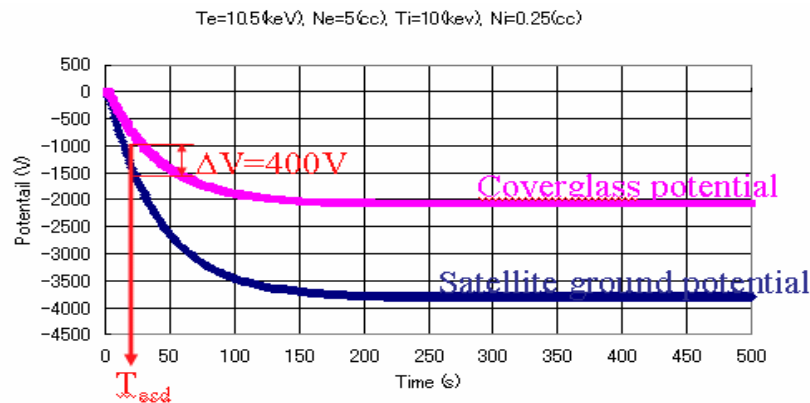
- T_{esd}: Time to reach $\Delta V = 400V$
- T_{chrg}: Charging duration
- N_{arc}: Number of arcs

$$N_{arc} = T_{chrg} \div T_{esd}$$

Figure 15.   Trigger arc frequency analysis concept

Table 9 shows total number of trigger arcs in 1 year.

Table 9.   Total number of trigger arcs in a year

	LST=0	LST=0	LST=6	LST=12	LST=18
	eclipse	sunlit			
Total numbur of trigger arcs in 1 year	556	151	478	487	95

As a result, WINDS solar array has about 12170 trigger arcs in sunlit of mission life, and it has about 14950 trigger arcs in total 5 years of lifespan. Figure 16shows Te dependency of charging duration of each LST.
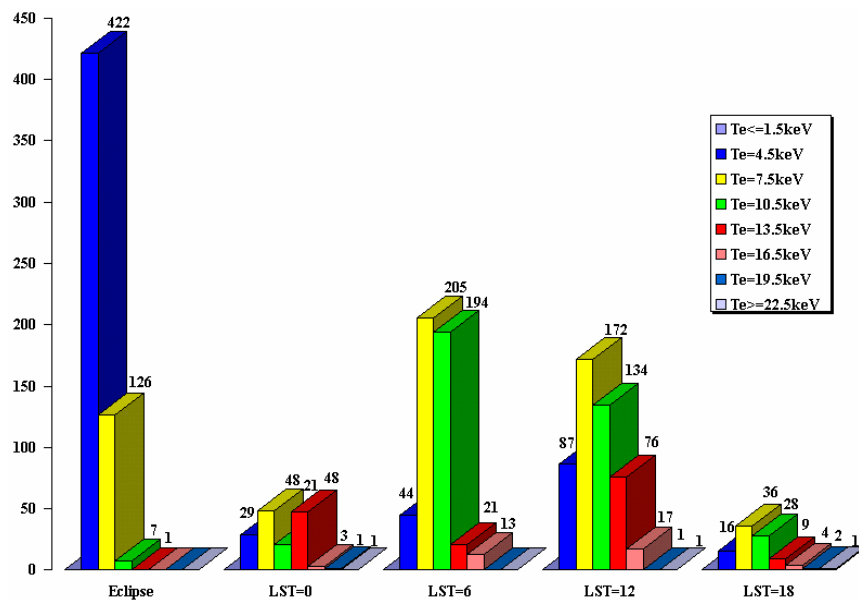
Figure 16.   Te dependency of trigger arcs

It had been comprehended that a critical time zone on the spacecraft charging is from end of eclipse to LST=12. According to the static analysis, however, it is shown that also LST=12 should been considered as a part of critical time zone for the spacecraft charging. This interpretation is supported by Figure 17. This figure shows that there is higher probability of occurrence for n_e (>10cm^{-3}) around LST=12.

(a) n_e>10cm^{-3}   **(b) T_e>3keV**
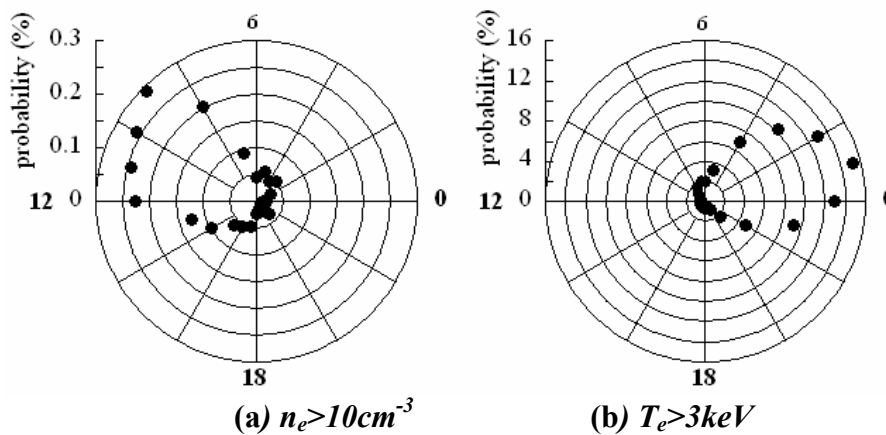
Figure 17.   Probability of occurrence for n_e>10cm^{-3} and T_e>3keV observed on LANL satellite

Conclusions

The ground ESD test and the NASCAP analysis were carried out for WINDS. There was no sustained arc in any coupons during the total 105 hours of the test. The extreme power degradation of 10 solar cells was observed in all the coupons by the total 1206 trigger arcs. It means that coating the cell edge with RTV was not perfect solution for trigger arc. On the other hand, the total number of trigger arcs was 14950 for 5 years, according to NASCAP static analysis. Therefore 124 solar cells were estimated for power degradation with trigger arcs for WINDS lifespan. It is necessary to consider the approximately 100 solar cells additionally for power degradation in WINDS solar array design. Also it was confirmed that exposing the bus bars to space without RTV coating did not show any-side effect. Therefore, to reduce the satellite mass and the risk of arcs at the cell edge, it determined not to coat the bus bars with RTV.

References

1. Cho M. et al, Laboratory tests on 110-Volt Solar Arrays in Simulated Geosynchronous Orbit Environment, Journal of Spacecraft and Rockets, vol.40, No.2, March-April 2003.

2. Cho M. et al, Laboratory tests on 110-Volt Solar Arrays in Ion Thruster Plasma Environment, Journal of Spacecraft and Rockets, vol.40, No.2, March-April 2003.

3. K.Toyoda et al, Development of Solar Array for a Wideband Internetworking Satellite:ESD Test, 8th SCTC, 2003.

4. Cho M. et al, ESD ground test of solar array coupons for a high power GEO telecommunication satellite,]]21st AIAA International Communications Satellite Systems Conference, Yokohama, 2003.

5. M. Frezet, E. J. Daly, J. P. Granger and J. Hamelin, Assessment of Electrostatic Charging of Satellites in the Geostationary Environment, ESA Journal Vol.13, 1989.

6. Gussenhoven M. S. and Mullen E. G., Geostationary environment for severe spacecraft charging, Jounal of Spacecraft and Rockets, 1983.

7. S.Kawakita et al, Influence of high energy electrons and protons on secondary electrons emission of cover glasses for space solar cells, 20th International Symposium on Discharges and Electrical Insulation in Vacuum, Tours, France, 2002.

8. M.Takahashi et al, ETS-VIII Solar PDL Plasma Approach, 7th Space Charging Technology Conference, 2002

DEVELOPMENT OF SOLAR ARRAY FOR A WIDEBAND INTERNETWORKING SATELLITE: ESD TEST

Kazuhiro Toyoda
Chiba University
Inage-ku, Chiba, JAPAN 263-8522
Phone: +81-43-290-3221
Fax: +81-43-290-3221
E-mail: **toyoda@faculty.chiba-u.jp**

Toshiaki Matsumoto
Yoshio Shikata
Mengu Cho
Kyushu Institute of Technology

Tetsuo Sato
JAXA (Japan Aerospace Exploration Agency)

Yukishige Nozaki
NEC TOSHIBA Space Systems, Ltd.

Abstract

This paper describes the details of ground based ESD test carried out for solar array of Wideband InterNetworking engineering test and Demonstration Satellite (WINDS).

An electron beam was used to simulate the inverted potential gradient conditions. The sustained arc was not observed for test coupons with RTV grouting at the inter-string gap and thicker RTV layer between cells and Kapton sheet. Arc pulses short-circuited the PN junction of triple-junction cells once the arcs occurred at the cell edges. Effects of exposing bus bars to space without coating with RTV were also investigated. There was no detrimental effect associated with the exposed bus bars.

Introduction

Since the last decade, the power level of Geosynchronous Orbit (GEO) satellite has increased dramatically to nearly 10 kW or even higher. To manage the large amount of power efficiently, the satellite bus voltage has increased to 100V. Nowadays many commercial telecommunication satellites employ solar arrays that generate the electricity at 100V.

As the voltage of solar array increases to 100V, the problems of arcing during the substorm condition have been recognized as serious hazard that sometimes threatens the stable supply of the solar array power. In GEO, when a satellite receives the sunlight, its charging is dominated by photoelectrons. As long as the satellite surface is well illuminated under the quiet condition, the photoelectrons keep the satellite potential within a few electron volts from the plasma potential. The insulator surface such as coverglass has similar potential. When a satellite encounters the substorm, the current due to high energy electrons increases and sometimes exceeds the current due to photoelectrons. Then the potentials of the satellite body and the insulator surface can become negative. Due to the difference of the secondary electron emission coefficients, the insulator potential may drop slower than the satellite body.

During that process, the coverglass potential can be more positive than the nearby conductor, e.g. interconnector. This situation is called "inverted potential gradient". As the potential difference builds up between coverglass and interconnector, an arc may occur.

The inverted potential gradient is the nominal case in LEO, where an arc can occur once the potential difference reaches 100 or 200 V [1]. If an arc occurs as a single pulse, it is called a trigger arc. The risk of one trigger arc growing to a catastrophic arc receiving energy from the array itself has increased recently as the power level of solar array has increased. TEMPO-2 satellite experienced the permanent loss of significant fraction of solar array output power when a severe substorm hit the satellite in 1997. The failure was attributed to an arc on solar array under the inverted potential gradient condition [2]. First, an arc occurred between adjacent array strings with different potential and short-circuited the two strings. Then the array output power of the two strings fed energy to the arc plasma. The arc current kept flowing and the underlying Kapton insulation layer was thermally broken leading to short-circuit between the array strings and the substrate. In the present paper, we call this type of sustained arc as "sustained arc".

Since the accident of TEMPO-2, the issue of sustained arc has been investigated at several research institutions all over the world. Cho et al [3] carried out an ESD test on solar array for Engineering Test Satellite VIII (ETS8). In the laboratory test, they verified that the inverted potential gradient could occur due to the difference of secondary electron coefficients of coverglass and conductive surface. The threshold voltage for the trigger arc inception was measured to be 400V. The sustained arc between the solar array string and the CFRP substrate occurred through a defect in Kapton sheet with the potential difference of 110V and the current capability of 2.64 A. Based on the test results, precaution was taken to minimize the possibility of a defect of Kapton sheet being exposed. The thickness of RTV layer between solar cells and the Kapton sheet was increased to 70 ~ 100 μm from the originally designed value of 50 μm. In addition, RTV was leaked out from the bottom of cell to cover the Kapton sheet near interconnector.

Toyoda et al [4] found that even trigger arcs may degrade the solar array output power during the ESD test on the ETS8 solar array. Excessive coating with RTV resulted in severe contamination over coverglass surface as the amount of silicon vapor produced by trigger arc increased. Short circuit of PN junction was also observed, that decreased the string output power by the output power of one cell. The results found in Ref. [4] imply that as the number of trigger arcs accumulates in orbit, the solar array output power may decrease gradually. Historically, the effects of trigger arcs in GEO have been neglected as long as the arcs ended as pulses of finite duration. If the repeated trigger arcs truly degrade the solar array in orbit, we might have noticed it already because a trigger arc due to the inverted potential gradient can occur on any satellite regardless the bus voltage.

There are three possible explanations why we have not noticed such power degradation yet. One is that the radiation dose effect on the solar cell power degradation has been overestimated. The second one is that there have not been so many trigger arcs during the satellite lifetime to have the effect distinguishable from the radiation dose effect. The third one is that the energy of each trigger arc was not large enough to cause the degradation because the satellite power level that is proportional to the area of solar array has been low. If the third hypothesis is correct, the power degradation due to trigger arcs may emerge in near future as the size of solar array increases and the total capacitance of coverglass increases. In that case we need a model to estimate the power degradation during the satellite lifetime and

reflect the result in the design phase of satellite power system. Once a trigger arc occurs, its energy is supplied by two types of capacitance; satellite capacitance and coverglass capacitance. The satellite capacitance that is typically of the order of 100 pF is responsible for the very beginning of trigger arc inception. As the trigger arc occurs, the electrons are ejected from the arc spot and the satellite potential rapidly reaches the zero potential. Then the coverglass surface becomes positive with respect to the space plasma.   The trigger arc
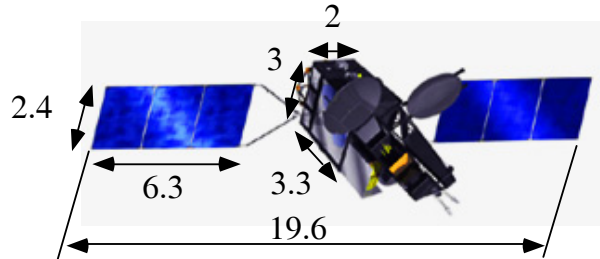
Figure 1.   Artist's image of WINDS. The sizes are shown in m.

plasma neutralizes the charge stored on the coverglass and the charge flows as the arc current. Therefore, the coverglass capacitance is responsible for the growing phase of the trig ger arc. In recent high power satellites, the total amount of coverglass capacitance is 10 µF or more. With the potential difference of 1 kV between the coverglass and the solar array string, the electrostatic energy available for the trigger arc is more than 1J. Leung [5] carried out an ESD test using a very large solar array coupon (11×19 cells with the size of 30 inch by 30 inch, approximately). He observed that the trigger arc plasma expanded up to the edge of the coupon and neutralized most of the charge stored on the coverglass before the trigger arc inception.

In the present paper we report the result of ESD tests carried out on solar array for WINDS (Wideband Inter- Networking engineering test and Demonstration Satellite) that will be launched by National Space Development Agency of Japan in 2005. Figure 1 shows an artist's image of WINDS. The satellite solar array generates a power of 5.2 kW at a voltage of maximum 55 V with triple-junction cells. The satellite bus voltage is 50 V. The purposes of the test are the following;

1. Confirm that the solar array suffers no sustained arc
2. Study how the amount of RTV coating applied to the cell edge affects the power degradation due to trigger arcs
3. Determine the flight design of solar array.

The solar array design of WINDS is based on the design of ETS8 [3]. Because WINDS uses triple-junction cells instead of silicon cells used for ETS8, the difference of coverglass material might lead to a different behavior under the inverted potential gradient condition. Also, because WINDS does not carry ion thruster unlike ETS8, there is no need to coat the bus bar with RTV to avoid the current leakage to the high density plasma generated by the backflow from the ion thruster plume. We need to confirm that exposing bus bar does not give rise to new problems in terms of ESD. The power degradation found in the previous study on ETS8 [4] should be investigated further to predict the power degradation at EOL (End-of-Life). In the present paper, we first describe the test system. Then, we discuss the test result. Finally we conclude the paper by describing the flight design of solar array.

Experiment

The solar array of WINDS consists of two solar array paddles where 292 parallel strings of solar cells are mounted. Each string is made by the series connection of 30 triple-junction cells. The output voltage and currents of each string are 55 V and 0.6 A. The maximum potential difference between adjacent cells is 55 V. The coverglass is CMG-100-AR and has a thickness of 100 μm. The coverglass capacitance is 0.76 nF each. Because one paddle has approximately 4200 cells, the total coverglass capacitance is 3.2 μF for each paddle.
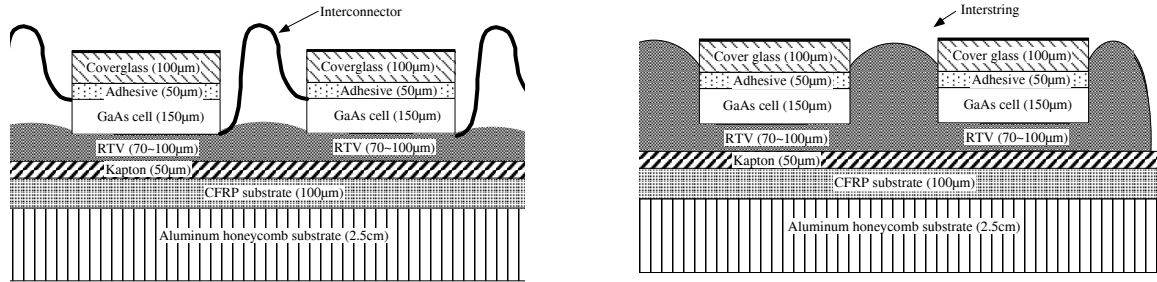
Figure 2.   Cross-sectional view of coupons 2 and 3.
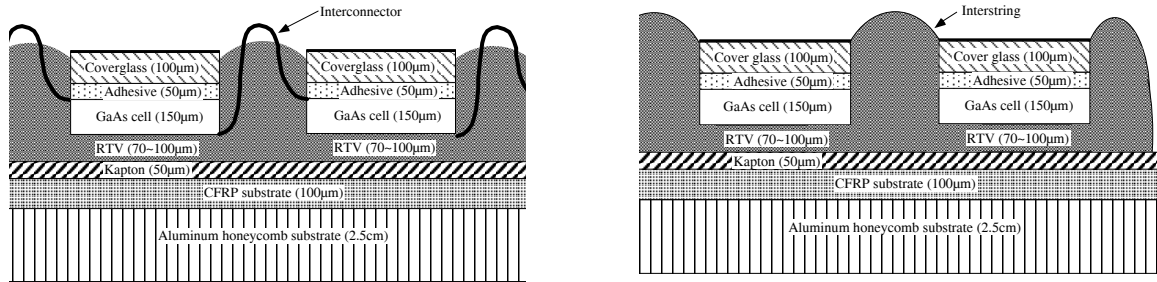
Figure 3.   Cross-sectional view of coupon 1.

We used three test coupons. The cross-sectional view of solar array coupon is shown in Figs. 2 and 3. A photograph is shown in Fig. 4. The summary of difference among the coupons is listed in Table. 1. A coupon consists of 15 cells (76 mm by 37 mm each). Five cells are connected in series making three parallel strings. At the corner of each cell, a bypass-diode is attached. We name each string as R, B, and G-strings. The R- and B-strings are connected in parallel at the backside of the coupon. Therefore they always have the same potential during the ESD test. Cells are glued on Kapton sheet of 50 μm thickness with RTV silicon. The Kapton sheet is placed on top of CFRP sheet (0.1 mm thickness) and aluminium honeycomb substrate (25 mm thickness). The side of aluminium honeycomb substrate is covered by Kapton tape not to have trigger arcs.

Table 1.   Difference of test coupons.

Coupon	Amount of RTV	Bass bar coating
1	large	yes
2	normal	yes
3	normal	no
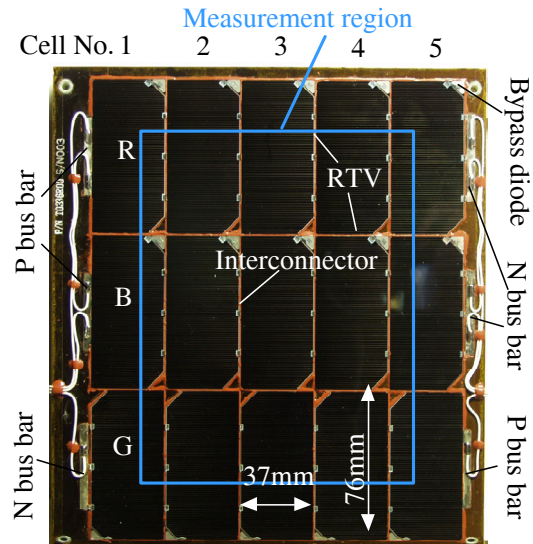
Figure 4. Photograph of a test coupon.
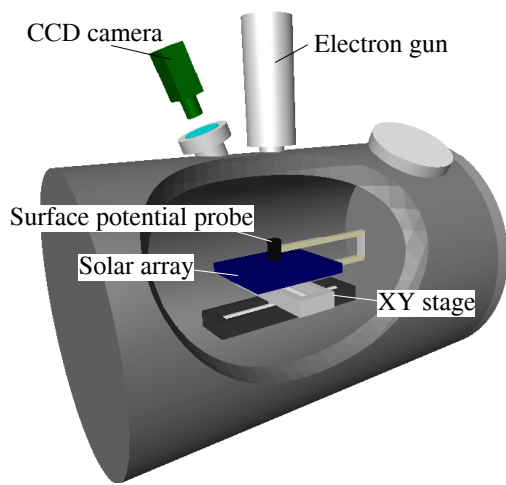
Figure 5. A schematic picture of chamber system.
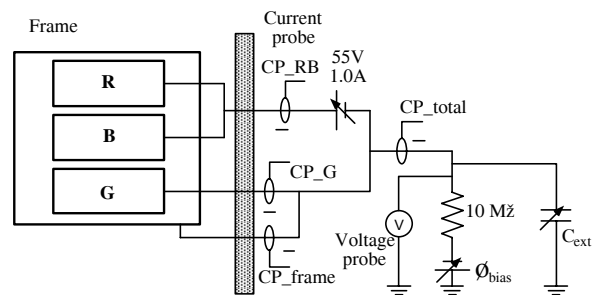
Figure 6. Layout of external circuit.

All the three coupons has the same thickness of RTV layer between cells and Kapton sheet, approximately 100 μm, inheriting the design from ETS8. The gap between strings is grouted by RTV also inheriting the design from ETS8. The coating of RTV at the cell edges of the coupon 1 is much thicker than the coating of ETS8, aiming at suppressing the trigger arc inception at the cell edges that lead to the short circuit of PN junction. The coating of RTV at the cell edges of the coupons 2 and 3 is the same as ETS8. The bus bars of the coupon 3 are not coated with RTV to save the satellite mass by a few kg. We can also expect that the bus bars act as lightning rods where a trigger arc occurs before it occurs at more dangerous points such as the string-gaps or the cell edges.

In Fig. 5, we show a schematic picture of the experiment. A coupon was placed on an acrylic plate in a vacuum chamber of 0.6m diameter and 0.9m length with the cell surface facing up. The vacuum chamber was evacuated by a turbo-molecular pomp and could reach a pressure of as low as 10^{-5} Pa before the test. During the test, the chamber pressure was 0.5 ~ 5×10^{-3} Pa. There was an electron beam gun at the top of vacuum chamber. The center of the electron beam was usually kept at the center of the coupons. The maximum beam voltage was 30 kV. At the beam energy of 3 kV that was a typical value during the test, the current density was 10 mA/m^2 and had the gaussian distribution of 150 mm diameter. The chamber

was also equipped with a Kaufman type argon plasma source that was used to remove the surface charge at the beginning of each ESD test.

A surface potential probe was attached to a XY stage to measure the two-dimensional distribution of surface potential. The surface potential probe could measure the potential up to ±20 kV. The probe moved over the coupon surface at the distance of 5mm. The probe motion was controlled by a PC and the potential was measured at the intervals of 10mm inside the area of 180mm×140mm. It took approximately 7 minutes to finish one measurement. The positions of trigger arcs were recorded by the arc position identification system [6]. The analog video image of coupon during the ESD test taken by a CCD camera was saved in real time to a PC as a digital video image sequence. After the test, the video sequence was analyzed by a computer program to identify the trigger arc positions from the optical flash associated with each trigger arc.

All the coupons were baked at 125°C for 5 hours at the factory before they were shipped to the laboratory for the ESD tests. Other than the baking, no special treatment of the coupon surface was applied before the shipment. Once a coupon arrived at the laboratory, we first took photographs of the cell edges by ×60 optical microscope. Once a coupon was placed in the vacuum chamber and the chamber was evacuated, we baked the coupon at 70°C ± 1°C for 2 hours. During the ESD test, the coupon temperature was kept at 40°C ± 1°C.
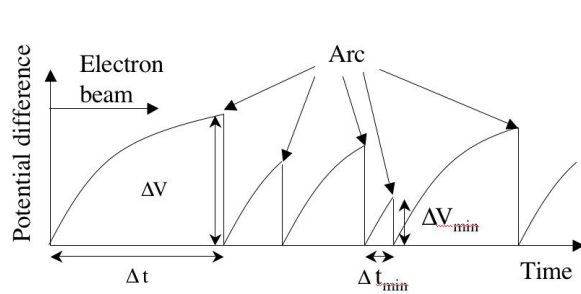
Figure 7.   A schematic model of temporal profile of potential difference during the electron beam irradia-
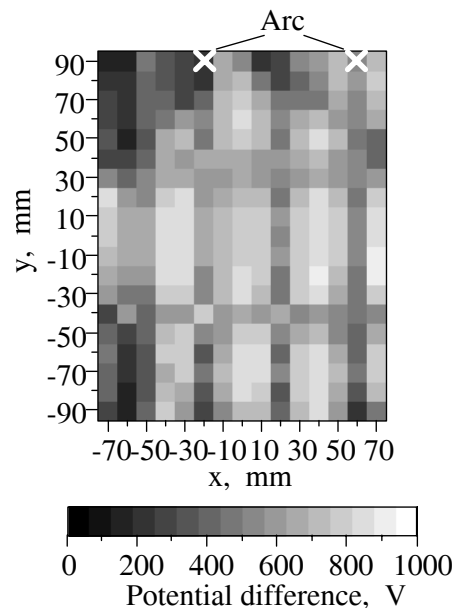
Figure 8.   Distribution of potential difference at 4 s after a trigger arc inception.

In Fig. 6, we show a layout of external circuit. The coupon was electrically insulated from the vacuum chamber. The cables from the bus bars were connected to a connector at the backside of a coupon. From the connector, the cable was connected to the external circuit through high voltage feed-throughs of the vacuum chamber. The solar array coupon was biased negatively via a DC power supply. In order to protect the power supply, the resistance of 10MΩ was connected. A high voltage probe measured the potential of the coupon, $\varnothing_{bias}$. Between the R and B strings and the G string, an inter-string voltage was applied by another DC power supply. The power supply usually acted as a constant voltage source of 55 V and

would have acted as a constant current source of 1.0 A once the strings had been short-circuited by the arc plasma.

The arc current was measured via current probes. In Fig. 6, the probes denoted as CP_{RB} and CP_{total} could measure the current from DC to 10 MHz. The probes denoted as CP_{frame} and CP_G could measure from 8.5 kHz to 100 MHz. The current probes and the high voltage probes were connected to two 4 channel digital oscilloscopes (bandwidth 100MHz). The oscilloscopes were triggered once $\varnothing_{bias}$ increases above a certain level due to the voltage drop of the trigger arc current. The waveforms measured by the oscilloscopes were transferred to PCs via GPIB cables.

The external circuit had a capacitance to simulate the coverglass capacitance which supplied the energy to the trigger arc plasma. The value of the external capacitance was set so that the amount of electrostatic energy was equal to the energy to be given in orbit. The electrostatic energy stored in the coverglass of one solar array paddle is given by

$$U_{cg} = \frac{1}{2} C_{cg} \Delta V^2 \qquad (1)$$

where C_{cg} is the total capacitance of coverglass, 4 µF for the case of WINDS, and ΔV is the potential difference between the coverglass and the solar array string when a trigger arc occurs. The external capacitance, C_{ext}, was determined by

$$C_{ext} = \frac{2U_{cg}}{V_{bias}^2} \qquad (2)$$

where V_{bias} was the bias voltage. In order to determine C_{ext}, we first measured ΔV before the ESD tests.

In Fig. 7 we show a schematic model of how the potential difference ΔV changes as trigger arcs occur repeatedly while the coupon is irradiated with the electron beam. We first remove the surface charge by the dense plasma generated by the plasma source. Then we irradiate the coupon with the electron beam at the constant energy and current density. The potential difference builds up as shown in Fig. 7. The potential difference follows the same temporal profile as long as the beam parameters are kept the same. At a time Δt from the start of electron beam, a trigger arc occurs at a potential difference of ΔV. Once an arc occurs, most of the coverglass charge is neutralized and the potential difference goes back to nearly zero. Because the electron beam is operated constantly, the potential difference starts to increase again immediately after the trigger arc. It is not guaranteed that the next trigger arc occurs at the same position and with the same ΔV as the previous one.

The threshold voltage for the trigger arc inception ΔV_{min} was obtained by measuring the minimum time interval between the trigger arcs, Δt_{min}. Because the real solar array consists of 4200 cells per one paddle, one cell would have the favorable conditions to arc at ΔV_{min} or less that was measured with a coupon of only 15 cells. We irradiated a solar array coupon biased to -3 kV with the electron beam of 3 keV for 1 hour. We measured the minimum time interval Δt_{min} during the one hour. Then, we irradiated the coupon with the beam and waited for an arc. Once an arc occurred, we switched off the beam at Δt_{min} from the arc inception. Then the surface potential distribution was measured to identify ΔV_{min} at the arc spot where the trigger arc occurred with the interval of Δt_{min}.

The coupon used to measure the threshold voltage ΔV_{min} was another one different from the three coupons used for the ESD test. The coupon consisted of 15 triple junction cells with CMG-100-AR coverglass. The cell layout was similar to the three ESD coupons. The only

difference from the ESD coupon was that the thickness between the cell and the Kapton sheet was 50 μm. The coupon was biased to -3 kV with an external capacitance of 100 nF. The minimum time interval was Δt_{min} = 4 sec. In Fig. 8 we show the surface potential distribution measured after the beam irradiation of 4s from an arc inception. The marks shown in Fig. 8 are the position of the arcs that had Δt_{min} = 4 sec. The maximum potential difference near the arc spot was 800 V. From this measurement we determined ΔV_{min} = 800 V. Substituting ΔV = 800 V into Eq. 1, we obtained 1.28J as the electrostatic energy given to a trigger arc. From Eq. 2 we determined C_{ext} so that the energy was close to 1.28J. During the test we used bias voltages of -3 kV, -4 kV and -6 kV. At each bias voltage we changed C_{ext} to 400 nF, 200 nF, and 100 nF to have the energy of 1.8J, 1.6J, and 1.8J.

Table 2. Test conditions.

Case	Coupon	$\varnothing_{bias}$, -kV	C_{ext}, nF	V_e, kV	t_{exp}, h
1	1	3	400	2.8 - 4.0	6
2	1	4	200	3.0 - 4.0	4
3	1	6	100	3.0 - 6.0	10
4	2	3	400	2.8 - 4.0	6
5	2	4	200	3.0 - 4.0	4
6	2	6	100	3.0 - 6.0	10
7	3	3	400	2.8 - 4.0	6
8	3	4	400	3.0 - 4.0	4
9	3	6	100	3.0 - 6.0	10
10	3	3	400	2.8 - 4.0	6
11	3	4	200	3.0 - 4.0	4
12	3	3	400	3.0 - 4.0	35

Figure 9. Distribution of potential difference at case 2.
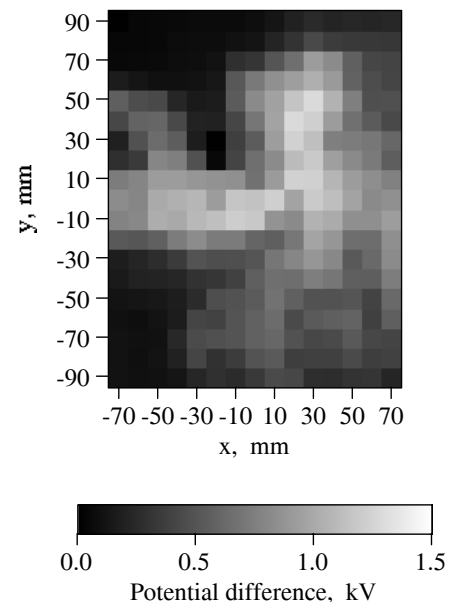
Figure 10. Distribution of potential difference at case 3.

On the basis of the potential difference measurement, the time on the inverted gradient condition is estimated as 60 hours for five years by employing NASCAP/GEO [7]. We

decided on 65 hours as the test time for coupon 3 to evaluate the power degradation due to arcing. Table 2 lists the test conditions. We tested the coupons 1 and 2 for 20 hours and the coupon 3 for 65 hours. For the cases 1~9, and case 11, the beam center was aligned to the center of the coupons. For the cases 10 and 11, the beam center was set to the center of No.1 cell of the B string, because the test purpose was to see the trigger arcs at the bus bars. The electron beam voltage, V_e was lowered gradually so that trigger arcs would occur frequently. The temporal profile of V_e was kept the same among the three test coupons. For the case 8, the external capacitance of 400 nF was used instead of 200 nF by mistake.

At every 10 hours from case 1 to 9, the coupons were removed from the chamber. After the photographs of the cell edges were taken by the 60 optical microscope, they were sent back to the factory to measure the output power. Each coupon was taken out from the vacuum chamber after the cases 2, 3, 5, 6, 8, 9, and 10. Once a coupon was put in the chamber, it was kept in vacuum for approximately three days. Every time the coupons were exposed to atmosphere, they were baked for 2 hours at 70°C before the ESD tests.

Test Results and Discussions

In Table 3 we list the number of arcs observed. During the 20 hour experiment, the number of arcs is 288, 392, and 266, respectively for the coupons 1, 2, and 3. The coupon 2 had arcs more than the other two coupons. The cases 10 and 11 had 260 arcs in 10 hours. The cases with higher arc rates had higher chamber pressures. With so many trigger arcs, there was no sustained arc and we confirmed that the solar array design is very effective at suppressing the sustained arc occurrence.

In Figs. 9 and 10, we show the distribution of potential difference, ΔV over a coupon. The case 2 has $\varnothing_{bias}$ = -4 kV and V_e = 3 kV. The case 3 had $\varnothing_{bias}$ = -6 kV and V_e = 3.4 kV. In the both cases the potential difference is higher than 1 kV but the distribution patterns are different. For the case 2, the center of the coupon that is also the center of the beam is charged to a high potential difference more than 1 kV. In this case, the coupon surface has a potential more positive than -3 kV and the electron beam of 3 kV can reach the surface even though it is decelerated. Therefore, the coverglass surface is charged due to emission of electron-induced secondary electrons. For the case 3 where the coupon is biased to -6 kV, however, even if the potential difference is 1.5 kV, the surface potential is still -4.5 kV. Therefore, the electron beam cannot reach the surface and the surface is charged by positive ions produced by ionization of neutral gas via the electron beam.

Table 3.   Number of arcs.

Case	Coupon	N_{arc}	t_{exp}, h	p, 10^{-3} Pa
1	1	78	6	1.12
2	1	78	4	1.25
3	1	132	10	0.98
4	2	58	6	1.10
5	2	1	4	0.65
6	2	333	10	2.46
7	3	60	6	0.86
8	3	41	4	0.62
9	3	165	10	0.83
10	3	150	6	2.51
11	3	110	4	1.73
12	3	84	35	0.56

In Fig. 11, we show the positions of all the arcs during the tests. Majority of the arcs occurred at the interconnectors that are exposed to space. The arc positions of cases 2 and 3 agree well with the potential distribution shown in Figs. 9 and 10. In cases 4, 5, 6, 10, and 11 many arcs are observed at the cell edges unlike other cases.

In Fig. 12, we show a typical example of arc current waveforms. This is the waveform measured by CP_{total} for an arc at an interconnector at the B string during the case 1. The pulse width is approximately 30 μs. From this kind of waveform, we identify the peak value and calculate the charge by integrating the current with respect to time. At the arc inception we also observed the jump of ionization gauge due to vaporization of the surface material near the arc spot.

Table 4 lists the results of the peak currents, the charge flown as the arc current, and the pressure increase at the arc inception. We also list the amount of charge stored in the external capacitance, $Q = C_{ext} jV_{bias} j$. The table lists the average and the standard deviation of each item. For the test using the coupon 2, we did not use the current probes that could measure up to DC. Therefore the results of the cases 4, 5, and 6 are not listed. The average of the peak current increases as the charge stored in the external capacitance increases. There is no significant difference between the coupons 1 and 3 as we compare the cases with the same external charge, Q.

After the test, we observed the power degradation for all the three coupons. In Fig. 13 we plot the ratio of degraded power to the initial power. The horizontal axis denotes the test time. The R and B strings were connected in parallel at the backside of the coupon, and were not separated as we measured the output power. The R and B strings degraded most severely, 23% in 59 arcs and 49% in 392 arcs. The coupon 1 suffered 19% degradation in 156 arcs but remained the same in 288 arcs. The coupon 3 showed little degradation up to 266 arcs but degraded severely after that. From these results, the power degradation is not simply proportional to the number of arcs. There is a certain type of trigger arc that damages the PN junction. The cell performance degrades only when such a damaging arc occurs.
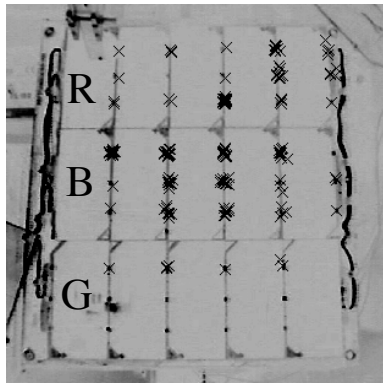
(a) Cases 1 and 2
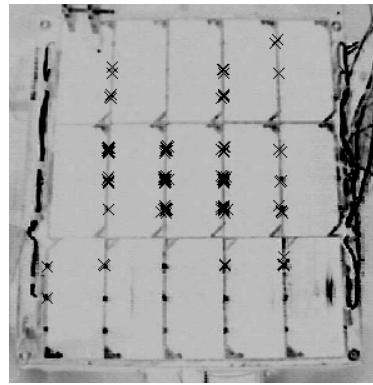
(b) Case 3
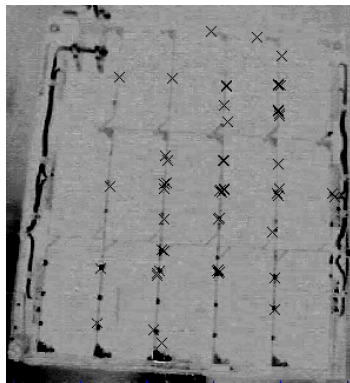
(c) Cases 4 and 5
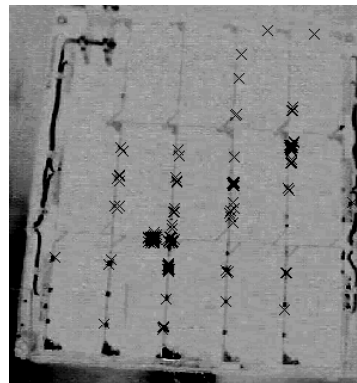
(d) Case 6
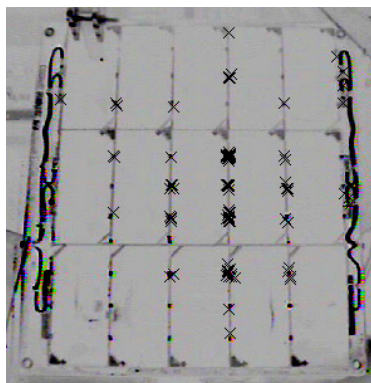
(e) Cases 7 and 8
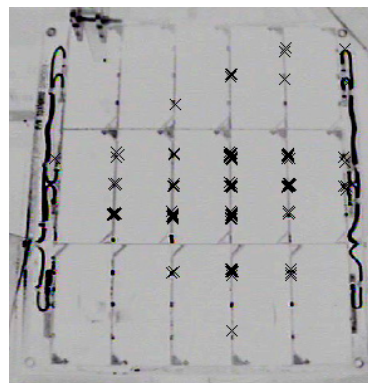
(f) Case 9
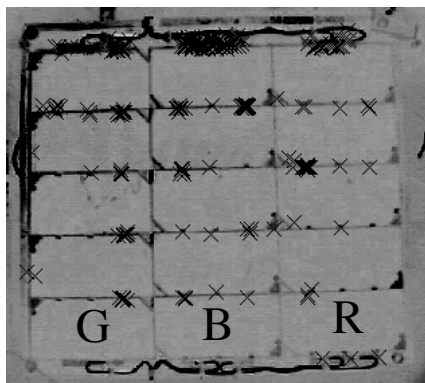
(g) Cases 10 and 11
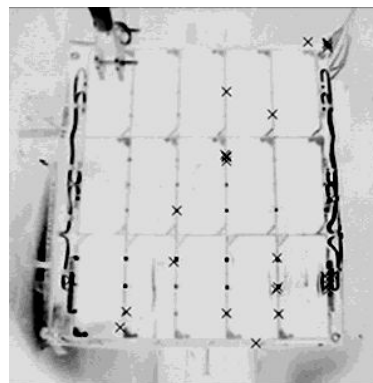
(h) Case 12

Figure 11.   Positions of arcs.

Table 4. Statistics of peak current, charge, and pressure increase dore to each arc.

Case	Q, mC	I_{ave}, A	I_{std}, A	Q_{ave}, mC	Q_{std}, mC	Δp_{ave}, mPa	Δp_{std}, mPa
1	1.2	123.5	50.8	1.12	0.23	1.32	0.14
2	0.8	105.5	49.0	0.80	0.06	1.15	0.08
3	0.6	81.6	33.1	0.64	0.04	0.97	0.08
7	1.2	151.5	108.7	1.22	0.22	1.38	0.14
8	1.6	159.4	65.1	1.56	0.16	2.06	0.11
9	0.6	71.2	27.0	0.63	0.02	0.94	0.99
10	1.2	144	66.5	1.27	0.13	1.53	0.15
11	0.8	111	69.5	0.80	0.01	1.12	0.10
12	1.2	155	59.9	1.27	0.13	1.60	0.19
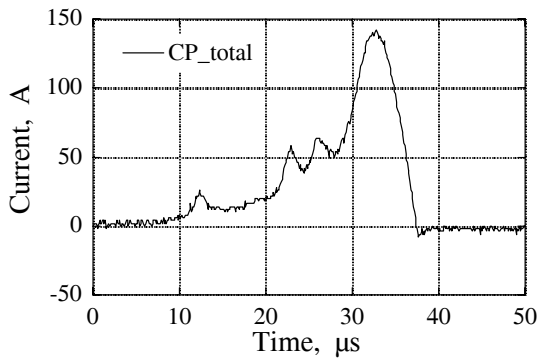
Figure 12. Typical example of arc current waveform.
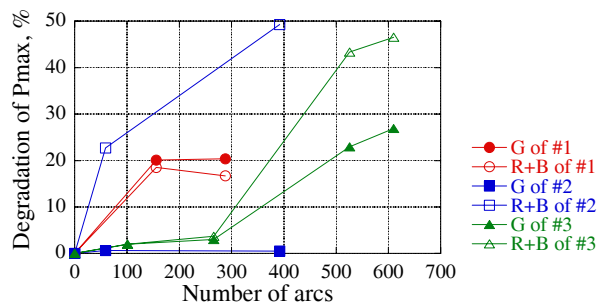
Figure 13. Degradation of solar array output power.

After the tests as for the coupon 2, the electric performance was measured with cutting the parallel connection between R and B string. The result showed that one cell in R string and two cells in B string were short-circuited. From this result, it was estimated that about 400 arcs could destroy 3 cells. From the analysis using NASCAP/GEO, the number of trigger arcs was estimated at 14950 during 5 years [7]. For WINDS satellite with 5 years lifetime, the number of the degraded cells is calculated at about 112 cells.

We identified the damaged cells of the coupon 2. The cell 2 and 4 of the B string and the cell 4 of the R string were short-circuited and generated little voltage. We carried out detailed analysis via the IR-OBIRCH method [4] on the cell 4 of the B string. The short-circuited PN junction was located at the cell edge. In Fig. 14 we show a microscope photograph of the short-circuited position taken after the test. There was an arc spot of silver color at the cell edge where the current leakage via the short-circuited PN junction was identified. The arc occurred at a void of RTV that should have covered the edge. Through the void, the cell edge was exposed to space. Trigger arcs often occurs at such void and if they occur at the cell edges they are likely to short-circuit the PN junction. It is difficult to prevent the formation of void in RTV during the manufacturing processes of solar array panels. We can fill in the void by putting additional RTV. The coupon 2 had the voids more than the other two coupons. We paid special attention to the other two coupons to inspect the cell edges and fill in the voids. Still, even for a coupon panel of 15 cells we can not completely prevent the formation of the voids. It is practically impossible to inspect all the edges of more than 8,000 cells and fill in the voids.
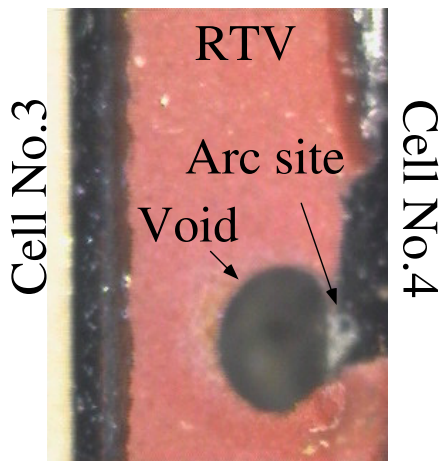
Figure 14. Photograph of the arc spot responsible for the short-circuit of PN junction of the B string of the coupon 2.
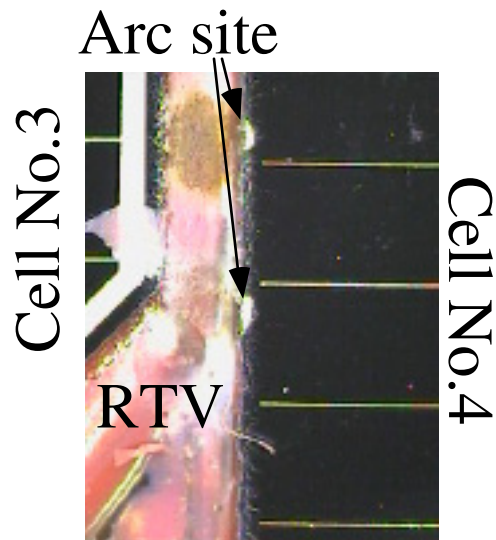
Figure 15. Photograph of the arc spot suspected to be responsible for the power degradation of the R string of the coupon 3.

In Fig. 16 we show a photograph of the cell 4 of the R string of the coupon 3 which had arcs during the case 10. There are two arc spots at the cell edge. They are very similar to the arc spot shown in Fig. 16 and probably the cause of power degradation after the last 10 hours of the coupon 3 as shown in Fig. 13. In Fig. 15, however, there is no void in RTV. The G string had a similar arc spot without a void nearby that was formed during the last 10 hours. Probably, the height of grouted RTV was not high enough to cover the conductive area at the cell edge. Therefore, the presence of void is not the necessary condition for the power degradation. The necessary condition is that a trigger arc occurs at the cell edge.

It is difficult to completely suppress the trigger arcs leading to the power degradation. Using an extra amount of RTV certainly reduces the probability of trigger arc inception. But at the same time, it increases the probability of void formation as the total volume of RTV increases. Also the more RTV coating leads to the more contamination of coverglass as reported in Ref. [4] and the more weight. Using little or no RTV increases the probability of trigger arc inception. Therefore, there is the optimum level of how much RTV coating should be used. To determine the optimum level, we need an estimate on how much the solar array output power really degrades in orbit and use the estimate as an input parameter of the system analysis.

In the first 20 hours of the test on the coupon 3, only few arcs occurred on the bus bars because the beam center was aligned with the center of the coupon. In order to see the effects of exposed bus-bars, we shifted the beam center toward the bus bar in the cases 10 and 11. During the test of total 30 hours, there was no sustained arc on the coupon 3. Therefore, exposing the bus bars does not increase the risk of the sustained arc.

In cases 10 and 11, there were 121 arcs at the bus bars. There were 137 arcs at the other parts, such as interconnectors or cell edges. Although trigger arcs occur at the bus bar as frequently as the other parts, they don't dominate the arc occurrence as we originally hoped. As long as an arc occurs at the bus bar, however, the trigger arc plasma initializes the charging processes at the other points. Therefore, the arcs at the bus bar reduces the risk of

trigger arcs at the other points, although the degree of reduction may not be so large. Nevertheless, there is no active reason for coating the bus bars with RTV, as long as exposing bus bars causes no harm.

Table 5.   Arc parameters depending on arc position.

Case	Position	I_{ave}, A	I_{std}, A	Q_{ave}, mC	Q_{std}, mC
10	Bus bar	122	36	1.23	0.08
10	IC	128	34	1.24	0.09
11	Bus bar	91	37	0.79	0.05
11	IC	88	24	0.75	0.04

In Table 5 we list the peak current and the charge of the trigger arcs at the bus bars and the interconnectors for the cases 10 and 11. There is no significant difference depending on the positions. We have concluded that there is no need to coat the bus bars with RTV as long as the satellite does not carry ion thrusters.

Conclusion

We carried out the laboratory tests on solar array for WINDS. We tested three types of solar array coupons. There was no sustained arc in any coupon during the total 105 hours of the test. We observed the power degradation in all the coupons. The power degradation was caused by trigger arcs at the cell edges that were exposed to space. Coating the cell edge with RTV was not a prefect solution because there were always voids in the RTV.

Exposing the bus bars to space without any coating with RTV did not show any side-effect. Therefore, to reduce the satellite mass and reduce the risk of arcs at the cell edge, we determined not to coat the bus bars with RTV.

We summarize the flight design of WINDS solar array in the following;

1. To suppress the inter-string sustained arc, the gap between strings is grouted with RTV.
2. To suppress the string-substrate sustained arc, the RTV layer between the cells and the Kapton sheet is specified as 100 μm and the RTV layer leaks out at the cell gap in the direction of series connection.
3. There is no coating of bus bar with RTV.
4. To avoid trigger arcs at the cell edges, we give the best effort to fill in the voids of RTV by additional RTV.

In the present test, the power degradation due to trigger arcs was also confirmed for triple-junction cells in addition to Si cells tested in Ref. [4]. We also found that the necessary condition for the power degradation is trigger arcs at the cell edge. We still don't know how large the trigger arc must be to cause the damage. In the present test, we assumed that the electrostatic energy stored in the entire paddle of solar array would be given to each trigger arc plasma. Whether this is really true or not is still under controversy and the present test was carried out assuming the worst case. In future we need to study the threshold of the trigger arc energy for the power degradation and whether such energy is really available for a trigger arc in orbit.

References

1. Hastings, D. E. and Garrett, H. : Spacecraft Environmental Interactions, Cambridge Univ. Press, 1996.

2. Katz, I. , Davis, V.A. and Snder, D.B. : Mechanism for Spacecraft Charging Initiated Destruction of Solar Arrays in GEO, AIAA 98-1002, 36th Aerospace Sci. Meeting, (1998).

3. Cho, M., Matsumot, T., Ramasamy, R., Toyoda, K., Nozaki, Y. Takahashi, M.: Laboratory Tests on 110V Solar Arrays in a Simulated Geosynchronous Orbit Environment AIAA 2002-0630, 40th Aerospase Sciences Meeting, Reno, January, 2002

4. Toyoa, K., Matsumoto, T., Cho, M., Nozaki, Y., and Takahashi, M.: Power reduction of solar arrays due to arcing under simulated GEO environment AIAA 2003-0682, 41st Aerospace Science Meeting, Reno, January, 2003.

5. Leung, P.: Plasma Phenomena Associated with Solar Array Discharges and Their Role in Scaling Coupon Test Results to a Full Panel AIAA 2002- 0628, 40th Aerospase Sciences Meeting, Reno, January, 2002

6. Toyoda, K., Cho, M., and Hikita, M.: Development of Position Identitifcation System of Arc Discharge on a Solar Array in Vacuum by Digital Processing of Video Images, J. Japan Soc. Aero. Space Sci.,Vol.51, No.589, pp.82-84, 2003.

7. Sato, T., Takahashi, M., Nakamura, M., Kawakita, S., Cho, M., Toyoda, K., and Nozaki, Y.: Development of Solar Array for a Wideband Internetworking Engineering Test and Demonstration Satellite: System Design, 8th Spacecraft Charging Technology Conference, Huntsville, USA, October, 2003.

GROUND-BASED SIMULATION OF LOW EARTH ORBIT PLASMA CONDITIONS: PLASMA GENERATION AND CHARACTERIZATION

John D. Williams
Mechanical Engineering Dept.
Colorado State University
Fort Collins, CO 80523
E-mail: johnw@engr.colostate.edu

Casey C. Farnell
Paul B. Shoemaker
Colorado State University

Jason A. Vaughn
Todd A. Schneider
NASA Marshall Space Flight Center

Abstract

A 16-cm diameter plasma source operated on argon is described that is capable of producing a plasma environment that closely simulates the low Earth orbit (LEO) conditions experienced by satellites in the altitude range between 300 to 500 km. The plasma source uses a transverse-field magnetic filter, and has been successful in producing low electron temperature plasmas that contain streaming ion populations. Both of these characteristics are important because the plasma in LEO is relatively cold (e.g., $T_e \sim 0.1$ eV) and the ram energy of the ions due to the motion of the satellite relative to the LEO plasma is high (e.g., 7,800 m/s which corresponds to ~ 5 eV for O^+ ions). Plasma source operational conditions of flow rate and discharge power are presented that allow the electron temperature to be adjusted over a range from 0.14 to 0.4 eV. The expanding plasma flow field downstream of the source contains both low-energy, charge-exchange ions and streaming ions with energies that are adjustable over a range from 4 eV to 6 eV. At low flow rates and low facility pressures, the streaming ion component of the ion population comprises over 90% of the total plasma density. In the work described herein, a large area retarding potential analyzer was used to measure both electron and ion energy distribution functions in the low density, expanding plasma produced downstream of the plasma source. The benefits of using this type of plasma diagnostic tool in easily perturbed, low-density plasma are identified, and techniques are also discussed that can be used to perform real-time measurements of electron temperature. Finally, recommendations are made that may enable lower electron temperatures to be produced while simultaneously decreasing the plasma source flow rate below 1 to 2 sccm.

Introduction

Simulation of the LEO plasma environment in ground-based vacuum facilities has been performed at various governmental space agencies and commercial aerospace companies for many years.[1,2,3,4] In most of these studies compromises have been made on the fidelity of the plasma environment simulations in regard to plasma composition, plasma density, electron

temperature, and ram (or streaming) ion energy. M.G. Cho et al.[5] used an argon ion source to simulate the LEO plasma environment ($n_e = 0.5 \times 10^6$ cm^{-3}) during high voltage solar cell arc tests where the reported electron temperature produced by their LEO plasma simulator was quite high at 2.4 eV compared to actual LEO electron temperatures of ~0.1 eV. Vaughn et al.[6] present results of studies on arcing in plasma and expansion of arcs into simulated LEO ambient plasmas produced by an orificed hollow cathode discharge operated on argon. The plasma density in this study was 1.5×10^6 cm^{-3} and the electron temperature was 1 eV at the sample location.   In earlier work, Konradi et al.[7] discuss plasma ion current collection on panels of various sizes biased at large negative voltages. The plasma was created in a large vacuum test facility using a Kaufman ion source which was also operated on argon. No biases were applied to the ion optics system, and, consequently, the energy distribution of the emitted ions was only dependent upon the plasma potential distribution within the discharge chamber and the potential variation from the source to the panels under test. The authors indicate that electron temperatures as low as 0.15 eV were obtained at plasma densities ranging from 0.5×10^6 cm^{-3} to 2.5×10^6 cm^{-3}, but that the ion flow field was dominated by low energy charge exchange ions that did not simulate orbital ram energies very well. Kern and Bilen[8] performed plasma current collection studies on breaches in wire insulation using a low energy plasma source where the plasma density and temperature at their sample location was $\sim 1 \times 10^7$ cm^{-3} and 1 eV, respectively. In their work, they report that the argon ions were streaming from the plasma source at energies of ~20 eV. Choiniere et al.[9] report on plasma electron collection to surfaces exposed to a high velocity xenon ion flow fields of 25 to 50 eV. The electron temperature in their experiments was measured to be 1.4 to 1.8 eV at quite high electron densities that were varied over a range from 0.5×10^9 cm^{-3} to 4×10^9 cm^{-3}.

The low electron temperature plasma source we describe in this paper utilizes a transverse-field magnetic filter. It is well known that plasma sources equipped with magnetic filters are capable of producing plasmas with unique properties. Magnetic filters have been exploited in neutral hydrogen injectors for fusion research[10,11] and in atomic nitrogen and oxygen ion sources for plasma processing applications.[12,13] Magnetic filter-equipped plasma sources that use multi-cusp magnetic field configurations are also finding applications as ion sources in focused ion beam (FIB) lithography systems because they are capable of producing very low-energy-spread ion beams with correspondingly high emittance.[14] These FIB plasma sources exhibit very low electron temperatures on the order of 0.1 eV in the region downstream of the magnetic filter and careful design of the filter layout and discharge chamber magnetic fields enables ion beams to be produced from plasma with ion energy spreads that are as low as 0.6 eV.[14]

To a very large extent, the plasma simulation facilities described in Refs. (1) through (9) have performed their task well, and results from these and other activities have guided the design and fabrication of both materials and hardware used in space flight applications. However, two problems have persistently plagued LEO simulation efforts and they include (1) difficulty in obtaining plasma sources that produce plasmas with adjustable, ultra-low electron temperatures on the order of 0.1 eV and streaming ion populations of 5 eV and (2) poor performance of plasma diagnostic equipment due to contamination buildup on probe surfaces, very large sheath growth at negative biases, or probe-induced perturbations at positive biases. Recent results obtained from the International Space Station (ISS) have indicated that electron current collection on positively biased solar cells may increase under low electron temperature conditions.[15] It would be desirable to study this phenomenon in the laboratory under well

controlled conditions, and our paper describes proof-of-concept experiments that have been performed on a LEO plasma simulator based on magnetic filters that could enable this sort of testing. We also describe the use of a large-area, multi-grided retarding potential analyzer (RPA) manufactured by EPL, Inc. that was used to characterize the electron and ion energy distribution functions in the low-density, expanding-plasma environment downstream of the plasma source. The benefits of using RPAs to measure expanding, low-density plasma properties are also discussed, and rf techniques are reviewed that would be useful for performing rapid measurements of electron temperature.

Apparatus and Procedures

Figures 1a and 1b contain photographs and schematic diagrams of our experimental setup. All testing was performed in a 1.2 m diameter by 5 m long stainless steel vacuum chamber that was pumped with a 0.9-m diameter, 20-kW diffusion pump. The base pressure of this facility with no flow was 1×10^{-6} Torr after 1 to 2 hr pump down times, and argon flow rates of 15 sccm increased the vacuum pressure to about 2×10^{-5} Torr. The magnetic filter-equipped plasma source is shown in the upper left and right hand photographs in Fig. 1a and on the left hand side of the schematic diagram shown in Fig. 1b. The photograph of the operating plasma source was taken through the view port shown in the lower left photograph, which only allowed for a partial image of the annular plasma emission region. The discharge chamber of the plasma source was 22 cm in diameter, and the active area of the ion optics system placed on the downstream end of the source was 16 cm. Although capable of extracting an ion beam, the multi-aperture, three-grid ion optics system was only used to reduce the open area of the source and increase the neutral density within the discharge chamber. An electrical and mechanical schematic diagram of the plasma source is displayed in Fig. 2a where the magnetic filter structure is shown immediately upstream of the ion optics system. A plasma is created within the discharge chamber by introducing argon flow to the source and by using a power supply connected between a hot filament cathode and an anode structure. Typical anode voltages of 35 to 55 V were investigated over discharge current ranges from 0.6 to 3 A. As indicated in Fig. 2a, the anode of the plasma source was connected to vacuum chamber ground for all testing described in this paper. In addition, the body of the plasma source including the magnetic filter was electrically connected to ground.

The discharge plasma contains both high-energy primary electrons and a Maxwellian electron group ($T_e \sim 2$ to 7 eV). Ions from the discharge plasma drift toward the magnetic filter structure and pass through into the region downstream of the filter, and they drag along low energy electrons with them. The magnetic field strength in the central regions of the magnetic filter region was ~45 Gauss for most of the testing described herein. Energetic electrons within the discharge chamber are prevented from following the ions due to the filtering effect of the radial magnetic field generated between the inner and outer magnet rings of the filter.[16] Although the magnetic field is strong enough to stop energetic discharge electrons, it is not strong enough to stop plasma from leaking through this region. The low energy electrons are able to diffuse through the filter (and follow the ions) via momentum exchange collisions amongst other low energy electrons, neutrals, ions, and possibly through other mechanisms. A large area retarding potential analyzer (RPA) manufactured by EPL, Inc was placed 61 cm downstream of the plasma source as shown in Figs. 1a and 1b. The RPA was used to

characterize the plasma flow field properties. An electrical schematic of the RPA is shown in Fig. 2b. The RPA uses three aligned grids that are spaced relatively far apart from one another for improved energy resolution purposes. However, the apertures in the grids are comprised of slots with widths that are only slightly smaller than the grid-to-grid separation distance. An analysis of the RPA design using SIMION 7.0 suggested that the potential within the apertures of the grid used to discriminate ion energy was varying significantly from the potential applied to the grid under some bias conditions. It was felt that the potential variation across the apertures could cause inaccurate energy distribution functions to be measured, and, in order to correct this problem, a high transparency (90%) nickel mesh manufactured by Buckbee-Mears was placed over the apertures of the grid located adjacent to the collector electrode. This change resulted in significantly improved performance of the RPA where ion and electron energy distribution characteristics less than 0.1 eV could be easily resolved.
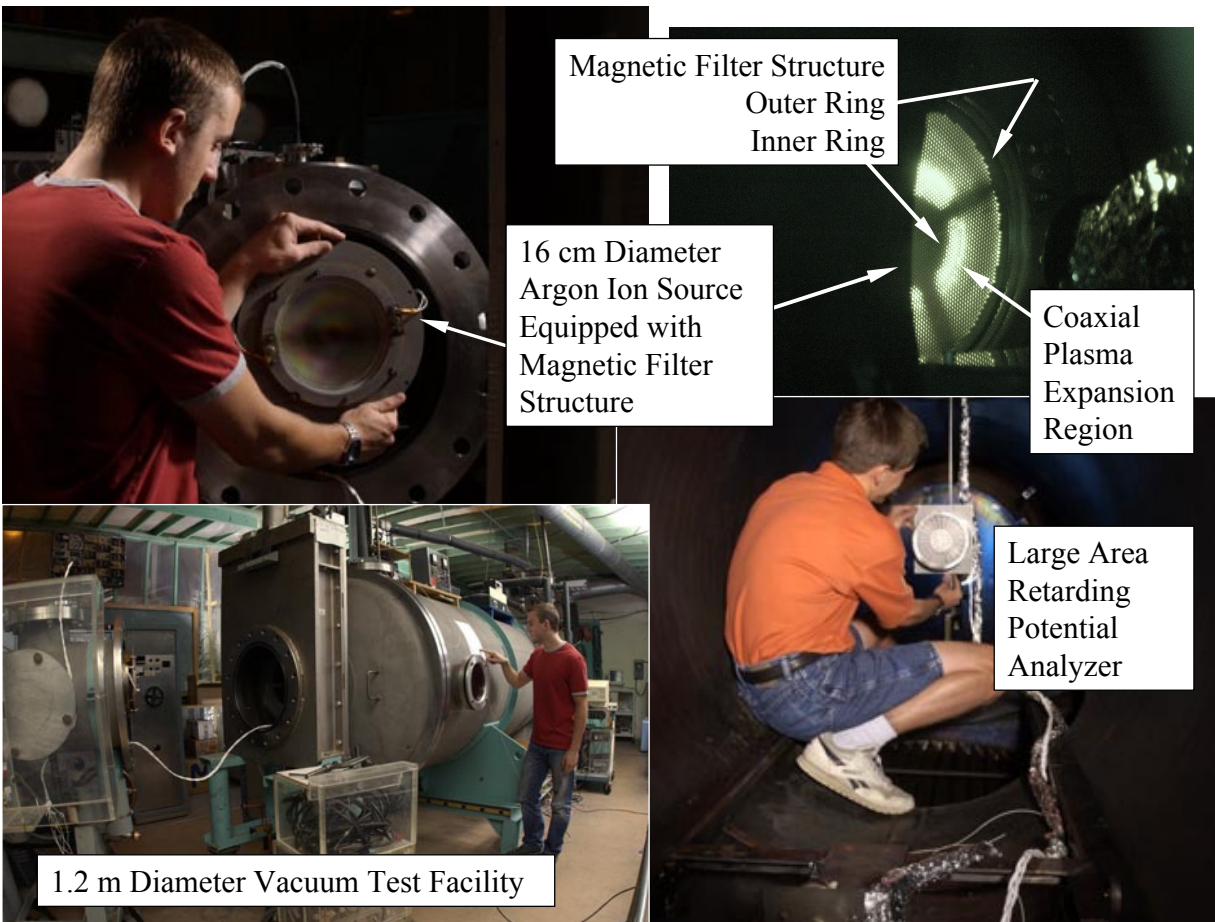
Figure 1a. Photographs of test setup.
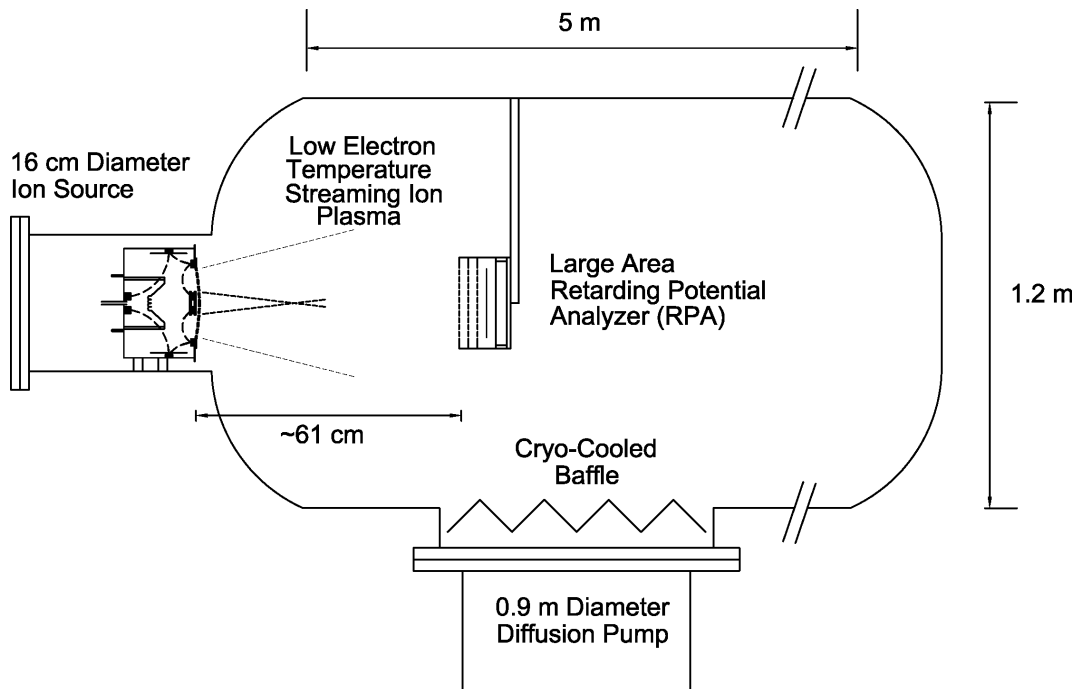
Figure 1b. Schematic diagram of LEO plasma simulation test facility.
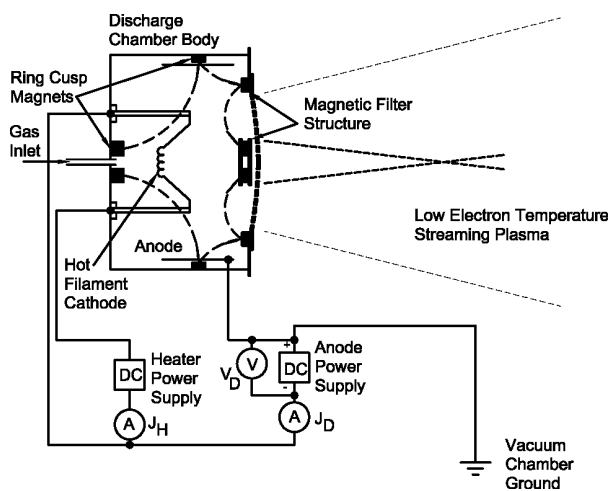
Figure 2a. Schematic of magnetic filter equiped plasma source.
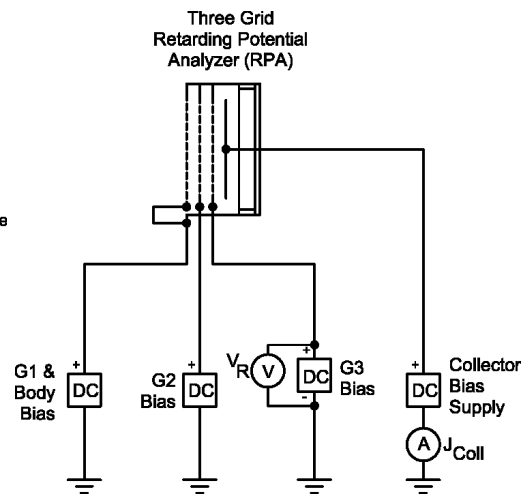
Fig. 2b Schematic of RPA

As configured for out tests, the RPA depicted in Figs. 1 and 2 is capable of providing high-resolution measurements of both ion and electron energy characteristics. RPAs are relatively inexpensive to build and easy to operate, and data analysis is simple compared to the analysis of Langmuir probe data due to the removal of the ion current from the sampling electrode when operated in the electron energy characterization mode. RPAs can also be used in non-uniform plasmas (i.e., freely expanding ones where plasma density varies with position) or in vacuum facilities that are not ultra clean without the concern that accompanies Langmuir probes.[17]   This

is a consequence of the energy selection grid being located within the device where it will not cause varying ion or electron sheaths to form and grow as it is being biased. RPAs are also more tolerant of contamination than Langmuir probes because charged particle collection occurs within RPAs on electrodes that are biased at relatively high potentials.

In addition to a low electron temperature, the plasma region downstream of the magnetic filter also contains a streaming ion population that is relatively mono-energetic at an energy that can range from ~4 eV to 6 eV depending upon plasma source operational conditions like flow rate, discharge power, discharge voltage, and discharge plasma uniformity. Although not confirmed at this time, it is believed that the streaming ions gain their energy through plasma expansion processes as the plasma density decreases from a relatively high value just downstream of the plasma source to much lower densities at distances further downstream. Some charge exchange ions are also created as ions stream from the source, but their relative numbers are low (less than 10%) and can be further minimized by reducing the flow rate required by the plasma source, and, thereby dropping the facility neutral background pressure.

As mentioned above, Fig. 2b contains an electrical schematic of the three-grid RPA that was used to measure both ion and electron energy characteristics. For electron energy characterization, the grid adjacent to the plasma was typically held at a constant potential that was slightly above plasma potential (~1 V). The next grid further into the RPA was typically held at +19 V to accelerate electrons from the plasma that pass through the first grid and to repel plasma ions from penetrating into regions located further into the RPA. The third grid from the plasma is used to energy select the electrons that pass through the second grid. At a given potential, this grid will allow electrons with an energy greater than this potential to pass through, but it will stop or retard all other electrons with insufficient energy to surmount this "retarding" potential. The collector electrode is typically biased positive of the discriminating grid (i.e., grid # 3) to avoid secondary electrons produced at the collector electrode from leaving this surface and flowing toward the third grid or other surfaces located within the RPA. A typical RPA data set consists of a list of the potentials applied to the first grid, second grid, and the collector electrode along with measurements of the collector current versus the potential applied to the third grid. A log-linear plot of the collector current versus the retarding potential can be used to estimate properties like plasma density, plasma potential, and electron temperature and/or energy. As mentioned above, one unique feature of RPA data collected with the set up shown in Fig. 2 is the automatic removal of the ion current. This simplifies the analysis of the current-voltage trace and also enables other more subtle plasma diagnostic techniques to be performed.

One novel use of an RPA can be implemented by superimposing an alternating sinusoidal voltage signal onto the retarding electrode as shown in Fig. 2 and described by Gill and Webb.[18] If implemented properly, this alternating voltage signal would cause the collector current to be modulated in a way that could be used to determine the electron temperature or electron energy distribution function.[19] It is noted that AC modulation techniques applied to Langmuir probes and RPAs have been performed since the 1930s. However, AC modulation of RPA energy discrimination electrodes has never been mentioned to our knowledge in the context of characterizing low-density plasmas that may be appropriate for producing LEO-like plasma environments. In addition, plasma properties of non-uniform, expanding plasmas may be characterized by applying AC modulation techniques to RPAs that would be impossible to

implement using Langmuir probes because of non-linear ion current collection effects caused by excessive sheath growth at negative biases in flowing, low density plasmas.

Application of an AC signal to the retarding grid of an RPA will partially rectify the collector current signal due to the exponential dependence of electron current on retarding potential. Analysis of the collector current frequency spectrum is then used to find the magnitudes of the first and second harmonics that are induced by the voltage waveform imposed on the retarding grid and the rectification effects, respectively. Similar to AC modulation of Langmuir probes, the RPA modulation technique would use the ratio of 2nd-to-1st harmonic amplitudes to determine the electron temperature. We plan to explore the use of AC modulation techniques in future work on low electron temperature, expanding plasmas in order to develop a faster method of determining electron temperature compared to methods that involve current-voltage data acquisition and subsequent analysis.

As mentioned above, the RPA was also used to measure ion energy characteristics. For these measurements, the grid adjacent to the plasma was typically held at a constant potential that was below plasma potential by 2 to 5 V. The next grid further into the RPA is typically held at -28 V to accelerate ions from the plasma that pass through the first grid and to repel plasma electrons from penetrating into regions located further into the RPA. The third grid from the plasma is used to energy select the ions that pass through the second grid. At a given potential, this grid will allow ions with an energy greater than this potential to pass through, but it will stop or retard all other ions with insufficient energy to surmount this "retarding" potential. The collector electrode is biased negative of the discriminating grid (i.e., grid # 3) to collect ions that make it past the third electrode. The derivative of the RPA trace was used to determine the ion energy distribution function. It is noted that Auger (or secondary) electron emission from the stainless steel collector electrode can occur and these electrons will flow to the discriminator electrode when it is biased positive of the collector. For argon ions, this effect can account for up to 20% of the measured ion current signal.

Results

A typical RPA electron trace is shown in Fig. 3 on both linear and log scales for the y-axis. This trace was taken at a relatively high plasma source flow rate of 73 sccm when the discharge voltage was set to 45 V and the discharge current was set to 2.2 A. Although not evident on the linear trace, a slight dc leakage current was detected and subtracted from the trace before plotting the data on the log scale. The break in the slope of the log trace at ~0.1 V is used to infer plasma potential, which was consistent with RPA ion trace data as described below. Once the current offset was removed, the log trace was fit to a straight line whose slope yielded an electron temperature of 0.14 eV. These same data were collected over a range of flow rates from 6 to 74 sccm (Ar), and the corresponding electron temperatures are plotted versus flow rate in Fig. 4. The electron temperature was observed to increase from 0.14 eV at high flow conditions to a value just above 0.35 eV at 6 sccm.

A study was also conducted to determine the effects of discharge voltage and current on electron temperature. The results of these tests are shown in Fig. 5 when the flow rate to the plasma source was fixed at 14.7 sccm. A low discharge current of 0.6 A was observed to

produce relatively high electron temperatures in the expanding plasma (~0.44 eV). As the discharge current was increased, however, the electron temperature decreased dramatically to a minimum value of 0.17 eV at a discharge voltage of 35 V and discharge current of 2.2 A. A relatively small effect of discharge voltage on electron temperature was observed in the preliminary experiments conducted to date, which was unexpected. Although more work needs to be completed to understand the data presented in Figs. 4 and 5, we are encouraged by the ability to control the electron temperature by varying the plasma source operating conditions.
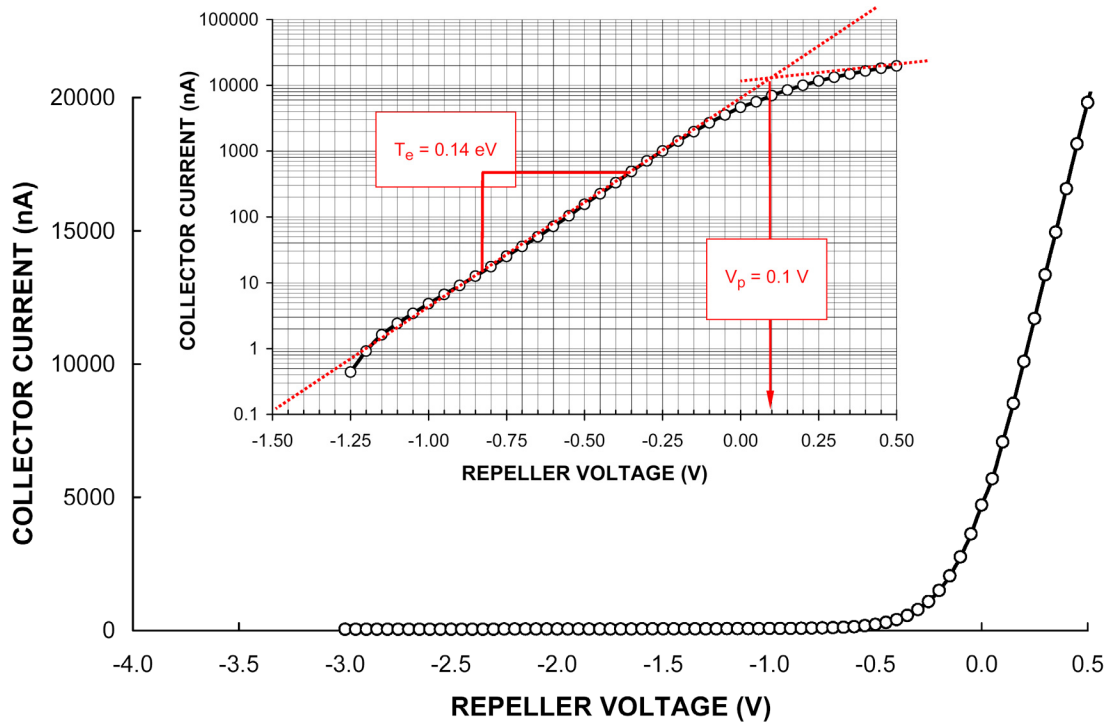
Figure 3. Typical RPA electron trace plotted on linear and log scale.
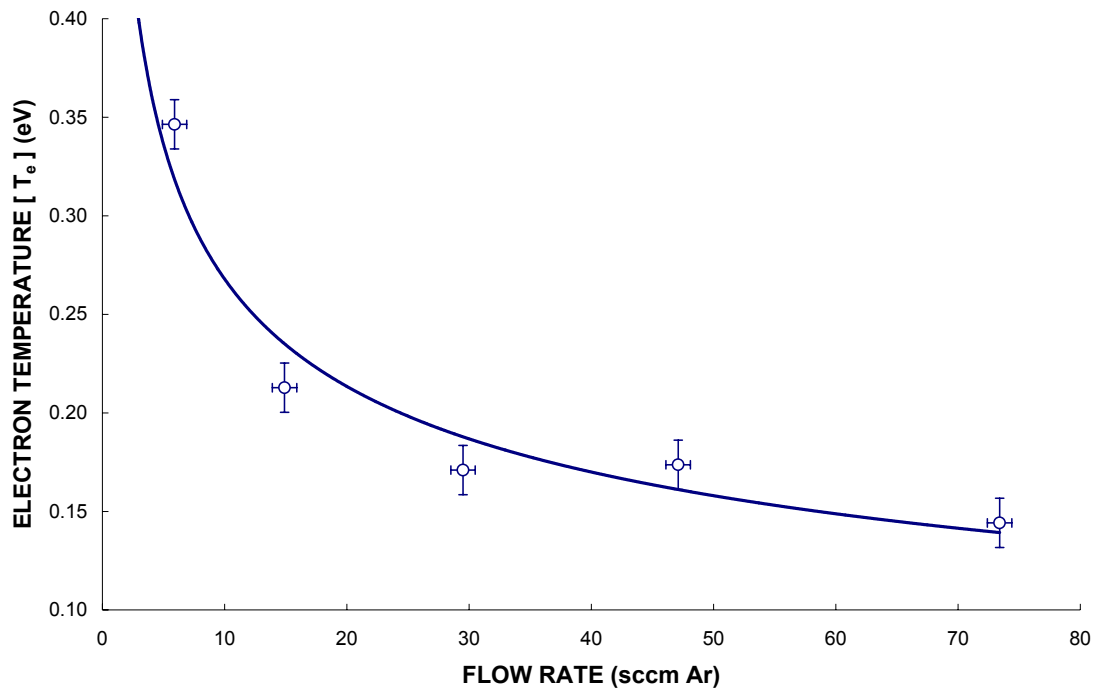
Figure 4. Effect of flow rate on electron temperature at a fixed discharge power level of ~90 W.
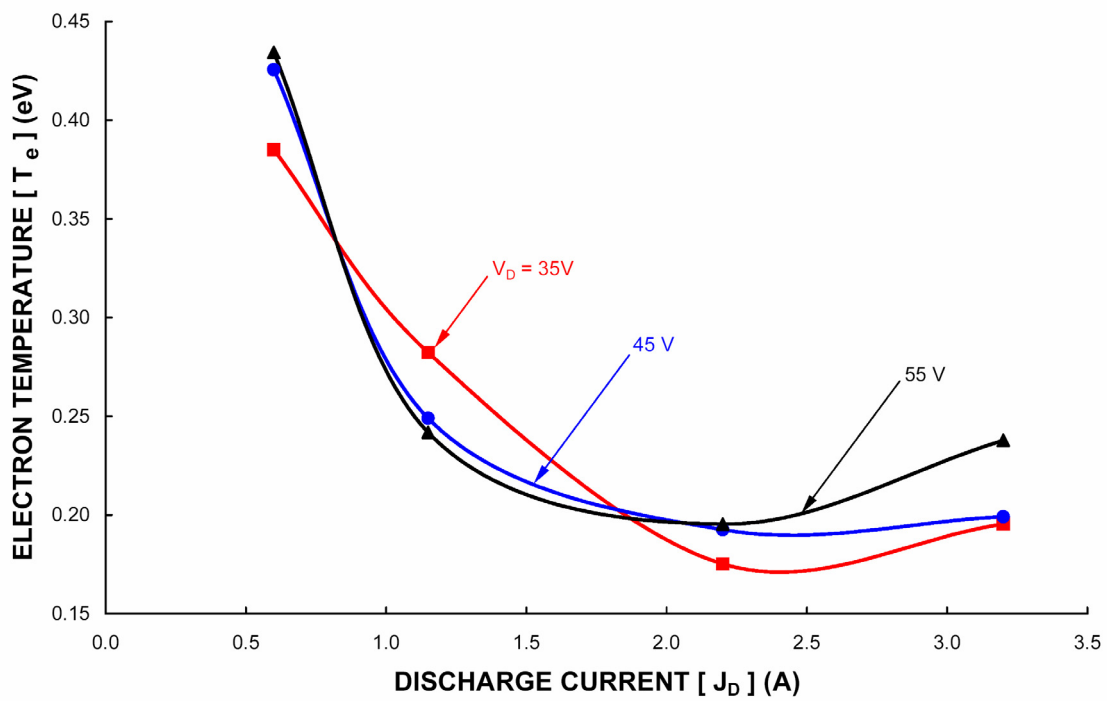
Figure 5. Effects of discharge voltage and current on electron temperature in the expanding plasma.

Figure 6 contains an RPA ion trace taken in the expanding plasma region when the plasma source was operated at a flow rate of 14.9 sccm (Ar) and at a discharge voltage and current of 46 V and 2.2 A, respectively. The derivative of the trace is shown in the inset figure, which is representative of the ion energy distribution function. As shown in the figure, the ion flow field is comprised of two components. One component corresponds to low energy ions that are created at plasma potential from charge exchange reactions between neutrals and streaming ions. This ion component signal is identified in Fig. 6 at a potential of 0.3 V. As mentioned earlier, measurements of plasma potential using RPA electron traces agreed well with measurements based on the low energy charge exchange ion signal. The other ion component corresponds to ions produced in the plasma source at a higher potential that are accelerated into the lower density plasma regions downstream. The streaming ion density at the RPA was calculated to be 4×10^5 cm^{-3} by assuming that the RPA transparency to ions was 0.59 and the area of the RPA collector electrode was 65 cm^2.

For the plasma source operating conditions of Fig. 6, the most probable streaming ion energy relative to the ambient plasma potential was 5 eV, and the full-width, half maximum (FWHM) energy spread of the streaming ions was 2 eV.   Similar measurements of the most probable ion energy (relative to the ambient plasma potential) and FWHM energy spread were made at different discharge voltages and currents, and these data are shown in Fig. 7. The streaming ion energy is shown to vary from about 4 to 6 eV while the FWHM energy spread varies from about 2 to 3 eV as the discharge current is varied from 0.6 to 3 A. A slight trend of increased ion energy and energy spread was observed with increasing discharge voltage. The streaming ion energy of 5 eV and the plasma density of $\sim4\times10^5$ cm^{-3} closely match the plasma conditions in LEO environments.
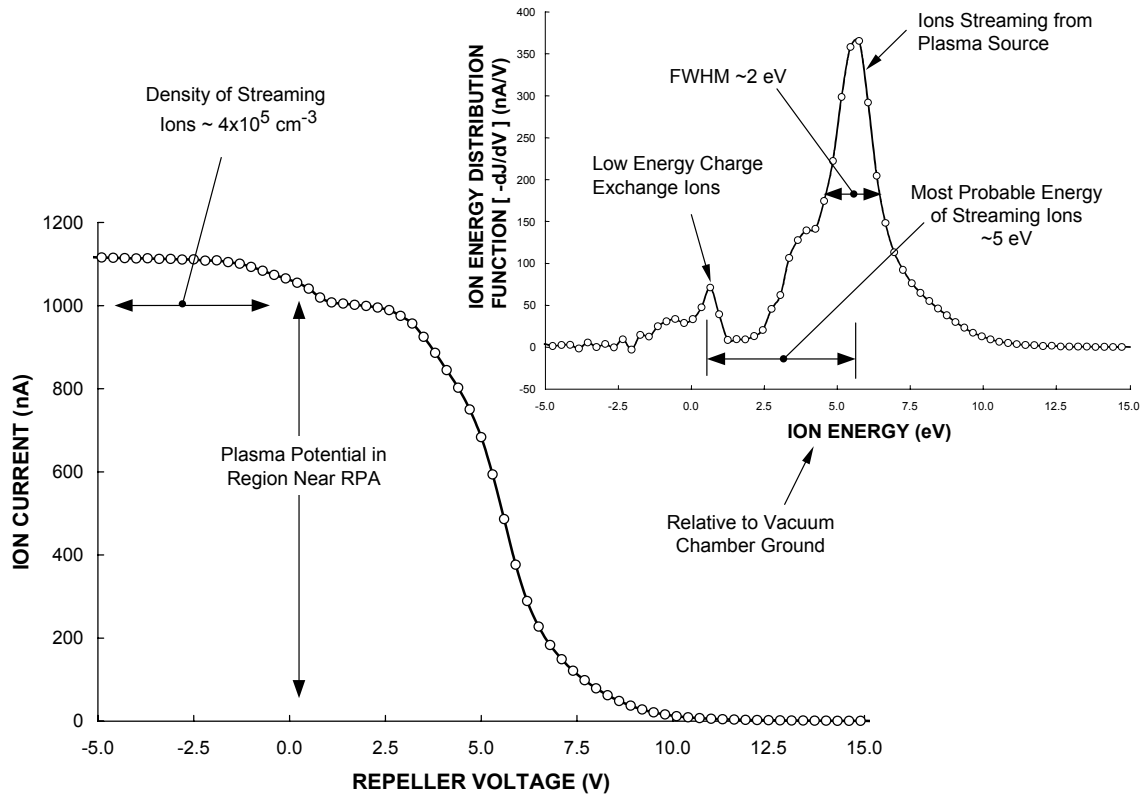
Figure 6. Typical RPA ion current trace and corresponding ion energy distribution function that shows presence of charge exchange and streaming ion populations.
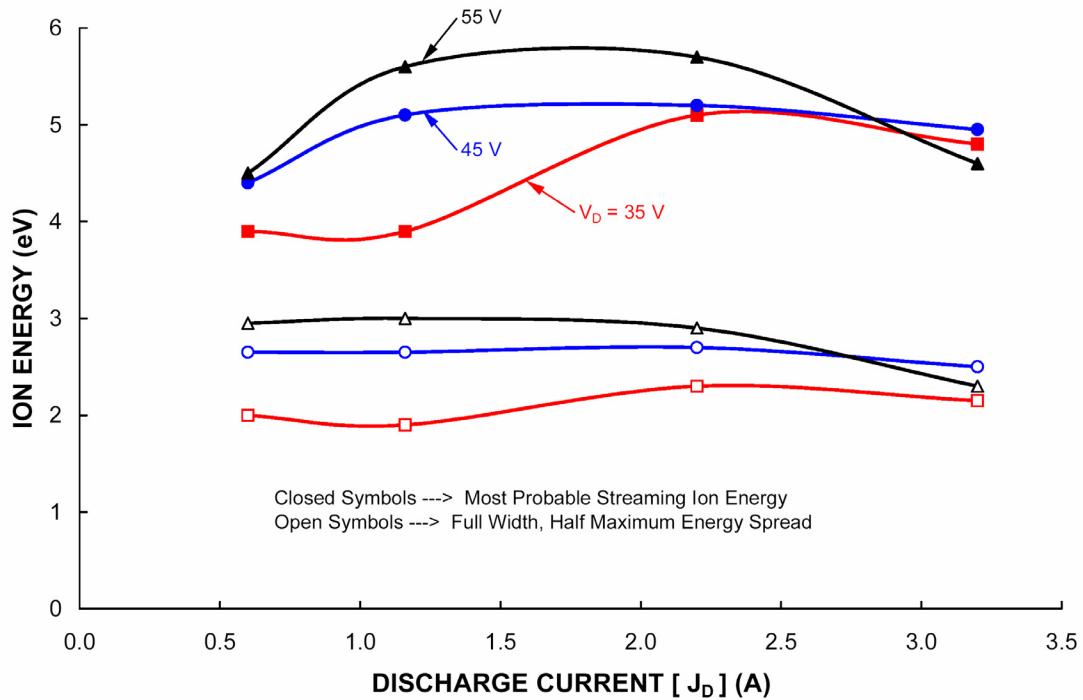
Figure 7. Effect of discharge voltage and current on streaming ion energy and energy spread.

Conclusions and Recommendations for Future Work

The preliminary data presented herein suggests that a magnetic filter-produced expanding plasma represents an excellent candidate for use as a LEO plasma simulator in that it produces plasma with both low electron temperature and streaming ion energies. Operating conditions of flow rate, discharge current, and discharge voltage were shown to enable production of plasma electron temperatures over the range from 0.14 to 0.45 eV and streaming ion energies over the range from 4 to 6 eV. Increasing the flow rate to the plasma source was observed to have the greatest effect on reducing the electron temperature, which was probably due to increased neutral densities within the plasma source. One recommendation for future work would be to improve the gas seals in the source and to mask down the ion extraction region in an effort to increase the neutral density within the plasma source at a given flow rate condition. Increasing the neutral density near the magnetic filter structure by injecting the gas at this location might also have a beneficial effect of reducing the electron temperature below 0.14 eV. In this study, high quality electron and ion energy distribution functions were obtained from a unique, large-area retarding potential analyzer that could be operated without perturbing the low density plasma environment. One disadvantage of this type of plasma diagnostic is the time it takes to acquire and analyze the current-voltage trace. To address this concern, an ac-based technique was proposed to improve the speed in which electron temperature measurements are obtained, and further work to pursue this approach is also recommended.

References

[1] H. Thiemann, and K. Bogus, "Anomalous Current Collection and Arcing of Solar-Cell Modules in a Simulated High-Density, Low-Earth-Orbit Plasma," ESA Journal, V. 10, 1986, pp. 43-57.

[2] J.T. Galofaro, et al., "Electrical Breakdown of Anodized Coatings in Low-Density Plasmas," J. Spacecraft and Rockets, V. 36, No. 4, 1999, pp. 579-585.

[3] B.G. Herron, J.R. Bayless, and J.D. Worden, "High-Voltage Solar Array Technology," J. Spacecraft, V. 10, No. 7, 1973, pp. 457-462.

[4] Banks, B.A., S.K. Rutledge, and J.A. Brady, "The NASA Atomic Oxygen Effects Test Program," 15th Space Simulation Conference, NASA CP-3015, Williamsburg, Virginia, Oct. 1988, pp. 51-65.

[5] M.G. Cho, et al., "Plasma Response to Arcing in Ionospheric Plasma Environments: Laboratory Experiment," J. Spacecraft and Rockets, V. 39, No. 3, 2002, pp. 392-399.

[6] J.A. Vaughn, et al., "Electrical Breakdown Currents on Large Spacecraft in Low Earth Orbit," J. Spacecraft and Rockets, V. 31, No. 1, 1994, pp. 54-59.

[7] A. Konradi, B. McIntyre, and A.E. Potter, "Experimental Studies of Scaling Laws for Plasma Collection at High Voltages," J. Spacecraft, Vol. 21, No. 3, 1984, pp. 287-292.

[8] O. Kern and S.G. Bilen, "Model of Current Collection to Small Breaches in Electrodynamic-Tether Insulation," AIAA 2003-4947, 39th Joint Propulsion Conference, Huntsville, AL, 2003.

[9] E. Choiniere, et al., "Measurement of Cross-Section Geometry Effects on Electron Collection to Long Probes in Mesosonic Flowing Plasmas," AIAA-2003-4950, 39th Joint Propulsion Conference, Huntsville, AL, 2003.

[10] K.N. Leung, "Characterization of Ion Sources: Multi-cusp ("Bucket" Type) Ion Source," appears in Chap. 2, Section 6 of Handbook of Ion Sources, B. Wolf, Ed., CRC Press, New York, 1995. See also Chap. 2, Section 13, "Large Area Ion Sources," and references therein.

[11] Y. Okumura, et al., "High Magnetic-field, Large-Volume Magnetic Multipole ion-Source Producing Hydrogen-Ion Beams with High Proton Ratio," Rev. Sci. Instrum., V. 55, No. 1, 1984, pp. 1-7. See also Y. Ohara, et al., "3D Computer Simulation of the Primary Electron Orbits in a Magnetic Multipole Plasma Source," J. Appl. Physics, V. 61, No. 4, 1987, pp. 1323-1328. Note that ring-cusp rather than line cusp magnetic field configurations are studied in these papers, which are similar to our plasma source and magnetic filter design. References that cite this family of ion sources also discuss the physics of electron temperature reduction across magnetic filters. e.g., M. Shirai, et al., "Theoretical

Investigation of Electron Temperature Variation Across Magnetic Filter in a Negative Ion Source," Rev. Sci. Instrum., V. 67, No. 3, 1996, pp. 1085-1087. And references therein.

[12] S.R. Walther, K.N. Leung, and W.B. Kunkel, "Production of Atomic Nitrogen Ion Beams," Rev. Sci. Instrum. V. 61, No. 1, 1990, pp. 315-317.

[13] J.N. Matossian, "Plasma Ion-Implantation Technology at Hughes Research Laboratories, J. of Vac. Sci. and Tech. B, V. 12, No. 2, 1994, pp. 850-853.

[14] Lee Y, et al., "Co-axial multicusp source for low axial energy spread ion beam production," Nuclear Instruments and Methods in Physics Research, Section A- Accelerators, Spectrometers, Detectors, and Associated Equipment, V. 433, No. 3, Sep. 1, 1999, pp. 579-586.

[15] D.C. Ferguson, et al., "ISS FPP Ionospheric Electron Density and Temperature Measurements-Results, Comparison with the IRI-90 Model, and Implications of ISS Charging," AIAA-2003-1083, 41st Aerospace Sciences Meeting, Reno, Nevada, 2003. See also R. Mikatarian, et al., "Electrical Charging of the International Space Station," AIAA-2003-1079, 41st Aerospace Sciences Meeting, Reno, Nevada, 2003

[16] K.W. Ehlers and K.N. Leung, "Effect of a Magnetic Filter on Hydrogen-Ion Species in a Multicusp Ion-Source," Rev. Sci. Instrum., V. 52, No. 10, 1981, pp. 1452-1458.

[17] E.P. Szuszczewicz and J.C. Holmes, "Surface Contamination of Active Electrodes in Plasmas: Distortion of Conventional Langmuir Probe Measurements," J. of Appl. Physics, V. 46, 1975, pp. 5134-5143.

[18] P. Gill and C.E. Webb, "Electron-Energy Distributions in Negative Glow and Their Relevance to Hollow-Cathode Lasers," J. of Appl. Physic D- Applied Physics, V. 10, No. 3, 1977, pp. 299-311.

[19] J.D. Swift and M.J.R. Schwar, Electrical Probes for Plasma Diagnostics, London Iliffe Books, American Elsevier Publishing Co., Inc., New York, 1969.

SECONDARY ARCS ON SOLAR GENERATORS – EMAGS 2 TEST CAMPAIGN

L. Gaillot
EADS ASTRIUM
31 Av. des Cosmonautes
31402 Toulouse Cedex 4 (France)
Phone: +33 5 62 19 98 43
Fax : +33 5 62 19 76 57
E-mail: ludovic.gaillot@astrium.eads.net

E. Boyer
P. Pélissou
EADS ASTRIUM, France

L. Lévy
D. Sarrail
ONERA-DESP, France

M-L. Fille
D. Caswell
ESA/ESTEC Keplerlaan, Netherlands

Abstract

For few years, many tests have been performed on solar array samples around secondary arcs in order to validate a theoretical model, to determinate the arcing conditions and to conceive some mitigating techniques.

EMAGS 2 (Solar Array Triggered Arc Phenomena Study - ESA contract) is the continued effort of ESA to try to better define how tests should be performed. This study consists in an extensive test campaign on different solar array samples issued from actual EADS ASTRIUM programs as on dummy SA samples.

In this paper are then presented the five different tests that will be performed from June 2003 to June 2004 in JONAS vacuum chamber at ONERA DESP – Toulouse.

Introduction

In 1997, it has been reported that 2 commercial satellites solar arrays suffered power losses in geostationary orbit, probably due to some destructive arc [RD1]. The reality of this phenomenon (low voltage self-sustained arc), linked to the fact that a satellite in GEO orbit tends to charge negatively because of the environment, has been demonstrated by ground tests.
Basically, self-sustained arcs between adjacent cells can be triggered if:
- the surface potential of coverglasses is less negative than the absolute potential of the satellite (this situation is called Inverted Voltage Gradient and allows the creation of ESDs between coverglasses and solar cells).
- a primary discharge (ESD) occurs in the gap between adjacent cells

- the voltage between these adjacent cells and the current available in case of secondary arc are sufficient to sustain the arc. The current available is at least the current of a string.

Self-sustained arcs can then result in a permanent short-circuit between adjacent cells or between cells and solar panel structure. The whole phenomenon theory is detailed in [RD2], [RD3], [RD4], [RD5] and [RD6]. Ground tests have also allowed to define some mitigating techniques (such as the installation of blocking diodes on each string) (eg [RD2]). Many tests are still performed on this subject to improve the theoretical model, to find new mitigating techniques or simply to check the immunity vs secondary arcs of new solar arrays. These tests can be performed either under electronic irradiation or in plasma. Contrary to tests in electron, tests in plasma allow to trigger more easily primary discharges but, on the other hand, are not representative of the GEO charging environment.

The first objective of EMAGS 2 is then to compare both methods by tests on dummy solar array samples using similar set-ups.

The second objective is to assess the voltage / current threshold for secondary arc triggering according to the cells type (GaAs triple junction or Si) and to the inter-cells gap (0.5 mm, 0.9 mm, 2 mm).

And finally, the last aim of EMAGS 2 is to determine the possible effects of repetitive primary discharges and secondary arcs on solar cells.

Comparison Between Tests in Electron and in Plasma (Test 1)

Introduction

During the first step of EMAGS 2, tests in inverted voltage gradient conditions have been performed on dummy solar array samples, first in an electronic charging environment and then in plasma. Tests on solar array samples under electronic irradiation, contrary to tests in plasma, are representative of the phenomenon but present some difficulties to trigger easily primary discharges in the gap between cells. A comparison of the results (occurrence and characteristics of primary discharges and secondary arcs) can then allow to validate the representativity of a test in plasma and also to determine the satellite capacitance to be used in plasma test. These tests have been performed on dummy samples (Cu) because the triggering of primary discharges is easier to control on such samples than on real solar array samples.

Test conditions

Tests in IVG under electronic irradiation (energy of about 6 keV and current density of about 1nA/cm^2) as tests in plasma (Argon with a density of 10^4/cm^3) have been performed in JONAS vacuum chamber (ONERA DESP) on identical samples. These samples consisted in an epoxy plan with two copper surfaces (about 5 x 5 cm) simulating solar cells. One of these surfaces was partly covered with a teflon SSM to trigger the primary ESD (see Figure 1).
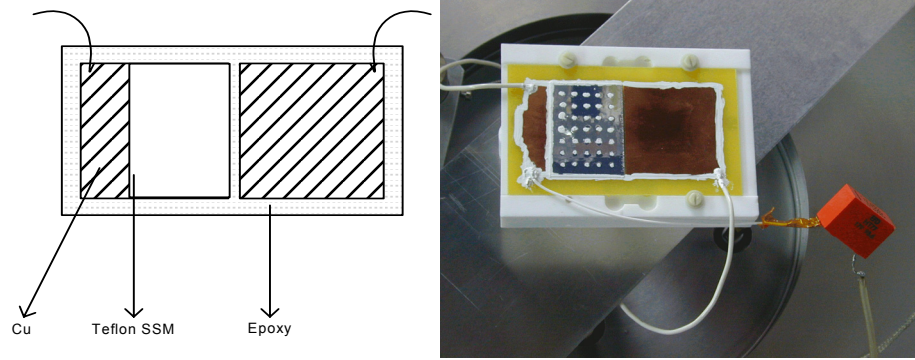
Figure 1. Dummy samples

The gap between both copper surfaces was about 0.9 mm, which is representative of SA samples.

Test set-up

The test set-up in electron was the following:
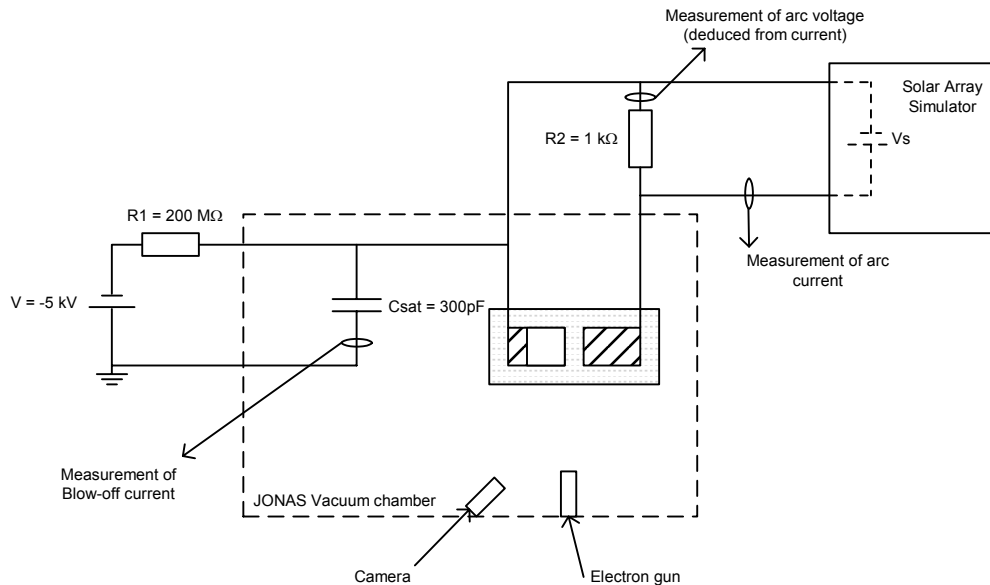
Figure 2 – Set-up for electron irradiation (Test 1)

During the tests, the following measurements were performed:
- blow-off current (Pearson current probe placed on the satellite capacitance)
- secondary arc current (current probe placed on the output of the solar array simulator)
- secondary arc voltage (current probe placed on the 1 kΩ resistance)

The whole circuit is floating with regard to chamber structure (except for the high voltage supply for which the return wire is connected to the chamber structure). The satellite capacitance is placed as close as possible to the sample.

Csat (about 300 pF) represents the absolute capacitance of a satellite wrt to the GEO plasma (assessed between 100 pF and 300 pF depending on the satellite). This capacitance is biased by a high voltage supply to –5kV through a decoupling resistance of 200 MΩ. In case of a primary discharge, the blow-off current is provided by Csat and also by a spurious capacitance of about 500 pF brought by the set-up (so a total capacitance of about 800 pF - the physical capacitance placed inside the vacuum chamber is nevertheless expected to have a prevailing influence wrt the blow-off current as the harness length wrt the sample is much shorter for this capacitance).

The solar array simulator (power supply with a current limiter at its output) allows to apply a voltage between the adjacent copper cells. In the case of a secondary arc triggering between these cells, the current is limited by the SAS. The used solar array simulator has the advantage to produce an acceptable current overshoot in case of secondary arc (duration < blow-off rise time and limited amplitude), which is an important aspect with regard to the representativity of the test.

For tests in plasma, the set-up is the same than the previous one except that the cells are biased to -1.5 kV instead of -5 kV. Indeed, at higher bias voltage values in plasma, we constate that most of the primary discharges are not triggered in the gap (so no risk of secondary arc).

Moreover, in order to obtain more easily primary discharges in the inter-cells gap, a conductive mask is placed between the plasma source and the sample.

In the test under electron irradiation, the satellite capacitance used was about 800 pF (total). The bias voltage being 3.3 times lower in plasma tests, the satellite capacitance to be used is then necessarily different.

To determine the value of Csat which allows a test in plasma to give results close to those obtained in electron, tests in plasma were performed with 3 different capacitance values:
- 3 nF to be representative of the charges amount (Q=C.V ; 800pF.5000V = 2.7nF.1500V)
- 10 nF to be representative of the total energy (E=C.V^2/2 ; 800pF.5000^{2}V^2/2 = 9nF.1500^{2}V^2/2)
- 300 nF (worst case approach)

Figure 3. Installation of the dummy sample in JONAS vacuum chamber

Tests have been performed at 5 voltage values between cells (set at SAS level): 30, 35, 40, 55 and 70 V.

The different limits of the available current in case of secondary arc were:
- 0.6 A (representative of the max current in a triple junction GaAs cells string)
- 1.1 A (representative of the max current in a Si cells string)
- 2 A

So, for each of the 4 test set-ups (electron with a capacitance of 800 pF, plasma with 3 nF, plasma with 10 nF and plasma with 300 nF), 15 voltage/current configurations have been tested (with at least 3 primary discharges in the gap in each case).

First results

No self-sustained arc has been observed during these tests probably because the current available in case of arc was limited to 2 A max.

Nevertheless, many secondary arcs with duration of few 10 µs (for low voltage / current configurations) up to few 100 µs have been measured.

In any case, tests in plasma don't give results very different from those obtained in electron, which tends to validate the representativity of such tests.

With regard to the arc occurrence rate (secondary arc triggering with respect to the number of primary discharges in the gap), the 10 nF capacitance in plasma (with a bias voltage of -1.5kV) allows to obtain results similar to the tests in electron (especially for currents of 1.1 A and 2 A).

With regard to the secondary arc average durations, the results in plasma are close to those in electron, for a capacitance value of 300 nF.

Before setting the capacitance value to be used in the next tests of EMAGS 2 (in plasma), many other comparisons between results have still to be done (arc voltage characteristics, arc impedance, primary discharge characteristics...).

<u>**Tests on solar array samples**</u>

The other tests of EMAGS 2 will be performed in plasma (Argon) in JONAS vacuum chamber at ONERA DESP on solar array samples issued from actual EADS ASTRIUM programs. All these tests will be based on the same test set-up including the satellite capacitance that will be determined after the complete review of the results of the first test.

These tests aim to assess the:
- influence of the cell type wrt secondary arcs triggering
- influence of the gap length wrt secondary arc triggering
- effect on solar cells of repetitive primary discharges
- effect on solar cells of repetitive secondary arcs (not self-sustained)

Test set-up

For all the next tests, the set-up will be the following:
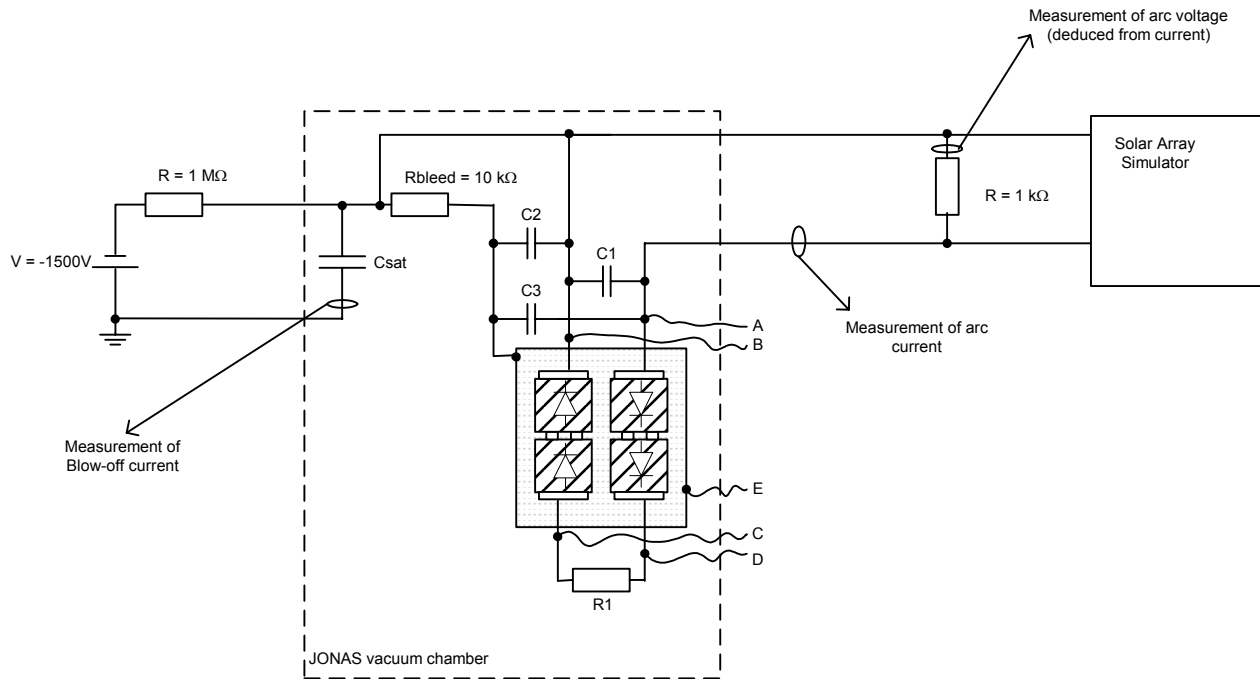
Figure 4. Test set-up

Csat will be determined according to the results of the first test (comparison electron / plasma).

R1 will be about 5 kΩ in order to create a steady state current in solar cells of about 10 mA.

C1 represents the junction capacitance of a whole string and will be set to about 300 nF for a GaAs string and 100 nF for a Si string (approximation based on the cell junction capacitance at the functional point and on the number of Si and GaAs cells by string).

C2 and C3 aim to represent the capacitance of the whole string wrt panel structure (kapton capacitance) and are then assessed considering the surface of a solar cell, the thickness of kapton and glue under a cell and the number of cells in a string. C2 and C3 values will then be set to about 15 nF in case of a string of GaAs cells and to about 50 nF in case of a Si string.

The test set-up used for a Si solar array sample will then be slightly different from the one used for a GaAs sample (C1, C2, and C3 necessarily different to be representative).

A, B, C, D and E wires will allow to perform the good-health check test on solar cells i.e. the measurement of the I(V) characteristic of both solar cells rows in darkness (between A and D or between B and C) and the isolation measurements between solar cells and structure (between A, B, C or D and E).

In order to obtain more easily primary discharges in the inter-cells gap, a conductive mask will be placed between the plasma source and the sample.

During all tests, arc voltage and current as blow-off transient current will be measured.

Influence of the cell type (Test 2)

The aim of this test is to assess the influence of the cell type in the secondary arc phenomenon. Comparative tests will then be performed on two solar array samples with either Si cells or triple junction GaAs cells and in each case, the voltage / current thresholds for secondary arc (and/or sustained arc) triggering will be determined.

The samples are similar: on each sample, 2 rows of 2 solar cells in serie (similar sizes and CMX coverglass in both cases) are bonded on a kapton layer. The support is a NIDA with two carbon fiber layers (see next figure).
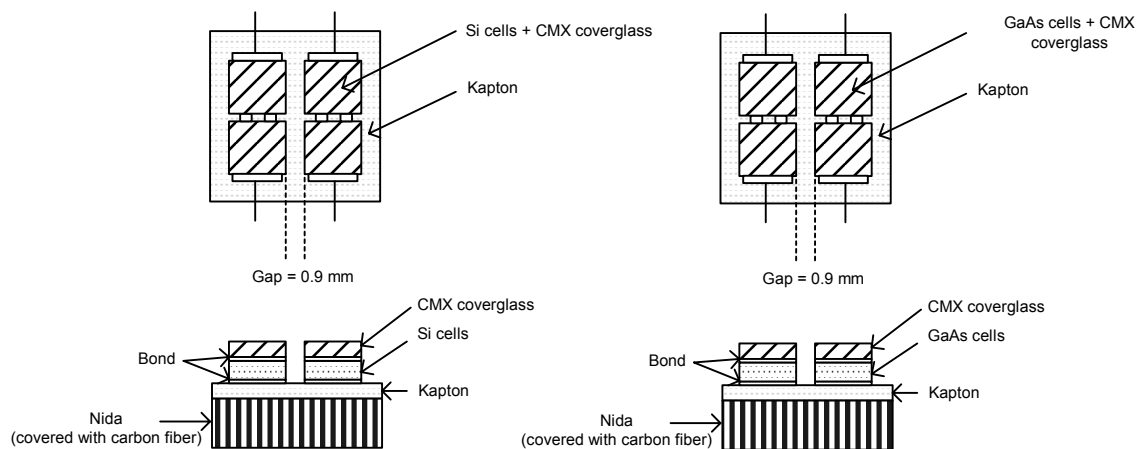
Figure 5. Samples definition (comparison Si / GaAs)

In both cases, the inter-cells gap is of 0.9 mm and the coverglass position on the cells doesn't present an overlapping in the gap.

Tests will be done for SAS current limits of 0.6 A (representative of the max current in a triple junction GaAs cells string), 1.1A (representative of the max current in a Si cells string), 2 A and 3 A. For current limits of 0.6 A and 1.1 A, tests will be performed only at 50 V, 70 V and 90 V because such current limits are not expected to present a high risk of self-sustained arc triggering.

For current limits of 2 A and 3 A, tests will be done at SAS voltage values from 30 V to 90 V (by step of 10 V).

So, for each of the 2 sample types, 20 voltage/current configurations will be tested (for each configuration, a minimum number of 3 primary discharges in the gap is required).

The following data will then be determined for each cell type:
- maximum values of voltage between cells and current limit for no secondary arcing (wrt GaAs coupon, this data is an input for the test of primary discharge cumulative effect)
- thresholds (voltage / current) for aborted secondary arcs (wrt GaAs coupon, this data is an input for the test of secondary arc cumulative effect)
- thresholds (voltage / current) for self-sustained arcs

The secondary arc sensibility to the solar cells material will then be assessed.

Gap sensitivity characterization (Test 3)

The aim of this test is to assess the influence of the inter-cells gap in the secondary arc triggering. Comparative tests will then be performed on three solar array samples (Si cells) with different gap values. In each case, the voltage / current thresholds for secondary arc (and/or sustained arc) triggering will be determined. On each sample, 2 rows of 2 solar cells in serie (Si with CMX coverglass in any case) are bonded on a kapton layer. The support is a NIDA with two carbon fiber layers (see next figure).

Gap = 0.5 mm, 0.9 mm or 2 mm
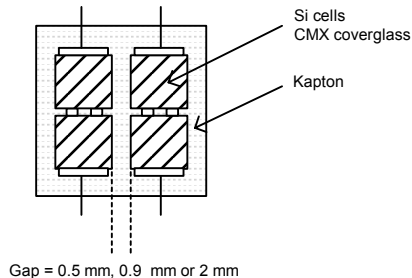
Figure 6. Samples definition (gap sensitivity)

The three samples are identical except with regard to their inter-cell gap:
- 0.5 mm (worst case gap)
- 0.9 mm (nominal gap value between adjacent cells of a same string for solar arrays)
- 2 mm (nominal gap value between adjacent cells of different sections for solar arrays)

In all cases, the coverglass position on the cells is identical (no overlapping in the gap).

Test will be performed for SAS voltages between cells from 30 V to 90 V (by step of 10 V) and for the current limits of 1.1A (representative of the max current in a Si cells string), 2 A and 3 A.

So for each of the 3 sample types (gap of 0.5mm, 0.9 mm or 2 mm with Si cells in any case), 21 voltage/current configurations will be tested (for each configuration, a number of 3 primary discharges in the gap, with or without secondary arc triggering, is required), which will allow to determine in each case:
- thresholds (voltage / current) for aborted secondary arcs
- thresholds (voltage / current) for sustained secondary arcs

The secondary arc sensibility to the gap distance can then be assessed.

Primary discharges cumulative effect (Test 4)

The aim of this test is to characterize the cumulative effect of primary discharges on a same solar array sample (triple junction GaAs cells with CMX coverglass and gap of 0.9 mm). This test will then be performed at a unique SAS voltage / current configuration (voltage between cells/ current limit) chosen with regard to results of tests 2 (configuration for which only primary discharges were observed on a GaAs sample). A solar cells characterization (measurement of I(V) cells characteristics) will be performed before and after the test (in full darkness) to check that repetitive primary discharges don't affect the solar cells performances (which is expected because of the low energy contained in primary discharges).

Secondary arcs cumulative effect (Test 5)

The aim of this test is to characterize the cumulative effect of aborted secondary discharges on a same solar array sample (triple junction GaAs cells with CMX coverglass and gap of 0.9 mm). This test will be performed for a unique configuration of voltage between cells/ current limit chosen with regard to results of tests 2 (configuration for which aborted secondary arcs only were observed on an identical sample). The possible effect of aborted secondary arcs on solar cells will be checked comparing the I(V) characteristics (in darkness) of the solar cells before and after many secondary arc (not self-sustained).

<u>**Conclusion**</u>

The tests performed in the frame of the second phase of EMAGS 2 (ESA study) will then allow to:
- compare with regard to secondary arcing, tests under electron irradiation (most representative) with tests in plasma (discharges more easy to obtain) in order to define a representative set up in plasma
- assess the sensibility of secondary arc triggering with regard to the solar cells material (Si, GaAs)
- assess the sensibility of secondary arc triggering with regard to the inter-cells distance (Si)
- determine the effect of repetitive primary discharges on solar cells (GaAs)
- determine the effect of repetitive secondary arcs on solar cells (GaAs)

A summary of the EMAGS 2 test campaign is given in the following table :

Test	Environment	Sample	Output
Set-up validation (Test 1)	- Electron irradiation - Plasma	- Copper cells covered by teflon SSM	- Comparison of secondary arcs and primary discharges - Determination of the satellite capacitance to use in plasma tests (input for tests 2, 3, 4 and 5)
Material comparison (Test 2)	Plasma	- Si cells / CMX / 0.9 mm gap - Triple junction GaAs cells / CMX / 0.9 mm gap	- Thresholds for aborted secondary arcs and self-sustained arcs (input to tests 4 and 5 wrt GaAs cells) - Secondary arc sensitivity to solar cells material
Gap sensitivity (Test 3)	Plasma	Si cells / CMX / - 0.5 mm gap - 0.9 mm gap - 2 mm gap	- Thresholds for aborted secondary arcs and self-sustained arcs - Secondary arc sensitivity to the gap between cells
Primary discharges cumulative effect (Test 4)	Plasma	Triple junction GaAs cells / CMX / 0.9 mm gap	Cumulative effect of primary discharges on solar cells (SAS voltage / current defined according to results of test 2)
Aborted secondary arcs cumulative effect (Test 5)	Plasma	Triple junction GaAs cells / CMX / 0.9 mm gap	Cumulative effect of aborted secondary arcs on solar cells (SAS voltage / current defined according to results of test 2)

Reference Documents

1. "Solar Array Triggered Arc Phenomena Studies and Modelling (EMAGS)" – Final report, RF/4748-00 DESP, L. Levy (ONERA), Oct 2000

2. "Solar Array Augmented Electrostatic Discharge in GEO" Christopher F. Hoeber, Ernest A. Robertson, Ira Katz, V. A. Davis, David B. Snyder, AIAA paper

3. "ESD Triggered Solar Array Failure Mechanism", I. Katz, V.A. Davis (Maxwell Technologies Inc.), David B. Snyder (NASA LeRC), Ernest A. Robertson (Space Systems / Loral) – 6th Spacecraft Charging Technology Conference, 1 Sept 2000

4. "ESD Initiated Failures on High Voltage Satellites", I. Katz, V.A. Davis(Maxwell Technologies Inc.), David B. Snyder (NASA LeRC), Ernest A. Robertson (Space Systems / Loral) – Space Environments and Effects Flight Experiments Workshop, 23-25 June 1998

5. "R&T CNES. Phénomènes d'Arcs Déclenchés par Décharge Electrostatique. Conductivité Induite sous Rayonnement de Matériaux Spatiaux", R. Reulet, B. Dirassen, D. Sarrail (ONERA), D. Payan (CNES), RP/CS313101 (AER 03131), Oct 2000

6. "Risks of Low Voltage Arcs Sustained by the Photovoltaic Power of a Satellite Solar Array during an Electrostatic Discharge. Solar Array Dynamic Simulator", D. Payan, D. Schwander, J.P. Catani (CNES)– 7th Spacecraft Charging Technology Conference, 23-27 April 2001

7. "Electrostatic Discharges on Solar Arrays. Physical Model of Inverted Gradient Electrostatic Discharge", D. Payan, F.Séverin, J-P. Catani (CNES), J-F. Roussel, R. Reulet, D. Sarrail (ONERA), 7th Spacecraft Charging Technology Conference, 23-27 April 2001

CHARACTERISTIC OF CHARGE ACCUMULATION IN GLASS MATERIALS UNDER ELECTRON BEAM IRRADIATION

H. Miyake
Musashi Institute of Technology
1-28-1 Tamazutsumi, Setagaya-ku, Tokyo158-8557, Japan
Phone: +81-3-5707-2156
Fax: +81-3-5707-2156
E-mail: miyake@me.musashi-tech.ac.jp

Y. Tanaka
T. Takada
Musashi Institute of Technology

Abstract

We observed space charge formation in various glass materials under electron beam irradiation. Spacecraft charging occurs in plasma and radiation environment. Especially we have focused on an accident caused by internal charging in glass material used cover of solar array panel. Therefore we have tried to measure the charge distribution in glass materials irradiated e-beam. The measurement is carried out using PEA (Pulsed Electro-Acoustic method) system. Two types of glass materials are used for samples. One is a quartz glass (pure SiO_2), and another are glasses including impurities of oxide metal. In the case of quartz glass, charge accumulation was not observed neither during nor after electron beam irradiation. On the other hand, charge accumulation was observed in glass sample including metal-oxide impurities. We found the polarity of the observed charges in bulk depends on the content of impurities. To confirm the existence of which impurity dominates the polarity of the accumulated charge, we measured charge distribution in several glass materials including various metal-oxide impurities.

Introduction

Glass materials are used as a cover of solar array panel for spacecraft. When the spacecraft moves in the radiation environment in space, it is affected some serious damage due to the discharge accident caused by irradiation of radioactive rays. We have paid attention to the effect on glass materials of electron-beam (e-beam) irradiation. The irradiation of e-beam may cause the electric discharge. Therefore, we have measured space charge distribution in various glass materials after e-beam irradiation.

Principles of PEA Method

The PEA (Pulsed Electro-Acoustic) method is one of widely used technique to measure the charge distribution in polymeric dielectrics.   The principle of the PEA method is shown in Figure 1.   Consider a sheet sample with thickness of d and charge distribution (z). When an externally applied pulsed electric field Ep(t) is applied to the sample, a perturbation force is induced on each charge.   This force generates a pressure acoustic wave which is proportional to the charge density.   A piezoelectric transducer is used to detect the acoustic wave and transform the propagated acoustic wave into an electric signal. Since, in the PEA measurement system, the detector of piezo-electric transducer is completely shielded and it separated from the sample, we can measure the charge distribution with low electric noise. The details of the measurement are described elsewhere [1]-[3].

Experimental Procedure

Measurement system

Figure 2 shows a schematic diagram of the PEA system. In the measurements, an ordinary PEA system for polymeric materials was used [1]. Irradiated electrons were reached to the surface of samples through the hole of upper electrode unit. Therefore, the measurements were carried out under short circuit condition during electron beam irradiation and after irradiation continuously.

Sample and e-beam irradiation

As shown in Table 1, five kinds of glass materials are measured. A quartz glass is pure SiO_2, and others include various oxidized metal impurities as shown in Table 1. Thicknesses of all samples are about 1mm. The e-beam was irradiated to samples in air atmosphere with acceleration energy of 500keV for 180sec. The current density of the e-beam was about 150nA/cm^2. This experiment was carried out using "2MeV, 60kW Dual-beam Type Electron Accelerator Irradiation Facility" which is operated by JAERI (Japan Atomic Energy Research Institute).

The measurement was carried out with the period of 10 seconds for 3 minutes during electron beam irradiation. After the irradiation, the decay process of the accumulated charge of bulk was also measured with the same period for approximately 6 minutes.

Table 1: Chemical component of glass

Sample	Chemical Composition (%)							
	SiO_2	Al_2O_3	CaO	MgO	Na_2O	B_2O_3	Fe_2O_3	Zr_2O_4
Quartz	99.9	-	-	-	-	-	-	-
NE-Glass	52〜56	12〜16	0〜10	0〜5	0〜1	15〜20	-	-
T-Glass	65	23	<0.01	11	<0.1	<0.01	0.1	<0.1
E-Glass	52〜56	12〜16	15〜25	0〜6	0〜1	8〜13	-	-
C-Glass	60〜65	2〜6	15〜20		8〜12	2〜7	-	-

Results and Discussion

Typical result of measurements of polymeric material and quartz glass

Figure 3 shows a typical result of space charge distribution under e-beam irradiation in PMMA. In the color chart, red and blue area shows the negative and positive charge distribution, respectively. We observed negative charge accumulation at the middle position of the bulk in PMMA. That negative charge signal gradually increased in time progress of electron beam irradiation. Figure 4 shows a charge distribution in pure quartz glass. We could not observe any signals in that bulk. From these results, it is assumed that the injected electrons are trapped in the bulk of PMMA stably while they are not trapped in the bulk of quartz glass.

Measurement results of various glass materials consisted of SiO$_2$ and some impurities

Figure 5 and 6 show results of space charge distribution in NE and T-glasses under and after electron beam irradiation. In these figures, the irradiation surface of the sample is described on the right side. From these results, the negative charge accumulations are observed between the middle of bulks and irradiation surfaces.

On the other hand, in the case of E and C-glasses shown in Figure 7 and 8, positive charges were observed in bulk near the irradiation surface. Those accumulated negative and positive charges were increased with increase of irradiation time. After irradiation, they gradually decreased.

In all glass samples except for quartz glass, the small amounts of negative charges are observed near the electrode which is opposite side to irradiation surface.

Figure 9 shows the time dependence of the amount of accumulated charges in samples during 10 minutes for measurement. These amounts of charges were obtained by calculating the integration of the observed charge distribution. From these results, charge amounts accumulated in NE and T glasses are five times larger than that in other glasses under electron beam irradiation.

Figure 10 shows the decay process of accumulated charge in the bulk for 30days. During relaxation process, there seems to be two types of decay characteristics. One is a quick decay process within several tens minutes observed in C-glass. Another is a slow decay process within several tens days observed in E, T and NE glasses.

Relationship between polarity of charges and species of impurities

Figure 11 shows the relationship between amount of accumulated charge polarities and impurities. From figure 9, it is found that a large amount of Na$_2$O is included in C-glass 10 or more times larger than that in other glasses. Therefore, we assumed that the Na$_2$O strongly affected the fast decay of accumulated positive charge.

A large amount of alkali (Na$_2$O, CaO and MgO) impurities (more than 20%) are contained in E and C-glass. Therefore, it can be thought that such kind of impurities may affect generation of the positive charge.

Judging from the relationship between the amount of impurities and negative charge accumulated in NE and T-glasses shown in Figure 9 and 10, the amount of negative charge seems to be affected with the existence of Al$_2$O$_3$. However, the above-mentioned assumption has not been confirmed yet. To know the details of the accumulation mechanism in e-beam irradiated glass, it is necessary to continue more experimental works.

Conclusion

From experiments, we found the followings.

1) No charge accumulation was observed in electron beam irradiated in pure SiO2.
2) Charge accumulations were observed in glass materials including oxidized metal impurities by e-beam irradiation.
3) The polarity of the accumulated charge seems to be strongly affected by the species of impurities.
4) Positive charge is accumulation was observed in alkali rich glasses.
5) Negative charge accumulation was observed in Al_2O_3 rich glass.
6) Fast decay process of accumulated positive charge was observed in Na_2O rich glasses.

Acknowledgement

Figure 1.   PEA measurement system

Figure 2.   Schematic diagram of PEA space charge measurement system
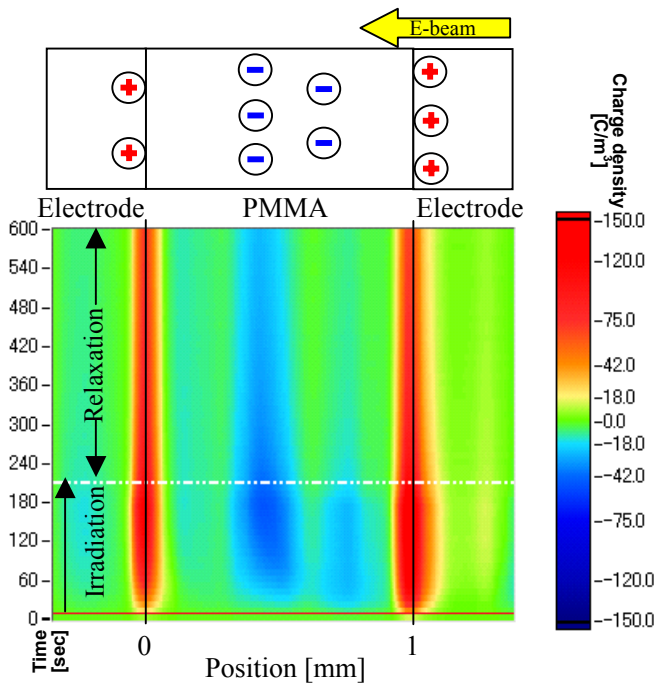
Figure 3. Space charge distribution in PMMA
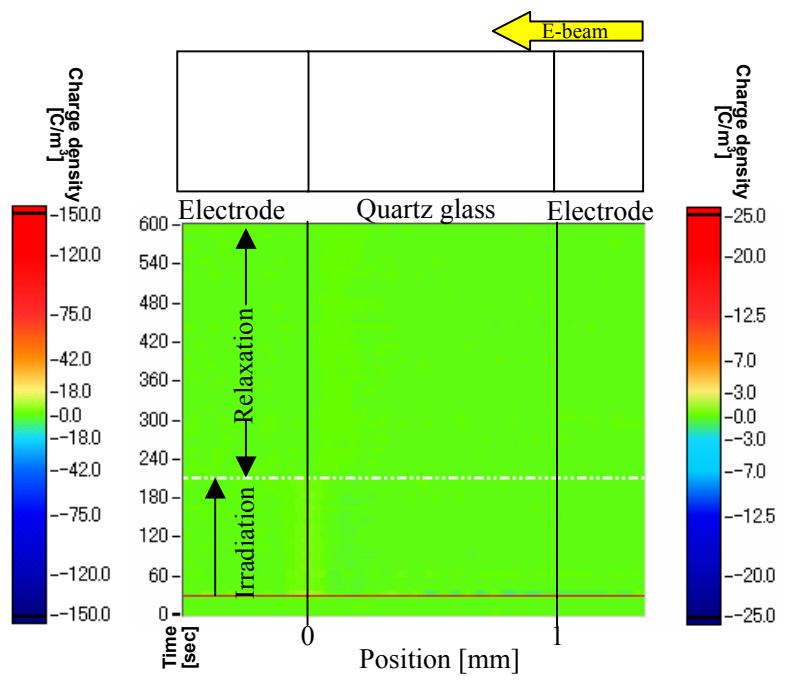
Figure 4. Space charge distribution in Quartz glass
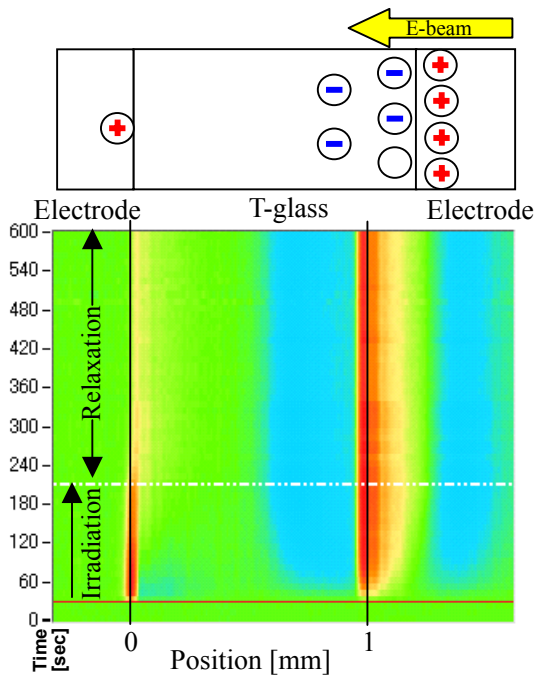
Figure 5. Space charge distribution in T-glass
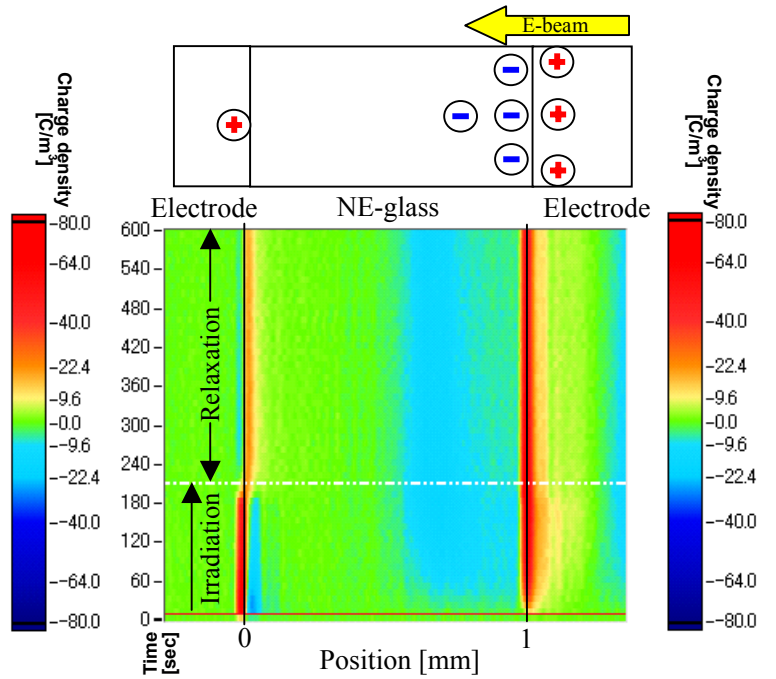
Figure 6. Space charge distribution in NE-glass
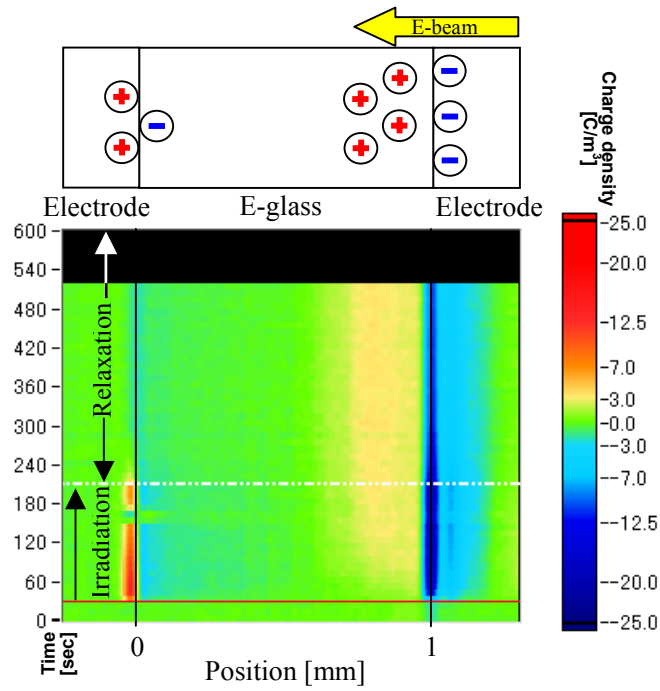
Figure 7. Space charge distribution in E-glass
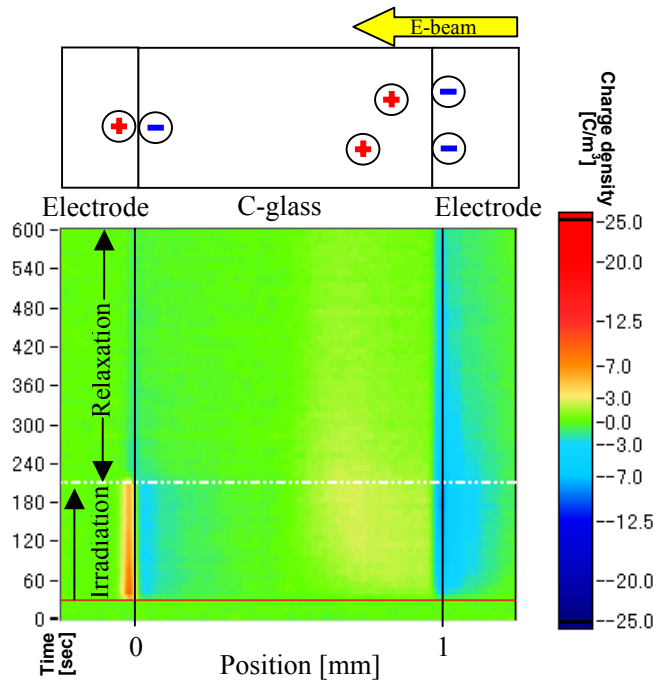
Figure 8. Space charge distribution in C-glass
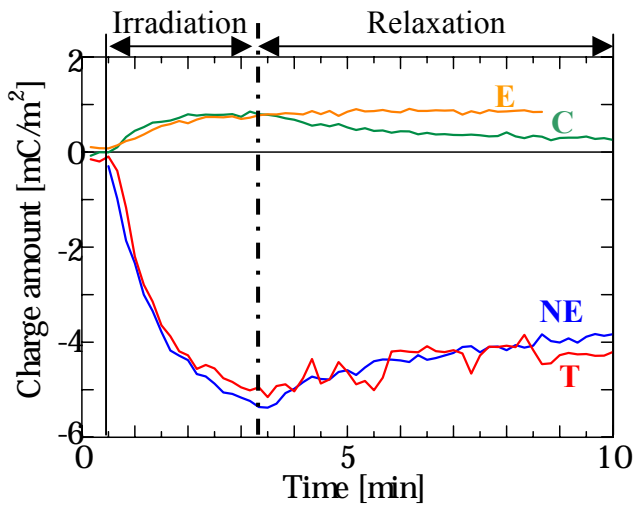
Figure 9. Time dependence of accumulation and relaxation process of bulk charge
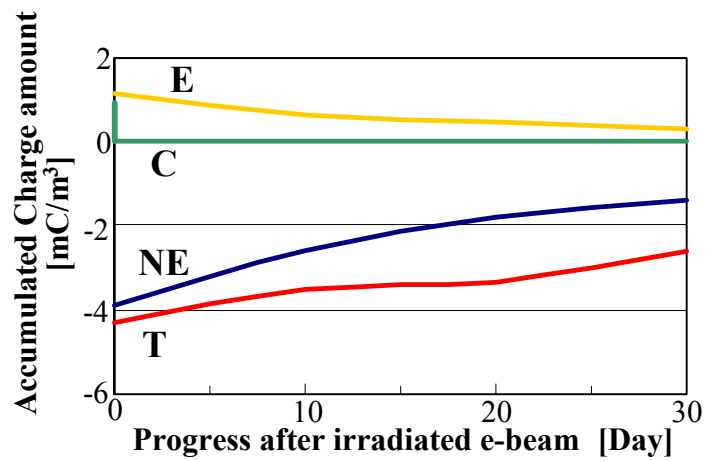
Figure 10. Time dependence of decay process of bulk charge for 30days
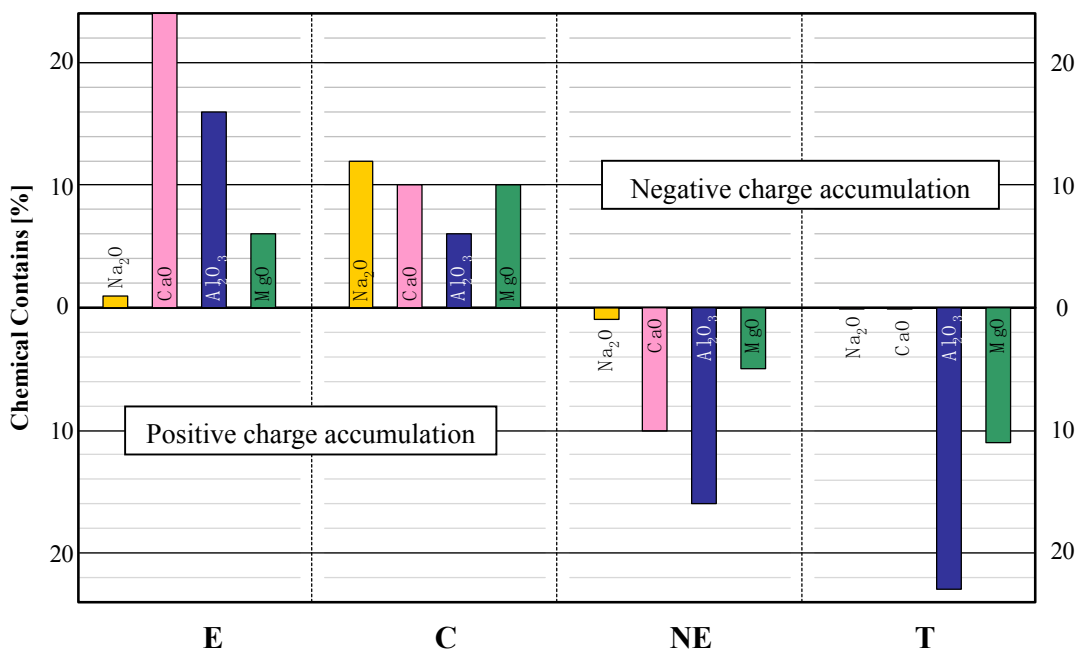
Figure 11. Relationship between accumulation charge polarity and each contained impurities

References

1. Y. Li and T. Takada: IEEE EI Magazine, Vol.10, No.5, pp. 16-28, 1994

2. T. Takada: IEEE Trans. DEI, Vol.6, No.5, pp. 519-547,1999

3. T. Takada: Y. Tanaka N. Adachi and X. Qin, IEEE Trans. DEI, Vol.5, No.6, pp. 944-951,1998

4. H. Miyake, Y. Ito, Y. Tanaka, T. Takada and M. Hanai: Space Charge Distribution for Various Glass Materials under DC Stress, IEEJ Trans. FM, Vol. 123, No.1, 2003 (in Japanese)

5. X. Qin, K. Suzuki, Y. Tanaka and T. Takada: Three-dimensional Space Charge measurement in a dielectric using the acoustic lens and PWP method, J. Phys. D: Appl. Phys. Vol.32, pp156-160 (1996)

MEASUREMENT OF BULK CHARGE IN DIELECTRIC MATERIALS IRRADIATED BY ELECTRON BEAM IN VACUUM ENVIRONMENT

N. Osawa
Musashi Institute of Technology
1-28-1 Tamazutsumi, Setagaya-ku, Tokyo 158-8557, Japan
Phone: +81-3-3703-3111 ex. 3931
Fax: +81-3-5707-2156
E-mail: osawa@me.musashi-tech.ac.jp

S. Takahashi
Y. Tanaka
T. Takada
R. Watanabe
N. Tomita
Musashi Institute of Technology, Japan

V. Griseri
L. Levy
ONERA/CERT, Toulouse, France

C. Laurent
LGET, Universite Paul Sabatier, Toulouse, France

Abstract

Bulk charge accumulation in thin dielectric materials under electron beam irradiation in vacuum environment was observed using newly developed measurement system. Recently, some accidents in spacecraft due to the charging up of electric potential have been reported. Some of them are caused by surface discharge normally happens in plasma environment. Some others seem to be caused by discharge due to and an accumulation of charge in bulk of materials at relatively higher altitude environment. Surface charge is usually measured using surface potential meter. However, there had been no useful method to measure the bulk charge in the materials. Therefore, we have been developing the bulk charge measurement system. We have already succeeded in measuring the bulk charge distribution in thick sample under electron beam irradiation in air atmosphere. However, to simulate the actual spacecraft in condition of high altitude space environment, it is necessary to carry out the measurement for thin materials in vacuum environment. Therefore, we have developed an improved measurement system applicable to a thin sample in vacuum environment. Using the improved system, we carried out the measurement of bulk charge distributions in 180 and 50 μm thick Kapton® and PET film under electron beam irradiation in vacuum of ca 10^{-6} Pa. In this report, some typical measurement results are introduced following the explanation of brief measurement principle.

Introduction

The spacecraft flying in GEO is always exposed to plasma and/or radioactive-rays such as α−, β− and γ−rays. In such condition, dielectric materials like cover glasses of solar battery or thermal blankets are charged up. Especially in GEO, they are expected to be irradiated by high-energy electron beam. In the case of high-energy electron beam irradiation, the electrons are injected into the bulk of dielectric materials and they accumulate in them. Because there are no basic data based on practical experiments, it seems difficult to simulate the accumulation and relaxation process of injected charge in dielectric materials. In other words,

it is difficult to expect when and how an accident of ESD caused by accumulated charge will happen on spacecraft. Therefore, we need to measure the charge distribution in the bulk of dielectric materials. We have been developing a system for measuring such a charge distribution in dielectric materials using, so-called, PIPWP (Piezo-induced pressure wave propagation) method.

Principle of PIPWP Method

The principle of PIPWP method is shown in Figure 1. By applying a pulse electric field to the piezo-device, a pulsive pressure wave is generated. When the acoustic wave propagates through the charged sample, the position of charge shifts slightly. The movement of the charge induces the change of surface charge on the electrode. Therefore, the displacement current flows the external circuit due to the change of induced charge on the electrodes. Since the displacement current flows when the acoustic pulse passes through the charge layer, we can observe the charge distribution by measuring the external current. A detail of the principle is described elsewhere [1].
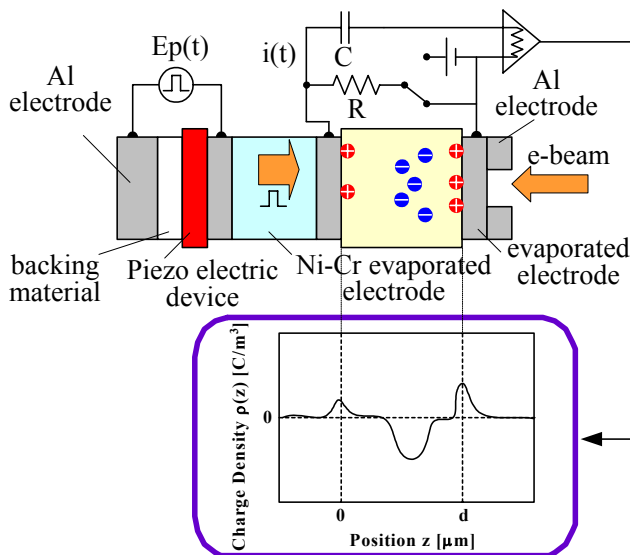
Figure 1. The principle of PIPWP method
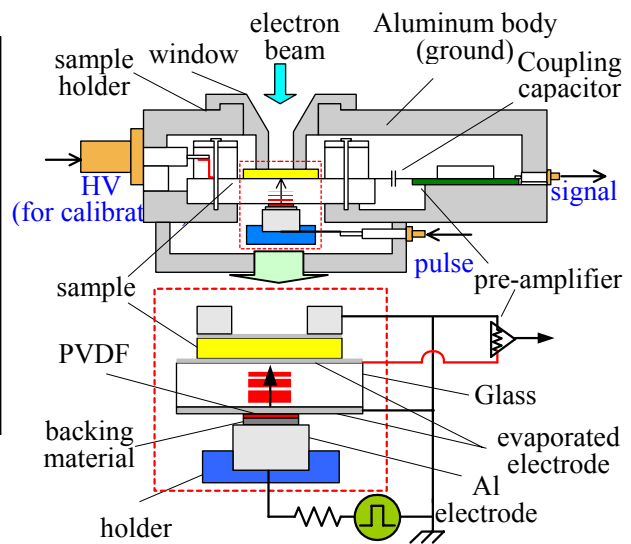
Figure 2. Diagram of the measurement apparatus

Measurement Apparatus

Diagram of the measurement apparatus is shown in Figure 2. [2] And Figure 3 shows Picture of the measurement apparatus. The apparatus have a window for the irradiation of the radioactive rays to the sample as shown in fig.2. The room for the sample should be completely shielded to reduce the noise from outside. Therefore the sample has an evaporated aluminum electrode on the topside surface, and it is connected tightly to the grounded flange of the window. To obtain the electric signal from the bottom side of the sample, a glass plate is inserted between the sample and the piezo-electric device. This glass plate is used to isolate the bottom side of the sample from the grounded level. As the aluminum electrode is evaporated on the bottom side of the glass plate for the shielding, the sample is completely covered by the grounded shield. The glass plate also has an evaporated electrode on the topside surface and it is connected to the detecting amplifier.

To generate a pressure wave, a pulse voltage is applied to the piezo-devise. The resolution of the apparatus depends on thickness of piezo-devise and the pulse width. In the experiment for measurement of Kapton® with 180 μm thickness, the PVDF film with 9 μm thick and 500ns width pulse were used as the piezo-devise and pulse voltage, respectively. To measure a thin film, we needed to improve the resolution of the measurement. Therefore, in the case of measurement for PET with 50 μm thickness, PVDF film with 4 μm thick and 1ns width pulse were used.
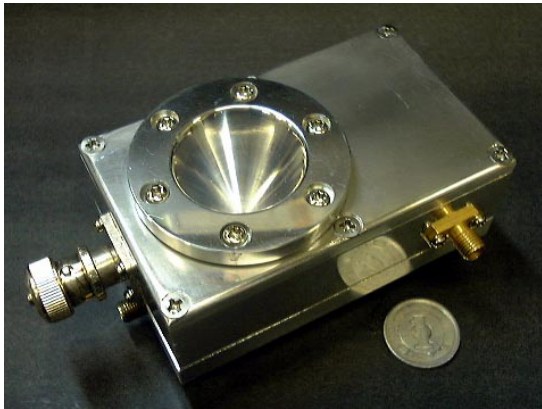
Figure 3.   Picture of the measurement apparatus

Figure 4.   Picture of SIRENE
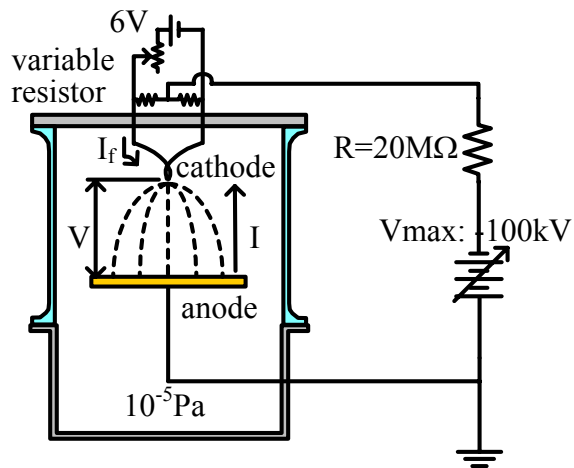
Figure 5.   Picture and diagram of the small test chamber

Electron Beam Irradiation System

In this experiment, two types of electron beam chambers were used. One is a named SIRENE in ONERA (Office National d'Etudes et de Recherches Aerospatiales), shown in Fig. 4. The range of acceleration energy and flux of electron beam in SIRENE are 10-400 kV and 0-2 nA, respectively. Another is small test chamber, shown in Figure 5, with dc high voltage generator up to 100 keV.
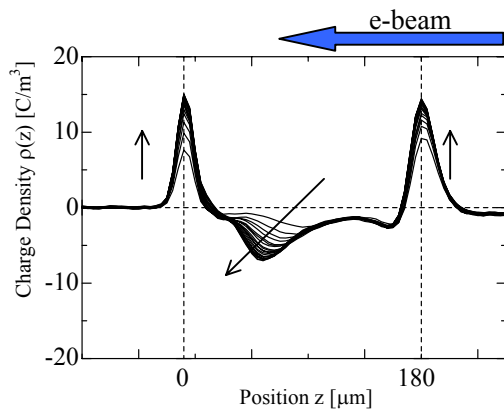
Figure 6. The Charge Density (under irradiation)
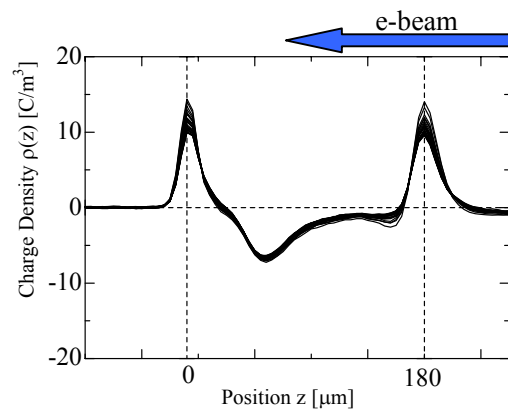
Figure 7. The Charge Density (after irradiation)
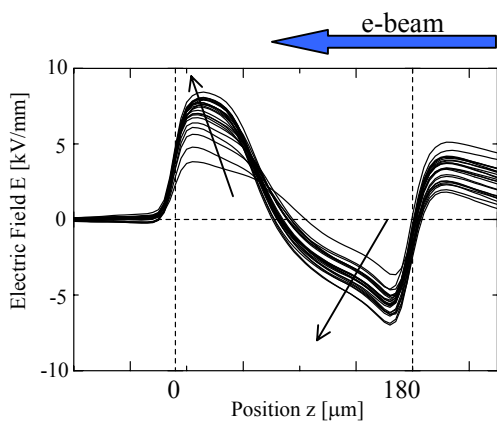
Figure 8. The Electric Field (under irradiation)
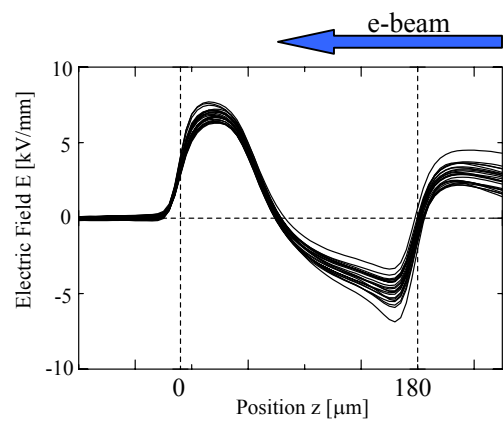
Figure 9. The Electric Field (after irradiation)
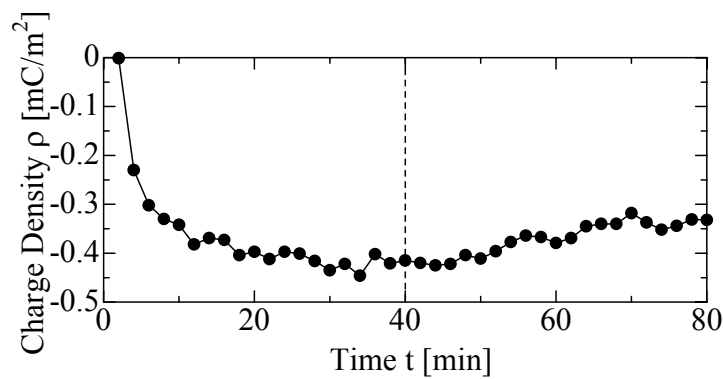
Figure 10. Amount of total charge (under and after irradiation)

Results and Discussion

Electron beam irradiated Kapton® of 180 μm thick

Figures 6 and 7 show the changes of charge distributions in 180 μm thick Kapton® under and after electron beam irradiation with acceleration energy of 125 keV in vacuum. This experiment was carried out using SIRENE. In these figures, the charge distributions of every 2 minutes are described. The electron beam is irradiated from right hand side in the Figs. As shown in Fig. 6, the negative charge gradually increases with increase of the irradiation time.

The peak of the negative charge is located around 120 μm from the irradiation surface described in right side in the figure. After irradiation, it is found that almost no changes are observed in this time range. Figures 8 and 9 show the electric field distributions that are obtained by integral calculation from the charge distributions shown in Figs. 6 and 7. As shown in Fig. 8, during e-beam irradiation, the electric field gradually increases with increase of the negative charge distribution. On the other hand, the electric field is stable after the irradiation as shown in Fig. 9. These results show the accumulated negative charge in Kapton® film may remains in the bulk for long time. Figure 10 shows the change of total amount of accumulated charge in Kapton® film under and after irradiation. The total amount of charge rapidly increases immediately after beginning of the irradiation.   However, the change of it becomes stable soon and seems to be saturated. After irradiation, the amount of charge seems to keep the maximum value

Electron beam irradiated PET of 50 μm thick

Figures 11 and 12 show the changes of charge distribution in 50 μm thick PET film under and after electron beam irradiation with acceleration energy of 40 keV in vacuum. This experiment was carried out using small test chamber. As shown in Fig. 11, the negative charge gradually increases with increase of the irradiation time. In these results, the distributions of every 1 minute are described. It is clear that the injected electrons increases rapidly near the opposite electrode as shown in Fig. 11. The peak of the negative charge is located around 41 μm from the irradiation surface described in right side in the figure. After irradiation, it is found that the charge distribution gradually decreases as shown in Fig. 12. Figures 13 and 14 show the electric field distributions calculated using the space charge distributions shown in Figs. 11 and 12. As shown in Fig. 13, during e-beam irradiation, the electric field gradually increases with increase of the negative charge distribution. The maximum electric field finally becomes 100 kV/mm. After irradiation, the electric field distribution gradually decreases. Figure 15 shows the change of total amount of charge accumulated in PET film under and after irradiation. It is found that the total amount of charge gradually increases in irradiation process.   After irradiation, however, it quickly decreases in this time range.

Since it is difficult to compare the results obtained from different samples, we do not mention the physical meaning of the results. However, it is clear that the developed measurement system seems to be useful for analysis of interaction between electron beam and dielectric materials.

Conclusion

We develop a measurement system of charge distribution in dielectric materials during electron beam irradiation in vacuum atmosphere. Using this system, we observed the change of charge distributions in Kapton® and PET films under and after electron beam irradiation. The developed measurement system seems to be useful for analysis of interaction between electron beam and dielectric materials.
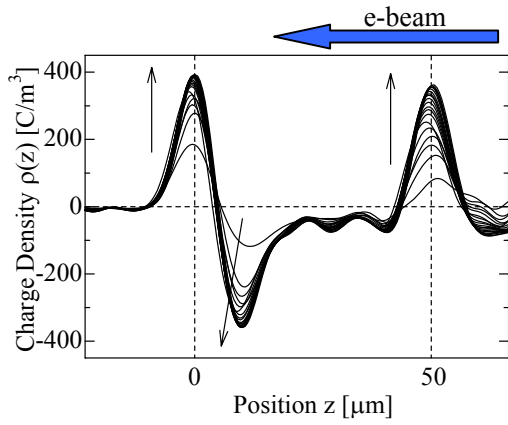
Figure 11 The Charge Density (under irradiation)
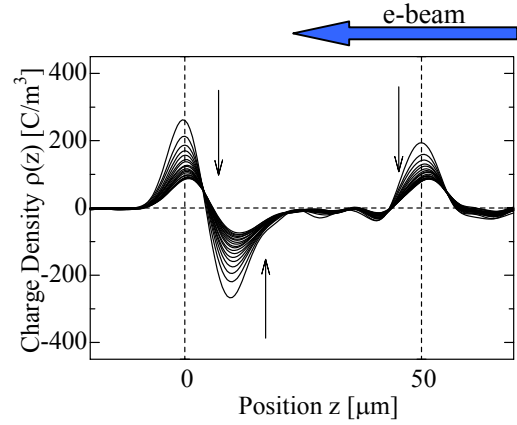
Figure 12 The Charge Density (after irradiation)
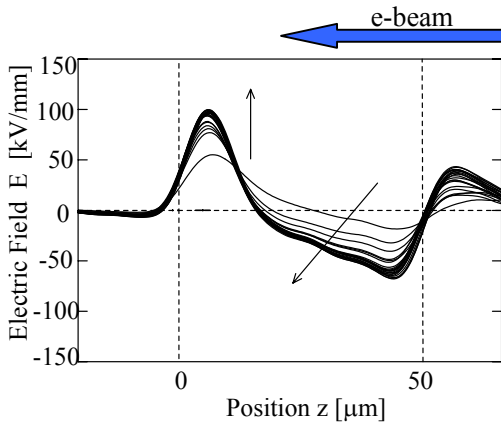
Figure 13 The Electric Field (under irradiation)
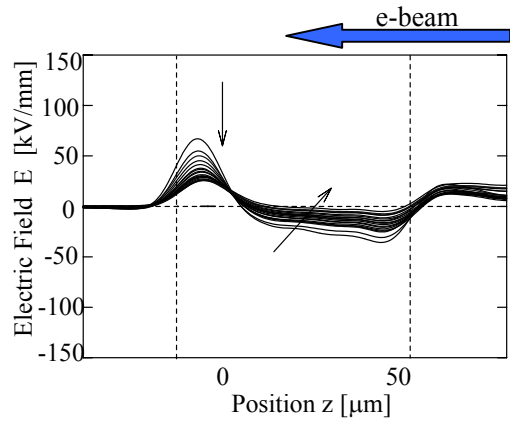
Figure 14 The Electric Field (after irradiation)
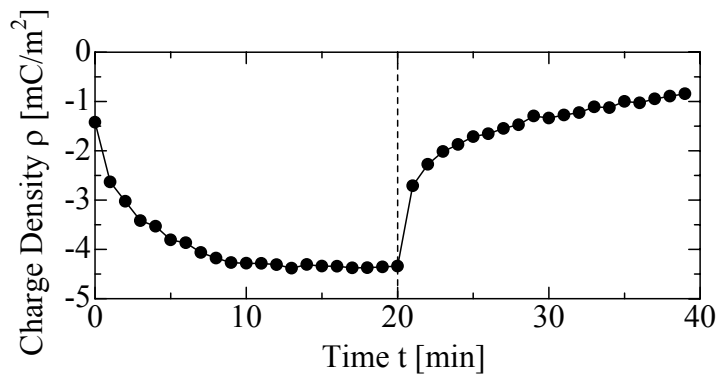
Figure 15.   Amount of total charge (under and after irradiation)

References

1. T.Takada, Y.Tanaka, N.Adatchi, X.Qin "Comparison between the PEA Method and the PWP Method for Space Charge Measurement in Solid Dielectrics'' IEEE Transactions on Dielectrics and Electrical Insulation Vol.5, No.6

2. Y.Tanaka, R.Watanabe, N.Tomita and T.Takada "Measurement techniques for charging in bulk of insulating materials irradiated by radioactive rays'' 7th Spacecraft Charging Technology Conference, 2001

IMPROVED DEMONSTRATION OF INTERNAL CHARGING HAZARDS USING THE 'REALISTIC ELECTRON ENVIRONMENT FACILITY' (REEF)

K. A. Ryden
QinetiQ Space Department
Cody Technology Park
Farnborough, Hampshire, GU14 OLX, United Kingdom
Phone: +44 (0)1252 393057
Fax: 44-1252-396320
E-mail: karyden@space.qinetiq.com

P A Morris
D J Rodgers
R Bielby
P R Knight
QinetiQ Space Department, United Kingdom

J Sorensen
ESA-ESTEC, The Netherlands

Abstract

Experimental ground testing has been carried out to determine whether digital latches can spontaneously change state in severe (space weather induced) outer-belt environments via the mechanism of internal spacecraft charging/discharging. A new facility is employed which improves simulations of the charging environment experienced by satellite equipment and materials. Results are presented which demonstrate the complete chain of events from environment to circuit anomaly. The anomaly rate shows dependence on both charging flux and circuit board temperature.

Introduction

Numerous spacecraft anomalies in the outer radiation belt have been attributed to electrostatic discharges (ESD) resulting from internal charging [1,2]. Charging occurs when intense fluxes of energetic electrons, typical of the outer belt, penetrate spacecraft shielding and are deposited in dielectrics or isolated metal components. Over periods of days, the build up of charge can result in intense electric fields and eventual ESD. This can induce a current 'spike' in electronic components resulting in upset or damage. Although there is convincing in-orbit evidence for a link between internal charging and spacecraft anomalies it is essentially circumstantial – for example anomalies are often seen to coincide with periods of enhanced electron flux. So far, laboratory simulations [3, 4, 5] and flight experiments [6, 7] have tended to concentrate on the charging process or ESD events *per se* rather than demonstrating their effect on electronics. As a result the complete chain of cause and effect (environment $\Rightarrow$ internal charging $\Rightarrow$ ESD $\Rightarrow$ electronic upset) has not been fully demonstrated leading to residual scepticism in some quarters about the reality of such effects [7]. The work presented here examines the behaviour of a digital electronic circuit while subjected to improved simulations of the environment experienced by electronic equipment in GEO. The basic approach is the irradiation of active circuit boards with an electron 'beam' well matched in intensity and spectrum to outer belt conditions. Observation of the behaviour

of the active circuit has been undertaken, as well as monitoring for discharges in general. The prime benefits of the study are:

- accurate simulation of on-orbit environmental conditions over long periods (days or even weeks);
- use of space-approved materials, components and structures;
- use of representative electronic circuits.

The Realistic Electron Environment Facility (REEF)

A high degree of realism was a basic aim of this work in order to properly simulate internal charging effects. Therefore a good simulation of the outer belt energetic electron spectrum was essential. While such simulations are available from some electron beam facilities [e.g. 5] via use of scattering foils, these facilities do not readily offer the capability to carry out very long duration testing, nor the ability to maintain and vary sample temperatures.

To undertake this work a new 'Realistic Electron Environment Facility' (REEF), was developed. REEF consists of a vacuum chamber ($<10^{-5}$ m bar) containing a ^{90}Sr source and the item under test. The temperature of the sample is maintained by coupling it to a thermally controlled plate. The plate's temperature can be stabilised to better than 1°C and controlled over the range -10°C to +40°C; this is important as the conductivity of dielectrics, and therefore the rate at which trapped charge will leak away, is strongly temperature dependent [8].

It was decided to use ^{90}Sr (a pure β-emitter) to simulate the space electron environment since it offers a number of advantages over conventional electron beams for this application and these are summarised in Table 1.

Sr90 source	Electron beam facility
spectrum is a good match to typical outer belt spectra from 0.1MeV up to 2.2MeV	mainly mono-energetic
current intensities can be made comparable to the worst-case GEO environment	minimum beam intensity is usually too high
spectrum is accurately known and fully repeatable between different laboratories the half life is 28 years and so the emission characteristics will be stable over long periods	at low currents, beam current variability over long periods can be significant
relatively small running costs are involved and long term testing is feasible	generally expensive to rent cannot readily be run continuously beyond one working day

Table 1. The advantages of 90Sr facility over an electron beam

The electron flux (usually quoted in terms of current density, pA/cm^2) at the sample can be altered by variation of source-sample distance. Integral spectra for the maximum and minimum source-sample distances possible within REEF are shown in Fig. 1 together with the average GEO electron environment from the NASA AE8 average model [9], the NASA Spacecraft Charging Handbook severe-case spectrum [10] and a 'worst-case' GEO environment predicted by the FLUMIC model [11]. FLUMIC is used in ESA's DICTAT internal charging analysis tool [12]. It can be seen that the REEF capability brackets the predicted GEO levels and provides a good spectral match up to approximately 2MeV.
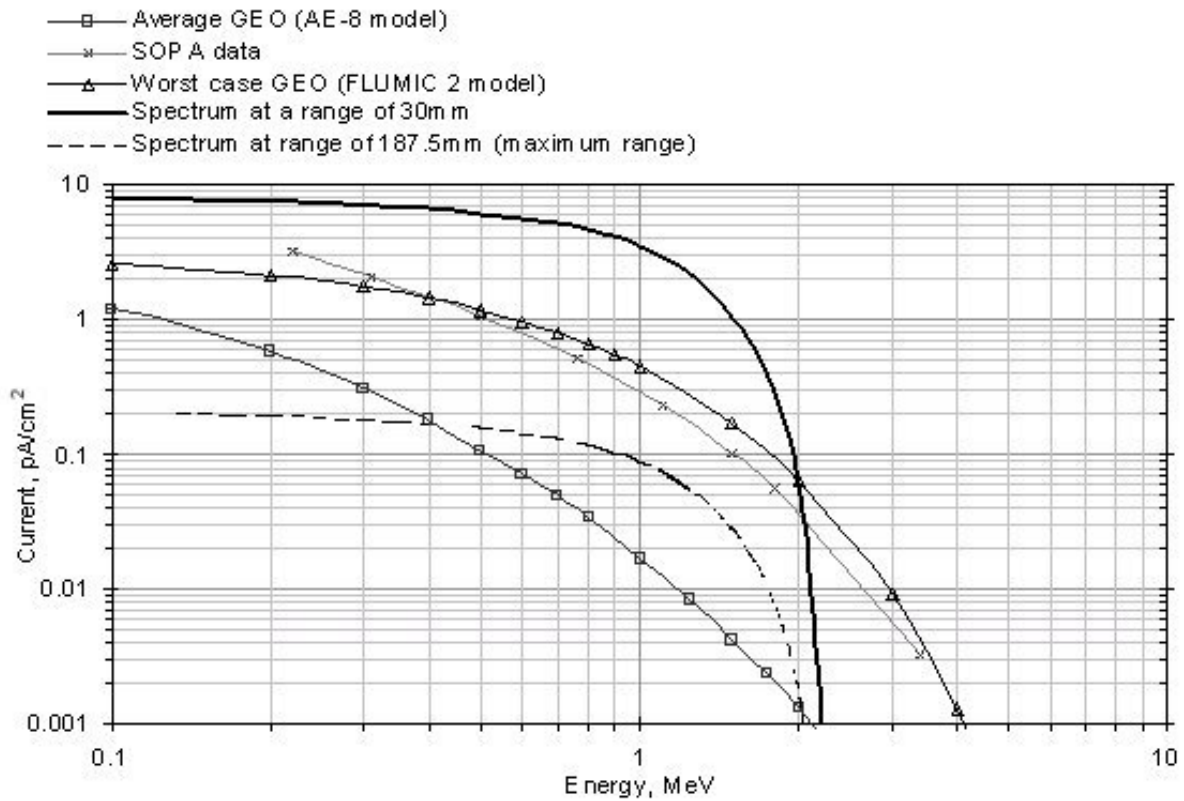
Figure 1. Integral electron spectra in REEF at the maximum and minimum source-sample distances compared with predicted worst-case and average GEO environments.

The electron current density at the sample varies approximately as the inverse square of the source-sample distance, except at very small distances where the finite source size (~5mm) makes the decrease somewhat slower.

The REEF spectra presented in Fig. 1 depict electron currents on the beam axis, but off-axis the current seen by a flat sample will decrease due to both the increased distance from the source and the oblique irradiation angle which results in unit sample area having a reduced effective area to collect current. This off-axis decrease has been measured and results are shown in Fig. 2 out to a radial distance of 40mm for source-sample distances of 37mm and 77mm. As would be expected the 'beam' is far more uniform at the larger source-sample distance; this may be important where uniform irradiation of a sample is critical. The electron flux can be reduced to zero by closing a shutter in front of the source when required.
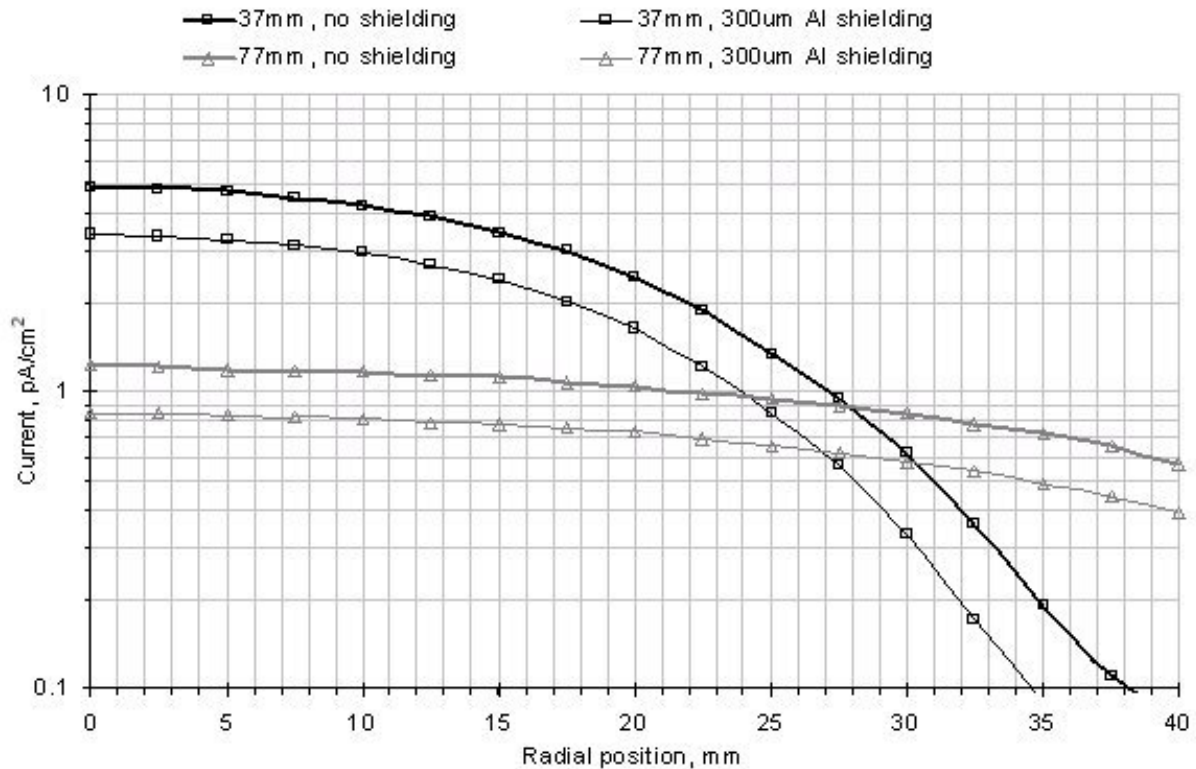
Figure 2. Measured electron current in REEF at source-sample distances of 37mm and 77mm as a function of distance from the beam axis.

Experimental Approach

Component selection

It was necessary to select a test circuit that represented generic elements of satellite electronic systems. To maximise the generality of the results the focus was placed on the so-called data, or D-type latch (also known as a flip-flop) which is a common building-block in many digital circuits. The dual CMOS latch 74HC74 was selected: in normal operation a rising edge on the clock line (CLK1/CLK2) simply latches the data at the inputs (D1/D2) through to outputs Q1/Q2. For these tests the inverted versions of Q1/Q2 (Q1' and Q2' are available on the chip) were fed back through to D1/D2 respectively (Fig. 3). This ensures that the data inputs are always different from the outputs, hence any false latch commands (i.e. CLK signals) will change the outputs and the occurrence of a false latching event is thus definitely detected. Since ESD can result in a ringing pulse with several rising edges, low pass filters with a time constant (10µs) much longer than the typical ESD duration (~100ns) were included in the feedback to prevent latch self-correction from an even number of rising edges.
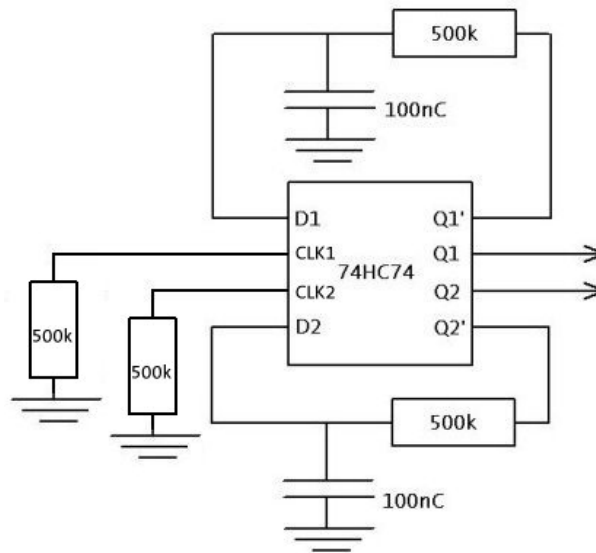
Figure 3. The circuit under test.

Circuit board and track layout

A widely used base material for space electronic circuit boards is woven glass-reinforced epoxy resin 'FR4', which has excellent electrical and mechanical properties. Because of this widespread usage and evidence from CRRES [6] which suggests that it is highly prone to generating discharges in the real space environment, FR4 was used for this work. The boards prepared had dimensions of 50mm x 50mm and two thicknesses were used: 1.6mm and 3mm. The PCB tracks were printed on one side for the circuit board using 1oz/sq. foot copper as shown in Fig. 4. A ground plane was incorporated on the rear of the PCB as this is good practice in electronic design. In fact a ground plane also has the benefit of providing a leakage path for charge stored in the board.
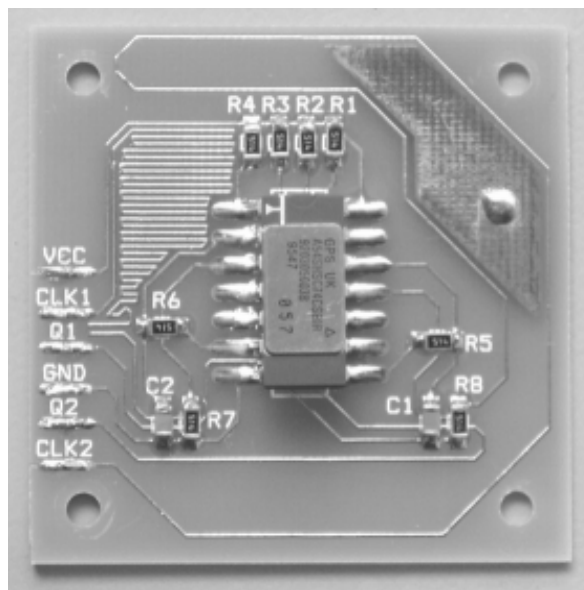
Figure 4. PCB with mounted 74HC74 chip.

There are an infinite number of possible track layouts and they strongly influence the likelihood of ESD coupling into the circuit. The board layout was relatively arbitrary except that the clock lines were made long and one clock line was routed in a wide loop whereas the other was kept to a more limited area of the board. Clock lines were pulled low via 500kΩ resistors. Another feature on the board was an island of copper, which could be left isolated if required in order to investigate the hazard that it presented. The mounting bolts could be isolated or grounded.
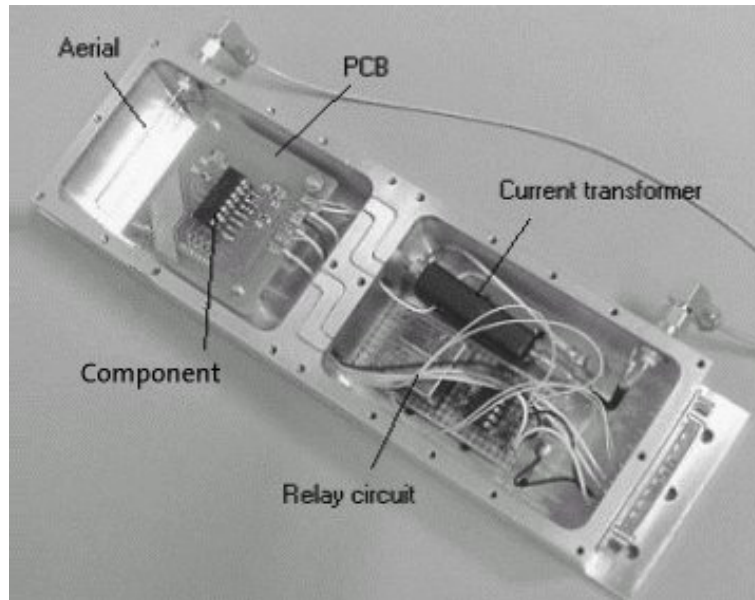
Figure 5. Test housing with all shields removed.

Installation in REEF

For the irradiations the PCB was housed in a machined aluminium box (Fig. 5) designed to mimic typical spacecraft equipment housings and surrounding structure. It is worth noting that backscatter and secondary radiation effects such as bremsstrahlung are all highly dependent on the properties of surrounding materials such as atomic number. Such secondary effects may influence the charging process. The test housing was divided into two compartments. The first compartment held the PCB under test and was positioned under the central beam axis. This compartment can be shielded using a lid if required. For the realistic experiments described below a minimal shield thickness of 300μm of aluminium was used solely to complete a Faraday cage around the sample and to maintain an even thermal environment. Note that the electron currents specified for the realistic testing are at the circuit board i.e. after the 300μm shield. Also contained in this compartment was an aerial, used to detect the occurrence of ESD, connected to a digital storage oscilloscope. The other compartment was heavily shielded and contains ancillary items (e.g. current transformer, interface for latch test circuit) which needed to be close to the D-latches to minimise the probability of noise pick up and signal attenuation. The current transformer was used to measure transients in the PCB ground plane.
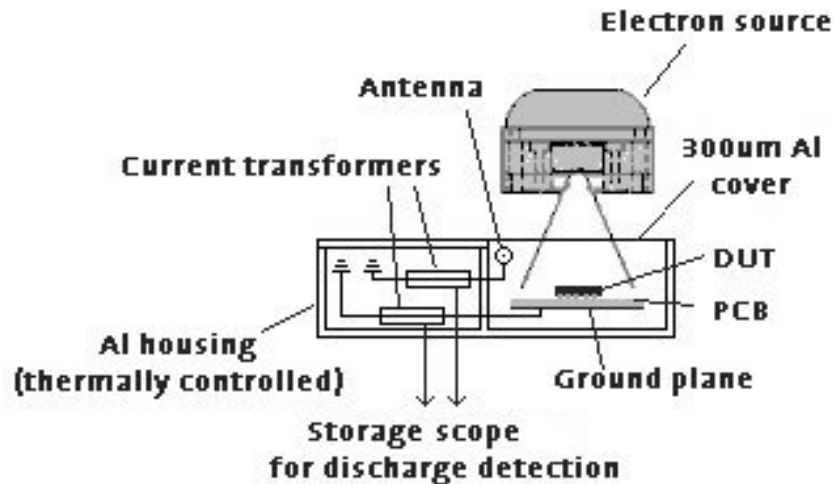
Figure 6. Schematic of the experimental arrangement.

Circuit Board Irradiations

Overview

All of the investigations used the circuit design and housing detailed above and the chip was spot shielded with 2mm of tantalum (grounded) to reduce the risk of total-dose damage. The following parameters were monitored and recorded continuously during the tests:

- Q1 and Q2 outputs to detect anomalies;
- current waveforms between PCB ground plane and ground;
- voltage waveforms from antenna;
- the DC current drawn by the circuit to check for total-dose damage.

Preliminary accelerated tests

Preliminary trials were aimed at determining whether anomalies would occur in particularly extreme (and somewhat unrealistic) circumstances, mainly as a test of the system as a whole. As such a very high (axial) electron current of ~5pA/cm^2 (incident on the PCB) was used - a level predicted for virtually unshielded components in GEO, and an order of magnitude greater than would usually be experienced by even lightly shielded (~0.5mm aluminium) components in GEO. No shield was used above the PCB. The D-latch used in this preliminary experiment was a commercial MM74HC74 device in a plastic package since it was unnecessary to risk damage to a more expensive device. The Ta shield prevented any flux reaching the chip and thus any charging of the package itself. The circuit board was made particularly susceptible to charging by:

- using a thick PCB (3mm);
- leaving metallic structures on the board (fastening bolts, isolated copper island, spot shield) ungrounded ('good practice' would be to ground such structures).

The PCB was irradiated at room temperature and the first anomaly (an uncommanded change of state of Q1 and Q2) was observed 4 hours into the irradiation and in total, 55 anomalies were observed during 231 hours of irradiation. Checks were carried out to ensure that these anomalies were not due to any type of local interference. Most of these anomalies were co-incident with large signals in both the aerial and ground plane consistent with ESD, however on two occasions these signals were measured without accompanying anomalies. After 114 hours of irradiation, the current drawn by the test circuit increased significantly and this is suspected to have been the result of ESD damage to the chip. These trials proved that electron irradiation would cause ESD and anomalies in the circuit, but under rather extreme conditions.

Realistic conditions (for GEO)

Next a set of irradiations using more realistic conditions were conducted in order to see how the rate of anomalies varied as a function of key parameters. A more typical PCB thickness of 1.6mm was used and the metallic elements (bolts and PCB floating island etc.) were grounded. The chip used was a 54HSC74 silicon-on-sapphire device from a European supplier which is frequently used on space missions. Despite being radiation-hard to 300krad(Si) the device was still fitted with a spot shield of 2mm Ta in order to avoid any possible total dose damage. The spot shield was grounded. The device came in a ceramic package and is pictured in Fig. 4. Prior to the irradiation, the board with the test components was 'baked out' at 60°C for a 24-hour period in order to remove absorbed moisture. The sample was then irradiated continuously for a period of a month without any re-pressurisation of the chamber. During this period it was subjected to a sequence of different flux and temperature conditions. Both the environment history and the latch status results are shown in Fig. 7 (lower section shows the electron current and temperature histories whereas upper section shows latch state) and summarised in Table 2. Occasionally the latch state was deliberately changed in order to test that the circuit was still functioning normally (these test flips are marked below the latch state trace in Fig. 7). A 300μm shield was used during these tests. Initially the electron current incident on the PCB was set to 0.6pA/cm^2 simulating the worst-case current predicted by FLUMIC under 0.5mm of Al which is a minimum likely shielding thickness for most spacecraft.

At room temperature (period 1 denoted P1 hereafter) no anomalies were observed but when the temperature was reduced to 0°C (P2) anomalies began occurring almost immediately. To prove that these were due to irradiation (rather than other electromagnetic interference) the source shutter was closed for a day (P3), during which time no anomalies occurred, and when it was re-opened (P4) further anomalies were seen. Over the next 12-days the temperature was initially increased to 10°C (P5) and then decreased to 0°C (P6) and -10°C (P7). It was found that the anomaly rate tended to be greatest at lower temperatures.

During 19th May the electron current was reduced to 0.14pA/cm^2 representing an average GEO level, whilst maintaining a sample temperature of -10°C (P8). Early the next day, two anomalies occurred in each channel but no further anomalies occurred over the next 4-days. It was speculated that this level was in fact too low to cause anomalies on its own but that the two anomalies that did occur were caused partly by irradiation at the higher level over previous days (during P7). When the current was again increased to the higher-level (P9)

anomalies resumed at a higher rate again. The anomalies over each period are summarised in Table 2. Note that an anomaly is defined by either of the two outputs spontaneously changing. Where both outputs changed simultaneously this is counted as only one anomaly. Test switches of the latches are excluded from the tables.

Variation in the anomaly rate for separate periods with the same current and temperature (e.g. P2, P4 & P6 or P7 & P9) was significant. This was possibly due to varying levels of residual charge from the preceding irradiation and the chaotic nature of the discharge process.

Example waveforms detected on the aerial and the ground plane are provided in Fig. 8 and Fig. 9. Virtually all anomalies were co-incident with the occurrence of such waveforms.
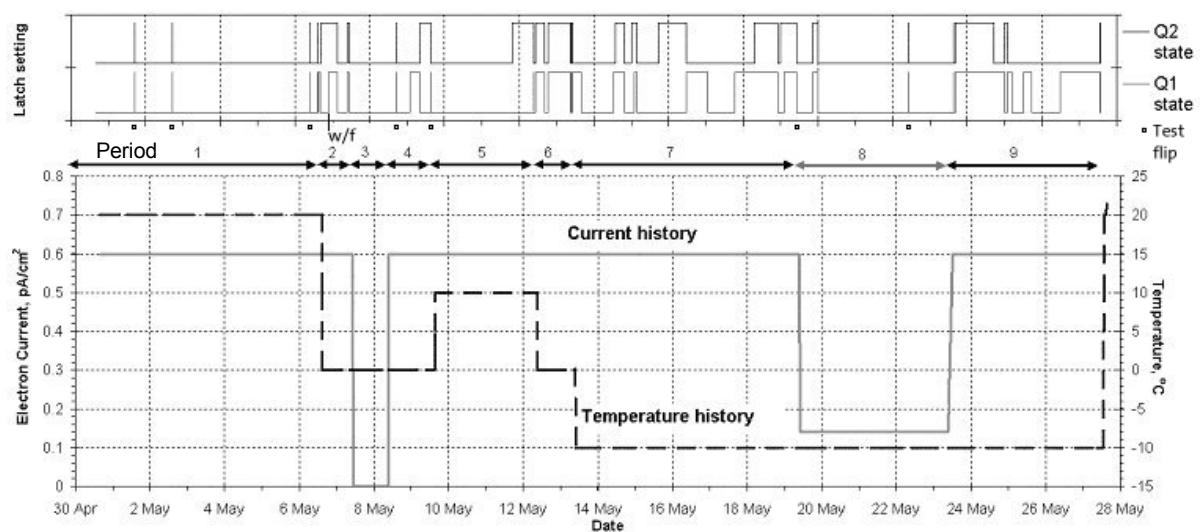
Figure 7. Test history. The top plate shows the two output states from the chip during testing. Changes in these two states represent the occurrence of anomalies (excepting tests of the normal functioning of the circuit – marked with squares below the axis). The lower plate shows the irradiation current and the temperature during the test.
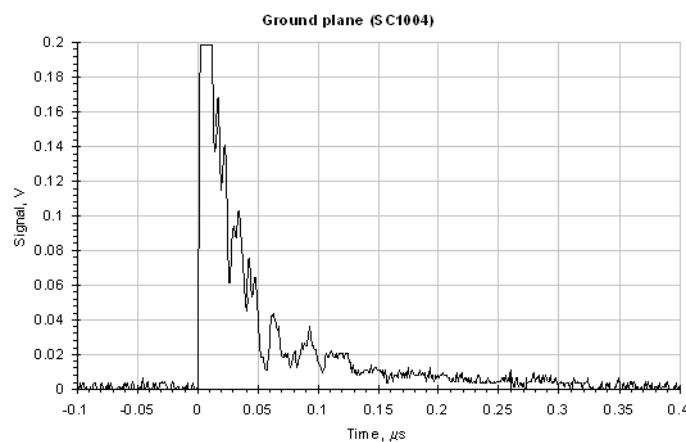
Figure 8. Typical waveform detected through the PCB ground plane (the waveform was recorded on 6th May and the corresponding event is marked by w/f in Fig. 7). The measured signal corresponds to a current from the ground plane of 0.2A/V.
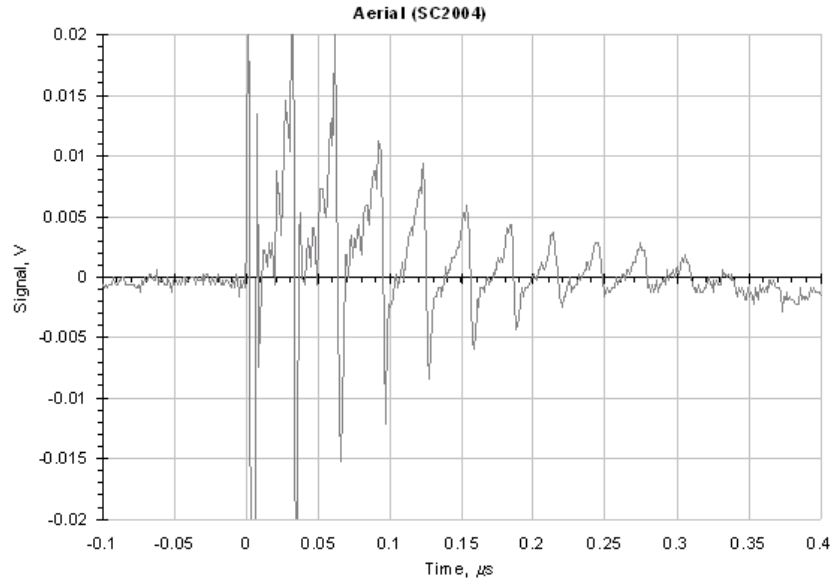
Figure 9. Typical waveform detected on the aerial (the waveform was recorded simultaneously with the ground plane waveform in Fig. 8).

Period	Temp °C	Current pA/cm^2	Time hours	Anomalies	Rate #/day
1	20	0.6	143	0	0
2	0	0.6	20	8	9.6
3	0	Shuttered	23	0	0
4	0	0.6	30	3	2.4
5	10	0.6	66	1	0.36
6	0	0.6	24	4	4.0
7	-10	0.6	136	18	3.2
8	-10	0.14	98	2	0.49
9	-10	0.6	97	8	2.0

Table 2. Summary of anomalies.

In order to examine repeatability of the results, the irradiation was repeated with a previously un-irradiated component and circuit board. All initial conditions were identical to the original test except that the initial temperature was set to -10°C so it was expected that anomalies would occur readily. The recorded latch outputs (Q1 and Q2) and the temperature and current histories are shown in Fig. 10. Markers below the trace again denote test flips (non-anomalous events) in the latch trace.

Conditions were maintained at a constant level for the first period of the investigation which lasted approximately 7 days. However, during this period, no anomalies occurred in the system. The decision was thus made after seven days to increase the irradiation current by a third (to 0.8pA/cm^2). Again, over the next 24 hours, the circuit again showed no signs of circuit anomalies or ESD events. A third period was thus undertaken for which the temperature was reduced to -20°C. The effect of this temperature reduction was immediate. Within 40 minutes of the reduction, an ESD event was recorded coinciding with changes of both Q1 and Q2. A total of 19 anomalies were observed in the circuit during the 23 hours

proceeding the change in temperature, seven of which could be directly associated with ESD events. A summary of this test is provided in Table 3.
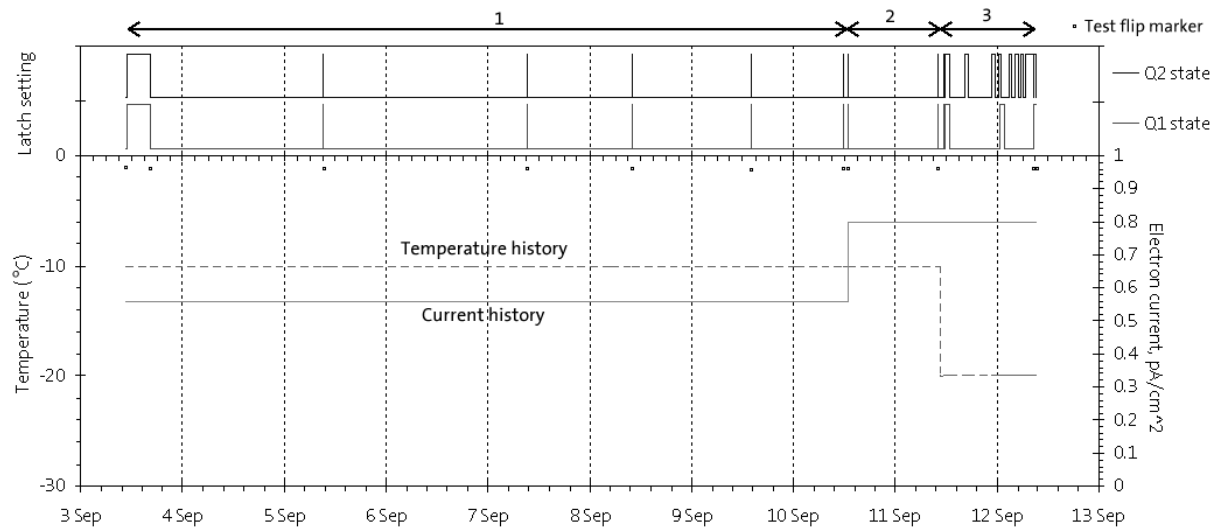
Figure 10. Test history of second test. The top plate shows the two output states from the chip during testing. Changes in these two states represent the occurrence of anomalies (excepting tests of the normal functioning of the circuit – marked with squares below the axis). The lower plate shows the irradiation current and the temperature during the test.

Period	Temp °C	Current pA/cm^2	Time hours	Anomalies	Rate #/day
1	-10	0.6	170	0	0
2	-10	0.8	22	0	0
3	-20	0.8	23	19	19.8

Table 3. Summary of anomalies in second test

Conclusions

It has been shown that anomalous changes of state can occur in a simple digital latch mounted on an FR4 board when irradiated in a close approximation of the worst-case (electron) environment expected in GEO under 0.5mm of aluminium shielding. In view of the co-incident transients detected by the antenna and ground-plane current monitor these anomalies are concluded to be due to electrostatic discharges occurring either on or within the PCB (there were no ungrounded metallic elements). Reducing the flux to near-average GEO intensities (at constant temperature) resulted in a much reduced anomaly rate compared to the worst-case flux, as would be expected.

It had been expected that the anomaly rate would increase at lower temperatures since dielectric conductivity reduces sharply with temperature [8]. Our results support this prediction to some extent, however there seems to be an important and unexpected effect resulting from (rapid) changes in temperature which, in both experiments, led to a sudden onset of discharge events. Further investigation is desirable to confirm this observation and determine its significance for spacecraft.

References

1. A R Fredrickson, 'Upsets related to spacecraft charging', IEEE Tran. Nuc. Sci., Vol. 43, No2 April 1996.

2. G. L. Wrenn, D. J. Rodgers and K. A. Ryden, 'A solar cycle of spacecraft anomalies', Annules Geophysicae, Vol.20, pp 953-956, (2002).

3. F. P. Wenaas, M. J. Treadaway et al, 'High energy electron induced discharges in printed circuit boards', IEEE Tran. Nuc. Sci., Vol.26, No. 6, Dec 1979, pp5152-5155.

4. A. R. Fredrickson, 'Bulk charging and breakdown ion electron-irradiated polymers', Spacecraft charging technology - NASA report 2182, pp33-50, 1980.

5. P. G. Coakley, M. J. Treadaway, P. A. Robinson, 'Low flux laboratory test of the internal discharge monitor (IDM)', IEEE Tran. Nuc. Sci, Vol.32, No.6, Dec 1985.

6. A. R. Fredrickson, E. G. Holeman et al, 'Characteristics of spontaneous electrical discharging of various insulators in space irradiation', IEEE Tran. Nuc. Sci., Vol. 39, No.6, pp1773-1982, 1992.

7. A. Ciccolella and J. Wolf, 'The Discharge Detector Experiment', Proc 7th SCTC, ESA-SP476, pp337-340, Nov 2001.

8. K. A. Ryden, P A Morris and S N Clucas, 'The effect of temperature on internal charging', Proc 7th SCTC, ESA-SP476, pp133-138, Nov 2001.

9. Vette, J. I., The NASA/National Space Science Data Center Trapped Radiation Environment Model Program (1964-1991), NSSDC/WDC-A-R&S 91-29, 1991.

10. A. Whittlesey, 'Avoiding problems caused by spacecraft on-orbit internal charging effects, NASA-HDBK-4002, Feb. 1999.

11. G. L. Wrenn, D. J. Rodgers and P. Buehler, 'Modelling the outer belt enhancements of penetrating electrons', J. Spacecraft and Rockets, Vol. 37, pp408-415, 2000.

12. http://www.spenvis.oma.be/spenvis/

HIGH VOLTAGE SOLAR ARRAY ARC TESTING FOR A DIRECT DRIVE HALL EFFECT THRUSTER SYSTEM

Todd Schneider
NASA Marshall Space Flight Center
Environmental Effects Group, Mailstop ED31
Huntsville, AL 35812
Phone: (256) 544-2595
E-mail: todd.a.schneider@nasa.gov

M.R. Carruth, Jr.
J.A. Vaughn
NASA Marshall Space Flight Center, Huntsville, AL

G.A. Jongeward
I.G. Mikellides
Science Applications International Corporation, San Diego, CA

D. Ferguson
T.W. Kerslake
T. Peterson
D. Snyder
NASA Glenn Research Center at Lewis Field, Cleveland, OH

A. Hoskins
Aerojet Corporation, Redmond, WA

Abstract

The deleterious effects of spacecraft charging are well known, particularly when the charging leads to arc events. The damage that results from arcing can severely reduce system lifetime and even cause critical system failures. On a primary spacecraft system such as a solar array, there is very little tolerance for arcing. Motivated by these concerns, an experimental investigation was undertaken to determine arc thresholds for a high voltage (200-500 V) solar array in a plasma environment. The investigation was in support of a NASA program to develop a Direct Drive Hall-Effect Thruster (D2HET) system. By directly coupling the solar array to a Hall-effect thruster, the D2HET program seeks to reduce mass, cost and complexity commonly associated with the power processing in conventional power systems. In the investigation, multiple solar array technologies and configurations were tested. The cell samples were biased to a negative voltage, with an applied potential difference between them, to imitate possible scenarios in solar array strings that could lead to damaging arcs. The samples were tested in an environment that emulated a low-energy, HET-induced plasma. Short duration "trigger" arcs as well as long duration "sustained" arcs were generated. Typical current and voltage waveforms associated with the arc events are presented. Arc thresholds are also defined in terms of voltage, current and power. The data will be used to propose a new, high-voltage (>300 V) solar array design for which the likelihood of damage from arcing is minimal.

Introduction

In the quest to create lighter more efficient spacecraft, the natural trend is toward higher voltage power systems. High voltage power systems offer more power for less mass – due to reduced resistive (I^2R) losses in conductors that carry lower currents but deliver the same power (Power = Current x Voltage). Unfortunately, the efficiency gains of operating at high voltage can be offset by spacecraft charging problems. Nowhere is this trade-off between system efficiency and spacecraft charging more evident than in the case of high voltage solar arrays operating in a plasma environment. High voltage solar arrays can exhibit parasitic current collection as well as arcing when immersed in a plasma.[1,2,3]

The Direct Drive Hall-Effect Thruster (D2HET) program is an excellent example of a power system design that benefits from mass savings as a result of high voltage solar array operation.[4,5] In the D2HET concept, the anode of a Hall-Effect Thruster (HET) is driven directly by a high voltage (300 V) solar array. Operation in this manner significantly reduces the mass of a Power Processing Unit, by eliminating the transformer stage that is usually responsible for increasing the standard 28 – 40 Volt array power to 300 Volts. However, the high voltage solar arrays in a D2HET system must be capable of operating in the charge exchange plasma that is generated in the HET plume. In addition, the arrays must also be capable of operation in the natural plasma environment around the Earth – as might be the case for orbit raising applications. Therefore, it was necessary for the D2HET program to find a robust high voltage solar array that would have minimal (electron) current collection and greatly reduced potential for arcing.

In order to find the next generation of high voltage solar arrays, the D2HET program investigated current collection phenomena and arcing thresholds using several existing solar array technologies. The results of the electron current collection studies are described by Mikellides.[6] The purpose of this paper is to describe the results associated with arc tests that have been conducted. The results of the current collection tests and the arcing tests have been used to create a hybrid solar array design that is expected to function efficiently in harsh charging environments.

Experiment Set-up

To accomplish the task of determining arc thresholds as well as understanding solar array arc characteristics, a plasma test chamber was set-up at NASA Marshall Space Flight Center. The test chamber (Figure 1) is a cylindrical vacuum chamber with a 1.2 m inside diameter and a useable length of 1.7 m. Two liquid nitrogen trapped diffusion pumps maintain the base vacuum pressure at 5×10^{-7} Torr. The plasma is created by a hollow cathode plasma source. In order to reduce interaction between the plasma source and the biased solar array, the "keeper" electrode of the hollow cathode is grounded. Using argon gas at an operating pressure of 8×10^{-5} Torr, the typical plasma conditions are: Density = $5\text{-}10 \times 10^6$ cm^{-3}, Electron temperature = 0.5-1 eV, and Plasma potential ~ -20 volts. The plasma parameters are determined by using a 3.8 cm diameter spherical Langmuir probe. To monitor the solar array samples in the chamber, a video camera is placed at one end of the vacuum vessel in line with a viewport. The camera is connected to a video system that provides a means of visually determining the position of an arc on the array.

To facilitate the reviewing process, the video system is equipped with a time-date generator as well as a title maker. The video system is shown in Figure 2.
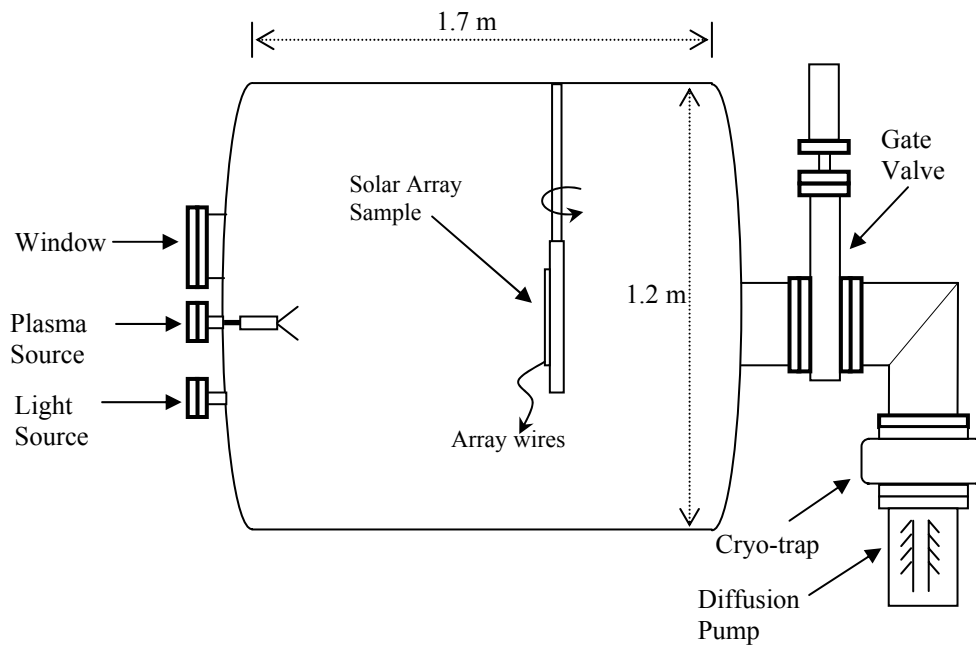
Figure 1. Plasma Test Chamber.
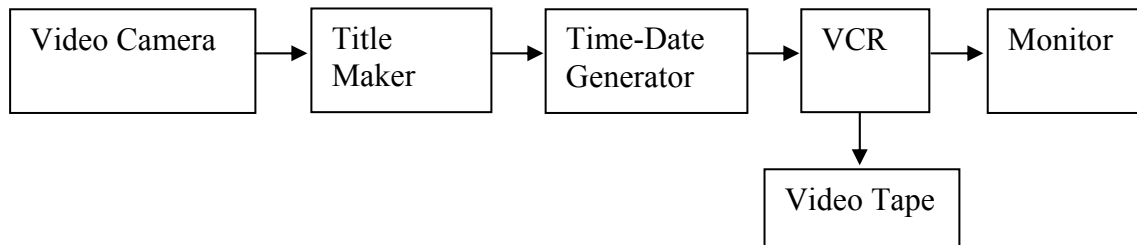
Figure 2. Block diagram of the video system used to capture arc events on tape.

In space, it has been observed that solar arrays biased negative with respect to the surrounding plasma are subject to experiencing arcing events.[7] The arcs vary in duration and peak current values.   Previous ground based test have confirmed the existence of two general categories of arcs: 1) Trigger Arcs and 2) Sustained Arcs.[8] Trigger arcs are characterized as short duration (~20 microseconds) high peak current (>20 amps) discharges. The primary energy source for a trigger arc is the intrinsic capacitance of the array. Trigger arcs are not usually responsible for damaging the solar array; however, they are considered a catalyst for sustained arc events. Sustained arcs, as the name implies, are long duration arcs (>1 millisecond), but with low current (<10 amps) demand. Sustained arcs represent the greatest

threat to the solar array survivability. Sustained arcs are likely to occur at the interface between two solar cells that have a significant differential voltage between them – as might be the case for two cells in separate strings on the array. Sustained arcs utilize the photovoltaic power generated from each string to supply their energy requirements.

In order to generate both trigger and sustained arcs in ground based testing, two separate circuits are required. Figure 3 shows the circuit used to generate a trigger arc. The trigger arc circuit requires a capacitor that is representative of the self-capacitance associated with a full array. For this experiment, the capacitance used was 1.0 microfarad. This value was chosen based on the design reference missions that were specified at the outset of the D2HET project.[9]
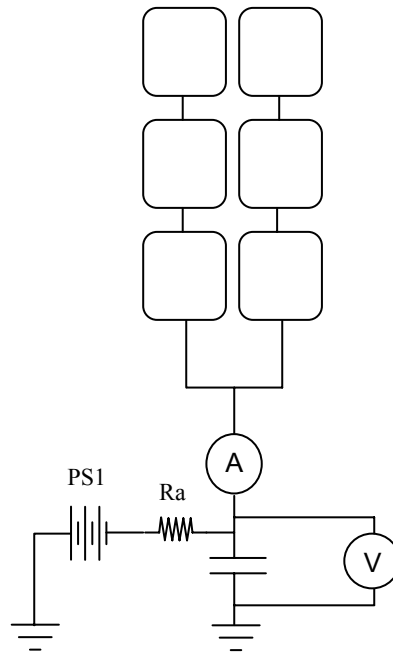
Trigger Arc Circuit

Figure 3. Basic schematic of the trigger arc circuit.

To generate a sustained arc, a power supply (PS2) is added to the trigger arc system (Figure 4). This supply, known as the differential power supply, is a current limited supply that simulates the power created by a solar array string under illumination. The events leading to a sustained arc have been described by Hastings[10] and Ferguson.[11] The process is believed to occur under conditions where a trigger arc is initiated at the interface between two adjacent cells that have a voltage difference between them. The arc plasma from the trigger arc creates a conductive "bridge" across the interface that allows for current to flow between the two adjacent cells. This current flow between cells can result in significant heating of the cell material, cover glass, and substrate. In fact, it has been observed in this experiment as well an in space, the heat from a sustained arc can cause significant damage by melting cell edges, damaging interconnects, and pyrolizing Kapton substrates – which can result in a conductive path of material (carbon) being created between two cells.

Cells in a string

Interface between strings →
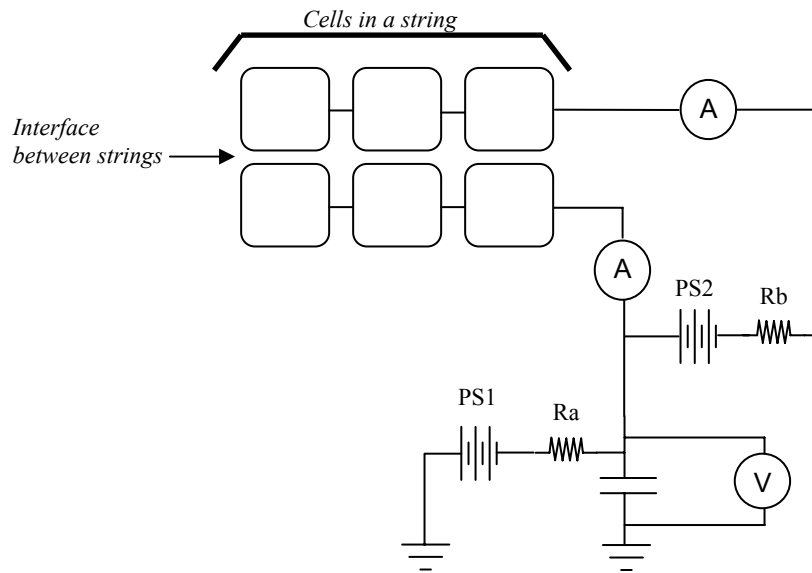
Sustained Arc Circuit

Figure 4. Basic schematic of the sustained arc circuit.

Given the potential for damage to an array as a result of a sustained arc event, it is important to determine the arc threshold for a given array and to either operate the array below this threshold or to initiate an array design that eliminates the possibility of sustained arcs. With this in mind, the D2HET program set out to determine if there was an existing array technology that was capable of operating at −300 volts without experiencing an arc event. If such an array were found, the electron current collection of the candidate array would be assessed and compared to the mission design goals before it would be chosen as the appropriate technology for a D2HET mission. On the other hand, if none of the technologies tested met the arc threshold specification, then a new array design could be created based on the test results.

Sample Descriptions

A wide range of solar array designs presently exists and new lightweight high-efficiency designs continue to be produced. To help reduce the number of candidate test samples for the D2HET program, an emphasis was placed on technologies that appeared to be suited for use at high voltages (300 volts). Ultimately, three different array technologies were chosen.

The first type of solar array tested was based on the design used for the International Space Station (ISS). ISS solar arrays have been designed to operate at relatively high voltage (160 volts) and have demonstrated continuous operation in space for years. A key feature of the ISS array is the use of interconnects which are completely covered by an insulating film (Kapton). However, the cell edges are exposed, which allows current collection. A picture of the sample coupon is shown in Figure 5.

The second technology chosen for testing was named "Planar TECSTAR".[12] In contrast to ISS, the Planar TECSTAR design employs exposed interconnects on some parts of the sample coupon. A picture of the coupon is shown in Figure 6. The connections at the top and bottom of the sample are exposed, however, the connections in the middle of each two cell module are covered by coverglass. The cells are mounted on top of a Kapton film. The film in turn rests on top of a rigid structure formed from graphite sheets with an aluminum honeycomb structure in the middle.
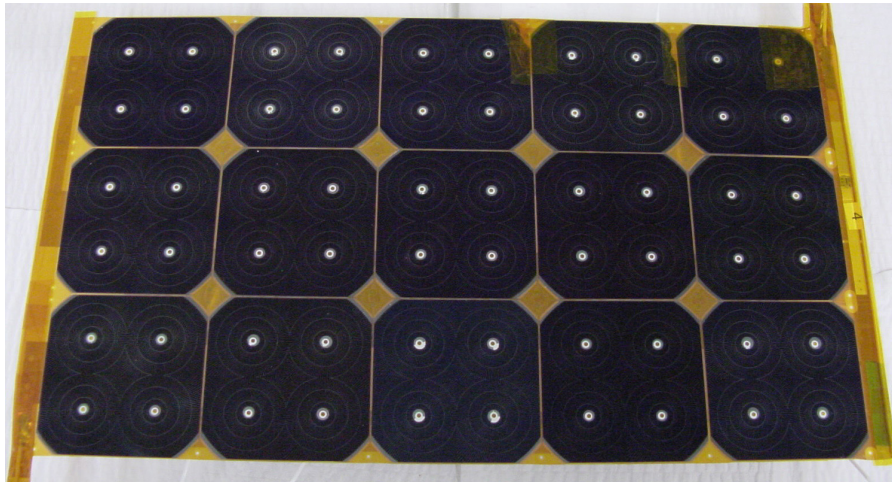
Figure 5. Photograph of the ISS Solar Array sample.

The third type of solar array sample tested was referred to as the "TECSTAR Concentrator". This sample design is unique due to the fact that a triangular shaped metallized dielectric film is placed between the two photovoltaic modules. This is part of a design that is intended to concentrate more light on each individual cell. As this is an emerging technology, and since the photovoltaic modules are separated by a greater distance, it is reasonable to expect a reduced chance of arcing between cells. The TECSTAR Concentrator sample is shown in Figure 7.

Although not a distinct technology, a fourth sample coupon was created to explore some of the fundamental aspects that may affect arc generation and duration. This sample was known as the "Mock Cell" sample. The cells in the Mock Cell sample are geometrically similar to the ISS cells. However, each cell is made of copper instead of the semi-conducting material used in the ISS coupon. The Mock Cell coupon provided flexibility in the geometric arrangement of the individual cells. Thus, the gap between cells, as well as the distance between the cell and the substrate, could be easily modified. A drawing as well as a picture of the Mock Cell coupon is shown in Figure 8.
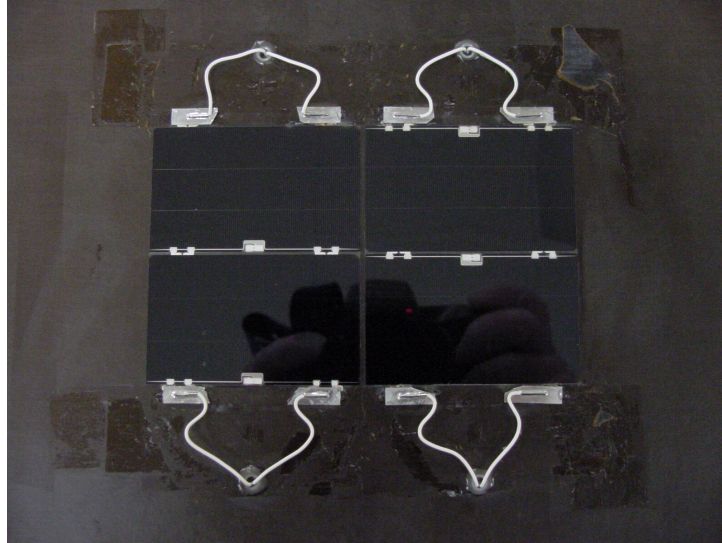
Figure 6. Picture of the Planar TECSTAR sample.

Regardless of the particular test coupon used, each sample shared the following characteristics: 1) The samples were mounted on top of a Kapton film substrate, 2) Each sample had a conductive region (typically photovoltaic semiconductors) that was exposed to the plasma, and 3) All of the solar cell modules had coverglass on top of the cell material. In most cases the coverglass sheet extended beyond the cell material. For example, in the ISS coupon the coverglass sheet overhang was a few mils (1 mil=1/1000 inch).

Figure 7. Picture of the Tecstar Concentrator sample.

Although the number of samples tested was relatively small, to accurately complete the assessment of the array, hundreds of arc events were required. To facilitate the process of creating an arc and capturing arc current and voltage information, a computerized control and acquisition system was assembled. A LabView™ program was created to control a personal computer equipped with a data acquisition card and an IEEE-488 card. The control system set the trigger arc power supply voltage and operated the switch attached to the differential power supply. An arc detection circuit was created to sense the initiation of a trigger arc. This circuit
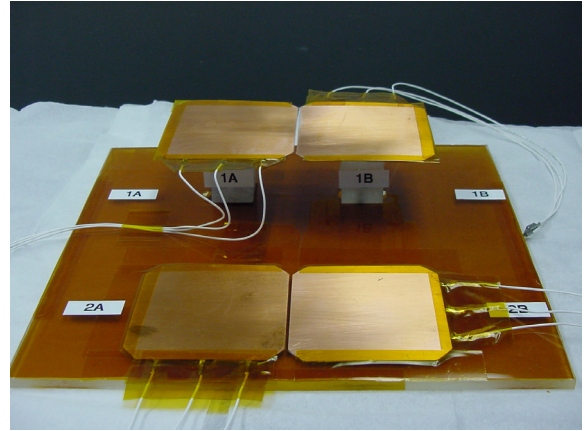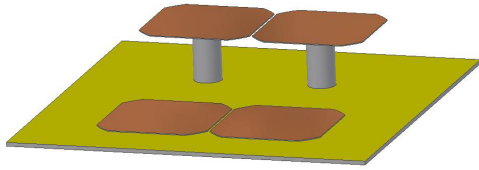
Figure 8. Drawing of the Mock Cell coupon (left). Picture of the test sample (right).
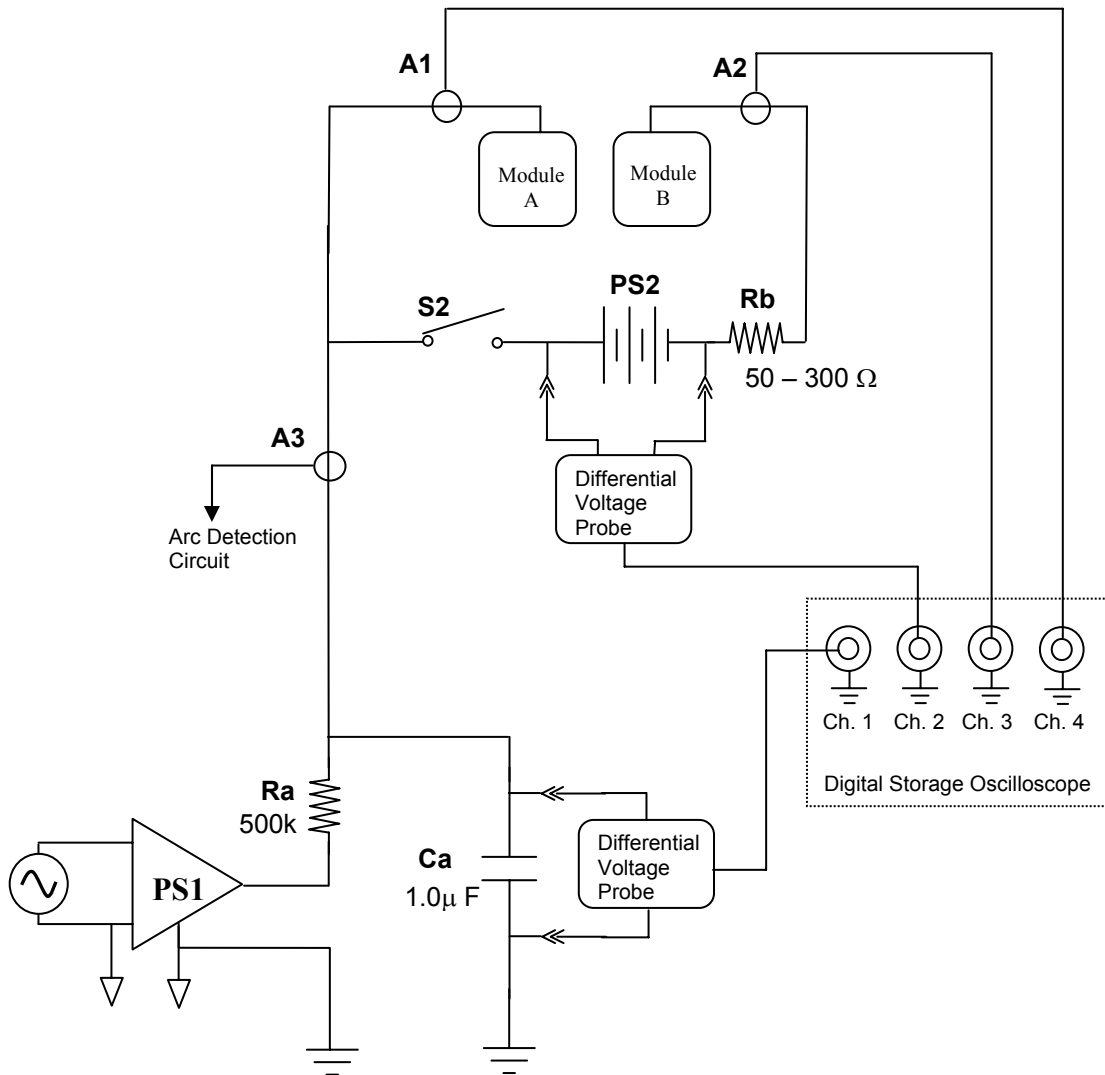
Figure 9. Schematic diagram of the components used to generate sustained arcs.

provided a pulse to the computer which shut down the power supplies and automatically transferred the current and voltage data from a digital storage oscilloscope to the computer. The LabView™ program then created an arc log file which contained information about the sample under test as well as the elapsed time between the application of power to the array to the detection of an arc. Figure 9 shows the arrangement of equipment used to conduct the tests.

Test Results

The trigger arc voltage threshold is a key parameter in determining whether or not an array technology is suitable for use as a high voltage source in a plasma environment. To determine the voltage at which a trigger arc would occur, a specific procedure was created. This procedure is captured in Figure 10. The current and voltage waveforms are captured for each arc event. A typical set of trigger arc waveforms is shown in Figure 11. Recall, a trigger arc is characterized by a very short duration with a large current peak. The results of the trigger arc tests conducted on the three array technologies are tabulated in Figure 12.

Upon completion of the trigger arc threshold tests, the next step was to determine the conditions necessary to generate a sustained arc. Although a given technology may have had a relatively low trigger arc threshold, it is still useful to study the sustained arc properties of the array to determine which technology is the least susceptible to long duration arcs.
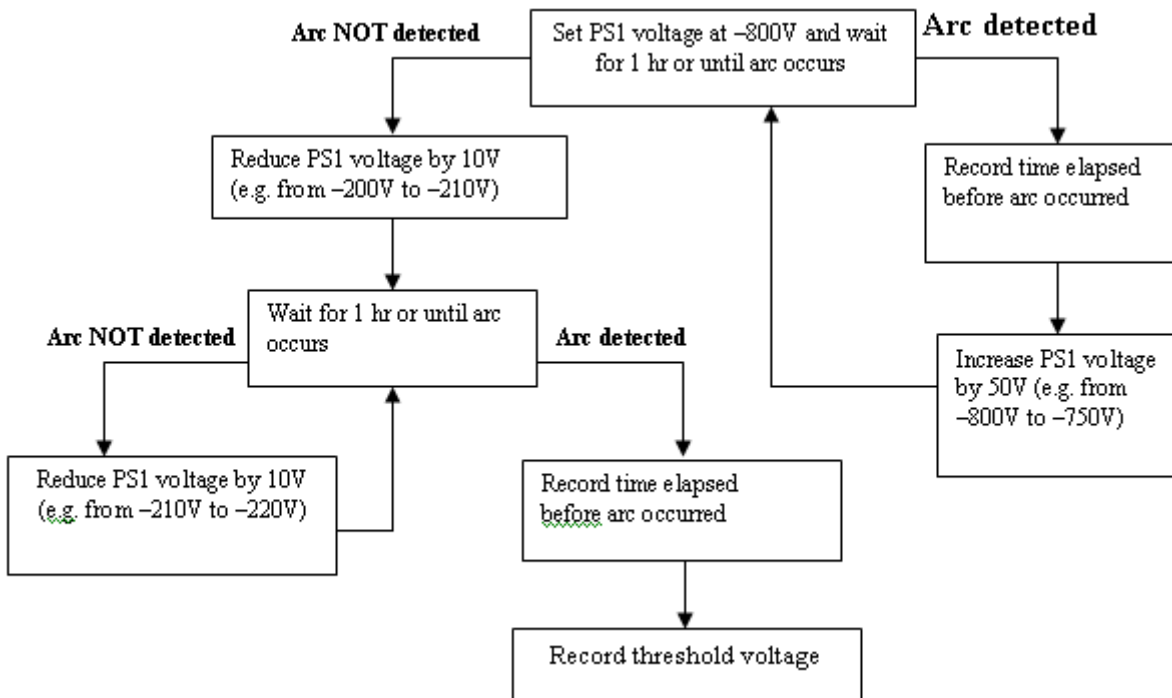
Figure 10. Procedure used to establish the trigger arc threshold.

The circuit shown in Figure 9 above is used to generate a sustained arc. An important part of the sustained arc circuit is the resistor (Rb) attached to the differential power supply. This series resistance is used to limit the current flow from the differential supply. This resistor was changed based on the voltage setting of the differential supply. By limiting the current from the differential supply (typically <3 amps), a more realistic simulation is created of the current available in a full array string. Typical sustained arc current and voltage waveforms are shown in Figure 13. Note the long duration time and low average current values, characteristic of a sustained arc.

During the course of a sustained arc test, the differential voltage and current levels are changed in order to survey the conditions that lead to damaging sustained arcs. By scanning the parameter space in this way, it is possible to determine voltage, current, and power thresholds for the generation of a sustained arc. Understanding these thresholds is key to designing a new solar array technology that is immune to sustained arcs. Figure 14 shows the sustained arc thresholds for two different array technologies.
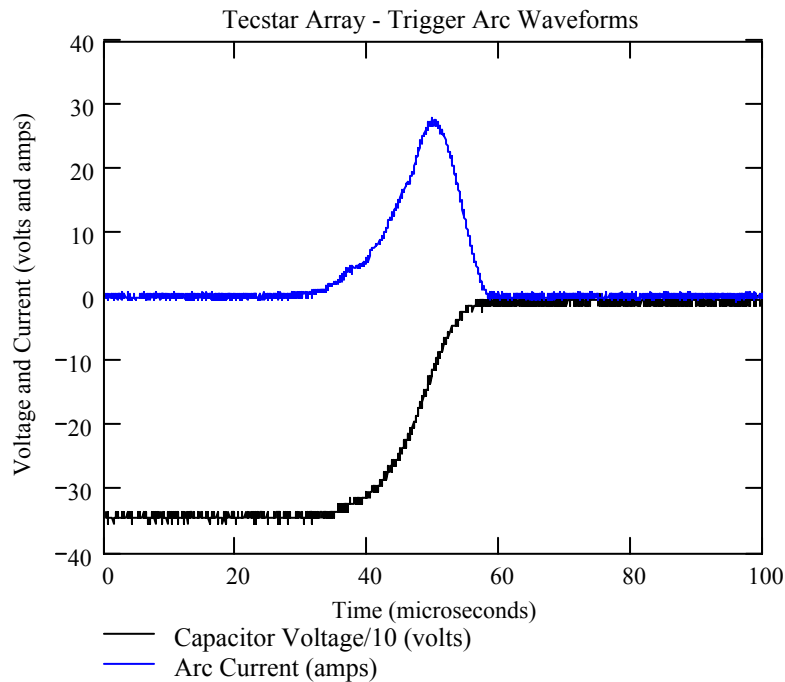
Figure 11. Representative trigger arc waveforms.

At the completion of the sustained arc testing of the solar array technologies selected by the D2HET program, a unique opportunity existed to create a custom solar array coupon which could be used to better understand some of the factors that contribute to the duration of sustained arcs. By creating a "Mock Cell" coupon, it was possible to focus on the role of substrate materials in sustained arc duration. One might imagine that heating of the substrate material leads to the release of neutral particles from the surface, through evaporation or even ablation. Depending on the rate with which these neutrals are released into the discharge, the local ionization rate, and the rate with which electrons are released from the conducting materials, the duration of the arc may change significantly. To explore this possibility, a Mock Cell sample

was created with two sets of "cell" pairs. One set of cells was placed "flat" against the Kapton substrate as is commonly found on commercial arrays. The other set of cells was "elevated" 5 cm above the Kapton substrate. Figure 8 above shows the arrangement of the cells in the Mock Cell coupon.

Trigger arc threshold results for ISS coupon.

Date of test: 25/2003		Date of test: 2/26/2003	
Applied Voltage (V)	Time elapsed before arc (min)	Applied Voltage (V)	Time elapsed before arc (min)
-500	0.159	-400	9.981
-450	1.629	-350	60.001
-400	24.985	-360	60.001
-350	60	-370	10.979
-360	60.001	-400	27.474
-370	49.416	-350	60.001
		-360	34.361

Trigger arc threshold results for TECSTAR planar coupon.

Date of test: 4/7/2003		Date of test: 4/8//2003	
Applied Voltage (V)	Time elapsed before arc (min)	Applied Voltage (V)	Time elapsed before arc (min)
-400	1.059	-250	12.636
-350	0.507	-200	60.001
-300	19.618	-210	54.448
-250	28.504		
-200	60.001		
-210	24.885		

Trigger arc threshold results for TECSTAR concentrator coupon.

Date of test: 5/5/2003	
Applied Voltage (V)	Time elapsed before arc (min)
-400	0.013
-350	0.024
-300	0.059
-250	0.266
-200	60.001
-210	0.874

Figure 12. Results of the trigger arc threshold tests.

Sustained arc tests were conducted on the Mock Cell coupon. The results are shown in Figure 15. It is clearly evident for this coupon that the elevated cells produced dramatically extended arc times. In some cases arcs in the elevated set sustained for one order of magnitude more than in the flat set. While this result is certainly interesting, more tests are required to rule

out the effect of factors such as variations in cell material composition or workmanship differences.   Certainly if the substrate material is found to play a role in arc sustainment, spacecraft designers would have a new option for controlling or eliminating sustained arcs.
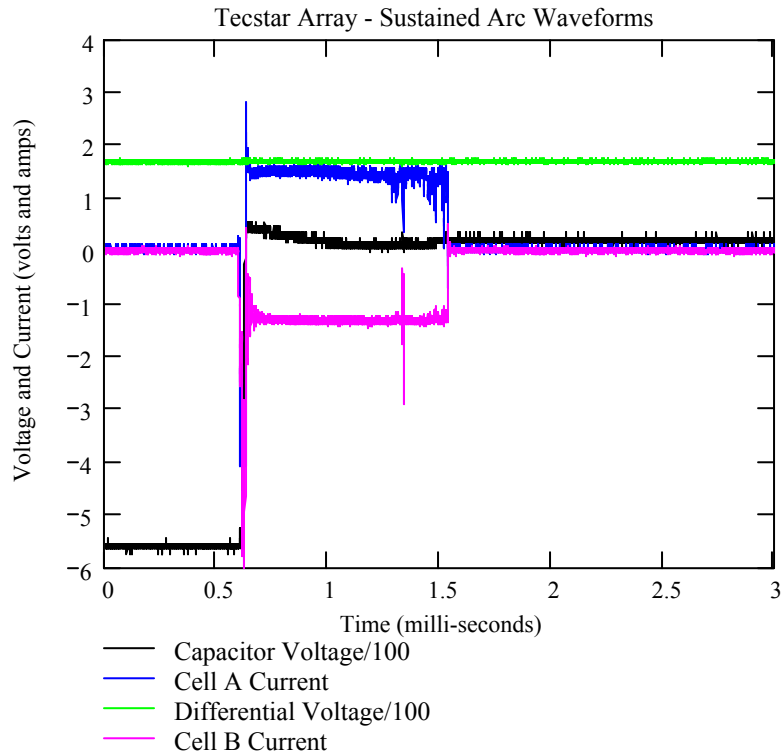
Figure 13. Representative sustained arc waveforms.
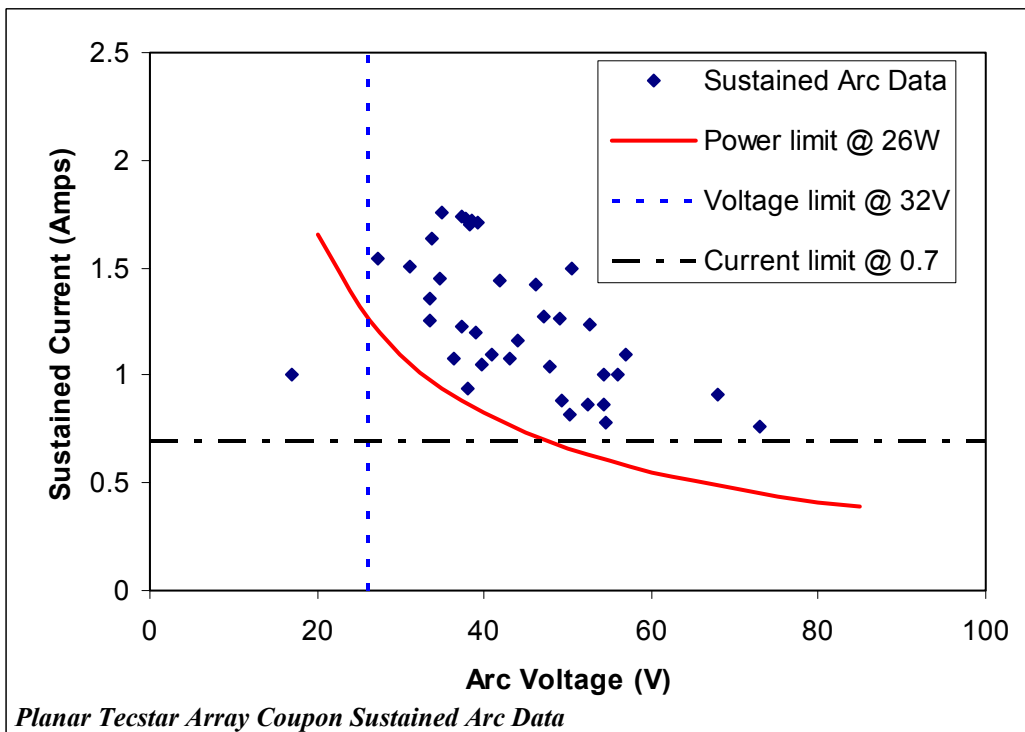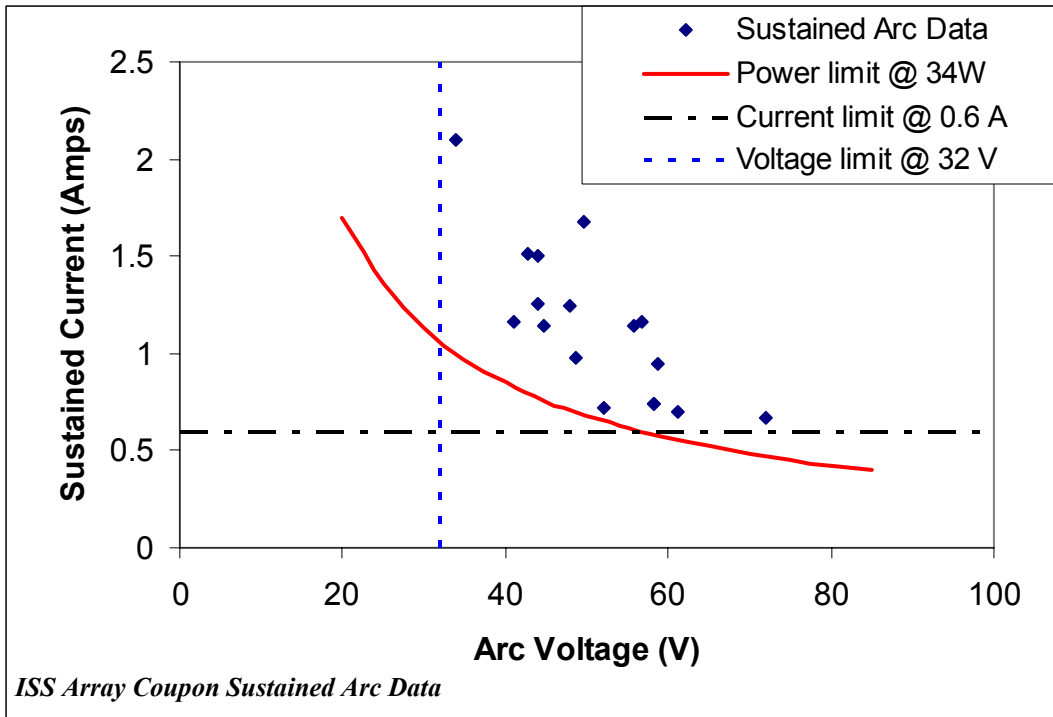
Figure 14. Current, Voltage, and Power thresholds for the ISS array (top) and the Planar Tecstar array (bottom)
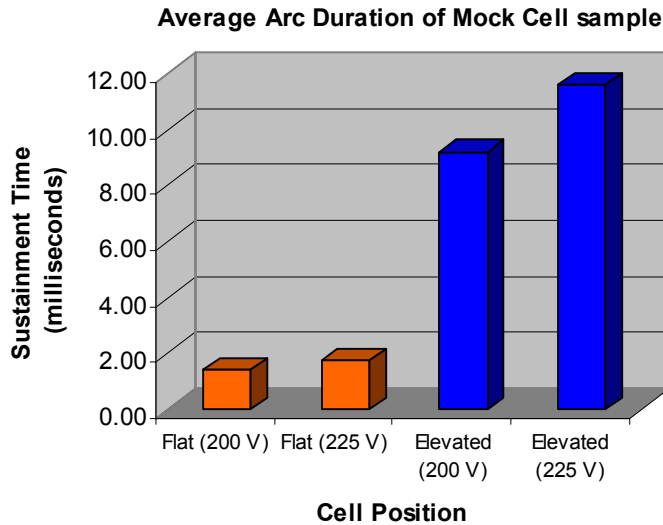
Figure 15. Results of the trigger arc threshold tests.

Conclusion

A set of tests has been completed which assess the susceptibility of some existing solar array technologies to arc when biased at high negative potentials in a plasma environment. The tests were broken into two broad categories: Trigger Arc tests and Sustained Arc tests. In the Trigger Arc tests, arc voltage thresholds were established for each array technology. In the sustained arc tests, voltage, current, and power thresholds were determined for two of the three solar array technologies. In addition to the tests conducted with commercially available array segments, a separate sustained arc test was conducted on a custom built Mock Cell sample. Results of the Mock Cell sample indicated the possibility that the substrate material that is in contact with the solar cells may play a role in the arc duration.

All of the tests described in this paper were conducted as a part of the Direct Drive Hall-Effect Thruster (D2HET) program. The D2HET program requires the use of high voltage (300 volt) solar arrays to directly supply the anode voltage for a Hall-effect thruster. This requirement is challenging due to the fact that the arrays will be immersed in a plasma. To ensure long solar array lifetimes it is important to minimize or eliminate arcing. None of the array technologies tested met the demands of the D2HET program. However, all of the tests combined to create a dataset that includes voltage, current, and power thresholds for arc generation. This dataset is being used to create a new solar array sample which is expected to operate at -300 volts without generating a sustained arc. The new sample is scheduled to be tested in early 2004. It is hoped that the new solar array technology will be useful not only for a D2HET mission, but also for any spacecraft designer that is interested in increasing array voltages without incurring spacecraft charging problems.

Acknowledgement

References

[1] Carruth, M.R., et al., "ISS and Space Environment Interactions Without Operating Plasma Contactor", 39th AIAA Aerospace Sciences Meeting, Reno, NV, January 2001, AIAA-2001-0401.

[2] Hastings, D.E., "A review of plasma interactions with spacecraft in low Earth orbit," Journal of Geophysical Research, Vol. 100, No. A8, Pages 14,457-14,483, August 1, 1995.

[3] Hikita, M. and Cho, M., "Charging and Discharging Phenomena in Simulated Space Environment," IEEE 19th Int. Symp. on Discharges and Electrical Insulation in Vacuum, 0-7803-5791-4/00, Xi'an, 2000.

[4] Hoskins, W.A., et al. "Direct Drive Hall Thruster System Study", 51st JANNAF Propulsion Meeting, Orlando, Florida, 19-21 November 2002.

[5] Oleson, S.R. and Sankovic, J.M., "Advanced Hall Electric Propulsion for Future In-Space Transportation," NASA TM-2001-210676, April 2001.

[6] Mikellides, I.G., et al. "Assessment of High-Voltage Solar Array Concepts for a Direct Drive Hall Effect Thruster System", 39th AIAA/ASME/SAE/ASEE Joint Propulsion Conference, Huntsville, Alabama, 20-23 July 2003.

[7] Davis, S., Stillwell, R., Andlario, W., Snyder, D., and Katz, I., EOS-AM Solar Array Arc Mitigation Design, SAE Technical Paper 1999-01-2582, August, 1999.

[8] Cho, M., et al., "Laboratory Tests on 110-Volt Solar Arrays in Ion Thruster Plasma Environment", Journal of Spacecraft and Rockets, Vol. 40, No. 2, March–April 2003

[9] Jongeward, G.A., et al., "Development of a Direct Drive Hall Effect Thruster System", SAE Power Systems Conference, Paper No. 02PSC-77, Coral Springs, Florida, 29-31 October 2002.

[10] Hastings, D.E., Cho, M., and Kuninaka, H., "Arcing rates for a high voltage solar array: Theory, experiment and predictions," J.Spacecraft and Rockets, Vol.29, No.4, 1992., pp.538-554.

[11] Ferguson, D.C., et al., "High Voltage Space Solar Arrays," 53rd International Astronautical Congress, The World Space Congress – 2002, IAC-02-IAA.6.3.03, 10-19 Oct 2002.

[12] The sample was manufactured by Tecstar, Inc., City of Industry, California.

MEASUREMENT OF CHARGE DISTRIBUTION IN ELECTRON BEAM IRRADIATED PMMA USING ELECTRO-OPTICAL EFFECT

Yusuke Usui
Musashi Institute of Technology
1-28-1 Tamazutsumi, Setagaya-ku, Tokyo 158-8557, Japan
Phone: +81-3-3703-3111(3931)
Fax: +81-3-5707-2156
E-mail: usui@me.musashi-tech.ac.jp

Toshiro Sakai, Masayasu Ishikawa,
Takeharu Isono, Yasuhiro Tanaka,
Tatsuo Takada, Rikio Watanabe,
Nobuyuki Tomita
Musashi Institute of Technology, Japan

Yoshihiro Murooka
Shibaura Institute of Technology, Japan

Abstract

In space environment, a spacecraft is exposed by high-energy cosmic rays. The electric potential of insulating materials on the surface of the spacecraft charged up when the cosmic rays are irradiated to the spacecraft. Sometimes, the change of the electric potential causes an unexpected accident of electrostatic discharge (ESD) with serious damage to the electric devices. To understand the mechanism of the ESD, the measurement of charge distribution in dielectric materials should be carried out. Therefore, we have proposed to use an optical method using Kerr effect for the measurement. Using this system, we have already succeeded in the measurement of PMMA after the electron beam is irradiated. In this paper, we would like to show the measurement results under the electron beam irradiation in air atmosphere.

Introduction

The dielectric materials are used for covering the surface of a spacecraft. Since they are exposed to high-energy cosmic rays, the electric potential is increased due to the accumulation of charge in the bulk and/or on surface of them. Sometimes the change of the electric potential causes an unexpected accident of ESD with serious damage to the electric devices. To prevent the accident, it is important to investigate the relationship between irradiation of cosmic rays and dielectric materials. Therefore, we have been developing a measurement system for the charge distribution using an optical technique [1,2]. In this report, the principle of measurement and some typical results are introduced.

The Principle of the Optical Measurement Method

Electro-Optical Kerr Effect

Figure 1 shows the principle of Electro-Optical Kerr effect. When the linearly polarized laser light is illuminated to a sample with electric field E, an optical phase retardation $\Delta\theta_s$ generates in the laser light during passing through it. The generated optical phase retardation

$\Delta\theta_s$ is proportional to square of the electric field E^2 as described in following equation,

$$\Delta\theta_s(x) = \frac{2\pi l}{\lambda}\gamma E(x)^2 \qquad (1).$$

Where l, λ and γ are light path length in the sample, wavelength of the light and Kerr constant, respectively.
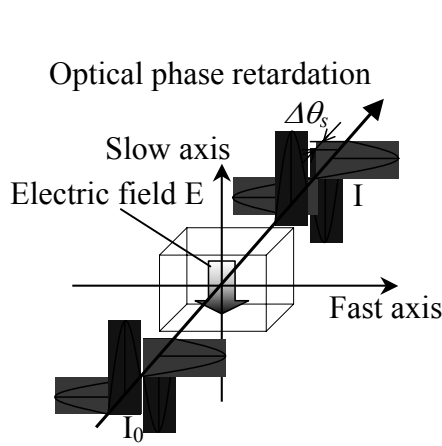
Figure 1.   The optical phase retardation $\Delta\theta_s$ by Kerr effect
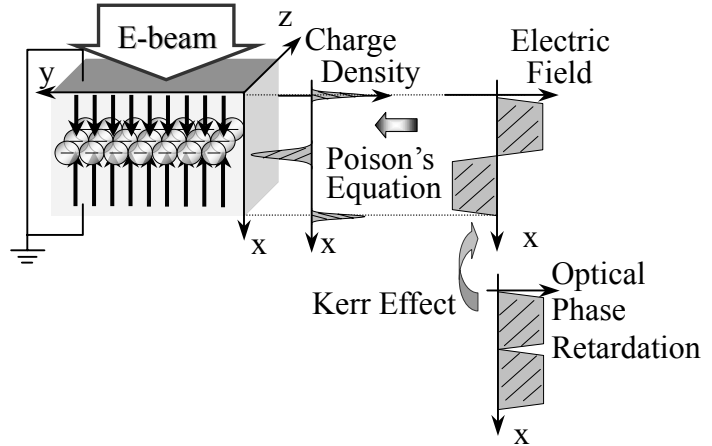
Figure 2. Model to measure charge distribution using Kerr effect and Poisson's equation

When the PMMA irradiated with electron beam, electric field $E(x)$ generated by accumulated charges. Since the birefringence is induced due to the generation of dielectric anisotropy of permittivity, the passing light has the optical phase retardation $\Delta\theta_s(x)$. By measuring $\Delta\theta_s(x)$, electric field $E(x)$ is calculated from following equation,

$$E(x) = \pm\sqrt{\frac{\lambda}{2\pi l\gamma}\Delta\theta_s(x)} \qquad (2).$$

In the experiments, the wavelength λ is 633nm, distance l is 10mm and Kerr constant γ is 1266×10^{-24} m^2/V^2 [3].

Poison's Equation

The charge density ρ is calculated by the electric field E. When the charges are assumed to be distribution in y-z plane as showing Fig.2, the relationship between charge density   and electric field $E(x)$ is expressed by following equations,

$$div\mathbf{E} = \frac{\partial E_x(x,y,z)}{\partial x} + \frac{\partial E_y(x,y,z)}{\partial y} + \frac{\partial E_z(x,y,z)}{\partial z} = \frac{\rho}{\varepsilon} \qquad (3),$$

$$\rho = \varepsilon\frac{d_x E(x,y,z)}{dy} \qquad (4).$$

Here, we used the value of 2.68 is used as the relative permittivity of PMMA.

<p style="text-align:center"><u>Measurement System</u></p>

Two-Dimensional Birefringence Measurement System

Figure 3 shows a schematic diagram of two-dimensional birefringence measurement system. The optical phase retardation $\Delta\theta_s(x,y)$ and the fast axis angle ϕ_s of the sample are measured using this system [4,5]. The output light intensity $I(x,y)$ is given by,

$$I(x,y) = \frac{I_0(x,y)}{2}\left[\begin{array}{l} 1+\left\{\cos 2\phi_A - 2\sin 2\phi_s \sin 2(\phi_s - \phi_A)\sin^2 \frac{\Delta\theta_s(x,y)}{2}\right\}\cos\Theta \\ -\sin 2(\phi_s - \phi_A)\sin\Delta\theta_s(x,y)\sin\Theta \end{array}\right] \quad (5).$$
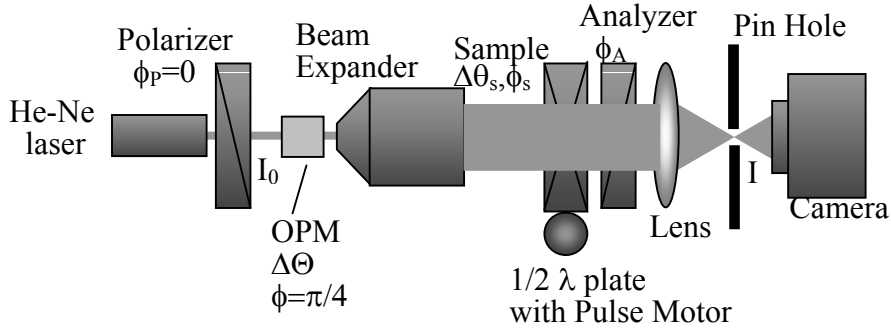
Figure 3. Two-Dimensional Birefringence Measurement System

Where, ϕ_A and Θ are optical rotation angle rotated by 1/2 λ plate and phase retardation modulated using BSO crystal, respectively. Modulated light intensities $I^+(x,y)$, $I^0(x,y)$, and $I^-(x,y)$ are described using following equations,

$$I^+(x,y) = \frac{1}{2}\gamma(x,y)I_0(x,y)\left[\begin{array}{l} 1+\left\{\cos 2\phi_A - 2\sin 2\phi_s \sin 2(\phi_s - \phi_A)\sin^2 \frac{\Delta\theta_s(x,y)}{2}\right\}\cos\Theta \\ -\sin 2(\phi_s - \phi_A)\sin\Delta\theta_s(x,y)\sin\Theta \end{array}\right] \quad (6),$$

$$I^0(x,y) = \frac{1}{2}\gamma(x,y)I_0(x,y)\left[1+\left\{\cos 2\phi_A - 2\sin 2\phi_s \sin 2(\phi_s - \phi_A)\sin^2 \frac{\Delta\theta_s(x,y)}{2}\right\}\cos\Theta\right] \quad (7),$$

$$I^-(x,y) = \frac{1}{2}\gamma(x,y)I_0(x,y)\left[\begin{array}{l} 1+\left\{\cos 2\phi_A - 2\sin 2\phi_s \sin 2(\phi_s - \phi_A)\sin^2 \frac{\Delta\theta_s(x,y)}{2}\right\}\cos\Theta \\ +\sin 2(\phi_s - \phi_A)\sin\Delta\theta_s(x,y)\sin\Theta \end{array}\right] \quad (8).$$

Where I_0 and $\gamma(x,y)$ are input light intensity and a parameter for the un-uniformity of output light intensity, respectively. From Eqs(6) and (8) the subtraction of $I^-(x,y)$ from $I^+(x,y)$ is given as,

$$I^+(x,y) - I^-(x,y) = -I_0(x,y)\sin\Theta \cdot \sin 2(\phi_s - \phi_A)\sin\Delta\theta_s(x,y) \qquad (9).$$

Here, we describe $I_0(x,y)\sin\Theta$ and $\sin 2(\phi_s-\phi_A)\sin\Delta\theta_s$ as a system function $I_M(x,y)$ and an intrinsic function $F(\Delta\theta_s,\phi_s)$. From Eqs.(6), (7) and (8), the system function $I_M(x,y)$ and the intrinsic function $F(\Delta\theta_s,\phi_s)$ are given as,

$$I_M(x,y) = \frac{\sin\Theta}{1-\cos\Theta}\left\{I^+(x,y) + I^-(x,y) - 2I^0(x,y)\cos\Theta\right\} \qquad (10),$$

$$F(\Delta\theta_s,\phi_s) = \frac{\left(I^-(x,y) - I^+(x,y)\right)\left(1-\cos\Theta\right)}{\sin\Theta\left(I^+(x,y) + I^-(x,y) - 2I^0(x,y)\cos\Theta\right)} \qquad (11).$$

When the optical rotation angle ϕ_A was set $\pm\pi/8$rad, the intrinsic function $F(\Delta\theta_s,\phi_s)$ is given as,

$$F_L(\Delta\theta_s,\phi_s) = \sin 2(\phi_s - \phi_{AL})\sin\Delta\theta_s(x,y) \qquad (12),$$

$$F_R(\Delta\theta_s,\phi_s) = \cos 2(\phi_s - \phi_{AL})\sin\Delta\theta_s(x,y) \qquad (13).$$

Therefore, using Eqs.(12) and (13), the optical phase retardation $\Delta\theta_s$ and the fast axis angle ϕ_s are given as,

$$\Delta\theta_s(x,y) = \sin^{-1}\sqrt{F_R(\Delta\theta_s,\phi_s)^2 + F_L(\Delta\theta_s,\phi_s)^2} \qquad (14),$$

$$\phi_s = \left(\frac{1}{2}\tan^{-1}\frac{F_L(\Delta\theta_s,\phi_s)}{F_R(\Delta\theta_s,\phi_s)}\right) + \phi_{AL} \qquad (15).$$

The Electron Beam Irradiation

When the sample is irradiated with electron beam, the birefringence generates in the sample. The test sample used were a rectangle PMMA with the size of 10mm in height, 20mm in width and 10mm in depth, respectively as shown in Fig.4. Thin conductive layers are put on top and bottom surfaces of the test sample. The electron beam with the current density of 35nA/cm^2 was irradiated to the sample with energy of 1.5MeV for 60seconds in air atmosphere. The measurement of the birefringence is carried out during electron beam irradiation and after irradiation.
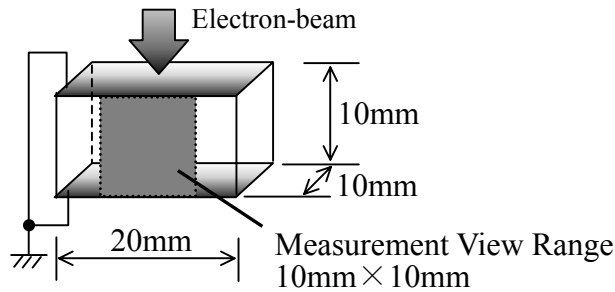
Figure 4.   The shape of sample and measurement view range

Result and Discussion

Figure 5 shows two dimensional phase retardation distributions $\Delta\theta_s(x,y)$ in PMMA during and after electron beam irradiation to the sample. With increase of irradiation time, a dark line that indicates the retardation is nearly zero is getting clear at the depth of ca 3.3mm from the irradiation surface.

Figure 6 shows the time dependent of the retardation distribution around the center of the sample. It is found that the bottom of the curves are located at ca 3.3mm from irradiation surface. Since the sensitivity of the system is too high, some of the value of the retardation $\Delta\theta_s$ exceeds the measurement limit. On the other hand, the birefringence behavior immediately after the start of the electron beam irradiation is observed because of the high sensitivity of this measurement system. The optical phase retardation $\Delta\theta_s$ before the electron beam irradiation is due to the originally remaining stress (photoelastic effect).

Figure 7 shows the time dependent charge density distribution in PMMA sample during and after electron beam irradiation. The results shown in figure 7 are calculated using equation (1)-(10). It is found that the negative charge is increasing at 3mm depth with increase of electron beam irradiation time. After irradiation, it is found that the accumulated negative charge gradually decreases. Judging from the results, it seems that the electro-optical method is applicable to the measurement of charge distribution in electron beam irradiated sample during irradiation.

Conclusion

We succeeded in the measuring of the charge density ρ in PMMA during and after electron beam irradiation. A typical result clearly shows the negative charge accumulation and its decay in electron beam irradiated PMMA sample.

Acknowledgement
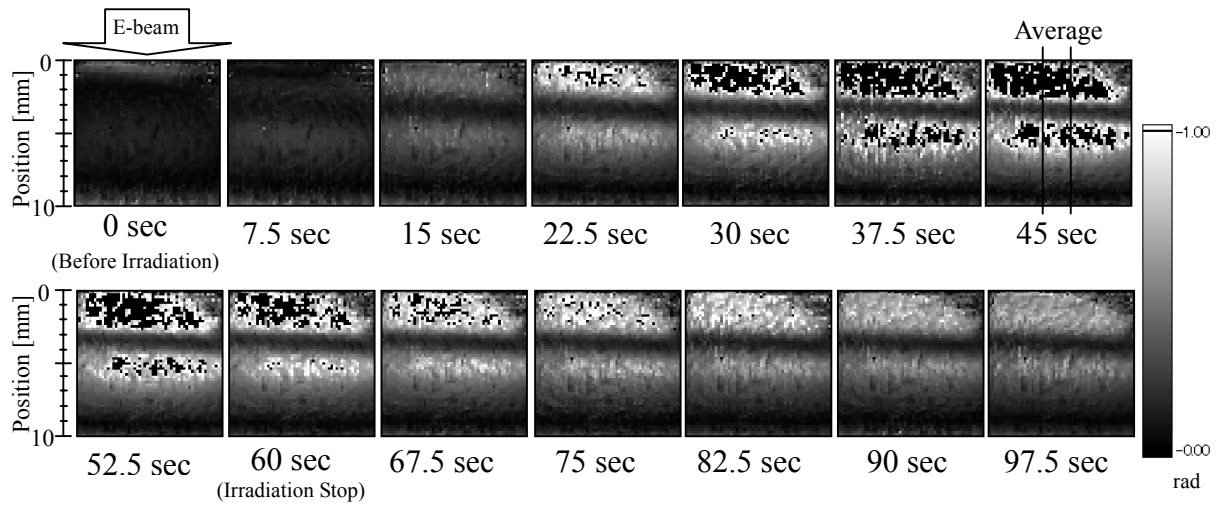
Figure 5. The two-dimensional distribution of retardation in PMMA sample

(a) Optical phase retardation $\Delta\theta_s$ during the electron beam irradiation

(b) Optical phase retardation $\Delta\theta_s$ after the electron beam irradiation
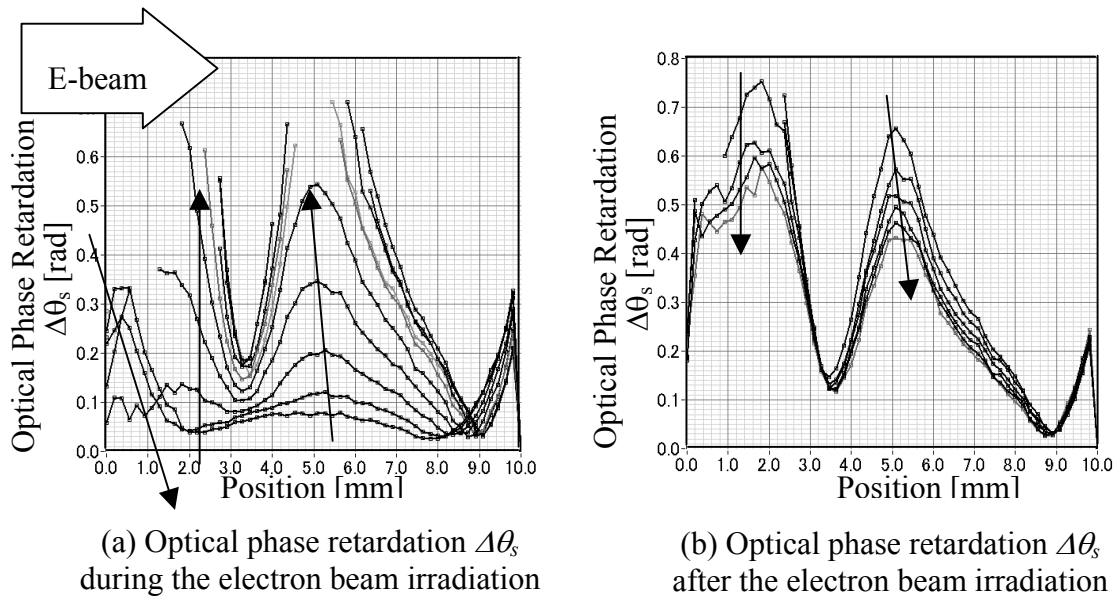
Figure 6. Time dependence of optical phase retardation distribution

(a) Charge density ρ during the electron beam irradiation

(b) Charge density ρ after the electron beam irradiation
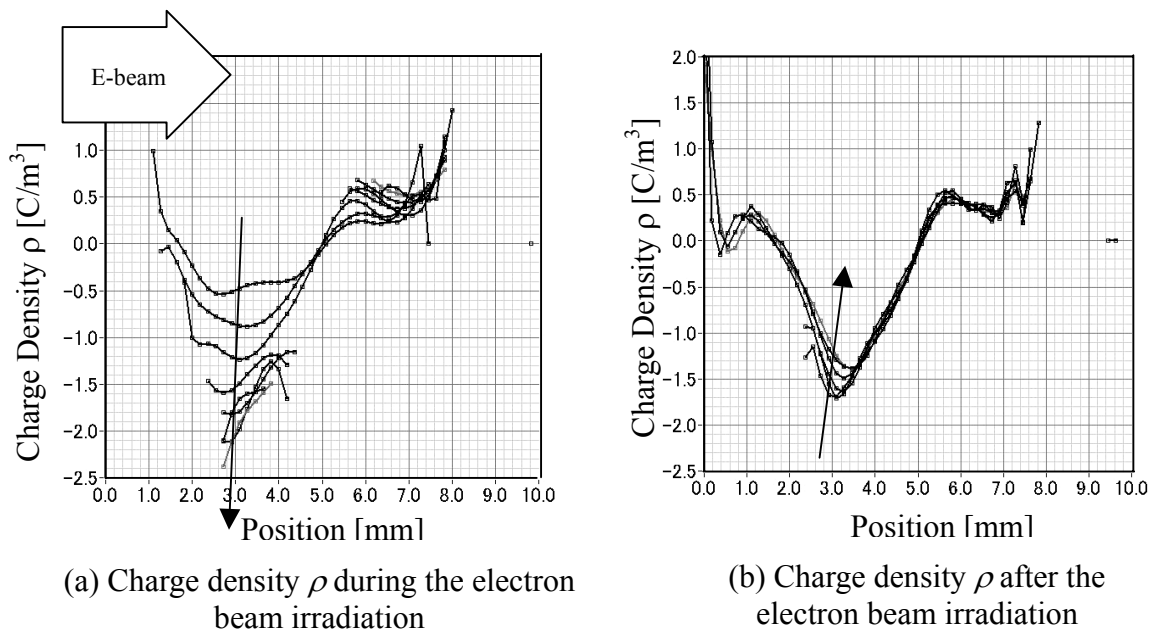
Figure 7. Charge density calculated using Poison's equation

References

1. H.Saito, T.Urabe, Y.Tanaka, T.Takada, Y.Murooka "Monitoring System for High Energy Cosmic Ray Observation in Space Environment using Advanced Electro-optic Pockels Techniques" Conference on Electric Insulation and Dielectric Phenomena, 2000.

2. M.Ishikawa, H.Saito, Y.Tanaka, Y.Murooka, T.Takada and N.Tomita "Development of Charge Distribution Measurement System using Pockels Effect" 7th Spacecraft Charging Technology Conference, 2001.

3. M.Zahn et al IEEE Transactions on Electrical Insulation Vol.El-22 No.2, April 1987 "Kerr Eectro-Optic Field Mapping Measurements In Electron Beam Irradiated Polymethylmethacrylater."

4. Y.Zhu, T.Koyama, T.Takada and Y.Murooka "Two dimensional measurement technique for birefringence vector distribution" Applied Optics, 1999.

5. T.Isono, G.Iketaka, Y.Tanaka, T.Takada and Y.Murooka "A New Optical Phase Modulator used Liquid Crystal" The 14th International Conference on Gas Discharges and their Applications, 2002.

PLASMA PHENOMENA ASSOCIATED WITH SOLAR ARRAY DISCHARGES AND THEIR ROLE IN SCALING COUPON TEST RESULTS TO A FULL PANEL

Philip Leung
Michael Bodeau
The Boeing Company
Boeing Satellite System
El Segundo, California

Abstract

On a solar array, different surface potential profiles could be developed under different environmental and spacecraft operation configurations. These potential profiles were simulated in the laboratory with solar cell coupons, and the resulting discharge phenomena were investigated. The results indicated that the propagation time of the discharge generated plasma between the discharge site and the edge of the test coupon is the critical parameter in determining the waveform of the discharge current.

Introduction

Within the last few years, several solar array test programs were conducted by Boeing Satellite System (BSS) to address issues related to solar array discharges. This paper will discuss some of the results. The focus will be on the plasma phenomena associated with solar-array discharges in the GEO environment. Our research indicated that an understanding the plasma phenomena associated with discharges is extremely important as they provide clues on how to scale the coupon test results to a full flight solar panel.

The potential profile resulting from the charging of a solar array by the energetic electrons during a substorm is dependent on the spacecraft configuration and on the condition of coverglasses. Under standard operation conditions[1], unless there are large photo-emission surfaces, a spacecraft (S/C) is usually charged to a negative potential with respect to the space plasma. The coverglasses on the solar cells are exposed to sunlight, photo-electron emission from coverglasses tend to keep the their potentials less negative than the S/C structure (Figure 1). The resulting potential profile is the so call "inverted gradient" potential profile[2]. In many applications, a MgF_2 anti-reflective coating is deposited on the coverglass. MgF_2 has a very high secondary yield[3]. Even in the absence of sunlight, the secondary yield from MgF_2 coating is sufficient to maintain the inverted gradient potential profile. Therefore, for MgF_2 coated coverglass, the charging of solar array will usually result in the "inverted gradient" potential profile even during eclipse and during the time that the coverglasses are shadowed.
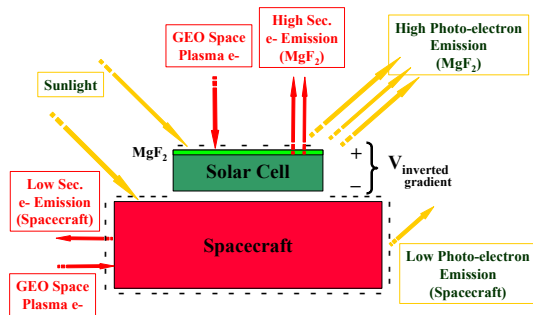
Figure 1. Inverted gradient potential profile
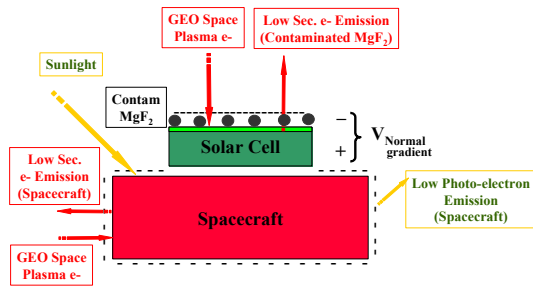
Figure 2. Normal gradient potential profile

For coverglasses without MgF$_2$ coating, or coverglasses that are contaminated (such that the secondary yield is dominated by contaminants), they will be charged to a more negative potential with respect to the spacecraft structure by substorm electrons when they are not exposed to sunlight. The resulting potential profile is the so-called normal gradient configuration (Figure 2).

Inverted Gradient Discharges

Laboratory simulation of the inverted gradient potential profile

In order to simulate the space environment, tests need to be conducted in a vacuum chamber. Since most test facilities are not large enough to accommodate a full solar panel, the satellite industry usually uses coupons, constructed to flight specifications, as test articles. Usually, coupons of different sizes were used so results could be scaled to a full panel. The larger the coupon, the better the accuracy is the scaling to the flight size. Figure 3 shows a picture of a large coupon used in one of our test programs.
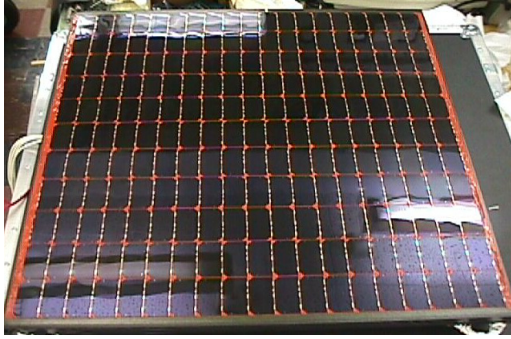
Figure 3. A large solar cell coupon. This coupon has 12x19 cells.

The inverted gradient potential profile can be simulated in the laboratory easily by the high voltage bias method[2,4,5]. Usually, a negative high voltage bias is applied to the structure, simulating the charging of the structure by the electrons. To create positively charge coverglass surfaces, the coverglasses are irradiated by electron beam or by an ultra-violet light source. In the electron beam method, the electron beam energy is selected such that the energy of electrons arriving at the coverglasses is ~ 1 KeV (for example, the electron beam energy is selected to be 3 KeV for a bias of −2 kV). For most materials[6], including coverglass materials, the secondary yield at 1 KeV is higher than 1. As a result, the coverglasses are charged to a positive potential with respect to structure, forming the inverted gradient potential profile. Figure 4 is a schematic of the high voltage biasing circuitry. In Figure 4, C_s is the capacitance of the coupon (127 pF for the coupon shown in Figure 3) with respect to chamber. A large panel/spacecraft has a capacitance of ~500 pF with respect to the space plasma. For tests to simulate the discharge from the structure of a large spacecraft, an external capacitor with a capacitance of 500 pF was placed in parallel with C_s.

In a typical test, various diagnostic instruments are used to monitor the charging and the discharging phenomena. A non-contacting voltage probe (Trek-probe) is usually used to measure the surface potential of coverglasses. Since the structure potential is at the biased voltage, this surface potential measurement provides a direct measurement of the potential difference (ΔV) between coverglasses and solar cells. Current probes, inserted at different locations of the coupon (Figure 4), are used to monitor the magnitude and the direction of the discharge current. Langmuir probes are used to detect the charge particles released in a discharge event. Figure 5 shows the arrangement of these diagnostic instruments for a typical test.
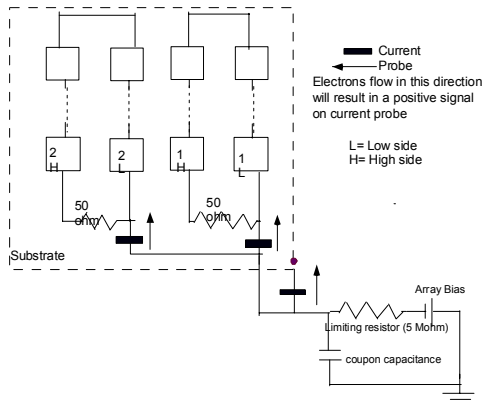
Figure 4. Schematics to simulate the inverted gradient potential profile.
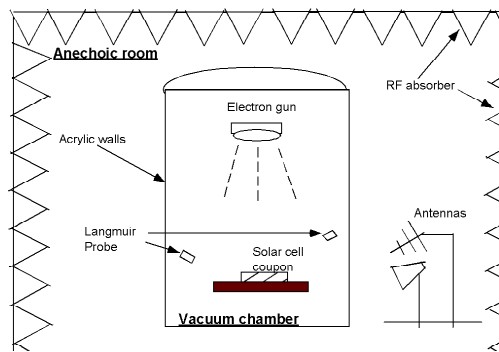
Figure 5. Diagnostic instruments.

Inverted Gradient Discharges and the Associated Plasma Phenomena

A typical example of an IG potential profile is shown in Figure 6. To create this potential profile, the structure was biased to −8 kV and the coupon was irradiated by electron beam with an energy of 9 KeV. A potential difference (ΔV) of 3 kV was developed between coverglasses and the solar cells (solar cell was at the structure potential). This ΔV was near the threshold of a discharge for this coupon, and discharges were observed. The potential profile of the coupon immediately after the discharge was also shown in Figure 6. These potential profiles indicated that the excess positive charges on the surface of the coupon were neutralized during the discharge event. The signal detected by a Langmuir Probe (LP), located at 1 meter from the coupon, was negative in sign (Figure 7) indicating electrons were emitted by the coupon during this discharge event. The coupon structure was at a potential of -8 kV with respect to ground. The electrons emitted must have energy of 8 KeV. Within the time resolution of the scope settings (~20 ns), the time delay between the onset of the discharge and the arrival of electrons was negligible, which provided another evidence that the electrons detected by LP are fast with energy of order of 5-10 keV.
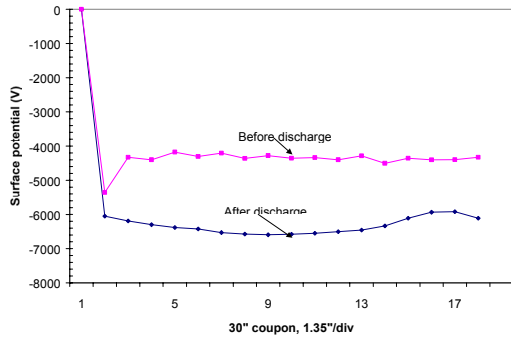
Figure 6. A typical inverted gradient potential profile. The structure was biased at –8 kV.
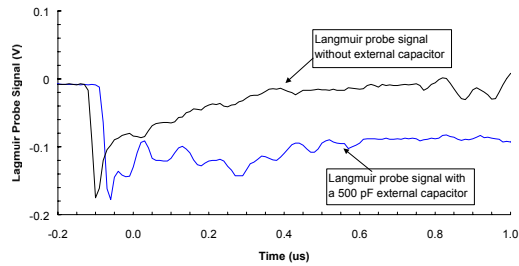
Figure 7. Langmuir probe signals.

Tests were also performed by adding a 500 pF capacitor in parallel with the existing coupon capacitance. The 500 pF capacitor was to simulate the structure capacitance of a spacecraft with large solar panels. With this external capacitor, the total capacitance was approximately 625 pF and was 5 times the capacitance of the coupon. The LP data for an IG discharge event with this external capacitor is also displayed in Figure 7. The LP data indicated that the duration of the electron pulse emitted by the coupon was 2 µs and was approximately 5 times the width without the external capacitor. The results showed that the charges stored in the structure capacitor provided the charges for the emitted electrons. The discharge current waveforms measured with and without the external capacitor are shown in Figures 8 and 9, respectively. The data show that the pulse widths were approximately equal for both waveforms, indicating that the structure capacitance did not play a role in the duration of the discharge event. At a peak current of 4 Amp, the charges stored in the structure capacitance will be depleted in 2 µs and 0.3 µs with and without the external capacitor, respectively. Consequently, the charges stored in the structure capacitance could not account for the entire current pulse and could only account for the fast electrons observed by the LP at the beginning of the discharge event.
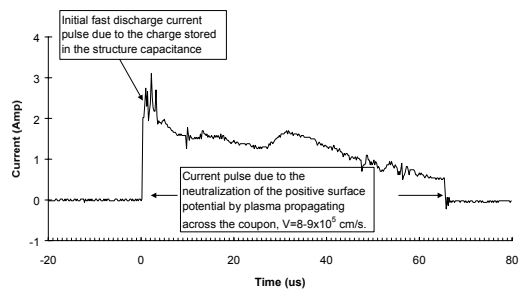
Figure 8. Inverted gradient current pulse without the external capacitor.
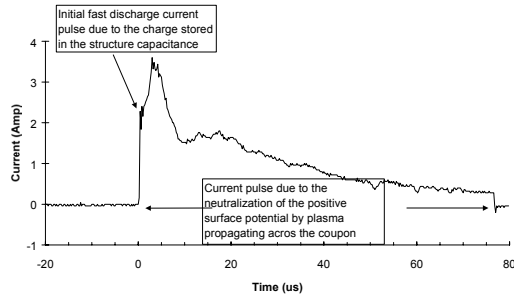
Figure 9. Inverted gradient current pulse with a 500 pF external capacitor.

Once electrons were emitted by the solar cells (at the edges or at the interconnects), they ionized the gaseous molecules in the vicinity of the solar cells producing a plasma[7]. The secondary electrons produced by ionization were attracted towards the coverglasses by the positively charged coverglasses. As a result, the secondary electrons were accelerated to energy sufficient for impact ionization producing more electrons and ions. This process kept cascading until the excess positive charges on all coverglasses were neutralized. An image of an inverted gradient discharge (Figure 10) provided evidence of this phenomenon. In this image, the bluish glow was due to excited gaseous atoms indicating the presence of a plasma. Figure 10 shows that the glow was visible throughout the entire coupon indicating the entire surface of the coupon was involved in this discharge event.
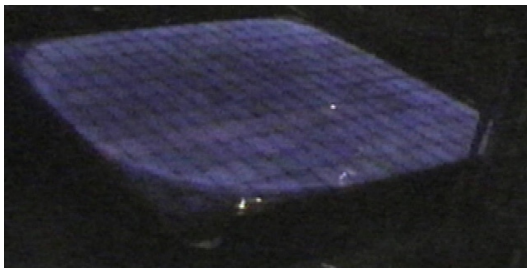
Figure 10. An image of an inverted gradient discharge.

The electron pulse detected by LP lasted for 0.4 μs (2 μs with the external capacitor). Although the duration of the discharge pulse is ~ 80 μs, the LP did not pick up any significant signal after the first couple of microseconds. The initial burst of electrons was due to the 8 keV electrons emitted by the coupon (at the solar cells or at the structure). After the charges stored in the structure capacitor were depleted, the structure potential dropped to ground potential and high-energy electrons could no longer be emitted. The plasma electrons that were responsible for neutralization of the positive charge on the coverglasses have their velocity vector pointing towards the coupon instead of away from the coupon and thus were not detected by the LP. Consequently, the high energy electron signal detected by the LP probe only lasted for microseconds.

The total charges released during an IG event can be obtained by integrating the current pulses of Figures 8 and 9. They were 84 μC for the event without the external capacitor (Figure 8) and 79 μC for the event with the external capacitor (Figure 9). The amount of charges is

much higher than the charges stored in the structure of the coupon (1 µC without the external capacitor and 6 µC with the external capacitor). For this coupon, the capacitance of each coverglass surface with respect to solar cell was 126 pF. There were 209 cells on the coupon, resulting in a total coverglass to solar cell capacitance of 0.026 µF. The potential difference between coverglasses and structure was 3.3 kV. Therefore, 87 µC (Q= CV) of charges were stored on the surface of coverglasses. This amount of charges was approximately equal to the charges released during a discharge event. Consequently, the majority (> 90%) of the charge released during an IG discharge event must originate from the coverglasses.
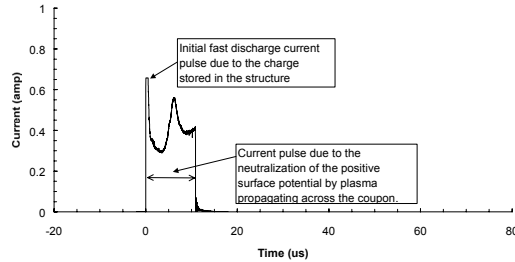
Figure 11. Inverted gradient current pulse generated by a 12" by 12" coupon.

In many applications, the scaling of the IG discharge current to a full-up solar panel is required. For this reason, tests were performed with a smaller coupon (12"x12") to determine the relevant scaling laws. A typical IG discharge current pulse obtained with the smaller coupon is shown in Figure 11. For this event, the inverted gradient potential profile was identical to the larger coupon. The structure potential was the same, i.e. at -8 kV and the ΔV between coverglasses and the solar cells was 3.3 kV. The observed pulse width of the current waveform was 12 µs. The pulse width (τ) of the ESD current pulse is related to the distance (d) between the trigger arc site and the edge of the coupon, and by the velocity of plasma (V_p) by the following relationship:

$$\tau = \frac{d}{V_p} \qquad (1).$$

Based on the dimensions of the large and small coupons, and the location of the current probes, the propagation velocities of the plasma were determined to be 8.7×10^5 cm/s and 9.5×10^5 cm/s for the large and small coupons, respectively.

Scaling to a Full Panel

For the satellite community, the major concern with IG discharges is the plasma generated by the discharge event. The plasma forms a low impedance path and could induce current to flow between cells, in particular if the cells are at a high potential with respect to each other. The current flow causes heating of the insulating substrate material and could result in a disastrous sustained short between the cells[8]. The standard industry practice is to perform tests to demonstrate new solar array designs for immunity to sustained discharge in the laboratory. In order to have a high fidelity test, the amount of plasma produces by a full panel IG discharge must be simulated properly. That is, the trigger arc[8] must produce the same amount of plasma as that of a full panel discharge. The discussions of sec. IIA and IIB provided the necessary

information to scale the IG current waveform from a coupon (and hence the plasma associated with the current pulse) to a full panel. The important points are summarized below:

1. The charges stored in the structure capacitance are responsible for the initial portion (~1 μs) of the current pulse. For the same structure capacitance, the peak current is independent of the coupon size.
2. The majority (>90%) of charges released during an IG discharge is due to the replacement current resulting from the neutralization of the charges stored on the coverglasses.
3. The width of the current pulse is proportional to the propagation time of the plasma to the edge of the coupon. For the inverted gradient condition, the plasma propagation velocity is ~9x10^5 cm/s.
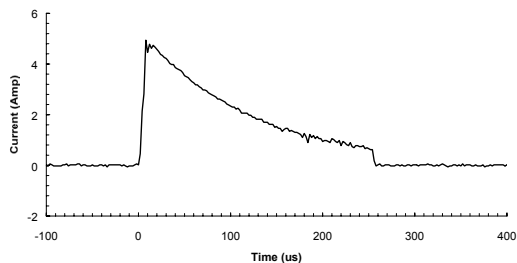
Figure 12. aveform to simulate a full panel inverted gradient discharge.

For a solar panel which has a length of 365 cm (144 in), the predicted pulse width of the discharge current is 200-400 μs. The peak current is independent of panel size. Based on the test results, the peak current is expected to be 4 Amp. Figure 12 shows a current waveform that can be used to simulate the full panel discharge.

Normal Gradient Discharges

Laboratory Simulation of the Normal Gradient Potential Profile

In the laboratory, the normal gradient (NG) potential profile is produced by irradiating the coverglasses with electron beam and with the structure of the coupon connected to chamber ground. Under this condition, the coverglasses will be charged to a negative potential with respect to the solar cells, resulting in the NG potential profile. Most of the tests[9,10] reported in literature were performed with the structure hard-grounded (i.e. grounded to chamber via a low impedance path). As the results presented in the next section shows, this method cannot simulate the space-charge phenomenon resulting from the emitted electron during a discharge event. A higher fidelity simulation method is to ground the structure of the coupon with a parallel resistor and capacitor network (Figure 13). In Figure 13, the 5 Mohm resistor isolates the structure from the chamber ground. As in the inverted gradient test, the 500 pF represents the capacitance of the spacecraft with respect to space.
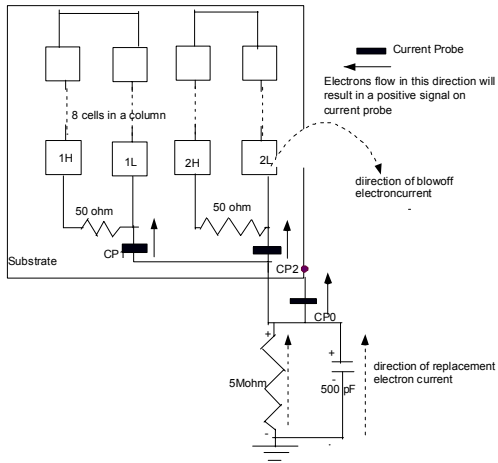
Figure 13. Normal gradient schematics with RC network grounding.

In the normal gradient test program at BSS, tests were performed with coupons of different sizes and with different cell layout configurations. One coupon had 2x4 cells (2 columns each column with 4 cells), another coupon had 4 by 8 cells (4 columns each with 8 cells). The latter coupon allowed different string configurations to be wired (1x8 and 3x8, 4x8). The different wiring configurations enabled the investigation of the scaling of ESD current with respect to cell layout configuration.

Normal Gradient Discharges and the Associated Plasma Phenomena

When the coupon was irradiated by electron beam of 22 keV, the coverglasses potential was measured to be -8 to -10 kV. Discharges were observed to occur readily. Figure 14 shows the potential profiles before and after a discharge. The data showed that >50% of the charges stored on the coverglasses were released during this discharge event. The current pulses have the waveforms shown in Figure 15. The data in Figure 15 were obtained with a 4x8 coupon wired as two 2x8 strings, and the coupon was hard-grounded. These waveforms indicated that electrons left the surface of coverglasses inducing a return current to flow in the solar cells. The peak current was measured to be 45 Amp. The pulse width was only 400 ns and was much less than the IG discharge current pulse width, indicating that NG discharge was a much faster event than IG discharge.
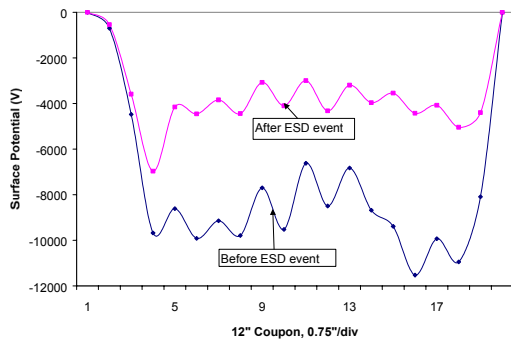
Figure 14. Normal gradient potential profiles before and after a discharge.
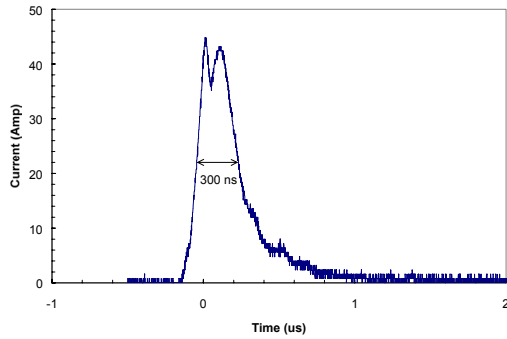
Figure 15. Normal gradient discharge current pulses
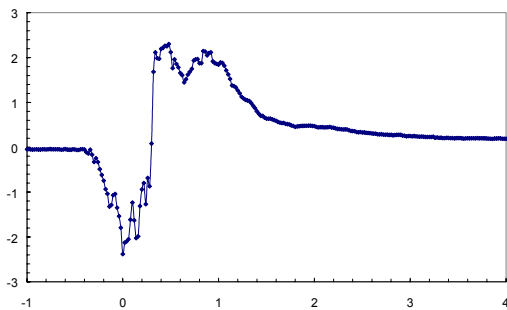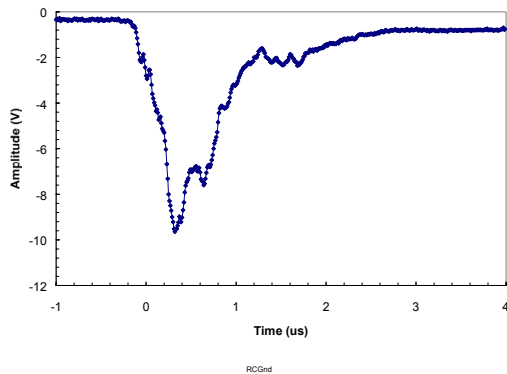
Figure 16. LP signal, NG discharge, hard-grounded (top) and via RC net work (bottom).

Tests were also conducted with the substrate grounded through the RC network. The discharge current waveforms were similar for both grounding configurations. The Langmuir probe signals, however, showed drastically different signatures (Figure 16).   With the hard ground case, the LP signal was negative in sign, indicated that only electrons were collected by the LP during the NG discharge. The pulse width of LP signal was approximately equal to the width of the current pulse in the solar cell string. With the RC grounding method, the LP only collected electrons for the first 300 ns. The LP signal then turned positive indicating that ions were collected. With the RC grounding scheme, the replacement current caused the structure to charge to a positive potential (Figure 13). As a result, electrons could not escape the coupon and were forced to return to the coupon via the solar cell (interconnects or the cells) or substrate/structure. The ions produced by ionization of gaseous environment in the vicinity of the solar cells were accelerated towards the chamber ground and were collected by the LP. In space with an isolated spacecraft, a negative space charge cloud will be formed around the

vehicle during a NG discharge. The electric field due to this space charge will force the electrons back to the spacecraft just like the RC grounding case.

Discharge Current Scaling for Normal Gradient Discharge

It is important to know the magnitude of the current induced in solar cells so that the susceptibility of the solar cells to discharge current can be quantified. In an actual solar panel, there are many ways to lay out the cells. Usually, the cells are arranged in strings so that the voltage output of each string is equal to the operation voltage of the array. For typical solar cells, a 50 Volt string requires ~30 solar cells while a 100 Volt string entails ~ 60 solar cells. These cells can be arranged in a long string of 30 to 60 solar cells or they can be arranged in a serpentine fashion with each segment of serpentine containing 5-10 cells.

Tests were performed to characterize the discharge current induced in the solar cells for the long string and for the serpentine configurations. For the long string configuration, tests were conducted on coupons with 2x4 cells and 2x8 cells. The test results are shown in Figure 17. The results show that for the long string configuration, the peak current is independent of the string length. However, the pulse width increases linearly with the length of the string. These results agreed with the results of Bogorad[9]. For a long string, the time required for the plasma generated at the discharge site to propagate the long dimension (end of the string) is much longer than the time to the short dimension (edge of the coupon). Consequently, the waveform of the discharge current is dominated by the length of the string (number of cells in a string). The discharge current (I_d) is given by:

$$I_d = \frac{\Delta Q}{\Delta t} \quad (2).$$

A longer string loses more charges (ΔQ) during a discharge event. However, the time duration (Δt) of the discharge is also longer. For this reason, the peak current was observed to be independent of the number of cells in a string. From the data, the plasma propagation speed was estimated to be 3.6×10^7 cm/s. The higher speed, as compared to IG plasma propagation speed, was due to the higher ΔV in the NG (8 kV vs 3 kV).

The discharge current of the serpentine configuration was investigated by wiring the 4x8 coupon into strings of 1x8, 2x8, 3x8 and 4x8. Current probes were inserted at each string to measure the discharge current. The results are shown in Figure 18. In this figure, only the highest peak current was plotted. The objective was to compare the results to the well-established Balmain area scaling relationships[10]. Balmain's test results indicated that the peak-current increased with the square root of the area. For our test configuration, the area is proportional to the number (N) of segment in the serpentine. Therefore, the peak current should scale with √N. Figure 18 shows that the data did follow the square root relationship indicating that Balmain area scaling law is valid for solar cells coupon/panel when the dimension of width and length were of the same order of magnitude. In this configuration, the total charge released is proportional to the area of the coupon, but the plasma propagation time is proportional to the linear dimension of the coupon. Consequently, the peak current (equation 2) is proportional to the linear dimension of the coupon, i.e. square root of the area.
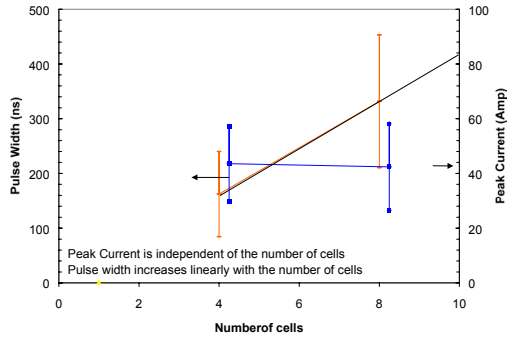
Figure 17. Peak discharge current and pulse width vs the number of cells in a string
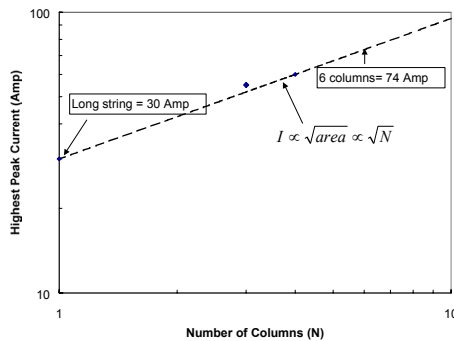
Figure 18. Peak current vs number of columns in a serpentine.

Summary

Results of laboratory simulation of solar array charging and discharging for both the inverted gradient and the normal gradient potential profiles were discussed in this paper. In an inverted gradient discharge, the initial current pulse is due to fast electrons emitted by the solar cell coupon. The fast electron emission is terminated when the charges stored in the structure capacitance of the solar array/coupon are depleted. For this reason, the peak current of a solar panel IG discharge is dependent on the structural capacitance only and is independent of the size of the solar panel. The displacement current resulting from the neutralization of the positive charge stored on the coverglasses is responsible for > 90% of the charge in the discharge current pulse. The time duration of this discharge current pulse is governed by the plasma propagation time from the discharge site to the end of the coupon, and hence scales linearly with the panel size.

In the normal gradient discharge, the discharge current waveform is again dominated by the propagation time of plasma from the site of the discharge to the edge of the coupon. The peak current of a square/rectangular segment obeys the Balmain's scaling law. That is, the peak current increases with the square root of the area. However, this scaling law is only valid for a solar panel segment where the dimensions of the length and width are of the same order of magnitude. For a long string, the peak current is independent of the number of cells in the string whereas the pulse width increases linear with the number of strings. The long string follows a modified scaling relationship as the time required for the discharge produce plasma to go from the discharge site to the edge of the solar panel is much longer in the long dimension than in the

short dimension. Consequently, the waveform of the discharge current is governed by the length of the string (number of cells in a string).

<u>Acknowledgement</u>

References

1.   Whipple,E.C., "The Equilibrium Electric Potential of a Body in the Upper Atmosphere," NASA X-615-65-296.

2.   Stevens, et al., "Voltage Gradients in Solar Array Cavities as Possible Breakdown Sites in S/C Charging Induced Discharges," IEEE Transactions on Nuclear Science, Vol. NS-28, No. 6, Dec. 1981, pp. 4558-4562.

3.   Krainshy, I., Lundin, W., Gordon, W.I., Hoffman,R.W., "Secondary Electron Emission Yield", Case Western Reserve University Report for NASA Grant NSG 3197. September 1981.

4.   Leung, P., "Discharge Characteristics of a Simulated Solar Cell Array," IEEE Transactions on Nuclear Science, Vol. NS-30, No. 6, Dec. 1983, pp. 4311-4315.

5.   Snyder, D., "Environmentally Induced Discharges in a Solar Array," IEEE Transactions on Nuclear Science, Vol. NS-29, No. 6, Dec. 1982, pp. 1607-1609.

6.   Garrett, H.B., "Spacecraft Charging: A Review", Space Systems and Their Interactions With Earth'' Space Environment, AIAA, New York, 1980.

7.   Leung, P. and Plamp G., "Characteristics of RF Resulting from Dielectric Discharges", IEEE Transaction on Nuclear Science, December 1982, p. 1610-1614, 1982.

8.   Katz, I., Davis, V., and Snyder, D., "Mechanism for Spacecraft Charging Initiated Destruction of Solar Arrays in GEO," AIAA 36th Aerospace Sciences Meeting, Reno, Nevada, 1998.

9.   Bogorad et. al., "The Effects of Conducting Breaks on Electrostatic Discharge (ESDs) on Optical Solar Reflector (OSR) Panels, IEEE NS-39, No.6, Dec 1992, p.1790-1796.

10.   Balmain, K.G., "Surface Discharge Effects", in Space Systems and Their Interactions with Earth's Space Environment, Edited by Garrett and Pike, AIAA, New York, 1980.

MATERIALS CHARACTERIZATION AT UTAH STATE UNIVERSITY: FACILITIES AND KNOWLEDGEBASE OF ELECTRONIC PROPERTIES OF MATERIALS APPLICABLE TO SPACECRAFT CHARGING

J.R. Dennison
Physics Department, Utah State University
Logan, UT, USA 84322-4415
Phone: 435.797.2936
Fax: 436.797.2492
E-mail: JR.Dennison@usu.edu

C.D. Thomson
J. Kite
V. Zavyalov
Jodie Corbridge
Physics Department, Utah State University

Abstract

In an effort to improve the reliability and versatility of spacecraft charging models designed to assist spacecraft designers in accommodating and mitigating the harmful effects of charging on spacecraft, the NASA Space Environments and Effects (SEE) Program has funded development of facilities at Utah State University for the measurement of the electronic properties of both conducting and insulating spacecraft materials. We present here an overview of our instrumentation and capabilities, which are particularly well suited to study electron emission as related to spacecraft charging. These measurements include electron-induced secondary and backscattered yields, spectra, and angular resolved measurements as a function of incident energy, species and angle, plus investigations of ion-induced electron yields, photoelectron yields, sample charging and dielectric breakdown. Extensive surface science characterization capabilities are also available to fully characterize the samples *in situ*. Our measurements for a wide array of conducting and insulating spacecraft materials have been incorporated into the *SEE Charge Collector Knowledgebase* as a *Database of Electronic Properties of Materials Applicable to Spacecraft Charging*. This *Database* provides an extensive compilation of electronic properties, together with parameterization of these properties in a format that can be easily used with existing spacecraft charging engineering tools and with next generation plasma, charging, and radiation models. Tabulated properties in the *Database* include: electron-induced secondary electron yield, backscattered yield and emitted electron spectra; He, Ar and Xe ion-induced electron yields and emitted electron spectra; photoyield and solar emittance spectra; and materials characterization including reflectivity, dielectric constant, resistivity, arcing, optical microscopy images, scanning electron micrographs, scanning tunneling microscopy images, and Auger electron spectra. Further details of the instrumentation used for insulator measurements and representative measurements of insulating spacecraft materials are provided in other Spacecraft Charging Conference presentations. The NASA Space Environments and Effects Program, the Air Force Office of Scientific Research, the Boeing Corporation, NASA Graduate Research Fellowships, and the NASA Rocky Mountain Space Grant Consortium have provided support.

Introduction

Up to one third of all spacecraft system anomalies and component failures are known to result from spacecraft charging [*1*]. Charging to high potentials can also lead to satellite material alterations and degraded instrumentation performance [*1-3*], as well as potential safety hazards for astronauts [4]. The extent and configurations of spacecraft charge buildup depends on spacecraft position and orientation, local environment parameters such as incident charged particle and photon flux, and material properties such as electrical properties (*e.g.,* resistivity and capacitance) and electron emission rates.

In an effort to improve the reliability and versatility of spacecraft charging models designed to assist spacecraft designers in accommodating and mitigating the harmful effects of charging on spacecraft, NASA, ESA and other agencies have developed an extensive set of engineering tools to predict the extent of charging in various spacecraft environments (e.g., NASCAP/LEO /GEO, POLAR, SEE Charging Handbook, NASCAP2K, SPARCS) [5-9]. The NASA Space Environments and Effects (SEE) Program is currently funding further extensions of the NASCAP2K charging code [6]. These codes model the spacecraft geometry orbit and orientation; plasma environment and particle flux; relevant materials properties; and charge absorption, distribution, transport and emission.

The original NASCAP databases lack relevant electronic properties of most spacecraft materials commonly in use today (only nine basic materials were incorporated in the original NASCAP database, [5]) so that many new spacecraft bulk materials and coatings need to be characterized. In addition, future charging codes will require better descriptions of materials properties plus the capability to model more complex materials and the effects of the evolution of materials properties due to contamination and other environmental effects [10-12]. Further, the codes will need to model more complex interactions between the emitted particles, charged spacecraft, ambient plasma environment and high-energy particle fluxes; this requires more sophisticated knowledge of the energy and angular trajectories of emitted and returning charged particles [13].

To enhance the effectiveness of these models, NASA SEE also sponsors the development of facilities and materials testing at Utah State University (USU) for measurement of the electronic properties of both conducting and insulating spacecraft materials [14,15]. The USU Materials Physics Group performs state-of-the-art ground-based testing of electronic properties of materials, particularly of electron emission and conductivity. Through the development of controlled ground-based experiments in vacuum chambers, essential electron yield parameters can be measured to update charging databases. In the laboratory, we use our knowledge of satellite-plasma environment interactions to design experiments that will provide us with an understanding of fundamental particle and material interactions that can occur in space. The objectives of the USU research are (i) to provide more accurate measurements together with sufficient materials characterization, (ii) to significantly extend the database to include a wider range of materials that are more representative of the myriad materials used in spacecraft design, (iii) to incorporate results of materials testing in parameterized form into electronic databases that are readily used by the charging codes, (iv) to explore extensions to the current modeling of these materials properties, and (v) to investigate additional charging topics such as the effects of contamination [9,11,16] or angular distribution of emitted electrons [13,16].
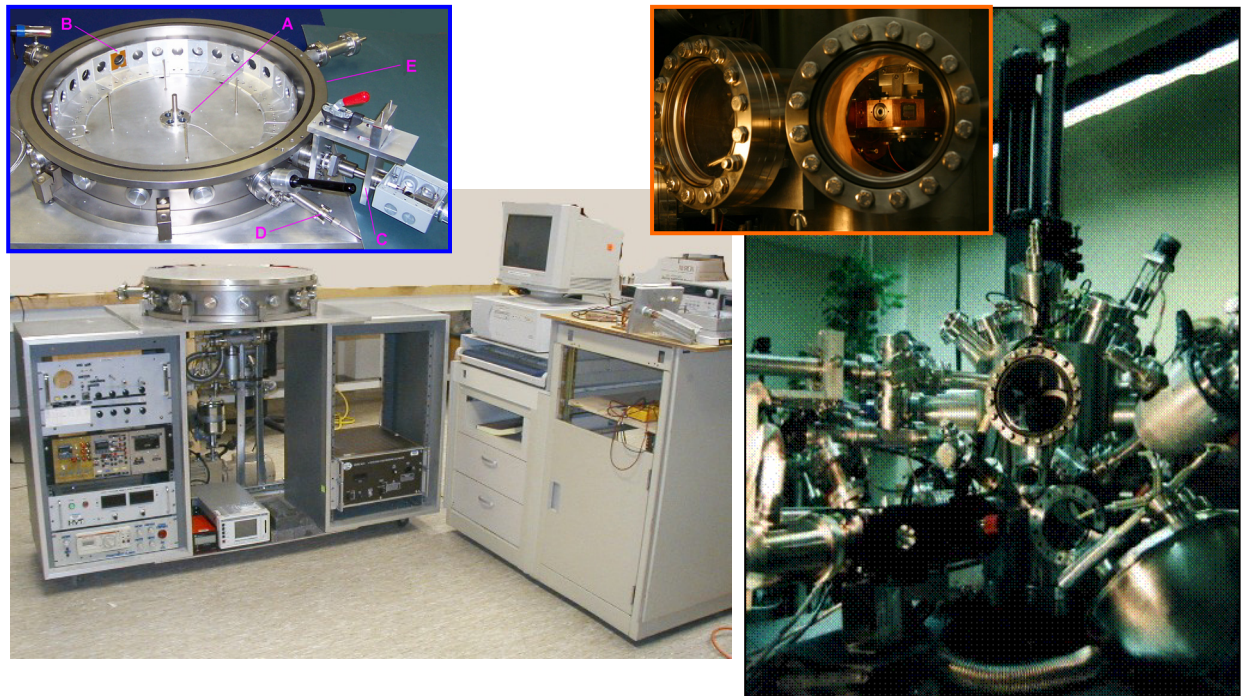
Figure 1. **(Left)** USU high vacuum Charge Storage Chamber for thin film insulator resistivity measurements [18-20]. **(Inset)** Interior view of the charge storage chamber showing the: (A) 32 sample carousel, (B) sample holders, (C) charge probe assembly, (D) sample cover manipulator, and (E) electron gun port.
(Right) USU *Fatman* UHV chamber for electron, ion and photon electron emission yields and emission spectra with extensive surface analysis capabilities. [14,21] **(Inset)** The sample stage, visible through the viewport, holds 11 samples that can be positioned before various sources and detectors is detachable for rapid change out.
(Bottom) USU *Little Boy* UHV chamber dedicated to energy- and angle-resolved electron emission studies provides a highly controlled environment for low current measurements [11,16]. **(Inset)** Sample mount and rotatable retarding field Faraday cup detector with ~ 0.3 eV and ~2 ° resolution.

In this paper, we begin with a description of the USU facilities and instrumentation [15,17,18], followed by a more detailed description of the specific required measurements and experimental methods used along with parameterization of materials properties for use with existing charging codes [13,14,19,21-23]. Representative measurements and analysis for a wide variety of materials are presented to illustrate these capabilities [22-24]. We also describe incorporation of our results into electronic databases [24]. A complete list of the materials already studied and those currently being tested are presented, as well as a justification of their selection for study [24]. We end with a review of recommendations for extensions to the parameterization of materials properties that should be incorporated into future charging models and a summary of additional related studies being performed at USU.

USU Facilities

This section provides an overview of our instrumentation and capabilities, which are particularly well suited to study electron emission and associated properties of both insulators and conductors, as related to spacecraft charging. These measurements include electron-induced SE and BSE yields, emission spectra, and angular resolved measurements as a function of incident energy, species and angle, plus investigations of ion-induced electron yields and emission spectra, photoelectron yields, conductivity, charge storage decay, internal sample charging, and dielectric breakdown. USU maintains three vacuum chambers with extensive space environment simulation capabilities (see Fig. 1). Other surface science and test capabilities are also available to fully characterize the samples.

Fatman surface analysis chamber

The primary instrument of the USU facility is a versatile ultra-high vacuum (UHV) chamber with surface analysis and sample characterization capabilities (see Fig. 1) [14-21]. This chamber can simulate diverse space environments including controllable vacuum ($<10^{-10}$ to 10^{-3} Torr) and ambient neutral gases conditions, temperature (<100 to >1500 K), electron fluxes, ion fluxes, and solar irradiation. The sample stage, visible through the viewport in Fig. 1, holds 11 samples that can be positioned before various sources and detectors and is detachable for rapid change out.

Electron sources include a low-energy gun (50 eV to 5 keV) and a high-energy gun (4 keV to 30 keV). Both guns provided monoenergetic electron beams ($\Delta E/E < 2 \cdot 10^{-4}$) with beam currents ranging from 0.1 nA to 10 μA, beam spot diameters ranging from ~50 μm to 2 mm (depending on beam energy), and pulsing capabilities from 1 μs to continuous emission. There are three ion guns with <0.1 to 5 keV mono-energetic sources for inert and reactive gases, one with rastering and pulsed deflection capabilities. The NIR-VIS-UV solar irradiance spectrum is simulated using a pair of monochromated lamp sources: (i) a Tungsten/halogen lamp system with a *Suprasil* envelope produces focused (~0.5 cm diameter) radiation from 0.4 eV to 7.2 eV (200 nm to 2000 nm) and (ii) a Deuterium RF powered continuum source with a MgF_2 window produces focused (~0.5 cm diameter) radiation from 3.1 eV to 11.1 eV (150 nm to 400 nm). Radiation from these sources passes through a nitrogen-purged monochromator. A UV Si photodiode was calibrated against a pyroelectric detector, as a UHV-compatible secondary intensity standard. Additional light sources include a helium resonance lamp (21.2 and 40.8 eV), broadband Hg discharge and W-filament sources; and a variety of quasi-monochromatic NIR/VIS/UVA LED sources.

The primary detector for emission studies is a custom hemispherical grid retarding field analyzer fully enclosing the sample, and particularly well suited and calibrated for absolute yield measurements [14,21,23]. The hemispherical grid detection system has been carefully calibrated (both through calculation and measurement) to account for detector losses, allowing yield accuracies of better than 5%. The suppression grid is used to discriminate between BSE's (energies >50 eV) and SE's (energies <50 eV). By ramping the grid bias, energy spectra of the emitted electrons can also be measured using this detector. For conducting samples, electron guns are operated in continuous emission mode, and dc-currents are measured with standard ammeters sensitive to several tens of picoamperes. For pulsed measurements on insulators, the electron guns deliver 5 μs, 20-60 nA incident pulses. Custom high speed, high sensitivity electronics have been developed at USU that allow <10 nA, <5 μs pulsed beam measurements for determining insulator emission with minimal charging effects [17,23]. Optically isolated fast

(1-2 μs rise time) sensitive/low noise (10^7 V/A / 100 pA noise level) ammeters have been built to measure electron emission bursts that are emitted from the sample and detecting surfaces [17,23]. Detected current pulses from the ammeters are then either converted to total charge using integrator circuits, or sent to a fast digital storage oscilloscope and then exported to a computer for further analysis. A custom low-energy electron flood gun (energies <1 eV) is used to neutralize positive surface charging between pulses [17,23,25]; UV/VIS light sources are also available for charge neutralization [17]. Both DC and pulsed measurements and data retrieval are fully computer automated, using GPIB interfacing and a DAQ card under Labview[TM] control. Other detectors in the Fatman chamber include a standard Faraday cup detector, an electrostatic hemispherical analyzer, a cylindrical mirror analyzer, and a time of flight micro-channel plate detector. A complete description of the DC-system setup, as well as the pulsed-system setup, along with additional insulator-yield and charging data is available in other works [14,17,21,23].

Little boy chamber for energy- and angle-resolved emission studies

The USU facility is also equipped with a second, smaller UHV chamber, shown in Fig. 1, dedicated primarily to angle-resolved SE emission measurements [10,11,14,16]. The Little Boy chamber provides a highly controlled environment for low current measurements. A custom retarding field analyzer Faraday cup detector [10,11,13], continuously rotatable about the sample, is used to obtain angle-resolved SE yield and spectra for both normally and obliquely incident electrons in the range of emission angles $-16°<\alpha<+76°$ [10]. Angular resolution of the instrument is ~1.5° and the energy resolution is 0.2 eV ± 0.1% of the incident beam energy [10]. The chamber is equipped with a 0.3-3 keV electron source and a 100-500 eV ion source. In addition to angle-resolved measurements, this chamber has been used to study the dynamic evolution of SE yields as a function of surface condition [10-12] and sample potential [13].

Charge storage resistivity chamber

A third high vacuum chamber is available for insulator conductivity measurements using the charge storage method [20]. This chamber (see Fig. 1) is a second-generation system designed so that up to 32 samples on a rotatable carousel can be tested simultaneously in a controlled, stable vacuum environment for the duration of month-long experiments. Charge is deposited separately on each sample using a custom electron flood gun. [17,23]. The charge on the each sample is measured using the TreK[TM] charge probe [27] via a novel retractable charge transfer probe. These charge storage measurements are compared with thin film insulator conductivity measurements made using classical ASTM capacitor methods in a smaller vacuum vessel [18,28]. Both conductivity chambers allow temperature control over a range of approximately – 100 °C to + 100 °C, and controlled humidity, vacuum and ambient gas. Instrumentation for both classical and charge storage decay methods has been developed and tested in a joint project with the Jet Propulsion Laboratory (JPL) and USU. Details of the apparatus, test methods and data analysis and preliminary results are given elsewhere [18,19].

Capabilities at USU

The NASCAP code designed to model spacecraft charging uses 19 parameters to characterize the electronic properties of a given material [5]. Table I identifies the experimental methods and apparatus employed at USU to determine these 19 physical properties for each sample. The measurements can be grouped under three headings:

(i) *sample characterization*, used to fully identify the specific materials tested and to allow end users to more accurately assess which material is most closely related to their specific spacecraft materials;

(ii) electron emission (induced by electrons, ions, photons) which determine a material's response to space environment fluxes; and

(iii) conduction related properties, used to model the response of materials to accumulated charge.

The measurement methods and instrumentation are described below in more detail for each of these three groups. A number of additional property measurements, highlighted in italics in column three of Table I, are included in the study; the intent of these additional measurements is to extend the description of the electronic properties of the materials with the goal of improving the modeling of spacecraft charging in future codes. Further details of the instrumentation used for these measurements are found elsewhere [12,14].

Sample preparation and characterization

Conducting 1 cm diameter sample disks are polished using 0.25 μm diamond. Thin film samples are glued to a Cu slug using a UHV-adhesive and silver powder and the surface is cleaned by using standard solvents immediately prior to introduction into the vacuum. Surface morphology is characterized *ex situ* using optical microscopy, scanning electron microscopy subsequently mounted on a sample carousel in a UHV chamber (base pressure 10^{-9} to 10^{-10} Torr). *In situ* characterization of surface morphology is made with SEM. Auger electron spectroscopy (AES) mapping before and after electron emission measurements determined surface contaminants to a level of ~10% of a monolayer. Prior to taking yield measurements, many samples were ion sputtered with 500 eV argon ions at a typical fluence of ~5 mC·cm^{-2} to remove adsorbed contamination monolayers. Additional sample characterization capabilities are also available, including: photoelectron spectroscopy, and secondary ion mass spectroscopy for contamination assessment and IR/VIS/UVA reflectivity.

Electron-induced emission measurements

A primary focus of the research at USU has been the development of instrumentation and methods for measuring *absolute* total, SE, and BSE yields of conductor and insulator materials to incorporate into materials databases [24]. Emitted electrons can be divided into two categories: (i) Secondary electrons (SE): lower energy electrons (<50 eV by definition) that originate within the material, produced by numerous inelastic scattering events of the incident electrons, (ii) Backscattered electrons (BSE): typically higher energy electrons (>50 eV by definition) that originate from the incident electron source, but may scatter either elastically or inelastically before leaving the target material. The electron yields are then defined as the ratio of the sample emitted electron current captured by the detector to the total incoming electron current.

Table I. Methods and apparatus used for properties measurements related to NASCAP fit parameters.

Property Category	Measured Property (Methods and Apparatus)	Related NASCAP Parameters [5, *]
Sample Characterization	Density (Gravimetric)	Density; ρ {9,19}.
	Bulk Composition (AA, ICP)	Mean atomic number $\langle Z \rangle$ {4} and weight $\langle A \rangle$ {10}.
	Surface contamination (*in situ* AES, AES mapping)	
	Surface morphology (*in situ* SEM.; *ex situ* STM/AFM, SEM, optical microscopy)	
	Coating thickness (*in situ* HEED; *ex situ* STM/AFM, SEM, optical microscopy)	Dielectric film thickness; d {2}.
Conduction Related Properties	Dielectric constant (*ex situ* capacitive measurements)	Relative dielectric constant; ε_r {1}.
	Bulk and surface conductivity (*ex situ* 4-point resistance probe measurements, ASTM capacitance resistance, charge storage decay)	Bulk conductivity; σ_o {3}. Surface resistivity; ρ_s {14}. *Temperature dependence of conductivity. Charge storage resistivity.*
	Electrostatic discharge (*in situ* I-V profiles of non-conducting films on conducting substrates)	Maximum potential before discharge to space; V_{max} {15}. Maximum surface potential difference before dielectric breakdown discharge; V_{punch} {16}.
	High-energy plasma radiation-induced conductivity (IV measurements for flux of monoenergetic electrons for non-conductive samples)	Two parameter fit of radiation-induced conductivity, σ_r; k and Δ {17, 18}.
Electron-Induced Emission	SE/BES total yields versus incident electron energy (Emission current for flux of monoenergetic electrons from 100 eV to 30 keV).	Maximum SE yield δ_{max} {5}. Energy for δ_{max}; E_{max} {6}. Effective atomic number, Z_{eff}, for $\eta(E_o)$ {4}. *Extended parameter fits for $\delta(E_o)$ and $\eta(E_o)$. Incident angle dependence of $\delta(E_o)$ and $\eta(E_o)$*
	Stopping power data.	Four-parameter bi-exponential range law fit for PE energy range derived from stopping power data; b_1, n_1, b_2, n_2 {7-10}.
	Energy- and angle- resolved BS/SE cross sections. (Cross sections using rotatable Faraday cup retarding field analyzer.)	*Parameters for Lambert cosine law fit of angular-resolved cross sections* [13]. *Parameters for Chung and Everhart* [26] *model of energy- resolved cross section. Parameters for coupled energy-angle resolved cross section* [12,13].
Ion-induced Emission	Total electron yield versus incident ion energy (Emission current from flux of monenergetic He ions at 100 eV to 5 keV)	SE yield due to 1 keV proton impact; $\delta^H(1keV)$ {11}. Incident proton energy for δ^H_{max}; E^H_{max} {12}. *Ion energy dependence of emitted electron yields. Energy spectra of emitted electrons. Species dependence of ion yields.*
Photon-induced Emission	Total electron yield versus incident photon energy (Emission current for flux of monoenergetic photons from discharge lamps)	Total electron yield from solar spectrum {13}. *Photon energy dependence of emitted electron yields. Energy spectra of emitted electrons.*

* The numbers of the materials database parameters used in the current version of NASCAP are indicated in curly brackets. Proposed additions to the database are indicated in italics.

Figure 2. Measurements of electron emission due to incident electrons. Various fits to the curves are defined in Ref. 24.
(Left) SE yield versus incident energy of Sheldahl Thick Film Black^{TM}. Note the logarithmic energy scale. The five parameter fit yielded δ_{max} = (1.14 ± 0.05) electrons / electron, E_{max} = (0.28 ± 0.02) keV, n_1 = (1.87 ± 0.01), n_2 = (0.53 ± 0.01), and b_2/b_1 = (1.18 ± 0.1) [24].
(Right) BSE yield versus incident energy for polycrystalline Au. For BSE, Z_{eff} =50.90.5 [12].
(Bottom) Pulsed electron emission spectrum at 100 eV incident energy for Ti alloy. [22]

Figure 2 shows the total, SE, and BSE yields as functions of normal incident electron energy over a range of ~<100 eV to 10 keV using the DC-yield apparatus and also the energy-resolved emission spectra using the pulsed-yield apparatus. Such measurements on conductors are straightforward, since a constant electron current source can be used and DC currents from the sample can be captured and quantified using the detector assembly and a sensitive slow-response picoammeter. Additionally, by grounding the conductor, any charge that leaves or is absorbed into the material can be immediately neutralized to ground. Electron yield measurements on dielectrics are more difficult to make than on conductors, since any charge that is deposited in the material cannot easily be dissipated. The surface and bulk potentials that develop can subsequently affect electron emissions by either influencing incident electron energies, or by creating internal electric fields that alter the escape mechanisms of SE's. Consequently, for insulators the pulsed-yield apparatus with neutralization methods must be used.

In order to predict the extent of spacecraft differential charging in modeling codes it is mandatory to accurately determine *absolute* SE yield parameters that include the maximum electron yield, δ_{max} and its corresponding energy, E_{max} as well as the first and second crossover energies, E_1 and E_2, at which the material transitions between positive and negative charging. The two parameters δ_{max} and E_{max} are used in NASCAP to model the SE yield as a function of incident energy. Four additional parameters, b_1, n_1, b_2, n_2, are used to describe the shape of the reduced yield curve $\delta(E_0)/\delta_{max}$ vs. E_o/E_{max}. They are typically determined from a bi-exponential range law fit for PE energy range derived from stopping power data [5]. They can also be determined directly from fits to the SE yield curve; in this case b_2 and n_2 describe the shape of the high energy tail of the curve while b_1 and n_1 model the region from E_{max} to a few keV incident energies [12,28]. In addition, we determined alternate fits to the reduced yield curve using a number of other models which potentially provide more accurate models, particularly in

Figure 3. Measurements of electron emission due to incident ions. Various fits to the curves are defined in Ref. 24.
(Left) Low energy He, Ar and Xe ion yields for HOPG graphite. [24]
(Right) Higher energy He ion yield for Al alloy 6061. Note the logarithmic energy scale. [24]
(Bottom) Energy spectrum of emitted electrons at 500 eV incident ion energy for ~25 μm thick Sheldahl Black Kapton[TM]. [14].

the high energy tail, including those by Sternglass [29], Schwartz [30], and Dionne [31]. The BSE yield curve is modeled in NASCAP using a very complex function with a single parameter, the effective atomic number, Z_{eff} [5]. Note that Z_{eff} is not related to the atomic number of the sample. This and a more elaborate empirical five parameter fit are shown in Fig. 2. A four-parameter fit, based on the work of Chung and Everhart [26], is used to model the emission spectra (see Fig. 2). Other measurement and analysis methods are being explored to determine insulator yield parameters free from charging distortions. For example, three approaches have been used at USU successfully to determine the second crossover energy, E_2 for insulating materials: (i) the mirroring method approach; (ii) the pulsed-total yield approach; and (iii) and the dc-spectral approach [22]. Of these two techniques, the dc-spectra approach is found to be most sensitive to sample negative charging, and therefore a more precise method for determining E_2.

Ion-induced emission measurements

Total electron yield due to ion bombardment as a function of incident ion energy and emission spectra (see Fig. 3) are measured using the same hemispherical grid retarding field analyzer used for SE/BSE emission measurements. A cold cathode ion gun is used as the source for monoenergetic He, Ne, Ar, Kr and Xe ions over the range of <100 eV to 5000 eV. The sample is biased to -20 eV to repel SE which would contaminate the emission measurements.

NASCAP requires two ion yield fitting parameters: (i) the SE yield due to 1 keV proton impact, δ^H_{1keV}, and (ii) the incident proton energy, E^H_{max}, for maximum ion yield, δ^H_{max} [5]. Our measurements do not go to high enough energies to determine E^H_{max}, which is typically 100 keV or higher; therefore, high energy yields from the literature are used to augment the USU low energy data. Figure 3 shows both the NASCAP fit and an extended 5 parameter empirical fit, plus the ion yield dependence on ion mass [14,24]. Our lowest mass measurements were done

with He rather than incident protons; however, this does not present a significant problem as the difference between H and He yields is typically not large, where data are available, and further NASCAP assumes that the emission is the same for all ion species, independent of mass [5].

Photon-induced emission measurements

Total electron yields due to photon bombardment as a function of incident photon energy (see Fig. 4) are determined by measuring incident beam and sample currents. The sample is biased to -20 eV to repel SE which would contaminate the emission measurements. NASCAP uses a single parameter, the total electron yield due to standard solar irradiance, to characterize photon-induced electron emission [5]. It is straightforward to determine this parameter from integration of the measured spectra of electron emission versus incident photon energy (see Fig. 4), by normalizing for the solar spectral intensity [32].

Conduction related properties

Conductivity of insulating materials is a key parameter to determine how accumulated charge will distribute across the spacecraft and how rapidly charge imbalance will dissipate. Instrumentation for both classical and charge storage decay resistivity methods has been developed and tested at JPL and USU. Details of the apparatus, test methods and data analysis are given elsewhere [18-20]. Classical methods use a parallel plate capacitor configuration to determine the conductivity of insulators by application of a constant voltage (E field) and the measurement of the resulting leakage current across the plates and through the insulator [18,28]. The capacitive resistance apparatus (CRA) at USU is designed as a versatile instrument for classical resistance measurements under tightly controlled conditions [18]. The sample environment—including sample temperature, ambient vacuum or background gas, and humidity—can be strictly controlled. Computer automation of voltage and current measurements, together with environmental parameters, allow rapid and prolonged resistance measurements. Thus, the apparatus is capable of parametric studies of variables that influence the resistivity, including sample material and thickness, applied voltage magnitude and duration, sample temperature, ambient gas or vacuum, and humidity. Figure 5 shows data obtained at USU using the classical resistance method following the ASTM D 257-99 standard method [28] for Sheldahl [33] thermal control blanket material at 26±2 °C in ambient room light at 30±5% ambient relative humidity with wet electrodes for a range of voltages. The curves showed linear behavior on a log-log plot with a slope of ~½ and converged to ~(3±1) $\cdot 10^{+16}$ Ω·cm at ~½ hr. The published resistivity value for Dupont Kapton HN is $1 \cdot 10^{17}$ Ω·cm [34].

However, recent works have shown that these classical methods are often not applicable to situations encountered in spacecraft charging [18,20,35]. Conductivity is more appropriately measured for spacecraft charging applications as the "decay" of charge deposited on the surface of an insulator. Charge decay methods expose one side of the insulator in vacuum to sequences of charged particles, light, and plasma, with a metal electrode attached to the other side of the insulator. Data are obtained by capacitive coupling to measure both the resulting voltage on the open surface and emission of electrons from the exposed surface, as well monitoring currents to the electrode.

Additional equipment is available for *ex situ* examination of conduction-related properties, including capacitance, bulk and surface conductivity, dielectric constant, dielectric strength and electrostatic discharge [24]. The relative dielectric constant and bulk resistivity were measured
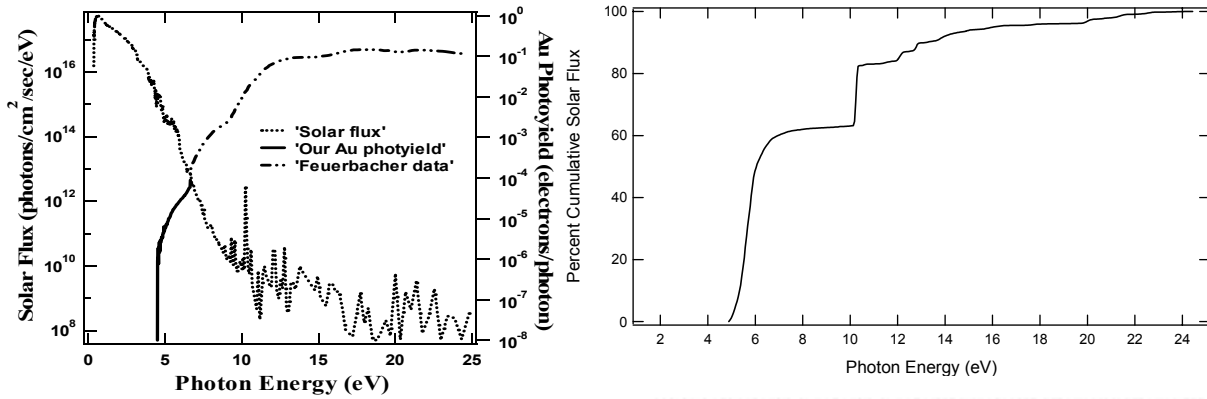
Figure 4. Measurements of electron emission due to incident photons.

(Left) Solar flux and solar photoelectron yield versus incident photon energy for polycrystalline Au. Data below ~7 eV are from measurements at USU. Data above ~7 eV are from Feuerbacher [14].
(Right) Percent cumulative solar yield versus incident photon energy for Au. The large jump at ~10 eV is due to intense Lyman alpha radiation [24].
(Bottom) Detail of photoyield as a function of photon energy for polycrystalline Au.
(Inset) Work function determination from photoyield threshold energy [24].

using a standard impedance analyzer (see Fig. 5). A standard four-point probe is used for *ex situ* measurements of bulk and surface conductivity of more conducting samples. The maximum potential difference that can exist between the material surface and the underlying conductor before dielectric breakdown or "punchthrough" is referred to as the punchthrough voltage or dielectric strength. The punchthrough voltage of thin insulating films was measured using the Utah State custom capacitor resistance apparatus by monitoring current across the sample while applying voltage across the sample electrodes. Alternatively, dielectric breakdown can be determined by high energy bombardment. Above 1600 eV incident electron beam energy, the anodized Al surface layer reached its breakdown potential and became conducting, passing DC-current through the sample as shown in Fig. 5.

Application to Spacecraft Charging

The primary object for the SEE projects at USU was to provide an extensive database of electronic properties of relevant spacecraft materials for use in charging codes. Table II lists values of the 19 parameters used to specify materials properties in NASCAP for a representative sample, Au. Our studies are posted on the web-browser based *Database of Electronic Properties of Materials Applicable to Spacecraft Charging* in the *SEE Charge Collector Knowledgebase* [36]. This *Database* contains a *Materials Report* for each sample studied which has a detailed description of the source of the sample, all measured characterization data, the raw emission data, the derived values for NASCAP parameters and other models of the data, and a review of the available literature on the material [24]. The parameters for NASCAP derived from a
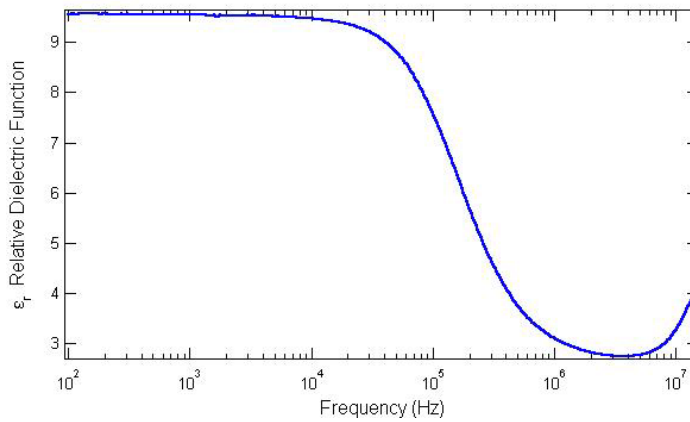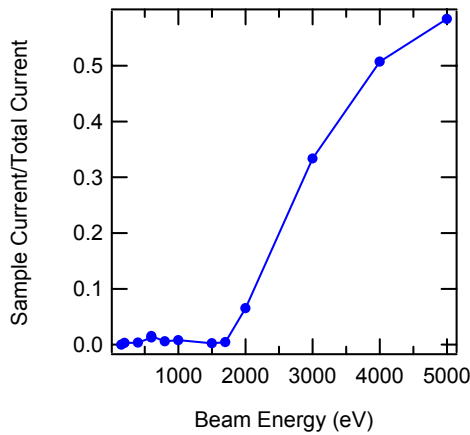
**Figure 5.Conduction related properties
(Top)** Relative dielectric constant versus frequency for 25 μm Kapton HN film with ~0.1 μm vapor-deposited Al and ~40 nm indium tin oxide (ITO) coatings. The sample was a composite material sold for applications as a low emissivity conductive thermal control coating material for spacecraft [33,34].
(Bottom) Classical resistivity versus time measurements for a sample of Sheldahl thermal control blanket material with a Kapton HN substrate and a 0.1 μm vapor-deposited Al coating [33,34].
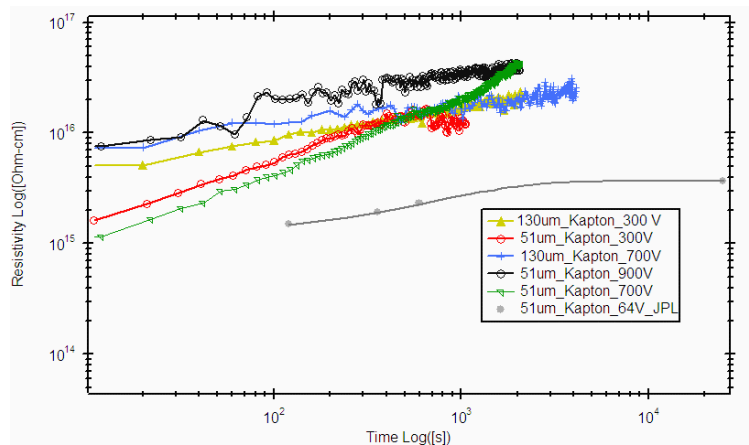
Data shown are from USU for 51 μm and 130 μm thick samples at 300 V, 700 V and 900 V uncoated sample at 64 V [22]. JPL data are for 51 μm thick uncoated sample at 64 V [19].
(Bottom) Discharge current versus electron beam incident energy for 1 μm thick chromic acid anodized Al 2219 alloy. Breakdown initiates at ~1600 eV incident energy, at the sample current threshold [22].

representative Au data set are listed in Table III. Additional analysis and parameterization for improved material modeling in future spacecraft charging codes (see below) is also included in each *Materials Report*.

Table III is a list of the materials already on reported in the *Database* and those currently being tested at USU. The prioritized list is based on extensive discussions with spacecraft charging community specialists, intended to meet two objectives: (i) extending the NASCAP database to include the most common spacecraft materials currently in use and (ii) investigating representative materials with wide ranging physical properties. The accurate remeasurement of NASCAP parameters for those materials already incorporated in current NASCAP databases serves to confirm our experimental methods or update existing data which are not fully reliable.

Suggested improvements to materials properties parameterization

Based on our experience with materials testing and characterization, data analysis, and evaluation of spacecraft charging, we can offer recommendations for additional measurements and improved parameterization of existing results that can be used to improve the modeling of spacecraft charging in future codes. Specifically, we suggest:

i) *Extended Parameterization*: Enhance modeling of electron emission data with extended parameter fits. Specifically, add a 6 parameter empirical BSE yield fit and a 5 parameter empirical ion yield fit.

ii) *Additional Emission and Optical Properties:* Extend modeling to include electron emission spectra, work functions, and angular distribution of emitted electrons to more fully model the effects of surface bias on yields and return currents. Add ion species (mass) dependence to ion yield models. Extend photoyield models to include photon energy dependant yields; this can model varying incident optical spectra and reflected or partially transmitted light. Incorporate reflectivity spectra to model fraction of incident light causing photoemission and indirect photoemission.

iii) *Data Modeling:* Add capabilities within NASCAP to fit data sets of new materials using the NASCAP parameterized models, especially the 5 parameter SE yield model.

Table II. Spacecraft Materials Tested at Utah State University.

Conducting Materials

Elemental Metals and Semiconductors	Alloys	Conductive Coatings
Aluminum (Al)	Al Alloy 6061-T6	Aquadag (C)
Beryllium (Be)	Stainless Steel Alloy 316	Amorphous Carbon (a-C)
Copper (Cu)	Ti Alloy Ti-A 16-v4	
Gold (Au)		Annealed Amorphous Carbon
HOPG Graphite (C)		
Molybdenum (Mo)		
Silver (Ag)		

Spacecraft Materials

Conductors	Insulators
Carbon-filled polyester (Sheldahl Thick Film Black)	Ge on 25 µm Kapton (Sheldahl thermal control blanket)
Black Kapton conducting (Sheldahl thermal control blanket)	ITO on 50 µm FEP with Ag/Inconnel backing (Sheldahl thermal control blanket)
	ITO on 25 µm Kapton with Al Backing (Sheldahl thermal control blanket)
	8 µm Kapton on Al backing (Sheldahl thermal control blanket)
	6.4 µm PET on Al backing (Sheldahl thermal control blanket)
	13 µm FEP on Ag/Inconnel backing (Sheldahl thermal control blanket)

Conductive Coatings	Non-Conductive Coatings
Al on 2 µm Kapton (JPL "Solar Sail")	RTV Adhesive (DC 93-500) on Cu
Al on 8 µm Kapton (Sheldahl thermal control blanket)	RTV Adhesive (CV-1147) on Cu
Al on 25 µm Kapton with ITO backing (Sheldahl thermal control blanket)	Anodized (Cr-Acid) Al Alloy
Al on 6.4 µm PET (Sheldahl thermal control blanket)	Anodized (S-Acid) Al Alloy
Ag/Inconel on 13 µm FEP (Sheldahl thermal control blanket)	

SEE Materials Database (Ver. 2) materials in green.
Materials currently under study at USU in red.

iv) *Charge Transport Capabilities:* Add charge storage method resistivity values to the database [24]. Add parametric models of resistivity (*e.g.,* temperature or electric field dependence) and dielectric spectra useful in charge transport modeling. Expand modeling of radiation-induced conductivity and electron emission based on the internal charge distribution of insulators [22].

v) *Multi-Material Geometries:* Enhance multi-material geometry capabilities to better model semi-transparent (to electrons, ions or light) thin-film conductors/insulators on conducting/insulating substrates. This capability will be essential to more fully model contamination and surface modification, in addition to optical, thermal and atomic oxygen resistant coatings [12,13].

Other Applications

In addition to direct contributions to the *Database of Electronic Properties of Materials,* there have been a number of studies at USU on specific aspects of the contributions of electron emission to the overall spacecraft charging problem. One such study has determined that, under certain circumstances encountered in near-earth orbits, incorporating more complete knowledge of the energy- and angle-resolved spectra of SE is necessary to fully model how SE emission and spacecraft charging are affected by re-adsorption of low energy electrons by the emitting surface or adjacent surfaces in the presence of charge-induced electrostatic fields [13]. Angular distribution of SE's were found to affect charging calculations when a spacecraft is charged positively and can also affect return current to adjacent surfaces [13]. Angle- and energy-resolved spectra $\eta(E,\alpha)$ and $\delta(E,\alpha)$ were measured for selected conducting materials [11,16], and these data were used to quantitatively model the effects of sample bias and the interplay between spacecraft geometry and angular emission.

These same angle- and energy-resolved emission spectra have also been compared to theoretical predictions of the emission cross sections. Semi-empirical theory assumes isotropic angular distribution, [37] while quantum theory predicts highly anisotropic angular production cross sections that become isotropic during transport to the surface [38]. Our studies indicate that there may still be anisotropic components to some energy ranges as vestiges of the underlying SE production mechanisms [11,16].

We have also studied the effects of bandgap and surface potential barriers on emission from semiconductors and insulators [21,23,39]. One study shows that $_{max}$ decreases by ~30% as the bandgap of graphitic amorphous carbon decreases from ~0.6 to ~0 eV upon thermal annealing [21,39]. Other studies look at the role of band gap and electron affinity on emission from insulators [23]. In this and other studies, we attempt to understand how the fundamental physics mechanisms and the interaction of electrons with matter underlying three phase models of the production, transport and emission from a surface are related to the observed emission [16,21,23].

Emission of low energy SE is very surface sensitive. Therefore, even monolayer contamination can significantly modify SE yield. USU studies of deposition of disordered carbon on Al/Al_2O_3 and Au surfaces found that modification of only a couple atomic layers led to changes in SE yields by a factor of 2 or more; further modeling of hypothetical satellites suggested monolayer C contamination of Au can swing charging 10^4 V! [10,12]

We have also studied the contribution to "snapover" from SE emission [40,41]. In snapover, insulators surrounded by positively biased conductors in a plasma experience a surface discharge phenomena. Our studies suggest that secondary emission is not the only factor that determines the onset positive voltage for snapover [23].

Spin-off application

While the primary motivation for our work at USU is based on charging of spacecraft materials [14,24], the electron emission properties of materials are relevant to many spin-off technical applications. Electron multipliers use high SE yield dynode materials [42]. Material and topographic contrast in scanning electron microscopy exploit the facts that the number of SE's produced depends on the electronic structure and angular distribution of emitted electrons, respectively [37,43]. Electron probe microanalysis and Auger electron spectroscopy are surface techniques based on details of backscattered electron energy loss mechanisms [44]. SE yield from emitters is critical in design of field emission devices [45]. Electron emission has important applications for next generation flat panel displays; electron emission sources must have high yields and the spacers between anodes and cathodes are required to be insulating and have low SE yields [46]. Advanced vacuum tube technology requires low SE yield materials [47]. SE yield of materials determines arc initiation, with important applications to high power arcing [48] and plasma discharge phenomena like flashover or snapover [40,41]. Disordered carbon is used to coat the inside of the plasma fusion confinement test reactors to reduce secondary electron emission that inhibits controlled fusion reactions [49].

Table III. NASCAP parameters for polycrystalline Au [14].

Parameter	Value
[1] Relative dielectric constant; ε_r (Input as 1 for conductors)	1, NA
[2] Dielectric film thickness; d	0 m, NA
[3] Bulk conductivity; σ_o (Input as -1 for conductors)	$(3\pm1)\cdot10^7\Omega^{-1}\cdot m^{-1}$
[4] Mean atomic number $<Z_{eff}>$	50.9 ± 0.5
[5] Maximum SE yield for electron impact; δ_{max}	1.47 ± 0.01
[6] Primary electron energy for δ_{max}; E_{max}	(0.57 ± 0.07) keV
[7-10] Fit to stopping power data; b_1, n_1, b_2, n_2	$n_2=1.39\pm0.04$ $b_2=1$, $n_1=0$, $b_1=0$
[9 and 19] Density; ρ	$(1.932\pm0.002)\cdot10^4$ kg·m^{-3}
[10] Mean atomic weight $<A>$	196.97
[11] SE yield due to proton impact $\delta^H(1keV)$	(0.336 ± 0.002).
[12] Incident proton energy for δ^H_{max}; E^H_{max}	(1238 ± 30) keV
[13] Photoelectron yield, normally incident sunlight	$3.64\cdot10^{-5}$A·m^{-2}
[14] Surface resistivity; ρ_s	-1 ohm, NA
[15] Max. potential before discharge to space; V_{max}	10000 V, NA
[16] Maximum surface potential difference before dielectric breakdown discharge; V_{punch}	2000 V, NA
[17, 18] Two parameter fit of radiation-induced conductivity, σ_r; k and Δ	NA

NA -- Not applicable or approximated for bulk conductors.

Acknowledgments

References

1. R.D. Leach, and M.B. Alexander: "Failures and Anomalies Attributed to Spacecraft Charging," NASA Reference Publication 1354, NASA Marshall Space Flight Center, November 1994.

2. D. Hastings, and H. Garrett, Spacecraft-environment Interactions, Cambridge University Press, 1996.

3. K.L. Bedingfield, R.D. Leach and M.B. Alexander,: "Spacecraft System Failures and Anomalies Attributed to the Natural Space Environment." NASA Reference Publication 1390, NASA MSFC, 1996.

4. M.R. Carruth Jr., T. Schneider, M. McCollum, M. Finckenor, R. Suggs, D. Ferguson, I. Katz, R. Mikatarian, J. Alred, and C. Pankop, "ISS and space environment interactions without operating plasma contactor," AIAA Paper #2001-0401, Proc. of the 39th AIAA Aerospace Sci. Meeting, Reno, Nevada, Jan. 8-11, 2001.

5. M.J. Mandell, P.R. Stannard and I. Katz, "NASCAP Programmer's Reference Manual," NASA LRC, 1993.

6. Myron Mandell, "NASCAP-2K – An Overview","" Proc. of 8th Spacecraft Charging Techn. Conf., October 20-24, 2003, Huntsville, Alabama.

7. Marc Van Eesbeek, Alain Hilgers, "European Approach to Materials Characterization for Plasma Interactions Analysis," Proc. of 8th Spacecraft Charging Techn. Conf.,, October 20-24, 2003, Huntsville, Alabama.

8. V.A. Davis, L.F. Neergaard, M.J. Mandell, I Katz, B.M. Gardner, J.M. Hilton, J. Minor, "Spacecraft Charging Calculations: NASCAP-2K and SEE Spacecraft Charging Handbook," AIAA 2002-0626, Proc. 40th AIAA Aerospace Sci. Meeting, January 14-17, 2002, Reno, Nevada.

9. Sebastien Clerc, S. Brosse, M. Chane-Yook, SPARCS: An Advanced Software For Spacecraft Charging Analysse," Proc. of 8th Spacecraft Charging Techn. Conf., October 20-24, 2003, Huntsville, Alabama.

10. R.E. Davies and J.R. Dennison, J. Spacecraft and Rockets, 34, 571-574 (1997).

11. R.E. Davies, "Backscattered and Secondary Electron Scattering Measurements with Applications to Spacecraft Charging," MS Thesis, Utah State Univ., 1996.

12. W.Y. Chang, J.R. Dennison, Jason Kite and R.E. Davies, "Effects of Evolving Surface Contamination on Spacecraft Charging," Proc. of the 38th AIAA Aerospace Sci. Meeting, Reno, NV, January 12, 2000.

13. N. Nickles, R.E. Davies and J.R. Dennison, "Applications of SE Energy- and Angular-Distributions to Spacecraft Charging," Proc. of 6th Spacecraft Charging Techno. Conf., (Hanscom Air Force Base, MA, 1999).

14. W.Y. Chang, J.R. Dennison, Neal Nickles and R.E. Davies, "Utah State University Ground-based Test Facility for Study of Electronic Properties of Spacecraft Materials," Proc. of 6th Spacecraft Charging Techno. Conf., (Hanscom Air Force Base, MA, 1999).

15. JR Dennison, NASA Space Environments and Effects Program Grants, "Electronic Properties of Materials with Application to Spacecraft Charging," 1998-2003; "Electronic Properties of Materials with Application to Spacecraft Charging—Extension of Materials Database," 2003-2004.

16. R.E. Davies, "Measurement of Angle-Resolved SE Spectra," PhD Thesis, Utah State Univ., 1999.

17. C.D. Thomson, V. Zavyalov, J.R. Dennison, "Instrumentation for studies of electron emission and charging from insulators," Proc. of 8th Spacecraft Charging Techn. Conf.,, October 20-24, 2003, Huntsville, Alabama.

18. Prasanna Swaminathan, A. R. Frederickson, J.R. Dennison, Alec Sim, Jerilyn Brunson, Eric Crapo, "Comparison Of Classical And Charge Storage Methods For Determining Conductivity Of Thin Film Insulators," Proc. of 8th Spacecraft Charging Techn. Conf., October 20-24, 2003, Huntsville, Alabama.

19. J.R. Dennison, A. R. Frederickson, Prasanna Swaminathan, "Charge Storage, Conductivity And Charge Profiles Of Insulators As Related To Spacecraft Charging," Proc. of 8th Spacecraft Charging Techn. Conf., October 20-24, 2003, Huntsville, Alabama.

20. A.R. Frederickson and J.R. Dennison, "Measurement of Conductivity and Charge Storage in Insulators Related to Spacecraft Charging," Proc. 2003 IEEE Nuclear and Space Radiation Effects Conference, Monterey, CA, July 21-25, 2003; to be published in IEEE Transaction on Dielectrics and Electrical Insulation.

21. Neal Nickles, "The Role of Bandgap in the SE Emission of Small Bandgap Semiconductors: Studies of Graphitic Carbon," PhD Dissertation, Utah State Univ., August 2002.

22. C.D. Thomson, V. Zavyalov, J.R. Dennison, Jodie Corbridge, "Electron Emission Properties Of Insulator Materials Pertinent To The International Space Station," Proc. of 8th Spacecraft Charging Techn. Conf., October 20-24, 2003, Huntsville, Alabama.

23. C.D. Thomson, Measurements of the SE Emission Properties of Insulators, Ph.D. dis., Utah State Univ., 2004.

24. J.R. Dennison, W.Y. Chang, N. Nickles, J. Kite, C.D. Thomson, Jodie Corbridge, and Carl Ellsworth, "Final Report Part III: Materials Reports," NASA Space Environments and Effects Program Grant, "Electronic Properties of Materials with Application to Spacecraft Charging," September 2002; J.R. Dennison, J. Kite, C.D. Thomson, Jodie Corbridge, Robert Berry, and Carl Ellsworth, "Final Report Part IV: Additional Materials Reports," May 2003. Available in electronic format through NASA SEE as part of the SEE Charge Collector Knowledgebase, http://see.msfc.nasa.gov/ee/db_chargecollector.html.

25. I. Krainsky, W. Lundin, W.L. Gordon, and R.W. Hoffman, <u>Secondary Electron Emission Yield Annual Report for Period July 1, 1979 to June 30, 1980</u>, Case Western Reserve University, Cleveland, OH, 1980 (unpub.).

26. Chung, M.S. and T.E. Everhart, "Simple calculation of energy-distribution of low-energy SEs emitted from metals under electron bombardment," J. Appl. Phys. 45,2, 707-709, 1974.

27. Operators Manual, Model 341A, High Voltage Electrostatic Voltmeter, Trek, Inc., 11601 Maple Ridge Road, Medina, New York 14103, USA. Telephone: (585) 798-3140, http://www.trekinc.com/.

28. ASTM D 257-99, "Standard Test Methods for DC Resistance or Conductance of Insulating Materials" (American Society for Testing and   Materials, 100 Barr Harbor drive, West Conshohocken, PA 19428, 1999).

29. Mandell, private communications, 2000.

30. Sternglass, E.J., "Theory of SE emission by high-speed ions," Phys. Rev. 108, 1, 1-12 (1957).

31. Schwarz, A., "Application of a semi-emperical sputtering model to secondary electron emission," J. Appl. Phys. 68 2382 (1990).

32. Gerald F. Dionne, "Origin of SE emission yield-curve parameters," J. Appl. Phys. 46 (8), 3347-3351 (1975).

33. B. Feuerbacher and B. Fitton, J. Appl. Phys. 41 1536 (1972).

34. The Red Book, RB 1, (Sheldahl Technical Materials, Northfield MN, 1995); http://www.sheldahl.com/Product/TechMaterials.htm, June 20, 2002.

35. Kapton polyimide film product information: Physical Properties, Report H-38492-1, (Dupont, Wilmington, DE, February, 1997); http://www.dupontteijinfilms.com/ , June 20, 2002.

36. A.R. Frederickson, C. E. Benson and J. F. Bockman, "Measurement of Charge Storage and Leakage in Polyimides," Nuclear Instruments and Methods in Physics Research B, 454-60, 2003.

37. NASA Space Environments and Effects Program SEE Charge Collector Knowledgebase, http://see.msfc.nasa.gov/ee/db_chargecollector.html.

38. L. Reimer, <u>Scanning Electron Microscopy. Physics of Image Formation and Microanalysis</u>, (Springer-Verlag., 1985), pp. 119-121.

39. M. Rösler and W. Brauer, "Theory of secondary electron emission I. General theory for nearly-free-electron metals," Phys. Stat. Sol. (b), 104, 161-175, 1981.

40. Jodie Corbridge and J.R. Dennison, "Effects of Bandgap on SE Emission for Graphitic Carbon Semiconductiors," Bull. Am. Phys. Soc. 48(1) Part II, 1146, (2003).

41. C.D Thomson, J.R Dennison, R.E Davies, B Vayner, J Galofaro, D.C Ferguson, and W. de Groot, "Investigation of the Snapover of Positively Biased Conductors in a Plasma," Proc. 38th AIAA Aerospace Sci. Meeting, January 10-13, 2000, Reno, Nevada.

42. C.D. Thomson, "Experimental Investigation of Snapover: The Sudden Increase of Plasma Current Drawn to a Positively Biased Conductor When Surrounded by a Dielectric," M.S. Thesis, Utah State University, 2001.

43. W. E Baumgartner, W. K Huber, "SE emission multipliers as particle detectors," J. Phys. E: Sci. Instrum., 9(5), 321-30 (1976).

44. H. Seiler, "SE emission in the scanning electron microscope," J. Appl. Phys. 54 (11), R1-R18 (1983).

45. H. Ibach, Electron Spectroscopy for Surface Analysis (Springer-Verlag, New York, 1977).

46. P. R Schwoebel, I. Brodie, "Surface-science aspects of vacuum microelectronics," J. Vacuum Sci. Techn., B, 13(4), 1391-410 (1995).

47. G. Auday, Ph. Guillot, and J. Galy, "Secondary emission of dielectrics used in plasma display panels," J. Appl. Phys. 88 (8), 4871-4874 (2000).

48. P. A Redhead, "The birth of electronics: Thermionic emission and vacuum," J. Vacuum Sci. Techn., A, 16(3, Pt. 1), 1394-1401 (1998).

49. G. R. Jones, M. T. C. Fang, "The physics of high-power arcs," Reports Prog. Phys., 43(12), 1415-65 (1980).

50. Kaoru Ohya, "SE emission from plasma facing materials and its impact on sheath voltage," Nuclear Instruments and Methods in Physics Research, Section B: Beam Interactions with Materials and Atoms (1999).

FEEDBACK ON THE PICUP3D EXPERIENCE AND THE OPEN SOURCE STRATEGY APPLIED TO A SPACECRAFT-PLASMA INTERACTION SIMULATION CODE

Julien Forest
Swedish Institute of Space Physics (IRF-K), Kiruna, Sweden
Planetary and Terrestrial Environment Study Centre (CNRS-UVSQ/CETP)
E-mail: julien@irf.se

Alain Hilgers
Space Environments and Effects Section, (ESA-ESTEC/TOS-EES)

Abstract

PicUp3D is an electrostatic multi-species 3D Particle-In-Cell (PIC) code dedicated to the modeling of the electrostatic sheath of spacecraft. Fully written in JAVA and able to model 3D realistic geometries, PicUp3D is designed to perform fine modeling for various purposes, especially scientific instruments calibration, and active device environment analysis such as ion thrusters. The development of PicUp3D was initiated in the context of the IPICSS project, for Investigation of Plasma Induced Charging of Satellite Systems, in partnership between IRF-K, ESA, CNRS/CETP and CNES, in the framework of the SPINE network and an ESA Academic Research Programme. The development time was followed by a long validation phase during which PicUp3D was intensively tested and used for mission supports at ESA. These application cases have confirmed the ability of PicUp3D models to simulate correctly modern spacecraft-plasma interactions problems. To induce a strong synergy with the scientific and the industrial communities, PicUp3D was developed with an open source software approach, such that the source code is freely accessible and the models can be tailored, validated or deeply modified by advanced users. PicUp3D has been released (http://www.spis.org) for the first time in December 2002 under the GPL license and is now freely available. Since then, feedback have been collected and contributed to improve the code by integration of new models, such as a multi-grid field description, or technologies, such as a script command layer. In parallel, this interaction with the user community have helped to identify key issues that should be taken into account to support a community based development of the next generation spacecraft-plasma interaction simulation library (SPIS). The current status of PicUp3D is presented and analyzed with respect to the initial objectives of the project.

Introduction

Spacecrafts interact with the surrounding plasma via many processes. By virtue of the thermal motion of plasma particles and via electrostatic interactions, exposed surfaces collect charged particles (electrons and ions), leading to the accumulation of a net electrostatic charge and a corresponding potential distribution. The potential is also modified by the ionization of surfaces by the UV and soft X-rays radiations and high energetic particle radiation. Charging may have many consequences for spacecraft systems including the scientific instruments. For example, strong charging events have been observed on geostationary orbit and in auroral regions and may generate sparks. Even moderate potential difference between the spacecraft and the plasma is a concern since it may prevent ambient particles to reach plasma sensors. Other spacecraft-plasma interaction phenomena may create disturbances of a few volts on spacecraft surfaces or in the space surrounding the spacecraft.

For instance ion wakes are observed on low Earth orbit where spacecraft speed is meso-thermal (i.e., higher than ion averaged thermal velocity but lower than electron averaged thermal velocity). The corresponding highly non-isotropic perturbations are difficult to model via analytical models. The need for in-flight plasma instrument calibration is now better perceived and detailed numerical simulations may clearly help to this [1,5].
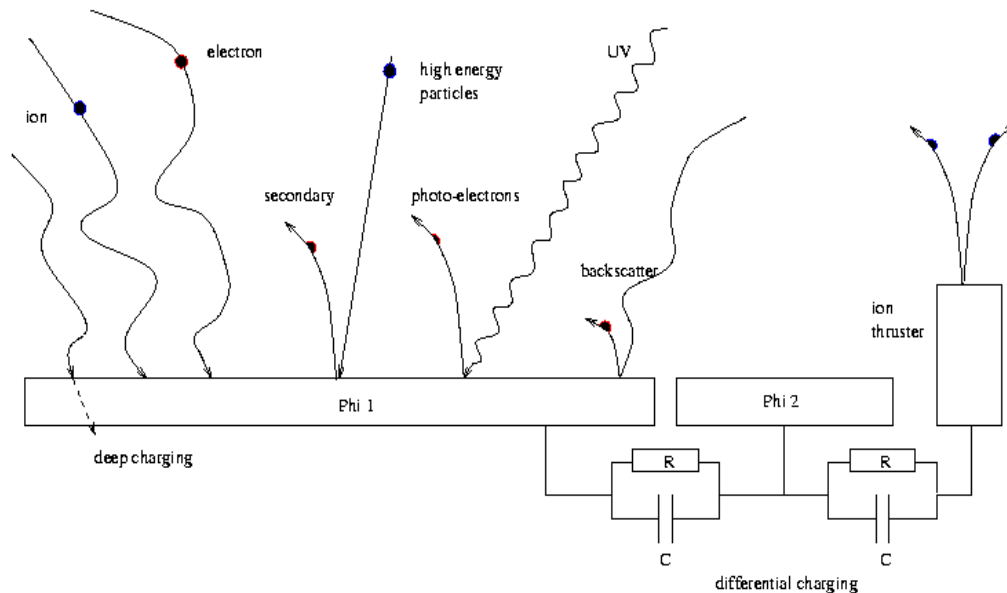
Figure 1. Sketch of surface processes which contribute to spacecraft charging.

On the technological side, new needs appear in Europe with the more common use of electrical propulsion (e.g. ESA missions GOCE and SMART-1). The interaction of the ion plume with the external environment (including the vehicle itself) constitutes a large and open domain of investigation. The new generation of high power solar arrays working with higher bus voltage presents new issues with risks of arcing and loss of power due to current leakage. These phenomena were not well modeled by the previous generation of charging codes and are still very challenging from the numerical point of view (e.g., complex processes involving various fields of physics, large range of scales) [cf 4, 8].

Historical Context and Approach

These new challenging requirements have emphasized the need for new and advanced simulation codes, based on more detailed models and using modern computing technologies. Because new problems are in many cases multi-disciplinary, a very good visibility of the implemented models and the access to the code constitute a critical issue. One solution is the Open Source Software (OSS) approach, according to which software are released with their source codes. This approach may appear as a clear breaking with respect to the pre-existing culture in the domain of simulation codes, especially in an industrial context. However, this approach has existed in the academic world for more than thirty years and may also be an answer to some constraints in the industrial environment. This is somehow the approach that was adopted with the NASA-USAF charging code, NASCAP, except for its geographical restriction [7]. Because simulation software are complex and costly to develop and validate, an in-house team of developers remains generally too small in terms of manpower and knowledge and cannot develop a complete software by its own excepted in very big

companies. By sharing the development costs on one hand and gathering the complementary knowledge on the other one, the open-source approach should reduce the development, validation and maintenance cost. Last, the open source approach should also decrease the dependence on only one specialist and break the effect "one-code one-specialist" and by this extends the frequency of use and the lifetime of the code.

The IPICSS project, for Investigation of Plasma Induced Charging of Satellite Systems, was initiated at IRF-K in the framework a PhD scholarship (ESA Academic Research Programme) in summer 1999, in partnership between IRF-K, ESA, CNRS/CETP and CNES (academic grant). It was performed in the context of the SPINE network (see http://www.spis.org/spine/). The objectives of this project were to analyze in depth the new requirements for spacecraft-plasma interaction modeling especially from the scientific community (e.g. for instrument calibration, interpretation of observations) and the industry (e.g., for analyzing active device and electric thrusters) and to develop a simulation tools to meet such requirements.

One of the main outputs of IPICSS was the development of a new spacecraft-plasma interaction simulation software, called PicUp3D, able to model 3D realistic geometry for a broad range of time varying space plasma environment [2,3]. This new code includes advanced numerical kinetic models and takes advantage of new computing technology such as the Object Oriented Approach and modern hardware (PC clusters). PicUp3D was designed since the beginning in the perspective of an open source strategy and was officially released under the GPL license in December 2002. Since it has been made publicly available its uses has significantly progressed within both communities, scientific and industrial.

The PicUp3D Code, Models and Technologies

Picup3D is based on a 3D electrostatic full multi-species Particles-In-Cell (PIC) model. The electrostatic potential is solved on a 3D Cartesian structured grid, using an optimized Gauss-Seidel iterative solver. An additional non-uniform static magnetic field can be taken into account. The motion of macro-particle is performed using a classic leap-frog scheme. The spacecraft is modeled using an unstructured meshing, allowing the possibility to optimize the surface meshing and facilitates the link with existing 3D modelers and Delaunay surface meshers. A very large range of plasma conditions may be taken into account, including non-Maxwellian sources (drifting or non-isotropic plasma). Currents of particles may be derived for each surface element.

PicUp3D is fully written in JAVA language and according to an Object Oriented Approach (OOA). The real reasons of this choice are directly related to the perspective of a public release and a future community based development. JAVA is a very popular language today, especially among the young generation of computer engineers. It benefits from the strong dynamics of the Web community and a large number of development tools and advanced libraries are freely available on the Net. The OOA allows a high modularity of the code and future extension by simple integration of new computing components (classes, methods). Actually, the OOA seemed especially appropriate for later insertion of new piece of codes by several developers. The rigorous and simple syntax of JAVA leads to more homogeneous, and then easier to maintain, codes than the C++ language.

Tests have been performed which demonstrate that JAVA programs are able to perform large numerical simulations with acceptable.
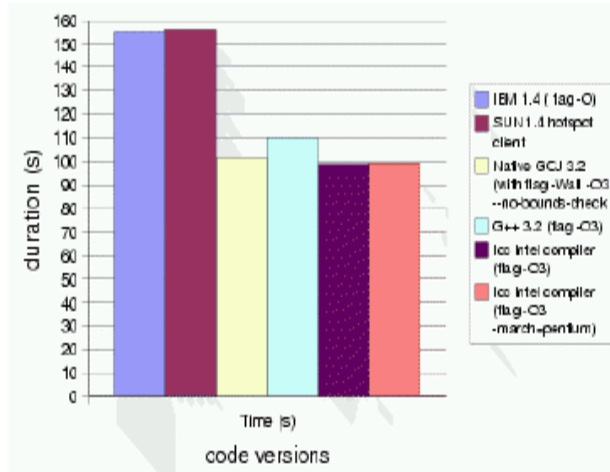
Figure 2. Comparative benchmarks between JAVA and C++ versions of the Poisson's solver implemented in PicUp3D.

Comparative benchmarks (see Figure 2) shows that for critical modules as the Poisson's equation solver, the JAVA byte-coded version of the code is about twice slower than its native equivalent written in C++. The corresponding run duration increase is nevertheless smaller than the time usually spent by the user to modified or adjust code parameters before a run for standard problems (typically a few days). The performance of the latest version of the GNU compiler, GCJ, able to compile JAVA source codes into native executable codes, has also been explored. In this case, the JAVA code performances become almost equivalent to the C++ ones and is even surprisingly sometimes faster than C++. This seems very promising and opens new possibilities for very large simulations with JAVA codes.

PicUp3D and its main library are completed by a set of pre and post-processing tools. A script layer, based on Jython, is under implementation in order to facilitate the access to the low level numerical methods via modules that can be called and manipulated directly by the user in a console mode.

Picup3D has been validated with several Langmuir's probe test case simulations (potential map, current-tension characteristics). The results were compared against Langmuir probe theory and outputs from other validated codes. A specific effort was dedicated to evaluate the accuracy of the code. Tests have confirmed that an accuracy better than 10% on potential and current on Langmuir's probe could be achieved [2].

Problems requiring runs on grids larger than 150^3 mesh nodes and with more than 6 millions of particles have been successfully modeled in support to some ESA missions [4,9,10].
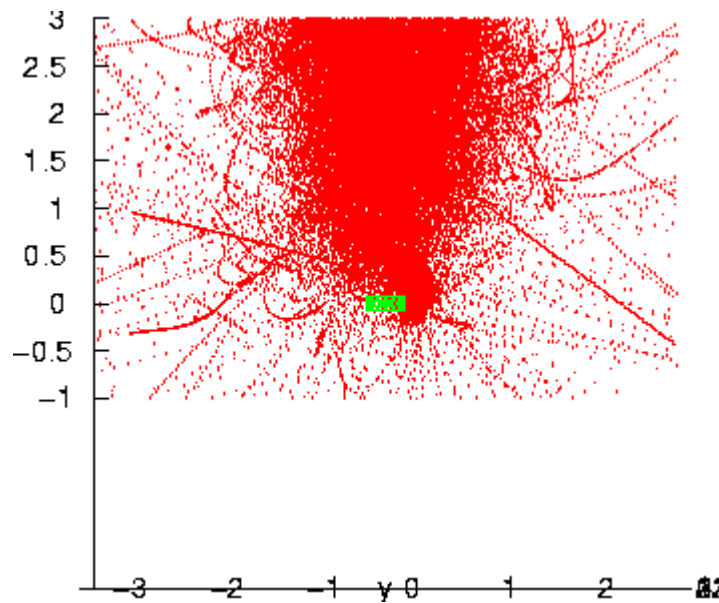
Figure 3. Photo-electron cloud attracted by the ion emitter (ASPOC) plume on the ESA CLUSTER-II mission [10].

Open Source Strategy

It has appeared from previous experiences, that a public release of an open source software should respect a set of rules to be successful. First of all, the released code should satisfy well-defined need. Generally, OSS are initiated by a reduced team of initial developers (kernel-team hereafter) until the development reaches a "critical mass" when the code is able to perform a minimum set of the required functionalities. The date of release in the development time-line is very variable depending on the objective of the software and its related communities. A project may have interest to be released the earliest possible to benefit from the community dynamics and inputs. Conversely, in some area it is better not to release the software before enough validation has been performed to create confidence on the applicability of the code. Another criteria of maturity is the characteristic time to install and learn how-to-use the code for a new user. If the learning curve is prohibitively long, the software will be rejected by the community. Presumably, the need to stimulate co-development from community members not belonging to the kernel team set even more constrained on the required maturity and structure of the code before release. These aspects are critical for the dynamics of a community-based development.

A Gant's diagram corresponding to the evolution of the PicUp3D project is shown on Figure 4. There are two well identified phases in the project. The first one, before the first release, corresponds to the design and the development of the simulation kernel. This was done by a very small team, typically one to three developers at a given time with the contribution of a few experts for validation which were performed in short iterative sequences most of the time on the complete chain of the simulation but lead sometimes to drastic revisions of some modules.
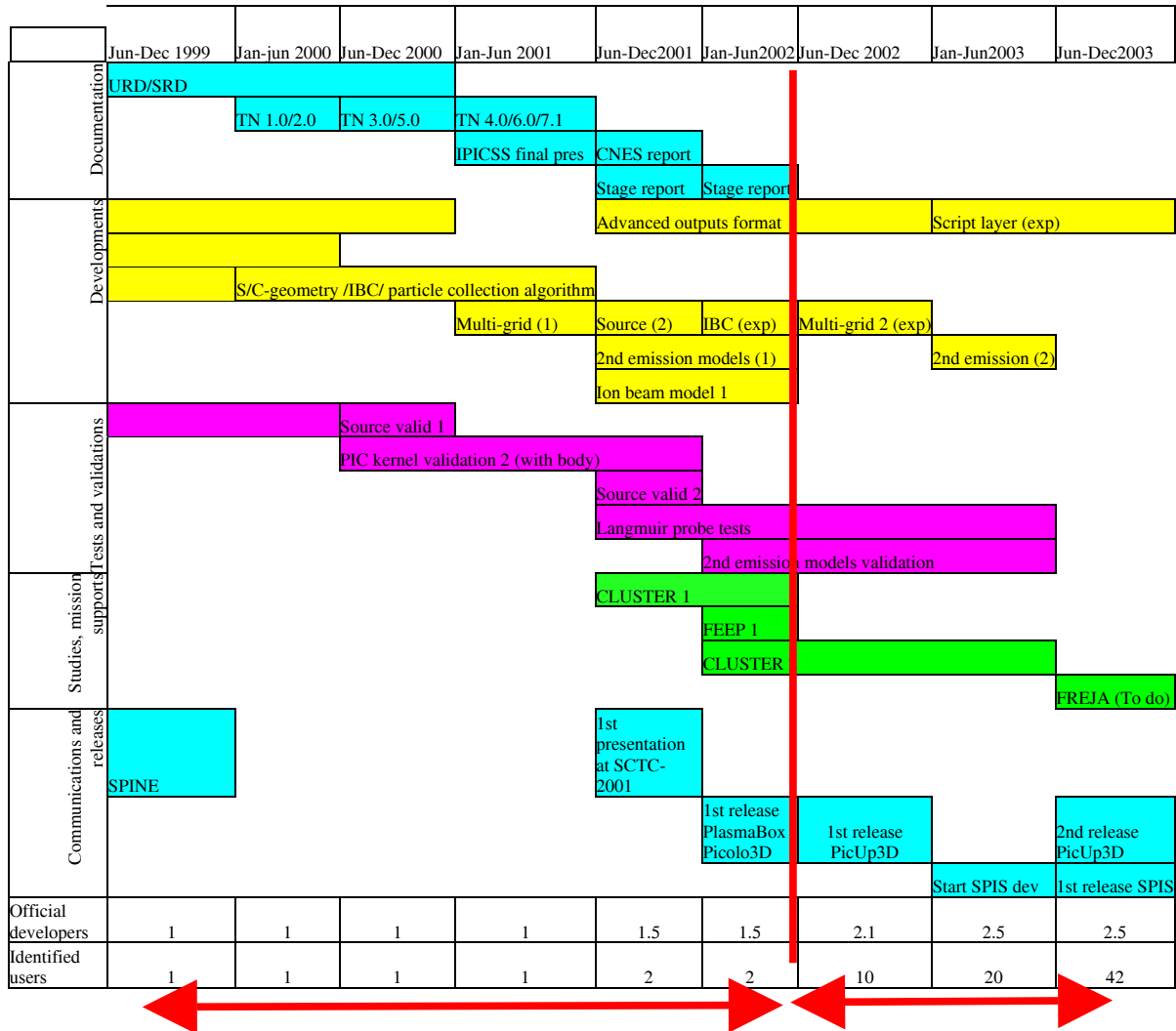
Figure 4 — Gantt's diagram corresponding to the evolution of the PicUp3D project.

Time columns: Jun-Dec 1999 | Jan-jun 2000 | Jun-Dec 2000 | Jan-Jun 2001 | Jun-Dec2001 | Jan-Jun2002 | Jun-Dec 2002 | Jan-Jun2003 | Jun-Dec2003

Documentation
- URD/SRD
- TN 1.0/2.0
- TN 3.0/5.0
- TN 4.0/6.0/7.1
- IPICSS final pres
- CNES report
- Stage report
- Stage report

Developments
- Advanced outputs format
- Script layer (exp)
- S/C-geometry /IBC/ particle collection algorithm
- Multi-grid (1)
- Source (2)
- IBC (exp)
- Multi-grid 2 (exp)
- 2nd emission models (1)
- 2nd emission (2)
- Ion beam model 1

Tests and validations
- Source valid 1
- PIC kernel validation 2 (with body)
- Source valid 2
- Langmuir probe tests
- 2nd emission models validation

Studies, mission supports
- CLUSTER 1
- FEEP 1
- CLUSTER
- FREJA (To do)

Communications and releases
- SPINE
- 1st presentation at SCTC-2001
- 1st release PlasmaBox Picolo3D
- 1st release PicUp3D
- 2nd release PicUp3D
- Start SPIS dev
- 1st release SPIS

	Jun-Dec 1999	Jan-jun 2000	Jun-Dec 2000	Jan-Jun 2001	Jun-Dec2001	Jan-Jun2002	Jun-Dec 2002	Jan-Jun2003	Jun-Dec2003
Official developers	1	1	1	1	1.5	1.5	2.1	2.5	2.5
Identified users	1	1	1	1	2	2	10	20	42

Figure 4. Gant's diagram corresponding to the evolution of the PicUp3D project.

At the date of the first release, the simulation kernel of PicUp3D was fully operational and had been already applied for problem solving in an operational context. The second phase, is based on a broader community contribution and has already seen improvement in terms of new models (new photo-electrons emission, multi-grid modules) or specialization of the code. During this phase, the initial effort of the kernel team has to be progressively re-oriented from the pure development toward the management of the community, the integration and the validation of the external contributions.

The last critical point is the choice of the license and the ownership of the intellectual rights. At the opposite of what is generally believed, the open source software approach does not imply that authors loose their intellectual property rights which should be defined carefully in relation with an appropriate license. A community-based development is based on an agreement and the choice of the license is essential. For PicUp3D distribution, it has been decided to use the well known GPL license which forces any software derived from PicUp3D to be distributed under the same license. The advantage of this license is that it tends to increase the resources available to the community of users and developers without discrimination.

PicUp3D Community Description and Feedback

PicUp3D and its derived versions (PlasmaBox and PicOlo3D) have been directly downloaded from the official web site by about 65 different users in less than 6 months. This is more than the community of users identified within the Spacecraft Plasma Interaction Network in Europe (SPINE) which consist of a few tens of members (www.spis.org/spine).

Users geographical distribution
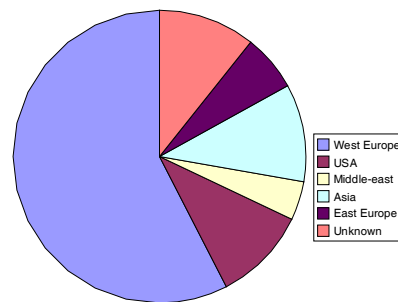
Figure 5. Geographical distribution of downloads of PicUp3D

The geographical distribution of locations from where code downloads have been performed is shown on Figure 5. It shows that PicUp3D was mainly downloaded from western European countries (mainly EU) with (about 57 % of the downloads), followed by USA (~11%). Eastern European and Asian countries together represent 21 % of the downloads. The high representation of western European countries is probably due in part to the active promotion made within the SPINE network. About 11 % of the downloads were performed without that any official identification has been provided. A majority of registered users expressed the wish to be kept informed of the future evolutions of the project.

The number of downloads according to academic organisations versus commercial companies is shown on Figure 6. It shows an almost even distribution with a slight advantage for the academic world (47% against 40%). This even distribution constitutes a real success regarding the initial goals of the project. It is difficult, however, to know how many downloads correspond to real applications and whether the applications have been extended beyond the spacecraft-plasma interaction domain.
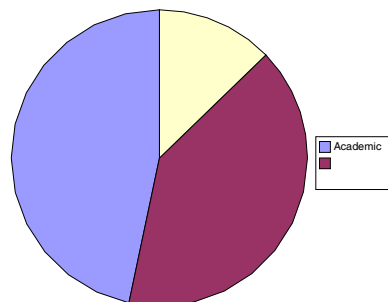
Figure 6. Academic versus commercial companies distribution of downloads

The feedback from the community is mainly organised through the SPINE meetings where discussion on the relevant issues can take place. The feedback takes several aspects ranging from provision of piece of new code to bug reports. Significant contributions have been done on multi-grid algorithm, secondary emission improvement. Ongoing analyses are being performed to take into account wire structures, wakes, magnetic field effects and to shorten computation time to reach equilibrium. It must be noted, however, that most of these activities are mainly funded via similar sources as the kernel team. A substantial feedback is also provided by the analysis and critics of the code by the users, regarding the models, the computing implementation and the user interface. PicUp3D, like many research codes, is still a prototype and is sometimes difficult to install and use. This is also partly due to the lack of official documentation (not released yet). Critics regarding the computing aspect may take various forms, from the simple bug report to a complete proposition of alternative design. The research of the inter-compatibility with another project is a very efficient way of contribution. It requires re-engineering of both codes, allows the quick introductions of new functionalities. The interaction users-developers on the basis of the first released version constitutes a very good source of new user requirements and may lead to define functional specifications of a new version or a new code. This is especially true in case of iterative development, or "development in spiral", typical of community based software development.

Future of PicUp3D

The observations made in the previous section show that the public release of a scientific code may actually help to increase the dynamics of a scientific community and that PicUp3D has played and may continue to play an efficient role in the development of the SPINE community. Initially designed as a simple technological demonstrator, PicUp3D's life lasted already longer than expected. It is now adopted by a large community which may even extend outside the boundaries of the SPINE network. Its development phase as an exclusively in-house code is now finished. A new phase is opening, based on the participation of the user and developers community. It is expected that the main effort in the SPINE network will be progressively dedicated to the future SPIS library of codes [8]. As a result PicUp3D will keep a simple structure and its distribution and installation will continue to be very simple. It is foreseen that it will be used as an educational tool by academia. In the very near future, it will assure a progressive transition of the community toward SPIS. In this perspective, PicUp3D has been imbedded in the first release of the SPIS-UI framework of the SPIS project [8]. The pre and post-processing tools will provide extended CAD capabilities and better surface meshing to PicUp3D (see Figure 7). Eventually, based on the already proven capability of PicUp3D it will also certainly be used as a benchmark for new codes.
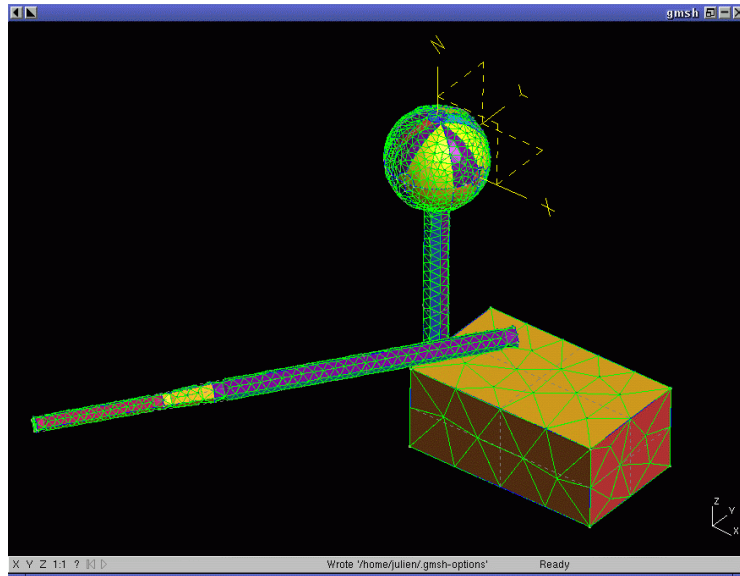
Figure 7. Example of set of Langmuir's probes modeled with the SPIS-UI framework and imported into PicUp3D's format.

Conclusion

Although it is still too early to draw a definitive conclusion about the new community based development phase of the PicUp3D project we can however notice a number of successful achievements made with this project. Tests and applications performed in an operational environment have confirmed the relevance of first principle based numerical models like 3D PIC simulations to address contemporary modelling requirements in spacecraft-plasma interactions. Tests and benchmarks have confirmed the capability of JAVA to perform large simulations with a reasonable computing cost. The JAVA language associated to a simple object oriented design seems also very well adapted to a community based development and future extensions of the code. The open source approach allows a very large range of possible extensions and adaptations of the code around the core numerical kernel. The most successful test is presumably the popularity of the code gained in less than one year within the SPINE community and world-wide as evidenced by the number of references made to it in this conference.

Acknowledgments

References

1. Eriksson, A.I., Wedin, L., Wahlund, J-E, and Holback, B.: "Analysis of Freja Charging Events: Modelling of Freja Observations by Spacecraft Charging Codes", IRF Scientific report 252, January 1999.

2. Forest J., Eliasson, L., Hilgers, A.: "A new spacecraft plasma simulation software, PicUp3D/SPIS", 7th Spacecraft Charging Technology Conference, Proceedings pp.515-520, ESA/SP-476, ISBN No 92-9092-745-3, ESA-ESTEC, Noordwijk, The Netherlands, 23-27 April 2001.

3. Forest J., A. Hilgers, B. Thiebault, L. Eliasson, J.-J. Berthelier, and H. de Feraudy, "A new open source spacecraft plasma interaction simulation software library, PicUp3D", to be submitted.

4. Forest, J., A. Hilgers, B. Thiebault and A. Popescu, "Modelling of the plasma environment of micro FEEP thrusters using PicUp3D PIC code", in Proceedings of the 8th Spacecraft Charging Technology Conf., Huntsville, USA, Oct. 20-24, 2003.

5. Hilgers, A. and B. Thiebault, "A review of spacecraft effects on plasma measurements", in Proceedings of the 8th Spacecraft Charging Technology Conference, Huntsville, AL, USA, October 20-24, 2003.

6. Mandell M. J., et al., "NASCAP programmer's reference manual", NASA contract No NAS3-22826, SSS-R-84-6638, La Jolla USA, 1984.

7. Roussel, J.-F., F. Rogier, M. Lemoine, D. Volpert., G. Rousseau, G. Sookahet, P. Séng, and A. Hilgers, Design of a New Modular Spacecraft Plasma Interaction Modeling Software (SPIS)," in Proceedings of the 8th Spacecraft Charging Technology Conference, Huntsville, AL, USA, October 20-24, 2003.

8. Thiébault, B., Hilgers, A., Forest, J., Escoubet, P., Fehringer, M. Laakso, H.: Modelling of the photo-electron sheath around an active mgnetospheric spacecraft, in Proceedings of the 8th Spacecraft Charging Technology Conference, Huntsville, AL, USA, October 20-24, 2003.

9. Thiébault, B., Hilgers, A., Sasot, E., Forest, J., Génot, V., Escoubet, P.: "Investigation of electrostatic potential barrier near an electron-emitting body", in Proceedings of the 8th Spacecraft Charging Technology Conference, Huntsville, AL, USA, October 20-24, 2003.

ON ORBIT DAYTIME SOLAR HEATING EFFECTS: A COMPARISON OF GROUND CHAMBER ARCING RESULTS

J. Galofaro

Photovoltaics and Environmental Effects Branch
John H. Glenn Research Center at Lewis Field
21000 Brookpark Road, Mail Stop: 302-1
Cleveland, Ohio 44135-3191
Phone: (216) 433-2294
Fax: (216) 433-6106
Email: Joel.T.Galofaro@grc.nasa.gov

B. Vayner

Ohio Aerospace Institute, Brook Park, Ohio

D. Ferguson

John H. Glenn Research Center, Cleveland, Ohio

Abstract

The purpose of the current experiment is to make direct comparisons between the arcing results obtained from the diffusion pumped vertical chamber and our newly renovated Teney vacuum chamber which is equipped with a cryogenic pump. Recall that the prior reported results obtained for the Vertical chamber were nominal at best, showing only a slight reduction in the arc rate after 5 heating cycles at the lower bias potentials and virtually no changes at high potential biases.[1, 2] It was concluded that the vertical chamber was unable to remove enough water vapor from the chamber to adequately test the arcing criterion. Because the cryo-pumped Teney chamber has a ten times better pumping speed, (40,000 liters per sec compared to 4,000 liters per sec for the diffusion pumped vertical chamber), a decision was made to retest that experiment in both the Teney and Vertical vacuum chambers. A comparison of the various data is presented with encouraging results.

Introduction

For the current experiments silicon photovoltaic arrays are placed under simulated daytime solar heating (full sunlight) conditions typically encountered in a Low Earth Orbit (LEO) environment. Assuming a 220 km LEO orbit the array will reach a temperature of about 80°C in full sunlight. It is our contention that a desorbed molecular ionization mechanism involving water vapor, at the triple junction sites on a solar array, is directly responsible for arcing onset of solar arrays in LEO.[3-10] The solar array arcing criterion is used to validate our hypothesis that the arc rate depends on the water vapor content stored in the array. Because solar heating of the array seeks to drive out absorbed water vapor, a reduction in water vapor should lead to a reduction in the arcing rare. Arc rates are established for individual arrays held at 11°C and are used as a baseline for further comparisons. As in the previous experiment the arrays were heated to a temperature of 80°C. Each thermal cycle was set to time duration of 40 minutes to approximate

the daytime solar heat flux to the array over a single orbit. The arrays are allowed to cool back down to ambient temperature before proceeding to the next thermal cycle. After 5 complete heating cycles the arc rates of the solar arrays are then retested at a temperature of $11^{\circ}C$.

Experimental Setup

Figure 1 shows a picture of the 2.2 meter (diameter) by 3.0 meter (length) Vertical Chamber (Left) and the 1.8 meter (diameter) by 2.0 meter (length) of the cryo-pumped Teney vacuum chamber (Right). Figure 2 shows two solar arrays hanging in front of an aluminum plate equipped with resistive heating elements which are used to simulate the solar heat flux to the array. Two type T thermocouples were used to monitor the array and heater plate temperatures. Arrays samples 62 and 63 are each composed of thirty-six 4 by 6 centimeter silicon solar cells arranged as 3 parallel strings, each string being composed of 12 cells wired in series. At experiment startup the base neutral background pressure (P_o) in the chamber at $14^{\circ}C$ was recorded at $P_o = 5.7x10^{-7}$ Torr. A Kaufman plasma source was used to ionize xenon gas neutrals via a hot wire filament for the experiments. In principle xenon gas is carefully metered into the chamber using a user controlled leak valve and an ionization gauge was used to read back the tank pressure. With the xenon gas flowing through the source (source not energized) a tank neutral pressure, $P_o = 4x10^{-5}$ Torr was established. Initially a programmable power supply source/measure unit (electrometer) is used to monitor electron flux to a Langmuir probe (Lp) which is mounted near the face of the array. A bias of +30V is applied to the Lp relative to tank ground and the current flowing to the surface of the probe is carefully monitored. Next the filament current in the plasma source is gradually increased until the electrometer reads +0.4 milliamps indicating ionization of xenon gas neutrals is occurring and that a plasma is present. The Langmuir probe is swept in voltage to obtain the plasma parameters and the filament current to the plasma source is further adjusted until the Lp diagnostic parameters match the ionospheric conditions for the specified orbit. The plasma electron number densities and electron temperatures measured for the current tests were: Ne=4.0x10-5cm^{-3} and Te = 0.89eV, about the same values used the previous arcing tests in the vertical chambers.

For the arcing tests the three strings in each array are shorted and biased negative through a 10k ohm resistor to the a power supply and back to ground through a 1μF capacitor wired in parallel (See Figure 3). A current probe amplifier, current and voltage probes, a four channel 400 MHz digital storage oscilloscope, data acquisition and control software were used to record the arcs. Other miscellaneous equipment used in the tests included a quadruple mass spectrometer to record the levels of partial pressure for water vapor and other species in the vacuum system.

Arc Test Results

A plot of the partial pressure of water in the Vertical chamber, after three forty minute thermal cycles, is plotted in Figure 1. The minimum partial pressure for water in the Vertical tank after three hundred hours pumping levels out at approximately 2 microTorr.[2] Therefore it was not necessary to proceed beyond 3 heating cycles for the vertical chamber tests. For comparison purposes note the over all level of reduction in the partial pressure of water is about 20 times less for the Teney vacuum chamber (after five complete thermal cycles) than is case for the Vertical chamber after three thermal cycles (see figures (4.a) and (4.b)).

Table A depicts in tabular form the arcing results obtained for the diffusion pumped vertical chamber and the cryo-pumped Teney vacuum chamber. Figures (5.a) & (5.b) graphically depict the arcing threshold potential (or arc inception voltage) obtained before heating and after thermal cycling for sample 63 (the 300 micron thick cover slide array) tested in the Vertical and Teney vacuum chambers. Similarly figures (5.c) & (5.d) plot the arcing threshold potential before and after thermal cycling obtained for sample 62 (the 150 micron thick cover slide array). Note that the arc inception voltages plotted for the Vertical and Teney vacuum chamber tests of array samples 62 and 63 (Figure's (5.a), (5.b) and (5.c),(5.d)) show that the arc inception voltage after heating is much more negative than is the case for the same samples before the arrays were heated.

	Diffusion Pumped Vertical Chamber				Cryogenic Teney Chamber			
	Strings #1, 2, & 3 (Sample 63) (300 micron thick cover slide)		Strings #4, 5, & 6 (Sample 62) (150 micron thick cover slide)		Strings #1, 2, & 3 (Sample 63) (300 micron thick cover slide)		Strings #4, 5, & 6 (Sample 62) (150 micron thick cover slide)	
	Bias	Arc Rate	Bias	Arc Rate	Bias	Arc Rate	Bias	Arc Rate
Before Heating:	-200 V	0 arcs in 30 minutes	-150 V	0 arcs in 15 minutes	-150 V	1 arc in 30 minutes	-110 V	0 arcs in 30 minutes
	-220 V	2 arcs in 30 minutes	-180 V	0 arcs in 15 minutes	-170 V	0 arcs in 30 minutes	-130 V	8 arcs in 30 minutes
	-240 V	4 arcs in 60 minutes	-200 V	2 arcs in 30 minutes	-200 V	4 arcs in 30 minutes	-150 V	21 arcs in 20 minutes
	-260 V	6 arcs in 30 minutes	-220 V	6 arcs in 38 minutes	-220 V	5 arcs in 30 minutes		
	-280 V	20 arcs in 30 minutes	-240 V	21 arcs in 30 minutes	-240 V	7 arcs in 30 minutes		
After Heating:	-220 V	0 arcs in 30 minutes	-200 V	0 arcs in 30 minutes	-150 V	0 arcs in 30 minutes	-150 V	1 arc in 30 minutes
	-240 V	0 arcs in 15 minutes	-240 V	4 arcs in 30 minutes	-170 V	0 arcs in 15 minutes	-170 V	0 arcs in 20 minutes
	-260 V	0 arcs in 20 minutes	-260 V	25 arcs in 20 minutes	-200 V	4 arcs in 30 minutes	-200 V	4 arcs in 30 minutes
	-280 V	0 arcs in 20 minutes	-270 V	15 arcs in 10 minutes	-220 V	5 arcs in 15 minutes	-220 V	9 arcs in 30 minutes
	-300 V	7 arcs in 30 minutes			-240 V	15 arcs in 5 minutes		
	-320 V	17 arcs in 30 minutes						
	-340 V	29 arcs in 30 minutes						

Table A: Summary of Arc Rate Test Results for Vertical and Tenny Chambers

Conclusion

The results from the thermal cycling tests appear to validate the arcing criterion that was forwarded earlier. The arcing criterion contends that the arc rate should drop as water is out gassed from the array due to heating. More importantly the arc inception voltage seems to be a better prognosticator in determining the effectiveness of thermal cycling on the out gassing of water from the array. In all cases the negative bias potentials recorded for initial arc inception voltage have been driven a great deal more negative after heating compared to the arc inception values recorded earlier before the arrays were heated. Furthermore the trend of lowering arc inception voltages after thermal cycling was observed in both the Vertical and Teney vacuum chamber tests.

As a result of the current measurements the amount of water in the chamber needs to be at or below the 1.6 microTorr minimum level after heating for the observed changes in the arc inception voltage to be seen. The observation of the required 1.6 microTorr level has caused us to rescind our earlier conclusion that the Vertical chamber was unable to remove enough water vapor to adequately test the arcing criterion. A careful reexamination of the data has revealed that the original thermal cycling tests were run in an inconsistent manner with changing plasma source and density parameters.[1, 2] The current tests were retested in the Vertical chamber with the same plasma source parameters, density and pressure set in the original thermal cycling tests of

samples 62 and 63 run in the Teney vacuum chamber. Finally we believe we have demonstrated the effectiveness of the thermal cycling technique to passively outgas water from a solar array in an attempt to stave off arcing in LEO.
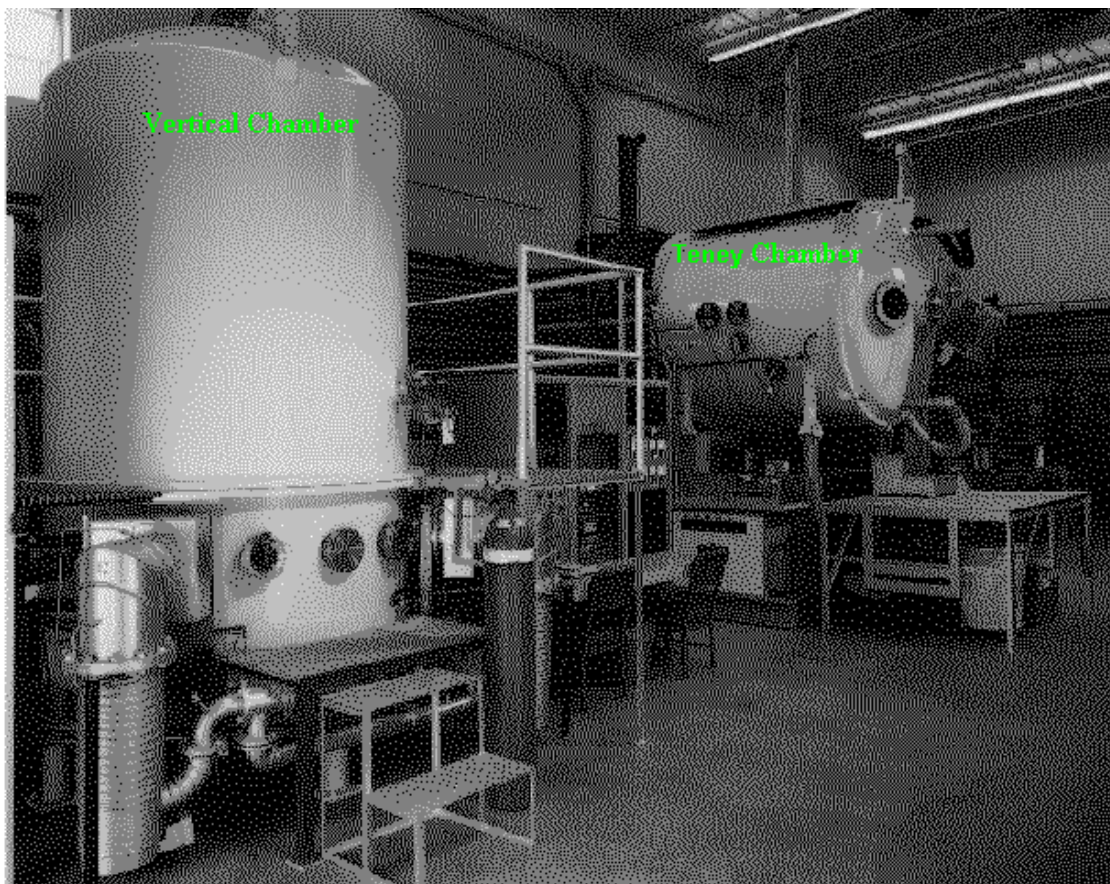
Figure 1:   NASA Glenn Plasma Interaction Facility showing the 2.2 x 3 meter Vertical Chamber and the 1.8 x 2 meter Teney Chamber
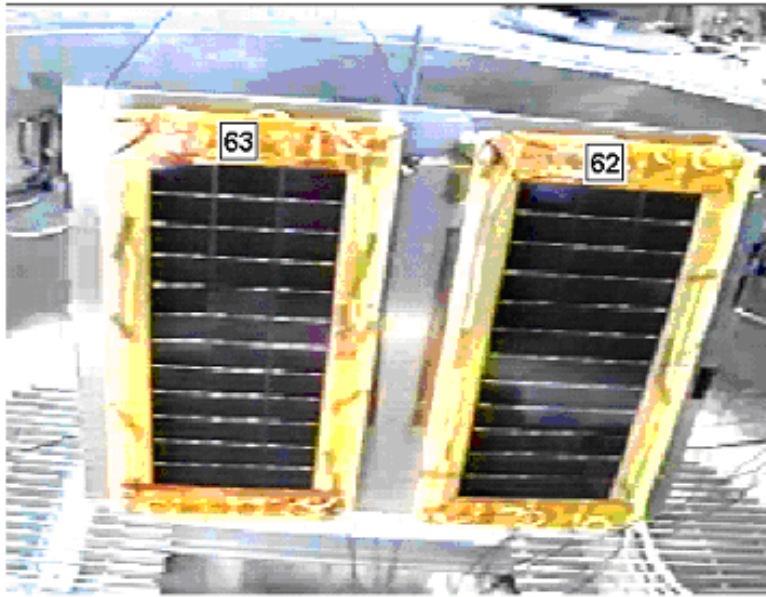
Figure 2: Solar array samples and the heater plate assembly mounted in the Vertical Chamber prior to test
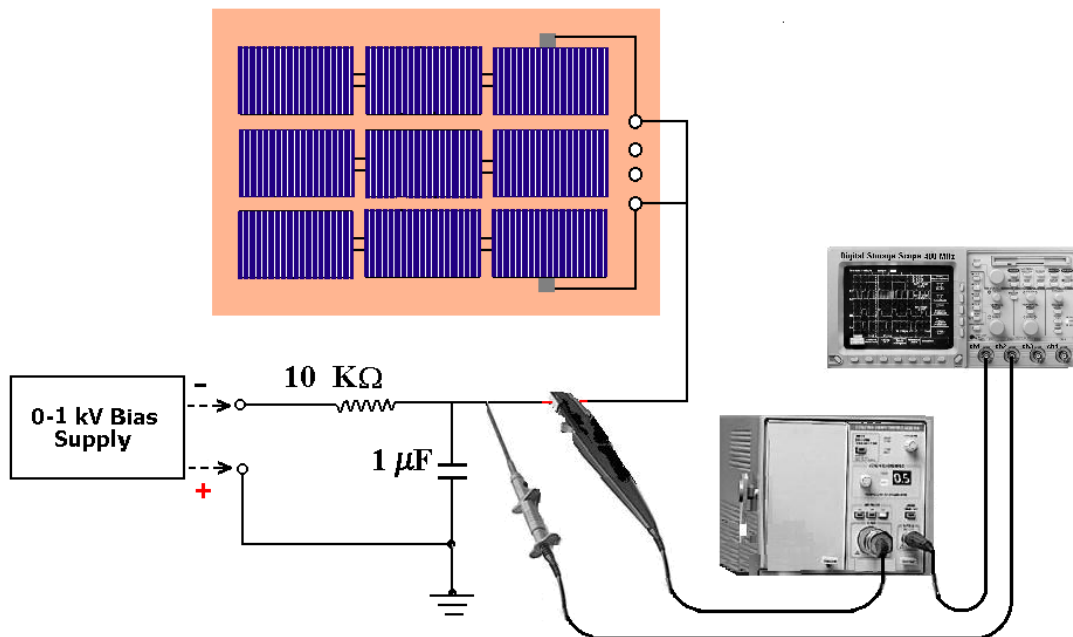
Figure 3: R-C circuit and hardware used for detecting arcs on solar arrays.
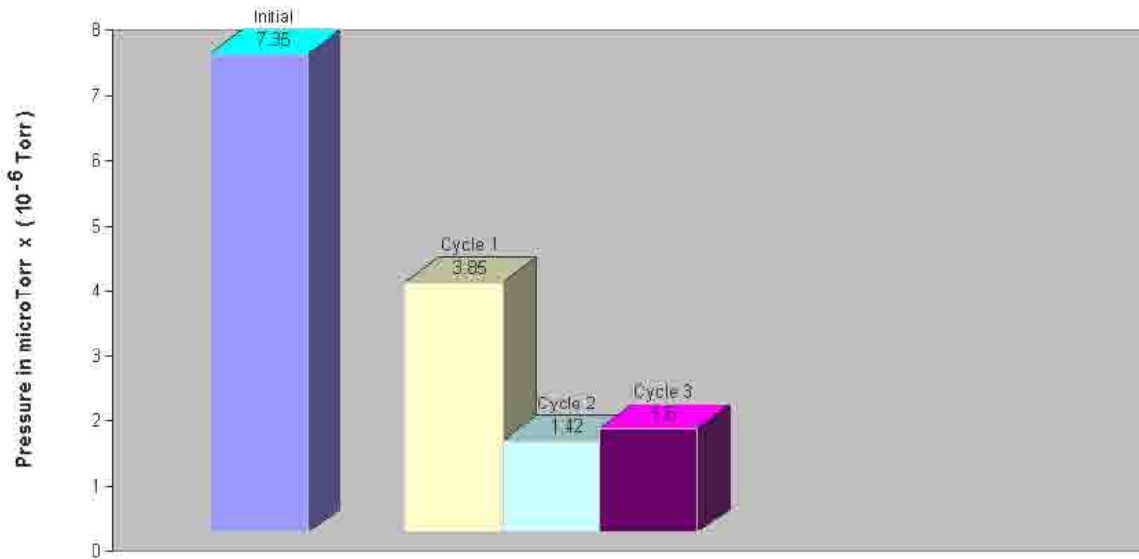
Figure 4.a: Partial pressure of water in the vertical chamber after each heating cycle. The recorded pressures were obtained after the arrays were cooled back down to the 11 deg. Celsius.
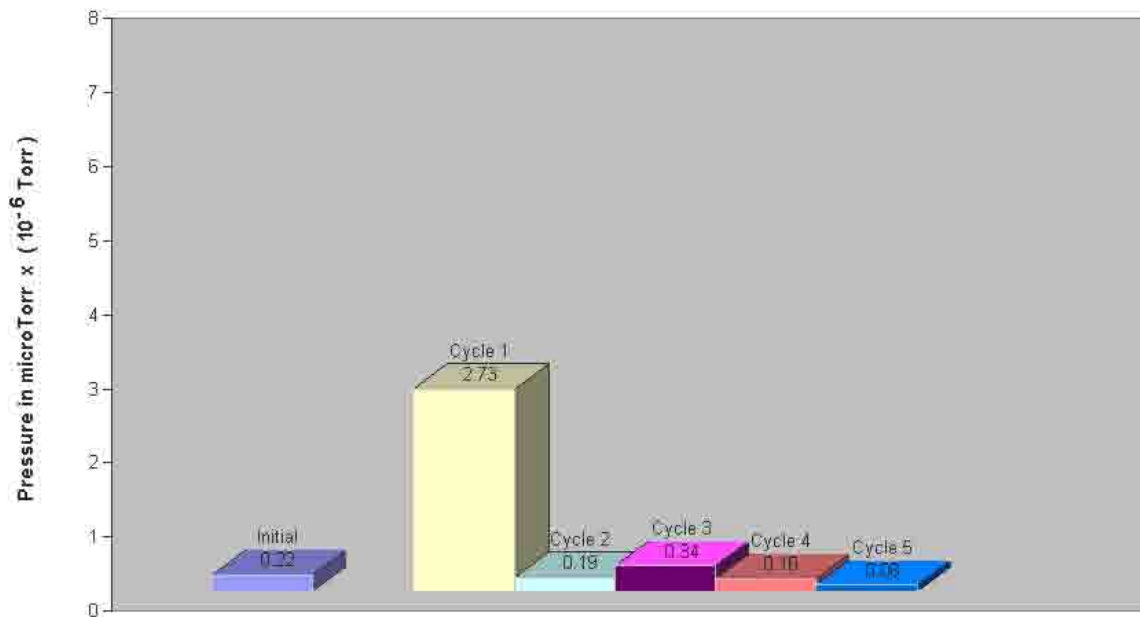
Figure 4.b: Partial Pressure of water in the Teney vacuum chamber after each heating cycle. Recorded pressures were obtained after the arrays cooled back down to 11 deg. Celsius.

Arc Thresholds Vertical Chamber, Sample #62
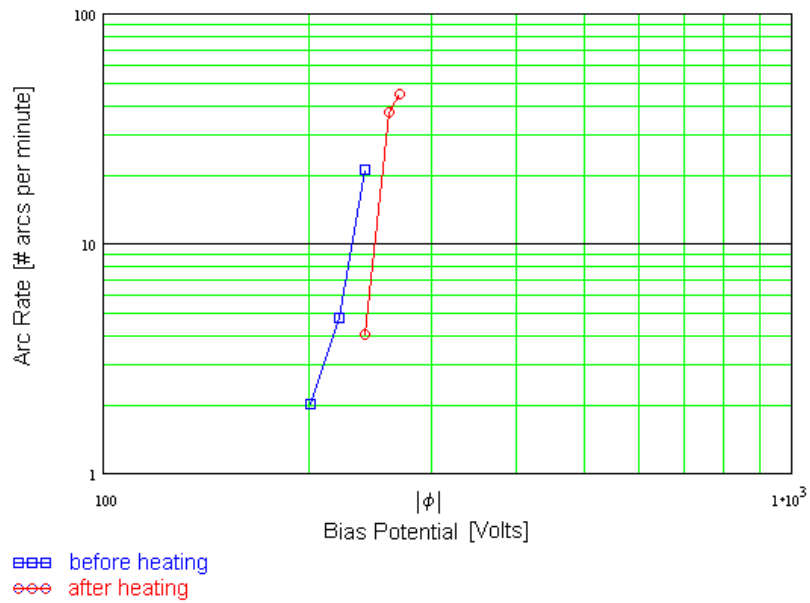
Figure (5.a): Arc inception voltage before and after 3 heating cycles

Arc Thresholds Teney Chamber, Sample #62
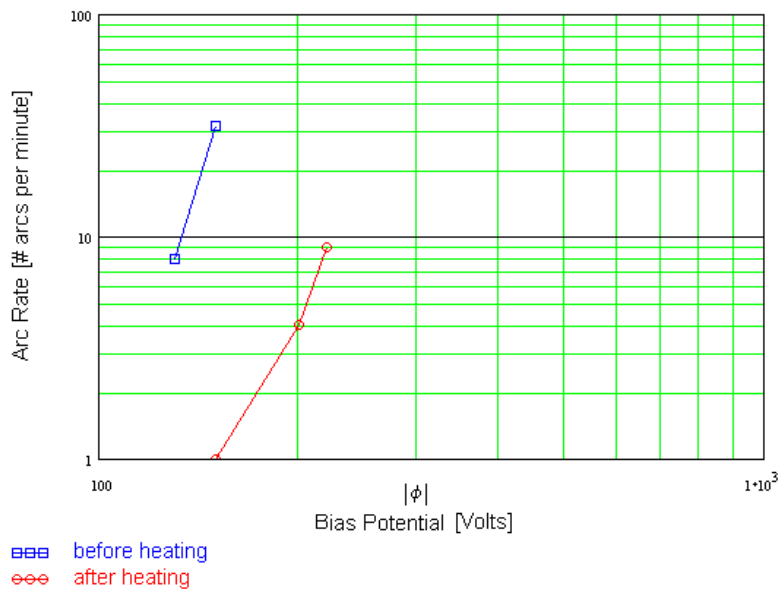
Figure (5.b): Arc inception voltage before and after 5 heating cycles

Arc Thresholds Vertical Chamber, Sample #63

Arc Rates in Vertical Tank, Sample 63

before heating
after heating
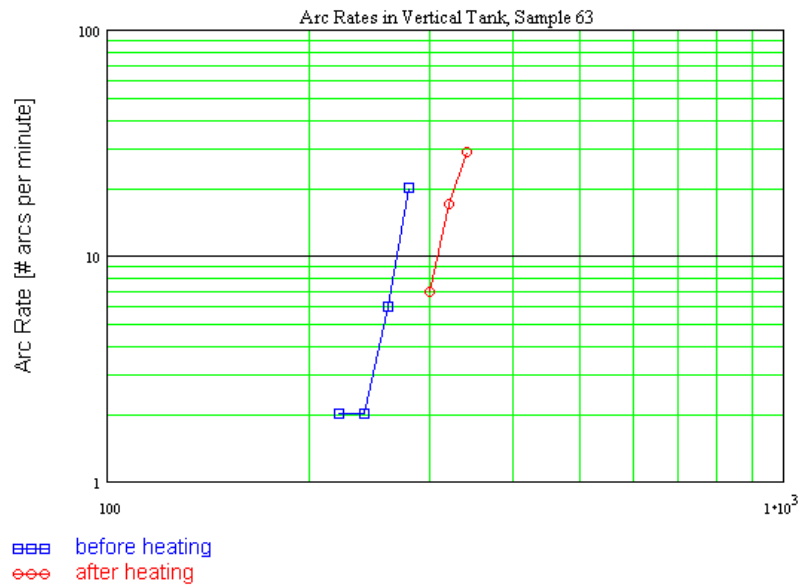
Figure (5.c): **Arc inception voltage before and after 3 heating cycles**

Arc Thresholds Teney Chamber, Sample #63

before heating
after heating
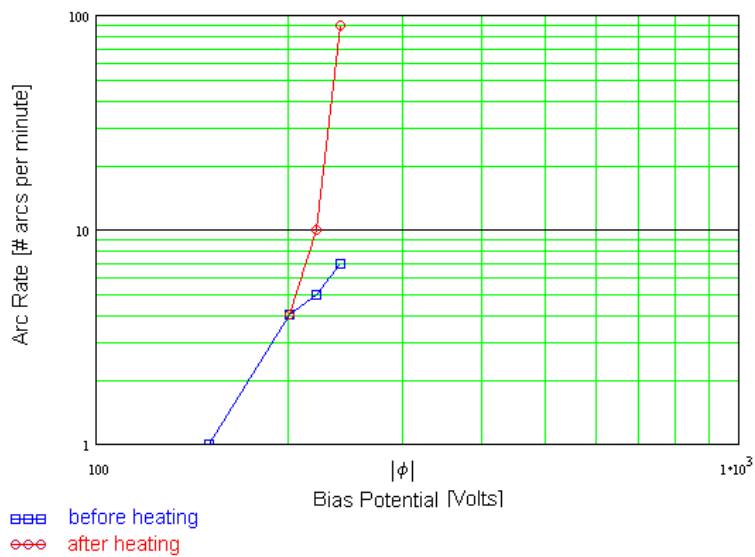
Figure (5.d): **Arc inception voltage before and after 5 heating cycles**

References

1. B. Vayner, J. Galofaro and D. Ferguson, "Interactions of High Voltage Solar Arrays with their Physical Environment: Physical Processes", Journal of Spacecraft and Rockets Volume TBD.

2. J. Galofaro, B. Vayner, and D. Ferguson "Daytime Solar Heating of Photovoltaic Arrays in a Low Density Plasma's", 34th Plasma dynamics and Lasers Conference, June 23-26, 2003 Orlando, Florida, AIAA 2003

3. B. Vayner, J. Galofaro, D. Ferguson, and W. Degroot "Conductor-Dielectric Junction in Low Density Plasma", 38th AIAA Aerospace Sciences Meeting and Exhibit, Jan 10-13, 2000 Reno, NV

4. B. Vayner, J. Galofaro, D. Ferguson, W. Degroot, L. Vayner, "Arcing Onset on a Solar Array Immersed in a Low Density Plasma", AIAA 2001-0400, 39th Aerospace Sciences Meeting & Exhibit, Jan 8-11, 2001 Reno, NV.

5. B. Vayner, J. Galofaro, and D. Ferguson "Arc Inception Mechanism ON A Solar Array Immersed IN A Low-Density Plasma", NASA/TM-2001-211070, June, 2001

6. J. Galofaro, B., Vayner, W. Degroot, D. Ferguson "The Role of Water Vapor and Dissociative Recombination Processes in Solar Array Arc Initiation" AIAA paper 2002-0938, 40th Aerospace Sciences Meeting and Exhibit, Jan. 14-17, 2002, Reno, Nevada.

7. Vayner, J. Galofaro, D. Ferguson and W. Degroot "Electrostatic Discharge Inception on a Height-Voltage Solar Array" AIAA Paper 2002-0631, 40th Aerospace Sciences Meeting and Exhibit, Jan. 14-17, 2002, Reno, Nevada.

8. J. Galofaro, B. Vayner, D. Ferguson and W. Degroot "A Desorbed Gas Molecular Ionization Mechanism for Arcing Onset in Solar Arrays Immersed in a Low-Density Plasma" AIAA Paper 2002-0938, 33rd Plasma dynamics and Lasers Conference, May 20-23, 2002, Maui, Hawaii.

9. B. Vayner, J. Galofaro and D. Ferguson "The Neutral Gas Desorption and Breakdown on a Metal-Dielectric Junction Immersed in a Plasma", Paper AIAA-2002-244, 33rd Plasma dynamics and Lasers Conference, Maui, Hawaii, May 20-23, 2002.

10. B. Vayner, J. Galofaro and D. Ferguson "Interactions of High Voltage Solar Arrays with their Physical Environment: Physical Processes, Journal article To Be Determined.

SPACE ENVIRONMENTS AND EFFECTS (SEE) PROGRAM: SPACECRAFT CHARGING TECHNOLOGY DEVELOPMENT ACTIVITIES

B. Kauffman
Space Environments and Effects Program
NASA Marshall Space Flight Center
Mail Code ED03
Huntsville, AL 35812
Phone: (256) 544-1418
Fax: (256) 544-8807
Email: billy.kauffman@nasa.gov

D. Hardage
J. Minor
NASA Marshall Space Flight Center

Abstract

Reducing size and weight of spacecraft, along with demanding increased performance capabilities, introduces many uncertainties in the engineering design community on how materials and spacecraft systems will perform in space. The engineering design community is forever behind on obtaining and developing new tools and guidelines to mitigate the harmful effects of the space environment. Adding to this complexity is the continued push to use Commercial-off-the-Shelf (COTS) microelectronics, potential usage of unproven technologies such as large solar sail structures and nuclear electric propulsion. In order to drive down these uncertainties, various programs are working together to avoid duplication, save what resources are available in this technical area and possess a focused agenda to insert these new developments into future mission designs. This paper will introduce the SEE Program, briefly discuss past and currently sponsored spacecraft charging activities and possible future endeavors.

Introduction

The Space Environments and Effects (SEE) Program was formed by the National Aeronautics and Space Administration (NASA) in 1993 to support the growing need for the development and maintenance of a preeminent program in space environments and effects technology. This initiative is intended to provide a coordinated national focus for innovative technology development to support design, development, and operation of spacecraft systems that will accommodate or mitigate effects due to the presence of the space environment. The program is unique in that it was initiated as a customer-driven and product-oriented endeavor. Considerable effort was made to ensure that the potential industry, academia, and government agency users of the products were consulted and made an integral part of the program. Their assessment and prioritizing of future research needs for space environment definition and techniques for calculating the effects of the space environment on spacecraft systems forms the basis for the SEE Program's activities. This direct involvement of potential customers also ensures that the SEE Program sponsored research products are made available in a timely manner to those most concerned with the information, i.e. spacecraft designers and operators.

SEE Program Objectives and Goals

The objectives of the SEE Program are to collect, develop, and disseminate the SEE-related technologies required to design, manufacture, and operate more reliable, cost-effective spacecraft for the Government and commercial sectors. In order to satisfy these objectives, the SEE Program has developed the following goals:

Advocate technology development, flight experiments, and databases by creating and maintaining:

- Engineering environments definitions
- Up-to-date engineering focused models
- Environmental and materials databases
- Engineering design guidelines
- Flight/ground simulation/technical assessments
- Integrated assessment tools
- Simplified access to modeling and assessment tools

Maintain cutting edge expertise in SEE-related technologies by:

- Coordination with other agencies, industry, and academia
- The incorporation of technical experts and specialists
- Sustained awareness of state-of-the-art SEE technologies

Heighten the awareness of SEE significance and program capabilities through:

- Internet access
- Bulletin
- Displays
- Workshops
- Publications[1,2,3,4,5,6]

SEE Program Structure

While the SEE Program was established with NASA sponsorship, it was recognized from the start that the program's success would depend on its ability to interact with research activities of other agencies, industry, and academia. This interaction has now become one of the principal strengths of the SEE Program. The SEE Program focuses on bridging the gap between the science community and the engineering community by improving environment definitions and tools for spacecraft design and operations planning.[7]

SEE Program Organization
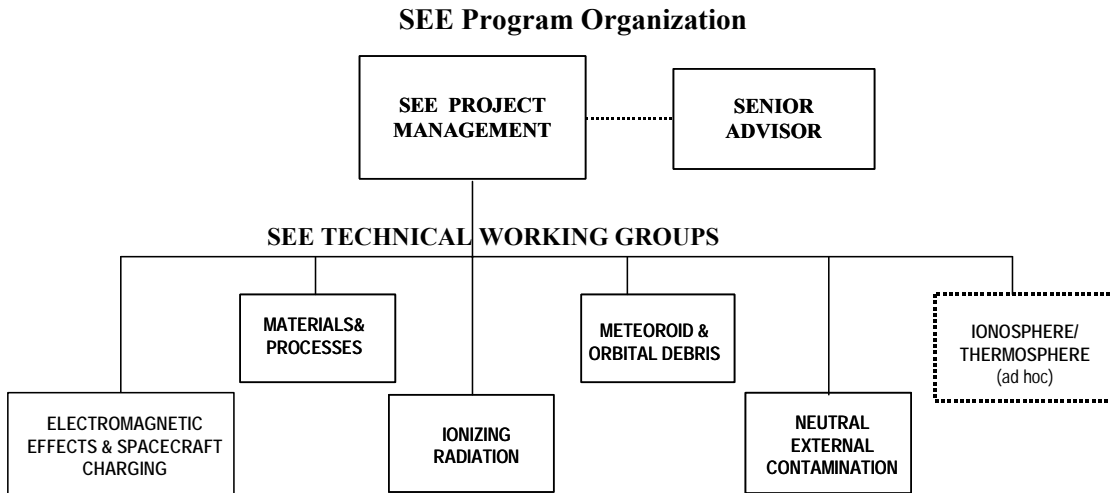
Figure 1. Space Environments and Effects Program Organization

    The Space Environments and Effects Program is organized (Figure 1) to facilitate the implementation of the Program's mission, which is directed toward research, development, verification, and transferring SEE-related technologies to the aerospace customers.[8]   While the program functions under the direction and oversight of the NASA Office of Aerospace & Technology Enterprise; Enabling Concepts and Technology Program at NASA Headquarters, the key to its ability to accomplish its mission is the Technical Working Groups (TWGs). These groups encompass the disciplines of electromagnetic effects & spacecraft charging, materials and processes, meteoroid and orbital debris, ionizing radiation, neutral contamination, and ionosphere and thermosphere (ad hoc). Their activities and responsibilities include: (1) ensuring communication with working group members, (2) coordinating development, evaluation, and maintenance of working group technical content and research areas, (3) coordinating research and development of new technologies and design issues that impact their respective space environmental areas, (4) coordinating development and use of engineering tools, models, and databases, and (5) coordinating development of spacecraft design and test techniques and methodologies for accommodating or mitigating space environment effects.

    The membership in the SEE Technical Working Groups is drawn from NASA, Department of Defense (DoD), National Oceanic and Atmospheric Administration (NOAA), industry, and academia.

    The six TWGs, as shown in Figure 1, are the Electromagnetic Effects & Spacecraft Charging, Ionizing Radiation, Materials & Processes, Meteoroid & Orbital Debris, Neutral External Contamination, Ionosphere and Thermosphere (ad hoc) Working Groups. Members of these groups direct and, in some cases, conduct studies and tests that meet a recognized need of the customer. The data from these studies are incorporated into databases, design guidelines, and/or models and provided to the customers.

Technology Development Activities

Since its inception in 1993, the SEE Program has released three separate NASA Research Announcements (NRAs) for technology development. To date, approximately fifty contracts have been awarded (not including direct funded contracts), using peer review, with the technical disciplines represented including all those encompassed by the SEE Technical Working Groups. Organizations receiving the contracts included industry, academia, and government agencies. The products of these contracted efforts from the 1994 and 1997 NRAs are now being realized and as the reports are received and processed, they are being distributed to the aerospace community through the SEE Program.[10] Results from two-year efforts from the 2001 NRA will become available in the spring of 2004.

Past SEE Program Funded Spacecraft Charging Activities

The following is a listing of activities pertaining to spacecraft charging that have been funded by the SEE Program. The list is intended to introduce and make one aware that a product exists. More information about each may be obtained by visiting the SEE Program website (given in the Conclusion section of this paper) or contacting someone in the SEE Program Office.

Title: Electronic Properties of Materials Applicable to Spacecraft Charging*
Organization: Utah State University
Principal Investigator: J.R. Dennison
Objective: Determine the electrical properties for a wide array of spacecraft materials and integrate this new information into relevant NASA databases and models. Specifically, measure secondary and backscattered electron total yields from electron-induced, ion-induced and photon-induced energies.

Title: Interactive Spacecraft Charging Handbook 3.01
Organization: SAIC (Formerly Maxwell Technologies)
Principal Investigator: Ira Katz
Objective: A browser-based, preliminary design spacecraft charging analysis tool with updated spacecraft charging models, updated design guidelines and analysis tools, including algorithms on deep dielectric charging, auroral charging and a 3-D modeling tool.

Title: Low-Earth Orbit (LEO) Spacecraft Charging Guidelines
Organization: NASA Glenn Research Center (GRC)
Principal Investigator: Dale Ferguson
Objective: Develop and publish a LEO spacecraft charging guideline and incorporate new test data as necessary.

* The SEE Program has been continuing this task and is currently testing new materials

Present SEE Program Funded Spacecraft Charging Activities

The following is a list of activities pertaining to spacecraft charging that are ongoing and being funded by the SEE Program. The list is intended to introduce and make one aware that an effort is underway and a product should be available in the future. More information about each may be obtained by visiting the SEE Program website (given in the Conclusion section of this paper) or contacting someone in the SEE Program Office.

Title: Electric Propulsion Interactions Code (EPIC): Integrated Guidelines and Tools for the Assessment of Electric Propulsion Impact on Spacecraft
Organization: Science Applications International Corporation (SAIC)
Principal Investigator: Myron Mandell
Objective: To enhance and combine existing plasma simulations codes into an integrated package, EPIC, to provide system designers with a tool for assessing electric propulsion spacecraft interactions.

Title: Measurement of Charge Storage Decay Time and Resistivity of Spacecraft Insulators
Organization: Utah State University
Principal Investigator: J.R. Dennison
Objective: Investigate the methods for measurement of charge storage and the magnitude of the effect in typical space applications through a combination of straightforward measurements and reference to existing theory on conduction in insulators. Specifically: (i) perfect methods and test protocols to study and quantify the effect, (ii) perform ground-based measurements of the effect in a limited number of controlled studies on near-term, ground-based measurement of the effect in a limited number of controlled studies on near-term missions and (iii) extend existing preliminary work to develop improved techniques so that a wider array of materials and their parameters can be efficiently tested in multiple-sample testing procedures.

Title: NASCAP-2K*
Organization: SAIC
Principal Investigator: Myron Mandell
Objective: A five year, collaborative effort with U.S. Air Force to develop a comprehensive revision to NASA's spacecraft charging analysis code. The code possesses new algorithms for LEO, GEO, polar orbits, deep-dielectric charging, radiation belts and interplanetary space. It also possesses a new interactive, object-oriented spacecraft design tool called Object Toolkit (OTk).

Title: L2 Charged Particle Environment Model and Extreme Event Case Studies
Organization: Jacobs Sverdrup
Principal Investigator: Joe Minow; Bill Blackwell
Objective: Develop a semi-empirical engineering model of electrons and ions (from a few 100's eV to approximately 1MeV) that include the thermal plasma distributions as well as bulk flow effects in the distant magnetotail.

* Co-funded with Hanscom AFRL

Title: Variability in LEO Plasma Environment
Organization: Jacobs Sverdrup
Principal Investigator: Joe Minow
Objective: Develop a model using a plasma variability database to specify statistical variations of plasma parameters (Ne, Te, Ni, Ti) in LEO environments (approximately 200 km to 2000 km).

Title: The "Charge Collector" – A Collection of Spacecraft Charging-Related Products
Organization: SEE Program
Principle Investigator: Multiple
Objective: A compilation of spacecraft charging-related products offered by NASA's SEE Program. The information contained was developed by various organizations of government, industry and academia, all under contract to the SEE Program. The type of information contained the Charge Collector includes databases, reports, tabulated data and design guidelines.

Past Living With a Star Program: Space Environment Testbeds Program Spacecraft Charging Funded Activities

The following is a listing of activities pertaining to spacecraft charging that were sponsored by NASA's Office of Space Science Living With a Star (LWS): Space Environment Testbeds (SET) Program. These activities were funded through the 2001 SEE Program NRA and were managed by the SEE Program. The list is intended to introduce and make one aware that an effort is close to completion or has been completed. More information about each may be obtained by visiting the SEE Program or SET Program websites.

Title: Characterization of Magnetospheric Spacecraft Charging Environments Using the LANL Magnetospheric Plasma Analyzer Data Set
Organization: Science Applications International Corporation (SAIC)
Principal Investigator: Victoria Davis
Objective: Spacecraft charging due to diurnal variations in the plasma environment produces spacecraft anomalies and failures. The current models of the plasma environment are not correlated to spacecraft charging events. This effort will identify those parameters that are important to spacecraft charging and allow for accurate predictive charging capabilities.

Title: Electrostatic Return of Contaminants
Organization: ROR Enterprises
Principal Investigator: Ray Rantanen
Objective: Develop a model capable of calculating the electrostatic return of spacecraft emitted molecules that are ionized and attracted back to the spacecraft by the spacecraft electric potential on its surfaces.

Title: Mining CRRES IDM Pulse and Environment Data
Organization: NASA Jet Propulsion Laboratory (JPL)
Principal Investigator: Robb Frederickson
Objective: Investigate IESD pulsing by insulators flown on the CRRES Spacecraft in relation to radiation-belt particle spectra.

Possible Future SEE Program Activities

The SEE Program is currently partnering with a new NASA Program, Jupiter Icy Moon Orbiter (JIMO), to develop 3D electric propulsion plume and integrated models. JIMO will possess unique, high energy, and multiple thruster plumes that introduce uncertainties and modeling requirements never experienced before. Currently, an effort is scheduled to begin in FY04 for multiple years and will leverage previous efforts (NASCAP-2K and EPIC).

The SEE Program is currently working with NASA HQs to determine if resources will be available for another SEE Program NRA to be released in FY04. If approved, several spacecraft charging topics will be solicited in this opportunity. Due to the sensitive nature, the areas of interest cannot be made available at this time. If FY04 resources cannot be secured, the SEE Program will delay the NRA and plan to release it in the 3rd quarter of FY04 using FY05 & FY06 resources.

Conclusion

Since 1993, NASA's Space Environments and Effects (SEE) Program has made significant progress towards updating and developing new products to mitigate spacecraft charging issues. As this paper illustrates, the SEE Program reflects an interagency and broad industry scope. The program also plays an important role as an advocate for space environments and effects related flight experiments. The program's success, however, depends upon the feedback from aerospace industry and government programs on their anticipated needs and the value of the program's products in their spacecraft systems development activities.

Those having interest in the SEE Program activities*, whether from opportunities for participation, information on products, or to contribute inputs on future spacecraft needs relative to space environment definition or effects of the space environment on spacecraft systems, are invited to visit the website homepage at *http://see.msfc.nasa.gov*.

Acknowledgements

The authors wish to acknowledge the contributions of Steve Pearson, Senior Advisor, at NASA's Marshall Space Flight Center.

* All non-U.S. citizens and foreign nationals living in the U.S. must obtain an International Agreement from NASA Headquarters to receive any products that have export control restrictions.

References

1.   Belk, C. A., J. H. Robinson, M. B. Alexander, W.J. Cooke, and S. D. Pavelitz (1997): "Meteoroids and Orbital Debris: Effects on Spacecraft." NASA Reference Publication 1408.

2.   Herr, J. L. and M. B. McCollum (1994): "Spacecraft Environments Interactions: Protecting Against the Effects of Spacecraft Charging." NASA Reference Publication 1354.

3.   Leach, R. D. and M. B. Alexander (1995): "Failures and Anomalies Attributed to Spacecraft Charging." NASA Reference Publication 1375.

4.   Vaughan, W. W., K. O. Niehuss, and M. B. Alexander (1996): "Spacecraft Environments Interactions: Solar Activity Effects on Spacecraft" NASA Reference Publication 1396.

5.   James, B. F, O. A. Norton, Jr., and M. B. Alexander (1994): "The Natural Space Environment: Effects on Spacecraft." NASA Reference Publication 1350.

6.   Bedingfield, K. L., R. D. Leach, and M. B. Alexander(Editor) (1996): "Spacecraft System Failures and Anomalies Attributed to the Natural Space Environment." NASA Reference Publication 1390.

7.   Pearson, S.D., B. Kauffman, S. Clifton and C. Upton, "Developing Tomorrow's Space Technology Today; NASA's Space Environments and Effects (SEE) Program," AIAA 96-4374, AIAA Space Programs and Technologies Conference, Huntsville, AL, September 24 – 26, 1996.

8.   Hayduk, R.J. and S.D. Pearson, "NASA's Space Environments and Effects Program Technology Development and Risk Mitigation for Spacecraft Design," IAF-97-I.3.03, 48th International Astronautical Congress, Turin, Italy, October 6 – 10, 1997.

9.   Pearson, S.D., K.S. Clifton and W.V. Vaughan, "NASA's Space Environments and Effects Program and Related Space-borne Experiments," AIAA 98-0294, 36th Aerospace Sciences Meeting and Exhibit, Reno, NV, January 12–15, 1998.

10.   Pearson, S.D., K.S. Clifton and W.V. Vaughan, "NASA's Space Environments and Effects Program and Related Space-borne Experiments," AIAA 98-0294, 36th Aerospace Sciences Meeting and Exhibit, Reno, NV, January 12 – 15, 1998.

SECONDARY ELECTRON EMISSION CAUSING POTENTIAL BARRIERS AROUND NEGATIVELY CHARGED SPACECRAFT

Eloy Sasot Samplón
Space Environments and Effects Section (ESA-ESTEC/TOS-EES)
Keplerlaan 1, 2200 AG Noordwijk, The Netherlands
Email: Eloy.Sasot@esa.int

Alain Hilgers
Benoit Thiébault
Space Environments and Effects Section (ESA-ESTEC/TOS-EES), The Netherlands

Vincent Génot
Centre d'Etudes Spatiales des Rayonnements (CNES-CNRS/CESR), France

Anders I. Eriksson
Swedish Institute of Space Physics (IRFU), Sweden

Abstract

Low-energy secondary electrons have been observed to be reflected back to the spacecraft during eclipse conditions. It has been argued that the presence of negative potential barriers can be caused by the secondary electron emission space charge and may play a role in the spacecraft charging process. The barriers turn back the low-energy spacecraft-emitted electrons and prevent the low-energy ambient electrons from reaching the detector. Two numerical methods previously presented by Whipple and by Parrot et al. in the literature have been used to study the effect of secondary electrons on potential barriers negatively charged spacecrafts. The former method provides an upper bound for the potential barriers when the sheath is large compared to spacecraft dimension. The latter one provides in principle the exact sheath profile subject to accurate integration of the density distribution over the energy. The application of the methods to data provided by the ATS6 and Freja spacecraft suggests that the high level negative charging is not due to barriers induced by secondary electron emission space charge.

Introduction

A key problem in plasma-body interaction studies is the self-consistent modelling of the plasma distribution in the electrostatic sheath. Numerous assumptions to tackle the problem in different ways have been set since the founder article by Mott-Smith and Langmuir [6]. The phenomenon is made even more complicated by the effect of secondary particles emitted at the body surface. This has been discussed by a number of authors (cf. e.g. Grard [4]). There has been evidence that under certain circumstances a potential barrier may be induced by the space charge due to an excess of secondary electron particles (cf. e.g. Whipple [10][11]). The electrostatic potential barrier has been suspected to play a role in high charging level. This has been invoked for ATS-6 spacecraft (cf. Whipple [10]) and more recently for the Freja spacecraft [2][9].

An example of a charging event observed on Freja spacecraft is shown on Figure 1 where the time series of the energy spectrograms of the ions (panel 1: Oxygen, panel 2: Helium and panel 3: Hydrogen) and of electrons (bottom panel) are shown. The pitch-angles of the ion

and electron detectors are shown respectively in panel 4 and 6. In panel 5 the integrated flux of electrons in a broad energy range is shown. The charging event can be monitored via the acceleration of ions seen for all species between 17:00 and 18:20 UT. Beyond 18:20 the spacecraft acceleration signature is unclear due to the overlap with other high energy ion phenomena probably of natural origin. When no energetic ions are seen one can observe the usual feature of ram ion flux with energy corresponding to the relative velocity of the spacecraft with respect to the plasma.
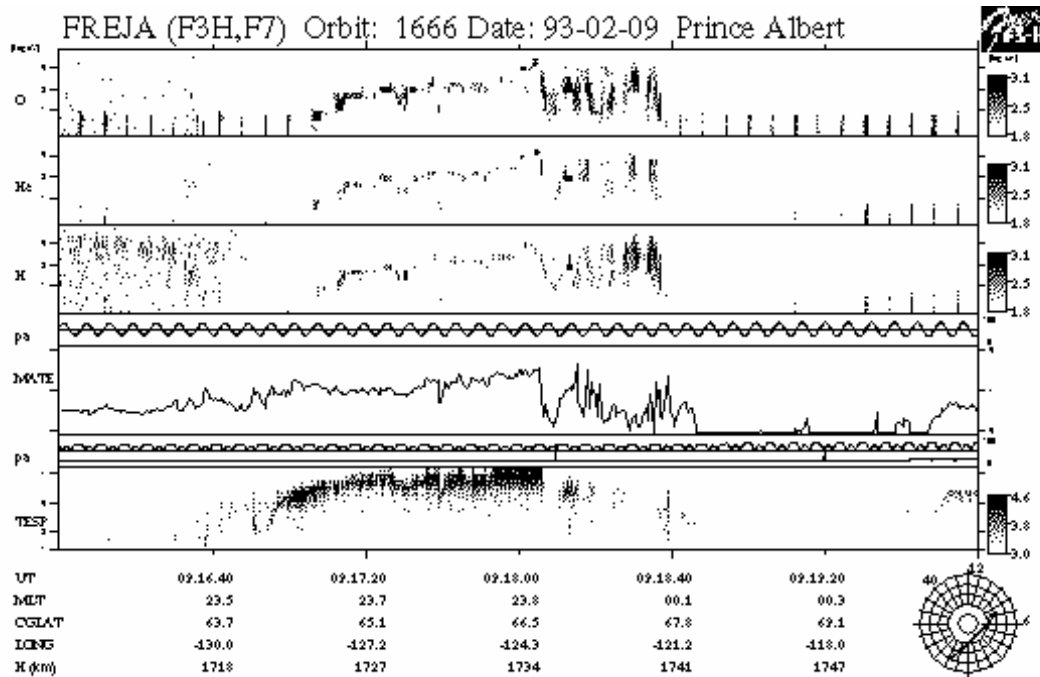
Figure 1. Time series plot of Freja particle measurements during a high level charging event [8].

Such a high charging level is relatively rare on Freja. The examination of 2 years of data (~7000 orbits) by Wahlund et al. [9] has identified about 170 charging events with negative potential below −10 V during auroral arc crossings. About 40 exhibited a potential lower than −100 V and 5 of the order of −1000 V.

The total distribution of the values of the potential for these events is shown in Figure 2 below. It must be noted that Freja manufacturers made use of material coating that are known to alleviate charging (especially ITO and cover glasses) therefore when −10 V was observed on Freja another spacecraft could have experienced a much more negative potential in the same environment.
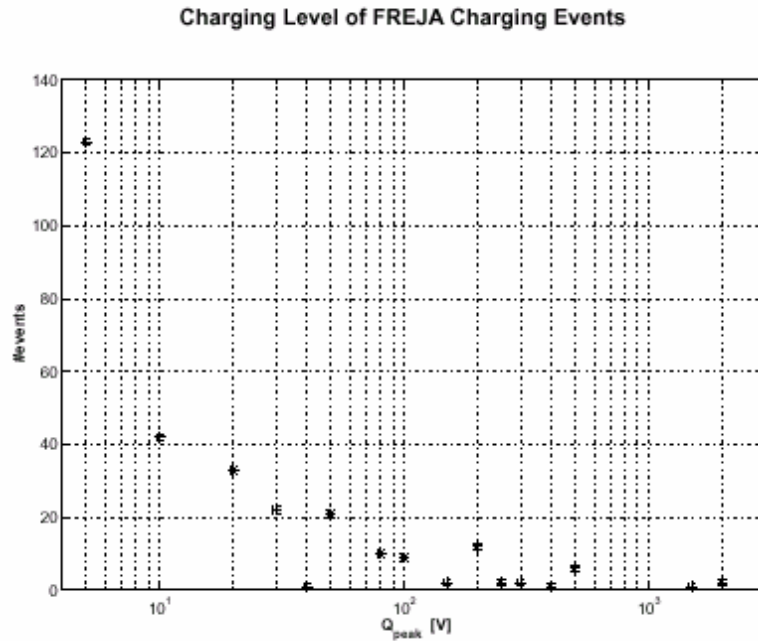
Figure 2. Distribution of observed charging events of Freja for potential below –10 V (from Wahlund et al. [9]).

An unresolved problem yet is how such very high level negative charging events are possible on Freja despite the presence of all the materials with high secondary electron emission yield which are grounded to the spacecraft structure. So far all attempts to reproduce this charging level taking into account the expected secondary electron emission have failed [2]. Three main effects have been proposed to block secondary electron emission and therefore reach high level negative charging: (1) the effect of the magnetic field parallel to electron-emissive surfaces, or the effect of a negative potential barrier either due to (2) differential charging or due to (3) the negative space charge of the secondary electrons. To check the influence of the first effect, a correlation of the level of charging with the angle of the spacecraft spin axis with respect to the ambient magnetic field had been sought but no correlation were found [9]. The second effect may occur will operate if significant surfaces with low secondary electron emission and low surface conductivity existed. However, the existence of such surfaces on Freja has not been identified yet [2]. The third effect which had not been investigated so far is the subject of the current study.

In this paper two methods for assessing the level of a potential barrier are used to investigate the applicability of such mechanism to Freja charging process. It is concluded that no significant space charge induced potential barriers may have played a role in Freja high level charging.

Methods of Barrier Level Assessment

In this paper one uses numerical approaches which have been developed in the past and published in the literature by Parrot et al. [7] and Whipple [10]. The unperturbed ambient plasma, composed of primary electrons, ions and secondary emitted electrons is assumed to be collisionless and Maxwellian. Plasma conditions are taken independent of time and not influenced by magnetic fields. Both methods solve the system of Vlasov-Poisson equations around a sphere equipotentially charged and therefore apply in principle to spherically symmetric problems.

The Vlasov-Poisson system of equations in spherical symmetry can be written as follows

$$V_i . \nabla f_i - q_i \nabla \Phi . \nabla_p f_i = 0$$

$$\Delta_R \Phi(R) = -\frac{\rho(R)}{\epsilon_0}$$

Where V is the particle velocity, f is the particle distribution function in speed, ρ is the particle density, Φ is the electrostatic potential, R is the radial distance, and Δ_R is the Laplacian in spherical coordinate for spherical symmetry. The density of various species is determined by counting particles accessible in each relevant phase and space domain. Two formulations have been proposed to count the particles: the Effective Potential and the Turning Point methods.

Effective Potential Method

The effective potential formulation (Bernstein and Rabinowitz [1]) has been used by Whipple [10] to analytically solve the Vlasov equation in the E-J^2 domain under the hypothesis of a very large Debye length compared to the spacecraft dimension. The particle counting in phase space is based on the fact that the energy E must be greater than the effective potential U for radial motion for the trajectories to exist:

$$E > U = q \cdot \phi + \frac{J^2}{2 \cdot m \cdot R^2}$$

Where U is the effective potential, ϕ is the electrostatic potential, q and m the charge and mass of the particle, R the distance from the probe and J the angular momentum of the particle. Particle densities at any point are given by an integral over velocities. Assuming spherical symmetry, they can be transformed into an integral over E and J^2. The result for secondary particles density n are, if Maxwelian distributions for both plasma and emitted electrons are assumed:

$$\frac{n}{n_0} = \frac{e^{\phi_S}}{2\pi^{1/2}x^2} \cdot \iint \frac{w \cdot e^{-E} \cdot dE \cdot dJ^2}{(E - \phi - J^2/x^2)^{1/2}}$$

Where n_0 is the nominal secondary particles density, x is the radial spatial variable (scaled to the satellite radius), ϕ_s is the satellite potential and w is a weight value which has the value unity in regions where only one-way trajectories are possible and has the value 2 in regions where particles from a given source can be going in both directions. The applicability of Maxwellian distribution for secondary electrons has been discussed by e.g., Grard [4].

Whipple [10] used the above equation with an approximation of the boundary of the particle trajectories (cf. Figure 3) in the E-J^2 domain. He developed a numerical scheme to find out an upper bound of the value of the potential barrier in a given plasma environment.
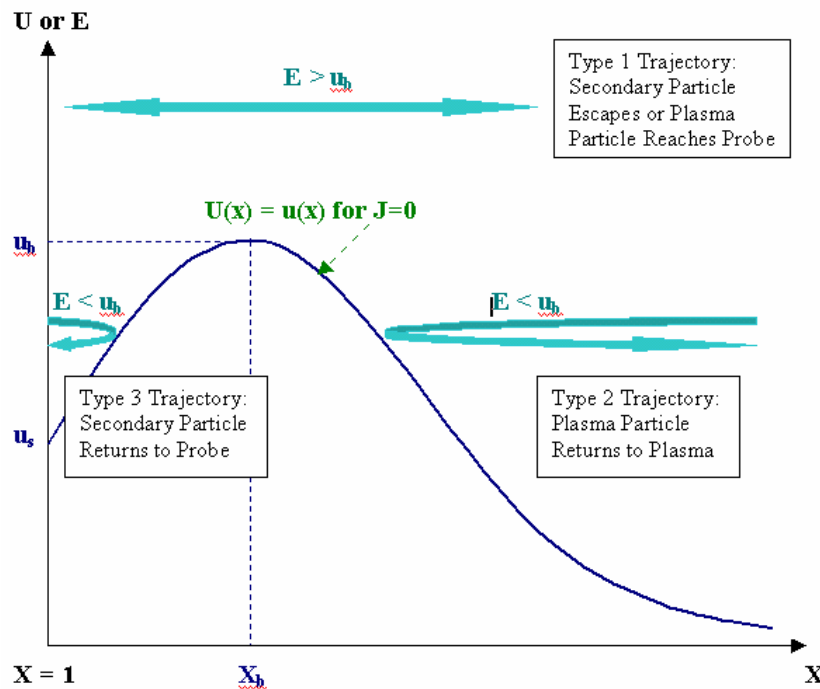
Figure 3. Orbit classification using the effective potential formulation

Turning Point Formulation Method

The turning point formulation described by Parrot et al. [7] and also by Thiébault et al. [8] is based upon the study of the possible particles orbits in the r-J^2 phase space to solve the Vlasov equation for a given potential profile. The Vlasov-Poisson system is then solved iteratively by under-relaxation.

This has been validated for the application of sheath modelling in presence of secondary electron by Thiébault et al. [8] by comparison with a 3D Particle-In-Cell (PIC) code developed by Forest et al. [3]. The main limitation of the turning point approach is that the full solution is obtained via a numerical integration over the particles energies which is very demanding in terms of computing time.

Application of the Turning Point Method to ATS-6

The effective potential method was further applied by Whipple to the ATS-6 satellite data for which a potential barrier had been observed thanks to the identification of a knee in the electron spectra [11]. The various plasma and potential values deduced from the ATS-6 satellite data by Whipple [10] for 4 events where potential barriers were identified are shown in Table 1.

Table 1. Plasma parameters derived from ATS-6 data by Whipple [10].

	Nph (p/cc)	Ne/Ni (p/cc)	Tph (eV)	Te (eV)	Ti (eV)	Vsat (V)	λe (m)	λph (m)
Day 198	10.3	0.2	4.9	65	7	-20	36.79	5.2
Day 199	90	1.2	2	32	10	0	9.59	1.1
Day 204	200	90	1.9	14.5	3.5	-2	1.08	0.73
Day 273	0.4	17	6	320	650	-2000	4.41	29.4

For each event three estimates of the potential barrier magnitude are available and are reported in Table 2 under the columns labelled **E**, **W**, and **P** which stand respectively for the **E**xperimental estimate of the potential barrier observed on ATS-6 data, an estimate of an **U**pper bound of the potential barrier based on the effective potential method, and the theoretical **P**rediction of the barrier based on the turning point formulation. In this table Vmin stands for the minimum of the potential while Vdiff is equal to Vsat-Vmin. The two first estimates were provided by Whipple [10] while the later one is provided by this study. An example of potential profile computed for day 204 is shown on Figure 4.

Table 2. Experimental, Upper bound and turning point method estimates.

Potential (V)	Day 198			Day 199			Day 204			Day 273		
	E	U	P	E	U	P	E	U	**P**	E	U	P
-Vsat	20			0			2			2000		
-Vmin	60	24.6	20	10	6.2	3.82	10	3.2	2.47	2050	2000	2000
Vdiff	40	4.6	0	10	6.2	3.82	8	1.2	0.47	50	0	0
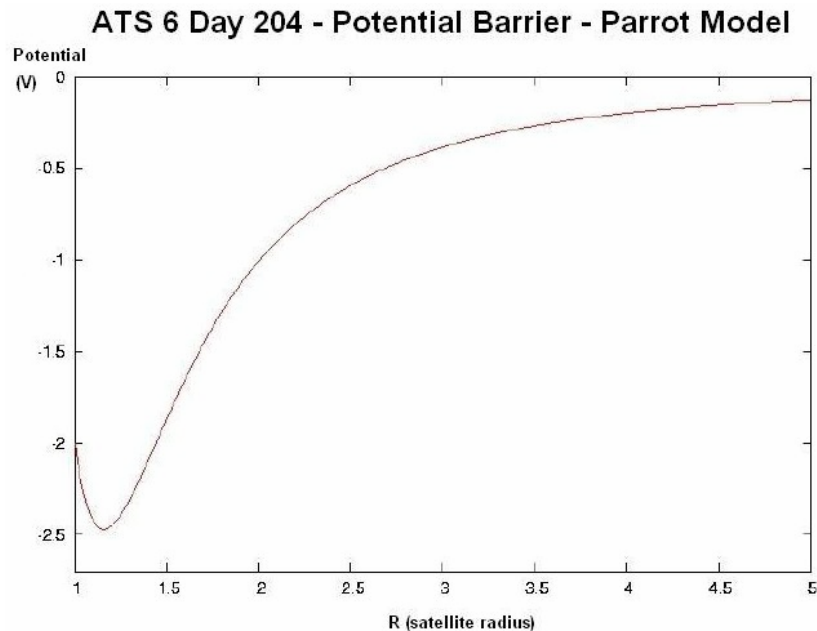
Figure 4. Potential barrier for ATS during the charging event of day 204 computed with the turning point method.

The upper bound and the exact prediction are consistent with each other. It can be noted that during day 198 the turning point formulation method even indicates that no potential barrier exists which is a significative refinement compared to the upper bound estimate

method. In all cases, however, the theoretical predictions and upper bound estimates are both significantly lower than the observed barrier. This is interpreted as an impossibility that the potential barrier actually observed is due to the secondary electron space charge.

Application to Freja Charging Events

Freja, which was on a low altitude polar orbit, encountered a somewhat different environment than ATS-6, which was on a geosynchonous orbit. The main difference during the charging events was especially the much higher background plasma density observed on Freja. The turning point formulation method and the upper bound estimate method have been used to derive an estimate of a possible potential barrier around Freja spacecraft during four well identified charging events. The environmental data and the spacecraft potential for each of these events have been derived from the data. The flux of secondary particle was chosen such as to remain in a realistic range but favouring the occurrence of negative electrostatic barrier. In all cases, no barrier could be found. A parametric study has been performed to find out the range of parameters for which barriers would occur on Freja. It was found that barrier would not occur for spacecraft potential lower than –7 Volts. We can therefore conclude that a secondary electron induced potential barrier is very unlikely to play a role in the process of high level charging observed on Freja.

Conclusion

The application of the turning point formulation to the modelling of electrostatic sheath has improved the prediction of secondary electrons induced potential barriers compared to previous studies. With this method the prediction made by Whipple of an upper bound of the expected secondary electron induced potential barrier has been refined. The conclusions of Whipple, however, remain unchanged. Applied to Freja, the turning point method shows that secondary electrons seem not to be causing potential barriers when the spacecraft is beyond a few volts negative in the polar region, where the density is relatively high (a few tens of particles per cc). Therefore, secondary electron induced potential barrier is unlikely to be involved in the building process of high level negative charging observed on Freja. Other aspects of the secondary electron emission process will have to be taken into account in order to explain the highly negative Freja charging events. This might still be due to differential charging effects although the reason for it is not understood yet. It must be also noted that certain characteristics of the secondary electron emission properties may not be well modelled yet and these could significantly affect the charging level too.

Acknowledgments

References

1.	Bernstein, I.B., and Rabinowitz, I.N.: "Theory of electrostatic probes in a low-density plasma", Phys. Fluids, 2, 112, 1959.

2.	Eriksson, A.I., Wedin, L., Wahlund, J-E, and Holback, B.: "Analysis of Freja Charging Events: Modelling of Freja Observations by Spacecraft Charging Codes", IRF Scientific report 252, January 1999.

3.	Forest J., Eliasson, L., Hilgers, A.: "A New Spacecraft Plasma Simulation Software, PicUp3D/SPIS", 7th Spacecraft Charging Technology Conference, Proceedings pp.515-520, ESA/SP-476, ISBN No 92-9092-745-3, ESA-ESTEC, Noordwijk, The Netherlands, 23-27 April 2001.

4.	Grard, R.J.L.: "Properties of the satellite photoelectron sheath derived from photoemission laboratory measurements", J. Geophys. Res., Vol.78, No.16, 2885, 1973.

5.	Hilgers, A., J.-E. Wahlund, L. Wedin, A. I. Eriksson, B. Holback and H. Koskinen, "Electrostatic Charging on Earth Polar Orbiting Spacecraft: Lessons Learned from Freja," ESA publication Preparing for the future, Vol. 9, No 3, December 1999.

6.	Mott-Smith, H.M., and Langmuir, I.: "The theory of collectors in gaseous discharges", Phys. Rev., 28, 727, 1926.

7.	Parrot M.J.M. Storey L.R.O. Parker L.W. Laframboise J.G.: "Theory of cylindrical and spherical Langmuir probes in the limit of vanishing Debye number", it Phys. Fluids, Vol. 25, No. 12, 2388-2400, 1982.

8.	Thiébault, B., Hilgers, A., Sasot, E., Forest, J., Génot, V., Escoubet, P.: "Investigation of Electrostatic Potential Barrier Near an Electron-Emitting Body", Proceedings of the 8th Spacecraft Charging Technology Conference, Huntsville, AL, October 20-24, 2003.

9.	Wahlund, J-E., L. J. Wedin, T. Carrozi, A. I. Eriksson, B. Holback, L. Andersson, H. Laakso, "Analysis of Freja Charging Events: Statistical Occurrence of Charging Events," ESA contract 11974/96/NL/JG(SC), WP 130 TECHNICAL NOTE (SPEE-WP130-TN), Version 2.0, Finish Meteorological Institute, Helsinki, February 22, 1999.

10.	Whipple, E.C. Jr.: "Theory of the Spherically Symmetric Photoelectron Sheath: A Thick Sheath Approximation and Comparison With the ATS 6 Observation of a Potential Barrier", J.Geophys. Res., Vol. 81, No. 4, 601-607, 1976a.

11.	Whipple, E.C. Jr.: "Observation of Photoelectrons and Secondary Electrons Reflected From a Potential Barrier in the Vicinity of ATS 6", J. Geophys. Res., Vol. 81, No. 4, 715-719, 1976b.

INVESTIGATION OF ELECTROSTATIC POTENTIAL BARRIER NEAR AN ELECTRON-EMITTING BODY

Benoît Thiébault
Space Environments and Effects Section (ESA-ESTEC/TOS-EES)
Keplerlaan 1, 2200 AG Noordwijk, The Netherlands
E-mail: Benoit.Thiebault@esa.int

Alain Hilgers
Eloy Sasot
Julien Forest
Space Environments and Effects Section (ESA-ESTEC/TOS-EES), The Netherlands

Vincent Génot
Centre d'Etudes Spatiales des Rayonnements (CNES-CNRS/CESR), France

Philippe Escoubet
Space Science Department (ESA-ESTEC), The Netherlands

Abstract

Electrons emitted on spacecraft surfaces can generate negative potential barriers. This may affect the equilibrium potential of the spacecraft, which can be driven more negative and jeopardise plasma measurements by repelling low energy particles. This phenomenon is investigated with the help of a numerical method based on the turning point formalism to classify orbits and which is validated with a PIC code. Comparison with spacecraft data in the magnetosphere is performed.

Introduction

Photoemission on spacecraft is an important issue for the operation of plasma detectors in space. Outside the ionosphere, the photoemission current may significantly influence the electrostatic potential of the spacecraft, which has been observed to be driven up to a few tens of volts positive [1]. Furthermore, detectors can be directly contaminated by photoelectrons emitted from sunlit surfaces and propagating toward the detector entrance [2][3][4][5].
Several authors have investigated in the past the possibility of the occurrence of electrostatic potential barrier due to the photoelectron space charge [2] [6] [7]. In this paper this issue is analysed with the help of a fully self-consistent numerical scheme presented by Parrot et al. [8]. Its application to the photoelectron sheath problem is validated by comparison with a particle in cell code (Forest et al, [10]). The model is then applied to the prediction of potential barriers around Geotail spacecraft. The results of this study predict a potential barrier located much closer to the spacecraft than indicated by earlier work.

Method

Thanks to the very long mean free path of the plasma particles and the short time scale to reach electrostatic equilibrium compared to change of the environment, collisions between particles and time dependence can be discarded. Furthermore, at the high altitudes relevant to the spacecraft considered in this paper, the magnetic field effects can be neglected. The sheath structure around the electron emitting body is therefore believed to be well described

by the Poisson-Vlasov system of equations with appropriate boundary conditions. The ambient plasma far away from the body and the photo-electron distribution at its source is assumed to be Maxwellian. Despite of the expected non-symmetry of the photo-electrons very close to the spacecraft it is assumed in the rest of the paper that their distribution, as well as the one of all plasma species are spherically symmetric.

With the above hypotheses, the Poisson-Vlasov system can be written as

$$\Delta_R \Phi(R) = -\frac{\rho(R)}{\epsilon_0}$$

$$V_i . \nabla f_i - q_i \nabla \Phi . \nabla_p f_i = 0$$

Where Φ is the electrostatic potential, R the radial distance, Δ_R is the Laplacian in spherical coordinate for spherical symmetry, ρ is the charge density, f_i is the density probability distribution function of species i.

The turning point method, extensively described by Parrot et al. [8], is based on the analysis of the possible particles orbits using the turning point formulation to simplify and solve the Vlasov equation of the distribution function in a given potential.

Each number density

$$N_i(R) = \iiint f_i(R, V) d^3 V_i$$

where V_i is the velocity, is calculated as a function of the radial distance and the potential distribution via the identification of the domain of accessibility in function of momentum l and energy ϵ using the orbit classification shown on Figure1.

It is then straightforward to obtain for the normalised density

$$n_i(r) = \frac{N_i(r)}{N_i^S}$$

the following dimensionless expressions [8]:

$$n_i(r) = \frac{2\alpha_i \cdot exp(\phi_i^S)}{\sqrt{\pi}} \int_0^\infty exp(-\epsilon_i) M_{n_i}(\epsilon_i) d\epsilon_i$$

$$\text{where} \qquad M_{n_i}(l_i^2) = \frac{1}{2r} \sqrt{g_i(r) - l_i^2}$$

$$g_i(r) = r^2(\epsilon_i - \phi_i)$$

$$\text{and} \qquad M_{n_i}(\epsilon_i) = \sum_j \xi_j \left[M_{n_i}(l_i^2) \right]_{(l_i^2)_{min\,j}}^{(l_i^2)_{max\,j}}$$
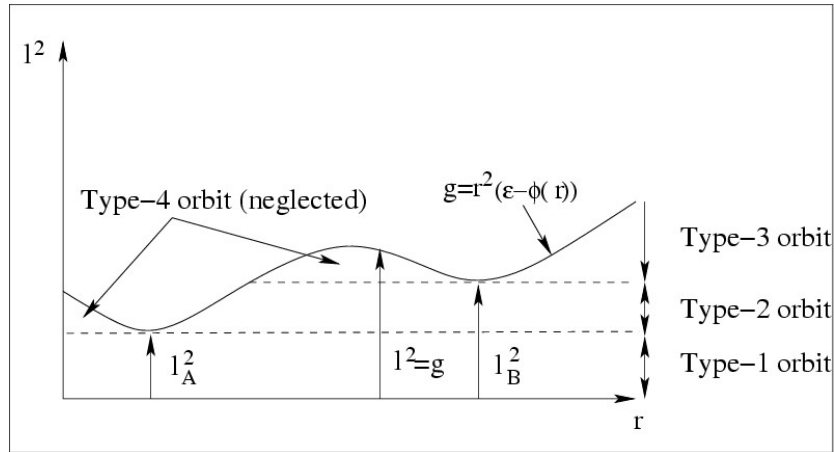
Figure 1. Orbit classification using the turning point formulation from Parrot et al. [8].

Once the density of each species is known one can compute the total electric charge and inject it in the Poisson equation, which is solved via a standard numerical scheme, e.g., Gauss-Seidel in one dimension. The solution to the Poisson-Vlasov system is then found iteratively using under-relaxation.

Test and Validation of the Method

To validate this method, two tests were performed. The first one is based on the comparison with the results obtained by Roussel [9] with the PIC code SILECS for a Langmuir probe in a dense Maxwellian plasma at rest without photoemission. The second test validates the photoelectron emission and propagation model with the use of the PIC simulation code, PicUp3D, developed by Forest et al. [10].

Comparison with SILECS

Roussel [9] computed the sheath structure for a Maxwellian plasma around a spacecraft without photo-emission which he validated by comparison of the density profiles with Laframboise results [11]. The corresponding potential profiles are shown in Figure 2 together with the potential profile predicted by the turning point formulation based method.
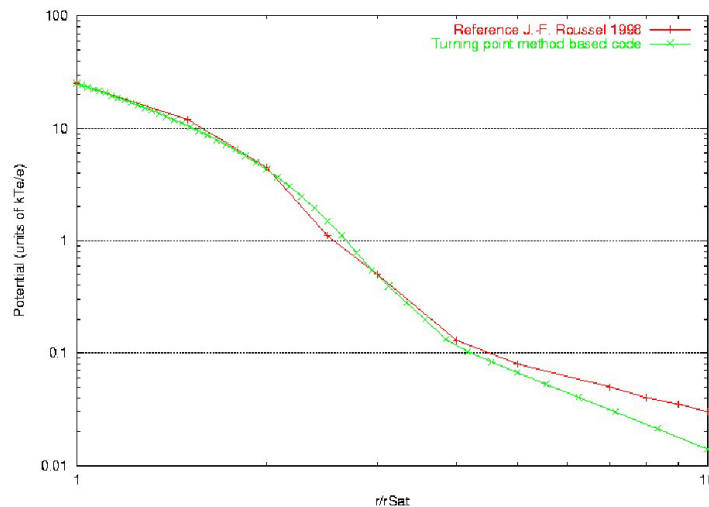
Figure 2. Comparison of the turning point method prediction with the results from [9]

The curves are in good agreement in the potential range above 0.1 k_BT_e/q_e.or distance beyond 4 spacecraft radii. At lower potential or higher distance the turning point method predicts a slightly lower potential up to 0.01 k_BT_e/q_e. It is not clear why such a discrepancy appears. It may be due to the difference of simulation box size and of the boundary conditions.

Comparison with PicUp3D

The PicUp3D [10] code is a simulation software dedicated to model spacecraft plasma interactions. It is an open source software written in java freely available on the web [12]. It is based on a 3D Particle-In-Cell (PIC) kinetic description of ions and electrons to simulate plasma dynamics. Several simulations have been performed for a Maxwellian plasma environment corresponding to a temperature of 1 eV for the ions and the electron and an electron density of 100 particles per cubic centimetre. With such a plasma, the Debye length is equal to 0.74 m, which is comparable to the size of the spacecraft. Therefore the PIC simulation can be made very accurate in a reasonable size computation box. The corresponding potential profiles are shown on Figure 3 below together with the profile computed with the turning point formulation based method.
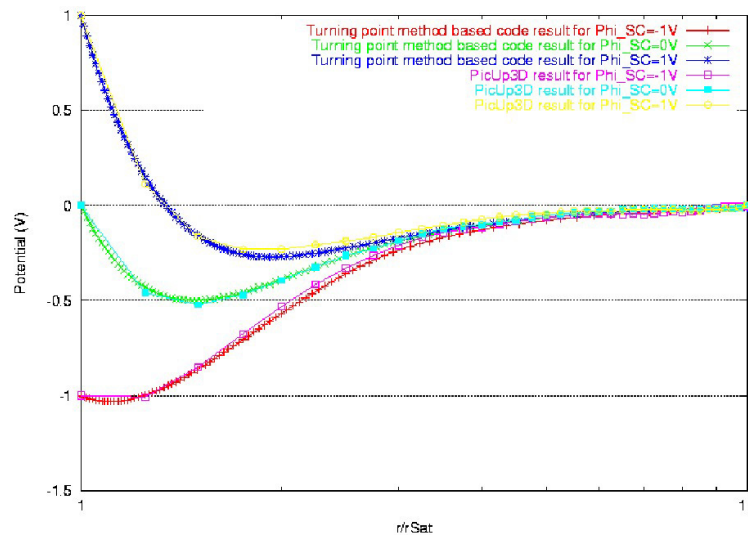
Figure 3. Comparison of the turning point formalism based method with simulations made with a PIC code for a small Debye length plasma.

The potential profiles shown on Figure 3 and computed with the two different methods are in very good agreement. Unlike the previously presented test, there is not even a discrepancy close to the edge of the simulation box, presumably because in the present test the same boundary conditions were used for both methods. This information is considered as a successful cross-validation test of the two methods especially for what regards their ability to simulate photo-electron expansion around a spacecraft.

Comparison with Geotail Data

Geotail observation

Zhao et al [7] have used the current balance equation to assess the value of the potential barrier around Geotail spacecraft:

$$J_{ph}(1+\Delta u)exp(-\Delta u)\frac{S}{4\pi R^2} = J_e\left(1+\frac{T_{ph}}{T_e}\Delta u\right)\cdot exp\left(-\frac{T_{ph}}{T_e}\Delta u\right)\cdot exp\left(-\frac{T_{ph}}{T_e}u_s\right)+\frac{I}{4\pi R^2}$$

Furthermore, they use a predefined and arbitrary parameterised potential profile to provide a barrier potential value and position. To this end Zhao et al. made the following hypotheses:

- o The spacecraft is modelled as a sphere;
- o The spherical symmetry applies on the potential and the plasma and photo-electron density;
- o The ion and electron temperature is 100 eV and the plasma density is 1 cm^{-3}

Predicted potential barrier with the turning point formulation

The turning point formulation based method was used to assess the characteristics of the potential barrier under the same set of hypotheses as used by Zhao et al. for the spacecraft and environment model. The results for the potential and the barrier locations are shown on Figures 4 and 5 below.
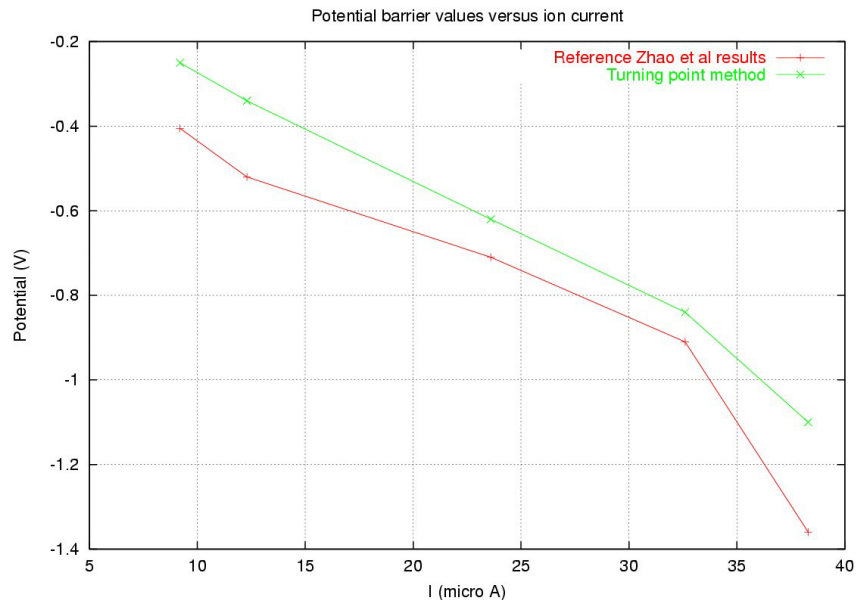
Figure 4. Minimum potential deduced from Geotail observation and computed by the turning point formulation based method as a function of the spacecraft potential.
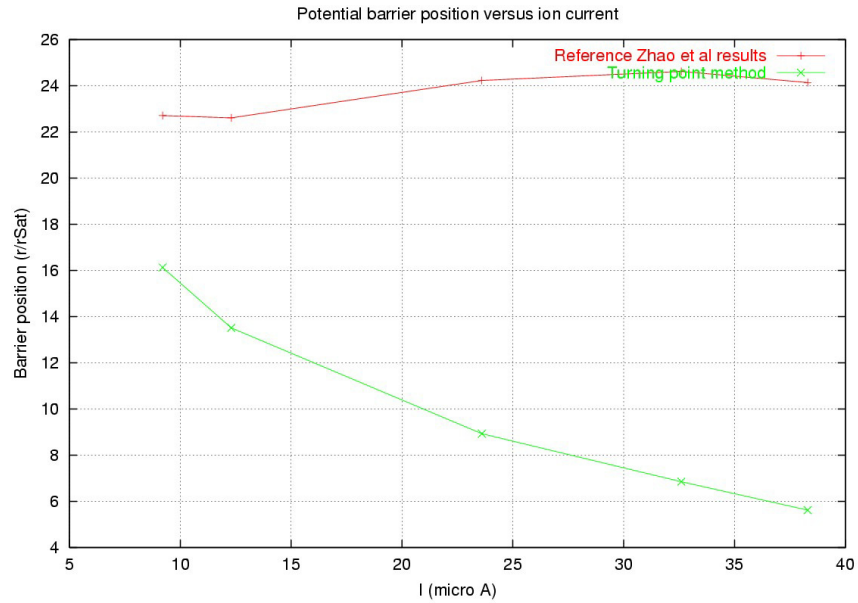
Figure 5. Location of the minimum of the potential deduced from the empirical technique of Zhao et al. and computed by the TPF based method as a function of the spacecraft potential

One can see that the potential profile computed by the two methods have the same shapes but differ by a constant value. It can be shown that the derivation of Zhao et al. actually is undefined within a constant value. We therefore conclude that our results on the potential are consistent with the ones of Zhao et al. The difference between the barrier location is more significant. It was explained by Zhao et al., that their assessment of the location of the barrier may be strongly depending on the actual hypothesis they have made for the a priori and arbitrary shape of the barrier. Our results confirmed this fact and suggest that the barrier location is actually closer to the spacecraft and its distance from the spacecraft decreases with decreasing potential unlike predicted by Zhao et al. [7].

Conclusion

The turning point formulation method presented by Parrot et al. [8] to model electrostatic sheath in spherical symmetry has been validated by comparison with two different PIC codes. It has been used for simulating photo-electron sheath in a large Debye length regime around a spherical body. The prediction of a potential barrier and of its magnitude is consistent with the results of Zhao et al. [7] based on the observations made on Geotail spacecraft. There is a discrepancy, however, for what regards the barrier location estimated on one hand by the analytical approach of Zhao et al. and on the other hand by the numerical model used in this study. Examination of Zhao et al.'s hypotheses leads to conclude that our predictions are less biased and therefore more realistic. We conclude that in the case of Geotail any potential barrier is located much closer to the spacecraft than it was predicted before and that its location decreases for decreasing potential. A main limitation of the applicability of the current study to a real case is the assumption of a spherical symmetry for the distribution of the photo-electrons cloud. This is currently under investigation with the help of 3D simulation codes and will be the subject of a forthcoming paper.

Acknowledgments

References

1. Pedersen, A., C. A. Cattel, C.-G. Faelthammar, V. Formisano, P.-A. Lindqvist, F. Mozer, and R. Torbert, Quasistatic electric field measurements with spherical double probes on the GEOS and ISEE satellites, Space Sci. Rev., 37, pp 269-312, 1984.

2. Guernsey, R.L., and Fu, J.H.M., Potential distribution surrounding a photoemitting plate in a dilute plasma, J. Geophys. Res., 75(16), 3193, 1970.

3. Wrenn G. and Heikkila, Photo-electrons emitted from ISIS Spacecraft, in Photon and particle interactions with surfaces in space, 221-230, 1973.

4. Szita, S., A. N. Fazakerley, P. J. Carter, A. M. James, P. Travnicek, G. Watson, M. Andre, A. Eriksson, and K. Torkar, Cluster PEACE observations of electrons of spacecraft origin, Ann. Geophys., 19, 1-10, 2001.

5. Hilgers, A. , Interaction between biased sunlit electron collectors in an infinite-Debye-length magnetoplasma: electron temperature threshold effect , J. Geophys. Res., 100, 5705-5713, 1995.

6. Whipple, E. C., Theory of the spherically symmetric photo-electron sheath: a thick sheath approximation and comparison with the ATS 6 observation of a potential barrier, J. Geophys. Res., 81, 601, 1976.

7. Zhao H., Schmidt R., Escoubet C.P., Torkar K., Riedler W., Self-consistent determination of the electrostatic potential barrier due to the photoelectron sheath near a spacecraft, Journal of geophysical research, Vol. 101, No. A7, 15,653--15659, 1996

8. Parrot M.J.M. Storey L.R.O. Parker L.W. Laframboise J.G., Theory of cylindrical and spherical Langmuir probes in the limit of vanishing Debye number, Phys. Fluids, Vol. 25, No. 12, 2388--2400, 1982.

9. Roussel J.-F., Spacecraft plasma environment and contamination simulation code: description and first tests, Journal of spacecraft and rockets, Vol. 35, No. 2, 205--211, 1998.

10. Forest J., L. Eliasson, A. Hilgers, A New Spacecraft Plasma Simulation Software, PicUp3D/SPIS, in proceedings of 7th Spacecraft Charging Technology Conference, pp.515-520, ESA/SP-476, ISBN No 92-9092-745-3, ESA-ESTEC, Noordwijk, The Netherlands, 23-27 April 2001.

11. Laframboise J.G., Theory of spherical and cylindrical Langmuir probes in a collisionless Maxwellian plasma at rest, Institute for aerospace studies, university of Toronto, 1966.

12. SPINE web site, http://www.spis.org

INSTRUMENTATION FOR STUDIES OF ELECTRON EMISSION AND CHARGING FROM INSULATORS

C.D. Thomson
Physics Department, Utah State University
SER 250 UMC 4415
Logan, UT, USA 84322-4415
Phone: 435.797.2936
Fax: 436.797.2492
E-mail: JR.Dennison@usu.edu

V. Zavyalov, J.R. Dennison
Physics Department, Utah State University

Abstract

Making measurements of electron emission properties of insulators is difficult since insulators can charge either negatively or positively under charge particle bombardment. In addition, high incident energies or high fluences can result in modification of a material's conductivity, bulk and surface charge profile, structural makeup through bond breaking and defect creation, and emission properties. We discuss here some of the charging difficulties associated with making insulator-yield measurements and review the methods used in previous studies of electron emission from insulators. We present work undertaken by our group to make consistent and accurate measurements of the electron/ion yield properties for numerous thin-film and thick insulator materials using innovative instrumentation and techniques. We also summarize some of the necessary instrumentation developed for this purpose including fast-response, low-noise, high-sensitivity ammeters; signal isolation and interface to standard computer data acquisition apparatus using opto-isolation, sample-and-hold, and boxcar integration techniques; computer control, automation and timing using Labview software; a multiple sample carousel; a pulsed, compact, low-energy, charge neutralization electron flood gun; and pulsed visible and UV light neutralization sources. This work is supported through funding from the NASA Space Environments and Effects Program and the NASA Graduate Research Fellowship Program.

Introduction: Absolute Electron Yield Measurements for Spacecraft Charging

A key contributor to the spacecraft charging process is electron-induced secondary electron (SE) emission. SE's are low-energy (<50 eV) electrons that are emitted from a material resulting from incident electron, ion, or photon bombardment. In order to predict the extent of spacecraft differential charging in modeling codes it is mandatory to accurately determine *absolute* SE yield parameters that include the maximum electron yield, δ_{max} and its corresponding energy, E_{max} as well as the first and second crossover energies, E_1 and E_2, at which the material transitions between positive and negative charging. Previous experimental studies have determined values for these parameters for some materials, but most measurements were taken in poor-quality vacuums, and were susceptible to contamination effects. Furthermore, most electron yield data has not been carefully referenced to accurate standards (Holliday, 1957). Furthermore, past

attempts to calibrate detector systems have only been partially successful. In all reviewed cases, second order corrections corresponding to absorption and scattering (within the detector apparatus) were neglected. Consequently, existing electron yield data that have been corrected against previous standards may be relatively correct, but the absolute accuracy remains uncertain.

A primary focus of the research at Utah State University (USU) has been the development of instrumentation and methods for measuring absolute total, SE, and back scattered electron (excited electrons with energies >50 eV, termed BSE) yields of numerous conductor and insulator materials to incorporate into the NASA/SEE Charge Collector material database (Dennison, 2002). For the last few years, measurements have been made on various conductor samples using a DC-measurement system that has involved continuous electron, ion, and photon sources along with sensitive slow-response ammeters used to measure electron currents. Improvements at USU described here include data acquisition in an ultra-high vacuum (UHV) environment for surface contamination control, and the utilization of a fully enclosing hemispherical grid detection system that has been calibrated (both through calculation and measurement) to account for detector losses. These corrections ensure the accuracy of our absolute yield measurements. A review of our recently extended capabilities to make insulator-yield measurements using pulsed electron-beam sources, in addition to optically isolated, fast-response sensitive electronics and various charge-neutralization techniques is given. Both the DC- and pulsed-yield setups are fully automated such that multiple measurements can be made in a short turn-around time. A complete description of the DC-system setup as well as the pulsed-system setup, along with additional insulator-yield and charging data is available in other works (Thomson, 2004; Nickles, 2002; Dennison, 2002).

This paper reports basic concepts, instrumentation, calibration and test results of both our DC- and pulsed- electron beam system to measure accurate SE and BSE yields of both insulators and conductors. Finally, validation of the pulsed-measurement system in comparison to the DC-measurement system will be shown along with pulsed-yield data on an anodized Al2219 alloy.

Overview of Insulators and Conductor Yield Measurements

Historically, SE and BSE yields have been measured by either using a sample biasing scheme (to either attract or repel SE's) or by using a retarding field grid (biased between 0 V and -50 V) detector. Of these two approaches, the grid/detector scheme is considered to be more accurate, although technically more complicated since all electron current entering or leaving the measuring apparatus needs to be accounted for (Nickles, 2002; Seiler, 1983). This often requires the utilization of several sensitive ammeters that can float independently. It has been well established that small changes in absolute magnitude of yield coefficients can have substantial effects on spacecraft potentials [Davies, 1997; Chang, 2000]. Hence, it is essential that our experimental investigations provide calibration of absolute electron yield measurements, with a target of ~5% accuracy.

Such measurements on conductors are straightforward since a constant electron current source can be utilized and DC-currents coming off of the sample can be measured using standard picoammeters. Additionally, by grounding the conductor sample, any charge that leaves or is

absorbed into the material can be immediately neutralized to ground. Electron yield measurements on dielectrics are more difficult to make than on conductors, since any charge that is deposited in the material cannot easily be dissipated. During measurements of electron emission properties of insulators, charge builds up near the sample surface because of low bulk and surface conductivity and lack of charge dissipation. The resulting sample potentials that develop can affect incident electron landing energies, and produce energy shifts of the emitted electrons, and consequently lead to significant errors in the measured SE and BSE yield measurements. To control insulator charging, pulsed-electron beams and neutralization sources are implemented.

An important phenomenon that limits the incident-electron pulse width and frequency practical for SE yield measurements on insulators is a surface potential buildup during the primary electron pulse. This potential is proportional to the total charge deposited on the insulator surface, which is directly related to the electron pulse duration and electron beam intensity, that is to total electron fluence. This implies a primary limitation on the pulse-measurement system design with regards to the speed and sensitivity of the ammeters used for detecting electron yield currents. Other limitations arise from the necessity to monitor low-level currents from several sources that are biased over a range of zero to hundreds of volts. The DC measurement scheme built at USU has proven to be one of the most accurate and versatile systems for the metrological absolute measurements of the emission properties of conducting materials. Based on this previous experience for conductive materials, a similar pulse measurement scheme for the insulating materials has been developed and tested.

General Experimental Setup

A simple schematic of the measurement setup is shown in Fig. 1. The sample is enclosed in the hemispherical detection apparatus, and an incident electron (or ion) beam enters into the assembly through a tubular aperture in the back of the detector housing. Sensitive ammeters are tied independently to the electron collector, biasing grid, sample, and sample stage to account for all incident and emitted electron current. The retarding grid can be biased negatively (or positively) to reject or pass electrons excited from the sample. Potentials on the suppression grid are controlled using a Keithley 230 voltage supply controlled via GPIB interfacing by a computer for both DC and pulsed-yield setups. The electron collector always remains at a +50 V bias (supplied by a standard power supply with the DC-yield setup and with batteries for the pulsed-yield setup) with respect to the retarding grid both to ensure that all electrons passing through the grid reach the collector, and also to ensure that any SE's emitted from the collector are returned to the collector. Total and BSE yields are directly measured by applying a 0 V or -50 V bias to the retarding grid, and then by taking the ratio of the collector current over the total incident current. The total incident current can be determined in three ways: i) by directly monitoring the electron gun emission current; ii) by measuring the total gun current using a Faraday cup; iii) or by simply summing the sample, grid, collector and stage currents. All three methods have been shown to produce results for the total incident current consistent to ~3 %; the third method is more expedient, and was therefore implemented most often.

Details of the USU surface analysis chamber are given in Dennison (2003). All measurements are performed in an UHV chamber pumped with turbomolecular and ionization

pumps to pressures ranging from 10^{-10} to 10^{-8} Torr (determined using ion gauges), depending on the sample data set. Ion gauges are turned off during measurements as they emit stray electron and ion current (fractions of nanoamperes) into the chamber. Hence, the gauges act as an agent for positive insulator charging, and also affect the yield measurements by introducing stray currents.
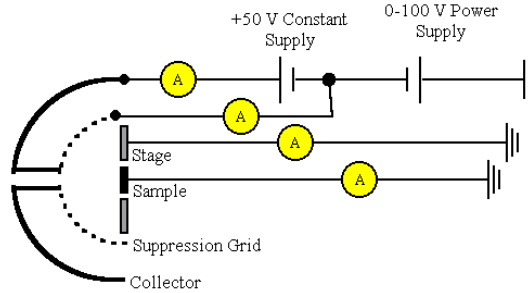
Figure 1. Basic schematic for DC- and pulsed- yield measurements. The incident electron beam enters through the detector aperture tube. Collector, retarding grid, sample, and stage currents are measured to calculate electron yields.

Two electron guns are available for making yield measurements: a low-energy gun (STAIB EK-5-S, energy range 50eV to 5 keV with pulsing capabilities from 1µs to continuous emission), and a high-energy gun (Kimball ERG-21, energy ranging from 4 keV to 30 keV, pulsing from 10 ns to continuous emission). Both guns provide beam currents ranging from 10-100 nA, with beam spot diameters ranging from 0.8 to 2 mm depending on the energy. Samples are placed on an 11-sample carousel that can be swung around to face the electron sources (Dennison, 2003). Thin-film conductor foils and insulator films are glued to 10.0 ± 0.1 mm diameter Oxygen Free High Conductivity (OFHC) copper cylinders using a UHV adhesive containing fine silver powder to provide electrical contact between the films and substrate.

DC-Yield Measurement System

Using the detector setup described above, electron yields are measured using the DC-setup shown in Fig. 2. Yields are then calculated as ratios of the emitted current to the total incident current. For total yield measurements, the grid bias is set to 0 V, and are calculated in terms of the collector, sample, stage and grid currents. BSE yields are measured and calculated in a similar manner, with the grid potential at -50 V. Yield equations are then

$$\sigma = \frac{I_{Collector}}{I_{Incident}} = \frac{I_{Collector}}{I_{Collector} + I_{Sample} + I_{Stage} + I_{Grid}(0V)} \quad \text{and}$$

$$\eta = \frac{I_{Collector}}{I_{Collector} + I_{Sample} + I_{Stage} + I_{Grid}(-50V)}$$

Finally, SE yields are calculated as the difference between the BSE and SE yields as $\delta = \sigma - \eta$.

To achieve our goal of 5% accuracy in yield measurements, a retarding field energy analyzer and direct current measurement using electrometers have been used by us and other investigators (Nickles, 2002), rather than more precise or sensitive energy analyzers or detectors. However, accurate absolute yield measurements using such grid analyzers require corrections for scattering off the grids and other detector surfaces and for other geometrical factors. Spherical or hemispherical retarding grids are most common, as their radial electrostatic fields provide better energy resolution. Corrections for spherical grids that fully surround the sample are much simpler to determine than those for hemispherical grids (Sternglass, 1953; Jonker, 1951). However, we have used hemispherical grids to facilitate use of a sample carousel for increased sample throughput (Nickles, 2002).
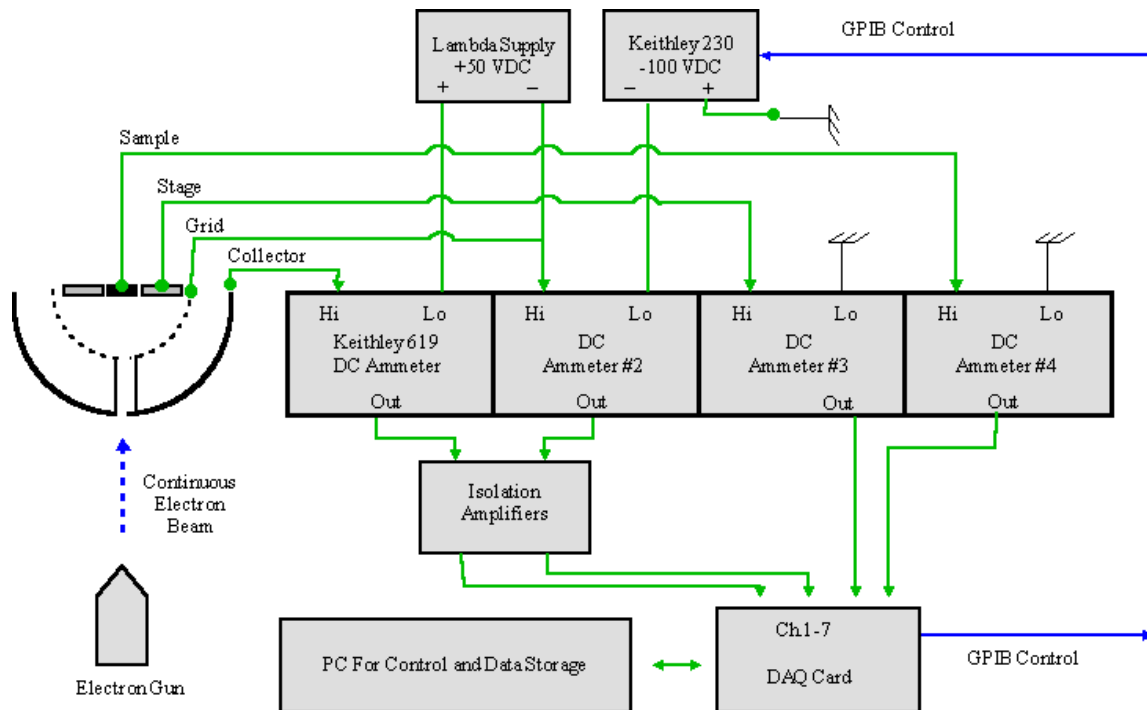
Figure 2. DC-yield measurement block diagram for conductors.

We have arrived at a consistent set of correction factors with <5% uncertainty for the various types of measurements performed using the USU detector. Determination of the correction factor values was based on consideration of: (i) numerous calibration measurements; (ii) detailed numerical modeling of the grid corrections for our apparatus; and (iii) comparison with previous yield measurements by other investigators, where available. Validation experiments and comparison with prior studies of SE, BSE and ion yields were made for polycrystalline Au samples, because Au has been studied extensively and is relatively free of contamination effects due to its inert nature. Uncertainties in the calibration measurements and modeling of the grid corrections were all at about the 5% level, consistent with our target objective for accuracy of absolute yield measurements.

A complete discussion of grid correction calculations for our detector for total yield, BSE yield, SE yield, ion yield, and photoyield are presented elsewhere (Nickles, 2002; Thomson, 2004). The largest grid correction is the opacity of the grids, accounting for ~75% of the full correction factor. Smaller "blocking" corrections of ~5%, based solely on the geometry of the detector, account for electrons not reaching the collector due to less than 10% of the solid half-sphere not subtended by the grids. This includes electrons lost out the electron beam incidence aperture and electrons that hit the beam tube or other detector surfaces before reaching the collector. The third largest correction is for BSE reflected from the collector. Coating the collector with colloidal graphite that has a particularly low BS yield of 0.07 [Sternglass, 1953] is a standard method used to reduce this correction; in our case it is reduced to a ~4% correction. Note that essentially all SE leaving the collector are returned to the collector because the retarding grid is always held at –50 V with respect to the collector. Also note that many high emission angle BSE have trajectories that return them to the collector before reaching the retarding grid. Additional smaller correction terms involve multiple SE or BSE scatter.

Overview of the Pulsed-Yield Setup

Although a completely independent measuring circuit was used for pulsed-yield measurements (see Fig. 3) the basic block diagram is much the same as for the DC-measurements (see Fig. 2). However, optically isolated fast (1-2 µs rise time) sensitive/low noise (10^7 V/A / 100 pA noise level) ammeters were developed to measure electron emission bursts that were emitted from the sample and detecting surfaces, and are described in more detail below. Careful shielding and grounding schemes were used to eliminate electromagnetic and power-line noise to the signals.

For pulsed measurements, a digital TTL signal from the computer DAQ card was used to activate a timing circuit that delivered a simultaneous trigger to both a pulse generator and signal-integrator circuits. Upon receiving this trigger, the pulse generator delivered a 5 µs square-wave firing pulse (100 ns rise time) to the electron gun. Total and BSE current pulses from the sample, stage, retarding grid, and collector were measured with the fast-response ammeter circuits described below. Typical emitted pulses are shown in Fig. 4 for the sample and collector. These pulses were integrated using either the integrator circuits or by storing the waveforms to a 500 MHz LeCroy digital storage oscilloscope and then exporting the data to a computer for further analysis. Both data acquisition and analysis were fully automated using Labview 5.0. After signal integration was performed, yields were calculated similar to the DC setup by taking the ratios of the emitted charge to the total incident charge as:

$$\sigma = \frac{Q_{Collector}}{Q_{Incident}} = \frac{\int I_{Collector}dt}{\int I_{Collector}dt + \int I_{Sample}dt + \int I_{Stage}dt + \int I_{Grid}(0V)dt} \quad ,$$

$$\eta = \frac{Q_{Collector}(>50V)}{Q_{Incident}} = \frac{\int I_{Collector}dt}{\int I_{Collector}(>50V)dt + \int I_{Sample}dt + \int I_{Stage}dt + \int I_{Grid}(-50V)dt} \quad \text{and}$$

$$\delta = \sigma - \eta$$
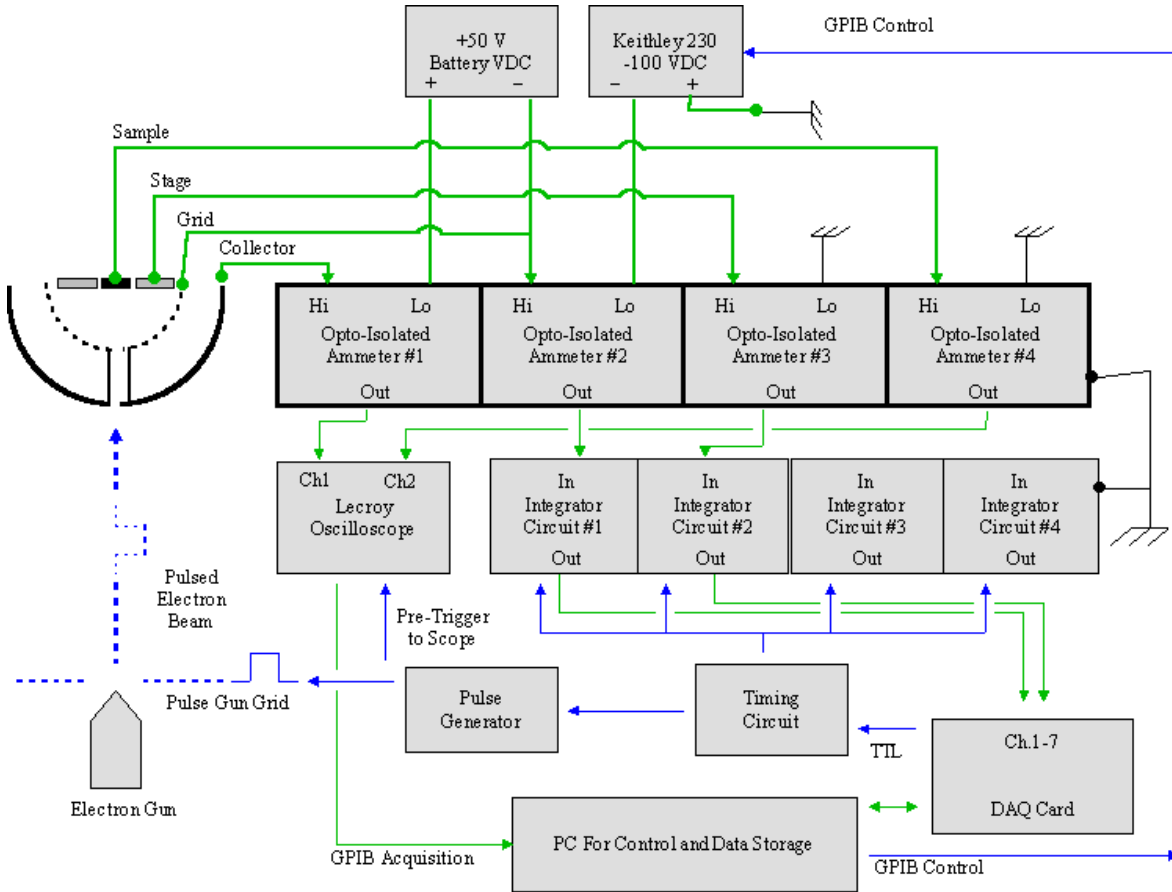
Figure 3. Pulsed-yield measurement block diagram for insulators.

Details of the Pulsing Circuitry

Most commercially available picoammeters have a low frequency bandwidth and are designed for current measurements with respect to the ground, and cannot be used for floating current measurements. To protect a data acquisition system from high floating voltages, and to avoid galvanic coupling between measurement and data acquisition circuitry, isolation amplifiers are needed as an interface between the input current detectors and the output voltage signals of the data acquisition system. Isolation amplifiers also reject large common-mode signals appearing at the input, and dampen ground loops since the inputs and outputs are floating relative to each other. For low current, low-noise, and wide frequency bandwidth floating current measurements, optically coupled isolation amplifiers are favored against modular devices using transformer-coupled modulation-demodulation. Optically coupled isolation amplifiers have the advantage of smaller size, wider bandwidth and integrated circuit reliability. Also, they use a DC-analog modulation technique that steers clear of problems associated with electromagnetic interference and coupling that most inductively coupled isolation amplifiers exhibit.

The circuit schematic of the opto-isolated ammeter (Fig 5) is composed of three stages. The first stage is a current-to-voltage converter that is a classic transimpedance amplifier based on a
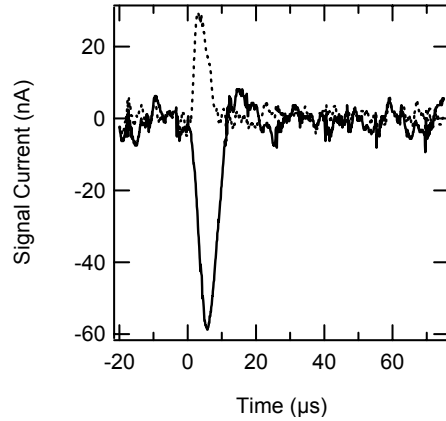
Figure 4. Measured sample (dot) and collector (solid) electron 5 µs, 50 nA pulses on Au at 800 eV. Similar pulsed signals were obtained for stage and grid surfaces. Delayed rise and fall times were caused by system capacitance and ammeter response times.

low-noise and low-leakage current OPA602BP DIFIT op amp. As a rule most of the noise is induced on the first transimpedance stage of the ammeter so that optimal design of this stage is crucial for the overall performance of the ammeter. The feedback resistor, R_f was selected as a compromise between sensitivity, low noise performance, and highest possible speed to fulfill the electron impulse magnitude and duration limitations discussed above. The signal-to noise (SNR) ratio of the transimpedance stage is SNR = 10 log(I_{in} R_f^2/ $2eB_f(1+R_f/R_s)^2$) where I_{in} is the input current (1-100 nA), R_f is the feedback resistance, B_f is the frequency bandwidth, and R_s is an effective current source resistance. It is seen that the higher the feedback resistance, the better the SNR. However, source C_s, feedback C_f, and input op amp, C_{in} capacitances slow down the time response of the transimpedance amplifier with time constants $\tau=R_fC_{in,s,f}$ and significantly limit the optimal value of the feedback resistor R_f. It is found that the ammeter frequency response for feedback resistor values R_f <100 MΩ is mostly defined by the input capacitance that is an order of 3-7 pF for most of the available op amps. Taking this into account, the optimal value for the feedback resistor was selected in a range of 10-100 kΩ that allows us to achieve good sensitivity in the nanoampere current region, and low-noise performance at the level of 2-5 pA/Hz$^{1/2}$, and a high frequency bandwidth of 200-400 kHz.

The second stage is a high linearity bipolar isolation amplifier with a gain of A_{op}=2 or 10, selectable by a switch on the front panel of the ammeter. A wide bandwidth (DC to >1 MHz) HCNR200 analog optocoupler, with a low nonlinearity of 0.01% and a stable transfer gain ($K_3=I_{pd1}/I_{pd2}$) was chosen for this stage. The stage transfers the voltage signal from the first transimpedance stage to the third amplifying stage through optical coupling. The optocouplers allow a large potential difference (~2.6 kV) between a common input ground and an output ground. Optical coupling is achieved through a light emitting diode (LED) with two matching photodiodes (PD1 and PD2) detecting optical signals from the same LED. Because of the unipolar nature of the LED, two optocouplers are combined together to provide bipolar optical coupling (see Fig. 5). Relatively small values of R_{in} and R_{11} (values recommended by the manufacture are typically >100 kΩ) are chosen to provide the optocouplers' wide frequency

band of ~1 MHz, given that the input and output time constants are defined primarily by the photodiode capacitance of $C_{pd} \sim 22$ pF as $\tau_{in}=C_{pd1}R_{in}$ and $\tau_{out}=C_{pd2}R_{11}$.

The third gain stage is composed of a standard inverting voltage amplifier, U7 with a gain of A=100. To provide amplification in a wide frequency bandwidth without any distortion of the signal detected by the first transimpedance stage, a low cost OP37GP op amp with a 63 Mhz frequency bandwidth was chosen for this stage as well as for optocoupler stages of the ammeter.

An overall output voltage of the 3 stage opto-isolated ammeter is thus defined as $V_{out}= T\ A_{op}$ $A= I_{in}R_f\ A_{op}\ A= I_{in}R_f\ K_3(R_{11}/R_{in})A \sim I_{in}R_f\ AR_{11}/R_{in}$ where T is the transimpedance stage gain, A_{op} is the opto-isolation amplifier gain, and A is the output stage gain. The overall gain may be selected by switches S1 (gain T) and S2 (gain A_{op}) on the ammeter front panel for a combined range of $2x10^6 - 1x10^8$ V/A (K_3=1 and A=100). The feedback potentiometer, R8, is used to set an overall amplifier gain to calibrate the ammeter, where $G=TA_{op}A$.
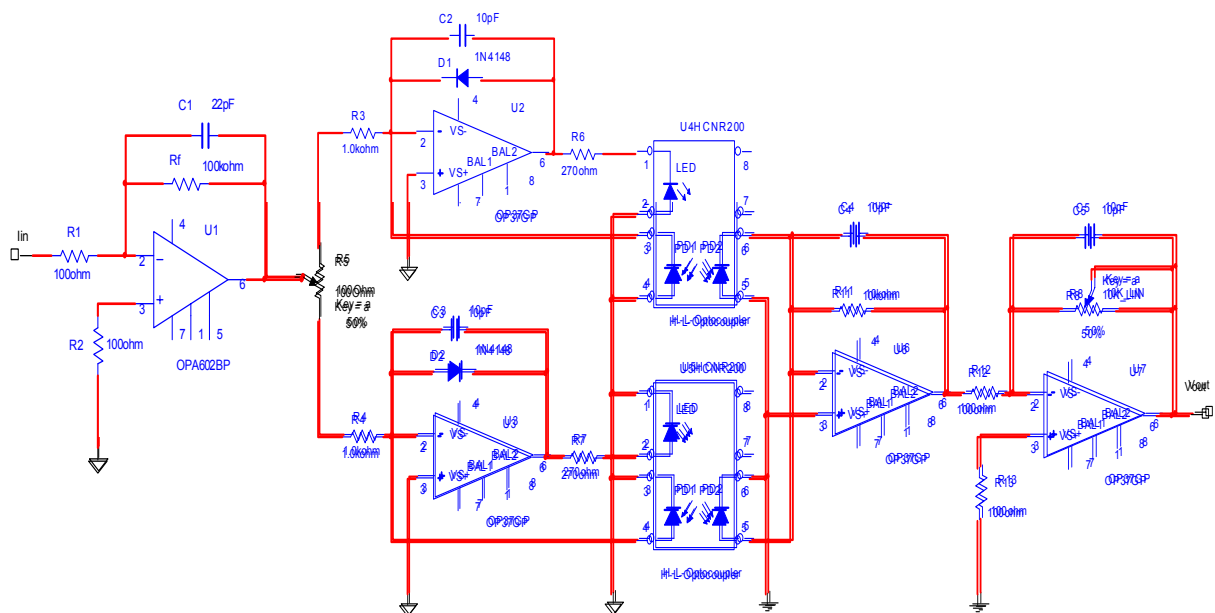
Figure 5. Circuit diagram of opto-isolated ammeter.
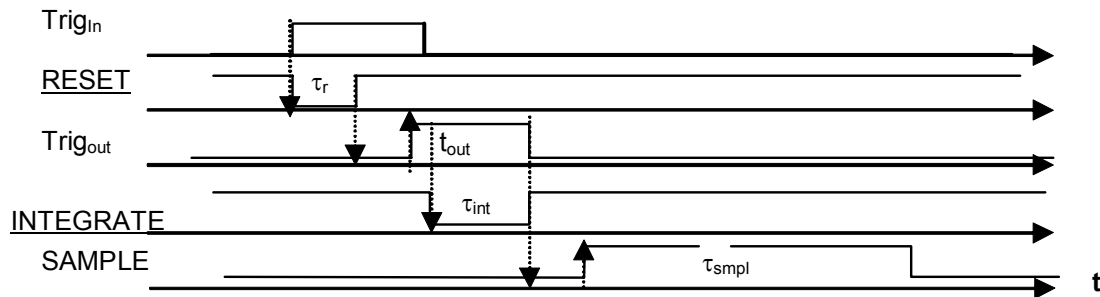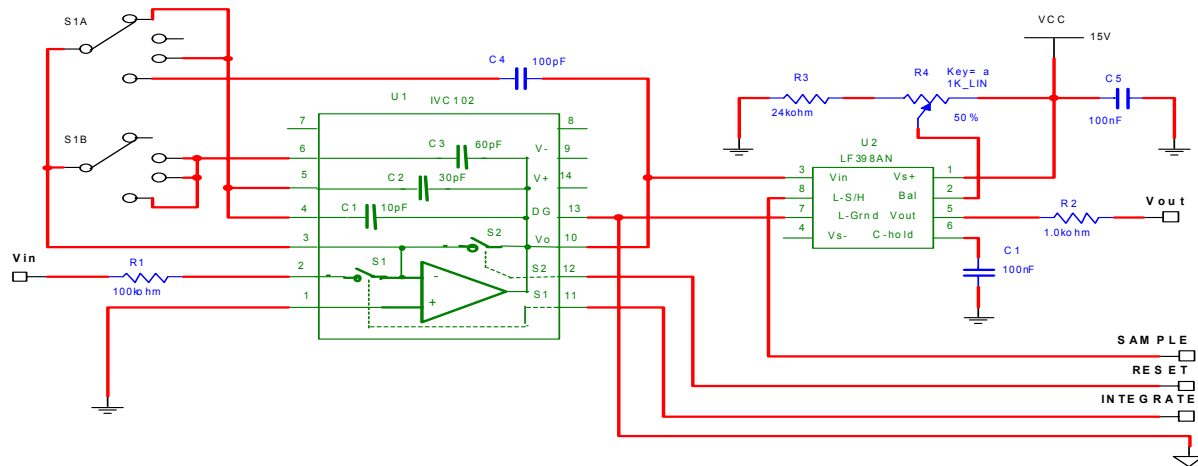
Figure 6. Circuit diagram of the switched integrator and timing diagram of the sample-and-hold circuitry.

To convert a short impulse voltage signal from the ammeter to the DC output voltage, which can then be recorded by the computer through a data acquisition board, a switched integrator is used. A circuit diagram of the integrator and sample-and-hold circuit is shown in Fig. 6. For the integrating stage, an IVC102 precision integrating amplifier was chosen. This amplifier is based on a low-bias current FET op amp with integrating capacitors (C_1-C_3), and low leakage FET switches (S_1 and S_2)—all integrated on the same chip. Since the complete circuit is on a single chip, the IVC102 eliminates many of the problems commonly encountered in discrete designs, such as leakage current errors, stray capacitance interference, voltage offset drift, and noise pickup. High quality metal-oxide internal capacitors with excellent dielectric characteristics provide high temperature stability and low nonlinearity of ~0.005% that is especially important for short integration times. TTL/CMOS-compatible timing inputs (switches S1 and S2) control the integration period, as well as hold and reset functions to set the effective transimpedance gain and reset (discharge) the integrator capacitor. The transfer function of the integrator is:

$$V_{out} = \frac{1}{T}\int_{t1}^{t2} V_{in}dt = \frac{1}{T}\int_{t1}^{t2} I_{in}(t)R_fGdt = \frac{R_fG}{T}\int_{t1}^{t2} I_{in}(t)dt$$

where $V_{in} = I_{in}(t)R_fG$ and V_{out} are input and output voltages of the integrator, $I_{in}(t)$ is a measured current at the ammeter input, R_f is the feedback resistor of the ammeter first transimpedance

stage, $\Delta t = t_2 - t_1$ is an integration time and $T = R_{int} C_{int}$ is the integrator time constant. The last integral is simply the charge measured for the time duration, Δt, so that the final expression is:

$$V_{out} = \frac{Q}{T} R_f G = (\Delta t/T) \, (I_{in} R_f G)$$

Note that the integration time, Δt, should be longer than or equal to the current impulse duration. The integration time and the integrator time constant may be set independently over a range of 4-100 µsec.

Finally, to control the proper operation of the switched integrator and sample-and-hold circuit, a simple digital pattern generator (not shown) is used. This generator creates TTL level digital signals to control the RESET, INTEGRATE, and SAMPLE switches at a rate controlled by the trigger signal $Trig_{In}$ from a computer. A timing diagram of these control impulses is shown in Fig. 6.

Neutralization Techniques

Methods for insulator charge neutralization included a low-energy electron flood gun source (energies <1 eV) mounted adjacent to the sample (see Fig. 7) in the sample block, separated (center of gun aperture to center of sample) by 11 mm. The gun extraction grid potential was switched from suppression to emission mode for a few seconds between each incident electron pulse to neutralize positive surface charging as described above. This process was self regulating in that once the positive insulator was neutralized, the low energy electrons were no longer attracted to the surface, and a steady state current corresponding to a near-zero surface potential was achieved. The amount of flood gun current drawn to the sample was dependent on the gun's filament current and extraction potential as well as the sample potential. To test the effectiveness of the flood gun, a gold sample was placed next to the gun. Sample current was monitored as the sample was biased to positive potentials ranging from 0-50 V for three different extraction potentials, while maintaining a constant filament current of 1.3 A as shown in Fig. 8. Each data set was fitted with an asymptotically approaching exponential function. At a sample potential of 0 V, the current drawn from the flood gun varied from 6-75 nA, depending on extraction potential. This indicated that operating the flood gun for 1 s would deliver 4-5 orders of magnitude more electron fluence to the sample surface than a typical 5 µs, 50 nA incident electron pulse containing $\sim 10^6$ electrons/pulse.

The effectiveness of the electron flood gun method remained questionable for eliminating negative surface charge or charge beneath the insulator surface. Either visible or UV light with energies of a fraction of the insulator bandgap (<10 eV) have been shown to stimulate photo-induced conductivity in materials such as Kapton[TM] and polyethylene, and thereby accelerate the discharging process (Bass, 1998; Levy, 1985). To assist in the neutralization of negative charge, a mercury-gas and tungsten-filament lamp were mounted next to a quartz view port with a focusing lens to irradiate the samples. Measured intensities of the focused beams at the sample faces were ~ 35 mW/cm^2. We found the electron flood gun to be the most effective tool for charge neutralization below 1 keV, based on yield-repeatability measurements. Preliminary discharging measurements on a chromic-anodized Al2219 alloy using the flood gun, mercury, and tungsten lamps are discussed elsewhere (Thomson, 2003).
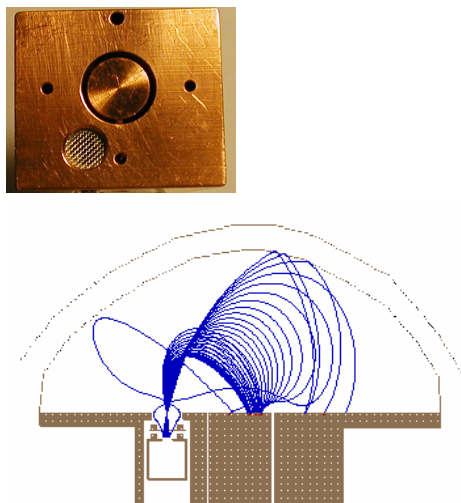
Figure 7. An electron flood gun sits adjacent to insulator samples and neutralizes positive surface charge. Top: a picture of the flood gun and sample. Bottom: a SIMION simulation of the flood gun inside the detector cavity next to a positively charged sample at +0.5 V and retarding grid at -1 V
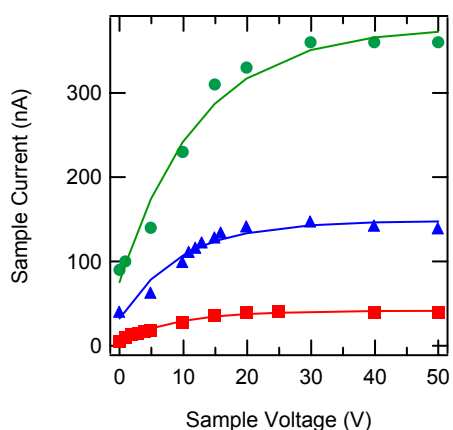
Figure 8. Flood gun current to a biased Au sample. I_{Fil}=1.3 A for all data; only the gun extraction potential is varied from 4 V (●), 3 V (▲), and 2 V (■). Sample current ranges from 5.5 nA to 75 nA at a 0 V sample potential, and from 42 nA to 380 nA at saturation.

Pulsed-Yield Measurements

The pulsed-yield setup was first tested on a conducting titanium sample to compare results directly to the DC-yield setup. The offsets and linearity of the four pulse ammeters were first calibrated using an oscilloscope (average of 100 traces of the pulse ammeters) and an accurate DC-ammeter over the range of 0-100 nA to an uncertainty of <0.5 nA using the low-energy electron gun in DC-mode (as a constant current source) at 400 eV. Next, operating the gun in single-pulsed mode at 5 μs pulse duration, 50 nA pulse magnitude, and at 400 eV the total collector charge was measured and calculated for each of the three ammeter amplification

settings ($2 \cdot 10^6$ V/A, $1 \cdot 10^7$ V/A, and $2 \cdot 10^7$ V/A) for all ammeters, and results were compared for consistency. Variations between ammeter settings $1 \cdot 10^7$ V/A and $2 \cdot 10^7$ V/A were less than the uncertainty of repeated measurements on an individual setting, <10%. However, variations between the $2 \cdot 10^6$ V/A setting and the other two settings ranged between 20-50% most likely due to the poor signal-to-noise-ratio of the lower gain setting.

Integrator circuits were tested in comparison to charge-integration calculations using the trapezoidal-rule. This was done for two different time duration/integration time constant settings: $\Delta t/T = 21.5/15.5$ μs and $\Delta t/T = 12.5/9.0$ μs for both $1 \cdot 10^7$ V/A and $2 \cdot 10^7$ V/A ammeter settings. Error between integrator circuit and computational integrations were ~10% for all settings, however, results were slightly better when using an ammeter amplification of $2 \cdot 10^7$ V/A with $\Delta t/T = 21.5/15.5$ μs settings. Variations in the integration results were attributed to small current DC offsets in the pulsed signals that were later adjusted for in Labview software data acquisitioning.
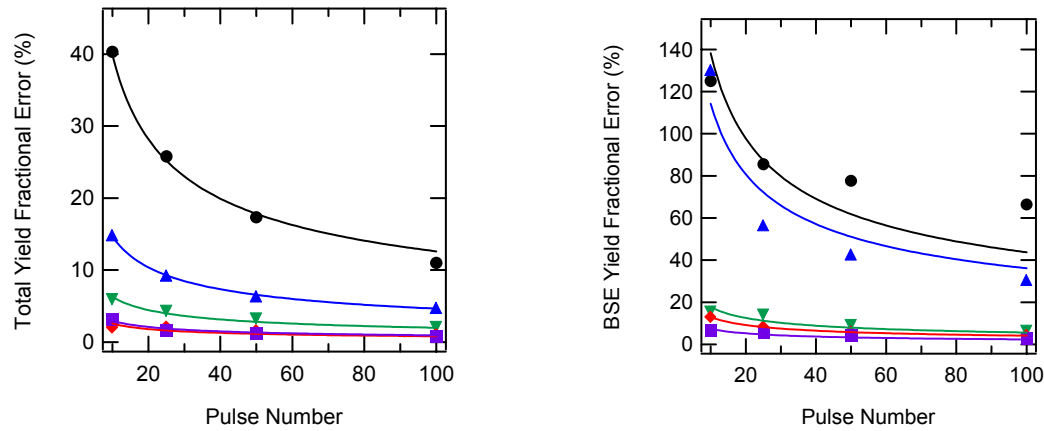
Figure 9. Fractional error as a function of pulse current magnitude and number of pulses for total yields (top) and BSE yields (bottom) using the low energy STAIB gun at 400 eV on conducting Ti at 10 nA (●), 25 nA (▲), 50 nA (▼), 75 nA (♦), and 100 nA (■) impulse magnitudes. Fits vary as the inverse of the root of the number of pulses.

Repeated insulator measurements at a given beam energy were averaged to decrease the electron yield uncertainty, but came at the expense of both greater data acquisition time (since the sample must be flooded between incident pulses) and increased sample radiation exposure. In order to balance measurement uncertainty with sample irradiation exposure, error diagnostics for the pulsed-yield system were performed by taking 100 single-pulse total and BSE yield measurements on conducting titanium at different 5 μs impulse magnitudes of 10 nA, 25 nA, 50 nA, 75 nA, and 100 nA (as measured by the collector) at a beam energy of 400 eV. Results for the percent fractional error for both total and BSE yields are shown in Fig. 9, and depended both on the signal amplitude and on the number of pulses/measurement. Data are fitted with

$$\% FE(N) = \frac{100}{\sqrt{N}} \left(\frac{YLD_{Stdev}}{YLD_{Mean}} \right)$$

where N is the number of pulses/yield measurement, YLD_{Stdev} is the yield standard deviation and YLD_{Mean} is the average yield value. Data was generally taken using ten pulses/measurement at 50 nA impulse magnitude such that the percent fractional errors were 5% and 20% for SE and BSE yields, respectively.

The absolute accuracy of the pulsed-yield measurements was tested on a titanium sample and compared to DC-yield results with discrepancies <5%. As can be seen in Fig. 10, the two approaches are quite comparable for total, SE, and BSE yields. Additionally, a pulsed SE spectrum was taken at beam energy 400 eV on titanium as shown in Fig. 11.

Finally, to demonstrate the pulsed setup on an insulator, a yield curve was taken on insulating anodized Al 2219 alloy as shown in Fig. 12 along with the Feldman semi-empirical fit used in the SEE Charge Collector Knowledge Base (Dennison, 2002). The flood gun was used after each electron beam pulse to neutralize the sample. Estimates for the maximum yield were δ_{max}=3.0±0.1 at E_{max}=300±50 eV, and the first and second crossover energies were E_1=50±10 eV and E_2=1400±100 eV. Further data on this and other insulator samples is provided in other conference proceedings (Thomson, 2003).
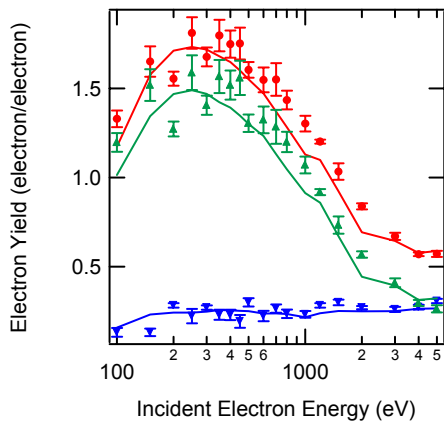
Figure 10. Comparison of pulsed total (●), SE (▲), and BSE (▼) yields with DC (solid lines) yields for Ti. Each data point is the mean of 10 pulses (standard error as bars), of time duration 5 μs and magnitude 50 nA.
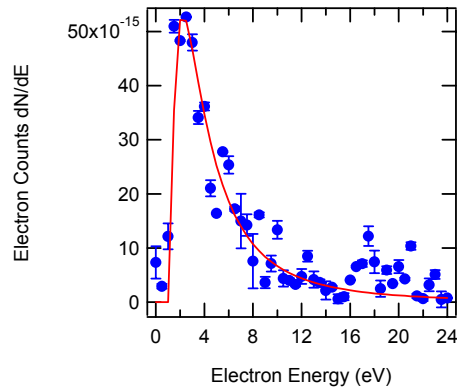
Figure 11. Pulsed-yield SE spectra on Ti at 400 eV. Data is fit with the Chung and Everhart model. Each data point is the mean of 10 pulses (standard error as bars), of time duration 5 μs and magnitude 50 nA.
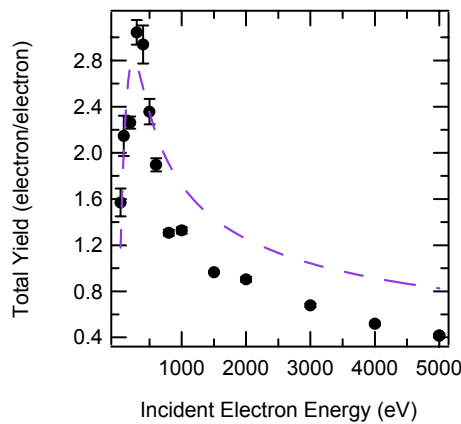
Figure 12. Pulsed-total yields (5 μs pulses with amplitudes 50 nA, each data point is 10 pulses) for insulating anodized Al2219 fitted with a Feldman Model.

Summary and Conclusions

The measurement of absolute SE, BSE, and total yields of both conductor and insulator materials provides important parameters for the NASA/SEE's Charge Collector material database. At USU, we have performed careful calibration of our detector setup to make accurate SE yields on conductors and insulator materials with absolute uncertainties of <5 %. We have also developed fast-response, optically isolated electron detection equipment that is synchronized with the pulsing of electron guns, integrator circuits, and computer data acquisition. Neutralization techniques such as electron flooding and UV sources have also been implemented. The absolute yields for a titanium conductor sample were measured, and have been shown to produce consistent results using both the pulsed-yield and DC-yield setup. Finally, pulsed-yield measurements on an anodized Al2219 aluminum alloy insulating sample have been demonstrated without significant charging distortions.

Acknowledgments

References

1. A.D. Bass, P. Cloutier, and L. Sanche, "Measurements of charge accumulation induced by monochromatic low-energy electrons at the surface of insulating samples," J. Appl. Phys. 84 (5), 2740-2748 (1998).

2. Davies, R.E and J.R. Dennison, "Evolution of Secondary Electron Emission Characteristics of Spacecraft Surfaces," J. Spacecraft and Rockets, 34, 571-574 (1997).

3. J.R. Dennison, W.Y. Chang, N. Nickles, J. Kite, C.D. Thomson, Jodie Corbridge, and Carl Ellsworth, "Final Report Part III: Materials Reports," NASA Space Environments and Effects Program Grant, "Electronic Properties of Materials with Application to Spacecraft Charging," September 2002; Available in electronic format through NASA SEE as part of the SEE Charge Collector Knowledgebase.

4. J.R. Dennison, C.D. Thomson, J. Kite, V. Zavyalov, Jodie Corbridge, "Materials characterization at Utah State University: facilities and knowledgebase of electronic properties of materials applicable to spacecraft charging," Proceedings of the 8th Spacecraft Charging Technology Conference, October 20-24, 2003, Huntsville, Alabama.

5. J.E. Holliday, and E. J. Sternglass, 1957, "Backscattering of 5-20 keV electrons from insulators and metals," J. Appl. Phys. 28, 1189-1193.

6. J.H.L. Jonker, "The angular-distribution of the secondary electrons of nickel," Philips Res. Rep. 6, 372-387 (1951).

7. L. Levy, D. Sarrail, and J.M. Siguier, "Conductivity and secondary electron emission properties of dielectrics as required by NASCAP," Proceedings of the Third European Symposium on Spacecraft Materials in Space Environment, Noordwijk, The Netherlands, October 1-4, 1985.

8. Neal E. Nickles, The Role of Bandgap in the Secondary Electron Emission of Small Bandgap Semiconductors: Studies of Graphitic Carbon, Ph.D. dissertation, Utah State University, 2002.

9. H. Seiler, "Secondary electron emission in the scanning electron microscope," J. Appl. Phys. 54 (11), R1-R18 (1983).

10. E. J. Sternglass, An Experimental Investigation of Electron Back-Scattered and Secondary Electron Emission From Solids, Ph.D. thesis, Cornell University, 1953.

11. C.D. Thomson, V. Zavyalov, J.R. Dennison, Jodie Corbridge, "Electron Emission Properties of Insulator Materials Pertinent to the International Space Station," Proceedings of the 8th Spacecraft Charging Technology Conference, October 20-24, 2003, Huntsville, Alabama.

12. C.D. Thomson, Measurements of the Secondary Electron Emission Properties of Insulators, Ph.D. dissertation, Utah State University, 2004.

AF-GEOSPACE 2.0

R. V. Hilmer
Air Force Research Laboratory, Space Vehicles Directorate
AFRL/VSBXR, 29 Randolph Road, Hanscom AFB, MA 01731
Phone: (781) 377-3211
Fax: (781) 377-3160
E-mail: Robert.Hilmer@Hanscom.af.mil

G. P. Ginet
Air Force Research Laboratory, Space Vehicles Directorate

T. Hall
E. Holeman
Institute for Scientific Research, Boston College

M. Tautz
Radex, Inc.

Abstract

The capabilities of the newest AF-GEOSpace space environment software program are reviewed. Released in 2002, AF-GEOSpace Version 2.0 is a graphics-intensive software program with space environment models and applications developed and distributed by the Space Weather Center of Excellence at the Air Force Research Laboratory (AFRL). A wide range of physical domains is addressed including solar disturbance propagation, radiation belt configuration, and ionospheric auroral particle precipitation and scintillation. The software is currently being used to aid with the design, operation, and simulation of a wide variety of communications, navigation, and surveillance systems. Building on the success of previous releases, AF-GEOSpace has become a platform for the rapid prototyping of automated operational and simulation space weather visualization products and helps with a variety of tasks, including: orbit specification for radiation hazard avoidance; satellite design assessment and post-event anomaly analysis; solar disturbance effects forecasting; frequency and antenna management for radar and HF communications; determination of link outage regions for active ionospheric conditions; scientific model validation and comparison, physics research, and education. Version 2.0 provides a simplified graphical user interface, improved science and application modules, and significantly enhanced graphical performance. Common input data archive sets, application modules, and 1-D, 2-D, and 3-D visualization tools are provided to all models while FTP scripts are provided to automatically update common daily global input parameters. Dynamic capabilities permit multiple environments to be generated at user-specified time intervals while animation tools enable, for example, the display of satellite orbits and environment data together as a function of time. Documentation examples include detailed instructions for investigating phenomena that have well known effects on communications and spacecraft systems. To obtain a copy of AF-GEOSpace Version 2.0 for Windows NT/2000/XP, please contact the first author.
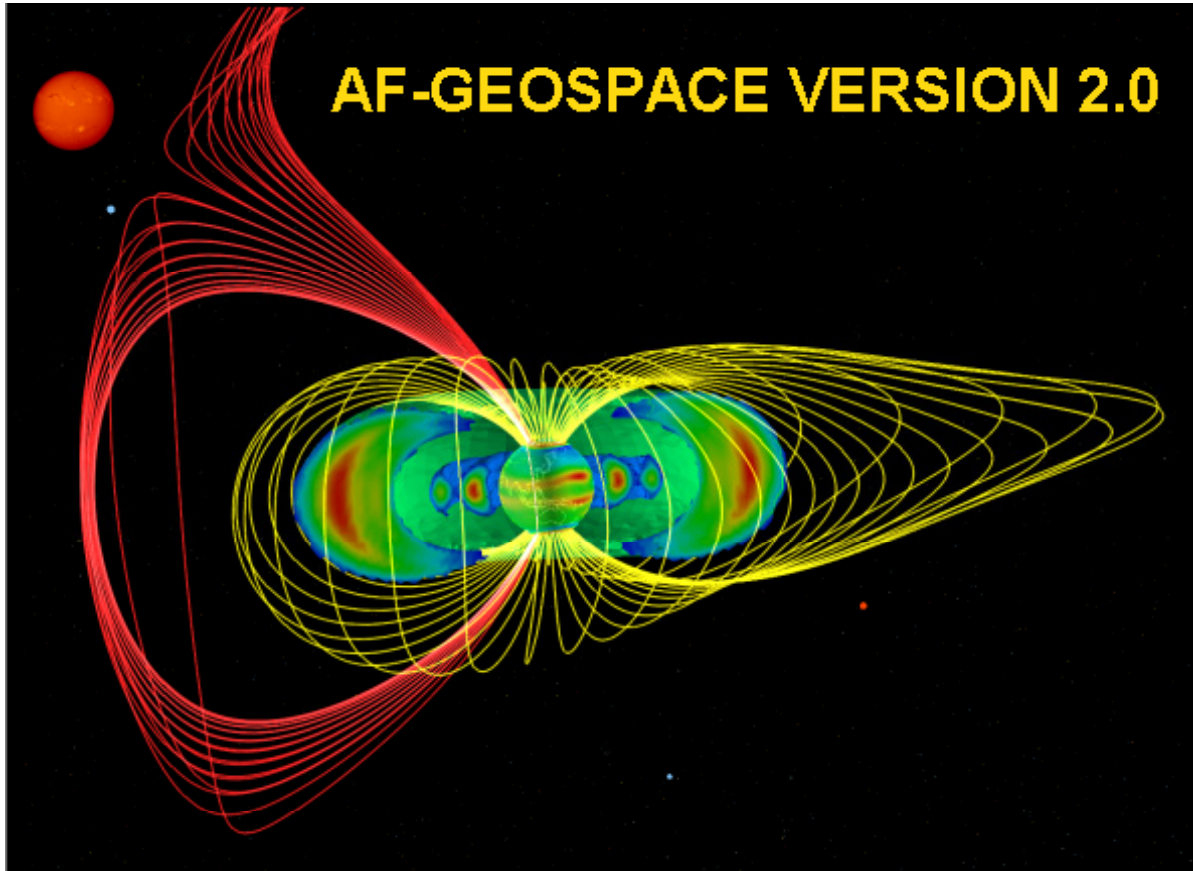
Figure 1. AF-GEOSpace Version 2.0 for Windows NT/2000/XP was developed by the Space Weather Center of Excellence at the Air Force Research Laboratory. With the Sun to the left, (yellow) geomagnetic field lines originating from constant magnetic latitude envelop the radiation belts and are stretched anti-sunward (to the right). Originating at higher latitude, the magnetic field lines of the northern dayside magnetic cusp (red) help to define the shape of the dayside magnetopause. Ionospheric electron densities are shown with peak bands at latitudes both above and below the Earth's geomagnetic equator.

Introduction

Space systems experience environmental effects ranging from intermittent communication outages caused by ionospheric scintillation to total satellite system failures caused by energetic magnetospheric particles. Motivated by the need to mitigate the impact of these hazards, space environment models are employed during the spacecraft design process and operations and provide environmental simulations for a wide variety of communication, navigation, and surveillance systems operating at altitudes between 100 km and geosynchronous orbit (6.6 Earth Radii). While our understanding of fundamental physical processes is still limited, useful empirical, statistical, and theoretical models have been developed to address topics ranging from solar coronal mass ejections to the Earth's trapped radiation belts to auroral particle precipitation.

AFRL is constantly expanding its space environment modeling capabilities and has integrated a collection of scientific codes and related applications into the AF-GEOSpace software program. A sample of the program's output is shown in Figure 1. The program has grown and evolved steadily in an effort to address the concerns of the space weather community. While some models may not be considered state-of-the-art, they are included to provide valuable historical validation baselines and the ability to easily relate output from models covering similar domains, e.g., to directly compare results from the CRRES and AE-8 electron radiation belt models. The flexibility to simultaneously view science model results and real-time data with a common set of visualization tools has allowed AF-GEOSpace to serve AFRL as a development platform for some of the automated visualization products required of the operational community. With all models running on a common platform, AF-GEOSpace becomes a vehicle for rapid model prototyping, model validation, environment specification for spacecraft design, mission planning, and anomaly resolution. In short, AF-GEOSpace becomes the backbone for an integrated space environment model.

This paper describes the software program AF-GEOSpace Version 2.0 released in 2002. We begin by highlighting the program's development history then provide a summary of current capabilities by reviewing the Windows pull-down menu functions, and the content of the science, application, data, and graphics modules. A complete reference list detailing model and application sources is provided.

Development Overview

The first public release of AF-GEOSpace (Version 1.21, 1996/IRIX on SGI) contained radiation belt particle flux and dose models derived from CRRES satellite data, an aurora model, an ionospheric model, and ionospheric HF ray tracing capabilities. The next public release (Version 1.4, 1999/IRIX on SGI)[1] added science modules related to the cosmic ray and solar proton environment, low-Earth orbit radiation dosages, single event effects probability maps, and ionospheric scintillation, solar proton, and shock propagation models. New application modules for estimating linear energy transfer (LET) and single event upset (SEU) rates in solid-state devices, and modules for visualizing radar fans, communication domes, and satellite detector cones and links were added. Automated FTP scripts permitted users to automatically update their global input parameter data set directly from NOAA/SEC (Space Environment Center). Real-time DMSP data modules for displaying auroral particle data and identifying enhanced outer zone electron belt populations remain exclusive to Version 1.4.

What's New? AF-GEOSpace Version 2.0 (for WindowsNT/2000/XP) includes the first true dynamic run capabilities and offers new and enhanced graphical and data visualization tools such as 3-D volume rendering and eclipse umbra and penumbra determination. The dynamic run capability enables the animation of all model results, in all dimensions, as a function of time. Version 2.0 also contains a new realistic day-to-day ionospheric scintillation simulation generator (IONSCINT), an upgrade to the WBMOD scintillation code, a simplified HF ionospheric ray tracing module, and applications built on the NASA AE-8 and AP-8 radiation belt models. User-generated satellite data sets can now be visualized along with their orbital ephemerides. A tool for visualizing MHD model results stored in structured grids provides a hint of where future space weather model development efforts are headed. A new graphical user

interface with improved module tracking and renaming features greatly simplifies software operation. Finally, a major restructuring of the code to an open architecture has greatly increased the code's portability and made it easier in integrate new modules.

AF-GEOSpace Version 2.0 is written in C++ for Windows NT, 2000, and XP. It is rigorously object oriented and contains separate user interface, kernel, and graphics libraries. Environment modules provide interfaces to the science models and related applications needed to investigate the solar, interplanetary, magnetospheric, auroral, and ionospheric environments and their effects on communications and spacecraft systems.

The software is divided into five explicit module classes to simplify the integration of new algorithms and increase portability. *Science Modules* control individual science models and produce output data sets on user-specified grids. *Application Modules* typically manipulate these data sets, e.g., by integrating dose calculated by a radiation belt model or tracing HF rays through a model ionosphere. They also provide capabilities like orbit generation and magnetic field line tracing. *Data Modules* read and assist with the analysis of user-generated data sets. *Graphics Modules* control the one, two, and three-dimensional viewport windows and enable display features such as isocontours, plane slices, magnetic field lines, line plots, axes, the Earth, stars, and satellites. *Worksheet Modules* provide transformations between the GEOC, GSM, SM, and GEI systems in spherical, cylindrical, and Cartesian coordinates and also provide calendar system conversion tools. This separation of modules by function permits the use of common inputs and visualization tools by all modules. Next we look at the new dynamic run capability.

Dynamic Run Environments

AF-GEOSpace Version 2.0 supports two basic environment module types: *static* and *dynamic*. Note that previous releases of AF-GEOSpace supported only *static* environments. Science or application module runs are called *static* if they produce output representing a single Universal Time. All environment models and applications are run using a fixed set of geophysical parameters, e.g., the geomagnetic activity index Kp. With the exception of the new ionospheric scintillation module and the satellite orbit generator and its associated applications, all environment models and applications are run for a fixed Universal Time. Runs are called *dynamic* if they produce output at more than one Universal Time. This dynamic run capability allows the user to animate results in all dimensions, e.g., simultaneously view a satellite's path through a generated data set in 3-D, view a 2-D projection on Earth of data slaved to a satellite's altitude, and view a 1-D plot of the time history of data values encountered by the satellite. Figure 2 shows 3-D and 2-D graphic frames for a single time from a dynamic run sequence representing a 2001 geomagnetic storm. A common set of global parameters was the key to generating this coordinated set of environments over the storm time interval.

Global Parameters

The purpose of the global parameter concept is to provide consistent inputs to the multiple models that can be created within a single static or dynamic environment. Global parameters are the date, time, and geophysical indices shared between many of the models, i.e., the geomagnetic activity index Kp, daily sunspot number (SSN), solar radio flux at 10.7 cm (F10.7), planetary

magnetic index Ap, geomagnetic activity index Dst, and the equatorward boundary of the diffuse aurora at midnight (AB). Most models have additional parameter inputs that are entered by the user when initializing a module. The last two parameters are included for reference purposes, i.e., Dst is useful when constructing magnetic field models and the AB values are useful as manual inputs to the aurora science module equatorward edge-mapping algorithm. A data archive covering 1932 to 2001 includes the indices Kp and Dst as well as DMSP-derived auroral boundaries. These data enable the user to run models over a wide variety of activity levels and space weather events. FTP scripts enable automated updates of some common parameters.
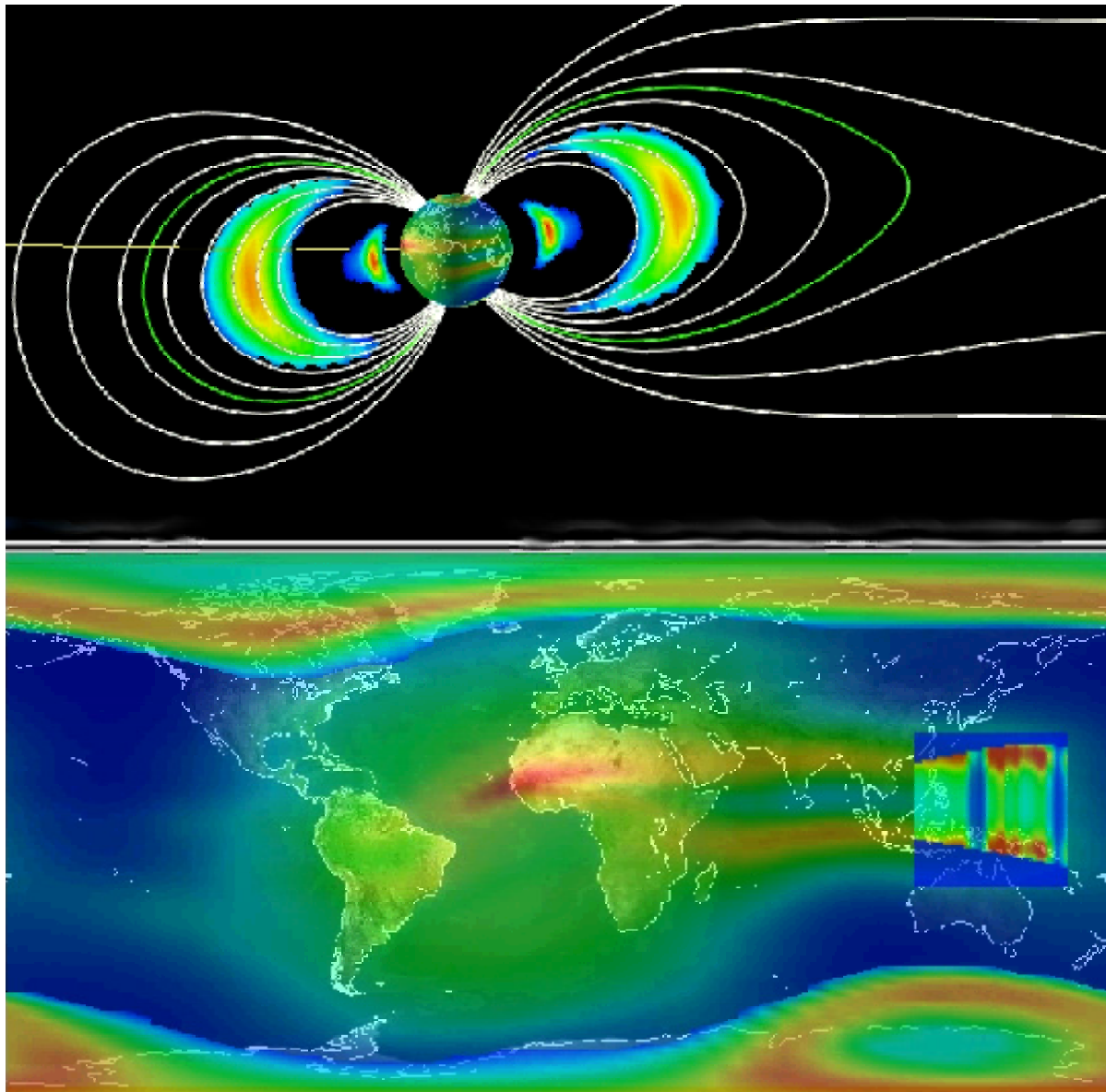
Figure 2. AF-GEOSpace 2.0 environment models representing 30 March 2001 at 1400 UT. *Lower*: Earth map with precipitating auroral electron flux at high latitudes, total electron content (TEC) in the ionosphere with peak over East Africa, and S4 scintillation index (inset) north of Australia. *Upper*: Earth with Sun axis to left, inner

proton belt (9.7 MeV), outer electron belt (1.6 MeV), and magnetic field lines in the noon-midnight meridians. Auroral and TEC from lower frame are also visible.

Menus

The functions of the AF-GEOSpace pull-down menus illustrate the software's capabilities.

The *File* menu provides options to load Environment Window inputs and run results of previously saved science and application modules. Module settings and output are saved as single Common Data Format (CDF) files. The contents of the active windows can be captured in Tagged Image File Format (TIFF) or Joint Photographic Experts Group (JPEG) format.

The *Edit* menu provides access to features enabling the user to run models, delete models, rename entries in the active modules lists, examine text representations of module produced data, setup computation grids, set dynamic run mode time step values and output parameter selection, and animate results from dynamic module runs (including satellite orbits in static mode).

The *Module* menu provides access to the five basic module classes: (1) *Science Modules* control individual science models and produce output data sets on user-specified grids, (2) *Application Modules* typically manipulate these data sets, e.g., by integrating dose calculated by a radiation belt model or tracing HF rays through a model ionosphere. Application modules also provide orbit generation and magnetic field line tracing capabilities, (3) *Data Modules* read and assist with the analysis of user-generated data sets, (4) *Graphics Modules* control the one, two, and three-dimensional windows and enable display features such as plane slices, magnetic field lines, line plots, axes, the Earth, stars, and satellites, and (5) *Worksheet Modules* provide commonly requested coordinate transformations and a calendar system conversion tools.

The *Windows* menu provides access to functions for creating, adjusting, and arranging graphics windows, i.e., create 1D, 2D, 3D or special 3-D Heliospace viewports, set background color, switch to full screen, or arrange windows in cascading or tile patterns.

The *Viewport* menu contains options for splitting the active viewport horizontally or vertically, transforming a viewport's dimensionality from 2D to 3D while retaining the displayed data, and fixing the viewer's position relative to a selected coordinate system.

In dynamic mode, the *Globals* menu provides read, write, and save access to the global parameters appropriate to the selected time period. A *Globals* popup window will appear showing the parameters Date, Time, Kp, Ap, SSN, F10.7, Dst, and AB. These values can be edited and line entries can be added or deleted directly in the text window. All science and application modules run will utilize using this same set of global input values. In static mode the global parameters used to represent the single selected time are contained in the Kp, SSN, F10.7, and Ap text boxes at the top of the Environment window.

The *Help* menu connects the user to a PDF version of the user's manual. The manual includes an extensive examples section with click-by-click instructions allowing the user to recreate the graphics presented.

Science Modules

Science modules provide methods for generating data sets from various space environment models. The following science modules are supported by AF-GEOSpace:

APEXRAD: The Advanced Photovoltaic and Electronics Experiment (APEX) space radiation dose model[2] specifies the location and intensity of the radiation dose rate behind four different thicknesses of aluminum shielding for five geomagnetic activity levels as specified by Ap15. It covers the Low Earth Orbit (LEO) altitude region (360-2400 km) and was developed to supplement the CRRESRAD model (see below) which has limited resolution in the LEO regime.

AURORA: Auroral precipitation models[3, 4] specify the location and intensity of electron number and energy flux, ion number and energy flux, Pederson and Hall conductivities, and the equatorward boundary at 110 km altitude. This module also provides the capability to map flux, conductivity, and equatorial boundary values up magnetic field lines into the three-dimensional magnetospheric grid.

CHIME: The CRRES/SPACERAD Heavy Ion Model of the Environment[5] (CHIME) specifies the location and intensity of galactic cosmic rays and/or solar energetic particle fluxes and/or anomalous cosmic ray fluxes.

CRRESELE: The Combined Radiation and Release Effects Satellite (CRRES) electron flux model[6] specifies the location and intensity of electron omni-directional flux over the energy range 0.5-6.6 MeV for a range of geomagnetic activity levels.

CRRESPRO: The Combined Radiation and Release Effects Satellite (CRRES) proton flux model[7] specifies the location and intensity of proton omni-directional flux over the energy range 1-100 MeV for quiet, average, or active geophysical conditions.

CRRESRAD: The Combined Radiation and Release Effects Satellite (CRRES) space radiation dose model[8] specifies the location and intensity of the radiation dose rate behind four different thicknesses of aluminum shielding for active or quiet geophysical activity levels.

IONSCINT: The High Fidelity Ionospheric Scintillation Simulation Algorithm (IONSCINT) model[9] provides realistic scenarios of disruptions in trans-ionospheric radio wave communications with spacecraft due to equatorial scintillation. IONSCINT addresses only intensity (or amplitude) scintillation of 244 MHz signals from geosynchronous satellites and represents statistically realistic climatology as well as the day-to-day variability of equatorial scintillations.

ISPM: The Interplanetary Shock Propagation Model[10] predicts the transit time of interplanetary shocks from the sun to the Earth and the shock strength upon arrival.

NASAELE: The NASA AE-8 radiation belt model[11] is used to compute the intensity and location of differential omni-directional electron flux for ten energy intervals between 0.5 and 6.6 MeV that correspond to the ranges of the CRRES HEEF instrument.

NASAPRO: The NASA AP-8 radiation belt model[11] is used to compute the intensity and location of differential omni-directional proton flux for 22 energy intervals between 1 and 100 MeV, which correspond to the ranges of the CRRES PROTEL instrument.

PIM: The Parameterized Ionospheric Model[12] (PIM) is a global ionosphere model that generates electron number density as well as maps of total electron content (TEC), Height of E and F2 peaks, and plasma frequencies at the E and F2 peaks as a function of a variety of geophysical activity indices.

PPS: The Proton Prediction System[13] (PPS) provides forecasts of the intensity and duration of solar proton events.

SEEMAPS: Single Event Effects Maps[14] (SEEMAPS) uses normalized flux and dose data for protons with energy > 50 MeV from the APEX and CRRES satellites to produce contour maps of relative probabilities of experiencing SEE in the Earth's inner radiation belts.

STOA: The Shock Time-of-Arrival Model[15] (STOA) predicts the transit time of interplanetary shocks from the sun to the Earth. STOA is a predecessor of ISPM.

WBMOD: The WideBand Model[16] (WBMOD) is an RF ionospheric scintillation model specifying S4, SI, and other scintillation parameters between any location on the globe and a satellite above 100 km altitude at any frequency above 100 MHz as a function of a variety of geophysical activity indices. A year 2000 update improves high latitude output.

Application Modules

Application modules provide orbit creation/prediction, dataset integration along orbits, magnetic field model generation, and access to specialized ionospheric ray-tracing, graphics, and scintillation products. The following applications are supported by AF-GEOSpace:

APEXRAD-APP: Advanced Photovoltaic and Electronics Experiments (APEX) radiation dose model[2] calculates expected accumulated yearly dose (in units of rads silicon/year) for four thicknesses of aluminum shielding during four levels of magnetic activity. For orbits with apogees greater than 2500 km, use CRRESRAD-APP described below.

BFIELD-APP: The B-Field application allows the generation of datasets representing the magnetic field in the near-Earth space environment. A variety of internal (dipole, IGRF) and external magnetic field models[17, 18, 19, 20] are used to generate gridded data set, and trace field lines and flux tubes.

CRRESELE-APP: The Combined Radiation and Release Effects Satellite (CRRES) electron flux model[6] is used to estimate of electron fluence, over the energy range 0.5-6.6 MeV, received along a user-specified satellite orbit under a wide range of magnetospheric conditions.

CRRESPRO-APP: The Combined Radiation and Release Effects Satellite (CRRES) proton flux model[7] is used to calculate proton omni-directional fluence (integral and differential) over the range 1 to 100 MeV for user specified orbits and quiet, active, or average geophysical activity levels.

CRRESRAD-APP: Combined Radiation and Release Effects Satellite (CRRES) space radiation dose model[8] is used to calculate the expected satellite dose accumulation behind four different thicknesses of aluminum shielding for user-specified orbits for active or quiet geophysical activity levels.

LET-APP: Calculates the linear energy transfer (LET) spectrum and its associated single event upset (SEU) rate in a microelectronic device resulting from the penetration of energetic space particles. Effects from both cosmic rays and the trapped protons are estimated by using the CHIME[5] and CRRESPRO[7] models.

NASAELE-APP: Calculates electron omni-directional fluence (differential and integral) for ten energy intervals in the range 0.65-5.75 MeV. A user-specified orbit is traced through the NASA AE-8 trapped electron model[11] to provide an estimate of electron fluence received by the satellite under a wide range of magnetospheric conditions.

NASAPRO-APP: Calculates proton omni-directional fluence (differential and integral) over the energy range 1.5-81.3 MeV for user specified orbits and quiet or active geophysical conditions using the NASA AP-8 trapped proton model[11].

RAYTRACE-APP: Calculates the behavior of MHz rays in an ionosphere specified by a Parameterized Ionosphere Model (PIM) data set generated using the PIM module.

SATEL-APP: Calculates orbital trajectories for satellites from a variety of user specified orbital element input sets.

WBPROD-APP: Gives a 24hr WBMOD[16] climatology prediction of the dB fade levels due to ionospheric scintillation effects for specific ground-to-satellite communication links.

Data Modules

Data modules provide methods for reading and displaying externally generated data sets. The following data modules are supported by AF-GEOSpace:

EPHEMERIS: Allows user-generated time-ordered data and satellite ephemeris to be loaded into AF-GEOSpace. Data and satellite trajectory can then be displayed using the ORBIT-PROBE (1D) and SATELLITE (3D) graphical modules, respectively. This feature enables data/model comparisons as the user-provided satellite trajectory can be used to sample other AF-GEOSpace environment models.

<u>PARAMESH</u>: Allows the user to load MHD simulation run results produced externally using the large-scale parallel grid meshing package called *Paramesh* and MHD science codes developed by the Navel Research Laboratory. Loaded data is then displayed within the special Heliospace viewport using the *Paramesh* related graphics modules described below. Details about the *Paramesh* package can be found at the NRL website (http://www.lcp.nrl.navy.mil/hpcc-ess/amrmhd3d.10.html). This module was a product of a CHSSI collaboration between NRL and AFRL. (Note that this module is actually accessed with the *File* menu option *Open Paramesh*.)

<u>Graphics Modules</u>

Graphics modules are used to visualize the data sets created through the Application, Data, and Science modules. The following graphics are supported by AF-GEOSpace:

<u>ANNOTATION</u>: Create and display descriptive text or time labels for viewports.

<u>AXES</u>: Plot a set of axes or sun vector.

<u>COORD-PROBE</u>: Provides a method for probing data along lines defined in user-specified coordinate systems.

<u>COORD-SLICE</u>: Slice the data set along a constant coordinate surface.

<u>DETECTOR</u>: Define and associate fixed or tracking detector cones with satellites or station locations.

<u>EARTH</u>: Plot an outlined or solid Earth. A variety of additional features are available including geographic, magnetic, and corrected geomagnetic latitude-longitude grids.

<u>EMITTER</u>: Define and associate fixed or tracking emitters, e.g., radar fan structures, with satellites or stations.

<u>FIELD-LINES</u>: Plot magnetic field lines and surfaces, flux tubes, and location of the auroral equatorward boundaries.

<u>GLOBAL INPUTS</u>: Produce a line plot of the global input data values, e.g., Kp or Dst, as a function of time.

<u>GRID</u>: Plot the 3-D grid associated with a data set.

<u>ISOCONTOUR</u>: Calculate an isocontour of a data set and plot the resulting surface.

<u>LINK</u>: View a line-of-sight link between stations and satellites or between satellites.

<u>ORBIT-PROBE</u>: Plot data sets from along satellite orbits.

ORBIT-SLICE: Cut the data set with a plane placed at the orbital plane of a satellite (or a plane perpendicular to or containing the satellite velocity vector) and plot the resulting slice.

PLANE-SLICE: Cut the data set with an arbitrary plane and plot the resulting slice.

RAY TRACE: Produce a depiction of the ionospheric rays traced through the PIM science model data sets.

SATELLITE: Provides a means of viewing satellite trajectories.

STARS: Plot the celestial background including stars, planets, and the moon.

STATION: Plot a labeled location on or above the surface of the Earth.

VOLUME: View the entire volume of a data set as a single three-dimensional object.

PARAMESH-COORDSLICE: Produce a slice or constant coordinate surface through a data set written using the *Paramesh* parallel meshing software.

PARAMESH-FIELDLINES: Produce field lines through a *Paramesh* data set.

PARAMESH-GRID: Display the grid, block structure (e.g., leaf and parent block), and overall domain of a *Paramesh* data set.

PARAMESH-ISOCONTOUR: Produce a surface of constant value through a *Paramesh* data set.

PARAMESH-VOLUME: View the entire volume of a *Paramesh* data set as a single three-dimensional object.

Graphical Module Options

Graphical option controls appear in the environment window of each active graphics module. The *Display* option is used to place or display a graphics object in an active viewport. The *Use Texture* mapping option improves the appearance of color data contours. An *Interactive* option controls whether or not graphical renderings are updated immediately as changes are made to the graphic inputs. The appearance of a graphical object can be manipulated using the *Clipping* (multiple planes with rotation and translation), *Transparency*, *Lighting* (e.g., ambient, specular), *Material* (e.g., emission and shininess), and *Color* (Red-Green-Blue and Hue-Saturation-Value slider) options. The *Color Map* option enables tailored modifications to the mapping of colors assigned to data values represented in the viewport color bar. The *Data Map* option controls the range and linear/log scale used to display data, e.g., to examine a subset of the data range.

Worksheet Modules

Worksheet modules provide auxiliary tools that are helpful in AF-GEOSpace calculations. The following worksheet modules are supported by AF-GEOSpace:

CALENDAR: A calendar showing month and day, day of year, and modified Julian day.
COORD_TRANSFORM: Perform coordinate transformations on point locations using different coordinate systems (GEOC, GSM, SM, GEI) and coordinate geometries (Cartesian, Cylindrical, Spherical) at a given Year, Day, and UT.

Final Comments

The AF-GEOSpace software suite provides the scientific community with a number of empirical, statistical, and physics-based models that address concerns about environmental hazards affecting real-world space systems. Recent improvements to the software have greatly increased its utility and portability. The authors encourage the community to make suggestions regarding the addition of new models and applications. AF-GEOSpace Version 2.0 software is distributed exclusively by AFRL and can be obtained by contacting the first author.

Acknowledgements

References

1. Hilmer, R V (Ed.), AF-GEOSpace User's Manual, Version 1.4 and Version 1.4P, AFRL-VS-TR-1999-1551, Air Force Research Laboratory, Hanscom AFB, MA, 1999

2. Bell, J T, and M S Gussenhoven, APEXRAD Documentation, PL-TR-97-2117, Phillips Laboratory, Hanscom AFB, MA, 1997

3. Hardy, D A, W McNeil, M S Gussenhoven, and D Brautigam, A statistical model of auroral ion precipitation, J. Geophys. Res., 94, 370, 1989.

4. Hardy, D A, M S Gussenhoven, and E Holeman, A statistical model of aurora electron precipitation, J. Geophys. Res., 90, 4229, 1985

5. Chenette, D L, J D Tobin, and S P Geller, CRRES/SPACERAD Heavy Ion Model of the Environment, CHIME, PL-TR-95-2152, Phillips Laboratory, Hanscom AFB, MA, 1995

6. Brautigam, D H, and J T Bell, CRRESELE Documentation, PL-TR-95-2128, Phillips Laboratory, Hanscom AFB, MA, 1995

7. Meffert, J D, and M S Gussenhoven, CRRESPRO Documentation, PL-TR-94-2218, Phillips Laboratory, Hanscom AFB, MA, 1994

8. Kearns, K J, and M S Gussenhoven, CRRESRAD Documentation, PL-TR-92-2201, Phillips Laboratory, Hanscom AFB, MA, 1992

9. McNeil, W, User's Guide for the High Fidelity Ionospheric Scintillation Simulation Algorithm, Prepared for AFRL/VSB by Radex, Inc., March 8, 2000

10. Smith, Z, and M Dryer, The Interplanetary Shock Propagation Model: A model for predicting solar-flare-caused geomagnetic storms, based on the 2 1/2 D, MHD numerical simulation results from the Interplanetary-Global Model (2D IGM) NOAA Tech. Mem., NOAA/ERL 89, 1995

11. Vette, J I, The NASA/NSSDC Trapped Radiation Environment Model Program (1964-1991), NSSDC/WDC-A-RS 91-29, 1991

12. Daniell, R E, Jr., L D Brown, D N Anderson, M W Fox, P H Doherty, D T Decker, J J Sojka, and R W Schunk, Parameterized Ionospheric Model: A global ionospheric parameterization based on first principles models, Radio Sci., 30, 1499, 1995

13. Smart, D F, and M A Shea, Modeling the time-intensity profile of solar flare generated particle fluxes in the inner heliosphere, Adv. Space Res., 12, No. 2-3, (2) 303, 1992

14. Mullen, E G, G Ginet, M S Gussenhoven, and D Madden, SEE relative probability maps for space operations, IEEE Trans. Nuc. Sci., 45, 2954, 1998

15. Smart, D F, and M A Shea, A simplified model for timing the arrival of solar flare-initiated shocks, J. Geophys. Res., 90, 183, 1985

16. Secan, J A, and R M Bussey, An improved model of high-latitude F-region scintillation (WBMOD version 13), PL-TR-94-2254, 1994

17. Hilmer, R V, and G -H Voigt, A Magnetospheric Magnetic Field Model with Flexible Current Systems Driven by Independent Physical Parameters, J. Geophys. Res., 100, 5613, 1995

18. Olson, W P , and K A Pfitzer, Magnetospheric Magnetic Field Modeling, Annual Scientific Report, Air Force Office of Scientific Research contract F44620-75-C-0033, McDonnell Douglas Astronautics Co., Huntington Beach, CA, 1977

19. Tsyganenko, N A, Global Quantitative Models of the Geomagnetic Field in the Cislunar Magnetosphere for Different Disturbance Levels, Planet. Space Sci., 35, 1347-1358, 1987

20. Tsyganenko, N A, A Magnetospheric Magnetic Field Model with a Warped Tail Current Sheet, Planet. Space Sci., 37, 5-20, 1989

A REVIEW OF SPACECRAFT EFFECTS ON PLASMA MEASUREMENTS

Alain Hilgers

Space Environments and Effects Section (ESA-ESTEC/TOS-EES)
Keplerlaan 1, 2200 AG Noordwijk, The Netherlands
E-mail: Alain.Hilgers@esa.int

Benoit Thiébault

Space Environments and Effects Section (ESA-ESTEC/TOS-EES), The Netherlands

Abstract

The spacecraft induced environment includes, secondary particles generated by primary radiation, outgassing material, particles emitted by thrusters or emitters, spacecraft generated electric and magnetic fields. All of these components may severely affect the behaviour of sensors and especially scientific instruments. In this presentation various effects are reviewed and methods to cope with, or to mitigate, them are discussed.

Introduction

This paper deals with unwanted effects on space plasma measurements related to the perturbation that spacecraft induces on the environment or directly on sensor themselves. These effects could be organised in several categories as follows:

-   spacecraft system anomaly (with various possible origins e.g., human, thermal, radiation...).
-   electromagnetic or magnetic perturbations;
-   electrostatic perturbations from spacecraft charged surfaces;
-   contamination by neutral or secondary particles originating from the spacecraft;
-   space charge effects from spacecraft electrostatic sheath.

Spacecraft anomalies may obviously affect the measurements via interrupting them or limiting the spacecraft resources available for them. Sensors themselves are subject to anomalies or degradation due to radiation, thermal and human error problems. The rest of the effects mentioned above are due to spacecraft induced environments such as secondary particles, generated by primary radiation, outgassed material, particles emitted by thrusters or emitters, spacecraft generated electric and magnetic fields. A list of the induced environment components is given in Table 1 below together with their effects on particle detectors.

This review is focused on three of the main effects on plasma instruments: contamination by spacecraft generated charged particles, surface charge effects and space charge effects on particle detection. A discussion of other effects can be found in previous reviews including the ones from Berthelier [1998], Pedersen et al. [1998], Hasting [1995], Laframboise and Sonmor [1993], Garret [1981] and Whipple [1981].

Table 1. Spacecraft induced environments and main effects on space systems.

Type and energy range when applicable	Main effect
Secondary charged particles (eV to MeV depending on primary radiation energy)	Background and false signal Space charge interference
Charged particles from thrusters and emitters	Space charge Secondary particles
Outgassed, sputtered and emitted neutral material	Deposit on surfaces and affect their properties
Electric and magnetic field	Affect field sensors and electronic Affect particle trajectories

Detector Contamination by Spacecraft Generated Garticles

Nearly all kind of particles ion, electron, atomic, molecular or photon can be generated by spacecraft surfaces artificially, spontaneously or under external influences. Spacecraft generated electron and ion can perturb sensors creating background and artefacts. Such effects are discussed in this section.

Photo-electrons are generated by primary UV and X photons impinging spacecraft material. The photo-electron yield varies very much with surface material (cf [Grard 1973 and Grard et al. 1983]) and the resulting flux leaving spacecraft surface depends of the electrostatic potential environment but saturation current level is typically of the order of a few tens of micro-Ampere per square meter. In addition, variation with time spent in space has been observed. This is explained by the contamination of surfaces by outgassed material or by atmospheric constituents.

There are numerous reports of photo-electron contamination of particle sensors [e.g., Wrenn and Heikkila, 1974, Szita et al., 2001] including Langmuir probes [Cauffman and Maynard, 1974; Pedersen et al., 1984, 1998; Hilgers et al., 1992, Hilgers 1995]. Photo-electrons generated inside the detectors can be minimising via the control of the amount of exposed internal surface to sunlight. Photo-electrons generated elsewhere over the spacecraft are much more difficult to avoid since they can travel a rather long distance away from the surface before being turned back to it.

An example is shown on Figure 1 on the electron energy spectrograms as a function of time as measured by PEACE electron detector onboard Cluster [Torkar et al., 2001]. The spacecraft generated photo-electrons appear as a low energy population with a well defined cut-off at the spacecraft potential (solid black line).

It must be noted that the photo-electron trajectories may be strongly influenced by the spacecraft generated electrostatic potential distribution (cf next section) and as result the photoelectron cloud can expand in the whole space around the spacecraft up to very long distances. Example of the photo-electron cloud expansion around a positively charged spacecraft is shown on Figure 2. The simulations were performed using the PicUp3D charging code [Forest et al., 2001; Thiébault et al., 2003a]. It can be seen that although the photo-emission takes place only on half of the cylindrical surface of the spacecraft, the photo-electrons easily propagate in all directions (including the anti-sunward one) and the iso-

density contours nearly follow the spacecraft surface iso-distance beyond a few spacecraft radii.
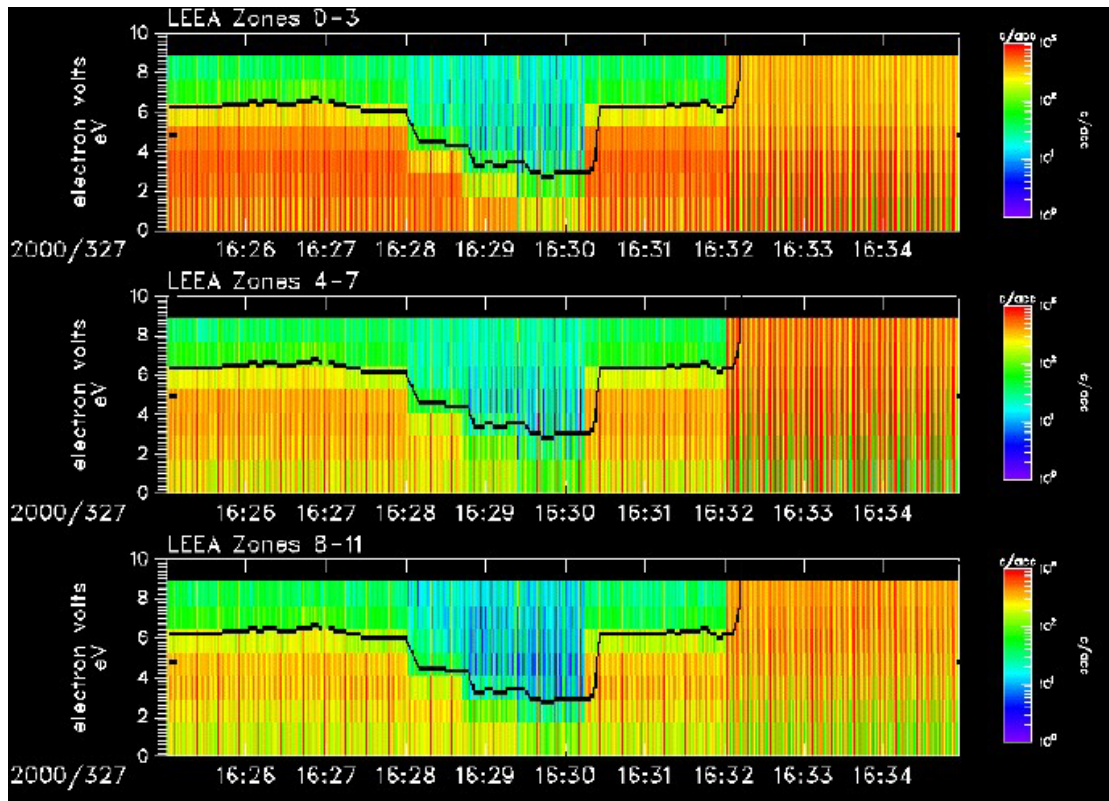
Figure 1. Electron energy spectrograms as a function of time as measured by PEACE electron detector on Cluster [Torkar et al.2001].
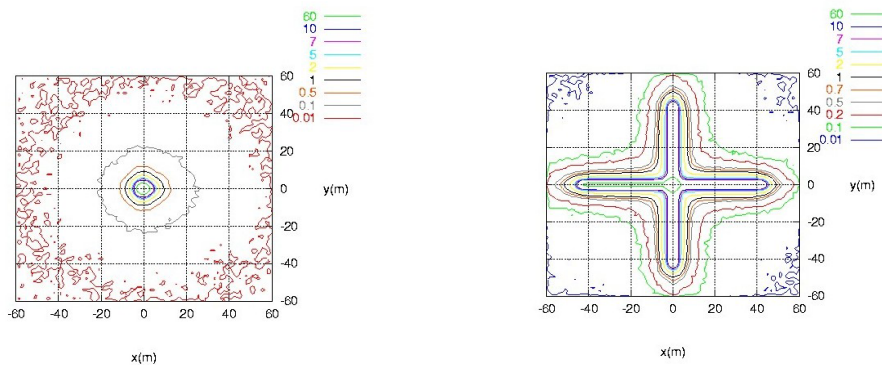
Figure 2. Photo-electron density contours in a plan perpendicular to a cylinder emitting photo-electron from its surface toward negative values of x as simulated with the 3D PIC code PicUp3D without boom antennas (left panel) and without (right panel).

Electrons are also emitted by spacecraft surface under irradiation by high energy particles (ions and electrons). One can distinguish the backscattered electrons from the secondary electrons. The former ones are electrons reflected by surfaces with nearly the same energy as the primary electrons and in specular direction. The secondary electrons are generated at much lower energy (typically a few eV) than the primary ones and in a broader range of directions. Secondary electron effects and behaviour are similar than for the photo-electrons except that currents are usually smaller and the emission occurs on nearly all external

surfaces because the high energy charged particle environment is far more isotropic than the photon environment. The number of secondary electrons emitted per incoming particles (yield) is a function of the incident particle energy. The yield can vary from nearly zero for incident particle with low energy (below 10 eV) or very high energy (above a few keV) to near one (and sometimes more than unity) around a few hundred eVs.

Since secondary electron and photo-emitted electron yields strongly depend of the surface material it is in principle possible to select material to be used according to such a property. However, it may be conflicting with other material requirements (e.g, conductivity and thermal properties). In addition, the yield may change with time spent in space due to material degradation and contamination.

Ions generated on spacecraft have been reported in data from various space missions including the Application Technology Spacecraft ATS-5 and ATS 6, the US Air force P78-2 (SCATHA) spacecraft and the magnetospheric science spacecraft ISEE 1 [Deforest, 1973; Olsen et al., 1981; Olsen and Norwood, 1991; Olsen and Whipple, 1988]. All these papers report observations when the spacecraft ground potential was very negative (typically more than 100 V) compared to the ambient plasma and the spacecraft generated ions were identified by a secondary peak at an energy typically lower than the primary accelerated ion peak through the potential drop.

Two mechanisms have been proposed to explain these ion populations. The first one invokes sputtering by energetic ions and the second one outgassing. Sputtered ions can be generated by high energy ions (pre-existing or from low energy ion population accelerated by negatively charged surfaces). Olsen and Norwood [1991] found that 10 to 100 keV Oxygen ions on glass could produce a yield of 0.5 to 1. particle per incident ions and roughly 2-4% of this yield is ionised. Outgassed material may be ionised by UV and X radiations. In principle, this type of spacecraft generated ions may be generated also in non high level charging conditions but should decrease with mission time.

Electric thrusters and ion and electron guns are designed to emit a significant amount of charged particles. Usually, they are emitted with a high enough energy and in an appropriate direction such that they are not turned back to particle detectors (unless especially designed this way). It must be noted, however, that certain electric thrusters devices also emit a significant amount of cold neutral gas which interact with the energetic ions via charge exchange and can be further scattered back to the spacecraft. A numerical model of these charge exchange ions around a simplified model of SMART 1 spacecraft predicts that the plasma cloud density outside of the main plume can be of the order of 10^{11} m^{-3} [Tajmar, 2001]. An example of such a numerical simulation is shown in Figure 3 for a spacecraft at the same potential as the plasma.
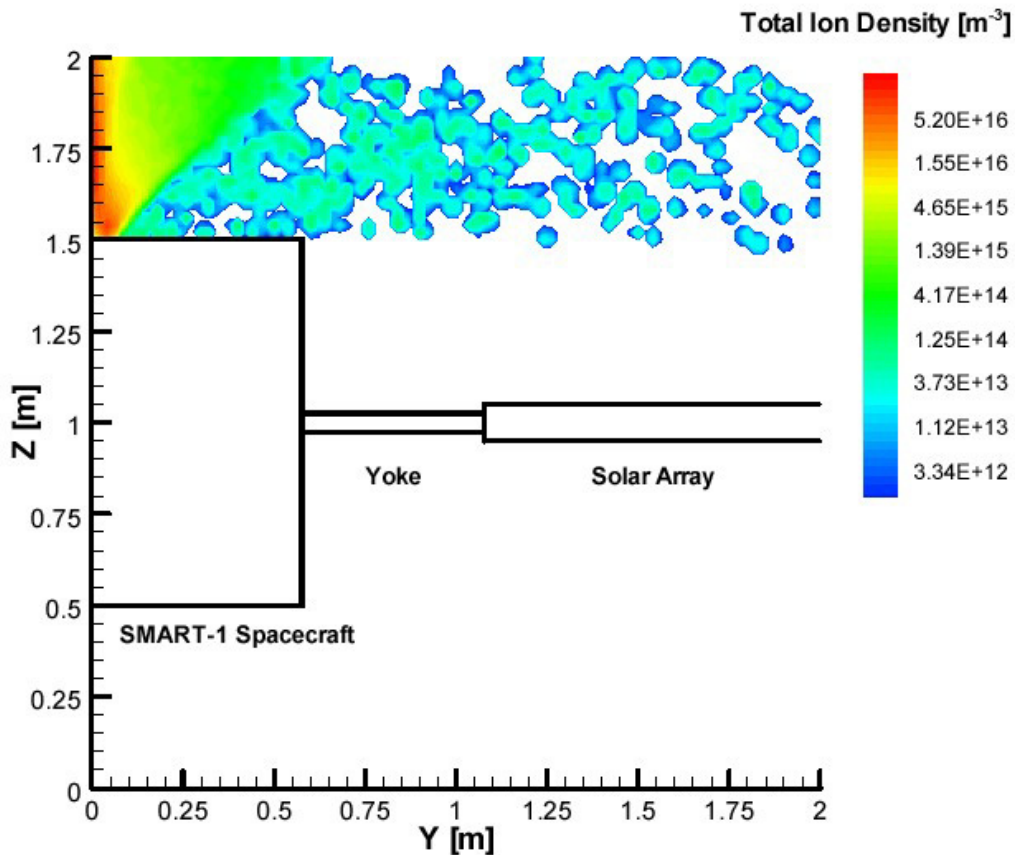
Figure 3. PIC simulation of SMART-1 ion plume density showing charge exchange ions backscattered toward the spacecraft [from Tajmar, 2001].

Surface Charge Effects

Electric charges (electrons and ions) of the plasma are free to move and may eventually get trapped on material surface. They cannot leave a surface as easily as in the atmospheric environment because the vacuum is far less conductive regarding this process. Also, secondary ion and electron emission processes (including photo-emission) contribute to change surface charges. The accumulation of charge (positive or negative) leads to the creation of an electric field distribution that eventually will prevent further charge accumulation by repelling the species of a given polarity and attracting the species of opposite polarity (cf sketch Figure 4). Indeed, the spacecraft is like a complicated electrical circuit with both active and passive elements that is non-linearly coupled to electrical current from space via its whole surface. Often, but not always, this system reaches an equilibrium corresponding to an overall current balance.
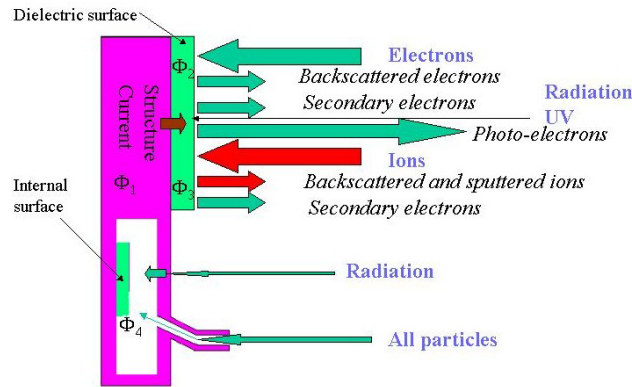
Figure 4. Sketch of the various electron and ion currents leading to charge deposition on a spacecraft surface element.

Because of the higher mobility of the electrons compared to the ions, surfaces in space plasma tend to charge negatively when the photo-electron current is negligible, i.e., in eclipse or in high density (ionospheric plasma). An equilibrium state would be mainly achieved by current balance of incoming ions and electrons, with possibly secondary and backscattered electrons when a significant amount of primary particles have energy around a few 100 eV (i.e., near maximum of the secondary electron yield; cf section 2). When the energy of the electrons is typically above a few keV (e.g., in the aurora or in storm and substorm accelerated particle environments) the secondary electron emission process is less efficient in mitigating the primary charging current and surfaces may reach very high negative potential level (of the order of 1 kV) in eclipse [Deforest, 1972; Garret and Rubin, 1978; Prokopenko and Laframboise, 1980; Olsen et al., 1983; Gussenhoven et al. , 1985; Wrenn and Johnstone, 19986; Yeh and Gussenhoven, 1987; Lai, 1991; Wahlund et al., 1999]. Spacecraft potential may severely affect spacecraft measurements [Olsen, 1982, Olsen et al. 1983] and in extreme case may also be a hazard to spacecraft system because of related electrostatic discharges [Katz and Mandel, 1982; Anderson and Koons, 1996].

On Figure 5 the time series of several plasma parameters are shown around a period of negative electrostatic charging on the Freja spacecraft [Wahlund et al. 1999]. Measurements of three different ion species are shown on the first three panels whereas electron measurements are shown on the two last panels. The energy range is shown on the vertical axis and the color level indicate the flux magnitude. The charging event is identified by an increase of the ion energy for all three ion species and all directions. This is because the ions are suddenly accelerated through the difference of potential toward the spacecraft and caught with the corresponding kinetic energy by the detector. One can see that such an event occur during a period where high energy electrons are observed. This type of electrons population is typically observed during auroral arc crossings at low altitudes (~800 to 10,000 km). Electron populations of similar energy are observed at higher altitudes on lower latitudes where high level negative charging may also occur, usually when the spacecraft is in eclipse.
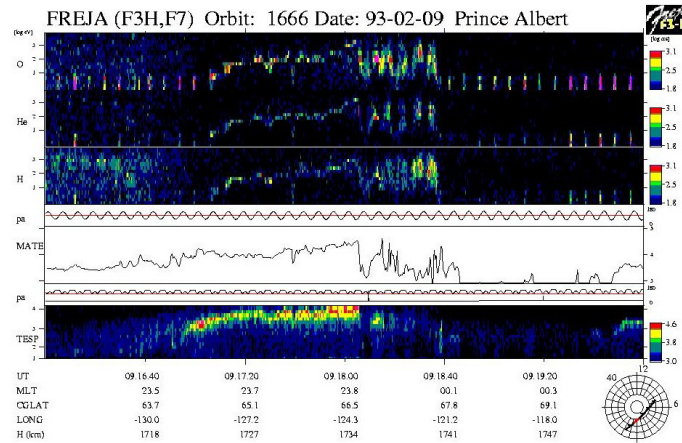
Figure 5. Time series plot of the particle measurement (from Wahlund et al., 1999).

It can be noted, however, that there have been a few reports of high level negative charging in sunlight {Mullen et al., 1986, Olsen and Whipple, 1988]. The event examined by Olsen and Whipple [1988] has been attributed to differential charging due to a degradation of the conductive coating of the spacecraft. As a result non-sunlit surfaces may have charged negatively and created negative potential barrier blocking photo-electron emission on the sunlit surfaces which in turn tend to charge negatively as well.

In general, sunlit surfaces, especially in the low density magnetosphere and the solar wind, are usually driven positively by photo-electron emission and so is the whole surface of a well conductive spacecraft. The positive voltage is about a few volts in the solar wind, the magnetosheath and the plasmasheet and a few tens of volts in very depleted magnetospheric regions (the so called magnetospheric lobes).

Even moderate positive potentials can strongly affect the accuracy of the measurements and re-calibration may require very sophisticated post-processing, e.g., relying on 3D modelling of the spacecraft potential and the electrostatic sheath. Several examples are given in the following.

An obvious effect is the repelling of ions with energy too low with respect to the required electrostatic potential to reach the detector. As a consequence the total number of density will be difficult to evaluate [Olsen, 1982; Olsen et al., 1986].

To cope with such a problem, it is sometimes possible to polarize negatively the detector. In this case however the trajectory of the lower energy ions is strongly perturbed and information is practically lost regarding their original direction of arrival which is a critical information for reconstructing the angular velocity distribution [Hamelin et al., 2002]. An illustration of the problem is given Figure 6 taken from Hamelin et al. [2003] where ion trajectory are computed for a spacecraft potential at +12 V and a detector at –4 V. The ion trajectories are strongly influenced by the potential on spacecraft surface and made even more complicated due to the complex geometry of the surface. Similar studies have been performed in order to simulate the response of the ion detector ROSINA onboard Rosetta spacecraft [Roussel and Berthelier, 2001; Nyffenegger et al., 2001]. One interesting aspect of this series of studies is that it includes comparison between numerical simulations and ground testing in plasma chambers [Roussel, 1998; Berthelier and Roussel, 2001].
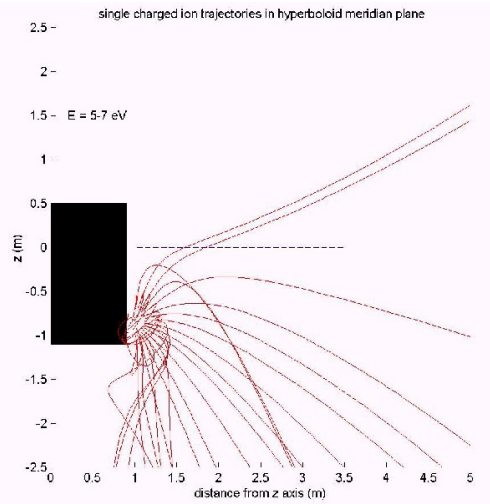
Figure 6. Projection of 3D ion trajectories on the A16 analyser plane for Vs = 12 V and Vh = 4 V [Hamelin et al., 2001].

Conversely, attracted species may experience a focusing effects. This effects on electron measurements has been investigated by a few authors [Garrett, 1981; Sing and Baugher, 1981; Sojka et al., 1984; Comfort et al., 1982]. Recently, Scime et al. [1994] have shown that taking into account electron trajectory bending by the spacecraft generated electrostatic field may considerably improve electron measurements.

Finally, it must be noted that if the spacecraft geometry is simple and its surface conductive enough the potential current relation of the spacecraft can be derived (using e.g., [Laframboise, 1966]) and the spacecraft potential can be used as a plasma diagnosis techniques [cf. e.g., Escoubet et al., 1997].

Space Charge Effects

In the cold ionospheric plasma or high speed streaming solar wind the relative velocity between the spacecraft and the plasma is such that the flow around the spacecraft is meso-sonic which means with relative speed higher than the thermal ion velocity but lower than the electron thermal velocity. It results an ion depleted region in the wake behind the spacecraft. The properties of spacecraft wakes on low Earth orbits have been recently reviewed by Hasting [1995]. In addition, to the plasma rarefaction effect which makes surfaces in the wake more prone to charging, there is a region with an excess of negative charge with more or less complicated structure [e.g., Parker, 1978, Singh et al., 1997]. The related electrostatic potential distribution may also affect the measurements of particles.

Some wake effects are intrinsically related to the Earth geomagnetic field. For instance, it has been noted that polar cap flow of cold ionospheric plasma may create a magnetic field aligned wake behind the spacecraft and that such a wake would be increased by the positive spacecraft potential usually observed in such regions. The resulting space charge is suspected to induce spurious electric field with double probe system measurements [Pedersen et al., 1984; Engwall et al., 2003]. Similarly, Langmuir probe current decreases observed when the probe and the spacecraft are magnetically connected have been interpreted as a field aligned magnetic wake of the spacecraft hub [Hilgers and Holback, 1993; Hilgers, 1995].

As already mentioned in section 2 above, several spacecraft are equipped with active plasma or particle emitter devices which may be active scientific experiments or systems used for propulsion or surface charge mitigation. The injected plasma is usually of much higher density compared to the ambient plasma and can significantly influence the electrostatic potential around the spacecraft even when there is no net space charge injected. In the case of the POLAR spacecraft, Singh et al. [2001] have shown on the basis of numerical simulations that while the use of a plasma contactor efficiently reduces the positive potential of the spacecraft the ion measurements were nevertheless significantly affected by the electric field generated by the expanding plasma.
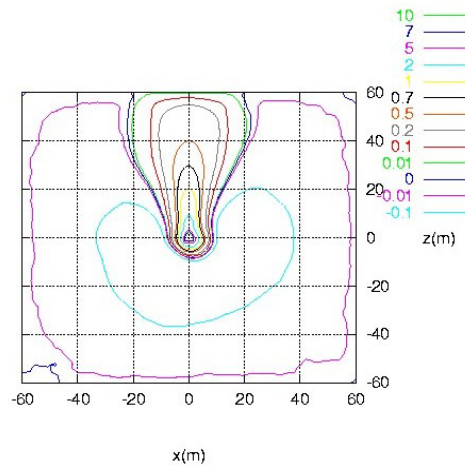
Figure 7. Electric potential contours around a spacecraft at 7 V in a plasma with a density of 1 cm^{-3} and a temperature of 10 eV.

An alternative system also used for charged mitigation but relying on ion emitter has been discussed by Torkar et al. [2001]. The space charge influence of the resulting ion beam in absence of neutraliser has been investigated via PIC plasma simulation method by Thiébault et al. [2003a]. An example of simulated electric potential contours around the ion plume when the spacecraft is at 7 V in a plasma with a density of 1 cm^{-3} and a temperature of 10 eV is shown in Figure 7. The effect of the ion beam space charge is clearly seen along the Z axis (perpendicular to the sun and to the spine plane). However, it can be seen that it is very efficiently shielded by the ambient plasma electrons and the photoelectrons in direction perpendicular to the Z axis. The positive potential typically vanishes within a few meters. A negative potential barrier appears instead which is created by the photo-electron space charge.

The existence of negative potential barriers around spacecraft generated by secondary or photo electrons induced space charge has been speculated for many years [cf e.g Whipple 1976 and reference therein]. Such barriers may affect the current balance on spacecraft surfaces especially via their limiting effect on secondary electron emission and/or the access of particles to detectors. Evidence in space are marginally conclusive [Whipple, 1976; Zhao et al., 1996] but some numerical simulations tend to confirm their existence [Schroeder, 1973; Sasot et al. 2003, Thiébault et al., 2003a, 2003b]. An example of simulation results from Thiébault et al. [2003b] is shown in Figure 7 in a 100 cm^{-3} density and 1 eV temperature plasma environment around a spherical body with isotropic secondary electron emission for three values of the potentials; -1 V, 0 V and +1 V suggesting that potential barriers could be

observed over a relatively broad range of potential and can be of the order of the secondary electron emission and ambient plasma thermal energy.
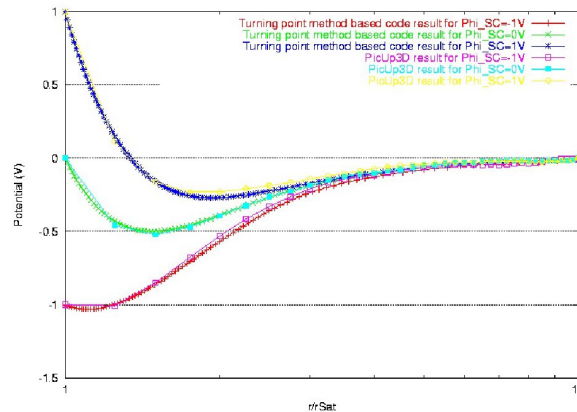
Figure 8. Simulation of the potential profile in a 100 cm^{-3} density and 1 eV temperature plasma environment around a spherical body with isotropic secondary electron emission for three values of the potentials; -1 V, 0 V and +1 V.

Conclusion

There are several spacecraft effects which may limit significantly the scientific return of plasma instruments. Some mitigation techniques exist. For instance positive surface potential can be mitigated by ion emission or plasma contactors, improvement can be obtained by mounting detectors on booms and/or making spacecraft geometry as simple as possible, spacecraft surface materials may be chosen according to their specific properties. However, some trade-off analyses are often necessary due to the possible impact the mitigation techniques may have on cost and/or the performance of other systems. Modelling is still required for optimising the set-up and/or retrieving a 'clean' signal. To this end numerical plasma simulation, laboratory testing and detailed space-based observation for validation would be useful. Currently, the analyses are mainly limited by the lack of information on material properties in space, and of space-based observations in general. Also numerical tools are in general not accurate enough to cope with the thin details required for simulating detector signals. Various recent initiatives are trying to address these issues, especially in the framework of ISSI working group on plasma instrument calibration, SPINE activities [Forest et al., 2001, Roussel et al., 2003] and ECSS standard on spacecraft charging [Rodgers and Hilgers, 2003].

Acknowledgments

References

1. Anderson, P.C. and H.C. Koons, Spacecraft Charging, Anomaly on a Low Altitude Satellite in an Aurora, J., Spacecraft Rockets, 33, 734-738, 1996.

2. Berthelier, J.-J., The effects of spacecraft-plasma interaction on plasma and electrostatic probe measurements, in Proceedings of the 6th Spacecraft Charging Technology Conference, November 1998, Hanscom, Ma, USA.

3. Berthelier J.-J. and J.-F. Roussel , Experimental tests of numerical simulation of the interaction of the Rosetta orbiter with the cometary plasma, in proceedings of 7th Spacecraft Charging Technology Conference, pp.515-520, ESA/SP-476, ISBN No 92-9092-745-3, ESA-ESTEC, Noordwijk, The Netherlands, 23-27 April 2001.

4. Berthelier J.-J., and J.-F. Roussel, A study of the electrical charging of the ROSETTA Orbiter: II - Experimental tests in a laboratory plasma, Submitted to Journal of Geophysical Research, 2003.

5. Cauffman D. P. and N. C. Maynard, A model of the effect of the satellite photosheath on a double probe floating system, J. Geophys. Res., 79, 2427, 1974.

6. Comfort, R. H., C. R. Baugher and C. R. Chappell, Use of teh thin sheath approximation for obtaining ion temperatures from ISEE 1 limited aperture RPA, J. geophys. Res., 87, 5109, 1982.

7. Deforest, S. E., Spacecraft charging at synchronous orbit, J. Geophys. Res., 77, pp 651, 1972.

8. Engwall, E. A. Eriksson, A. Pedersen, J. Forest, G. Paschmann, J. Quinn, R. Torbert, K. Torkar, Wake effects on positively charged spacecraft in flowing tenuous plasmas: Cluster observations and modeling, in Proceedings of the 8th Spacecraft Charging Technology Conference, Huntsville, AL, USA, October 20-24, 2003.

9. Escoubet, C.P., A. Pedersen, R. Schmidt and P.A. Lindqvist, Density in the magnetosphere inferred from ISEE-1 spacecraft potential, J. Geophys. Res., 102, 17, 585- 17, 609, 1997.

10. Forest J., L. Eliasson, A. Hilgers, A New Spacecraft Plasma Simulation Software, PicUp3D/SPIS, in proceedings of 7th Spacecraft Charging Technology Conference, pp.515-520, ESA/SP-476, ISBN No 92-9092-745-3, ESA-ESTEC, Noordwijk, The Netherlands, 23-27 April 2001.

11. Forest J. and A. Hilgers, Feedback on the PicUp3D experience and the open source strategy applied to spacecraft plasma interaction simulation code, in Proceedings of the 8th Spacecraft Charging Technology Conference, Huntsville, AL, USA, October 20-24, 2003.

12. Garrett, H.B., The charging of spacecraft surfaces, Rev. Geophys. Space Phys., 19, 577-616, 1981.

13. Garrett, H.B. and A.G. Rubin, Spacecraft charging at geosynchronous orbit – Generalized solution for eclipse passage, Geophys. Res. Letters,5, 865-868, 1978

14. Grard, R.J.L.: "Properties of the satellite photoelectron sheath derived from photoemission laboratory measurements", J. Geophys. Res., Vol.78, No.16, 2885, 1973.

15. Grard, R., K. Knott and A. Pedersen, Spacecraft charging effects Space Sci. Rev., 34, 289-304, 1983.

16. Gussenhoven, M.S., D.A. Hardy, F. Rich, W.J. Burke and H.C. Yeh, High-Level Spacecraft Charging in the Low-Altitude Polar Auroral Environment, J. Geophys. Res, 90, 11,009-11,023, 1985.

17. Hamelin, M., M. Bouhram, N. Dubouloz, M. Malingre, S.A. Grigoriev, and L.V. Zinin, Electrostatic interaction between Interball-2 and the ambient plasma. 2 Influence on the low energy ion measurements with Hyperboloid, Ann. Geophys., 20, 377, 2002.

18. Hamelin M. , M. Bouhram , N. Dubouloz, M. Malingre, S. A. Grigoriev and L.V. Zinin, Combined effects of satellite and ion detector geometries and potentials on the measurement of thermal ions. The Hyperboloid instrument on Interball, in proceedings of 7th Spacecraft Charging Technology Conference, pp.515-520, ESA/SP-476, ISBN No 92-9092-745-3, ESA-ESTEC, Noordwijk, The Netherlands, 23-27 April 2001.

19. Hastings, D.E., A review of plasma interactions with spacecraft in low Earth orbit, J. Geophys. Res., 100, 14,457-14,483, 1995.

20. Hilgers, A., B. Holback, G. Holmgren, R. Boström, Probe measurements of low plasma densities with application to the auroral acceleration region and AKR sources, Journal of Geophysical Research, 97, 8631-8641, 1992.

21. Hilgers, A., and B. Holback, Some Aspects of Satellite spin effects on spherical probe measurements in a magnetized plasma, Geophysical Research Letters, 20, 347-350, 1993.

22. Hilgers, A. , Interaction between biased sunlit electron collectors in an infinite-Debye-length magnetoplasma: electron temperature threshold effect , Journal of Geophysical Research, 100, 5705-5713, 1995.

23. Katz, I. and M.J. Mandell, Differential charging of High Voltage Spacecraft: equilibrium potential of insulated surfaces, J. Geophys. Res., 87, 4533-4541, 1982.

24. Laframboise J.G., Theory of spherical and cylindrical Langmuir probes in a collisionless, Maxwellian plasma at rest, Institute for aerospace studies, university of Toronto, 1966.

25. Laframboise J. G. and L.J. Sonmor, Current collection by probes and electrodes in space magnetoplasmas: a review, J. Geophys. Res., 98 337-357, 1993.

26. Lai, S.T., Theory and Observation of Triple – Root Jump in Spacecraft Charging, J. Geophys. Res., 96, 19269-19281, 1991

27. Mullen, E.G., M.S. Gussenhoven, D.A. Hardy, T.A. Aggson, B.G. Ledley and E. Whipple, SCATHA Survey of High Level Spacecraft Charging in Sunlight, J. Geophys. Res.,91, 1474- 1480, 1986.

28. Nyffenegger, O., M. Mildner, P. Wurz, K. Altwegg, H. Balsiger and J.J. Berthelier, Influence of electric charging on the Rosina instruments in the plasma environment of comet 46p/Wirtanen, in proceedings of 7th Spacecraft Charging Technology Conference, pp.515-520, ESA/SP-476, ISBN No 92-9092-745-3, ESA-ESTEC, Noordwijk, The Netherlands, 23-27 April 2001.

29. Olsen, R.C. and C.W. Norwood, Spacecraft–generated Ions, J. Geophys.Res., 96, 15,951 – 15,962, 1991

30. Olsen, R.C., The hidden population in the magnetosphere, J. Geophys. Res., 87, 3481-3488, 1982

31. Olsen, R.C., P.M. Decreau, J.F. Johnson, G.L. Wrenn, A. Pedersen and K. Knott, Comparison of thermal plasma observations on SCATHA and GEOS, in Proc. of the 17th ESLAB Symposium on Spacecraft/Plasma Interactions, 1983

32. Olsen and Whipple, An unusual charging event on ISEE-1, J. Geophys. Res., 93, 5568-5578, 1988.

33. Parker, L.W., Differential charging and sheath asymmetry of non conducting spacecraft due to plasma flows, J. Geophys. Res., 83, 4873-4876, 1978

34. Parrot M., J.M. Storey L.R.O. Parker L.W. Laframboise J.G.,Theory of cylindrical and spherical Langmuir probes in the limit of vanishing Debye number, it Phys. Fluids, Vol. 25, No. 12, 2388--2400, 1982.

35. Pedersen, A., C. A. Cattel, C.-G. Faelthammar, V. Formisano, P.-A. Lindqvist, F. Mozer, and R. Torbert, Quasistatic electric field measurements with spherical double probes on the GEOS and ISEE satellites, Space Sci. Rev., 37, pp 269-312, 1984.

36. Pedersen, A. F.S. Mozer and G. Gustafsson, Electric measurements in a tenuous plasma with spherical double probes, in Measurement Techniques in Space Plasmas, ed. by R. F. Pfaff, J. E Borowsky and D. T. Young, AGU Mongraph, 1998

37. Prokopenko, S.M.L. and J.G. Laframboise, High-Voltage charging of geostationnary spacecraft, J. Geophys. Res., 85, 4125-4131, 1980

38. Rodgers, D., and A. Hilgers, ECSS-E-20-06 draft standard on spacecraft charging: environment-induced effects on the electrostatic behaviour of space systems, in Proceedings of the 8th Spacecraft Charging Technology Conference, Huntsville, AL, USA, October 20-24, 2003.

39. Roussel J.-F., Spacecraft plasma environment and contamination simulation code: description and first tests, Journal of spacecraft and rockets, Vol. 35, No. 2, 205--211, 1998.

40. Roussel J.-F, and J.-J. Berthelier, Numerical simulation of the electrical charging of the Rosetta orbiter, in proceedings of 7th Spacecraft Charging Technology Conference, pp.515-520, ESA/SP-476, ISBN No 92-9092-745-3, ESA-ESTEC, Noordwijk, The Netherlands, 23-27 April 2001.

41. Roussel, J.-F. J.-J. Berthelier, A study of the electrical charging of the Rosetta Orbiter: I- Numerical Model, submitted to J. Geophys. Res., 2003.

42. Roussel, J.-F., F. Rogier, M. Lemoine, D. Volpert, G. Rousseau, G. Sookahet, P. Sèng, A. Hilgers, Design of a new modular spacecraft plasma interaction modeling software (SPIS), in Proceedings of the 8th Spacecraft Charging Technology Conference, Huntsville, AL, USA, October 20-24, 2003.

43. Sasot Samplon E., A. Hilgers , B.Thiébault, J. Forest, V. Genot, and A. I. Eriksson, Secondary electron emission causing potential barriers around negatively charged spacecraft, in Proceedings of the 8th Spacecraft Charging Technology Conference, Huntsville, AL, USA, October 20-24, 2003.

44. Scime, E. E., J. Phillips, and S. Bame, Effects of spacecraft potential on three-dimensional electron measurements in the solar wind, J. Geophys. Res., 99, 14,769-14,776, 1994.

45. Singh, N., and C. R. Baugher, Sheath effects on current collection by particle detectors with narrow acceptance angles, Space Sci. Instrum., 5, 295, 1981.

46. Singh, N., W. C. Leung and B. I. Vashi, Potential structure near a probe in a flowing magnetoplasma and current collection, J. Geophys. Res., 102, 195-208, 1997

47. Singh, N., W. C. Leung, T. E. Moore, and P. D. Craven, Numerical model of the plasma sheath generated by the plasma source instrument aboard the Polar satellite, J. Geophys. Res., 106, A9, 19,179-19,192, 2001.

48. Sojka, J. J., G. L. Wrenn and J. F. E. Johnson, Pitch angle properties of magnetospheric thermal protons and satellite sheath interference in thier observation, J. Geophys. Res., 89, 9801, 1984.

49. Szita, S., A. N. Fazakerley, P. J. Carter, A. M. James, P. Travnicek, G. Watson, M. Andre, A. Eriksson, and K. Torkar, Cluster PEACE observations of electrons of spacecraft origin, Ann. Geophys., 19, 1-10, 2001.

50. Szuszczewicz, E. P. and P. Z. Takacs, Magnetosheath effects an cylindrical Langmuir probes, Phys. Fluids, 22, 2424-2428, 1979.

51. Tajmar, M., J. Gonzalez, and A. Hilgers, Modelling of Spacecraft-Environment Interactions on SMART-1", AIAA Journal of Spacecraft and Rockets, Vol. 38, No. 3, pp. 393-399, 2001.

52. Thiébault, B. A. Hilgers, Forest, J., Escoubet, P., Fehringer, M. Laakso, H., Modelling of the photo-electron sheath around an active magnetospheric spacecraft, in Proceedings of the 8th Spacecraft Charging Technology Conference, Huntsville, AL, USA, October 20-24, 2003a.

53. Thiébault, B., Hilgers, A., Sasot, E., Forest, J., Génot, V., and P. Escoubet, Investigation of electrostatic potential barrier near an electron-emitting body, Proceedings of the 8th Spacecraft Charging Technology Conference, Huntsville, AL, October 20-24, 2003b.

54. Torkar K., W. Riedler, M. Fehringer, C.P. Escoubet , K. Svenes, B.T. Narheim, A. Fazakerley, S. Szita, and M. André, Effect of active spacecraft potential control on Cluster plasma observations – first results, in proceedings of 7th Spacecraft Charging Technology Conference, pp.515-520, ESA/SP-476, ISBN No 92-9092-745-3, ESA-ESTEC, Noordwijk, The Netherlands, 23-27 April 2001.

55. Wahlund, J-E., L. J. Wedin, T. Carrozi, A. I. Eriksson, B. Holback, L. Andersson, H. Laakso, "Analysis of Freja Charging Events: Statistical Occurrence of Charging Events," ESA contract 11974/96/NL/JG(SC), WP 130 TECHNICAL NOTE (SPEE-WP130-TN), Version 2.0, February 22, 1999.

56. Whipple, E. C., Theory of the spherically symmetric photo-electron sheath: a thick sheath approximation and comparison with the ATS 6 observation of a potential barrier, J. geophys. Res., 81, 601, 1976.

57. Whipple, E.C., Potentials of surfaces in space, Rep. Prog. Phys., 44, 1197-1250, 1981.

58. Wrenn G. and Heikkila, Photo-electrons emitted from ISIS Spacecraft, in Photon and particle interactions with surfaces in space, 221-230, 1973.

59. Wrenn, G.L. and A.D. Johnstone, Spacecraft charging: Meteosat experience, in Proc. of the AGARD Conference on The Aerospace Environment at High Altitudes and its implications for Spacecraft Charging and Communications, 1986

60. Yeh H.-C., and M. S. Gussenhoven, The statistical environment for defense meteorological satellite program eclipse charging, J. Geophys. Res., 92, 7705-7715, 1987.

61. Zhao H., Schmidt R., Escoubet C.P., Torkar K., Riedler W., Self-consistent determination of the electrostatic potential barrier due to the photoelectron sheath near a spacecraft, Journal of geophysical research, Vol. 101, No. A7, 15,653--15659,

OBSERVATIONS OF VEHICLE SURFACE CHARGING IN DUSTY PLASMA

Aroh Barjatya
ECE Dept, Utah State University, 4120 Old Main Hill, UT 84322
Phone: (435) 881-1616
E-mail: arohb@cc.usu.edu

Dr. Charles M. Swenson
ECE Dept, Utah State University

Abstract

The NASA Sudden Atom Layer (SAL) rocket was launched in February of 1998 from Puerto Rico into an approximately 5 km thick sodium layer that peaked at 94 km altitude. This layer was observed from ground based sodium lidar as well as the Arecibo Radar. The instrument payload consisted of a charged dust detector, an electric field probe, a DC Langmuir probe, and a RF impedance probe. The instruments experienced an anomalous charging event as the rocket passed through this sodium layer. We present here an analysis of the DC Langmuir probe data and the RF impedance probe data to compute the amount of vehicle charging attributed to charged dust. Possible scenarios that could lead to the observed charging effects on the instruments are investigated using a novel SPICE model. The model development and its features are also presented in this paper.

Introduction

Since the first report on charging of the spacecraft surface in geosynchronous orbit [DeForest, 1972] and the subsequent realization that charging could lead to serious operational anomalies [Rosen, 1976], the understanding of spacecraft charging has increased significantly [Garrett and Whittlesey, 2000]. Although the low Earth orbits (LEO) are largely immune to charging due to higher ambient plasma density, analysis of a series of DMSP satellites has proved that high latitude LEO is subject to severe kilovolt charging, lasting tens of seconds [Gussenhoven et al, 1985; Frooninckx and Sojka, 1992].

All the above scenarios pertain to satellites and interplanetary spacecrafts flying through hot collision-less plasma with little or no dust present in the environment. The 80-100 Km altitude range, where most of the sounding rockets fly, presents a different charging dynamics situation then the one present at 'satellite orbit' altitudes. The difference is manifested by enormous amount of meteoric material that condenses into dust particles and is suspended in the Earth's mesosphere between 80-100 Km. The presence of dust at such a low altitude where the Debye length and the mean free path is small, constitutes a "dusty plasma", as compared to the "dust in plasma" at higher 'satellite orbit' altitudes. The Earth's atmosphere at these low altitudes also presents us with anomalous physical phenomena like noctilucent clouds, polar summer mesospheric echoes (PMSE) and sporadic sodium layers. The occurrence of each of these phenomena has been researched extensively in the literature, and in some or the other way each of these phenomena has been linked with the presence of charged dust in the lower Earth atmosphere.

Positive and Negative
Ion Mass Spectrometer

Langmuir Probe

Dust Detector

Electrostatic Shield

Langmuir Probe
Electronics

Sodium and Potassium
Lamps

Telescopes

Photomultipliers

90

180

135

TM

ACS

PFP and
E-field
Electronics

3.0 m

E-field Probes

Dipole PFP

DC Probe

0

315

270

SAL Payload Concept
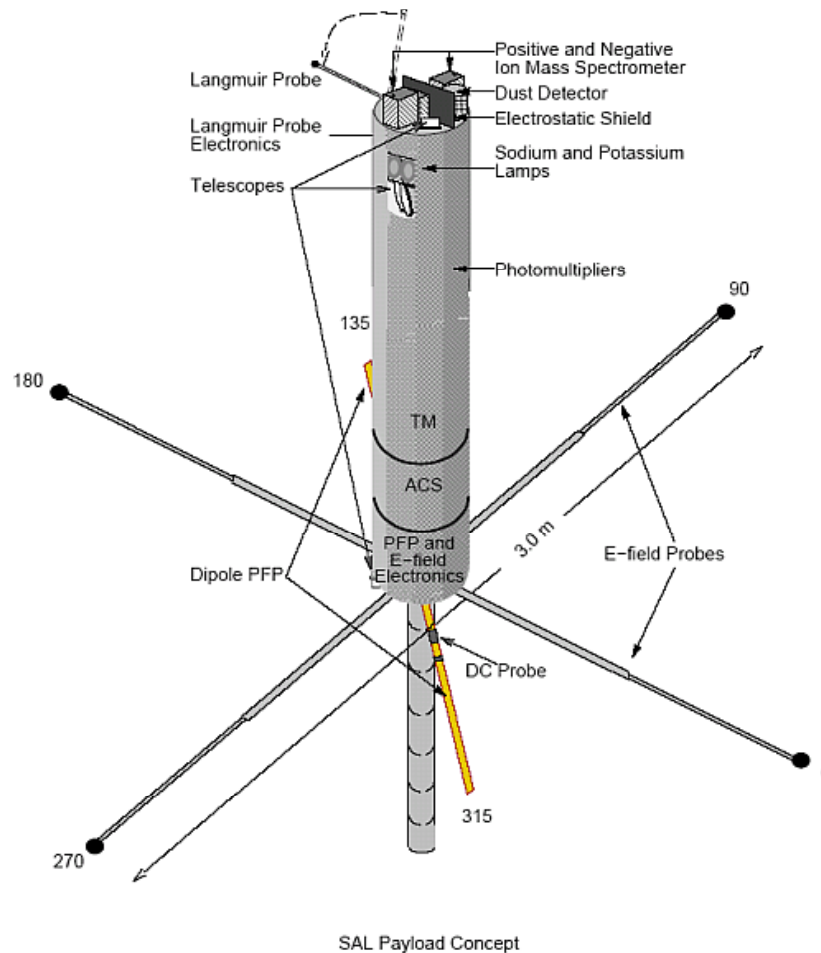
Figure 1. The Sudden Atom Layer Rocket (NASA 21.117) was launched February 20, 1998 at 2009 Local Time. This Cornell University payload included instruments from Utah State University, University of New Hampshire, Naval Research Labs, NASA and Aerospace Corporation.

One of the ways to settle these speculations is to perform in-situ observations of the atmosphere when these anomalies occur. The NASA Sudden Atomic Layer investigation sounding rocket program [Gelinas et al, 1998] was such an attempt to facilitate an understanding of the sporadic sodium layers. The rocket flight detected a layer of charged dust near a sporadic sodium layer. Amongst the large instrument suite that the rocket carried, it carried a radio frequency Swept Impedance Probe (SIP) for absolute electron density measurement and a DC Langmuir Probe (DCP) for relative electron density measurements. There was a significant disagreement between the two probes during a short phase of the flight. The data points to a case of rocket surface charging which the DCP is sensitive to and the SIP insensitive to.

A significant amount of mathematical modeling work has been done in literature to understand the behavior of a spacecraft during charging incidences. Although for a detailed spacecraft-specific analysis tedious mathematical modeling is imperative, for just understanding the behavior of spacecraft at a higher level, a simpler approach is desired.
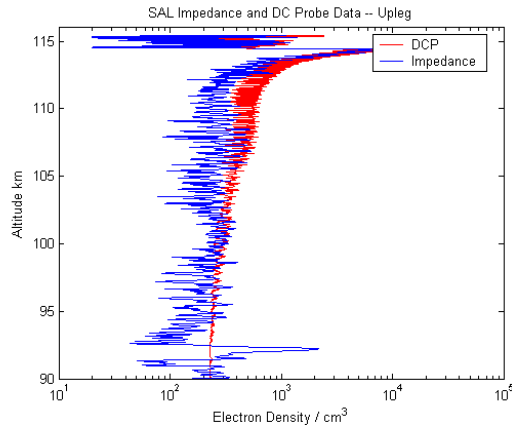
Figure 2(a). Upleg trajectory electron density profile
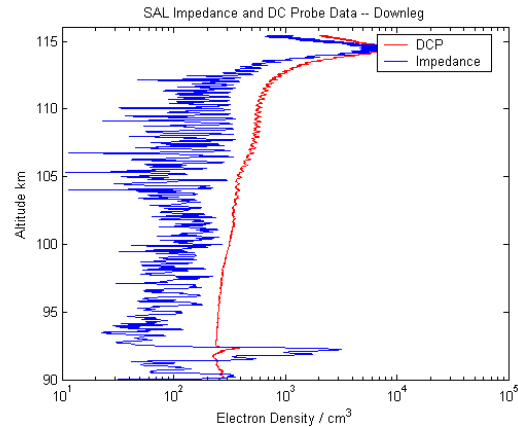
Figure 2(b). Downleg trajectory electron density profile.

In this work we first give an overview of the NASA Sudden Atom Layer (SAL) rocket payload along with the data from the SIP and the DCP. We then develop a simple SPICE (Simulation Program with Integrated Circuit Emphasis) model that can be used to simultaneously calculate spacecraft floating potential and instrument response using the numerical solvers available within SPICE. SPICE is an industry standard simulation program used by electrical engineers for simulating networks of linear and non-linear circuit elements [Keown, 2001]. This model is then applied to the SAL scenario in order to understand the anomaly observed in the DCP data.

Sudden Atom Layer (SAL) Investigation.

Cornell Universities Sudden Atomic Layer (SAL) Investigation sounding rocket was launched from Puerto Rico on 19 Feb 1998 at 2009 LT. The rockets main scientific goal was the investigation of the phenomenon of sporadic sodium layers (Na_s), which are thin (1 Km) layers of neutral atomic metal that form in the mesosphere, roughly at an altitude of 90-100 Km. The payload is as shown in Figure 1. The payload instruments included a charged dust detector to measure mesospheric dust over a mass range of 1,000 –10,000 amu, a Langmuir probe operating as Fast Temperature Probe to measure plasma temperature, electric field booms to measure fields from DC to 5 KHz, telescopes to measure sodium airglow, photometers and lamps to measure neutral sodium and potassium densities, a positive ion mass spectrometer, and a Swept Impedance Probe (SIP) & DC Langmuir Probe (DCP) to measure the absolute and relative electron density respectively.

The SAL rocket flight reached a maximum altitude of 115.5 Km and flew through two thin Na_s layers at 94 Km and 97 Km, with peak densities of 6000 cm^{-3} and 4000 cm^{-3}, as determined by the Arecibo sodium resonance density lidar. The dust detector observed a positive dust layer at the bottom of the lower Na_s layer at 92 Km altitude [Gelinas et al, 1998]. The SIP, provided by Utah State University/Space Dynamics Lab, successfully measured electron density and the measurement techniques included in this version of the probe provided valuable insight into electron density structures associated with sudden sodium layers. The SIP recorded a high electron density layer at 92 Km and an intermediate layer at 114 Km. The SIP data is shown in
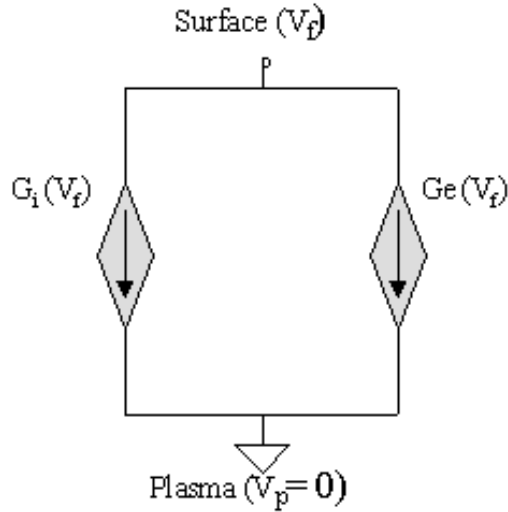
Figure 3. The SPICE sub-circuit Model for a generic spacecraft

Figure 2. Also shown is the DC Langmuir probe relative density data that has been normalized to the SIP data at 114 Km altitude. The important point to note is that the DC Langmuir probe completely missed the 92 Km electron density layer in the rockets upleg trajectory and registered a faint signal on the downleg trajectory. Although at first sight itself we realize that this is related to rocket surface charging, but the relation of charging to the presence of charged dust is unknown and we also do not realize the reason as to why a faint signal was observed in the downleg trajectory and almost nothing on the upleg. We now present a simple charging model to analyze this problem at a very crude level.

Model Development

A Maxwell-Boltzmann distribution is assumed for electrons and ions. The basic process behind spacecraft charging is that of current balance at equilibrium, i.e. all currents must sum to zero. The potential at which this is achieved is the potential difference between the spacecraft surface and the space plasma ground. The former is referred to as the floating potential of the spacecraft surface and the latter as plasma potential. The equation expressing this current balance can be stated as:

$$I_E(V) - [I_I(V) + I_{SE}(V) + I_{BSE}(V) + I_{PH}(V) + I_B(V)] = I_T \qquad (1)$$

Where

V	Spacecraft potential	I_{BSE}	Back-scatter electron current
I_E	Electron current to spacecraft surface	I_{PH}	Photo-electron current
I_I	Ion current to spacecraft surface	I_B	Active current sources such a ion beams
I_{SE}	Secondary electron current	I_T	Total current (= 0 at equilibrium)

In this paper the plasma potential will be taken as zero and hence as circuit electrical ground in the SPICE model. A SPICE sub-circuit model, as shown in Figure 2, can be conceptualized

considering only the positive electron current (current going out) and the negative ion current (current coming in) and disregarding all other currents given in equation (1). Each of these current sources is modeled as a voltage-controlled-current-source (VCCS), since both the ion and electron currents are dependent on the potential of the spacecraft with respect to the plasma. In this paper VCCS is represented as G (V), keeping in line with the syntax used in SPICE. Hence, ion current is written as $G_i(V_f)$ and electron current as $G_e(V_f)$, where V_f is the potential of the spacecraft surface.

The sub-circuit is modeled using SPICE 'Analog Behavioral Modeling' features, that allow an entire equation governing the behavior of the circuit to be modeled. Our model, as a first step, models $G_i(V_f)$ and $G_e(V_f)$ with the retardation and saturation region equations for a cylindrical Langmuir probe in collision-less plasma.

For relative potential of the surface with the plasma greater than zero, the electron current is referred to be as being in the saturation region. The ions, however, are retarded by the positive potentials, leading to an exponential decrease in the ion current as the potential increases. The opposite is true when the potential is negative, the ion current referred to as being in saturation region while the electron current in retardation region.

The current equation for electrons [Chen, 1965; Pfaff, 1996] is given as follows, where the first equation governs the current in saturation region and the second one in retardation region. The ion current is governed by similar equations except that the relational condition for spacecraft potential V with respect top plasma potential V_p and the direction of current, both are reversed.

$$G_e(V) = A n_o e \sqrt{\frac{k_b T_e}{2\pi m_e}} \sqrt{\left(1 + \frac{e(V - Vp)}{k_b T_e}\right)} \quad V \geq V \tag{2}$$

$$G_e(V) = A n_o e \sqrt{\frac{k_b T_e}{2\pi m_e}} \exp\left(\frac{e(V - Vp)}{k_b T_e}\right) \quad V \leq Vp \tag{3}$$

Where

A	Surface area	T_e	Electron temperature
n_o	Plasma density	V	Surface potential
e	Fundamental charge	V_p	Plasma potential (taken by model as 0)
k_b	Boltzmann Constant	m_e	Electron mass

These equations are then solved to find out the floating potential of the spacecraft. In earlier similar models developed, that constitute multiple numbers of such current sources [Smithtro and Swenson, 2002] the equations are solved for V_x, where x stands for a particular instance of the current source, and then the resulting expression simulated using commercially available mathematical tools to find the floating potential of all the elements in the model. The benefit of using SPICE for modeling these equations is that the SPICE software itself solves for V, while doing a bias-point analysis, giving the floating potential of the surface, such that the total current
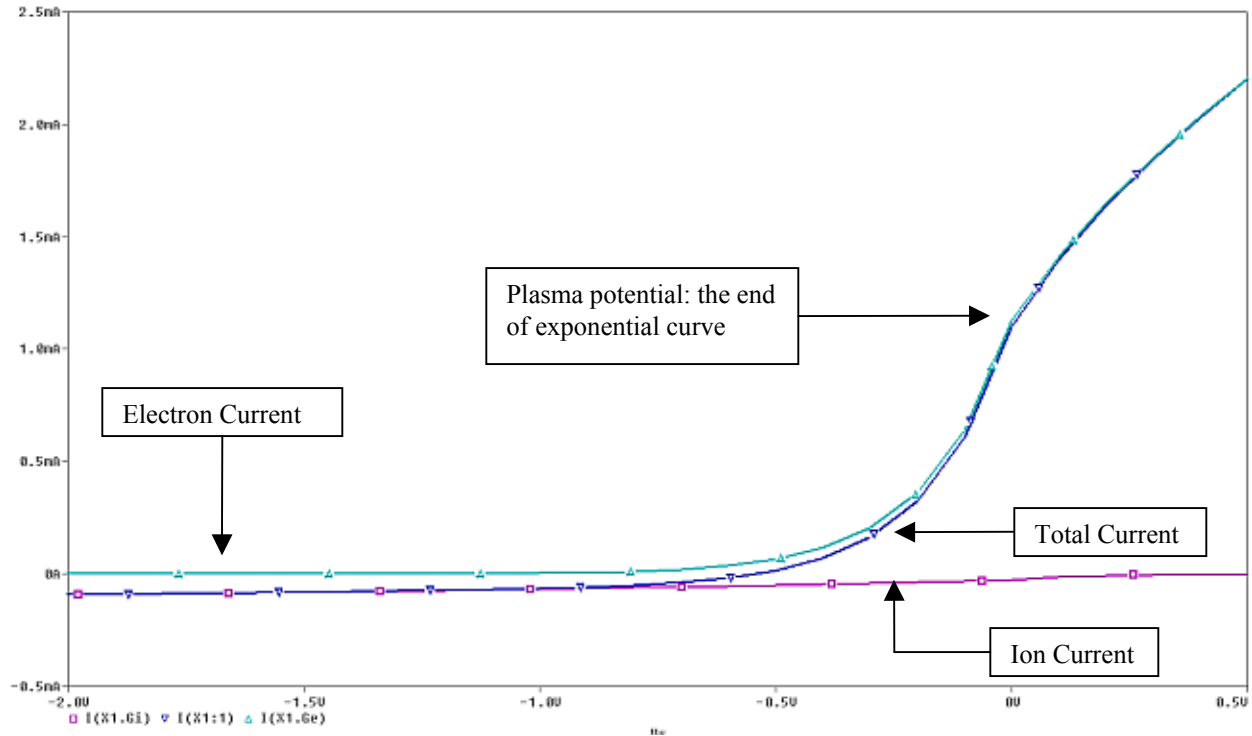
Figure 4. The I-V plot of the cylindrical probe

due to electrons and ions is zero. The model user does not need to bother about the complexity of nonlinear equations as the number of elements in the model increase. This capability becomes a boon when the model is expanded to include multiple number of dielectric surfaces, electric probes and biased solar array. Where mathematical simulation would lead to solving a complexly coupled nonlinear differential equations, the SPICE model is just a couple of lines long, iteratively calling the sub-circuit model for each of the elements.

A sub-circuit of the type shown in Figure 3 can be modeled for each of the geometries: plate, cylinder and sphere, by specifying the current sources with equations appropriate for a particular probe geometry. The sub-circuits then take A, n_o, and T_e as parameters. Having area as a parameter gives the same sub-circuit capability to model various parts of spacecrafts. Hence, each of these sub-circuits can be used to model different parts of a big spacecraft that comes closest to the geometry of the sub-circuit model. Complex spacecraft geometry can be modeled using this method leveraging on the 30+ years of development of SPICE by the electrical engineering community. Seen from a different perspective, the sub-circuit is a function that can be called any number of times, with different function parameters, to model different elements in same environment or same part in different environments. Furthermore, a parametric analysis can be performed on the model with varying parameters like area or ambient density, giving plots of potential with respect to the parameter. The model can also be used to generate I-V plots.

As a test of the above model we do a SPICE DC sweep of the sub-circuit from –2.0 volts to 0.5 volts, in a general LEO environment with $T_e=T_i=2050$ K, A = 1m^2, and plasma density as 1e11 m^{-3}. We can then generate I-V plot showing not only the individual currents for both the ion
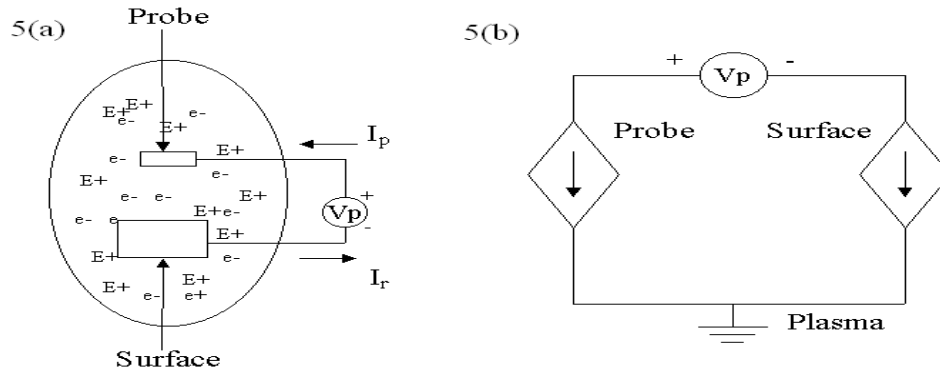
Figure 5. Spacecraft and attached Langmuir probe in plasma

and electron current sources but also the total current. The plot is shown in Figure 4. The curve is as expected from solving the equations manually or using any other mathematical models. The point where the total-current curve breaks away from an exponential rise is the plasma potential, and the point where the total current is zero (at -0.56V) is the floating potential. If we just need to find the floating potential without doing a voltage sweep or looking at plots, all that is required is to do a bias-point analysis and SPICE gives us the floating potential.

A very simple geometry of a spacecraft with a Langmuir probe be modeled as shown in Figure 5(a). The spacecraft and the probe are both assumed to be cylindrical but with significantly different surface areas. Each of these can be modeled using the cylindrical sub-circuit model with their areas passed as the parameter. The model can then be analyzed using SPICE as represented in Figure 5(b).

We can take the above simple example and expand it further to model the SAL rocket. The SAL rocket SPICE model is as shown in Figure 6. As above, plasma is modeled as the spacecraft ground. Node 'Surface' represents the spacecraft surface. Node 'DCP' is the DC Langmuir probe which is biased into the electron saturation region by 3 Volts relative to the spacecraft surface. Node 'FPP' represents the Floating Potential Probe, which were 4 identical carbon spheres extending out on the booms. Node 'FTP' is the Fast Temperature Probe. The FTP was designed [Siegfring et al., 1998] so as to keep it always biased in the electron retardation region. In order to avoid any effect of surface charging, FTP was biased by the amount that was the difference between the FPP and the spacecraft surface (V_{fpp}). It was then further biased by an additional volt. The dependence of the FTP bias on the voltage difference between the FPP and the spacecraft surface is modeled as Vd, which is a voltage-dependent-voltage-source with a 1:1 ratio to the voltage V(FPP - Surface). Cylindrical probe sub-circuit models the rocket surface and the DC probes, whereas spherical probe sub-circuit models the FPP and the FTP.

Each of the above sub-circuit models employ the standard colliosion-less plasma theory equations for the ions and the electrons which are modeled as thermal species. We realize that at this low altitude the plasma is cold and collisional, but our intention is to make a simple model to understand the behavior of the DC probe and not to quantitatively justify the collected current values. The plasma is considered collisional in cases where the mean free path is not greater then the spacecraft radius and the debye length. In the case when the mean free path is smaller then the spacecraft radius and is of the same order as the debye length, the current to a surface is just the collision-less scenario current scaled by a factor of lambda/a, where lambda is the mean free path and a is the spacecraft radius.

The ion thermal speed at T=180K is a maxwellian distribution around the mean value of 375 m/s. This is on the order of the rocket velocity, which is 660 m/s at 92 Km altitude. We thus chose to model the ions as a thermal species in our SPICE model of SAL. On the other hand, the dust being much heavier is relatively immobile and needs to be modeled as ram current. In the case of ram current, we assume the dust particle speed distribution to very narrow around the ram speed and therefore the current drops as a unit step function when the surface potential exceeds the directed ram energy. We then add another voltage-dependent-current-source in the sub-circuit models above for the dust ram current given by the following equation.

$$G_{dust}(V) = A_{ram} \, n_d \, Z_d \, V_{ram} \, H[\varepsilon - eV] \qquad V \geq Vp \qquad (4)$$

$$G_{dust}(V) = A_{ram} \, n_d \, Z_d \, V_{ram} \qquad\qquad V \leq Vp \qquad (5)$$

Where

A_{ram}	Cross-sectional surface area facing ram	V_{ram}	Spacecraft ram velocity
$n_d \, Z_d$	Dust charge density	V	Surface potential
e	Fundamental charge	V_p	Plasma potential (taken as 0V)
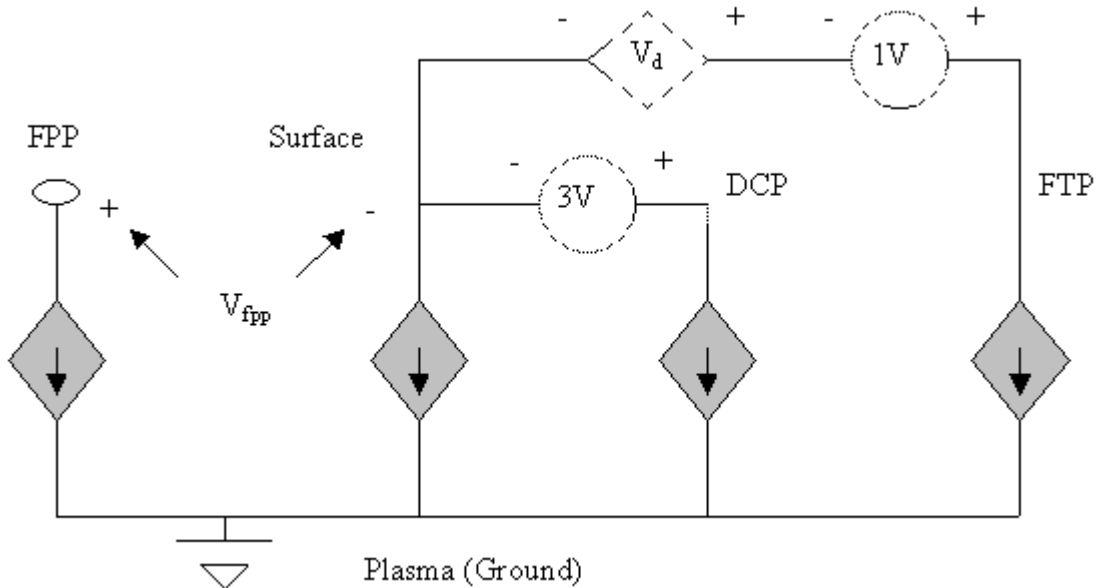
Figure 6. SAL rocket SPICE model

By the convention of our model, this current will be positive (going out) if the dust is negative and will be negative (coming in) if the dust is positive. We now pass additional parameters to the sub-circuits, the cross-sectional area A_{ram} and the dust charge density n_dZ_d. The energy ε is found using the relation $(1/2) \, m \, v^2$, where m is the mass of the dust and v is the rocket ram velocity.

Discussion

The charging of a dust particle due to collisions with ions and electrons leads it to acquire a negative charge, similar to a spacecraft acquiring a negative floating potential. On the other hand, charging by photoemission due to solar radiation leads to a positive charge on the dust. The SAL dust detector saw a layer of positively charged dust at an altitude of 92 Km, which coincides with the high electron density layer, observed by the SIP and the ground based lidar. The existence of positive dust at the same altitude with high electron density at nighttime is highly anomalous and is still not explicable. However we assume that the dominant charging process at the time of launch was photoemission, rather then electron attachment [Gelinas, 1999]. The fact that this high electron density layer disappeared shortly after the completion of the rocket flight (as observed by lidar) also indicates that it was indeed an artifact of photoemission from dust particles and later recombined as night progressed. If the high electron density was largely due to photoemission from dust particles, then it is safe to assume that at that altitude and at that time, the dust charge density constituted a higher percentage of positive charge density of the quasi-neutral plasma.

We define $\beta = (n_dZ_d / n_e) * 100$ as the percentage of positive charge attached to the dust. Where n_dZ_d is the dust charge density and n_e is the electron density. Figure 7 shows a plot of current observed in the DCP for the profile of electron density recorded by the SIP with varying β. As can be seen the higher the dust charge density the lower is the current observed. Comparing this with the Figure 2 where the DCP charged, it can be deduced that the dust layer present at 92 Km altitude had a high β rendering the fixed bias DCP and the vehicle surface unable to collect current from plasma.
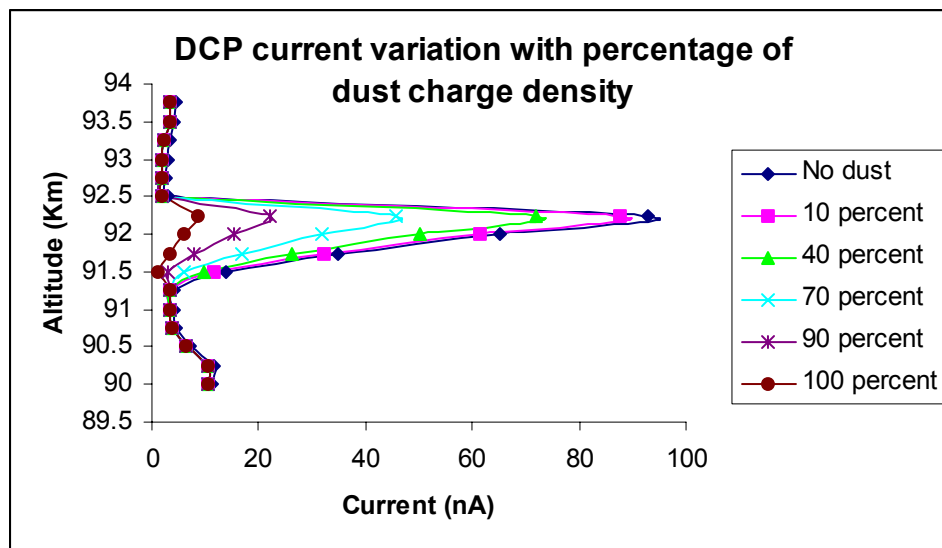
Figure 7. Variation in the current observed in the DCP with varying dust charge density as a percentage of total positive charge in the quasi-neutral plasma.
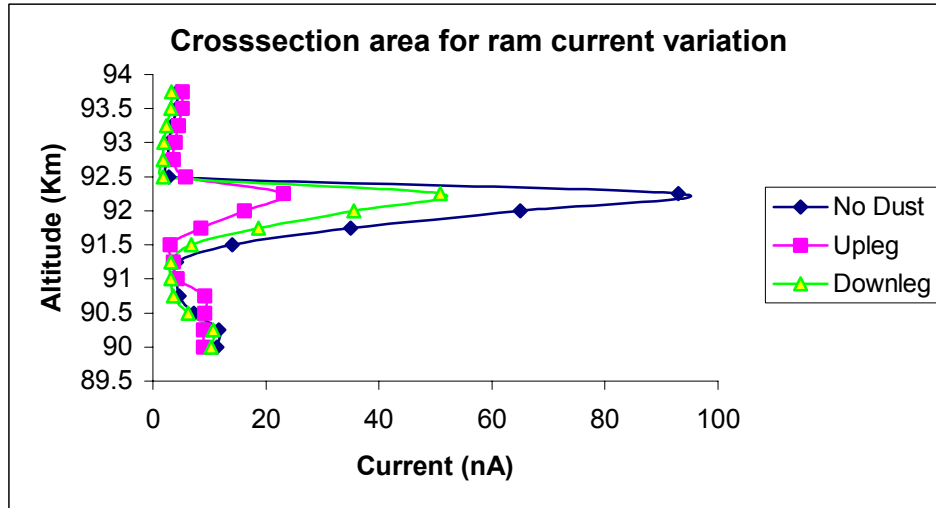
Figure 8. Variation in cross section area for the dust ram current leads to an over all variation in the total current.

Figure 7 explains why the DC probe registered a small electron density variation as compared to the SIP. It, however, does not explain why the upleg signal was fainter then the downleg signal. One of the simplest explanations could be the variation in the dust ram current collection due to rocket attitude variation between upleg trajectory and downleg trajectory. The rocket had an 8 degree inclination with the vertical during downleg, where as the inclination during upleg was only 2 degree. The variation in the ram area of the rocket was calculated based on this data and fed to the SPICE model. Two separate models were created, one each for upleg and downleg, with the only difference being the ram collection area for the dust current. The variation in the current collected by the DC probe is as shown in Figure 8. This plot, which was made assuming a β of 90% clearly shows us that the current collected during upleg will be lesser then the current collected on the downleg.

This feature is also explained in Figure 9. The Upleg shows us the upleg trajectory case when the inclination is 2 degrees to the vertical and hence the ram cross-section area is small. Due to a smaller ram cross-section area dust ram current is low and hence the rocket surface charges more negative to repel larger number of thermal electrons, leading to reduction in the current collected by the positive biased DC probe. The Downleg part shows us the downleg trajectory case when the inclination to the vertical was 8 degrees and the ram cross-section area increases by 3%. As the dust ram current collection is higher, the surface charges comparatively less negative and the current observed by the DC probe is higher. The interesting thing to note here is the fact that even 3% increase in cross-sectional area could lead to a significant change in floating potential.
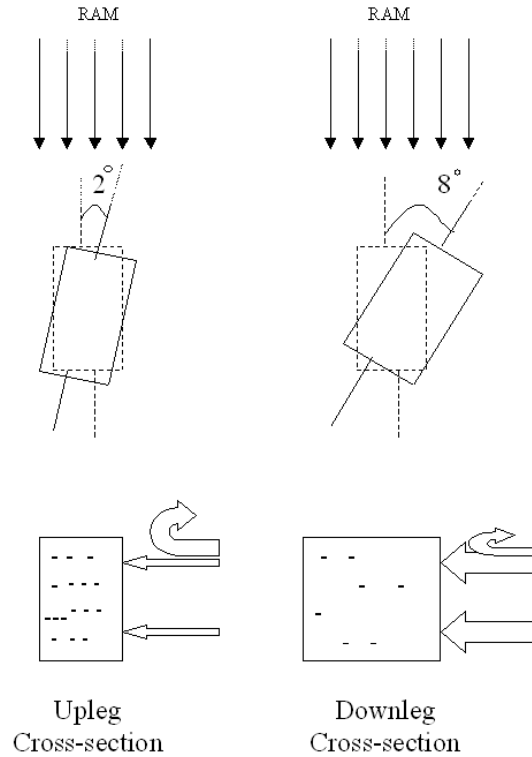
Figure 9. During Upleg the surface charges more negative to repel more electrons due to less positive charges striking its surface.

One of the things the model doesn't help us explain is the spike in the DCP observed current during the downleg trajectory. This phenomena is again shown in Figure 10, which is a zoomed in picture of the DCP collected current between the altitude of 90 to 100 Km. The same effect is observed in the upleg trajectory also although the effect is very subdued and the probe registers almost no current for the complete dust layer. One of the possible reasons for this difference between the upleg and downleg observations could be that the dust charge density is more at the bottom of the layer then at the top of the layer. This would lead to more surface charging during when the rocket hits the dust layer during its upleg trajectory. On the downleg trajectory the probe seems to track the high electron density layer for a very short time period, as shown by the spike, which slowly dies out even though the electron density layer continues further down. This feature of the observation is still not explicable. It seems that there is some capacitance in play during the charging event. We added the sheath capacitance parallel to the spacecraft surface in the SPICE model to try to model this transient effect. The sheath capacitance was calculated using the following equation:

$$C = \frac{\varepsilon\,A}{\lambda_{d}} \tag{6}$$

Where
ε Permittivity of free space
A   Surface area of the spacecraft
λ_{d} Debye length
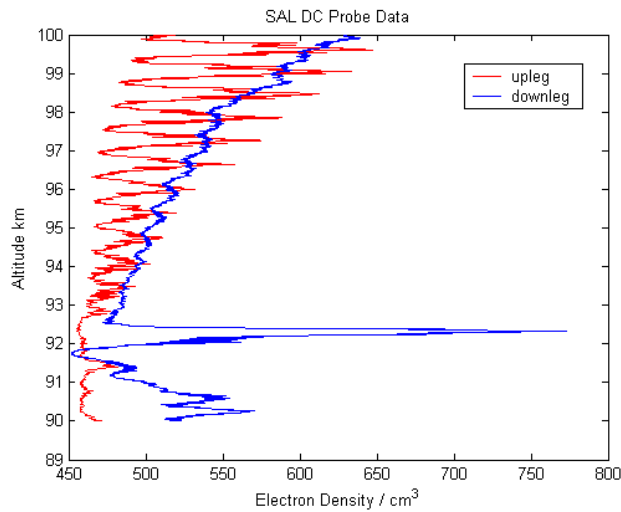
Figure 10. P current profile for upleg and downleg trajectory.

Using the sheath capacitance, the transient effect shown by the SPICE model is so short that complete profile generated using the model, sampling the current at the same rate as the actual probe, misses any transient effect. However, if the DCP current in the model is sampled faster we do see this transient effect. This transient effect, at the DCP sampling rate, is more visible in the model if the sheath capacitance is increased by a factor of 10. However, in order to observe the effect as shown in figure 10 the capacitance needs to be increased by a factor of 100, which seems unrealistic but could be possible. We are still looking into this feature of the observed DCP current profile.

Conclusion

In this work we have developed a simple SPICE model for spacecraft charging analysis that can be applied to various spacecraft geometries in varied conditions, in a relatively simple manner. This model can not only be used to evaluate and test electric probes on sounding rockets and satellites but also evaluate spacecraft charging for a particular spacecraft in specific orbital conditions. The model is largely for high-level understanding of the system characteristics and behavior with variations in plasma characteristics or spacecraft configuration. The model makes use of the existing theory for collision-less plasma, and as the theory for collision-less plasma is fairly robust the model itself also gives accurate representation of spacecraft charging. Although, if collisional plasma theory equations are developed carefully, then the model can also be used for fairly detailed analysis in collisional plasma conditions. This SPICE model can be used to emulate the behavior of fairly complex spacecraft by modeling various parts of the spacecraft as planar, cylindrical or spherical surfaces. The complex interdependence of the non-linear charging equations is solved by the numerical solver built with in SPICE, which has stood the test of time over the 30+ years of development in the industry.

This SPICE model was used to understand the anomalous behavior of the DC Langmuir probe on the SAL sounding rocket. The analysis done with the model tells us that for a sounding rocket to experience surface charging in a dusty plasma, the two important parameters are the percentage of positive charge density constituted by dust charge density, and the ram cross section of the rocket in the velocity direction. The higher the dust charge density percentage with

respect to the total positive charge, the higher the charging on the rocket surface. The higher the ram cross-section of the rocket surface, the lesser is the susceptibility of the surface to charging.

As SPICE is an electrical engineering tool, it is fairly simple to model transient effects of spacecraft charging by adding capacitors in the model. However, we are still trying to postulate a possible scenario to explain the spike in the DCP observed current during the downleg trajectory of the rocket.

References

1. Cen, F. F., Electric Probes, Chapter 4, Plasma Diagnostic Techniques, Edited by Huddlestone R.H. and Leonard S.L., Academic Press Inc. 1965.

2. DeForest, S.E., Spacecraft Charging at synchronous orbit, J. Geophys. Res., Vol. 77, No. 4, Feb, pp 651-659, 1972.

3. Frooninckx, T. B., and J. J. Sojka, Solar cycle dependence of spacecraft charging in Low Earth Orbit, J. Geophys. Res., Vol. 97, No. A3, Mar, pp 2985-2996, 1992.

4. Garrett, H.B. and A. C. Whittlesey, Spacecraft Charging, An update, IEEE Tran. Plasma Science, vol 28, no. 6, pp 2017-2028, Dec 2000.

5. Gelinas, L. J. et. al, First observation of meteoric charged dust in the tropical mesosphere, Gepphysical Research Letters, Vol 25, No. 21, 4047-4050, 1998.

6. Gelinas, L. J., An in-situ measurement of charged mesospheric dust during a sporadic atom layer event, University of New Hampshire, PhD Thesis, 1999.

7. Gussenhoven, M. S., D. A. Hardy, F. Rich, W. J. Burke and H. C. Yeh, High-level spacecraft charging in the low altitude polar auroral environment, J. Geophys. Res., Vol. 90, No. A11, Nov, pp 11,009-11,023, 1985.

8. Katz, I., and D. E. parks, Space Shuttle orbiter charging, J. Spacecr. Rockets, 20, 22, 1983.

9. Keown, J., OrCAD Pspice and Circuit Analysis, Fourth Edition, Prentice Hall, 2001

10. Pfaff, R.F., In-Situ measurement techniques for ionospheric research, Laboratory for extraterrestrial physics, NASA, 1996.

11. Rosen, A., Spacecraft charging: Environment-induced anomalies, J. Spacecr. Rockets, 13, 129, 1976.

12. Smithtro, C., and C. M. Swenson, A time dependent model of spacecraft charging with application to the International Space Station, AIAA Conf, 2002.

SPACECRAFT CHARGING IN A QUASI-STATIC AND DYNAMIC PLASMA ENVIRONMENT AND THE SCALING LAWS FOR ESD-INDUCED CURRENT TRANSIENTS

Richard Briët
Electrical and Electronic Systems Dept., Electromagnetic Effects
©2003, The Aerospace Corporation, M/S. M4-935
2350 E. El Segundo Blvd.
El Segundo, CA 90245
Phone: (310) 336-1912
E-mail: Richard.Briet@aero.org

Objective

The objective of this paper is to present a general expression for predicting characteristics of an electrical pulse from a surface discharge. Scaling laws are presented for various shapes of the dielectric surface.

Abstract

For many years satellite design engineers and manufacturers used a **($\sqrt{Area}$))-scaling** law to estimate peak current amplitudes from electrostatic surface discharges (ESDs) on satellites in orbit. Balmain proposed this scaling law (BSL) in 1978. In some applications, Balmain's scaling law generates overly conservative design requirements.

This paper presents a general expression for the pulse shape of surface discharges. For a given surface discharge, the peak current depends on the shape of the surface and on the location of the discharge; the pulse duration depends on the longest linear distance from the site of a discharge to an edge of the surface.

Introduction

Applied physicists always face the challenge of using small-scale laboratory test results to predict what would or could happen to full-scale systems when they are exposed to postulated worst-case environments. Their predictions become the basis for systems design requirements (SDRs). Management must make the difficult decision to implement, or to ignore the recommendations that the technical staff made on the basis of their best technical judgement. Management's concern is that overly conservative requirements drive costs up without corresponding benefit. The alternative of not implementing the recommended design guidelines might result in significant losses from a degraded or lost mission. The economic impact of recent spacecraft anomalies, such as GOES 8, Anik 1, and Anik 2 [1][2] reminded the industry that spacecraft charging cannot be ignored: this rekindled interest in spacecraft charging, and revived the search for better ways to prevent ESDs.

In the mid-1970s Balmain [3] and others [4] studied the problem of surface discharges in the laboratory. Based on his observations, Balmain proposed a **($\sqrt{Area}$))-Scaling Law** for estimating

peak currents from ESDs **[3]** on satellites in orbit. The Balmain Scaling Law is now widely used throughout the industry, because it is convenient and it is easy to use. However, this convenience can be expensive.

Throughout the industry engineers apply BSL regardless of shape or size of a dielectric surface area. Lack of understanding of the physics of surface discharges and subsequent misapplication of BSL led to unrealistic predictions of thousands of amperes of peak currents from surface ESDs on some spacecraft. Basic physics shows that size and shape of a dielectric surface and the location of a discharge determine the pulse shape and its duration.

Contents

In the first part of this paper we present a brief review of the quasi-static theory of differential surface charging in plasma. We establish the existence of a surface shielding distance, L_B, which explains total-surface and partial-surface discharges by diffusion.

In the second part of this paper we present the complete one-line derivation of the general expression for the pulse shape of a surface discharge. We show that BSL is a special case. Each surface has its own characteristic discharge signature that yields considerable information about the charged surface[1].

Glossary

$kT/q = V_{Plasma}$	is the plasma potential
$K_B = \sqrt{((J\rho/t)/(kT/q))}$	is the inverse of the effective surface shielding distance
$L_B = \sqrt{((kT/q)/(J\rho/t))}$	is the effective surface shielding distance
t	is the thickness of the dielectric film/charge-depth
ρ	is the bulk-resistivity of the dielectric
ρ/t	is the surface resistivity
J	is the net normal-incident plasma current density[2]
$\sigma_q \approx Q/A = [Q/(LW)]$	is the surface charge density

I. Theory of Differential Surface Charging

In a 1987 paper titled " *ASCAT, A Surface Charging Analysis Technique,"* **[5]** the author derived an expression for the differential surface potential across a rectangular dielectric surface of width, **W**, and length, **L**. ASCAT models a rectangular surface that is grounded at both ends ($x = 0, \boldsymbol{L}$).

---

[1] This observation suggests that surface charging/discharging could be useful as a tool for non-destructive evaluation (NDE) of surface materials.
[2] The components of the net charging current density include the ambient plasma current, $J_o=neu$, the back-scattered electron current density, J_{bs}, the current density from secondary electrons, J_{se}, the current density from photo-emissions, J_{ph}, and the contributions from positive ions and radicals.

Surface Voltage Profiles

In the ASCAT model the steady-state surface-voltage profile[3] across the dielectric strip is

$$V(x) = \left(\frac{kT}{q}\right)\left[1 - \frac{\cosh\left(K_B\left(x - \left(\frac{1}{2}\right)L\right)\right)}{\cosh\left(\left(\frac{1}{2}\right)K_B L\right)}\right] \qquad (1)$$

The maximum voltage at the midpoint, where $x = (L/2)$, is:

$$V(L/2)|_{Max} = 2(kT/q)(\sinh(K_B L/4))^2/\cosh(K_B L/2) \qquad (2)$$

_For **(L) << (L_B)**_ the maximum voltage is given by: $V_{max} = (1/8)J(\rho/t)\,L^2$. It is half of the incident current, $(1/2)J(LW)$ multiplied into the mean resistance in either grounded half-strip, $R|_{Ave} = (1/2)(\,(\rho(L/2))/(tW))$. We could have used Ohm's Law to derive the same.

_For **(L) >> (L_B)**_ the maximum voltage approaches the plasma potential: $V_{Max} = V_{Plasma} = kT/q$. This is a result a physicist would have guessed without doing any analysis at all. It is consistent with the theories of thermodynamics and electrostatics. In thermodynamics we learned that an object immersed in a heat bath will eventually acquire the temperature of the heat bath. In electrostatics we learned that an object suspended in plasma will reach equilibrium at the plasma potential.

Surface Field Distribution

The electrical stress across the dielectric surface is defined by $E(x) = -dV(x)/dx$. It is:

$$E(x) = \left(\frac{kT}{q}\right) \cdot K_B \cdot \frac{\sinh\left(K_B\left(x - \frac{1}{2}L\right)\right)}{\cosh\left(K_B\left(\frac{1}{2}L\right)\right)} \qquad (3)$$

The maximum stress occurs at both grounded edges:

$$E(x=L,0)|_{Max} = \pm\,(kT/q).K_B.\tanh(K_B\,(L/2)) \qquad (4)$$

_For moderately conductive surfaces and **L << L_B**_ this stress is $E(L,0)|_{Max} = \pm J(\rho/t)(L/2)$.

The maximum stress can also be written as $E(L,0)|_{Max} = \pm\,4\,(V_{max}/L) = \pm\,2\,\mu u$, where the mobility, μ, is given by $\mu = (n\,q_e\,\rho) = \sigma_q\,(\rho/t)$, and $u = <E>_{Ave}/\mu$. The factor "2" accounts for the averaging process where $<E>_{Ave} = (E_{max}+E_{min})/2 = E_{max}/2$. The _average_ electrical stress can also be calculated from the derivative of the maximum voltage.

---

[3] The general surface voltage profile is a function of the grounding configuration and the surface resistivity. It is the basis for a grounding guideline that is more effective than the existing multiple-point grounding guideline.

For example, for $(L) << (L_B)$:

$$(d(V_{max})/dL)|_{Ave} = \pm(d/dL) [((1/8) J (\rho /t) L^2)] = \pm(1/4) J (\rho /t) L \qquad (5)$$

As it should be, this is half the value for the maximum electrical stress for $(L) << (L_B)$.

For high-resistant surfaces and $L >> L_B$ the stress is $E(L,0) = \pm (kT/q)K_B = \pm V_{Plasma}/L_B$. The maximum stress is the slope of the surface voltage profile at the grounded terminals where $x = L$, and $x = 0$. This slope crosses the plateau of the surface voltage at a distance of $x = L_B$ from a reference ground.

Surface Current Distribution

The steady-state current distribution across the surface is given by [3]:

$$I(x) = (W \cdot K_B) \cdot \left(\frac{kT}{q}\right) \cdot \left(\frac{t}{\rho}\right) \cdot \left(\frac{\sinh(K_B(x - (\tfrac{1}{2})L))}{\cosh(K_B \cdot (\tfrac{1}{2})L)} \right) \qquad (6)$$

In the middle of the strip, $I(L/2)=0$. At the grounded edges on either end of the strip (at $x=0$ *and* at $x=L$) the leakage current is given by

$$I(0,L)_{Max} = mJ \cdot (W \cdot L_B) \cdot \tanh(K_B \cdot (\tfrac{1}{2})L) \qquad (7)$$

For $(L) << (L_B)$ $\tanh(K_BL/2) \approx (K_BL/2)$. Therefore, the magnitude of the leakage current at either grounded edge is $|I(0,L)| = (1/2)J(LW)$. This is half the captured plasma current.

For $(L) >> (L_B)$ $\tanh(K_BL/2) \approx 1$. Therefore, the magnitude of the leakage current is $|I(0,L)| = J.(W.L_B)$. Note that this leakage current is a local phenomenon, i.e., only that fraction of the total area that is effectively within the surface shielding distance, L_B, from reference ground captures the plasma current. The area beyond L_B is at equilibrium with the plasma potential, kT/q: on those outlying areas, the resident charges shield the surface against incident charges from the plasma.

Total-Surface vs. Partial-Surface Charge (Diffusion) Discharges

The discussion in the previous section suggests that surface discharges on moderately conductive dielectric surfaces[4] where $L << L_B$ tend to be total-surface discharges. Surface discharges on high-resistant materials where $L >> L_B$ tend to be partial-surface discharges. For the ASCAT model, only that fraction ($f = \# L_B/L$) of the total surface area that falls within several shielding lengths, L_B, will discharge. This is an important concept, because it answers the question about the existence of an upper bound for BSL. It has implications about the total amount of charge (and therefore energy) that can be dissipated in an ESD [5], i.e., *high-resistant dielectrics will not release all surface charges in a single surface discharge*. Since not all of the energy stored on a

---

[4] "Moderately conductive" means the bulk and/or surface resistivity is sufficiently low that $L << L_B$.

charged dielectric surface will be dissipated in a single surface discharge, we may conclude that there is justification to relax some ESD design requirements. In Part II of this paper we will explore this issue in further detail from the perspective of the transient nature of an ESD. Let us review the lessons learned until this point.

Lessons Learned

(L#1): For moderately conductive surfaces and $L << L_B$ the entire surface area, $A=(LW)$, captures and diverts the plasma current, $I=JA$, to both grounded terminals[5].

(L#2): For high-resistant surfaces and $L >> L_B$ only a relatively narrow strip of area $A_B=WL_B$ within a few shielding lengths, L_B, from a reference ground captures and diverts the *locally* captured plasma current to the nearest reference ground. The remainder of the surface is at equilibrium with the plasma potential, (kT/q). This surface deflects the incoming plasma current away from the dielectric surface.

(L#3): The concept of a "*locally* captured plasma current," $I_B=JA_B=(L_B/L)(JA)$ is important. It means that around every reference ground there is a strip of land that is as wide as several shielding lengths, L_B. Beyond the borders of this island, surface charges do not move. If the separation distance between two islands is more than $2 L_B$, then the charges on one island may not interact with the charges on a second island. Charges on separate islands interact strongly when the borders of two or more islands overlap. We can interpret L_B as the surface analogue of the Debye length in a plasma, L_D.

Theory of Surface Discharges

Surface discharges occur when the electrical stress exceeds the breakdown strength of the medium. There is a general understanding, and laboratory tests confirm it is true **[4]**, that high-resistant materials tend to break down more often than more conductive materials do. This concept is in fact the basis for one of the standard charge mitigation techniques in the industry. Therefore, we limit our discussion to high-resistant dielectrics, and we postulate that breakdown occurs when the electrical stress reaches the breakdown strength of the material. From Equation (4) and $L >> 2 L_B$ we can calculate the electrical surface stress for high-resistant materials, and postulate that breakdown occurs if

$$|E(0)|_{Max} = (kT/q).K_B = \sqrt{((\rho J/t)(kT/q))} \geq E_{BD} \qquad (8)$$

Based on Equation (8) a charge-mitigation design requirement is that the electrical surface tension or stress be kept below the surface dielectric strength of the material. Testing to show compliance takes time and money. Therefore, to cut down on laboratory time, accelerated testing is common practice. Such tests are performed at elevated levels of J and the voltage of the electron beam used to simulate the plasma potential, kT/q. Equation (8) shows that there is an other option to enhance accelerated testing. It is based on the trade-off between two simultaneously occurring effects. (1) For most dielectrics, lowering its temperature increases its

---

[5] In general, captured charges diffuse to all grounded strips: the longer the grounding strip is, the better the diffusion rate will be, and therefore the more effective the charge mitigation will be.

surface resistivity, thereby accelerating the electrical surface tension to reach the breakdown level **[4]**, and (2) lowering the plasma temperature will lower the electrical surface tension, thereby delaying the electrical surface tension, $|E(0)|_{Max}$, to reach the breakdown level, E_{BD}. A log-log plot of (ρ/t) vs. (*sample temperature*) shows that the surface resistivity increases with falling temperature. It is a plot often used to determine the activation energy in solids. At phase transitions, such as occurs at the melting point, one observes an abrupt change in the slope, and therefore the activation energy. Test results and on-orbit data showed that some dielectrics, such as nylon, do break down more often at low temperatures. Thus, for the tested samples, the temperature dependence of the surface resistivity, (ρ/t), dominated the observed breakdown. This suggests that testing at lower temperatures is a viable third option for accelerated testing. (One must not confuse the temperature of a sample that affects (ρ/t) with the plasma temperature in kT/q.)

Summary of Part I: Surface Charging Theory

The first part of this paper provided a set of useful equations. In particular,

i)   for estimating the maximum steady-state surface potential on dielectric surfaces use Equation (2): $V(L/2)|_{Max} = 2(kT/q)(sinh(K_B L/4))^2/cosh(K_B L/2)$

ii) for estimating the maximum electrical stress,   use Equation (4): $E(x=L,0)|_{Max} = \pm (kT/q) K_B \tanh(K_B (L/2))$

iii) for estimating the maximum steady-state diffusion/leakage current at the grounded terminals, use Equation (7): $|I(L,0)|_{Max} = \pm J (W L_B) \tanh(K_B L/2)$

iv) for identifying controllable parameters to accelerate achieving test objectives, use Equation (8): $|E(0)|_{Max} = (kT/q) K_B = \sqrt{((\rho J/t)(kT/q))} \geq E_{BD}$

From "*iv)*" above and the effect of sample temperature on its surface resistivity it is noted that low-temperature testing is a third viable alternative for accelerated testing.

In Part I of this paper we compared the response of moderately conductive materials with the response of high-resistant materials. We showed that for high-resistant materials, only the part of surface area inside a few shielding lengths, L_B, from reference ground captures and diverts the plasma current to reference ground. The remainder of the surface is at equilibrium with the plasma potential, and as such, it serves as a shield against the incoming plasma current. We noted that the shielding length **[5]**, $L_B = \sqrt{((kT/q)/(\rho J/t))}$, is the surface-analogue of the Debye length in a plasma, L_D. It is a shielding distance, i.e., it is the mean free path, or the diffusion length of electrons across the surface of a dielectric material. The shielding length, L_B, is the basis of our postulate that a single electrostatic discharge on high-resistant materials will not dissipate all surface charges and partial-surface discharges will not dissipate all available energy stored on the surface. This may have a significant impact on current ESD mitigation design requirements.

In Part I of this paper we discussed only the quasi-static model of spacecraft charging. Most of the discussion is based on a paper published in 1987 **[5]**. For convenience, we list the most significant results in **Table 1**.

Table 1. Summary of Steady-State Solutions for Surface Charging Effects

Description	Maximum	$L \ll L_B$:[1A]$^\bullet$	$L \gg L_B$:[fA]$^\bullet$
Voltage Profile: $V(x) =$ **Eqn. (1)**	**Eqn. (2):** $V(\frac{L}{2}) = 2\left(\frac{kT}{q}\right)\dfrac{\left(\sinh\left(K_B\frac{L}{4}\right)\right)^2}{\cosh\left(K_B\frac{L}{2}\right)}$	V_{Max}: $V = (\frac{1}{8})J(\frac{\rho}{t})\cdot L^2$	V_{Max}: $V = V_{Plasma} = \frac{kT}{q}$
Electrical Stress $E(x) =$ **Eqn. (3)**	**Eqn. (4):** $E(0,L) = \mathfrak{m}\left(\frac{kT}{q}\right)\cdot K_B \cdot \tanh\left(K_B \cdot \frac{L}{2}\right)$	E_{Max}: $E = (\frac{1}{2})J(\frac{\rho}{t})L$	E_{Max}: $E = \left(\frac{kT}{q}\right)/L_B$
Current: $I(x) =$ **Eqn. (6)**	**Eqn. (7):** $I(0,L) = \mathfrak{m}J \cdot W \cdot L_B \cdot \tanh\left(K_B \cdot \frac{L}{2}\right)$	I_{Max}: $I = (\frac{1}{2})J(LW)$	I_{Max}: $I = J\left(W \cdot L_B\right)$
• **1A:** Candidate for total-surface discharge			
• **fA:** Fractional, or partial-surface discharge if (distance between grounding) $> (2L_B)$.			

In Part II of this paper we discuss the transient nature of ESD. The objective is to predict the pulse shape, $I(\tau)$, the peak current, $I_{pk} = I(\tau)|_{max}$, and the pulse width, τ_{pw}, or pulse duration, τ_{Total}, of an ESD. After a brief listing of our assumptions, we will present the complete one-line derivation of the general expression for a surface discharge current.

II. Theory of ESD Transients

Since the early work by Ohm (1827), much research was done on conduction in gasses, metals and dielectrics. (Debye, Thomson, Seebeck, and Lorentz). These and many other authors studied the more complex subjects of how an ESD is triggered and how an arc discharge is sustained: those are subjects beyond the scope of this paper. We only discuss a transient ESD pulse from the time the discharge was triggered until the pulse stops. We derive a general expression for the shape of the pulse, and we apply our expression to representative geometrical shapes. We show that BSL is a special case of a more general scaling law.

Derivation of Scaling Laws

Introductory Remarks In Part-I of this paper we showed that L_B is the surface analogue of the Debye length. L_B is a surface shielding length or diffusion distance. A little later we explain how L_B affects spacecraft mitigation design requirements. However, to keep this simple, we make the following assumptions:

1• A single surface discharge occurred at some point along an edge of a dielectric tile
2• The surface charge density is constant everywhere: $dQ/dA \approx (Q/A) = \sigma_q =$ constant
3•, Regardless its shape, a surface discharge clears the entire surface, *A,* of all charges
4• The discharge travels across the surface at a <u>constant *radial* velocity</u>, $u=dr/d\tau =r/\tau$

Clarification: These simplifying assumptions *do not negate the facts* that (1) mid-surface discharges do occur, and (2) at the grounded boundaries the surface charge density is not constant. The third assumption implies that $L << L_B$, i.e., we model a surface area that is electrically small. Later we discuss partial-surface discharges on electrically large surfaces where $L >> L_B$. The fourth assumption is justified by virtue of the second and third assumptions. The *average* velocity of a discharge is proportional to the *average* electrostatic stress across the surface of the dielectric material, i.e.: $u = <E_{Max}>/(2\sigma_q.\rho/t)$.

Complete Derivation of Surface Discharges

An electrical current is defined as the rate of change of local charges, i.e., $I = dQ/d\tau$. Subject to the above assumptions, this equation can be written in the following form:

$$I(r) = \frac{dQ}{d\tau} = \frac{d(\sigma_q A)}{d\tau} = \sigma_q \cdot \frac{dr}{d\tau} \cdot \frac{dA}{dr} = (\sigma_q \cdot u) \cdot (r \cdot \theta) = \frac{E_{Max}}{2(\rho/t)} \cdot (r \cdot \theta) \quad (9A)$$

This completes the derivation of the general expression for the pulse shape from a total-surface discharge.[6] Since $r = u\tau$, equivalent time-dependent expressions are:

$$I(\tau) = \left(\frac{E_{Ave}}{(\rho/t)} \cdot u\right) \cdot \theta \cdot \tau = \left(\frac{1}{\sigma_q}\right)\left(\frac{E_{Ave}}{(\rho/t)}\right)^2 \cdot \theta \cdot \tau = \sigma_q \cdot u^2 \cdot \theta \cdot \tau \quad (9B)$$

Our studies of surface-ESD transients will be based in part on Equation (9A):

$$\boxed{I(r) = (\sigma_q \cdot u) \cdot (r \cdot \theta) = \frac{E_{Max}}{2(\rho/t)} \cdot (r \cdot \theta)} \quad (10)$$

Applications to Specific Geometrical Shapes

Circular tile

The first shape to which we will apply Equation (10) is the circular tile. This is the shape Balmain studied in the 1970's **[6].** His test-results led him to suggest we use the **($\sqrt{(Area)}$)** Scaling Law (BSL) to predict peak ESD amplitudes on large dielectric surfaces.
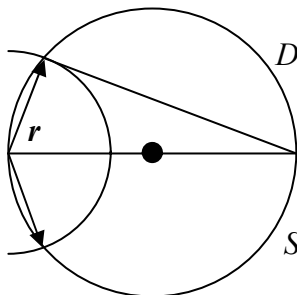
Disk Geometry   R = Radius of Disk
D = Diameter = 2R
$r\theta$: Arc-length = 2r Acos(r/D)
$r\theta$: 2r Acos(r/D) = 2D θ cos(θ)

Surface Discharge Current:

---

[6] The characteristic pulse shape of natural lightning is remarkably similar. This is not coincidental.

$$I(r) = \left(\sigma_q u\right)\left(2 \cdot r \cdot A\cos\left(\frac{r}{D}\right)\right) = 2 \cdot \left(\sigma_q u\right)\left(\theta \cdot \cos(\theta)\right) \cdot D \qquad (11)$$

The peak current occurs when $dI/d\tau = (dr/d\tau)(d\theta/dr)(dI/d\theta) = u \, d\theta/dr)(dI/d\theta) = 0$:

$$\frac{dI}{d\tau} = 2\sigma_q u^2 \cdot \frac{d\theta}{dr} \cdot \left(\cos(\theta_x) - \theta_x \cdot \sin(\theta_x)\right) \cdot D = 0$$

Thus, at $\theta_x = (\cos(\theta_x))/(\sin(\theta_x))$ the peak-current is given by

$$I(r)\big|_{Pk} = 2 \cdot \left(\sigma_q u\right)\left(\frac{(\cos(\theta_x))^2}{\sin(\theta_x)}\right) \cdot D \qquad (12)$$

These results show that both the pulse-shape (Eqn. (11)) and the peak-current (Eqn. (12)) scale with $D \sim \sqrt{(Area)}$. ***This is the famous Balmain Scaling Law***. The question is: "Are we doing the right thing in industry when we apply Balmain's Scaling Law to all surface shapes?" To answer that question we next consider a square tile.

*Square Tile, dimensions L*W = a*a: Discharge at a corner (0,0)*

We assume a discharge occurs at a corner. As long as surface charges sustain a spark, we visualize a radial wave front starting at the corner and sweeping across the charged surface. For a square tile, the arc length, $r\theta$, is a piece-wise continuous function of time: it changes abruptly when the wave front meets a corner. For each continuous segment we must write a different equation for $r\theta$.
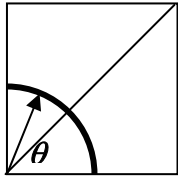
This diagram shows a square tile of dimensions *"a"-by-"a"*.
For $0 < r < a$ $\theta = \pi/2$ radians $I(r) = (\sigma_q.u) \, r \, (\pi/2)$
For $a < r < a\sqrt{2}$ $(\theta) = (A\sin(a/r) - A\cos(a/r))$ $I(r) = (\sigma_q u) \, r \, (\theta)$

For the square tile the peak current is $I(a)|_{Pk} = (\sigma_q u) \, a \, (\pi/2)$. This shows that the peak current scales with $a = \sqrt{(Area)}$. This is consistent with Balmain's Scaling Law. However, is this true for other shapes as well? Let's consider a rectangular tile next.

*Rectangular Tile, dimensions L*W = 2a*a: Discharge at a corner (0,0)*
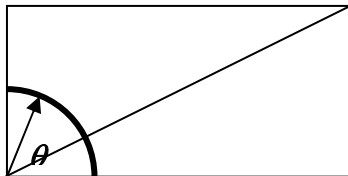
Here we show a rectangular tile of dimensions *"2a"-by-"a"*.
For $0 < r < a$ $\theta = \pi/2$ radians $I(r) = (\sigma_q.u) \, r \, (\pi/2)$
For $a < r < 2a$ $\theta = A\sin(a/r)$ $I(r) = \sigma_q u \, r \, A\sin(a/r)$
For $2a < r < a\sqrt{5}$ $(\theta) = (A\sin(a/r) - A\cos(a/r))$ $I(r) = \sigma_q u \, r \, (\theta)$

For this rectangular tile the peak current is $I(a)|_{Pk} = (\sigma_q u) a(\pi/2)$. Note that its value is *the same* as the value of the peak amplitude for the square tile. It seems that the ambiguity regarding

scaling laws for a square tile is removed: On rectangular tiles the peak current scales with the width of the tile. Other researchers have suggested such a scaling law. The total duration of the pulse scales with the longest distance from the arc to an edge of the tile. In this example it is the time to reach the opposite corner. However, most of the surface charge, and therefore surface energy is dissipated after $(L/u) = ((2a) / u)$ seconds.

To get a better understanding of the scaling laws we will compare the pulse shape from a surface discharge at half the width, **W/2**, with one occurring at **L/2** = a of the rectangle.

*Rectangular Tile, dimensions L*W = 2a*a: Discharge at W/2*
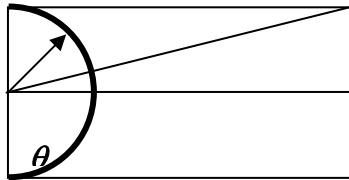
The diagram shows the same *"2a"-by-"a"* rectangular tile.
For: $0<r<a/2$ $\theta = \pi$ radians $I(r) = \sigma_q u \pi r$
$a/2<r<2a$ $\theta = Asin(a/r)$ $I(r) = \sigma_q u r Asin(a/r)$
$2a<r<(a/2)\sqrt{17}$ $(\theta) = (Asin(a/r)-Acos(a/r))$ $I(r)=\sigma_q u r (\theta)$
The peak current for this configuration is $I_{pk} = \sigma_q u (a/2) \pi$

*Rectangular Tile, dimensions L*W = 2a*a: Discharge at L/2*
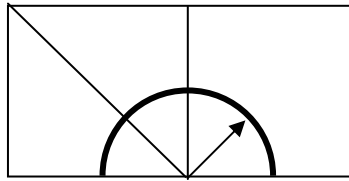
For $0<r<a$, $\theta = \pi$ radians $I(r) = \sigma_q u \pi r$
For $a<r<a\sqrt{2}$, $\theta=(Asin(a/r)-Acos(a/r))$ $I(r)=\sigma_q u r (\theta)$
The peak current for this configuration is $I_{pk} = \sigma_q u (a) \pi$
The calculated peak currents for all five examples are listed in **Table 2**, and correlated with the pulse shapes in **Figure 1.**

If we agree to call the diameter of a circle its width, then we can say that for each shape the peak current scales with the width of the surface. The three examples for the rectangle clearly show that the peak current also depends on the location of the discharge. However, in all cases, the pulse duration for a given discharge is always such that the time integral of the pulse equals the total charge stored on the surface: $\int I dt = Q = \sigma_q A$.

This is found to be true for all examples, and the reason is simple: *By our 3rd assumption, we modeled a pulse from a total-surface discharge*. In **Figure 2** we show that for a discharge at a corner of a rectangle, the peak current is not changed as the length of the rectangle is increased. However, the pulse duration increases in such a way that the additional surface under the curve of $I(r=u\tau)$ equals the charge stored on the added surface area. This is the law of conservation of charge, and it is very different from the way we used scaling laws in the past. For a partial-surface discharge, the area that will discharge is within one to seven shielding lengths, L_B, from a site of a discharge.

Putting it all together

Brief summary of accomplishments

The pulse shape of an ESD from a surface discharge is governed by a simple geometrical relationship. For any surface shape of a dielectric tile, the discharge current amplitude is directly proportional to the arc-length of the wave front sweeping across the surface. For the examples in this paper, the center of the traveling wave is located at the site of an ESD[7]. Having said this much, we must be able to qualitatively guess what the pulse shape of a discharge at any point on a dielectric surface of arbitrary shape must look like. We listed the peak-currents for the five examples **Table 2**. The last entry in this table is the universal scaling law for surface discharges. In **Figure 1** we show what each pulse looks like. Equation (9A) shows: $I(r)=(\rho\, E_{Ave}/t)$ $(r\theta)=(1/2)(\rho\, E_{Max}/t)\, (r\theta)= (\textbf{\textit{Coefficient}}) * (r\theta).$ Because it is important, we will say this one more time for emphasis in plain English.

> *The amplitude of a current pulse from a surface discharge to reference ground, measured at the site of the surface discharge, is directly proportional to the arc-length of the wave front that travels across the face of a dielectric surface.*

How to extract Relevant Information from Test Results

In Part II we derived the general expression for the pulse shape for a surface discharge and found that surface discharges scale with the arc-length of a traveling wave front of a discharge. We applied the formula to circular, square, and rectangular shapes, and we showed that Balmain's $(\sqrt{Area})$-Scaling Law (1978) is a special case: it is the exact solution for circular tiles.

To verify this theory we could perform tests on carefully selected shapes of dielectric material, or we could do a literature search to find what others have done and published since spacecraft charging became an issue. Balmain tested circular samples of varying diameter **[6]**, and so it seems reasonable to say that Balmain had in fact completed the tests for circular samples more than 20 years ago. Therefore, additional testing should be performed on rectangular samples over the temperature range at which satellites might operate. By comparing the measured current pulse shape with predicted pulse shapes one can determine all relevant parameters needed for surface charging assessment purposes. Here is a suggested list of parameters one may want to measure on rectangular samples.

(1) *Average velocity, u, method 1:* From the measured time to reach the first peak and the measured distance between a spark and the nearest corner on a rectangular sample, we can calculate the average speed, u, of a propagating surface discharge. $u = (distance\ between\ the$ *site of the spark to the nearest corner, a*) / (*measured time to reach the first peak in the wave shape,* τ) = a/τ.

---

[7] In all examples in this paper, the arc of the traveling wave front is always in direct line-of-sight with the location of the discharge. For shapes where this is not the case, we may have to use Huygens' Principle of wave propagation to determine the location and the direction of motion of the wave front at any time.

(2) *Average velocity, u, method 2:* An alternative method for finding u is to measure the peak surface potential, and to calculate the theoretical value, $u = <E_{Max}>/(2\sigma_q.\rho/t)$, where expressions for E_{Max} are given in Part I, **Table 1**.

(3) *Surface Charge Density, σ_q:* For a corner discharge the peak-current is $Ipk = (\sigma_q.u).(a\,\pi/2)$, and $u = a/\tau$. Therefore, the surface charge density, $(Q/A)=\sigma_q = 2Ipk.\tau/(\pi a^2)$.

(4) *Total Surface Charge:* The total charge is the surface charge density times the area, $Q =\sigma_q A$. We may want to know if the total area, A,[8] is discharged, or only part of it.

(5) From a numerical integration of the ESD pulse we obtain the value for the total charge dissipated in a surface discharge. The ratio between the integrated discharge current and the estimated total surface charge, Q (See #(4) above), is the fraction of surface area that was discharged. This ratio is expected to be of the order of (L_B/L).

Example

Consider a charged rectangular dielectric tile of dimensions WxL = 1m x 2m, and assume that an ESD occurs at a corner. Assume also that we have a total-surface discharge, i.e., we assume $L_B >> L$. If the measured peak current was 120 amps, and the velocity of propagation was $u = 6E5$ m/sec, then

A• Estimate the total accumulated charge on the tile just before an ESD is triggered.
B• Estimate or find the pulse duration
C• Estimate or find the average current from a surface discharge

(A•) The third entry in **Table 2** lists the equation for the peak current. It is given by $I_{pk} = \sigma_q.u.(\pi/2)W.$ All the parameters needed to calculate the surface charge density, σ_q, are known. Therefore,

$$\sigma_q = (I_{pk})/(\,u(\pi/2)W) = (120)/(6E5\,(\pi/2)\,1) = (400/\pi)\mu C/m^2 = \mathbf{127.3\ \mu C/m^2}$$

The accumulated charge is $Q = \sigma_q A = (I_{pk})L/(\,u(\pi/2)) \approx \underline{\mathbf{255\ \mu C}}$.

(B•) The pulse duration is $(\sqrt{(W^2+L^2)})/u = \underline{\mathbf{3.7\ \mu sec}}$.
<u>Note</u>: One must not confuse the "*Pulse Duration*" with the "*Pulse Width.*"

(C•) The average ESD current is $<I>_{Ave} \approx Q/(Pulse\ Duration)$. Therefore,
$I_{ave} \approx \sigma_q\,Au/(\sqrt{(W^2+L^2)}) = (I_{pk})L/(\pi/2)/(\sqrt{(W^2+L^2)}) = (120)2/(\pi/2)/(\sqrt{(1+4)})= \underline{\mathbf{68.33\ amps}}$.
<u>Note:</u> For a long sample, the sustained arc reaches a steady state value given by $I\approx\sigma_q\,ua= I_{pk}/(\theta)$ $= I_{pk}/(\pi/2) = \mathbf{76.4\ amps}$.

Summary and Conclusions

The amplitude of the instantaneous discharge current is proportional to the arc length of an expanding spherical wave front of surface discharge: in our examples, the wave front is centered about the site of an arc. In mks-units arc length is measured in (*meters*) x (*radians*). Therefore, a

---

[8] How we calculate *Area* is crucial: For a highly resistive material, a recommended estimate is $A=7(L_B)^2$.

universal scaling law for peak currents must be based on a comparison of the maximum arc length, $(r\theta)_{\text{Max}}$ of an expanding wave front. Geometry dictates that $(r\theta)_{\text{Max}}$ is a function of the shape and size of a charged surface, as well as the location of an arc-discharge. It was shown that Balmain's **($\sqrt{(Area)}$)**-scaling-law is a special case that applies only to circular shapes. One could take liberty to apply Balmain's **($\sqrt{(Area)}$)**-scaling-law to square tiles. However, for all other shapes one must use the universal scaling law: it corresponds to the last entry (in **boldface** font) in **Table 2.**

An important discovery is the fact that the peak amplitude of a surface discharge is less affected by the size of the surface area as it is by the location of the discharge. The pulse duration, however, scales with the distance between the site of a discharge and the most distant point on an edge of the charged dielectric surface.

<div align="center">

Recommendations

</div>

For the purpose of specifying ESD-induced peak current amplitudes, one must apply the Universal Scaling Law presented in this paper, i.e., $I_{pk} = \sigma_q\, u\, (r\theta)_{Max} = (E_{Ave}\, /(\rho/t))(r\theta)_{Max.}$ For proper implementation of recommended spacecraft charging mitigation requirements, the Industry needs data for the surface resistivity, (ρ/t), for the operating temperature range for satellites on orbit. This data is needed for estimating $(\sigma_q\, u) = (E_{Ave}/(\rho/t)) = ((E_{Max}/2)/(\rho/t))$ under breakdown conditions.

For partial-surface discharges, one may use **Table 2** to determine the maximum area from which charge is dissipated in a single discharge. **Table 2** shows that beyond $(7\, L_B)$, the electrical surface tension, $|E(0)|_{\text{Max}}$, is too weak to pull charges into the funnel of a discharge.

Table 2.Percent Surface Discharged as a function of the shielding length, L_B.							
(L / L_B)-->>	0.10	0.25	0.50	1.00	3.00	5.00	7.00
Residual Charge	5%	12%	24%	46%	91%	99%	100%
Amount Discharged	95%	88%	76%	54%	9%	1%	0%

References

1. Major Space Losses (1994-1998), in International Space Industry Report, 2(17), 28, 12 October 1998.

2. Satellite Failures linked to ESD?, in Conformity, 3(10), 14, October 1998.

3. Dr. K.G. Balmain, "Scaling Laws and Edge Effects for Polymer Surface Discharges," NASA Conference Publication 2071, AFGL-TR-79-0082, Spacecraft Charging Technology-1978, p.646.

4. P.R. Aron, J.V. Staskus, NLRC, "Area Scaling Investigations of Charging Phenomena," NASA Conference Publication 2071, AFGL-TR-79-0082, Spacecraft Charging Technology-1978, p.485.

5. Dr. Richard Briët, "ASCAT, A Spacecraft Charging Analysis Technique," Proceedings of the 1987 IEEE/NSREC, Snowmass, CO.

6. Dr. K.G. Balmain, personal communications at the IEEE Conference on EMI/EMC in Montréal, Canada, August 17, 2001.

MODELING OF THE PLASMA THRUSTER IMPACT ON SPACECRAFT CHARGING

S. Brosse
Alcatel Space Industries
100 Bd du Midi, 06156 Cannes La Bocca Cedex France
Phone: 33 4 92 92 64 83
Fax: 33 4 92 92 69 70
E-mail: sylvie.brosse@space.alcatel.fr

S. Clerc
Alcatel Space Industries, France

Abstract

This paper presents the recent investigations done by the Research Department of Alcatel Space in the modelling of the electrostatic impact of plasma thruster on spacecraft charging. In particular, we will question the validity of the generally accepted hypothesis of Maxwell-Boltazmann distribution for the electron especially to take account of the plasma contactor effect.

In a first part, we will present the problem of the Maxwell-Boltazmann distribution to correctly model the spacecraft charging modification due to plasma thruster in the software SPARCS developed by Alcatel Space.

We will show that the plasma contactor effect of a plasma thruster is essential to estimate and model the electrostatic impact of the thruster. We will show too that the Maxwell–Boltzmann distribution for the electron is not adapted to model the current flow between spacecraft and GEO ambient plasma.

In a second part, we will present the plasma contactor principle and the physical mechanisms which generates charges exchange between spacecraft and ambient plasma. We will show that we can compare the physical mechanisms of the expansion of high-density plasma (the plasma generated by the thruster) into another plasma (the GEO ambient plasma) with the mechanism appearing in a PN junction. The region of high-density plasma is similar to the N region (electrons majority) of the junction and the region of low density is similar to the P region (electron minority). So, with this analogy we can understand how a current flow can circulate between the spacecraft and the ambient plasma through the plasma of the thruster. Finally, we will present a model for electrons to take account of this current flow and its impact on spacecraft charging.

Introduction

The always increasing of satellite on orbit life and mass make the Electric Propulsion Thruster more and more attractive for station keeping on geostationary telecommunication satellites. First developed by Russian researchers, the Stationary Plasma Thrusters (SPT) technology will be commonly used on commercial satellite in Europe in a nearest future. The Alcatel Space next satellite platforms will use SPT 100 for north-south station keeping. However, the introduction of an electric propulsion subsystem on our telecommunication

satellite represents an innovation that requires to study their potential repercussion on the other systems of the satellite.

In a SPT thruster, the propellant (Xenon) atoms are ionised in a discharge chamber (anode). An electrostatic field is then used to accelerate the positive ions to produce the required thrust. To prevent the spacecraft from charging, the positive ion beam must be neutralised by an equivalent negative charge. In SPT 100 this electrons source is a hollow cathode. The plasma ejected by the SPT is then neutral, cold and very dense (about 10^{17} m^{-3} 30 cm away from thruster exit). Moreover a secondary plasma is created by charge exchange collisions between fast ions (primary ions) and slow neutral atoms. This relatively dense (about 10^{12} m^{-3}) low energy plasma can expand around spacecraft. These plasmas constitute charged particles store which can modify the natural environment, generate current due to the interaction between plasma and spacecraft and so modify the electrostatic charge of the spacecraft.

Spacecraft charging is considered as a phenomenon associated with the interactions between plasma and spacecraft surfaces. Charging effects can produce potential differences and high electrical field between spacecraft surfaces or between spacecraft surfaces and spacecraft ground. Above breakdown threshold, an electrostatic discharge (ESD) can occur. The transient phenomenon generated by this discharge may couple with spacecraft electronics (Electromagnetic Compatibility) and cause upsets ranging from logic switching to complete system failure. Discharges can also lead to degradation of exterior surface coatings and induce contamination of surfaces.

The charge and discharge phenomena due to the natural plasma in geostationary environment are studied for a long time. Methods and design rules have been set out to prevent from spacecraft charging and ESD occurrences in this environment. These design rules are mainly based on passive techniques of charge control like for example:

- The use of conductive surfaces connected to spacecraft ground.
- The careful selection of materials in terms of photoemission and secondary emission.
- The use of metallization and conductive coatings.

There are others spacecraft charging mitigation methods said actives methods. The principle of these methods is to eject a current. This active current source modifies the current balance equation and can control the spacecraft potential. When the potential of spacecraft is negative relative to the 0V of the surrounding plasma (typical case of the geostationary orbit), the objective of the active current source is to eject a current of electrons to bring the potential back to 0V. There are various methods to eject a current [1]. For example the sharp spikes method, see figure 1. Sharp spike protruding from charged surfaces generate very high electric field. At sufficiently high fields, field emission of electrons occurs reducing the negative potential of the conductive surfaces connected to the spike. Another method used the thermal emission, this is the hot filament emission method, see figure 1. The electrons are emitted from hot filaments.

These two methods are simple but their effectiveness is limited due to tips sputtering for example and electron guns are retained more effective [2]. An electron gun basically consists of a heated cathode and a series of collimating and accelerating electrodes (here referred as anode.
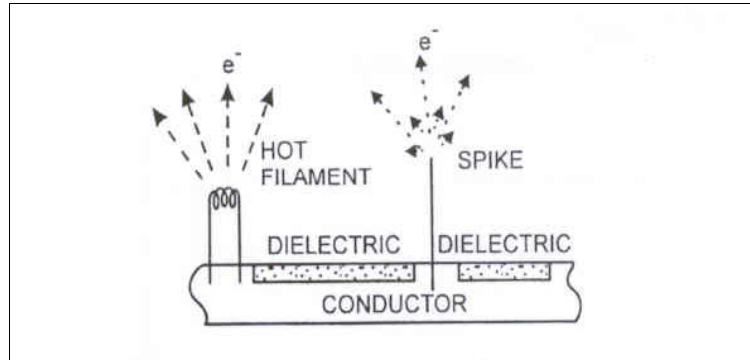
Figure 1. Electron emissions from a sharp spike and a hot filament

These methods based on electrons emission can be used only if the spacecraft is negatively charged. When the spacecraft is positively charged, ions emitters can be used [2]. But the inherent limitation of these devices based on charged particles emitters is that they can deal only with absolute charging situation. In case of differential charging, they can do nothing and the change in potential of only one part of the S/C could even trigger discharges between differently charged areas, thus worsening the situation.

The main interest of plasma source called plasma contactor to mitigate the spacecraft charging is that they can be employed to address charging situations of both signs and, more important, they can also alleviate differential charging problems. The principle of a plasma contactor is to emit a high-density and low temperature plasma. This plasma provides a conductive path between charged spacecraft and the ambient plasma environment. This is the same function as electrical grounding wire. The principle of a plasma thruster like SPT is precisely to generate a high-density and cold plasma. So, we can think that a plasma thruster will act more or less as a plasma contactor.

The software SPARCS (SPAcecRaft Charging Software) developed in the Research Department of Alcatel Space simulates the electrostatic impact of plasma thruster on the spacecraft charging in geostationary environment. In the development of SPARCS, we have seen that the plasma contactor effect of a plasma thruster is essential to correctly estimate and model its electrostatic impact on the spacecraft charging. But we will see that the generally accepted hypothesis of Maxwell-Boltazmann distribution for the electron with the neutrality assumption is not adapted to take account of the plasma contactor effect.

Problem of the Maxwell Boltzmann and Neutrality Hypothesis in SPARCS

SPARCS will be used to make the spacecraft charging analysis. It will be used to predict the surface potentials when spacecraft is submitted to both geostationary environment and plasma from the electric thruster [3]. Now we have the 2D axi-symetrical version and a first version of the 3D. The parallel version is under development. The magnetospheric plasma is assumed to be collisionless, low density and hot whereas the propulsion plasma is characterised by fast and slow ions. So the Vlasov equation is used to model the ions. For the SPT plasma electrons, in a first step the Maxwell-Boltzmann has been used. In fact this distribution is valid only close to the plume. The potential of the SPT plume (plasma potential) decreases away from spacecraft. The primary ion density decreases in n_0/r^2 and as we use the assumption of the neutrality $n_i=n_e$ in the plume, the electron density decreases too in n_0/r^2. With the Maxwell-Boltzmann distribution, we finally obtain that the potential

decreases in $\phi_0-2\log(r)$. So inside the plume where r is small, this is correct but outside the plume where $r \to \infty$, the potentials tends towards $-\infty$, which is not valid. In fact it is impossible to describe the electron distribution near the plume (cold electrons 1-2 eV, dense 10^{15} m^{-3}, potential reference -10kV-0V) and at infinity (hot electron 10 KeV, low density 10^6 m^{-3}, potential reference 0V) with a single Maxwell-Boltzmann equilibrium function. Moreover, there is a problem too on the results of the potentials of spacecraft surfaces. As we have seen, in the plasma thruster plume we have $n_i=n_e$ with $n_e = n_{ref}. Exp[(\phi-\phi_{ref})/KT_e]$ with ϕ_{ref} and n_{ref} at the thruster exit, see figure 2. Due to the thruster functioning, the potential ϕ_{ref} is referenced to the potential of the cathode ϕ_{crp} and ϕ_{crp} is referenced to the conductive parts ϕ_{pc} (spacecraft ground) so $\phi_{ref} = Vc + \phi_{pc}$.
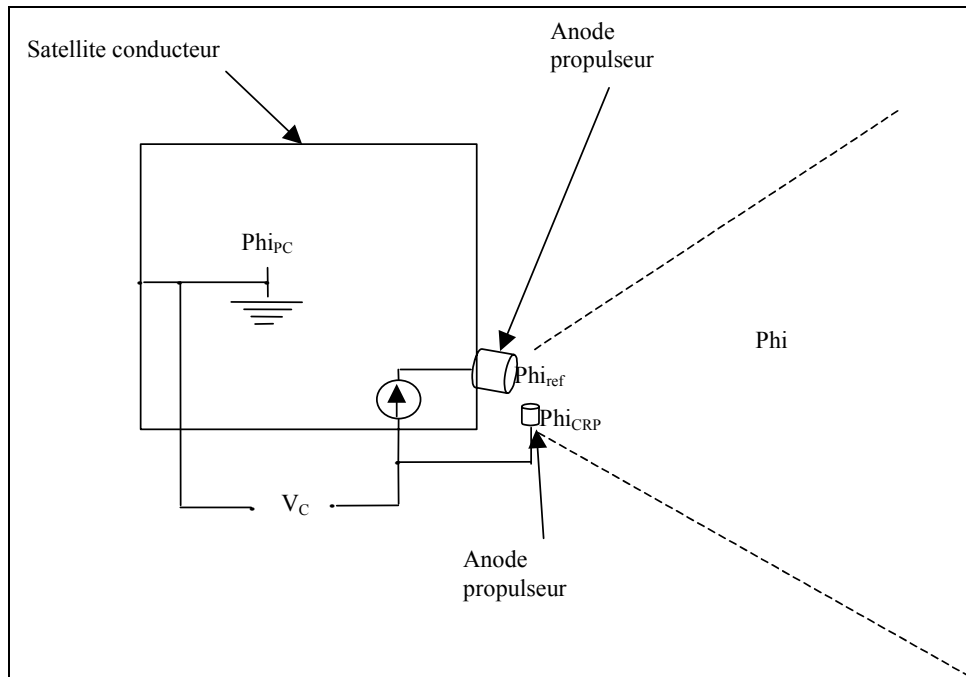
Figure 2. Configuration of potentials

Finally the current density can be written as $j_e = j_{ref}.\exp[(\phi-Vc-\phi_{pc})/KTe]$. But on the spacecraft surfaces $\phi = \phi_{pc}$ and $j_e = j_{ref}.\exp[(-Vc)/KTe]$. We see that the current is independent of ϕ_{pc} that is not realistic. Moreover, in these conditions the electronic current from the plasma plume is lower than the ion current. So, it is the electronic current from ambient geostationary plasma that balances this positive current. As the electronic current from GEO plasma is very low, the equilibrium potential is high (+40000V) that is not physical. So we can see that with the Maxwell-Boltzmann distribution and with the neutrality it is impossible to have good results. In fact, there is another relation between the plasma potential of the plume, the spacecraft potential and the magnetospheric potential which is impossible to model with the Maxwell-Boltzman distribution and neutrality. This relation is due to the plasma contactor effect of the plasma thruster. There is an electric circuit through the conductive path created by the plasma plume of the thruster. This circuit connects the spacecraft potential with the potential of the geostationary ambient plasma (0V). The plasma contactor effect is very important to determine the impact of the plasma thruster on spacecraft charging. Without this effect we could not explain the neutralisation of potentials observed in orbit. For example, in the case where the thruster is directly connected to the spacecraft ground, the spacecraft potential (ϕ_{pc}) is not directly modified by the particles of plasma

thruster. The plasma potential of the plume is equal to the spacecraft potential, so the particles of the plume are not attracted by the potential of the spacecraft surfaces (grounding). The plasma is neutral and there is no net current so there is no modification of the spacecraft charge by the charged particles ejection. This is the plasma contactor effect due to the plasma conductivity that creates a conductive path between spacecraft and 0V magnetosphere. There is an electronic current flow from the spacecraft to the 0V that discharges the absolute potential of the spacecraft. Even when the thruster is electrically floating, the plasma contactor effect discharges indirectly the spacecraft potential. So in conclusion of this part, we see that the modelling of plasma contactor effect of the plasma thruster is essential but it is impossible with the Maxwell-Boltzman distribution and neutrality assumption.

Plasma Contactor Principle and Physical Mechanism

As we have seen before the plasma contactor principle is to create a conductive path between charged spacecraft and ambient plasma by the ejection of a high-density and low temperature plasma. In the case where the spacecraft is negatively charged for example, there is a electrons current flowing from spacecraft towards the ambient plasma through the plasma ejected by the plasma contactor, see figure 3.
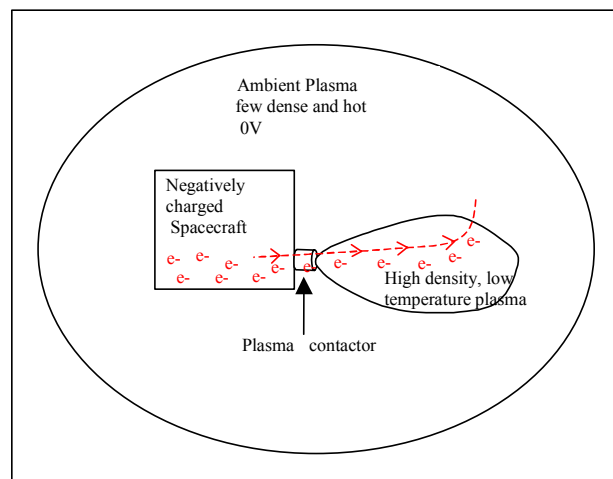
Figure 3. Plasma contactor principle

To model the plasma contactor effect it is necessary to understand the physical mechanism for current flow through the plasma plume. It can be illustrated with the examination of the no current flow case (no external perturbation).

The particles ejected by the plasma contactor (or the thruster) flow from regions of higher density to regions of lower density, this is the diffusion, see figure 4.

But the electrons move faster than the ions (due to ions high mass) and therefore reach the regions of lower density faster. This electrons flow leaves an excess of positive charge (see figure 4) and a electric field appears which retards electrons until there is no net electron flow [6]. A space charge region (a potential barrier) is created. The net force on the electron is zero: $F_e = F_d$. F_d is the diffusion force and at the equilibrium, D grad(n) = e.n.grad(V).

In fact, the physical mechanism of the expansion of high-density plasma into another plasma can be compared with the mechanism appearing in a PN junction, see figure 5.

Figure 4.

Geostationary Plasma
Few dense and hot

N

⊕ Giver Atom

- Free Electron

Neutral zone

P

⊖ Acceptor Atom

+ hole

Neutral zone

E_{int}
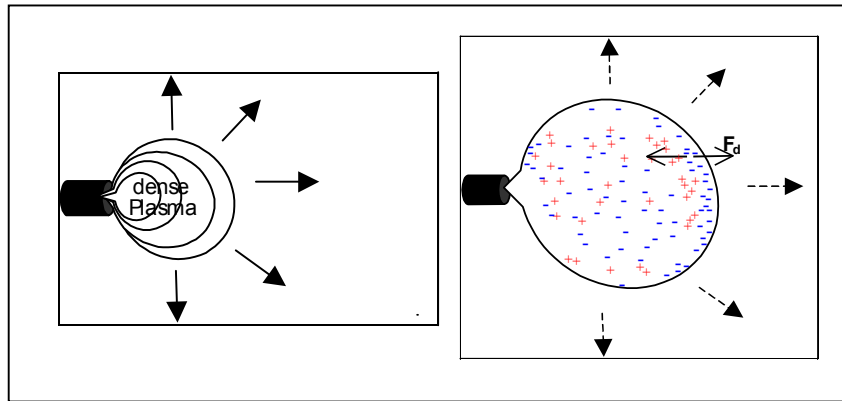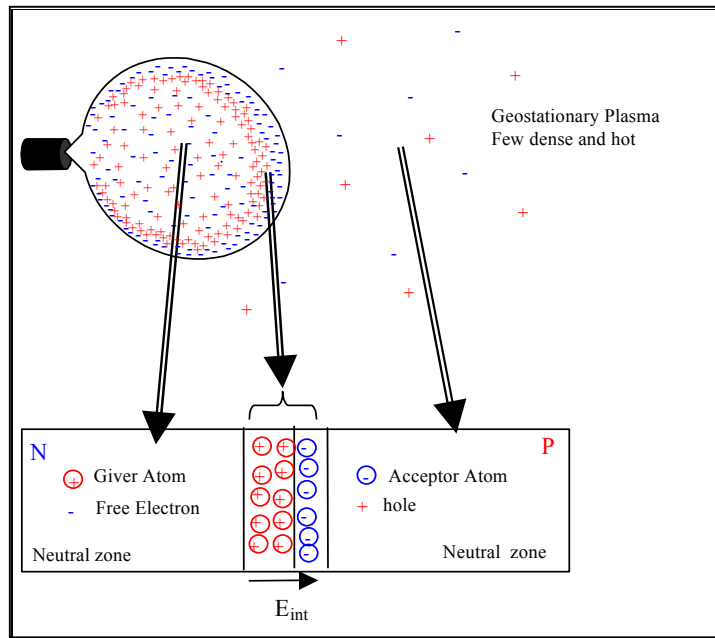
Figure 5. Analogy with PN junction

The region of high-density is similar to the N region of the junction and the region of low density is similar to the P region. At the junction, there is a space charge region created by the electrons diffusion from the N region where they are the majority carriers towards the P region where they are minority carriers. This current flow leaves an excess of positive charges in the N region and a negative charges in the P region. There is a space charge region and so a potential barrier.

Examine now the case where there is an external field. For the plasma contactor this external field is created by the difference between the potential of the plasma contactor (V_{ps}) and the potential of geostationary plasma (V_{pGEO}). For negatively charged spacecraft, the potential of plasma contactor (plasma thruster) is negative relative to GEO plasma (plasma contactor or thruster connected to spacecraft ground), so this corresponds to the forward biased in PN junction, see figure 6.
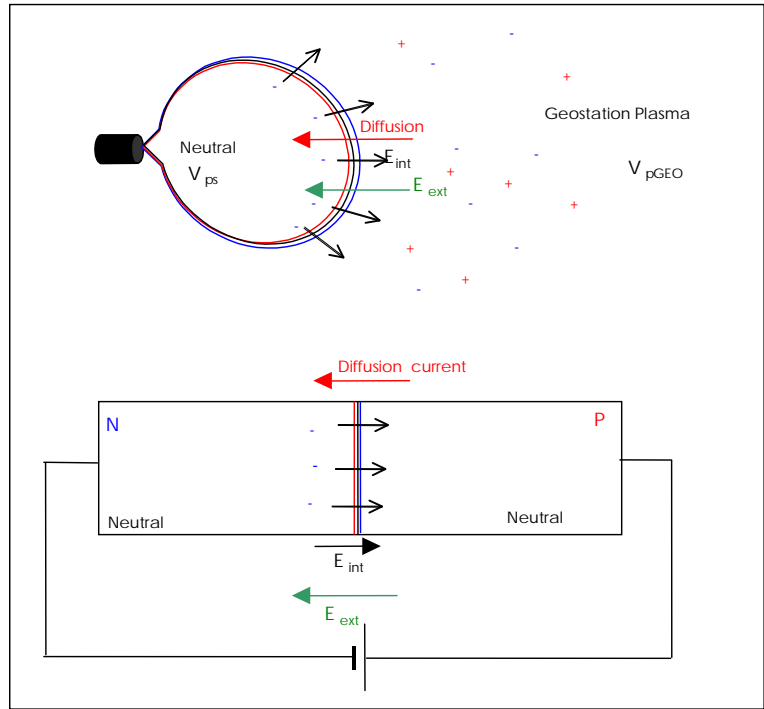
Figure 6. Forward bias

In these conditions, the external field E_{ext} reduces the internal field E_{int} (the potential barrier), and the electrons can diffuse from N region (from the dense region for the plasma contactor) to the P region (the GEO ambient plasma). So the electrons flow from spacecraft ground to ambient GEO plasma reducing the absolute floating potential of the spacecraft.

In the case of reverse bias, so when thruster potential is positive relative to GEO plasma, the external field is added to the internal field, see figure 7.
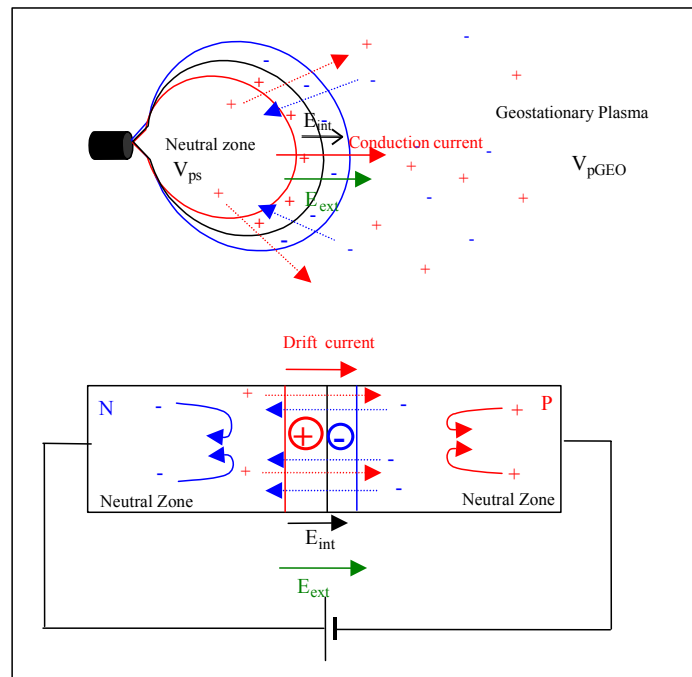
Figure 7. Reverse biased

The depletion region (space charge region) increases and the potential barrier grows. In the N region or dense plasma region, the electron have not enough energy to climb this barrier. The diffusion current becomes negligible. But the ions can flow from dense plasma to ambient plasma (GEO) and electrons of GEO plasma can flow towards the plasma source. This current is similar to minority carriers current (drift current) in the PN junction (electrons in the P regions and hole in the N region). The ions of the dense plasma are nearly motionless and the density of the electron in GEO plasma is very small so the drift current from GEO towards plasma source is small. The floating absolute potential of spacecraft is neutralise but more slowly than in the case of forward bias. When the field in the space charge region is very high, the electrons coming from GEO plasma gain sufficiently energy through the space charge region to ionise neutrals and the current rapidly grows. This is an avalanche phenomenon similar to the Zener effect in diode.

Finally, the phenomena of current circulation between spacecraft and GEO ambient plasma through plasma plume are similar to the ones appearing in a biased PN junction. If we compare the plasma contactor current/voltage characteristic measured with the diode characteristic, we can see that they are very similar, see figure 8 [4].
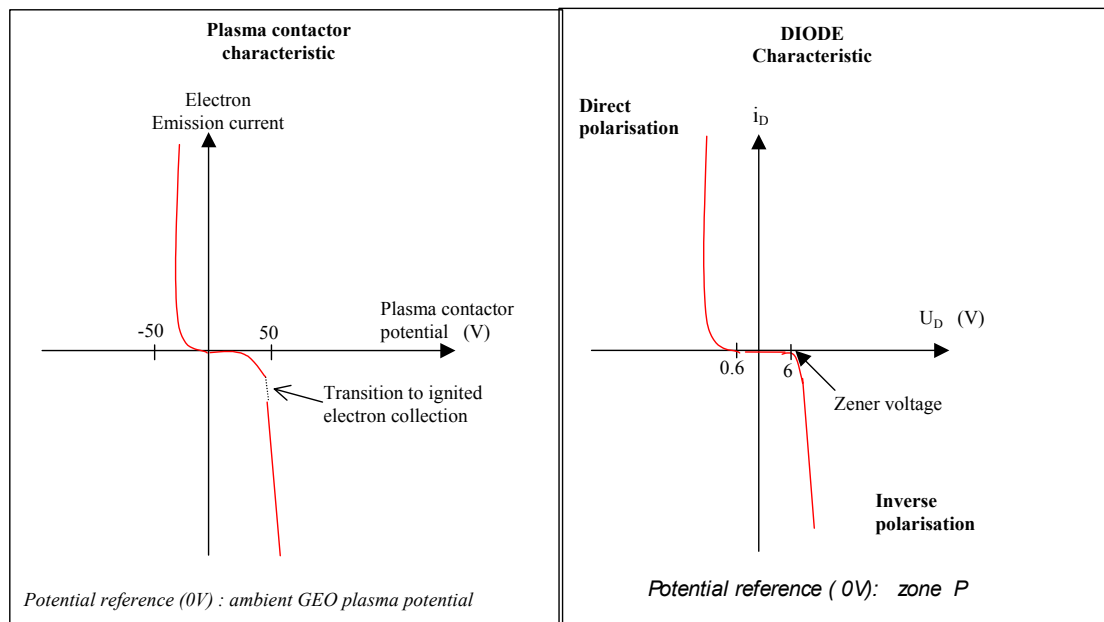
Figure 9. Diode and plasma contactor current/voltage characteristic

Plasma Contactor Modelling

We have seen that the Maxwell-Boltzmann distribution and neutrality model are not adapted to correctly model this current circulation We have seen too that the phenomena of current circulation between spacecraft and GEO ambient plasma through plasma plume are similar to the ones appearing in a biased PN junction.. So, this current for the plasma contactor can be calculated the same way as it is calculated in a biased junction.

So in a first step we will precisely calculate the current through a PN junction in function of the biased voltage.

In semiconductors, there are two kinds of current: the diffusion current and the drift current. So for holes and electrons, the total current density is:

$$J_p = q \cdot p \cdot \mu_p \cdot E - q \cdot D_p \cdot \frac{\partial p}{\partial x}$$

$$J_n = q \cdot n \cdot \mu_n \cdot E + q \cdot D_n \cdot \frac{\partial n}{\partial x} \quad \text{with} \quad \frac{D_p}{\mu_p} = \frac{D_n}{\mu_n} = \frac{kT}{q} \quad \text{The constants } D_p \text{ et } D_n \text{ are the}$$

diffusion constants and μ_p and μ_n are the mobility.

In the case of the no biased junction, at the equilibrium, there is no net current. The diffusion current exactly balances the drift current. So for the hole for example, we have:

$$J_p = q \cdot p \cdot \mu_p \cdot E - q \cdot D_p \cdot \frac{\partial p}{\partial x} = 0 \quad \text{so} \quad \frac{kT}{q} \frac{\partial p}{\partial x} = p \cdot E \quad \text{with E=-dV/dx.}$$

With the boundary conditions we can write that $\ln \dfrac{p_{n0}}{p_{p0}} = -q \dfrac{V_0}{kT}$

In the notation used, « n » and « p » are respectively the electrons and holes concentration, the index « n » and « p » show the region where this concentration is measured, and finally the index « 0 » shows a concentration at the equilibrium.

So, the potential barrier is $V_0 = \dfrac{kT}{q} \cdot \ln \dfrac{N_a N_d}{n_i^{\,2}}$ with N_a and N_d the doping concentration in the P region and in the N region respectively.

With forward external bias, the potential of the P region is positive relative to the region N.

In this case $n_p = n_{p0} \cdot \exp(\dfrac{qV}{kT})$ and $p_n = p_{n0} \cdot \exp(\dfrac{qV}{kT})$, V is the bias voltage.

At the quasineutral N region input ($x=x_n$), in stationary state and in assuming there is no carrier generation, the continuity equation gives for holes:

$$-U_p - \frac{1}{q} div \vec{J}_p = 0 \quad \text{with} \quad U_p = \frac{p_n - p_{n0}}{\tau_p} \quad , \quad \tau_P \text{ is the hole lifetime and } L_p = \sqrt{D_p \cdot \tau_p} \text{ is the}$$

diffusion length. At this point (neutral zone) we have only a diffusion current:

$$J_p = -q \cdot D_p \cdot \frac{\partial p_n}{\partial x} \quad \text{and finally we have} \quad -\frac{p_n - p_{n0}}{\tau_p} - \frac{1}{q} \cdot \frac{\partial}{\partial x}(-q \cdot D_p \frac{\partial p_n}{\partial x}) = 0 .$$

The solution of the differential equation with the boundary conditions is

$$p_n(x) = p_{n0} \left[(\exp(\frac{qV}{kT}) - 1) \cdot \exp(-\frac{x - x_n}{L_p}) + 1 \right] .$$

So J_p can be calculated : $J_p(x) = q \cdot \dfrac{D_p}{L_p} \cdot p_{n0} \cdot (\exp(\dfrac{qV}{kT}) - 1) \cdot \exp(-\dfrac{x - x_n}{L_p}) .$

We can make the same for electrons in the P region, and we have:

$$J_n(x) = q \cdot \frac{D_n}{L_n} \cdot n_{p0} \cdot (\exp(\frac{qV}{kT}) - 1) \cdot \exp(\frac{x + x_p}{L_n})$$

In stationary state, the total current $J = J_p(x) + J_n(x)$ is constant in x. The recombination in the space charge region is assuming negligible.

$$J = J_n(-x_p) + J_p(x_n) = (q \cdot \frac{D_n}{L_n} \cdot n_{p0} + q \cdot \frac{D_p}{L_p} \cdot p_{n0}) \cdot [\exp(\frac{qV}{kT}) - 1]$$

that is often written as $J = J_s \cdot [\exp(\frac{qV}{kT}) - 1]$. This is the well-known expression of the

current in the diode with $J_s = (q \cdot \frac{D_n}{L_n} \cdot n_{p0} + q \cdot \frac{D_p}{L_p} \cdot p_{n0})$.

In reverse bias, the current can be calculate exactly in the same way and gives the same expression with V< 0.

For the calculation of the current between plasma contactor and ambient plasma, we can make the same calculations. In this case we suppose that the dense plasma is not in expansion. It is like a fixed dense plasma bubble into another plasma (few dense), see figure 10.
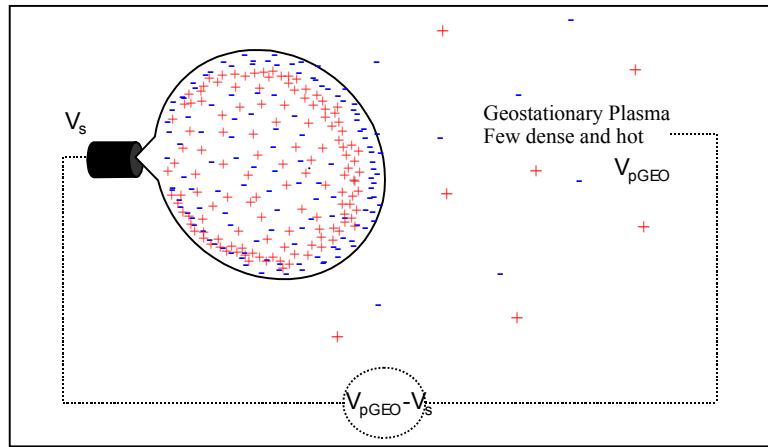
Figure 10.

As for holes and electrons of the junction, we can use the drift-diffusion equation for

electrons and ions of the plasma. For so we can write $J_i = q \cdot n_i \cdot \mu_i \cdot E - q \cdot D_i \cdot \frac{\partial n_i}{\partial x}$ and

$J_e = q \cdot n_e \cdot \mu_e \cdot E + q \cdot D_e \cdot \frac{\partial n_e}{\partial x}$ and we can calculate the barrier potential : $V_0 = \frac{kT}{q} \cdot \ln \frac{n_e^s}{n_i^{GEO}}$

with n_e^s the electrons density in the dense plasma bubble (so in the plasma plume of the plasma contactor or thruster) and n_i^{GEO} the ions density of the plasma in geostationary environment.

In the plume n_e^s is about 10^{15} m^{-3} and for geostationary environment n_i^{GEO} is about 10^6 m^{-3}. So we find that V_o is about 20V – 40V (T_e = 1-2eV).

From this drift diffusion equation and from these assumptions, the electrons current calculation can be made exactly in the same way as for the PN junction with adapted boundary conditions. Finally we can write that the current circulating between the plasma source and the GEO plasma through the dense plasma bubble can be written as: $J = J_0$ exp[(qV/KT)-1] with $V = V_{pGEO} - V_s$. When the spacecraft is negatively charged, its potential is more negative than the potential of the GEO plasma and then V is positive.

In fact, this model is very simplified, nevertheless it is coherent with the plasma contactor current-voltage characteristic that has been measured (see figure 9) and it shows that the current can be calculated and taken into account when the drift-diffusion equation (fluid model) is used for electrons. For a more realistic model, it should be necessary to add a temperature equation. The plasma plume of the plasma contactor or thruster is cold (1-2 eV) whereas the plasma of the GEO environment is hot (few 10 KeV). Moreover, the temperature in the plasma plume varies.

We have assumed too that there is no expansion of the plasma plume and that it is like a fixed plasma bubble. This assumption is not valid as the principle itself of the plasma contactor and thruster is to continuously eject a dense plasma. So, in fact the plasma plume expands in the ambient GEO plasma. This means that the model for ions is more complex (Vlasov) with charge exchange collisions. This means too that electrons and ions don't have the same characteristic speed. For the same reason the assumption of stationary state is perhaps not really verified. Last, another delicate point is to determine the limit of the dense plasma. Nevertheless, we can think that a fluid model for electrons of plasma plume is more adapted to taken into account of the current circulation than the Maxwell-Boltzmann distribution.

This model has not been yet implemented in SPARCS but it is planned for next year.

Impact of the Plasma Contactor Effect on Differential and Absolute Charge on Spacecraft

We have seen before that the plasma contactor effect is to generate a conductive path like a circuit between the spacecraft and the ambient GEO plasma. We have seen too that when the spacecraft is charged relative to the ambient GEO plasma (the 0V), a current circulates between the spacecraft and the ambient plasma.

When the plasma contactor or the plasma thruster is directly connected to spacecraft ground, there is a current flow between conductive spacecraft surfaces and the ambient GEO plasma (0V) until the potential of the conductive surfaces of the spacecraft (the absolute potential) is equal to the potential of the ambient GEO plasma (0V). So, there is a direct neutralisation of floating potential of the spacecraft. This neutralisation is rapid, see figure 11.

Moreover, the particles of the secondary plasma (backflow) created by charge exchange collisions between primary ions and slow neutral atoms are attracted by the electric field generated by the differential potential (difference between potential of dielectric surfaces ϕ_s, and potential of the spacecraft ground ϕ_{PC}). For example if $\phi_s < \phi_{pc}$ as $\phi_{pc} = \phi_{pp}$ (plasma thruster connected to spacecraft ground and there is neutralisation of absolute potential), the

ions of secondary plasma are attracted by ϕ_s and come to neutralise the surface until $\phi_s = \phi_{pc}$, see figure 11.

When the thruster is perfectly isolated from spacecraft ground, the plasma thruster provides particles (secondary plasma) which are attracted by potential of spacecraft surfaces (dielectric and conductive). In the same time, due to the plasma contactor effect, there is a current flow between thruster and the ambient plasma environment until $\phi_{pp} = 0V$, see figure 12. So, finally there is indirect neutralisation of floating potential (slow) and differential potentials.
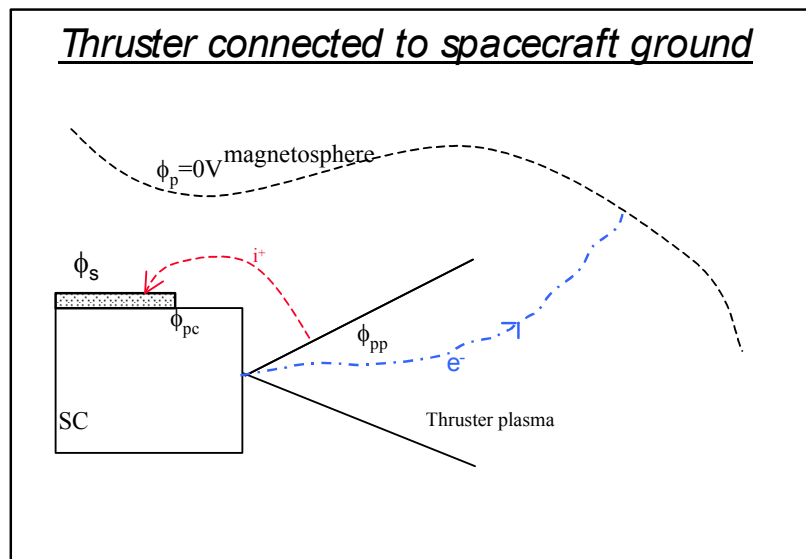
Figure 11. Thruster connected to spacecraft ground
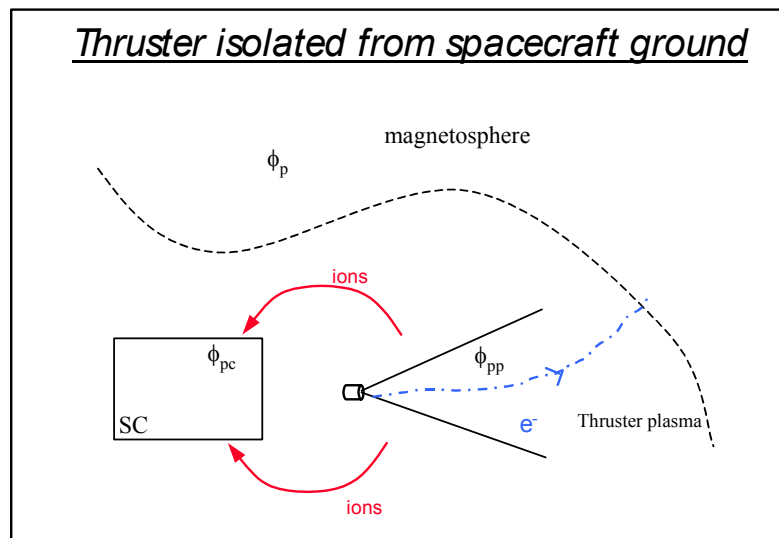
Figure 12. Thruster isolated from spacecraft ground

In a realistic case, as it is the case on Alcatel platforms, the thruster is not perfectly isolated from spacecraft ground. There is a parasitic electric circuit between thruster and spacecraft ground. As for a perfectly isolated thruster, the particles of secondary plasma are attracted by potential of spacecraft surfaces and neutralise them, see figure 13. And in the

same time there is a current flow between spacecraft conductive surfaces (spacecraft ground) and the ambient plasma through the parasitic electric circuit and the conductive path provided by the plasma plume of the thruster (plasma contactor effect). So there is neutralisation of potentials but the dynamic and the neutralisation phenomenon depends on the characteristics of the parasitic electric circuit.
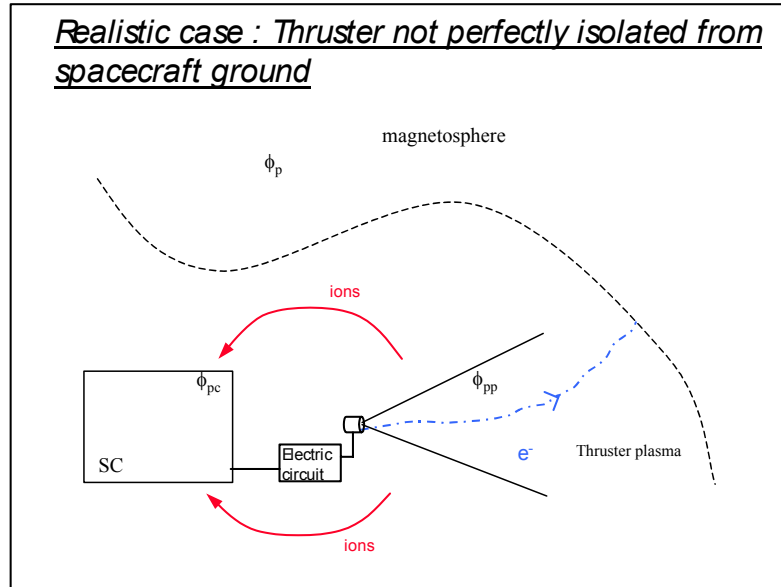
Figure 13. Thruster not perfectly isolated from spacecraft ground

Conclusion

The modelling of the plasma contactor effect of a plasma thruster model is essential to simulate the impact of the plasma thruster on spacecraft charging. During the development of SPARCS we have seen that the generally accepted hypothesis of Maxwell-Boltazmann distribution for the electron of the plasma plume is not adapted to take account of the plasma contactor effect. As the plasma contactor physical mechanisms are similar to the ones of the PN junctions, we think that a fluid model for electron is more adapted to take into account the current circulation between spacecraft and GEO plasma through the thruster plasma plume. Nevertheless, there are still some difficulties like the determination of the neutrality region limit, the necessity to add a temperature equation and the validity of stationary state. For the Alcatel platforms, the parasitic circuit between thruster and spacecraft ground should be modelled too. The fluid model for electron will be implemented in SPARCS next year. Alcatel will have then a complete, innovative and accurate tool for spacecraft charging analysis.

References

1. A critical Overview on Spacecraft Control Methods. Shu T. Lai, Air Force Research Laboratory, 6th Spacecraft Charging Technology Conference.

2. Active Devices for the control of S/C charging. Alberto MATUCCI, Proel Technology Division of Laben, Cours de technologie spatiale. Environment Spatial prévention des risques liés aux phénomènes de charge. juin 96.

3. SPARCS: An Advanced Software for Spacecraft Charging Analyses. S. Clerc, S. Brosse, Alcatel Space, M. Chayne-Yook, Inria, 8th Spacecraft Charging Technology Conference (Huntsville, Alabama)

4. An Experimental investigation of the plasma contacting process. Paul J. Wilbur, John D. Williams, Colorado State University, AIAA-87-0571

5. Hollow-cathode Plasma contacting insights gained from the electrodynamic tether mission. P.J. Wilbur, D. Burtner, Colorado State University, IEPC-99-218.

6. Plasma Sources for Spacecraft Neutralization. V. Davis, I. Katz and M. Mandell, M. Mandell. AIAA 90-1556.

THE VIABILITY OF USING WEIGHT SAVING MATERIAL FOR FUTURE LONG TERM SPACE VEHICLES (I.E. SATELLITES)

Nicola Burgess
Raytheon Missile Systems, E3 Technology Section
P.O. Box 11337, Bldg. MO2
Tucson, Arizona 85734-1337 USA
Phone: 520.794.0845
Fax: 520.794.9087
E-mail: Nicola_Burgess@raytheon.com

Sarah Splitek
R. Michael Lassise
Raytheon Missile Systems

Abstract

The potential hazards of the natural space environments to a composite structure and to the systems within the structure are compared to an all conductive (metal) structure. Low Earth Orbit (LEO) will be the focus of the evaluation. The natural space environments comprise a multitude of risks, with a primary concern being the natural space plasma and the resulting spacecraft charging. Various other aspects of the environment and their impacts on a composite structure will also be examined.

The evaluation of spacecraft charging demonstrates a high probability of electrical overstress (EOS). The majority of space vehicles are made of a combination of metal and composites, indicating a concern of EOS (arcing) between the materials. To avoid EOS, you must have the entire vehicle at the same potential. Different materials will not have the same discharge voltage, allowing one to charge at a higher voltage than the other. This causes a potential difference and allows for EOS. The composite is not a good conductor and has a dielectric constant associated with it. The rate of charging and the distribution of charge will vary non-linearly, causing a non-uniform distribution of charge. EOS allows degradation of the on board systems, leading to possible mission failures. EOS may cause physical damage to composites, which can lead to a loss of structural integrity.

Introduction

With the advancement of man's presence in space, the cost and weight of objects being launched have become major concerns; as a result, composite materials are being widely used for space travel. The cost to launch a spacecraft into space is predicated by weight; as composites are generally more lightweight than traditionally used metals, they are cheaper to launch. Also when considering the cost of building a spacecraft, the cost of the material has to be taken into consideration. Not only are launch costs made lower by lighter material the cost of the material itself is also lower than commonly used metal, making both launching and building composite spacecrafts more attractive in an economic sense.

Along with composites being financially more attractive, the mechanical properties of composites often are more appealing. Due to the longevity required of spacecraft, mechanical strength is a major concern for designers. The mechanical strength of a composite can be stronger than a lot of the commonly used metals, thus composites are appealing to make a successful mission. Also due to the manner in which composites structures are composed (via computer), all the boltholes and apertures are built into the structure when it is wound, unlike its metal counterpart, which needs drilling and boring to complete the structure. This, from a mechanical standpoint, makes a composite vehicle easier to work with.

The third major reason for using composites is the thermal properties. Composites have been proven to provide good thermal conductivity, thus they have the ability to adjust to high temperature variations. Due to the nature of the space environment, structures will have to undergo numerous temperature differentials when traveling into and out of the sunlight. Due to the thermal properties of composites this constant changing is easily handled.

The above thermal and mechanical properties and cost effectiveness are three reasons why composites are being widely used in long-term space missions. There are, however, some consequences of using composites. The natural space environment is made up of 9 components: the neutral thermosphere, the thermal environment, plasma, meteoroids and orbital debris, the solar environment, ionizing radiation, the magnetic field, the gravitational field, and the mesosphere[1]. The environment of primary concern for spacecraft charging is plasma. Plasma exists in the ionosphere and is caused by the interaction of the gas in the ionosphere and solar particles. In the ionosphere the electron and ion densities are equal and as a rule vary depending on the location in the ionosphere. Due to this the altitude will make a difference in the amount of plasma flux a spacecraft encounters. Low Earth Orbit (LEO) will be of primary concern in this discussion.

While reviewing the environments for space travel it is obvious that there are more considerations than the cost and the thermal and mechanical properties. Along with mechanical and thermal considerations, electromagnetic considerations have to be evaluated as well. All of the systems being launched currently are using very sophisticated electrical devices and these devices are very susceptible to the electromagnetic space environment. To protect these devices there needs to be adequate shielding provided by the body of the craft. Typically, a method of shielding these devices is to provide a metal (conductive) enclosure referred to as a faraday cage. This also ties into the grounding scheme as a faraday cage provides the ground to prevent arcing between pieces of the spacecraft. When a composite is used this faraday cage becomes impossible to achieve as the composite is not, in general, a good conductor. This leaves an opening anywhere there is composite thus exposing sensitive electrical devices to a hostile electromagnetic environment. Also if there are any metal structures the composite between them will act as a dielectric, thus creating a capacitor.

Existing information

Spacecraft charging and its effects are widely known and discussed in various papers and conferences. Many failures have been documented and blamed on spacecraft charging. For

---

[1] NASA Reference Publication 1350

example, the Telsat, Canada's Anik E-1 communications satellite began to spin out of control on 20th January 1994. Within two hours Anik E-2 also lost control[2]. This caused over $50 million in recovery, repair, and lost revenue costs. It has been determined that this anomaly was caused by ESD from a build up of charge from a solar flare. Other various spacecraft anomalies have been blamed on spacecraft charging or the electromagnetic environment in general with more that have not been identified. Much is understood about the natural space environment and its possible effects on spacecraft, first studied in detail by SCATHA. The following figure from NASA Reference Publication 1350 outlines the issues that are faced in the natural space environment.

Natural Space Environments

	DEFINITION	PROGRAMMATIC ISSUES	MODELS/DATABASES
NEUTRAL THERMOSPHERE	Atmospheric density, Density variations, Atmospheric composition (Atomic Oxygen), Winds	GN&C system design, Materials degradation/ surface erosion (atomic oxygen fluences), Drag/decay, S/C lifetime, Collision avoidance, Sensor pointing, Experiment design, Orbital positional errors, Tracking loss	Jacchia/MET, MSIS< LIFTIM, upper atmospheric wind models
THERMAL ENVIRONMENT	Solar radiation (albedo and OLR variations), Radiative transfer, Atmospheric transmittance	Passive and active thermal control system design, Radiator sizing/material selection, Power allocation, Solar array design	ERBE database, ERB database, NIMBUS database, ISSCP database, Climate models, General Circulation Models (GCM's)
PLASMA	Ionospheric plasma, Auroral plasma, Magnetospheric plasma	EMI, S/C power systems design, material determination, S/C heating, S/C charging/arcing	International Reference Ionosphere Models, NASCAP/LEO NASCAP/GEO, POLAR
METEOROIDS AND ORBITAL DEBRIS	M/OD flux, Size distribution, Mass distribution, Velocity distribution, Directionality	Collision avoidance, Crew survivability, Seconary ejecta effects, Structural design/ shielding, Materials/solar panel deterioration	Flux models
SOLAR ENVIRONMENT	Solar physics and dynamics, Geometric storms, Solar activity predictions, Solar/geomagnetic indices, Solar constant, Solar spectrum	Solar prediction, Lifetime/drag assessments, Reentry loads/heating, Input for other models, Contingency operations	EL Laboratory model, NOAA prediction data, Statistical models, Solar database
IONIZING RADIATION	Trapped proton/electron radiation, Galactic cosmic rays (GCR's), Solar particle events	Radiation levels, Electronics/parts dose, Electronics/single event upset, Materials dose levels, Human dose levels	CREME, AE-8MIN, AE-8MAX, AP-8MIN, AP-8MAX, Radbelt, Solpro, SHIELDOSE
MAGNETIC FIELD	Natural magnetic field	Induced currents in large structures, Locating South Atlantic Anomaly, Location of radiation belts	IGRF85, IGRF91
GRAVITATIONAL FIELD	Natural gravitational field	Orbital mechanics/tracking	GEM-T1, GEM-T2
MESOSPHERE	Atmospheric density, Density variations, Winds	Re-entry, Materials selection, Tether experiment design	Earth-GRAM 90, UARS database, "science" GRAM

MSFC   EM & Environments Branch/EL54

Figure 1. Table outlining space environments and their concerns

As can be seen from the above table, there are numerous concerns due to the space environment and these concerns are identified and understood. Much is understood about composites and how they react in certain environments as can been seen in the "Handbook of Composites" and NASA's "Design Guidelines for Shielding Effectiveness, Current Carrying Capability, and the Enhancement of Conductivity of Composite Materials". What is not completely understood, however, are the interactions of composites and the natural space electromagnetic environments. Since the composite has a conductive and dielectric component, it is necessary to identify when each is dominant.

---

[2] NASA Reference Publication 1375

Current Work

Spacecraft charging has been a primary concern for the aerospace and defense industries since the launch of the first spacecraft. Numerous analyses have been conducted to determine the possibility of spacecraft charging and the effects this would have to a vehicle within the LEO environment. These analyses have focused on an all metal structure and approximated it to be a sphere thus allowing the use of probe theory[3]. This is a reasonable assumption due to the fact that the spacecraft is immersed in the natural space plasma. The primary method of charging is particle collisions within the metal structure. The source of this charging is primarily the electrons that are released from the sun in the form of solar winds. Solar winds have a 50:1 ratio of electrons to protons and have a measured charging rate of 10V/s and up to 1MV/s during high solar flare activity. Other effects that contribute to charging are secondary electrons, back scattered electrons, and photoelectrons.

There are two major components of spacecraft charging. The first is surface charging. Spacecraft charging has the possibility to build up enough difference in potential to cause ESD (arcing). The second is internal dielectric charging. Once a surface is charged there is only a matter of time before it discharges. Discharges can exceed 40 amps and last longer than 150 nanoseconds. Due to the severity of this effect it needs to be fully understood and analyzed.

The surface charging, attributed to the aforementioned sources, has various effects on the vehicle. The phenomenon and severity of charging is dependent on the materials of the spacecraft. For dielectrics the electrons are absorbed or captured until sufficient numbers are present. The material then discharges in the form of an arc to neighboring material or to the surrounding space. Arcing can occur as low as 300V in Low Earth Orbit (LEO).

Another concern is coronal discharging. A corona is most likely to occur at sharp points or when a circulating current is induced. A corona discharge is a potential breakdown (not total or arcing) and occurs when arcing potential is not met. Coronal discharge is the ionization of the space plasma and comes in various forms. The ionized plasma fluoresces causing a "glow" or, if unstable, streamers. Corona discharge is looked at in more detail in section 3.0.

The third concern is internal dielectric charging. Internal dielectric charging occurs when there are energetic electrons in the plasma. The electrons can penetrate the surface of the satellite, thus charging an internal surface. When the surface has sufficiently charged with electrons captured, a discharge will occur. This internal discharging can couple directly to subsystems, exposed circuits and cables in a pulse-like manner causing major problems with the internal systems of the satellite, thus has a higher potential of damage.

Surface Charging

Surface charging will occur when a vehicle is immersed in space plasma. To calculate the potential on the surface of a vehicle in space, probe theory is used. Probe theory is when a sphere is placed in plasma, and the resulting cloud of electrons and ions is a function of the particles energies and densities and the surface potential. This is reasonable due to the fact that

---

[3] Handbook of geophysics

the satellite is immersed in the natural space plasma. The potential on the surface is calculated in two steps: 1) finding the currents to the surface of the vehicle, which are based on functions of ambient conditions and the vehicle geometry. 2) the vehicle potential is then based on the current balance (this also includes sheath particles trapped close to the vehicle). Current balance theory is based on the assumption of charging a sphere of radius r and capacitance C_0 (capacitance at infinity, $C_0 = 4\pi\varepsilon_0 r$) using certain time scales. The following derivation is based on the "Handbook of Geophysics". The time for charging the sphere relative to space is given

by:
$$\tau_s = \frac{C_0 V}{4\pi r^2 J} = 2x10^{-3} \text{ sec}$$
(1)

where r = 1 meter, V = 1 kV and J = 0.5nA/cm^2 (the ambient current).

The time for charging a dielectric of area A is given by: $\tau_s = \tau_D = \frac{C_D V}{AJ}$
(2)

where A is the area and C_D is the dielectric capacitance, leading to τ_D, the charging time for a dielectric. For example, the dielectric constant of composites without metal mesh is between 2 - 10, thus the charging time of the sphere is less than the charging time of the dielectric, therefore the dielectric will charge. The probe method as outlined in The Handbook of Geophysics is commonly used in various computer codes such as NASCAP. It should be noted however, that the computer codes assume either a pure conductor or a pure insulator; composites have properties of both, thus putting the results in question. Also, all of the data on the electrical properties treat composites primarily as conductors, such as the Composite Handbook and NASA's "Design Guidelines for Shielding Effectiveness, Current Carrying Capability, and the Enhancement of Conductivity of Composite Materials."

Corona

An aspect of discharging that is a possible concern is that of a coronal discharge. A coronal discharge is the ionization of a surrounding gas which occurs when that potential gradient exceeds the ionization potential of the gas but is not sufficient to cause arcing (arcing begins at 300V in LEO). A corona is caused by a build up of electrons on a surface, thus when enough electrons are collected, they cause a "glow" by means of discharging into an inhomogeneous electric field. If these currents are circular, charge build up becomes possible at various points. Some examples of where this can happen are antennas and bore sights. In these cases build up of charge can lead to ionization of the surrounding area leading to corona discharge. Corona discharge at the end of a cylindrical tube can seriously impact the performance of electro-optic devices due to the fact that a corona may be luminescent. Also, communications equipment can be severely interfered with when a corona forms around antennas.

Corona discharge is a partial breakdown of the plasma. There are various methods used in the investigation of corona discharge[4]. The first is using coaxial cylinders assuming the center

---

[4] Electrical Breakdown of Gasses

cylinder is a cathode and the outer cylinder is an anode. From this assumption the electric field intensity between the coaxial cylinders is given by the following:

$$E = \frac{V}{r \ln\left(\frac{r_c}{r_a}\right)}$$

(3)

where E is the electric field intensity at a point r in between the two cylinders, V is the potential on the electrode (cathode), r_c is the radius of the cathode, and r_a is the radius of the anode. The electric field accelerates electrons toward the anode and if enough electrons start to accelerate there can be an avalanche of electrons leading to a breakdown or corona.

Another way to evaluate the possibility of coronas is to assume a radial current distribution around a disk. From the current, magnetic flux can be found by:

$$B = \frac{b\mu_0 I}{2\pi a^2}$$

(4)

where B is the radial magnetic flux, b is some point inside the cylinder, μ_0 is the permeability of free space, I is the current, and a is the radius of the cylinder. Given that B=µH, the magnetic field intensity is found by:

$$H = \frac{bI}{2\pi a^2}$$

(5)

From H, and given E=377H in free space, the electric field can be solved for:

$$E = 377\frac{bI}{2\pi a^2}$$

(6)

This electric field is then compared to known values for breakdown.

Internal Dielectric Charging

Along with the importance of investigating surface charging, internal charging is also of great concern. Internal charging has the potential to be more damaging than surface charging as it is within the satellite itself. Internal dielectric charging is due to high-energy electrons (E > 100eV) that penetrate though diffusion, into the satellite and build up on internal structures, including inside the satellite. These high-energy electrons are present in the natural space plasma the surrounds the satellite. High-energy electrons are more common in polar orbits, like the orbit of this vehicle, due to aural events. Diffusion is the mechanism in which charge that is built up on the outside of the space vehicle will diffuse though the outer vehicle and build up on the inner surface thus creating the possibility of arcing. Once the initial diffusion has taken place it becomes a continuous process whereby allowing a current to pass though from the outer surface to the inner wall. Thus internal charging and discharging will be a continual occurrence.

The internal electric field can build up when the charge leakage rate is less than the charge collection rate. The time it takes to charge is thus related to the dielectric leakage rate, however given enough time sufficient charging will occur resulting in arcing. This arcing will appear as a pulse to the internal systems, cables, exposed circuits, etc. Pulse's usually last approximately 10's nanoseconds. The likelihood for a discharge to occur is a function of both the voltage potential and the electric field. But first before the electric field is calculated the range of the energetic electrons has to be calculated to see if there would indeed be a charge build up. The range that the electrons penetrate is given by Weber's equation (1),

$$R = 0.55 \frac{E}{\rho}\left[1 - \frac{0.9841}{(1+3E)}\right] \tag{7}$$

where R is the maximum range an electron with energy E can travel in cm, E is in MeV, and ρ is the density of the material. The electrons within the dielectric are not all distributed at R but spread throughout the material, and there is a fall-off in the current as the range is approached. Sorensen (1) estimated that fall off was linear, though a gaussian might fit better the improvement is too small for the additional computation, thus the linear approach is used,

$$a(g/cm^2) = 0.238xE \tag{8}$$

where a is the fall off distance.

The electric field also needs to be calculated this can be done with the use of the dielectric current density,

$$J = \phi\, q \tag{9}$$

where J is in A/cm^2, ϕ is the electron flux, and q is the charge of an electron. Just to note that a capacitor plate behavior is assumed, and thus the electric field buildup may be determined from the conductivity of the material,

$$E(t) = \frac{V(t)}{d} = \frac{J}{\sigma}\left(1 - e^{-t/\tau}\right) \tag{10}$$

where σ is the dielectric conductivity, τ is the time constant, and d is the thickness of the material. The time constant is a function of the material,

$$\tau = \frac{\varepsilon}{\sigma} \tag{11}$$

where ε is the dielectric constant. The above electric field can be calculated and then compared to the breakdown strength of the dielectric to determine if arcing will occur.

Arcing

Arcing occurs between either different metals or two pieces of metal at different potentials separated by a gap. Due to the fact that various areas of the craft are made up of different materials there could be arcing from one material to another. The vehicle will have a net potential induced by the plasma that will be the same for all the materials, however the current balance for each material will not be the same due to the differences in conductivity, thus arcing will occur. A simple form of Ohm's law can be used to calculate this imbalance,

$$I = \frac{V}{Z} \qquad (12)$$

where V is the potential and Z is the impedance. Let I_1, I_2 and I_3 be the currents for 3 materials the potential across each material can be found by the following. Given the definition of current,

$$dq = Idt \qquad (13)$$

and then the fact that,

$$C = \frac{\varepsilon_0 A}{d} \qquad (14)$$

where d is the distance between the materials and A is the area of the material. Thus the potential is given by,

$$q = CV$$
$$\Delta q_1 - \Delta q_2 = C\Delta V \qquad (15)$$

where ΔV is the voltage across the imbalance and C is the capacitance between the two. Given that the internal discharging also acts like a capacitor it will discharge in the same manner.

Charging of a Composite

Charge build up and arcing

The outlined effects of being in the natural space plasma are also evaluated with a composite structure in mind. It is determined that surface charging and internal dielectric charging are greater concerns when composites are used in conjunction with metal for the structure of the space vehicle this is due to the electrical properties of composites. As previously mentioned composites are a concern due to the fact that they are poor conductors and have dielectric matrix associated with them. Due to the poor conductivity, the rate the composite can charge and the distribution of charge vary non-linearly, causing a non-uniform distribution of charge. This allows for areas of the composite to charge differently from other areas, thus punch through or flash over[5] may occur. Also as various materials have different discharge voltages, there can be

---

[5] Spacecraft Charging by Dr. Holbert

a potential difference reached before the discharge occurs. Thus a metal will charge to a different potential than a composite, allowing for a potential difference between the two materials and in essence creating a capacitor and allowing for arcing.

If the charge builds up faster than current moves then the charge will "stack up" eventually building up enough charge to arc or corona. The time for current to move is dependent on the material under question; this is known as the relaxation time. The relaxation time is determined by the resistivity and the dielectric constant of the material. For any material, if the charging time is less than the relaxation time, charge has the opportunity to build up leading to corona or arcing. This can become a major concern when composites are being taken into account as the relaxation time is commonly higher than the charging time as shown with the dielectric time constant (equation 2). The following table lists the electrical properties for some common materials including some composites.

Table 1. Typical Resistivity and Conductivity Values[6]

MATERIAL	THICKNESS		RESISTIVITY			CONDUCTIVITY		
			Volume		Surface			
	mil	cm	ohm-meter	ohm-centimeter	ohm/square	mho/meter	mho/cm	relative
Copper		0.100	1.72E-08	1.72E-06	1.72E-03	5.81E+07	5.81E+05	1.00E+00
Aluminum		0.100	2.87E-08	2.87E-06	2.87E-03	3.48E+07	3.48E+05	6.01E-01
Cold rolled steel		0.100	1.01E-07	1.01E-05	1.01E-02	9.90E+06	9.90E+04	1.71E-01
Stainless steel		0.100	8.62E-07	8.62E-05	8.62E-02	1.16E+06	1.16E+04	2.00E-02
Steel filaments in plastic		0.100	2.00E-03	2.00E-01	2.00E+02	5.00E+02	5.00E+00	8.62E-06
10% stainless filaments		0.320	8.20E-03	8.20E-01	2.56E+00	1.22E+02	1.22E+00	2.10E-06
Zinc plating	1	0.003	5.70E-08	5.70E-06	1.90E-03	1.75E+07	1.75E+05	3.02E-01
GFRP (typ.)		0.100	1.80E-05	1.80E-03	1.80E+00	5.56E+04	5.56E+02	9.58E-04
GFRP (meas.)		0.360	8.64E-05	8.64E-03	2.40E-02	1.16E+04	1.16E+02	2.00E-04
40% Carbon fiber	70	0.178	1.00E+00	1.00E+02	5.62E+02	1.00E+00	1.00E-02	1.72E-08
5% Ni coated graphite in polycarbonate	125	0.318	3.40E+02	3.40E+04	1.07E+05	2.94E-03	2.94E-05	5.07E-11
10% "	125	0.318	5.20E-01	5.20E+01	1.64E+02	1.92E+00	1.92E-02	3.32E-08
15% "	125	0.318	1.60E-03	1.60E-01	5.04E-01	6.25E+02	6.25E+00	1.08E-05
20% "	125	0.318	1.10E-03	1.10E-01	3.46E-01	9.09E+02	9.09E+00	1.57E-05

As can be seen from the above table the resistivity is considerable higher for the composite materials than for the metal materials (it should also be noted that the GFRP typical value is greater than the measured value, as the means of measurement is not know the typical value will be of most curiosity). This leads to a longer relaxation time and the possibility of charge build up. To calculate the relaxation time equation 2 is used.

$$\tau_c = RC = \frac{CV}{AJ}$$

[6] NASA Contractor Report 4784

where τ_c is the relaxation time, R is the resistance and C is the capacitance. Then using the following equations,

$$R = \frac{\rho d}{A}$$
$$C = \frac{\varepsilon A}{d}$$
(16)

the relaxation time becomes,

$$\tau_c = \rho \varepsilon$$
(17)

where ρ is the resistivity and ε is the relative permittivity given by $\varepsilon = \varepsilon_0 \, \kappa_\varepsilon$.

The following table shows the resistivity, for those materials listed above when calculated for a thickness of 0.5cm (a typical body tube thickness).

Table 2. Resistivity at 0.5 cm

Material	Surface Resistivity (Ω-square)	Volume Resistivity (W-m) (based on 0.5 cm thickness)
Copper	1.72E-03	8.60E-06
Aluminum	2.87E-03	1.44E-05
Cold rolled steel	1.01E-02	5.05E-05
Stainless steel	8.62E-02	4.31E-04
Steel filaments in plastic	2.00E+02	1.00E+00
10% stainless filaments	2.56E+00	1.28E-02
Zinc plating	1.90E-03	9.50E-06
GFRP (typ.)	1.80E+00	9.00E-03
GFRP (meas.)	2.40E-02	1.20E-04
40% Carbon fibor	5.62E+02	2.81E+00
5% Ni coated graphite in polycarbonate	1.07E+05	5.35E+02
10% "	1.64E+02	8.20E-01
15% "	5.04E-01	2.52E-03
20% "	3.46E-01	1.73E-03

From the above table it can be seen that the resistivity is much higher for the composite material as expected. Due to the fact that the dielectric matrix is non-linear for composites it can be determined that with a charging mechanism of up to 1MV/s during auroral conditions the composite will charge in a non-linear manner until arcing potential is reached. The material will then arc or corona and charge again, repeating this process. As can be inferred from above, composite materials will have the time to build up enough charge to arc more rapidly than metal.

It should be noticed that the above analysis talks about arcing, however does not talk about different materials. This is due to the fact that composite materials charge differentially as well as non-linearly. With this differential charging parts of the composite will charge at a different rate than other parts thus allowing for different potentials to build up and allowing for surface arcing or arcing through the material in a channel like manner.

Along with surface charging and arcing there is a concern with internal arcing. Internal arcing occurs when the internal surface of the composite (assuming a tube) becomes charged enough to arc (internal dielectric charging). This arcing can occur between different parts of the composite as previously mentioned, or to equipment located inside the composite. Charge will build up on the inside of most composite materials due to the fact that there is little to no shielding effectiveness provided by the material, thus a current on the outside of the composite will be on the inside also, due to short diffusion time of composite materials. This will be looked at in more detail in the next section.

Spacecraft Charging with Composite Materials

As is discussed previously the natural space environment is such that if not protected against is of great concern. Also as previously mentioned, spacecraft charging is even more concerning with the use of composites. Surface charging is calculated in the same manner as before using probe theory, however that composite will charge at a faster rate than metal because of the longer relaxation time. Also due to the nonlinear dielectric properties of the material, the material will not all charge to the same potential. This differential charging allows for the possibility of punch though and flashover as mentioned in section 4.1. Both of these effects are of concern with composites due to their destructive manner. With both punch through and flashover there is the possibility of physical damage to the vehicle in the form of holes and degradation of the composite. Due to the make up of the composite it is possible to melt during one such arc.

Again like metals there is also a threat of corona. Coronas can occur when enough electrons are deposited on a surface and then discharge into the surrounding environment causing "glow" or "streamers". Composites will have a larger "stack up" of charge thus there is a higher probability of a corona. As opposed to the physical damage that can occur with surface arcing, a corona can interfere with sensors, receivers, and antennas or anything on the outside of the vehicle. For example if an electro-optic detector has a corona "glow" around it, it will make it almost impossible to obtain any reliable data. This corruption of data could possibly result in failure. The best way to avoid corona is to minimize sharp points and use metals to negate charge buildup.

Finally internal dielectric or bulk charging is most likely when using composites. This is due to the lack of conductivity. Composites typically have little to no shielding thus impinging electrons will drive straight through the material deeper than if the material was metal. This leads to a build up of charge on the inside of the vehicle. Not only can arcing occur within the vehicle, but due to the magnetic field within the vehicle, caused by the moving charge, there is the possibility of inductive coupling to cables, wires, and internal systems. The electrons built up on the inside of the vehicle will arc as they do on the outside surface. When arcing inside

occurs, the arc will go to the internal systems or to other parts of the composite. As is shown above, spacecraft charging is a major concern in general and even more so with composites.

Conclusion

With composites becoming more prevalent in today's and tomorrow's aerospace industry, the effects of natural space environment and other extreme electromagnetic environments have to be evaluated. The electromagnetic properties of composites must be understood to provide an integrated design which provides protection of electronic equipment from the external hostile environments. As previously mentioned, composites have good thermal and mechanical properties, and these are well understood in the community. But the electromagnetic properties of composites are incomplete. Most analyses treat composites as conductors. However, the literature reports that composites have dielectric properties. This makes the response of composites to the mentioned environments a dispersive or non-linear material. This has been discussed in this paper by the fact that composites not only act as conductors, but also dielectrics-they charge!!

Due to the fact that composites have dielectric components implies a dielectric matrix is associated with them. With this knowledge the internal charging of composites becomes a major issue in the analysis of the material. To thoroughly understand the interaction of the composite to the space plasma and other extreme electromagnetic environments this dielectric matrix along with the accompanying conductivity matrix must be studied. The response of the material is directional and complex. To provide complete protection of the internal systems, this knowledge needs to be acquired. With future missions into space looking to survive longer and at the same time be cost conscious, composite material usage will grow. Therefore, the electromagnetic analysis and testing of these materials becomes a major program issue in order to insure mission success.

References

1. Ryden, K. A., D. J. Rodgers, and G. L. Wrenn, "Engineering Tools for Internal Charging", Establishment of Engineering Specification for Internal Charging, England 1999.

2. Jursa, A. S. ed., "Handbook of Geophysics and the Space Environment", Air Force Geophysics Laboratory, USAF Systems Command, 1985.

3. Meek, J. M. and J. D. Craggs, ed., "Electrical Breakdown of Gases", John Wiley & Sons, New York, 1978.

4. Leach, R. D. and M. B. Alexander, ed., "Failures and Anomalies Attributed to Spacecraft Charging", NASA Reference Publication 1375, NASA Marshall Space Flight Center, August 1995.

5. Vaughan, W. W., K. O. Niehuss, and M. B. Alexander, ed., "Spacecraft Environments Interactions: Solar Activity and Effects on Spacecraft", NASA Reference Publication 1396, NASA Marshall Space Flight Center, November 1996.

6. James, B. F. Coordinator, "The Natural Space Environment: Effects on Spacecraft", NASA Reference Publication 1350, NASA Marshall Space Flight Center, November 1994.

7. Herr, J. L., M. B. McCollum, "Spacecraft Environments Interactions: Protecting Against the Effects of Spacecraft Charging", NASA Reference Publication 1354, NASA Marshall Space Flight Center, November 1994.

8. Leach, R. D. and M. B. Alexander, ed., "Electronic Systems Failures and Anomalies Attributed to Electromagnetic Interference", NASA Reference Publication 1374, NASA Marshall Space Flight Center, July 1995.

9. Bedingfield, K. L., R. D. Leach, M. B. Alexander, ed., "Spacecraft System Failures and Anomalies Attributed to the Natural Space Environment", NASA Reference Publication 1390, NASA Marshall Space Flight Center, August 1996.

10. Casper, Jeffrey E., ed., "High Power Microwave Harding Design Guide for Systems Volume I: HPM and Interpreting Harding Requirements", Final Design Guide, US Army Laboratory Command Harry Diamond Laboratories Adelphi, April 1992

11. "Avoiding Problems Caused by Spacecraft On-Orbit Internal Charging Effects", NASA Technical Handbook 4001, NASA, February 1999

12. Evans, R. W., "Design Guidelines for Shielding Effectiveness, Current Carrying Capability, and the Enhancement of Conductivity of Composite Materials", NASA Contractor Report 4784, NASA Marshall Space Flight Center, August 1997

13. Sorensen, J., "Engineering Tools for Internal Charging", ESA Final Report, ESA, January 1999

14. Peters, S. T., ed., "Handbook of Composite 2nd ed.", Chapman and Hall, New York, 1998

15. Gaier, James R., "Intercalated Graphite Fiber Composites as EMI Shields in Aerospace Structures", IEEE Transactions on Electromagnetic Compatibility, Vol. 34, No. 3, August 1992

16. Whittlesey, Albert and Dr. Henry B. Garrett, "NASA's Technical Handbook for Avoiding On-Orbit ESD Anomalies Due to Internal Charging Effects", 6th Spacecraft Charging Technology Conference, AFRL-VS-TR-20001578, September 2000

17. Holbert, Dr., "Spacecraft Charging", Retrieved 8 May 2003, Online: http://www.eas.asu.edu/~holbert/eee460/spc-chrg.html

18. Sorensen, J., "An Engineering Specification of Internal Charging", ESA, Retried 22 January 2003, Online: www.estec.esa.nl/conferences/96a09/Abstracts/abstract35/paper/

19. Holbert, Dr., "Space Radiation Environmental Effects", Retrieved 16 May 2003, Online: http://www.eas.asu.edu/~holbert/eee460/spacerad.html

SIMULATIONS OF SOLAR WIND PLASMA FLOW
AROUND A SIMPLE SOLAR SAIL

Henry B. Garrett
The Jet Propulsion Laboratory,
The California Institute of Technology
4800 Oak Grove Dr.
Pasadena, CA 91109
Phone: 818-354-2644
E-mail: Henry.Garrett@jpl.nasa.gov

Joseph Wang
Department of Aerospace and Ocean Engineering
Virginia Polytechnic Institute and State University

Abstract

In recent years, a number of solar sail missions of various designs and sizes have been proposed (e.g., Geostorm). Of importance to these missions is the interaction between the ambient solar wind plasma environment and the sail. Assuming a "typical" 1 AU solar wind environment of 400 km/s velocity, 3.5 cm^{-3} density, ion temperature of ~10 eV, electron temperature of 40 eV, and an ambient magnetic field strength of 10^{-4} G, a first order estimate of the plasma interaction with square solar sails on the order of the sizes being considered for a Geostorm mission (50 m x 50 m and 75 m x 75 m corresponding to ~2 and ~3 times the Debye length in the plasma) is carried out. First, a crude current balance for the sail surface immersed in the plasma environment and in sunlight was used to estimate the surface potential of the model sails. This gave surface potentials of ~10 V positive relative to the solar wind plasma. A 3-D, Electrostatic Particle-in-Cell (PIC) code was then used to simulate the solar wind flowing around the solar sail. It is assumed in the code that the solar wind protons can be treated as particles while the electrons follow a Boltzmann distribution. Next, the electric field and particle trajectories are solved self-consistently to give the proton flow field, the electrostatic field around the sail, and the plasma density in 3-D. The model sail was found to be surrounded by a plasma sheath within which the potential is positive compared to the ambient plasma and followed by a separate plasma wake which is negative relative to the plasma. This structure departs dramatically from a negatively charged plate such as might be found in the Earth's ionosphere on the night side where both the plate and its negative wake are contiguous. The implications of these findings are discussed as they apply to the proposed Geostorm solar sail mission.

Nomenclature

$$\lambda_{\mathrm{D}} = \sqrt{\frac{KT_e}{4\pi n e^2}}$$ plasma Debye length (based on electron temperature)

Φ electric potential

Φ_s solar sail to ambient plasma potential difference

B_o solar wind magnetic field

d_{sh} solar sail sheath thickness

L_x, L_y solar sail size

n_{sw} solar wind plasma density

T_e, T_i electron and ion (proton) temperature, respectively

v_{sw}, v_{ti}, v_{te} solar wind flow velocity, ion thermal velocity, and electron thermal velocity, respectively

$I_T(\Phi_s) =$ Total current to/from solar sail; $= 0$ for current balance at potential $\Phi = \Phi_s$.

$J_e(\Phi_s) =$ Average electron current per unit area to solar sail at potential Φ_s

$J_i(\Phi_s) =$ Average ion current per unit area to solar sail at potential potential Φ_s

$JS_e(\Phi_s) =$ Average secondary electron current per unit area from solar sail at potential Φ_s

$JBS_e(\Phi_s) =$ Average backscattered electron current per unit area from solar sail at potential Φ_s

$JS_i(\Phi_s) =$ Average ion induced secondary electron current per unit area from solar sail at potential Φ_s

$J_{pho}(\Phi_s) =$ Photoelectron current per unit area from solar sail at potential Φ_s

$A_e =$ Ambient electron impact area

$A_i =$ Ambient ion impact area

$A_{pho} =$ Photoelectron emission area

Introduction

In recent years, a number of solar sail missions of various designs and sizes have been proposed. Indeed various groups, both private and governmental, are in the process of building either flight or prototype solar sails. Of potential importance to these missions is the interaction

of the ambient solar wind plasma environment with the sail. To evaluate this interactions and establish a baseline for future studies, we will assume a "typical" 1 AU solar wind environment of 400 km/s velocity, 3.5 cm^{-3} density, ion temperature of ~10 eV, electron temperature of 40 eV, and an ambient magnetic field strength of 10^{-4} G. This environment will be used to carry out a first order estimate of the plasma interaction with square solar sails on the order of the sizes being considered for a Geostorm mission (50 m x 50 m and 75 m x 75 m corresponding to ~2 and ~3 times the Debye length in the plasma). As will be discussed in more detail below, the first step will be to carry out a crude current balance for the sail surface immersed in the plasma environment and in sunlight to estimate the surface potential of the model sails (the surfaces in this initial study are assumed to be made of thin, uniformly conducting aluminum). A 3-D, Electrostatic Particle-in-Cell (PIC) code is then used to simulate the solar wind flowing around the solar sail. Assuming that the solar wind protons can be treated as particles while the electrons follow a Boltzmann distribution, the electric field and particle trajectories are solved self-consistently to give the proton flow field, the electrostatic field around the sail, and the plasma density in 3-D. The sail is found to be surrounded by a plasma sheath within which the potential is positive compared to the ambient plasma and followed by a separate plasma wake which is negative relative to the plasma. The structure departs dramatically from a negatively charged plate such as might be found in the Earth's ionosphere on the night side where both the plate and its negative wake are contiguous. Finally, the implications of these findings are discussed as they apply to a sample mission, the Geostorm Solar Sail.

Basic Characteristics

Spacecraft in the interplanetary environment experience a number of effects from the sun: surface charging (either positive or negative) and/or deep dielectric charging that can result in damaging arcs, UV and radiation effects on materials, and plasma wake or sheath effects that could impact experiments or instruments on the spacecraft. Of importance here are plasma interaction effects due to the solar wind. The solar wind is a fully-ionized, electrically neutral, magnetized plasma that flows outward from the Sun. The solar wind plasma in interplanetary space can vary over a wide range: from <1 cm^{-3} to ~80 cm^{-3} in density, from ~200 km/s to over 2000 km/s in velocity, and from 0.5 eV to ~100 eV in temperature. Although the solar wind is highly variable, in this study we will concentrate on the typical or average solar environment in order to establish a baseline for future studies. We will thus assume the following "average" solar wind parameters for our test environment:

$$v_{sw} \sim 400 \ km/s; \ n_{sw} \sim 3.5 \ cm^{-3}; \ T_i \sim 10 \ eV \ ; T_e \sim 40 \ eV \ ; B_o \sim 10^{-4} \ Gauss$$

(For simplicity, here we only consider the core population for the solar wind electrons and ignore the halo population.)

Based on these solar wind parameters, the following basic plasma parameters can be determined:

$$\lambda_D \sim 25 \ m; \ v_{te} \sim 2.65 \ x \ 10^3 \ km/s; \ v_{ti} \sim 30 \ km/s; \ c_s = (T_e/m_p)^{1/2} \sim 62 \ km/s$$

$$\Omega_i \sim 1 \ rad/s; \ \Omega_e \sim 1.8 \ x \ 10^3 \ rad/s$$

The basic characteristics of the solar wind flowing around a solar sail are thus the same as that of a collisionless, mesothermal plasma flowing around an obstacle. That is, since the solar wind flow is such that $v_{ti} << v_{sw} << v_{te,}$, the plasma is mesothermal. Moreover, as both the ion gyroradius, $r_{ci} = v_{sw}/\Omega_i \sim 400$km, and the electron gyroradius, $r_{ce} = v_{te}/\Omega_e \sim 1.5$ km, are much larger than the typical solar sail dimension ($L_{sail} \sim 100$m), the solar wind flow may be considered as an unmagnetized, collisionless plasma flow for our problem.

The floating potential of the solar sail relative to the ambient solar wind plasma can be estimated from current balance (Garrett, 1981). That is, for a thin, conducting aluminum sheet, it is assumed that current balance is given by:

$$I_T(\Phi_s) = 0 = -A_e \cdot J_e(\Phi_s, T_e, n_{sw}) + A_i \cdot J_i(\Phi_s, T_i, n_{sw}) + A_e \cdot JS_e(\Phi_s, T_e, n_{sw}) +$$
$$+ A_e \cdot JBS_e(\Phi_s, T_e, n_{sw}) + A_i \cdot JS_i(\Phi_s, T_i, n_{sw}) + A_{pho} \cdot J_{pho}(\Phi_s) \qquad (1)$$

An accurate calculation of the solar sail floating potential requires knowledge of the detailed spacecraft specification so that all the current sources can be properly accounted for. In this paper, we shall consider a very simple geometric model—a conducting flat plate. For the solar wind conditions listed in section I, the assumed model (Garrett, 1981) estimates that the floating potential in sunlight ranges $\Phi_s \sim 6$ V to ~ 14 V based on the details of the current collection (e.g., ion ram current, orbit limited, etc.). Hence, in this study, we take the sail potential to be $\Phi_s \sim 10$V.

Simulation Model

A 3-D, Electrostatic Particle-in-Cell (PIC) code is used to simulate the solar wind flowing around a solar sail. In this code, the solar wind protons are treated as particles. The electron component is assumed to be an isothermal fluid and hence its density follows the Boltzmann distribution. The electric field and particle trajectories are then solved self-consistently. A dynamic alternating direction implicit (DADI) solver is used to solve the nonlinear Poisson's equation in a 3-dimensional space. More detailed description of the code can be found in Wang et al. (2001).

The model setup is shown in Fig.1. When geometric symmetry is considered, the simulation setup needs to include only a quarter of the sail. The $x = 0$ and $y = 0$ boundaries are symmetric surfaces while all other boundaries are "open" boundaries. Macro-particles representing the solar wind protons are injected into the simulation domain along the z axis at every time step. The solar sail is taken to be a conducting, thin plate with the assumed 10 V potential.

Simulation Results

As a base model, we consider a square conducting sail with dimensions of $Lx = Ly$. Table 1 listed the solar sail sizes being considered for the Geostorm mission: $Lx = 50$ m for Sail-1 and $Lx = 75$ m for Sail-2, respectively. If one normalizes the dimension by the electron Debye length, one finds that the two sail sizes are $Lx/\lambda_D \sim 2$ and $Lx/\lambda_D \sim 3$, respectively. For these dimensions

and an assumed sail potential to be $\Phi_s \sim 10$ V, the model parameters for Geostorm simulations have been determined and are listed in Table 1 in both normalized units and physical units. A series of test runs with varying resolutions were performed to ensure that the results do not depend on the simulation parameters.

Geostorm Solar Sail Results

The simulations results for the two sails considered are shown in figures 2 and 3. In each figure, the top panel shows electric potential contours on a z-y plane cutting through the center of the sail; the middle panel shows potential contours on a x-y plane containing the sail surface, and the bottom panel compares the potential profile along a z-axis through the center of the sail surface and that along a z-axis through the center of the sail edge. The following conclusions can be drawn from the simulations:

- The sail is surrounded by a plasma sheath (within which the potential is positive compared to ambient) and followed by a plasma wake (within which the potential is negative).
- The plasma sheath in the ram side starts at a distance of ~ 2 λ_D in front of the sail, or a distance of ~ 50 m in front of the sail for the typical solar wind conditions listed in section 1.
- For the two solar sail sizes considered, the sail size has a minimum effect on the plasma sheath. (Although the potential in the wake region is significantly different.)
- While the plasma sheath extends to a distance of ~ 50 m in front of the sail, its effects on solar wind electron measurement made near the sail surface should be minimum. This is because the solar sail floating potential is only about 10 V while the solar wind electron temperature is $T_e \sim 40$ eV. However, the sheath may have some effects on solar wind proton measurements made within the sheath.

Parametric Simulation Results

To better understand the global structure of plasma sheath and wake, we have also performed parametric simulations for various sail sizes and floating potentials. To generalize the results for different solar wind conditions, we will present results in normalized parameters. (Note that the results scale with the plasma Debye length.) This section presents simulation results for a solar sail with a dimension of $Lx = Ly = 8$ λ_D (i.e., $L \sim 200$ m for the solar wind conditions listed in section 1. For comparison, we also include simulation results for a conducting plate with a negative floating potential. The parametric cases are summarized in Table 2. The results are shown in figures 4 through 8.

It is interesting to compare the plasma interaction of solar sail with that of a large space platform in the ionosphere. A spacecraft in low Earth orbit (LEO) also sees a collisionless, mesothermal plasma flow. However, a LEO spacecraft typically has a negative floating potential. The problem of ionospheric plasma flowing around a large, negatively biased structures has been studied extensively (for instance, *Wang and Hastings*, 1992a,b; *Wang et al.*, 1994, and references therein). In such a problem, the dominate physics is formation of a plasma wake. When the spacecraft flowing potential is low, the wake is formed through plasma expansion. An expansion fan will be generated at plate edge which serves as a presheath to connect the ambient

plasma flow and the plasma sheath surrounding the plate. Hence, for a negatively biased sail, the plasma sheath and wake is a unified structure, as shown in Fig.5. On the other hand, for a solar sail with a positive floating potential, the sheath and wake are two distinct regions. In this configuration, the protons are decelerated within the sheath but still undergo the same expansion process in the wake region.

Conclusions

We find, for base solar wind plasma conditions, that a solar sail is surrounded by a plasma sheath followed by a plasma wake (within which the potential is negative). The sheath thickness in front of the solar sail is a few Debye lengths thick for moderate charging potentials. Since the solar wind Debye length is in the range of $O(10)$ m to $O(10^2)$ m, comparable to typical solar sail dimensions, one would expect to observe some sheath effects within a distance of tens of meters on the ram side. However, since the solar sail floating potential is found to be moderate (a few volts), sheath effects on solar wind measurements performed near the sail are *not* expected to be significant.

Acknowledgements

Tables

Table 1. Geostorm Solar Sails

	$Lx \times Ly$ (λ^2_D)	Lx (m)	Φs (T_e)	Φs (V)	dsh (λ_D)	dsh (m)
Sail-1	2X2	50	0.25	10	~ 2	~ 50
Sail-2	3X3	75	0.25	10	~ 2	~ 50

Table 2. Parametric Cases

	$Lx \times Ly$ (λ^2_D)	Φ_s (T_e)
1	8X8	.25
2	8X8	-2.25
3	8X8	1.00
4	8X8	-1.00
5	8X8	-10.00

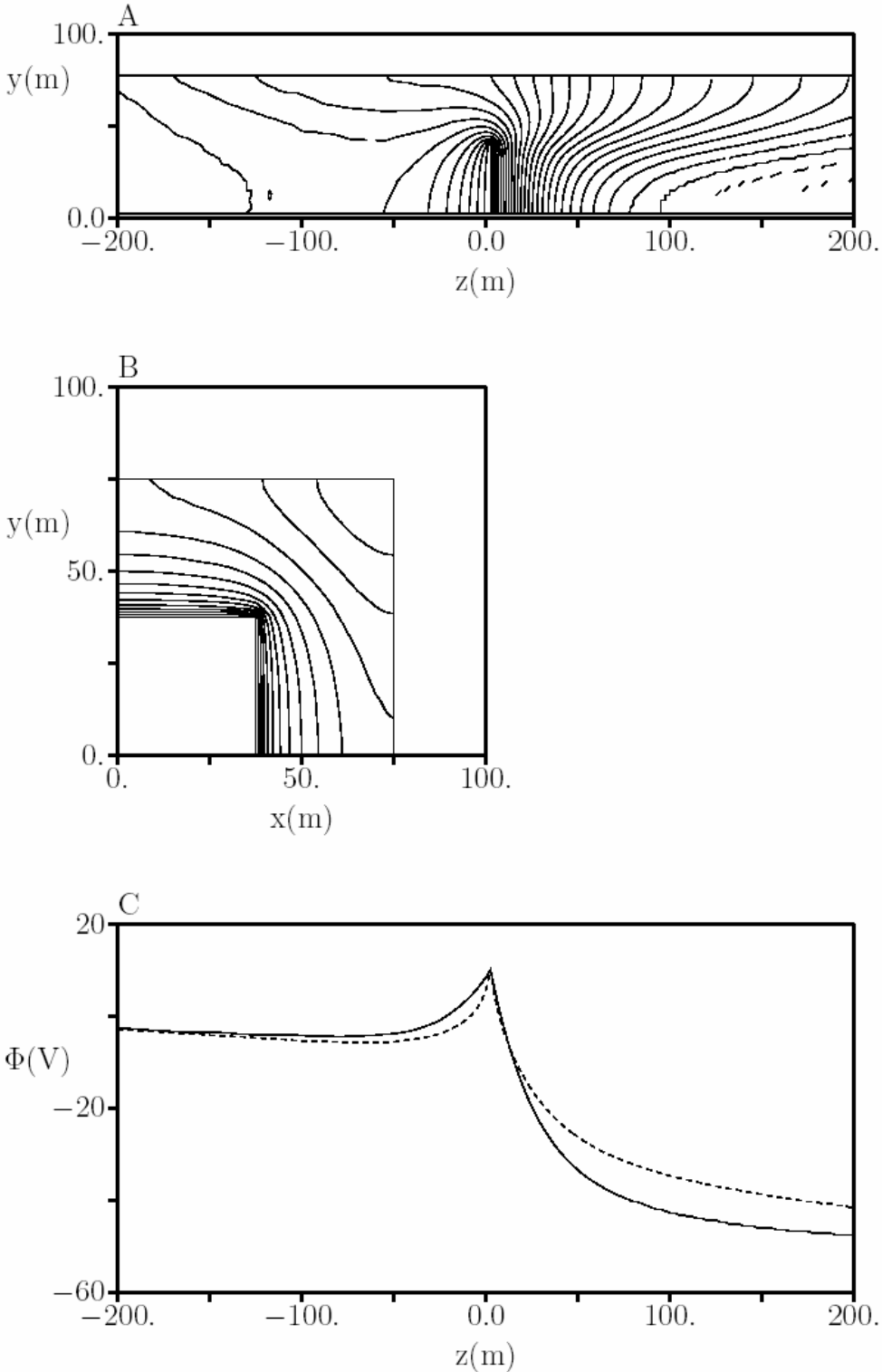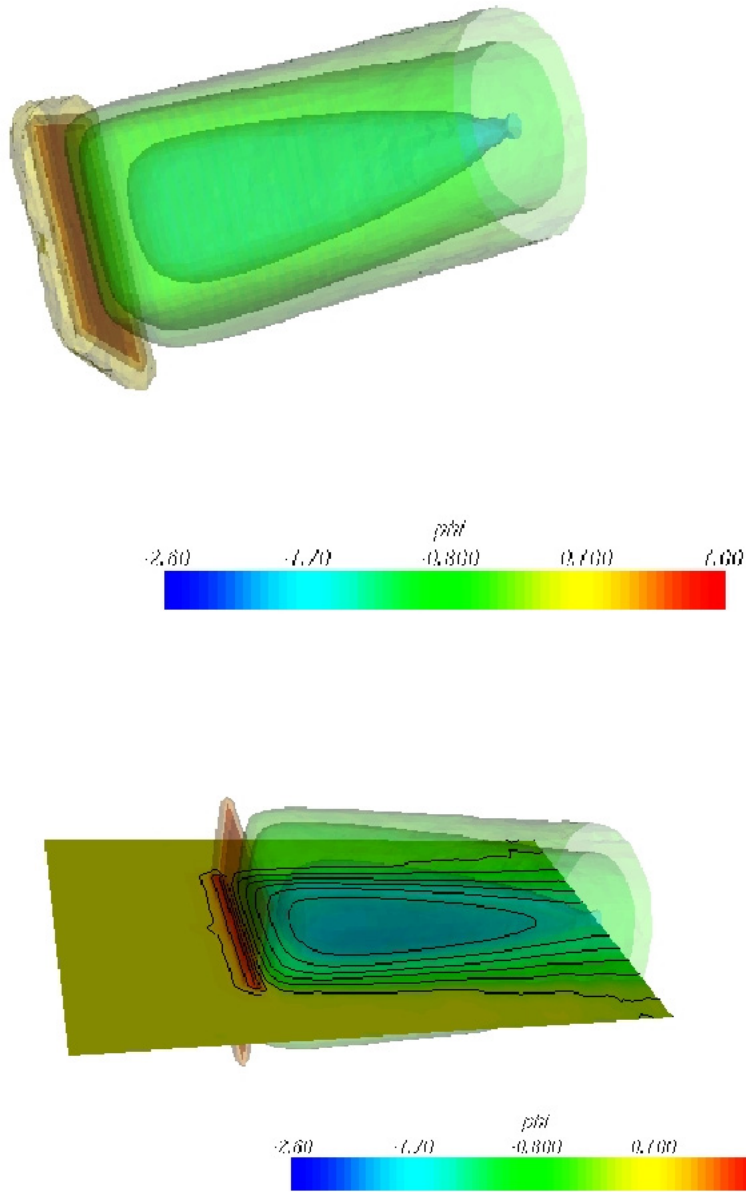# Figures
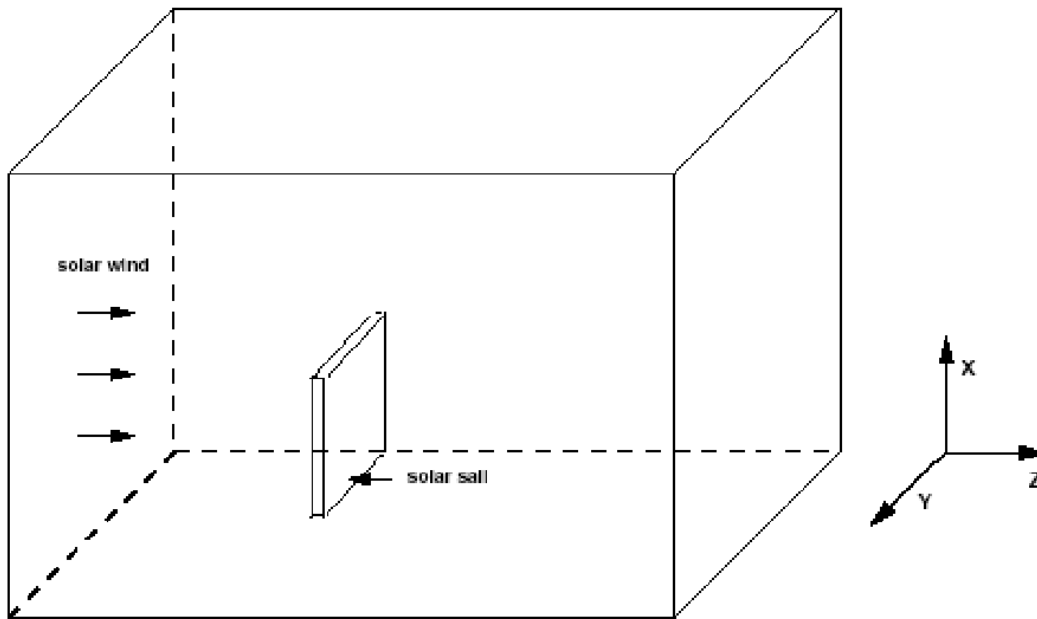
Figure 1. Simulation Setup. 3-D simulations are performed for a quarter size solar sail. Solar sail is modeled as a thin conducting plate with a potential. Solar wind is injected from the upstream surface along the z direction. Solar wind is modeled as particle protons and fluid electrons.
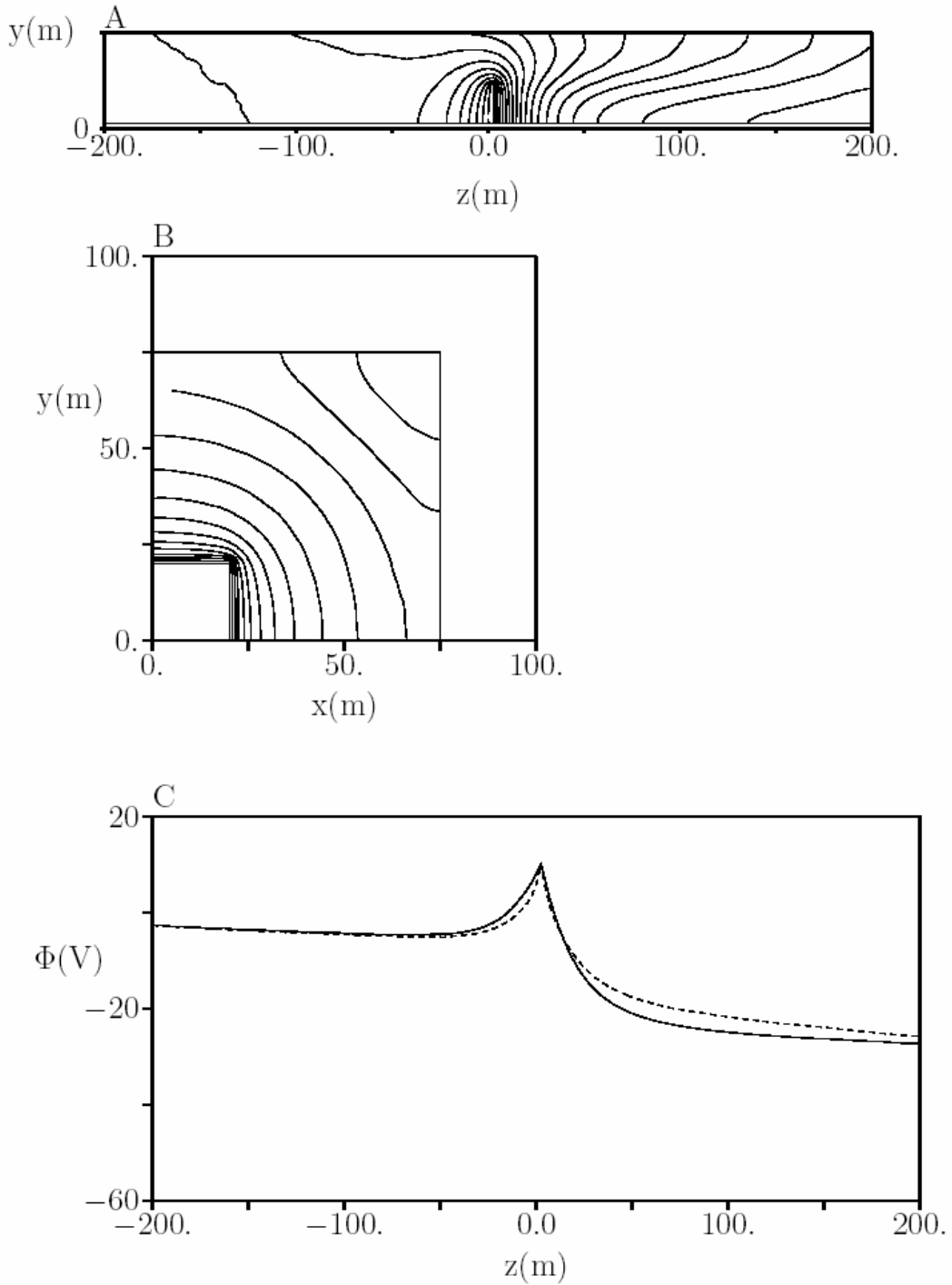
Figure 2. Simulation Results for Sail-1. Dimension: 50 m X 50 m. Sail Potential: 10V. A: electric potential contours on a z-y plane cutting through sail center. B: electric potential contours on a x-y plane containing sail surface. (contour level difference=2 V) C: potential profile along a z axis through the center of the surface and a z axis through the center of the edge.

Figure 3. Simulation Results for Sail-2. Dimension: 75 m X 75 m. Sail Potential: 10V. A: electric potential contours on a z-y plane cutting through sail center. B: electric potential contours on a x-y plane containing sail surface. (contour level difference=2 V) C: potential profile along a z axis through the center of the surface and a z axis through the center of the edge.
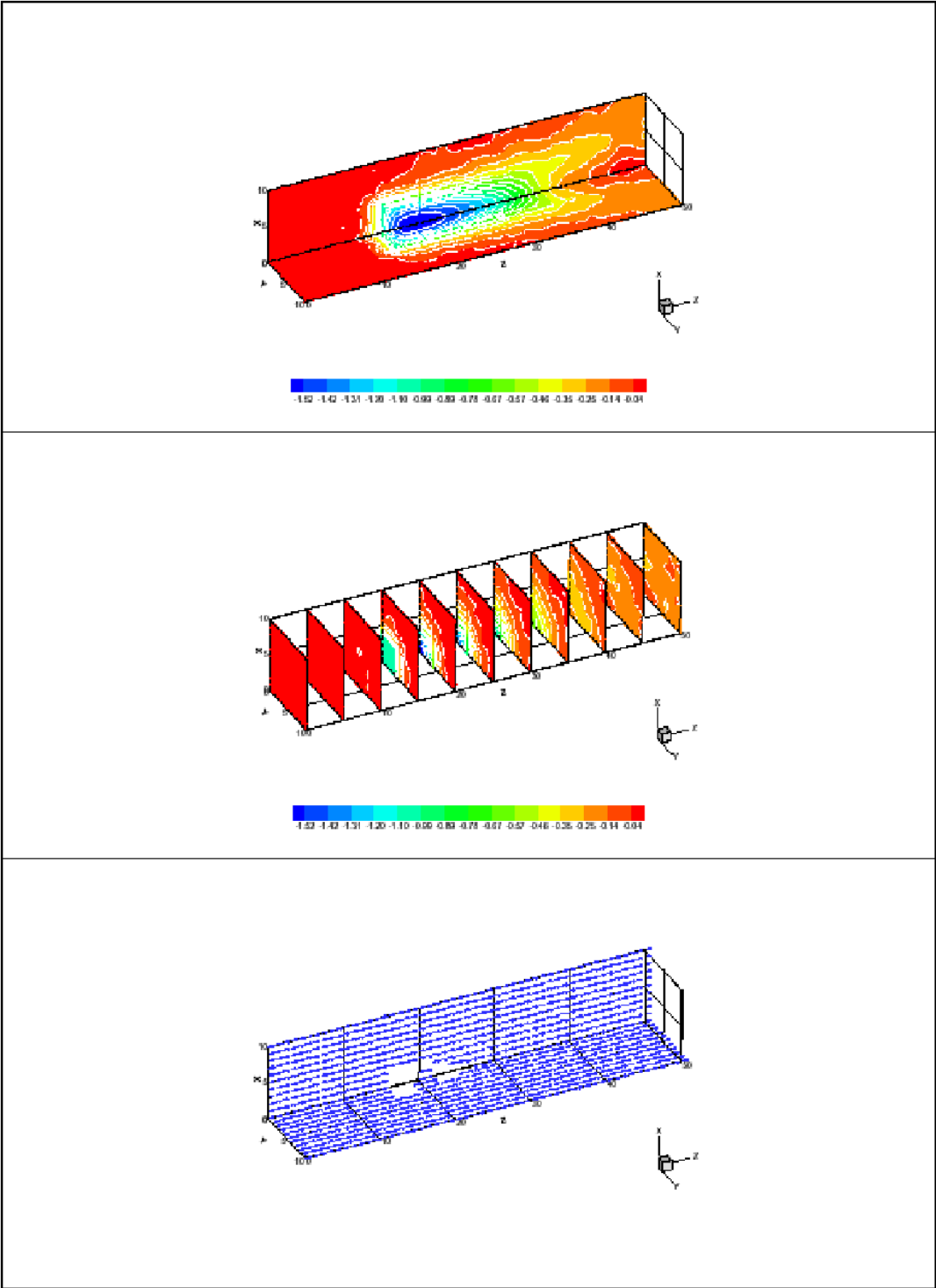
**Figure 4. Parametric Case 1. (Potential Isosurfaces. Potential values are normalized by T_e.
Sail potential: 0.25 T_e)**
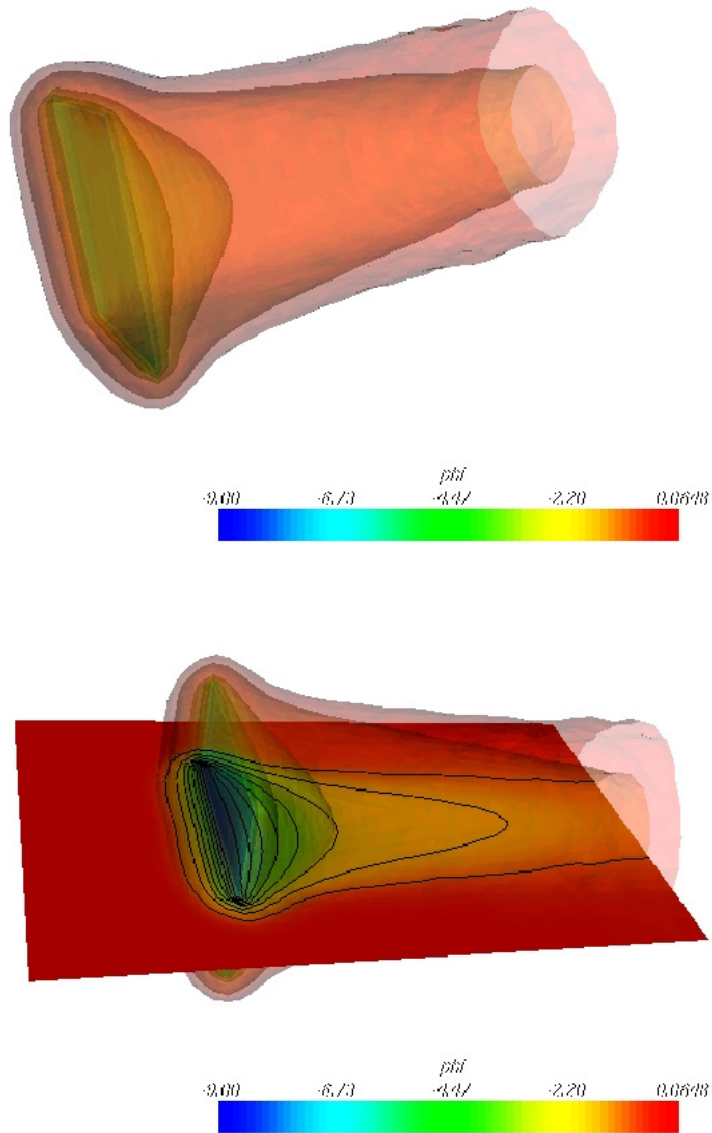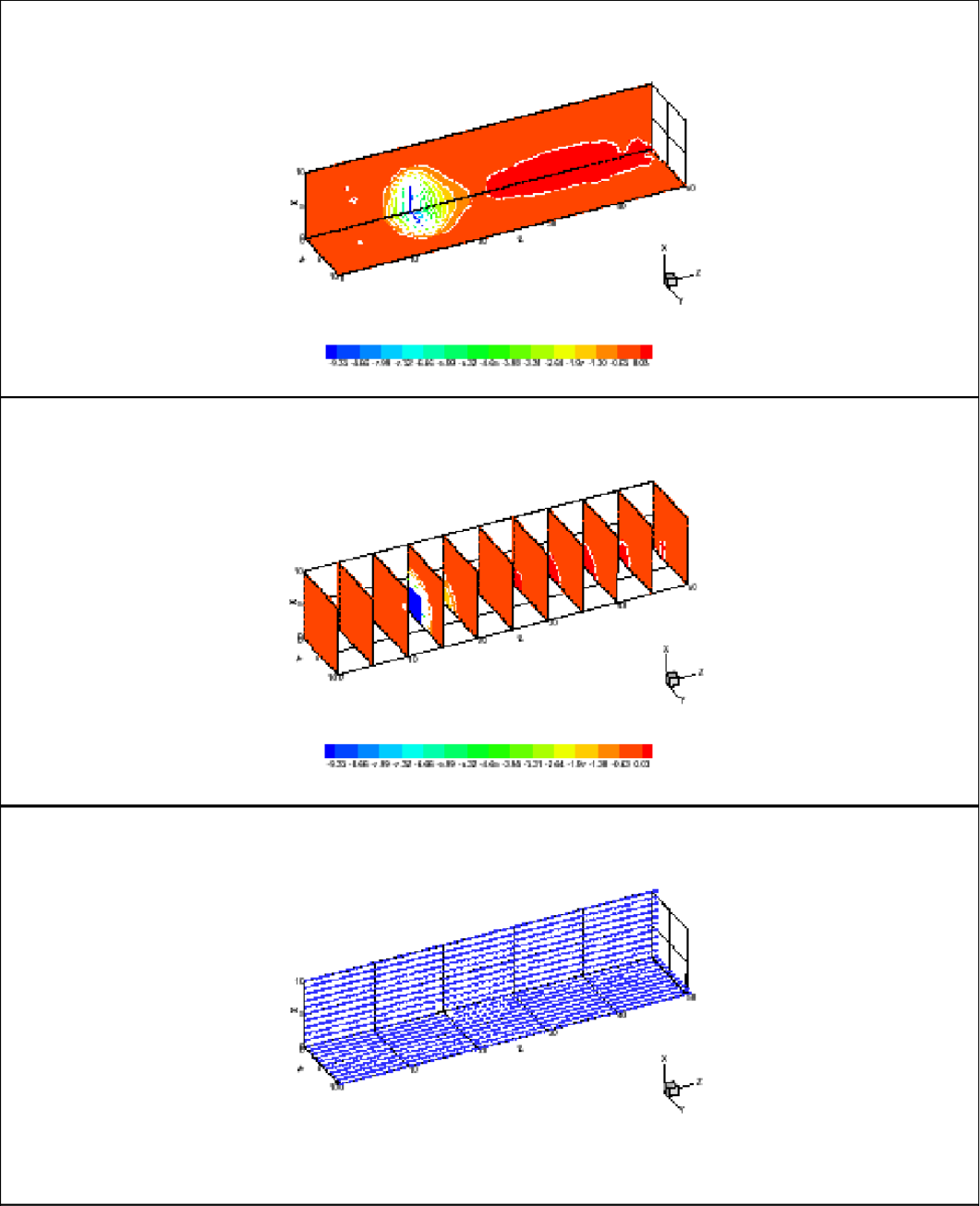
Figure 5. Parametric Case 2 (Potential Isosurfaces. Potential values are normalized by T_e. Sail potential: -2.25 T_e)
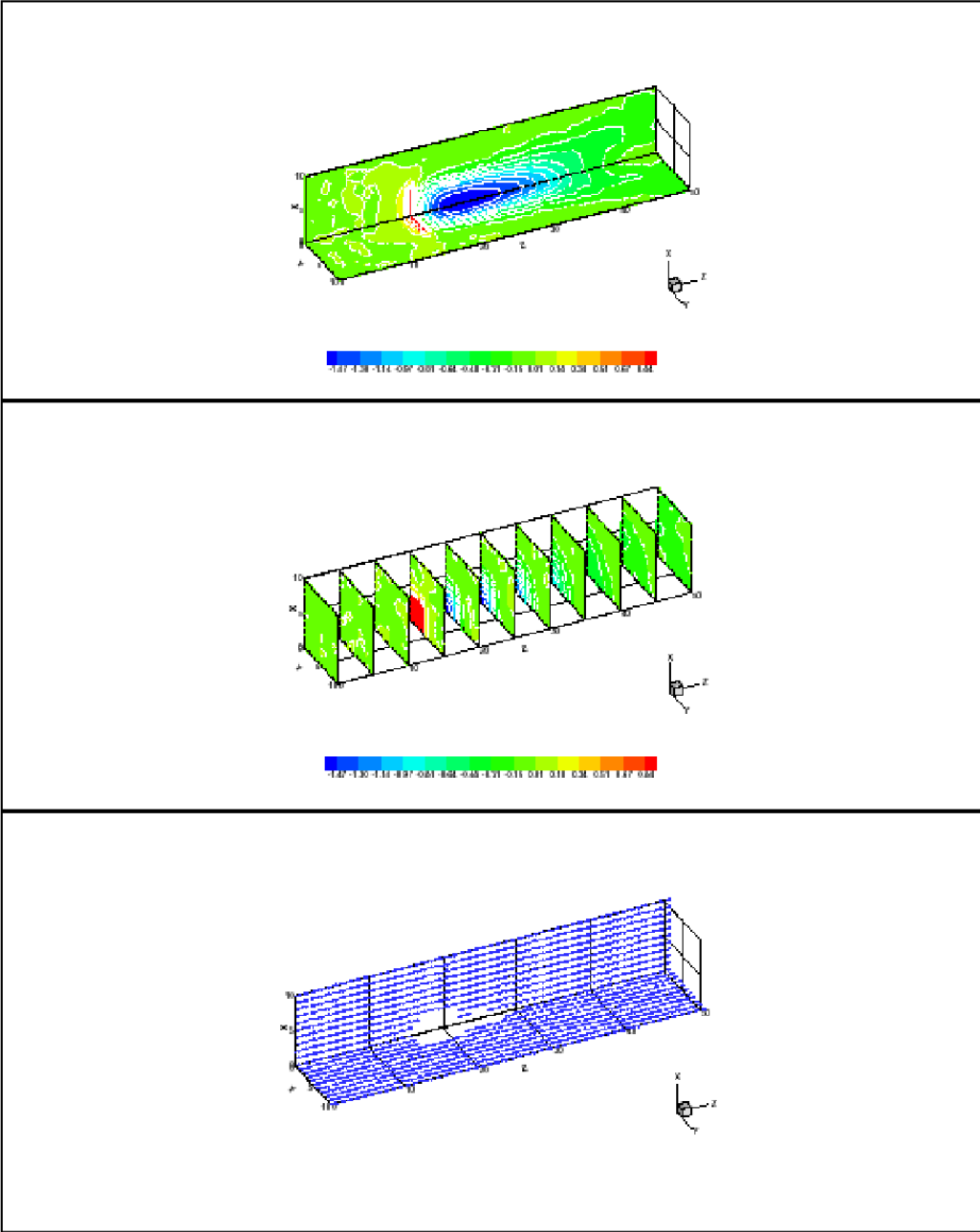
Figure 6. Parametric Case 3 (Potential contours and ion velocity vectors. Potential values are normalized by T_e. Sail potential: 1 T_e)

Figure 7. Parametric Case 4 (Potential contours and ion velocity vectors. Potential values are normalized by T_e. Sail potential: -1 T_e)

Figure 8. Parametric Case 5 (Potential contours and ion velocity vectors. Potential values are normalized by T_e. Sail potential : -10 T_e).

References

1. Garrett, H.B., "The Charging of Spacecraft Surfaces", <u>Rev. Geophys, 19</u>, No. 4, 577-616, 1981.

2. Wang, J., and D.E. Hastings, Ionospheric plasma flow over large high voltage space platforms I: Ion-plasma time scale interactions on a plate at zero angle of attack, Phys. Fluids B, 4(6), 1597-1614, 1992a.

3. Wang, J., and D.E. Hastings, Ionospheric plasma flow over large high voltage space platforms II: The formation and structure of the plasma wake, Phys. Fluids B, 4(6), 1615-1629, 1992b.

4. Wang, J., P. Leung, H. Garrett, and P. Murphy, Multibody-Plasma Interactions: Charging in the Wake, J. Spacecraft, 31 (5, September-October), 889-894, 1994.

5. Wang, J., D. Brinza, and M. Young, Three-Dimensional Particle Simulations of Ion Propulsion Plasma Environment for Deep Space 1, 31 (3, May-June), 433-440, 2001.

HIGH VOLTAGE SOLAR ARRAY FOR 400V OPERATION IN LEO PLASMA ENVIRONMENT

Satoshi Hosoda
Kyushu Institute of Technology
1-1 Sensui Kitakyushu, Japan 804-855
Phone: +81-93-884-3228
Fax: +81-93-884-3228
E-mail: hosoda@ele.kyutech.ac.jp

Teppei Okumura
Mengu Cho
Kyushu Institute of Technology, Japan

Kazuhiro Toyoda
Chiba University, Japan

Abstract

To realize a MW-class space platform, the power must be delivered at least 400 volts. In order to realize 400 volts operation in LEO, arcing caused by interaction between the spacecraft and the surrounding LEO plasma must be overcome. The purpose of the present paper is to report on the results of laboratory experiment carried out to develop solar array capable of generating electricity at 400V in LEO plasma environment. We tested various types of solar array designs. We biased solar array coupon panels negatively inside a vacuum chamber and measured the arc inception rate for each design. The arc sites were also located to identify the weakness of each design. These data are compared to the characteristics of conventional solar array for 100V bus satellite.

We confirmed that covering array strings by transparent film and by large coverglass is promising. The advanced coverglass coupon is most realistic design

Introduction

The use of high power in future space missions calls for high voltage power generation and transmission to minimize the energy loss during power transmission and the cable mass. In order to promote industrial use of Low Earth Orbit (LEO), such as manufacturing, sightseeing, or power generation, the power of a large LEO platform after the International Space Station (ISS) will soon reach the level of MW. In principle, the transmission voltage scales to the square root of the power to be delivered. Therefore, in order to realize a MW-class space platform, the power must be delivered at 400 volts, at least. In order to realize 400 volts operation in LEO, arcing caused by interaction between the spacecraft and the surrounding LEO plasma must overcome. The development of 400V solar array benefits not only a large space platform but also a satellite with a hall thruster, because the voltage is high enough to directly drive the electric propulsion system without raising the voltage via a DC/DC converter [2]. When a solar array generates

electricity in LEO, most of the voltage becomes negative with respect to the surrounding plasma due to mass difference between ions and charge it positively. Then the electric field near triple junction, where interconnector (conductor), adhesive (dielectric) and vacuum meet together is enhanced and an arc occurs [1]. There have been numerous studies on arcing on high voltage solar array in LEO condition. It is now known that an arc occurs once an array has a negative potential as low as –100V with respect to plasma. An arc on solar array surface is usually a pulse of current whose energy is supplied by the electrostatic energy stored on the coverglass surface due to charging via positive ions. Such an arc is often called trigger arc or primary ESD (electrostatic discharge). Repeated arcs lead to surface degradation and electromagnetic interference. Destruction of solar array cell PN junction due to the intense arc current is another concern. Moreover, a single arc might shorten momentary the array circuit and the current flows for a much longer time than a trigger arc by recalled secondary arc. A secondary arc might lead to permanent short-circuit in the array circuit and the arc current keeps flowing until thermal breakdown of insulative layer occurs. Such an arc is called sustained arc and believed to be the cause of the failure of Tempo-2 [4].

The purpose of the present paper is to report the results of laboratory experiment carried out to develop solar array capable of generating electricity at 400V in LEO plasma environment. The development effort is carried out in the two directions; (1) Suppress the inception of arcing completely (2) Minimize the damage caused by each arc. In this paper, we focus on the first items. We tested various types of solar array designs. We biased solar array coupon panels negatively inside a vacuum chamber and measured the arc inception rate for each design. The arc sites were also located to identify the weakness of each design. These data are compared to the characteristics of conventional solar array for 100V bus satellite.

Test Coupons

In the experiments we use various types of solar cell array coupon. Figure 1 shows a picture of base coupon. The base coupon is based on the standard design for a 100V bus satellite and serves as the reference for all the coupons with mitigation techniques. The coupon is made of $7cm * 3.5cm$ Si cell with IBF (integrated bypass function). Four cells are connected in series and three strings are placed in parallel. In order to distinguish each string, the strings are named as R, B and G strings as shown in Fig. 1. Between the strings, RTV-Si rubber is grouted to prevent short-circuit between the adjacent strings. The cells are mounted on the polyimide sheet on top of the aluminum honeycomb / CFRP substrate.

All the new coupons were designed following concepts:

1. Prevent charging the coverglass from ambient ions
2. Prevent interacting between electrons emitted from triple junction and ambient plasmas

Considering these concepts and the results of previous tests, we designed four new coupons. The schematic drawing of coupons tested in this study are shown in Fig. 2 ~ Fig. 5. These coupons are designed with the results of the previous test coupons [6]. There are two types of coupons using large coverglass and using the Teflon film.

Figure 2 shows the advanced film coupon. This coupon has a transparent Teflon film covering over all the strings. The Teflon film made of ETFE (Ethylene-Tetra Fluoro Ethylene copolymer). It has a transmittance of about 95% between $400 nm$ to $1 \mu m$ wavelength. ETFE has the characteristic of radiation resistance. Because it is hard to adhere the film to substrate, the film is attached by covering the front and back sides by adhesive at edges. To reduce gaps between the film and substrate due to the cables as low as possible, doubled size of film and substrate are utilized. All the bus bars are coated by RTV-Si rubber. Figure 3 shows the advanced film strip coupon. In this coupon, cells are covered only the cell edges by Teflon film strip concerning degradation of film transmittance. At the previous film strip coupon, many arcs occurred through small gaps around the adhesive. Therefore, RTV-Si rubber is grouted between all inter cells and bus bars. Figure 4 shows the large coverglass coupon. A large coverglass is adhered and covers over each cells, so that emitted electrons can't diffuse to ambient plasma. The bus bars and the outer cell edges are covered by the Teflon film strip. No RTV-Si rubber is utilized. Figure 5 shows the roof coverglass coupon. This coupon is similar to the large coverglass coupon. The large coverglass is adhered and supported by one cell which located near its center, and it overhang to other cells. RTV-Si rubber is grouted between all inter cells and bus bars.

Experimental Apparatus

Figure 6 shows a schematic of experimental set-up. The vacuum chamber is $1 m$ in length and $1.2 m$ in diameter. The chamber can be pumped to a pressure of as low as $10^{-6} Torr$. In order to simulate the LEO plasma environment, an ECR plasma source generates Xenon plasma with a density of $2 * 10^{12} m^{-3}$ at $3 \sim 7 eV$. The plasma source operates at a flow rate of $0.2 sccm$ and the chamber pressure during the operation is $8 \sim 9 * 10^{-5} Torr$. In order to keep the coupon temperature constant, halogen IR lamps was utilized. The chamber has also equipped with a metal-halide lamp to simulate the sum light. Using the lamp, we can monitor the cell electrical output without opening the chamber door. During the experiment, a negative bias voltage of $-100 V \sim -800 V$ is applied to each coupon. Each bias voltage is applied for 90 minutes considering the orbital period in LEO. The bias voltage is raised from a lower value to a higher (more negative) value. In Fig. 7, we show a schematic picture of external circuit connected to an array coupon. The strings are biased to a negative potential via a DC power supply through a limiting resistance of $100 k\Omega$. In order to simulate the arc current supplied by coverglass on the solar array panel as a capacitance [8], we connect an external circuit. The external circuit consists of a capacitance, inductance and resistance. We have attached a capacitance, $5 \mu F$, and an inductance, $270 \mu H$, and a resistance, 5Ω during the bias voltage from $-100 V$ to $-400 V$. In case of $-500 V \sim -800 V$ test, we have unavoidably changed the capacitance to $20 nF$ and removed the inductance and resistance due to current limitation of circuit.

The data recorded are the following:

- Arc position
- Arc current waveform
- Fluctuation of the background plasma condition
- Increase of background pressure

We have developed an experimental system that can record all the arc events. A video camera takes the picture of the array coupon during the experiment. The video image is directly recorded via a computer. We have developed a computer program to decompose the video stream into frames, compare each frame, detect the optical flash associated with arcs, record the coordinate of the arc flash and the time of arcing. Using this system, we can identify the position of every arc immediately. We have also developed a high-speed data acquisition system which can acquire 4 channels of current waveform data in 33ms and automatically analyze the waveform data to calculate the peak value and electrical charge flown. The data acquisition speed is fast enough to record all the arc current waveforms. Using the two systems, we can easily know when, where, and what arc occurred on a coupon panel.

Test Results

Figure 8 shows the arc positions observed on the base coupon. All the arc position is plotted on the figure for the bias voltages of –100 ~ -400V. The location of arcing was roughly classified on bus bars, interconnectors and cell edges. Figure 9 shows the relation between bias voltage and the arc number on each location in 90 minutes. The number of arc, especially on the cell edge increased with increasing the bias voltage. In case of –400V, we observed 164 arcs on the strings. Among the arc number of 164, 63 occurred on bus bars, 33 occurred on interconnectors, and 68 occurred on cell edges which not coated by RTV-Si rubber. To estimate cell degradation due to arcs, we measured the electrical output of R-string (see Fig. 10). After the test, the maximum output power dropped to about 70% of the initial value, which means two cells were damaged by arcing [6].

At first, we report on the results of the coupons used the improved cover film. In this experiment, the advanced film coupon has never been suffered arcing during the bias voltage of –800V. Comparing the result of the previous film coupon which suffered 14 arcs at –800V[6], the performance of arc mitigation has been greatly improved. The reason of this improvement is due to reduce the gap between the film and substrate. This coupon is most realistic design from a viewpoint of manufacturing and cost. Figure 11 shows the result of the advanced film strip coupon. The figure shows the relation between bias voltage and arc number on each location. This coupon suffered only 4 arcs at –800V. All the arcs occurred on the bus bar and interconnectors. The electrical output of cells hardly changed. Cell edges that covered by RTV-Si rubber did not experience arcing. As shown in the previous paper [6], the film strip coupon and the interconnector film rap suffered so many arcs in spite of –400V of bias voltage. With respect to electrical output, the maximum power dropped by 20~30%. Therefore, extremely improvement for the arc mitigation using film strip was confirmed.

Next, we report on the results of the coupons which improved the coverglass. Figure 12 shows the result of the large cover glass coupon. This coupon suffered several hundred of arcs at –700 ~ -800V as shown in Fig. 12. However, the arc that was occurred on the outer cell edges came up to as much as 10% of all the arcs. Furthermore, no arc occurred on interconnector and cell edge covered by large coverglass. With respect to the outer cell edges where arcs occurred, there are some gaps between the film and the substrate due to the power cables. Ions probably entered through these gaps and charged the dielectric along the edge. Figure 13 shows the result of the roof coverglass coupon. This coupon suffered about 20 arcs at –800V. Almost all

arcs occurred on so-called the stress-relief which is only expose from bas bar with RTV coating to plasma. No arc occurred on the cell edge. The results of arc number at each bias voltage for different coupons are shown in Fig. 14.

The results of cell degradation in each coupon are shown in table 1. The power drops was estimated as shown in Fig. 10. Measured values of power drop contained about 4% of error so that the no degradation of cell electrical output was confirmed almost all the coupons though some coupons suffered many arcs. As the above experiment results show, we obtained satisfactory results for arc mitigation.

Conclusion

(1) Solar array coupons with arc mitigation function have been tested in LEO plasma environment
(2) Covering array strings by transparent film is promising. The advanced film coupon is most realistic design.
(3) Covering array strings by large coverglass is promising

Acknowledgement

Table 1.   Degradations of cell electrical output in each coupon

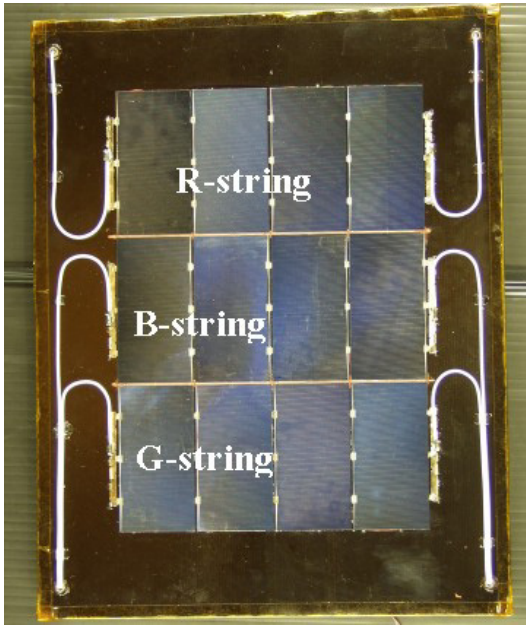| Coupon	Base coupon	Large coverglass coupon	Roof coverglass coupon	Advanced film coupon	Advanced film strip coupon
Power drop	30%	2%	3%	<1%	1%
Total arc Number	259	312	66	0	13
Total arc number on cell edge	82	26	0	0	0

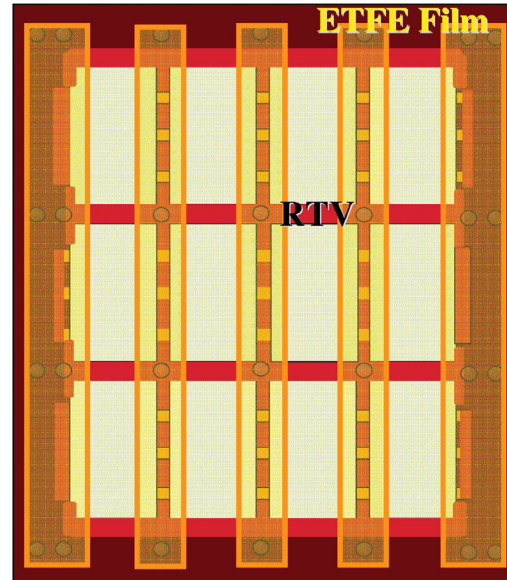**Figure 1.   Picture of the base coupon.**

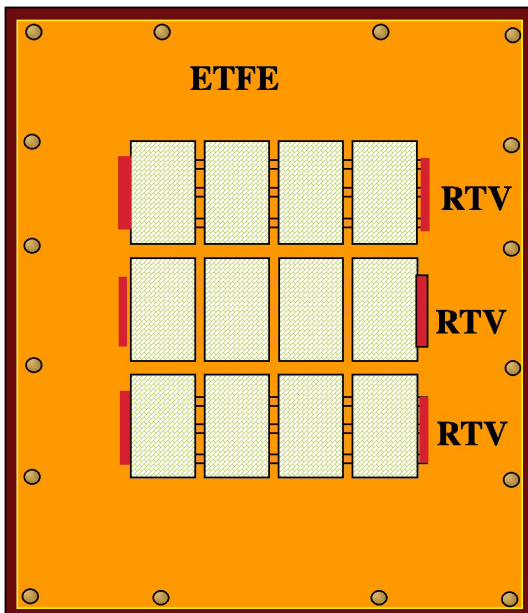**Figure 3.   Schematic drawing of the advanced film strip coupons.**

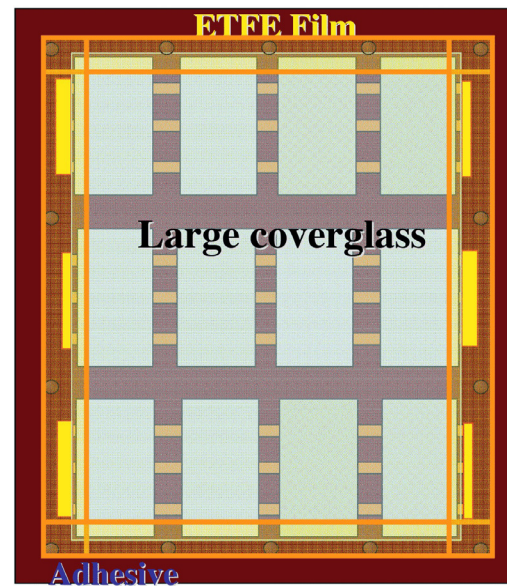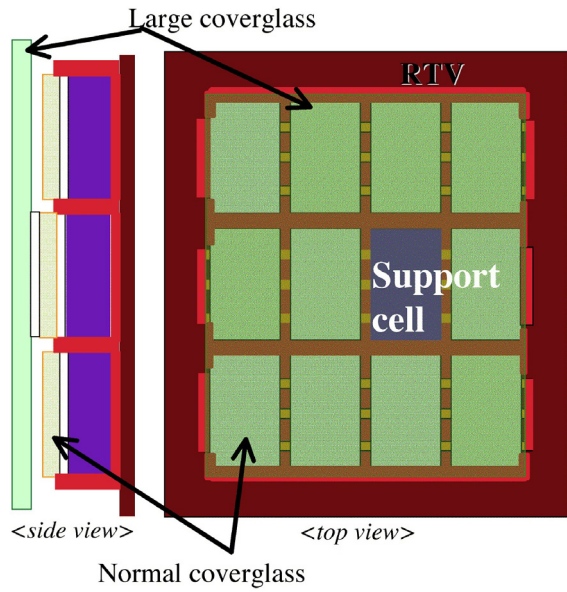**Figure 2.   Schematic drawing of the advanced film coupons.**
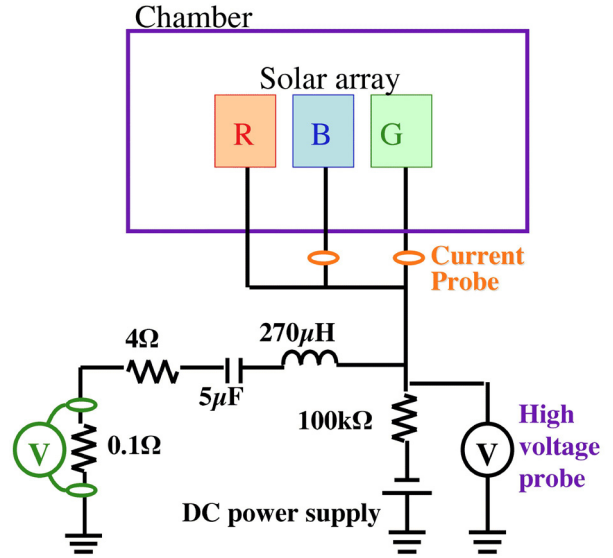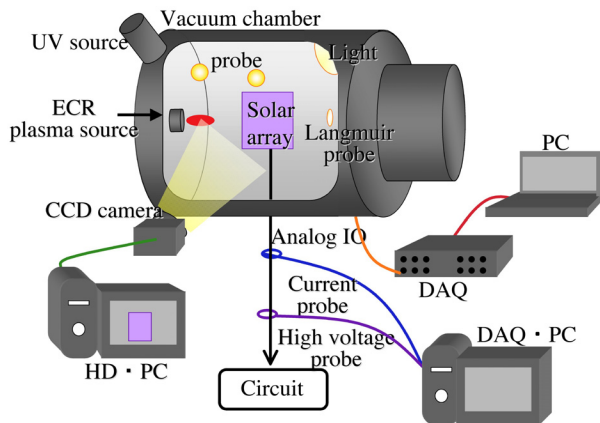

Figure 4.   Schematic drawing of the large coverglass coupons.

Figure 5. Schematic drawing of the roof coverglass coupons.

Figure 7. Schematic illustration of experimental circuit from –100V to –400V

Figure 6. Schematic illustration of experimental apparatus.
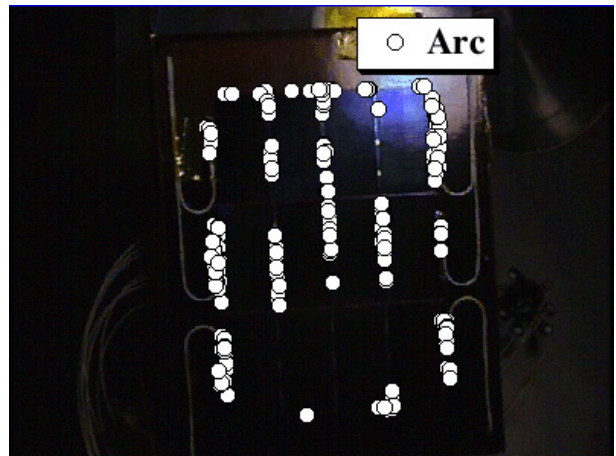
Figure 8. All the arc positions observed on the base coupon from –100V to –400V
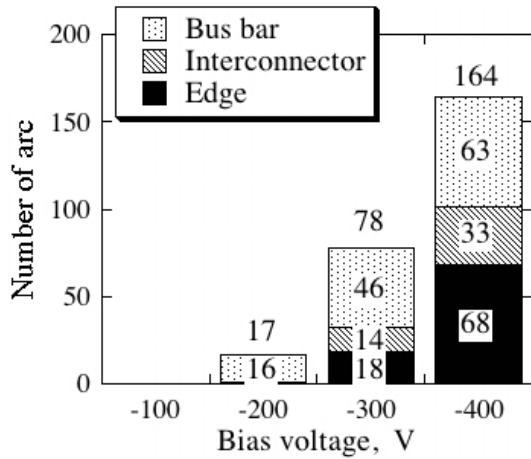
Figure 9. The arc positions observed on the base coupon

Figure 11. The arc positions observed on the advanced film strip coupon.

Figure 10. Degradation of cell electrical output. Result of R-string of a base coupon.

Figure 12. The arc positions observed on the large coverglass coupon.

Figure 13. The arc positions observed on the roof coverglass coupon.
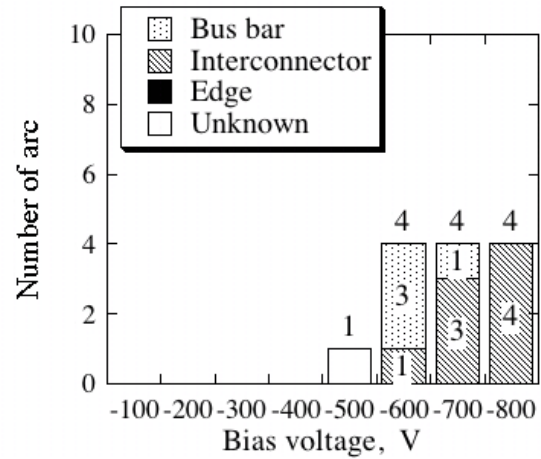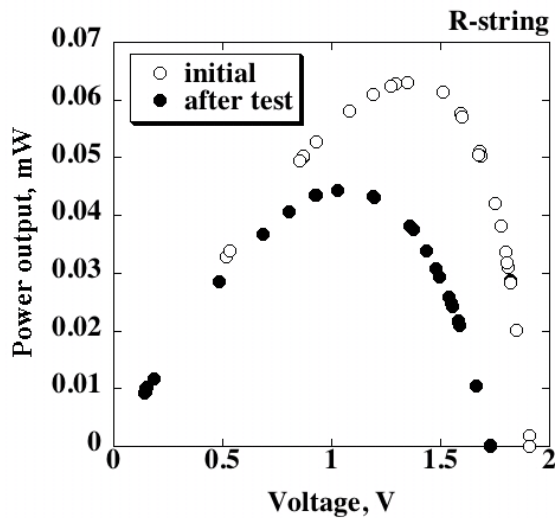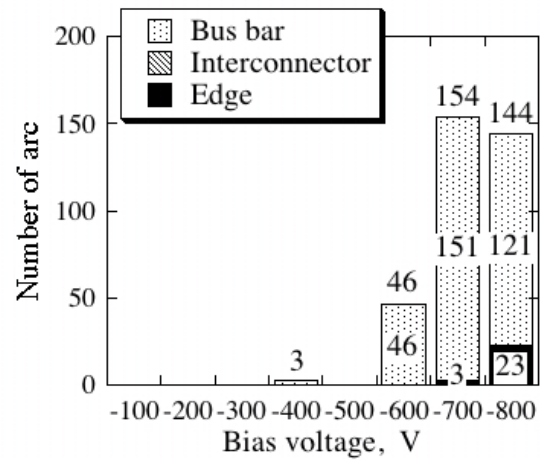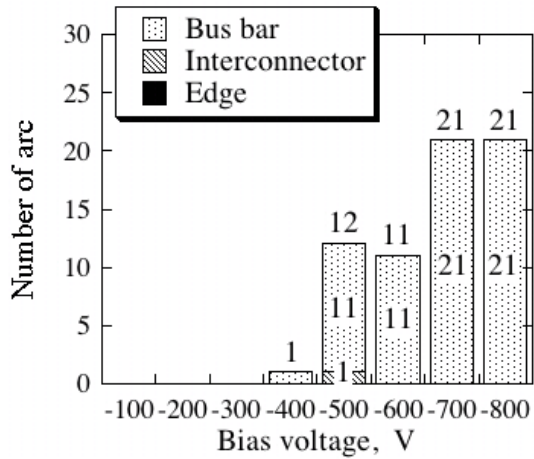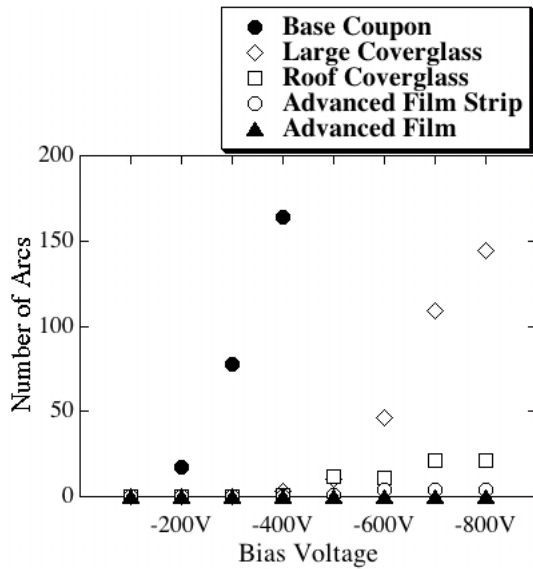

Figure 14. Number of arcs in 90 minutes at each bias voltage for different coupons.

References

1. Hastings, D. E., Cho, M. and Kuninaka, H. "The Arcing Rate for a High Voltage Solar Array: Theory, Experiment and Predictions,", J. Spacecraft and Rockets, 29, 1992, pp. 538-554.

2. Jongeward, G. A., Katz, I., Carruth, M. R., Raph, E. L., King, D. Q. and T. Peterson, "High Voltage Solar Arrays for a Direct Drive Hall Effect Propulsion System", Proceedings of 27th IEPC, IEPC-01-327.

3. Hastings,D.E., Garrett,H., "Spacecraft-Environmental Interactions", Cambridge Univ.Press, New York, 1996.

4. Katz, I., Davis, V.A; and Snyder, D.B, "Mechanism for Spacecraft Charging Initiated Destruction of Solar Arrays in GEO", AIAA paper 98-1002, January 1998.

5. Ferguson, D. C., Snyder, D. B., Vayner, B. V., and Galforo, J. T., "Array Arcing in Orbit from LEO to GEO", AIAA paper 98-1002, January 1999.

6. Cho, M., Saionji, A., Toyoda, K. and Hikita, M., "High Voltage Solar Array for 400V Satellite Bus Voltage: Preliminary Test Results", AIAA 2003-0683, 41st Aerospace Science Meeting, 6-9 January, Reno, USA, 2003.

7. Cho, M., Shiraishi, K., Toyoda, K. and Hikita, M., "Laboratory experiments on mitigation against arcing on high voltage solar array in simulated LEO plasma environment", AIAA02-0629, 40th Aerospace Sci. Meeting, 2002.

8. Cho, M., Ramasamy, R., Hikita, M., Tanaka, K., Sasaki, S., "Plasma Response to Arcing in Ionospheric Plasma Environment: Laboratory Experiment", J. Spacecraft and Rockets, May-June, pp.392-399, 2002.

HIGH-LEVEL SPACECRAFT CHARGING AT GEOSYNCHRONOUS ALTITUDES: A STATISTICAL STUDY

Shu T. Lai
Space Vehicles Directorate
Air Force Research Laboratory
Hanscom AFB, MA 01731-3010

Maurice Tautz
Radex, Inc.

Abstract

We present the results of a statistical study on high-level spacecraft charging at geosynchronous altitudes. Below the critical temperature T* for a surface material, no spacecraft charging occurs. The spacecraft charging potential data are obtained from the ion line of the ion energy spectrum. If the ion line can not be clearly identified, the data point is flagged. We do not use flagged data in our analysis. Since T* depends on the surface material and since each satellite has its own surface material or materials, each satellite is expected to have its own critical temperature. The coordinated space environmental parameter data of the Los Alamos National Laboratory (LANL) geosynchronous satellites include spacecraft charging data measured on several geosynchronous satellites in eclipses and in sunlight over years. We have obtained statistical results of T* for each satellite studied and found that, beyond T*, the high-level spacecraft potential increases almost linearly with the ambient electron temperature. Amazingly, the critical temperature in sunlight remains the same as in eclipse, agreeing with the monopole-dipole differential charging model. This work offers a useful method not only for predicting the onset of spacecraft charging in eclipse and in sunlight but also for predicting high-level spacecraft charging potential with reasonable accuracy at any given ambient electron temperature in the geosynchronous environment.

Introduction

Spacecraft charging can detrimentally affect electrical operations on space systems. Most communication and surveillance spacecraft are at geosynchronous altitudes and many more such spacecraft will be deployed in the new millennium. The plasma density in the geosynchronous environment varies from over 100 cm^{-3} to 0.1 cm^{-3} and the energy varies from a few eV to tens of keV depending on local time and geomagnetic conditions. Spacecraft surface charging occurs at high plasma energies. While surface material properties and spacecraft geometry are defined by spacecraft design, spacecraft charging is controlled by the dynamic plasma condition which varies in time. It is important to identify the most reliable space environment parameters for predicting spacecraft charging.

We have identified the most reliable space environment parameter for predicting spacecraft charging is the plasma electron temperature. Historically, *Rubin et al.* [1980], first reported, though with a few data points only, the linear dependence of spacecraft potential as a function of the ambient electron temperature. Their graph of spacecraft potential versus electron

temperature showed an intercept at a finite temperature. *Laframboise et al.* [1982], *Lai et al.* [1982, 1983], and *Prokopenko and Laframboise* [1983] put forth the theory of the critical temperature. Below the critical temperature, spacecraft charging does not occur; above it, spacecraft charging occurs. The theory is now included in standard textbooks on spacecraft-plasma interactions [*Hastings and Garrett*, 1996].

For many years, there was no systematic observation of spacecraft charging together with the coordinated space environment parameters and therefore no way to validate the theory. Recently, the spacecraft charging data obtained on the Los Alamos National Laboratory (LANL) geosynchronous satellites LANL-89-046, LANL-90-95, LANL-91-80, LANL-94-084 and LANL-97A have become available. A recent study [*Lai and Della-Rose*, 2001] using four weeks of spacecraft charging data obtained on LANL-94-084 has uncovered new evidence for the existence of critical temperature of the space plasma electrons for a given spacecraft surface material. Below the critical temperature, little spacecraft charging occurs, while above the critical temperature, the spacecraft potential increases almost linearly. The evidence that a critical temperature exists is abundant and was seen in every charging event on the LANL satellite.

In order to establish the critical temperature theory beyond a doubt, it is necessary to study more data for validation. We report on our results in this paper.

Theory

In the geosynchronous environment, the ambient electron flux exceeds that of the ambient ions by two orders of magnitude, because the electrons are lighter and faster. Measurements on the LANL-94-084 satellite confirmed the flux difference [*Lai and Della-Rose*, 2001].

Suppose a satellite is initially uncharged and the ambient electron temperature is increasing. Eventually, the electron flux increases to a level for charging to occur. At the threshold, the current balance is between the incoming ambient electrons and the outgoing secondary and backscattered electrons.

$$\int_0^\infty dE E f(E) = \int_0^\infty dE E f(E)\left[\delta(E) + \eta(E)\right] \qquad (1)$$

*(E) and 0(E) are the coefficients of secondary electron emission and backscattered electron emission respectively. For a Maxwellian space plasma, the distribution function $f(E)$ is of the form:

$$f(E) = n\left(m/2\pi kT\right)^{1/2}\exp\left(-E/kT\right) \qquad (2)$$

Substituting eq(2) into eq(1), one readily obtains two theorems, (I) and (II): -

- (I) Since the density n is multiplicative, it cancels out on both sides. Therefore, the threshold condition is independent of the plasma density n.
- (II) The solution T* to eq(1) is the critical temperature for the onset of spacecraft charging.

To solve eq(1), one needs to input the functions *(E) and 0(E). If the ambient electrons are coming in at various angles 2, one needs to use angle dependent functions of *(E,2) and 0(E,2).

Including the angles, the algebra becomes more complicated. The results are given in Table 1.

Table 1. Critical Temperature (keV)

MATERIAL	ISOTROPIC	NORMAL
Mg	0.4	---
Al	0.6	---
Kapton	0.8	0.5
Al Oxide	2.0	1.2
Teflon ©	2.1	1.4
Cu-Be	2.1	1.4
Glass	2.2	1.4
SiO$_2$	2.6	1.7
Silver	2.7	1.2
Mg Oxide	3.6	2.5
Indium Oxide	3.6	2.0
Gold	4.9	2.9
Cu-Be (Activated)	5.3	3.7
MgF$_2$	10.9	7.8

Spacecraft Potential

For the onset of spacecraft charging, we have neglected the ions because the ion current is about two orders of magnitude smaller than that of the electrons. However, to determine the resulting spacecraft equilibrium (negative) potential, one needs to include the ions that are attracted. It is often a good approximation to describe the electron repulsion by means of the Boltzmann factor (the exponential term) and the ion attraction by means of the factor of Mott-Smith and Langmuir (the term in parenthesis following the ion current $I_i(0)$) in the following current-balance equation:

$$\Sigma I(\phi) = I_i(\phi) - I_e(\phi) = I_i(0)\left(1 - \frac{q_i\phi}{kT_i}\right) - I_e(0)\exp\left(-\frac{q_e\phi}{kT_e}\right) = 0 \quad (3)$$

where $I_e(N)$ and $I_i(N)$ are the currents of the repelled and attracted species, respectively, collected by the spacecraft at potential N. Including secondary and backscattered electrons, the electron current $I_e(N)$ in eq(3) is replaced by the net electron current , which is of the form:

$$I_e^{'}(\phi, T_S) = I_e(\phi)\left[1 - <\delta + \eta>\right] \quad (4)$$

where

$$<\delta + \eta> = \frac{\int_0^\infty dE E f(E, T_e)[\delta(E) + \eta(E)]}{\int_0^\infty dE E f(E, T_e)} \quad (5)$$

Using eq(5), the current-balance equation, eq(3), becomes

$$I_i(0)\left(1 - \frac{e_i\phi}{kT_i}\right) - I_e(0)[1 - <\delta + \eta>]\exp\left(-\frac{e_e\phi}{kT_e}\right) = 0 \quad (6)$$

where the subscripts e and i label electrons and ions, $e_e = -e$ and $e_i = e$, and e is the elementary charge. For spacecraft potential lower than the ambient ion temperature, that is $eN << kT_i$,

which is usually valid initially, one expands eq(3.6) in a Taylor series of eN / kT_i and obtains

$$e\phi = \frac{T_i / T_e}{T_i / T_e + 1} kT_e \log \frac{I_i(0)}{I_e(0)} + ... \quad (7)$$

which gives a straight line of eN as a function of kT. For higher values of eN, the quadratic term needs to be included.

Observations of Spacecraft Charging in Eclipse

The ion to electron temperature ratio T_i / T_e obtained on LANL1994-084 is mostly between 1 and 3 approximately. If the ratio is almost a constant in eq(7), the potential N plotted as a function of kT_e would be almost a straight line. It is not really a straight line, because the log term is also a function of T_e.

The LANL spacecraft potential data are deduced from the shift of the ion distribution $f_i(E)$. Occasionally, the ion shift (ion line) is not clear. Instead of discarding those points which have unclear ion shifts, the LANL team deduced the spacecraft potential for those points in the following manner [*M.F. Thompsen*, personal communication., 2002]. They have observed an empirical curve of spacecraft potential plotted against electron temperature, although they have made no mention of critical temperature. They put the 'unclear' points on this empirical curve according to their electron temperature. Such data are flagged. We have examined the flagged data points in three different months of sample data [courtesy, *M.F. Thompsen*, 2002] and found that the flagged data are all on the sunlight charging curve and none on the eclipse charging curve. Therefore we conclude that the flagged data probably do not affect our eclipse charging study at all.
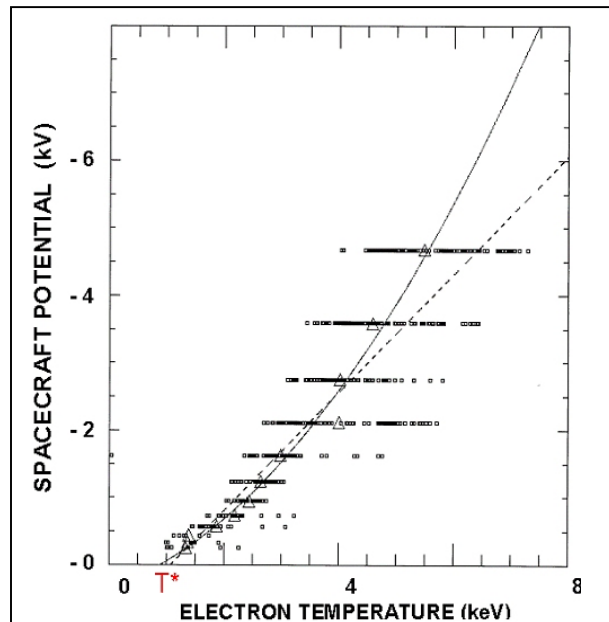

Figure 1   Spacecraft potential and electron temperature measured on LANL-1989-046 during the eclipse periods of Mar 13-28, 1993-2001.
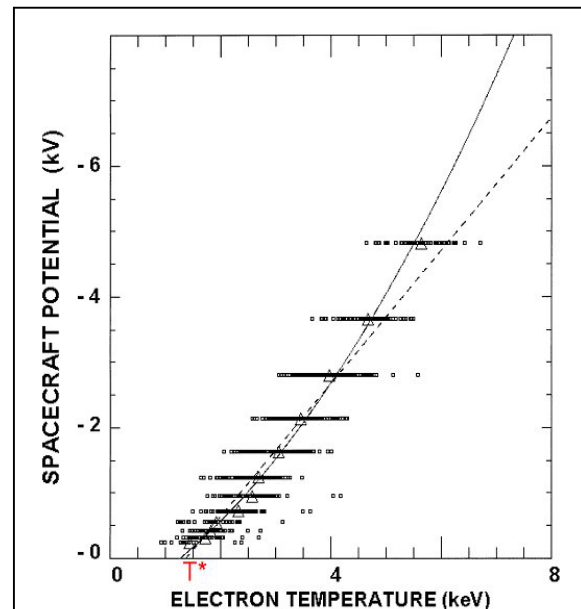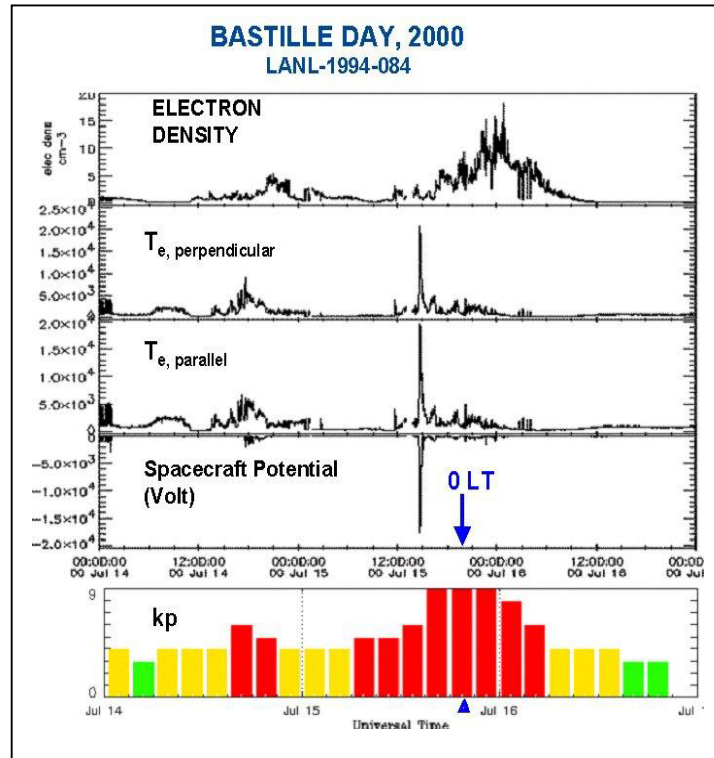

Figure 2   Spacecraft potential and electron temperature measured on LANL-90-095 during the eclipse periods of Mar 14-29, 1993-2001.

Figure 1 shows a plot of LANL 1989-046 spacecraft potential vs. electron temperature for the eclipse periods of Mar 13 to 28, 1993 to2001. Figure 2 shows a similar plot of LANL 1990-095 spacecraft charging and ambient electron temperature data taken in the eclipse periods of Mar 14 to 29, 1993 to 2001. We have also obtained similar results by using eclipse data for the LANL-1994-084, LANL 1991-80 and LANL-1997A satellites. Each of these results shows that (1) the trend of each plot is almost a straight line. (2) there exists an intercept T* (its value being 1.5 to 2 keV approximately), (3) a quadratic function would fit better than a straight line, (4) the values of T* are lower with quadratic fits, but are of the same order of magnitude.

Figure 3. The spacecraft potential mirrors with the electron temperature - not with the electron density or kp.

The most well known storm in the recent solar max was the Bastille Day storm of 2000. Figure 3 shows the magnetic index kp going up to the maximum possible level (k=9) during the storm. The parallel and perpendicular electron temperatures jumped to high values at the arrival of the solar disturbance. The electron density rose later but not simultaneously with the electron temperature. This offers a good opportunity to observe the spacecraft potential in response to these two space parameters, namely, electron temperature and electron density. Indeed, the data measured on LANL 1994-084 shows that the spacecraft potential mirrored the electron temperature but not with the electron density at all.   It had been previously assumed that electron flux and electron density were the principal factors.

Spacecraft Charging in Sunlight

Photoelectron emission from spacecraft surfaces often dominates over all other ambient currents.   Therefore, it seems impossible for spacecraft to charge to negative potentials in

sunlight. Yet, the LANL satellites often charge to hundreds or thousands of negative volts in sunlight. We are going to present that the LANL satellite charging data agree well with the monopole-dipole model.

In the following, we will present an important finding: "The level of spacecraft charging in sunlight is usually about 1/3 of that in eclipse". As a collorary, we have another important finding: "The onset of spacecraft charging occurs at the same critical temperature no matter the satellite is in clipse or in sunlight."

Photoelectron Current in Sunlight

Laboratory measurements show that typical spacecraft surface materials generate in space conditions photoemission currents of the order of $J_{ph} = 2 \times 10^{-9}$ A/cm^2 [*Stannard, et al.*, 1978]. For comparison, the average electron current density measured on the SCATHA (Spacecraft Charging at High Altitudes) satellite was $<J> = 0.115 \times 10^{-9}$ A/cm2 [*Purvis and Garrett*, 1984]. Thus, the photoemission current density J_{ph} exceeds the average ambient electron current J by a factor F = 20.

$$I_{ph} = 20 < J > \qquad (8)$$

If a spacecraft is charged to a negative potential in steady state, the potential must satisfy the current balance equation.   For example, current balance in the Mott-Smith and Langmuir model is of the form:

$$I_e(0)\exp\left(-q_e\phi / kT_e\right) - I_i(0)\left(1 - \frac{q_i\phi}{kT_i}\right) = I_{ph} \quad (9)$$

where the notations are as usual, $q_e = -e$, $q_i = e$, and   is negative.   If $I_{ph} > I_e(0)$, there is no solution for the above equation.   How, then, can spacecraft charging to negative potentials occur?

Monopole-Dipole Potential in Sunlight

Consider a negatively charged satellite with dielectric surfaces in sunlight. The shadowed side charges to a higher (negative) potential than the sunlit side. Taking the first two terms of an infinite series in Legendre function of a general potential distribution, one obtains a monopole-dipole potential distribution [*Besse and Rubin*, 1980]:

$$\phi(\theta, R) = K\left(\frac{1}{R} - \frac{A\cos\theta}{R^2}\right) \qquad (10)$$

where A is the dipole strength which is less than unity. The angle $2 = 0^o$ is the normal sunlight direction (Figure 4). We have conducted an explicit validation, for the first time, of the monopole-dipole distribution in sunlight charging.

For unit radii satellite, the radial distance $R=1$ at the satellite surface, and $K = N(90^o, 1)$ equals the monopole potential. The potential barrier is located at R_S, where the potential is the maximum for $2 = 0^o$.

$$\left[\frac{d\phi(0^o, R)}{dR}\right]_{R=R_S} = 0 \qquad (11)$$

which gives $R_S = 2A$. Therefore, $A > \frac{1}{2}$, otherwise the barrier is located inside the spacecraft.

The barrier height B is given by

$$B = \phi(0^o, R_S) - \phi(0^o, 1) = K\frac{(2A-1)^2}{4A} \qquad (12)$$

The fraction f of photoelectron flux (Figure 5) escaping through the potential barrier is given by

$$f = \frac{\int_B^\infty dEE\exp(-E/kT)}{\int_o^\infty dEE\exp(-E/kT)} = \left(\frac{B}{kT}+1\right)\exp\left(-\frac{E}{kT}\right) \qquad (13)$$

where the photoelectron distribution is Maxwellian and has a typical temperature T of 1.2 eV [*Whipple*, 1982]. Since the photoelectron temperature is low, very small barrier height will block most of the photoelectrons.
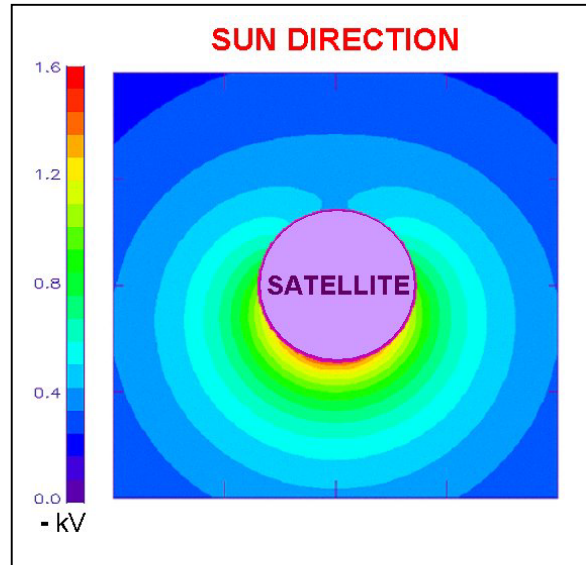
Figure 4. Typical potential contours in a monopole-dipole potential distribution. The contours wrap from the dark side to the sunlit side.
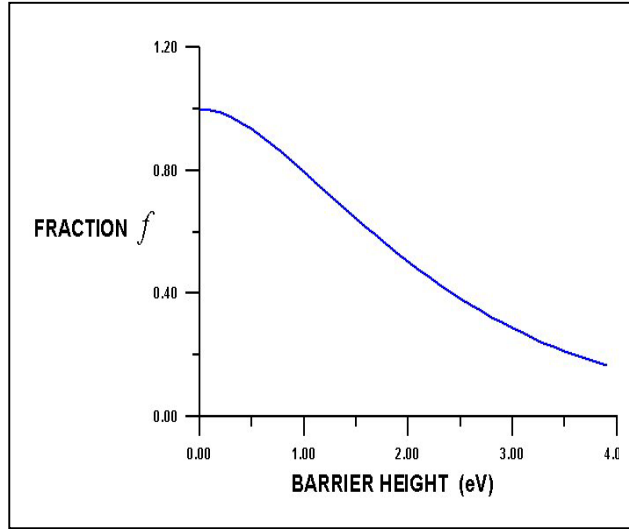
Figure 5. Fraction of photoelectron current escaping through the barrier. A small barrier height is sufficient to block most of the photoelectron current.

In particular, for high level charging, the ratio B/K of the barrier potential to the monopole potential is usually nearly zero. Substituting B/K ≈ 0 in eq(12) gives A ≈ ½. As a result, the ratio of the sunlit surface potential to that of the shaded surface is given by (Figure 6):

$$\frac{\phi(0^o,1)}{\phi(180^o,1)} = \frac{1-A}{1+A} = \frac{1-1/2}{1+1/2} = \frac{1}{3} \qquad (14)$$

Observations of Spacecraft Charging in Sunlight

We have analyzed several years of the Los Alamos National Laboratory (LANL) satellite charging data and obtained very useful statistical results on the behavior of charging in sunlight. The results agree surprisingly well with the monopole-dipole model.

Figure 7 presents a compilation of charging data obtained on the LANL 1991-80 Satellite for the period March 13-28, 1994-2001. The March period is chosen because of the following reason. The geosynchronous satellite, being in the equatorial plane, undergoes eclipse around midnight in March and September. Therefore, both eclipse charging and sunlight charging data are available for comparison during the March period. A statistical curve fit shows clearly that there are two trends in Figure 7. The ratio of the potentials in eclipse and in sunlight is approximately 1/3. For example, when the sunlight charging potential is -1 kV at electron temperature of about 4.4 kV, the eclipse charging potential at the same temperature is about -3 kV . This result is a strong evidence supporting the validity of the monopole-dipole model.
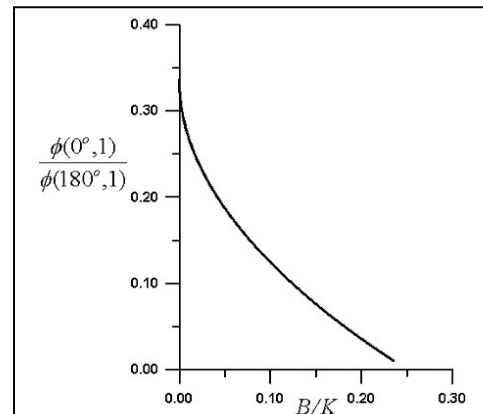
Figure 6. Ratio of potentials of sunlit and shadowed surfaces as a function of barrier potential.

Since 1/3 of a finite number is finite while 1/3 of zero is obviously zero, the onset of spacecraft charging occurs at the same critical temperature of the space plasma electrons. Below the critical temperature, there is no charging. Above it, the charging level increases with the temperature. This new and important finding is clearly seen in Figure 7.

To add more credence to the above findings, we present another statistical graph (Figure 8) showing the charging data of a different satellite, viz., LANL-1997A, during the periods September 14-28, 1997-2001. Again, the period September 14-28 is chosen because both eclipse charging and sunlight charging events are available for comparison. In Figure 8, the ratio of potentials in sunlight to that in eclipse is again approximately 1/3. For example, the sunlight charging potential is about -1 kV at the temperature of about 4.4 kV; that of the elipse charging at the same temperature is about -3 kV. The onsets of eclipse charging and sunlight charging occur at approximately the same value of critical temperature. Similar results have been obtained for the other LANL satellites. We conclude that these results strongly support the validity of the monopole-dipole model.

Figure 7.   Charging voltage in sunlight is 1/3 that in darkness.

Figure 8.   Charging voltage in sunlight is 1/3 that in darkness.
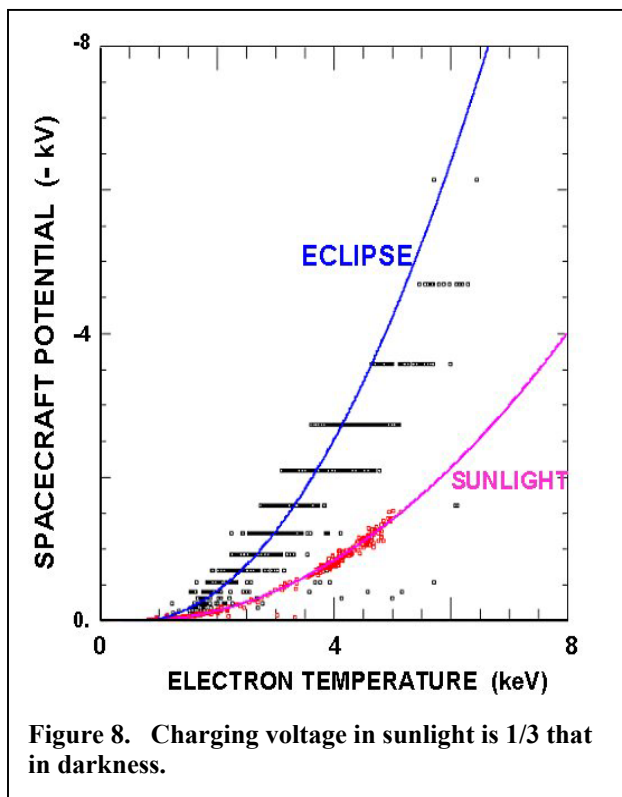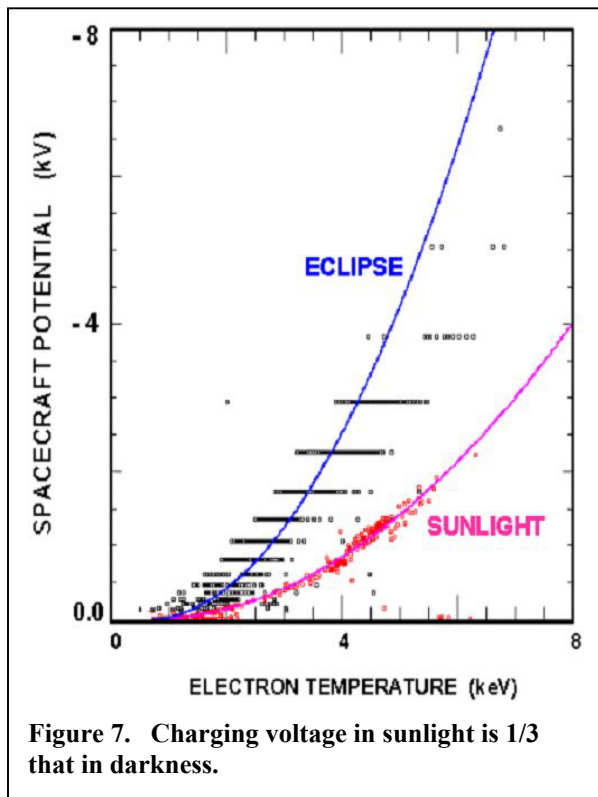
Summary and Discussion

The geosynchronous altitudes are the most important region for spacecraft charging. Most communication satellite are there, while the ambient plasma varies in temperature and density depending on the local time and space weather. A most important problem is to seek the most reliable space environment indicator of the onset of spacecraft charging. By studying the LANL geosynchronous satellite data, we have found that spacecraft charging depends strongly on the ambient plasma electron temperature, and not as much on the other space environment parameters such as electron density, ion temperature, ion density, and even high kp. The exact level of charging depends on the spacecraft geometry, configuration of surfaces, etc. The average potential is, however, almost a straight line as a function of temperature. The line deviates from being absolutely straight, because there is a quadratic term in the Taylor series of potential as a function of temperature and, furthermore, the plasma distribution may resemble a kappa distribution at high temperatures.

It has long been known from laboratory measurements that the photoemission flux from sunlit surfaces should exceed the ambient plasma electron flux at geosynchronous altitudes. How then can satellites charge to negative voltages? To solve this problem, one realizes that there is always a shadowed surface when a satellite is in sunlight. High negative charging can occur on the shadowed surface when the plasma electron temperature is hot.

A bootstrap mechanism then occurs as follows. The negative potential contours extend from the high voltage (dark) side to the low voltage (sunlit) side, thereby trapping the photoelectrons with a potential barrier. Since photoelectrons have a few eV only in energy, a small potential barrier is sufficient to trap most of the photoelectrons. With photoemission partly suppressed, the sunlit side can charge to high negative potentials. The results of the monopole-dipole model predicts that the ratio between the eclipse charging potential to the sunlit charging potential under the same space plasma conditions is approximately 1/3.

Amazingly, we have found abundant evidence that this ratio is valid statistically by studying years of charging data obtained on LANL satellites, . Since R of a finite number is finite and R of a zero is zero, the critical temperature for the onset of spacecraft charging is therefore unchanged - it is the same whether in eclipse or in sunlight. We believe that this is a significant finding for developing a reliable indicator in the future for predicting spacecraft charging in changing space weather.

Acknowledgment

References

1. Besse, A.L. and A.G. Rubin, A simple analysis of spacecraft charging involving blocked photo-
2. electron currents, J. Geophys. Res., **85**, 2324-2328, 1980.

3. Hastings, D., and Garrett, H.B., Spacecraft-Environment Interactions, Cambridge University Press, Cambridge, UK., 1997.

4. Laframboise, J.G., Godard R. and Kamitsuma M., Multiple Floating Potentials, Threshold Temperature Effects, and Barrier Effects in High Voltage Charging of Exposed Surfaces on Spacecraft, in Proceedings of International Symposium on Spacecraft Materials in Space Environment, Toulouse, France, 1982, pp.269-275.

5. Laframboise, J.G. and Kamitsuma, M., The Threshold Temperature Effect in High Voltage Spacecraft Charging, in Proceedings of Air Force Geophysics Workshop on Natural Charging of Large Space structures in Near Earth Polar Orbit, AFRL-TR-83-0046, ADA-134-894,1983, pp .293-308.

6. Lai, S.T., H.A. Cohen, T.L. Aggson and W.J. McNeil, Charging of booms on a satellite rotating in sunlight, J. Geophys. Res., **91**, No.A11, 12137-12141, 1986.

7. Lai, S.T., Gussenhoven, M.S. and Cohen, H.A., Energy Range of Ambient Electrons Responsible for Spacecraft Charging, EOS Trans. Am. Geophys. U., Vol.63, No.18, 1982, pp.421.

8. Lai, S.T., Gussenhoven, M.S., and Cohen, H.A., The Concepts of Critical Temperature and Energy Cutoff of Ambient Electrons in High Voltage Charging of Spacecraft, in Proceeedings of the 17th ESLAB Synposium, edited by D.Guyenne and J.H. A. Pedersen, pp. 169-175, European Space Agency, Noordwijk, The Netherlands, 1983.

9. Lai, S.T., Spacecraft Charging Thresholds in Single and Double Maxwellian Space Environments, IEEE Trans. Nucl. Sci., Vol.19, 1991, pp.1629-1634.

10. Lai, S.T. and D. Della-Rose, Spacecraft charging at geosynchronous altitudes: New evidence of existence of critical temperature, J. Spacecraft & Rockets, Vol.38, pp.922-928, Dec., 2001.

11. Purvis, C., H.B. Garrett, A.C. Whittlesey and N.J. Stevens, Design guidelines for assessing and controlling spacecraft charging effects, NASA Tech. Paper 2361, 1984.

12. Prokopenko, S.M. and Laframboise J.G.L., High Voltage Differential Charging of Geostationary Spacecraft, J. Geophys. Res., Vol. 85, No.A8, 1980, pp.4125-4131.

13. Rubin, A., Garrett, H.B., and Wendel, A.H., Spacecraft Charging on ATS-5, Air Force Geophysics Laboratory, AFGL-TR-80-0168, ADA-090-508, 1980.

14. Stannard, P.R., et al., Analysis of the charging of the SCATHA (P78-20) satellite, NASA CR-165348, 1981. Sanders, N.L.and G.T.Inouye, Secondary Emission Effects on Spacecraft Charging: Energy Distribution Consideration, in Spacecraft Charging Technology 1978, edited by R.C.Finke and C.P. Pike, pp. 747-755, AFGL, Hanscom AFB., Massachusetts, 1978. NASA-2071, ADA ADA-084626.

15. Whipple, E.C., Potentials of surfaces in space, Reports on Progress in Physics, vol. 44, pp.1197-1250, 1981.

DEGRADATION OF HIGH VOLTAGE SOLAR ARRAY DUE TO ARCING IN LEO PLASMA ENVIRONMENT

Teppei Okumura
Department of Electrical Engineering
Kyusyu Institute of Technology
1-1 Sensui Tobata-ku Kitakyusyu 804-8550,Japan
Phone: +81-93-884-3228
Fax: +81-93-884-3228

Satoshi Hosoda
Kazuhiro Toyoda
Mengu Cho
Department of Electrical Engineering
Kyusyu Institute of Technology, Japan

Abstract

A degradation test for a solar array coupon against ESD was performed under simulated Low Earth Orbit environment. All tests were performed in a vacuum chamber with a plasma source. A test coupon was biased at -400V with the aim of developing the next generation 400V high voltage solar array. The LCR circuit was used in order to simulate the arc current that flows by gathering the charge stored on coverglasses. Tests were repeated until the solar array coupon was damaged. The arc locations and waveforms of both current and voltage were detected for all the arcs during the tests. The electrical performance of the coupon was measured after every test without opening the vacuum chamber. Many arcs occurred and caused the cell degradation. The cell was damaged by only one arc that occurred at the edge of cell, not at electrodes.

Introduction

The spacecrafts, such as satellites and space station, have larger structures and longer lifetimes year after year. These spacecrafts need a large amount of the electric power generation, nowadays up to several kW power level. The International Space Station (ISS) can generate 65kW electric power. The higher bus voltage is indispensable for the large spacecrafts to reduce both the increase in power line's weight and the power loss resulting the joule heating due to the increase in electric power generation. The bus voltage over 100 V is employed for the kW class spacecrafts, and the output voltage of the solar array becomes over 100 V. In the case of ISS, the electric power is generated at the voltage of 160 V by the solar array, and is transmitted at 120 V. In near future, the electric power will increase when the lager spacecrafts appear. Taking into account that the bus voltage is generally proportional to the square root of the electric power, the spacecrafts generating the 1 MW class electric power need the output voltage of about 400 V.

The negative end of the solar array is connected to the spacecraft body in many spacecrafts. Under the Low Earth Orbit (LEO) environment, the space plasma, whose density is on the order of $10^{10} \sim 10^{12}$ m^{-3}, can charge the spacecrafts at the negative potential with respect to the plasma, because of electron's higher velocity than ions. When the positive end of the solar array has the same potential as the ambient plasma, the spacecraft body and the negative end of the solar array have the negative potential equal to the voltage in power generation.
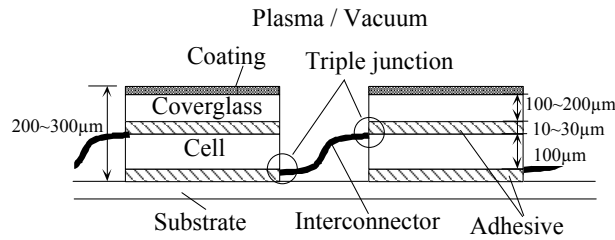
Figure 1.   Cross-section of the solar array.

When the solar array generates the electric power at 400 V, almost part of the spacecraft and the solar array have negative potential with respect to the plasma, and especially the negative end of the solar array is –400 V.

The arcing is observed on the spacecraft and the solar array, when the spacecraft has the negative potential of from 100 V to 200 V with respect to the ambient plasma [1]. The arcing can cause the degradation of the solar cells, the malfunction of the electrical devices, and the short-circuit of the solar array circuit [2]. The influences on the solar array due to the arcing depend on both the number and the energy of arcs. The more negative the spacecraft is charged, the higher the arc rate becomes because the potential difference between the cover-glass and the conductor increases. The arc energy also becomes larger so that the energy depends on the amount of the positive charge gathered from the charged coverglass (dielectric) during arcing.

The cross-sectional view of the solar array for space use is shown in Fig. 1. The solar cells are glued on the Kapton substrate by adhesive, and connected in series each other by the interconnectors (conductor). The coverglasses are also glued on the cells. When the space-craft has negative potential with respect to the plasma, the cells and the interconnectors also have negative potential. Therefore ions are attracted to cells and attack the coverglasses. The coverglass surface is charged to positive by ions. This potential difference between the coverglass and the interconnector enforces the electric field at the triple junction, which con-sists of the interconnector, the coverglass, and plasma. The electrons emitted by the field emission from the triple junction collide with the side wall of the coverglass. The electric field is enforced by the charging of the coverglass. As the result, an arc occurs.

So far, we had developed the 400V high voltage solar array on LEO environment [3,4]. From this result, it was verified that the most effective techniques of mitigating arcs was to cover the coupon with a transparent film. This coupon could suppress the arcing completely up to the negative potential of –1000 V. However in space, the space debris can attack the solar array and make a hole on the film. In such case, it is difficult to suppress completely arcing on the solar array. Therefore for both the mitigation of the solar array degradation and the power generation system design containing the solar array in the spacecraft, it is impor-tant to investigate whether the solar array is degraded or not by arcing, and what degree the solar array is degraded.

The purpose of this study is to investigate the degradation of the 400 V high voltage solar array in LEO.

Charge Supplied by the Charged Coverglass

Before arcing, the surface of the coverglass (a dielectric with 100μm thicness) has the positive potential with respect to the cell and the interconnector, because the coverglass sur-

face has almost same potential as the plasma though most part of the spacecraft has the negative potential with respect to the plasma. After arcing, the charge stored in the capacitance between the spacecraft and the plasma is discharged, and the spacecraft potential rises up to the plasma potential. Then the coverglass surface becomes positive against the plasma. The arc plasma spreads from the arc site with neutralizing the charge on the coverglass. This neutralization of the coverglass charge is observed in the ground tests. The maximum size of the coupon used for such an experiment is 1m square because of the spatial limit of the experimental facility on the ground [5]. For real space use, in the case of ETS-VIII which generates 8 kW at 110V for example, one wing of the solar array is about 10 m in length [6]. The solar array operating at 1MW at 400V will have a large number of solar cells and a huge area. Many coverglasses exist (capacitance) on this large area of the solar array and can supply a lot of charge to the arc plasma in arcing. It is important for the degradation test to estimate the charge supplied from the coverglasses, since it is thought that the degree of the cell damage due to arcing depends on the amount of the charge flowing to the arc site. Then we estimated the amount of the charge neutralized by the arc plasma on the basis of the experimental result [7].

In this experiment, it was observed that the arc plasma could neutralize the charge stored on the film which simulated the coverglass and was placed at 4m far from the arc site. Therefore it was assumed that the arc plasma could neutralize the charge of the coverglass within 4m from the arc site [7]. It was also assumed that the ratio of the neutralized charge to the total charge stored on the coverglass, γ_c, was 100% at the arc site, and was inversely proportional to the distance from the arc site, r, and was 0% at 4 m from the arc site. The velocity of the arc propagating with neutralizing the charge on coverglass was 7×10^4 m/s from the experimental result. We also put the capacitance of the coverglass to C_{cg}=286.5 nF/m^2.

The charge on the coverglass is neutralized radially at the velocity, v, from the arc site. The charge, $C_{cg}|\Delta V|$, is stored on the coverglass per unit area before arcing, where ΔV is the potential difference between the coverglass and the cell. We put that $\gamma_c = 1 - 0.25r$ on the condition, γ_c=0 at r=4 m, where r represents m in unit. The time duration from the beginning of arcing is t s. We also put the charge neutralized at r during dt to dC, and from $r = vt$, the discharge current, I, is
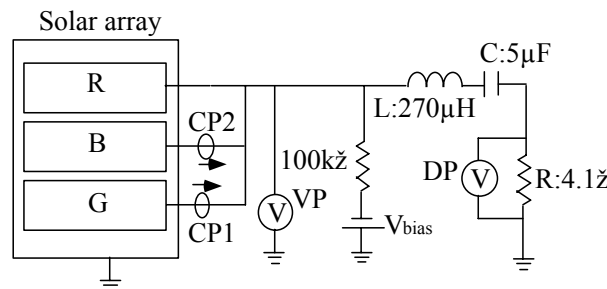
$$I = \frac{dC}{dt} = \frac{(\pi(r + dr)^2 - \pi r^2)C_{cg}|\Delta V|\gamma_c}{dt} \qquad (1)$$

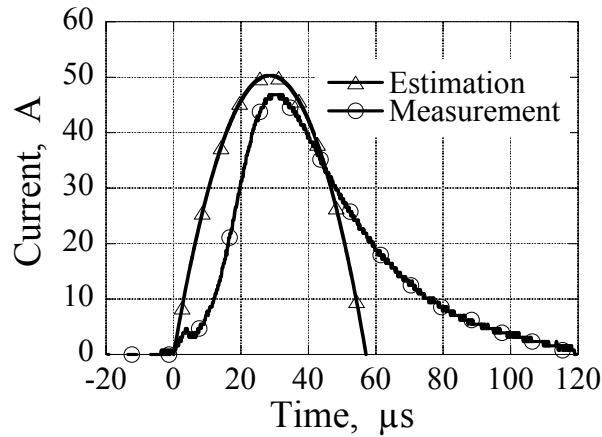$$\cong 2\pi r C_{cg}|\Delta V|\gamma_c \frac{dr}{dt} \qquad (2)$$

$$= 2\pi C_{cg}|\Delta V|v^2 t(1 - 0.25vt) \qquad (3)$$

Substituting the value of the constant, we have

$$I = 3.52 \times 10^6 t(1 - 1.75 \times 10^4 t), \text{A} \qquad (4)$$


Figure 2. Experimental circuit.

Figure 3. Waveform of arc current.

From this equation, the peak of the arc current, I_{max}, is 50 A, and the amount of the charge is 2 mC. In the previous experiment, the external capacitance was connected to the circuit to simulate the coverglass capacitance. In this method, the charge stored in the external capacitance flows via the arc plasma with several Ω between the solar array and the camber wall in the arc inception. Therefore the charge flows during such short time as a few microseconds, the peak of the current is very large. Then we controlled the discharge current close to Eq. (4) by means of adding a resistance and an inductance besides a capacitance to the circuit. The experimental circuit is shown in Fig. 2. The voltage of –400 V was applied to the solar array during the experiment. The capacitance of 5 µF was used so as to set the charge to 2 mC. The inductance, H, is 270 µH, and the resistance, R, is 4.1 Ω. These values were estimated by a circuit simulator in advance of the experiment and were corrected slightly by the experiment. The circuit showed the waveform of the discharge current (Fig. 3).

The peak of the discharge current was 47 A in Fig. 3 and was close to the estimated value, 50 A. This circuit could suppress the large current such as the rush current over 100 A. The amount of charge was about 2 mC, and all amount of the charge stored in the capacitance was discharged during arcing.
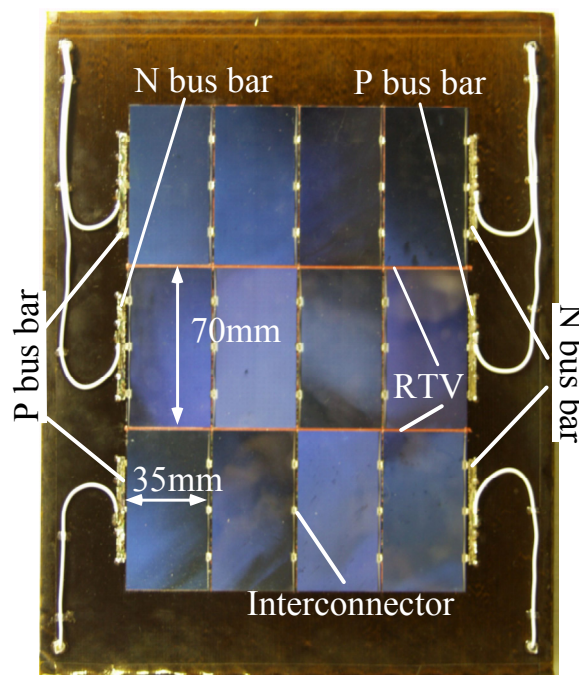

Figure 4. Picture of the coupon.

Experiment

Solar array coupon

The picture of the solar array coupon used in the experiments is shown in Fig. 4. This coupon is the basic design for the 100 V solar array used currently in the space. The substrate is 25 mm aluminum honeycomb which is covered with Carbon Fiber Reinforced Plastics (CFRP), and the top of the substrate is covered with the Kapton film. The twelve silicone cells (70mm×35mm) are glued on the Kapton film. Four cells are connected in series by the interconnectors. The electrodes of both end of the series connection are called the bus bars. Three parallel connections are called as R, B, G strings, respectively. We also call the cells by the numbers as shown in Fig. 4. The cells have IBF (Integration Bypass Fumction), which allows the current flow from N to P electrode in the cell even if the cell can not generate the electric power. The gap between strings are glued by RTV (Room Temperature Vulcanizing) silicone rubber to prevent the sustained arc [8, 9].
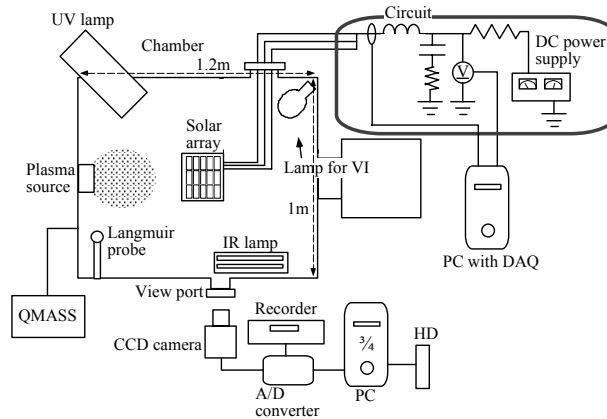
Figure 5.   Experimental setup.

Measurement system

The sketch of the measurement system is shown in Fig. 5. The experiments were performed in a vacuum chamber, which was 1 m in diameter and 1.2 m in length. The pressure in the chamber could reach up to about 5×10^{-4} Pa, and was 1×10^{-2} Pa during the experiments. The plasma was produced by an ECR plasma source [10]. The plasma density around the coupon was about 5×10^{12} m^{-3} and the electron temperature was about from 3 eV to 7 eV with xenon gas of 2×10^{-8} kg/s. The coupon was kept at 40 ºC by an IR lamp to simulate the temperature on orbit during the experiment.

The arc location on the coupon was identified by a position identification system of arc discharge [11]. During the experiments, the video image of the coupon was recorded in a hard disk drive connected to a PC as the digital video image. After the experiments, the arc location was identified by means of analyzing the digital video image with a computer program in the PC.

All waveforms of the array potential and the discharge current were acquired by a high speed data acquisition system [12]. This system consists of a high speed data acquisition board, a PC, and a LabVIEW program, and can record the waveforms within about 30 ms intervals after a waveform is recorded. This system can also perform the real-time recording

and display of the peak, the amount of charge, and the pulse width of the discharge current.
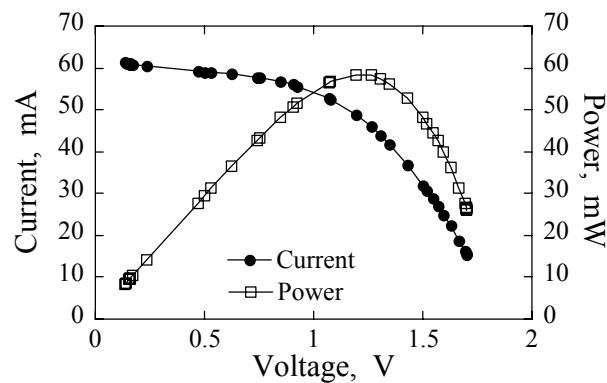
Figure 6.   VI Characteristic.

The circuit used in the experiments is shown in Fig. 2. Here the current probes, CP1 and CP2, were HIOKI 3274 (DC ~ 10 MHz). The current supplied from the capacitance C was measured by measuring the potential of R using the differential probe DP.

The metal halide lamp mounted in the chamber enabled to acquire the electrical performance of the coupon without opening the chamber during the experiments. The electrical performance was acquired in each string by means of measuring both the output voltage and current with shifting the value of resistance connected to the string (VI characteristics). The example of the VI characteristic is shown in Fig. 6. The output power is also shown in this figure. The maximum power gives the electric performance of the strings. The illumination of this lamp was 19000 lx at the center of the coupon. The plasma source was stopped during the VI measurement. The VI curve was corrected by the coupon temperature, which was measured simultaneously, since the electric performance of the solar cell depended on its temperature.

Result and discussions

The experimental condition is listed

Table 1 Test conditions.

Work gas	Xe
Mass flow rate	0.2 sccm
Plasma density	5×10^{12} m^{-3}
Chamber pressure	9.7×10^{-3} Pa
Neutral density	2.3×10^{18} m^{-3}
Bias voltage	-400 V
Array temperature	40 ℃
External capacitance	5 µF
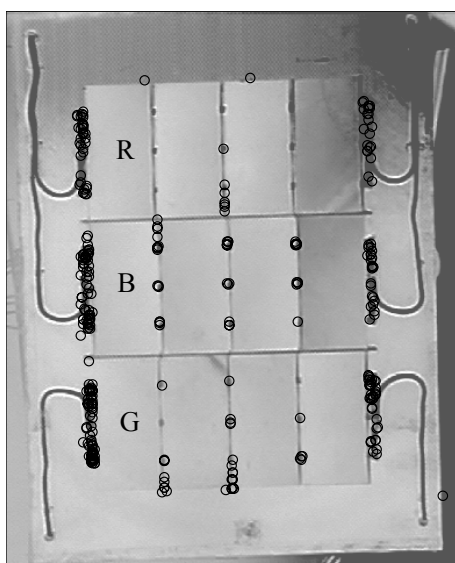
Figure 7.   Position of arc.

Table 2.   Experimental result.

Case	Experimental duration, s	Number of arcs		
		Total	Electrode	Cell edge
1	100	53	53	0
2	62	29	29	0
3	26	18	18	0
4	40	28	26	2
5	39	25	23	2
6	78	41	38	3
7	37	18	18	0
8	76	34	30	4
9	55	26	19	7
10	52	23	15	8
Total	565	295	269	26

in Table 1. The work gas of the plasma source was xenon, and the plasma density at the center of the coupon was about 5×10^{12} m^{-3}. Table 2 shows the experimental result, and Fig. 7 shows the arc location on the coupon during the experiments. The coupon was biased at –400 V in the plasma environment. The experimental case contains about 20 arcs, and was repeated until the coupon was degraded. After each experimental case, the electric performance was acquired by the VI measurement without opening the chamber. The 10 cases were performed totally, and the total experimental

Figure 8.   Peak of output power.

time was 565 s, the total number of arcs was 295. The 269 arcs of all arcs occurred at the electrodes, like the bus bar and the interconnector, which were exposed to the space, and the 26 arcs occurred at the side edges of the cells except for the exposed electrode. This result showed that the arc occurred easier at the exposed electrode than at the cell edge.

(a) Case 4

(b) Case 5

(c) Case 6

(d) Case 8

(e) Case 9

(f) Case 10

Figure 9.   Position of arcs.

The peak of the output electric power measured after every case was shown in Fig. 8. The maximum power was normalized by the value measured before the experiment. The maximum power did not change in any strings by case 5. After case 6, the R-string showed degradation of electric power. After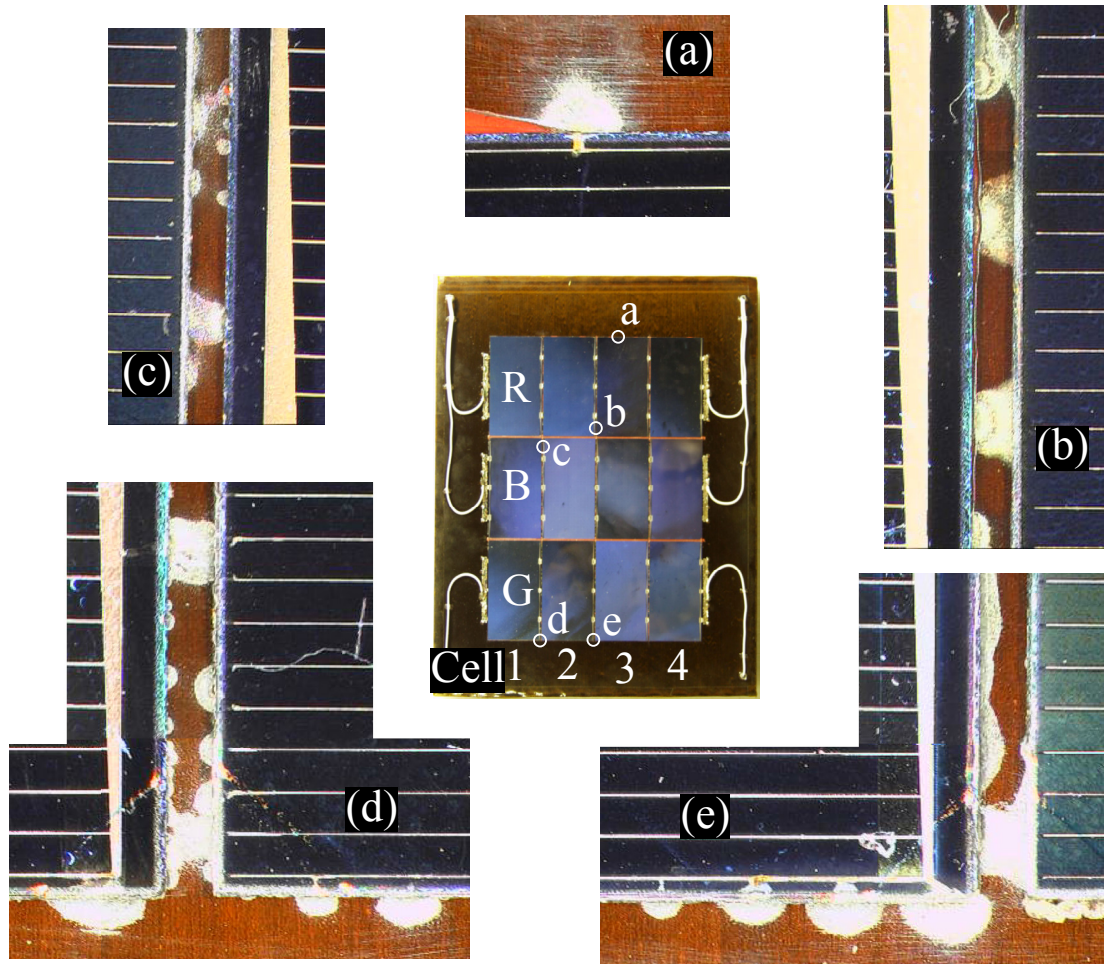 case 9, the G-string suffered the degradation of 20 %, and then suffered moreover the 20 % degradation after case 10. After all, the total power degradation was 40 % in the G-string.

Figure 10.   Microscopic picture at the cell edge.

The arcs occurred at the side edge of the cells in both R and G-strings, when the electric power of the strings was degraded. The distributions of the arc location in the cases 4, 5, 6, 8, 9, and 10, which had the arcs occurred at the side edge of the cells, are shown in Fig. 9. In the cases 4 and 5, three arcs occurred at the cell edge between the cells No. 2 and No. 3 in the R-string. In case 6, an arc occurred at the same position as cases 4 and 5, and at the top of the cell No. 1 and 3 in the R-string, respectively. No arc at the cell edge except for the cell edge between the cells occurred until case 6, and no degradation also occurred until case 6. In case 8, the cells were not degraded, though 4 arcs occurred at the cell edge between No. 1 and No. 2 in the B-string. In case 9, 7 arcs occurred in the G-string totally at the cell edge between No. 2 and No. 3, and at the bottom edge, and then the cells were degraded. In case 11, the arcs occurred in the G-string at the cell edge between No. 1 and No. 2, between No. 2 and No. 3, and at the bottom edge of both No. 1 and No. 2., and then the electric performance decreased

moreover. It was verified that the arcs at the electrode exposed to the space did not degrade the cells, however the arcs at the side edge of the cells could degrade the cells.
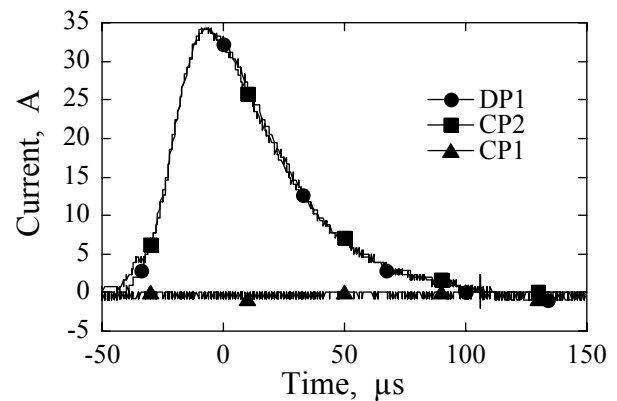
Figure 10 shows the microscopic picture of cells that had arcs at their side edge. Each position of the cell edge was named as (a) ~ (e). The P electrode was melted out of the backside of the cell in the case of arcing at the cell edge. When the arcs occurred at the exposed electrode like the interconnector, there was no such an arc track.

At most of the positions where the arcs occurred at the cell edge between the cells, the cell seems to be connected to the adjacent cell by the arc site. If the P electrodes of the backside of the cells are short-circuited each other, the P and N electrodes are short-circuited in one cell, and this leads to the decrease in electric power. The arc sites between the cells were observed in all strings. To clarify whether two cells were short-circuited or not, the resistance was measured between the adjacent cells, No. 1 and No. 2 in the G-string. The three interconnectors connecting two cells were cut in order to measure the resistance. The result showed that the insulation was kept between the two cells. From this result, the decrease in electric power resulted from the short-circuit of the PN junction in the cell.

Figure 11. Waveform of the arc degrading the cell.
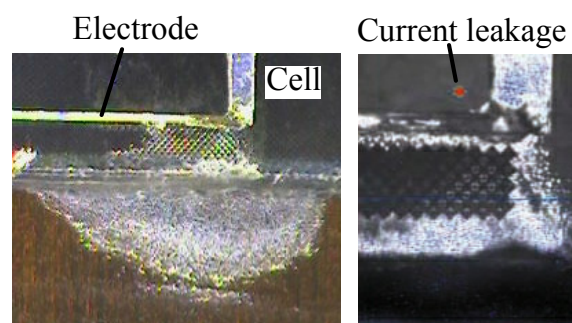
Figure 12. Microscopic picture of current leakage point.

In case 6 which the R-string was degraded in, the arcs occurred at the top edge of the cells besides at the gaps between cells. As shown in Fig. 10 (a), an arc site attached at the top edge by the arcing at the cell edge. The parallel lines in this picture were the N bar electrodes at the cell surface, and were insulated from the space by the coverglass. In Fig. 10 (a), the N electrode seemed to be connected to the cell edge by the arc site. In the R-string, such an arc site from the N electrode between the coverglass and the silicon was observed only in Fig. 10 (a). In the B-string, there was no arc site like this.

In the G-string, both the power degradation and the arcing at the cell edge occurred in cases 9 and 10. The arc sites like Fig. 10 (a) were also observed in the G-string, one arc site in the cell No. 1, and five arc sites in No. 2. The position of the current leakage in the cell was identified.

At first, in the G-string, the degraded cells were identified by measuring the open-circuit voltage (Voc) of each cell with exposing one cell to the light and shading the other cells. The Voc of the cells No. 1 and 2 was about the one tenth of the other cells, and these cells were identified as the degraded cells. This result was consistent with the arcs occurring at the cell edge of these cells.

Table 3.   Parameters of arcs.

Variable	Minimum	Maximum	Points	Mean	Std Deviation
I_{max}, A	13.7	46.1	289	37.5	7.42
Charge, mC	0.98	2.00	289	1.73	0.23
Pulse width, µs	97	154	289	111	8
V_0, V	-389	-201	289	-347	46

Next, the current leakage position was identified in the No. 1 cell identified as the degraded cell. The identification method was identified by detecting the IR radiation from the leaking position with applying the inverse voltage to the string. The identified current leakage position is shown in Fig. 11. This position corresponds to the bottom edge in Fig. 10 (d). The current leakage position identified in the No. 1 cell was only one place shown in Fig. 11. From the arc location identification result, the only one arc occurred at the arc site in Fig. 11, and this arc caused the power degradation of the No. 1 cell. From this result, it was confirmed that only one arc could destroy the PN junction in the cell.

The current waveforms of the arc, which occurred at the bottom edge of the No. 1 cell and caused the current leakage in the cell, was shown in Fig. 12. These current waveforms in this figure were measured by the differential probe DP and the current probes CP1 and CP2 in the circuit (Fig. 2). Table 3 lists the quantities, the minimum, the maximum, the average, and the standard deviation for the peak value of the current, the amount of the charge, the pulse width, and the array potential before arcing, respectively. Here the charge and the pulse width were calculated for the waveform within 95 % of the peak value of the current. The discharge current flew in G-string where the emission of the arc was observed. The current waveform of this arc which destroyed the cell was similar to other arcs, and the peak value of the current was 34 A, the amount of the charge was 1.2 mC, the pulse width was 116 µs, and the array potential before arcing was –381 V.

Figure 13.   Relation between I_{max} and V_0.
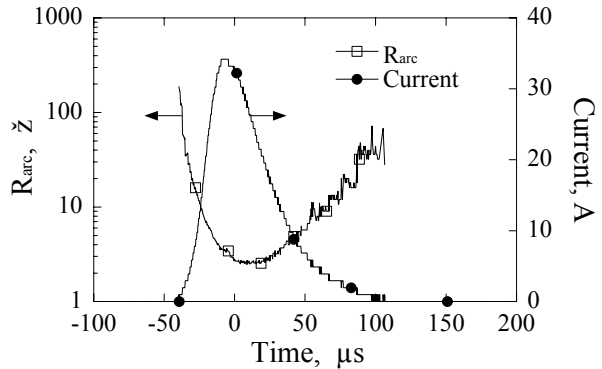
Figure 14.   Waveform of R_{arc} and current.

As shown in Table 3, the current waveform in Fig. 12 was the average value with no difference from the other arcs. Since it takes finite time to charge the capacitance from 0 V to –400 V after arcing when the arc rate becomes high, the arc can occur before the array potential reaches to –400 V. Therefore the array potential before arcing, V_0, has various values. Figure 13 shows the relation between the V_0 and the I_{max} for the arcs at the cell edge and at the interconnector or the bus bar, respectively. Naturally, the V_0 was proportional to the
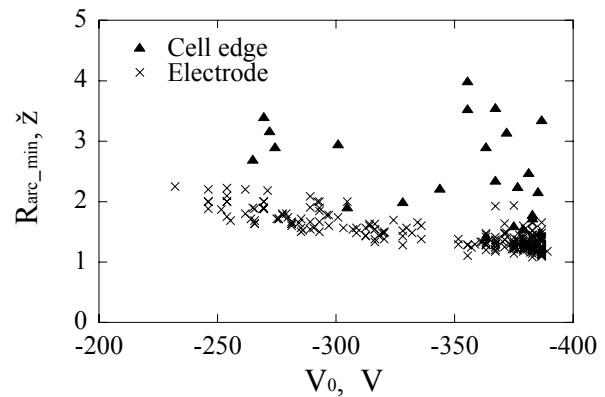
charge stored in the external capacitance before arcing, Q_0. If the Q_0 is large, the I_{max} becomes large, too. In the case of the arcs at the electrodes, the $|V_0|$ was proportional to the I_{max}. On the contrary, the I_{max} of the arcs at the cell edge was smaller than the arcs at the electrodes. This means that the resistance R_{arc} between the array (cathode) and the vacuum (anode) was larger in arcs at the cell edges than in arcs at the electrodes.
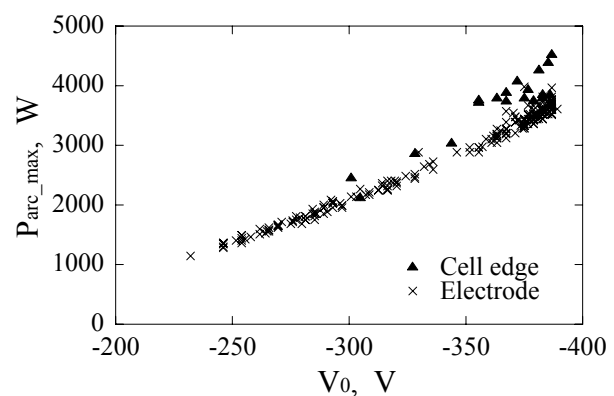
To investigate R_{arc} in detail, the waveform of R_{arc} was calculated by means of dividing the absolute value of array potential by the current. The example waveform of R_{rac} is shown in Fig. 14. The R_{arc} decreased after arcing and was minimum after the current was maximum, and then increased. This resistance is the sum of the resistance between the array and the chamber via plasma, and the resistance in the array circuit including the inside of cells. The minimum value of R_{arc} was put as R_{arc_min} and was calculated over all discharge waveforms.

Figure 15 shows the relation between R_{arc_min} and V_0 for the arc both at the cell edge and at the electrode. In the case of the

Figure 15. **Relation between R_{arc_min} and V_0.**

Figure 16. **Relation between Parc_min and V0.**

arcs at the electrode, R_{arc_min} showed a tendency to decrease with increase in $|V_0|$. The resistance between the electrode and the chamber decreases with increase in the energy of electrons emitted from the electrode. Therefore the resistance decreased since the energy of electrons accelerated from the cathode was large with increase in $|V_0|$. The resistance was larger in the cell edge arcs than in the arcs at the electrode. In the case of the arc that degraded the cell (Fig. 11), the V_0 was –384 V, and the R_{arc_min} was 2.5Ω. The average of R_{arc_min} at the electrode over 350 V of $|V_0|$ was 1.3Ω, and the R_{arc_min} in the case of the arc degrading the cell was about 1Ω larger than in the cell edge case. It is one of this reason that the electrons were emitted easier from the electrode exposed to space than from the P electrode at the backside of the cell between the cell and the substrate. The P electrode was melted out from the backside of the cells in the case of the cell edge arcs, though the interconnectors were not damaged by the arcs. From these results, the cell can be heated from the arc as the arc occurred at the cell edge.

To investigate the heat energy supplied to the cell by arcs, the power P_{arc} wasted by R_{arc} was calculated by multiplying the current and the array potential. In Fig. 16, the maximum P_{arc}, P_{arc_max} , was plotted against V_0. As shown in Fig. 16, the P_{arc_max} of the cell edge arcs was larger than that of the electrode arcs. This result means that the cell edge arcs can heat the cell harder than the electrode arcs. It is thought as one of the reasons for the cell degradation that the cell edge arcs heated the cell locally and melted the cell edge and then short-circuit PN junction of the cell.

In the experiment, the arc site between the coverglass and the silicone cell was observed at the current leakage point. If the adhesive between the coverglass and the cells is absence, the arc current can flow into N electrode as an arc occurs at the cell edge. The N+ diffusion layer just under the adhesive is about 0.1 μm in depth. Since this layer can be destroy easily by the arc site, PN junction is short-circuited. This is one of the reasons for the cell degradation.

The array was biased at –400 V in the experiment, and the arcs caused the power degradation. The power degradation was 10 % in the R-string, and 40 % in the G-string. Because of 4 cells in each string, the 2 cells were destroyed totally. The 295 arcs occurred during the experimental time of 565 s. From this result, the probability of one arc destroying one cell is about 0.7 %. Limiting at the cell edge, 26 arcs occurred. The probability of one cell edge arc destroying one cell is high, about 7.7 %. Since the arc rate decreases with time, and the plasma density in the experiment is the maximum value in LEO, to estimate the degraded cells in the satellite lifetime is overestimation. We can estimate that 5.7×10^5 cells are degraded during the lifetime of 10 years using the probability of 0.7 %. Generating the power of 1 MW at 400 V, the number of the silicon cell generating 1 A at 0.5 V is 2×10^6, the series of 800 cells and 2500 string. A fourth of all cells is destroyed. This degradation is harder than the radiation degradation. In real case of 400 V power generation, the arc mitigation methods must be applied to the coupon. However, it is difficult for these methods to mitigate arcs completely. From these results, the double mitigation method, which means that the arc do not occur at the cell edge if the arc occur, is needed.

Conclusions

The ESD test of the 400 V power generation solar array for space use was performed in the vacuum chamber simulating the LEO plasma environment. The waveform of arc current was controlled close to the waveform considering the neutralization by arc plasma of coverglass charge by means of using LCR circuit. The system, which can measure the electrical performance of the solar array without opening the chamber, was constructed.

A lot of arcs occurred on the solar array biased at –400 V and caused the degradation of the electric performance of solar array. From the results of identifying the degraded cells and current leakage point of the cells, it was observed that only one arc destroyed the PN junction of the cell. The arc destroying the cell occurred at the cell edge but at the electrode exposed to space. The interconnector and the bus bar had little damage due to arcing. On the other hand, as the arcs occurred at the cell edge, the P electrode melting out from the backside of cell, and the arc site between coverglass and the silicone were observed. From these results, it was thought that the arcs at the cell edge added heat stress locally to the cell edge and could destroy the cell.

In real use of the high voltage solar array in space, it is necessary to apply the mitigation method to the solar array. In addition of applying the mitigation method, it is is important to prevent the arcs at the cell edge if the arc occurs on the solar array.

Acknowledgement

References

1. Grier, N. T.: Plasma Interaction Experiment II (PIX II): Laboratory and Flight Results, Spacecraft Environmental Interaction Technology-1983, NASA CP-2359, 1985, pp.333-347.

2. Katz, I., Davis, V. A. and Snyder, D. B.: Mechanism for Spacecraft Charging Initiated Destruction of Solar Arrays in GEO, AIAA paper 98-1002, 36th Aerospace Sciences Meeting, Reno, 1998.

3. Cho, M., Shiraishi, K., Toyoda, K., Hikita, M.: Basic Developmental Experiment of Arc-Resistive High Voltage Solar Array for Low Earth Orbit, Journal of the Japan Society for Aeronautical and Space Sciences, Vol.50, No.581, (2002), pp.215-222.

4. Toyoda, K., Saionji, A., Cho, M., and Hikita, M.: Experimental Study of Mitigating Arcs on a High Voltage Solar Array in LEO, Proceedings of the 23rd International Symposium on Space Technology and Science, Matsue, Japan, 2002, pp. 379-384.

5. Leung, P.: Plasma Phenomena Associated with Solar Array Discharges and Their Role in Scaling Coupon Test Results to a Full Panel AIAA 2002- 0628, 40th Aerospace Sciences Meeting, Reno, January, 2002

6. Meguro, A., Tsujihata, A., Hamamoto, N., and Homma, M.: Technology status of the 13 m aperture deployment 21 antenna reflectors for Engineering Test Satellite VIII, Acta Astronautica, Vol. 47, No. 2 (2000), pp. 147-152.

7. Cho, M., Miyata, N., Hikita, M., and Sasaki, S.,: Discharge over Spacecraft Insulator Surface in Low Earth Orbit Plasma Environment, IEEE Transactions on Dielectrics and Electrical Insulation, Vol.6, No.4 (1999), pp. 501-506.

8. Cho, M., Ramasamy, R., Matsumoto, T., Toyoda, K., Nozaki, Y., Takahashi, M.,: Laboratory Tests on 110-Volt Solar Arrays in Simulated Geosynchronous Orbit Environment, Journal of Spacecraft and Rockets, Vol. 40, No. 2 (2003), pp. 211-220.

9. Cho, M., Ramasamy, R., Toyoda, K., Nozaki, Y., Takahashi, M.,: Laboratory Tests on 110-Volt Solar Arrays in Ion Thruster Plasma Environment, Journal of Spacecraft and Rockets, Vol. 40, No. 2 (2003), pp. 221-229.

10. Hayashi, H., Saionji, A.,Toyoda, K., Cho, M., and Kuninaka, H.: Development of Plasma Interaction Acceleration Test Facility for Study on Space Material Deterioration, 23rd Int. Symp. Space Tech. Sci. ISTS 2002-b-28, Matsue, Japan, 2002.

11. Toyoda, K., Cho, M., and Hikita, M.: Development of Position Identification System of Arc Discharge on a Solar Array in Vacuum by Digital Processing of Video Images, Journal of the Japan Society for Aeronautical and Space Sciences, Vol.51, No.589, (2003), pp. 82-84.

12. Saionji, A., Toyoda, K., and Cho, M.: Development of Automatic Data Recording and Analysis System for Laboratory Experiments on High Voltage Solar Array in Space Environment, Proceedings of ACED & K-J Symp. on ED and HVE, Seoul, 2002, pp.63-66.

ECSS-E-20-06 DRAFT STANDARD ON SPACECRAFT CHARGING: ENVIRONMENT-INDUCED EFFECTS ON THE ELECTROSTATIC BEHAVIOUR OF SPACE SYSTEMS

D. J. Rodgers
ECSS-E-20-06 Working Group
Space Department, QinetiQ, Farnborough, GU14 0LX, UK
Phone: +44-1252-394297
Fax: +44-1252-396330
E-mail: djrodgers@space.qinetiq.com

A. Hilgers
ESA/ESTEC, 2000 AG Noordwijk, The Netherlands

Abstract

ECSS (European Co-operation on Spacecraft Standardisation) is an initiative to develop a coherent, single set of user-friendly standards for use in all European space activities. One part of this initiative has covered environment-induced effects on the electrostatic behaviour of space systems, including spacecraft charging. This has resulted in a draft standard, ECSS-E-20-06, that describes the performance and verification requirements needed to control these effects.

Contributions to the standard have come from European governmental agencies, the European Space Agency and industry. Before adoption, the standard will be subject to wider circulation and amendment as a result of feed-back.

This draft standard attempts to bring together good practice and de facto standards, from a wide range of sources, into a single reference document. In addition, it provides an explanation of the main physical processes of spacecraft electrical interactions and their effects, covering sheath effects, wakes, tethers, electric propulsion, internal and surface charging, and discharges and transients. Requirements are given for surface materials, solar arrays, internal materials, tethers and electric propulsion systems. Finally, useful information is provided into ways of carrying out the required tests and simulations.

Introduction

The European Cooperation for Space Standardisation (ECSS) is a joint initiative between ESA, European national space agencies and European space industry. It is progressively establishing a system of standards covering all aspects of space system development and operation, including engineering, management and product assurance [1]. The objectives of the ECSS system are to improve the efficiency and quality of the procurement and engineering processes associated with space systems development and operation, and to improve the competitiveness of European space industry. ECSS standards are harmonised to the maximum extent possible with international standards or working practices where these have been adopted by European space industry and the preparation of ECSS standards takes into account information and opinions of all interested parties. ECSS intends to establish a formal status for a part of the ECSS standards as European Standards (EN) through the European Committee for Standardization (CEN), as appropriate.

Figure 1 shows a top-level documentation tree of the ECSS system. The Level 2 standards (e.g. ECSS-Q-60, ECSS E-20, etc.) describe the required objectives and functions for all aspects in the individual domain (electrical engineering, quality assurance, system engineering, etc.). Level 3 documents describe methods, procedures and recommended tools to achieve the requirements of Level 2 documents. In addition they define the constraints and requirements. Level 3 documents are guidelines and are allowed to be adapted to the projects' needs. The subject of this paper, a new standard ECSS-E-20-06 "Charging: Environment-Induced Effects on the Electrostatic Behaviour of Space Systems", is in preparation and defines in more detail the methods to be used for the control of hazards arising from spacecraft charging and spacecraft/plasma interactions.
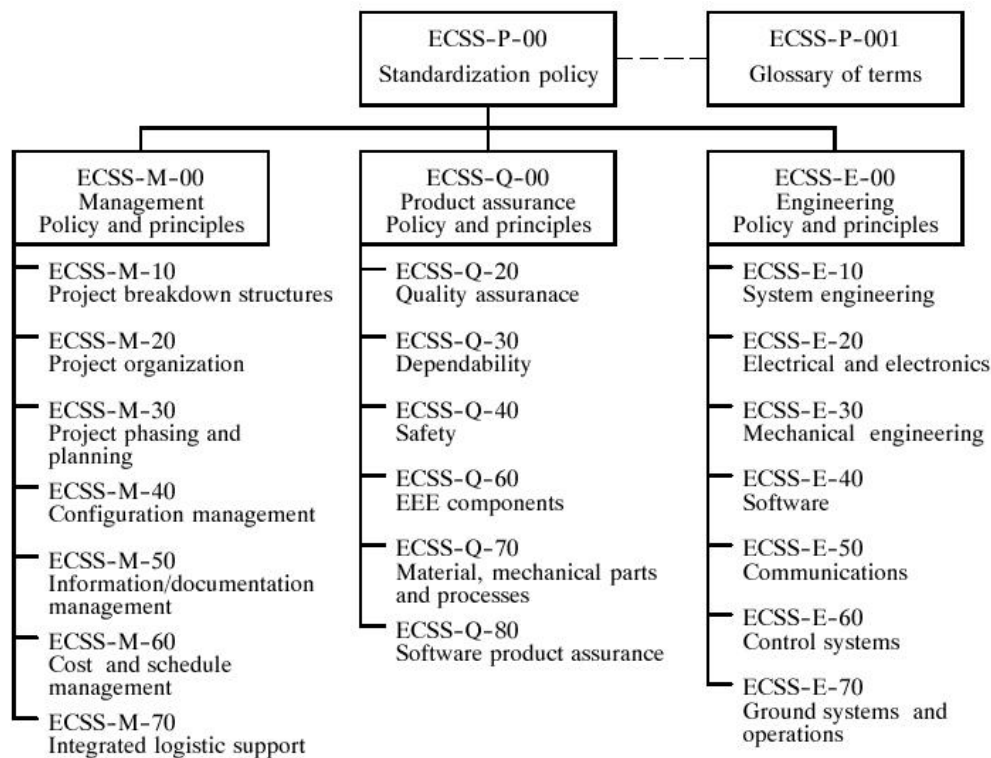
Figure 1. The ECSS documentation architecture showing level 2 documents. Level 3 includes E-10-04 on space environment and E-20-06 on spacecraft charging and environment induced effects on electrostatic behaviour.

Related Standards

A number of existing and planned level 3 standards are related to this standard:

– ECSS-E-10-04 (Space environment) [2], describes the environmental plasma and radiation that influence charging – including the radiation belts and the thermal plasma populations in the ionosphere, plasma sphere and plasma sheet/ ring current. The current version has been implemented as an active document within the 'Space Environment Information System' (www.spenvis.oma.be/spenvis/). ECSS-E-10-04 is planned to be updated next year.

- ECSS-E-10-12 (Radiation dosimetry methodology), in preparation, has relevance to internal charging effects.

- ECSS-E-20-07 (EMC test), is in preparation. Testing of electrostatic behaviour shares many techniques with general electromagnetic cleanliness.

- ECSS-E-20-01 (Multipaction), now in public review, shares a common interest in secondary electron emission with spacecraft charging analysis.

- ECSS-E-20-05 (Control of vacuum-related electric breakdown) has relevance to charging-induced electrostatic discharge.

- ECSS-E-20-08 (Space Voltaic Assemblies), in preparation, describes one of the key spacecraft systems for the charging hazard.

- ECSS-Q-70-71 (Data for selection of space materials), relates to choice of materials. This, is a draft in public review and is an update to ESA's PSS-01-701 [3].

- ECSS-E-10-02 (Verification) and ECSS-E-10-03 (Testing) describe verification and testing strategies and documentation.

In addition to ECSS efforts on standardisation., the International Standards Organisation (ISO) has established a working group on the space environment under its subcommittee responsible for standardisation in the field of space systems and operations (TC20/SC14) [4].

Scope and Content of ECSS-E-20-06

The standard is intended to provide a clear and consistent guide to the application of measures to assess and avoid/minimise hazardous effects arising from spacecraft charging and other environmental effects on a spacecraft's electrical behaviour. It aims to improve the efficiency of European space industry by ensuring that collaborative developments proceed on the basis of a common understanding of the processes and their effects and common requirements for their control. An overview of the types of electrical effects occurring in space is given and there is a detailed description of the physical processes behind them. The requirements, in terms of spacecraft design, testing and analysis that arise from these processes form the core of this standard. Finally, there is a discussion of types of orbits and how to tailor the requirements according to an individual mission.

Although spacecraft systems are clearly subject to electrical interactions while still on Earth (e.g. lightning and static electricity from handling, re-entry plasmas), these aspects are not covered. Many are common to terrestrial systems and covered elsewhere. Instead the standard covers electrical effects occurring in space (i.e. from the ionosphere upwards).

Electrical interactions between the space environment and a spacecraft may arise from a number of external sources including the ambient plasma, radiation, electrical and magnetic fields and sunlight. The nature of these interactions and the environment itself may be modified by emissions from the spacecraft itself, e.g. electric propulsion, plasma contactors, secondary emission and photo-emission. The consequences, in terms of hazards to spacecraft systems depend strongly on the sensitivity of electronic systems and the potential for coupling between sources of electrical transients and fields and electronic components.

Processes and Effects

Sheath effects

Due to the nature of the space plasma, an electrostatic sheath will develop around any object immersed in it. The sheath is a layer of net space charge that will screen the distant plasma from the surface charges. The sheath confines all of the significant electric fields, therefore its geometry relative to the spacecraft dimensions is important for estimating the interaction between the spacecraft and the surrounding plasma.

Ambient charged particle fluxes (ions and electrons), photoelectrons, back-scattered and secondary electrons from the surfaces as well as actively emitted particles from, e.g., thrusters, together with spacecraft geometry and velocity and external magnetic fields contribute to determining the properties of the sheath. The standard includes discussion of the characteristic shielding length, the Debye length and the thin-sheath (space-charge limited) and thick sheath (orbit limited) sheath models. For example, a guide to typical Debye lengths in natural plasma regions is shown in Table 1.

Plasma region	Density (m^3)	Temperature (eV)	Debye length (m)	N_d (m^{-3})
Interstellar	10^6	10^{-1}	1	10^6
Solar corona	10^{13}	$1 - 10^2$	$10^{-2} – 10^{-3}$	$10^4 - 10^7$
Solar wind	$10^3 - 10^9$	$1 - 10^2$	$1 - 10^2$	10^{10}
Magnetosphere	$10^6 - 10^{10}$	$10 - 10^3$	$1 - 10^2$	$10^9 - 10^{13}$
Ionosphere	$10^8 - 10^{12}$	10^{-1}	$10^{-1} - 10^{-3}$	$10^4 - 10^6$

Table 1. Typical Debye lengths and Nd, (the number of particles in a Debye sphere) for different regions of space.

Surface charging

Surfaces in space naturally charge as a result of charged particle collection and emission. Sunlit insulated surfaces tend to charge positively due to photo-electron emission while non-sunlit insulated surfaces tend to charge negatively because of the higher mobility of ambient electrons compared to ambient ions. Grounded surfaces have either positive or negative potential depending on the balance of the various contributing currents to exposed surfaces, possibly involving currents from active devices. High level negative surface charging is widely recognised by designers as a hazard to spacecraft operations especially on geostationary orbit during eclipses. It occurs when primary high energy (typically above a few keV) environmental electrons are collected on spacecraft surfaces, leading to large negative potentials on the spacecraft as a whole and large potential differences between different spacecraft components which can lead to electrostatic discharges. Other consequences include increased sputtering and surface contamination. Electrons from around 1-40keV are needed to produce this effect, which is strongly material-dependent. Electrons of this energy are typical of the trapped plasma of the outer magnetosphere but are generally absent within the plasmasphere and ionosphere, except in auroral regions. In the ionosphere, auroral charging may be facilitated by wake effects. Negative surface charging is countered by a number of processes that cause a positive current to flow onto a surface, e.g. ion currents, secondary electron emission, and photo-emission. A worst-case charging

environment was described in ECSS-E-10-04, based on a severe charging event seen on the SCATHA spacecraft.

Even moderate potential (positive or negative) needs to be carefully assessed and possibly controlled for certain types of scientific spacecraft carrying instruments with very sensitive gain or specifically dedicated to low energy particle measurements.

Wakes

The interaction between a moving object and a stationary plasma leads to a disturbance in the local plasma, resulting in rarefaction on the downstream or wake side and, in the case where plasma is back-scattered, plasma compression on the upstream or ram side. These changes have consequences on the currents to surfaces and thus on the charging characteristics of the spacecraft. ECSS-E-20-06 describes the acoustic velocity, the Mach number and the structure of wakes. The wake void region is larger for large spacecraft and those with high Mach numbers. From Table 2 it can be seen that wakes are most important at low altitudes.

Altitude km	Circular velocity km/s	Ion Acoustic velocity km/s	Mach no.	Mach angle degrees
200	7.8	1.4	5.5	10
500	7.6	2.1	3.7	16
1000	7.3	3.6	2.0	29
1500	7.1	4.3	1.6	38
2000	6.9	5.7	1.2	55
GEO	3.0	30 – 500	0 – 0.1	n/a

Table 2. Typical plasma parameters for LEO orbits and GEO (adapted from [5]). A range of electron temperatures from 2eV to 2keV is estimated for GEO.

Tethers

Tethers currently represent a novel technology with prospects for being useful in many ways. Proposed applications include power generation, orbit raising/lowering, aerodrag compensation, inclination changing, atmosphere skimming, as a re-entry mechanism, as an antenna, for towing, to maintain fixed separations between two bodies, to permit improved 3-d pointing stability and for active modification of ambient plasma.

Most proposed uses involve conductive tethers, in which the interaction with the magnetic field is used to generate power or to modify the spacecraft velocity. ECSS-E-20-06 describes how induced potentials are calculated and the forces acting on a current-carrying wire. Problems associated with adequate current collection and tether oscillations, which make the application of tethers difficult in practice, are discussed.

Active plasma sources

Plasma environments may be generated around a spacecraft using active plasma sources - generally electric propulsion thrusters which use a plasma beam to generate a thrust. There is now a wide range of thruster technology available, including field-emission electric propulsion (FEEP), gridded ion engines (e.g. Radio-frequency and Kaufmann), electro-

dynamic thrusters (e.g. Hall effect) and magneto-plasma dynamic thrusters. Neutralisers form an integral component of many of these systems and may be used separately (e.g. to counter natural charging).

The standard describes the different types of thrusters and their particle emissions (primary, charge exchange and neutral). The effects these produce on the spacecraft potential and on surface properties through sputtering and contamination are discussed.

Internal charging

Internal charging is the build-up of electric charge, due to particles from the external space environment, within the spacecraft structure. In many cases, this occurs inside dielectrics. However, it may also occur on electrically isolated conductors within the spacecraft. ECSS-E-20-06 describes the charging and leakage currents and how they arise. Internal charging is associated with small currents of a high-energy (>0.5MeV) radiation-belt electrons which typically vary on time-scales of hours to days. The time-scale for charging is often days or longer and is typically determined by the capacitive time-constant across the material.

Internal charging becomes a problem when the high electric fields initiate electrostatic breakdown. Immediate effects include the direct injection of large transient currents into electronic circuits or the indirect production of transient currents through electromagnetic coupling. Additionally, a discharge may cause permanent changes in material properties e.g. causing a material to be degraded as an insulator. The main contributors to the charge balance within internally charged components are current deposition from penetrating electrons and current leakage through bulk electrical conductivity which is small but not negligible in insulators. Conductivity is particularly complicated in dielectrics and varies with temperature, electric field and radiation dose-rate.

Discharges and transients

Electrostatic discharge (ESD) is a single, fast, high current transfer of electrostatic charge. It results from direct contact between two objects at different potential or high electrostatic field between two objects in close proximity, as is often the case in space. ESD may occur both on dielectrics and conductors within or outside the spacecraft. It is the main mechanism by which surface and internal charging can cause major disruption to satellite operations.

The standard describes discharge mechanisms for dielectrics including 'punch-through', 'flash-over' and 'blow-off'. A charged metal component may discharge slowly through field emission or via adjacent dielectrics through inverted potential gradient discharge.

Design and validation requirements

Surface materials

Requirements for surface materials have the effect of restricting differential surface charging to acceptable levels and thus minimising the probability of electrostatic discharge due to surface potentials. The requirements in this section reflect, to a large extent, good practice as described in NASA's 'Design Guidelines for Assessing and Controlling Spacecraft Charging Effects' [6].

Control of surface potentials is achieved principally by effective grounding throughout the spacecraft e.g.

–   where practical all surface materials should be conductive. This implies the use of conductive coatings on insulating materials.

–   coatings should be sufficiently thick to survive predicted erosion due to sputtering and atomic oxygen.

–   where possible coatings should be selected to have high secondary electron yield, in order to control absolute charging levels.

–   grounding of surface materials shall be assured:

    –   metals with small resistance to ground

    –   partial conductors (e.g. paints) with a low resistivity- thickness product

    –   conductive coatings with low resistivity–thickness product and small distance to ground.

In the event that some surfaces are left insulating, an analysis is required to show that the design is acceptable from a surface charging standpoint. The analysis must use the worst-case environment as defined in ECSS-E-10-04.

More stringent requirements are needed for scientific spacecraft, which have the measurement of ambient electric field or of low energy particles as part of their mission. In this event, surface materials must be conductive and conductive coatings must have high secondary electron yield, in order to control overall charging levels. In addition, appropriate modelling must be performed to verify charging levels. In the event that modelling reveals that charging levels are too high, then active neutralisation must be implemented.

Each design requirement requires a validation procedure and for surface materials these include visual inspection of the equipment, testing of continuity and resistance, material characterisation and charging simulation. On solar arrays, ESD can trigger secondary arcing sustained by the power of the photo-voltaic cells. Hence specific test requirements for solar arrays are described.

Internal parts and materials

Internal charging and subsequent discharge effects need to be considered early in the design cycle of spacecraft intended for the outer radiation belt, including geostationary orbit. This is because simple mitigation procedures, like conductive coatings for surface materials, are not effective for internal charging. Instead careful design of dielectric components, choice of materials and sufficient shielding are required. As was seen for surface charging, grounding is a key requirement. Metallic components must be supplied with a grounding path. This requirement includes structural elements, spot shielding, transformer cores, metal packaging of components, unused tracks on PCBs etc. Conductive paths need not be highly conductive however - a resistance of less than 10^{12} Ω will suffice for internal charging but it is practice for lower resistance to be specified for other EMC reasons.

Dielectric structures (e.g. cables) external to the main spacecraft body represent a particular hazard. These components must have the minimum thickness of dielectric insulation consistent with their primary function. This requirement arises because there is a direct relation between dielectric thickness and internal electric fields. In order to minimise the occurrence of discharges due to internal dielectric charging, electric fields within dielectric materials must be kept below 10MV/m. This can be ascertained either by simulation of sensitive dielectric components or laboratory testing in an appropriate environment. In determining the maximum electric field, a suitable worst-case model of outer belt electron fluxes must be used. A time-averaged radiation-belt model, such as AE-8 is not appropriate.

Validation is performed through a combination of inspection, testing and calculation:

−   Inspection of the structure, cable harnesses etc. to verify that there are no ungrounded metal components.

−   Resistance testing on grounded metal components

−   Testing of circuits by the application of appropriate voltage spikes

−   Verification that dielectric electric fields are acceptable:

    −   Experimental validation is difficult because a worst-case environment must be reproduced in a laboratory chamber.

    −   Computer simulation may be used to assess electric fields. For simple structures with 1-d planar or cylindrical symmetry, a 1-d analytical charge deposition and conductivity code can be used. For complicated structures, 3-d Monte Carlo simulations can be used. Both types of calculation requires knowledge of a worst case environment and the electrical properties of the material.

Testing or simulating every dielectric component is onerous and so the standard describes how this may be omitted if one of the following can be established:

−   **The material conductivity is very high**, i.e. the material of the part in question has an intrinsic bulk conductivity, at the lowest temperature in which it is to be used, that is too high to permit the creation of high electric fields. ($>2.5 \times 10^{-14} \Omega^{-1} m^{-1}$, or in geostationary orbit only $>2.5 \times 10^{-1}$ $\Omega^{-1} m^{-1}$)

−   **The part is very well shielded**, i.e. the part is sufficiently shielded that currents under worst-case natural environments will always be too small to cause hazardous levels of charging. (>5.6mm Al equivalent, or on geostationary orbit only >3mm Al)

−   **The charging current is very low**, i.e. The part is subject to a very low current density under a worst-case environment when consideration of the amount of shielding and thickness of the part is made. ($<1 \times 10^{-10}$ A m^{-2})

Tethers

Because tethers are still regarded as an experimental technology, the standard does not define quantitative requirements for the electrostatic aspects of their design. Instead, it requires that consideration be given to the key issues:

− Hazards that may arise due to voltages generated by conductive tethers.

− Current collection and resulting problems.

− Hazards arising from high currents flowing through the tether and spacecraft structures, e.g. Ohmic heating and extraneous magnetic fields.

− Continuity of insulation.

− Hazards from undesired conductive paths.

− Hazards from electrodynamic tether oscillations.

− Mechanical hazards to the spacecraft and the debris hazards to other spacecraft associated with a tether that breaks due to electrical burn-out.

− Electrostatic sticking from static electricity or environmentally induced charging.

Electric Propulsion

Electric propulsion (EP) systems employ plasmas and electric fields to provide thrust. Hence the interaction with the plasmas and electric fields of the environment may be complex. The standard makes a distinction between electrostatic processes that concern the thruster's fitness for its purpose (which are not its concern) and processes that disturb the environment and hence other spacecraft systems or environmental effects which affect the thruster (which are both the concern of this standard). Sometimes there is overlap between these areas. Both thrusters and neutralisers (even when no thruster is present) are covered.

The spacecraft charging current arising from the operation of the EP system must be completely neutralised. In general, this means there must be a neutralisation system with capacity to supply more current than the EP beam. This needs to have excess current capacity to cover natural charging currents in a worst case charging environment. For some low thrust systems e.g. FEEPs, in LEO, it may be possible that neutralisation can be achieved through natural ionospheric currents although this expected to be highly unusual and would need to be implemented only after analysis using worst case low density plasma conditions for the appropriate orbit.

Neutralisation of the space charge in the beam itself should be achieved as close to the spacecraft as possible. This is necessary to limit spacecraft contamination from charge exchange ions produced in the beam. Neutralisers should normally be located as close as possible to the EP system however, there may be instances where designers may desire to trade these effects against benefits of a simpler design e.g. where one neutraliser serves two

thrusters. Such a strategy must be based on evidence that the beam neutralisation remains acceptable.

To limit contamination, propellant for thrusters and neutralisers shall be selected with this in mind and the atoms emitted from the EP system and their spatial distribution shall be assessed. Acceptable levels of contamination will vary and need to be established on a case by case basis e.g. optical surfaces and thermal control surfaces may have lower acceptable levels than other surfaces.

Except for transient trajectories during switch-on, there should be no ion trajectories from the EP system that impinges on any other surface of the spacecraft. This is necessary to avoid sputtering of surface materials and undesirable thrust torques. Some types of thruster have strong beam dispersion at low energies and if, as a result, it is unavoidable that some ion trajectories do impinge on another part of the spacecraft, it must be established that sputtering and torques are acceptably small.

EP systems may emit substantial quantities of neutral gas. The level of plasma density around the spacecraft due to neutral gas emission must be assessed and consequential discharging through the gas must be considered.

Validation of EP systems is achieved mainly through ground testing and computer modelling. Both of these approaches have limitations and careful consideration needs to be given to using complementary experimental and computer simulations to provide confidence in different aspects of a design. For systems with flight heritage, in-flight performance monitoring may provide further validation.

Informative section

Requirements for validation of a design are termed in ways that exclude references to specific analysis techniques and tools. However, it can be useful for users how they can to meets these requirements with currently available methods. The standard includes an informative section where some of the techniques and tools are described, including measurement sensors, surface and internal charging simulation codes and material characterisation methods.

Conclusions

We have presented some aspects of the ECSS-E-20-06 standard, currently nearing completion. It brings together best practice from a number of areas to form a comprehensive set of requirements governing the control of hazards resulting from spacecraft/plasma interactions. The draft standard is expected to be issued soon for review and the spacecraft charging community is invited to contribute to its improvement before it is, hopefully, formally adopted by ECSS.

Members of the ECSS-E-20-06 Working Group

A.Hilgers, E.Daly, L.Gerlach, A.Ciccolella, M.van Eesbeek, M.Fehringer, J.Gonzales, M-L.Fille, E.Gengembre (ESTEC, Noordwijk, The Netherlands)

D.J.Rodgers, N.Wallace (QinetiQ, Fanborough,UK)

L.Eliasson (IRF, Kiruna, Sweden)

D.Payan, J.P.Catani, C.Predine (CNES, Toulouse, France)
M.Tajmar (ARC Siebersdorf, Austria)

P.Pelissou (Astrium, France)

P.Hill (Astrium, Germany)

L.Levy, A Bondiou-Clegerie (ONERA, Toulouse France)

J-J.Berthelier, (IPSL, France)

References

1. ECSS-P-00A, Standardisation Policy, ECSS Secretariat, ESTEC, The Netherlands, issued April 2000.

2. ECSS-E-10-04A Space environment, issued 21 January 2000

3. PSS-01-701, Data for Selection of Space Materials, EUR 20 Rev.3, 15 March 1994

4. ISO TC20/SC14 WG4 Space Environment web site http://www.magnet.oma.be/iso/

5. Martin A.R., D.J.Rodgers, R.L.Kessel, A.D.Johnstone, A.J.Coates, B.N.Maehlum, K.Svenes and M.Friedrich, 'Spacecraft/Plasma Interactions and Electromagnetic Effects in LEO and Polar Orbits', Final report on ESA contract no., 7989/88/NL/PB(SC), Culham Report no. CLM/RR/E5/7, 1990

6. 'Design Guidelines for Assessing and Controlling Spacecraft Charging Effects', NASA TP-2361, 1984.

MODELING OF THE PHOTOELECTRON SHEATH AROUND AN ACTIVE MAGNETOSPHERIC SPACECRAFT WITH PICUP3D

Benoît Thiébault
Space Environments and Effects Section (ESA-ESTEC/TOS-EES)
Keplerlaan 1, 2200 AG Noordwijk, The Netherlands
E-mail: Benoit.Thiebault@esa.int

Alain Hilgers
Julien Forest
Space Environments and Effects Section (ESA-ESTEC/TOS-EES), The Netherlands

Philippe Escoubet
Michael Fehringer
H. Laakso
Space Science Department (ESA-ESTEC/SCI), The Netherlands

Abstract

Emission of photoelectrons by the sunlit surfaces of a spacecraft can affect the plasma environment via the resulting spacecraft potential but also via the induced space charge. The photoelectron cloud structure around Cluster has been investigated with the PicUp3D plasma simulation software taking into account the plume of the onboard ion emitter. Preliminary results are presented related to the shielding of the ion emitter plume by the photoelectron and on the propagation of the photoelectrons around the spacecraft and along the wire booms. Conclusions are drawn related to the possible influence of these effects on electrostatic sensors mounted at the end of long (>40 meters) wire boom antennas.

Introduction

A number of scientific spacecraft have embarked scientific payload dedicated to the investigation of the solar wind interaction with the magnetosphere and other magnetospheric phenomena and massively rely on plasma and field measurements in three dimensions of space. In many occasions, electric field measurements are performed via pairs of electric sensors mounted at the extremity of long wire booms. Occasionally, a spurious electric field has been observed in the spin plane. Four main processes have been suspected to be the cause of such spurious electric fields:

- a wake effect which creates asymmetric environment around the probes [1];
- the effect of active ion emitters plume space charge when operating;
- the effect of the photoelectron space charge [1];
- the effect of asymmetric currents of photo-electrons to the probes [1];

The recent Cluster experiment which is constituted by a fleet of four magnetospheric spacecraft equipped with slightly redundant instruments to measure the electric field allowed to investigate in depth the occurrence of spurious electric field and their possible cause. The modelling of the first effect is currently being studied by the IRF group in Uppsala (Eriksson, private communication) while efforts to model the last three effects have been made at ESA-TOS/EES using the PicUp3D simulation code [2] and the preliminary results are reported in this paper.

Spacecraft and environment characteristics

Each spacecraft of the Cluster mission is approximately a cylinder with height 1.2 m and diameter 3 m. The booms in the spine plane are about 42 meters long with electrostatic sensors at the extremities opposite to the spacecraft. The wire booms thickness is of the order of 1 mm. An ion emitter called ASPOC is mounted on near the edge of the top side of the spacecraft. It is used to reduce the floating potential of the satellite, which can otherwise reach up to 40 V in the magnetospheric lobes.
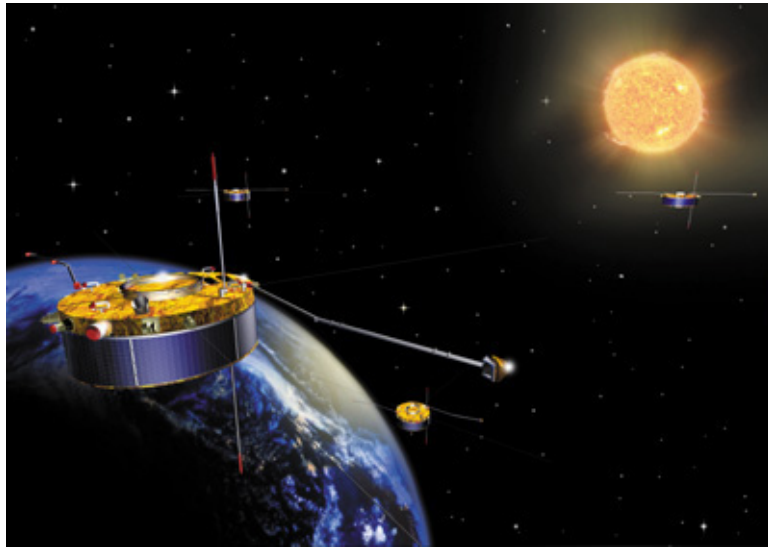
Figure 1. Artist's view of the Cluster satellite

Electrostatic and plasma environment

The Cluster satellite crosses different plasma regions along its orbit with very diverse plasma conditions. It was reported that the spurious electric field was mainly observed in the magnetospheric lobes were the plasma temperature is about 100 eV and the density as low as 0.1 particle cm^{-3} which implies a Debye length is about 235 m. With such plasma conditions and due to the photo-electron emission, the spacecraft potential is typically of about 40 Volts when the ion emitter is off and about 7 Volts positive when the ion emitter is on. The photo-electron emission current density at saturation has been measured and is of about 50 μA m^{-2}.

Simulation parameters and constraints

The code used in this study is PicUp3D [2]. It is a simulation software designed to model spacecraft plasma interactions. It is developed with an open source approach, written in Java programming language and is freely available on the web. The algorithms are based on a 3D Particle-In-Cell (PIC) kinetic description of ions and electrons to simulate plasma dynamics.

The size of the simulation box is driven by the need to include the spacecraft and the antenna and its sheath (typically a few Debye length), which is expected to be even more extended along the ion beam. Therefore, a very large computation box is required. For this study simulation box with a size L_{box} varying between 120 m and 450 m has been used. Since PicUp3D algorithms are based on a rectangular mesh the use of such box sizes together with the memory limitation implies a rather low spatial resolution. Typical values of the

spatial resolution were of the order of 1 meter allowing the number of computation node to be between 80x80x80 and 150x150x150. Therefore the spacecraft geometry could not be very accurately described, and especially the booms, nor the electric field very close to the surfaces.

Furthermore, a very accurate potential description was required (± 0.1 V) to match the observed level of the spurious electric field. Therefore, a high number of macro particles was used (typically 5.10^6) to achieve a good statistical description and averaging over many plasma periods was necessary.

A small time step, dt, had to be used to accurately compute the particles trajectory (dt < $0.1* 1/\omega_{pe}$, where ω_{pe} is the plasma frequency) and the time of computation to reach the equilibrium was very long (~ 100 * $1/\omega_{pe}$).

All these constraints lead to highly demanding simulations in term of computing resources. They also have an impact on the accuracy of the results and doubts could be raised on the relevancy of the results in the most extreme situations. Therefore, the approach used in this study was to perform a series of simulations corresponding to increasing complexity in term of the constraints put on the simulation. Typically, one performed a series of three simulations with increasing Debye length. Only the last one corresponds to the relevant environment where the spurious electric field is observed, however, the reality of the phenomena can be checked with the two first simulations for which the confidence of the results is higher. The simulation parameters are shown in Table 1 below.

Simulation parameters

Table 1. Simulation parameters for 3 cases corresponding to increasing Debye length.

Simulation	n_0 (cm^{-3})	T_0 (eV)	λ_D (m)
Case 1	1	1	7.43
Case 2	1	10	23.5
Case 3	0.1	100	235.

Where n_0 is the plasma density, T_0 the temperature and λ_D the Debye length. The ion emitter was simulated only through its ion space charge that was assumed constant and only depending on the ion emitter current, I_{ASPOC}. For all simulations the following parameters to describe the ion emitter plume and the photo-electron current were used.

T_{pe} = 2.5 eV (photo-electron temperature)
J_{pe} = 50 µA/m^2 (photo-electron current density at saturation)
I_{ASPOC} = 10 µA (Ion emitter current)
E_{ASPOC} = 10 keV (Energy of emitted ions)

Furthermore, the simulations were performed in all cases once with the wire booms and another time without the wire booms.

Simulation results

Ion beam shielding

Figure. 2 shows a meridian cut of the potential in the simulation cases 2 and 3 without wire booms. The effect of the ion beam space charge is clearly seen along the Z axis (perpendicular to the sun and to the spine plane). However, it can be seen that it is very efficiently shielded by the ambient plasma electrons and the photoelectrons in direction perpendicular to the Z axis.
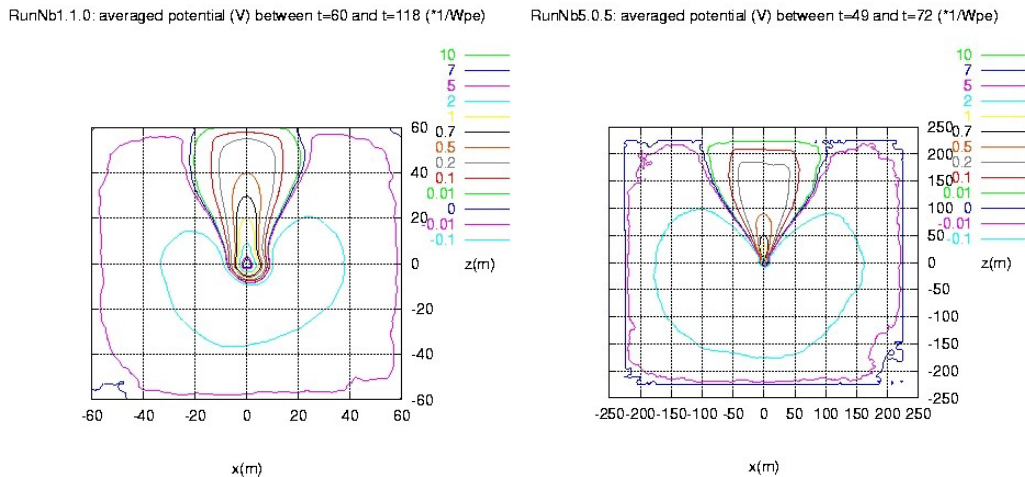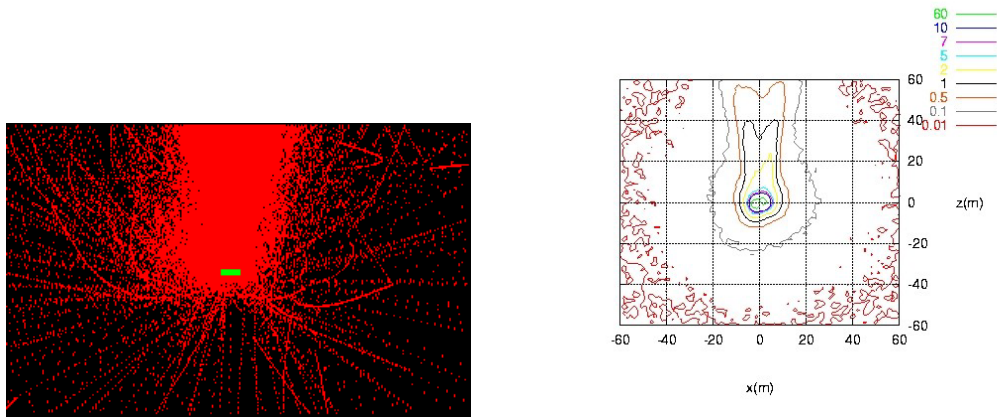

Figure 2. Case 2 (left) and case 3 (right) potential maps. The sunlight comes from the left

The positive potential typically vanishes within about 20 meters from the Z axis. Therefore, the possible influence of the ion space charge on the electrostatic probes located 40 meters apart from the spacecraft can be ruled out.

Photoelectron space charge

A set of photo-electron trajectories shown in Figure 3 below in a case without wire booms illustrates how the photo-electron are shielding the ion space charge. Furthermore, a significant amount of photo-electrons propagates relatively easily very far from the spacecraft. The photo-electron density is shown on the right panel of Figure 3. This photo-electron behaviour explains why instead of a positive potential one rather observes a negative potential beyond 20 meters across the ion beam. It results a negative potential barrier as shown in the potential profile along the X axis drawn on Figure 4. The reality of such barriers is discussed elsewhere in this conference [3]. The value of the photo-electron induced potential disturbance is relatively high (slightly less than 0.01 V) but marginal compared to the magnitude required to induce the observed spurious electric field. Furthermore, it must be noted that in absence of wire booms, the PicUp3D simulations predict a rather symmetric photo-electron cloud beyond a few meshes from the spacecraft surfaces. However, this aspect must be taken with caution since it may be an artefact due to the poor resolution near the spacecraft surface.

Figure 3. Set of photoelectron trajectories around the spacecraft and the ion emitter plume (left panel) and corresponding density contours in Z*X plane (right panel).The sunlight comes from the negative X values.
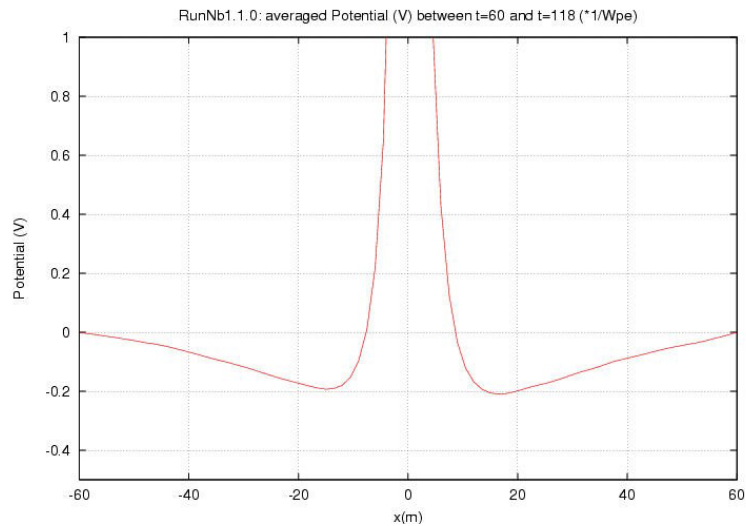

Figure 4. Case 2 potential cut along the sunlight axis. The sunlight comes from the left

Asymmetric photoelectron cloud and possible influence of the booms

The photoelectron density dominates over the ambient plasma density up to a factor 60 near the sunlit surfaces. However, at the electrostatic probe position, the photoelectron density is negligible with respect to the ambient density and should not in this case directly induce an asymmetry of the measurements.

The simulations performed while taking into account the wire booms provide a completely different picture. The density of photo-electrons and the corresponding potential distribution when booms potential is taken into account are shown in Figure 5. As shown on the density map, the positive boom may guide photo-electrons very efficiently toward the end of it. In absence of any active potential barrier, the density at the electrostatic probe would be dominating over the ambient plasma. Furthermore, the density is this time asymmetric, more photo-electrons propagating in the sunward direction than in the anti-sunward one. However,

in reality there are small a few centimeters segments of the boom biased at a negative potential which may repel the photo-electrons. Unfortunately, the resolution accessible on current standard computing machines with PicUp3D does not allow testing properly the efficiency of these guards.
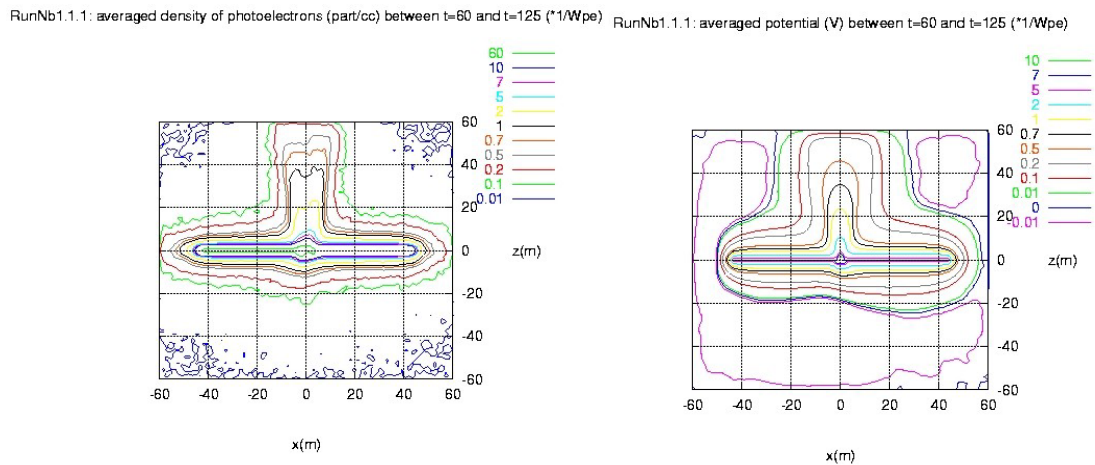
Figure 5. Case 2 photoelectron density map (left) and potential map (right) in a simulation taking the wire booms into account. The sunlight comes from the left

Conclusion

A full 3D modelling of the electrostatic sheath of a magnetospheric spacecraft equipped with an ion emitter has been attempted in plasma regions where the Debye length is very large compared to the spacecraft hub dimension. Although the quantitative output suffers from a strong uncertainty related to the coarse meshing, these preliminary results give evidence of complicated sheath structures influenced by the following factors:

- Ion beam space charge (but not beyond a few meters across the beam).
- Photo-electrons (evidence of negative potential barrier and long ranging influence, i.e., up to 40 meters away from the spacecraft hub).
- Wire booms (guide photo-electrons to very long distance with sun/shade asymmetry).

The photoelectron cloud has been identified as a potential problem that may induce spurious electric field due to an asymmetric guiding along the booms. However, a quantitative prediction of the spurious electric field requires much more detailed geometric description of objects (booms, guards detectors and sources). This would be possible only with the use of meshing techniques, which may cope with ratio of size varying from 1 mm for accurate modeling of the wire booms to hundred meters (boom length), which is the size of the sheath.

Acknowledgments

References

1. Pedersen, A., C. A. Cattel, C.-G. Faelthammar, V. Formisano, P.-A. Lindqvist, F. Mozer, and R. Torbert, Quasistatic electric field measurements with spherical double probes on the GEOS and ISEE satellites, Space Sci. Rev., 37, pp 269-312, 1984.

2. Forest J., Eliasson, L., Hilgers, A.: "A New Spacecraft Plasma Simulation Software, PicUp3D/SPIS", 7th Spacecraft Charging Technology Conference, Proceedings pp.515-520, ESA/SP-476, ISBN No 92-9092-745-3, ESA-ESTEC, Noordwijk, The Netherlands, 23-27 April 2001.

3. Thiébault, B., Hilgers, A., Sasot, E., Forest, J., Génot, V., Escoubet, P.: "Investigation of Electrostatic Potential Barrier Near an Electron-Emitting Body", Proceedings of the 8th Spacecraft Charging Technology Conference, Huntsville, AL, October 20-24, 2003.

FEASIBILITY STUDY OF AN EXPERIMENTAL PLATFORM WITH ACTIVE PLASMA EMISSION FOR JAPAN EXPERIMENTAL MODULE ONBOARD ISS

Hideyuki Usui
Radio Science Center for Space and Atmosphere, Kyoto University,
Gokasho Uji, Kyoto 611-0011, Japan
Phone: +81-774-38-3817
Fax: +81-774-38-3817
E-mail: usui@kurasc.kyoto-u.ac.jp

I. Funaki
Japan Aerospace Exploration Agency

Y. Nakayama
National Defense Academy, Japan

H. Tashima
RASC, Kyoto University, Japan

H. Kuninaka
Japan Aerospace Exploration Agency


M. Okada
National Institute of Polar Research, Japan

Abstract

A Japanese experimental module (JEM) onboard the international space station (ISS) is directly exposed to space, hence if a plasma device is equipped to the exposed facility of JEM, many kinds of new plasma experiment become possible. However, there is a concern that by emitting plasmas, spacecraft charging and corresponding discharge will severely damage JEM and even ISS. We are proposing an experimental module for JEM in order to clarify such spacecraft-plasma interaction by operating a sub-scaled plasma-emitting floating body that can be deployed from JEM with some diagnostic equipment. Prior to the design of such a plasma experimental facility, strict assessment on the plasma environment around the plasma emitting device should be finished. We particularly focus on the transient response to the plasma emission. In this paper, the need and concept of the plasma experimental module for JEM are described with some initial results obtained in ground experiments as well as PIC simulations.

Introduction

Since 1960s, there were many space plasma experiments that actively emit charged particles in such forms as electron- or ion-beam from the satellites. Among them, spacecraft charging experiment by such projects as SCATHA, ATS-6, in which the first spacecraft charging, and even successful control by those plasma beams were completed [1]. However, these experiments require a whole spacecraft system that is developed for the specific experiments and available for

only a short-term mission period. If a platform for plasma experiment is continuously executable in ISS, international space station, these opportunities will place a great impact on both scientific as well as engineering point of view. Based on such an idea, we try to propose a plasma experimental module for Japanese Experimental Module (JEM), that utilizes JEM's unique feature, whose experimental module is directly exposed to space [2], accordingly, ideal plasma experiment in semi-infinite space becomes possible. Prior to the design of such a plasma experimental facility, strict assessment on the plasma environment around the plasma emitting device should be finished. In this paper, the need and concept of the plasma experimental module for JEM are described with some initial results obtained in ground experiments as well as PIC simulations.
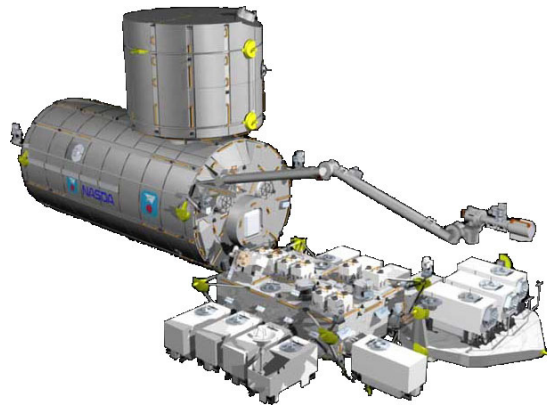
**Figure 1. Japanese Experimental Module (JEM) on ISS.**

Problems Caused by Artificial Plasma Emission from Spacecraft

Among several charge exchange mechanisms such as inflow- and outflow-charged-particles, and photoemission, current accompanied by active plasma emission can be very large and dominant. In the ionosphere, a spacecraft is usually charged to a negative potential because of high energy electrons incident on the spacecraft. To prohibit charging and corresponding discharging, a plasma contactor is employed for the ISS. Because a floating body emitting electron tends to fix its potential to that of surrounding plasma, the plasma contactor can be used to adjust the spacecraft potential to the space potential. For this case depicted in the left figure in Fig.2, electrons will flow into a positively biased solar paddle, leading to electrical power loss. In contrast, if a spacecraft emits only ions, the spacecraft potential becomes a negative value around the beam potential. From the negatively biased spacecraft, the ions cannot leave the spacecraft, hence ions will reflect back to the spacecraft. This case corresponds a spacecraft with an ion engine system that has a disordered neutralizer [3].

These cases of steady state charging are easy to consider. Some difficulties arise when a transient profile has to be considered. Transient change of spacecraft potential is roughly expressed as,

$$C dV/dt = I_b + I_{etc} \qquad (1)$$

where V is spacecraft potential, I_b is artificially emitted current, I_{etc} is other current other than I_b. Here, C, capacitance of a spacecraft, is proportional to the spacecraft size, hence, if a small spacecraft ejects large current, V changes very quickly. For example, a $1m^3$ size satellite emitting 100mA/1.5kV ion beam, V changes 1.5 kV in less than 1 ms. For such a rapid potential change, ambient plasma cannot respond, hence the spacecraft potential will continue changing, leading to severe discharging between the spacecraft with a negative potential and ambient plasma, which could damage the spacecraft electrical system. For the case of ISS's plasma contactor is in disorder, the above mentioned discharge and corresponding damage of the ISS can occur. However, such interaction is difficult to predict because the phenomena will depend on: how far the emitted artificial plasma is extended when the discharge starts; or whether the discharge is restricted to only near the spacecraft surface, or large scale discharge involving ambient plasma is expected. These parameters will be determined by the spacecraft size, the scale of artificial plasma emission, and ambient plasma condition. Since artificially emitted plasmas are moving fast and the potential change and expansion is very rapid, a ground testing simulating the real plasma field, or even numerically prediction, is difficult. A mixture of dense near-field plasma and weak far-field plasma further complicates the problem. Our purpose of plasma experimental module for JEM is to scale down such interaction by changing C/I_b values.
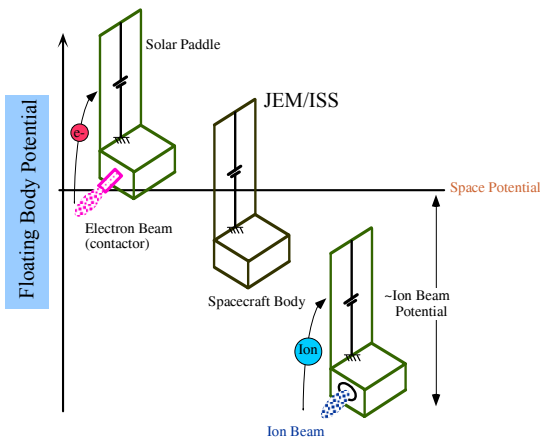
Figure 2. Spacecraft charging by artificial plasma emission
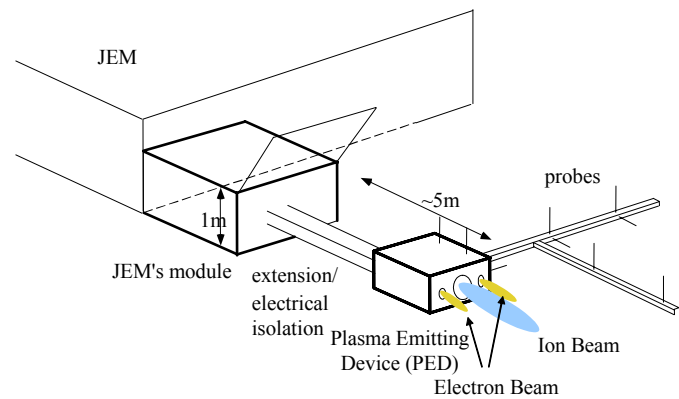
Figure 3. Plasma experimental module for JEM

Concept of Plasma Experimental Module on JEM

Preliminary design of the plasma experiment module is as follows. It consists of an ion source and electron sources both are powered by C-band microwave as shown in Fig.3. Both sources can be operated separately, hence, by starting up or shutting down each of the sources, transient potential profile of both bodies as well as ambient plasma response can be evaluated, the latter of which will be conducted by a diagnostic package of the module using Langmuir probes. Also, by throttling the ion source and changing the bias voltage between the two electron sources, the setup easily operates in a plasma contactor mode, in which ambient plasma parameters are independently changed into a desired parameters by the leaking plasma from the

ion source; this is possible because the ion or the electron source can be easily controlled by changing microwave power. The first plasma experiment is, as mentioned, a scaled down simulation of the charging process of ISS itself. In the experiment, the transient profile of the coupling among a scaled-down plasma contactor, ambient plasma, and the module's body, will be measured. To obtain such transient plasma, plasma emission device (PED), which consists of an ion source and two electron sources, is powered by a battery. As in Fig.4, when opening SW3, PED's battery is charged up. Then, SW1 and SW2 is opened, and power of the battery is supplied to power supplies of PED such as microwave amplifier, and DC power supplies, after a controller start the PED's operation. For a period the battery continues, we have a transient plasma evolution both from the ion source and the neutralizers (NEUT1 and NEUT2). The PED is one of subsystems of our plasma experimental module (PEM). We have three ion/electron sources (PED1 to PED3), whose batteries are powered by the base system of PEM. This base system not only supplies the power to the PEM, but also controls a plasma diagnostic package (PDP) to qualify the transient plasma evolution around the spacecraft. Hence, the PEM will acquire data concerning the operation of PED, and plasma data near the PED. The PEM itself follows the standard guideline of the design of JEM; it is powered from JEM, it will receive and forward any command and acquired data via JEM's telemetry system directly connected to a ground station. The experimental module will be firstly placed in one of the JEM module in a size 1 m x 1.8 m x 1 m, then being deployed to the PED and the PDP as was depicted in Fig.3. The PEM and its subsystem hence contain a motor driver that extends/stores the PEM for that purpose.
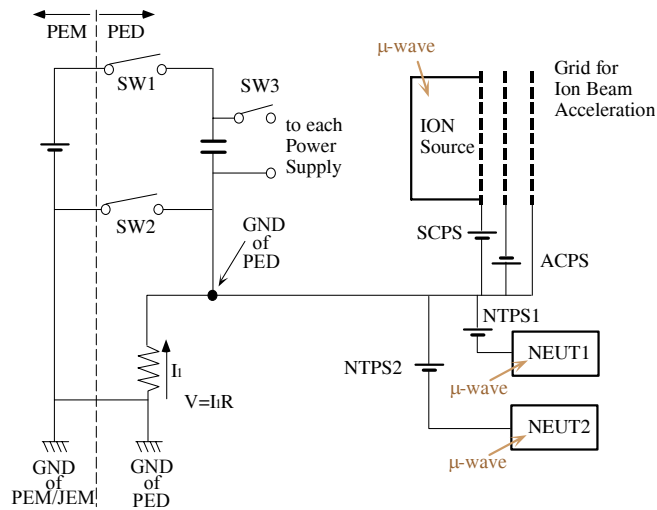
Figure 4. Electrical connections of plasma experimental module

Note that as in Fig.4, PEDs are electrically isolated from PEM, hence a change of spacecraft potential is directly measured by obtaining I_1 in Fig.4. Such a floating system requires careful assessment whether the plasma emission affects the entire system or not. The below experimental device is being prepared to conduct such assessment prior to the specific design of the PEM.
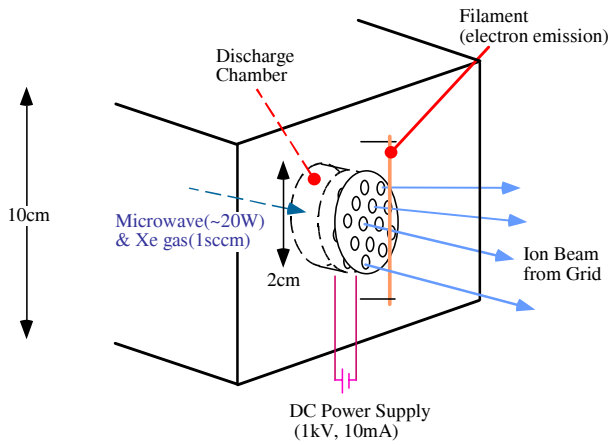
Figure 5. Plasma emitting device (lab. model)
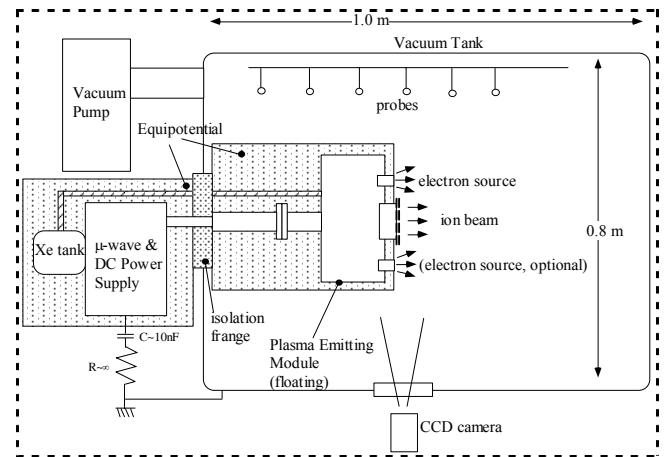
Figure 6. Experimental setup for charging test

Experimental Setups for Preliminary Ground Tests

We have completed preliminary evaluation of the low-power plasma emitter in a space chamber in the institute of space and astronautical science (ISAS). The plasma emitter shown in Fig.5 is located in a conductor body, and operated in a total power of 30 W, including an ion optics that accelerates ions up to 1 kV beam, and a filament type neutralizer.

The main body of the ion source features a very small discharge chamber of 18 mm inner diameter, which almost coincides with microwave neutralizer [4]. The Xe propellant pressure inside the chamber is controlled by a 4-mm-wide orifice diameter; with the conductance of the orifice below 1, the inner pressure is kept at 0.67 to 1.3 Pa for the Xe mass flow rate of 0.5 - 2.0 sccm. Microwave of 4.2 GHz is fed through a coaxial line followed by an L-shaped antenna, whose tip is inserted into a magnetic field formed by front- and back- yokes and block magnets. The strong magnetic field above the ECR condition enables easy startup of the neutralizer, so plasma density, hence the available ion current, can be increased just by increasing the microwave power for this type of discharge chamber. With its quick ignition feature, the microwave powered source is considered appropriate for transient study because there is no time delay after the switch on. However, at this time, only the ion source was powered by microwave.

To simulate floating spacecraft in space, the plasma emitter and the power supplying unit outside the space chamber are electrically isolated from the ground (Fig.6).

Charging Experiment of Plasma-Emitting Floating Body in Vacuum Chamber

For the experimental configuration in Fig.6, steady plasmas with ion and electron emission were achieved. Plasma parameters are summarized in Table.1. By scaling down the plasma source and the body size, the ratio between the body size and the Debye length was almost the same both for the real scale, 1m^3 satellite, and for the simulated scaled-down model. This proves that such a scaling-down is effective to study the interaction between the spacecraft and the plasma emitter as far as steady plasma is concerned.

Table 1. Plasma environment for laboratory model

|	Small plasma source	1m^3 satellite with ion thruster
Ion beam diam.	20mm	100mm
Ion beam current	8mA	140mA
Ion beam current density	18Am^{-2}s^{-1}	25Am^{-2}s^{-1}
Ambient Plasma Density	3e14m^{-3}	1e12m^{-3}
Beam Plasma Density	1e16m^{-3}	2e15m^{-3}
Ambient Debye length (l_{Denv})	1mm	16mm
Beam Debye length (l_{Dbeam})	0.16mm	0.37mm
Representative length (L)	10cm	1m
L/ l_{Denv}	100	62.5
L/ l_{Dbeam}	625	2700
Capacitance	2nF	10pF
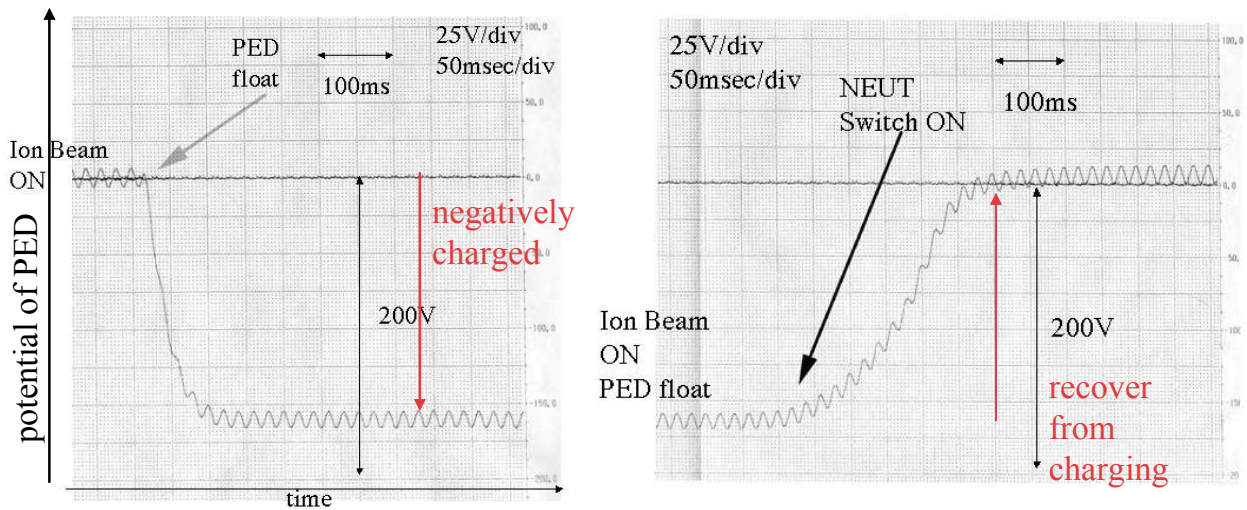
**Figure 7. Transient potential profiles of floating body.
Ion beam emission (left) and neutralization by electron emission (right).**

   In addition to these representative plasma emission, data for some unusual operation was obtained: for example when a neutralizer is switched off. The body potential dropped to a negative value around the beam potential, accompanied by a virtual cathode in front of the ion source. From the virtual anode, ions are reflected back to the body, which will suppress further charging by ion emission. This is why the ion emitting spacecraft stays at its beam potential. For steady operation including this unusual case, interactions are confined to the field only near the body. Thus if the module is located far from the JEM, no interaction is expected.   However, we need to obtain an evidence of this fact for our experimental module, in particular, for transient plasma, that is not examined in the above experiment. Most of such cases can be checked in ground tests, but difficulties are associated when considering the effect of the vacuum chamber wall. The assessment hence requires a numerical technique that will bridge the ground test condition and the model for the JEM.

As for transient plasma evolution, we have obtained only limited test cases. The result in Fig.7 shows potential profiles of the floating body; in left panel of Fig.7, while only ion beam is emitted and GND of the body is set to chamber's GND, the GND of the body was suddenly changed to floating. For the ion beam voltage 200 V, the potential of the body was reduced to -160 V, whose absolute value is close to the beam voltage. Also, characteristic time to reach its steady state is discussed. Follows the approximation of Eq.(1), that is, $dt \sim CdV/I = 2e-9[F]*200[V]/4e-3[A] = 100ms$, which corresponds to characteristic time for charging. In Fig.9-b, after following the procedure in right panel of Fig.7, the neutralizer was switched on. The charging was stopped and the potential of the floating body was recovered to around 0 V. Transient changes of the above cases are, however, rather quiet cases because of a large time scale. This large time scale is a result of large capacitance between the PED and GND, which was inevitably inserted due to electrical connections between the PED and the power supply. For a rapid charging experiment to execute, we have to reduce this capacitance, and to increase the current emitted from the body. Such fast time scale experiment is the next step of our research.
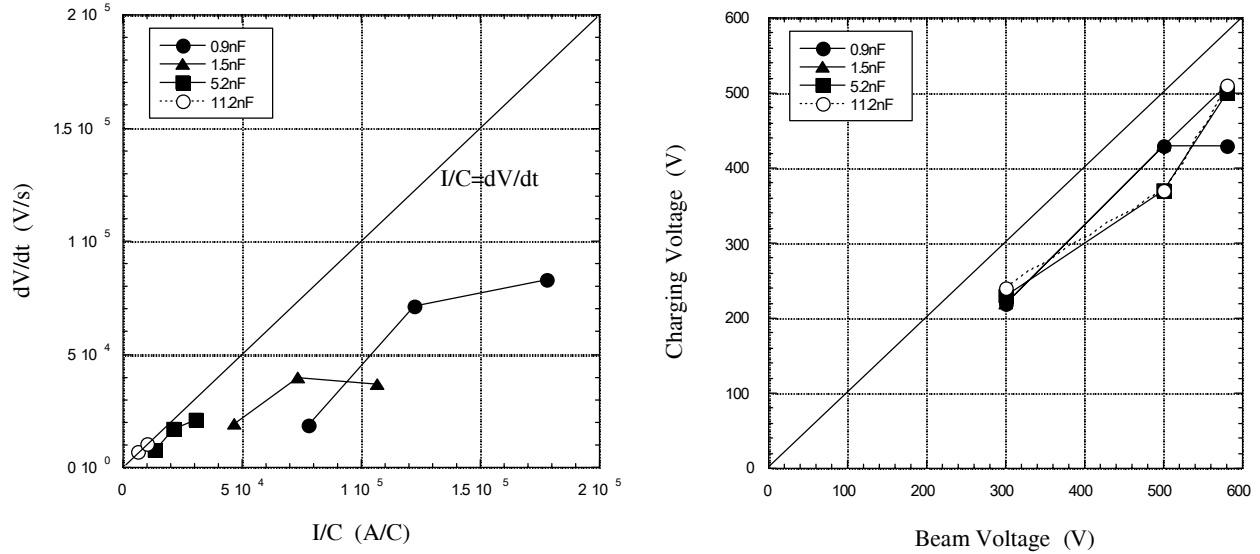
Figure 8. Transient responses of the floating body potential (left panel) and steady state charging (right panel) at ion beam emission; experimental results of the ground test; total capacitance is 0.9nF, 1.5nF, 5.2nF and 11.2 nF; ion beam voltage is 300 to 580 V.

In the next step, transient charging phenomena of the body were experimentally studied for various ion beam currents and ion beam voltages. The currents and the voltages of the ion beam can be easily controlled by changing the acceleration voltage of the small ion source. Also, by inserting an additional capacitance to the circuit, total capacitance of the body, hence the time scale of charging, will be selected for each condition (i.e., a combination of an ion beam current and a voltage) following the equation below.

$$I = I_b = CdV/dt \qquad (2)$$

In left panel of Fig.8, voltage changes at the time that the ion beam emitting body being connected to a ground was suddenly isolated, and the beam emitting body becomes "floating

body". I/C=dV/dt line in left panel of Fig.8 corresponds to the case the charging time scale is strictly determined by (2), however, for larger I/C values, the values of dV/dt deviate from (2), which means transient responses of the floating body potential is complicated than expected. In contrast to these transient responses, charging voltages at their steady states are not affected by the parameters, I and C, as shown in right panel of Fig.8. The charging voltages are slightly different from the ion beam voltages due to the secondary electron emission by ion impacts.

It is important to discuss how the above transient charging tests in the ground chamber will apply to a realistic spacecraft. To simulate spacecraft charging in space, in addition to the parameters in Table 1 (body size, the ion beam current, the ion beam voltage, the ambient plasma), the I/C parameter should be carefully chosen. Since the capacitance of the spacecraft is roughly approximated by a conductor body with known radius, the relation between the spacecraft size and the capacitance is easily obtained.   Then, the I/C is determined if the beam current I is available. The beam current I will depend on the condition what kind of plasma device is operated in what power level. For example, the ISS employs 10A-class plasma contactors, while many commercial satellites are equipped with 0.1 to 0.5 A-class ion thrusters for north-south station keeping.   We are planning to make a device that can simulate charging phenomena which occurs in a very short time scale, two orders of magnitude smaller than our current experiment. Such a fast charging will be discussed in the future with a compact but large beam current source.

Numerical Simulation

Aside from the experimental works, numerical evaluation of the spacecraft charging is very important. One reason is that the spacecraft charging always occurs in an infinite space, that is very difficult to realize in a limited space inside the space chamber on the ground. In this sense, a numerical code is a versatile tool for the evaluation of the spacecraft charging. Another reason is that for the ground testing, due to the effect of electrical connections accompanied by additional capacitances to the circuit, the charging tests cannot obtain a very fast time scale as in space even if the current of the beam is increased. As a result, only some similarity rules on spacecraft charging can be achieved from the ground tests, but a realistic situation should be predicted by the numerical method. Both the experiments and the simulations hence have different roles, therefore we need both tools to assess the transient phenomena of the spacecraft charging.

We performed three-dimensional electrostatic PIC simulations including charge-exchange effect which produces slow ions in the vicinity of plasma emitting device and can affect the plasma plume distribution as well as the dynamics of exhausted ions. Figure 9 shows preliminary simulation results of one of the charging experiment in the space chamber that was already described in this paper.   In three panels of Fig.9, we show the spatial distribution of emitted ions. Near the center of the space chamber, a floating body starts emitting an ion beam, which is just leaving the floating body at an early stage of the charging experiment. Then the potential of the body decreases as in the right bottom panel of Fig.9, because the floating body ejects positively charged particles. The ions leaving the floating body then slowdowns due to the potential slope and a potential hill is formed near the beam emitter where slow ions reside and accordingly the space potential in front of the beam emitter increases. The potential of the body continues

decreasing, until most of the emitted ions will be reflected back to the floating body, forming a current loop. This situation is shown in Fig. 10 as a velocity phase plot of emitted ions. Lastly, the potential of the body will reach its steady state. In this process, some beam-instability can occur by the interaction between forward emitted ions and returning ones. This possibility should be carefully examined because the plasma instability may cause the turbulence of plasma environment in terms of particle heating and field interference in the vicinity of spacecraft. We will examine this possibility by changing the beam parameters as well as the spacecraft configuration as a future work. The preliminary simulation successfully reveals the movements of charged particles, and the process of the transient charging of the body. Using this code, variety of transient charging phenomena can be investigated. Also, we are now incorporating the effect of insulators to evaluate realistic spacecraft to plasma interaction.
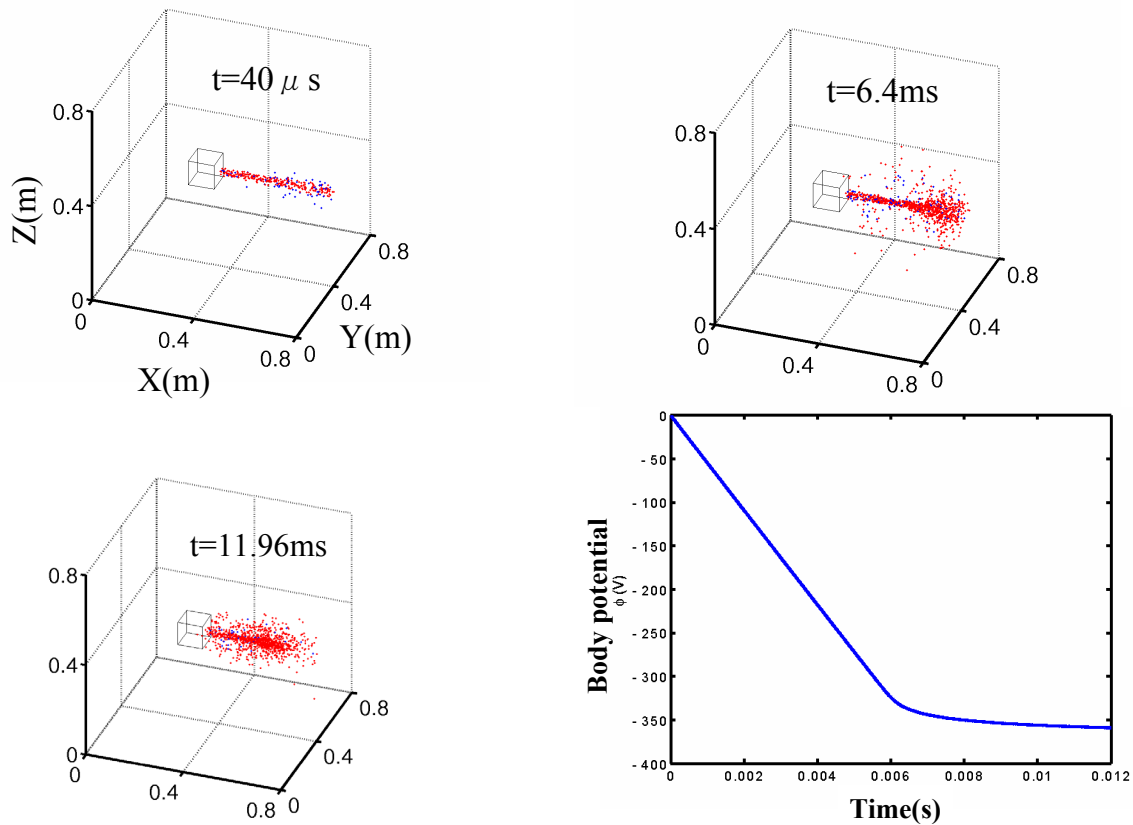
Figure 9. Temporal evolution of ion distribution obtained by PIC simulation. Ion current is 0.07mA, Ion beam voltage is 300 V (three panels). Temporal variation of the body potential (the right bottom panel).
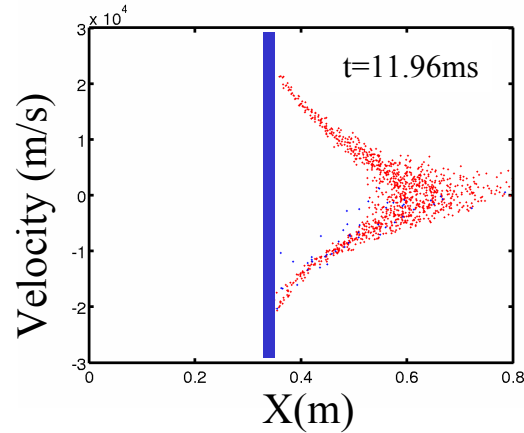
Figure 10. Ion velocity versus position. Most of the emitted ions stagnate and return to the body location at X=0.35m

Summary

We proposed a plasma experimental module that is targeting at and designed for JEM's outside modules. Utilizing JEM's unique feature, that is, a compact space experiment is directly exposed to space, many plasma experiments in infinite space become possible. Future evolution includes high powered electric propulsion, the interaction of SSPS (Space Solar Power System) and plasma, or to demonstrate difficult physical and engineering problem like mini-magnetosphere plasma propulsion. However, before going into a full-scaled experiment, an assessment is required for the interaction between manned spacecraft, JEM, and active plasma experimental module (PEM). Because we don't know the detailed scaling of such interactions, our first mission of the PEM is decided as a scaled-down demonstration of the interaction between emitted plasma and the PEM. This module for demonstration includes both plasma generator and a plasma diagnostic module, which can be deployed as one of JEM ⊐ s module. The main purpose of the scaled-down module is to reveal transient plasma evolution and transient potential change of the PEM, that will lead to severe discharging, hence hazardous for JEM. An operational limit below which the plasma system is safely used should be surveyed and decided in the future studies by ground experiments and PIC simulations.

References

1. Lai, S.T., An Overview of Electron and Ion Beam Effects in Charging and Discharging of Spacecraft, IEEE Trans. Nuclear Science, Vol.36, No.6, Dec. 1989, pp.2027-2032.

2. http://jem.tksc.nasda.go.jp/iss/doc09.html

3. Kuninaka, H., Funaki, I., Nishiyama, K., and Nakayama, Y., Virtual Anode Phenomena due to Lack of Neutralization on Ion Thrusters Based on MUSES-C Program, AIAA2001-3785, 37th AIAA/ ASME/ SAE/ ASEE Joint Propulsion Conference & Exhibition, Salt Lake City, U.S.A., July 2001.

4. Funaki, I., and Kuninaka, H., Overdense Plasma Production in a Low-power Microwave Discharge Electron Source, Japanese Journal of Applied Physics, Vol.40, Part 1, No.4A, 2001, pp.2495-2500.

ONSET OF SPACECRAFT CHARGING IN SINGLE AND DOUBLE MAXWELLIAN PLASMAS IN SPACE: A PEDAGOGICAL REVIEW

Shu T. Lai
Space Vehicles Directorate
Air Force Research Laboratory
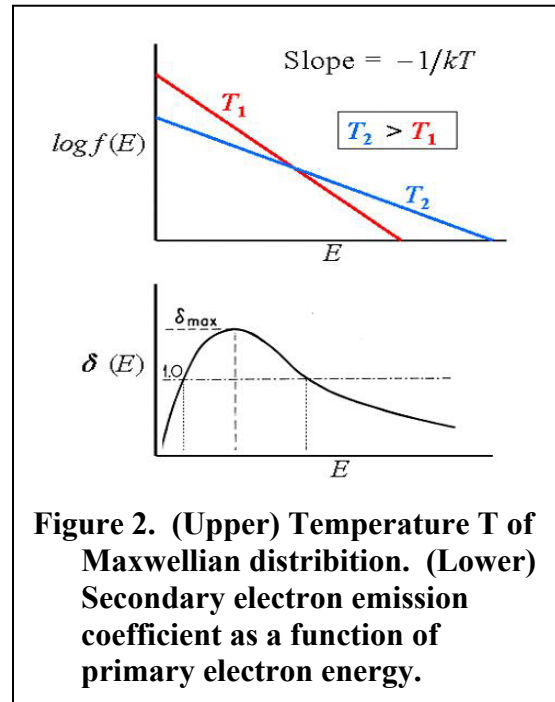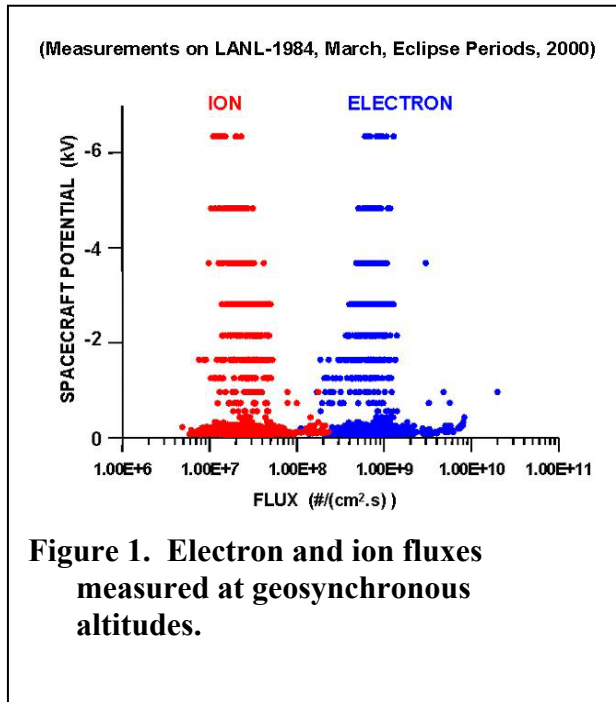29 Randolph Road
Hanscom AFB, MA 01731-3010

Abstract

This paper reviews some recent advances in the onset of spacecraft charging. Current balance determines the spacecraft potential. The electron flux intercepted by an object in a plasma exceeds that of ions by orders of magnitude because of the ion-electron mass difference. Negative voltage charging occurs when the incoming electron flux exceeds the outgoing secondary and backscattered electron flux. The secondary electron emission coefficient depends on the surface material, typically exceeds unity at about 40 to 1800 eV of primary electron energy, and falls below unity at higher energies. Beyond a critical temperature T*, the incoming electron flux exceeds that of the secondary electrons, thereby negative charging occurs. Scarce evidence of T* was observed on ATS-5 and ATS-6 satellites. Recently, abundant evidence was observed on the Los Alamos National Laboratory geosynchronous satellites. The existence of T* enables accurate prediction of spacecraft charging onset. In double Maxwellian plasmas, the onset of spacecraft charging depends on the density and temperature of both distributions. We explain pedagogically the onset of charging in double Maxwellian plasmas. Triple-root jumps in spacecraft potential can occur.

Physical Reason of Critical Temperature

The spacecraft potential is governed by current balance. When the incoming electron flux exceeds the fluxes of the incoming ions and outgoing secondary electrons, negative charging occurs. In the geosynchronous environment, the electron flux exceeds that of the ions by nearly two orders of magnitude, because of their mass difference [Figure 1]. Negative charging is important at geosynchronous altitudes. However, the ambient flux difference alone is insufficient to obtain negative charging because the secondary electrons play an important role in the current balance.

Plotting the log of a Maxwellian electron distribution $f(E)$ as a function of electron energy E gives a straight line. The inverse of its slope gives the temperature T. Higher temperature corresponds to more abundant higher energy electrons [Figure 2 Upper]. The secondary electron coefficient *(E) exceeds unity, meaning more outgoing secondary electrons than incoming primary electrons, in the energy E range of about E_1=40 to E_2=1800eV of primary electron energy, depending on the surface material. [Figure 2 Lower]

Figure 1. Electron and ion fluxes measured at geosynchronous altitudes.

Figure 2. (Upper) Temperature T of Maxwellian distribution. (Lower) Secondary electron emission coefficient as a function of primary electron energy.

Combining the two concepts of $f(E)$ and $*(E)$, the temperature T controls the competition between the two camps of electrons, viz., the low energy camp generating more outgoing secondary electrons and the high energy camp generating less secondary electrons than primary electrons. A spacecraft put in an initially low T plasma would not charge negatively, because there are more low energy electrons. As the temperature reaches a critical value T*, the population of higher energy electrons begins to dominate, suppressing the secondary electron emission.

Maxwellian Space Plasma Environment

We now consider a mathematical formulation of the onset of charging to negative potentials. At equilibrium, the spacecraft potential N is determined by current balance. At the threshold of charging onset, the potential N is zero. For uniform charging, it is sufficient to consider balance of fluxes — the incoming flux equals the outgoing flux:

$$\int_0^\infty dE E f(E) = \int_0^\infty dE E f(E)[\delta(E) + \eta(E)] \qquad (1)$$

where $f(E)$ is the distribution function of the incoming electrons, $*(E)$ and $0(E)$ are the secondary and backscattered electron emission coefficients. To calculate eq(1), one needs the functional forms of $f(E)$, $*(E)$ and $0(E)$. For a Maxwellian plasma,

$$f(E) = n(m/2\pi kT)^{1/2} \exp(-E/kT) \qquad (2)$$

Simple analytical forms of *(E) and 0(E) for normal incidence has been given by Sanders and Inouye [1979] and Prokopenko and Laframboise [1980] respectively.

$$\delta(E) = c[\exp(-E/a) - \exp(-E/b)] \qquad (3)$$

and

$$\eta(E) = A - B\exp(-CE) \qquad (4)$$

Substituting eqs(2,3,4) into eq(1), one obtains:

$$c\left[(1+kT/a)^{-2} - (1+kT/b)^{-2}\right] + A - B(CkT+1)^{-2} = 1 \qquad (5)$$

The Maxwellian distribution $f(E)$ is a function of electron energy E, electron density n and electron temperature T. The energy variable E in eq(1) has been integrated out in the definite integral. Since the density n is multiplicative, it cancels out on both sides of eq(1). Therefore, the onset condition (eq.1) for charging is independent of the plasma density n. In other words, the condition for the onset of charging is a function of T only. The solution to eq(5) is the critical temperature T* for the onset of spacecraft charging.

Angular Dependence

The angular dependent forms of secondary and backscattered electron emission coefficients have been given by [*Darlington and Cosslett*, 1972] as follows:

$$\delta(E,\phi) = \delta(E,0)\exp\left[\beta_S(E).(1-\cos\phi)\right] \qquad (6)$$

and

$$\eta(E,\phi) = \eta(E,0)\exp\left[\beta_b(E).(1-\cos\phi)\right] \qquad (7)$$

where N is the angle of incidence of the primary electrons. β_S and β_b are empirical factors. By fitting experimental data, *Laframboise et al.* [1982] have obtained the forms of β_S and β_b:

$$\beta_S(E) = \exp(\zeta) \qquad (8)$$

and

$$\beta_b(E) = 7.37Z^{-0.56875} \qquad (9)$$

where

$$\zeta = 0.2755(\xi - 1.658) - \left\{[0.2755(\xi - 1.658)]^2 + 0.0228\right\}^{1/2} \qquad (10)$$

and

$$\xi = \ln(E/E_{max}) \qquad (11)$$

In eq(9), Z is the atomic number of the surface material. E_{max} in eq(11) is the primary

electron energy where the secondary emission is maximum. Substituting eqs(3,4,6-11) into eq(1), one obtains the critical temperature T* for given surface materials [Table 1].

Table 1. Critical Temperatures

MATERIAL	ISOTROPIC	NORMAL
Mg	0.4	---
Al	0.6	---
Kapton	0.8	0.5
Al Oxide	2.0	1.2
Teflon ©	2.1	1.4
Cu-Be	2.1	1.4
Glass	2.2	1.4
SiO_2	2.6	1.7
Silver	2.7	1.2
Mg Oxide	3.6	2.5
Indium Oxide	3.6	2.0
Gold	4.9	2.9
Cu-Be (Activated)	5.3	3.7
MgF_2	10.9	7.8

Evidences of Critical Temperature

Early evidences of the existence of T* were given by Rubin et al. [1980]. The Los Alamos National Laboratory (LANL) geosynchronous satellites provide abundant co-ordinated data of spacecraft charging and the space environment. The data span over several years and are available on the CDCWeb. Using these data, we have found abundant evidences of the existence
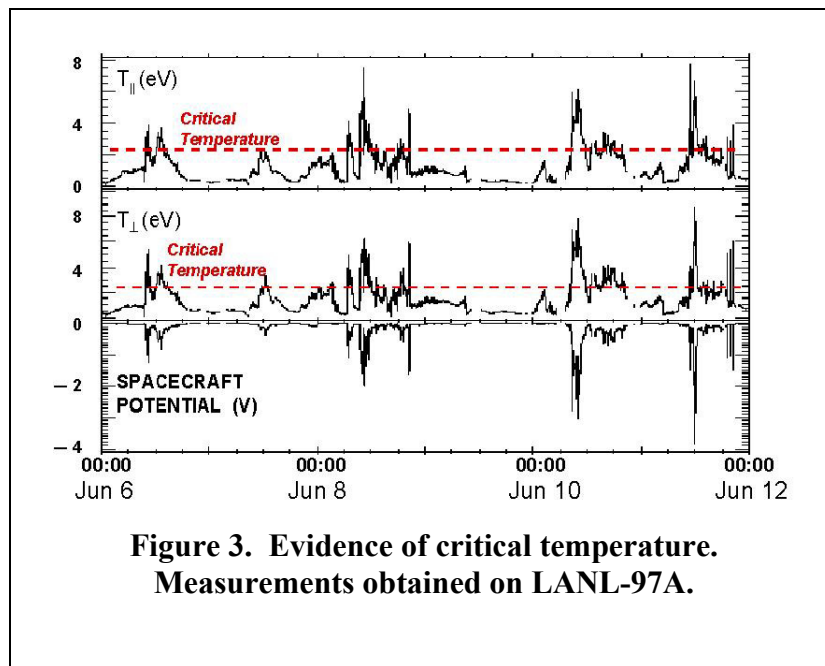
**Figure 3. Evidence of critical temperature.
Measurements obtained on LANL-97A.**

of critical temperature, not only on one LANL satellite but on all of them, and not only in one year but in all years.   Abundant observational evidences have been reported in Lai and Della-Rose [2001] and in Lai and Tautz [2003]. Figure 3 shows an example of the existence of critical temperature T*. Below T*, no charging occurs; above T*, the charging level increases almost

Figure 4. A triple-root situation. The even roots are unstable.
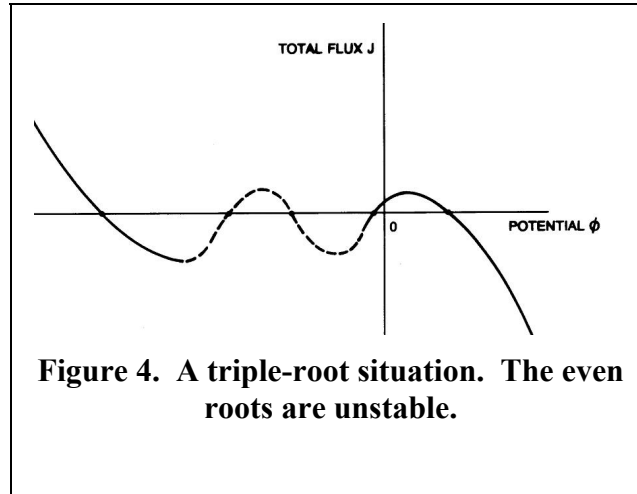
linearly with T. Using several years of data, we now know without a doubt the existence of critical temperature for the onset of spacecraft charging. More details are given in Lai and Tautz [2003].

Double Maxwellian Plasma Environment

In general, the current balance equation is of the form $J(N) = 0$ where J is the total (or net) flux. It is possible that the equation has multiple roots, i.e. solutions [Whipple, 1981; Besse, 1980; Laframboise, et al., 1982, 1983; Meyer-Vernat, 1982; Lai, 1991a, 1991b; Garrett and Hastings, 1996]. If it has three roots, the $J(N)$ curve as a function of N is a "triple-root curve". The spacecraft potential is at one of the roots. As the ambient plasma condition changes in time, a "triple-root jump" may occur. That is, the spacecraft potential may jump from one root to another. This behavior will be explained in the double Maxwellian plasma model.

A General Theorem on Multiple Roots

Our sign convention is that incoming flux of positive ion is positive, and so is outgoing electron flux.   In a general curve of flux-voltage [Figure 4], there exists at least one root, $J(N) = 0$, where J is the total flux. This is because at high positive potential $N > 0$, incoming electron flux must dominate and therefore $J < 0$. At high negative potential $N < 0$, incoming ion flux must dominate and therefore $J > 0$.   In between these two extremes, there must exist at least one or an odd number of zero crossings, $J(N) = 0$.

Therefore, we have a **general theorem: The number of roots, $J(N) = 0$, must be odd**.

The even roots are unstable, because their slopes, dJ/dN, have the wrong sign, corresponding to negative resistance. Only the odd roots are stable. Since the spacecraft potential cannot be multiple valued at the same time, it is at one of the odd roots only.

As the space plasma environment changes, it may happen that two neighboring roots, including the spacecraft potential, disappear together [Figure 5]. The spacecraft potential would jump to the next neighboring (the third) root. When the space plasma parameters reverse their course, the two lost roots may appear again. Yet, the spacecraft potential may remain at the new root. A return to its first root may occur but at different values of plasma parameters. This is a hysteresis behavior.
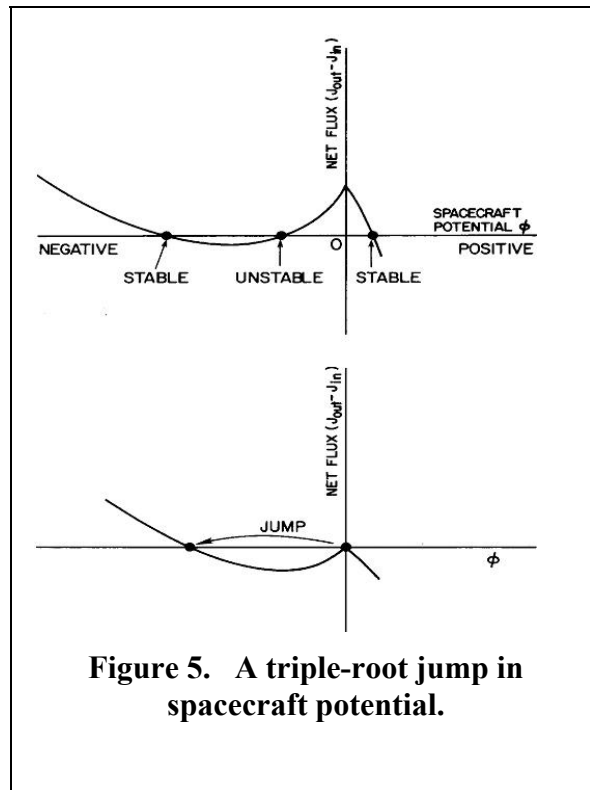
Figure 5.   A triple-root jump in spacecraft potential.

Double Maxwellian Space Plasma

The space plasma environment varies in time. In the outer region of the geosynchronous orbit, energetic plasma clouds from the magnetotail may come in at about midnight hours. Due to the curvature of the magnetic field, the energetic electrons tend to drift eastwards and the energetic ions westwards. As they move nearer the Earth, the co-rotation effect tends to move everything eastwards. This describes what usually happens during a 'substorm injection', which may occur from once in many days to a few times a night.

In quiet time, it is often a good approximation to describe the energy distribution of the space plasma at geosynchronous altitudes as a Maxwellian $f_1(E)$. When a new plasma cloud arrives, the plasma distribution changes. It is often convenient to describe the distribution, f, as a double

Maxwellian, which is a sum of a low temperature, T_1, component and a high temperature, T_2, component.

$$f_e = f_{e,1} + f_{e,2} \tag{12}$$

and

$$f_i = f_{i,1} + f_{i,2} \tag{13}$$

By convention, the first Maxwellian f_1 is the one that has the lower electron temperature $T_{e,1}$. The density of f_1 is greater than that of f_2, otherwise the population is called 'inverted' which is rare.

$$T_{e,1} < T_{e,2} \tag{14}$$

$$n_{e,1} > n_{e,2} \tag{15}$$

The Triple-Root Situation of Spacecraft Potential

Firstly, at very high positive surface potential N, the flux must be predominantly that of incoming electrons (total $J<0$). Secondly, at very high negative surface potential, the flux must be predominantly that of incoming ions (total $J>0$). Consider the potential N as a variable. Let N decreases from the $J<0$ region. If $J(N)$ climbs above 0 and then decreases to below 0, we have a triple-root situation (Figure 7).

In a double Maxwellian plasma, the total (or net) flux J is given by

$$J = J_1 + J_2 \tag{16}$$

J_1 and J_2 must have opposite signs at roots of $J(N) = 0$ where the potentials are moderate, i.e. small enough for ion currents to be negligible. In order for J_1 and J_2 to have opposite signs, T_1 must be below T*, while T_2 above T*.

$$T_2 > T^* > T_1 \tag{17}$$

which gives $J_1 > 0$ while $J_2 < 0$.

The condition for the existence of a positive flux $J(N) > 0$ is

$$|J_1| > |J_2| \tag{18}$$

where, neglecting the ions, the net fluxes are given by

$$J_1 = \int_0^\infty dE E f_1(E) \left[1 - (\delta(E) + \eta(E)) \right] \exp\left(-\frac{e\phi}{kT_1} \right) \tag{19}$$
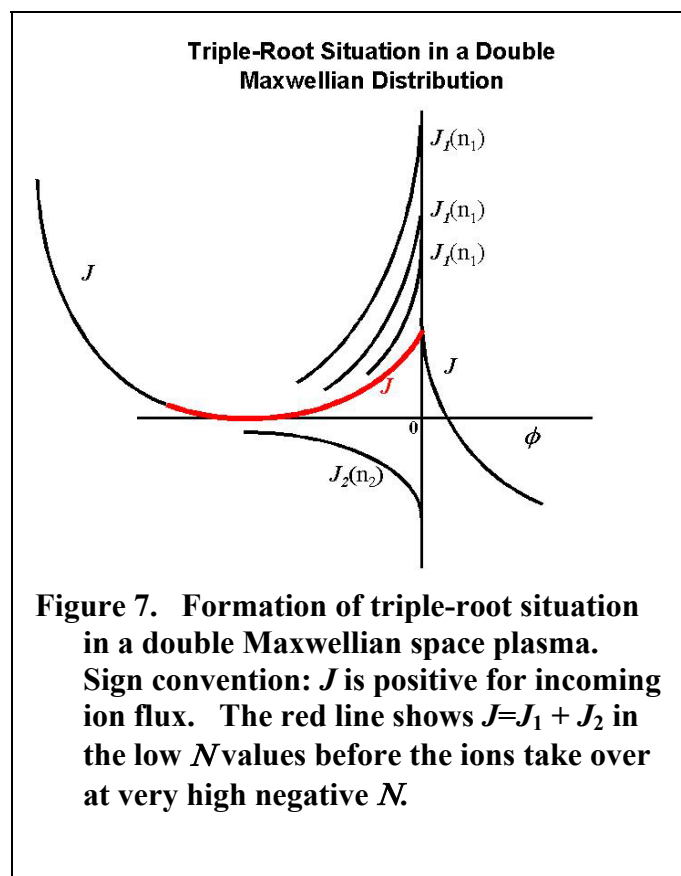
and

$$J_2 = \int_0^\infty dE E f_2(E) \left[1 - (\delta(E) + \eta(E)) \right] \exp\left(-\frac{e\phi}{kT_2} \right) \tag{20}$$

Since $T_2 > T_1$, $J_1(N)$ decreases faster than $|J_2(N)|$ as the magnitude of (negative) N increases (i.e. to the left side in Fig.7). At a sufficiently large magnitude of (negative) N, $J_1(N)$ decreases to a value so small that the equality (18) is not satisfied, rendering the total J negative. Whether the inequality (18) is violated depends mainly on the relative densities n_1 and n_2. If n_1 decreases, J_1 decreases accordingly. Eventually, when $J_1 = J_2$ in magnitude, the total flux $J(N) = J_1(N) + J_2(N) = 0$. A root is at this value of N. As the magnitude of (negative) N increases to very large values, eventually the ambient ions must take over. That is, eventually, at such high magnitude of (negative) N, the curve $J(N)$ must have negative slope, crossing the $J(N) = 0$ again. Counting the roots, we already have one at positive N, now one at negative N, and eventually there must be one at a high magnitude of negative N. Thus, a triple-root situation is formed. A triple-root jump occurs when two of the adjacent roots coalesce and disappear.

A Potential Adverse Effect of High Secondary Electron Emission

As a corollary, the use of spacecraft surface materials with high secondary electron emission coefficient ∗ poses a potential adverse effect, viz., triple-root jump in spacecraft potential. High ∗ value makes J positive (because of outgoing electron) at or near $N = 0$. This property prevents the surface from onset of charging until the ambient electron temperature is high. However, in a double Maxwellian plasma (Figure 7), high J_1 at $N = 0$ may increase the likelihood of a triple-

Figure 7. Formation of triple-root situation in a double Maxwellian space plasma. Sign convention: J is positive for incoming ion flux. The red line shows $J=J_1 + J_2$ in the low N values before the ions take over at very high negative N.

root situation with a high negative root.   If the space weather changes in such a manner that n_1 decreases rapidly, the sum J of J_1 and J_2 may decrease to zero at $N = 0$. If so, a triple-root jump in spacecraft potential occurs. The amplitude of the jump may be very large. The time of jump may be very short, depending on the surface capacitances involved. For example, the jump in Day 114 of SCATHA occurred on the copper-beryllium surface, which has $* = 4$ approximately. It occurred when n_1 was dropping rapidly, while the other space environment parameters stayed relatively constant in the period of the event.

Summary and Conclusion

When an object is placed in a plasma, whether in space or in the laboratory, the object intercepts more electrons than ions, because the electrons are lighter than ions and therefore the electron flux is higher. When electrons impact on a surface, secondary and backscattered electrons are emitted from the surface. Secondary electrons are much more abundant and therefore more important than backscattered electrons. At a range of primary electron energy, typically between 50 to 1500 eV depending on the surface material, the outgoing electron flux exceeds the incoming primary electron flux. This property prevents negative-voltage charging of the surface for incoming electrons in this range of energy.

However, primary electrons from space plasma are not mono-energetic but form a distribution in energy. At equilibrium, the distribution is Maxwellian, which is characterized by the electron density and electron temperature. Because of the secondary-emission property of a given surface material, the electrons in a Maxwellian distribution can be thought of falling into two camps. The low energy camp generates more outgoing (secondary) electrons than incoming electrons and therefore tends to drive the surface potential positive. The high-energy camp generates less outgoing electrons than incoming electrons. Therefore this camp tends to drive the surface potential negative. The competition between these two camps determines the onset of spacecraft charging. As the electron temperature increases, the number of electrons in the high-energy camp increases. Eventually, at sufficiently high temperature (the critical temperature), the two camps are even, meaning onset of charging. At higher temperatures, the high-energy camp wins and therefore the surface potential is negative. Abundant evidences have been observed on the LANL geosynchronous satellites confirming, without a doubt, the existence of critical temperature for the onset of spacecraft charging.

In general, a spacecraft surface flux-voltage curve (or equation) can yield an odd number of roots. The even roots are unstable because they are opposite to Ohm's law. A triple-root situation does not necessarily imply a triple-root jump in potential. To have a jump, two of the adjacent roots have to coalesce and disappear together. The amplitude of a jump can be very large, kV, for example. The time of jump, being limited mainly by surface capacitances, can be extremely fast.

A double Maxwellian distribution is often a good approximation for describing the space plasma, especially when a new plasma cloud has arrived and an equilibrium has not achieved. Conventionally, the first Maxwellian $f_1(E)$ is the one with the lower temperature. Although the concept of critical temperature T* was developed for single Maxwellian plasmas, surprisingly the concept plays an important role in double Maxwellians and triple-roots.   When the

temperatures of f_1 and f_2 are both less than T*, no negative voltage charging occurs. When the temperatures of f_1 and f_2 both exceed T*, there must be negative charging. If $T_1 <$ T*, while T $>$ T*, the fluxes J_1 and J_2 of the two Maxwellians must be of opposite signs. Therefore J_1 and J_2 compete with each other. At low negative potentials, the ions can be legitimately neglected. If J_1 greatly exceeds J_2, their sum J exceeds 0. A triple-root situation may form. If the density n_1 of J_1 decreases, J_1 decreases accordingly. When J_1 decreases to below J_2, J falls below 0, allowing a triple-root jump to occur.

As a corollary, spacecraft surfaces of high secondary emission coefficient *$_{max}$ are more likely to suffer from triple-root jump. It has been a common belief that using surfaces of high *$_{max}$ is a good mitigation method. Not so! When the space plasma environment becomes hot while the first Maxwellian density is dropping steadily, there is danger for a triple-root jump to occur for such surfaces. With this corollary, we close this paper by bringing this important message to the attention of the community of spacecraft charging and space vehicle designs.

Acknowledgment

References

1. Besse, A.L., Unstable potential of geosynchronous spacecraft, J. Geophys. Res., Vol. 86, No.A4, 2443-2446, 1981.

2. Hastings, D., and Garrett, H.B., Spacecraft-Environment Interactions, Cambridge University Press, Cambridge, UK., 1997.

3. Darlington, E.H. and Cosslett, V.E., Backscattering of 0.5-10 keV electrons from solid targets, J. Phys. D., App. Phys. 5, pp.1961-1981, 1972.

4. Laframboise, J.G., Godard R. and Kamitsuma M., Multiple Floating Potentials, Threshold Temperature Effects, and Barrier Effects in High Voltage Charging of Exposed Surfaces on Spacecraft, in Proceedings of International Symposium on Spacecraft Materials in Space Environment, Toulouse, France, 1982, pp.269-275.

5. Laframboise, J.G. and Kamitsuma, M., The Threshold Temperature Effect in High Voltage Spacecraft Charging, in Proceedings of Air Force Geophysics Workshop on Natural Charging of Large Space structures in Near Earth Polar Orbit, AFRL-TR-83-0046, ADA-134-894,1983, pp .293-308.

6. Lai, S.T., Gussenhoven, M.S. and Cohen, H.A., Energy Range of Ambient Electrons Responsible for Spacecraft Charging, EOS Trans. Am. Geophys. U., Vol.63, No.18, 421, 1982.

7. Lai, S.T., Gussenhoven, M.S., and Cohen, H.A., The Concepts of Critical Temperature and Energy Cutoff of Ambient Electrons in High Voltage Charging of Spacecraft, in Proceeding of the 17th ESLAB Synposium, edited by D.Guyenne and J.H. A. Pedersen, pp. 169-175, European Space Agency, Noordwijk, The Netherlands, 1983.

8. Lai, S.T., Spacecraft Charging Thresholds in Single and Double Maxwellian Space Environments , IEEE Trans. Nucl. Sci., Vol.19, pp.1629-1634,1991.

9. Lai, S.T., Theory and observation of triple-root jump in spacecraft charging, J. Geophys. Res., Vol.96, No.A11, 19269-19282, 1991.

10. Lai, S.T. and D. Della-Rose, Spacecraft charging at geosynchronous altitudes: New evidence of existence of critical temperature, J. Spacecraft & Rockets, Vol.38, pp.922-928, Dec., 2001.

11. Lai, S.T. and M. Tautz, High-level spacecraft charging at geosynchronous altitudes, A statistical study, 8th Spacecraft Charging Technology Conference, Huntsville, AL, Oct 20-24, 2003.

12. Meyer-Vernet, N., Flip flop of electrical potential of dust grains in space, Astron. Astrophys., Vol.105, 98-106, 1982.

13. Prokopenko, S.M. and Laframboise J.G.L., High Voltage Differential Charging of Geostationary Spacecraft, J. Geophys. Res., Vol. 85, No.A8, 1980, pp.4125-4131.

14. Rubin, A., Garrett, H.B., and Wendel, A.H., Spacecraft Charging on ATS-5, Air Force Geophysics Laboratory, AFGL-TR-80-0168, ADA-090-508, 1980.

15. Sanders, N.L.and G.T.Inouye, Secondary Emission Effects on Spacecraft Charging: Energy Distribution Consideration, in Spacecraft Charging Technology 1978, edited by R.C.Finke and C.P. Pike, pp. 747-755, AFGL, Hanscom AFB., Massachusetts, 1978. NASA-2071, ADA-084626.

16. Whipple, E.C., Potentials of surfaces in space, Reports on Progress in Physics, Vol.44, pp. 1197-1250, 1981.

SOLAR ARRAY IN SIMULATED LEO PLASMA ENVIRONMENT

Boris Vayner
Ohio Aerospace Institute, NASA Glenn Research Center
MS 302-1, 21000 Brookpark Road
Cleveland, OH 44135
Phone: (216)-433-8058
Fax: (216)-433-6106
E-mail: vayner@grc.nasa.gov

Joel Galofaro
Dale Ferguson
NASA Glenn Research Center

Abstract

Six different types of solar arrays have been tested in large vacuum chambers. The low Earth orbit plasma environment was simulated in plasma vacuum chambers, where the parameters could be controlled precisely. Diagnostic equipment included spherical Langmuir probes, mass spectrometer, low-noise CCD camera with optical spectrometer, video camera, very sensitive current probe to measure arc current, and a voltage probe to register variations in a conductor potential. All data (except video) were obtained in digital form that allowed us to study the correlation between external parameters (plasma density, additional capacitance, bias voltage, etc) and arc characteristics (arc rate, arc current pulse width and amplitude, gas species partial pressures, and intensities of spectral lines). Arc inception voltages, arc rates, and current collections are measured for samples with different coverglass materials and thickness, interconnect designs, and cell sizes. It is shown that the array with wrapthrough interconnects have the highest arc threshold and the lowest current collection. Coverglass design with overhang results in decrease of current collection and increase of arc threshold. Doubling coverglass thickness causes the increase in arc inception voltage. Both arc inception voltage and current collection increase significantly with increasing a sample temperature to 80 C. Sustained discharges are initiated between adjacent cells with potential differences of 40 V for the sample with 300 μm coverglass thickness and 60 V for the sample with 150 μm coverglass thickness. Installation of cryogenic pump in large vacuum chamber provided the possibility of considerable outgassing of array surfaces which resulted in significant decrease of arc rate. Arc sites were determined by employing a video-camera, and it is shown that the most probable sites for arc inception are triple-junctions, even though some arcs were initiated in gaps between cells. It is also shown that the arc rate increases with increasing of ion collection current. The analysis of optical spectra (240-800 nm) reveals intensive narrow atomic lines (Ag, H) and wide molecular bands (OH, CH, SiH, SiN) that confirms a complicated mechanism of arc plasma generation. The results obtained seem to be important for the understanding of the arc inception mechanism, which is absolutely essential for progress toward the design of high-voltage solar array for space application.

Introduction

The purpose of the current paper is to test a possibility of significant increase of arc thresholds by modifications of conventionally designed solar arrays. Previous studies of arc inception mechanism [1-4] suggest that such modifications can be done in the following directions: I) to insulate conductor-dielectric junction from a plasma environment (wrapthrough interconnects); II) to change a coverglass geometry (overhang); III) to increase a coverglass thickness; IV) to outgas areas of conductor-dielectric junctions, V) to use coverglass with lower dielectric permittivity and higher conductivity. The operation of high-voltage array in LEO produces also the parasitic current power drain on the electrical system. Moreover, the current collected from space plasma by solar arrays determines the spacecraft floating potential that is very important for the design of spacecraft and its scientific apparatus. In order to verify the validity of suggested modifications and to measure current collection six different solar array samples have been tested in large vacuum chamber. Five samples (36 silicon based cells) consist of three strings in each sample containing 12 cells connected in series. One sample contains nine cells (2x4 cm) arranged in three strings, and this sample is used for measuring arc plasma optical spectra. Thus, arc rate and current collection can be measured on every string independently, or on a whole sample when strings are connected in parallel. The heater installed in the chamber provides the possibility to test samples under temperature as high as 80 C that simulates the LEO operational temperature. The experimental setup is described below.

Experimental Setup

Low Earth Orbit (LEO) plasma environment was simulated in two different vacuum vessels: 1) horizontal vacuum chamber (1.8 m diameter and 2 m long) equipped with cryogenic pump; 2) large vacuum tank (2.2 m diameter and 3 m height) with four diffusion pumps. The vacuum equipment provided pressure as low as 0.5 μTorr. The essential difference between these two tanks is that the residual water vapor partial pressure in horizontal chamber is five times lower than in vertical tank. Each vessel has one Kaufman plasma source that generates xenon plasma with electron density $n_e=(0.1-10)\cdot10^5$ cm^{-3} , temperature T_e=0.6-1.2 eV, and neutral gas pressure p=(0.7- 7)$\cdot10^{-5}$ Torr which can be kept steady during the experiment. To measure plasma parameters, Langmuir probes with diameter 2 cm were employed (two in each tank). To determine an ion distribution function and to improve measurements of electron temperature one retarding potential analyzer (RPA) was mounted on the bottom of vertical tank. It was found that the ion (xenon) thermal flux in the experiment is about three times lower than ram ion flux in LEO, and the electron temperature is 5-10 times higher than in ionosphere. However, the number densities are simulated with a quite high accuracy, and one can believe that the results of high-voltage experiments in vacuum chambers are fairly adequate to the outcomes of processes in LEO plasma. To control plasma chemical composition (particularly, water vapor and oil partial pressures) a quadruple mass spectrometer was installed in each tank.

The sample (or set of samples) is vertically mounted in the middle of the chamber, and it is biased to a voltage power supply through a capacitor and a 10 kΩ resistor network back to ground. An additional power supply (Solar Array Simulator-SAS) is used to generate electrical field perpendicular to the dielectric side surface for investigating arc inception on semiconductor-dielectric junction and inception of sustained discharges between adjacent strings. Diagnostic

equipment includes two current probes to measure discharge current and SAS current, and one voltage probe that allows us to register voltage pulse on the sample during the discharge. To measure optical spectra of arc plasma an intensified CCD (1024x512 pixel) camera with optical spectrometer is installed. The arc sites are determined by employing a video camera and VCR. Most experiments were performed at room temperature (15C), but some tests had been done at the temperature +80 C simulating the exposure of solar array to full sun in LEO.

Arc Spectra

Previous experimental data and theoretical analysis have demonstrated that water molecules adsorbed on the side surface of dielectric (coverglass+adhesive) can play a decisive role in the process of arc inception [5-7]. It is known that spectra of vacuum arcs consist of cathode metal lines only [8] but adding air in vacuum chamber (10^{-4} Torr) results in appearance of hydrogen and hydroxyl lines [9]. Partial pressure of water vapor and nitrogen is always below 10^{-5} Torr for the current experiment. Thus, the presence of hydrogen and hydroxyl in the arc plasma would be a good indicator of water ions dissociative recombination. The presence of other species in arc plasma may reveal other important processes in the discharge development. To elucidate all these problems the measurements of optical spectra have been performed for silicon solar array sample (nine cells). All dielectric-conductor junctions besides one interconnect area were insulated by tape to exclude spectra from arcs between cells. The spectral resolution was determined as 0.12 nm/pixel by using standard calibration lamps. To increase the arc luminosity an additional capacitor (usually 1 μF) was installed between negatively biased electrode and ground. Gate pulse generator provided varying both gate pulse width and time delay; thus, it was possible to measure the intensities of spectral lines on different stages of a discharge development. In addition to hydrogen (H_α), hydroxyl (OH), and metal lines (Ag) arcing on the sample revealed also some molecular radicals identified according to Ref. 10 (Fig.1).

The results of spectral measurements, observation of decreasing arc rate with number of arcs (conditioning), and theoretical estimates [11] are very strong argument in favor of the idea that in order to raise arc threshold solar array surfaces must be thoroughly outgassed. The validity of this hypothesis has been confirmed by ground tests described in Sec. 5 below.

Outgassing of Solar Array Samples

When spacecraft is coming out of eclipse, solar array temperature is rising due to exposure to Sun radiation. Operational temperature of an array in LEO conditions is approximately 80-100 C. It is believed that the adsorbed contaminants from the array surface are evaporating at a high rate due to heating. On another hand, when solar array sample is installed in a vacuum chamber its surface is contaminated not only by "natural" species (adsorbed water, atmospheric gases, and products of a technological process) but also other contaminants. The most abundant of these contaminants is vacuum pump oil. To measure chemical composition of background vacuum and to determine plasma contamination due to heating, the quadruple mass-spectrometers are installed in both large chambers. Two solar array samples are mounted on an aluminum sheet with electrical heater placed on the back (Fig.2). This heater provides enough power to radiantly heat sample from 15 C to 80 C for about 50 minutes (Fig.3). It is seen that the increase in water
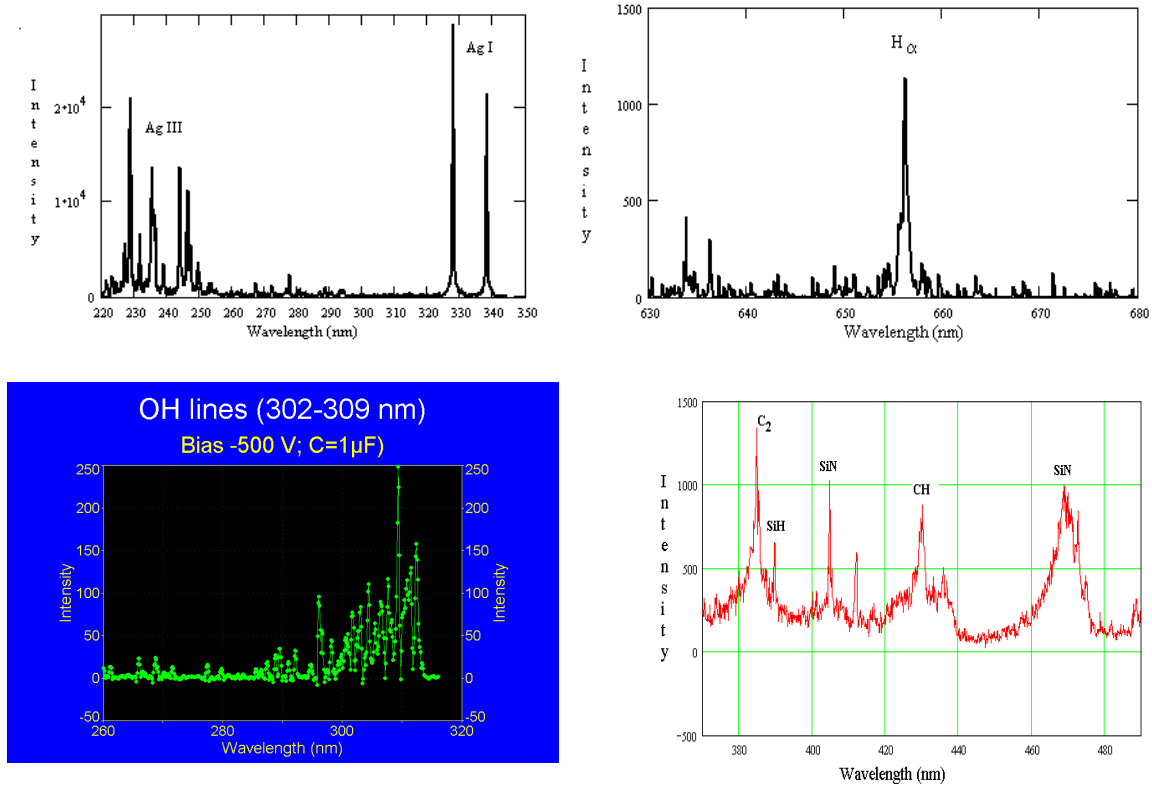
Figure 1. One example of emission spectrum of arc plasma.

vapor partial pressure is considerably higher than the plain isochoric increase $\dfrac{\Delta p}{p_0} = \dfrac{\Delta T}{T_0}$,and this observation confirms the presence of water adsorbed on solar array surface.

Five cycles of heating-cooling sample in vacuum chamber resulted in significant drop of residual water vapor pressure (Fig.4).
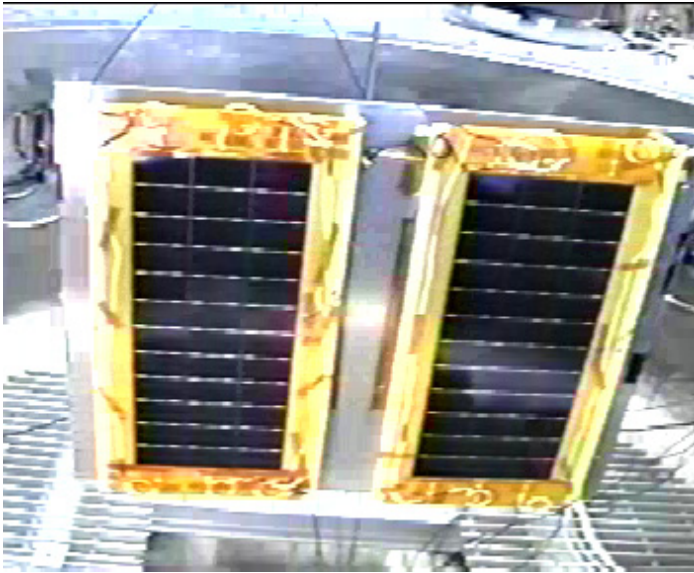
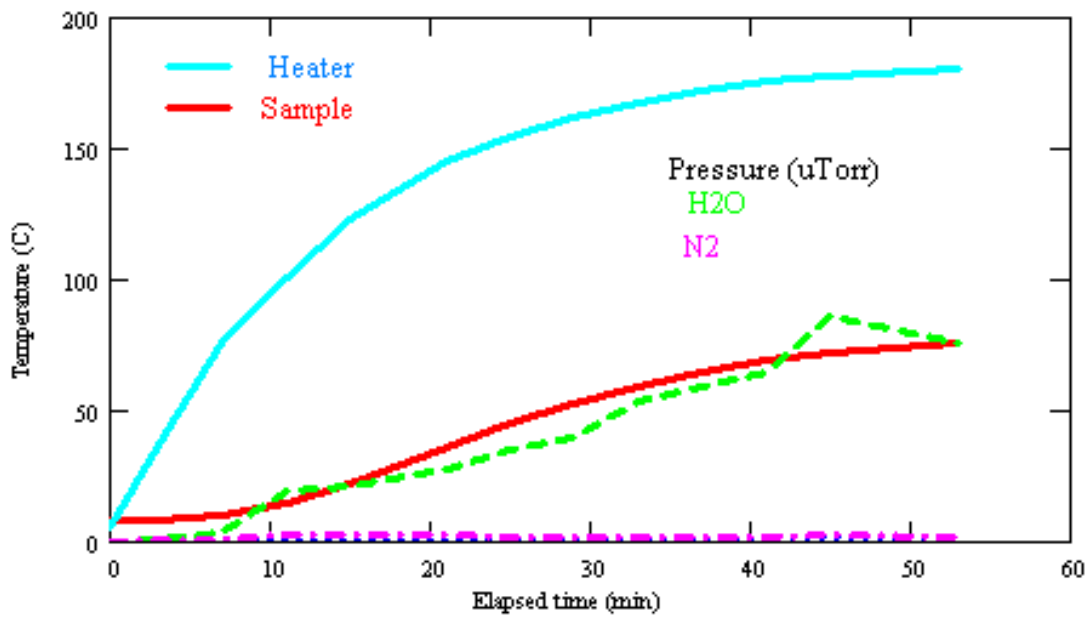**Figure 2. Solar array samples installed in vacuum chamber.**
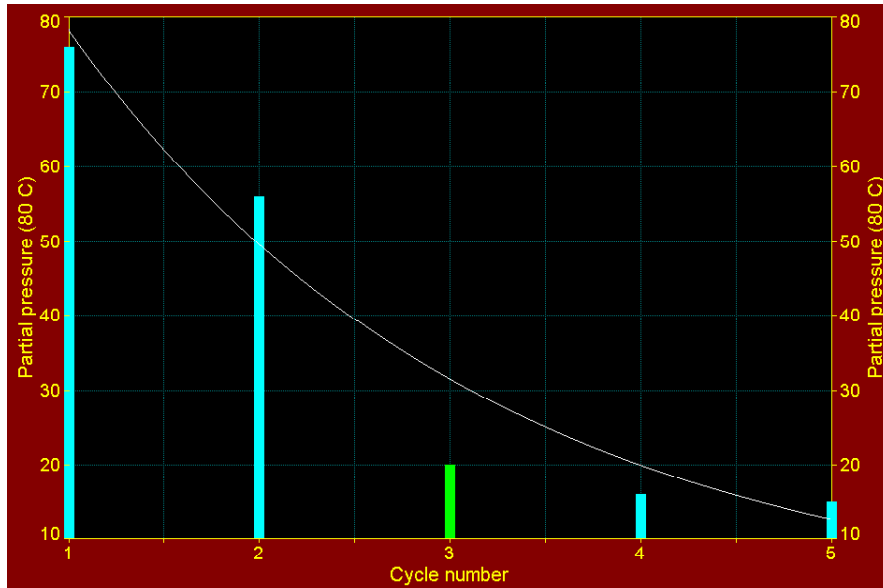

Figure 3. Increase of water vapor pressure is considerably higher than plain isochoric increase.

Figure 4. Water vapor partial pressure in course of thermal cycling (rel. units).

Arcing in Plasma

Five types of tested solar arrays are shown in Table 1. Each string (12 cells in series) is tested separately to measure arc inception voltage and arc rate. Measurements reveal significant differences in these parameters even for strings belonging to one sample. There are two reasons explaining such observations: manufacturing process peculiarities and geometrical design of a sample. In fact, the middle string is separated from neighboring strings by narrow gaps (0.8 mm) covered with a thin RTV layer while two other strings have edges with underlying semiconductor and dielectric exposed to the plasma. Manufacturing peculiarities demonstrate themselves when one compares arc parameters for two outer strings and finds considerable differences. And arc sites are located mostly on interconnects for middle string while great part of arcs on outer strings has been observed on cell edges. To preserve the homogeneity of collected data one common experimental procedure is used for all measurements of arc inception voltages and arc rates: 1) string is initially biased to voltage well below an expected arcing threshold; 2) 15-30 minute time interval is allowed to register (or to not register) an arc; 3) voltage is increased on 10-20 V; 4) arc rate is defined as an average over a respective time span. On the first stage of the test, two samples (#1 and #2 in Table 1) are mounted on the heater plate and installed in chamber. The results of measurements for middle strings at the room temperature are shown in Fig.5. Obviously, arc inception voltage is lower for the panel with thinner coverglass, and arc rates differ significantly. Arc rates have been also determined at high temperature (Fig.6).

Arc rates are widely scattered over a range of voltages 280-380 V. In general, the temperature rise to 80 C results in significant increase of arc inception voltage (40-60 V). In particular, inner strings are not arcing below 300 V. It is worth noting that measurements shown above have been done at comparatively high water vapor partial pressures: 4 µTorr at 15 and 15-30 µTorr at 80 C. These values are much higher than one can anticipate in LEO conditions. The

Table 1. Five types of solar array samples tested in the large chambers.

Sample No	Coverglass Thickness (µm)	Material	Overhang (µm)	Cell size (cm)	Interconnect
1	300	UVR	0	4x6	exposed
2	150	UVR	0	4x6	exposed
3	150	CMX UVR	0	4x6	exposed
4	150	UVR	250	4x6	exposed
5	150	UVR	0	8x8	wrapthrough

decrease of an arc rate during the process of continuing arcing (conditioning) has been measured by biasing the whole sample #2 to -400 V and measuring average arc rate for every four minutes. Additional capacitance is increased from 0.22 µF to 1µF to accelerate conditioning. After about 70 arcs, arc rate drops from 3.25 arc/min to the magnitude of 1 arc/min and stays practically steady for the next 30 arcs. To verify the influence of plasma density on arc rate this parameter has been increased by factor 1.5, and arc rate was measured for the next 100 arcs. Finally, arc rate has decreased to 0.25 arc/min after about 200 arcs. Thus, the influence of conditioning on previous measurements of arc rates for separate strings belonging to different samples is insignificant, particularly because of low capacitance (0.22 µF) used in these tests.
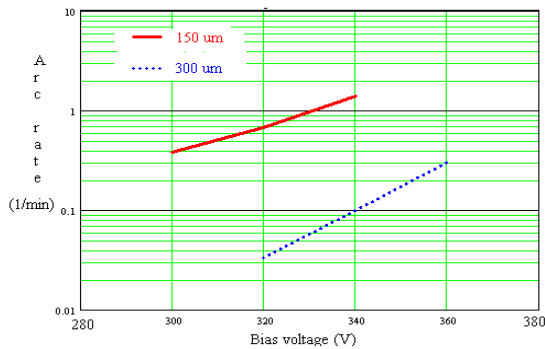

Figure 5. Arc rate on the middle strings (samples #1 and #2).
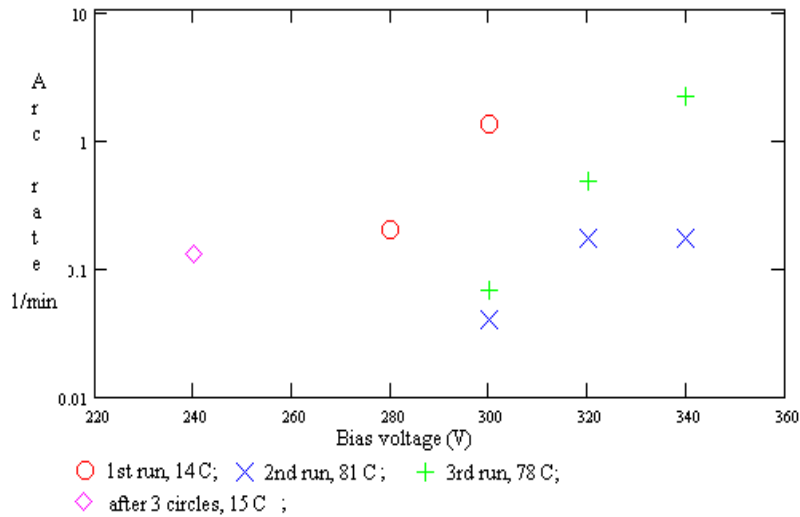
Figure 6. Arc rate on the middle string of sample #2.

To test the possibility of outgassing of the whole sample by heating it to 80 C and pumping out an excess of water vapor the sample #2 has been undergone to five thermal cycles (see Fig.4). Arc rates are measured for all three strings connected in parallel at room temperature before the first cycle and after the fifth cycle. The results are shown in Fig.7.
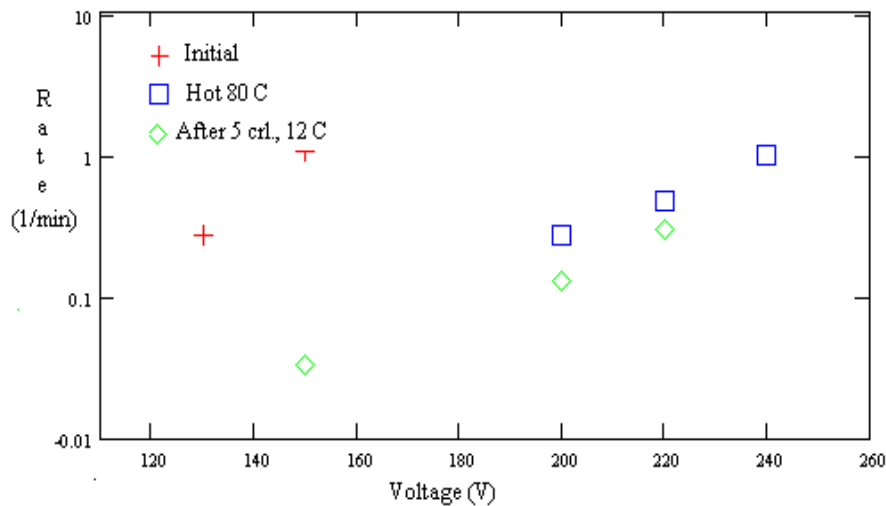
Figure 7. Arc rate on sample #2 (three strings in parallel).

It is seen in Fig.7 that arc rate decreases about 30 times and arc threshold increases approximately 30 V due to outgassing. It should be noted that minimum partial pressure of water vapor in xenon plasma reached in these experiments was 1.4 μTorr that seems not low enough to outgas sample surfaces to the degree expected in LEO.

Arcing on the sample #3 (middle string, CMX UVR coverglass) demonstrates significant increase in arc threshold (80-100 V) comparatively to arcing on sample #2. Arc inception voltage

for the middle string is 360 V, and two other strings are arcing at lower voltages due to considerable percentage of arcs on the cell edges. This observation can be explained by difference in dielectric permittivity for borosilicate and CMX glasses. Really, electric field strength in the vicinity of a triple junction is higher for dielectric with high permittivity (Fig.8). If one suggests that all other characteristics of samples #2 and #3 are identical the observed difference in arc threshold voltages can be understood. It should be noted that the conductivity of coverglass also influences the arc threshold voltage, and the direction of this effect is opposite to the previous one because of higher resistivity of CMX glass (10^{13} Ohm*m vs. 10^{12} Ohm*m for borosilicate). That may explain lower than expected from the Fig.8 observed discrepancy in arc thresholds but this problem needs more thorough investigation. The test results for the sample #4 (250 μm overhang) look also prospective. Arc inception voltage is 80-100 V higher, and arc rate is lower for the middle string. Two other strings have also demonstrated the decrease of arc rate in spite of arcing on cell edges. The increase of arc inception voltage to 480 V for the hot sample is particularly important. It seems that the array with coverglass overhang and additional insulation of cell edges can operate at 400 V in LEO conditions.
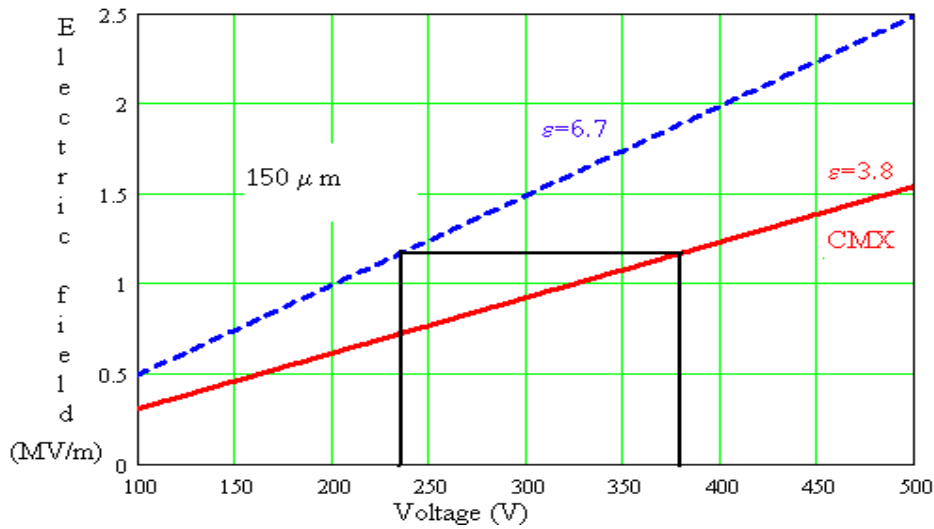
Figure 8. The difference in arc thresholds between samples with CMX and borosilicate coverglasses should be about 130 V according to the calculations of electric field strengths.

According to existing model of arc inception [12,13] the most probable arc site on an array surface is a conductor-dielectric junction exposed to the plasma. Thus, if all interconnects are insulated from the surrounding plasma the probability of a discharge decreases significantly. One of the possible realizations of this idea is the array design with wrapthrough interconnects (sample #5, Fig.9). Such design cannot prevent arcing at very high negative potential because edge of semiconductor (silicon, germanium, or other) stays exposed to the plasma, and many tests (including ones described in this paper) have demonstrated intensive arcing on cell edges. However, considerable increase of arc inception voltage can be expected, particularly for the middle string. Test results confirm these expectations (Fig.10). The inception of arc is observed on the middle string at bias voltage 440 V that is 60 V higher than arc inception voltage for the
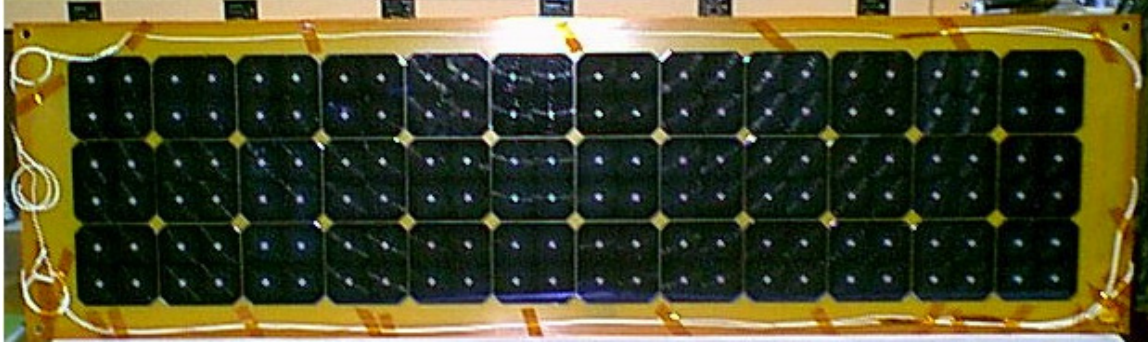
Figure 9. Solar array sample with wrapthrough interconnects.

string with coverglass overhang. Arc sites are located between adjacent cells belonging as to middle string as to neighboring strings. Two other strings demonstrate much lower arc inception voltages due to arcing on edges. Unfortunately, experimental setup has not provided a possibility to heat this sample above room temperature but even the results obtained to date show that this kind of solar array can be used in LEO to generate power at voltage 450 V if array edges are electrically insulated.

Short electrostatic discharges studied above are certainly undesirable events that must be prevented for reliable operation of the spacecraft. However, this kind of transients are not damaging solar array irreversibly, at least in cases of low additional capacitances used in current experiments. Sustained discharges initiated between adjacent cells with a few tens volt potential difference are much more dangerous [14,15] because they can destroy cells and underlying substrate that results in considerable loss of power. Samples #1, #2, and #4 have been tested against an inception of sustained arc between two strings. Test starts with lower limits on SAS voltage and current. After the registration of 5-10 arcs these parameters are gradually changed and more arcs are generated until initial sign of sustained discharge is seen on the oscilloscope. This sign represents the SAS current pulse that continues much longer than original arc. The corresponding SAS voltage and current are considered as threshold parameters because even a small increase of them (10 V and 0.25 A) results in spectacular event shown in Fig.11. In this case the sustained discharge has been quenched after 20 s by turning SAS off. Damaged part of the sample is shown in Fig.12. Threshold parameters depend on solar array design: they are 40 V and 1 A for sample #1, 60 V and 2 A for sample #2, and 80V and 1.6 A for sample #4.

Scaling of Arc Current Pulse Width and Amplitude

Even short transients are detrimental for spacecraft, and the degree of damage increases with the increase of arc current amplitude and pulse width. These two parameters depend on the amount of electrical charge leaking into surrounding plasma during the discharge time. There are currently two theoretical models that allow estimating lost electrical charge and its dependence on the array capacitance. First model [16] is based on the suggestion that the discharge generates an expanding plasma sheath neutralizing positive charge on top of coverglass. If plasma expands with a constant speed the discharge time is proportional to the array linear dimensions, or, in another terms, to the square root of an array capacitance. This dependence has been proved in many experiments [16,17]. However, the distance that plasma can expand on is limited to about

1 m in simulated LEO conditions [18]. Thus, according to the first model the upper limit for the effective capacitance is the capacitance of the part of solar array with area approximately 1 m^2.
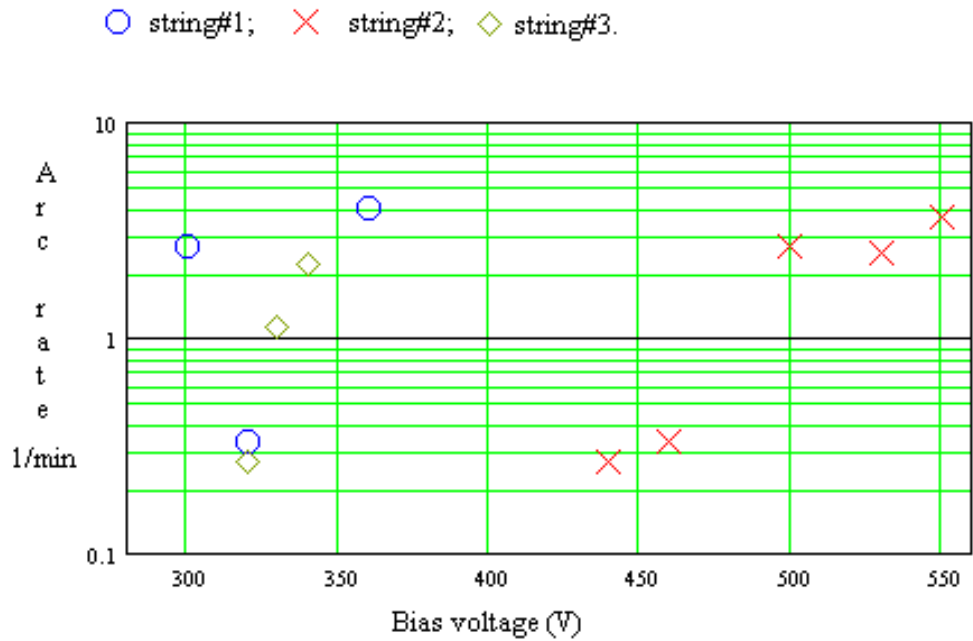

Figure 10. Arc rate on sample #5.

Figure 11. Sustained arc between adjacent strings on sample #2.

The second model also envisages that both arc current amplitude and pulse width are proportional to the square root of a capacitance but this prediction is based on the dynamics of ionization-

recombination processes in the discharge plasma [6]. If the second model is correct the effective capacitance is only two-three times less than the capacitance of a whole solar array. A simple experiment has been performed to verify the validity of the second model. Two solar array samples (sample #2) are mounted on aluminum panel with grounded aluminum plate installed between samples. The height of the plate is 7.5 cm bigger than the distance between aluminum panel and top of the sample. Such arrangement prevents the expansion of plasma sheath from one sample to another. The additional capacitor of 1000 pF is used in this particular experiment.
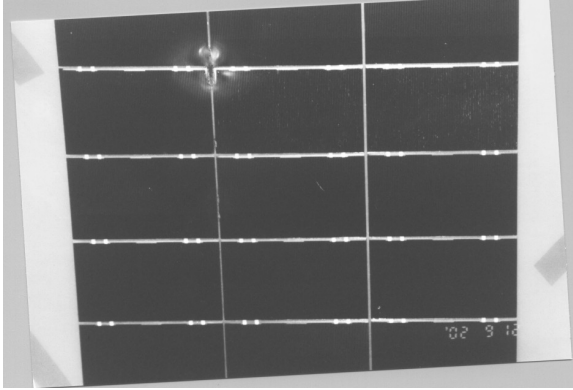
Figure 12. Damage induced by sustained arc.

The capacitance of one cell can be calculated as

$$C_1 = \frac{\varepsilon_0 \varepsilon_1 S_1}{d_1} \left(1 + \frac{\varepsilon_1 d_2}{\varepsilon_2 d_1}\right)^{-1} \qquad (1)$$

where $\varepsilon_{1,2}$ are dielectric constants of coverglass and adhesive, $d_{1,2}$ are their thicknesses, and S_1 is a cell area.

Dielectric constants are: for borosilicate coverglass ε_1=6.7, and for epoxy ε_2=3.6. Thus, a quite reliable estimate can be obtained: C_1=590 pF/cell. Moreover, the scaling does not practically depend on exact numbers for largest capacitances. Ten measurements of arc current pulse widths for each configuration have been done by biasing one string, three strings, and six strings in parallel. The results are shown in Fig.13. The scaling is confirmed with a very high accuracy, which means that adequate ground simulations of arcing on spacecraft surfaces have to be performed with a very large additional capacitance (for instance, about 1000 µF for ISS).

Current Collection

One solar cell provides current of 1 A in order of magnitude while collected current is scaled in hundred micro amps. Thus, the role of collected current in a parasitic power drain is certainly negligible. However, the floating potential of the spacecraft strongly depends on the current collected by the solar array [19]. There are three main factors that influence the magnitude of collected current: I) solar array design; II) solar array temperature; III) parameters of surrounding

plasma. Obviously, the design with coverglass overhang and with wrapthrough interconnects offers arrays with considerably decreased collected currents. Electron number density and electron temperature also influence on current collection. Ground tests that simulate an electron component of LEO plasma quite reasonably provide reliable data for current collection by cells with positive potentials with respect to surrounding plasma. Test data containing measurements of collected current for negatively biased cells are applicable to the analysis of spacecraft floating potential not better than in order of magnitude because the characteristics of ion component are different in ground tests and in LEO.
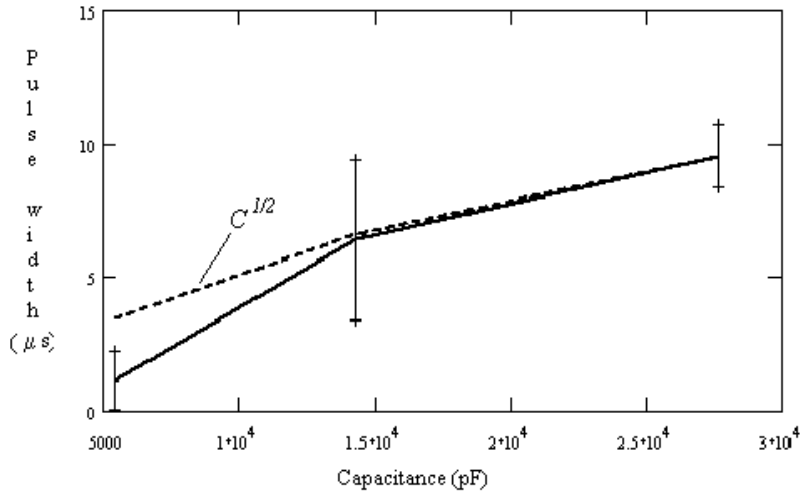

Figure 13. Pulse width scaling measured by biasing to -340 V one, three, and six strings of sample #2. Error bars (±1σ) are calculated from ten measurements for each point.

A few examples of the dependence of electron current collection on bias voltage are shown in Fig.14. It is seen than the increase of electron number density results in the almost proportional increase in current collection. But the dominant factor in the current collection is an array temperature. The magnitude of collected current grows more than three times when array temperature reaches 79 C. This observation must be taken into account for the computations of spacecraft floating potentials. Ion currents are measured by biasing separate strings up to 100 V negative, and these currents do not exceed 1 μA for all situations studied even though the same effect of significant increase due to heating is also found.

Measurements of collected currents for the sample with coverglass overhang have demonstrated the decrease in magnitude close to the factor 2 comparatively to sample with a standard design. Cell with wrapthrough interconnects collects not much less current than cell with coverglass overhang but it generates three times higher power. It seems that tests in simulated plasma environment are suitable for creation a data base for further computations of the spacecraft floating potentials in LEO.

Conclusions

Comprehensive tests of five different types of solar array samples in simulated LEO plasma environment have demonstrated that the highest arc threshold (440 V) can be achieved for an array with wrapthrough interconnects if edges of strings are not exposed to the plasma. This design is also effective in decreasing of an array current collection. The design with exposed interconnects but with coverglass overhang also provides significant improvement comparatively to the conventional design. Particularly, arcing on the sample cannot be initiated at potentials below 300 V even under room temperature, and arc threshold increases to 420 V under temperature 72 C. The increase of coverglass thickness also results in some improving of array parameters. Thorough outgassing of solar array surfaces may result in significant decrease of arc rate for a conventionally designed solar array.

a)

b)
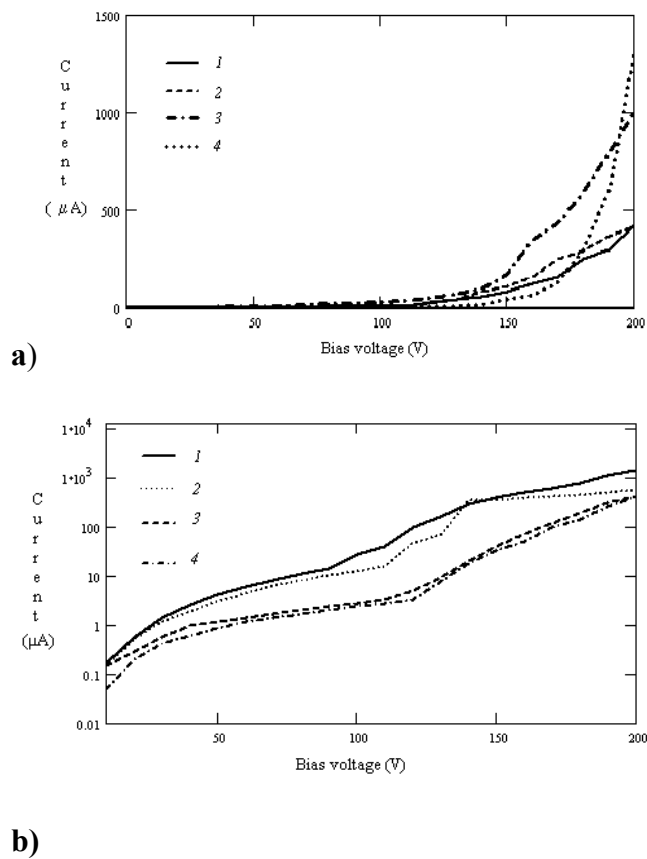
Figure 14. Electron current collection:
a) *1*-sample #2, str.2, $n_e=2*10^5$ cm^{-3},15 C; *2*-sample #1, str.1, $n_e=7*10^5$ cm^{-3},15 C; *3*-sample #1, str.2, $n_e=2*10^6$ cm^{-3},15 C; *4*-sample #2, str.1, $n_e=5*10^5$ cm^{-3}, 79 C.
b) b)*1*-sample #3, str.2, $n_e=1*10^6$ cm^{-3}; *2*- sample #4, str.2, $n_e=1*10^6$ cm^{-3}; *3* and *4*-sample #5, str.1 and 2 respectively, $n_e=3.5*10^5$ cm^{-3}, temp. 15 C.

References

(1)   Stevens, N.J. "Interactions Between Spacecraft and the Charge-Particle Environment", Proc. Spacecraft Charging Technology Conference, NASA CP-2071, 1978, p.268-294.

(2)   Ferguson, D.C. "Solar Array Arcing in Plasmas", NASA CP-3059, 1989, p. 509.

(3)   Hastings, D.E. "A Review of Plasma Interactions With Spacecraft in Low Earth Orbit", Journal of Geophys. Research, Vol.100, No.A8, 1995, pp.14,457-14,483.

(4)   Parks, E.D., Jongeward, G., Katz, I., and Davis, V.A. "Threshold-Determing Mechanisms for Discharges in High Voltage Solar Arrays", Journal of Spacecraft and Rockets, Vol.24, No.4, 1987, pp.367-371.

(5)   Upschulte, B.L., Marinelli, W.J., Carleton, K.L., Weyl, G., Aifer, E., and Hastings, D.E. "Arcing on Negatively Biased Solar Cells in a Plasma Environment", Journal of Spacecraft and Rockets, Vol.31, No.3, 1994, pp.493-501.

(6)   Vayner, B., Galofaro, J., Ferguson, D., and Degroot, W. "Electrostatic Discharge Inception on a High-Voltage Solar Array", AIAA Paper 2002-0631, Jan.2002.

(7)   Galofaro, J., Vayner, B., Ferguson, D., and Degroot, W. "A Desorbed Gas Molecular Ionization Mechanism for Arcing Onset in Solar Arrays Immersed in a Low-Density Plasma", AIAA Paper 2002-2262, May 2002.

(8)   Anders, A., and Anders, S. "Emission Spectroscopy of Low-Current Vacuum Arcs", Journal of Physics D: Appl. Phys., Vol.24, 1991, pp.1986-1992.

(9)   Yotsombat, B., Davydov, S., Poolcharuansin, P., Vilaithong, T., and Brown, I.G. "Optical Emission Spectra of a Copper Plasma Produced by a Metal Vapor Vacuum Arc Plasma Source", Journal of Physics D: Appl. Phys., Vol.34, 2001, pp.1928-1932.

(10)   Pearse, R.W.B., and Gaydon, A.G. "The Identification of Molecular Spectra", 3rd edition, Chapman & Hall LTD, London, UK, 1963, 347p.

(11)   Vayner, B.V., Galofaro, J.T., and Ferguson, D.C. "The Neutral Gas Desorption and Breakdown on a Metal-Dielectric Junction Immersed in a Plasma", AIAA Paper 2002-2244, May 2002

(12)   Cho, M., and Hastings, D.E. "Computer Particle Simulation on High-Voltage Solar Array Arcing Onset", Journal of Spacecraft and Rockets, Vol.30, No.2, 1993, pp.189-205.

(13)   Hastings, D.E., Weyl, G., and Kaufman, D. "Threshold Voltage for Arcing on Negatively Biased Solar Arrays", Journal of Spacecraft and Rockets, Vol.27, No.5, 1990, p.539-544.

(14)   Hoeber, C.F., Robertson, E.A., Katz, I., Davis, V.A., and Snyder, D.B. "Solar Array Augmented Electrostatic Discharge in GEO", AIAA Paper 98-1401, Jan. 1998.

(15)   Snyder, D.B., Ferguson, D.C., Vayner, B.V., and Galofaro, J.T." New Spacecraft-Charging Solar Array Failure Mechanism" 6th Spacecraft Charging Technology Conference, Nov. 2-6, 1998, Air Force Res. Lab., Hanscom AFB, MA, USA, pp.297-301.

(16)   Balmain, K. G., and Dubois, G. R. "Surface Discharges on Teflon, Mylar and Kapton," IEEE Transactions on Nuclear Science, Vol. 26, No.12, 1979, pp.5146-5151.

(17)   Snyder, D.B. "Characteristics of Arc Currents on a Solar Cell Array in a Plasma", IEEE Transactions on Nuclear Science, Vol.31, No.4, 1984, pp.1584-1587.

(18)   Cho, M., Ramasamy, R., Hikita, M., Tanaka, K., and Sasaki, S. "Plasma Response to Arcing in Ionospheric Plasma Environment: Laboratory Experiments", Journal of Spacecraft and Rockets, Vol.39, No.3, 2002, pp.392-408.

(19)   Ferguson, D.C., and Hillard, G.B. "In-Space Measurements of Electron Curren Collection by Space Station Solar Arrays", AIAA Paper 95-0486, Jan. 1995.

CHARGE STORAGE, CONDUCTIVITY AND CHARGE PROFILES OF INSULATORS AS RELATED TO SPACECRAFT CHARGING

J.R. Dennison
Physics Department, Utah State University
Logan, UT, USA 84322-4415
Phone: (435) 797-2936
Fax: (435) 797-2492
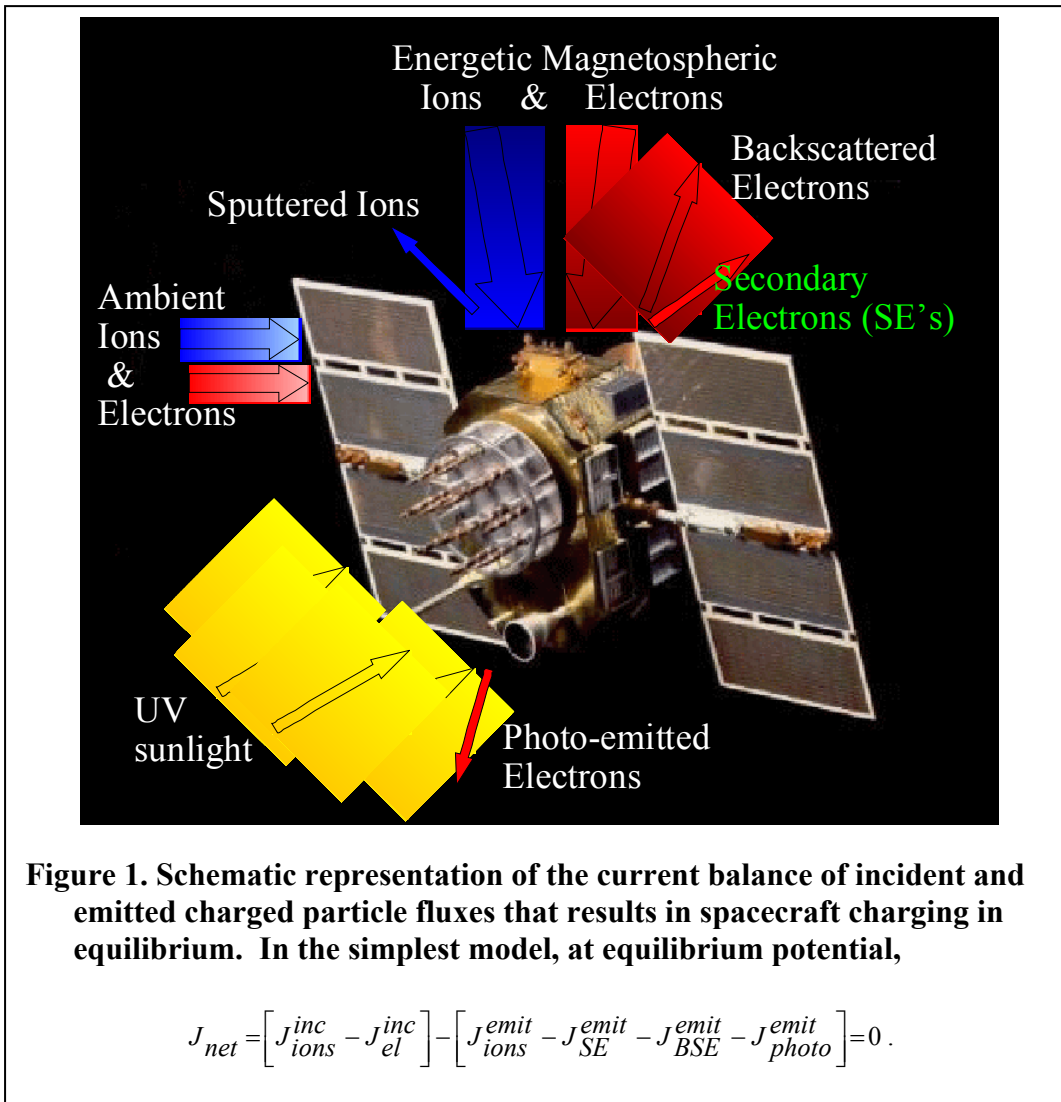E-mail: JR.Dennison@usu.edu

Prasanna Swaminathan
Physics Department, Utah State University

A. R. Frederickson
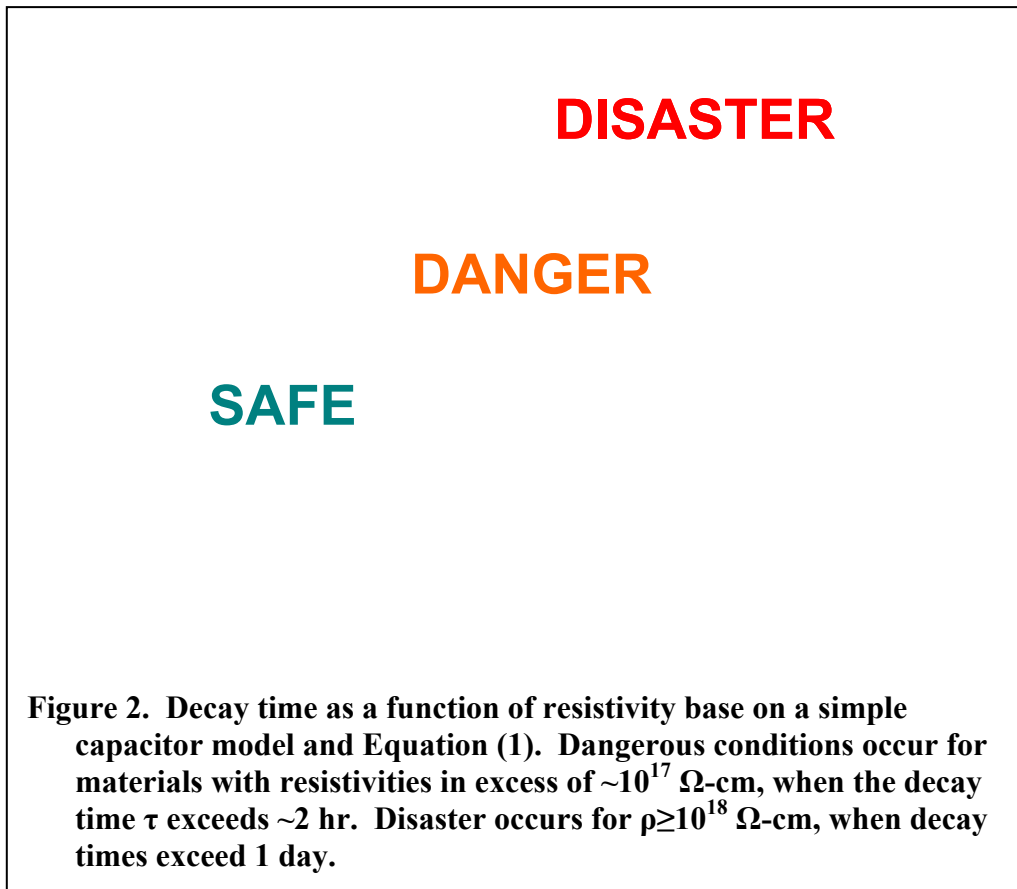Caltech Jet Propulsion Laboratory

Abstract

Dissipation of charges built up near the surface of insulators due to space environment interaction is central to understanding spacecraft charging. Conductivity of insulating materials is key to determine how accumulated charge will distribute across the spacecraft and how rapidly charge imbalance will dissipate. To understand these processes requires knowledge of how charge is deposited within the insulator, the mechanisms for charge trapping and charge transport within the insulator, and how the profile of trapped charge affects the transport and emission of charges from insulators. One must consider generation of mobile electrons and holes, their trapping, thermal de-trapping, mobility and recombination. Conductivity is more appropriately measured for spacecraft charging applications as the "decay" of charge deposited on the surface of an insulator, rather than by flow of current across two electrodes around the sample. We have found that conductivity determined from charge storage decay methods is 10^2 to 10^4 smaller than values obtained from classical ASTM and IEC methods for a variety of thin film insulating samples. For typical spacecraft charging conditions, classical conductivity predicts decay times on the order of minutes to hours (less than typical orbit periods); however, the higher charge storage conductivities predict decay times on the order of weeks to months leading to accumulation of charge with subsequent orbits. We found experimental evidence that penetration profiles of radiation and light are exceedingly important, and that internal electric fields due to charge profiles and high-field conduction by trapped electrons must be considered for space applications. We have also studied whether the decay constants depend on incident voltage and flux or on internal charge distributions and electric fields; light-activated discharge of surface charge to distinguish among differing charge trapping centers; and radiation-induced conductivity. Our experiments also show that "Malter" electron emission occurs for hours after turning off the electron beam. This Malter emission—similar to emission due to negative electron affinity in semiconductors—is a result of the prior radiation or optical excitations of valence electrons and their slow drift among traps towards the surface where they are subsequently emitted. This work is supported through funding from the NASA Space Environments and Effects Program.

Figure 1. Schematic representation of the current balance of incident and emitted charged particle fluxes that results in spacecraft charging in equilibrium. In the simplest model, at equilibrium potential,

$$J_{net} = \left[J_{ions}^{inc} - J_{el}^{inc} \right] - \left[J_{ions}^{emit} - J_{SE}^{emit} - J_{BSE}^{emit} - J_{photo}^{emit} \right] = 0 \, .$$

Introduction

In the space environment, charge is deposited on the surface of the spacecraft as it orbits. Hence, the orbital periodicity sets the relevant time scale for the problem; typical orbits of near-earth satellites range from 1 to 24 hours. For example, satellite orbit or rotation period determines the time surfaces are exposed to sunlight and subject to photoemission. Charge accumulated on the insulating spacecraft surfaces typically dissipates through the insulator to a conducting substrate. To better understand the charging phenomena, one then needs to relate conductivity or charge mobility to a suitable time scale. The charge storage decay time to the conducting substrate depends on the (macroscopic) conductivity or equivalently the (microscopic) charge mobility for the insulator. If the charge decay time exceeds the orbit time, not all charge will be dissipated before orbital conditions again charge the satellite, and charge can accumulate. As the insulator accumulates charge, the electric field rises until the insulator breaks down and generates a pulse.

In the simplest model of spacecraft charging, the charge on satellite surfaces accumulates in such a way as to produce an electric field that modifies the incident and emitted charge particle fluxes so that a net current balance and charge equilibrium is achieved. This current balance is depicted in Figure 1. The model is plausible, if simplistic, for a fully conductive spacecraft for which the charge will readily redistribute over the entire satellite in the case of absolute charging (or over isolated sections, for differential charging). The surface of conductors will charge to the point where the incident currents from the environment fluxes are equal to emission currents. By contrast, as insulating spacecraft materials accumulate charge, their low charge mobility causes

Figure 2. Decay time as a function of resistivity base on a simple capacitor model and Equation (1). Dangerous conditions occur for materials with resistivities in excess of ~10^{17} Ω-cm, when the decay time τ exceeds ~2 hr. Disaster occurs for ρ≥10^{18} Ω-cm, when decay times exceed 1 day.

charge to accumulate where deposited, and the local electric fields to rise until the leakage current from the insulators to underlying conductors equals the accumulation current from the environment (or until the charge stored in the insulator actually breaks down and generates a charge pulse). Hence, conductivity of insulating materials is a key transport parameter to determine how accumulated charge will distribute across the spacecraft, how rapidly charge imbalance will dissipate, and what equilibrium potential an insulator will adopt under given environmental conditions [1].

Treating a thin film insulator as simple capacitor, charge decay time is proportional to resistivity. As a first approximation, the thin-film insulator can be treated as a planar capacitor (with the charged front surface and conducting rear electrode acting as the electrodes); all charge resides at the interfaces, that discharges in an Ohmic fashion through the bulk of the insulator. In
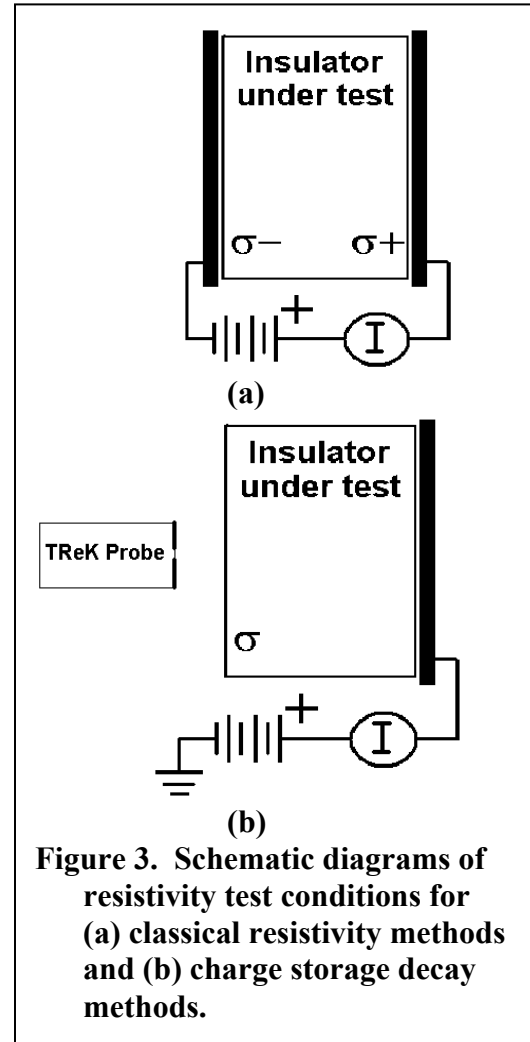
this approximation, the RC-time constant or relaxation time, τ, for discharging insulator can be written as:

$$\tau = \rho \varepsilon_r \varepsilon_0 \qquad\qquad (1)$$

where ρ is the material resistivity, and ε_o is the permitivity of free space. The relative dielectric constant, ε_r, of nearly all spacecraft insulators lie within a narrow range, 2-10, and is well known for most materials; thus, determination of the resistivity follows directly from measuring the relaxation time. The decaying surface potential can then be estimated as a function of time as $\sigma(t) = \sigma_0 \cdot e^{-t/\tau}$, where σ_o is the initial sample surface charge induced by electron beam irradiation, and σ is the decayed surface charge after a time interval, t. Therefore, τ is equivalently the relaxation time or the charge storage decay time, the time it takes for the surface charge to drop to 1/e of its initial value. Note that in this simple model, decay time is an intrinsic material property, independent of surface area or thickness.

Figure 2 shows a plot of decay time as a function of resistivity, Equation (1), for a relevant range of resistivity values. Values of typical spacecraft insulator material resistivities found in handbooks are in the range of 10^{13} to 10^{17} Ω-cm [2]. These corresponding to decay times of ~1 sec to ~2 hr, suggesting that in most cases charge collected by common spacecraft insulators will dissipate faster than the charge is renewed. Considering these results, dangerous conditions occur for materials with resistivities in excess of ~10^{17} Ω-cm, when τ exceeds ~2 hr. Disastrous conditions occur for $\rho \geq 10^{18}$ Ω-cm, when decay times exceed 1 day.

(a)

(b)

Figure 3. Schematic diagrams of resistivity test conditions for (a) classical resistivity methods and (b) charge storage decay methods.

Thus, it becomes critical for reliable spacecraft charging modeling to determine appropriate values of resistivity for typical thin film insulating materials [1,3,4]. The bulk resistivity values of insulators used to model spacecraft charging have traditionally been obtained from the handbook [2] values found by the classical ASTM/IEC methods [5,6]. However, recent work has shown that these classical methods are often not applicable to situations encountered in spacecraft charging [1,3,4,7,8]. The charge storage method—described below—was developed to measure the resistivity in a more applicable configuration. Results from charge storage resistivity methods find ρ values 10^1-10^4 times larger than classical handbook values, based on tests performed by Frederickson and coworkers on approximately ten different materials, including polyimides, Mylar^{TM}, Teflon^{TM}, silicate glasses, and circuit boards [1,3,4]. Returning to Figure 2, the relevant decay times corresponding to the higher charge storage resistivities of

these typical spacecraft insulators in the range of 10^{14} to 10^{21} Ω-cm are ~1 min to several years, clearly in the danger or disaster zones. Resistivity values based on the charge storage method have recently been used to correctly predict charging events observed in real satellite data, through modeling of pulses occurring aboard the CRESS satellite (see below) [8]. Given these results, we have concluded that charge storage resistivity methods are more appropriate than classical methods for many spacecraft charging problems.

This paper describes measurements of the decay of charge deposited on the surface of insulators or within a narrow region below the surface. The work is a joint project by the Jet Propulsion Laboratory (JPL) and Utah State University (USU) sponsored through the NASA Space Environments and Effects (SEE) Program [7]. All data presented in this paper were taken at JPL. Preliminary studies using the charge storage method and further details of the methods and instrumentation are found elsewhere [1,3,4]. Swaminathan, *et al*. provides a detailed comparison between classical and charge storage methods used to measure resistivity [1].

Comparison of Resistivity Test Methods

Classical methods use a parallel plate capacitor configuration to

(a)

(b)

Figure 4. (a) Fractional charge (proportional to surface voltage decay) versus elapsed time measurements on four samples. The top three curves are for 25 µm (proprietary) silicate glass samples, initially charged to -300 V DC. The bottom curve is for a 0.8 mm thick FR4 printed circuit board sample, initially charged to -600 V DC. [4] (b) Surface voltage decay for the two polyimide samples. Low-energy electron charging occurred at 0 days and resulted in the solid data points. Electron beam charging occurred at 23.7 days resulting in the open data points. [3]

determine the conductivity of insulators by application of a constant voltage (**E**-field) and the measurement of the resulting leakage current across the plates and through the insulator [1,5,6]. Figure 3(a) shows the preferred experimental arrangement for the ASTM-IEC or classical resistance method that is valid in the range of $10^7 < \rho < 10^{21}$ $\Omega \cdot$cm [6,7]. An adjustable high voltage is applied to one sample electrode. Current flow to the sample electrode held at ground is measured by a picoammeter. The resistance of the sample is then given by $R = \rho d / A_{eff}$, where ρ is the resistivity, A_{eff} is the effective area slightly larger than the metal electrode surface area, and d is the sample thickness. The resistance R is determined from an I-V curve using Ohm's law.
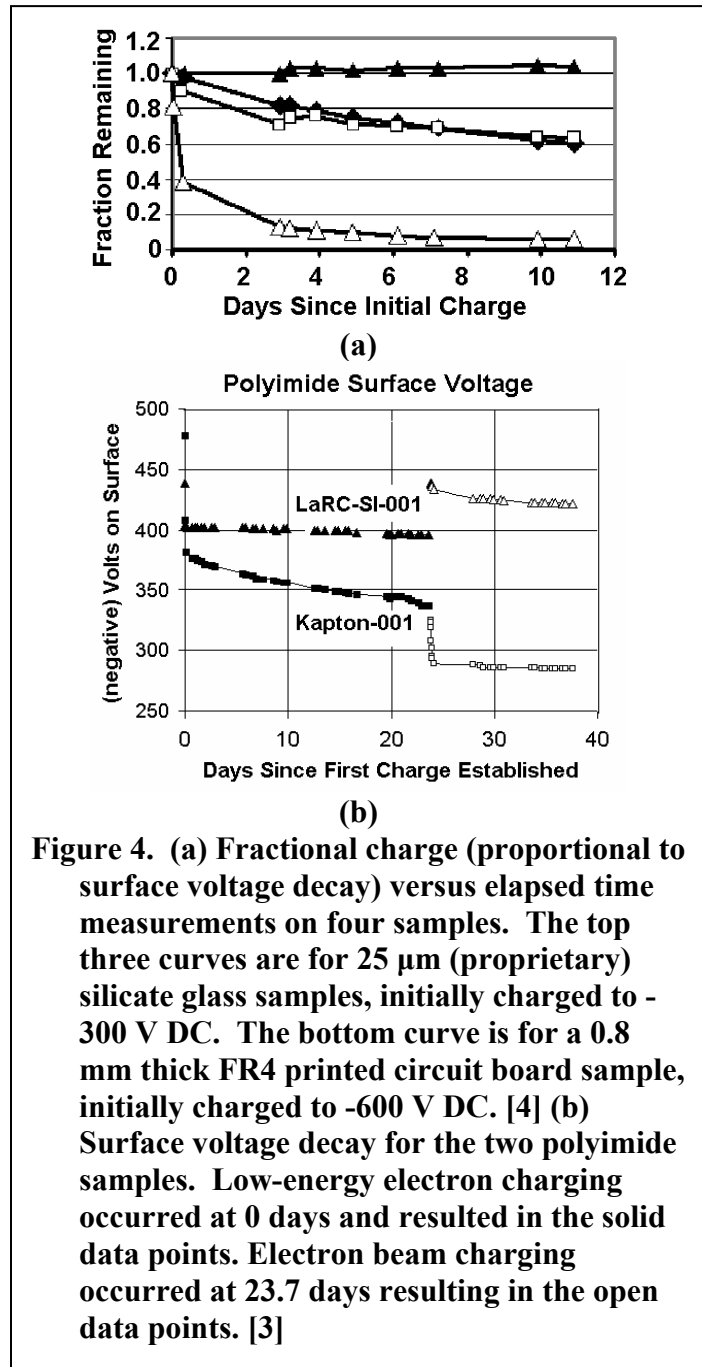
Data obtained using the classical resistance method for specific spacecraft materials such as Kapton H [9] and FR4 printed circuit board [4] materials are provided in other references [1,3,4]. Comparisons between classical and charge storage decay methods for some specific samples are made below; other such results are given in Refs. 1 and 4.

The voltages developed in space are usually generated by impressing charge into the insulation, not by the application of voltage from a power supply onto electrodes. Conductivity is more appropriately measured for spacecraft charging applications as the "decay" of charge deposited on the surface of an insulator. The arrangement for charging and measuring the surface charge (or voltage) on an insulated surface is shown in Figure 3(b). Charge decay methods expose one side of the insulator in vacuum to a charge source for deposition and treatments or to a field probe for charge monitoring. The other surface of the sample is in good contact with a conducting electrode and is connected to wiring so that it can be biased relative to ground or electron source, and can be monitored for currents. A TReK^{TM} electrostatic voltmeter [10] is used, that can sense surface voltages from –20 kV to +20 kV relative to local "ground," and from this infer local surface charge distributions. No electrical contact is made to the nearby HV surface. A custom capacitance transfer probe was constructed at JPL to make electric field measurements at sample surfaces *in situ* in a vacuum chamber, using a TreK^{TM} probe external to the chamber; this isolates the sensitive TreK^{TM} probe from the charge sources and sample treatments.

A variety of charged particle sources for deposition and sample treatment are available. For the basic charge storage measurements, a low energy (<10 eV) electron-emitting filament is used to provide uniform surface charge that does not penetrate far into the sample. This method (described in detail in Ref. 1) places the electrons gently onto the front surface, not deeper into the bulk of the insulator. Alternately, a broad-beam electron gun with accelerating potentials from 0 to 75 keV is available for uniform, stable charge deposition at energies in the few keV regime near the second crossover energy and at higher energies for study of internal sample charging. In addition, samples can be pre-treated using, low-energy electron fluxes, the higher energy electron beam, VIS/UV light photon fluxes, plasma sources, ion fluxes, and thermal treatments.

Table 1. Resistivity Models for CRRES Data from FR4 Printed Circuit Board Samples.

Method Used to Determine Resistivity	Dark Resistivity (Ω-cm)	Radiation-Induced Resistivity (Ω-cm)	Total Resistivity (Ω-cm)	Relaxation Time (hr)
Classical Method	5×10^{17}	3×10^{18}	2×10^{17}	5
Charge Storage Method	2×10^{18}	same	1×10^{18}	31
Best Fit to Pulse Data	6×10^{18}	same	2×10^{18}	52

Figures 4(a) [4] and 4(b) [3] show charge storage decay curves for six different materials. In each case, the resistivity is two to four orders of magnitude larger than that obtained with classical methods. For example, the charge storage value of resistivity for aluminum-backed 51 μm Kapton H samples [4] was $>5 \cdot 10^{+19}$ Ω·cm [see Fig. 4(b)], compared to a value of ~(3±1)

$\cdot 10^{+16}$ Ω·cm measured with classical methods and a handbook value of $1 \cdot 10^{+17}$ Ω·cm [9]. Note that charge decay is measured on timescales reasonably similar to that experienced in space, at least a month, to correctly evaluate appropriate decay.

Application of Charge Storage Resistivity to Charging Modeling

Frederickson and Brautigam have recently completed a study [8] of Internal Discharge Monitor (IDM) pulse data [11] from sample aboard the *Combined Release and Radiation Effects Satellite* (CRRES) [12], which provides compelling evidence for the validity of using charge storage resistivity values in spacecraft charging modeling. The project used only basic laboratory-derived materials properties (including resistivity) and data from on-board environmental charge flux monitors as inputs to models for internal charge deposition and migration within test samples to successfully predict the sample electrostatic discharge (ESD) pulsing amplitude and frequency over a time scale of hundreds of days and more than a thousand orbits. Central to the success of the project was the use of the charge storage resisitvity in place of the classical value of resistivity.

Specifically, data records were mined for IDM pulse data as a function of elapsed time for a variety of insulator samples, including a 0.8 mm thick FR4 printed circuit board sample, shown in the middle graph of Figure 5. Concurrent electron environmental data over a range of energies from ~0.1 to 5 MeV were also mined and parameterized to obtain a dosage profile impinging on the sample as a function of elapsed time over the ~15 month lifetime of the satellite. These parameterized dosage profiles for each half-orbit (~5 hr period) were used, together with stopping power and conductivity data for the sample materials, to model the charge deposition profile, the
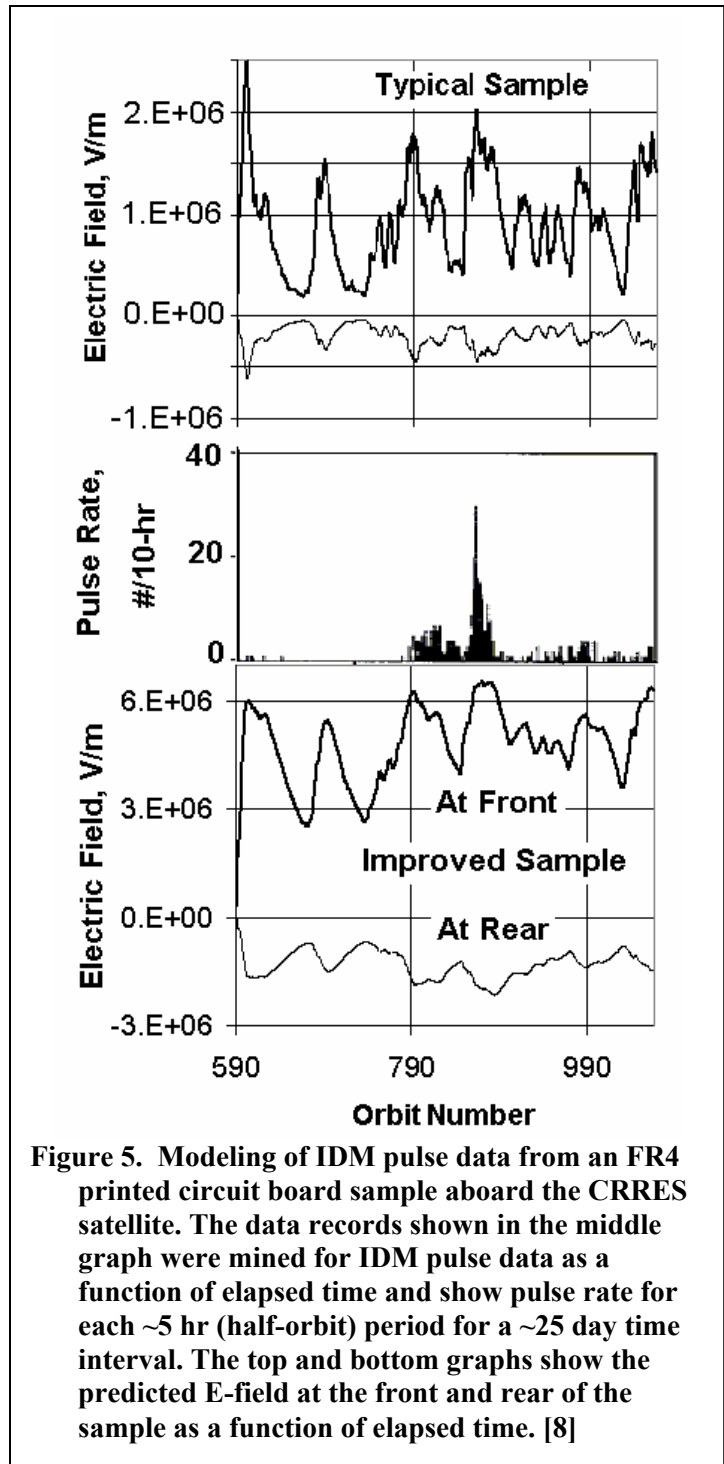

Figure 5. Modeling of IDM pulse data from an FR4 printed circuit board sample aboard the CRRES satellite. The data records shown in the middle graph were mined for IDM pulse data as a function of elapsed time and show pulse rate for each ~5 hr (half-orbit) period for a ~25 day time interval. The top and bottom graphs show the predicted E-field at the front and rear of the sample as a function of elapsed time. [8]

charge transport, and the time evolution of the internal charge distribution. The NUMIT code [13] was then used to calculate and time-evolving **E**-field profile.

The top and bottom graphs in Figure 5 show the predicted **E**-field at the front and rear of the sample as a function of elapsed time. The top panel is based on the classical resistivity value of FR4 board and an estimated value of the radiation-induced conductivity based on results for similar materials (values are listed in Table I). Note that at no time does the **E**-field in the top panel of Figure 5 exceed 25% of the value of $1 \cdot 10^7$ V/m, which is typically needed to induce occasional pulsing. This prediction of no pulsing is consistent with the observation that the relaxation time from the total resistivity (dark resistivity and radiation-induced resistivities added in parallel) based on Equation (1) of ~5 hr is less than the orbit time of ~10 hr. However, when the measured charge storage resistivity is used to predict the **E**-field evolution (see lower panel of Figure 5), the **E**-field exceeds $0.6 \cdot 10^7$ V/m near 600, 790, 850 and 1050 orbit number. In each case, there is corresponding pulse activity observed in the central panel of Figure 5, with the pulse rate amplitude correlated to the magnitude of the **E**-field. Again, the prediction of pulsing is consistent with the predicted relaxation time of ~31 hrs from Equation (1), which is well in excess of the orbit time. Finally, a value of dark resistivity that best fits the pulse data was determined. Note that because the charge storage resistivity and the estimated radiation-induced resistivity are comparable, the total resistivity of the best fit is only a factor of two larger than the total resistivity using the measured charge storage resistivity.

Effects of Internal Charge Distributions

Given the preliminary results from charge storage measurements of spacecraft insulators and the successful use of these measurements to model charge storage and dissipation and to predict pulsing in real world applications, it is tempting to consider the problem solved and simply use charge storage resistivities in place of classical resistivities for future modeling. However, the question of why the classical and charge storage methods produce resistivity values that differ by as much as four orders of magnitude still needs to be addressed, if for no other reason than to know which resistivity value to use for different circumstances (to say nothing of understanding the questions of the underlying physics).

While there is yet no clear explanation as to why the two methods produce such divergent results,
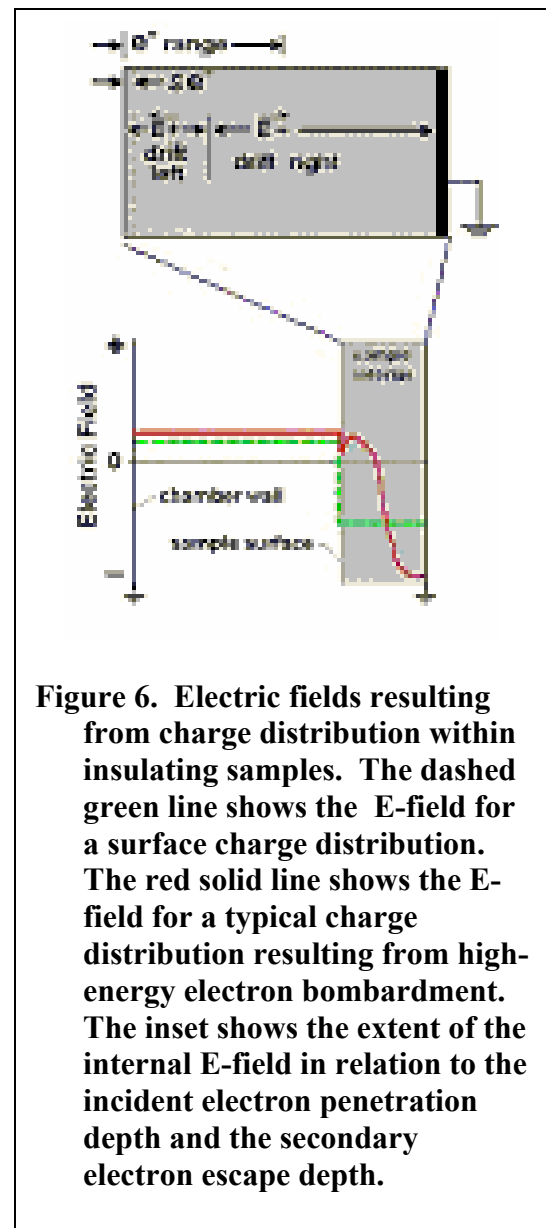
Figure 6. Electric fields resulting from charge distribution within insulating samples. The dashed green line shows the E-field for a surface charge distribution. The red solid line shows the E-field for a typical charge distribution resulting from high-energy electron bombardment. The inset shows the extent of the internal E-field in relation to the incident electron penetration depth and the secondary electron escape depth.

preliminary results suggest internal charge distribution and electric fields are critical to understanding the underlying physics. To illustrate these processes requires knowledge of how charge is deposited within the insulator, the mechanisms for charge trapping and charge transport within the insulator, and how the profile of trapped charge affects the transport and emission of charges from insulators. One must consider generation of mobile electrons and holes, their trapping, thermal de-trapping, tunneling, mobility, recombination and emission from the sample.

A number of experiments have been conducted in this project to investigate the role of charge deposition, charge transport and charge decay in materials properties such as conductivity and electron emission. In general, these experiments involve determining the effects of different sources and sample treatments, such as high-energy electron beams and radiation sources, ion sources, plasma sources, visible and UV light treatments, thermal treatments, or other treatments of the samples [4]. To evaluate conduction in unaltered insulators, their surfaces must be charged with low-energy electrons, as described above. Kilovolt electron beams, ions, or other treatments alter the sample as they excite secondary processes that repopulate trapping states in the insulator, or otherwise alter the material.

Charge deposition and distribution

We begin by describing where charge is deposited in an insulator and how this is affected by the incident particle energy and the charge distribution already present in the insulator. Consider the electric fields resulting from charge distributions in the insulator depicted for a 1D scenario schematically in Figure 6. For very low incident energies, the mean free path of the incident electrons is very small (on the order of nanometers) and, to a good approximation, charge is deposited on the insulator surface. Such a surface charge distribution is also appropriate for a biased conducting surface [14] where charge produced in the interior rapidly migrates to the surface. A charge distribution confined to the surface results in a uniform **E**-field everywhere within the ideal insulator between the charged surface and the grounded rear electrode. The field is also constant external to the charged surface between a parallel grounded plate and the charge plane. The magnitude of the external field is typically much less than the internal field, as the ratio of the **E**-fields scales with the inverse ratio of the distances from the charged surface and the grounded planes. The surface charge on an insulator presents a barrier to incident electrons in the same manner as for a biased conductor [14]. Those incident electrons with insufficient energy to overcome the surface potential barrier are turned away; those with higher energies have their landing energies reduced.

Higher energy electrons penetrate further into the surface; for kilovolt electrons this can be on the order of μm for insulators. Because space radiation injects charge into the interior of the insulator, generally the highest voltage is achieved internal to the insulator. A simple approximation is that all charge is deposited in a plane at a uniform depth, equal to the mean free path of the incident electrons. Note that this approximation is that used for the stopping power in the Sternglass formulation of the secondary electron yield formula [15]. If the plane of charge is moved into the insulator to the depth of the mean free path, the electric displacement on the left side of the charge plane remains unchanged, but the constant electric field inside the left side of the insulator is decreased by a factor of $1/\varepsilon_r$. An alternate approximation for high-energy electron penetration is that the number of energy loss scattering events (or equivalently, the

number of SEs generated) for the incident electrons is independent of depth (or equivalently, that the stopping power is constant), up to the penetration depth where all incident electron energy has been dissipated. (Note, this approximation is used for the constant loss formulations of the secondary electron yield formula [16]. Other models for SE yield, termed power law models, assume stopping power is proportional to the incident electron energy to the nth power, where $1 < n \leq 2$; these reflect that higher energy electrons will produce more SE's and lead to a higher SE production near the surface [16].) Any of these models provide a way to model the charge distribution inside an insulator, assuming that charge is not mobile and that the subsequent deposition is not affected by the presence of an internal charge distribution.

A more reliable picture for a typical charge distribution set up by high-energy electron bombardment is substantially more complex, if we consider charge mobility and the affect of the charge distribution of subsequent deposition. An appropriate model for this is illustrated by the solid line of the main curve in Figure 6 and the accompanying inset. Negative charge is deposited in the insulator up to some range of the incident energy electrons, typically on the order of μm. For typical insulators, the stopping power is found to be a larger exponent than for most metals, leading to non-linear charge deposition and reflecting the effect of charge build up in the insulator on deposition [17]. Over a narrow depth below the surface—determined by the mean free path of low-energy SEs, which are most commonly on the order of a few eV—the number of secondary electron that leave the sample often exceeds the number of electrons deposited by the incident beam; this leads to a net positive charge distribution in the SE electron region indicated in Figure 6. Thus, there can be a charge double-layer at the surface. That is, there is a sample region near the surface with an **E**-field to the left, a sample region on the right with an **E**-field to the right, and a zero-field plane between these two regions. The zero-field plane is typically found between the incident electron penetration depth and the SE escape depth and is the depth where the voltage is most negative [22]. The depth of the zero-field plane will increase with increasing penetration depth or incident beam energy.

Figure 6 illustrates a specific situation where the thickness of the sample is about 1/3 of the distance to the vacuum wall, and therefore the electric field in the vacuum region is roughly 1/3 of that in the sample assuming surface charge only. In real spacecraft arrangements, the distance to ground in the vacuum is very much greater than the sample thickness. Thus, in real spacecraft, the electric field strength in the back of the insulator is perhaps a hundred times larger than that in the front. Figure 6 also illustrates incident electrons with a penetration depth about ⅔ of the sample thickness. As incident electron energy increases, the incident electron range increases and the maximum voltage at the zero-field plane approaches the grounded rear electrode, resulting in an increased electric field strength.

Charge migration

We next look at how the internal charge distribution can affect the migration of charge (conductivity). Figure 7 shows a qualitative picture of the simplified band level diagrams of an insulating sample exposed to successively higher fluxes of high-energy electron irradiation, beginning with a virgin sample in Figure 7(a). As high-energy electrons enter the insulator, they deposit energy in the region up to the penetration depth, which excites electrons into the conduction band [see Figure 7(b) and (c)]. There is typically one electron-hole pair generated for

each ~ 30 eV (that is ~3 E_{gap}) lost by the incident electron, and perhaps 40 such electron-hole pairs can be generated for each kilovolt of incident electron energy dissipated. As charge builds up within the insulator, the maximum voltage at zero-field plane increases, resulting in the band-bending behavior illustrated in Figures 7(b) and (c).

Electrons in the region to the left of the zero-field plane are driven to the left. The conductivity of an insulator is altered as radiation-induced excited electrons accumulate and trapped states are filled with electrons. Thermal emission from shallow traps to the conduction band occurs (slowly) everywhere that shallow traps are occupied. This is typically a small effect at room temperature. The conduction electrons are then preferentially driven in the direction of the **E**-field, but are quickly recaptured in another trapped state. This leads to what is referred to as hopping conductivity, as the electrons preferentially progress in short "hops" from one trapped state to the next, with a net motion in the direction of the **E**-field. As these hopping electrons reach the surface, they can be thermally excited from a trapped state to an energy sufficient to overcome the surface potential barrier. The distance from the zero-field plane, where the voltage is maximum, through the sample surface and across the vacuum is large, and therefore the electric field in this region is relatively small.

If the interior charge build up is large enough, the peak voltage can exceed the vacuum level of the sample. This means that as hopping electrons progress towards the surface they will encounter a point at which they will be excited to a conduction band state above the vacuum level. At this point, the sample is said to have a negative electron affinity and the electrons can proceed unimpeded to the surface and across the surface barrier. This negative electron affinity effect can greatly extend the region over which SEs can escape the material, thereby dramatically increasing SE yield [18]. Because electrons involved in hopping conductivity undergo slow transitions from trapped states to the conduction band states, after the irradiation stops, thermal emission currents may persist for some time until the shallow traps have emptied. This is called the Malter Effect [19].

Trapped electron moving from the zero-field plane to the right can proceed via hopping conductivity, or by an alternate method called tunneling [see Figures 7(d), (e) and (f)]. From the zero-field plane, the distance to the sample electrode is short and therefore the electric field near the electrode is large. The field can be further enhanced by using higher energy electrons to bring the penetration depth, as well as the maximum voltage zero field plane, closer to the rear electrode of the sample. This field in the back of the sample can become so large that shallow-trapped electrons tunnel to the conduction band and provide enhanced conductivity. This can occur in a range of field strength similar to that in which electrical breakdown *easily* occurs (>5×10^5 V/cm), and may either contribute to breakdowns or prevent them by reducing charge build-up through increased conductivity, depending on the nature of the defects that are responsible for the breakdowns.
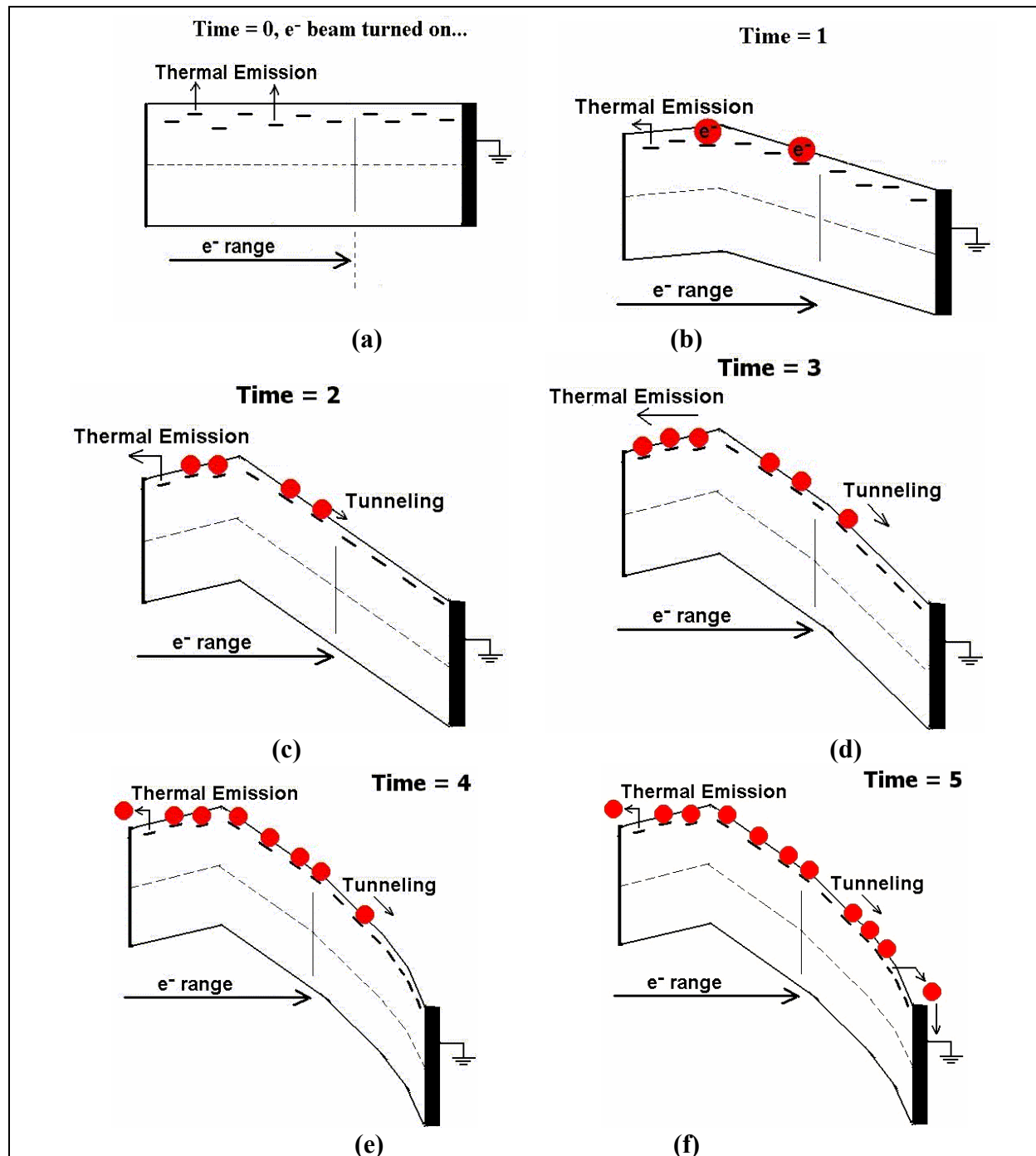
Figure 7. Simplified band diagrams for an insulating sample exposed to successively higher fluxes of high-energy electron irradiation. The horizontal axis is depth into the sample, from the charged surface on the left to the grounded rear electrode on the right. The incident electron penetration depth (typically on the order of μm) shown is approximately ⅔ of the sample thickness, so that the zero-field plane where peak voltage occurs is about ⅓ of the way into the sample. The vertical axis is energy, beginning at the bottom with the valance band at E_{VB} (solid line), then the Fermi level at E_F (dashed line), localized trapped states (long dashes), and conduction band at E_{CB} (solid line). The position of the Fermi level will move towards the conduction band as the concentration of localized trapped states increases. The vacuum level, E_{vac}, is typically somewhat above E_{CB}. To set the scale, note that typical insulator band gaps, $E_{gap} \equiv E_{CB}$-E_{VB}, are ~5 eV to 10 eV. The red dots represent electrons excited by the incident high-energy electrons into the conduction band, that have subsequently decayed into trapped states.

Observed effects due to high-energy electron pre-treatments

Figures 8(a) and 8(b) shows Q-V electron-beam charging data for three similar 25 μm silicate glass samples (proprietary, undisclosed materials) [also shown in Figure 4(a)]. Here Q is the cumulative charge incident on the sample surface from a series of short high-energy electron beam pulses and V is the measured incremental surface voltage proportional to surface charge. For Figure 8(a) [top curve in Figure 4(a)], a 10 keV electron beam was used for which the electron penetration depth was less than 10% into the insulator and the **E**-field at the rear of the insulator was relatively small. Currents arriving at the sample surface and the sample electrode were small and not affected by the developing surface voltage, as demonstrated by the straight line in Figure 8(a) for the good, non-leaky insulator. The material used for Figure 8(b) [middle curve in Figure 4(a)] was manufactured to be more conductive. The slight curvature of the trace in Fig. 8(b) indicates the occurrence of conduction currents during the time of charge-up irradiation, that is that this is a slightly leaky insulator. The insulator's capacitance was determined from the slope of the curve at small Q.

This contrasts with the behavior shown in Figure 8(c) for which, the sample behaves as a capacitor during early irradiation, whereas it behaves as a voltage regulator during continued irradiation. Figure 8(c) shows data for the same glass samples irradiated with 40 keV electrons, where the deepest incident electrons penetrate nearly 90% into the sample. In this case, the zero-field plane is much closer to the rear grounded electrode; thus, the electric field in the rear of the sample is much larger, many electrons are excited into traps near the rear electrode, and tunneling currents are larger.

(a)   (b)   (c)
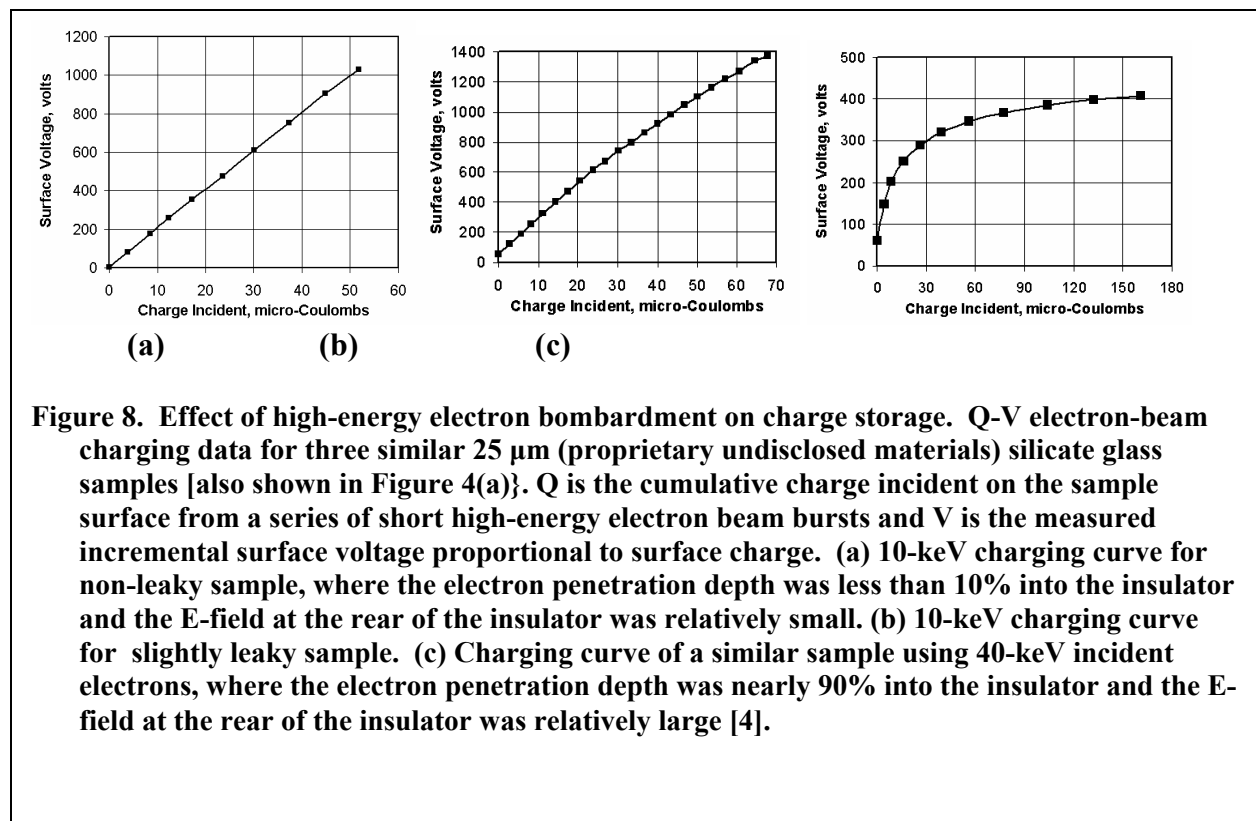
Figure 8. Effect of high-energy electron bombardment on charge storage. Q-V electron-beam charging data for three similar 25 μm (proprietary undisclosed materials) silicate glass samples [also shown in Figure 4(a)}. Q is the cumulative charge incident on the sample surface from a series of short high-energy electron beam bursts and V is the measured incremental surface voltage proportional to surface charge. (a) 10-keV charging curve for non-leaky sample, where the electron penetration depth was less than 10% into the insulator and the E-field at the rear of the insulator was relatively small. (b) 10-keV charging curve for slightly leaky sample. (c) Charging curve of a similar sample using 40-keV incident electrons, where the electron penetration depth was nearly 90% into the insulator and the E-field at the rear of the insulator was relatively large [4].

Figure 8(c) hints that the various radiation-generated conduction mechanisms in these glass samples prevent the development of a strong electric field, provided there is sufficient beam that penetrates throughout the sample. On these samples with 40-keV beams, much smaller surface voltage is produced than is produced with 10- or 20-keV electron beams even though at all three energies all of the electrons are stopped in the insulator. This is evidenced by the large curvature and low surface voltage in Figure 8(c), resulting from large charge bleed-off due to the enhanced conductivity. Charging induced by electron irradiation is strongly modified by the electron-hole pairs that the irradiation generates in the insulator. High field effects at or above 10^6 V/cm act strongly on the electron-hole pairs and on electrons in shallow traps to provide extended conductivity which can be evaluated by measuring surface voltage on the insulator. Also note that monitoring surface voltage while irradiating with electrons that stop just short of penetrating the insulator provides a way to roughly evaluate electron mean free path in an insulating material.
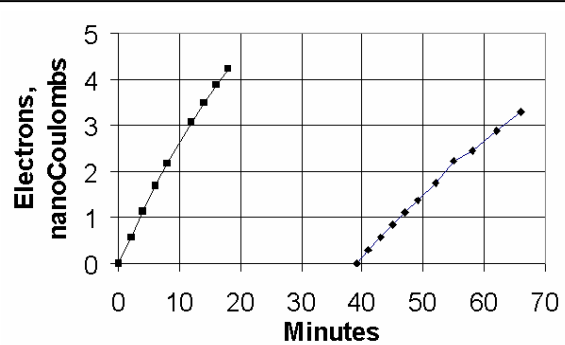
Figure 9. Electron emission into the vacuum after irradiation ceases. The 25 μm (proprietary undisclosed materials) silicate glass sample (also see Figures 4 and 8) was charged to – 1100 Volts by 10 keV electrons. The emission current was monitored by measuring the collection of electrons on the sensor field plate. By also knowing the capacitance of the sample (Cf = 35 pF), the surface voltage decay due to the emission of charge onto the sensor field plate was calculated. After 18 minutes the measurement was discontinued, and started again after 38 minutes.

Our experiments also show that "Malter" electron emission occurs for hours after turning off the electron beam. This Malter emission—similar to emission due to negative electron affinity in semiconductors—is a result of the prior radiation or optical excitations of valence electrons and their slow drift among traps towards the surface where they are subsequently emitted. Evidence for this comes from 10 keV-electron irradiation samples shown in Figure 9, where electrons are continually emitted for hours from the irradiated surface after the irradiation ceases. The long emission duration indicates that hopping is a dominant mechanism and that the conduction band is not significantly below the vacuum level. Additionally, monitoring current from the rear grounded electrode indicted that similar emission occurs at the rear electrode as well [4].

Light-induced conductivity

Visible light has been used after charging the sample to investigate the conduction contributed by electrons (or holes) emitted from shallow trapping levels separately from the natural dark conductivity [4]. Kilovolt electron irradiations excited electrons into the conduction band, from where they decayed into traps. After irradiation, the trapped population was probed by exciting these trapped electrons into the conduction band to enhance conductivity so that the

sample surface voltage decayed. Light of frequency ν can excite an electron transition from a trapped level into the conduction band provided that hν > ΔE, where the trapped states are an energy ΔE below the bottom of the conduction band. Thus, the relative currents for increasing light frequency provide information about the energy distribution of trapped states. In these experiments, a light source illuminated the pre-charged sample while a minimal positive battery voltage was maintained so that charge did not escape the surface of the sample. The light-induced conductivity caused the surface voltage to decay, and this voltage decay provided a sensitive monitor for conductivity.

In some samples, the effects of visible light-induced conductivity were found to be dominant while in other samples visible light provides negligible conductivity. A Teflon ™ sample that was irradiated with an electron beam at 1 kV surface voltage showed almost no discharge. By contrast, polyimide samples 50 μm thick that underwent similar irradiation were discharged in a few hours by a 1-watt incandescent filament. (A caution is evident from this result: the light emitted by an electron gun filament can potentially modify the charging process induced by the gun's electrons.) In some samples, light has been used to neutralize internal charging induced in prior tests so that further electron emission testing may proceed without initial charge in the sample [20,21].

Acknowledgments

References

1. Prasanna Swaminathan, A. R. Frederickson, J.R. Dennison, Alec Sim, Jerilyn Brunson, Eric Crapo, "Comparison Of Classical And Charge Storage Methods For Determining Conductivity Of Thin Film Insulators," Proceedings of the 8th Spacecraft Charging Technology Conference, October 20-24, 2003, Huntsville, Alabama.

2. W. Tillar Shugg, Handbook of Electrical and Electronic Insulating Materials, 2nd Ed; The Guide to Plastics by the Editors of Modern Plastics Encyclopedia, McGraw Hill, Inc., N.Y., 1970.

3. A.R. Frederickson, C. E. Benson and J. F. Bockman, "Measurement of Charge Storage and Leakage in Polyimides," Nuclear Instruments and Methods in Physics Research B, 454-60, 2003.

4. A.R. Frederickson and J. R. Dennison, "Measurement of Conductivity and Charge Storage in Insulators Related to Spacecraft Charging," accepted for publication in IEEE Trans. Nuc. Sci., Dec. 2003.

5. ASTM D 257-99, "Standard Test Methods for DC Resistance or Conductance of Insulating Materials" (American Society for Testing and Materials, 100 Barr Harbor drive, West Conshohocken, PA 19428, 1999).

6. IEC 93, International Electrotechnical Commission Publication 93, Methods of Test for Volume Resistivity and Surface Resistivity of Solid Electrical Insulating Materials, Second Edition, 1980.

7. J.R. Dennison and A.R.Frederickson, "Electronic properties of materials with application to spacecraft charging", NASA Space Environments and Effects (SEE) Program Grant NAS8-02031,.2002-2004.

8. A. Robb Frederickson and Donald H. Brautigam, "Mining CRRES IDM Pulse Data and CRRES Environmental Data to Improve Spacecraft Charging/Discharging Models and Guidelines," Final Report: NASA SEE Program Contract No. NAS7-1407, Task Order 10676, 2003; to be published.

9. Kapton polyimide film product information: Physical Properties, Report H-38492-1, (Dupont, Wilmington, DE, February, 1997); http://www.dupontteijinfilms.com/ , June 20, 2002; The Red Book, RB 1, (Sheldahl Technical Materials, Northfield MN, 1995); http://www.sheldahl.com/Product/TechMaterials.htm , June 20, 2002.

10. Operators Manual, Model 341A, High Voltage Electrostatic Voltmeter, Trek, Inc., 11601 Maple Ridge Road, Medina, New York 14103, USA. Telephone: 1 (800) 367-8735 or 1 (585) 798-3140, http://www.trekinc.com/ .

11. A.R. Frederickson, E.G. Mullen, K.J. Kerns and P.A. Robinson, "The CRRES IDM Spacecraft Experiment for Insulator Discharge Pulses," IEEE Trans. Nuc. Phys. 40(2), 233-241 (1993).

12. E. Mullen and M. Gussenhoven, "Results of Space Experiments: CRRES," in R.N. DeWitt, D. Duston, and A.K. Hyder (eds.) The Behavior of Systems in the Space Environment, pp. 605-654, (Kluwer Academic Publishers, 1993).

13. A.R. Frederickson, "Radiation Induced Electrical Current and Voltage in Dielectric Structures," AFCRL-TR-74-0582, 1974.

14. N. Nickles, R.E. Davies and J.R. Dennison, "Applications of SE Energy- and Angular-Distributions to Spacecraft Charging," Proc. of 6th Spacecraft Charging Techno. Conf., (Hanscom Air Force Base, MA, 1999).

15. E.J. Sternglass, "Backscattering of Kilovolt Electrons from Solids," Phys. Rev. 95, 345-358 (1953); "An Experimental Investigation of Electron Back-scattering and Secondary Electron Emission From Solids, Ph.D. Dissertation, Cornell University, Ithica, NY, 1953.

16. A.J. Dekker, Solid State Physics, edited by Seitz and Turnbull (Academic Press, New York, 1958).

17. G.F. Dionne, "Origin of Secondary-electron-emission Yield-curve Parameters," J. Appl. Phys. 46 3347-3351 (1975); "Effects of Secondary Electron Scattering on Secondary Electron Emission," J. Appl. Phys. 44, 5361-5364 (1973).

18. J.E. Yates, A. Shih and Abrams, "Electron transport and emission properties of C(100)," Phys. Rev. B, 56, R4410-R4413 (1997).

19. R. Coelho, P Jestin, L. Levy and D. Sarrail, "On the Return-Voltage Buildup in Insulating Materials," IEEE Trans. Elec. Insul. 22, 683-90 (1987).

20. C.D. Thomson, V. Zavyalov, J.R. Dennison, Jodie Corbridge, "Electron Emission Properties of Insulator Materials Pertinent To The International Space Station," Proceedings of the 8th Spacecraft Charging Technology Conference, October 20-24, 2003, Huntsville, Alabama.

21. C.D. Thomson, Measurements of the Secondary Electron Emission Properties of Insulators, Ph.D. dissertation, Utah State University, 2004.

22. B. Gross and M. M. Perlman, J. Appl. Phys. 43, 853-7 (1972).

ELECTRON EMISSION PROPERTIES OF INSULATOR MATERIALS PERTINENT TO THE INTERNATIONAL SPACE STATION

C.D. Thomson
Physics Department, Utah State University
Logan, UT, USA 84322-4415
Phone: 435.797.2936
Fax: 436.797.2492
E-mail: JR.Dennison@usu.edu

V. Zavyalov
J.R. Dennison
Jodie Corbridge
Physics Department, Utah State University

Abstract

We present the results of our measurements of the electron emission properties of selected insulating and conducting materials used on the International Space Station (ISS). Utah State University (USU) has performed measurements of the electron-, ion-, and photon-induced electron emission properties of conductors for a few years, and has recently extended our capabilities to measure electron yields of insulators, allowing us to significantly expand current spacecraft material charging databases. These ISS materials data are used here to illustrate our various insulator measurement techniques that include:

i)   Studies of electron-induced secondary and backscattered electron yield curves using pulsed, low current electron beams to minimize deleterious affects of insulator charging.

ii) Comparison of several methods used to determine the insulator 1st and 2nd crossover energies. These incident electron energies induce unity total yield at the transition between yields greater than and less than one with either negative or positive charging, respectively. The crossover energies are very important in determining both the polarity and magnitude of spacecraft surface potentials.

iii) Evolution of electron emission energy spectra as a function of insulator charging used to determine the surface potential of insulators.

iv) Surface potential evolution as a function of pulsed-electron fluence to determine how quickly insulators charge, and how this can affect subsequent electron yields.

v)   Critical incident electron energies resulting in electrical breakdown of insulator materials and the effect of breakdown on subsequent emission, charging and conduction.

vi) Charge-neutralization techniques such as low-energy electron flooding and UV light irradiation to dissipate both positive and negative surface potentials during yield measurements.

Specific ISS materials being tested at USU include chromic and sulfuric anodized aluminum, RTV-silicone solar array adhesives, solar cell cover glasses, Kapton[TM], and gold. Further details of the USU testing facilities, the instrumentation used for insulator measurements, and the NASA/SEE Charge Collector materials database are provided in other Spacecraft Charging Conference presentations (Dennison, 2003b). The work presented was supported in part by the NASA Space Environments and Effects (SEE) Program, the Boeing Corporation, and a NASA Graduate Fellowship. Samples were supplied by Boeing, the Environmental Effects Group at Marshall Space Flight Center, and Sheldahl, Inc.

Introduction

The electron emission properties of materials have been studied for over fifty years and are relevant to many technical applications including the continued development of electron multiplier detectors (Shih, 1997), scanning electron microscopy (Reimer, 1985; Seiler, 1983), electron probe microanalysis, Auger electron spectroscopy (Belhaj, 2000), plasma fusion devices, high-current arcing, and flat panel displays (Auday, 2000). The specific motivation for our work at Utah StateUniversity (USU) comes from NASA's concern for the charging of spacecraft materials in the space environment (Dennison, 2003d; 2002). The extent and configurations of spacecraft charge buildup depends on the spacecraft orbit, orientation, ion, electron and photon flux, and on electrical material properties such as resistivity and dielectric constant, and electron emission rates. At USU, we have expanded the material electron emission database used by NASA's current model for spacecraft charging, NASCAP 2K, to include numerous uncharacterized materials that are used in spacecraft construction. Our ground-based experiments provide us with an understanding of fundamental particle and material interactions that can occur in space (Dennison, 2003b; 2002).

The focus of recent research has been the development of instrumentation and techniques for measuring the electron-induced electron emission properties of thick and thin-film insulating materials. These efforts have led to the development of novel electronics and methodologies for making very short-duration, low-signal measurements as well as various charge-neutralization techniques (Zavyalov, 2003). To demonstrate these capabilities, we present the results of measurements made for selected insulating and conducting materials used on the International Space Station (ISS). These data demonstrate the electron-yield charging characteristics of conducting and insulating materials, as well as various techniques used to measure electron emission parameters that are used in spacecraft charging models.

Electron Emissions From Insulators and Conductors

When charged particles impinge on a solid they can impart energy, exciting electrons within the material. If this energy is sufficient to overcome surface energy barriers (*e.g.* work function or electron affinity) electrons can escape from the material, leading to material charging. The emitted electrons can be divided into two categories: i) Secondary electrons (SE); typically lower energy electrons (<50 eV by convention) that originate within the material, produced by numerous inelastic scattering events of the incident electrons; ii) Backscattered electrons (BSE); typically higher energy electrons (>50 eV by convention) that originate from the incident electron source, but scatter either elastically or inelastically before leaving the target material

(Reimer, 1985; Seiler, 1983). SE and BSE yields are defined as the ratios of the sample emitted electrons to the total incoming electrons. Such measurements on conductors are straightforward since a constant electron current source can be used and DC currents from the sample can be captured and quantified using a retarding-grid detector assembly (with a zero or -50 V suppression used to discriminate between SE's and BSE's) and picoammeters. Additionally, by grounding the conductor, any charge that leaves or is absorbed into the material can be immediately neutralized to ground.

Electron yield measurements on dielectrics are more difficult to make, since any charge that is deposited in the material cannot easily be dissipated. The surface and bulk potentials that develop can subsequently affect electron emissions by influencing incident electron energies, or by creating electric fields that affect the escaping SE's. Without the implementation of neutralization techniques, an irradiated insulator will eventually charge to a steady state current equilibrium such that the net current to the sample is zero or the total electron yield is equal to one (Reimer, 1985; Seiler, 1983).

The polarity of insulator charging is dependent on incident electron energies. Positive (negative) charge will build up when the total number of electrons leaving the insulator sample is greater than (less than) the total number of incoming electrons. If the energy of incident electrons is below the insulator first crossover energy, E_1, (<100 V for most good insulators) negative charging results, since few SE's are excited by absorbed electrons. Likewise, if the incoming electron energies are above the second crossover energy, E_2 (>1 keV for most insulators) negative charging will again result since incident electrons penetrate deep into the material (up to several microns), exciting SE's (escape length tens of nanometers) that are too deep to escape from the material. However, if the incident electrons have energies between E_1 and E_2, more electrons will be emitted from the insulator than are incident, and net positive charging will occur. SE yield curves are commonly parameterized by the energy, E_{max}, that gives a maximum SE yield δ_{max} (or total yield, σ_{max}) as well as by the first and second crossover energies, E_1 and E_2. Furthermore, the magnitude of insulator charging can depend on a number of other parameters that include the BSE and SE yield properties, incident beam angle (Davies, 1999; Yong, 1998), substance purity, crystalline structure (Whetten and Laponsky, 1959), temperature (Johnson, 1953; Johnson, 1948; Mueller, 1945), insulator thickness (Yu, 2001; Goto, 1968; Ishikaw, 1967), surface cleanliness (Davies, 1997; Whetten, 1964; Whetten, 1959; 1957), sample potential (Yi, 2001), surface topography (Yong, 1998), and previous electron irradiation exposure leading to increased defect density and imbedded charge (Shih, 1997; Vigouroux, 1985). Numerous conductor electron spectra, yield curves, and yield parameters have been measured at USU and are available on the NASA SEE Charge Collector Knowledge Base (Dennison, 2002).

DC and Pulsed-Yield Measurement Setup and Sample Preparation

The general electron yield measurement procedure is briefly described here, but is covered more thoroughly in other SCC conference proceedings (Zavyalov, 2003, Dennison, 2003b). All measurements of thin-film conductor foils and insulator films were performed in the USU UHV test chamber at pressures ranging from 10^{-10} to 10^{-8} Torr, depending on the sample data set. Two electron guns were available for making yield measurements: a low-energy gun (STAIB EK-5-S,

energy range 50 eV to 5 keV), and a high-energy gun (Kimball ERG-21, energy ranging from 4 keV to 30 keV). Both guns provided beam currents ranging from 10-100 nA, with beam spot diameters ranging from 0.1 to 2 mm (depending on the energy), and pulsing capabilities from 1 μs to continuous emission. Emitted electrons were captured using a fully enclosing hemispherical grid detection system with a suppression grid used to discriminate between BSE's (energies >50 eV) and SE's (energies <50 eV) and to make energy-resolved measurements. For conducting samples, electron guns were operated in continuous emission mode, and dc-currents were measured with standard ammeters sensitive to several tens of picoamperes. For pulsed measurements on insulators, the electron guns delivered 5 μs, 20-60 nA incident pulses. A low-energy electron flood gun (energies <1 eV) was used to neutralize positive surface charging between pulses (Zavyalov, 2003; Dennison, 2003b; Krainsky, 1981).

Four specific materials used on the ISS—gold foil, a chromic acid anodized aluminum disk, and RTV thin films—were studied. The gold foil and Al alloy disk were glued to copper sample mounts using UHV compatible conductive silver adhesive paint. Both samples were cleaned using acetone and methanol immediately before introduction into the vacuum. Additionally, the gold sample was sputtered *in situ* with argon to remove adsorbed contamination monolayers, and sample cleanliness was confirmed using Auger spectroscopy. The thin-film RTV coatings on copper substrates were prepared by McDonald Douglass Corporation and included two DC 93-500 silicone space-grade encapsulant films and two NuSil CV-1147 controlled volatility RTV silicone films (Dennison, 2003c). The coatings were sprayed onto 10 mm dia. copper substrates (one side only), and were vacuum baked at 65 °C for 1 hr at ~10^{-3} Torr. The bake out procedure was designed in part to mimic conditions that the materials would experience in the space environment and also reduced possible outgassing of volatile components in the USU vacuum chamber during electron emission measurements (Dennison, 2003c). No cleaning methods at USU were used for the DC 93-500 or NuSil CV-1147 samples before introduction to vacuum. Further descriptions of each of the samples are given in Dennison (2003c) and in the sections that follow.

Finally, similar measurements are in progress or are planned for the near future for other ISS materials, including sulfuric acid anodized Al (NASA MSFC, 2002-2003), Kapton[TM], solar cells and cover glasses (Dennison, 2003b).

## **Gold Sample: Conductor Yields and Surface Potential-Induced Spectral Shifts**

The gold sample was a high-purity polycrystalline gold foil (10 mm dia., 0.1 mm thick). Au is used as a standard conductor for validation and calibration tests for electron-yield measurements (Zavyalov, 2003). Au coatings are also used on the soon-to-be-employed ISS Floating Potential Measurement Unit (FPMU) plasma charging monitor (Swenson, 2003) and on other spacecraft surfaces. SE and BSE yields of Au were taken over energies ranging from 100 eV to 10 keV using the dc-measurement setup described above (Zavyalov, 2003; Dennison, 2003b). Shown in Fig. 1 is the SE energy distribution for gold while being irradiated with a continuous 80 eV electron source. As can be seen from the spectrum, the SE energy distribution peaks at 2.3±0.5 eV, and ~70% electrons are emitted with energies ranging from 0-20 eV. Similar emission spectrum attributes are characteristic of both insulator and conductor materials. Shown in Fig. 2 are the total, SE and BSE yields as a function of incident beam energy. As can

be seen in the figure, the SE and total yields increase with increasing incident electron energy up to 600 eV, but then fall off as the beam penetration depth exceeds the mean SE escape depth (<10 nm).

Measuring shifts in the SE spectral emission peak provides a method for determining the sample surface potential of any material (particularly of charged insulator materials) while under continuous electron bombardment. Sample potentials can have considerable affects on SE escape kinetic energies. Typically, a material with 0 V surface potential displays a SE emission peak near 2 eV (Fig. 1). However, if the sample potential is negative, SE's will be accelerated away from the sample surface. The increased energy of escaping SE's can be observed in the spectra as a shift of the SE emission peak to higher energies. Alternatively, a few-volt positive sample potential will pull the majority of SE's back to the surface. A positive potential from the retarding grid can be used to extract the SE's from the sample, producing a shift of the SE emission peak to the left in the spectra (Girard, 1992; O. Jbara, 2001; Y. Mizuhara, 2002).
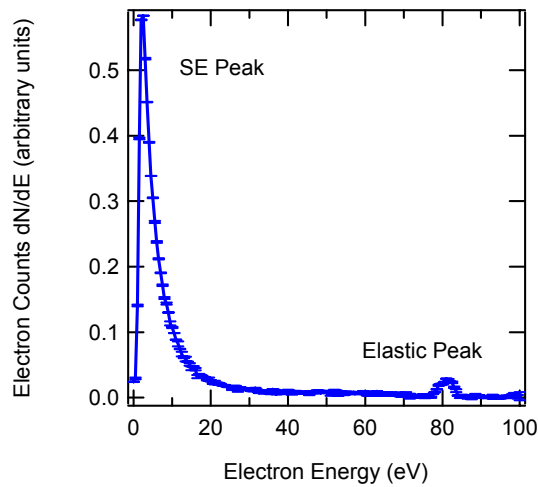
Figure 1. Electron energy spectrum for Au, induced from a 80 eV electron beam. SE peak at 2.3±0.5 eV.
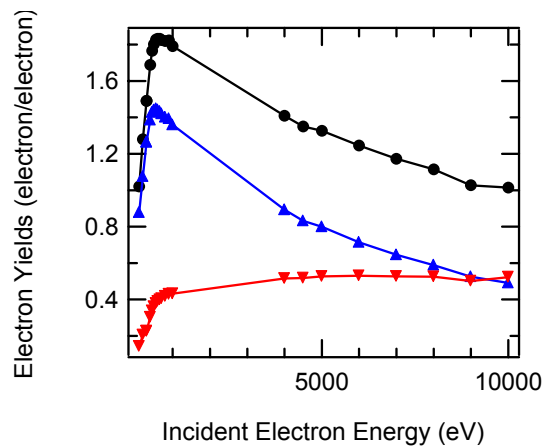
Figure 2. Total (●), SE (▲), and BSE (▼) electron yields for Au as a function of incident electron beam energy. Total yield parameters are σmax=1.8±0.1 at Emax=600±50 eV.

This SE spectral method for determining negative sample potentials was demonstrated on gold, and was used later on insulating samples to determine surface potentials induced by a continuous electron beam. Shown in Fig. 3 are four SE emission spectra taken with a 1 keV incident beam while biasing the sample negatively to 2 V, 5 V, 10 V, and 15 V. Due to the repulsion of emitted SE's from the negatively biased sample, the SE peak is right-shifted to values corresponding to the applied sample potential (see Fig. 3). A "false" SE emission peak is observed at 1.8±0.5 eV in all the spectra caused by electron scattering from the grounded inner detector grid, positioned between the sample and the retarding grid. This false SE peak did not vary with sample type or bias, and was taken as a ground-reference potential for shifted sample SE peaks. Also, the height of the grid SE peak, with respect to the shifted sample SE peaks, provided a relative measure of the number of SE's emitted from the material. Incidentally, since this inner grid remained grounded throughout the experiments, and screened out retarding-grid accelerating potentials, positive sample potentials were not measured in this way.
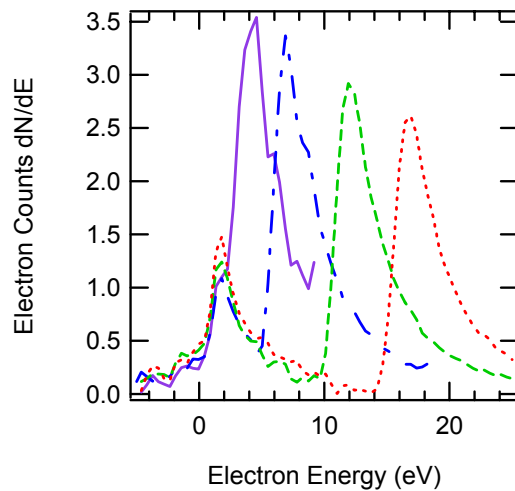
Figure 3. SE spectra on negatively biased gold for -2 V (solid), -5 V (dash-dot), -10 V (short dash), and -15 V (dot). Measured with respect to the grounded grid peak (1.8 eV), the SE peak positions correspond to the applied potentials, accurate to ± 1eV.
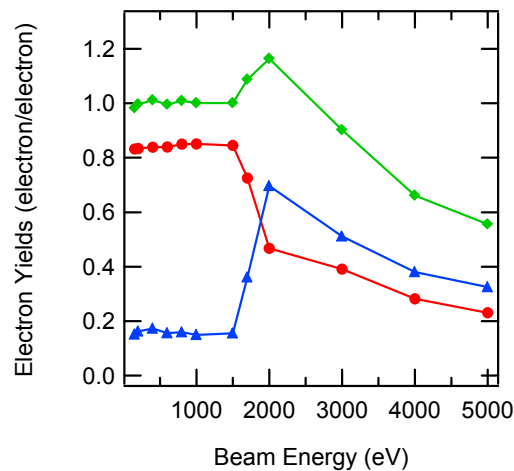
Figure 4. DC-total (♦), SE (●), and BSE (▲) yields for Al2219. The sample remained charged until 1500 eV, where dielectric breakdown occurred.
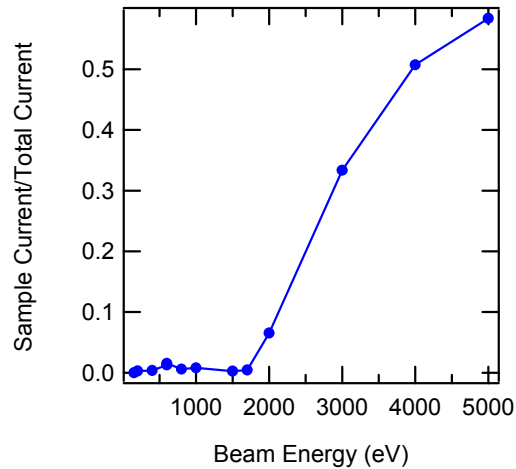
Figure 5. Monitoring Al2219 sample current confirmed dielectric breakdown at 1600 eV, where the sample began to conduct DC current.
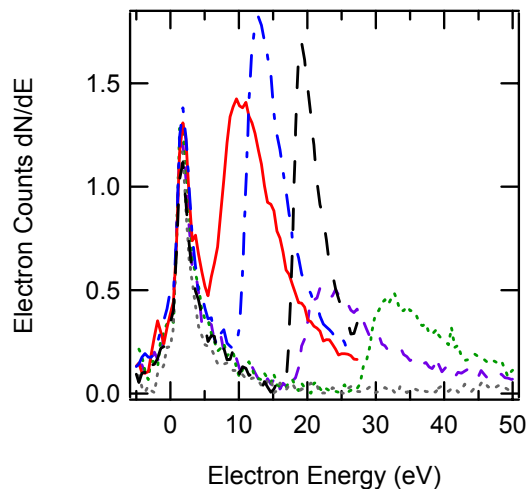
Figure 6. SE DC spectra of Al2219 showed increasingly negative surface potentials at beam energies of 200 eV (9±1 V) (solid), 500 eV (11±1 V) (dash-dot), 1000 eV (17±1 V) (long dash), 1250 eV (21±2 V) (short dash), 1300 eV (32±2 V) (dot). Decline of SE peak magnitude at 1250 eV indicated dielectric breakdown once more at a surface potential of 21±2 V.

Al2219 Insulator Yields, Emission Spectra, Electrical Breakdown, and Trapped Charge

A chromic acid anodized Al2219 alloy is used throughout the ISS body as a structural material and for micrometeriod and orbital debris shielding. The Al2219 alloy sample (2 mm thick, 10 mm diameter with a 1.3 μm chromic acid anodized surface coating on each side) was taken from a witness sample plate that was created at the same time as the large plates used on the ISS (NASA, 2002-2003). Specific aims in studying this sample were to compare the results of the dc- and pulsed-yield measurements for insulator to determine the effectiveness of the pulsed-yield setup. Additionally, evolving sample potentials under both continuous- and pulsed-incident electron beams were studied. Finally, discharging techniques including electron flooding, UV, and visible light irradiation were explored.

DC-yields were taken first using a continuous electron source at ~20 nA beam current. As shown in Fig. 4, for energies ranging from 100 eV to 1500 eV, the insulator quickly charged such that a steady-state current equilibrium was established where the total yield reached unity, and no net current flowed to or from the sample. However, after 1600 eV, a transition in the yield values occurred. As shown in Fig. 5, the sample current suddenly increased, indicating dielectric breakdown of the anodized coating. For this measurement, the exact value of the surface potential at electrical breakdown was not measured, but from the known thickness and dielectric strength for Al_2O_3 (see Table 1) was estimated to be ~35 V. Previous measurements on this material have demonstrated a breakdown potential ranging from 60-80 V (Schneider, 2003).

After letting the sample sit for a day, the breakdown surface potential was once again explored using a continuous incident electron beam and measuring the SE spectra. The incident beam energy was increased for each successive spectral measurement (starting from 200 eV up to 1300 eV) until signs of breakdown occurred. As shown in Fig. 6, (and as demonstrated with the gold sample), right-shifting of the SE emission peak was used to determine the magnitude of the sample potential.

Table 1. Insulator sample characteristics. RTV sample thicknesses, resistivities, dielectric constrants, dielectric strengths are from Dennison (2003c), Alred (2001), Dow Corning (1998), and NuSil (1998, 2001). Anodized A1 thickness is from Schneider (2003), resistivity from Goodfellow (2003), dielectric sonstrant from Carruth (2001), and dielectric strength from alumina data CRC (2001). Breakdown potentials were calculated from dielectric strengths and thicknesses. The estimate alumina data CRC (2001). Breakdown potentials were calculated from dielectric strengths and thicknesses. The estimate for E_2 for anodized A1 was obtained from the best fitting model (Variable n) to the yield curve data. Estimates for E_2 for RTV samples were obtained using total yield (Variable n model), spectral, and mirror-method techniques. Uncertainties in the mirror method data were obtained from decays in the surface potential over a measurement period of 1-3 min.

Samp.	Material	Thick. (μm)	Resist. (Ω·cm)	Rel. Diel. Const.	Diel. Strength (MV/m)	Brkdwn. Pot. (V)	Tot. Yld E_2 (eV)	DC-Spectral E_2 (eV)	Mirror Meth. E_2 (eV)
Al2219	Chromic Acid Anod. Al	1.3±0.5	>10^{14}	5.0-9.3	13	35	1400±100	No data	No data
RTV 1	CV-1147	34±3	10^{15}	2.6	22	743	1470±40	1225±25	1200±200
RTV 2	CV-1147	30±3	10^{15}	2.6	22	644	No data	No data	1100±200
RTV 5	DC93-500	49±3	10^{15}	2.6	19	917	No data	No data	1400±400
RTV 6	DC93-500	26±3	10^{15}	2.6	19	499	1050±30	1275±25	Data not conclusive

From the data, it was observed that the sample potential remained negative at energies between E_1 and E_2, and increased in magnitude with increasing incident energy. It must be noted that a negative potential was not expected between the crossover energies since the total electron yield for nearly all materials is greater than unity in this energy regime (and positive surface charging should occur). However, previous experimental studies on Al_2O_3 have shown that the measured

polarity of charging does not always correspond to that predicted by the electron yield parameters (Cazaux, 1999; Melchinger, 1995). A possible explanation for such behavior for our specific sample is that the previous electron irradiation produced residual trapped charge (embedded in the bulk) that provided a cumulative negative sample potential regardless of any positive SE surface charging taking place at beam energies between the crossovers. Data presented in the next two paragraphs support this hypothesis.
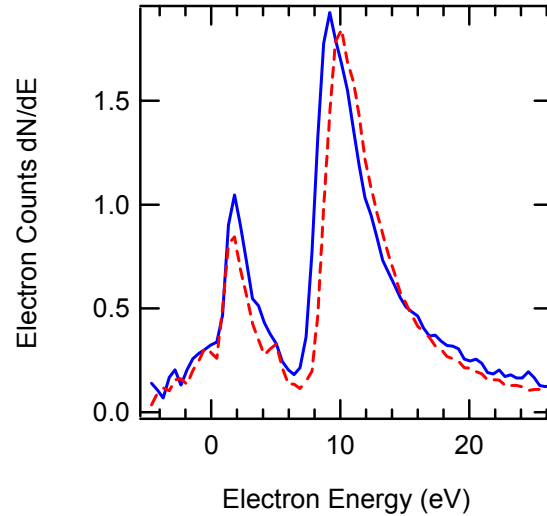
Figure 7. DC-Spectra taken at 500 eV (solid) and 1000 eV (dash) after 5 keV irradiation on Al2219 showed "locked" negative surface potential of 7-9 V resulting from imbedded electron charge.
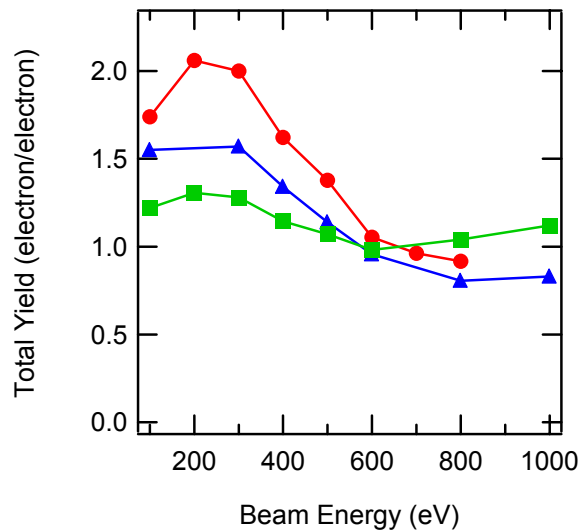
Figure 8. Three consecutive yield curves for Al2219. Each data point consists of one pulse (~106 electrons/pulse). No neutralization methods were used. The first (●), second (▲), and third (■) yield curves quickly flatten towards unity as the sample charged.

As shown in Fig. 6, as the beam energy was increased to 1250 eV and 1300 eV the surface potential reached -21±2 V and -31±2 V, respectively and the SE peaks for these energies showed a significant decrease in relative amplitudes, indicative of the electrical breakdown. From the SE spectral data, the breakdown surface potential occurred near -21 V (at beam energy 1250 eV). This value was slightly lower than the calculated estimates of -35 V, and 3-4 times smaller than previously measured values (Schneider, 2003). The value may be slightly lower since the sample had previously been irradiated and broken down on the day before at 1600 eV (see Figs. 4 and 5).

Once breakdown had occurred, the sample was irradiated for 15 min. at 5 keV beam energy to determine if subsequent SE spectra would be affected. Subsequently, the incident beam was once again lowered to 500 and 1000 eV, and SE spectra were measured. As seen in the spectra of Fig. 7, the sample potentials (both at 500 eV and 1000 eV) no longer showed dependence on incident beam energy (compare to Fig. 6 at 500 and 1000 eV), but remained locked at -8±1 V. This demonstrated the hysteresis of the sample, where residual charge from the high-energy incident beam remained trapped, keeping the sample potential at a negative value regardless of subsequent lower-energy electron irradiation between the crossover energies—where positive surface charging should have occurred.

Before proceeding with pulsed-yield measurements, the sample was allowed to discharge. Based on calculations using the standard resistivity and dielectric constant for alumina (see Table 1), and treating the sample as a discharging capacitor, a 8 V surface potential should relax within a time frame ranging from minutes to hours. However, the sample was allowed to sit for one week after irradiating with light from both tungsten and mercury lamps for several hours to stimulate photo-induced conductivity (Zavyalov, 2003). Additionally, the surface was flooded occasionally with the low-energy flood gun at a current density of 50-500 nA/cm^2 for five minutes to neutralize any positive surface charge (Zavyalov, 2003).

The first pulsed yields were taken to explore the rate of sample charging from a pulsed-electron beam. Three consecutive pulsed-total yield curves (5 μs, 40-60 nA impulses) were taken without implementation of any neutralization techniques, as shown in Fig. 8. After just a few incident pulses, the yield curves were significantly dampened towards unity, even though the incident source was only depositing ~10^6 electrons/pulse over a beam-spot area of ~1 mm^2. Treating the sample as a standard parallel plate capacitor (with an area of the beam spot), this amount of charge was estimated to change the surface potential by only 10-100 mV/pulse (positive). However, a significant portion of SE's are emitted with energies less than 5 eV (see, for example, Fig. 1 for gold) such that a cumulative positive surface potential of just 1 V can significantly suppress escaping SE's. Therefore, a small change in the positive surface potential could have large effects on electron yields. These results substantiate the use of neutralization techniques (in addition to pulsed electron beam) in measuring insulator electron yields. After these initial pulsed measurements, the neutralization sources were turned on (as before), and the sample was once again allowed to sit for several days.

To further explore the rates of sample charging as well as the effectiveness of the various neutralization methods, pulsed yields were taken repeatedly at a constant energy of E$_{beam}$=500 eV (using single 5 μs, 40-60 nA impulses) without any neutralization between incident electron

pulses. After the initial sequence (20-30 pulses were used in each sequence) of yield measurements, the electron flood gun was turned on for five minutes to test its discharging effectiveness. Then, a second pulsing sequence was repeated. Next, the sample was irradiated with a mercury gas lamp for 15 minutes, and a third yield sequence was taken. Finally, the sample was irradiated with the tungsten filament lamp for 15 minutes, and a fourth pulsing sequence was taken. As can be seen from Fig. 9, for the initial pulsing sequence, the total electron yield decayed asymptotically towards unity (steady state condition) with repeated pulsing, consistent with the flattening of yield data in Fig. 8. In the second yield sequence (after flooding) the total yield was restored to its original uncharged value (within the error), and then once again declined at roughly the same charging rate towards unity. In the third and fourth sequence, it was observed that the mercury lamp was only partially effective in neutralizing the sample, while the tungsten lamp had no effect on the yield values. Although these results were preliminary, they showed that in the energy regime between the crossover energies, the flood gun was very effective in neutralizing positive surface potentials, providing a way to measure repeatable electron yields. However, UV and visible light irradiation in this energy regime were not as effective, but still provide methods for negative-charge neutralization for beam energies beyond the second crossover energy (Levy, 1985).

    After exploring the effectiveness of the different neutralization techniques, the sample was once again allowed to discharge for a week, and then a total-yield curve for anodized aluminum was measured and fitted with various electron-yield models (Dennison, 2002) as shown in Fig. 10. Flood gun neutralization was alternated with electron beam pulsing to ensure neutralization. Additionally, yields were taken in order of increasing beam energy since it had already been observed that high-energy incident electrons could deposit negative charge that would remain trapped in the sample and influence yield measurements. From the best fit to the data, yield parameters were extracted and are given in Table 3. However, it must be mentioned that this yield data was obtained after extensive electron radiation and will need to be measured again (along with BSE and SE yield discrimination) in the near future on a virgin sample.

Silicone-RTV Samples: Methods for finding the Second Crossover Energy

    Two sets of thin-film RTV coated samples were tested: the first was a DC 93-500 coating used to bond cover glass materials to solar cells on the ISS, and the second was a NuSil CV-1147 coating used to bond solar cells to Kapton^{TM} sheeting on the ISS. Both RTV materials were relatively volatile; concerns that these materials would produce contamination layers on ISS surfaces have prompted the investigation of these thin-film materials on a conducting substrate (Dennison, 2003c). Similar contamination layers have been shown to potentially have a large impact on the charging of spacecraft surfaces (Dennison, 2001). Table 1 shows the thicknesses and electrical properties of the RTV coatings. Thicknesses were determined using a "depth of field" method with a microscope at 100 x magnification (Dennison, 2003c). The relative dielectric constants and bulk resistivities were measured using a standard impedance analyzer by the manufacturer (see Table 1). Ex $situ$ measurements of the volume resistivities of the thin-film silicone samples were also measured at USU using the ASTM—or capacitor resistance method—and ranged between $2\text{-}5 \cdot 10^{15}$ $\Omega \cdot$cm (Dennison, 2003a; Swaminathan, 2003). These insulator samples were studied primarily to determine accurate methods for measuring the total yield second crossover energy, E_2. Total yield curves as a function of incident electron energy

were also measured. A short description of each method for measuring E_2 is outlined below.
Details of the measured data follow.
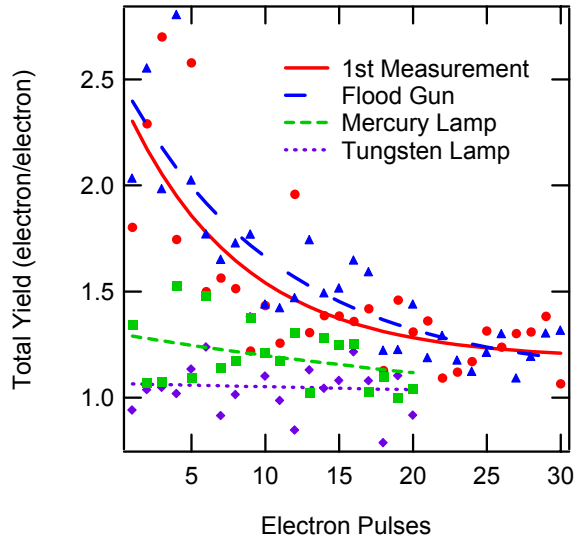
Figure 9. Dampening of total yields at 500 eV as a function of electron pulses (5 μs pulses with amplitude 50 nA) for Al2219, along with exponential fits. First yield sequence (●) and sequence following electron flooding (▲) produced similar yield decay curves indicating that flooding discharged the sample effectively. Yield sequences following mercury (■) and tungsten filament (◆) lamp irradiation remained close to unity, indicating ineffective neutralization.
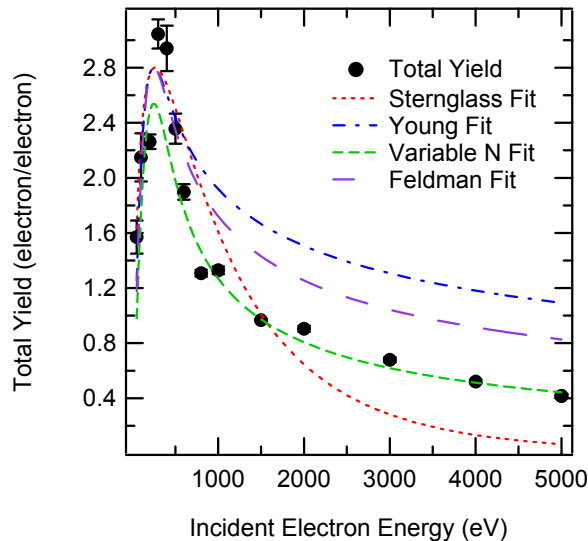
Figure 10. In contrast to Fig. 8, reliable absolute total yields were obtained with flooding the sample between yield measurements. This yield curve for Al2219 (5 μs pulses with amplitudes 50 nA, each data point was the average of 10 pulses) is fitted with various analysis models. Best estimates for yield parameters are provided in Table 3.

Pulsed Total Yield Approach: The first method was the most straightforward: total yields as a function of incident energy were taken using the pulsed-beam method, and E_2 was determined from the best fitting model to the data. The low-energy electron flood gun was used between pulses to neutralize any latent positive surface charge induced by the incident electron source.

DC-Spectra Approach: A continuous incident electron source <50 nA was used to measure DC-electron energy spectra. Regardless of the incident energy, under a DC-electron beam an insulator quickly charges to steady state where no net current arrives at or leaves the sample. When this steady state condition is met, the total yield equals unity (Reimer, 1985), and depending on the incident energy, the corresponding value of the sample potential can either be positive (for energies below E_2) or negative (for energies above E_2). As described above, the DC-SE emission spectra can be used to measure the surface potential at steady state. As the beam energy was increased towards E_2, the evolution of the surface potential was monitored using the position of the sample SE peak. The beam energy associated with the initial right-shifting of the sample SE peak (indicated by a separation of the sample SE peak from the inner grid reference peak) was taken to be the second crossover energy.

Mirroring Method: An incident electron beam at an energy beyond E_2 was used to charge the samples negatively to several hundred volts. However, as will be discussed below, it was important not to exceed the beam energy threshold corresponding to the electrical breakdown of the insulator, or else erroneous values of E_2 would result. When charged negatively with a high-energy electron beam, the sample surface potential, φ_s, of an ideal infinite-resistance insulator material will adjust such that the landing energy of incident electrons becomes equal to E_2, thus satisfying the steady state condition of $\sigma=1$. The relationship between the landing energy (E_2 at steady state), the beam energy, and the surface potential is governed by:

$$E_2 = E_{beam} - e\varphi_s \qquad (1)$$

where e is electron charge and E_{beam} is the incident electron energy used to induce the negative surface potential (Reimer, 1985). However, for most thin-film insulators, some leakage current will occur either through the bulk or across the surface that must be accounted for. As a first approximation, the thin-film insulator can be treated as a planar capacitor (with the conductor substrate and charged surface acting as the electrodes) that discharges in an ohmic fashion through the bulk of the insulator. Then, the RC-time constant, τ, for discharging insulator can be written as:

$$\tau = \rho\varepsilon_r\varepsilon_0 \qquad (2)$$

where ρ is the material resistivity, ε_r is the relative dielectric constant, and ε_o is the permitivity of free space. The decaying surface potential can then be estimated as a function of time as:

$$\varphi_s(t) = \varphi_{s0} \cdot e^{-t/\tau} \qquad (3)$$

where φ_{so} is the initial sample potential induced by electron beam irradiation, and φ_s is the decayed potential after a time interval, t. Using Eqs. (1) through (3), one needs only to determine the original sample potential (φ_{so}) induced by E_{beam} to calculate the second crossover

energy. Note that this potential decay can be measured directly using a non-contacting surface charge probe; this forms the basis for the charge storage decay method for determining thin-film insulator resistivities developed by Frederickson (Dennison, 2003a; Swaminathan, 2003, Frederickson, 2003). However, the vacuum chamber used in these studies was not equipped with a non-contacting potential probe, so indirect methods for determining φ_s were employed.

Following an experimental procedure similar to that of Wong (1997), the samples were irradiated with a defocused electron beam to uniformly charge the samples to φ_{so}. Then, a low-amplitude, modulated probe electron beam, with a much smaller diameter was used to probe the surface potential of the insulators. In doing this, it was assumed that by using a low-amplitude modulated probe beam, the surface potential would not be significantly altered. Then, by slowly increasing the probing beam energy, E_{probe}, the kinetic energy of the incident electrons eventually overcame the potential barrier of the sample. This critical beam energy was marked by a sudden rise in the sample displacement current, and the surface potential was assumed to be equal to $\varphi_s = E_{probe}/e$. Once the surface potential was determined, E_2 was calculated from Eq. (1) after correcting for any suspected leakage current [using Eqs. (2) and (3)] that had transpired during the time of the probing experiment.

Finally, for all three methods described above, the order of measurements was planned carefully to minimize charging errors. For example, negative charge build-up (to up to several hundreds or thousands of volts) induced by beam energies beyond E_2, can be very difficult to dissipate. Consequently, precautions were taken to minimize sample exposure to the high-energy (>1 keV) incident electrons until all lower-energy (<1 keV) measurements were made by initially taking pulsed-yield measurements (in order of increasing incident energies), followed by DC-spectra at energies near E_2, and lastly, the mirror method technique (that induced significant negative charging).

Pulsed-yields as a function of incident energy were taken on samples 1 and 6 using 5 μs, 50 nA incident pulses. The sample surface was neutralized with the flood gun after each incident electron pulse, and ten pulsed measurements were averaged for each data point,. The pulsed-yield measurements were started at beam energies of 100 eV, and then increased to 1 keV (yields beyond 1 keV were not taken until after DC-spectral measurements). The yield curves along with their best-fitting semi-empirical models are shown in Figs. 11 and 12. When the total yield curves began to approach unity for samples 1 and 6 (close to E_2), the electron gun was switched from pulsed to continuous-emission mode, and DC-spectra were taken (at ~30 nA incident beam current) on the samples as the beam energy was increased. Eventually, E_2 was crossed, and double-peak SE emission spectra (as described above) were observed due to negative charging as shown in Figs. 13 and 14. Estimates for E_2 as determined from both the pulsed-yield (best fitting model estimate) and DC-spectral methods are given in Table 1. Of the two techniques, the spectral measurements were considered to be a more precise method for determining E_2 since SE emission energies were very sensitive to sample potentials of even a few volts (causing the double-peaks in Figs. 13 and 14). However, there were concerns that for the DC-spectral method, continuous electron-beam bombardment could have altered yield parameters, including E_2, resulting from charge deposition in the bulk of the material.

When pulsed-yield and DC-spectral measurements were completed, mirror-method potential measurements were taken on all samples for E_{beam}=2 keV, 2.3 keV, 2.5 keV, and 3 keV (measurements were always taken in order of increasing beam energy on a given sample). The RTV samples were irradiated with a defocused (~10 mm diameter for uniform charging) electron beam at 100 nA for 5 minutes for each beam energy. During this irradiation period, DC sample current was monitored to check for dielectric breakdown of the insulators. At these incident energies, sample current was found to be lower than the noise level ±1 nA, except for sample 6 (see below). After this irradiating period, the electron gun was suppressed temporarily, and the beam energy was decreased of the insulator film as outlined above. Shown in Fig. 15 is a plot of the sudden rise in sample displacement current in response to the incident probe beam energy where the critical energy was reached, and the sample potential barrier was breached.
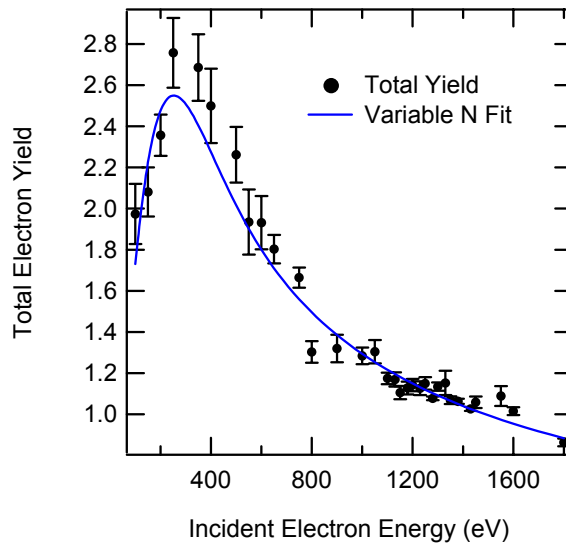
Figure 11. Pulsed-yield curve versus beam energy for CV-1147 sample 1 with flood gun neutralization after each pulse. Each yield point was the average of 10 pulsed-yield measurements (5 µs pulse with amplitude 50 nA) with standard errors as the error bars. The best model estimates for the total yield parameters were: σ_{max}=2.5±0.1 at E_{max}=250±10 eV, E_1=40±20 eV, and E_2=1470±40 eV. Model estimates for the maximum yield were low compared to the data.
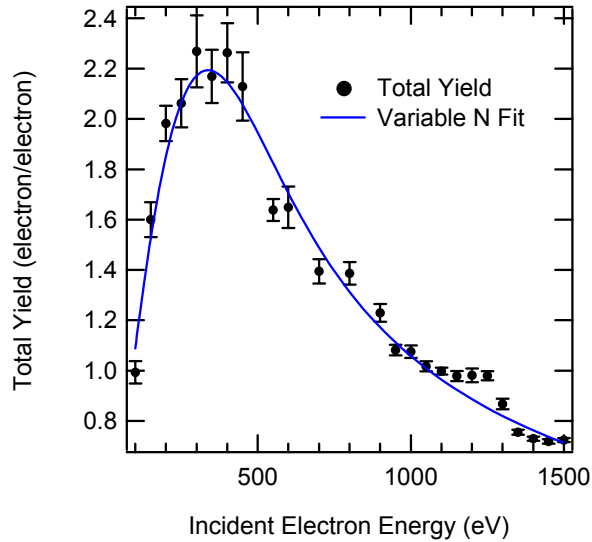
Figure 12. Pulsed-yield curve versus beam energy for DC 93-500 sample 6 with flood gun neutralization after each pulse. Each yield point was the average of 50 pulsed-yield measurements (5 μs pulse with amplitude 50 nA) with standard errors as the error bars. The best model estimates for the total yield parameters were: σ_{max}=2.2±0.1 at E_{max}=340±10 eV, E_1=90±10 eV, and E_2=1050±30 eV. Model estimates for the maximum yield were low compared to the data.
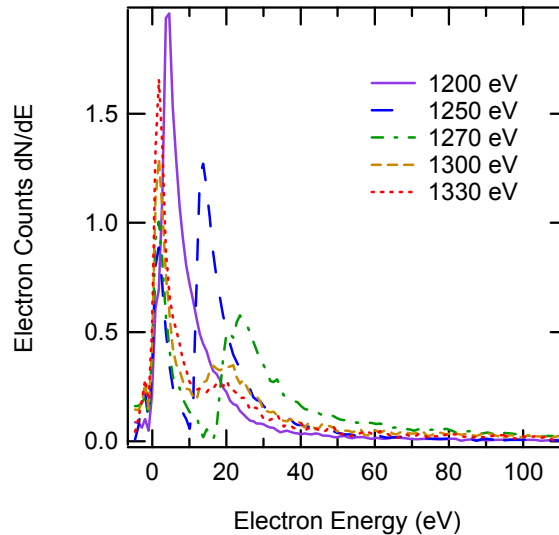
Figure 13. Shown are evolving SE spectra for sample 1 for increasing electron beam energies of 1200 eV (solid), 1250 eV (long dash), 1270 eV (dash-dot), 1300 eV (short dash), and 1330 eV (dot). The emergence and right-shifting trend of the 2nd SE peak was caused by a negative sample potential caused by the incident electron beam energy exceeding E_2. These spectra indicated a crossing of E_2 at 1200-1250 eV.
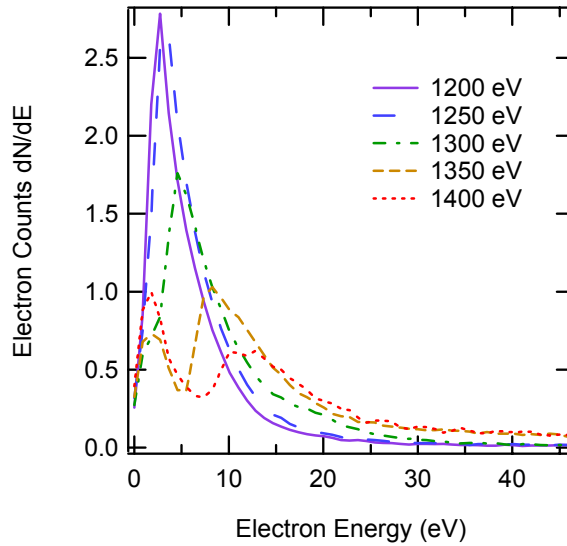
Figure 14. Shown are evolving SE spectra for sample 6 for increasing incident electron beam energies of 1200 eV (solid), 1250 eV (long dash), 1300 eV (dash-dot), 1350 eV (short dash), and 1400 eV (dot). These spectra indicated a crossing of E_2 at 1250-1300 eV.
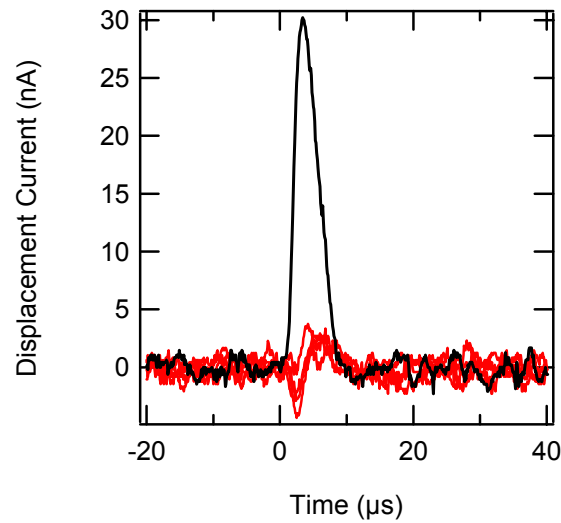
Figure 15. Shown is a plot of the rise in displacement current of a probing electron pulse (5 μs at 100 nA) once the incident energy overcame the surface potential barrier induced by a high-energy electron beam. In this case, the small displacement currents are induced by probe beam energies ranging from 900-1200 eV, while the large displacement current curve occured at 1250 eV. From this, the surface potential was taken to be 1250 eV.

Table 2. Mirror method results for the sample surface potential and E_2, for RTV samples at different irradiation energies, E_{beam} calculated from Eqs. (1) and (3) using the measured surface potential, φ_s and a RC time constant of 4 min. as determined from Eq. (2). Variations in E_2 resulted from uncertainties in the measurement time interval of 1-3 min. E_{beam} values indicated with a * induced surface potentials, φ_s, exceeding the sample dielectric breakdown potential (shown in Table 1), and therefore produced inaccurate estimates for E_2 (also indicated by *). Sample 6 appeared to have already undergone electrical breakdown at E_{beam} <2 keV.

Sample	E_{beam} (eV)	φ_s (V)	E_2 (eV)
RTV 1	2000	475 ± 25	1200±200
	2500*	775 ± 25	1150±300*
	3000*	875 ± 25	1500±400*
RTV 2	2000	500 ± 100	1100±200
	2300*	850 ± 100	800±400*
	2500*	1250 ± 50	300±550*
	3000*	1800 ± 100	-100±800*
RTV 5	2000	290 ± 10	1500±100
	2300	525 ± 25	1400±200
	2500	625 ± 50	1400±300
	3000*	1140 ± 10	1000±500*
RTV 6	2000*	175 ± 25	1700±100*
	2500*	150 ± 50	2200±100*
	3000*	250 ± 50	2500±100*

Table 3. Summary of measured total electron yield parameters and the electrical breakdown potentials of studied materials. Maximum yields, maximum yield energies were taken directly from the raw data since estimates from the fitting models were too low. Crossover energies were obtained from the best-fit of the yield data, except for CV-1147 and DC93-500, where estimates for E_2 were obtained from the SE spectral method. Measured breakdown potentials were obtained from SE spectra for anodized Al and the mirror potential method for the two RTV samples.

Sample	Maximum Total Yield	Maximum Total Yield Energy (eV)	First Crossover Energy (eV)	Second Crossover Energy (eV)	Measured Breakdown Potential (V)
Gold	1.8±0.1	600±50	100±20	10000±1000	Not applicable
Al2219	3.0±0.1	300±50	50±10	1400±100	>21
CV-1147	2.8±0.2	250±50	40±20	1225±25	700±200
DC93-500	2.3±0.2	350±50	90±10	1275±25	850±250

Mirror-method results for measured surface potentials along with calculated values for E_2 were calculated using Eqs. (1) through (3). Using the manufacturer material specification data provided in Table 1, estimates for the leakage RC time constant, τ, were calculated to be 4 min. [from Eq. (2)] for all RTV samples. In comparison, probing measurements lasted anywhere from 1 to 3 min. Consequently, during the course of an experiment, the sample surface potentials decreased as determined by Eq. (3). After making these corrections, estimates for E_2 were calculated using Eq. (1), and are given in Table 2 for different values of E_{beam}.

From the data in Table 2, it can be seen that E_2 values derived at higher E_{beam} (>2.5 keV) were typically inconsistent with respect to values derived from E_{beam}=2.0 keV, and were also prone to large errors. It is conceivable that electrical breakdown (in the form of small sustained arcs through the bulk of the films) occurred at higher-energy electron irradiation as indicated by * in Table 2. Dielectric breakdown potentials of the four samples were calculated based on dielectric strength values (see Table 1). As seen in Table 2, (with the exception of sample 6, see below), E_2 values were consistent for each sample for surface potentials, φ_s, lower than the calculated breakdown potentials. This observation provides some evidence that the mirroring method approach to finding E_2 was obfuscated by low breakdown potentials of thin-insulating films, and may be a more suitable method for finding the crossover energies of thicker samples. Table 1 summarizes all estimates for E_2 as determined from the three methods described above.

Finally, in contrast to the other RTV samples, the surface potential of sample 6 did not rise with increasing radiation energy, and stayed at relatively low potentials between 150 V to 300 V as shown in Table 2. As mentioned earlier, for sample 6, a sample current of ~2 nA was measured at beam energies ranging from 2-3 keV. It was speculated that the sample had undergone dielectric breakdown (prematurely) at beam energies <2 keV. This assumption was consistent with the fact that sample 6 had been prepared with the thinnest RTV coating (compared to the other three samples), and should therefore have demonstrated the lowest breakdown potential (see Table 1). Other samples displayed similar breakdown behavior at higher beam energies. For example, when E_{beam} was pushed to 5000 eV at 30 nA for sample 1 the sample current suddenly rose >20 nA. Then, upon decreasing E_{beam} to energies as low as 800 eV (keeping the incident current at ~30 nA), the sample remained open to current conduction on the order of 4 nA. Although the electrical breakdown of sample 6 did not influence pulsed-yield or DC-spectral estimates for E_2, since these measurements were taken before mirror method measurements, E_2 values derived from the mirror method were considered to be inconclusive for this sample.

Summary and Conclusions

Total electron yield measurements have been presented for one conductor and three types of insulators used in ISS construction. SE emission spectra demonstrated shifting energy distributions in response to samples with nonzero surface potentials. The spectra on gold demonstrated that as the sample surface potential was biased negatively, the SE peak shifted to higher energies (to the right in the spectral graphs) by an amount that corresponded to the applied sample potential. This technique was used to determine the potentials of charged insulator samples under continuous electron beam bombardment.

Measurements on Al2219 chromic-acid anodized aluminum showed that charging can occur very quickly on an insulator sample, even at low electron fluences of ~10^6 electrons/pulse over a ~1 mm^2 area. Charging, both under continuous and pulsed-electron irradiation, drove the total yield of the sample towards unity as current steady state was reached. Additionally, it was found that at a critical incident electron energy (initially 1500 eV, then 1250 eV on a subsequent run), the surface potential became sufficiently high (>20 V) to initiate dielectric breakdown of the thin anodized layer. After irradiating the sample with high incident energies of 5 keV, it was found that trapped charge in the sample maintained the surface potential at a negative value on the order of ten volts, even while being irradiated with an electron beam at energies (500 eV and 1000 eV) that should have induced positive surface charging. This behavior may later provide information on trapped internal charge distributions caused by higher-energy (> 1 keV) electron irradiation. Finally, electron yields were measured for the sample, and results are reported in Table 3.

With the two types of RTV-Silicone adhesive samples (CV-1147 and DC93-500), three approaches were explored for determining the second crossover energy, E_2: i) the pulsed-total yield approach; ii) the DC-spectral approach; iii) and the mirroring method approach. Of these three methods, the DC-spectra approach was assumed to be most sensitive to sample negative charging, and therefore a more accurate method for determining E_2. However, there were concerns that continuous electron beam irradiation may have altered yield parameters, including E_2. Also, it became apparent that the mirror method for determining E_2 was only valid when the beam energy threshold for dielectric breakdown was not exceeded. This may restrict the mirror method to thicker insulators (>100 μm). Results for the three methods are reported in Table 1. Best estimates for yield parameters for all the materials studied are reported in Table 3.

From these measurements, continuous- and pulsed-beam techniques for determining insulator yield parameters have been demonstrated. For both Al2219 and RTV samples, there was also clear evidence that >1 keV electron bombardment left residual charge under the surface that affected subsequent yields. Clearly, more work is needed to quantitatively asses charging effects on insulator potentials and electron emissions for different materials. Available tools and techniques demonstrated here are adequate to perform further required tests with carefully controlled sample bombardment history.

Acknowledgments

References

1. John Alred, Boeing Corporation (private communications), 2001.

2. G. Auday, Ph. Guillot, and J. Galy, "Secondary emission of dielectrics used in plasma display panels," J. Appl. Phys. $\underline{88}$ (8), 4871-4874 (2000).

3. M. Belhaj, S. Odof, K. Msellak, and O. Jbara, "Time-dependent measurement of the trapped charge in electron irradiated insulators: Applications to Al_2O_3-sapphire," J. Appl. Phys. $\underline{88}$ (5), 2289-2294 (2000).

4. M.R. Carruth Jr., T. Schneider, M. McCollum, M. Finckenor, R. Suggs, D. Ferguson, I. Katz, R. Mikatarian, J. Alred, and C. Pankop, "ISS and space environment interactions without operating plasma contactor," AIAA Paper #2001-0401, Proceedings for the 39th Aerospace Sciences Meeting and Exhibit, Reno, Nevada, Jan. 9-11, 2001.

5. J. Cazaux, "Some considerations on the secondary electron emission δ, from e⁻ irradiated insulators," J. Appl. Phys. $\underline{85}$ (2), 1137-1147 (1999).

6. CRC Handbook of Chemistry and Physics, 82nd Ed. (CRC Press, Boca Raton, FL, 2001).

7. Robert Davies, "Measurement of Angle-resolved Secondary Electron Spectra," PhD Dissertation, Utah State University, Logan, Utah, May 1999.

8. R.E Davies and J.R. Dennison, "Evolution of Secondary Electron Emission Characteristics of Spacecraft Surfaces," J. Spacecraft and Rockets, $\underline{34}$, 571-574 (1997).

9. J.R. Dennison, A. R. Frederickson, Prasanna Swaminathan, "Charge Storage, Conductivity And Charge Profiles Of Insulators As Related To Spacecraft Charging," Proceedings of the 8th Spacecraft Charging Technology Conference, October 20-24, 2003a, Huntsville, Alabama.

10. J.R. Dennison, C.D. Thomson, J. Kite, V. Zavyalov, Jodie Corbridge, "Materials characterization at Utah State University: facilities and knowledgebase of electronic properties of materials applicable to spacecraft charging," Proceedings of the 8th Spacecraft Charging Technology Conference, October 20-24, 2003b, Huntsville, Alabama.

11. J.R. Dennison, C.D. Thomson, and Jodie Corbridge, "Electronic Properties of ISS Materials," Boeing Company Final Report, Contract No. M/C H014-B419, 2003c.

12. J.R. Dennison, J. Kite, C.D. Thomson, Jodie Corbridge, Robert Berry, and Carl Ellsworth, "Final Report Part IV: Additional Materials Reports," NASA Space Environments and Effects Program Grant, Electronic Properties of Materials with Application to Spacecraft Charging, May 2003d.

13. J.R. Dennison, W.Y. Chang, N. Nickles, J. Kite, C.D. Thomson, Jodie Corbridge, and Carl Ellsworth, "Final Report Part III: Materials Reports," NASA Space Environments and Effects Program Grant, Electronic Properties of Materials with Application to Spacecraft Charging, September 2002.

14. J.R Dennison, Jason Kite, W.Y. Chang, and R.E. Davies, "Absolute and Differential Spacecraft Charging as a Result of Evolving Surface Contamination," Proceedings of the 7th Spacecraft Charging Technology Conference, (2001, Noordwijk, Netherlands).

15. Dow Corning 93-500 Space-Grade Encapsulant Product Information, Ref. No. 10-1062A-01, DC 3367, (Dow Corning Corporation, Midland MI, 05/01/1998).

16. A.R. Frederickson and J. R. Dennison, "Measurement of Conductivity and Charge Storage in Insulators Related to Spacecraft Charging," accepted for publication in IEEE Trans. Nuc. Sci., December, 2003.

17. K. Goto and K. Ishikawa, "Secondary electron emission from diffusion pump oils II. δ-η analysis for DC-705," J. Jap. Appl. Phys. 7 (3), 227-231 (1968).

18. P. Girard, P. Charpenel, and H. Martin, "Determination of the noncharging electron-beam energy on insulators," J. Appl. Phys. 71 (6), 2871-2876 (1992).

19. Goodfellow online catalogue, 2003.

20. K. Ishikawa and K. Goto, "Secondary electron emission from diffusion pump oils I," J. Jap. Appl. Phys. 6 (11), 1329-1335 (1967).

21. O. Jbara, M. Belhaj, S. Odof, K. Msellak, E.I. Rau, and M.V. Andrianov, "Surface potential measurements of electron-irradiated insulators using backscattered and secondary electron spectra from an electrostatic toroidal spectrometer adapted for the scanning electron microscope applications," Rev. Sci. Instrum. 72 (3), 1788-1795 (2001).

22. J.B. Johnson, "Secondary electron emission from targets of Barium-Strontium Oxide," Phys. Rev. 73 (9), 1058 (1948).

23. J.B. Johnson and K.G. McKay, "Secondary electron emission of crystalline MgO," Phys. Rev. 91 (3), 582-587 (1953).

24. I.Krainsky, W. Lundin, W.L. Gordon, R.W. Hoffman, Secondary Electron Emission Yield Annual Report for Period July 1, 1980 to June 30, 1981, Case Western Reserve University, Cleveland, OH, 1981 (unpublished).

25. L. Levy, D. Sarrail, and J.M. Siguier, "Conductivity and secondary electron emission properties of dielectrics as required by NASCAP," Proceedings of the Third European Symposium on Spacecraft Materials in Space Environment, Noordwijk, The Netherlands, October 1-4, 1985.

26. A.Melchinger, and S. Hofmann, "Dynamic double layer model: Description of time dependent charging phenomena in insulators under electron beam irradiation," J. Appl. Phys. $\underline{78}$ (10), 6224-6232 (2003).

27. Y. Mizuhara, J. Kato, T. Nagatomi, Y. Takai, and M. Inoue, "Quantitative measurement of surface potential and amount of charging on insulator surface under electron beam irradiation," J. Appl. Phys. $\underline{92}$ (10), 6128-6133 (2002).

28. C.W. Mueller, "The secondary electron emission of pyrex glass," J. Appl. Phys. $\underline{16}$, 453-458 (1945).

29. NASA Marshall Space Flight Center Materials, Processes, and Manufacturing Department, 2002-2003.

30. NuSil CV-1147 Controlled Volatility RTV Silicone Atomic Oxygen Protective Coating Product Profile, NT/061801/REVA (NuSil Technology, Carpinteria, CA, 06/18/2001).

31. NuSil CV-1147 Material Safety Data Sheet, (NuSil Technology, Carpinteria, CA, 03/09/1998).

32. L. Reimer, Scanning Electron Microscopy. Physics of Image Formation and Microanalysis, (Springer-Verlag., 1985), pp. 119-121.

33. Todd Schneider, NASA Marshall Space Flight Center Materials, Processes, and Manufacturing Department, (private communications) 2002-2003.

34. H. Seiler, "Secondary electron emission in the scanning electron microscope," J. Appl. Phys. $\underline{54}$ (11), R1-R18 (1983).

35. A.Shih, J. Yater, P. Pehrsson, J. Butler, C. Hor, and R. Abrams, "Secondary electron emission from diamond surfaces," J. Appl. Phys. $\underline{82}$ (4), 1860-1867 (1997).

36. Prasanna Swaminathan, A. R. Frederickson, J.R. Dennison, Alec Sim, Jerilyn Brunson, and Eric Crapo, "Comparison Of Classical And Charge Storage Methods For Determining Conductivity Of Thin Film Insulators," Proceedings of the 8th Spacecraft Charging Technology Conference, October 20-24, 2003, Huntsville, Alabama.

37. Charles Swenson, "Calibrating the Floating Potential Measurement Unit," Proceedings of the 8th Spacecraft Charging Technology Conference, October 20-24, 2003, Huntsville, Alabama.

38. J.P. Vigouroux, J.P. Duraud, A. Le Moel, C. Le Gressus, and D.L. Griscom, "Electron trapping in amorphous SiO_2 studied by charge buildup under electron bombardment," J. Appl. Phys. <u>57</u> (12), 5139-5144 (1985).

39. N. Rey Whetten, "Cleavage in high vacuums of alkali halide single crystals-secondary electron emission," J. Appl. Phys. <u>35</u> (11), 3279-3282 (1964).

40. N. Rey Whetten and A.B. Laponsky, "Secondary Electron Emission from MgO Thin Films," J. Appl. Phys. <u>30</u> (3), 432-435 (1959).

41. N. Rey Whetten and A.B. Laponsky, "Secondary electron emission of single crystals of MgO," J. Appl. Phys. <u>28</u>, 515 (1957).

42. W.K. Wong, J.C.H. Phang, and J.T.L. Thong, "Estimation of the second crossover in insulators using the electrostatic mirror in the scanning electron microscope," Appl. Phys. Lett. 71 (9), 1270-1272 (1997).

43. W. Yi, S. Yu, W. Lee, I.T. Han, T. Jeong, Y. Woo, J. Lee, S. Jin, W. Choi, J. Heo, D. Jeon, J.M. Kim, "Secondary electron emission yields of MgO deposited on carbon nanotubes," J. Appl. Phys. <u>89</u> (7), 4091-4095 (2001).

44. Y.C. Yong, J.T.L. Thong, and J.C.H. Phang, "Determination of secondary electron yield from insulators due to a low-kV electron beam," J. Appl. Phys. <u>84</u> (8), 4543-4548 (1998).

45. S. Yu, T. Jeong, W. Yi, J. Lee, S. Jin, J. Heo, and D. Jeon, "Double-to single-hump shape change of secondary electron emission curve for thermal SiO_2 layers," J. Appl. Phys. <u>79</u> (20), 3281-3283 (2001).

46. V. Zavyalov, C.D. Thomson, J.R. Dennison, "Instrumentation for studies of electron emission and charging from insulators," Proceedings of the 8th Spacecraft Charging Technology Conference, October 20-24, 2003, Huntsville, Alabama.

EUROPEAN APPROACH TO MATERIAL CHARACTERISATION FOR PLASMA INTERACTION ANALYSIS

Marc Van Eesbeek
Materials Physics and Chemistry Section
European Space Technology and Research Centre
NL2200AG Noordwijk, The Netherlands
Phone: Int+31 71 565 3896
Fax: Int+31 71 565 4992
E-mail: marc.van.Eesbeek@esa.int

Alain Hilgers
European Space Technology and Research Centre, Noordwijk, The Netherlands

Rene Reulet
Bernard Dirassen
Leon Levy
ONERA/DESP, Toulouse, France

Isabel Montero
Luis Galàn
ICMM/CSIS, Madrid, Spain

Abstract

The European Space Agency (ESA) has initiated an activity on material characterisation for plasma interaction analysis.

This work is part of a mini-project in the frame of the ESA Technology Research Program, which is also covering two other main aspects of the research and industry community needs, i.e.

(1) Spacecraft plasma interaction analysis and simulation software toolkit and
(2) Guidelines for spacecraft charging and plasma interactions.

The activities in the three parts will be harmonised in the framework of SPINE (Spacecraft Plasma Interaction Network in Europe).

The main objectives of the activities described in this paper are:

(1) Definition of required material characteristics needed for the different simulation software, the comparison of different characterisation techniques and the available test houses in Europe.
(2) Design of a database for relevant properties on materials used in spacecraft manufacturing; largely concentrated on external surfaces.
(3) Collection and integration of existing, and verifiable, material property data into an easy accessible database, compatible with the software under development.
(4) Measurement of properties on a set of newly proposed materials.

Special attention will also be drawn to the influence of other environmental parameters onto these properties, natural ones, such as solar radiation, as well as induced ones e.g. contamination, material ageing, temperature.

The paper presents the approach taken to achieve the objectives above, and gives the most recent developments in the different parts of the activity.

Introduction

The need for modelling of spacecraft plasma interactions in Europe becomes more and more obvious. Deleterious charging interactions are well known to occur in nearly all orbits (GEO, MEO, Transfer, and even LEO) and have in the last decades and also in the recent past led to so called "anomalies", leading in extreme cases to a definitive failure of the system. For instance, charging and (subsequent) discharging has caused recently severe and definitive damage to solar arrays. So, the charging and discharging effects might jeopardize the nominal operation of a satellite. The risk for attaining critical differential charging levels (range of kVolts) is clearly dependent on the use of insulators as external coatings (polymers, paints, glasses), unable to dissipate the incoming charged particles from the environment, and able to accumulate and store charge, up to critical discharging levels.

Furthermore external coatings of scientific satellites are most often required to be completely conductive. The concerns are the instruments measuring the low energy plasma: the measurements are affected by the (positive) satellite potential induced by photoemission. Measuring photoemission properties together with the energy distribution of the photo-emitted electrons is a real challenge to be tackled in this project.

The need for a capability of modelling spacecraft plasma interactions is obvious for a large community of users such as those in Europe including space research agencies (ESA, CNES), space industries, and scientific experimenters.

As a result of this need, SPINE was created in 2000. SPINE stands for Spacecraft Plasma Interactions Network in Europe. The objective of this network is to share resources and to co-ordinate efforts in all domains related to the interaction of spacecraft with the space plasma, including:

- Development of numerical analysis methods and algorithms, software architecture and data interface (code implementation, validation techniques, testing and post-processing, common Library of generic routines for s/c-plasma-interaction simulations).

- Development of a database on material properties, environmental data and space flight observations.

- Development of a Database of results and publications.

- Access to Environmental data

- Preparing in orbit investigations

- Establishment of standard procedures and method for hardware design, including qualification and testing

- Training of young scientists and engineers.

- Establishment of External collaborations

  In this general frame, ESA planned a mini project in the field of Spacecraft plasma interactions covering different aspects of the research and industry community needs.

  Next to the database for characterisation of material properties, the main topic of this paper, the two other main aspects covered are:

- A toolkit for spacecraft plasma interaction analysis and simulation software

- Guidelines for spacecraft charging and plasma interactions.

(1) A toolkit for spacecraft plasma interaction analysis and simulation software

The development of the analysis and simulation software toolkit, called SPIS (Spacecraft-Plasma Interaction System) has been started beginning of 2003.

It includes a general infrastructure, allowing a convenient embedding of an increasing number of modules, or routines. Within the contract, the contractor is responsible for the design and implementation of the framework as well as the implementation and integration of some of the numerical routines.

The SPINE community has been able to provide guidelines or requirements so that this software will answer its needs; It is also requested to develop some of the routines and to test the software on a number of pre-defined test cases.

(2) Guidelines for spacecraft charging and plasma interactions.

The guidelines for the spacecraft projects will address the need of the space research and space industry community for the assessment of problems related to spacecraft plasma interactions.

It will also promote the use and the sharing of European resources, especially regarding knowledge and expertise for spacecraft design and operations and test facilities.

The guidelines shall consist of a paper version, including text and graphs of the guidelines, and a public interactive version that shall include simple formula computational capabilities and a list of assets and contact points for support and access to facilities and expertise.

Identification of Needs

The identification of needs for the material characterisation programme is believed to be of outmost importance because it appeals to basic physics, it will drive several tasks in the frame of this activity, and it requires contacts with the users community.

The view of the needs might evolve in time, e.g. after attending to the SPINE meetings or as a result of exchange with the community users. Recommendations for updating the existing facilities could be formulated during this project.

The physics incorporated into NASCAP or other charging codes shall be reviewed and the need of new properties or of different modelling of a given process will be searched from basic physics and needs expressed by the users community (Spine). The importance of material properties for local charging (at material level) and overall charging of a satellite (absolute charging) will be addressed.

Although through performance of numerous NASCAP simulations with variable parameters, an assessment of the sensitivity of charging to given material properties could be made, this information is felt to be too coarse and is already known through previous NASCAP sensitivity studies; The basic outcome is the importance of secondary emission(s) and conductivity(ies). An alternative approach allowing an extended testing of properties sensitivity is proposed. It will use simple 0D codes to compute current balances in specific situations, as e.g. charging effect in GEO in presence of potential barrier, or enhancement of currents through secondary emission (effects of snapover, multipactor, hopping along a surface…), or photo-emission-driven charging situations. The required accuracy for each property will thus be determined in regard to their relative impact on the charging. Codes, similar to EQUIPOT in SPENVIS, but using other customised laws will be written for this study. These 0D codes may require information from 3D codes (e.g. potential barrier height in GEO as a function of differential charging), which will be obtained from analytical computations or numerical runs of in-house codes (e.g. ONERA code SILECS).

Material properties are not stable during the orbital life of a satellite and consequently, the properties should be measured according to agreed methods with considerations of environmental and ageing effects. Secondary emission and photo-emission are surface properties which are affected by contamination effects (all orbits are concerned) or by structural effects from atomic oxygen (LEO). Surface conductivity is also highly dependent on contamination and adsorbed gases. Conductivity is dependant on the applied field, on the temperature, on the (instantaneous) dose rate (Grays/s) and on the history (accumulated dose in Grays). Photo-conduction (a kind of radiation induced conductivity) has similar effects on coloured materials (Kapton is an example of a highly sensitive photo-conductive material).

Applicable Test Methods and Available Test-Houses

Recognising the need for material characterisation, e.g. when charging problems and related anomalies were recognised as a threat for the nominal operation of satellites, the European users have already developed in house capacities. An inventory through Europe of available facilities for the measurement of different properties will be made. The applicable test methods for the properties determination will be reviewed. Preferred methods and procedures will be stated.

In the field of material charging in the space environment, ONERA-DESP has many facilities, and has performed many studies and material measurements. Facilities and measurement methods in the field of secondary emission have also been developed at ICMM/CSIC. Each facility implies a cost (development, maintenance) making a common development at European level very cost-effective. ONERA-DESP and ICMM/CSIC will

join their expertise in a collaborative program set up in the frame of this activity. This is a framework which in the future will hopefully not be limited to these test houses, since after the test houses facilities will be reviewed, a proposal for developing or adapting new facilities cannot be excluded.

Pushed by space industries to meet their needs, and supported by space agency R&D efforts, ONERA-DESP and ICMM/CSIC have developed and maintained such facilities: CEDRE : CEDRE is equipped with low energy electrons (5-35 keV) for dark conductivity measurements. It features a temperature controlled holder, and much of DESP work on Kapton, Teflon, Cover glasses, paints was performed (with temperature effects) on this facility.

SIRENE: SIRENE is a more sophisticated DESP facility. It combines a high energy accelerator (400 keV Van De Graaff) and a low energy electron gun (5-20 keV). It has the unique feature to reproduce the geo-stationary electron spectrum (a stormy day, in the range of 10-400 keV). It allows a much more realistic assessment of voltage build-up in geo-stationary orbit since it involves both the charging (low energy) surface electrons, and the penetrating electrons able to enhance the material conductivity. The spectral range (10-400 keV) allows the study of materials up to 300 μm thickness, well fitting with most common external materials.

JONAS: Jonas is the DESP big plasma chamber to simulate the ionospheric plasma environment: high density and low energy plasma. Jonas can receive very big (meter size) samples. It combines a low energy electron gun with the ionospheric plasma and is fitted for experimental studies of wake charging (likely to occur in the polar LEO due to auroral precipitation).

LH 10 & VG ESCALAB (secondary emission facilities): ICMM/CSIC has developed facilities and expertise in surface physics. The equipment features Auger spectroscopy, secondary emission yield measurement, residual gas analysis and electron stimulated desorption measurements.

OTHER EUROPEAN FACILITIES (not in this consortium): All test houses in ESA member states should be listed. In Germany, the university of Giessen has been active as well as PTS in Freiburg. In the United Kingdom, QinetiQ is using radioactive strontium sources to investigate internal charging. Some Universities in Europe might as well have high-energy accelerators or low energy electron or ion guns, (basic equipment used in a variety of fields of physics).

Design of Database

It was considered important to build a database compatible with other already existing databases. This would save considerable effort (reusing database basic structures) and allowing importing and exporting data from other sources. In the frame of a partnership between ONERA and CNES, ONERA will use an already existing database (ARCAM = Aide à la Recherche des CAractéristiques des Matériaux), developed by CNES using Access as a tool. The database documents many materials related to European projects and a dedicated module is under study to include special material properties for space applications (outgassing, thermo-optical and radiation effects).

It is proposed to use the same database and add to it an "electric properties" module, to enable within this structure to exchange files already existing between ONERA, CNES and ESA. Specific interrogation requests will be defined.

The basic request for data will be by specifying the material. All the properties will then available so they can be either read or transferred as a file.

For each property, links will allow retrieving information about the data origin (article or report reference), and a summary of relevant attached conditions (temperature, value at beginning of life or after ageing test, history, contamination,..).
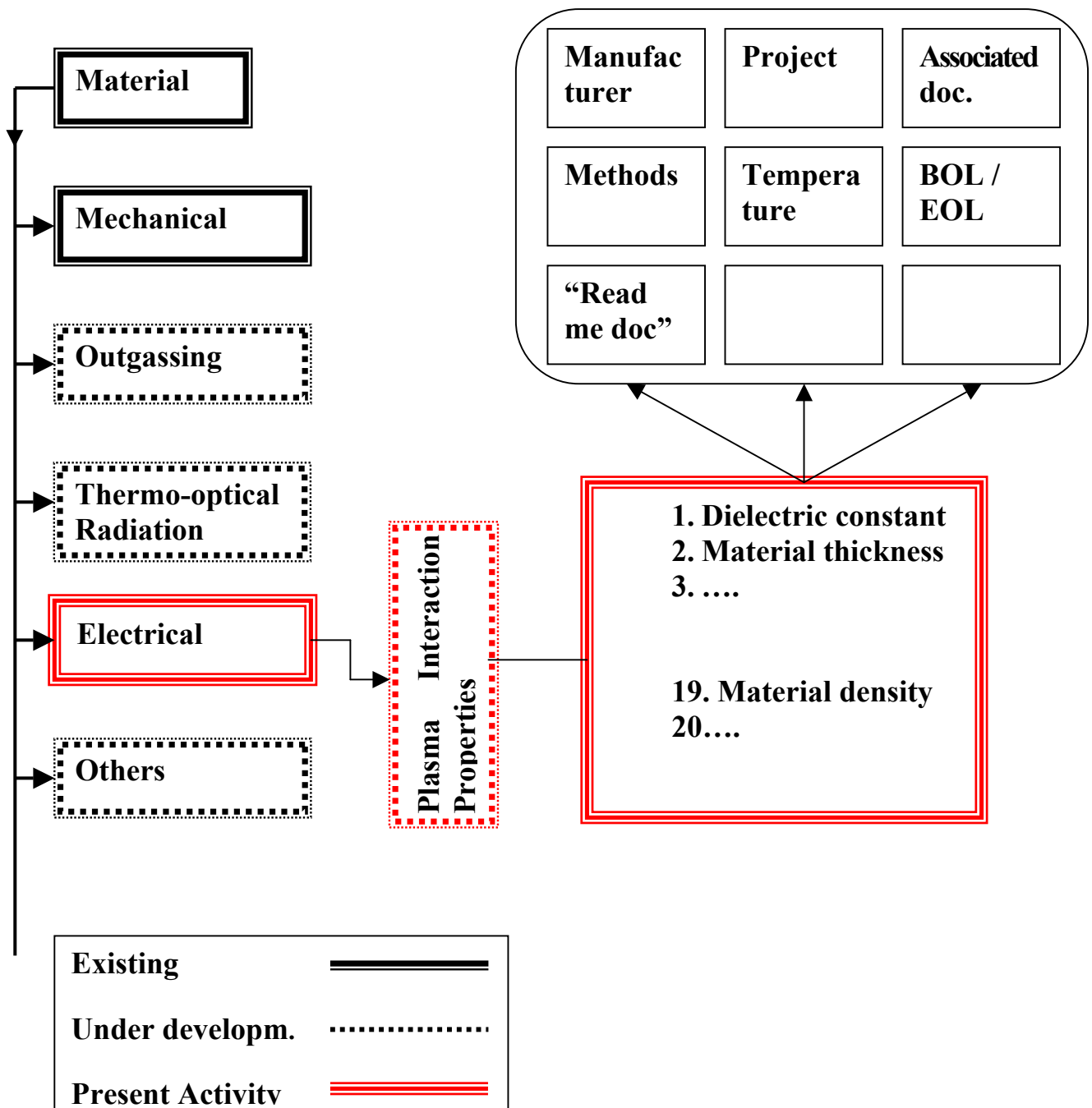
All data belonging to the public domain (published articles, data obtained in the frame of an ESA contract) will have a free access status for the Spine community. The SPINE community is diverse, including agencies, research institutes, universities and research laboratories.

Information on materials might be created on a private basis, the initiative coming from a company that would like to keep information confidential and proprietary. Such proprietary data will have a "protected status", i.e. limited access.

ESA's responsibility is to regulate the access to the database. Access will be given on condition to companies and organisations within the ESA member states.

The database will contain basic information about how the data is obtained (methods). The methods will be described in an informative didactic "read me" document.

The database will include editing possibilities to list all the materials inside the base, and the range of extreme values for each property.

The database includes also possibilities of editing the list of non-measured materials or non available properties.

Collection and integration of existing material properties in the database

The database will provide existing data to users and it will be first filled with already available data. When further data are produced, the database shall be updated.

In order to guarantee the validity of the data incorporated in the base, the different measuring methods shall be reviewed and recommendation for a preferred one (if possible) will be issued. The data shall give information about the method which was used to produce it. Full or restricted accessibility to the database shall be set up in close agreement with ESA.

The need of updating the database will depend on the production of new data on already existing materials or on new materials. A team will formally and periodically keep in contact to assess the status and importance of new data and the need of updating. Therefore, a group of identified personnel involved in material properties will be formed to evaluate the information. The group will communicate through a "moderator", collecting and dispatching available (non proprietary) information.

The database will document not only the existing and available data, but also give additional relevant information (how it was measured, article reference, etc).

Measurement of Properties on a Set of Proposed Materials

New materials (on use today or scheduled for use in the future) or new properties should be measured. An experimental program will be set up for a number of materials with considerations of environmental and ageing effects.

Users, i.e. through space industries, agencies and the Spine community, will be invited to express their non-covered needs. This should reveal required properties are not available.

This will help driving efforts towards new materials, new properties and eventually designing new (or adapted) facilities and measurement methods.

As already indicated, one of the properties playing a major role in the charging of spacecraft is the secondary electron emission.

The experimental set-up for the measurement of secondary electron emission yield is given below.
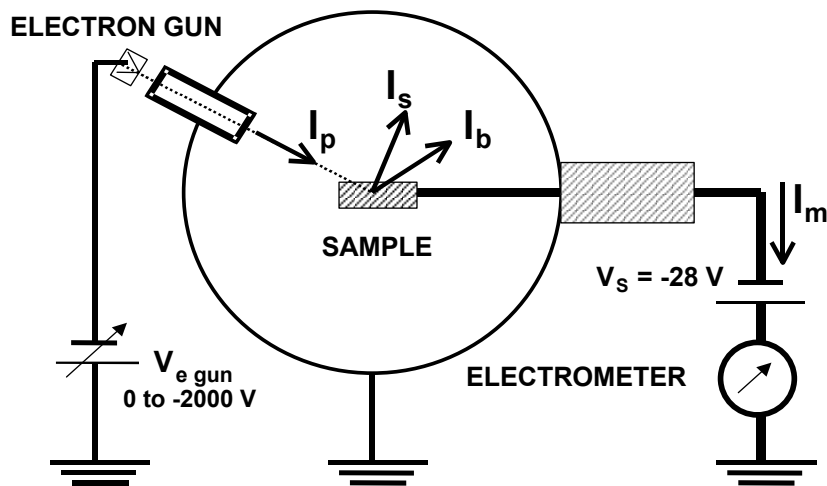
Experimental set-up for Secondary Electron Emission (SEE) measurements

The sample (to be measured) is irradiated with a calibrated electron gun. The figure below indicates the different categories of electrons re-emitted: The true secondary electrons (I_s), backscattered primary electrons (part of I_b) and elasctically reflected electrons do not have the same energies.
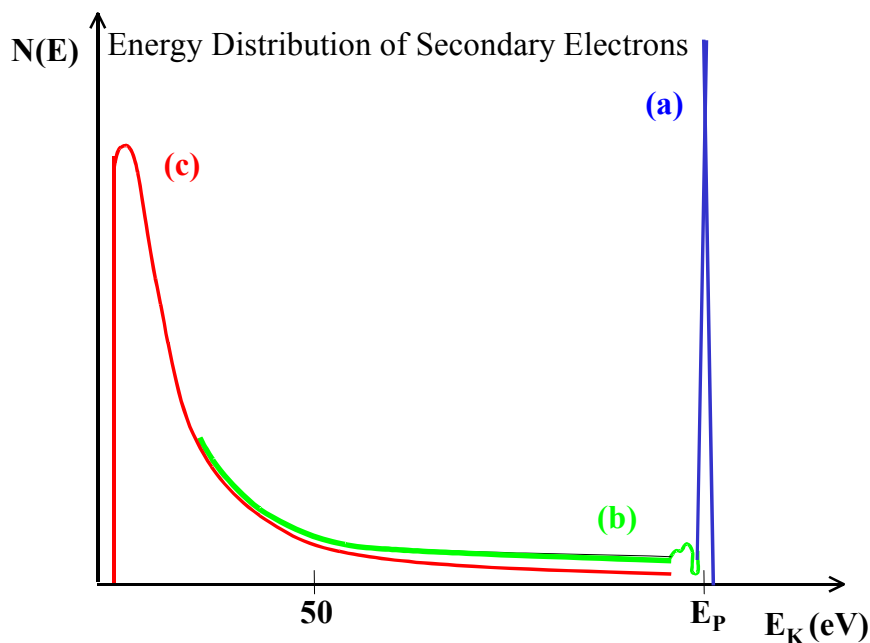
Three categories of electrons reemitted by the surface (a = reflected primaries; b = backscattered ; c = true secondary)

With a proper bias of the sample (up to 50 eV), true secondaries with low energies are allowed or not to escape the surface and two coeffcents can be measured, the true secondary electron emission (δ= Is/Ip) and the backscattered coefficient (η= Ib/Ip). The "total secondary emission" σ is computed as: $\sigma = \delta + \eta$.

Facilities and experience should also allow:

Measurement of secondary electron emission properties of spacecraft dielectric materials:

- Dependence of total secondary emission yield on primary energy, incident and emission angle
- Dependence true secondary emission yield on primary energy, incident and emission angle
- Energy distribution (spectra) of secondary emission

Study of dependence of secondary emission properties on:

- air exposure
- electron bombardment (conditioning: relevant for space dose effects)
- ion bombardment (conditioning: as above)
- heat treatment (relevant to contamination effects)

Analysis of the relation of secondary emission properties with:

- surface chemical composition
- surface roughness (relevant to ATOX influence)
- surface work function (academic interest)

Surface conditioning:

The total dose effect from electrons, ions or photons has been found to decrease the secondary electron yield and to result in a value of σm or δm which can be even lower than the measured value for the base material. The physical process, which causes this reduction of σm is related to the surface ion desorption. Electron conditioning treatment can be performed by use of electrons of 500 eV, $1\mu A/mm^2$ for variable duration.

Parallel Programmes

Outside Europe, major US research institutions dealing with spacecraft charging are carrying out a program very similar to this project. In the frame of the Space Environment and Effects Program, two actions similar to this study have started:

A data base (Satellite Contamination and Materials Outgassing Knowledgebase) has been attributed to the Bob Wood Aerospace Consulting Services, Inc., and an experimental program for the measurement of Charge Storage Decay Time and Resistivity of Spacecraft Insulators. The program is conducted by the Utah State University. Nearly 63 materials that are either in use today or provide a promising future in tomorrow's spacecraft design have been identified in this program.

Conclusion

The European Space Agency initiated and funded an activity to characterise the physical material properties needed for the modelling of material-plasma interaction. The subsequent contract has a nominal duration of 2 years. It is expected that by the end of this contract relevant properties for a large amount of materials, as well as the impact of ageing and space exposure on these properties will be assessed and integrated into a database.

AN IMPROVED METHOD FOR SIMULATING THE CHARGE OF DIELECTRICS IN A CHARGING ELECTRON ENVIRONMENT

D. Payan
CNES-Centre de Toulouse
18 Av. Edouard Belin, F31401 Toulouse – cedex 9

J. P. Catani
CNES-Centre de Toulouse

R. Reulet
B. Dirassen
L. Levy
ONERA-Centre de Toulouse

Abstract

Due to their dielectric nature and under the effect of the different forms of radiation encountered in space, dielectrics accumulate electrical charges up to the point where electrostatic discharges may occur. To prevent and avoid harmful interference due to discharges, their behaviour under irradiation must therefore be investigated in the laboratory before they are used in space applications. A current and widely used practice is to submit the tested materials to the bombardment of monoenergetic electron beams. Such a practice ignores the presence in space of a spectrum of electrons with energies reaching several MeV, and leads solely to surface charging and surface potentials generally higher than those really induced in space. The new approach used by "SIRENE" is to build an electron source as similar as possible to the one existing in orbit. This paper describes the SIRENE facility, which was developed for simulating the spatial geo-stationary environment during great geomagnetic activity. The range of available electrons goes from 10 to 400 keV. From a monoenergetic electron beam of 400 keV and thanks to a complex diffusion foil (made of several foils of different thicknesses and surface areas) the quantity of electrons of each energy level present in this particular environment is reproduced. However, it is always possible to work at lower energy levels in the monoenergetic range, for instance to simulate the inverted gradient mode. This paper provides information on the spectrum used for testing materials in the geo-stationary environment, and on the potential for adapting it to other orbits. It also gives the first results demonstrating the interest of this new approach. It also mentions the new instruments used to measure the surface potential as well as the space charge through the complete thickness of the material.

Introduction

The space environment may be responsible for numerous disturbances on the various parts of a satellite. Concerning the electrical hazards, the flux of electrons from space may result in problems caused by the electrostatic charging phenomena and the possible resulting discharges [1][2]. Laboratory tests are required for assessing this risk in order to prove, beforehand, the compatibility of the materials with their future environment (these tests can be validated by means of on-board experiments). The complexity of the space environment, and the fact that it is

impossible to reproduce all of its components make it difficult to perform any simulation. Several points must be considered:

· The utilization of electron flux only when, in space, the protons and photoelectrons emitted by the surfaces exposed to the sun also contribute to generating the charge (balance of all the interactions) and, consequently, the discharge.

· The locking in the laboratory of the structure potentials by the grounding of the metallizations when these structures, which are the "local grounds" for the electronic equipment, are also charged by the environment.

· The experiments are carried out over relatively short periods of time (some hours or days) whereas, in space, the key properties governing the charging of the materials (conductivity, secondary emission, etc.) undergo changes over much longer periods of time (several months).

· The electron guns or the accelerators generally used for the tests deliver monoenergetic electrons, whereas the electrons from space are distributed over a spectrum with a maximum energy level of several MeV.

This last point, which is particularly important, had to be considered to achieve an experimental simulation representative of the charging environment. Indeed, by taking into account the energy distribution of the electrons from space it is possible to integrate an essential factor relative to a materiel's level of charging which is its conductivity induced under the effect of radiation. Because the effect of an electron's charge is not neutral with respect to its energy, the multienergetic spectral approach is necessary and contributes to giving the tests performed their "qualifying" nature.

ONERA's DESP (SPace Environment Department) based the design and construction of the SIRENE facility on these considerations. The goal is to obtain a simulation system whose electron source reproduces the spectrum of the electrons in the geostationary environment (GEO) as well as possible, on a particular magnetic storm day, chosen because it is considered to be typical of a critical "charging" condition whose hazards must be assessed.

The development of the SIRENE facility was undertaken in technical cooperation with and with the financial backing of the CNES (French Space Agency) through multi-year investment and study actions [3]. The purpose of these actions was to design, construct and qualify a test facility that makes it possible to predict the level of charging of a dielectric material used in space.

The implementation of SIRENE therefore fits into the development of laboratory tests with better performances than those currently performed, avoiding the systematic recourse to more costly evaluations in space.

Geostationary Orbit Electron Flux – Reference Spectrum

The utilization of SIRENE poses the problem of choosing the energy spectrum of the geostationary-type natural environment for an experimental simulation of the electrostatic charging and discharging phenomena. The DESP has adopted the spectrum designated Kp>5 as reference, since AE8MAX is not sufficiently representative for this type of study. In fact, AE8MAX was defined using time-integrated environmental data, only concerning solar cycle No. 20 (low activity). Consequently, AE8MAX is better suited to studies on the effects of aging, where the dose is the decisive factor, than for studies on electrostatic charge phenomena. A comparison between the Kp>5 and AE8MAX integrated spectrums is given in Fig. 1.
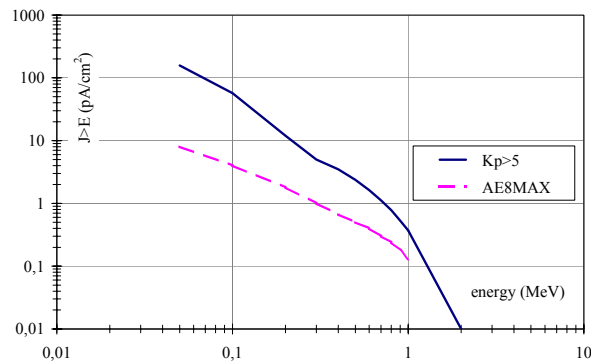
Figure 1. AE8MAX and Kp>5 integrated spectrums

The characteristics of the Kp>5 reference spectrum are described in detail in the study carried out for ESA (European Space Agency) [4]. This spectrum is defined by means of statistics on the flight data recorded on geostationary satellites during agitated periods of geomagnetic activity with a Kp index > 5. This Kp indicator varies between 0 and 9 according to the geomagnetic activity; the measurements were performed on the ground.

The Kp>5 energy-integrated spectrum is interpolated well by the following equation (with E in keV).

$$J(>E) = A \exp(-\frac{E}{Ea}) + C \exp(-\frac{E}{Ec}) \quad [4]$$

A=9.52*10^7 Ea= 268.64 keV
C=2.8*10^9 Ec =44.16 keV

The Kp>5 spectrum simulates a high-amplitude magnetic storm while remaining realistic, and it was established using dynamic data. Furthermore, it is well-correlated with the GEO models (ONERA/DESP's Salambô) and with the worst-case measurements recorded by the LANL's geostationary satellites [5]. This explains why Kp>5 seems well-suited to serve as reference spectrum for studies examining the problems of electrostatic charging.

Once the reference spectrum has been chosen, the goal is to reproduce it, as well as possible, over the widest possible spectral range. The solution adopted consists of transforming the mono-

energetic beam delivered by an electron accelerator into an energy-distributed beam, using complex diffusion foils.

Given the very great dynamics of the space flow according to the energy, it is practically impossible to reproduce this spectrum in its entirety using a single radiation source. In practice, each experimental device can only reproduce part of the Kp>5 reference spectrum. The energy range is chosen so that it corresponds more specifically to an application area. We therefore use two of the devices installed at the DESP as our example (DESP's various simulation systems are described in detail in [6]):

· firstly GEODUR which is a device suited to studies on the phenomena linked to the internal charge. Thus, the structures or materials tested are irradiated behind a shielding representative of the satellite's outer casing. The energy spectrum is representative of the GEO spectrum in the energy range comprised between 0.2 and 1 MeV, and it is obtained by transforming the 1.1 MeV monoenergetic beam from a Van de Graaff accelerator.

· secondly SIRENE, which is a facility designed for external charge studies on materials with a thickness of less than approximately 450 µm (equivalent thickness of aluminium), or for internal charge studies when the thickness of the shielding is slight (< 200 µm of aluminium). The energy spectrum is representative of the GEO spectrum in the energy range comprised between 40 and 400 keV, it is obtained by transforming a 400 keV mono-energetic beam delivered by a Van de Graaff accelerator. For many of the applications in SIRENE (without shielding), the electron spectrum's low-energy component, which is the most intense, has to be reinforced with a second radiation source. An electron gun is used to do this. It is possible, using the same procedure, to simulate spectrums other than the Kp>5 reference spectrum. However, it must be underlined that the development of complex windows suited to these spectrums, and the experimental validation of the beams obtained, represent a significant amount of costly work.

Another solution for carrying out this type of simulation is to use radioactive sources. However, although they have the advantage of providing energy-distributed radiation, they do have major safety and procurement drawbacks.

SIRENE Experimental Facility

The originality of the SIRENE experimental simulation facility is that it includes equipment making it possible to reproduce the effects of the charges induced by the electrons from the space environment in an energy range lower than or equal to 400 keV.

Description of the SIRENE Facility

The SIRENE facility has the following main components:

➢ A large-dimension cylindrical vacuum chamber (L≈1.5 m, Ø≈0.5 m) designed in 3 sections to ensure modularity. The horizontal opening of the chamber makes it easy to set up experiments *in situ*. At the level of the vessel, the influence of the terrestrial magnetic field

on the electron flow trajectory is compensated for by the magnetic field induced by the two pairs of windings (vertical and horizontal) surrounding the chamber. The body of the chamber is fitted with several standardised diameter extensions enabling the installation of various control and metrology instruments (vacuum gauge, visualisation camera, electrical outputs, analysis probes, connections to the radiation sources, etc.).

➢ A primary and secondary pumping unit which ensures a pressure of the order of 10^{-6} hPa after some hours in operation.

➢ A specimen door, with temperature regulation within a range comprised between -180°C and +100°C.

➢ The facility is equipped with two electron sources:

· A Van de Graaff type accelerator capable of delivering a monoenergetic electron beam whose energy level can be adjusted between 100 and 400 keV. In the case of experiments carried out using a simulation of electron flux from space whose energy spectrum is distributed, the accelerator's operating energy is of the order of 400 keV (most frequent case).

· A low-energy electron gun which delivers a beam whose energy level can be adjusted between 1 and 35 keV. This electron beam can be used alone (many tests are requested on the basis of specifications such as: E=20 keV, Φ=1 nA/cm^2). It is also used to complete the flow of the Van de Graaff accelerator's electron beam at low energy levels.

➢ A set of "complex" diffusion windows designed to transform the 400 keV monoenergetic beam delivered by the accelerator into an energy-distributed beam according to a reference spectrum chosen to simulate a type of orbit.

➢ The analysis instruments specific to the electrostatic studies, that is to say:

· current probes for detecting discharges and analysing current transients,

· A potential probe used for analysing charge potentials along a vertical axis.

A further development phase being carried out at present with the CNES concerns the metrology of the charge potentials. The instruments currently in place only enable *in situ* measurements of the potentials according to a vertical axis (d ≤ 15 cm) and no other analysis probe movements are possible. In the case of studies on a relatively large number of simple specimens, or on more complex structures (solar arrays, antennas, etc.), these instruments are insufficient. Consequently, a new potential probe movement system is in the process of being designed. It should make it possible to analyse charge potentials in a 20 cm x 20 cm plane.

A general view of the SIRENE experimental facility is shown in Fig. 2.

Figure 2. General view of SIRENE

The facility's various components with the positioning and the trajectory of the two electron beams delivered by the electron gun and the Van de Graaff accelerator are symbolised in Fig. 3 (shown in the horizontal plane).
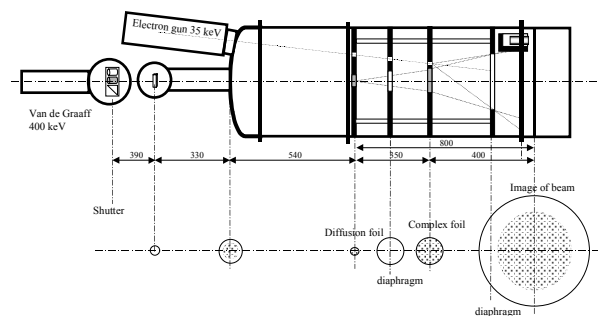
Figure 3. SIRENE schematic diagram

Definition and adjustment of the electron spectrum of SIRENE

The role of the complex diffusion window is to transform the monoenergetic beam delivered by the Van de Graaff accelerator into an energy-distributed beam that is as close as possible to the Kp>5 reference spectrum. The design of these complex windows is based on the association of simple diffusion foils, of different thicknesses and surface areas. The analysis of the flux transmitted by the simple or complex diffusion foils was carried out in cooperation with the CESR laboratory (Radiation Space Studies Centre) using the ERMD detector (EPIC Radiation Monitor Detector) [7].

Fig. 4 shows an example of the flux transmitted by the diffusion foils whose thickness varied between 0 and 550 μm when they were bombarded by a 400 keV electron beam which had been diffused by two 9 μm diffusion foils beforehand. The complex window was designed in such a way that from the 400 keV monoenergetic beam delivered by the Van de Graaff accelerator, the transmitted flow corresponds as well as possible to the Kp>5 spectrum in the 40-400 keV range. Although their density was slight, electrons whose energy was lower than 40 keV were present in this spectrum. It was not possible to quantify them with the ERMD detector since its detection

threshold is of the same order. The low energy component was provided by the electron gun by means of a virtually monoenergetic flow of 20 or 30 keV.

The SIRENE integrated spectrum (GEO orbit) is compared with the Kp>5 integrated reference spectrum in Figure , and a good match can be seen between the two spectrums.
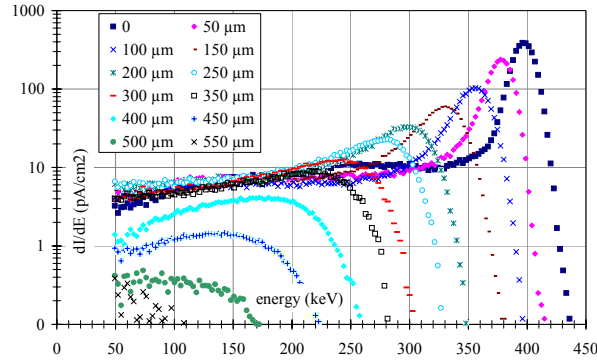
Figure 4. Differential spectrums of the flux transmitted by aluminium shieldings bombarded by a 400 keV electron beam
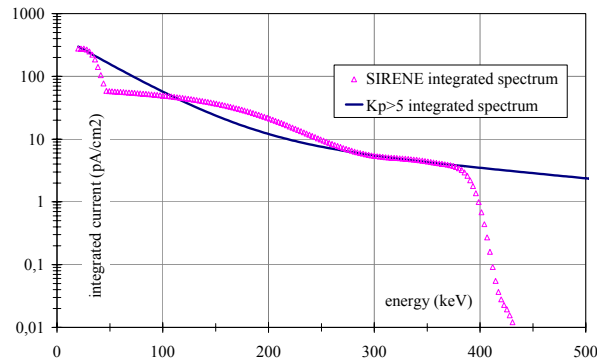
Figure 5. Integrated spectrum delivered by the complex window and Kp>5 integrated reference spectrum

A charge detection system embedded in the volume of polymer films (Teflon®, Kapton®, epoxy resin, etc.) has been developed in SIRENE [8]. The measurements are carried out *in situ* during the irradiation. This test bench, called the PEA (Pulse Electro Acoustic), is based on the pulsed electro-acoustic method. It was developed in cooperation with the Communications Research Laboratory (CRL) in Japan, the LGET (Toulouse Electrical Engineering Laboratory) and the CNES.

Experimental Results - Influence OF The Irradiation Mode

The influence of the irradiation mode on the materials' charge has been assessed in the SIRENE facility with two types of electron irradiations. The flow levels were chosen so that they correspond approximately to the integrated flow of the Kp>5 reference spectrum (E>20 keV). The following parameters were analysed to make this comparison: charge limit potential and the resistivity according to the square root of the electrical field.

– The first series of tests was carried out using the conventional irradiation conditions usually adopted for performing charge tests in the laboratory; in this case the energies were virtually monoenergetic. The conditions for the first irradiation mode were as follows:

$E=20$ **keV,** $\Phi=250$ **pA/cm^2**

– The second series of tests was carried out with SIRENE's 0 to 400 keV energy-distributed beam delivered simultaneously by the two radiation sources (see Figure). The conditions for this second irradiation mode were as follows:

$E=20$ **keV,** $\Phi=250$ **pA/cm^2 + E distributed from 0 to 400 keV,** $\Phi=50$ **pA/cm^2**, giving a total flow of 300 pA/cm^2.

Several representative dielectric materials were tested, they were all metallised on their rear face. When performing the tests, 2 specimens made of different materials were associated so that the charge kinetics were relatively close.

Influence of the irradiation mode on the charge potential (T≈20°C)

For both irradiation modes, the results presented correspond to tests performed at the laboratory's ambient temperature (T≈20°C).

The following materials were tested simultaneously in this way:

➢ 50.8 μm Kapton®, and 25.4 μm Kapton® (supplied by ASPI Toulouse, with germanium used for the rear metallisation)

➢ 127 μm FEP Teflon®, and 127 μm Kapton® (supplied by ASPI Toulouse)

➢ 127 μm RT/duroid®6002 (supplied by Rogers Corp.), and Second Surface Aluminium Coated FEP Tape with 966 Acrylic Adhesive (supplied Sheldahl, ref.: 146379, 127 μm FEP Teflon®)

Different specimens were used for each irradiation series so that that the changes made to the characteristics of the materials by the experiment did not disturb the results of the following tests. However, to ensure that the comparison of the irradiation modes was coherent, all the specimens were taken from the same test bars.

The comparison of the two irradiation modes on the charge potential is illustrated in Figure for the 50.8 μm and 25.4 μm Kapton®, in Fig for the 127 μm FEP Teflon® and Kapton®, and in Figure 8 for the 127 μm RT/duroid®6002 and SSM aluminuium (127 μm Teflon®). The recorded data show the variations of the charge potential versus the irradiation time.
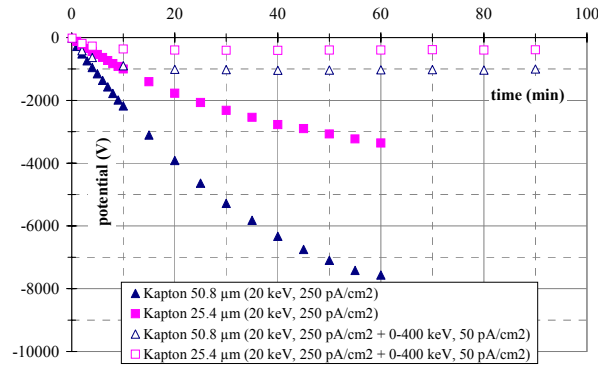
Figure 6. Variation in the charge potential versus the irradiation time for the 50.8 μm and 25.4 μm Kapton® according to the two irradiation modes
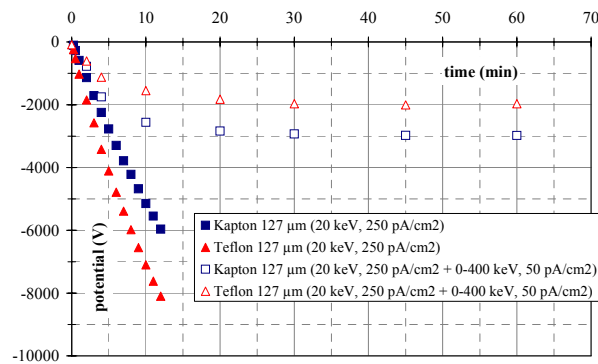
Figure 7. Variation in the charge potential versus the irradiation time for the 127 μm FEP Teflon® and Kapton® according to the two irradiation modes
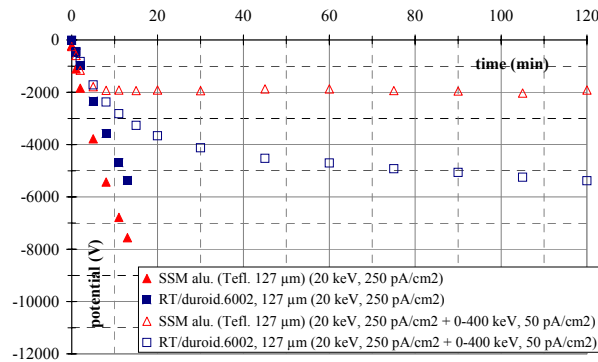
Figure 8. Variation in the charge potential versus the irradiation time for the 127 μm RT/duroid®6002 and SSM alu.(127 μm Teflon®) according to the two irradiation modes

The results shown in Fig. 6, Fig. 7 and Fig. 8 clearly show the large differences observed according to the irradiation mode, both on the charge kinetics and on the maximum potential.

The three tables below summarise the differences observed for the six materials on the maximum charge potential (expressed as an absolute value) according to the two electron flow simulation modes for the GEO orbit.

maximum charge potential (V)	
Kapton® thick=25.4 μm	Kapton® thick=50.8 μm
20 keV, 250 pA/cm²	$\lvert V \rvert >$ 3360	$\lvert V \rvert >$ 7500
20 keV, 250 pA/cm² + 0-400 keV, 50 pA/cm²	$\lvert V \rvert \approx 390$	$\lvert V \rvert \approx$ 1030

maximum charge potential (V)	
Teflon® thick=127 μm	Kapton® thick=127 μm
20 keV, 250 pA/cm²	$\lvert V \rvert \gg$ 8100	$\lvert V \rvert \gg$ 6000
20 keV, 250 pA/cm² + 0-400 keV, 50 pA/cm²	$\lvert V \rvert \approx$ 2000	$\lvert V \rvert \approx$ 3000

maximum charge potential (V)	
RT/duroid® 6002 thick=127 μm	SSM Alu. thick=127 μm
20 keV, 250 pA/cm²	$\lvert V \rvert \gg$ 5500	$\lvert V \rvert \gg$ 8000
20 keV, 250 pA/cm² + 0-400 keV, 50 pA/cm²	$\lvert V \rvert > 5000$	$\lvert V \rvert \approx$ 2000

It should be noted that for all the irradiations with a 20 keV monoenergetic flow, the irradiation times were intentionally limited to prevent the specimen from discharging. The purpose of this limitation was to prevent the profile of the maximum potential from being disturbed. Indeed, the material's resisitivity is calculated from the relaxation of this potential with respect to time.

Influence of the irradiation mode on the materials' resistivity (T≈20°C)

The resistivity of the materials is defined on the basis of the relaxation of the charge potential versus time after the irradiation is stopped.

It is worth pointing out right from this point that the resistivity value of the experimental results are deducted from registration of the potential relaxation versus to time. The different points of relaxation are acquired when the irradiation is stopped. So the different calculated values do not exactly correspond to real value of radiated induced conductivity (RIC) under irradiation but more to a residual or a delayed conductivity. Naturally, this effect decreases with time.

An example of this relaxation according to time is shown in Figure for the 127 µm Teflon® and Kapton® and in Figure for the 127 µm RT/duroid®6002 and SSM aluminium (127 µm Teflon®). These data, recorded after firing had been stopped, are reported for both irradiation modes. In this case, the charge potential obtained from the monoenergetic flow irradiation (20 keV, 250 pA/cm^2) was intentionally limited. The purpose of this limitation was to ensure that the electrical fields corresponding to the two irradiation modes were of the same order of magnitude.
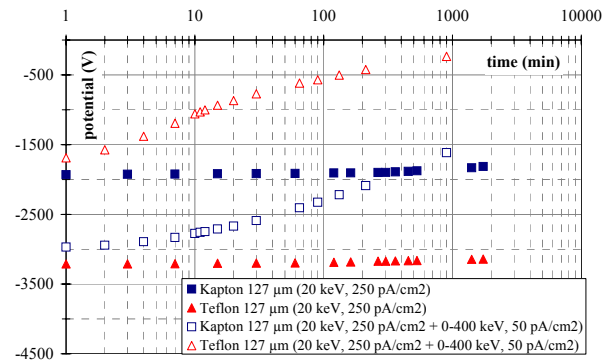
Figure 900. Relaxation of the charge potential versus time for the 127 µm Teflon® and the 127 µm Kapton®
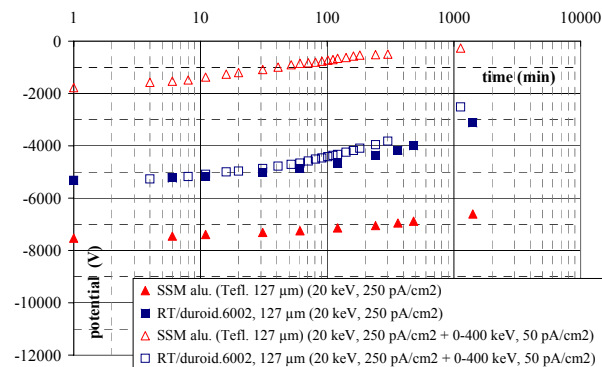
Figure 10. Relaxation of the charge potential versus time for the 127 µm RT/duroid®6002 and SSM alu.(127 µm Teflon®)

The resistivity of each material was calculated from the relaxation kinetics of the charge potentials, using the relation: $\rho = -\dfrac{1}{\varepsilon_0 \varepsilon_r} \dfrac{V}{\dfrac{dV}{dt}}$.

The parameters used for these materials are given in the table below.

	density	e⁻ (E=20 keV) penetration	permittivity
Kapton®	1.42	≈ 6.6 µm	3.46
Teflon®	2.15	≈ 4.9 µm	2.2
RT/duroid ® 6002	2.1	≈ 4.9 µm	2,94 (10 GHz)

The resistivity values calculated according to the square root of the electrical field $\rho = f\left(\dfrac{V}{e}\right)^{\frac{1}{2}}$ are given in Figure for the 127 µm Teflon® and Kapton® and in Figure for the 127 µm RT/duroid®6002 and SSM alu.(127 µm Teflon®).
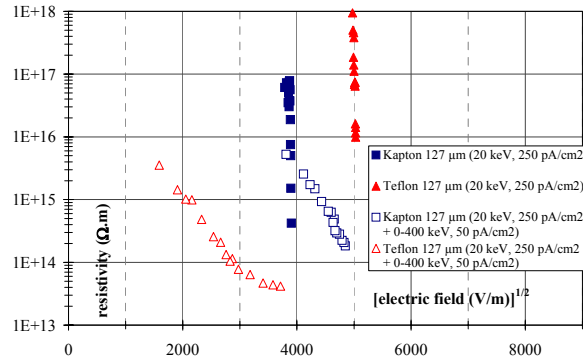
Figure 11. Resistivity variation according to the square root of the electrical field for the 127 µm Teflon® and the 127 µm Kapton®
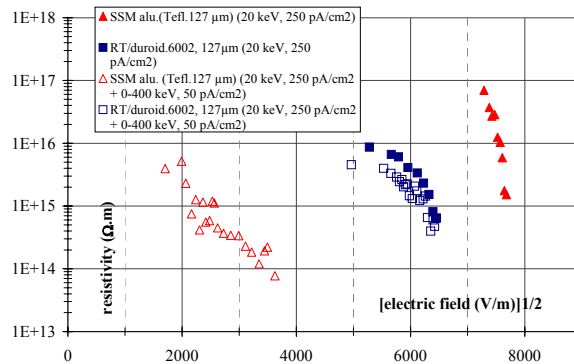
Figure 12. Resistivity variation according to the square root of the electrical field for the 127 µm RT/duroid®6002 and SSM alu.(127 µm Teflon®)

The singular behaviour of the resistivity should be noted in the case of monoenergetic flow irradiation (20 keV, 250 pA/cm^2) in particular on the Kapton®. This singularity concerns the first values calculated immediately after the charging, and which consequently corresponded to the first minutes of relaxation (t ≤ ≈ 10 min). The resistivity values were low and were not consistent with those calculated for longer relaxation times. Without developing explanations that do not come within the scope of this article, the possible influence of several points must be underlined.

− Concerning the experimental conditions:
   · the first resistivity values were calculated from the $\frac{dV}{dt}$ ratios presenting the greatest uncertainty given the slight decrease in the potential. However, since the drift of the signal from the electrostatic probe was systematically taken into account in the measurements, this point would not seem to explain the phenomenon.

   · the passing of the probe in front of the specimens could be a source of disturbances.

− Concerning the materials:

   · the conductivity of the irradiated thickness of the material (≈ 4 to 6 µm) may enable, at the beginning of relaxation, the flow of the charges through the edges of the specimens.

The results presented underline the importance of taking into account the conductivity induced under radiation. Generally speaking, the differences observed between the irradiation modes depend, of course, on the materials.

SIRENE operation involves sufficient levels of energy to create X-radiation in the chamber that could modify the conductivity characteristics of the treated specimens. The effect of this radiation has been quantified. It has not been possible to detect any influence of X-radiation for the flow levels specific to conventional tests.

Conclusion

In the framework of laboratory tests, the SIRENE facility makes a new and significant contribution in terms of representativeness concerning the spectral energy distribution of the flux of electrons in space. Its operational possibilities can be summarised as follows:

• treatment of specimens in a temperature range comprised between -150°C and +100°C

• irradiation with a virtually monoenergetic beam:

   − in an energy range comprised between 1 and 35 keV (electron gun)
   − in an energy range comprised between 100 and 400 keV (Van de Graaff accelerator)

• irradiation with a 0 to 400 keV energy-distributed beam:

- irradiation according to a spectrum close to Kp>5 (GEO orbit),
- possible irradiation according to an orbit of another type (GTO, MEO),
- in all cases, the representativeness of this type of test is limited to specimens whose thickness is of the order of 450 to 600 μm depending on the density,
- no influence of any possible X-radiation in the chamber has been detected.

The results presented on some dielectric materials show the importance of taking into account the conductivity induced under radiation on the charge limit potential. They thus demonstrate the importance of the way the charge electrons from space are simulated. These results clearly underline that, for most of the dielectric materials used on satellites, the conventional tests carried out with 20 or 30 keV monoenergetic beams are poorly suited and, very often, lead to an overestimation of the risks.

References

1. Lévy L., Material charging. Space Technology Course-Space Environment: "Prevention of risks related to spacecraft charging" - April 2002 - Toulouse (CEPADUES-EDITIONS)

2. Payan D., Vacuum electrostatic discharges. Space Technology Course-Space Environment: "Prevention of risks related to spacecraft charging" - April 2002 - Toulouse (CEPADUES-EDITIONS)

3. Reulet R., Dirassen B., Inguimbert C., Aït Zaïd L., Simulation en laboratoire des effets de charge par électrons. Instrumentation et analyse du faisceau d'électrons du nouveau dispositif SIRENE. Contrat CNES - RTS 2/05408 DESP - November 2001

4. Soubeyran A., Estienne J. P., Borde J., Rudenhauer F. G., Fehringer H. M., Betz G., Kensqek R. P., INTERNAL ELECTROSTATIC CHARGING - FINAL REPORT - ESTEC Contract N°9203/90/NL/JG. July 1992

5. Inguimbert Ch., Bourdarie S., Etude de l'environnement électronique en orbite MEO et GEO. Contrat CNES – RTS 1/07608 DESP – Mars 2003

6. Viel-Inguimbert V., Bourdarie S., Reulet R., Lévy L., Laboratory Ground Simulation of GEO and LEO Environment. 7th Spacecraft Charging Technology Conference, Noordwijk, The Netherlands, 23-27 April 2001

7. Reulet R., Dirassen B., Liébart S., Simulation en laboratoire des effets de charge par électrons. Rénovation du dispositif SIRENE. Contrat CNES - RF/CS0306501 DESP - Octobre 2000

8. Griseri V., Fukunaga K., Maeno T., Payan D., Laurent C., Levy L.. Internal space charge measurement of materials in a space environment. 9th International Symposium on "Materials in a Space Environment", Noordwijk, The Netherlands 16-20 June 2003

CLEAR, CONDUCTIVE, TRANSPARENT, FLEXIBLE SPACE DURABLE COMPOSITE FILMS FOR ELECTROSTATIC CHARGE MITIGATION

Kent A. Watson
National Institute of Aerospace
144 Research Drive
Hampton, VA 23666-1399
Phone: (757) 864-4287
Fax: (757) 864-8312
E-mail: k.a.watson@larc.nasa.gov

John W. Connell, Donavon M. Delozier,* and Joseph G. Smith, Jr.
National Aeronautics and Space Administration
Langley Research Center

* National Research Council Research Associate

Abstract

Space environmentally durable polymeric films with low color and sufficient electrical conductivity to mitigate electrostatic charge (ESC) build-up have been under investigation as part of a materials development activity. These materials have potential applications on advanced spacecraft, particularly on large, deployable, ultra-light weight Gossamer spacecraft. The approach taken to impart sufficient electrical conductivity into the polymer film while maintaining flexibility is to use single wall carbon nanotubes (SWNTs) as conductive additives. Approaches investigated in our lab involved an in-situ polymerization method, addition of SWNTs to a polymer containing reactive end-groups, and spray coating of polymer surfaces. The work described herein is a summary of the current status of this project. Surface conductivities (measured as surface resistance) in the range sufficient for ESC mitigation were achieved with minimal effects on the physical, thermal, mechanical and optical properties of the films. Additionally, the electrical conductivy was not affected by harsh mechanical manipulation of the films. The chemistry and physical properties of these nanocomposites will be discussed.

Introduction

Large, deployable, ultra-light weight spacecraft require polymeric materials that possess a unique combination of mechanical and optical properties.[1] Specific requirements for the materials are determined by the mission and orbital environment of the spacecraft. A few of the desired properties include atomic oxygen (AO) resistance [for spacecraft in low Earth orbit (LEO)], low solar absorptivity (low color), high thermal emissivity, resistance to ultraviolet (UV) and vacuum UV radiation, good mechanical properties, good processability, tear resistance, the ability to be folded and unfolded, and sufficient electrical conductivity for

mitigation of electrostatic charge (ESC) build-up. The overall goal of this work is to prepare clear, colorless, flexible, anti-static, space environmentally durable polymer films to satisfy material needs for future NASA missions.

Many of the property requirements for these applications are met by using aromatic polyimides due to their exceptional mechanical properties as well as resistance to UV and charged particle radiation. By proper choice of the constituent monomers, low color (low solar absorptivity) and AO resistant polyimides can be prepared.[2-4] However, the incorporation of sufficient electrical conductivity to mitigate ESC build-up without adversely effecting low color and flexibility has been difficult to achieve.

Particles in the Earth's orbital environment include electrons/ions, solar flare protons and cosmic rays.[5-7] Because of the high energies of these particles, they can penetrate spacecraft materials and cause destructive effects including loss of optical and/or mechanical properties. Energetic charged particles, particularly electrons, can also penetrate spacecraft surface layers, depositing a charge onto insulators and other electrically isolated surfaces on a spacecraft. This can result in ESC build-up and development of large electric fields and consequent discharging. Discharge of the built-up charge can cause catastrophic damage to sensitive spacecraft electronics.[8,9] The surface resistivity needed to mitigate ESC build-up on insulators such as polymer films is in the range of 10^6 to 10^8 Ω/square.

One approach to imparting surface resistivity into polymer films without severely detracting from the desired optical and thermo-optical properties is through the use of single walled carbon nanotubes (SWNTs). Discovered in the early 1990s,[10,11] SWNTs exhibit great potential for improving the electrical properties of materials. However, achieving good dispersion of SWNTs throughout a polymer matrix has been difficult due to the insolubility of the SWNTs and/or incompatibility with the host resin. SWNTs tend to agglomerate in solvent and the host resin and even if dispersed, typically re-agglomerate soon thereafter due to electrostatic attraction.

Three methods that use SWNTs as conductive additives have been investigated for incorporating surface resistivity into space environmentally durable polymer films. These are 1) an in-situ polymerization approach,[12-14] 2) the addition of SWNTs to amide acid polymers containing reactive alkoxysilane end-groups,[15-17] and 3) the coating of SWNTs onto the surface of polymer films.[13] The first two approaches impart bulk and surface conductivity while the last approach imparts surface conductivity. The best results have been achieved with the last two methods.

This paper discusses two of the aforementioned methods used to prepare clear, conductive space durable materials: 1) end-capping a low color, space environmentally durable polyimide (LaRC™ CP2) with alkoxysilane groups and 2) surface coating polymers with SWNTs. The preparation and physical properties of the materials are described and compared herein.

Experimental

Starting materials

Aminophenyltrimethoxysilane (APTS, Gelest Inc., 90% meta, 10% para) and 1,3-bis(3-aminophenoxy)benzene (APB, Mitsui Chemicals America, Inc. mp 107-108.5 °C) were used as-received. 4,4'-Oxydiphthalic dianhydride (ODPA, Imitec, Inc., mp 224-225.5 °C) and 4,4'-hexafluoroisopropylidene diphthalic anhydride (6FDA, Hoechst Celanese Inc., mp 241-243 °C) were sublimed prior to use. [2,4-Bis(3-aminophenoxy)phenyl]-diphenylphosphine oxide (3-APPO, mp 195-196.5 °C) was prepared as previously reported.[2] HiPco SWNTs (BuckyPearls™) were obtained from Carbon Nanotechnologies Inc. (batch # P0222) and were treated as described below. m-Cresol (Fluka) was vacuum distilled prior to use. Isoquinoline, N,N-dimethylacetamide (DMAc, anhydrous), N-methyl-2-pyrrolidinone (NMP, anhydrous), N,N-dimethylformamide (DMF, anhydrous), tetrahydrofuran (THF, anhydrous), 1,2-dichlorobenzene (DCB), sodium methoxide (powder), pyridine, and acetic anhydride were used as-received (Aldrich).

SWNT treatment

The SWNTs were treated as follows: A 250 mL round-bottom flask was charged with SWNTs (0.100 g) and DCB (220 mL) and the mixture sonicated for 3 hrs at room temperature. In a separate flask, pyridine (80 mL) and sodium methoxide (0.264 g) were stirred under nitrogen at room temperature. The SWNT/DCB mixture was added to the flask containing the pyridine/sodium methoxide mixture and the resulting mixture heated to 80°C. After 16 hrs at 80°C, the temperature of the reaction mixture was increased to reflux. Pyridine was removed by distillation and the reaction mixture was stirred in refluxing DCB for 3 hrs. The mixture was then cooled to room temperature. The SWNTs were isolated via centrifugation, washed numerous times with methanol, and dried in a vacuum oven at 150 °C for 6 hrs. The treated tubes exhibited enhanced solubility properties (stable suspension). The mechanism for the enhanced solubility is currently under investigation. All SWNTs were treated via this process prior to use.

Polymer synthesis

APB (6.7470 g, 0.0231 mol) and DMAc (30.0 mL) were placed into a 250 mL three neck round-bottom flask equipped with a mechanical stirrer, nitrogen gas inlet, and drying tube filled with calcium sulfate. Once dissolved, 6FDA (10.3044 g, 0.0232 mole, 0.5% offset) was added with additional DMAc (38.2 mL) to afford a solution with a solids content of 20% (w/w). The solution was stirred overnight at ambient temperature under a nitrogen atmosphere. The polymer was chemically imidized by the addition of 7.1 g of acetic anhydride and 5.5 g of pyridine and stirring at ambient temperature overnight. The polymer was precipitated in a blender containing water, filtered, washed with excess water and dried in a vacuum oven at 110 °C overnight to afford a white, fibrous material. All other polyimides were prepared as reported.[2]

Synthesis of polymers end capped with alkoxysilanes

The alkoxysilane terminated amide acids (ASTAAs) were prepared by the reaction of 6FDA with APB and end-capped with APTS at a 2.5% molar offset. The calculated number average molecular weight ($\overline{M}_n$) was ~27,700 g/mole. The oligomer was prepared by dissolving APB (4.9522 g, 0.0169 mol) and APTS (0.1853 g, 0.0009 mol) in DMAc (7 mL) in a three neck round-bottomed flask equipped with a mechanical stirrer, thermometer and nitrogen gas inlet. The flask was then immersed in a water bath to regulate the temperature. 6FDA (7.7184 g, 0.0174 mol) was added in one portion as a slurry in DMAc (10 mL) and rinsed in with 9 mL of DMAc to afford a solution with a solid content of ~34.4% (w/w). The reaction was stirred for ~24 hrs at ambient temperature under nitrogen. An aliquot was removed to determine inherent viscosity. For film casting, the solution was diluted with an additional 21 mL DMAc to afford a solids content of ~22.5% (w/w).

Films

ASTAA-LaRC™ CP2 solutions in DMAc (with and without SWNTs in the bulk) were doctored onto plate glass and dried to tack-free state in a low humidity chamber at ambient temperature. The films were then staged to 300 °C for 1 hr in a forced air oven.

Spray coating of SWNT

ASTAA-LaRC™ CP2 film solutions in DMAc were doctored onto plate glass and dried to a tack-free state in a low humidity chamber. A SWNT/DMF mixture (1.0 mg SWNT per 5.0 g DMF) was placed in an ultrasonic bath operating at 40 MHz for 6 to 8 hrs. An airbrush (Badger Model 250) was used to apply the SWNT/DMF suspension to the tack-free ASTAA-LARC™ CP2 films. The films were placed in a low humidity chamber for 16 hrs and then staged to 300°C for 1 hr in a forced air oven.

Polyimide (LaRC™ CP2, TOR-NC[3] and PPO-6FDA, Figure 1) solutions in DMAc (23% wt/wt) were doctored onto plate glass and placed in a low humidity chamber for 15 minutes. A SWNT/THF mixture (1.0 mg SWNT per 5.0 g THF) was placed in an ultrasonic bath operating at 40 MHz for 1 to 2 hrs. An airbrush (Badger Model 250) was used to apply the SWNT/THF suspension to the films. The coated polyimide films were placed in a low humidity chamber for 16 hrs and then staged to 220 °C for 1 hr in a forced air oven.

Other characterization

Inherent viscosity was obtained on a 0.5% (w/v) amide acid solution in DMAc at 25 °C. Melting point ranges (tangent of onset to melt and the endothermic peak) were determined by either differential scanning calorimetry (DSC) at a heating rate of 10 °C/min or visually on a Thomas-Hoover capillary melting point apparatus (uncorrected). The % transmission at 500 nm was obtained on thin films using a Perkin-Elmer Lambda 900 UV/VIS/NIR spectrometer. Solar absorptivity (α) was measured on an AZ Technology Model LPSR-300 spectroreflectometer

with measurements taken between 250 to 2800 nm using a vapor deposited aluminum on Kapton® film (1st surface mirror) as a reflective reference for air mass 0 per ASTM E903. An AZ Technology Temp 2000A infrared reflectometer was used to measure thermal emissivity (ε). Surface resistivity was measured using a Prostat® PSI-870 Surface Resistance and Resistivity Indicator per ASTM D-257 and reported as an average of three readings. High-resolution scanning electron microscopy (HRSEM) images were obtained using a Hitachi S-5200 field emission scanning electron microscope (FE-SEM) equipped with a "through-the-lens" secondary electron detector. The FE-SEM was operated in the low voltage mode in order to setup a stable local electric field on the surface of the sample while minimizing beam induced sample damage.

Results and Discussion

Alkoxysilane terminated amide acid synthesis

The ASTAA of LaRC™ CP2 was prepared at a 2.5% molar offset corresponding to a calculated $\overline{M}_n$ of ~27,700 g/mol as illustrated in Scheme 1.[14] The diamine and amine-containing end-cap were initially dissolved in DMAc. The dianhydride was then added to the stirred solution. To prevent premature reaction of the alkoxysilane groups due to a temperature increase arising from heat of reaction, the reaction flask was immersed in a water bath at room temperature. The ASTAA mixture was stirred overnight at room temperature under a nitrogen atmosphere. The inherent viscosity of the ASTAA was 0.73 dL/g. This solution was used to cast thin films. For ASTAA samples containing SWNTs, the tubes were sonicated in DMAc for 6 hrs and subsequently added to an aliquot of the ASTAA solution. ASTAA-LaRC™ CP2 samples were prepared with 0, 0.03, 0.05 and 0.08 % (wt/wt) SWNTs.
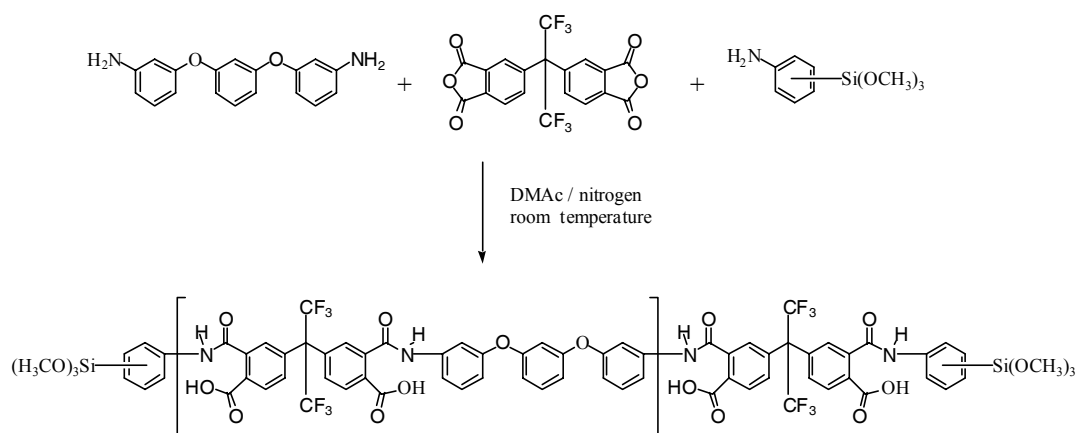
Scheme 1. Alkoxysilane-Terminated Amide Acid (ASTAA) of LaRC™ CP2 Synthesis

Polyimide synthesis

Three polyimides (Figure 1) were prepared as shown in Scheme 2. For LaRC™ CP2 and TOR-NC, the polyimides were prepared via the chemical imidization method using pyridine and acetic anhydride as the cyclo-dehydrating agents. PPO-6FDA was prepared in *m*-cresol resulting in the one-step formation of the polyimide. All polyimides were recovered as white fibrous materials.

The three polyimides were chosen for this study because of their low color and space environmental durability. LaRC™ CP2 is resistant to UV radiation and is presently in use on spacecraft in geosynchronous orbit. TOR-NC and PPO-6FDA are low color, UV stable polyimides that are structurally similar to LaRC™ CP2. However, these two polyimides contain pendant phosphine oxide groups that impart AO resistance to the materials, potentially making the polymers suitable for applications on spacecraft in LEO where AO is prevalent.
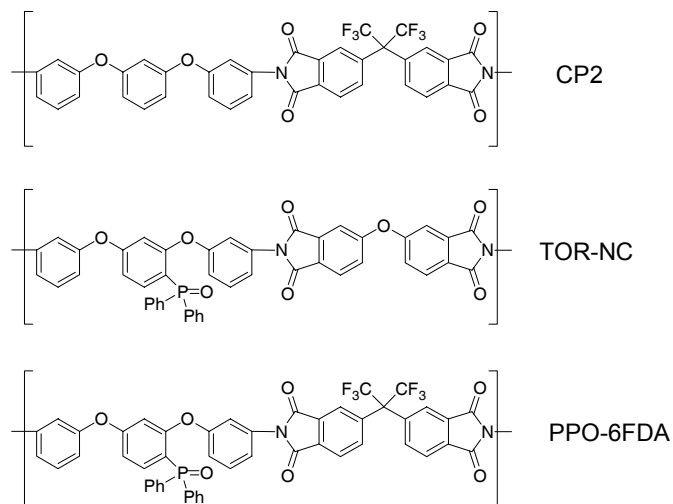
Figure 1. Structures of Polyimides

CP2: X = H, Y = C(CF$_3$)$_2$
TOR-NC: X = PO(Ph)$_2$, Y = O
PPO-6FDA: X = PO(Ph)$_2$, Y = C(CF$_3$)$_2$
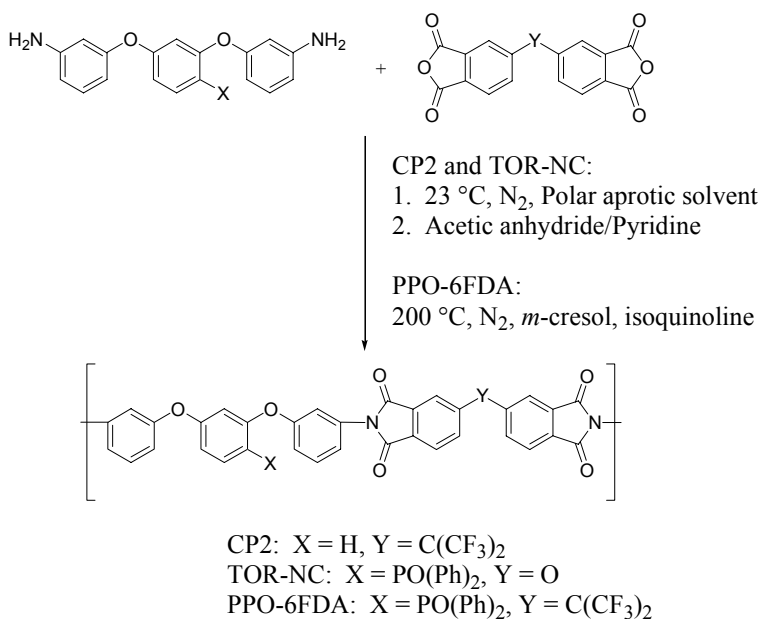
Scheme 2. Polyimide Synthesis

Spray-coating SWNTs onto polyimide films

To date, sufficient surface resistivity for ESC mitigation has been achieved by dispersing the SWNTs throughout the bulk of the polymer film. By this approach, the loading level needed to attain the percolation threshold has led to visual darkening of the films resulting in changes in the optical and thermo-optical properties of the nanocomposite as compared to the neat material.

Many applications on advanced spacecraft require conductivity on only one surface of the film. One approach to impart sufficient conductivity to one surface for ESC mitigation is by spray-coating the film with SWNTs. Typically a homogeneous solution is used in spray-coating processes; however, homogeneous dispersions of the SWNTs in DMF or THF were found to work well. After several trials, the best results for coating LaRC™ CP2, TOR-NC and PPO-6FDA were obtained using films that were cast from 23% solids in DMAc. These three polyimides (Figure 1) were coated with solutions containing 0.5, 1.0 and 2.0 mg of SWNTs. In addition, a series of alkoxysilane end-capped LaRC™ CP2 films were coated with SWNTs using this spray-coat method.

Surface resistivity

The conductivity of the films was determined as surface resistivity under ambient conditions with the results presented in Table 1. It was observed that the spray-coated films exhibited surface resistivities that were acceptable for ESC mitigation (range of 10^6 to 10^8 Ω/square). For ASTAA LaRC™ CP2, LaRC™ CP2, TOR-NC and PPO-6FDA coated with SWNTs the percent SWNT (wt/wt) for each sample is unknown; instead the amount of SWNT (in milligrams) sprayed is indicated. For LaRC™ CP2, TOR-NC and PPO-6FDA, SWNTs were sprayed in amounts ranging from 0.5 to 2.0 mg of SWNT. One sample of LaRC™ CP2 was sprayed with a solution containing 4.0 mg of SWNT. To maintain consistency, the polyimide films were cast from 23% solutions using 1.0 g of polymer and a doctor blade set at 14 mils. The resulting films had a surface area of approximately 150 cm^2.

The surface resistivities for the spray-coated films (P2 through P5, P8, P9, P11 through P15) were comparable to those obtained for the films containing the SWNT dispersed throughout the matrix (P18 and P19). The films that were not spray coated (P1, P6, P10) and P16, which did not contain SWNTs, were insulative with surface resistivities of 10^{12} Ω/square. Film P7 exhibited a surface resistivity of 7.0 x 10^{10} Ω/square even though other films spray coated with a comparable quantity of SWNTs (P2, P11) exhibited values of 10^7 Ω/square. As anticipated, the spray-coated films were conductive on only one surface with the opposite surface being insulative (>10^{12} Ω/square). Although the SWNTs were dispersed throughout the matrix in P17, the loading level was not sufficient to achieve the percolation threshold needed for conductivity. Previous work with this polymer has indicated that a loading level of 0.04 % (wt/wt) is needed.[17] Film P5 exhibited the lowest surface resistivity of 2.2 x 10^5 Ω/square. However, a tradeoff in properties occurred as this sample exhibited a higher α and lower percent transmission at 500 nm as compared to P3 and P4 (discussed in next section). From Table 1 it is shown that there is little difference in the surface resistivities between polymers spray-coated with 0.5, 1.0, and 2.0 mg of SWNTs (P2 through P4, P8 and P9, P11 through P13) with the exception being P7. Film P15

exhibited an order of magnitude decrease in surface resistivity as compared to P14 presumably due to the greater amount of SWNTs sprayed onto the surface.

Table 1. Surface Resistivity

ID	Polyimide	% SWNT (wt/wt)[a]	mg of SWNT[b]	Surface Resistivity, Ω/square
P1	LaRC™ CP2	--	0	2.5×10^{12}
P2	LaRC™ CP2	--	0.5	1.6×10^{7}
P3	LaRC™ CP2	--	1.0	6.1×10^{6}
P4	LaRC™ CP2	--	2.0	2.0×10^{7}
P5	LaRC™ CP2	--	4.0	2.2×10^{5}
P6	TOR-NC	--	0	2.8×10^{12}
P7	TOR-NC	--	0.5	7.0×10^{10}
P8	TOR-NC	--	1.0	4.5×10^{7}
P9	TOR-NC	--	2.0	7.6×10^{7}
P10	PPO-6FDA	--	0	2.1×10^{12}
P11	PPO-6FDA	--	0.5	6.1×10^{7}
P12	PPO-6FDA	--	1.0	3.4×10^{7}
P13	PPO-6FDA	--	2.0	4.5×10^{7}
P14	ASTAA LaRC™ CP2	--	0.4	1×10^{8}
P15	ASTAA LaRC™ CP2	--	1.1	1×10^{7}
P16[c]	ASTAA LaRC™ CP2	0	--	$> 10^{12}$
P17[c]	ASTAA LaRC™ CP2	0.03	--	$>10^{11}$
P18[c]	ASTAA LaRC™ CP2	0.05	--	1.7×10^{7}
P19[c]	ASTAA LaRC™ CP2	0.08	--	9.2×10^{6}

[a] Weight percent SWNTs in the bulk
[b] Amount of SWNTs in THF sprayed onto 1.0 g of polymer
[c] Reference 14

Optical properties

The nanocomposite films were measured for optical properties with the results presented in Table 2. The α pertains to the fraction of incoming solar energy that is absorbed by the film and is typically low (~0.1) for a low color film. The thermal emissivity (ε) is a measure of the films ability to radiate energy from the film surface.

When SWNTs were distributed throughout the bulk (P17 through P19), the films were observed to be visually darker than the neat polymer (P16). This was quantified by the decrease in % transmittance and increase in α. The ε also increased. These films were all of comparable thickness thus allowing for the direct comparison of these properties.

Due to the loss of the deuterium lamp in the instrument, the α values for P1-P13 were calculated from measurements taken between 420 and 2800 nm and are not valid for air mass 0. Therefore, relative comparisons can only be made between these samples (and not with P14 – P19). Comparisons of P1 through P13 can be made due to essentially comparable film thickness

with the exception being P10. The increase in α and decrease in %T with increased amount of SWNTs sprayed (P2 through P5, P7 through P9, P11 through P13) is minor as compared to the pristine materials (P1 and P6, respectively), especially considering the increase in surface conductivity. In general, the ε increased slightly with higher amounts of SWNTs sprayed.

A noticeable increase in α and decrease in % transmittance was observed for P14 and P15 as compared to the neat polymer (P16). However a direct comparison cannot be made due to a difference in film thickness.

Table 2. Thermo-Optical and Optical Properties of Films

ID	Polyimide	% SWNT (wt/wt)[a]	mg of SWNT[b]	Thickness, m	% Trans. @ 500 nm	α[c]	ε
P1	LaRC™ CP2	--	0	38.1	87	0.02	0.52
P2	LaRC™ CP2	--	0.5	40.6	86	0.03	0.54
P3	LaRC™ CP2	--	1.0	38.1	83	0.03	0.56
P4	LaRC™ CP2	--	2.0	38.1	82	0.06	0.56
P5	LaRC™ CP2	--	4.0	38.1	72	0.21	0.52
P6	TOR-NC	--	0	38.1	86	0.02	0.60
P7	TOR-NC	--	0.5	38.1	84	0.03	0.58
P8	TOR-NC	--	1.0	38.1	81	0.07	0.60
P9	TOR-NC	--	2.0	40.6	78	0.08	0.62
P10	PPO-6FDA	--	0	27.9	88	0.02	0.54
P11	PPO-6FDA	--	0.5	38.1	84	0.04	0.60
P12	PPO-6FDA	--	1.0	40.6	83	0.05	0.60
P13	PPO-6FDA	--	2.0	38.1	81	0.06	0.60
P14	ASTAA LaRC™ CP2	--	0.4	30.5	81	0.12	0.52
P15	ASTAA LaRC™ CP2	--	1.1	32.5	68	0.20	0.56
P16[d]	ASTAA LaRC™ CP2	0	--	38.1	86	0.07	0.59
P17[d]	ASTAA LaRC™ CP2	0.03	--	38.1	67	0.21	0.63
P18[d]	ASTAA LaRC™ CP2	0.05	--	40.6	59	0.30	0.65
P19[d]	ASTAA LaRC™ CP2	0.08	--	38.1	53	0.35	0.67

[a] Weight percent SWNTs in the bulk
[b] Amount of SWNTs sprayed onto 1.0 g of polymer
[c] The α for Samples P1 through P13 was calculated from taken between 420 and 2800 nm.
[d] Reference 14

Charge dissipation

A study to determine charge decay and capacitance loading for ASTAA LaRC™ CP2 polymers with SWNTs dispersed throughout the bulk (P16 – P19) was performed (Table 3). The films were charged to 3000 V for 60 ms. The initial peak voltage for P18 was -145.4 V, and for P19 was -65.50 V. For P16 (neat material), this was -3160 V and -3020 V for P17. According to the data, P18 and P19 (0.05 and 0.08 wt % SWNT, respectively) do not build-up and hold an electrical charge. It is apparent from both the surface resistivity and the charge decay data that P17 (0.03 wt % SWNT) does not contain enough SWNTs to reach the percolation threshold, as

similar values for surface resistivity and charge dissipation were observed for P16 (neat ASTAA). The results indicate that values from the two different methods (surface resistivity and charge decay) of determining charge dissipation are consistent.

Table 3. Charge Dissipation Data Comparison

ID	SWNT, %	Initial Voltage Peak, V	Surface Resistivity, Ω/square
P16	0	-3160	$> 10^{12}$
P17	0.03	-3020	$>10^{11}$
P18	0.05	-145.5	1.7×10^7
P19	0.08	-65.50	9.2×10^6

Film toughness

Transparent, conductive coatings on films commonly used on spacecraft such as indium tin oxide (ITO) are extremely brittle and cannot tolerate folding or bending. In order to assess the robustness of the SWNT spray-coated surface, qualitative handling tests were performed. These tests included creasing, folding and crumpling (Figure 3) a spray-coated LaRC™ CP2 film, measuring surface resistivity after each manipulation. In separate tests, scotch tape was applied to the spray-coated surface and removed several times. Additionally, the film was also placed in a sonicating bath operating at 40 Hz. This was repeated several times. In all of these qualitative tests, the surface resistivity of 10^7 Ω/square did not change. A similar result was obtained for P18 (where the SWNTs were distributed throughout the bulk), which was folded several times and crumpled into a ball.[14] Such tests applied to an ITO coated film would have resulted in loss of conductivity due to fracture of the coating. These tests indicate that the application of a SWNT dispersion by spray coating and SWNTs distributed throughout the bulk are viable methods to fabricate transparent, conductive, flexible coatings for films.

Figure 3. Mechanical Manipulation of a LaRC™ CP2 film Spray-Coated with SWNT

High resolution scanning electron microscopy

Figures 4 and 5 are HRSEM images of polymer films surface coated with SWNTs at a magnification of 20,000x. The sample in Figure 4 (P2) has a surface resistivity of 1.6×10^7 Ω/square and the sample in Figure 5 (P5) has a surface resistivity of 2.2×10^5 Ω/square. From the HRSEM images, P2 shows a layer of SWNTs on the film surface with small regions of

polymer that are uncoated (lower right corner of the image). Sample P5, however, was spray coated with a solution containing eight times the amount of SWNTs as compared to P2. This is evident from the image as what appears to be a thicker layer of SWNT on the film surface. The increased amount of SWNTs on the surface of P5 accounts for both the increased conductivity as well as the changes in optical properties (re: Tables 1 and 2) as compared with P2.
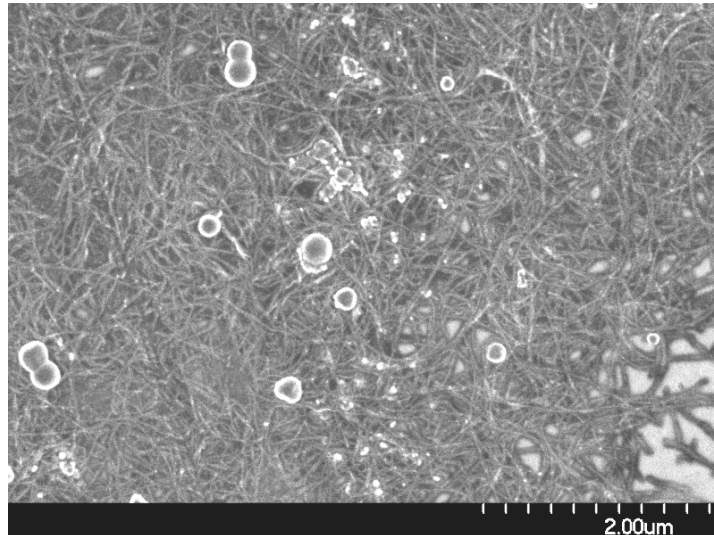
Figure 4. HRSEM of P2
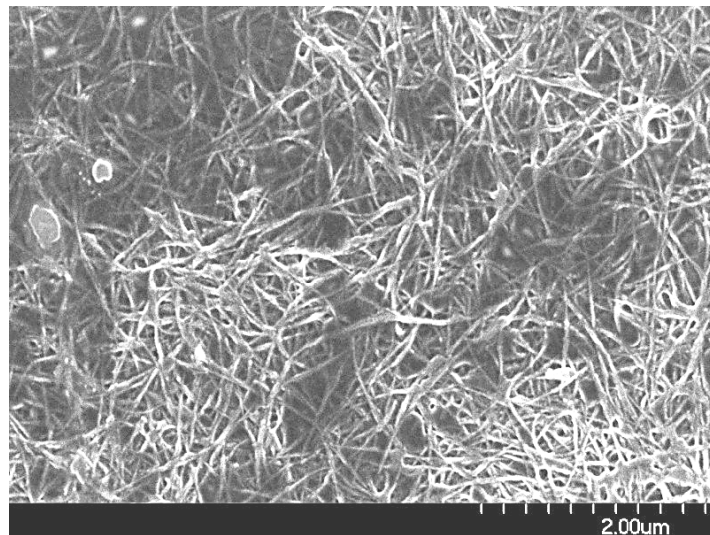
Figure 5. HRSEM of P5

<u>Summary</u>

Methods to prepare clear, colorless, flexible, space environmentally durable polymers with surface resistivity sufficient for ESC mitigation (10^6 to 10^8 Ω/square) are summarized. One

method involved preparing nanocomposites from alkoxysilane terminated amide acid polymers of LaRC™ CP2 and SWNTs distributed throughout the bulk to afford surface and bulk conductivity. The second method involved spray-coating one surface of the ASTAA films as well as low color polyimides (LaRC™ CP2, TOR-NC and PPO-6FDA) with a suspension of SWNTs in either DMF or THF to afford surface conductivity. Spray coated nanocomposite films exhibited surface resistivities sufficient for ESC mitigation with little degradation in the optical properties (%T and α). For nanocomposites containing SWNTs distributed throughout the bulk, noticeable changes in the optical properties as compared to the neat polymer were evident. Additionally, a 0.05 % (wt/wt) SWNT loading was needed to attain surface resistivities sufficient for ESC mitigation. Nanocomposite films prepared by both methods exhibited a high degree of flexibility and robustness as evidenced by retention of surface resistivity after harsh manipulation.

References

1. C.H.M. Jenkins, "Gossamer Spacecraft: Membrane and Inflatable Structures Technology for Space Applications", Vol. 191, American Institute of Aeronautics and Astronautics, 2001.

2. K.A. Watson, F. L. Palmieri and J. W. Connell, Macromolecules, Vol. 35(13), 4968, 2002.

3. Triton System, Inc. Chelmsford, MA 08124, www.tritonsys.com.

4. SRS Technologies, Huntsville, AL 35806, www.srs.com.

5. R. E. Smith and G. S. West, compilers, "Space and Planetary Environment Criteria for Use in Space Vehicle Development", 1982 Revision (Volume 1), NASA TM 82478, 1983.

6. A.S. Jursa, sci. ed., Handbook of Geophysic and the Space Environment, Air Force Geophysics Laboratory, Air Force Systems Command USAF, NTIS Document ADA 167000, 1985.

7. The Radiation Design Handbook, ESA PSS-01-609, European Space Agency, Paris, 1989.

8. P.A. Robinson, Jr., "Spacecraft Environmental Anomalies Handbook", Geophysics Laboratory, Air Force Systems Command, GL-TR-89-0222, 1989.

9. A.R. Frederickson, L. Levy and C. L. Enloe, "Radiation-induced Electrical Discharges in Complex Structures", IEEE Transactions on Electrical Insulation, 27, p. 1166, 1992.

10. S. Iijima and T. Ichihashi, Nature, Vol. 363, 603 (1993).

11. D.S. Bethune, C. H. Kiang, M. S. deVries, G. Goreman, R. Savoy, J. Vazquez and R. Beyers, Nature, Vol. 363, 605, 1993.

12. K.A. Watson, J .G. Smith Jr. and J. W Connell, Science for the Advancement of Materials and Process Engineering Technical Conference Series, Vol. 33, 1551, 2001.

13. C. Park, Z. Ounaies, K. A. Watson, R. E. Crooks, J. G. Smith Jr., S. E. Lowther, J. W. Connell, E. J. Siochi, J. S. Harrison and T. L. St. Clair, Chemical Physics Letters, Vol 364, 303, 2002.

14. K.A. Watson, J. G. Smith Jr., and J. W. Connell, "Space Durable Polyimide/Nanocomposite Films For Electrostatic Charge Mitigation", Science for the Advancement of Materials and Process Engineering Proceedings, Vol. 48, 1145, 2003.

15. J.G. Smith, Jr., K. A. Watson, C. M. Thompson and J. W. Connell, Science for the Advancement of Materials and Process Engineering Technical Conference Series, Vol. 34, 365, 2002.

16. J.G. Smith, Jr., K. A. Watson, D. M. Delozier and J. W. Connell, "Carbon Nanotube/Conductive Additive/Space Durable Polymer Nanocomposite Films for Electrostatic Charge Dissipation, 35th International SAMPE Technical Conference, September 28-October 2, 2003.

17. J.G. Smith, Jr., K. A. Watson, J. W. Connell, D. M. Delozier, P. T. Lillehei, Y. Lin, B. Zhou, and Y.-P. Sun, Polymer, submitted, 2003.

AN EDUCATIONAL MULTIMEDIA PRESENTATION ON THE INTRODUCTION TO SPACECRAFT CHARGING

E. Lin
DPL Science Inc.
2388 Tally Ho
St. Lazare, Quebec, Canada J7T 2B1
Phone: (450)458-0852
Fax: (450)458-2151
E-mail: info@dplscience.com

M. de Payrebrune
DPL Science Inc.

Background

Over the last few decades, significant knowledge has been gained in how to protect spacecraft from charging; however, the continuing technical advancement in the design and build of satellites requires on-going effort in the study of spacecraft charging.

A situation that we have encountered is that not all satellite designers and builders are familiar with the problem of spacecraft charging. The design of a satellite involves many talented people with diverse backgrounds, ranging from manufacturing and assembly to engineering and program management. The complex design and build of a satellite system requires people with highly specialized skills such that cross-specialization is often not achievable. As a result, designers and builders of satellites are not usually familiar with the problems outside their specialization. This is also true for spacecraft charging. Not everyone is familiar with the definition of spacecraft charging and the damage that spacecraft charging can cause. Understanding the problem is an important first step in getting everyone involved in addressing the appropriate spacecraft charging issues during the satellite design and build phases.

To address this important first step, an educational multimedia presentation has been created to inform the general engineering community about the basics of spacecraft charging. The content of this educational presentation is based on relevant published technical papers. The presentation was developed using Macromedia Flash. This software produces a more dynamic learning environment than a typical 'slide show', resulting in a more effective learning experience. The end result is that the viewer will have learned about the basics of spacecraft charging.

This presentation is available to the public through our website, *www.dplscience.com*, free of charge. Viewers are encouraged to pass this presentation to colleagues within their own work environment.

This paper describes the content of the multimedia presentation.

Description of the Presentation

Macromedia Flash was selected as the software tool for this presentation due to its powerful animation capability and its ability to support different media (CD, DVD, Video and Internet). The software allowed us to create the presentation as a stand-alone unit by combining text, pictures, video and audio tracks. We were able to successfully illustrate key points by maximizing the visual content and synchronizing the visual images with the audio track, resulting in an effective learning experience.

The information presented was gathered from various technical sources. A listing of these sources is provided at the end of this paper and includes the Canadian Space Agency, the European Space Agency, and NASA. Technical reviewers included Mr. Richard Adamo (SRI International), Dr. Keith Balmain (University of Toronto), and Mr. Jody Minor (NASA SEE Program). We are grateful for their comments.

The presentation is divided into six major sections. Figure 1 is a snapshot taken from the presentation, identifying the six sections.

Figure 1. The six major sections of the presentation.

Section 1: The sun and spacecraft charging

The presentation begins with a description of the sun and its role in spacecraft charging. We introduce the concepts of sunspot cycle, flares and eruptions, coronal mass ejection, solar wind and high-energy particles. Figure 2 is a snapshot taken from this section, comparing the size of the earth to that of a typical solar flare. The objective of this section is to explain to the viewer that the sun is the main contributing factor to the existence of high-energy particles and that the

presence of these high-energy particles is one of two primary reasons why spacecraft charging occurs.

Figure 2. A snapshot from Section 1 of the presentation, showing the size of a typical solar flare compared to the earth. (Photo credit NASA)

Section 2: Scope of the Problem

The second section focuses on the scope of the spacecraft charging problem. By 'scope of the problem', we aim to define the causes of spacecraft charging and hence explain why charging occurs. Spacecraft charging can exist because of the following situations:

- high-energy particles found in the natural space environment plus the existence of ungrounded metal, or

- high-energy particles found in the natural space environment plus the use of dielectric material.

The three components (high-energy particles, ungrounded metal and dielectric material) are then discussed.

The discussion on high-energy particles was presented in Section 1 so that only a brief summary is made here.

The discussion on ungrounded metal essentially advises the viewer that floating metal should be avoided. We emphasize that discharges from a floating metal can be more powerful than a

discharge from a dielectric because more electrons are involved in the discharging process, due to the high mobility of electrons in a conductor.

The discussion on dielectric material is the heart of this section. We explain that dielectric materials are abundantly used in spacecraft design and that their use cannot be avoided. The viewer learns that the unavoidable use of dielectric materials in spacecraft design is the other primary reason why spacecraft charging exists. Since it is necessary to use these materials, we need to understand their properties and behaviour. We introduce the concepts of resistivity and dielectric strength. Figure 3 is a snapshot taken from this section, illustrating the concepts of resistivity and dielectric strength. We explain that the continuing technical advancement in the design and build of satellites means that we cannot take previously used materials for granted. This includes commonly used materials such as Second Surface Mirrors, Sunshields and Thermal Blankets. We emphasize that the constant evolution in spacecraft design and technology implies that spacecraft designers must always be mindful about what dielectric materials are being used and where.

Figure 3. A snapshot from Section 2 of the presentation, illustrating the concepts of resistivity and dielectric strength.

Discharge effects are described briefly and include physical damage to the material and electromagnetic effects.

The section ends with a positive note: reference is made to the role of the Spacecraft Charging Specialist and how this technical authority can help in the mitigation and prevention of spacecraft charging and its effects.

Section 3: The Two Types of Charging

The third section describes the two types of charging: surface charging and internal charging. The objective is to differentiate the two and to explore ways in which the charging can be minimized.

We begin with the definition of surface charging and proceed to the design techniques to prevent surface charging. A simplified summary of some of the design guidelines found in NASA Technical Paper 2361 (Ref [11]) is presented to the viewer.

Next, we present the definition of internal charging and the design techniques to prevent internal charging. Figure 4 is a snapshot taken from this section, illustrating the meaning of internal charging. A simplified summary of the design guidelines found in NASA Handbook 4002 (Ref [9]) is presented to the viewer.

Figure 4. A snapshot from Section 3 of the presentation, illustrating the meaning of internal charging.

Since the selection of dielectric material will not always conform to the guidelines, we also look at the use of tests and analyses as methods of validating the choice of a dielectric material. Spacecraft charging tests and analyses are rarely straightforward and we identify some of the difficulties that are frequently encountered: lack of proper information on dielectric material properties (resistivity values over temperature, dielectric strength values), inaccuracies in the characterization of the space environment, limitations of a test set-up, uncertainty in the sensitivity of the victim circuit, etc.

Section 4: Test Facilities

The fourth section includes photographs of two spacecraft charging test facilities: SRI International in Palo Alto, California and the University of Toronto in Canada. The authors had the opportunity to work with Mr. Adamo and Dr. Balmain in past projects and were pleased to be able to include descriptions of their facilities in this presentation. Figure 5 is a snapshot taken from this section, showing Dr. Balmain's internal charging test set-up at the University of Toronto. This section gives the viewer a look at the practical aspects of spacecraft charging work, complementing the previous theoretical sections.

Figure 5. A snapshot from Section 4 of the presentation, with a look at Dr. Balmain's internal charging test set-up.

Section 5: Publications

The fifth section directs the viewer to some excellent publications available for further study. Figure 6 is a snapshot taken from this section, showing some of the suggested publications. We wished to emphasize to the viewer that this presentation is only a general introduction to the topic of spacecraft charging and that there are many articles and documents available for further reading.

Figure 6. A snapshot from Section 5 of the presentation, with a look at some of the suggested publications.

Section 6: Conclusions

The conclusion re-iterates the need for some of the on-going work in the field of spacecraft charging, namely: studies on the changing space environment and the characterization of dielectric material properties. Figure 7 is a snapshot taken from this section, reviewing the need to have more information on dielectric material properties. We wished to make this emphasis since the definition of the space environment and the identification of dielectric material properties have immediate impact on the ability to accurately assess spacecraft charging effects for any satellite program.

Figure 7. A snapshot from Section 6 of the presentation, emphasizing once again the need to have more information on dielectric material properties.

When played from start to end, the entire presentation will last approximately fifty (50) minutes. The viewer can pause the presentation at any time then resume playing when desired. Re-plays are also possible by using the 'play back' button. The viewer can also directly access a specific part of the presentation by using the Table of Contents feature. Figure 8 is a snapshot of the Table of Contents taken from the presentation.

Figure 8: The 'Table of Contents' in the presentation.

Conclusion

An educational multimedia presentation has been created to inform the general engineering community about the basics of spacecraft charging. The presentation is a general introduction to the topic and is intended for spacecraft designers, builders and project managers of all disciplines within the satellite industry. Topics covered in the presentation include the Sun and its role in spacecraft charging, the use of dielectric materials in spacecraft design, surface charging, internal charging, basic design guidelines to minimize charging, and spacecraft charging test facilities.

The presentation may be downloaded from our website *www.dplscience.com*, free of charge. We would appreciate feedback from the engineering community as to the effectiveness of this presentation as an educational tool.

Acknowledgements

We would like to thank the following organizations and individuals for their valuable support and assistance:

Canadian Space Agency	Mr. Richard Adamo
ESA	Dr. Keith Balmain
NASA	Mr. Larry Harding
SRI International	Mr. Jody Minor
University of Toronto	

References

Technical information for the presentation was obtained from the following sources:

1.   Balmain K.G., "Surface Discharge Effects", American Institute of Aeronautics and Astronautics 1979.

2.   Czepiela S.A., Hastings D., McManus H., "Charging of Composites in the Space Environment", American Institute of Aeronautics and Astronautics 1997.

3.   Fennell J.F., Koons H.C., Roeden J.L., Blake J.B., "Spacecraft Charging: Observations and Relationship to Satellite Anomalies", The Aerospace Corporation, Los Angeles, CA 90009, USA.

4.   Garrett H.B., "The Charging of Spacecraft Surfaces", Reviews of Geophysics and Space Physics, Vol. 19, No. 4, Pages 577-616, November 1981.

5.   Herr J.L., McCollum M.B., "Spacecraft Environments Interactions: Protecting Against the Effects of Spacecraft Charging", NASA Reference Publication 1354, November 1994.

6.   Inouye G.T., Sanders N.L., Komatsu, G.K., Valles J.R., Sellen Jr. J.M., "Thermal Blanket Metallic Film Grounstrap and Second Surface Mirror Vulnerability to Arc Discharges", Spacecraft Charging Technology 1978.

7.   Joselyn J.A., Whipple E.C., "Effects of the Space Environment on Space Science", American Scientist, Volume 78.

8.   Leach R.D., "Failures and Anomalies Attributed to Spacecraft Charging", NASA Reference Publication 1375, August 1995.

9.   Mulville D.R., "Avoiding Problems Caused by Spacecraft On-Orbit Internal Charging Effects", NASA-HDBK-4002, February 1999.

10.   Nanevicz J.E., Adamo R.C., "Occurrence of Arcing and its Effects on Space Systems", American Institute of Aeronautics and Astronautics, 1980.

11.   Purvis C.K., Garrett H.B., Whittlesey A.C., Stevens N.J., "Design Guidelines for Assessing and Controlling Spacecraft Charging Effects", NASA Technical Paper 2361, 1984.

12.   "Environment Spatial Prevention des Risques Lies aux Phenomenes de Charge", CNES, Cepadues-Editions, 1996.

13.   "Proceedings of the 7th Spacecraft Charging Technology Conference, ESA Publication Number SP-476, November 2001.

14.   "Surface Charging / ESD Analysis", NASA Preferred Reliability Practices PD-AP-1301.

15.   "Thick Dielectric Charging / Internal Electrostatic Discharge", NASA Preferred Reliability Practices PD-AP-1316.

16.   www.spacedaily.com/news/eo-01r.htmp

17.   www.estec.esa.nl/conferences/98c05

NASCAP-2K – AN OVERVIEW

M. J. Mandell
Science Applications International Corporation
10260 Campus Point Dr., M.S. A1, San Diego, CA, 92121
Phone: 858-826-1622
Fax: 858-826-1652
E-mail: myron.j.mandell@saic.com

V. A. Davis
B.M. Gardner
I. G. Mikellides
Science Applications International Corporation

D. L. Cooke
Air Force Research Laboratory/VSBS

J. Minor
NASA Marshall Space Flight Center

Abstract

Nascap-2k is the modern replacement for the older 3-D charging codes NASCAP/GEO, NASCAP/LEO, POLAR, and DynaPAC. Built on the DynaPAC kernel and incorporating surface charging, environment and space potential models from the older codes, Nascap-2k performs charging calculations for a wide variety of space environments under control of a unified graphical interface.

In this paper we illustrate the use of Nascap-2k for spacecraft charging calculations. We touch on some of the unique physical and mathematical models on which the code is based. Examples/demos include the use of Object Toolkit, charging calculations in geosynchronous substorm, solar wind, low earth orbit, and auroral environments, and display and analysis of surface potentials, space potentials and particle trajectories.

Introduction

The recently released version 2.0 of Nascap-2k builds on the physical principles, mathematical treatments, computational algorithms, and user experience developed during over two decades of spacecraft charging research. Using Nascap-2k's graphical user interface (GUI) a scientist or engineer with minimal knowledge of spacecraft charging can easily set up, run, and analyze standard problem types in geosynchronous, low-earth-orbit, auroral, and solar wind environments. A more adventurous user can, within the Nascap-2k framework, go beyond the standard problem types to investigate novel or specialized spacecraft environment interactions.

Nascap-2k presents three GUIs to the user. The main Nascap-2k GUI is concerned with environment specification, calculation strategy, and results display and analysis. Object Toolkit

(OTk) is used to build spacecraft surface models for Nascap-2k analysis (as well as for analysis by other codes). GridTool is used to build nested cubic grids about the spacecraft model for calculation of electrostatic potentials and particle trajectories in the external space. In addition to these, the SEE Spacecraft Charging Handbook is an extremely useful companion application to Nascap-2k.

Beneath the Nascap-2k GUI are the calculation engines written in Fortran and C++. The potential solver (for potentials in the external space) and particle tracker (for charge densities, visualization, and PIC capabilities) are of DynaPAC (Mandell *et al.*, 1992) heritage. New is the BEM (Boundary Element Method, Brebbia 1981) module (written in C++) which incorporates the BEM charging algorithms (Mandell *et al.*, 2001), together with environment and surface charging physics treatments inherited from NASCAP/GEO (Katz *et al.*, 1977), NASCAP/LEO (Mandell and Davis, 1990), and POLAR. The BEM module also serves as the main line of communication between the Nascap-2k GUI and the detailed information stored in the Nascap-2k database (also of DynaPAC heritage).

Among the virtues of Nascap-2k is that electric fields in space are strictly continuous. This is done by expanding the space of the interpolation functions so that the electric field (as well as the potential) is defined at each node. Figure 1 compares trajectories of particles passing over a slab computed using trilinear interpolation and using Nascap-2k's approach. In Figure 1a, the result of a code using the standard trilinear interpolation, the trajectories are split by the grid points, clearly an artifact due to inadequate representation of electric fields in this trilinear code. Figure 1b shows the same calculation, done with the continuous field treatment. The particle deflection varies continuously (albeit non-monotonically) with position.

Object Toolkit (OTk)

Object Toolkit was initially written to define spacecraft surface models for Nascap-2k. The reason for writing a new geometry engine was to avoid dependence on third-party software, which has proven to be expensive, difficult to learn, and awkward to adapt to our specific needs. OTk is customizable for use with other applications via an external file. To date, OTk has been customized for use with EPIC (Electric Propulsion Interactions Code) and at least one other code. OTk is written in pure Java, so that it is portable to any platform that supports a full Java implementation.

Figure 2a shows a solar array truss displayed in OTk. The truss was defined in OTk by manipulating and editing primitive "BOOM" objects. Such an object might also be defined by a standard finite element preprocessor (*e.g.* Patran) and imported into OTk.

Figure 2b shows the truss attached to a solar panel to form a "Wing." Note that the model was designed such that the nodes on the truss and panel matched precisely. When this happens, OTk automatically deletes the abutting surface elements.

The spacecraft body was defined as a "Box" primitive to which two "Panel" primitives were attached as radiators, and some editing was done to achieve the desired distribution of materials. Figure 2c shows the "Wing" attached to the spacecraft body. This common type of attachment is done by a "Wizard", which automatically orients the two parts, positions them, and edits the

mesh to be fully "compatible." Less common attachments can be done by performing the individual operations "manually" via menu choices and dialogs. The final model (body with two "Wings") is shown in Figure 2d. In subsequent sections, we will show charging calculations for this model in geosynchronous, interplanetary, and auroral environments. We will show charging of a different model in LEO environment.

OTk contains a default selection of common spacecraft materials. Properties of these materials govern secondary emission, conductivity, etc. The properties can be edited, and new materials can be added and assigned properties. The SEE Program provides a library of additional materials with well-documented, recently measured properties in a format that can be easily imported into OTk.

Geosynchronous Charging

To perform a simulation of charging at geosynchronous altitudes, we use the Nascap-2k GUI to define a plasma environment (Maxwellian or Double Maxwellian), sun direction and intensity, and a timestepping strategy. Initial surface potentials and/or conductor bias can be defined as appropriate. Since the Boundary Element Method is used for surface charging, external gridding is not required. However, if the external potentials and electric field and/or particle trajectories are of interest, GridTool is used to appropriately grid the external space in preparation for such calculations.

Figure 3 shows the result of a calculation of geosynchronous charging in sunlight, using the "NASA Worst Case" plasma environment (Purvis *et al.*, 1984), displayed in the Nascap-2k GUI. The maximum differential charging occurs toward the outboard end of the solar array, and the saddle point potential structure can be seen. Detailed results for selected surface elements can be shown in popup windows, and we can also readily obtain the time histories of potentials and currents to individual cells or groups of cells.

Solar Wind (Interplanetary) Charging

A spacecraft outside Earth's magnetosphere is exposed to an interplanetary environment that consists of solar UV radiation and the solar wind plasma. The approximate mean parameters of the solar wind plasma (Vilas *et al.*, 1988) at 1 AU are shown in Table 1. The plasma currents are well below the solar-induced photoelectron currents (above 10^{-5} Am^{-2} for most materials). Therefore, illuminated surfaces tend to charge to positive potentials (often tens of volts) to the point where the attenuated photoemission matches the enhanced collection of plasma electrons. To model this charging requires a model of the photoemission electron spectrum, which falls off much more slowly in the range of tens of volts than it does in the range of a few volts.

Figure 4ab shows an example of a charging calculation in an interplanetary environment. The solar cells maintain, on average, a positive potential of order 15 volts. As the dark insulators gradually charge, bootstrap charging takes over and takes the spacecraft negative. Note that the time-history post-processing facility can present both potentials and currents for groups of cells or individual cells, and the plotted results can be retrieved as text for pasting into a spreadsheet or other program for further analysis.

Table 1. Approximate average solar wind parameters at 1 AU.

Plasma Density	7×10^6 m^{-3}
Proton Velocity	430 km s^{-1}
Proton Energy	1 keV
Proton Current	5×10^{-7} A m^{-2}
Electron Temperature	15 eV
Electron Thermal Current	7×10^{-7} A m^{-2}

Auroral Charging

Spacecraft passing through auroral arcs, especially at night during dropouts of cold plasma, have been observed to charge to potentials of a kilovolt or more. (Gussenhoven *et al.*, 1985.) Figure 5a shows the Nascap-2k definition of an auroral environment in Fontheim (Fontheim *et al.*, 1982) form. In addition to the cold plasma environment, energetic electrons are divided into Gaussian, Maxwellian, and power law components. The SEE Spacecraft Charging Handbook (Katz *et al.*, 2001) provides two once-observed examples of such environments. From the complexity of this environment, it seems clear that further research is needed to provide guidelines as to how the auroral environment should best be represented for the purpose of charging analysis.

Figure 5b shows time-dependent charging of our model spacecraft in this environment. After about one second, the model has developed about 150 volts of overall charging and over 100 volts of differential charging; both types of charging are continuing to increase, albeit at a lesser rate.

Figure 5c shows a display of ion trajectories superimposed on surface and space potentials. These trajectories were specified to originate on a potential contour in a plane near the potential cutplane. The plot shows that ram ions entering this contour that do not impact the ramward side of the solar array eventually strike the rear of the charged spacecraft, slowing the charging process.

Low-Earth Orbit Charging

The cold, dense plasma that prevails in low-Earth orbit is a fairly benign environment for most purposes. However, applied high voltages (Mandell and Katz, 1990), a significant magnetic field, ram-wake effects, and sensitive scientific instruments can lead to interesting calculations. As an example, we consider the charging of an octagonal satellite whose three ram-facing facets consist of conductive experiment plates and ITO coated solar cells, and the remaining five facets (zenith, nadir, and three wake facets) are covered with uncoated cells or other insulators. The ends are also conductive. The environment is a plasma with density 3×10^{11} m^{-3} and temperature of 0.15 eV. The magnetic field is 0.25 gauss northward (parallel to the long axis) and 0.25 gauss vertical.

Figure 6abc shows the results of the calculation after 0.5 seconds. The vertical component of the magnetic field induces an end-to-end potential of nearly one volt, with the positive end at about -0.2 volts and the negative end at about -0.9 volts. The nadir and zenith insulating surfaces are in equilibrium at about -0.75 volts, while the wake surfaces have reached about -1.3 volts and continue to charge slowly. (The wake surface potentials are limited by photoemission when in sunlight, or by bulk conductivity of the coverglasses.) The wake structure behind the spacecraft is clearly shown by both potential contours and ion trajectories in Figure 6a.

Of interest is the current balance to the spacecraft. Electrons are collected predominantly on the southern (less negative) conducting end (conductor 3 in Figure 6c), and on the nearby ram facing surfaces. The conductive ram-facing surfaces (conductor 1 in Figure 6c) primarily collect ram ions. Thus, a parasitic plasma current of about 0.4 mA flows though the spacecraft from negative to positive (as in a battery), with the negative terminal distributed over the ram-facing surfaces, and the positive terminal located primarily on the southern end of the spacecraft. Reversing the sign of the vertical component of magnetic field moves the positive terminal to the northern end.

Summary

Nascap-2k is a modern computer code that simulates spacecraft charging in a variety of environments. Among the modern features of Nascap-2k are use of the Boundary Element Method (BEM) for surface charging, and space potentials with strictly continuous electric fields.

This paper outlined the definition of a simple spacecraft model using Object Toolkit, and showed results of charging calculations for that model in Geosynchronous, Auroral, and Interplanetary environments. A different spacecraft model was used to show magnetic field and wake effects for a low-Earth orbiting satellite. These calculations can be done in Nascap-2k with both a relative ease and a high degree of flexibility. In addition, several different types of diagnostics are provided to study and understand the results.

For additional information or to obtain *Nascap-2K*, contact Jody Minor, jody.minor@nasa.gov.
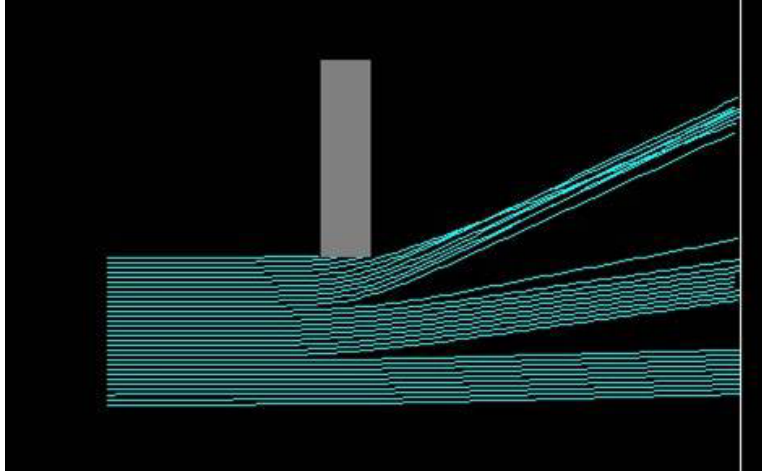
Figure 1a. Particle trajectories over a charged slab using a code with trilinear potential interpolation.
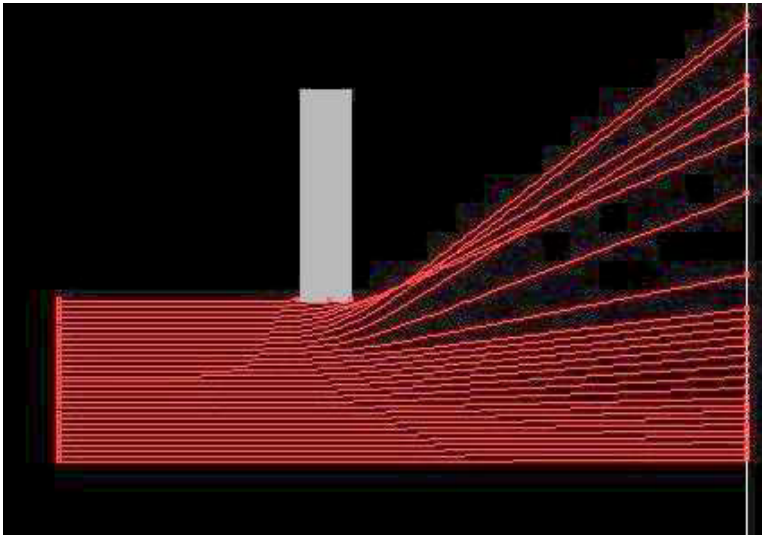
Figure 1b. Particle trajectories over a charged slab calculated using Nascap-2k with continuous electric fields.
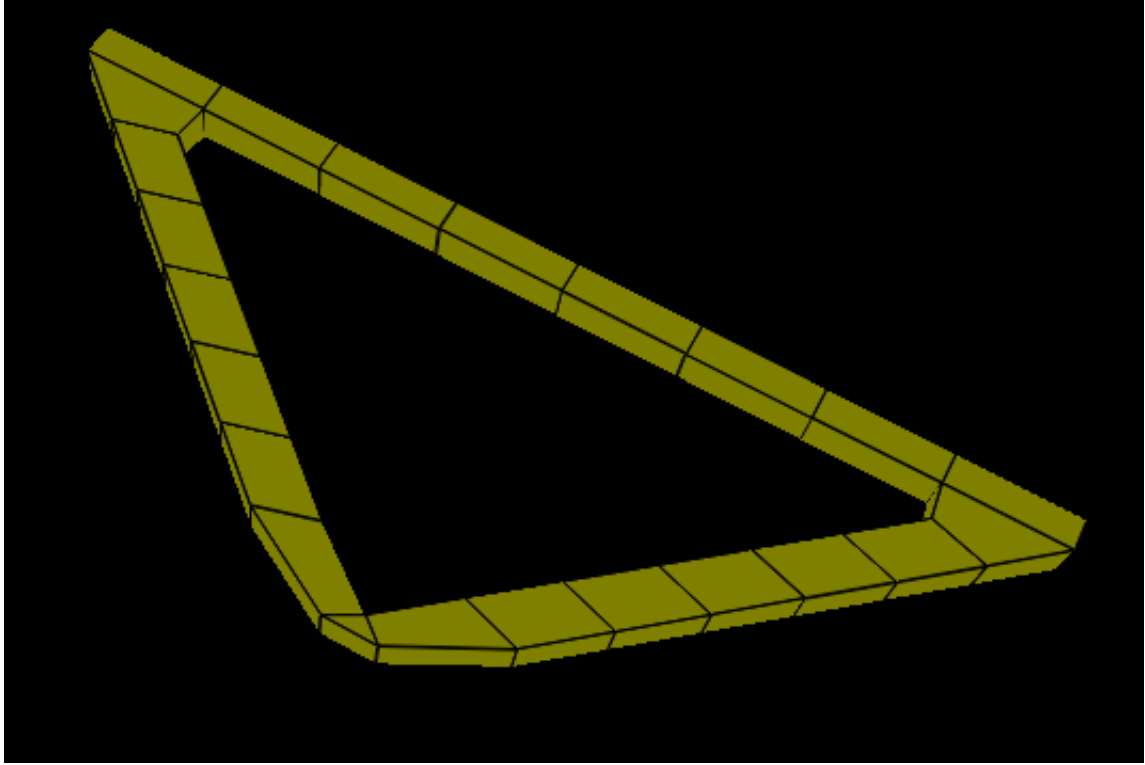
Figure 2a. Object Toolkit model of truss for mounting solar array.
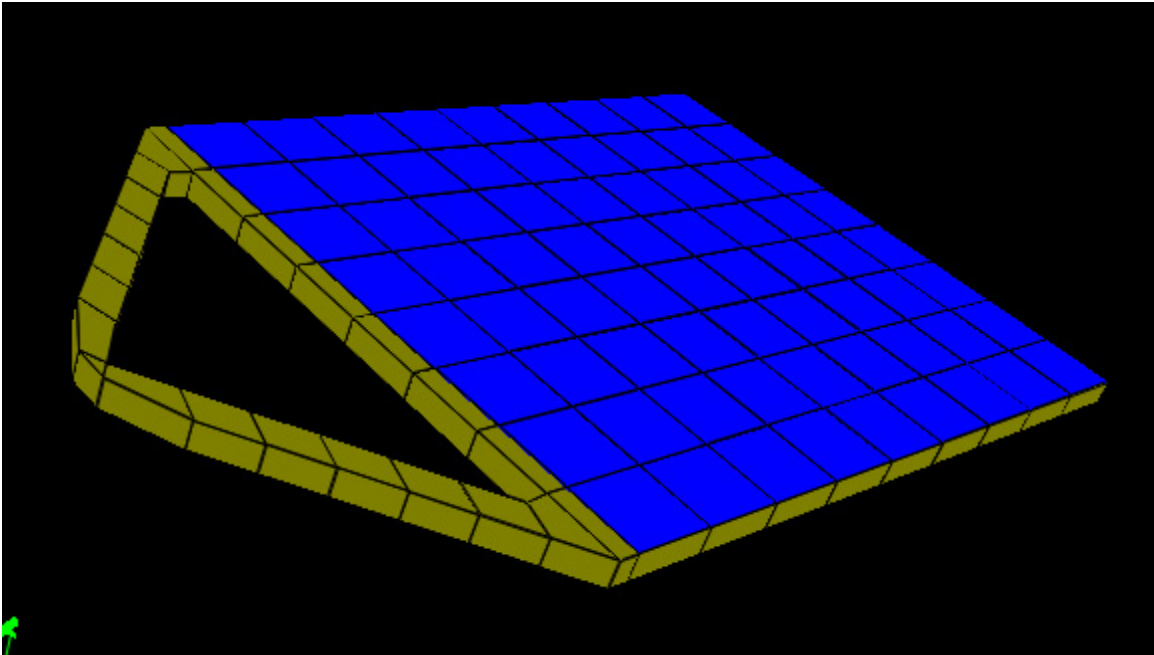
Figure 2b. Object Toolkit model of solar array wing.
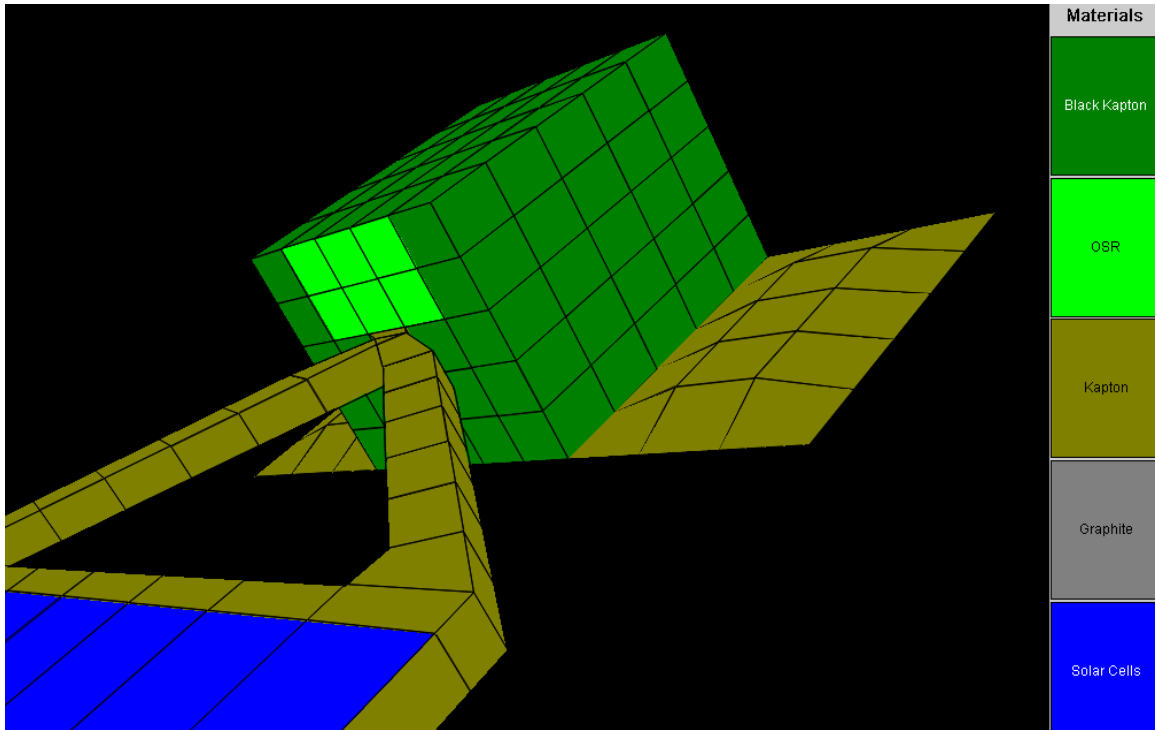
Figure 2c. Object ToolKit model of spacecraft body with wing attached.
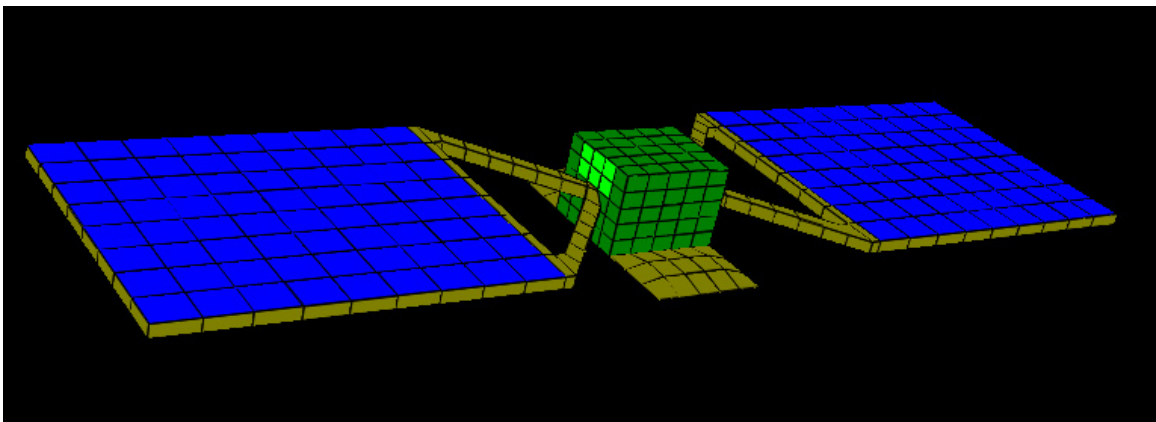
Figure 2d. Object Toolkit model of spacecraft.
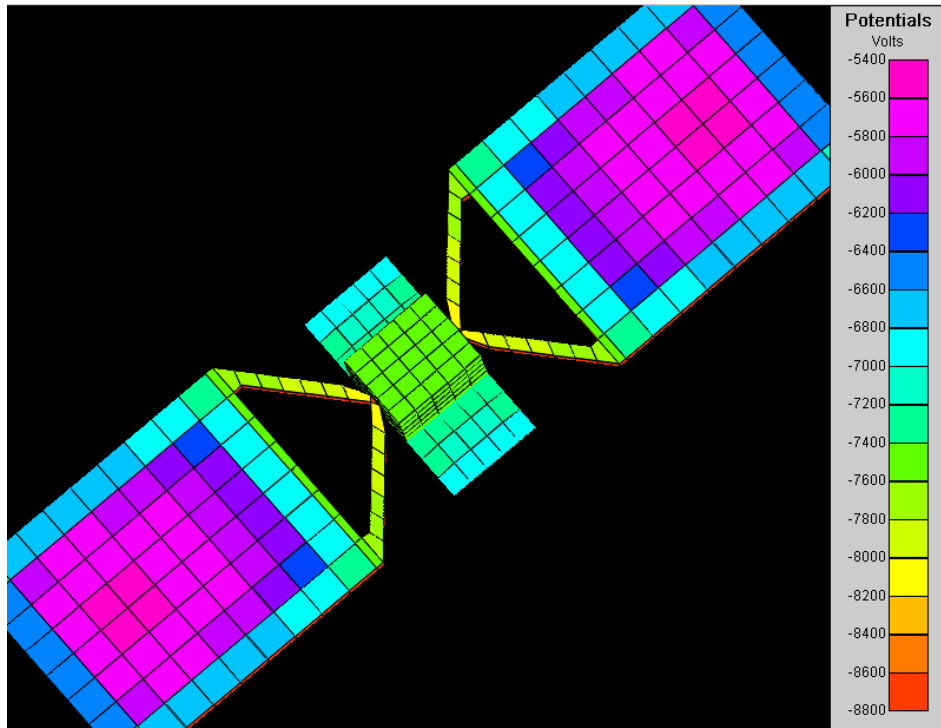
Figure 3a. Geosynchronous charging result, showing maximum differential charging toward outboard end of solar panels.
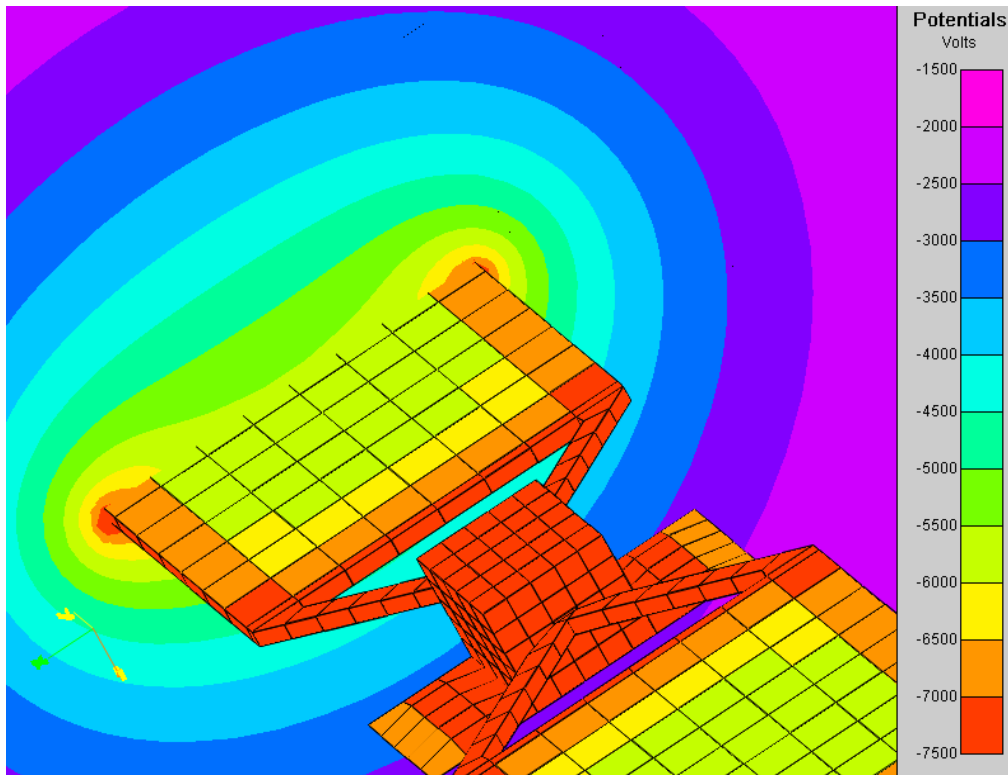
Figure 3b. Geosynchronous charging result, showing saddle point over solar panel.
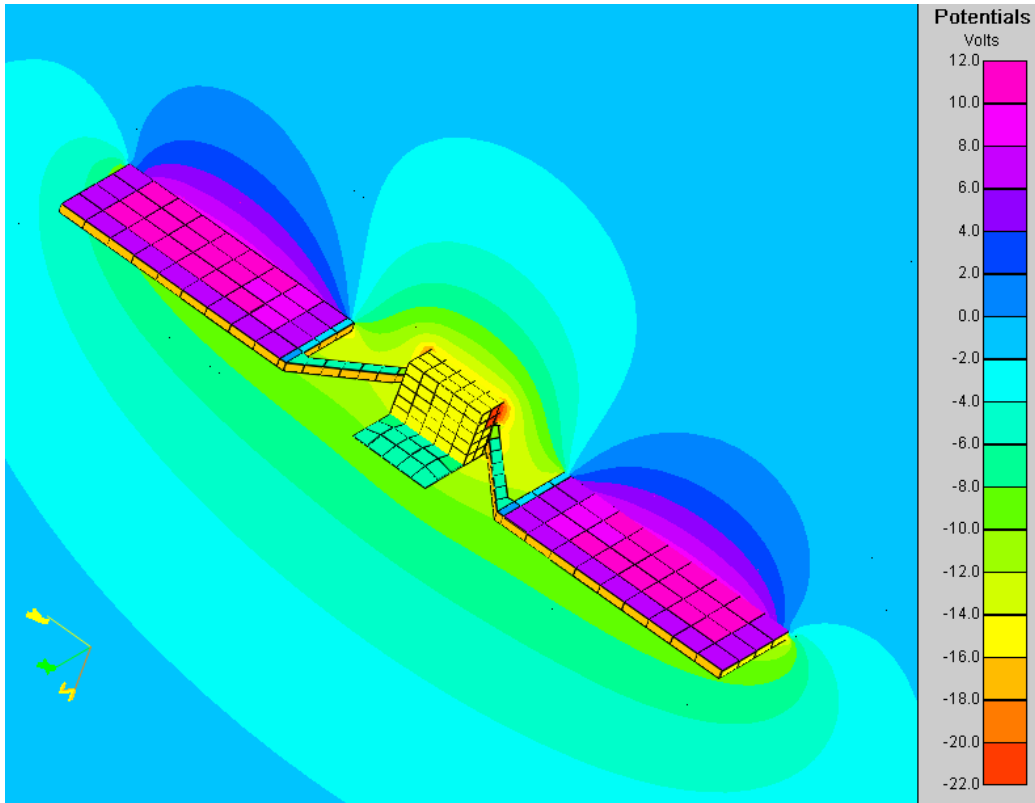
Figure 4a. Potentials calculated for spacecraft in solar wind environment.
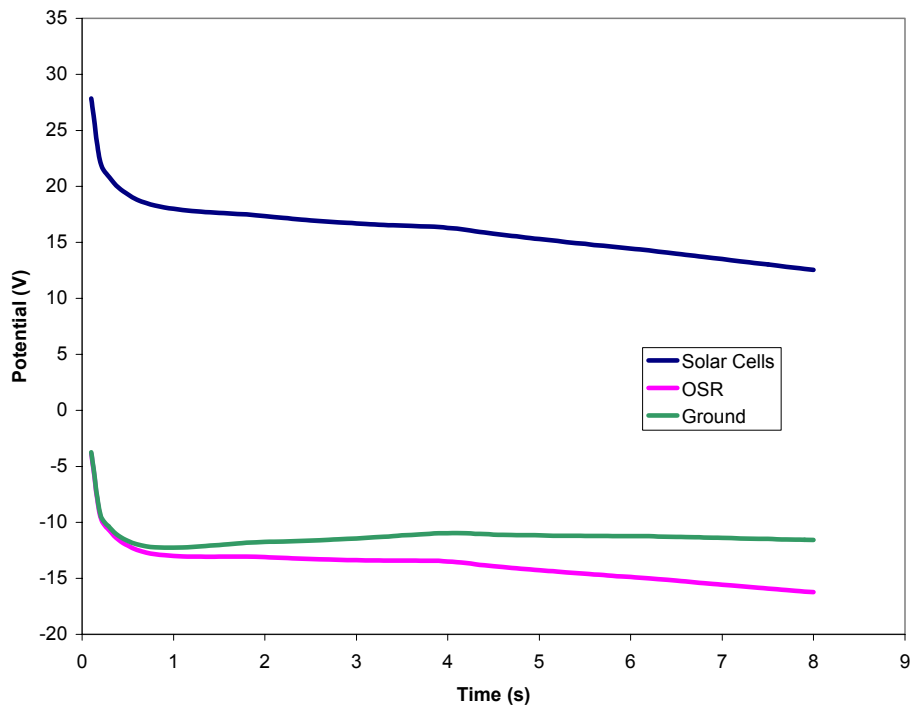
Figure 4b. Time history of potentials for solar wind calculation.

Polar Environment

Auroral Environment Plasma

Low Energy
Density (m^{-3}): 3.550E9
Temperature (eV): 0.200
Debye Length (m): 5.580E-2
E. Current (Am^{-2}): 4.256E-5
Ion Current (Am^{-2}): 2.492E-7

Maxwellian
E. Current(Am^{-2}): 1.400E-6
Temperature (eV): 8000.
Density (m^{-3}): 5.808E5
Coefficent: 4.346E4

Gaussian
E. Current(Am^{-2}): 1.400E-5
Energy (eV): 2.400E4
Width (eV): 1.600E4
Density (m^{-3}): 7.770E6
Coefficent: 4.075E4

Power Law
E. Current(Am^{-2}): 6.700E-7
1st Energy (eV): 50.00
2nd Energy (eV): 1.600E6
Exponent: 1.100
Density (m^{-3}): 1.034E6
Coefficent: 3.049E11

Sun

Sun Direction
X: 0.0 Y: 0.0 Z: -1.000

Relative* Sun Intensity: 0.0

*(value at Spacecraft) / (value at Earth Orbit)

Particle Species

Type	Mass (amu)	Charge (C)	%
Electron	5.486E-4	-1.602E-19	100.0
Oxygen	16.00	1.602E-19	100.0
HYDROGEN	1.000	1.602E-19	0.0

Add Species   Delete Species

Magnetic Field (T)
Bx: 0.0   By: 0.0   Bz: 0.0

Spacecraft Velocity (m/s)
Vx: 0.0   Vy: 0.0   Vz: -7500.

Figure 5a. Example of auroral environment, as used in sample auroral charging calculation.

Max0
Avg0
Min0
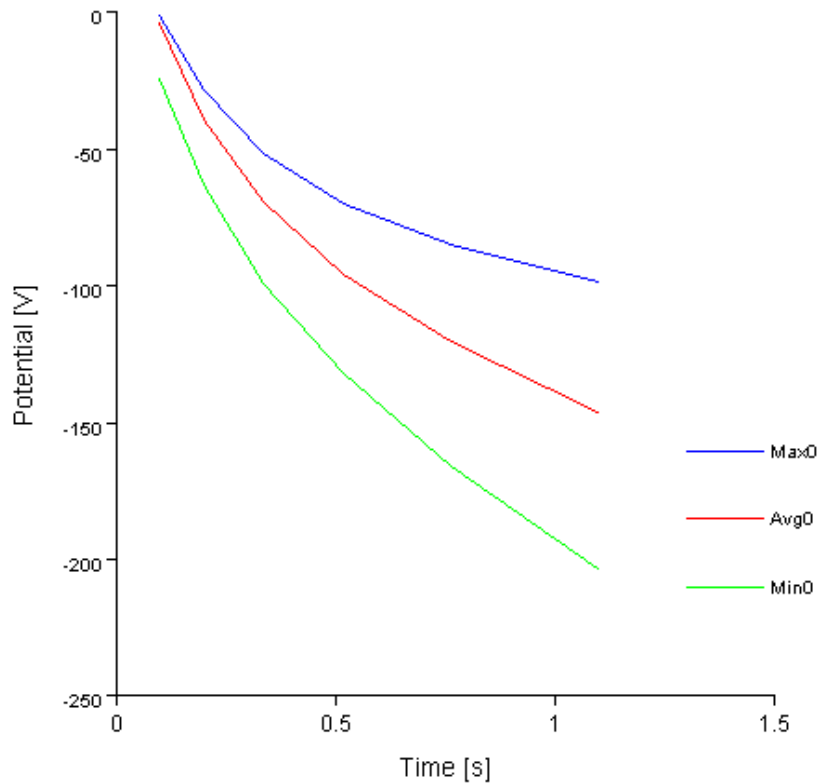
Figure 5b. Time dependence of overall and differential charging for the sample auroral charging calculation.
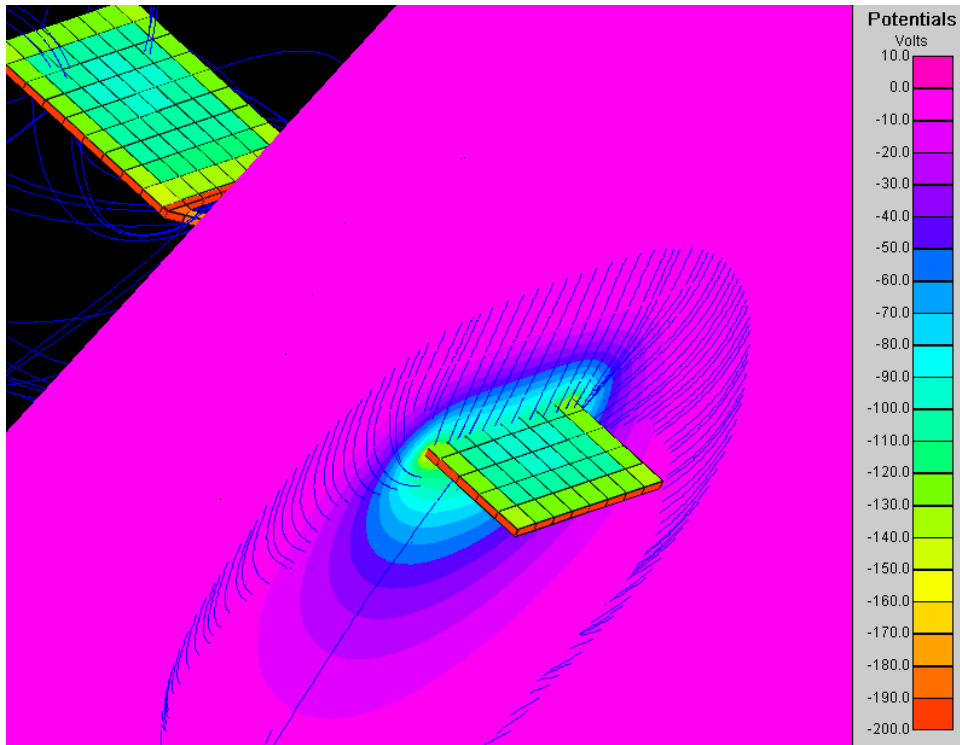
Figure 5c. Surface potentials, space potentials, and particle trajectories for the auroral charging example.
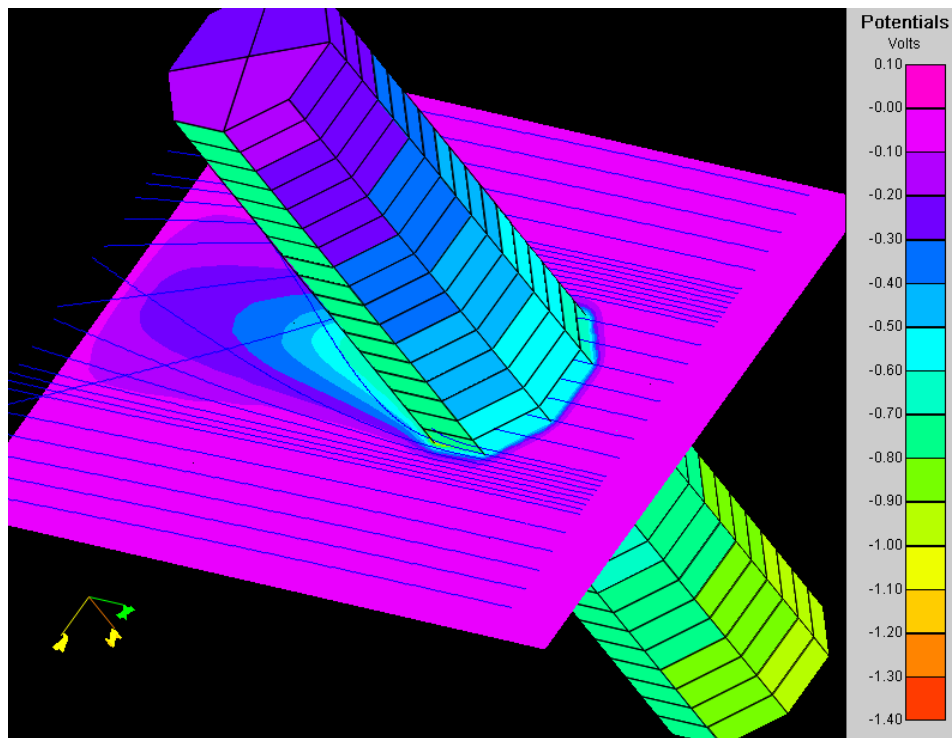
Figure 6a. Charging and wake structure of an octagonal satellite in low-Earth orbit. (See text for details.)
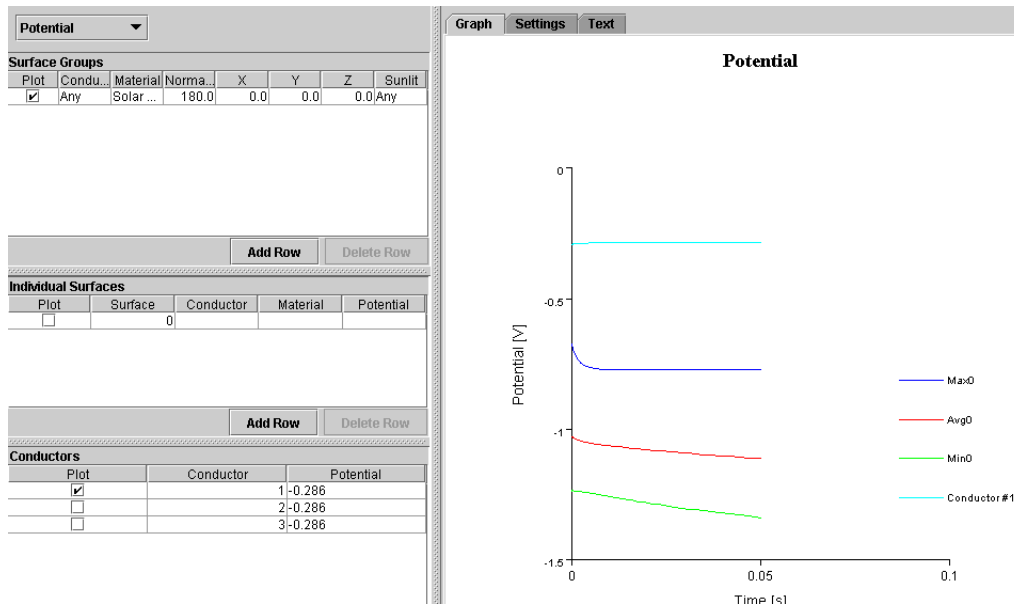
Figure 6b. Surface potentials for the octagonal satellite. The upper line represents the ground potential (to which v×B variation must be added). Second line is for nadir and zenith solar cells, and bottom line is for wake-facing solar cells.

Conductors		
Plot	Conductor	Charging Current
✔	1	4.127E-4
✔	2	5.522E-6
✔	3	-3.912E-4

Figure 6c. Current collected by the ram-facing conducting cells (top), negative-end conducting cells (middle), and positive-end conducting cells (bottom).

References

1. S.A. Brebbia, Boundary Element Methods, Springer Verlag, New York, 1981.

2. E.G. Fontheim, K. Stasiewicz, M. O. Chandler, R. S. B. Ong, "Statistical Study of Precipitating Electrons, Journal of Geophysical Research 87, 3469, 1982.

3. M.S. Gussenhoven, D. A. Hardy, F. Rich, W. J. Burke, H.-C. Yeh, "High-Level Spacecraft Charging in the Low-Altitude Polar Auroral Environment", Journal of Geophysical Research 90, 11009, 1985.

4. I. Katz, D. E. Parks, M. J. Mandell, J. M. Harvey, D. H. Brownell, S. S. Wang, and M. Rotenberg, A Three Dimensional Dynamic Study of Electrostatic Charging in Materials, NASA Rep. CR-135256, August 1977.

5. I. Katz, V. A. Davis, M. J. Mandell, B. M. Gardner, J. M. Hilton, A. R. Fredrickson, D. L. Cooke, J. Minor, "Spacecraft Charging Interactive Handbook," 7th Spacecraft Charging Technology Conference, Noordwijk, The Netherlands, 23-27 April 2001.

6. M.J. Mandell and I. Katz, "High Voltage Plasma Interactions Calculations Using NASCAP/LEO", AIAA Paper AIAA-90-0725, 1990.

7. M.J. Mandell and V. A. Davis, User's Guide to NASCAP/LEO, 1990.

8. M.J. Mandell, T. Luu, J. Lilley, G. Jongeward, and I. Katz, Analysis of Dynamical Plasma Interactions with High Voltage Spacecraft, (2 volumes), Rep. PL-TR-92-2258, Phillips Lab., Hanscom Air Force Base, MA, June 1992.

9. M.J. Mandell, I. Katz, J. M. Hilton, D. L. Cooke, J. Minor, "Nascap-2K Spacecraft Charging Models: Algorithms and Applications," 7th Spacecraft Charging Technology Conference, Noordwijk, The Netherlands, 23-27 April 2001.

10. C.K. Purvis, H.B. Garrett, A.C. Whittlesey, and N.J. Stevens, Design Guidelines for Assessing and Controlling Spacecraft Charging Effects, NASA TP 2361, 1984.

11. F. Vilas, C. R. Chapman, M. S. Matthews (editors), MERCURY, Tucson: University of Arizona Press, 1988.

VALIDATION OF NASCAP-2K SPACECRAFT-ENVIRONMENT INTERACTIONS CALCULATIONS

V.A. Davis
Science Applications International Corporation
10260 Campus Point Dr., M.S. A1
San Diego, CA, 92121
Phone: 858-826-1608
Fax: 858-826-1652
E-mail: victoria.a.davis@saic.com

M.J. Mandell
B.M. Gardner
I.G. Mikellides
Science Applications International Corporation

L.F. Neergaard
Jacobs Sverdrup Technology

D.L. Cooke
Air Force Research Laboratory/VSBS

J. Minor
NASA Marshall Space Flight Center

Abstract

The recently released *Nascap-2k*, version 2.0, three-dimensional computer code models interactions between spacecraft surfaces and low-earth-orbit, geosynchronous, auroral, and interplanetary plasma environments. It replaces the earlier three-dimensional spacecraft interactions codes NASCAP/GEO, NASCAP/LEO, POLAR, and DynaPAC. *Nascap-2k* has improved numeric techniques, a modern user interface, and a simple, interactive satellite surface definition module (Object ToolKit).

We establish the accuracy of *Nascap-2k* both by comparing computed currents and potentials with analytic results and by comparing *Nascap-2k* results with published calculations using the earlier codes. *Nascap-2k* predicts Langmuir-Blodgett or Parker-Murphy current collection for a nearly spherical (100 surfaces) satellite in a short Debye length plasma depending on the absence or presence of a magnetic field. A low fidelity (in geometry and time) *Nascap-2k* geosynchronous charging calculation gives the same results as the corresponding low fidelity NASCAP/GEO calculation. A high fidelity calculation (using the *Nascap-2k* improved geometry and time stepping capabilities) gives higher potentials, which are more consistent with typical observations. *Nascap-2k* predicts the same current as a function of applied potential as was observed and calculated by NASCAP/LEO for the SPEAR I rocket with a bipolar sheath. A *Nascap-2k* DMSP charging calculation gives results similar to those obtained using POLAR and consistent with observation.

Introduction

The three-dimensional spacecraft plasma environment interactions computer code *Nascap-2k*[1, 2, 3, 4] version 2.0 has recently been released. *Nascap-2k* computes a wide variety of plasma phenomena. These include spacecraft charging in geosynchronous, interplanetary, auroral, and low-earth-orbit plasmas, volume potentials, particle trajectories, and resulting variations in plasma density. The user interface is designed so that the non-expert user can do common problems and the expert can tackle questions that have not been previously contemplated. *Nascap-2k* takes advantage of improvements in computer technology, advances in understanding of the phenomena, and enhanced charging algorithms to improve upon the earlier three-dimensional computer codes. (NASCAP/GEO,[5, 6, 7, 8] NASCAP/LEO,[9, 10, 11, 12, 13] POLAR,[14] and DynaPAC[15, 16, 17]). While each code works well for the range of problems for which it was designed, by today's standards, these codes are complicated to use and require expertise to use properly. In addition NASCAP/GEO and POLAR are limited with respect to geometry. *Nascap-2k* builds on our experience with these codes and is designed to address their limitations. It incorporates all of the DynaPAC computational modules.

Previous papers have described *Nascap-2k*,[1, 2, 3, 4] its algorithms, and the new numeric techniques used. This paper focuses on comparison of *Nascap-2k* results with analytic solutions and with the results of NASCAP/GEO, NASCAP/LEO, and POLAR calculations.

Current Collection by a Sphere

We first validate that *Nascap-2k* reproduces analytic results for current collection by a sphere in a dense plasma. *Nascap-2k* incorporates the algorithms developed for NASCAP/LEO to model charge density and current collection in plasmas with Debye lengths short with respect to the mesh size of the calculational grid.[11, 14, 18, 19]

Nascap-2k provides a number of charge density models to use when solving Poisson's equation to obtain volume potentials. These include both analytic functions of the potential (and local electric field) and various combinations of tracked particle densities and analytic functions (such as the sum of a tracked ion density and a barometric function for electrons). In a dense plasma, when the spacecraft velocity and Earth's magnetic field have minimal effect on the charge density within the sheath, the non-linear analytic formula developed for NASCAP/LEO[11, 18] is generally appropriate. This analytic function of the potential smoothly interpolates between linear Debye screening at low potentials and the charge density of a single accelerated and converging species at high potentials.

$$\rho/\varepsilon_0 = -\left(\phi/\lambda_{nl}^2\right)\frac{\max\left(1, C(\phi, E)\right)}{1 + \sqrt{4\pi}\left|\phi/\theta_{nl}\right|^{3/2}}$$

$$\left(R_{sh}/r\right)^2 = 2.29\left|E\,\lambda_{nl}/\theta_{nl}\right|^{1.262}\left|\theta_{nl}/\phi\right|^{0.509}$$

$$C(\phi, E) = \min\left(\left(R_{sh}/r\right)^2, 3.545\left|\phi/\theta_{nl}\right|^{3/2}\right)$$

$$\lambda_{nl^2} = \max(\lambda_{Debye}^2/g, D^2)$$

$$\theta_{nl} = \theta(\lambda_{nl}^2 g/\lambda_{Debye}^2)^{2/3}$$

where the symbols refer to the local potential, ϕ, the local electric field, E, the plasma temperature, θ, the debye length, λ_{debye}, the local mesh spacing, D, and the local reduction in plasma density due to wake effects (neutral model), g.

Generally the charge density is multiplied by a convergence factor, C, which is a function of the local potential and electric field. This factor accounts for the increase in charge density as charged particles from a large area are attracted to a small region. The function was developed to fit the results of Langmuir and Blodgett[20] for current collection by a sphere.

Current is computed by tracking macroparticles from a sheath edge. The sheath is the region from which the repelled species is excluded. Because the sheath absorbs the attracted species, the density of the attracted particles at the sheath edge is one-half the ambient plasma density. By quasi-neutrality, the density of the repelled species is the same, giving a sheath edge potential of $\phi_s = \pm\theta\ln(n/n_o) = \pm\theta\ln(0.5)$.

The charge stabilization algorithm,[14, 19] which makes solution of Poisson's equation possible in these dense plasmas, limits the potential drop in a single volume element. In the lowest potential regions of the computational space, this leads to computed potentials dropping off more slowly than the real potentials. This would lead to an error in the physical location of the sheath edge. To account for this, the calculation places the sheath edge at a potential that depends on the mesh size of the grid within which the sheath falls.

The current density through the sheath is the one-sided plasma thermal current, $J = e\,n\sqrt{\dfrac{e\phi}{2\pi m}}$.

Langmuir and Blodgett[20] analytically solved for the current collected by a biased sphere. Figure 1 shows the current collected by a sphere as a 0.1 m radius function of density as computed using Langmuir and Blodgett's results and by *Nascap-2k*. Figure 2 shows the current collected as a function of potential. *Nascap-2k* reproduces the Langmuir-Blodgett results.

In the presence of a significant magnetic field, the collected current is reduced. Parker and Murphy[21] developed an upper limit on the amount of current that can be collected in the limit of zero temperature and cylindrical symmetry. They accounted for the difficulty of attracting current into the sheath across magnetic field lines. *Nascap-2k* includes the magnetic field in
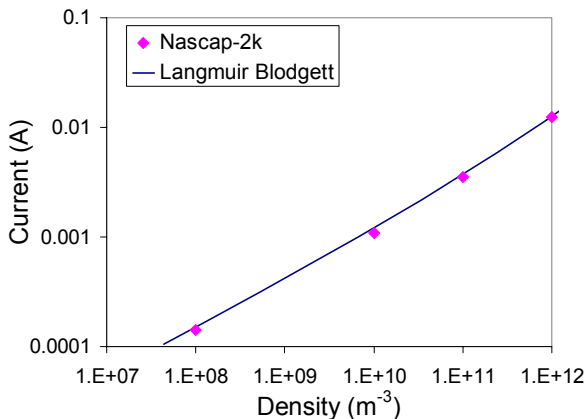
Figure 1. Electron current collected by a 100 V sphere from a 0.2 eV plasma, for no magnetic field.
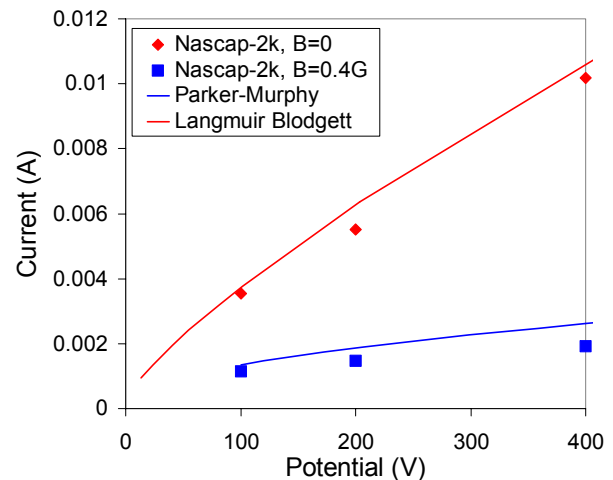
Figure 2. Electron current collected by a sphere from a 1011 m–3, 0.2 eV plasma.
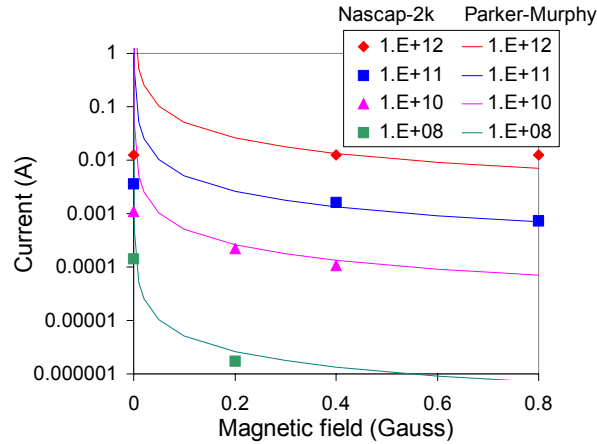
Figure 3. Electron current collected by a 100 V sphere from a 0.2 eV plasma. Densities are in m^{-3}.

Table 1. 90% worst case environment for geosynchronous orbits as defined in Reference 24.

	Temperature (keV)	Density (cm^{-3})
Ions	29.5	0.236
Electrons	12.0	1.12

current calculations in two ways. First, the magnetic field is included in the computation of macroparticle trajectories. With high magnetic fields, some of the particle trajectories that start at the sheath edge leave the sheath and cross the problem boundaries and other particles circle within the sheath and are never collected. Physically, these trapped particles provide an increased charge density that shrinks the sheath, thus reducing the current. However, this effect is *not* included in the analytic non-linear charge density model. The second way the magnetic field enters *Nascap-2k* calculations is when the Larmor radius exceeds the mesh size of the outer most grid by a factor of two, *Nascap-2k* reduces the sheath current by the cosine of the angle between the magnetic and electric fields. This accounts for the reduction of current to the sheath across magnetic field lines.

Figure 3 compares the current collected by a 0.1 m radius sphere as a function of magnetic field for a range of densities. Figure 2 shows the current collected as a function of sphere potential for a 0.4 Gauss magnetic field. The 10^{12} m^{-3} calculations were done with a small grid and *Nascap-2k* computed the sheath current in the same manner as in the absence of a magnetic field. In all the other calculations, the cross field sheath current was reduced. The *Nascap-2k* calculations are in agreement with the Parker-Murphy limits.

Charging in a Geosynchronous Plasma[22]

To validate *Nascap-2k* for geosynchronous charging calculations, we compare potentials computed using *Nascap-2k* with those computed with the industry standard NASCAP/GEO. To further illustrate the differences, we also compare the results with those obtained using the SEE Interactive Spacecraft Charging Handbook.[4, 23] The SEE Handbook is an interactive spacecraft charging code for the non-expert. It computes spacecraft surface charging for geosynchronous

and auroral zone spacecraft along with internal charging due to the deposition of high-energy (MeV) electrons.

A very simple spacecraft geometry, illustrated in Figure , was created to facilitate the comparison. The orientation of the solar arrays is appropriate to a spacecraft at 6 am local time. The proportions of the spacecraft were chosen to fit neatly in the NASCAP/GEO grid structure. The proportions of actual spacecraft almost always must be distorted in order to fit within the 17 x 17 x 33 grid. The SEE Handbook and *Nascap-2k* do not have this constraint.

The calculations use the environment recommended in Reference 24 (see Table 1) for initial modeling during the spacecraft design process. The spacecraft charges for 15 minutes, which is longer than any spacecraft would be exposed to such a severe environment.

The sun is taken to be incident on the spacecraft from the (0.92, 0.39, –0.02) direction. This is appropriate to a spacecraft in geosynchronous orbit at 0 longitude at 6 am GMT on January 1, 2000, consistent with the geometry model.

An important part of defining any spacecraft charging calculation is the determination of the appropriate values to use for the material properties for each surface. NASCAP/GEO, the SEE Handbook, and *Nascap-2k* all use the same fourteen material properties and incorporate them into the calculation in the same way. The focus here is in understanding variations between the results given by these codes. Therefore, the specific values are not important as long as they are consistent. We use the *Nascap-2k* provided default values for all the materials except the non-conducting paint on the antenna. For these surfaces, the values for Npaint[5] provided as a default material of NASCAP/GEO are used.

NASCAP/GEO calculations are done within a nested grid structure, with the innermost main grid 17 x 17 x 33 units in size. With the exception of booms that can extend beyond the
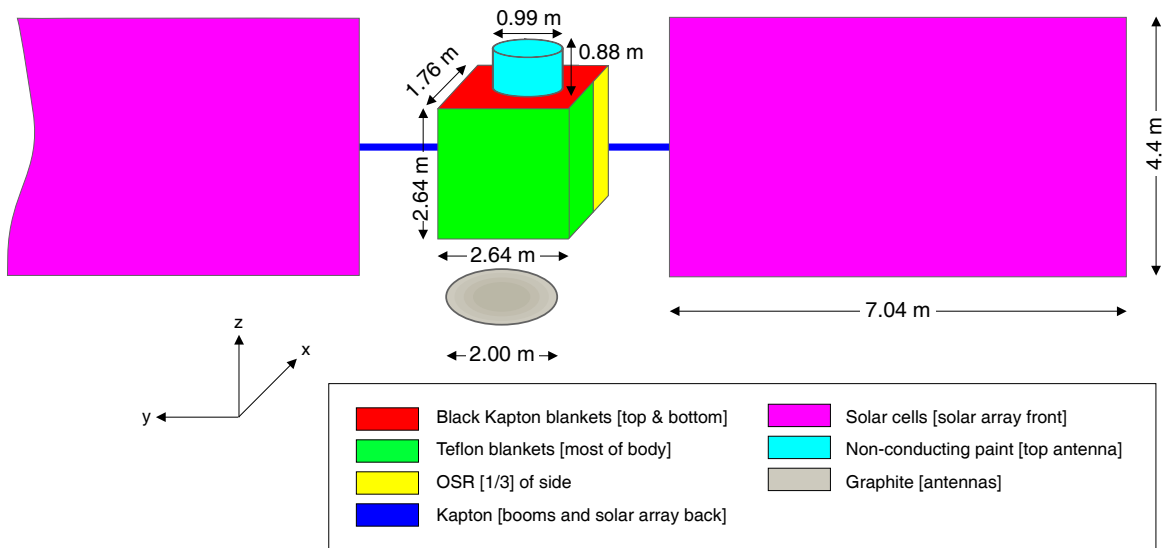
Figure 4. Illustrative spacecraft used for comparison of *Nascap-2k*, NASCAP/GEO, and SEE Interactive Spacecraft Charging Handbook.

main grid, the complete object must fit within this main grid. The object is made up of cubes, plates, wedges, tetrahedrons, and what is left of a cube after a tetrahedron is cut off of it. Booms (long cylindrical projections of arbitrary radius) can also be used. Booms must extend along the X, Y, or Z direction. Figure shows potentials on the best fidelity model that can be made. The Optical Solar Reflector (OSR) area is one-half rather than two-thirds of the spacecraft side and a cube represents the omni antenna. Actual spacecraft require even more distortion in order to fit them within the grid.

The SEE Handbook sets the location of each of the components. The user has no control over the distance between the various components or the zoning. This was done in order to insure stability and reasonable calculation speed in the tool, which is intended for general investigations. The orientation of the solar arrays is set by the longitude, date, and time.

Nascap-2k has a flexible geometric modeling capability. The user can control the size, shape, and gridding of each component. The omni antenna is represented by an octagonal cylinder and the side antennas are concave dishes.

The calculations were set up for 99 timesteps for a time period of 1000 seconds. The timesteps were chosen in the way most natural for each code. The NASCAP/GEO calculation uses geometrically growing timesteps starting with 1 second, with subsequent timesteps of 1.045 times the previous timestep. The SEE Handbook uses geometrically-distributed timesteps that the user cannot control. For the *Nascap-2k* calculation, we used the default geometrically distributed timesteps with a minimum of 0.1 seconds and a maximum of 60 seconds.

Table 2 compares the time required for an expert user to build a model and set up a calculation. This does *not* include the time needed to determine the most reasonable parameters for a specific problem. The determination of the appropriate material properties, geometry, environment, and calculation parameters for an actual analysis is typically days to weeks. It takes approximately as long to build a *Nascap-2k* model as to build a NASCAP/GEO model. However, the model created has the actual geometry and the resolution required. Sometimes it is necessary to build two NASCAP/GEO models at different resolutions in order to resolve questions.

The results of these sample calculations are summarized in Table 3. The potentials at 1000 seconds are shown in Figure 5 through Figure 7. The three codes give consistent results. The least negative surfaces are the ends of the solar arrays. The shaded Teflon surfaces are the most negative. All the surfaces that are more negative than the chassis are shaded insulators. In the center of the sun-facing side of the spacecraft body, the Teflon is slightly positive with respect to the chassis. This is most pronouced in the highest resolution *Nascap-2k* model. The sunlit insulators on the body are near the chassis potential or positive with respect to the chassis.

With the exception of the solar arrays, the surface potentials computed by the three codes are within approximately 35% of each other. The differences are primarily driven by the difference in the chassis potential. At the ends of the solar arrays, where the conductivity of the coverglass and barrier formation dominate the relative potentials, the differential potentials predicted by all three codes are within 4%. At the inner edges of the solar arrays, where the geometry is complex, the differentials vary by almost a factor of two between the minimum and the maximum.

There are two main contributions to differences between the solutions obtained using these three codes: resolution of the geometry and time fidelity.

In order to obtain a stable solution, the variation of the potential within a single timestep is limited. The algorithms for this limiting are complex and different for each of these codes. The SEE Handbook uses a strong limiting algorithm in order to ensure that the results are stable for a wide variety of problems. In NASCAP/GEO the limiting is partially under user control and moderate limiting (the default) was used for this calculation. *Nascap-2k* uses much less stabilization as the user is assumed to understand the code well enough to make the appropriate adjustments in the number and distribution of the timesteps in order to obtain a stable solution. As can be seen in Figure 8, the charging in *Nascap-2k* is faster than in either of the other two codes.

Table 2. Comparison of ease of use.

Code	Number of surfaces	Time to build model (min)	Time to set up calculation (min)	Time for charging calculation to complete on 800 MHz PC (min)
NASCAP/GEO	296	30	5	0.8
SEE Handbook	166	15	2	2
Nascap-2k	623	30	3	12

Table 3. Results of NASCAP/GEO, *Nascap-2k*, and SEE Handbook calculations, given in kV.

	Chassis	Kapton	OSR	Solar Cells	Teflon	Non-conducting paint
Absolute potentials (kV)						
NASCAP/GEO	−10.0	−8.2 to −13.1	−8.23 to −10.7	−5.2 to −7.68	−7.5 to −12.7	−8.3 to −10.3
SEE Handbook	−8.6	none in model	−7.3 to −9.6	−3.6 to −5.7	−6.8 to −11.3	−7.5 to −8.9
Nascap-2k	−12.0	−11.5 to −14.4	−10.0 to −13.7	−7.2 to −10.8	−7.9 to −14.0	−10.0 to −12.2
Differential potentials (kV)						
NASCAP/GEO		1.8 to −3.1	1.77 to −0.7	4.8 to 2.3	2.5 to −2.7	1.7 to −0.3
SEE Handbook		none in model	1.3 to −1.0	5 to 2.9	1.8 to −2.7	1.1 to −0.3
Nascap-2k		0.5 to −2.4	2 to −1.7	4.8 to 1.2	4.1 to −2	2 to −0.2
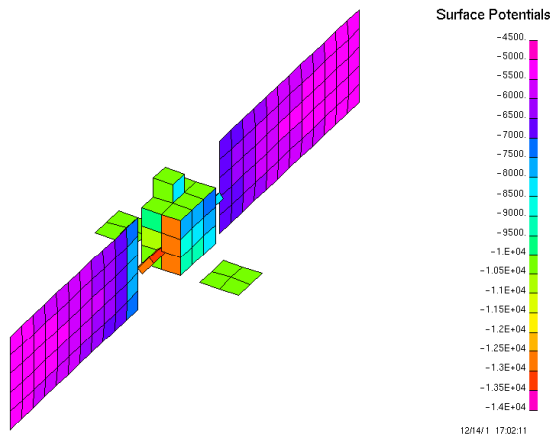
Figure 5. Results of spacecraft charging calculation using NASCAP/GEO.
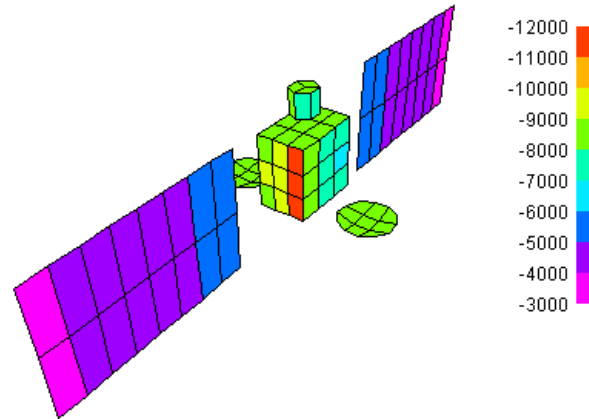
Figure 6. Results of spacecraft charging calculation using SEE Handbook.
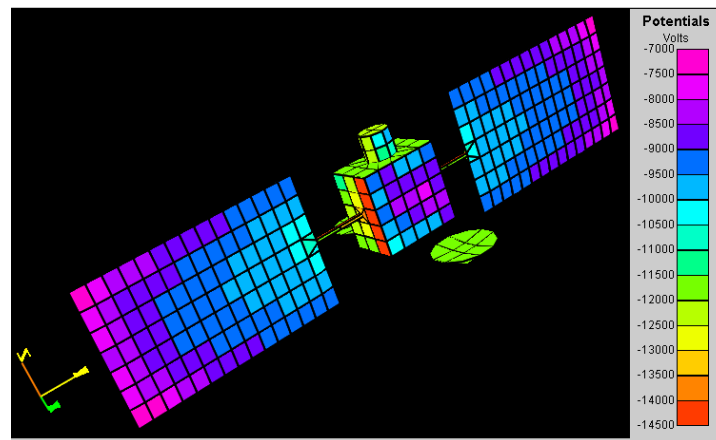
Figure 7. Results of spacecraft charging calculation using Nascap-2k.

The importance of geometric resolution can be illustrated by a comparison of the equilibrum solution given by the three codes as shown in Table 4. In order to further understand the differences due to geometry, a *Nascap-2k* object very similar to the SEE Handbook object was built and *Nascap-2k* used to compute potentials on it. The maximum negative differential in the NASCAP/GEO and *Nascap-2k* calculations are on the Kapton booms supporting the solar arrays. The SEE Handbook model and the simplified *Nascap-2k* model do not have these booms and the maximum negative differential potential is smaller than in the other cases. The chassis potentials computed by all three codes are within 13% of each other. The maximum positive differential potential is on the ends of the solar arrays. After 15 minutes of charging, all three codes give 5 kV differential. At equilibrum, the results are within 30% of each other. Most of this difference appears to be due to the differences in the geometric resolution, as the *Nascap-2k* calculation with the simplified model gives a differential closer to the SEE Handbook than the full geometry model. In all cases the maximum positive differential is about half of the chassis potential.

Nascap-2k improves our ability to model spacecraft surface charging, including improved geometric resolution and time fidelity. The surface charging calculated by *Nascap-2k* using low geometric and time fidelity is similar to the charging calculated by NASCAP/GEO.
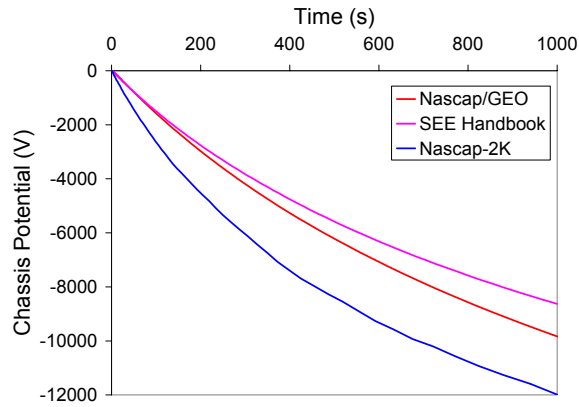
Figure 8. **Comparison of chassis potential versus charging time as computed by NASCAP/GEO, SEE Handbook, and *Nascap-2k*.**

Table 4. Comparison of equilibrum solutions (kV).

	Chassis	Max Differential	
		Positive	Negative
NASCAP/GEO	−20.3	10.8	−2.5
SEE Handbook	−17.8	10.4	−0.14
Nascap-2k	−19.5	7.8	−3.6
Nascap-2k with **Handbook object**	−19.2	9.4	−0.06

Potentials and Currents in Dense Plasmas

A common issue on low-earth-orbit spacecraft is the prediction and control of interactions between a spacecraft with high-voltage components (ranging from a few volts to kilovolts) and the ionospheric environment. Since electron guns were first placed on rockets, the voltage on the main body necessary to collect ionospheric electrons and complete the circuit has been the subject of numerous theoretical and experimental studies. A large-scale effort to address such issues was the Space Power Experiments Aboard Rockets (SPEAR) series of experiments. SPEAR-I[10] was designed to measure whether or not the Earth's magnetic field impedes electron collection, SPEAR-II to test pulsed high-voltage components, and SPEAR-III[17] to test proposed spacecraft grounding mechanisms. An analysis of the bipolar sheath using NASCAP/LEO (and POLAR) was published[10]. We compare key published results with results computed using *Nascap-2k*.

The PATRAN object originally used for the NASCAP/LEO calculations and used here for a *Nascap-2k* calculation is shown in Figure 9. It consists of gold-plated spheres mounted on cylindrical nickel booms. The nickel booms are bushings constructed with grading rings that are connected by resistors. The graded boom created a uniform potential gradient from the positively biased sphere to payload ground. The booms are connected to a cylindrical support boom covered with plastic. This boom is in turn connected to the main (aluminum) rocket body.

Nascap-2k requires a finer resolution computational grid around the spheres than that used in the earlier NASCAP/LEO calculations. Five nested grids, with an outer grid resolution of 1.1 m and an inner grid resolution of 0.06875 m, were used in the *Nascap-2k* calculations.

The calculations use a density of 5 x 10^{10} m^{-3}, a temperature of 0.1 eV, and Oxygen ions. The 0.4 Gauss magnetic field is normal to the plane determined by the spheres and the axis of the body. *Nascap-2k* provides a selection of space charge density models. As this is a steady-state calculation in a short Debye length motionless plasma, the non-linear analytic space charge density model, including convergence, is used.

The *Nascap-2k* and NASCAP/LEO potential calculations give similar results. Figure 10 and Figure 11 show space potential contours as computed by the two codes for the same applied potentials. The shapes and locations of the contour levels are the same. Figure 12 and Figure 13 show sample electron trajectories as computed by the two codes. The differences in the trajectories are due to the differences in the potential solution (different grid structure and interpolation functions) and the initial position of the trajectory.
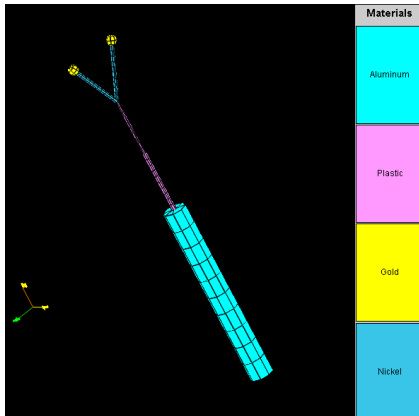
Figure 9. PATRAN model of SPEAR I used for the study of current collection in a bipolar sheath in a low-earth-orbit environment.
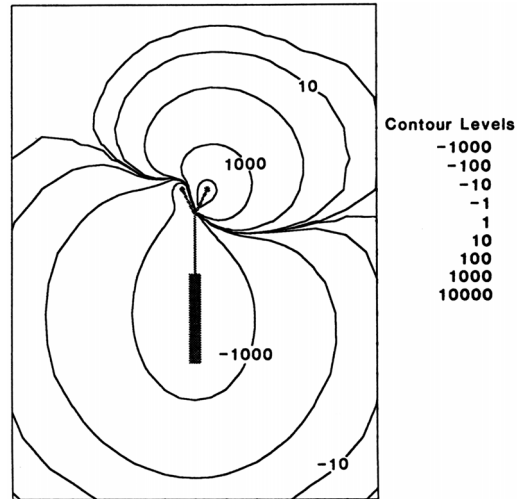
Figure 11. NASCAP/LEO potential contours for one sphere at +46 kV with respect to spacecraft ground and spacecraft ground at −6 kV.10 Reproduced by permission of American Geophysical Union.
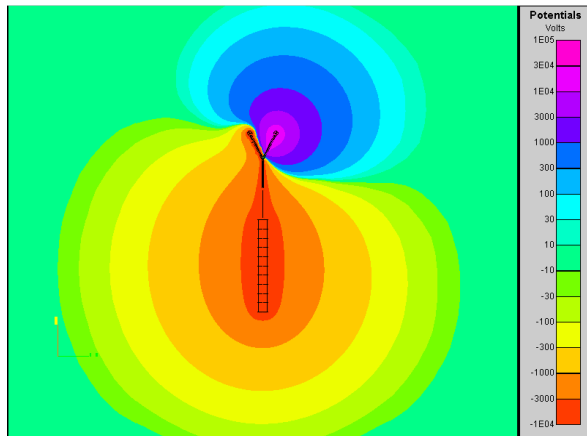
Figure 10. Nascap-2k potential contours with one sphere at +46 kV with respect to spacecraft ground and spacecraft ground at −6 kV.
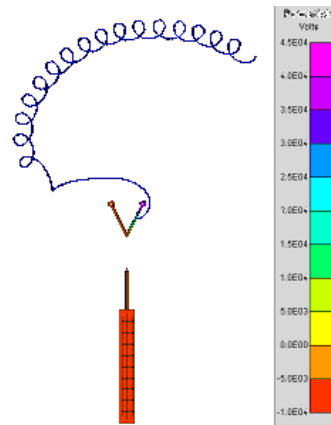
Figure 12. Sample electron trajectory in potential contours shown in Figure 10.
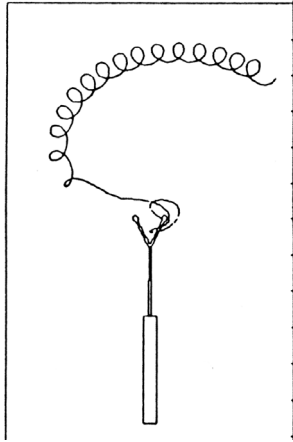
Figure 13. Sample electron trajectory in potential contours shown in Figure 11 .[10] Reproduced by permission of American Geophysical Union.

Table 5. Calculated Chassis Floating Potential and Current as computed by NASCAP/LEO and *Nascap-2k*.

Sphere Bias (kV)	Chassis floating potential (kV)		Sphere and bushing current (mA)	
	LEO	N2k	LEO	N2k
46	−8.3	−5.9	45.2	40.6
24	−5.3	−3.9	26.9	21.6
12	−3.3	−2.6	13.4	10.9
1	−0.6	−0.58	1.4	0.61
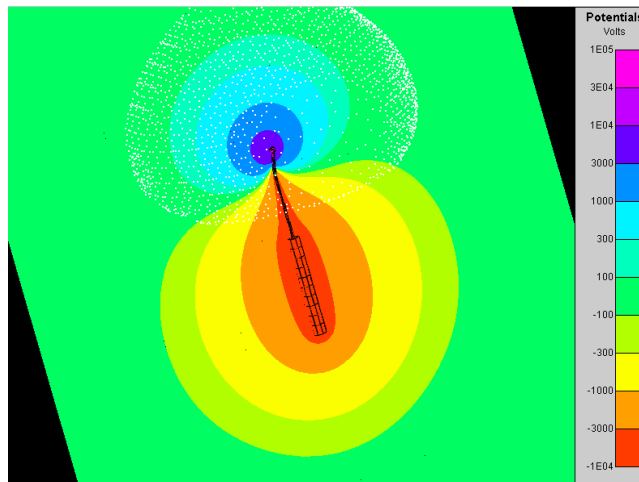
Figure 14. The white dots show the electron sheath edge with 46 kV bias and –8.3 kV chassis potential as computed by *Nascap-2k*.

Reference 10 compares NASCAP/LEO calculations with flight measurements of the spacecraft ground floating potential and the current collected by the biased sphere as a function of the bias value. The high energy cutoff in the ion flux spectra of the energetic particle detectors gives the floating potential. The width of the peak limited the accuracy of the floating potential measurement to within only an order of magnitude. The NASCAP/LEO results are near the center of the range.

The NASCAP/LEO and *Nascap-2k* calculated floating potentials and sphere and bushing currents are given in Table . The *Nascap-2k* floating potentials are slightly less as the electron currents computed by *Nascap-2k* are about one-third those computed by NASCAP/LEO for the same potentials. This is a result of the reduction in sheath current due to the magnetic field, a phenomenon that is not accounted for in NASCAP/LEO. Figure 14 shows the location of the

electron sheath. The magnetic field limits the plasma thermal current entering the sheath from the top, significantly reducing the electron current.

The measured collected electron current as a function of applied bias can be fit by a line I(mA) = 0.880 V(kV). The NASCAP/LEO results can be fit by a line I(mA) = 0.985 V(kV). The *Nascap-2k* results can be fit by a line I(mA) = 0.886 V(kV). The *Nascap-2k* currents as a function of floating potential agree with the flight measurements even better than the earlier NASCAP/LEO results do.

Auroral Spacecraft Charging

To validate *Nascap-2k* for auroral charging, a comparison of results obtained using *Nascap-2k* with those obtained using POLAR for the Defense Meteorological Satellite Program spacecraft (DMSP) was done.[25] The DMSP spacecraft definition used for the calculations described in Reference 25 was used for the *Nascap-2k* calculations.

Charging in eclipse from an initial potential of −10 V was computed for a period of 6 s with 45 timesteps varying from 0.0125 s to 0.2 s. In all cases, the charging currents were computed using an analytic model for the electrons and tracked ions. The charge density can be computed either analytically or self-consistently with the ion trajectories. In the first case, the ion currents are computed by tracking macroparticles from the sheath and in the second case by tracking macroparticles from the boundary of the computational space. The environment is described by a low energy plasma and high energy auroral electrons. The low energy plasma is a Maxwellian. The high energy electrons are described by a three component Fontheim[26] distribution.

$$\text{Flux}_{\text{Font}}\left(E\right) = \sqrt{\frac{e}{2\pi\theta_{\max}m_e}}\frac{E}{\theta_{\max}}\,n\exp\left(-\frac{E}{\theta_{\max}}\right) + \pi\zeta_{\text{gauss}}E\exp\left(-\left(\frac{E_{\text{gauss}}-E}{\Delta}\right)^2\right) + \pi\zeta_{\text{power}}E^{-\alpha}$$

The plasma environment parameters used are shown in Table 6. The spacecraft is moving at 6565 m/s in the −X direction.

Calculations can be done for two different charge density models: the analytic charge density model used in the SPEAR I calculation, and the self-consistent with ion trajectories model. We used the second charge density model as it is more appropriate for moving spacecraft. Ions are tracked from the problem boundaries and their spacecharge deposited on grid nodes at each step. Each ion is tracked until it reaches the spacecraft or leaves the grid. After the tracking step, the charge density is computed from the resulting ion density and a barometric description of the electrons.

**Table 6. Parameters used to describe auroral environment.**

Low energy plasma	**Density**	3×10^9 m^{-3}
	Temperature	0.2 eV
	Hydrogen fraction	9%
High energy electrons		
Maxwellian component	**Density**	2.49×10^5 m^{-3}
	Temperature	3200 eV
Gaussian component	**Coefficient**	1.5×10^4
	Energy	3.5×10^4 eV
	Width	1.8×10^4 eV
Power law component	**Coefficient**	2×10^{10}
	Minimum energy	50 eV
	Maximum energy	1.6×10^6
	Exponent	1.05
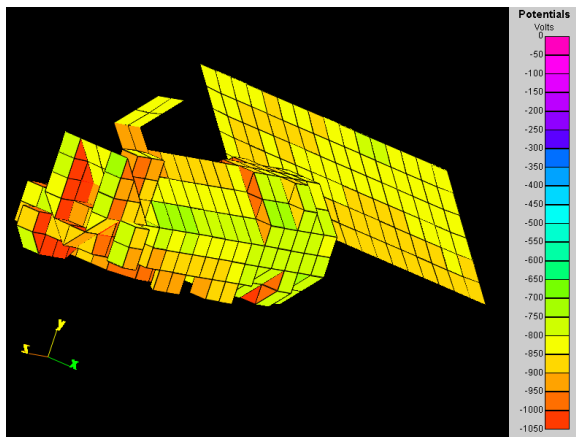
Figure 15. Resulting surface potentials for case with self-consistent charge density computed by *Nascap-2k*.
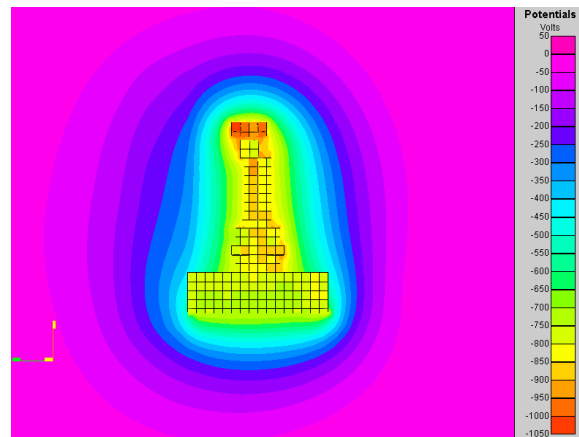
Figure 16. Resulting space potentials for case with self-consistent charge density computed by Nascap-2k.
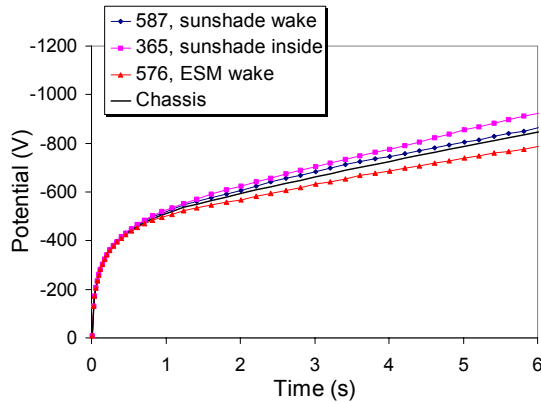
Figure 17. Time history of charging with self-consistent charge density computed by Nascap-2k.
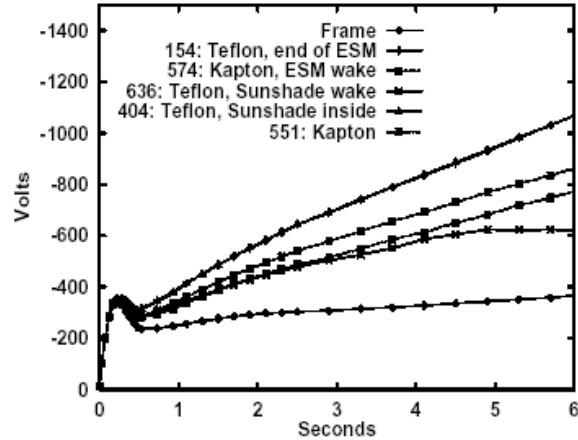
Figure 18. Figure 5 of Reference 25.

The results of the calculations are given in Figure 15 through Figure 17. With these choices for parameters, the resulting chassis potential is –845 V and surface potentials vary between –710 and –1025 V. The well-shadowed surfaces are the most negative. The chassis rapidly charges to the –500 V level and continues to charge at about 60 V per second. With more timesteps, the results might be slightly different.

These results can be compared with Figure 5 of Reference 25, shown here as Figure 18. The *Nascap-2k* results do not have the, presumably spurious, hump at 0.2 sec, show more charging, and are continuing to charge. The charging of the surfaces with respect to each other is not the same, but as the selected surfaces are probably different, no firm conclusions can be drawn.

Another set of calculations in the same paper was also repeated. The thickness of Teflon was set to 2.8 x 10^{-3} and all the Kapton was changed to Teflon. The results are shown in Figure 19 through Figure 21. These results can be compared with Figure 22 through Figure 24 obtained from POLAR. Again, the results using the two codes are similar in character. The shaded surfaces are the most negative and the ram-wake difference is small. Using POLAR, the wake side charges more than the ram side. Using *Nascap-2k*, the ram side charges slightly more than the wake side. The incident ions are focused onto the wake side of the spacecraft. The *Nascap-2k* and POLAR auroral charging results have the same character.

Conclusions

Nascap-2k is already proving valuable with its improved geometric modeling and surface electric field accuracy. It can be used to do the highest accuracy three-dimensional spacecraft-plasma interaction calculations with a single, straight-forward user interface. Calculations of interactions of a sphere with a surrounding plasma using *Nascap-2k* are consistent with analytic solutions. *Nascap-2k* reproduces or improves upon results from NASCAP/GEO, NASCAP/LEO, and POLAR for a selection of typical interactions calculations. *Nascap-2k* includes the limitation of collected current due the magnetic field in low-earth-orbit problems and provides much improved geometric and time fidelity in tenuous charging calculations.
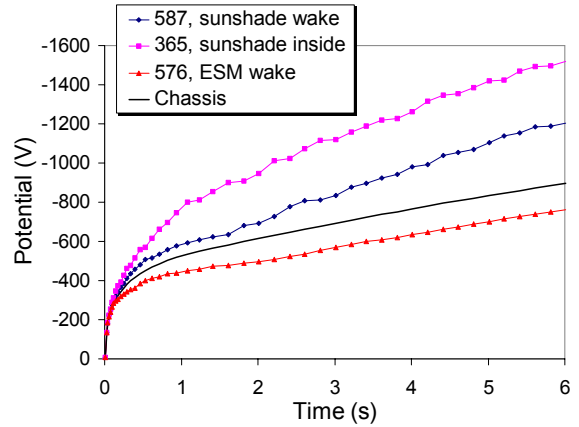
Nascap-2k can be obtained from NASA's SEE Program. Contact Jody Minor, jody.minor@nasa.gov or David Cooke david.cooke@hanscom.af.mil (Air Force users).
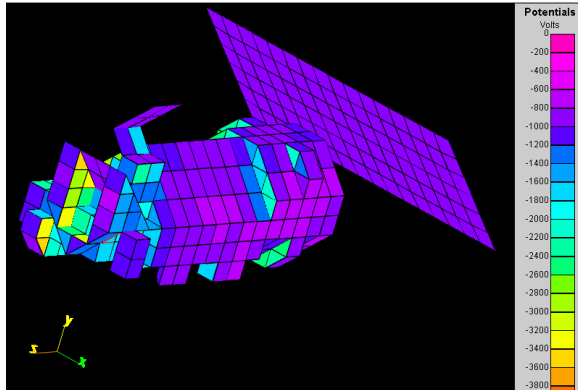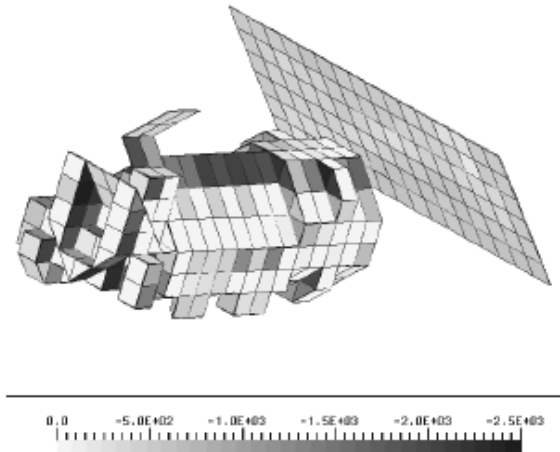

Figure 19. Resulting surface potentials for case with all Teflon and self-consistent charge density computed by *Nascap-2k*.
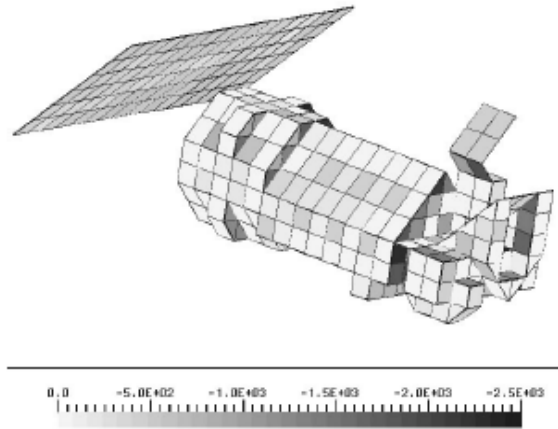

Figure 21. Time history of charging with all Teflon and self-consistent charge density computed by *Nascap-2k*.
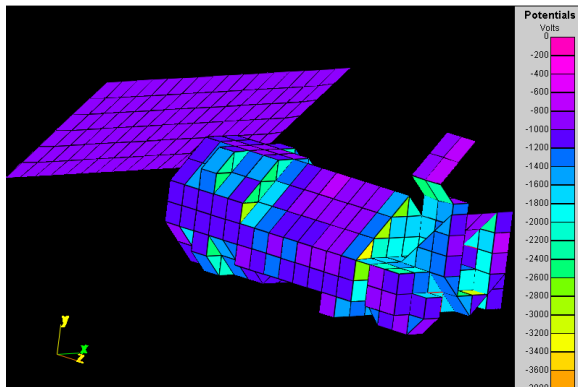
Figure 20. Resulting surface potentials for case with all Teflon and self-consistent charge density computed by *Nascap-2k*.

Figure 22. Resulting surface potentials using POLAR for Teflon only case from Reference 25.

Figure 23. Resulting surface potentials using POLAR for Teflon only case from Reference 25.
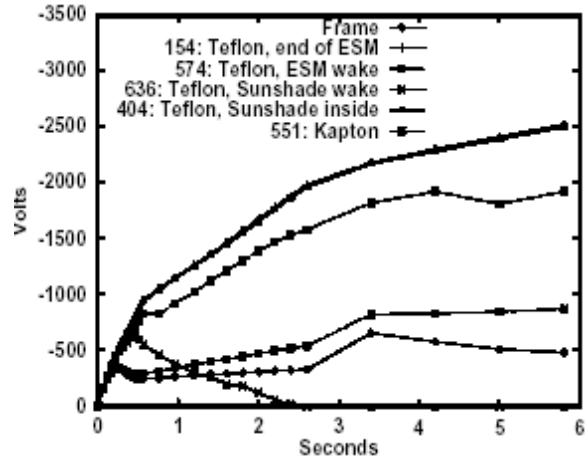
Figure 24. Time history of surface potentials using POLAR for Teflon only case from Reference 25.

References

1. M.J. Mandell, I. Katz, J.M. Hilton, J. Minor, D.L. Cooke, *Nascap-2k*, A Spacecraft Charging Analyis Code for the 21st Century, AIAA Paper 2001-0957, *AIAA Aerospace Sciences Meeting & Exhibit, 39th, Reno, NV,* Jan. 2001.

2. M.J. Mandell, I. Katz, D. Cooke, *Towards a more robust spacecraft charging algorithm*, AIAA Paper AIAA 99-0379, 1999.

3. M.J. Mandell, V.A. Davis, B.M. Gardner, I.G. Mikellides, D.L. Cooke, J. Minor, *Nascap-2k*—An Overview, This proceedings.

4. V. A. Davis, L. F. Neergaard, M.J. Mandell, I. Katz, B.M. Gardner, J. M. Hilton, J. Minor, *Spacecraft Charging Calculations: Nascap-2k and SEE Interactive Spacecraft Charging Handbook*, AIAA Paper, AIAA 2002-0626, 2000.

5. M.J. Mandell, P.R. Stannard, I. Katz, *NASCAP Programmer's Reference Manual,* NASA CR 191044, 1993.

6. P.R. Stannard, I. Katz, L. Gedeon, J.C. Roche, A.G. Rubin, M.F. Tautz, *Validation of the NASCAP model using spaceflight data,* AIAA Paper AIAA 82-0269, 1982.

7. I. Katz, P.R. Stannard, L. Gedeon, J.C. Roche, A.G. Rubin, M. F. Tautz, NASCAP simulations of spacecraft charging of the SCATHA satellite, *Spacecraft/Plasma Interactions and their Influence on Field and Particle Measurements*, ESA SP-198, p. 109, 1983.

8. I.Katz, D.E. Parks, M.J. Mandell, J.M.Harvey, S.S. Wang, J.C. Roche, NASCAP, a three-dimensional charging analyzer program for complex spacecraft, *IEEE Trans. Nucl. Sci., NS-24*, p. 2276, 1977.

9. M.J. Mandell, and I. Katz, *High Voltage Plasma Interactions Calculations Using NASCAP/LEO*, AIAA Paper AIAA-90-0725, 1990.

10. I.Katz, G.A. Jongeward, V.A. Davis, M.J. Mandell, R.A. Kuharski, J.R. Lilley, Jr., W.J. Raitt, D.L. Cooke, R.B. Torbert, G. Larson, and D. Rau, Structure of the Bipolar Plasma Sheath Generated by SPEAR I, *J. Geophys. Res., 94*, A2, p. 1450, 1989.

11. M.J. Mandell, V.A. Davis, *User's Guide to NASCAP/LEO*, S-CUBED Division of Maxwell Laboratories, SSS-R-85-7300-R2, 1990.

12. T. Neubert, M.J. Mandell, S. Sasaki, B.E. Gilchrist, P.M. Banks, P.R. Williamson, W.J. Raitt, N.B. Meyers, K.I. Oyama, I. Katz, The sheath structure around a negatively charged rocket payload, *J. Geophys. Res., 95*, p. 6155, 1990.

13. M.J. Mandell, J.R. Lilley, Jr., I. Katz, T. Neubert, N.B. Myers, Computer modeling of current collection by the CHARGE-2 mother payload, *Geophys. Res. Lett., 17*, p. 135, 1990.

14. J.R. Lilley, Jr., D.L. Cooke, G.A. Jongeward, I. Katz, *POLAR User's Manual*, GL-TR-89-0307, 1989.

15. M.J. Mandell, T. Luu, J. Lilley, G. Jongeward, and I. Katz, *Analysis of Dynamical Plasma Interactions with High Voltage Spacecraft,* (2 volumes), Rep. PL-TR-92-2258, Phillips Lab., Hanscom Air Force Base, MA, 1992.

16. V.A. Davis, M.J. Mandell, D.L. Cooke, C.L. Enloe, High-voltage interactions in plasma wakes: Simulation and flight measurements from the Charge Hazards and Wake Studies (CHAWS) experiment, *J. Geophys. Res., 104,* A6, p. 12445, 1999.

17. M.J. Mandell, G.A. Jongeward, D.L. Cooke, W.J. Raitt, SPEAR 3 flight analysis: Grounding by neutral gas release and magnetic field effects on current distribution, *J. Geophys. Res., 101*, A1, p. 439, 1998.

18. M.J. Mandell, I. Katz, P.G. Steen, G.W. Schnuelle, The effect of solar array voltage patterns on plasma power losses, *IEEE Trans. Nucl. Sci., NS-27*, p. 1797, 1980.

19. D.L. Cooke, I. Katz, M.J.Mandell, J.R. Lilley Jr., and A.J. Rubin, Three-Dimensional Calculation of Shuttle Charging in Polar Orbit, *Proc. of the Spacecraft Environmental Interactions Technology Conference 1983*, ed by Carolyn K. Purvis and Charles P. Pike, NASA Conf. Pub. 2359, AFGL-TR-85-0018, p. 205, 1985.

20. I. Langmuir, K.B. Blodgett, Currents limited by space charge between concentric spheres, *Phys. Rev., 24*, p. 49, 1924.

21. L.W. Parker, B.L. Murphy, Potential buildup on an electron-emitting ionospheric satellite, *J. Geophys. Res., 72,* p. 1631, 1967.

22. This section originally published in Reference 4 copyright © by the American Institute of Aeronautics and Astronautics, Inc. Reprinted with permission.

23. I. Katz, V.A. Davis, M.J. Mandell, B.M. Gardner, J.M. Hilton, J. Minor, A.R. Fredrickson, D.L. Cooke, *Interactive spacecraft charging handbook with integrated updated spacecraft charging models*, AIAA paper AIA 2000-0247, 2000.

24. C.K. Purvis, H.B. Garrett, A.C. Whittlesey, N.J. Stevens, *Design guidelines for assessing and controlling spacecraft charging effects*, NASA TP 2361, p. 3, 1984.

25. D.L. Cooke, Simulation of an Auroral Charging Anomaly on the DMSP satellite, *6th Spacecraft Charging Technology Conference,* AFRL-VS-TR-20001578, 2000.

26. E.G. Fontheim, K. Stasiewicz, M.O. Chandler, R.S.B. Ong, E. Gombosi, R.A. Hoffman, Statistical study of precipitating electrons, *J. Geophys. Res., 87*, p 3469, 1982.

NASCAP-2K AS A PIC CODE

M. J. Mandell
Science Applications International Corporation
10260 Campus Point Dr., M.S. A1,
San Diego, CA, 92121
Phone: 858-826-1622
Fax: 858-826-1652
E-mail: myron.j.mandell@saic.com

D. L. Cooke
Air Force Research Laboratory/VSBS

Abstract

Nascap-2k can be used to calculate plasmadynamic effects as well as steady-state charging and current collection. In this paper we consider electron dynamics in the sheath of a VLF antenna. We estimate the sheath size, and show 1-D calculations for both sine wave and square wave excitation. The results show strong electrostatic plasma oscillations at the sheath edge. Then we use Nascap-2k to duplicate the square wave results through the first maximum in the plasma oscillation, obtaining excellent agreement with the 1-D results. This opens the door to fully 3-D dynamic VLF antenna calculations.

Introduction

There is current interest in generating VLF waves in space for the purpose of controlling the trapped electron population (Inan *et al.*, 2003). A transmitting antenna for this purpose would be several inches in diameter, tens of meters long and have bias amplitudes of hundreds of volts. It would interact with a large volume of the surrounding plasma, and be a major driver for spacecraft potential. Thus, it is of major interest to be able to simulate dynamically and in 3-D the antenna together with its host spacecraft and the surrounding plasma.

Nascap-2k, through its DynaPAC heritage, contains the features needed to do this type of problem. However, these features have not been fully exercised since the days of SPEAR II (Cohen, 1995). In studying the CHAWS experiment (Davis, *et al.*, 1999), ion trajectories were used to calculate steady-state, self-consistent charge densities and space potentials, and we have exercised the ability to do PIC ions with barometric electron densities. For the antenna problem we would like to do both electrons and ions using PIC. (Note, however, that Nascap-2k only solves Poisson's equation, rather than the full Maxwell equations, so it computes only curl-free, quasi-static fields.)

In this paper we describe the antenna problem, and, for baseline parameters, show the solution, as calculated by a 1-D PIC code, for electron dynamics in the sheath. We then pose a nearly identical problem for solution with Nascap-2k, demonstrate that the solutions agree, and show the graphics. We were nearly able to do the problem using the current release of Nascap-

2k, editing scripts within the GUI and some of the generated ASCII input files. In the end, one line of code had to be changed to obtain a correct result.

Statement of Problem

The objective is to simulate the dynamic sheath around a negative thin rod. We avoid positive polarity because the positive half of the antenna will collect copious electrons, so the maximum potential it can reach is determined by numerous unknown factors, such as the relative size of the spacecraft and antenna. We wish to do this with realistic values of plasma density, ion mass, applied voltage, frequency, magnetic field, and spacecraft velocity. The arbitrary directions of the latter two require a 3-D code. A 1-D (radial) code can handle magnetic field either parallel to the antenna or circumferential (as would be caused by current flowing in the antenna).

Sheath Size Estimate

The sheath (defined as the region from which electrons are excluded) can be quite large, even for a fairly modest potential of about 100 volts. To calculate the sheath size, we specify the electric field at the antenna radius, R_0. We assume that the external space between the antenna and the sheath is filled with ions at ambient density, ρ. The electric field at any radius, r, between the antenna and the sheath is

$$E(r) = \frac{\rho e (r^2 - R_0^2)}{2\varepsilon_0 r} - \frac{a}{r} E(R_0)$$

The sheath condition is $E(R_s)=0$, where R_s is the sheath radius. We then integrate the electric field from R_s to R_0 to determine the corresponding potential.

Figure 1 shows the relation between applied potential and sheath radius for a 10 cm diameter antenna. At a density of 10^{12} m^{-3} the sheath radius at 100 volt bias is about 15 cm, and grows to nearly a meter at a density of 10^{10} m^{-3}. The calculations to follow assume a density of 3×10^{11} m^{-3}, giving a sheath radius of about 20 cm.

Baseline Parameters

Table 1 shows the baseline parameters for the calculation. Density of 3×10^{11} m^{-3} is chosen so that the sheath is large compared with the wire but still very tractable computationally. In general the plasma is cold, but 0.1 eV is used in those places where temperature is required. The antenna frequency is set to 100 kHz, and the process is followed for a half-period of 5 microseconds. To see the effect of magnetic field, a field of 0.5 gauss is chosen. The ordering of the plasma frequency, electron gyrofrequency, and applied frequency is $\omega_p > \omega_c > 2\pi f$.

Table 1. Parameters for baseline calculations.

Plasma Density	3×10^{11} m^{-3}
Electron Temperature	0.0 or 0.1 eV
Plasma Frequency	3.1×10^7 s^{-1}
Antenna Frequency	100 kHz
Magnetic Field	0.0 or 0.5 gauss
Electron Gyrofrequency	0.0 or 8.8×10^6 s^{-1}
Ion Species	O$^+$

1-D Calculations

A simple one-dimensional finite element code was written to simulate quasistatic plasma-dynamics about a long cylindrical antenna. The computational domain extended out to one meter from an antenna radius of 5 cm, and was divided into 1000 zones in equal increments of r^2. Two ion macroparticles and two electron macroparticles were placed in each zone, with each macroparticle having equal charge. The simulation was run for 2000 timesteps of 2.5 nanoseconds each, making up the 5 microsecond half-period for the 100 kHz frequency. When electrons left the computational space they were replaced by thermal electrons.

Figure 2 shows the potential profile at various times in the calculation. As expected, the potential is rapidly screened to about the expected sheath radius as electrons are expelled from the sheath. At certain times a positive potential region appears. This is an effect of electron inertia, as the moving electrons do not stop of their own accord, but must be attracted back towards the sheath boundary. In Figures 3-6 we plot (1) the maximum potential at times when a positive region appears; (2) the location of the maximum potential; and (3) the location of the sheath edge, indicated by a sharp drop in the charge density from nearly the ambient ion density to nearly zero.

Figures 3 and 4 show results for a half sine wave, for which the applied negative potential continuously rises and returns to zero. The magnitude of the potential maximum is 8-10 volts, and the oscillation frequency is somewhat less than the electron plasma frequency. The sheath edge occurs at a radius of about 20 cm as calculated above, with oscillations of about two cm. The potential maximum, when it occurs, is just inside the sheath edge.

Two differences can be noted between the unmagnetized (Figure 3) and magnetized cases. First, in the unmagnetized case the potential goes completely non-positive between peaks, whereas in the magnetized case a positive peak forms inside the outer boundary. This occurs because the magnetic field inhibits inward diffusion of the thermal electrons. Second, in the unmagnetized case the sheath remains at the end of the pulse, even though the potential goes to zero, while in the magnetized case the sheath disappears. This occurs because the magnetic field traps inbound electrons in the sheath region, whereas in the absence of magnetic field inbound electrons collide with the antenna.

Square wave calculations were done in 1-D to compare with the Nascap-2k calculations below, and are shown in Figures 5 and 6. Much stronger plasma oscillations are seen, with the

initial oscillation at 75 volts. The sheath edge oscillates 10 cm on either side of its average position at 20 cm, and the peak potential occurs well inside the sheath. Application of the 0.5 gauss magnetic field doubles the rate of decay of the oscillations.

3-D Calculations

Three-dimensional calculations were done with Nascap-2k to demonstrate the feasibility of such calculations. Figure 7 shows the Nascap-2k antenna model embedded in a nested grid. The antenna consists of two square rods, each 10 cm on a side and 4 m long. The outer boundary of the grid is a square 1.32 m on a side. The coarse resolution is 11 cm, with 5.5 cm resolution near most of the antenna, and 2.75 cm resolution in a limited region. Initially, 8 electron macroparticles and 8 ion macroparticles were placed in each zone, positioned so as to represent a uniform charge distribution in the context of the nonlinear interpolants. A negative 100 volt square wave was applied to half of the antenna, and each timestep consisted of (1) tracking the particles for 2.5 nanoseconds, (2) sharing the particle charge to the nodal coefficients in accordance with the nonlinear interpolants, and (3) recalculating the potential in preparation for the next tracking phase.

The initial state is represented in a 3-D view in Figure 8, and a planar view in Figure 9. Each of Figures 9-12 shows a plane of potentials with a plane of electron macroparticles just above it, positioned as shown in Figure 8. (Ion macroparticles have the same initial configuration, but move negligibly during the simulation time.) Note that the apparent high density of particles in the subdivided region is balanced by correspondingly reduced particle weight. Comparing Figure 10 with Figure 9, we see that the potentials change little in the first 25 nanoseconds, but they change considerably in the next 25. Figure 11 shows the electron motion, leading to sheath radii of 9 cm at 25 nanoseconds and 18 cm at 50 nanoseconds. Figure 11 shows the effects of the square cross-section. Particles that started out near the flat, low-field region have moved considerably less than those that started out near the high-field corners.

The simulation was run up to the first potential maximum, which occurred at 137.5 nano-seconds. Figure 12 shows that, at this time, there is a high, broad maximum in the potential, with electrons excluded from a region that extends well beyond the location of the potential maximum. Figure 13 shows another view of the final configuration, with potentials in a plane containing the antenna. Note that there is no apparent difference between the potentials in the highly resolved region and in the less resolved region, suggesting that the highest level of resolution may not be needed.

Figure 14 shows the development of the sheath radius and maximum potential calculated by Nascap-2k, compared with the 1-D sheath radius result. The maximum potential of 75 volts, as well as the time of first maximum (140 ns) is in excellent agreement with the one dimensional result. The maximum sheath radius calculated by Nascap-2k is larger than the 1-D result in proportion to the effective larger size of the 10 cm square antenna vs. the 10 cm diameter round antenna.

Conclusions

Electron dynamics are important in the very large sheaths of VLF antennas under space conditions. Large electrostatic oscillations are to be expected, producing at times positive potential regions about a negative antenna. The amplitude of the oscillations is waveform dependent.

Nascap-2k is shown to have the ability to perform quasi-electrostatic PIC simulations of sheath dynamics in fully 3-D geometry. This is important because such simulations can take into account the presence of the host spacecraft and arbitrary directions of magnetic field and spacecraft velocity.

To do the calculations shown here, scripts needed to be edited within the GUI, and ASCII input files needed to be edited. Only one line of source code had to be changed to obtain a correct result. Thus, an advanced user could do such calculations with the current Nascap-2k release, provided he was given access to the one altered DLL. Future Nascap-2k development will include tuning to make quasi-electrostatic PIC calculations more accessible to less advanced users, as well as features needed for more lengthy calculations, such as introducing thermal electrons at boundaries.
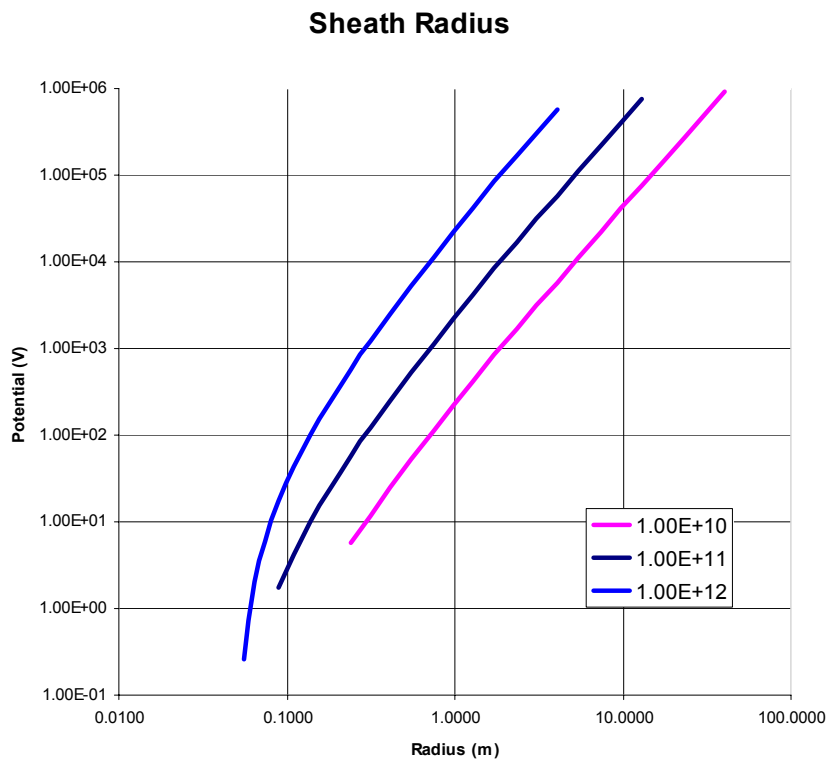
Sheath Radius

Figure 1. Potential vs. sheath radius for negative applied potential on a 10 cm diameter antenna. Curves for three different plasma densities are shown.
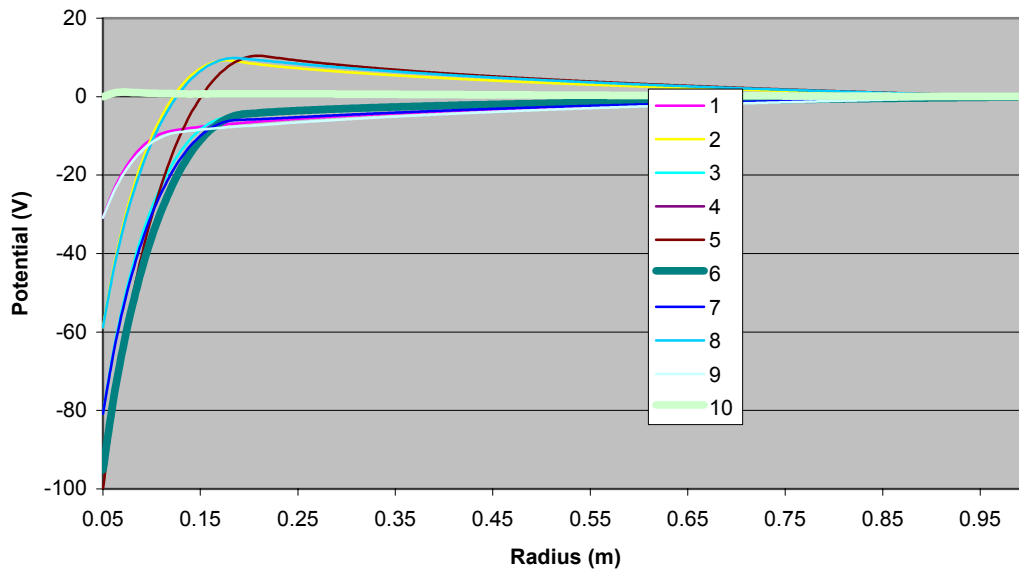
Figure 2. Potential profile at various times during the 1-d calculation.
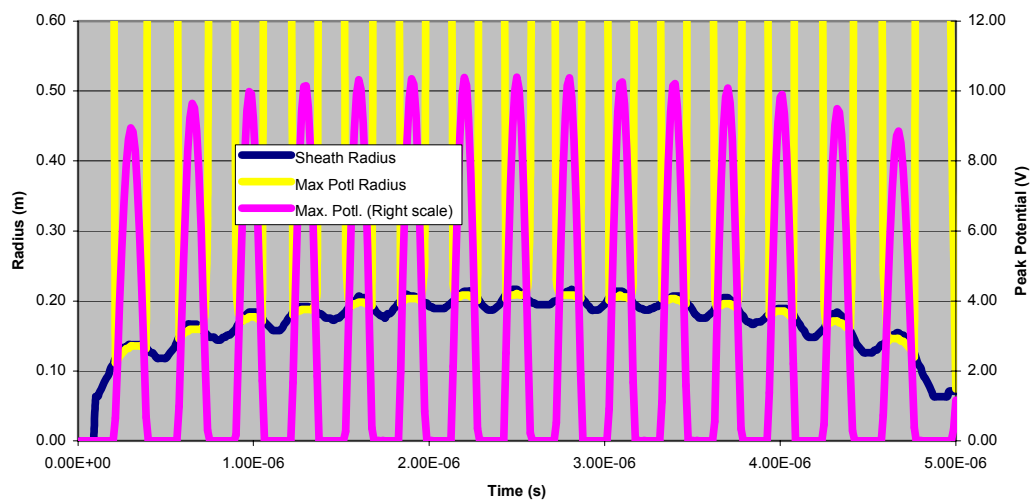
Figure 3. Simulation results for half sine wave and no magnetic field, showing peak positive potential (magenta curve, right scale), location of peak (yellow curve, left scale) and location of sheath edge (dark curve, left scale).
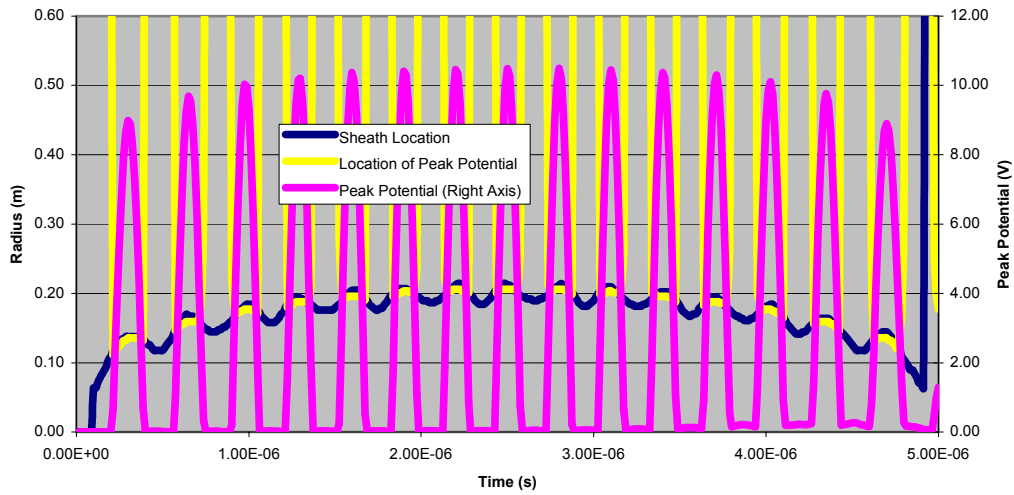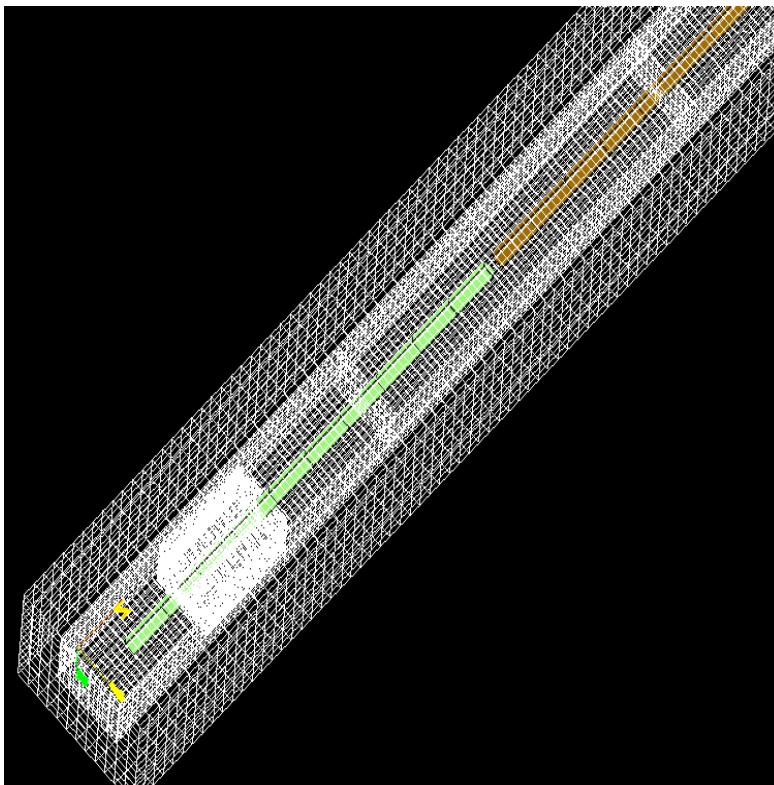
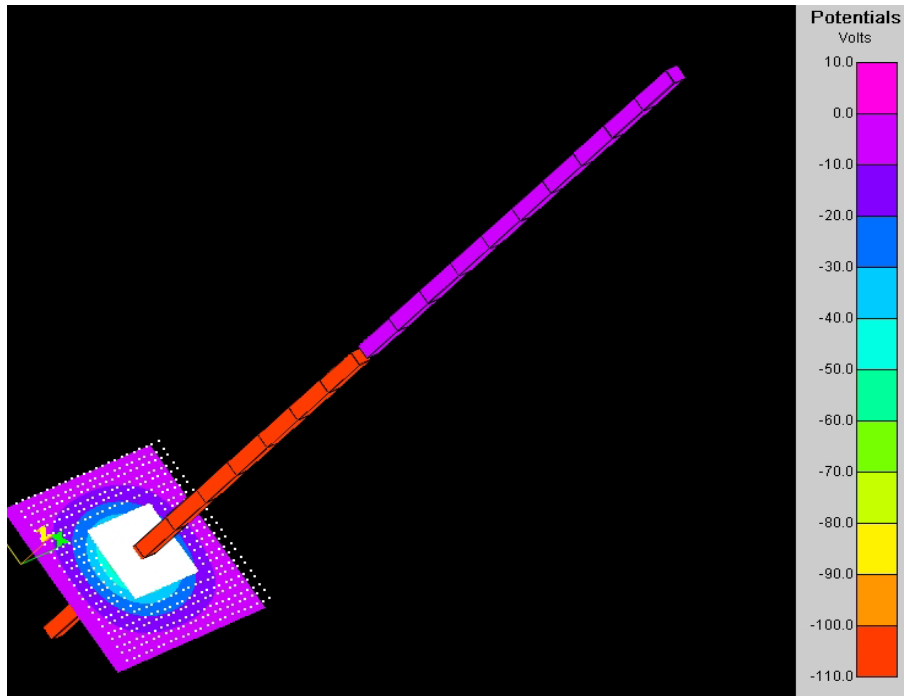**Figure 4. Same as Figure 3, for half sine wave with magnetic field of 0.5 gauss.**
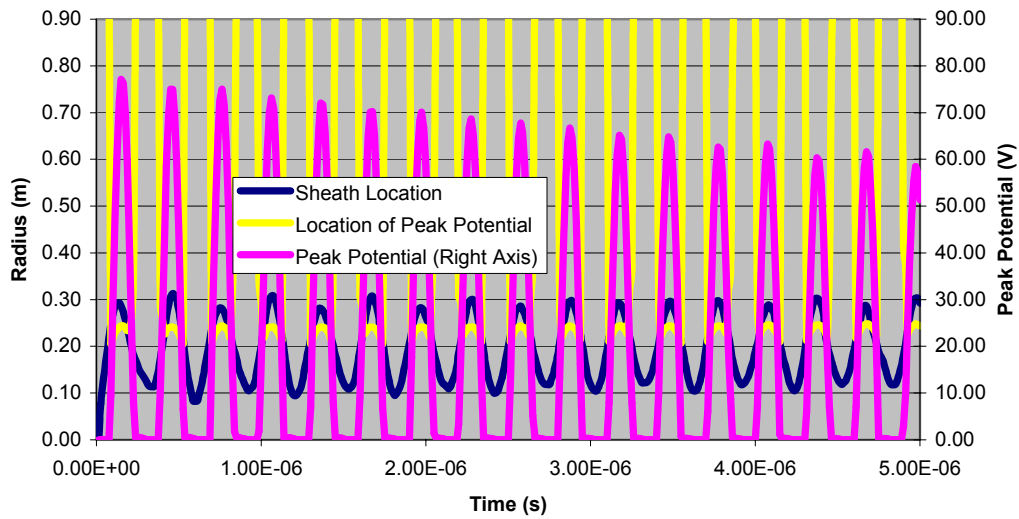
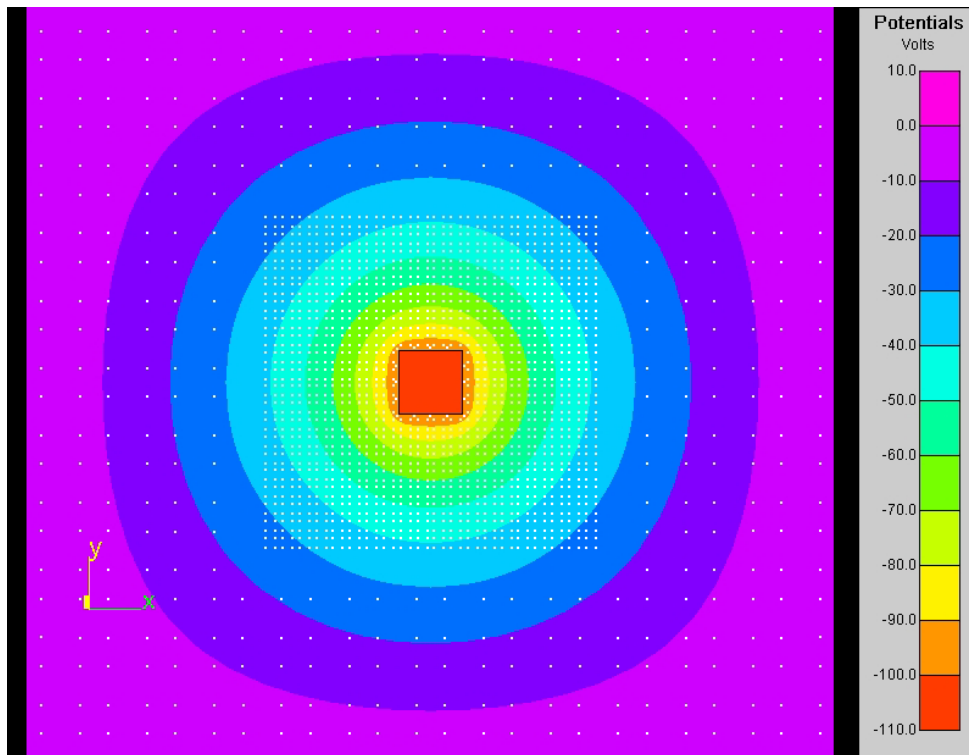**Figure 5. Same as Figure 3, for square wave and zero magnetic field.**
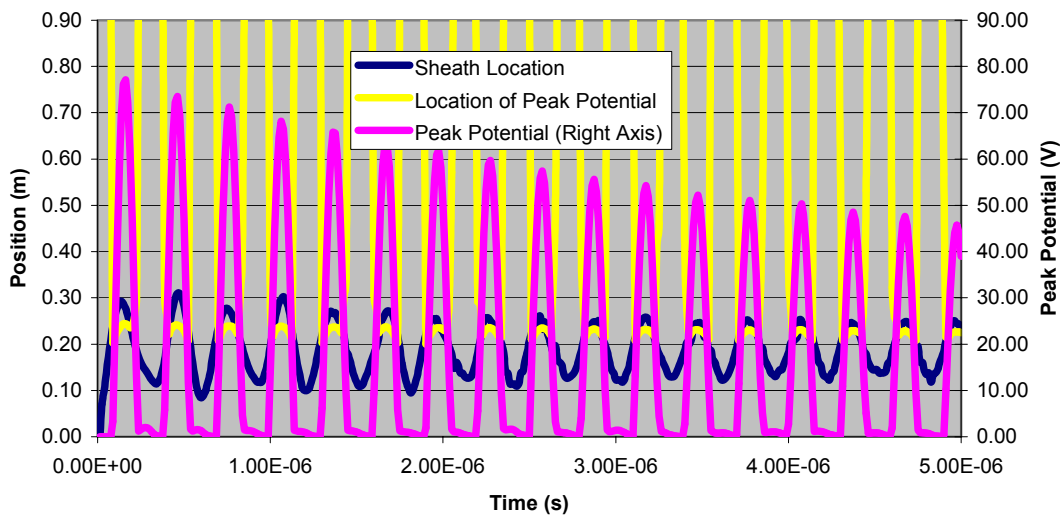
Figure 6. Same as Figure 3, for square wave with 0.5 gauss magnetic field.

Figure 7. Nascap-2k antenna model, showing antenna and gridding.

**Figure 8. Nascap-2k antenna model showing potentials and particle positions after 2.5 nanoseconds.**

Figure 9. Planar view of initial potentials and particles, as shown in Figure 8.
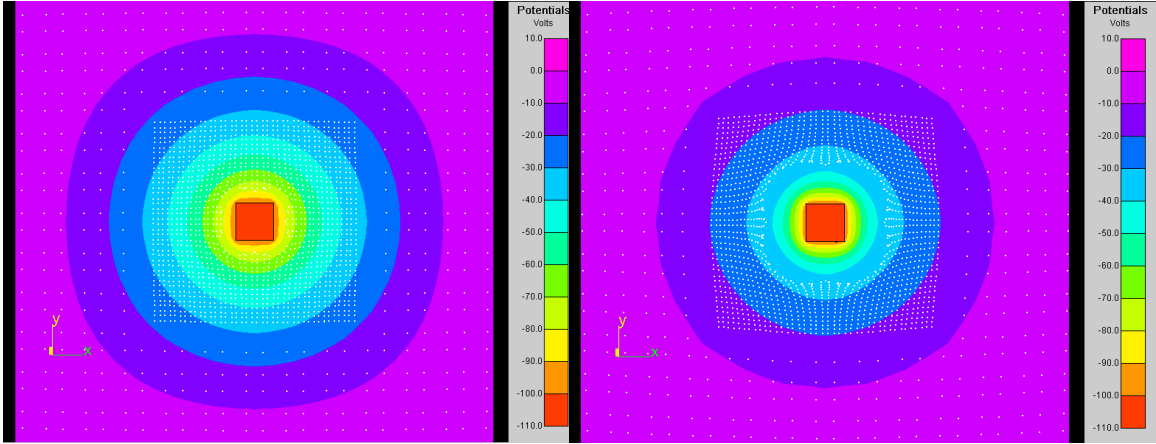
Figure 10. Particles and potentials after 25 nanoseconds (left) and 50 nanoseconds (right).
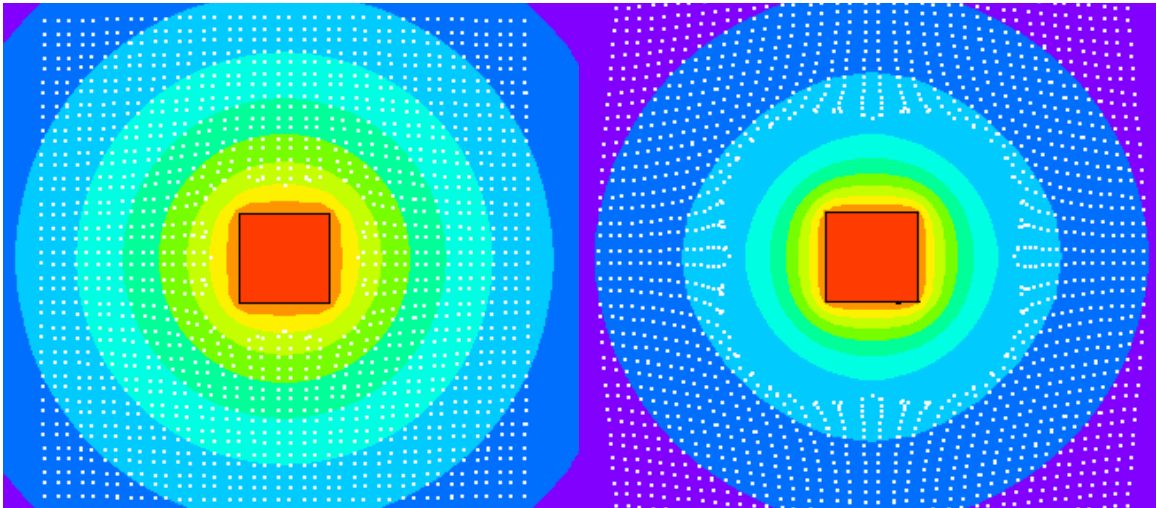
Figure 11. Blowup of Figure 10, showing a sheath radius of 9 cm after 25 nanoseconds (left), and about 18 cm after 50 nanoseconds (right).
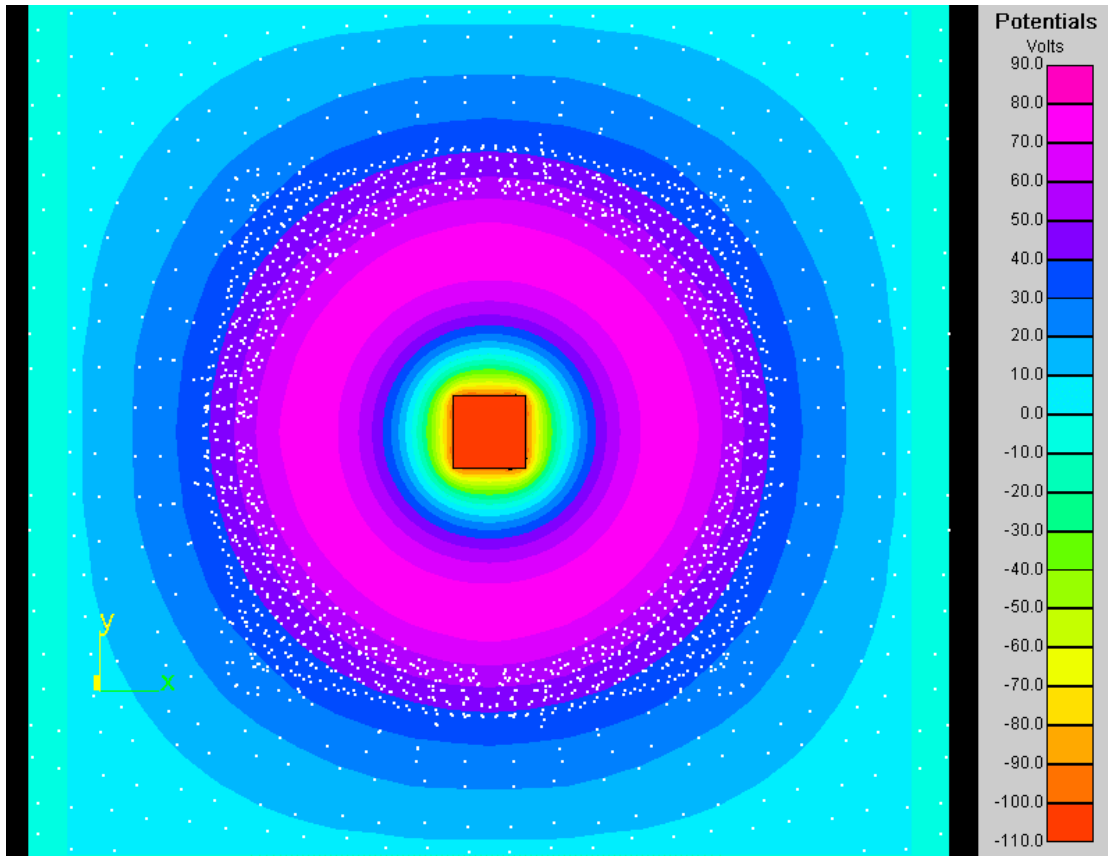
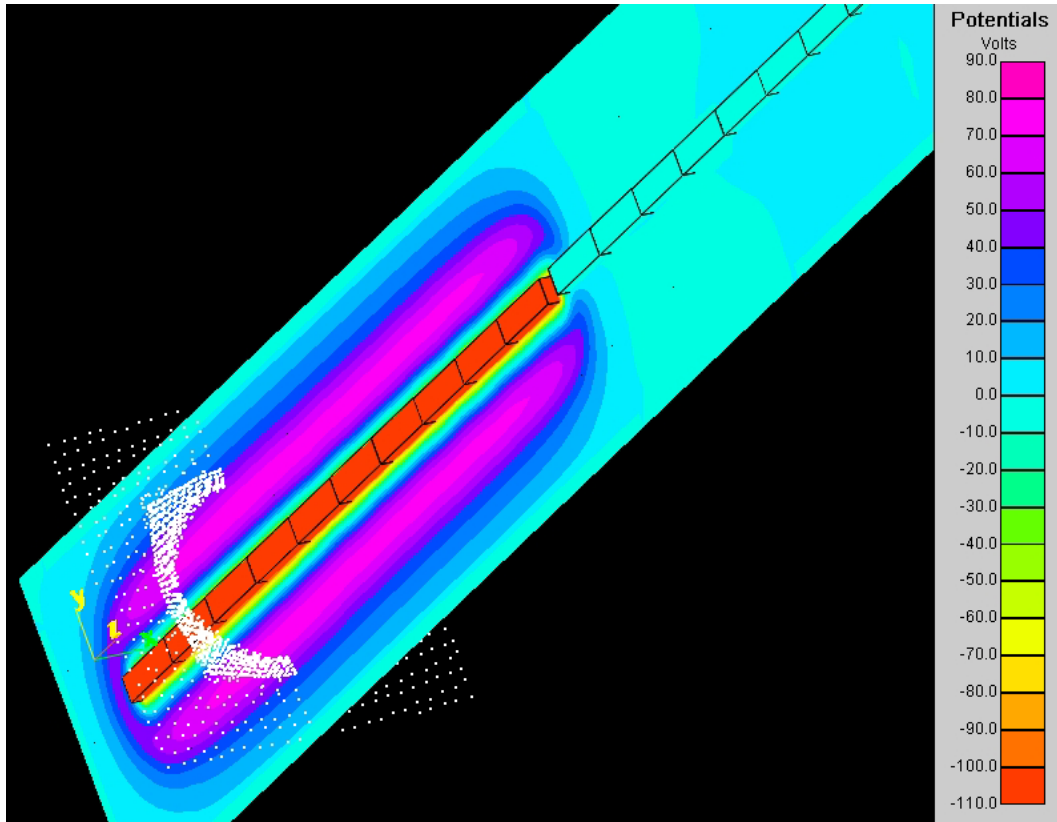**Figure 12. Potentials and particles at time of maximum positive potential.**

Figure 13. Another view of the final configuration (at 137.5 ns), showing potentials in a plane containing the antenna.
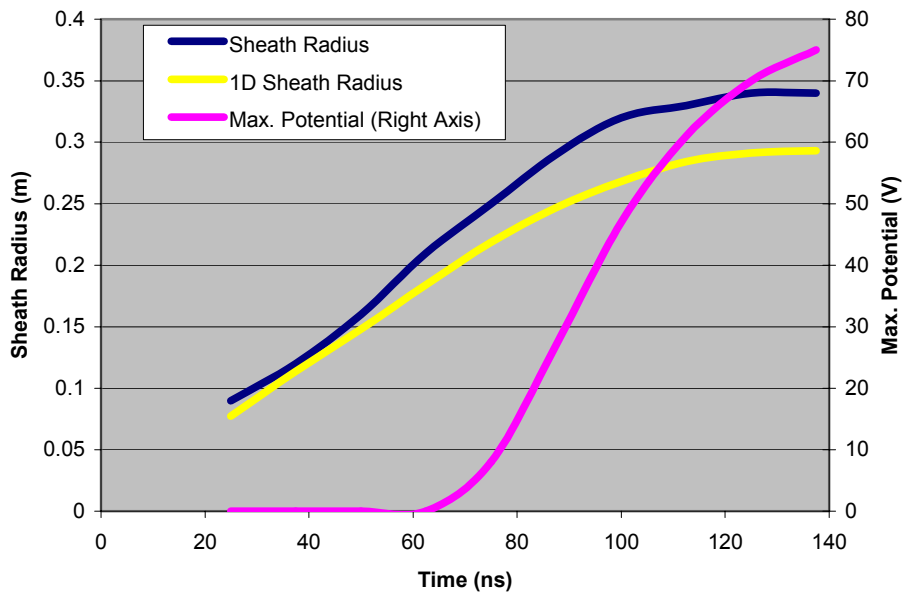

Figure 14. Nascap-2k results for sheath radius (dark curve) and maximum potential (magenta curve, right scale) compared with 1-D sheath radius results (yellow curve).

References

1. Cohen, H. A., F. M. Lehr and T. G. Engel (eds.), Spear II – High Power Space Insulation, Lubbock: Texas Tech University Press, 1995.

2. Davis, V.A., M.J. Mandell, D.L. Cooke and C.L. Enloe, "High-voltage interactions in plasma wakes: Simulation and flight measurements from the Charge Hazards and Wake Studies (CHAWS) experiment," Journal of Geophysical Research 104, No. A6, 12,445-12459, June 1999.

3. Inan, U. S., T.F. Bell, J. Bortnik and J.M. Albert, "Controlled precipitation of radiation belt electrons", Journal of Geophysical Research 108, No. A5, SMP 6-1, May 2003.

ASSESSMENT AND CONTROL OF SPACECRAFT CHARGING RISKS ON THE INTERNATIONAL SPACE STATION

Steve Koontz
NASA Johnson Space Center
Houston (JSC), Texas, USA
2101 NASA Road 1 Houston, TX 77058
Phone: 281-483-8860
E-mail: steven.l.koontz@jsc.nasa.gov

Mark Valentine
Thomas Keeping
Marybeth Edeen,
William Spetch
NASA Johnson Space Center

Penni Dalton
NASA Glenn Research Center

Abstract

The International Space Station (ISS) operates in the F2 region of Earth's ionosphere, orbiting at altitudes ranging from 350 to 450 km at an inclination of 51.6 degrees. The relatively dense, cool F2 ionospheric plasma suppresses surface charging processes much of the time, and the flux of relativistic electrons is low enough to preclude deep dielectric charging processes (1,2). The most important spacecraft charging processes in the ISS orbital environment are: 1) ISS electrical power system interactions with the F2 plasma, 2) magnetic induction processes resulting from flight through the geomagnetic field and, 3) charging processes that result from interaction with auroral electrons at high latitude.

Ironically, the cool, dense F2 plasma itself is necessary for the most important ISS spacecraft charging process identified to date. Electrical interactions between the F2 plasma and the 160 V photovoltaic (PV) electrical power system on ISS can produce significant electrical potential differences between ISS conducting structure and the surrounding ionospheric plasma, i.e. ISS floating potentials (FP). The negative-polarity-grounding scheme utilized in the 160 V PV power system leads naturally to negative FP values for ISS conducting structure. A negative FP results in the application of electrostatic fields across the dielectrics that separate ISS conducting structure from the ambient F2 plasma, enabling dielectric breakdown and arcing.   Degradation of thermal control coatings and noise in electrical systems can result. ISS is presently equipped two plasma contactor units (PCUs), each of which is designed to control ISS FP to within $\pm$ 40 V of the ambient F2 plasma during all phases of ISS construction and operations.

Recently, the continuing review and evaluation of putative ISS charging hazards required by the ISS Program Office revealed that ISS charging could produce an electrical shock hazard to the ISS crew during extravehicular activity (EVA).

ISS charging risks are being evaluated in an ongoing measurement and analysis campaign. The results of ISS charging measurements are combined with a recently developed model of ISS charging (the Plasma Interaction Model) and an exhaustive analysis of historical ionospheric variability data (ISS Ionospheric Specification) to evaluate ISS charging risks using Probabilistic Risk Assessment (PRA) methods. The PRA combines estimates of the frequency of occurrence and severity of the charging hazards with estimates of the reliability of various hazard controls systems, as required by NASA's safety and risk management programs, to enable design and selection of a hazard control approach that minimizes overall programmatic and personnel risk. The PRA provides a quantitative methodology for incorporating the results of the ISS charging measurement and analysis campaigns into the necessary hazard reports, EVA procedures, and ISS flight rules required for operating ISS in a safe and productive manner.

Introduction

Safety and reliability engineering for manned spaceflight is conducted in a regulatory environment, not unlike the regulatory environment that governs civil aviation, characterized by rules, processes, and procedures that may be very different from those applicable to robotic space flight programs or basic space science research projects. The identification, evaluation, and management of spacecraft charging risks for the ISS Program must be accomplished in a manner that is consistent with the regulatory environment that NASA has established for ISS design, development, and flight operations. Basic and applied science studies, flight operations data, and engineering analysis must be integrated in a balanced and objective manner so as to produce safety and reliability products that enable decision-making with a high degree of confidence. Both measurement data and engineering analysis must be subjected to validation and verification processes before acceptance for use in the development of safety engineering products. The safety and reliability products themselves are subject to an exhaustive programmatic review and approval processes. Because the likelihood of occurrence of any risk or hazard can never really be driven to zero, risk management is an essential part of the regulatory process and the question "how much risk is acceptable?" is important, as is the question "how is the risk accepted or declined?" Failure to integrate the science, engineering, operations, and management components of a manned flight risk assessment in an objective and balanced manner can be catastrophically costly. The Columbia Accident Investigation Board Report, Vol. 1, August 2003 provides a detailed example of such a failure.

The regulatory environment applicable to the ISS Program is defined in a series of Space Station Program (SSP) documents. Copies of the subject documents can be obtained from the authors on request, subject to U.S. export control regulations.

1) SSP-50200-01, <u>Space Station Program Risk Implementation Plan Vol. 1: Station Program Management Plan Annex E: Safety and Mission Assurance/Program Risk Plan, Revision A</u> Feb. 9, 2000

2) SSP-50021, <u>Safety Requirements Document</u> Dec. 12, 1995

3) SSP-50175, <u>ISS Risk Management Plan</u> April 10, 2002

4) SSP-30309, <u>Safety Analysis and Risk Assessment Document Rev. C</u> July, 1992

5) SSP-30599, <u>Safety Review Process, Rev. A</u> Jan. 11, 1995

NASA wide risk management and Probabilistic Risk Assessment (PRA) methods are defined in the NASA Headquarters requirements documents listed below.   PRA methods provide a rigorous logical and quantitative approach to answering the three most important questions that arise in the ISS spacecraft charging risk assessment: 1) "What is the likelihood of the hazardous condition?" 2) What is the severity of the consequences of an event caused by the hazardous condition and, 3) "what is the likelihood of failure of the hazard control system?"

1) NPG 71250.5A, <u>NASA Program and Project Management Processes and Requirements</u>

2) NPG 8000.4, <u>Risk Management Procedures and Guidelines</u>

3) NPG8705.x (draft), <u>PRA Applications and Guidelines</u>

ISS is pioneering the use of high-voltage, high power output, photovoltaic power systems on large spacecraft. Spacecraft charging as a result of interaction between photovoltaic electrical power systems with negative polarity grounds plagued early attempts to measure ionospheric temperature and density with satellite mounted Langmuir probes (3).   Therefore, the possibility of ISS spacecraft charging hazards or risks resulting from interactions of the 160 V PV array Electrical Power System (EPS) with the ionospheric plasma was recognized early in ISS development (4-13) and ISS is equipped with a ship set of two plasma contactor units (PCUs) (14, 15) to mitigate any possible charging hazards.

It should be noted that negative polarity grounding of the 160 V ISS PV EPS is only one component of the ISS spacecraft charging risk. The choice of thermal control coating on the micrometeoroid and orbital debris (MM/OD) shields employed on the NASA, ESA, and JAXA pressurized elements is an important factor in determining the magnitude of the possible hazards.

As an example, consider a spherical conducting structure that is 10 meters in radius (a reasonable size compared to ISS pressurized elements). If the free space capacitance (C_{fs} = $4\pi\varepsilon\varepsilon_o r$ = 1112 pF; ε = dielectric constant, ε_o = free space permittivity) of the structure is charged to -134 V, the stored energy is only $E = 0.5CV^2$ = 10 micro Joules.

Covering the sphere with a thin dielectric surface coating changes the character of the charging hazard dramatically. On the ram facing side of the sphere, the FP of the external surface of the dielectric film will approach 0 V as a result of positive charge collection from the ionosphere, and -134 V is applied across the dielectric.   Now the sphere is best described as a parallel plate capacitor (the conducting structure is one plate and the conducting ionosphere is the other) able to store energy

$$E = 0.5\ CV^2 = 0.5\ \varepsilon\varepsilon_o(A_{ram}/d)V^2\ =\ (0.5)(8.85 \times 10^{-12})\varepsilon(2\pi r^2/d)\ V^2,$$

where A_{ram} is the area of the hemisphere able to collect positive charge from the ionosphere. If d is 1 micron (1.3 microns is the thickness of the anodic coating on the US Lab and Node 1 meteoroid and debris shields) and $\varepsilon = 5$ for aluminum oxide, the stored energy becomes $E = 250$ Joules. Now, dielectric breakdown of the thin surface coating can discharge the parallel plate capacitor, releasing enough energy to damage the dielectric coating itself and producing enough voltage and current to present a possibly lethal hazard to any EVA crew who may become inserted into the discharge circuit as a result of arcing on exposed dielectric-coated metallic components on the EMU suit.   The high-density, low-resistance dielectric-breakdown arc plasma provides the conductive path connecting the negatively charged conducting structure to the positively charged dielectric film surface (5-8,11).

Note that the stored energy is inversely proportional to the dielectric film thickness. Simply increasing the film thickness from 1.0 micron to 100 microns reduces the stored energy from 249.5 Joules to 2.49 Joules while greatly reducing the risk of damage resulting from dielectric breakdown arcing and the current available for electric shock.   The thick (>120 microns) dielectric coatings on Sky Lab minimized any charging hazards that might have been generated by the 90 V PV array on that spacecraft. Similarly, the Russian elements of ISS and the ISS Truss Structure contribute little to the charging hazard because surface dielectric coatings are between 10 and 100m microns in thickness.

Stored energy is also directly proportional to V^2, and reducing the FP at the negative end of the PV array to –40V reduces the stored energy to 0.9 micro Joules for the uncoated conducting sphere, and 22 Joules for the dielectric coated sphere.

The ISS PV array design was subjected to extensive plasma chamber testing to assure that PV array damage due to arcing on the array was not an issue (9,10). Additional plasma chamber testing and analysis of structural and thermal control materials (5-8, 11) combined with the then limited flight data led to design requirements to control ISS structural floating potential to within ±40 V of the ambient plasma. More recently, the ISS FP requirement for control of the critical arcing hazard only during nominal flight operations has been changed. The new operational requirement, approved by the ISS Safety Review Panel (SRP), is that FP shall be no more negative than –60 V.

Two plasma contactor units (PCUs) designed to actively limit ISS FP to within ± 40 V of the ambient plasma, became part of the basic ISS design during 1990, thereby enabling the use of the negative polarity EPS grounding scheme at low risk by controlling ISS FP in a single-fault-tolerant fashion (14,15). At the time PCUs were adopted by the Program, only the critical hazard associated with dielectric breakdown arcing of specific thermal control coatings had been identified. Electrical interference with critical avionics and inadvertent firing of pyrotechnics as a result of surface dielectric breakdown arcing were both determined to be non-issues by the Russian and American Programs during the course of the safety review process before the first launch of 160 V PV array wings during late November 2000. Critical hazards require a single-fault-tolerant approach to hazard control, though either a zero-fault tolerant hazard control or no-hazard-control (i.e. acceptance or the risk) are also possible after exhaustive review and approval of a suitable Non-Conformance Report (NCR). The NCR quantifies the risk being accepted and justifies the approach, as required by SSP-50021, SSP-30309, and SSP-30599.

More recently, as a result of the continued review and assessment of spacecraft charging risks required by the ISS Program a possible catastrophic hazard, electrical shock to ISS crew during extra vehicular activity (EVA), was identified for the first time. ISS FP is required to be less negative than –40 V on all EVA translation paths and work sites during EVA. Catastrophic hazards require a two-fault-tolerant approach to hazard control, or a single-fault-tolerant hazard control with exhaustive review and approval of an NCR that quantifies the risk being accepted and justifies the approach.

PV array driven charging is only one contributor to possible ISS FP requirements violations. Magnetic induction potentials resulting from the flight of ISS thorough the geomagnetic field have been verified as an important contribution to FP as is shown in the following sections. Additional contributions to FP requirements violations can result of surface and structural charging following flight through auroral electron streams (16,17) though no direct observations of such charging have been made to date. Because PV array driven charging, magnetic induction potential charging, and auroral charging are independent processes to first order, the FP contributions of each simply add at any point on ISS.

Identified ISS Spacecraft Charging Hazards

The expectation or observed occurrence of spacecraft charging does not, in itself, constitute a risk or hazard requiring controls. Proper attention to electrical bonding and grounding practices (isolation of avionics from ground plane disturbances or radiated electromagnetic interference) during the design, development and test phase of a spaceflight program can effectively eliminate spacecraft charging concerns during flight operations. Adherence to the recommendations found in NASA Technical Paper 2361, Design Guidelines for Assessing and Controlling Spacecraft Charging Effects, (18) can eliminate most of the adverse effects of spacecraft charging events. Space Station Program Requirements for electrical grounding requirements (SSP-30240 Rev. C, Dec. 22, 1998) and electromagnetic compatibility (SSP-30423, Rev. E, June 9, 1998) assure that critical ISS avionics and pyrotechnics are not affected by spacecraft charging and dielectric breakdown arcing and the absence of such affects has been verified by testing. Slow degradation of the thin anodic thermal control coatings on the NASA, ESA, and JAXA pressurized elements as a result of dielectric breakdown arcing when FP is more negative than –60 V for long periods of time (> 6 months) is the only critical spacecraft charging hazard identified to date.

The design of the US extravehicular mobility unit (EMU) suit does not comply with the recommendations of NASA TP-2361, SSP-30240 or SSP-30423 as a result of necessary functionality and performance requirements. The only electrical connection between various large areas of partly exposed metallic conductors on the exterior of the suit is the astronaut's body. At the same time, stainless steel safety tethers assure that the astronaut can be grounded to ISS conducting structure in a variety of EVA configurations. It follows that an arc on one of several dielectric coated metallic EMU components can form an expanding, high-density arc plasma that moves outward and may provide a conducting path to discharge all or part of the NASA, ESA and or JAXA pressurized elements through the astronaut (5). The shock hazard to EVA crew is the only catastrophic ISS spacecraft-charging hazard identified to date. The FP control requirement that mitigates the hazard, FP no more negative than –40 V, is a requirement

established by NASA Flight Surgeons and is based on the minimum voltage necessary to drive a potentially lethal current through a perspiring (perspiration is a conductive electrolyte solution that reduces skin resistance dramatically) human being.

ISS Charging: in-Flight Observations and Data

PV array and magnetic induction driven charging of ISS has been the subject of numerous published studies both before and after the activation of the first set of 160 V PV array wings on ISS during early December of 2000 (4-15, 19-25).

PCU emission currents have validated the occurrence of the PV array driven charging mechanism, albeit with currents well below those expected before flight. PCU emission currents have also demonstrated the existence of substantial exposed conducting structure as a result of current collection enabled by magnetic induction voltages in ISS conducting structure.

As discussed below, flight measurement and analysis of U.S. Lab and Node 1 FP, with all FP controls disabled and PV array driven charging enabled, have not been more negative than –28 volts during 2001 (19-25).   Plasma chamber testing (5) has shown that the dielectric breakdown voltage for the 1.3-micron thick anodic film on the US Lab and Node 1 meteoroid and debris shields is more negative than -60 volts. Therefore, the PCU system has not been in continuous operation since May 2001.

The ISS FP not-to-exceed-limit for EVA safety is no more negative than –40 V, however, and two PCUs are operated routinely during EVA in a single-fault-tolerant hazard control strategy.   A two-fault-tolerant hazard control strategy is not required at this time because a PRA, demonstrating that the likelihood of violating the EVA safety FP requirement is less than 10^{-6} until the next set of 160 V PV array wings is installed on ISS (22-24), enabled approval of an NCR by the ISS Safety Review Panel. Floating Potential Probe measurements (19,20) were used to develop and partly validate a new charging model of ISS (22, 23, 25), which was used in conjunction with the recently developed ISS Plasma Environment Variability Specification (24) to demonstrate the very low likelihood of FP requirements violations.

PCU Emission Current Data

PCU emission current measurements have proven valuable in characterizing PV array driven and magnetic induction charging processes on ISS. PCU emission current from the ISS structural ground to the ambient ionosphere is measured with an LT-1006A operational amplifier in a linear current-to-voltage converter configuration calibrated so that an 8 V amplifier output corresponds to 12 amps of emission current. The amplifier is digitized for telemetry by a 12-bit analog to digital converter (with a sign bit) so that the least significant bit corresponds to 0.004 amps of emission current. The observed baseline noise during flight operations has been on the order of $\pm$ 0.005 amps with a zero offset of + 0.015 amps. Circuit analysis shows that the current-to-voltage converter circuit should be linear over the entire range from the noise band to 12 amps.

PCU emission current directly proportional to the net electron collection by the ISS PV-EPS system can be observed as abrupt increases in emission current at ISS orbital sunrise when the PV arrays are operating in sun tracking mode. Another means of measuring net PV-EPS electron collection is available via commanded full shunting of PV-array wings. Net PV-EPS electron collection measurements show the total amount of electron collection from the ionosphere that is not offset by conducting structure ion collection and as such is a good relative measure of the severity of the charging PV-EPS driven charging hazard.

Figure 1 shows measured eclipse-exit plasma contactor emission currents since January 2001. The eclipse exit emission currents show considerable variation both during a given 24-hour day and over the past 3 years. Large variations of Ne and Te with time of day, altitude, ISS latitude and longitude, geomagnetic field, solar activity, and season are expected and can explain much of the observed variability in the eclipse exit emission currents and the implied eclipse exit charging hazard. Detailed models of ISS PV array driven charging show that the magnitude of PV-array-driven charging will vary in a similar way with changes in the natural environment (22-25).
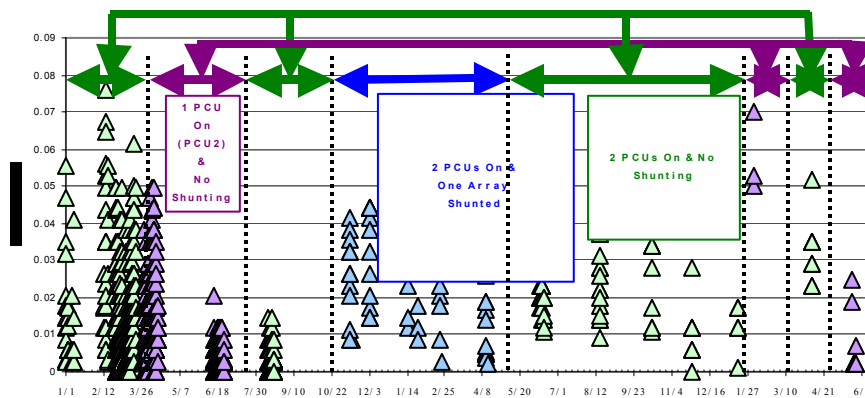
Figure 1. ISS plasma contactor emission current increase at eclipse exit: January 2001 to June 2003; US 160 V PV arrays, sun tracking and not shunted

The ISS PV arrays are automatically shunted whenever the ISS batteries are fully charged and ISS electrical loads do not demand full PV output. PV array wing full shunts can also be commanded from the ground. Commanding a shunt also provides a direct measure of the net PV array electron collection that isn't offset by ion collection by conducting surfaces. Figure 2 shows the orbital flight path corresponding to the commanded-shunting ISS telemetry data shown in Figures 3 and 4.

The top panel in Figures 3 and 4 shows the angular position of the individual PV array wings, P6-2B or P6-4B, in the ISS reference frame. The middle panel displays a number (PVCE-Error 3) that can be used to calculate the number of PV strings in each individual wing that are shunted at the indicated GMT time. The bottom panel shows the net PCU emission current from the ISS ground plane back to the ionosphere and including contributions from both 160 V PV array wings as well as ion and electron collection by ram oriented (i.e. forward facing) conducting structure.

Day 88 2001:88:20:04
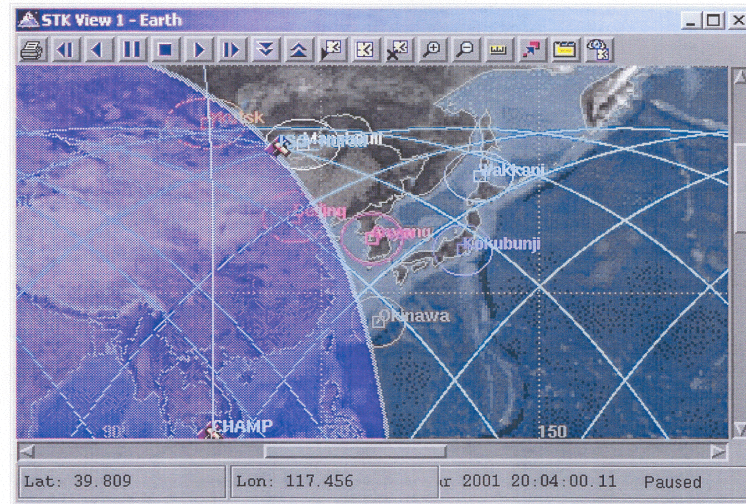
Figure 2. ISS orbital position and flight path corresponding to the commanded PV array shunt data shown in Figures 3 and 4.
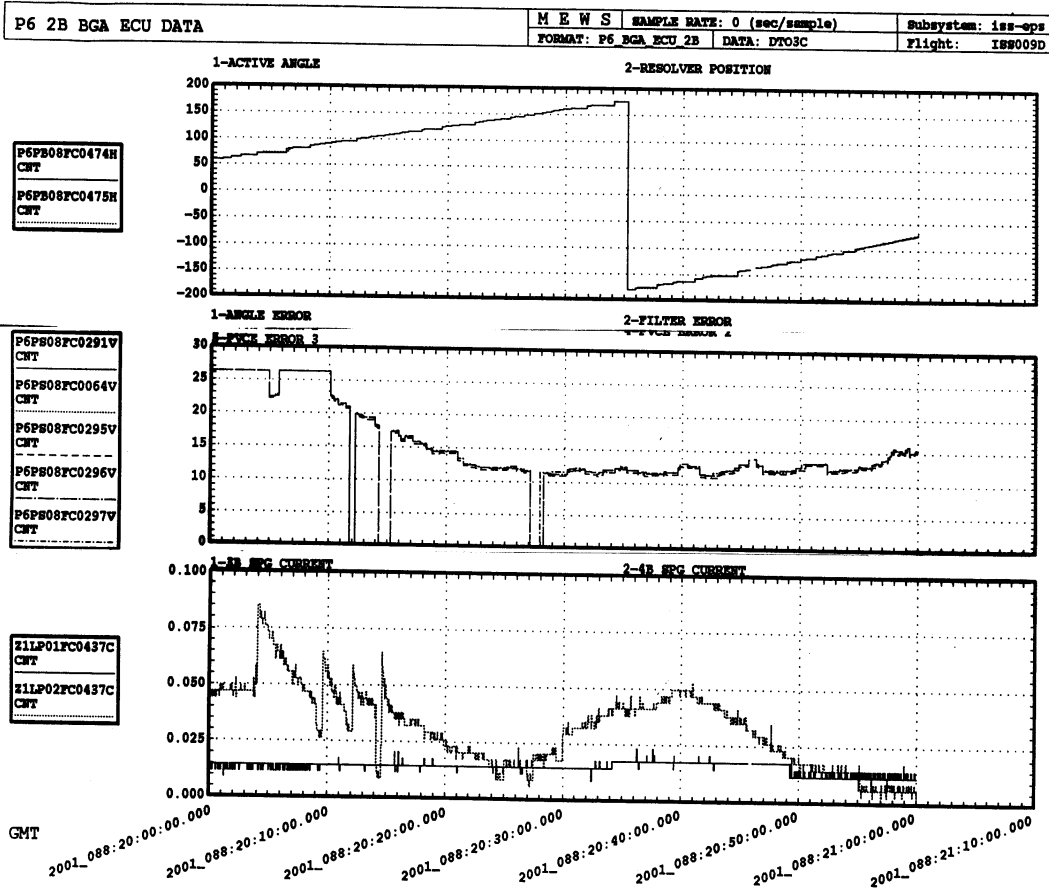
Figure 3: Changes in PCU emission current following commanded full-wing shunting of PV array wing P6-2B. Top panel – PV array wing angle in ISS coordinate system; Middle panel – Shunt voltage (0 = all PV strings shunted); Bottom panel – PCU emission current from ISS ground plane back to the ionosphere. PCU emission current contains contributions from PV array-EPS driven charging processes as well as current collection by ram oriented (forward facing) conducting structure biased by magnetic induction. Approximate number of un-shunted strings = 4.352 x (PVCE error – 4.66): PVCE < 5 => commanded shunt; all strings shunted.
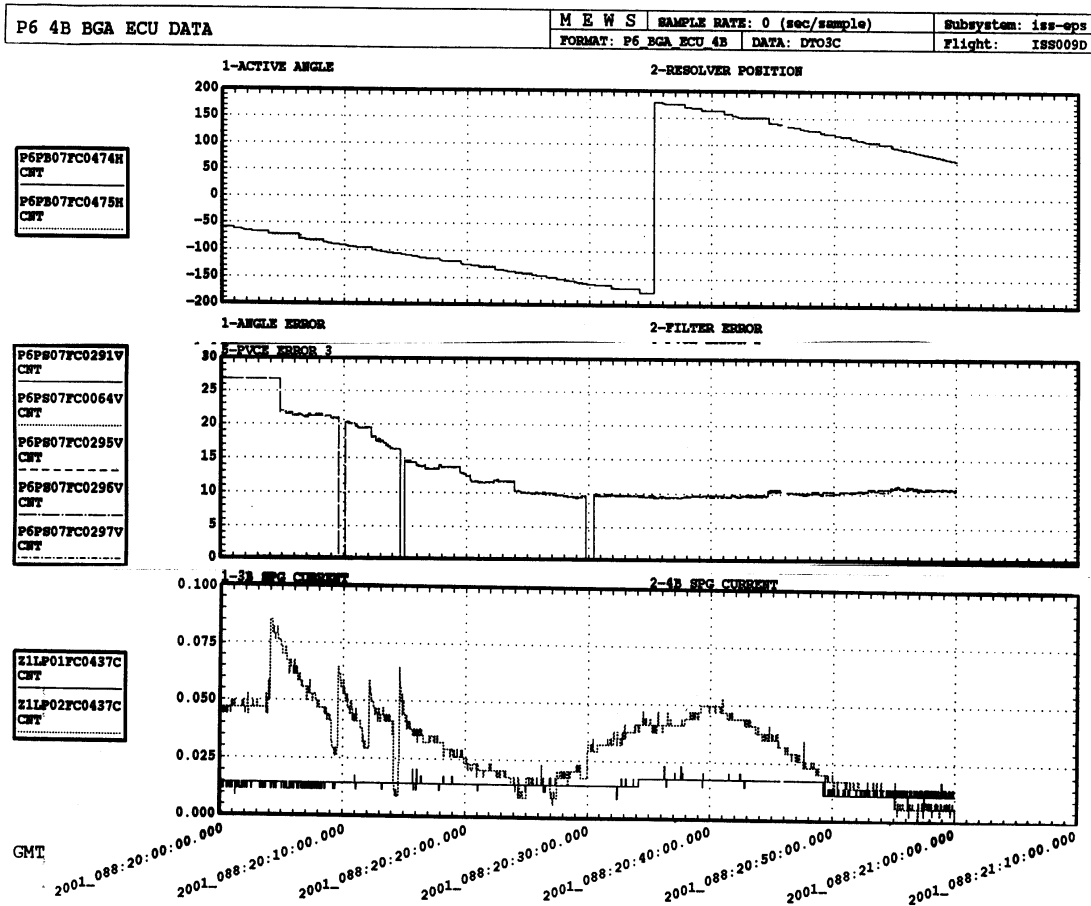
Figure 4: PCU emission current reductions associated with commanded shunting of PV array wing P6-4B. Top panel – PV array wing angle in ISS coordinate system; Middle panel – PV String Shunting PVCE = 0 => all PV strings shunted by command); Bottom panel – PCU emission current from ISS ground plane back to the ionosphere. PCU emission current contains contributions from PV array-EPS driven charging processes as well as current collection by ram oriented (forward facing) conducting structure biased by magnetic induction. Approximate number of un-shunted strings = 4.352 x (PVCE error – 4.66): PVCE < 5 => commanded shunt, all strings shunted.

The 160V ISS PV array cells are able to collect electron current from the ionosphere so as to contribute to charging hazards only when the active surface of the PV array is illuminated, not shunted, and not facing into wake. Figures 3 and 4 both show an abrupt increase in PCU emission current at eclipse exit (2001 88:20:04), (with an immediate small reduction in PVCE indicating that some strings were automatically shunted) with the active surface of the arrays facing forward, nearly perpendicular to the velocity vector. As the PV arrays track the sun past orbital noon (2001 88:20:36) the active surface the PV arrays turn into wake and further electron

collection by the PV array is suppressed. Beginning at 2001 88:30:00 electron collection by forward facing conducting structure becomes prominent again as it was at eclipse exit.

PCU emission current data needs accurate local environmental (Te, Ne) parameters quantitative interpretation. Nonetheless, the existence of the magnetic induction and PV array driven charging processes have been demonstrated and full wing commanded shunting and well as wake orientation have been shown to be viable non-PCU based charging hazard controls. The large changes in eclipse exit emission current, both seasonally and from orbit-to-orbit highlight the important role of environmental variability (24) in characterizing ISS spacecraft charging hazards. The hazards are not continuously present at a fixed level of severity and the hazards may disappear for considerable lengths of time. Therefore, likelihood of occurrence of the hazard as determined by PRA analysis becomes an important part of hazard characterization and control.

Floating Potential Probe Data

The results of in-flight floating potential probe (FPP) (19-25) measurements of ISS FP characterizing both the PV array driven charging process and the contribution of the **VxB$^.$L (V =** spacecraft velocity**, B** = geomagnetic field**, L** = length of conducting structure**)** magnetic induction voltages, with the plasma contactor system off, are shown in Figure 5 and Tables 1.

FPP measurements of ISS FP were made during several days in 2001, including intervals when the Space Shuttle was docked to ISS. On January 31, FPP data measurements of ISS FP were made with active side (the side with PV cell strings) of the active surface of the PV arrays in shallow wake flight attitude verifying that wake orientation of the arrays prevents PV array driven charging.

With the plasma contactor system off and PV arrays sun tracking, FPP data was collected on April 10-12, April 15, and on April 21 (before and after Space Shuttle docking).   A total of 46 FP measurements characterizing PV array driven charging were made in 2001, encompassing a wide range of ionospheric conditions.   Langmuir probe measurements of electron temperature, Te, at eclipse exit ranged from 0.08 to 0.23 eV while electron density, Ne, ranged from 10^9 to 10^{12}/m^3.   To date, the observed range of PV array-driven charging FP values range from –4 to –24 V.   It should be noted that the FPP could not provide Te or Ne if Fp exceeded –10V negative as a result of the limited range of the Langmuir probe sweep voltage.

The April 11 data is fairly typical, despite the geomagnetic storm starting about 13:30 universal time (UT).   Figure 5 shows the ISS FP at the FPP measurement point as a function of universal time on April 11, 2001. In Table 1 the total FP for the April 11, 2001 eclipse-exit charging peaks, shown in Figure 2, are broken down into the magnetic induction and PV array driven components for the locations on ISS defined in Figure 6.

Magnetic induction voltage is a significant fraction of the total FP in all cases, and must be considered in any ISS charging assessment. As shown in Figure 2, the agreement between calculated magnetic induction voltage and measurement is excellent in all cases.   Figure 6 shows a calculated magnetic induction voltage map of ISS when passing south of Australia on April 11,

2001. Flight south of Australia, in the flight attitude indicated in Figure 6, generates the more magnetic induction voltage on ISS than any other ISS flight path.

The data shown in Figure 5 and Table 1 span 6 orbits or 9 hours. During that time, the rotation of the Earth changed the geographic location of ISS eclipse exit from near the west coast of South America to Australia. The magnetic induction voltage peaks twice on each orbit, at $\pm$ 51.6 degrees latitude. Eclipse-exit PV array driven charging peaks are superimposed on the $-$ 51.6 latitude magnetic induction peaks. The $+$ 51.6 magnetic induction voltage peak occurs during eclipse. The measured FP consists only of magnetic induction voltage when ISS is in eclipse or when the PV arrays are shunted or in wake. When sun tracking, the active surface of the PV arrays move into wake at orbital noon. Figure 2 also shows a comparison of magnetic induction voltages calculated using a first principle model (22, 23, 25) with the flight data, demonstrating excellent agreement between the magnetic induction model and the flight data. The ISS magnetic induction voltage map shown in Figure 3 was calculated using the model (22, 23, 25).

Table 1: Post Eclipse Exit ISS Charging Peaks (maximum negative FP in volts) from Figure 2, April 11, 2001 at GMT time indicated (PCU system off)

12:38	2B	LAB	FPP	4B
vxB	2.034	-6.51	-3.42	-9.56
Chg	-19.6	-19.6	-19.6	-19.6
Total	-17.5	-26.1	-23.0	-29.1

14:10	2B	LAB	FPP	4B
vxB	2.571	-7.38	-4.19	-11.5
Chg	-17.0	-17.0	-17.0	-17.0
Total	-14.4	-24.4	-21.2	-28.5

15:41	2B	LAB	FPP	4B
vxB	2.812	-8.22	-4.96	-13.5
Chg	-15.2	-15.2	-15.2	-15.2
Total	-12.4	-23.5	-20.2	-28.7

17:15	2B	LAB	FPP	4B
vxB	3.429	-9.7	-6.55	-17.2
Chg	-7.0	-7.0	-7.0	-7.0
Total	-3.5	-16.7	-13.5	-24.2

18:46	2B	LAB	FPP	4B
vxB	3.775	-10.2	-7.35	-19.1
Chg	-4.7	-4.7	-4.7	-4.7
Total	-0.9	-14.9	-12.0	-23.8

20:18	2B	LAB	FPP	4B
vxB	3.903	-10.1	-7.65	-19.7
Chg	-5.2	-5.2	-5.2	-5.2
Total	-1.3	-15.3	-12.9	-25.0

Table 1 definitions: vxB=magnetic induction voltage; Chg=PV array driven charging; Total=vxB + Chg; For ISS locations 2B, 4B, Lab and FPP see figure 3
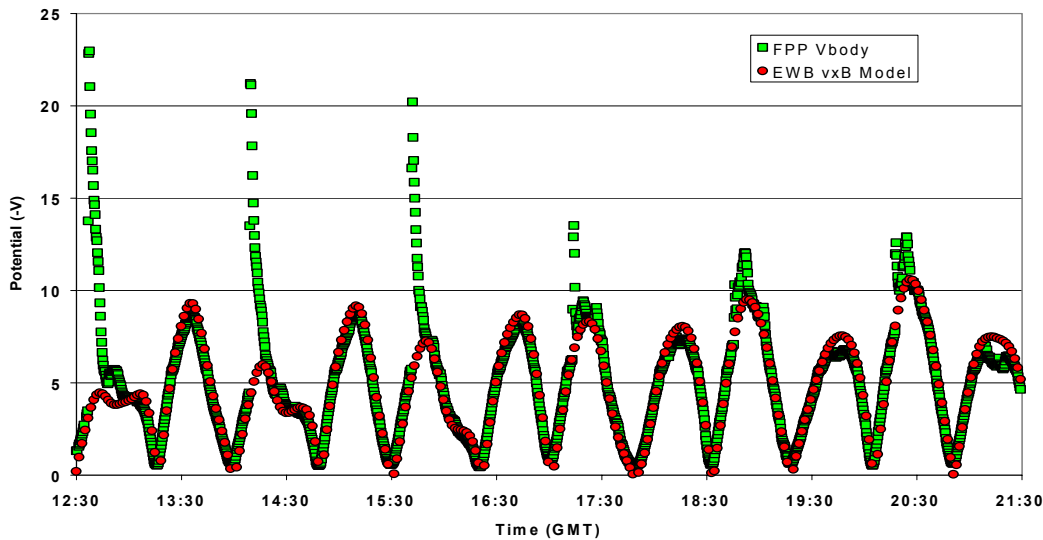
Figure 5: ISS FP at the FPP measurement point (FPP Vbody) with the plasma contactor system off. Calculated magnetic induction FP is compared with measured FP. April 11, 2001
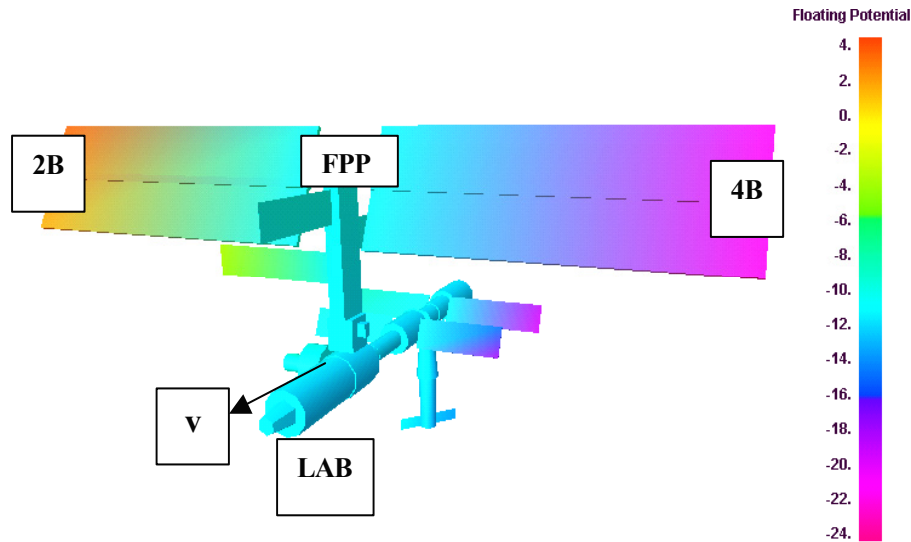
Figure 6: Calculated worst-case magnetic induction voltage map of ISS in +XVV flight attitude (velocity vector v), with 10 degrees down pitch. April 11, 2001

High Latitude Auroral Electron Charging

The possibility of spacecraft charging by auroral electrons at high latitudes, during geomagnetic storms or other geomagnetic disturbances, is a subject of some concern on the part of the spacecraft charging community (16,17, 26-30). Analysis of historical satellite charging and anomaly data for the United States Defense Meteorological Satellite Program (DMSP) satellites and the European Space Agency Freja satellite both suggest that auroral charging may be observed on ISS at high magnetic latitudes (26-30), especially at night during solar minimum. Charging of the Freja and DMSP vehicles has been correlated with ionospheric plasma densities of $10^4/cm^2$, or less, combined with fluxes of energetic auroral electrons (7-10 keV) greater than 10^8 electrons/(cm²sec sr) (26-30).   The DMSP and Freja satellites both orbit the Earth at or above 800 km, in the topside ionosphere, well above ISS operational altitudes.   Nonetheless, the required combinations of ionospheric plasma density and energetic electron flux are expected to occur at ISS altitudes, albeit infrequently, at or near the extreme latitudes of the ISS orbit ($\pm$ 51.6°).   Inspection of the auroral precipitation maps produced hourly by the US National Oceanics and Atmospherics Administration (NOAA) Polar Orbiting Environmental Satellite (POES) constellation show that ISS passes through the precipitating auroral electrons several times every day, whenever ISS passes south of Australia at night and Kp is greater than about 4 (31).

The question of whether or not flight through the same kind of environment that produces charging and the occasional recoverable anomaly on DMSP constitutes a risk or hazard for ISS or ISS EVA crew remains open. The absence of severe anomalies on the Freja spacecraft in a similar, if not more severe, charging environment highlight the important effect of spacecraft design on spacecraft charging effects.   More detailed assessments of the frequency of

occurrence of the auroral charging environment at 350 to 400 km altitude as well as detailed analysis and modeling of the expected ISS and EVA suit charging processes in that environment are in work at this time.   ISS and the EVA suits used on ISS are not identical to DMSP or Freja, when treated as electrical systems interacting with the auroral charging environment. Materials properties and materials interactions with the auroral charging environment will likely determine the outcome of the assessments. Secondary electron yields, dielectric coating thickness compared to energetic electron range, and total area of exposed conducting surfaces and vehicle or subsystem capacitance are all important factors.   The ISS plasma contactor system also contributes to control of any auroral charging risk by both increasing local plasma density and providing a return path to the ionosphere for any charging of ISS conducting structure produced by auroral electrons.

During the first two years of flight (during the current solar maximum), no ISS equipment anomalies have been reported that correlate with geomagnetic storms or flight through either the diffuse or visible auroras.   The ISS crews have reported flying through visible Aurora Australis on at least two occasions. The following excerpt from Commander William Shepherd's deck log of Nov. 10, 2000 is an interesting example.

"11:30: Transited through a very unusual aurora field. Started as a faint green cloud on the horizon, which grew stronger as we approached. Aurora filled our view field from SM (Service Module) nadir ports as we flew through it. A faint reddish plasma layer was above the green field and topped out higher than our orbital altitude."

Figure 3 shows southern hemisphere auroral precipitation maps produced by NOAA POES Satellites 15 (Nov. 10, 2000 10:56 UT) and 16(Nov. 10, 2000 12:26 UT). Both NOAA SEC satellites show auroral activity levels of 9 and hemispheric powers of 60 to 90 gigawatts, resulting from relatively intense diffuse auroral electron precipitation over Tasmania and southern New Zealand showing that that ISS was well within the precipitating electron environment during the visible auroral arc fly through reported by Cmdr. Shepherd (31).   Figure 8 shows an aurora over Greenland photographed by Cmdr. Culbertson during ISS expedition 3.
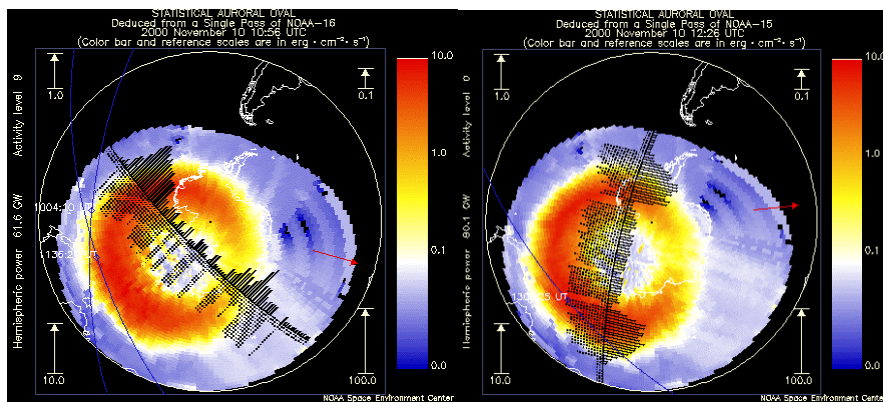
Figure 7. Statistical auroral oval with ISS and NOAA-15 and NOAA-16 ground tracks on November 10, 2000.

Figure 8: Photograph of Auroras over Greenland taken from the ISS Service Module by Cmdr . Frank Culbertson during Expedition 3.

Managing ISS Charging Risks: Probabilistic Risk Assessment (PRA)

The variability of the environment and the resulting variability in the severity of ISS spacecraft charging risks as well as realistic concerns about the reliability of the hazard control hardware leads naturally to the use of Probabilistic Risk Assessment methodology for both assessing and mitigating charging risks.

The ISS Plasma Hazard Evaluation Process (PHEP) consists of five major components all of which provide input into the PRA product.

1) The Floating Potential Measurement Unit (32) – A recently developed flight instrument designed to measure FP along with Te and Ne.   The data from the FPMU is subject of several stages of validation screening, beginning with parity error checks on telemetry data, continuing with quality-of-fit screening applied to the theoretical relationships to which flight data is fitted for reduction and analysis and completing with comparisons with measurements made on other spacecraft or by ground based incoherent scatter radar facilities. The FPMU is not used for validation of hazard control systems during EVA because the instrument only shows that at least one hazard control is operating when the requirement is for verification of either a single-fault or a two-fault tolerant hazard control system. The FPMU can and will be used for periodic functionality checks on individual hazard controls. The prime function of the FPMU is to provide data to validate the Plasma Interaction Model.

2) The Plasma Interaction Model (22, 23, 25) – Simple FPMU measurements on a given day or over a given limited time frame do not provide a reliable indication of the severity of the hazard simply because the environmental factors causing the hazard are so variable. In order to calculate the frequency of occurrence of FP requirements violations a validated model providing reasonably accurate predictions of ISS FP given ISS configuration, attitude, flight path, and flight environment is needed. FPMU data will be used to validate the charging model and only then can the frequency of occurrence of the FP requirements violation can be

calculated using the frequency of occurrence of the environmental conditions leading to the violation. If model validation is not possible then no relaxation of the two-fault-tolerant hazard control based on low likelihood of FP violations is possible.

3) The Specification of ISS Plasma Environment Variability (24) provides the likelihood of occurrence of flight environments corresponding to various levels of charging risk. The specification is based on a critical evaluation and statistical analysis of all available satellite and ground based data applicable to the ISS charging problem.

4) Critically evaluated and statistically valid test data (33) determining the arcing threshold for various materials on the ISS outer surface and on the outer surface of the EMU suit are essential for setting meaningful FP requirements needed for definition of effective hazard mitigation.

5) Probabilistic Risk Assessment provides the methodology needed to logically characterize the necessary and sufficient conditions for a hazard to exist, evaluate the likelihood of occurrence of FP requirements violations, and assess the reliability of the ISS electrical power system and command and data handling components that comprise the hazard control system.   If the likelihood of hazard control failure is low enough then a single-fault-tolerant hazard control system can be deemed adequate for mitigation of a catastrophic hazard, even if the likelihood of occurrence of the hazard itself is high enough to require a two-fault-tolerant approach.

These five essential components are assembled in the PHEP to produce the hazard reports, flight rules and procedures that assure the lowest risk and highest benefit for the ISS vehicle and ISS crew.

References

1. NASA Technical Memorandum 4527; <u>Natural Orbital Environment Guidelines for Use in Aerospace Vehicle Development</u>; Anderson, Jeffery B., Editor; Smith, Robert E., Compiler; June 1994

2. <u>Handbook of Geophysics and the Space Environment</u>; Jursa, Adolph S., Editor, Air Force Geophysics Laboratory, Air Force Systems Command, United States Air Force, 1985

3. Brace, Larry H.; "Langmuir Probe Measurements in the Ionosphere," in <u>Measurement Techniques in Space Plasmas: Particles</u> Geophysical Monograph 102, American Geophysical Union, 1998, page 33.

4. Garrett, H. B., Whittlesey, A. C.; "Spacecraft Charging, An Update," AIAA 96-0143, 34th AIAA Aerospace Sciences Meeting and Exhibit, 15-18, January 1996, Reno Nevada

5. Vaughn, J.A., Carruth, M. R., Katz, I., Mandell, M., Jongeward, G. A.; "Electrical Breakdown Currents on Large Spacecraft in Low Earth Orbit," J. Spacecraft and Rockets, Vol. 31, No. 1, January-February 1994, pp 54-59

6. Snyder, David B.; "Dynamic Interactions Between Ionospheric Plasma and Spacecraft," The Radio Science Bulletin, No. 274, Sept, 1995, pp 29-36

7. Ferguson, D. C., Hillard, G. B.; "In Space Measurement of Electron Current Collection by Space Station Solar Arrays," AIAA 95-0486, 33rd Aerospace Sciences Meeting and Exhibit, January 9-12, 1995, Reno NV.

8. de la Cruz, C. P., Hastings, D. E., Ferguson, D., Hillard, B.;"Data analysis and model comparison for Solar Array Module Plasma Interactions Experiment," J. Spacecraft and Rockets, Vol.. 33, No. 3, pp 438-446, May-June 1996

9. Hastings, D. E., Cho, M., Kuninaka, H., "The Arcing Rate for a High Voltage Solar Array," Journal of spacecraft and Rockets, 29, No.4, 538-554, 1992

10. Hastings, D. E.; "A Review of Plasma Interactions with Spacecraft in Low Earth Orbit," Journal of Geophysical Research, 100, No. A8, PP. 14457-14484, 1995

11. Galofaro, J. T., Doreswaamy, C. V., Vayner, B. V., Snyder, D. B., Ferguson, D. C.; "Electrical Breakdown of anodized Structures in a Low Earth Orbit Environment," NASA/TM – 1999-209044, April, 1999

12. Vayner, B. V., Galofarno, J., Ferguson, D. C., de Groot, W., Thompson, C., Dennison, J. R., Davis, R.; "The Conductor- Dielectric Junctions in a Low Density Plasma," NASA/TM – 1999-209408, Nov. 1999

13. Murphy, G., Croley, D., Ratliff, M., Leung, P.; "The Role of External Circuit Impedance in Dielectric Breakdown," AIAA 92-0821, 30th Aerospace Sciences Meeting and Exhibit, Jan. 6-9, 1992/Reno, NV

14. Patterson, M. J., Verhey, T. R., Soulas, G., Zakany, J.; " Space Station Cathode Design Performance and Operating Specifications," IEPC Paper Number 97-170, 25th International Electric Propulsion Conference, Cleveland Ohio, Aug. 1997.

15. Lambert, J. C., Chaky, R. C.; "The ISS Plasma Contactor," AIAA 96-0627, 34th Aerospace Sciences Meeting, Jan. 15-18, 1996, Reno NV.

16. Minow, J. I., Neergaard, L. F., Maurits, S., Hwang, K., Suggs, R. M.; "High Latitude Plasma Electrodynamics and Spacecraft Charging in Low-Earth Orbit," ESA/SCTC, 23-27, April, 2001

17. Purvis, C. K., Snyder, D. B., Jongeward, G. A.; "Auroral Interactions with ISSA," NASA Technical Memorandum 106794, December 1994

18. Purvis, C. K., Garrett, H. B., Whittlesey, A. C., Stevens, J. N.; Design guidelines for Assessing and Controlling Spacecraft Charging Effects, NASA Technical Paper 2361, 1984

19. Ferguson, D. C., Morton, T. L., Hillard, B. G.; "First Results from the Floating Potential Probe (FPP) on International Space Station," AIAA-2001-0402, 39th Aerospace Sciences Meeting and Exhibit, Jan.   2001, Reno, Nevada

20. Morton, Tl L., Minow, J. I.; "Floating Potential Langmuir Probe Data Reduction Results," AIAA-2002-0936, 40th AIAA Aerospace Sciences Meeting and Exhibit, 14-17, January 2002, Reno Nevada

21. Bering, E. A., Koontz, S., Katz, I., Gardner, B., Evans, D., Ferguson, D.; "The Plasma Environment of the International Space Station in the Austral Summer Auroral Zone Inferred from Plasma Contactor Data," AIAA 0220-0935, 40th AIAA Aerospace Sciences Meeting and Exhibit, 14-17, January 2002, Reno Nevada

22. Mikatarian, R.R., Kern, J.W., Barsamian, H.R. and Koontz, S.L., "Plasma Charging of the International Space Station", IAC/COSPAR World Space Congress, Houston, Texas, October 2002

23. Mikatarian, R.R., Barsamian, H., Alred, J., Minow, J., Koontz, S; "ISS Plasma Interactions: Measurements and Modeling," Proceedings of the 8th International Spacecraft Charging Conference, Oct. 20-24, 2003, Huntsville Alabama, USA

24. Minow, J. I., Neergaard, L., Bui, T. H., Mikatarian, R. R., Barsamian, H., Koontz, S., "Specification of ISS Plasma Environment Variabilit," Proceedings of the 8th

International Spacecraft Charging Conference, Oct. 20-24, 2003, Huntsville Alabama, USA

25. Gardner, B., Mandell, M. J., Davis, V. A., Jongeward, G. A.; "Electron Collection by International space Station Solar Arrays," Proceedings of the 8th International Spacecraft Charging Conference, Oct. 20-24, 2003, Huntsville Alabama, USA

26. Martin, A. R.; "Spacecraft/Plasma Interactions and Electromagnetic Effects in LEO and Polar Orbits," Final Report for ESA/ESTEC Contract Number 7989/88/NL/PB(SC), Vol. 3, 1991

27. Cooke, D. L.; "Simulation of an Auroral Charging Anomaly on the DMSP Satellite," 6th Spacecraft Charging Technology Conference, AFRL-VS-TR-20001578, 1 Sept., 2000

28. Gussenhoven M. S., Hardy, D. A., Rich, F., Burke, W. J.; Yeh, H-C.; "High-Level Spacecraft Charging in the Low-Altitude Polar Auroral Environment," Journal of Geophysical Research, Vol. 90, NO. A11, 11,009-11-023, November 1985

29. Wahlund, J-E., Wedin, L. J., Carrozi, T., Eriksson, A. I., Holback, B. Anderson, L., Laakso, H.; "Analysis of Freja Charging Events: Statistical Occurrence of Charging Events," WP-130 Technical Note (SPEE-WP130-TN), Version 2.0, ESA contract 11974/96/NL/JG(SC), 22 February, 1999

30. Stevens, N. J., Jones, M. R.; "Comparison of Auroral Charging Predictions to DMSP Data," AIAA 95-0370, 33rd Aerospace Sciences Meeting and Exhibit, January 9-12, 1995, Reno NV.

31. **http://www.sec.noaa.gov/pmap/**

32. Swenson, C. M., Barjatya, A., Thompson, D., Fish, C.; "Calibrating the floating Potential Measurement Unit," Proceedings of the 8th International Spacecraft Charging Conference, Oct. 20-24, 2003, Huntsville Alabama, USA

33. Schneider, T. A., Carruth, M. R., and Hansen, H.: "Minimum Arc Threshold Voltage Experiments on Extravehicular Mobility Unit Samples," 40th AIAA Aerospace Sciences Meeting, Reno, NV, January 14-17, 2002, AIAA 2002-1040.

ISS PLASMA INTERACTION: MEASUREMENTS AND MODELING

H. Barsamian
International Space Station Environments
The Boeing Company
13100 Space Center Blvd, Mail Stop: HB3-20
Houston, Texas 77059-3556
Phone: (281) 226-6734
Fax: (281) 226-6099
E-mail: Hagop.R.Barsamian@boeing.com

R. Mikatarian
J. Alred
The Boeing Company

J. Minow
Jacobs Sverdrup

S. Koontz
NASA Johnson Space Center

Abstract

Ionospheric plasma interaction effects on the International Space Station are discussed in the following paper. The large structure and high voltage arrays of the ISS represent a complex system interacting with LEO plasma. Discharge current measurements made by the Plasma Contactor Units and potential measurements made by the Floating Potential Probe delineate charging and magnetic induction effects on the ISS. Based on theoretical and physical understanding of the interaction phenomena, a model of ISS plasma interaction has been developed. The model includes magnetic induction effects, interaction of the high voltage solar arrays with ionospheric plasma, and accounts for other conductive areas on the ISS. Based on these phenomena, the Plasma Interaction Model has been developed. Limited verification of the model has been performed by comparison of Floating Potential Probe measurement data to simulations. The ISS plasma interaction model will be further tested and verified as measurements from the Floating Potential Measurement Unit become available, and construction of the ISS continues.

Introduction

The International Space Station (ISS) becomes electrically charged due to electron collection by the exposed positively charged edges of solar cells in its photovoltaic (PV) arrays. This electron current collected depends on the temperature and density of the ionosphere plasma. A Floating Potential Probe (FPP) flown on ISS in 2001 showed that the highest charging voltages occurred at orbital eclipse exit. Modeling of the charging process shows that high voltages require a combination of low electron temperature and high plasma density. For hazard

management and operational control, the ISS program needs methods for predicting charging voltages for the different ISS configurations through Assembly Complete.

Therefore, the charging of ISS surfaces with respect to the plasma in lower earth orbit occurs due to the main following mechanisms:

- Induction electric potentials (v×B·L) due to the motion of the spacecraft relative to the ambient plasma in the earth's magnetic field

- Electron collection on the edges of positively charged photovoltaic (PV) cells in the solar arrays

- Electron loss to the ambient plasma due to recombination with plasma ions on electrically conducting surfaces of the spacecraft

- Second order effects including electron loss due to photoemission and secondary emission

The variability of plasma parameters (electron-ion density, electron and ion temperatures, and spacecraft velocity relative to the plasma) results in substantial variations of charging with solar cycle, space weather, solar illumination, vehicle configuration, vehicle material and construction, and operational configuration and orientation.

The following paper addresses these mechanisms and applies them to give predictions of charging on the ISS. Each of these mechanisms is discussed below. Some discussion of on-orbit measurements is given followed by the introduction of the ISS plasma interaction model. Results of model predictions are followed by a brief section of the variability of plasma parameters.

On-Orbit Measurements

The FPP flown on ISS Flight 4A provided measurements of on-orbit structure potential from December 2000 to April 2001. The FPP device failed after April 2001 from unknown causes. This device also provided Langmuir probe plasma density and temperature measurements. At charging peaks, FPP Langmuir probe measurements of plasma density and temperature data suffered telemetry dropout when the FPP voltage went below –10V.[1,2]

When the PCUs are off, the FPP shows negative voltage spikes at ISS eclipse exit. The maximum voltage measured at the FPP in 2001 was –23V, including (v×B·L) induction potentials (Figure 1). This charging of ISS results from electron collection on the PV arrays. The transient nature of the charging was unanticipated, as was the low magnitudes of the peak voltages. Also, unanticipated were the small values of the PCU emission currents (< 0.1A compared to expected values of about 1A). Figure 2 shows that with the PCUs activated, the ISS structure voltages clamp at low values, consistent with (v×B·L) induction potentials. PCU #2 discharge current over an orbit is shown in Figure 3. The current does not exceed 100mA. The figure also delineates the International Reference Ionosphere (IRI 2001) electron temperature

prediction. The electron temperature increase at eclipse exit is consistent with peak eclipse exit potential decrease as indicated in Figure 1.

Early program modeling of the PV array electron collection gave relatively large collection currents, predicting large PCU emission currents with PCUs on. With PCUs off, large electron collection currents result in large negative potentials unless electron loss mechanisms are available to offset electron collection. Electron collection occurs on the exposed, positively charged edges of solar cells in gaps between cells on ISS arrays.

Electron collection is enhanced by a condition known as "snapover" which increases the effective collecting area of the arrays. Snapover is a condition of increased electrical conductivity of the array surface, resulting from a high positive bias voltage on the solar cells. This condition was assumed for both gap and exterior surfaces of the arrays in the first analytical model of electron collection. Felder, et al. (1993) estimated the threshold for snapover of the ISS PV arrays at 160V.[3]

Early modeling of ISS plasma interactions neglected electron loss mechanisms to estimate upper limits for PCU emission currents for design purposes. The present model incorporates an "ion collection" area that summarizes the various electron loss mechanisms in a single term. Electron loss mechanisms are described in the next section.

Plasma Interaction Model

The Plasma Interaction Model (PIM) results from a collaboration between The Boeing Company and SAIC (under subcontract to The Boeing Company). Figure 4 gives a schematic of the PIM. Input parameters for the PIM consist of the environmental parameters (Te, Ne and B), the vehicle's location in latitude, longitude and altitude, the configuration of the PV arrays (shunt configuration and array position angles) and the ion collecting area and current-voltage relation. Collection of electrons and ions on the arrays, masts[4] and structure are indicated as contributing to the total current to the vehicle. The induction voltage arising from the motion of the vehicle through the ionospheric plasma and the geomagnetic field contributes to the vehicle potential for both quasi-steady and time-dependent cases. This potential, due to Faraday's Law, is (v×B·L).

A small negative potential ($\sim-0.2V$) arises in the model due to the difference between ion and electron fluxes at the surfaces of the solar cell cover glasses. This potential prevents electron collection everywhere except between cell gaps. Both analytic and numerical-simulation solutions support this model of electron collection on the PV arrays.[5,6] This methodology is discussed in Mikatarian, et al. (2002).[7]

There are a number of mechanisms available to reduce ISS' net electron collection and therefore the magnitude of the negative structure potential. These include (** second order effect for ISS):

- Electron recombination with thermal or ram ions on conducting vehicle surfaces, including conducting wires in the PV array mast structures (also called "ion collection")

- Electron loss or ion collection at gaps between solar cells with low positive potentials in PV arrays

- Ion collection by conducting, grounded materials on vehicle thermal blankets, connectors, etc.

- Photo-emission of electrons due to solar UV radiation **

- Secondary electron emission due to energetic electron or ion impacts **

- Field emission from charging to keV potentials by energetic electrons (auroral charging) **

Any electron loss or ion collection mechanism reduces the net electron current available to charge the vehicle structure. Evaluating these mechanisms, we find that electron loss through ion collection dominates.

Treating the totality of electron loss and ion collection mechanisms as a single "effective ion collection area", a value of about $35m^2$ minimizes the differences between FPP measurements and model–calculated values. Conducting areas are most likely found on ISS pressurized elements, near the centerline of the ISS configuration through Flight 12A. The electrical effect of this area is to ground the ISS to the ambient plasma near the centerline of the vehicle.

Analysis

Some of the pertinent input parameters to the PIM discussed above are shown in Figure 1. The parameters are plotted against FPP measurements. The parameters shown here include the PV array normal to the ISS velocity vector, the latitude and longitude variation and the number of strings shunted on each of the arrays for ISS configuration 5A. All of these parameters must be accounted for in simulations of ISS charging to predict similar variations observed as the FPP measurements. In addition, the plasma properties are generated using IRI.

The magnetic field obtained through IRI plays an important role and effects the potentials on the ISS based on (vxB.L). Figure 5 delineates a potential contour of the ISS due to magnetic induction. This potential does not include the collection effect of the PV arrays. The spacecraft location is south of Australia where the largest magnitude of magnetic field strength has been shown to occur. While the pressurized segments of the ISS structure are near –10V, the variation from the tip of one PV array to the other is in the range of 30V.

In order to identify the 'ion collection' area of the ISS, all FPP eclipse exit charging data during nominal operations were compared to PIM predictions. The comparisons are consistent with a value of $35m^2$ as the amount of ion collection area present on the ISS. As discussed earlier, the ion collection area is an effective term that may account for other ISS plasma interaction mechanisms. Therefore, one must be careful when using this as a physical area present on ISS surfaces.

Comparison between the FPP potential measurements and PIM predictions at the charging peaks (occurring at eclipse exit) are shown in Figure 6. The effect of variability of the plasma properties must be accounted for due to the uncertainty of eclipse exit temperatures at high latitudes.[8] The indication of 3σ variability uses values obtained from Figure 7.[9] The combination of −3σ on Te values and +3σ on ne values are the predictions for extreme cases with very low probability of occurrence.

Concluding Remarks

A model describing the plasma charging on the International Space Station has been presented. The model accounts for solar array charging, magnetic induction, ion collection, and the variability of the ionospheric plasma properties. The model can be used to assess the various ISS build configurations and the effect of seasonal and solar cycle effects upon the vehicle charging.

The computer model has been used to calculate ISS structure potentials for comparison between the calculations and FPP flight measurements. High latitude electron temperatures derived from the IRI 2001 model ionosphere are highly variable. This necessitates adoption of "worst-case" values for charging hazard assessments by the ISS program.

During ISS Flight ULF1.1, the Program will be integrating into ISS a Floating Potential Measurement Unit (FPMU) which will be used to measure structure potential and ionospheric plasma (electron temperature and number density) properties. During CYs 2005 and 2006 additional arrays will be deployed which should yield enhanced charging on the structure. Comparisons between the computer model calculations and the FPMU flight measurements will be made on a continuing basis as the flight data is obtained.
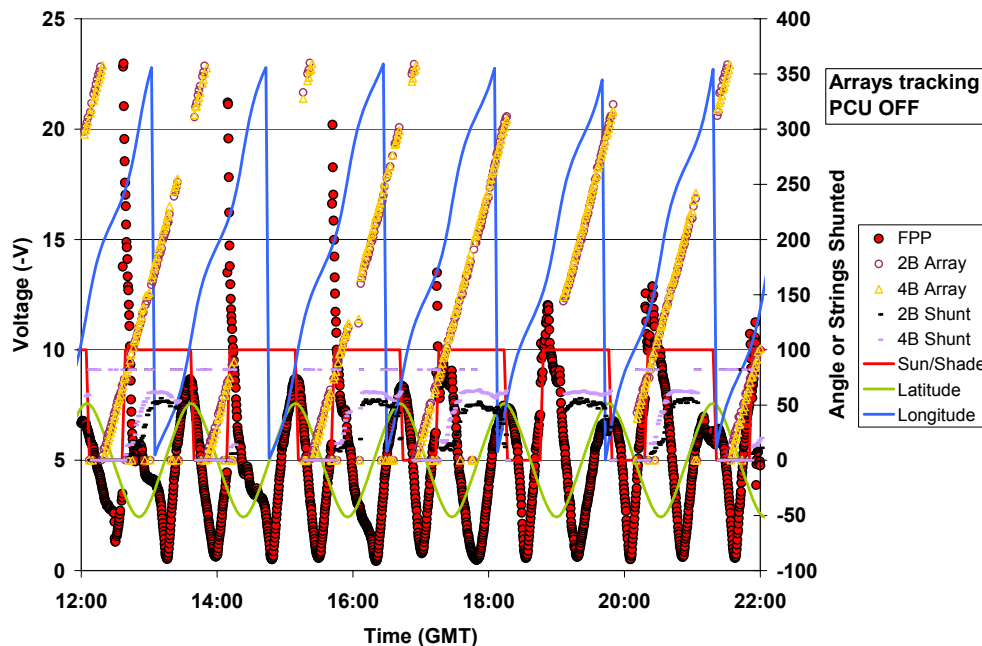
Figure 1. FPP Potential and pertinent parameters for an ISS orbit (PCUs in standby mode).
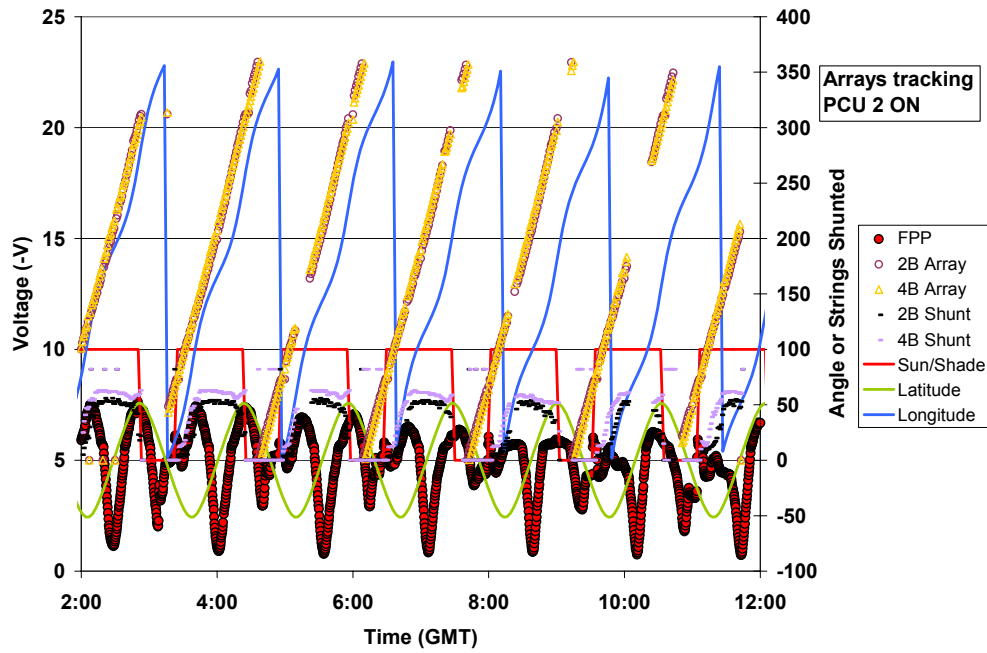
Figure 2. FPP Potential and pertinent parameters for an ISS orbit (PCU 2 in discharge mode).
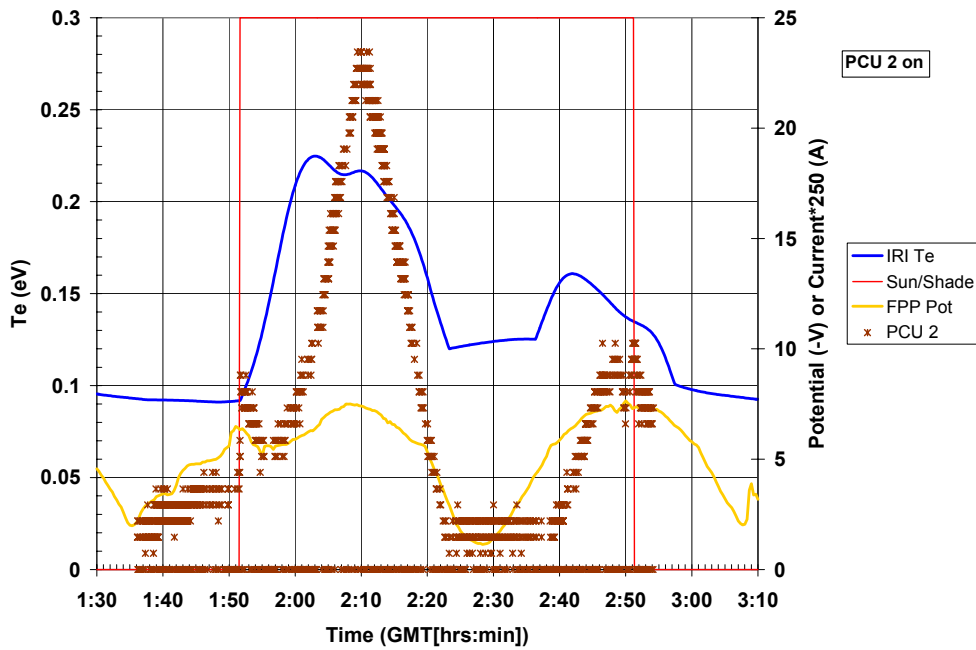
Figure 3. PCU #2 discharge current over full orbit.
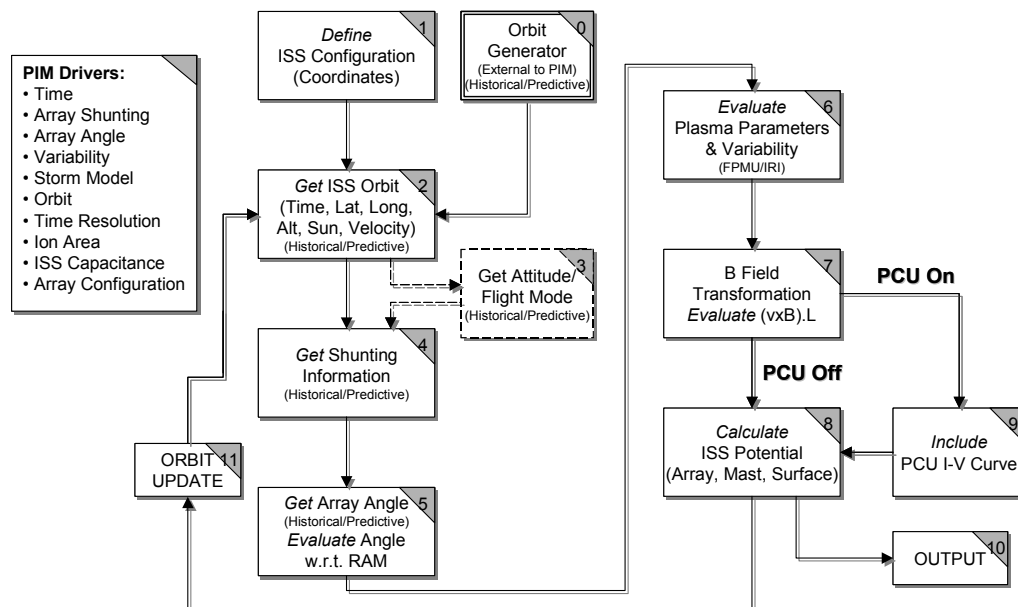
Figure 4. Overview of ISS Plasma Interaction Model.
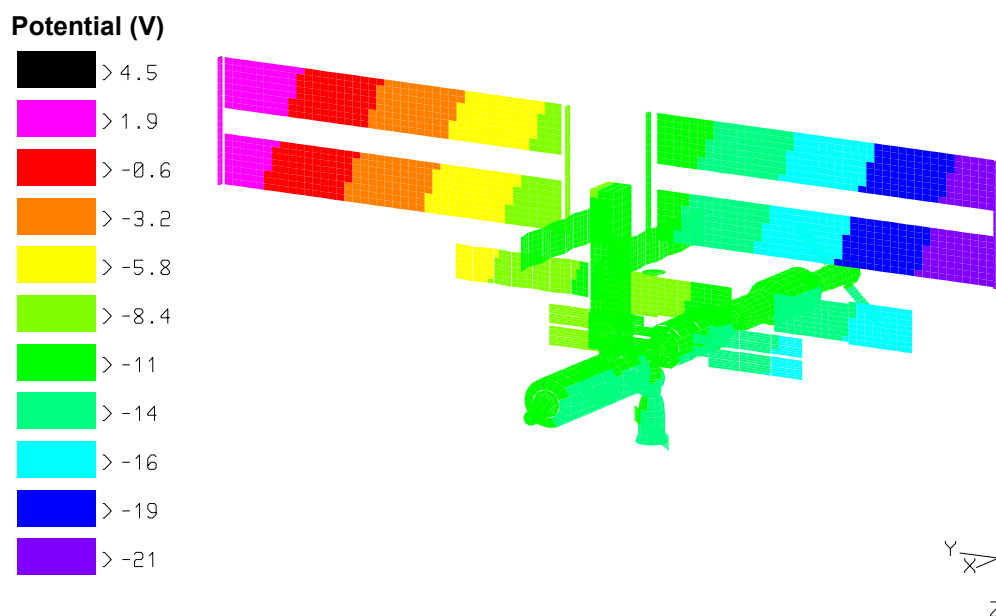
Figure 5. ISS potential variation due to magnetic induction.
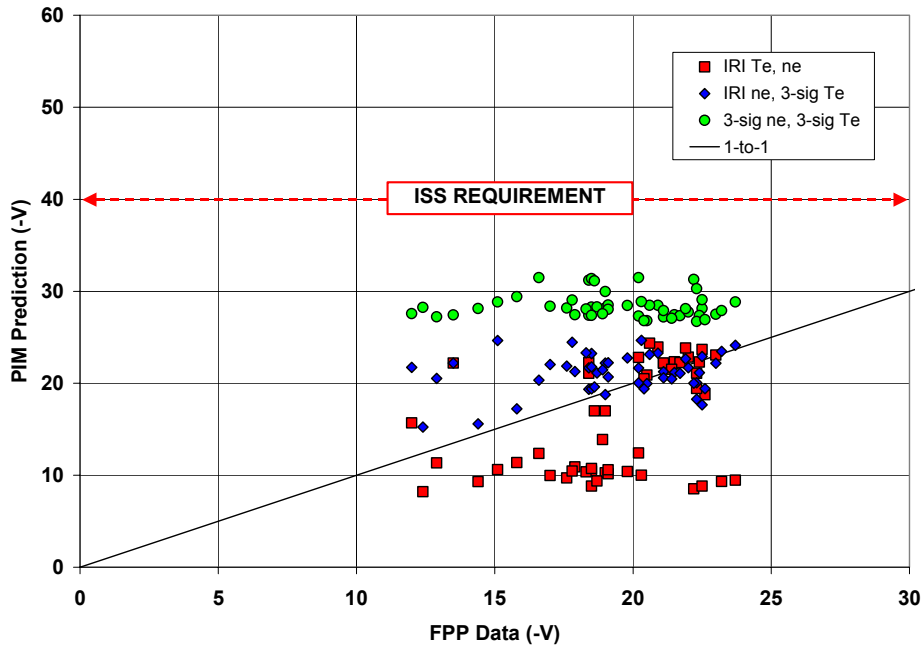
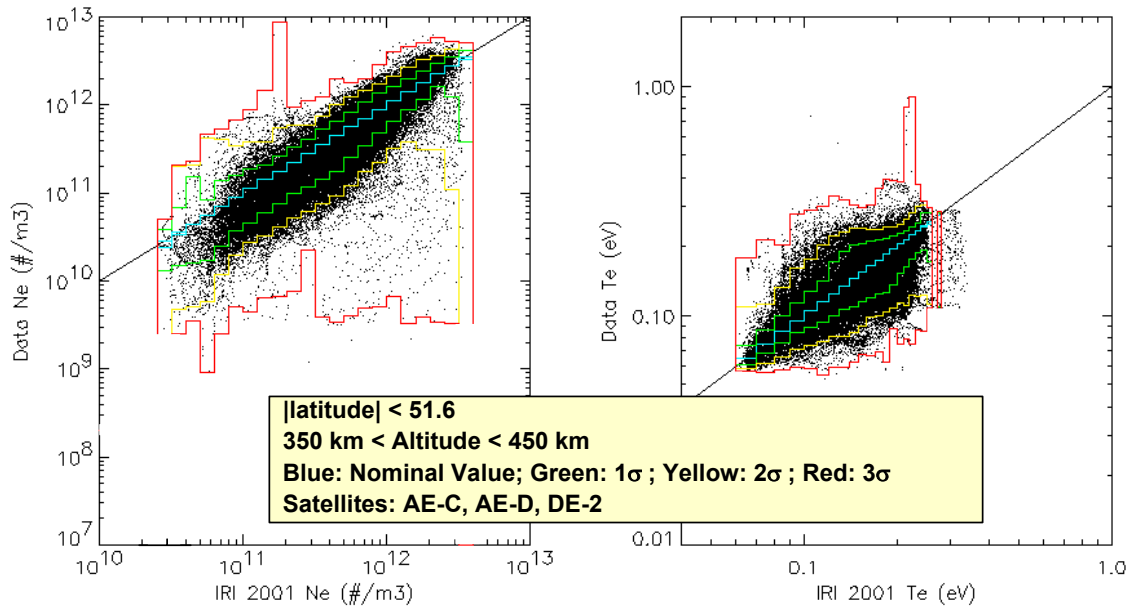**Figure 6. PIM predictions compared to FPP data (including variability).**

Figure 7. Satellite data plotted as a function of IRI temperature and density values for ISS orbit.

References

1. D.C. Ferguson, et al., First Results from the Floating Potential Probe (FPP) in the International Space Station, AIAA-2001-0402.

2. T.L. Morton, J.I. Minow, Floating Potential Probe Langmuir Probe Data Reduction Results, AIAA-2002-0936.

3. M.C. Felder, B.L. Sater, P.E. Paulsen, D. Thompson, R. Olsafsky, Results of Testing Conducted in Tank 5 for Interactions Between Space Station Freedom and Plasma, Preliminary Information Report 268, NASA Lewis Research Center, January 1993.

4. I. Katz, Thin Wire Collection Model for EWB, SAIC Memorandum, private communications, March 19, 2001.

5. M.J. Mandell, V.A. Davis, G.A Jongeward, B.M. Gardner, ISS Solar Array Electron Collection Model, SAIC Report: SAIC 02/2014, May 2002.

6. M.J. Mandell, V.A. Davis, B. Gardner, G. Jongeward, Electron Collection by International Space Station Solar Arrays, to be presented at the 8th Spacecraft Charging Technology Conference, October 20-24, 2003, Huntsville, Alabama.

7. R.R. Mikatarian, H.R. Barsamian, J.W. Kern, S.L. Koontz, J-F.Roussel, Plasma Charging of the International Space Station, 53rd International Astronautical Congress, The World Space Congress – 2002, 10-19 Oct 2002, Houston Texas.

8. R.R. Mikatarian, H.R. Barsamian, J.W. Alred, J.W. Kern, J. Minow, S.L. Koontz, Electrical Charging of the International Space Station, AIAA-2003-1079.

9. J.I. Minow, Development and Implementation of an Empirical Ionosphere Variability Model, 34th COSPAR Scientific Assembly, the World Space Congress – 2002, 10-19 October 2002, Houston, Texas, USA.

SPECIFICATION OF ISS PLASMA ENVIRONMENT VARIABILITY

Joseph I. Minow
Jacobs Sverdrup, Marshall Space Flight Center Group
MSFC/ED44, Huntsville, AL 35812
Phone: (256) 544-2850
Fax: (256) 544-0242
E-mail: joseph.minow@msfc.nasa.gov

Linda F. Neergaard
Jacobs Sverdrup, Marshall Space Flight Center Group

Them H. Bui
Microcraft, Inc., MSFC Group

Ronald R. Mikatarian
H. Barsamian
The Boeing Company

Steven L. Koontz
NASA, Johnson Space Center

Abstract

Quantifying spacecraft charging risks and associated hazards for the International Space Station (ISS) requires a plasma environment specification for the natural variability of ionospheric temperature (Te) and density (Ne). Empirical ionospheric specification and forecast models such as the International Reference Ionosphere (IRI) model typically only provide long term (seasonal) mean Te and Ne values for the low Earth orbit environment. This paper describes a statistical analysis of historical ionospheric low Earth orbit plasma measurements from the AE-C, AE-D, and DE-2 satellites used to derive a model of deviations of observed data values from IRI-2001 estimates of Ne, Te parameters for each data point to provide a statistical basis for modeling the deviations of the plasma environment from the IRI model output. Application of the deviation model with the IRI-2001 output yields a method for estimating extreme environments for the ISS spacecraft charging analysis.

Introduction

Empirical ionosphere models are used in applications requiring electron and ion density (Ne, Ni) and temperature (Te, Ti) predictions for spacecraft design and mission analysis studies although the output of these models are typically limited to mean values. In many applications, however, knowledge of the electron temperature and density variations about the mean and the magnitude of extreme deviations are important parameters as well, particularly for spacecraft designers and operations support personnel conducting space environment analysis for low Earth orbit missions. Quantifying the spacecraft charging risks and corresponding hazards for the International Space Station (ISS) is such a case where the mean plasma environment is not

Table 1. Historical Satellite Records

Spacecraft	Records in Study
•AE-C	[1973-12-16 to 1978-12-11]
–Circular, 68.1 deg in	608,139 records
–Elliptical 150 km x 4300 km	
–68.1 deg inc	
•AE-D	[1975-10-06 to 1976-01-29]
–Circular, 90.1 deg inc	100,395 records
–Elliptical, 154 km x 3816 km	
–90.1 deg inc	
•AE-E	[1975-12-01 to 1981-05-24]
–Circular, 19.7 deg inc	464,690 records
–Elliptical, 156 km x 2983 km	
–90.1 deg inc	
•DE 2	[1981-08-06 to 1983-02-15]
–Elliptical, 300 km x 1000 km	693,112 records
–89.99 deg	

sufficient to determine the maximum range of spacecraft potentials that may be expected during the construction phase of the vehicle and after assembly complete. Specification of ionospheric Ne, Te conditions for a spacecraft charging analysis requires not only the mean environment for mean charging conditions but estimates of the extreme values as well to determine if the maximum spacecraft potentials anticipated for any configuration of the vehicle will remain within the –40 volt program requirement. This paper describes the development of a prototype empirical ionosphere variability model for the ISS program intended for use with the International Reference Ionosphere (IRI) to provide ionospheric mean Ne and Te values as well as predictions of the range of variations in Ne and Te about the IRI output values.

Database

Satellite observations of electron density and temperature measurements are used to provide the database in the portion of the study reported here (although current work is underway to include ground based incoherent scatter radar observations as well). Data sets used in the study were obtained from the National Space Science Data Center (NSSDC), Goddard Space Flight Center, and are listed in Table 1. Since many of the satellites included in the database are the same satellites used in constructing the IRI topside models (Bilitza, 1994, 1997, 2001) the data set is particularly useful for examining variations in Ne and Te about the IRI values. Analysis of spacecraft charging data from the Floating Potential Probe instrument onboard the ISS during the winter and spring of 2001 (Ferguson, 2001; Ferguson et al., 2001) demonstrated that the
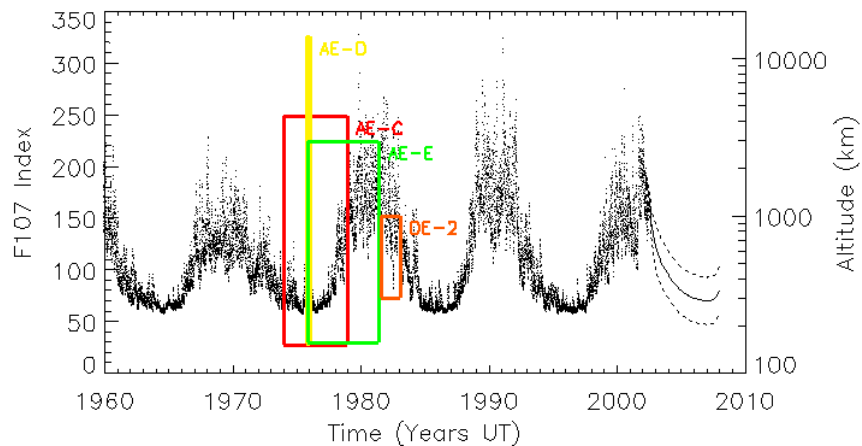
Figure 1. Altitude, solar cycle distribution of Ne, Te records. Altitude range and mission dates for the satellites are indicated by the colored boxes. The F107 EUV proxy index (in Solar Flux Units =10^{-22} W/m^2/Hz) is given to demonstrate phase in the solar cycle. Although the complete database covers nearly two solar cycles, only the AE-C, D, E and DE-2 data is included in the analysis (AE-E was removed) and results for this paper.

vehicle negative potential increases with increasing Ne and decreasing Te values and that the threat condition for maximum negative potential is high Ne, low Te values (Ferguson et al., 2001, 2003; Mikatarian et al. 2002, 2003). Since both Ne and Te parameters are required to determine the spacecraft potential, only data where simultaneous Ne and Te values are available are included in the study since these are required for estimates of spacecraft potential.

The data from the Atmosphere Explorer and Dynamics Explorer satellites, the subject of this paper, covers nearly a complete solar cycle. Electron density and temperature values were obtained from Langmuir probes on the Atmosphere Explorer series (Brace et al., 1973) and DE-2 (Krehbiel et al., 1981). Density values are available from the AE satellites over a range from 5.0×10^7 to 1.0×10^{12} electrons/cm^3 and temperatures from 0.03 to 0.86 eV with an accuracy of approximately 10% to 20% (Brace, 1998). Additional data appropriate for the ISS study is currently being processed and incorporated into the database including the AEROS A satellite (~200 km to 800 km) and a large selection of incoherent scatter radar observations from Arecibo (Puerto Rico), Millstone Hill (Massachusetts), Jicamarca (Peru), and St. Santin (France). Finally, over three years of data from the Challenging Minisatellite Payload (CHAMP) satellite (circular orbit at ~400 km altitude) will also be available in the near future to include in the database. Results from the extended database will be provided elsewhere in a future report.

Data is available over a wide range of altitudes for low Earth orbit. All AE and DE-2 satellite data from 200 km to 1000 km is shown in Figure 2-a although only a restricted range of altitudes is useful for the ISS study. Figure 2-b are all data values (including both night and day) for the 350 km to 450 km altitude range appropriate for the ISS study. Night time data is not of interest to the ISS charging study since biased solar arrays are required for the electron collection process on the solar arrays to occur (Mikatarian et al., 2003; Gardner et al., this conference).

Further filtering of the data set by rejecting nighttime values finally yields the remaining data shown in Figure 2-c.
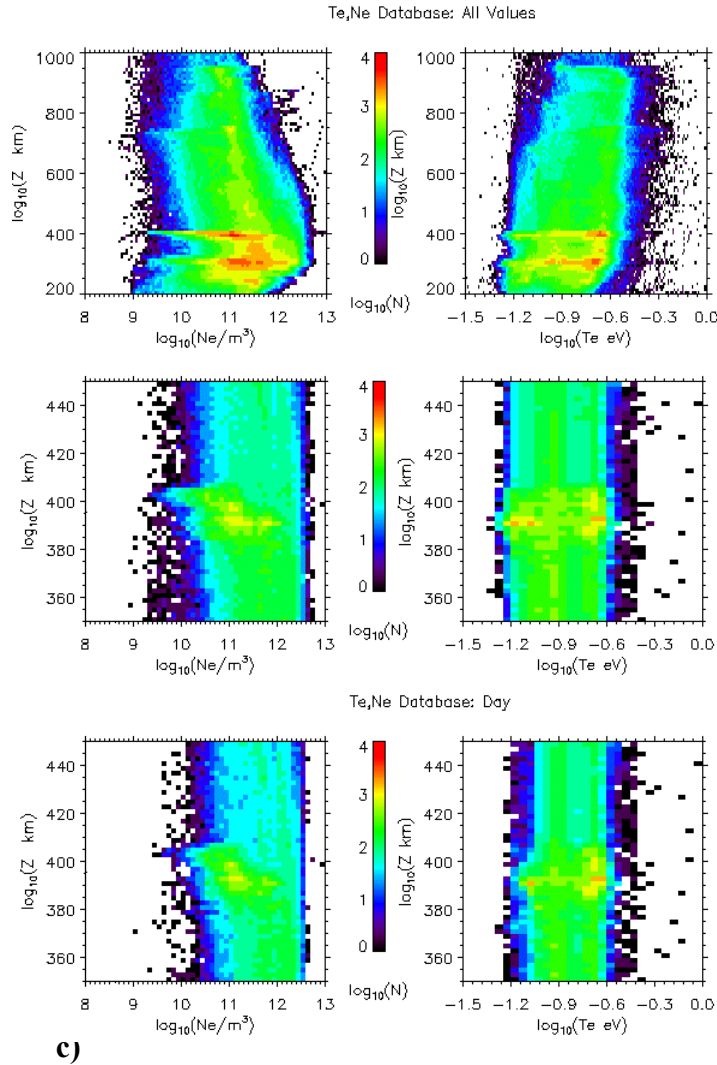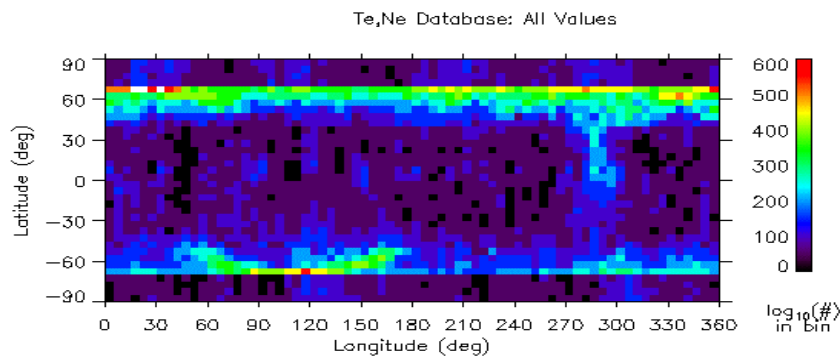

Figure 2. Distribution of Ne, Te values in database. Two-dimensional histograms of Ne-altitude (left panels) and Te-altitude (right panels) are shown for (a) all data from 200 km to 1000 km, (b) all data within 350 km to 450 km, and (c) only daytime data in 350 km to 450 km altitude range.

A two-dimensional histogram of the number of Ne, Te pairs is given in Figure 3 showing the number of values available in the ISS study set (350 km to 450 km) as a function of latitude and longitude. Coverage of the database is global since both polar and low inclination satellites are included in the database but only values with latitudes in the range $-55° < \lambda < +55°$ are retained for the ISS study.

Although there are nearly two million individual records available in the original data sets obtained from NSSDC, not all records contain paired Ne and Te values. In addition, when specific application requires a subset of the complete database (for example, the ISS study),

restricting latitude and altitude ranges further reduces the available data. For example, Table 2 demonstrates the impact of restricting the data to only those values appropriate to the ISS charging study. Of the original 1.96 million data records available from the NSSDC archives, only 1.89 million remain after removing records with missing latitude and longitude information, invalid Te or Ne values, and other data problems. Requiring coincident Te and Ne values further reduces the database to 1.17 million data records. Although this may seem like a large number of records, they are distributed over all latitudes and longitudes providing minimal statistics in localized regions. For example, there would be a few tens of values in a single 1° x 1° cell assuming a random distribution of data points distributed over a 200 km to 1000 km altitude range, not a very extensive database for deriving statistical variations in plasma parameters! If the geographical range is increased to a 5° x 5° cell then there would be approximately 700 values distributed over the altitude range. Restricting the database to the ISS altitude range and daytime conditions further reduces the amount of [Ne, Te] pairs to less than 100,000 records. Clearly the quality of any statistical analysis based on the database will benefit from a large amount of data and results are anticipated to improve with the introduction of additional satellite data and the incoherent scatter radar observations into the data set.

Scatter plots of Ne,Te values are shown in Figure 4-a for the complete historical dataset while Figure 4-b is a subset where the database has been filtered to retain only data available for the specialized application of determining the range of electron density and temperatures at sunrise and through the daytime period over the range of altitudes and latitudes available to the International Space Station. Filtering the data is required to obtain statistics appropriate for a very specific set of conditions but at the cost of reduced statistical quality of the results due to due to the reduction in the number of records in the database.


Figure 3. Latitude and Longitude Distribution of Ne, Te Data. The two-dimensional histogram shows the number of [Ne,Te] pairs of AE-C, AE-D, and DE-2 data values in 5 degree latitude/longitude bins. Only data within the 350 km to 450 km ISS study altitude range is included in the figure.

Table 2. Available Data

- **1,959,651 records in NSSDC data distribution**
- **1,894,008 remain after removing bad records**
  - –Missing lat/lon information
  - –zero or missing Ne, Te values
  - –other problems
- **1,173,581 records with coincident Ne, Te values**
  Distributed over all latitude, longitudes, altitudes:
  - ~29 values/(1° x 1°)
  - ~731 values/(5° x 5 °)
- **ISS specific application: 280,683 records**
  350 km < z < 450 km   -51.6º < latitude < 51.6º
  - ~4 values/(1° x 1°)
  - ~108 values/(5° x 5°)

a)   b)
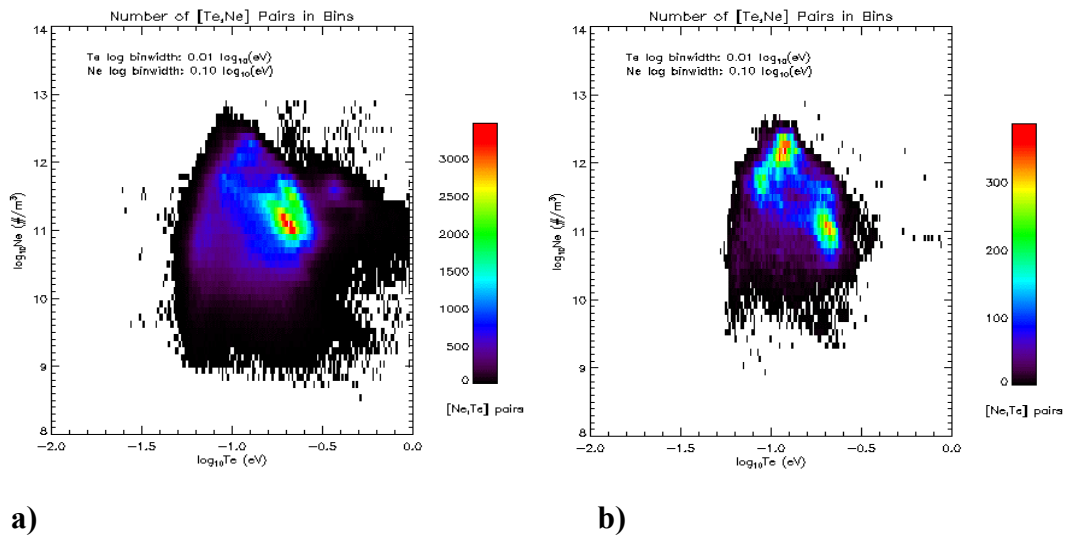
Figure 4. Ne, Te scatter plots. (a) Historical database of all 1.07x10^6 values and (b) the subset of 0.88x10^6 values applicable for ISS orbit (±51.6° latitude, 350 km < z < 450 km) with solar zenith angles sza < 120°. Color coding provides the number of data values within each bin. The threat condition for ISS charging occurs in the high Ne, low Te sector of the scatter plots.

Implementation of the Variability Model

The variability model is derived from the variance of individual Ne, Te values from IRI-2001 model results.   For each set of Ne, Te data values in the database, the corresponding IRI-2001 values are computed and compared to the data values. This requires using the IRI-2001 input parameters (latitude, longitude, altitude, time, and solar and/or geomagnetic conditions) for each Ne, Te pair in the historical database.Plots of differences between the data and model values are shown in the top panels of figure 5. Density values typically vary by orders of magnitude about

the mean IRI output.   There are numerous physical processes that result in plasma density variations that are not included in the climatological IRI model including equatorial plasma depletions associated with spread-f conditions during night in the equatorial regions, plasma depletions associated with sub-auroral enhanced plasma convection and stable auroral red arcs at mid latitudes, and plasma cavities associated with auroral arcs at high latitudes.   Similarly, transient enhancements in electron temperatures due to auroral processes (particle and Joule heating) are not included in the IRI model and appear as deviations from the mean model output in the current analysis.

Histograms of differences between the IRI-2001 model and the data are provided in the bottom panels of Figure 5. The distributions are nearly Gaussian only for small deviations from the model but exhibit strongly non-Gaussian features for large deviations suggesting that simply computing mean and standard deviations of the differences will underestimate the extreme deviations in the database.

a)   b)
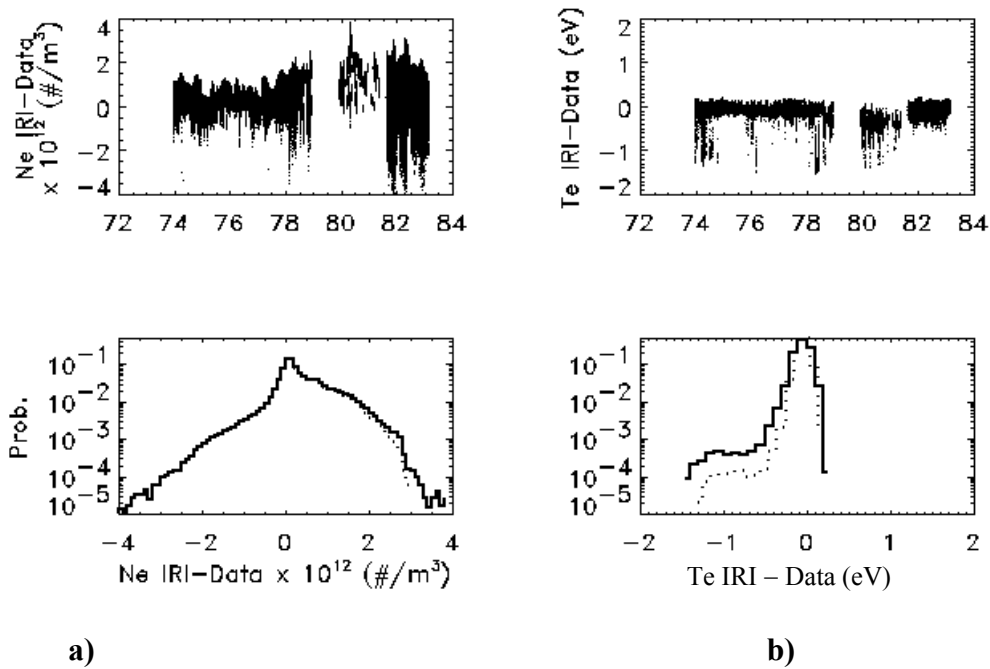
Figure 5. IRI Model and Data Differences. Differences between the IRI-2001 values and the Ne, Te values in the database (top) and histograms of the differences (bottom) for electron number density (a) and electron temperature (b). The solid lines in the histogram include data from AE-C, AE-D, AE-E, and DE-2 spacecraft while the dotted line indicates histograms where the AE-E data has been removed. in the dotted line.

Te values from the AE-E satellite appeared biased to anomalously high Te values in comparison to the AE-C, AE-D, and DE-2 data, even during 1976 and 1977 when data is available from both satellites and direct comparison is possible.   The AE-E values appeared to be spurious and were removed from the analysis for the ISS study.   The histograms in Figure 5 include both the complete Atmosphere Explorer and Dynamics Explorer data sets for all latitudes and altitudes in the database (solid lines) as well as histograms with the AE-E data removed (dotted line).   A set of high Te values is lost when removing the AE-E data although there does not appear to be a systematic bias in the measurements since the peak of the histograms with and without the AE-E data are at the same value.   Since the threat condition for extreme ISS charging is low Te, loss of the high Te AE-E data is not important to the study.
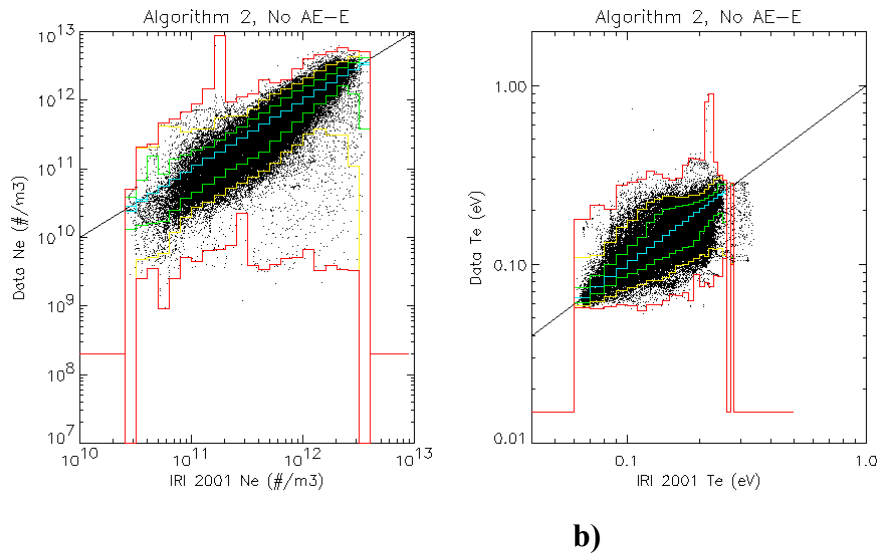
a)   b)

Figure 6. Comparison of historical Ne and Te database with IRI-2001. (a) Density values in the data are distributed about the IRI-2001 values. (b) Temperatures are similarly distributed. Lines drawn on each plots indicate bounds of 68%, 95%, and 99.9% of the data values for each bin (from Minow, 2002).

Scatter plots of data Ne and the corresponding IRI model Ne values are given in Figure 6a and data Te with corresponding IRI model Te values in Figure 6b. Density values in the database typically vary over an order of magnitude about the IRI values with extremes of approximately two orders of magnitude. Electron temperature variations in the historical database are typically within an order of magnitude of the corresponding IRI Te values.

Quantitative estimates of the variability are obtained by computing Ne and Te statistics for the historical database. For example, consider the process of obtaining electron density variability. The process begins with establishing Ne bins based on the IRI values then sorting the historical Ne database values into the appropriate density bins. Within each bin, statistical variation of the electron density is determined by finding the density values in the historical database that bound 50%, 68%, 95%, and 99% of the data values within each bin. Although the values are often referred to generically in this work as the "mean" and "1, 2, and 3 σ"variability estimates, the distributions within each bin are typically far from Gaussian and the technique is

generally applicable in terms of the percentiles. Te variability is derived from a similar process using IRI Te bins and the historical Te database.

Results from the variability study can be applied to estimate potential threats to the ISS program in a very simple way by taking the greatest Ne and least Te values that appear in Figure 4-b and Figure 6 and use them as a "worst case" ionosphere for the ISS orbit. This technique was used by Mikatarian et al. (2003) to demonstrate that the current ISS configuration will not exceed the –40 volt limit on the structure floating potential. Since the program limit is not exceeded even for a non-physical worst case (although Ne and Te values are typically anti-correlated in the daytime ionosphere it is not readily apparent that the highest Ne and lowest Te value in Figure 6 will ever occur at the same time). More detailed analysis of the correlations between the Ne, Te pairs will be required when the predicted potentials approach or exceed the limit of –40 volts, a possibility in future construction of the vehicle.

The second method of applying the variability statistics is to use the results of the statistical analysis to develop a computer model of Ne and Te variations. Computation of the percentiles shown in Figure 5 within a spatial range of altitudes, latitudes, and local times yields a database of deviations from the IRI-2001 model results that may be applied to IRI output to estimate
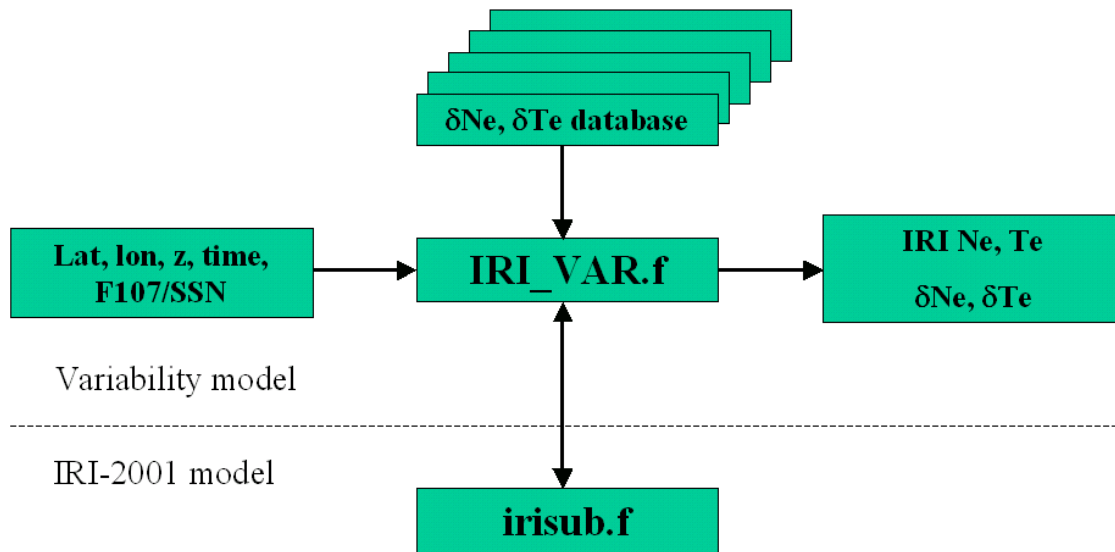
Figure 7. Schematic of Ne, Te Variability Model. The model takes the δNe, δTe results generated from the variability study to provide deviations from the IRI-2001 output for a given set of input parameters.

deviations in Ne, Te that are not contained in the average IRI model. Figure 7 provides a schematic of a FORTRAN program written to automate the process. A user runs the variability model by providing the standard IRI-2001 model input (latitude, longitude, altitude, time, solar activity, etc.) to a "wrapper" program that drives the IRI-2001 subroutines and includes access to the variability database. Ne, Te values from the IRI-2001 model are used to select which set of

statistics to use from the variability study and the software then provides the appropriate offsets to add or subtract from the 50% values in the bin.   Output from the "wrapper" program is both the standard IRI-2001 output as well as the deviations from the IRI-2001 values based on the historical database. This computer model is incorporated in the Plasma Interaction Model developed by Boeing and SAIC to predict ISS floating potentials (Gardner et al., this conference; Mikatarian et al., this conference).

   Variations in solar and geomagnetic activity have not been included in the analysis described above. Simply collecting together all data within a given altitude and latitude range without sorting by geophysical conditions requires accepting wide deviation in Ne and Te values. For example, Figure 7 provides the distribution of Ne and Te values both day and night data in the ISS altitude range where daytime values are coded red and nighttime blue.   The simple local time relation

$$LT = [UTC + longitude/15] \mod 24$$

is used to organize the Ne, Te values and solar zenith angle is used to determine if the individual measurement was made in illuminated or night conditions (the modulus operation assures all local times are in the range of 0 hours to 24 hours). Overlap of day and night values near dawn

a)   b)
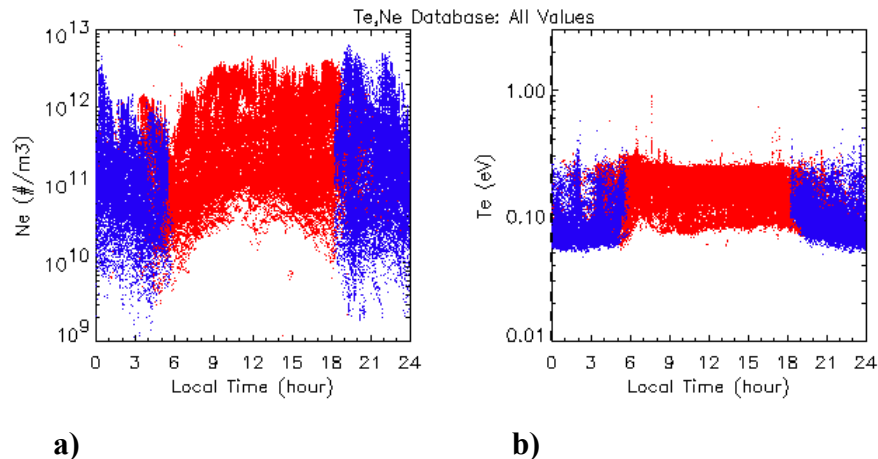
Figure 8. Ne-LT and Te-LT scatter plots. Day (night) values are indicated by the red (blue) colors. The vertical dashed line is sunrise where SZA(z) of a data value is equal to the solar zenith angle of sunrise SZA$_{SR}$ at altitude z of the [Ne, Te] data pair (SZA refers to the solar zenith angle, the angle between the satellite zenith-nadir axis and the direction of the Sun).

and dusk are due to variations in sunrise and sunset times over the latitude range from -55° to -
+55° included in the ISS study set.   The typical ionospheric behavior is apparent with night
density values decreasing until sunrise where they begin to rise.   Midday Ne values in Figure 7-a
are a maximum, ranging from 5×10^{10} #/m^3 to 5×10^{12} #/m^3, and Ne begins to decrease in the
evening hours and into the night.   Te values exhibit an abrupt increase at sunrise due to rapid
heating of the electron gas by photoelectrons, decrease in midday when Ne is a maximum,
increase in the late afternoon hours as Ne decreases, and finally decrease after sunset and into the
night time hours as the ionosphere cools.

In addition to the typical diurnal behavior of the ionosphere, an obvious feature in Figure 8 is
the large range of Ne and Te values at any given local time.   Ne values in Figure 6-a vary
approximately two orders of magnitude while the Te values vary by factors of two or three.
Some of the wide range in the Ne and Te values can be attributed to the variations in solar
activity. Pre-sunrise Ne and Te values obtained from incoherent scatter radar measurements at
Arecibo (Puerto Rico) during ionosphere World Day observations over a complete solar cycle
are given in Figure 9 as a function of the F107 proxy index for solar EUV activity.   The figure
demonstrates that the two order of magnitude variation in pre-sunrise Ne values in Figure 8-a is
due to variations in solar activity.   Current work on including both F107 and a geomagnetic
proxy index (either Kp or Ap) to reprocess the database is underway to reduce the variations.

ISS Eclipse Exit and Daytime Ne, Te Environment

Mikatarian et al. [2002, 2003] describe the spacecraft charging analysis used to demonstrate
the maximum values of ISS potentials for the current configuration are within the –40 volt limit
even if the Plasma Contactor Units install to discharge excess electron current are not used. An
important input to this work is an estimate of the mean and extreme Ne and Te values in the ISS
orbit. Analysis of on-orbit ISS potential measurements showed that charge collection by the
high voltage ISS solar arrays is linearly related to electron density and inversely proportional to
electron temperature (Ferguson et al., 2001). The greatest negative potentials are found when
the density is high and the temperature is low at eclipse exit (as the spacecraft enters sunlight)
and prediction of extreme charging events requires an estimate of the maximum electron density
and minimum electron temperatures in the ISS orbit.

A simple version of the statistical model was implemented for this work since it was
sufficient to demonstrate that ISS potentials do not exceed the –40 volt limit anywhere over the
range of altitudes and latitudes available to the ISS. In addition, since the extreme charging
conditions require a bias on the solar arrays, it is only necessary to consider conditions where the
spacecraft is illuminated by the Sun.   Therefore, a variability model applicable over the 350 km
to 450 km ISS altitude and within a latitude range of ±51.6° for daytime conditions satisfies the
program requirements to determine a plausible worst case environment for input into the
charging analysis.
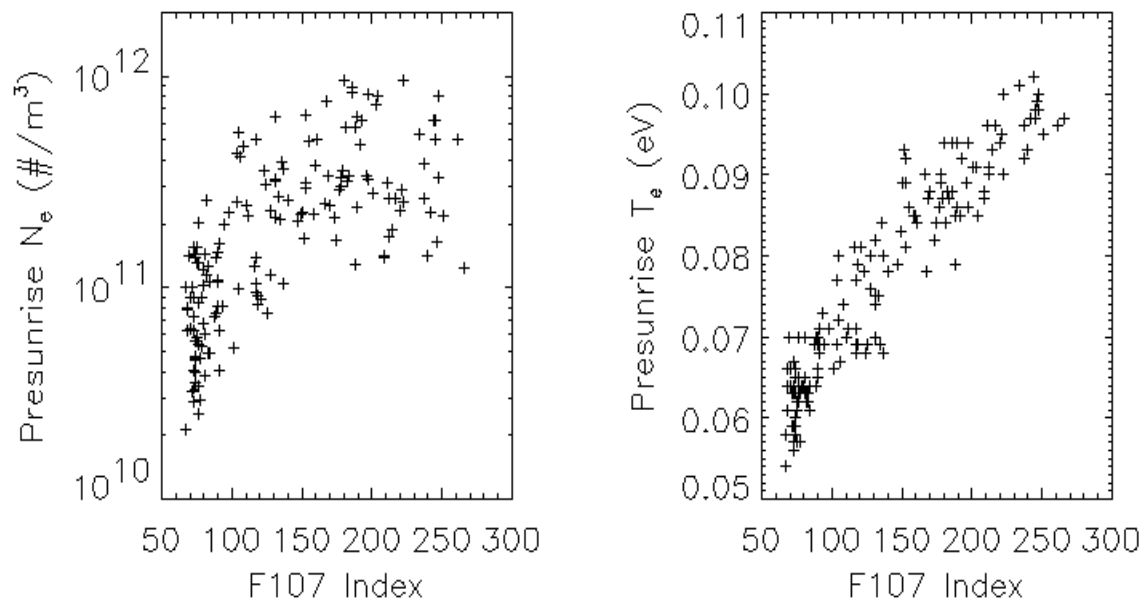
Figure 9. Pre-sunrise Ne, Te Measurements at Arecibo, Puerto Rico. (a) Ne and (b) Te values at ISS altitudes both exhibit a strong correlation with F107. Including solar activity in the analysis of the database will provide an opportunity to reduce the variability in the deviation model (from Mikatarian et al., 2003).

Figure 10 provides a case for comparing results from the Ne and Te variability model with data values. The top and middle panels are time series of Ne and Te altitude profiles obtained by the incoherent scatter radar at Arecibo, Puerto Rico, for a series of days in March 1988. The daily electron temperatures rise at sunrise due to photoelectron heating of the neutral gas is apparent in the plots with a decrease in Te during the middle of the day where the electron density is a maximum (electron cooling is dependent on the electron density). Finally, as the electron density begins to decrease late in the day the electron cooling rate also decreases and the electron temperature rises again before sunset. After the sunlight no longer illuminates the ionosphere both the electron density and temperature decay to the nighttime values.

Electron densities and temperatures from the 404.5 km radar range gate, an altitude typical of the ISS orbital altitude, is plotted in the bottom panel of Figure 4. Results from the IRI-2001 model are overplotted to show the model representation of the Te values and statistical results are indicated for sunrise and daytime periods. Statistics for these results include all data in the database from 350 km to 450 km altitude, solar zenith angle < 120 degrees, and latitudes between +/- 51.6 degrees. Note that while the extreme low temperature values indicated by the -"3σ" level are not significantly less than the night time observations, the daytime extreme values can be much greater than the observations.
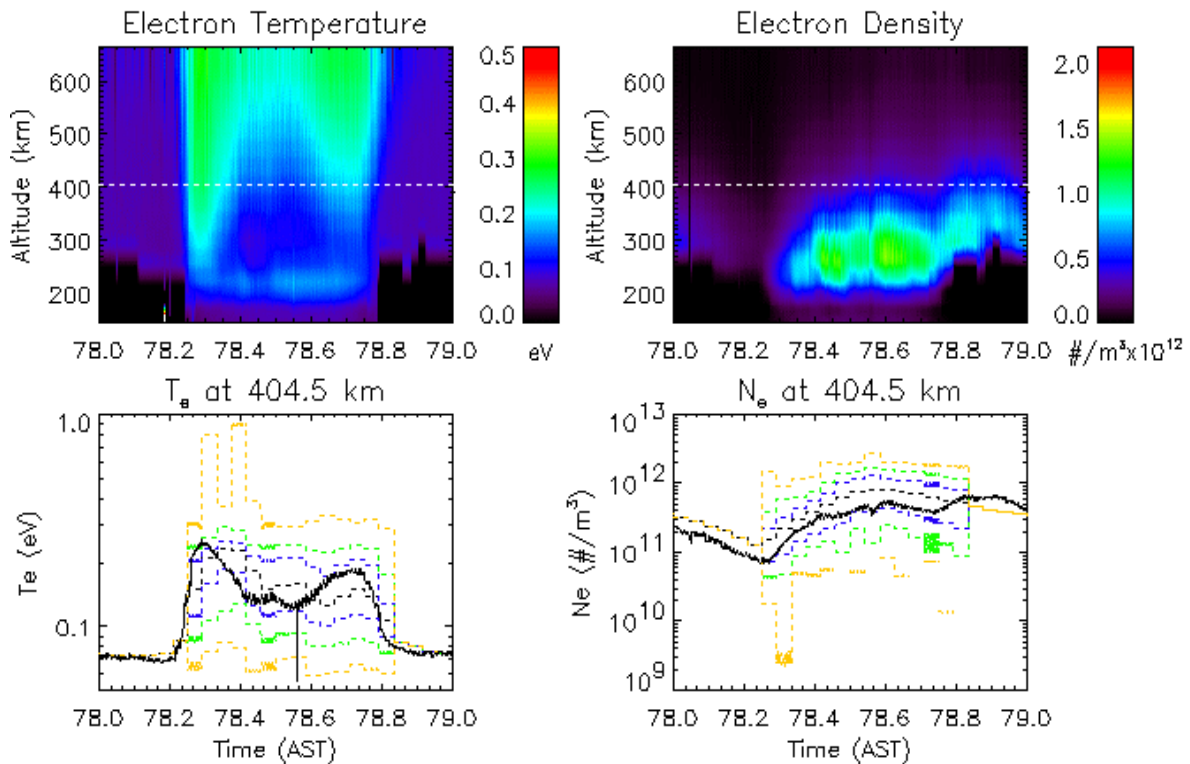
Figure 10. Incoherent scatter radar Ne and Te measurements on 18 March 1988 at Arecibo, Puerto Rico. Ne (top left) and Te (top right) are altitude profiles as a function of time (day 78 of year 1988 in Atlantic Standard Time) with the values of temperature and density given by the color scale. The Ne, Te values from ~405 km are plotted in the bottom panels (solid black line) with the corresponding IRI-2001 values (dotted black line). Estimates of the "1,2, and 3 σ" variability (blue, green, and yellow, respectively) are given for daytime periods when the variability database is applicable (from Minow, 2003).

Determination of the maximum charging levels anticipated for future ISS configurations will similarly require estimates of plausible worst case charging conditions as well as estimates of how frequently these conditions may be encountered. Implementation of the variability model provides a convenient method of incorporating Ne and Te statistics based on historical values into a simple computer model.

Summary

Preliminary results from a technique developed to provide statistical variations in electron density and temperature values in addition to the mean values available from standard empirical ionosphere models has been descirbed. Historical in-situ observations of Ne and Te from the AE-C, D, and E and DE-2 satellites provide a database of observations from which deviations

from the IRI-2001 empirical ionosphere model can be derived.   Deviations of Ne and Te values in the database from the IRI model results provide the variability about the model results.

Current activities are focused on collecting additional data sets to enhance the historical database.   The current set of satellite data contains over a million data values.   Adopting a set of 10 degree latitude bins, 10 degree longitude (or local time) bins, and 100 kilometer altitude bins will require the data to be distributed among 5832 bins. Assuming the data is relatively uniformly distributed, there will be between 100 and 200 points per bin.   The data however is not uniformly distributed in altitude or latitude due to the orbital dynamics of the spacecraft and some altitude regions or range of latitudes will contain many more data values than others. Work is underway to acquire additional satellite and incoherent scatter radar data sets that will fill out the database. Implementation of algorithms for computing density and temperatures over a range of altitudes based on observations at a single altitude are also a possible technique for enhancing the database.

References

1. Mikatarian, R., H. Barsamian, J. Kern, S. Koontz, and J.F Roussel, Plasma charging of the International Space Station, presented at the 53rd International Astronautical Congress, The World Space Congress 2002, 10-19 October, Houston, TX, 2002.

2. Mikatarian, R., H. Barsamian, J. Alred, J. Kern, J. Minow, and S. Koontz, Electrical Charging of the International Space Station, AIAA-2003-1079, presented at the 41st AIAA Aerospace Sciences Meeting, Reno, NV, January 6-9, 2003.

3. Minow, J.I., Development and Implementation of an Empirical Ionosphere Variability Model, 34th COSPAR Scientific Assembly, Houston, TX, October 10-19, 2002.

4. Bilitza, D., Topside models: status and future improvements, Adv. Space Res., 14, 17-26, 1994.

5. Bilitza, D., International Reference Ionosphere - status 1995/96, *Adv. Space Res.*, 20, 1751-1754, 1997.

6. Bilitza, D., International Reference Ionosphere 2000, *Radio Science* 36, 261-275, 2001.

7. Brace, L.H., R.F. Theis, and A. Dalgarno, The cylindrical electrostatic probes for Atmosphere Explorer –C, -D, and –E, *Radio Science*, 8, 341 – 348, 1973.

8. Krehbiel, J., L.H. Brace, R.F. Theis, W.H. Pinkus, and R.B. Kaplan, The Dynamics Explorer Langmuir probe instrument, *Space Science Instrumentation*, 5, 493, 1981.

9. Brace, L.H., Langmuir probe measurements in the ionosphere, in *Measurement Techniques in Space Plasmas: Particles*, edited by R.F. Pfaff, J.E. Borovsky, D.T. Young, pp. 23 – 35, American Geophysical Union, Washington, D.C., 1998.

10. Ferguson, D.C., "Charging of the International Space Station due to its High Voltage Solar Arrays", presented at the 17th Space Photovoltaic Research and Technology Conference, Ohio Aerospace Institute, Cleveland, OH, September, 2001.

11. Ferguson, D.C., G.B. Hillard, T.L. Morton, R. Personen, ISS FPP Ionospheric Electron Density and Temperature Measurements - Results, Comparison with the IRI-90 Model, and Implications for ISS Charging', AIAA-2003-1083, 2003.

12. Ferguson, D. C., T. L. Morton, and G. B. Hillard, First results from the Floating Potential Probe (FPP) on the International Space Station, AIAA-2001-0402, 2001.

ELECTRON COLLECTION BY INTERNATIONAL SPACE STATION SOLAR ARRAYS

M.J. Mandell
Science Applications International Corporation
10260 Campus Point Drive, San Diego, CA 92121
Phone: 858-826-1622
E-mail: myron.j.mandell@saic.com

V.A. Davis
B. Gardner
G. Jongeward
Science Applications International Corporation

Abstract

A solar array electron collection model was developed in 1991 for Space Station Freedom, for the purpose of determining the maximum current emission required for the hollow cathode plasma contactor to "ground" the station. Now that the International Space Station (ISS) is on-orbit and the first pair of solar array wings has been deployed, it has been observed that the electron collection by the solar array cell edges is significantly less than that predicted from preflight test results and the original model. A new model was developed that eliminates snapover and takes proper account of the role of plasma density. The model is validated by integration into Environment WorkBench (EWB), which models the station geometry, current-voltage relationships of station elements, point on orbit, plasma environment, v×B induced potentials, and attitude and movement of station solar arrays and performs a circuit analysis to compute the floating potential of the station chassis. These results are then compared with string currents (inferred from measurements of plasma contactor emission currents during targeted DTOs) and from measurements of charging by the Floating Potential Probe (FPP).

History

More than 10 years ago, plasma physicists (the *Space Station Plasma Interactions and Effects Working Group*) pointed out that the floating potential of (then) Space Station Freedom (SSF) would be negative to a major fraction of its solar array voltage. Other spacecraft were known to routinely float around thirty volts negative with no problems, but it was determined that sputtering of thermal coatings was likely at the higher SSF voltages. Therefore, a decision was made to put a hollow cathode plasma contactor on the SSF. To determine the required current capability of the plasma contactor, laboratory measurements of array collection were performed, and a computational model was built. The computational model was based on studies of electrostatic potentials in and near the solar cells performed with the 2-D *Gilbert* code by (then) S-Cubed, Maxwell Laboratories physicists. The model was integrated into the Environment Workbench (EWB). Given the purpose of this effort, the modeling focused on conditions and assumptions leading to the highest plausible solar array collection.

In December of 2001, the first two wings of International Space Station (ISS) solar arrays were deployed and became operational. Measurements indicated that the arrays collected far less electron current from the ionosphere than had been predicted. Thus far, charging has been limited to a few tens of volts, and, in the course of normal operations, occurs only on eclipse exit. However, the specification that no point on the station be more than forty volts negative of the plasma potential is now based on a criticality one hazard due to concern over astronaut safety. Clearly, a new array collection model is required to predict ISS floating potentials to within the accuracy necessary to meet this requirement. There is a need to re-examine the collection model and develop a new or revised model based on first-principles physics that is in agreement with the on-orbit performance of the array.

Previous Collection Model

The solar array collection model developed in 1991 was focused on the sizing of the plasma contactor unit (PCU), specifically to set its maximum current emission capability. As a result, the model parameters were tuned to predict maximum currents. In retrospect, it is not surprising that currents were over-predicted. The two main factors contributing to over-prediction of currents were (1) allowing snapover of any surface for which this was a stable state, and (2) performing calculations (using the *Gilbert* code) only at plasma densities of 1×10^{12} m^{-3}, scaling linearly to other densities. Since present results show that current rises faster than linearly with density, this resulted in overestimated currents at the more common lower densities.

A major uncertainty in the previous treatment was the effective "width" for electrons passing over a potential barrier. Lacking a clear theoretical treatment, this "width" was obtained by measurements of the electrostatic potential plots, even though the plots showed that the potential structure was not amenable to such treatment. In hindsight, the "width" was overestimated.

Nonetheless, the treatment predicted currents in excellent agreement with the laboratory measurements deemed most trustworthy.[1] Also, the model predicted many qualitative features (*e.g.,* temperature dependence) observed in flight, and could be coaxed into quantitative agreement with flight results by simply scaling back the collected current.

The "new" model described here is derived from the "old" model by reviewing the various assumptions and treatments that went into its development, and revising them to give realistic currents over a wide range of orbital configurations and plasma conditions (rather than maximum currents). In doing so, we have the benefit of a substantial set of on-orbit measurements, and need not rely on laboratory experiments under non-space-like conditions, or flight experiments on small coupons.

Components of the Model

Several components contribute to a model of electron current collection from the ionosphere by the ISS solar array cells. Note, however, that the collection model by itself is not sufficient to determine the floating potential of ISS. ISS build geometry and attitude, magnetic field induced voltages, orbital configuration, the amount, distribution and nature of ion-collecting surfaces and other current emitting elements (such as plasma contactors), and possible dynamic effects are

additional components of a predictive floating potential model. These components are included in the floating potential module of the Environment WorkBench (EWB) ISS plasma effects tool that is used to validate the array electron collection model.

The components of the array current collection model that need to be treated in some detail are discussed in this section.

Array geometry

The cross-sectional structure of the gap region between solar cells needs to be modeled at a resolution of tens to hundreds of microns. Because this gap cross-section is very small compared with the length of the gap (*i.e.,* the 8 cm side dimension of the solar cells) we can treat array collection as a locally two-dimensional problem.

Surface potentials

The potentials of the coverglass surfaces as well as the insulating surfaces interior to the gap play a role. In this model we consider all these surfaces to be at the potential calculated using the plasma temperature and the angle of the array to the ram (see the Section Surface and Gap Potentials for details). In particular, we do not allow any surfaces to be snapped over. This is one of the major differences between this model of ISS array current collection and the previous one. The decision to suppress snapover is based on the low values of collected current measured in flight.

Gap potential

The "gap" is an imaginary surface between the edges of two adjacent coverglasses and at the same level as the coverglass surface, so that what we refer to as the "gap" actually lies above the true gap surface. This "gap" potential is calculated from the coverglass and cell potentials as described below. Along with the coverglass, this surface forms the boundary of the external space through which electrons are collected, so that its potential is the main determinant of the plasma electron current collected. All but a negligible fraction of electrons crossing the gap surface are eventually collected by the solar cells.

Barrier formation

Under most conditions an electron's trajectory to the gap surface must cross a region of negative (electron-repelling) potential. The least repelling such potential (which occurs on the symmetry plane of the gap as shown in Figure 2) is designated "the barrier" for that set of parameters. The barrier structure results from the superposition of the repulsive coverglass-induced potential and the attractive gap-induced potential. The importance of the barrier is that it reduces the electron population energetically able to reach the gap and be collected by a factor of $e^{-V_b/T}$, where V_b is the magnitude of the barrier and T is the electron temperature.

Orbit-limited collection (corrected by particle tracking)

Rather than trying to identify a geometric width in the potential structure, we assume orbit-limited collection of electrons by the gap surface. As a first approximation, we assume that only energetic considerations limit an electron's ability to reach the gap, and conservation of the distribution function along a trajectory determines the current density to the gap. We refine this estimate by actually tracking electrons (in the reverse sense) to the gap surface. The particle tracking leads to an additional 10% to 30% current reduction, with the larger reductions occurring for the more compact potential structures (*i.e.*, for the higher densities).

String geometry

The array is laid out in compact strings. This provides the gap area per string and the distribution of cell potentials.
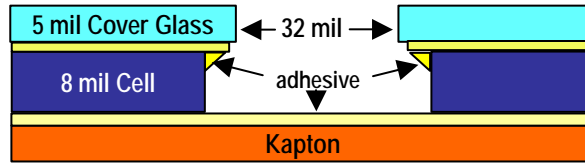
Figure 1. Composition and dimensions of the gap between two solar cells.

Array Geometry

Figure 1 shows the gap region between two solar cells. The cell itself can be at a high potential (up to 160 V), while the other surfaces are at small negative potentials. As mentioned above, we define the "gap" as an imaginary surface extending across the gap at the level of the top of the coverglass, so that the gap surface plus the coverglass surface form a plane boundary to the external space. Note also that the gap dimensions of less than one millimeter are smaller than the Debye length of any anticipated plasma environment encountered by ISS, which would be at least a few millimeters.

An aspect of the gap that has been somewhat controversial is the adhesive coverage on the edge of the solar cell.

Surface and Gap Potentials

We set the potentials of all insulating surfaces to that calculated by current balance between plasma ions and electrons:

$$j_{th}e^{\phi/T} = nev\cos\theta + j_{th}\left(\frac{m_e}{m_i}\right)^{1/2} \quad (1)$$

where the electron thermal current, j_{th}, is given by

$$j_{th} = ne\left(\frac{eT}{2\pi m}\right)^{1/2} \quad (2)$$

where T is the electron temperature (eV), v is the spacecraft velocity, θ is the angle between the surface normal and the ram direction, and φ is the surface potential. The surface potential varies from about -2T for a ram-facing surface to -5T for a ram-normal surface. We are not concerned with wake-facing surfaces. No snapover is allowed. This estimate is certainly valid over most of the coverglass area. It may well be questioned for the portion of the coverglass near the gap edge and for the gap interior surfaces, as these surfaces are at least somewhat inaccessible to plasma when the cell is on. Nonetheless, we posit departures of surface potentials from these estimates will be small enough to have little effect on the ultimate results.

Potentials in a plasma are screened by the space charge of the ambient plasma, which results from reduced density of the repelled species and acceleration and convergence of the attracted species. For low potentials (linear screening), only the repulsion is important, and the potential falls off exponentially with characteristic distance given by the "Debye length." For high potentials the acceleration and convergence effects are important, so that the geometry of the problem must be self-consistently taken into account. To calculate the gap surface potential we use the finite element electrostatic potential solver of the 2-D *Gilbert* code. *Gilbert* allows us to obtain excellent resolution within the gap while including the full coverglass surface and extending an adequate distance into the external space. In this case, plasma screening has little effect on the gap surface potential both because of the small dimensions of the gap (relative to the plasma Debye length) and because of the high potentials and fields within the gap. As a result, the mean gap potential is a simple linear function of the cell edge potential and the insulator surface (coverglass) potential.

We will see below that we need two different averages for the gap surface potential. For calculating the barrier we use the simple average

$$\langle \phi \rangle_{gap} = 0.01035 \phi_{cell} + 0.982 \phi_{glass}. \quad (3)$$

For calculating the orbit-limited current collection, however, we use

$$\langle \phi^{1/2} \rangle^2_{gap} = 0.00969 \phi_{cell} + 0.926 \phi_{glass}. (4)$$

Note that these coefficients are appropriate only to the geometry shown in Figure 1.

Barrier Formation

The "barrier potential," ϕ_B, is the least negative potential that an electron trajectory must encounter between its origin in the ambient plasma and the "gap surface." Figure 2 shows the potential structure for "baseline" conditions ($n_e = 1 \times 10^{11}$ m^{-3}, T=0.1 eV, ϕ_{cell}=150V). A negative potential barrier of about 0.05 volts is clearly seen about 7 millimeters in front of the gap surface. If a barrier is present, the current to the gap surface is reduced by a factor of exp(-ϕ_B/T). The barrier was calculated using the 2-D electrostatic finite element *Gilbert* code, both in the original 1991 study and in the current work. However, as the barrier potential of order 0.1 volts is a small fraction of the solar cell potential of order 150 volts, it is reasonable to question the accuracy of these calculations. Therefore, an analytic treatment was developed as a check on the numeric results. Also, an analytic treatment is better for use in a full computer model than a suite of numeric results spanning a rather large parameter space.
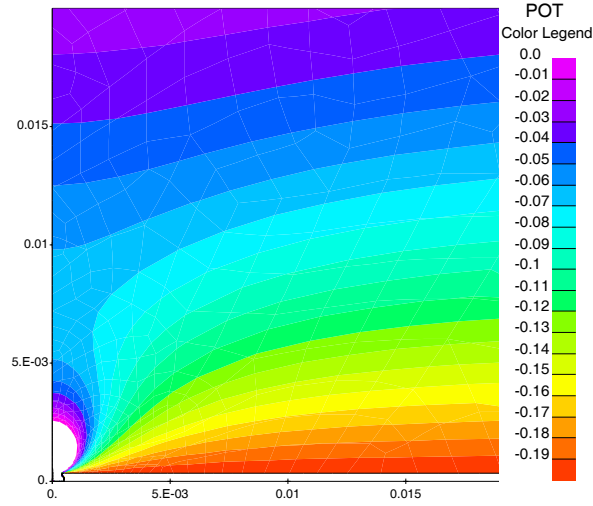
Figure 2. Potential structure above a solar array gap, showing saddle-point potential barrier. Structure is for n_e=1×10^{11} m^{-3}, T=0.1 eV, ϕ_{cell}=150V. White circular area above gap is region of positive potential.
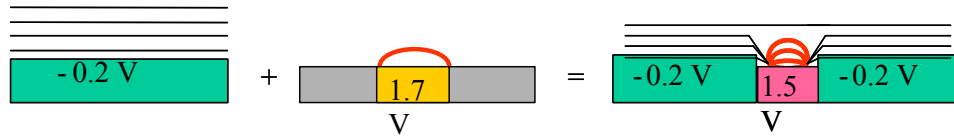
Figure 3. Superposition of coverglass (-0.2 V) potential plus gap surface potential (1.7 V on 0.0 V background) gives spatial potential induced by –0.2 V coverglass with 1.5 V gap surface.

Therefore, we have developed an analytic model for the potential on the symmetry plane (through the center of the "gap surface"). We approximate this potential as a superposition of the potential of a uniform coverglass surface plus the potential of the gap surface, as shown in Figure 3 (Superposition would be exactly correct if the potential were linearly screened. Since the plasma screening is nonlinear, this is an approximation which is good to the extent that the potentials are high enough and the distances short enough that the departure from linear screening is small.)

Coverglass-induced potential

The coverglass-induced potential is the one-dimensional solution to the nonlinear Poisson equation
$$-\varepsilon_0 \nabla^2 \phi = ne(1 - e^{\phi/T}) \qquad (5)$$
where the constant on the right hand side represents the ram ion density (unaffected by low potentials) and the exponential term represents reduced electron density (due to negative potentials comparable in magnitude to the electron temperature). In one dimension, this equation can be integrated once by multiplying by the electric field, $E = -\dfrac{\partial \phi}{\partial x}$, to get a relation between the electric field and potential.

$$2\varepsilon_0 \frac{d\phi}{dx}\frac{d^2\phi}{dx^2} = -2ne\frac{d\phi}{dx}(1-e^{\phi/t}) \qquad (6)$$

$$E^2 = \frac{2ne}{\varepsilon_0}(Te^{\phi/T}-\phi-T) = \frac{2T^2}{\lambda_D^{\,2}}\left(e^{\phi/T}-\frac{\phi}{T}-1\right) \qquad (7)$$

With this relation between the potential and electric field, it is straightforward to integrate the potential outward from the coverglass to obtain the coverglass-induced potential.

The *Gilbert* code was modified to optionally use the above charge density formula in negative potential regions. That brought the *Gilbert* and analytic calculations for the potential above the center of the coverglass into perfect agreement. All *Gilbert* calculations presented here use this charge density formulation.

Gap-surface induced potential

To find the gap-surface induced potential, we solve for the two-dimensional Laplace potential, $\phi(x,y)$, (where x is the distance from the gap center in the plane of the array and y is the distance above the array plane) subject to the boundary condition

$$\phi(x,0) = (<\phi_{gap}> - \phi_{glass}) \text{ for } |x| <= w/2 \qquad (8)$$
$$\phi(x,0) = 0 \quad \text{for } |x| > w/2$$

To solve this, we find the Fourier transform of ϕ, $g(t)$:

$$g(t) = \int_{-\infty}^{\infty} dx\,\phi(x,0)\cos xt = \frac{2\sin(wt/2)}{t}. \qquad (9)$$

Since $\cos xt\,\exp(-yt)$ satisfies Laplace's equation, we Fourier transform back to find

$$\phi(x,y) = \frac{1}{\pi}\int_0^{\infty} dt\,g(t)\cos xt\,\exp(-yt) = \qquad (10)$$
$$\frac{1}{\pi}\int_0^{\infty} dt\,\frac{2\sin(wt/2)}{t}\cos xt\,\exp(-yt)$$

Specializing to x=0 (*i.e.,* on the centerline of the gap) and using the standard tabulated integral

$$\int_0^{\infty} dx\,\frac{e^{-ax}}{x}\sin mx = \arctan(\frac{m}{a}) \qquad (11)$$

gives $\quad \phi(0,y) = \frac{2(<\phi_{gap}> - \phi_{glass})}{\pi}\arctan\frac{w}{2y} \qquad (12)$

Of course, this result includes no screening whatsoever. To obtain a maximally screened result, we multiply the Laplacian result by the factor $\exp(-y/\lambda_D)$, where λ_D is the plasma Debye length $(\varepsilon_0 T/ne)^{1/2}$.

Barrier calculation

   To determine the barrier potential, we add the coverglass-induced and gap-surface-induced potentials and find the minimum in the resulting curve. We have, however, two curves, depending on whether we consider the gap-surface-induced potential to be screened or unscreened, with the screened version giving a larger barrier. By comparison with *Gilbert* calculations, we set the barrier estimate to 0.76 times the unscreened (smaller) barrier plus 0.24 times the screened (larger) barrier value. Figure 4 shows the two curves for the baseline case of $n_e=1\times10^{11}$ m^{-3}, T=0.1 eV, ϕ_{cell}=150V. The two curves give barrier bounds of 0.0374 and 0.0759 volts, so that our analytic estimate for the actual barrier is 0.047 volts.

Orbit-Limited Collection

   Having established that there is (usually) a barrier to electron collection does not determine the electron current actually collected at the gap surface. The well-established way to determine particle collection is to track electron trajectories to the surface in the reverse sense (Figure 5) to see which trajectories correspond to actual environment electrons. Phase space considerations convert this information to the actual current. The approximation that all such trajectories correspond to environment electrons (and thus no particle tracking is necessary) is called the "orbit-limited" approximation.
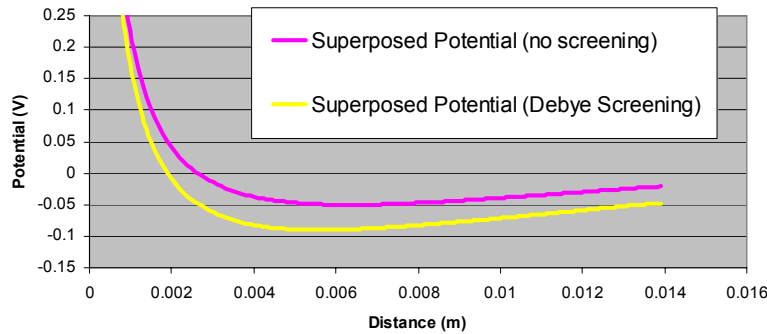
Figure 4. Potential as a function of distance from gap midline, giving screened and unscreened estimates for the barrier potential.
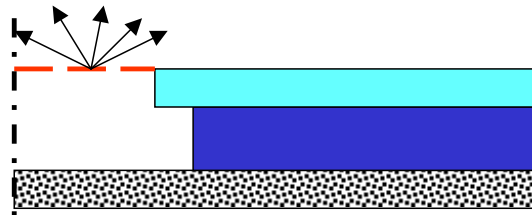
Figure 5. Reverse trajectory scheme to calculate current to surface.

   We treat the gap as infinitely long, so that the z-dimension (parallel to the gap length) is ignorable, leaving a two-dimensional problem. The integral to determine the collected current is then

$$j = \frac{n}{2\pi T} \int_{-\pi/2}^{\pi/2} d\theta \int_{\sqrt{2\phi}}^{\infty} (v\cos\theta)vH(v,\theta)dvd\theta e^{-(v^2/2-\phi)/T} \qquad (13)$$

where ϕ is now the potential at the gap surface, and $H(v,\theta)$ is unity for trajectories that connect to the environment and zero otherwise. If, for the moment, we assume $H=1$ everywhere, we can manipulate the integral to get

$$j = \frac{n}{\pi}\sqrt{2T}\sqrt{\frac{\phi}{T}}\int_0^\infty \sqrt{1 + \frac{wT}{\phi}}e^{-w}dw \qquad (14)$$

which can be expanded in a series for $\phi \gg T$

$$j \cong 2j_{th}\sqrt{\frac{\phi}{\pi T}}\left[1 + \tfrac{1}{2}\tfrac{T}{\phi} - \tfrac{1}{4}(\tfrac{T}{\phi})^2 + ...\right] \qquad (15)$$

or integrated exactly

$$j = 2j_{th}\sqrt{\frac{\phi}{\pi T}}\left\{1 + \frac{1}{2}\sqrt{\frac{\pi T}{\phi}}e^{\phi/T}\left[1 - erf(\sqrt{\phi/T})\right]\right\} \qquad (16)$$

where $j_{th} = ne\sqrt{\dfrac{eT}{2\pi m}}$ is the normal plasma thermal current.

If we take the potential barrier into account, we get

$$j = \frac{n}{\pi}\sqrt{2T}\sqrt{\frac{\phi}{T}}\int_{\sqrt{\phi_B/T}}^\infty \sqrt{1 + \frac{wT}{\phi}}e^{-w}dw \qquad (17)$$

$$j = \frac{n}{\pi}\sqrt{2T}\sqrt{\frac{\phi}{T}}e^{-\phi_B/T}\int_0^\infty \sqrt{1 + \frac{\phi_B}{\phi} + \frac{wT}{\phi}}e^{-w}dw \qquad (18)$$

which eventually leads to

$$j = 2j_{th}\sqrt{\frac{\phi + \phi_B}{\pi T}}e^{-\phi_B/T}\left\{1 + \frac{1}{2}\sqrt{\frac{\pi T}{\phi + \phi_B}}e^{(\phi + \phi_B)/T}\left[1 - erf(\sqrt{\frac{\phi + \phi_B}{T}})\right]\right\} \qquad (19)$$

This differs mainly in the exponential reduction by the barrier, since $\phi_B \ll \phi$ for all gaps collecting substantial current.

Departure from Orbit-Limited Collection

Orbit-limited collection, even with the exponential attenuation by the barrier, provides an upper bound to the collected current. In fact, not all reverse trajectories that are energetically allowed to escape over the gap actually do so; many are attracted back to the originating surface. Such trajectories represent portions of the environment phase space that do not contribute to the surface current. In general, a more compact potential structure leads to a greater fraction of excluded trajectories.

Figure 6 shows the fraction of trajectories connecting to the environment (function $H(v,\theta)$ averaged over angle) for two cases. The fraction goes to zero at the barrier energy, and rises

rapidly but continuously to nearly unity. Figure 7 shows the effect on the integrand for the current to the surface.
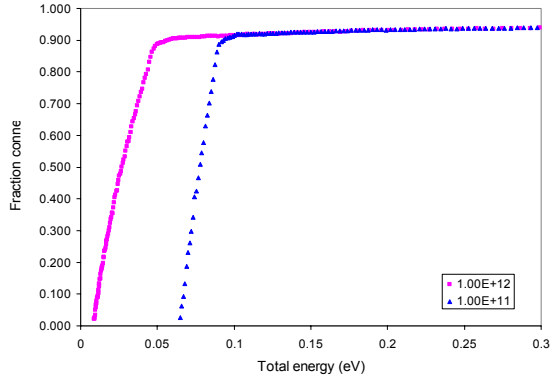
Figure 6. Fraction of trajectories connecting to environment as a function of energy.
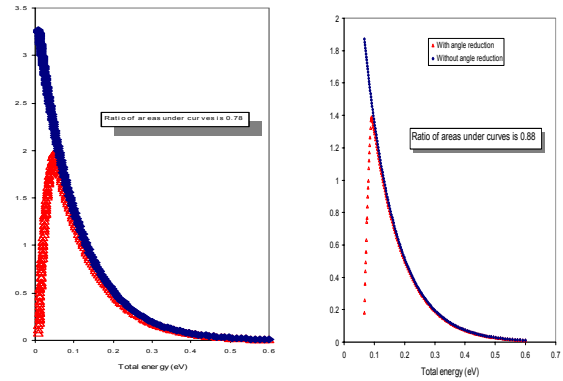
Figure 7. Decrease in integrand due to trajectories that do not connect to environment.

As a result of numerous *Gilbert* calculations, we have developed a simple numeric formula for the reduction in current, <H> due to departure from orbit-limited conditions. The formula is:

$$< H >= 0.89 + 0.62T^2 + 0.039\frac{\phi_{glass}}{T} - 0.02\ln\left(\frac{0.00744}{\lambda_D}\right) \qquad (20)$$

where T is the plasma temperature, ϕ_{glass} is the coverglass potential, and $\lambda_D = \left(\frac{\varepsilon_0 T}{ne}\right)^{1/2}$ is the

plasma Debye length. This expression is based on calculations done with temperatures between 0.1 and 0.25 eV (although it is still valid for temperatures down to .05 eV as it changes by only ~2% over this range), plasma densities between 10^{10} and 10^{12} m^{-3}, and coverglass potentials between -0.2 and -0.5 V. It is this expression that defines the parameter range over which the model is valid.

Gap Surface Current Collection

Compiling all of the above results, we find the current per unit length of gap to be

$$\frac{I}{L} = wj_{th}e^{-\phi_B/T} < H >< OL > \qquad (21)$$

where
w = gap width = 8.13×10^{-4} m

j_{th} = plasma thermal current = $ne\sqrt{\frac{eT}{2\pi m}}$

ϕ_B = potential barrier
<H> = current reduction due to departure from orbit-limited current
<OL> = orbit limited current enhancement:

$$2\sqrt{\frac{\phi}{\pi T}}\left\{1+\frac{1}{2}\sqrt{\frac{\pi T}{\phi}}e^{\phi/T}\left[1-erf(\sqrt{\phi/T})\right]\right\} \qquad (22)$$

Note that <OL> is calculated using the square-mean-root gap potential,

$$\left\langle \phi^{1/2} \right\rangle^2_{gap} = 0.00969\phi_{cell} + 0.926\phi_{glass} \,,$$

whereas the potential barrier, ϕ_B, is calculated with the mean gap potential,

$$\left\langle \phi \right\rangle_{gap} = 0.01035\phi_{cell} + 0.982\phi_{glass} \,.$$

The coverglass potential, ϕ_{glass}, is determined by

$$j_{th} e^{\phi_{glass}/T} = nev\cos\theta + j_{th}\left(\frac{m_e}{m_i}\right)^{1/2}$$

where v is the ram velocity and θ is the angle between the spacecraft velocity and the array normal.

String Current Calculations

To determine the current collected by a string, we need to multiply by the total gap length of the string, and average the collection over the range of cell voltages.

An infinite array of solar cells would have 2 edges per cell. However, the cells are arranged in 4×10 subpanels, leading to 14 extra edges per 40 cells or 2.35 actual edges per cell. With 400 cells per string and 8 cm per edge, each string has a total effective gap length of 75.2 m. Including the gap width gives an effective collection area per string of 0.06 m², with is about 2.4% of the actual cell area. Each array or wing contains 82 strings.

Dependence of Solar Array Electron Collection Model on Plasma Environment

Figure 8 below shows how the ISS solar array current, using this model of electron collection by the solar cells, depends on temperature and density. These curves assume sunlit, ram-facing conditions with all 82 strings on and the station chassis held to zero potential (that is, the solar cells on the array have voltages with respect to the plasma of from 0 to 160 volts).

Validation of Solar Array Collection Model

Environment Work Bench (EWB)

We validate the ISS solar array collection model by integrating it into Environment WorkBench (EWB), and comparing calculated array current collection with Plasma Contactor Unit (PCU) emission currents. EWB is an engineering trade study tool for the assessment of space environments effects on spacecraft. EWB was developed under contract to NASA[2] as the ISS plasma interactions and effects analysis tool. As such it has been used to support the plasma contactor design, development and integration efforts and more recently the initial analysis of the ISS Floating Potential Probe (FPP) and Plasma Contactor Unit (PCU) data.
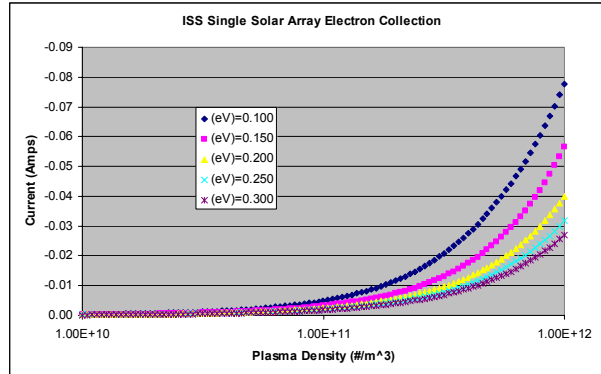
Figure 8. Electron collection of single ISS solar array increases with plasma density and decreases with increasing plasma temperature.
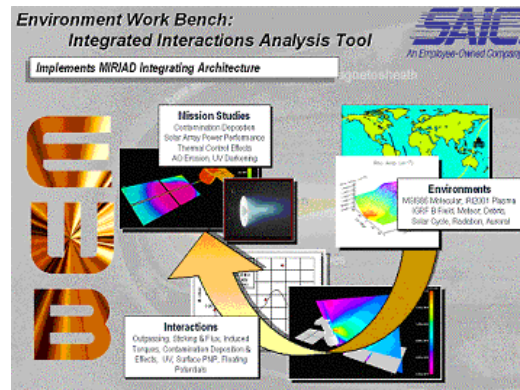
Figure 9. EWB was developed as the ISS plasma analysis tool to support development of the PCUs.

EWB was designed specifically to provide a verifiable methodology for combining the myriad of component interactions that need to be addressed in the calculation of ISS floating potentials. It is more than just a code with many models; it is an integration architecture that supports software in the loop testing.

EWB simulates a fully integrated system. Using ISS two-line element sets, it calculates the position of ISS at the time specified by the user and calculates the plasma, geomagnetic and solar environments at that point on orbit. The ISS model implemented in EWB includes attitude and sun-tracking of the solar arrays. Potentials are calculated over the entire system, including vxB induced potentials, by performing an iterative current balance calculation. Each "component" of ISS, e.g., solar arrays, conducting and insulating surfaces and PCUs has a model of its current/voltage relationship with the surrounding plasma. To change the electron collection of the solar arrays, one need only "plug in" a different model for that one component.

EWB includes standard environment models such as MSIS-86, IRI(90 & 2001), AP-8, AE-8, and IGRF-87, and standard Brouwer and NORAD orbit generators. A database of commonly used spacecraft materials allows selection from a variety of polymers, composites, thermal control coatings, etc., while the constructive geometry system definition enables the user to explore

spacecraft configuration issues. Space environment effects models in EWB include electromagnetic and plasma interactions, atomic oxygen erosion, surface contamination (including power system degradation effects), UV absorptivity, meteoroid and debris damage, and others.

Comparison with PCU data

On March 29, 2001 a DTO (delta-to-operations) was performed to shunt and unshunt the ISS solar arrays with the PCUs on. The purpose of this was to observe the jump or dip in the plasma contactor current as a measure of the collection of the arrays. When an array is unshunted, all 82 strings turn on at once, and the current collected on the cell edges is seen in the increased emission from the plasma contactor:

$$I_{pc}(V_s)=I_{mast}(V_s) + I_{body}(V_s)$$
$$I_{pc}(V_u)=I_{mast}(V_u) + I_{body}(V_u) + I_{array}(V_u)$$
$$I_{pc}(V_u)- I_{pc}(V_s)= I_{array}(V_u) + (V_u-V_s)*(dI_{mast}/dV + dI_{body}/dV)$$

V_s is the voltage at the PCU when the arrays are shunted and V_u is the voltage at the PCU when the arrays are unshunted. Since the PCUs are on and grounding the station, V_u is very close to V_s and, to first order the jump in the PC current is just the array current. A series of shuntings and unshuntings of the arrays was performed for each of four orbits as described in Table 1.

Table 1. Times and shunt/unshunt events for each of four orbits on March 29, 2001.

Time	Event
Sunrise + 5:00 (min)	Shunt Port Solar Array (4B)
Sunrise + 5:30	Unshunt Port Solar Array (4B)
Sunrise + 7:30	Shunt Stbd Solar Array (2B)
Sunrise + 8:00	Unshunt Stbd Solar Array (2B)
Sunrise + 10:00	Shunt both Solar Arrays
Sunrise + 10:30	Unshunt both Solar Arrays
Orbit Noon -10:00	Shunt Port Solar Array (4B)
Orbit Noon -9:30	Unshunt Port Solar Array (4B)
Orbit Noon -7:30	Shunt Stbd Solar Array (2B)
Orbit Noon -7:00	Unshunt Stbd Solar Array (2B)
Orbit Noon -5:00	Shunt both Solar Arrays
Orbit Noon -4:30	Unshunt both Solar Arrays

Figure 10 shows a sample of data from the first of four orbits for the March 29 DTO. The magenta line is the PC current. The jumps and dips due to unshunting and shunting of the arrays can be seen clearly. The blue and green points are the number of strings on for 2B and 4B (~26 corresponds to 82 strings on).

Using the newly developed solar array collection model implemented in EWB, we calculate the string current for each of the post sunrise unshunting events for all four orbits. The post-sunrise times were chosen over the pre-noon times because the arrays collect the greatest amount of current when they are in sunlight and into the ram. The data and calculated values are shown in Figure 11,

where the red marks are for array 2B and the blue for 4B. The darker square symbols are the data (jump in PCU current normalized to one string) and the lighter round ones, the calculated values. While this is a limited validation effort, these initial results are encouraging.
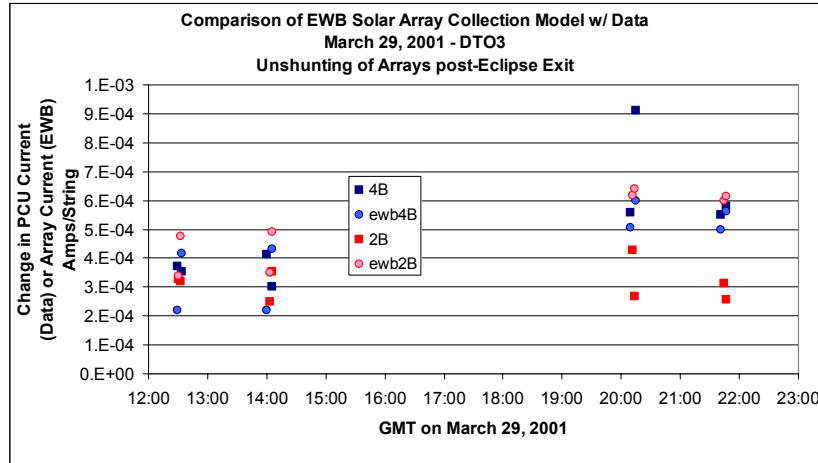
Calculation of ISS Potentials

The significance of current collection by solar arrays is that it can drive a system negative with respect to the plasma by as much as ~90% of the voltage on the arrays, which in the case of ISS is 160 volts. ISS has a requirement that no point on the station accessible to the astronauts during EVA be more than 40 volts negative of the plasma. Calculation of the station floating potential requires accurate models of the current/voltage characteristics of all surfaces and subsystems. It also requires accurate knowledge of the electron temperature of the plasma. We will discuss these two issues below.

In the case of ISS the major current collecting or emitting components are: electron emission by the PCUs, electron and ion collection by the solar array mast structures, electron and ion collection by the solar array cell edges, and ion collection by exposed conducting surfaces all over the station. In the case of ISS, the one we know the least about that has the largest impact on array driven charging is the effective ion collecting area of the station nodes and truss structures, etc.
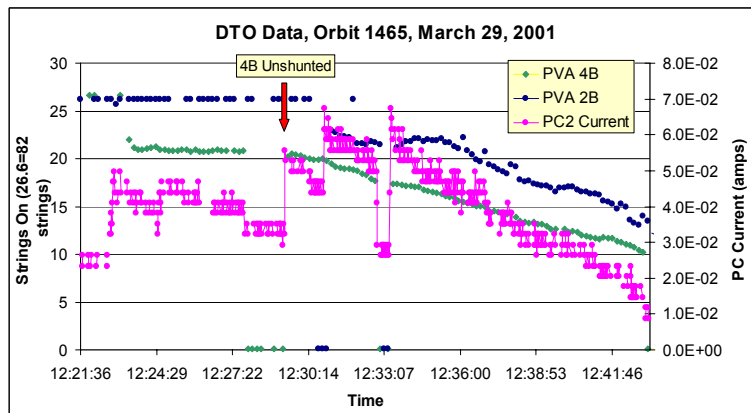
Figure 10. Sample of data from March 29, 2001 DTO. Arrow points to example of 4B unshunting with jump in PCU current.

Figure 11. Comparison of string current calculated using EWB, and March 29 DTO data.

Figure 12 shows a typical EWB calculation of chassis potential at the ISS FPP over several orbits on April 11, 2001. These are actually negative potentials but the values have been multiplied by minus one. Also shown is the FPP data for those same orbits. The PCUs were deliberately turned off in order to measure the array driven charging of the station. The ~10 volt lobes are vxB induced potentials while the ~20+volt peaks are ISS charging due to array current collection at eclipse exit. The three EWB calculations shown are done using three different values for the effective ion collecting area of ISS, 25m^2, 30m^2 and 35m^2. This illustrates the effect that ISS ion collecting area has on array driven charging, with a smaller effect on vxB induced potentials. The smaller the ion collecting area, the more negative the system is driven to reduce the electron collection area of the arrays until current balance is achieved.

Another variable that has a large effect on eclipse exit charging levels is the electron temperature of the plasma (as shown in Figure 8), typically .08 to .2 eV for ISS orbit. While the FPP measured the plasma density and temperature, due to the limited range of the Langmuir probe sweep, the environment data is most suspect just when we need it most, *i.e.*, when ISS is charging. Additionally our best models of the plasma environment, such as IRI2001 used here, is climatological. It is not designed to predict the electron temperature at a specific point in time and space at the level of accuracy needed for these calculations.
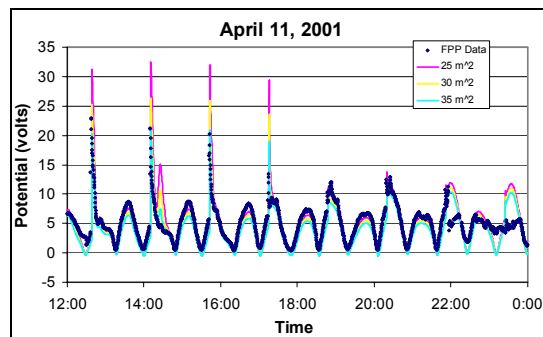

Figure 12. FPP data and EWB calculations of ISS potentials for several orbits on April 11, 2001.

To examine the effect of ion collecting area (A_i) on ISS charging levels over the range of anticipated plasma environments, we use a set of environment data gathered by the AEC satellite[3]. Figure 13 and Figure 14 show calculations done for ~8000 data points. These points were selected to lie within the latitudes seen by ISS, to be sunlit and to be in the morning. The date, time, location, plasma density (n_e) and electron temperature (T_e) were set and the potential at the FPP calculated for each point. Figure 13 shows the maximum potentials calculated for A_i =37m^2 are between 20 and 25 volts (green), while Figure 14, using A_i=20m^2, shows maximum potentials of 40-45 volts (red).

All of the FPP charging data was taken over 10 days, from April 10-21, 2001, with a total of about 50 charging peaks. The maximum charging value in the data set is 24 volts which would appear to point strongly to the appropriateness of using approximately 37m^2 as the effective ISS ion collecting area. However, the small size of our data set and brief time period over which it was taken gives little confidence that we have sampled the entire environment parameter space. We compare the distribution of the data, shown in the Figure 15 histogram, to the distribution of calculated values over the same time period, Figure 16. The calculations were done using A_i=35m^2 and IRI2001 calculated environments. The difference in these distributions leads us to believe we are not seeing a wide variation in the plasma environments for these peaks. If we look at the black circles in Figure 13 and Figure 14, we see that the data is consistent with two different areas in environment parameter space depending on what ion collecting area is assumed. In fact, for each value of A_i there is a "region" in n_e-T_e space that fits the range of the April, 2001 FPP data, with T_e being the bigger environmental driver.
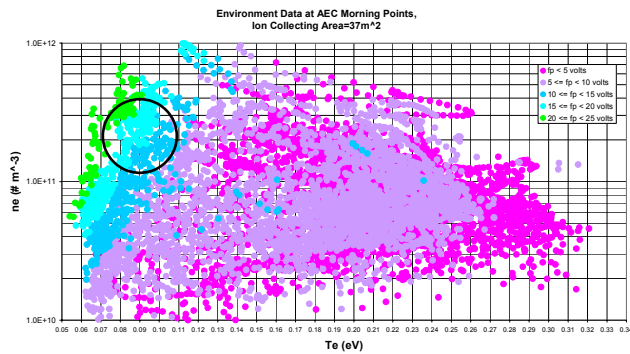

Figure 13. Calculation of ISS potentials at FPP location for ~8000 plasma environment data pairs from the AEC satellite. Assumes 37 m^2 of ion collecting area.
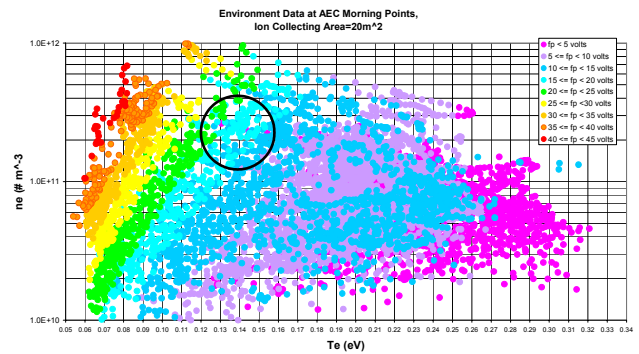
Figure 14. Calculation of ISS potentials at FPP location for ~8000 plasma environment data pairs from the AEC satellite. Assumes 25 m2 of ion collecting area.
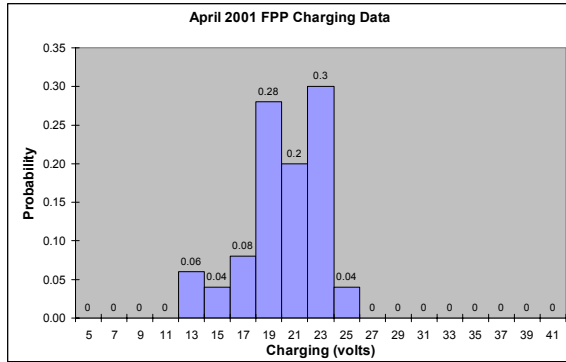
Figure 15. Histogram ISS FPP potentials for 50 observed charging peaks, April 10-21, 2001. Values range from 12 to 24 volts.
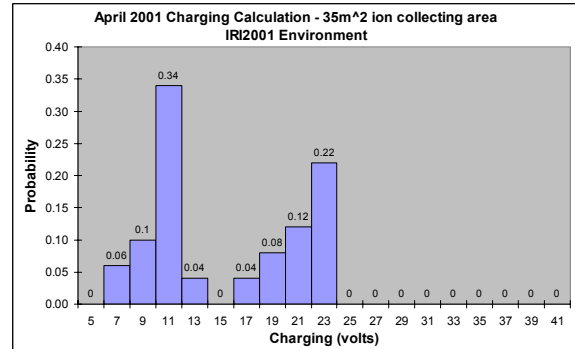
Figure 16. Histogram of calculated ISS FPP potentials for 165 eclipse exits, April 10-21, 2001. Values range from 5 to 23 volts.

Conclusions

Data from the ISS PCUs and FPP are inconsistent with predictions made using the original ISS solar array electron current collection model developed in 1991. With advances in knowledge, codes, and computers, and with on-orbit data for validation, we developed a new model of ISS solar array current collection. The biggest difference between the two models is the addition of a nonlinear electron density dependence and the assumption of no snapover.[4] Preliminary calculations done with the new model integrated into EWB show good agreement with PCU emission current data from the March 29, 2001 DTO. However, maximum ISS potentials cannot be predicted at this time due to our lack of both knowledge of the ISS effective ion collecting area and accurate measurements of the plasma environment. Additionally, we cannot be sure that the next set of solar arrays will collect in the same manner as the present pair. This adds additional uncertainty to the problem.

A Floating Potential Monitor Unit (FPMU) is being developed to fly on ULF1 and should give us the needed environment measurements. What is needed additionally is thorough validation of the array current collection model. This includes revalidation at each PVA-set deployment via targeted DTOs such as that performed on March 29, 2001. This information should allow, at each mission build, calculation of an effective ion collecting area to be used in predictions of 3-sigma worst-case charging of ISS.

References

1. Kaufman, B.A., Chrulski, D., Myers, R.M., "Photovoltaic Plasma Interaction Test II", Nasa Lewis Research Center, July 14, 1995.

2. EWB 5.0 User's Reference Manual, NASA/Glenn Contract NAS#-25347, July 31, 1997.

3. Joe Minow, Private Communication.

4. Stevens, N.J., "Review of Biased Solar Array-Plasma Interaction Studies, NASA TM82693, 1981.

THE ELECTRIC PROPULSION INTERACTIONS CODE*

I.G. Mikellides
Science Applications International Corporation
10260 Campus Point Drive, San Diego, CA 92121

M.J. Mandell
R.A. Kuharski
V.A. Davis
B.M. Gardner
Science Applications International Corporation

J. Minor
NASA Marshall Space Flight Center

Abstract

Science Applications International Corporation is currently developing the Electric Propulsion Interactions Code, *EPIC*, as part of a project sponsored by the Space Environments and Effects Program at the NASA Marshall Space Flight Center. Now in its second year of development, *EPIC* is an interactive computer tool that allows the construction of a 3-D spacecraft model, and the assessment of a variety of interactions between its subsystems and the plume from an electric thruster. These interactions may include erosion of surfaces due to sputtering and re-deposition of sputtered materials, surface heating, torque on the spacecraft, and changes in surface properties due to erosion and deposition. This paper describes the overall capability of EPIC and provides an outline of the physics and algorithms that comprise many of its computational modules.

Introduction

More than one hundred satellites are currently operating in space with onboard electric propulsion (EP). Many more missions with EP systems - both near-Earth and deep space - are being considered. A critical engineering issue in the integration of EP on spacecraft is the potentially unfavorable interaction of their high-energy plumes with surrounding critical components and diagnostic equipment. Such interactions may affect mission lifetime and sometimes even threaten mission success. As NASA considers more powerful EP technologies for long-duration missions, the need to predict pertinent interactions becomes even more critical. Only a few programs with the goal to produce large-scale, 3-D, global computer tools for the assessment of such interactions exist - two in the U.S.[1,2] and one in Europe.[3] One of the two U.S. programs aims in the development *EPIC*.

EPIC is currently developed by Science Applications International Corporation (SAIC) as part of a 2-year effort that is sponsored by the Space Environment and Effects (SEE) Program at

---

the NASA Marshall Space Flight Center (MSFC). The objective is to produce an integrated modeling package that can be used to aid the design of spacecraft with onboard electric propulsion. The suite of computer tools is intended to allow both expert and novice users to investigate EP plume-S/C interactions. The code is built on the Module Integrator and Rule-based Intelligent Analytic Database (MIRIAD) architecture, which has formed the core of several NASA and Department of Defense programs.

Overview

In general, the spacecraft designer provides the following input to *EPIC*: satellite geometry and surface materials, thruster locations and plume parameters, case study parameters such as sputter yield coefficients, orbit and hours of thruster operation. The output may be in the form of contour plots of the plume map in space and of surface interactions on the 3-D spacecraft, 1-D plots along surfaces (e.g. erosion depth on a solar array as a function of distance from the thruster), integrated results over duration of mission (e.g. total induced torque in a given direction, total deposition of eroded material at a specific location on the spacecraft), list of results in text format for post-processing. *EPIC*'s various components have already been used to asses EP-spacecraft interactions for both the government[1,4] and industry.[5]

The computer tool (built for the Win32 platform) consists of the following main components:

- An enhanced version of the 3-D geometry-definition tool Object Toolkit (OTk) to facilitate interactive generation of the spacecraft geometry and materials.
- A 3-D interactions code built using the Module Integrator and Rule-based Intelligent Analytic Database (MIRIAD) architecture.
- A 2-D plume code that generates the plume map from an electrostatic thruster in the R-Z plane. A fast, 1-D Hall effect thruster (HET) algorithm is also part of the plume modeling capability. The algorithm is intended to provide a more quantitative estimate of the conditions near the thruster exit.

EPIC Architecture

The bulk of *EPIC*'s capability is the 3-D plume-surface interactions code. The code is built on the MIRIAD architecture, which has formed the core of several NASA and DoD programs, and has allowed spacecraft designers to quickly and affordably model interactions between the spacecraft and the space environment. MIRIAD's open architecture provides a framework for integrating a variety of physical models and their constituent data into a single executable application. The application then allows the user to define systems of interest and perform parametric studies with relative ease. Ideally, any variable in MIRIAD can be included in a parametric study.

The main *EPIC* user interface and the code that integrates the various components are programmed in C# (C-sharp). C# is a new language developed by Microsoft that provides an easy-to-use object orientated way to program the windows user interface, and makes it extremely easy to combine components written in different languages using either the new Common

Language Runtime (CLR) or the Component Object Model (COM) that has been the backbone of windows programs for years. The combination of C# and the CLR foundation classes is a very powerful and easy way to get the desired functionality in the user interface.

The most natural and powerful way to communicate with the MIRIAD data server that coordinates *EPIC* calculations is through COM. It was therefore particularly important to be able to use COM components in *EPIC*. Any COM or dot net client can access *EPIC*'s COM data server. For example EXCEL can be used to script calculations and manipulate data produced by *EPIC*. C# allows easy use of our COM- based 3-D viewer (MxOpenGlArena) for viewing the system and displaying surface information and spatial data.

Main Computation Components of *EPIC*

Spacecraft model

Object Toolkit is *EPIC*'s 3-D object generator. Originally developed to create spacecraft surface models for the *Nascap-2k* plasma interactions code,[6] OTk has been generalized to allow for the definition of spacecraft models for other analysis codes. In particular for *EPIC*, employment of "Special Objects" has been allowed to facilitate the specification of thrusters as illustrated in Figure 1. "Special Objects" are objects understood by the target application that are included in Object Toolkit primarily to specify and display their location. They are therefore not a part of the spacecraft surface model. Each special object instance has an object type name (*e.g.* "Hall Thruster"), an instance name (*e.g.* "SPT100-1"), and a set of properties that includes, at minimum, its position ("x", "y", "z"), thrust unit vector, and the color with which it is to be displayed ("r", "g", "b"). The properties can be edited for each special object instance in similar fashion to the attribute property values. Figure 2 shows the OTk spacecraft model of Figure 1 imported into the main *EPIC* interface, and the list of all materials associated with the spacecraft.
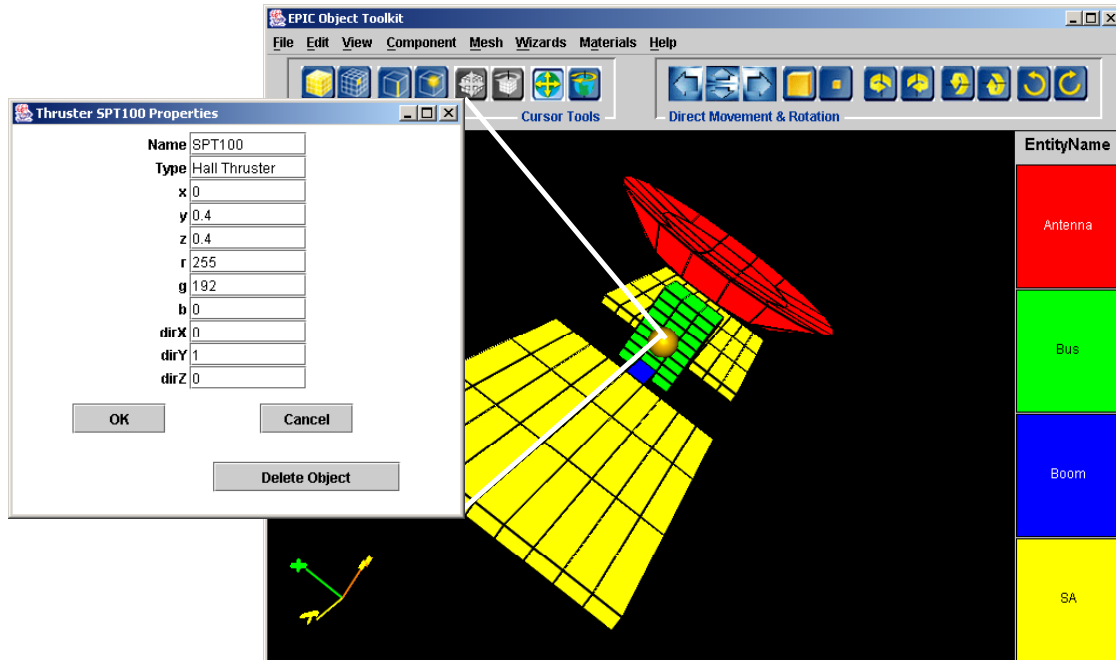
Figure 1. Object ToolKit-generated spacecraft showing various entity definitions and the thruster (in this case a Stationary Plasma Thruster, SPT-100) location.

Electric propulsion plumes

Thruster plume definition in *EPIC* is performed using "PlumeTool" (Figure 3). The 2-D plume generation computational module allows the spacecraft designer to either import a plume map (produced by other codes) or generate it using the existing 2-D plume code. The 2-D plume code was written to model low-density EP exhausts such as those associated with electrostatic thrusters. The code uses parts from an existing, finite element (FE) code (*Gilbert*) that has been used in the past to solve a variety of problems involving Poisson's equation (e.g. see Mikellides, I.G., *et al.*[7]). The generated plume maps consist of the spatial distributions of ion density and velocity. The model consists of three main components: a Lagrangian algorithm for determining the expansion of the main ion beam, a Particle-in-Cell (PIC) solver for computing the dynamics of the charge-exchange plasma, and an ideal-scattering algorithm that calculates the density and velocity of ions that are produced by elastic collisions with neutral atoms. The physics and numerics of each component have been described in detail in previous publications.[1,8,9,10] Highlighted below are some of the fundamental principles behind the various plume model components.
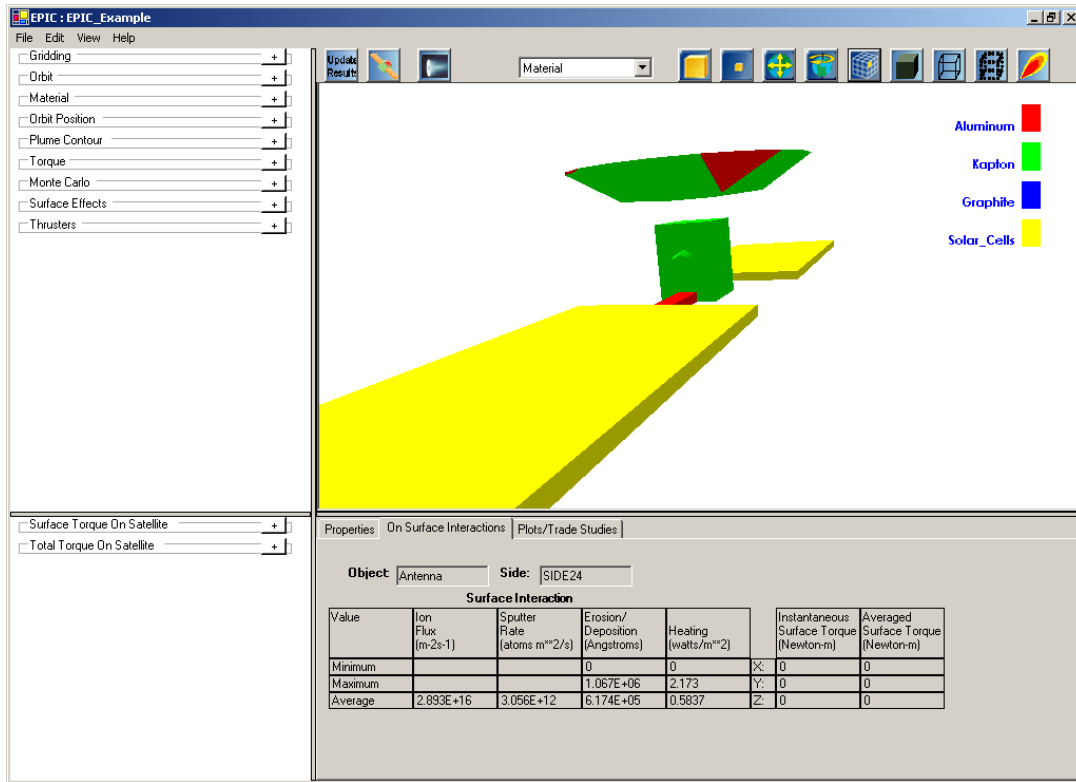
Figure 2. Main *EPIC* interface showing imported spacecraft object and thruster properties.

2-D Plume Physics Models. The main ion beam is assumed to be a collisionless, singly-ionized, quasi-neutral plasma expanding under the influence of the electric field. The latter is assumed to exist due to the presence of density gradients in the plasma. By comparison to heavy-particle motion, electrons reach dynamic equilibrium at much smaller characteristic times. The electron inertia term may therefore be neglected in the equation of motion. In the absence of electron-ion collisions and magnetic fields, integration of the conservation of momentum for the electrons leads to the Boltzmann relation, which can be expressed in terms of the electric potential as follows:

$$\phi(n, T_e) = T_e \ln(n / n_\infty) \tag{1}$$

where, ϕ is the electric potential, n is the plasma density ($n = n_e = n_i$), T_e is the electron temperature and n_∞ is the reference plasma density at zero potential.
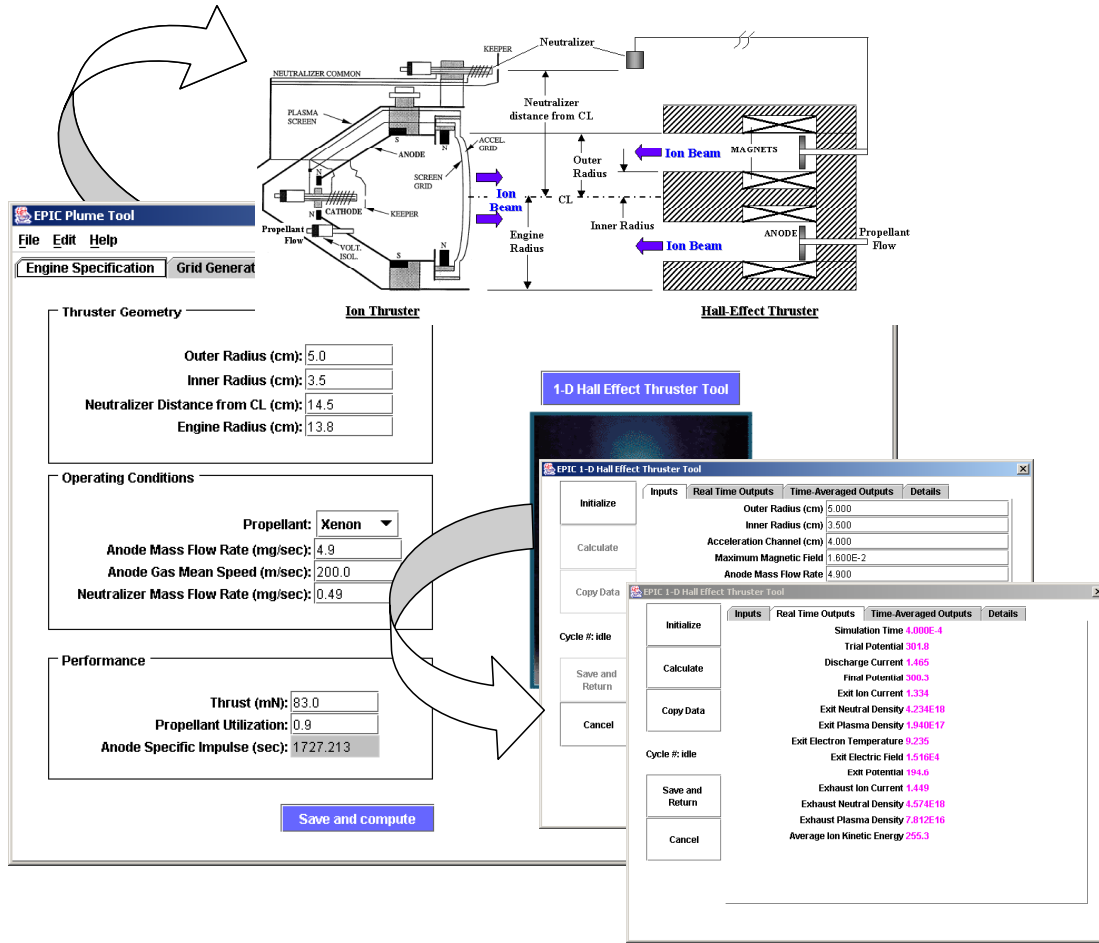
Figure 3. PlumeTool's Engine Specification window may be launched from the *EPIC* main interface.

Ions are accelerated by the electric field, $\vec{E} = -\nabla\phi$ according to,

$$m_i \, \frac{D\,\vec{v}_i}{D\,t} = -\,e\,\nabla\,\phi \qquad (2)$$

where m_i and e are ion mass and electron charge, respectively. Since the drift velocity of the ions, $\vec{v}_i$, is much greater than their thermal velocity, the high velocity ions are modeled as a fluid. The steady state, conservation equations of mass and momentum are solved in 2-D (R-Z) geometry. The numerical algorithm for computing the expansion of the main ion beam is based on a Lagrangian approach in which discrete mass elements, or otherwise "macroparticles" are released from the thruster exit and are then "tracked" using fundamental trajectory kinematics.[10] The (normalized) current density profiles presently implemented along the exit of Ion and Hall thrusters are shown in Figure 4. For an Ion thruster the current density profile is assumed to vary parabolically with radius, *i.e.* as $[1-(r/r_{outET})^2]$, where r_{outET} is the thruster outer radius. The ion velocity components V_r and V_z are determined by assuming that all ions are emitted from a point

source behind the acceleration grid, with a maximum divergence angle of α (currently set at 20 deg). Thus,

$$\bar{u}_r \equiv \frac{V_r}{|V|} = \frac{\tan\alpha}{\sqrt{\tan^2\alpha + \frac{1}{(r/r_{outET})^2}}}, \quad \bar{u}_z \equiv \frac{V_z}{|V|} = \sqrt{1 - \bar{u}_r^2}$$

$$V = \sqrt{\frac{2eE_b}{m_i}}$$

(3)

where E_b is the main beam energy. For Hall thrusters the current density and velocity profiles at the exit are based on extrapolation of integrated measurements from the Busek-Primex Hall thruster (BPT-4000).[5]
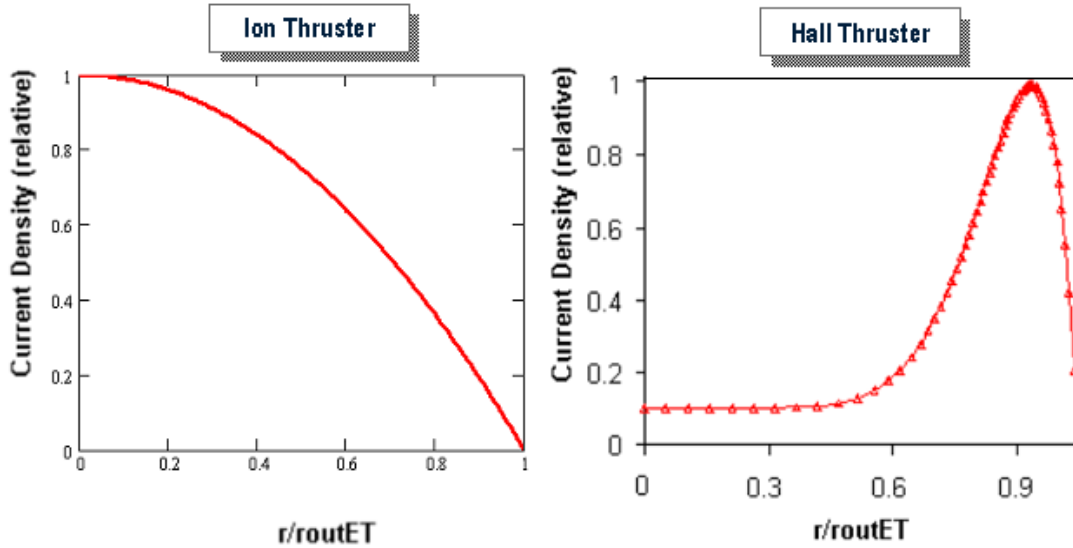
Figure 4. Normalized current density profiles for Ion (left) and Hall thrusters (right).

The neutral gas density in space is mainly due to particles from the thruster and from the hollow cathode. The beam of neutrals from the thruster is computed using an annular anode gas flow model with isotropic emission from a ring. The profile of neutrals from the thruster is computed using two disk emissions defined by the solid angles subtended by each disk, and subtracting the smaller from the larger.[8] The flow rate of neutrals from the thruster exit is estimated using the known anode flow rate and propellant utilization. The hollow cathode is offset by a distance r_{HC} from the thruster. Its axial location is assumed to be at $z=0$. The constant-temperature neutrals are emitted isotropically from the neutralizer, and their speed is estimated based on the same assumptions used for the thruster neutrals.

Fast ions from the main beam undergo charge-exchange (CEX) with neutral particles, resulting in slow-moving ions and fast-moving neutrals,

$$_{fast}Xe^+ + {}_{slow}Xe \rightarrow {}_{slow}Xe^+ + {}_{fast}Xe$$

(4)

In *EPIC*'s 2-D plume code, charge-exchange is computed using a two-dimensional PIC method. The rate of CEX-ion production rate $\dot{n}_{CEX}$ is determined by,

$$\dot{n}_{CEX} = n\,\vec{v}_i \sigma_{CEX} n_o \tag{5}$$

In eqn (5) n_o is the particle density of neutrals and σ_{CEX} is the cross section associated with the charge exchange collision. In contrast to the approach for the calculation of the main beam ions, where direct use of equation (1) provides the potential, the PIC algorithm solves the 2-D Poisson's equation on a finite element grid and iterates until steady state CEX densities and potentials are consistent. The plasma density in Poisson's equation is the sum of the main-beam and CEX densities. The first (computed by the Lagrangian method), and the prescribed neutral gas profile (above), are used as input for the calculation. The computed (total) ion particle density in Figure 5 shows clearly the CEX ion regions in the plume of an SPT-100.
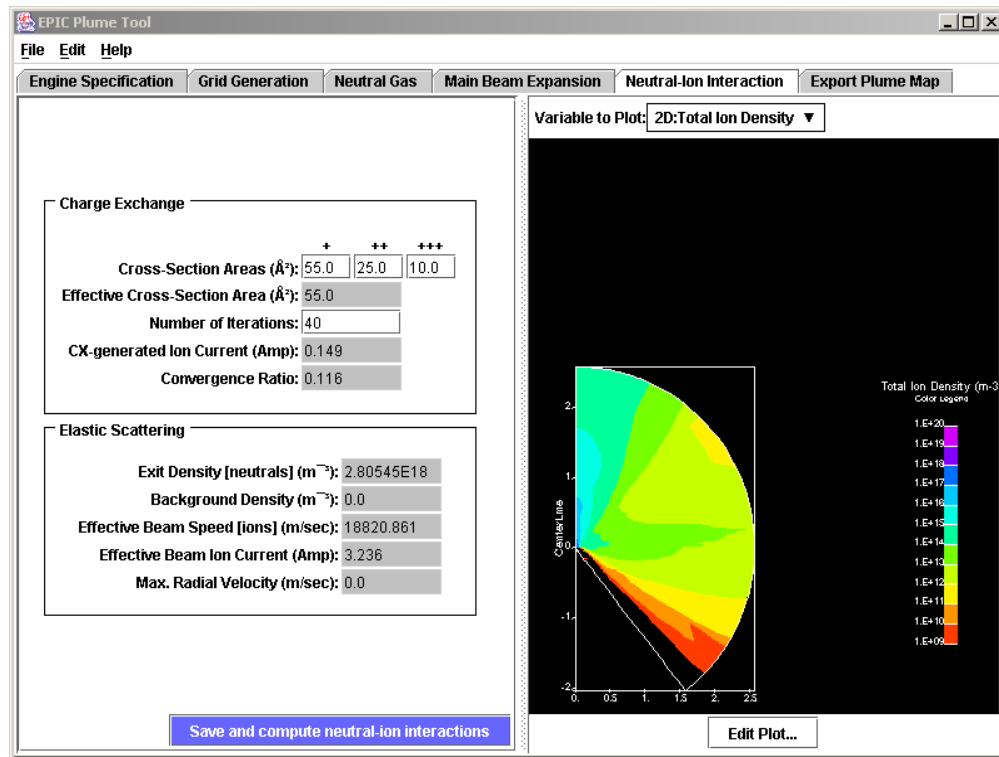
Figure 5. Total ion particle density in the plume of an SPT-100 as computed by PlumeTool's 2-D code.

With the revival of nuclear sources in space flight many EP systems are projected to operate at high power levels (>10 kW) for increased specific impulse and thrust. Main beam ion energies in such missions can range in the thousands of electron-volts (>5000 eV) with ion flow rates exceeding a few milligrams per second (>3 mg/sec). In these propulsion systems the need to quantify the effects of high-energy ions (>300 eV) that are produced by elastic scattering

between main beam ions and neutral particles becomes critical. The main reason is that these ions can be scattered to angles greater than those associated with the divergence of the main beam (which usually does not exceed 45 deg) and can therefore pose significant damage to surrounding spacecraft structures and diagnostics. An algorithm that determines the flux and energy of elastically scattered ions is part of PlumeTool; we outline here the basic approach.

In the classical sense, the differential cross section associated with an atomic collision can be calculated from the deflection angle, $\Theta(b,E_c,)$[11]

$$\Theta(b, E_c) = \pi - 2b \int_{r_m}^{\infty} \frac{dr}{r^2 \sqrt{1 - (b/r)^2 - (V(r)/E_c)}} \tag{6}$$

where E_c is the center-of-mass collision energy, b is the impact parameter, r is the interatomic distance, r_m is the *classical turning point* (point of nearest approach), and $V(r)$ is the interatomic potential energy. In the center of mass frame, θ, is given by $\theta = |\Theta|, \quad 0 < \theta < \pi$.

The differential cross section is obtained from equation (7) as follows:

$$I(\theta, E_c) \equiv \frac{\partial \sigma}{\partial \Omega_{CM}} = \left| \frac{b}{(d\theta / db) \sin \theta} \right| \tag{7}$$

where σ is the collision cross section. The solid angle is given by $d\Omega = 2\pi \sin\theta \, d\theta$. In the numerical model, given the angle and energy for each scattering pair (s-point to f-node as it will be shown later), the impact parameter is obtained by solving equation (6) using a Newton-Raphson method. The solution requires *apriori* knowledge of the interatomic potential function, $V(r)$, which may in general have both attractive and repulsive contributions. At the high energies of interest in the present work (>300 eV) the deflection function barely exhibits a minimum as the scattering is almost solely governed by the repulsive part of the interaction potential. In such cases the classical approach (vs. the more rigorous quantum mechanical approach[12]) is sufficiently accurate. Currently, only the repulsive potential function is included in the model. The coefficients that define the functional form of $V(r)$ have been derived from averaged potentials by Amarouche, M., *et al.*[13] and are listed in Katz, I., *et al.*[14] The derivative in equation (7) is computed using a first order forward finite difference.

We refer to Figure 6 to describe the formulation used for the determination of the density, average velocity and average energy of the elastically scattered ions. It is assumed that at the scattering point "s", one scattering event occurs as the main beam ion flux, $F_b = n_{b,s} u_{b,s}$ impacts one stationary neutral particle. Once scattered, each ion does not undergo another collision. Then the particle flow rate dN/dt (#particles N per unit time t) through the incremental surface $dS = \rho^2 d\Omega$, is given by:

$$\frac{dN}{dt} = F_b I_{ion} \frac{dS}{\rho^2} \tag{8}$$

where $d\Omega$ is the solid angle subtended by dS at point "s", $I_{ion}(\theta) = \frac{1}{2}I(\theta) + \frac{1}{2}I(\pi - \theta)$ and ρ is the distance between "s" and field node "f". The particle flow rate is also equal to,

$$\frac{dN}{dt} = n_{sf} u_{sf} dS \qquad (9)$$

where, n_{sf} and u_{sf} are the elastically scattered particle density and speed, respectively, at the field node "f". Combining equations (8) and (9) we obtain,

$$F_{sf} = n_{sf} u_{sf} = \frac{4 F_b I_{ion} \cos \vartheta_{sf}}{\rho^2} \qquad (10)$$

Equation (10) expresses the magnitude of the flux vector, $F_{sf} = |\mathbf{F}_{sf}|$, at the field node location $f(r_f, z_f, 0)$ due to scattering of the main beam flux F_b by a neutral at the scattering point $s(r_s, z_s, \phi)$. We note the additional term $4\cos\vartheta_{sf}$ introduced in equation (10) by the transformation from the center-of-mass frame to the laboratory frame.[9]

It is also assumed that the distance between nodes is much larger than the mean free path for ion-neutral collisions. Since both momentum and kinetic energy are conserved in the scattering event we can write,

$$u_{sf}^2 = u_{b,s}^2 \cos^2 \vartheta_{sf} \qquad (11)$$

which also yields the density of scattered ions at "f", n_{sf} as follows:

$$n_{sf} = \frac{F_{sf}}{u_{sf}} = \frac{4 n_b u_{b,s} I_{ion} \cos \vartheta_{sf}}{\rho^2 u_{b,s} \cos \vartheta_{sf}} = \frac{4 n_b I_{ion}}{\rho^2} \qquad (12)$$

The contributions to "f" from all points "s" along the scattering ring defined by each scattering node at $s(r_s, z_s, 0)$, and by all nodes is summed as shown in equation (13),

$$n_f(r,z) = \int_V \frac{4 n_b I_{ion}}{\rho^2} n_o dV \qquad (13)$$

where n_o is the neutral particle density at the scattering node.

Finally, we compute the average energy of the scattered ions at each field node using the energy flux and the particle flux as shown in equation (14) below. E_{sf} is computed using equation (11).

$$\overline{E}_f(r,z) = \frac{\int_V E_{sf} F_{sf} n_o dV}{\int_V F_{sf} n_o dV} \qquad (14)$$
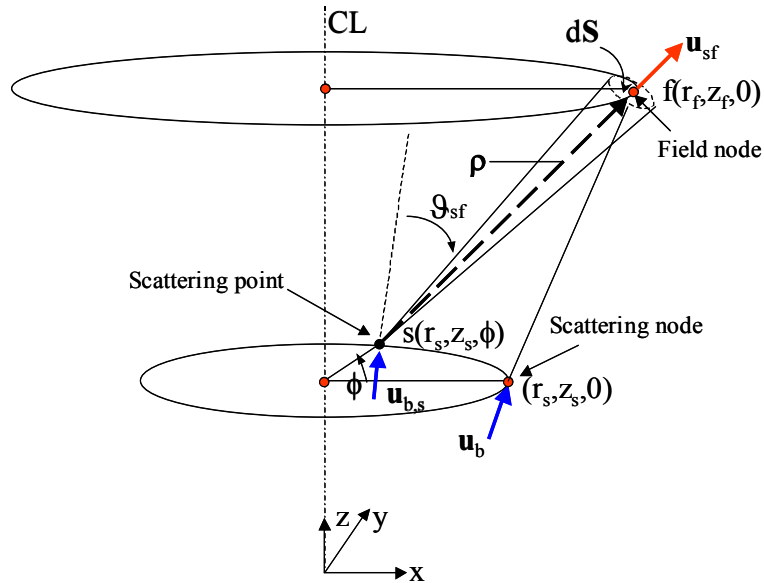
Figure 6. Elastic scattering geometry used to formulate the generalized algorithm in *EPIC*'s plume code. The four (red) corners define a portion of the plume computational plane.

Comparisons with idealized test problems and measurements have been conducted for the purpose of validating the algorithm. The comparisons showed good agreement and are described in Gardner, B.M., *et al.*,[10] and Mikellides, I.G., *et al.*[9] An example calculation for the BPT-4000 plume is shown in Figure 7 (the computed main beam only is shown on the left). The computed particle density of the elastically scattered ions, when the thruster was operated in the laboratory, is depicted in Figure 7, right. The value of background pressure for this plume calculation was taken to be 3.3e-5 Torr. Figure 8 shows the plume map for an SPT-100 imported in the main *EPIC* interface.
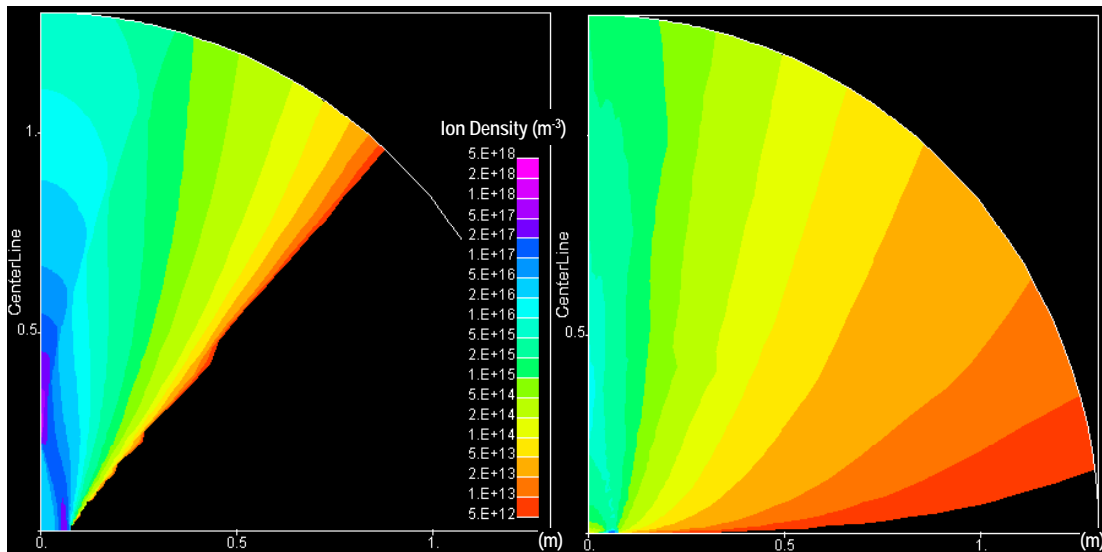
Figure 7. Computed main beam (left) and elastically-scattered ion density (right) (using the *EPIC* algorithm), in the plume of the BPT-4000 engine operating in the laboratory (P=3.3e-5 Torr).
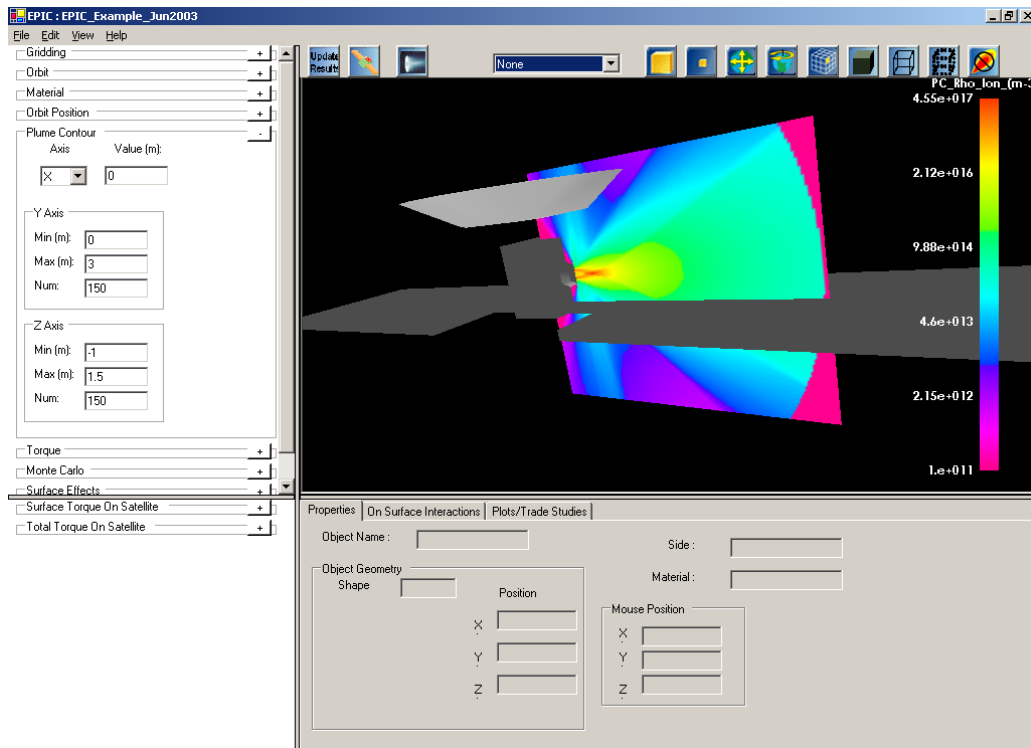
Figure 8. Imported SPT-100 plume showing ion particle density profile.

1-D HET Code. In electric propulsion systems such as HETs for example, it is difficult to predict conditions at the exit using empirical measurements exclusively. Furthermore, the effect of thruster geometry and operating conditions on the exhaust, and consequently the surrounding

S/C surfaces, is difficult to assess by simple extrapolation of measured quantities associated with a given thruster. Therefore, specifically for Hall thruster plumes *EPIC* incorporates a one-dimensional computer model of the acceleration region, which can be launched from within PlumeTool, as shown in Figure 3. The physics include collisions of electrons with neutrals, ions, and walls. The electron energy treatment includes ohmic heating, thermal diffusion and convection, and losses due to ionization, collisions with walls and atomic excitation.[15]

Plume-spacecraft interactions

The ability to assess a variety of spacecraft interactions with electric propulsion plumes, in three dimensions, is the bulk of *EPIC*'s capability. The interactions models presently allowable by *EPIC* have been described in greater detail elsewhere.[16] We summarize here the most commonly used interactions capabilities of *EPIC*. It is noted *apriori* that *EPIC* does not account for any plume perturbations caused by the presence of the spacecraft. Therefore, except for straight-line shadowing, all interactions calculations are carried out using a fixed plume profile (as provided by PlumeTool).

Fluxes to Surfaces. The ion flux F_{ijk} (atoms m^{-2} s^{-1}) at any point, i, on a surface j, due to plume component k, is calculated as follows:

$$F_{ijk} = \rho_{ik} \mathbf{v}_{ik} \cdot \mathbf{n}_j \tag{15}$$

where ρ_{ik} is the density at point "i" due to component "k", $\mathbf{v}_{ik}$ is the ion velocity (m/s) at point "i" of component "k", and $\mathbf{n}_j$ is the outward normal to surface "j". Fluxes to points on surfaces account for the interference ("blocking") by other spacecraft surfaces. Specifically, if a straight line between the point in question and the thruster orifice intercepts any other surface the flux is zero.

Surface Sputtering. The instantaneous sputtering rate (atoms m^{-2} s^{-1}) of a spacecraft surface "j" at a point "i" due to thruster plume impingement, R^S_{ij}, is

$$R^S_{ij} = \Sigma_k Y_{ijk} F_{ijk} \tag{16}$$

where "k" is summed over the plume components and Y_{ijk} is the sputter yield at point "i" of surface "j" from plume component "k". The sputter yield depends on the material, the energy of the ions impacting the surface and the angle between the flux vector and the surface-normal. All formulae are fits to sputtering measurements using the following functional form:

$$Y(E, \theta) = (a+bE)(1.00-0.72\,\theta +11.72\,\theta^2 -3.13\,\theta^3 -2.57\,\theta^4) \tag{17}$$

The yield is given in atoms/ion. The angular dependence is from Roussel *et. al.*[17]

Erosion/Deposition. The erosion/deposition rate at point "i" of surface "j" is the difference between the deposition and erosion rates.

$$R_{ij} = R_{ij}^D - R_{ij}^S \tag{18}$$

If $R_{ij} > 0$ it is a net deposition rate; if $R_{ij} < 0$, it is a net erosion rate.

The deposition rate is given by

$$R_{ij}^D = \Sigma_n \left(R_n^S \cos\left(\theta_{ijn}\right) \frac{\Omega_{in}}{2\pi} \right) \tag{19}$$

where R_n^S is average sputtering rate of all the points of surface "n," Ω_{in} is the solid angle subtended by surface "n" viewed from point "i" and θ_{ijn} is the angle between the normal of surface "j" and a ray from the centroid of surface "n" to the point "i".

The thickness or depth is calculated from the total particle deposition/erosion and the material "Density (gm cm^{-3})" and "Molecule mass" of the underlying material. Material properties are displayed on the "Material" sub-panel. The net erosion/deposition rate is computed at a randomly chosen selection of points over the mission (as specified in the "Monte Carlo" sub-panel) and then averaged. The mission averaged value is the product of the mission averaged rate and the "Mission Duration (days)" shown in the Orbit sub-panel. This ensures that time-dependent changes in spacecraft geometry (such as solar array sun-pointing) are included in the calculation.

For example, one may be interested in determining how long the thruster can be operated before material from the solar array is eroded below a critical thickness. The user can plot erosion of a specific element as a function of time of thruster operation as shown in Figure 9. The solar array element chosen is shown on the spacecraft. Additional variables may be plotted in this manner. The green line depicted on the plot of Figure 9 is material deposited on the antenna element that is highlighted in red in Figure 2.
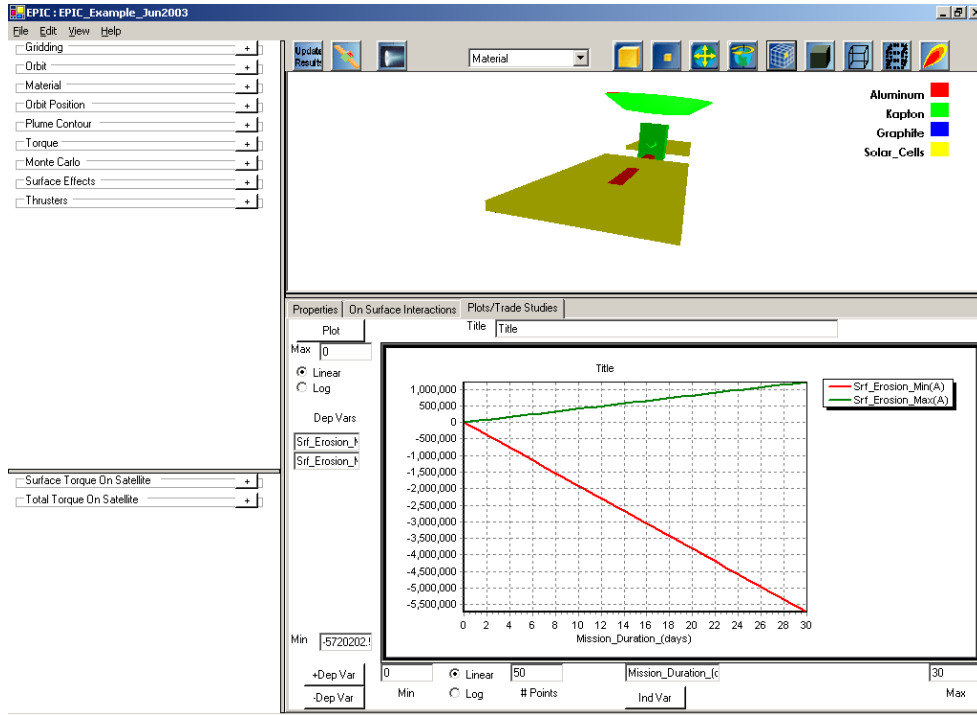
Figure 9. Trade studies may be performed using the Plots/Trade Studies tab. The plot shows erosion and deposition on critical spacecraft surfaces as a function of thruster operation time.

Induced Torques. Many electric thrusters produce torques that are comparable to or larger than those produced by gravity gradient, solar radiation, magnetic and aerodynamic effects, but are generally far smaller than torques resulting from chemical propulsion. Thrusters used for station-keeping or other purposes may produce unwanted torques, either directly or through the reflection of plume ions and neutrals from spacecraft surfaces.

There are in general two limiting cases for the reflection of plume particles from surfaces. In *specular* elastic reflection the component of momentum normal to the surface is reversed. Reflection from rough surfaces leads to *diffuse* reflection in which the outgoing particle travels in a random direction, *i.e.*, particles are reflected in all directions regardless of the angle of incidence. In the case shown in Figure 10 (torque results are shown on the bottom left), specular reflection has been chosen. The general *EPIC* model used to determine the induced torques on the spacecraft during thruster operation accounts for contributions from the thrust and from the impingement of the exhaust on surfaces:

$$\mathbf{\Gamma} = \sum_{T} \Delta \mathbf{R}_T \times (-\mathbf{f}_T) + \sum_{j} \Delta \mathbf{R}_j \times \mathbf{f}_j \tag{20}$$

where, $\mathbf{f}_j$ is the force imparted onto a surface j from plume particles, $\mathbf{f}_T$ is the thrust vector, $\mathbf{\Gamma}$ is the torque, $\Delta \mathbf{R}_T$ is the position vector of a thruster from a reference point and $\Delta \mathbf{R}_j$ is the position vector of a surface j from a reference point. In the model, the contribution from plume

impact is computed using one of the two limiting cases mentioned above: *specular* (elastic) reflection from the surface and *fully diffuse* reflection.
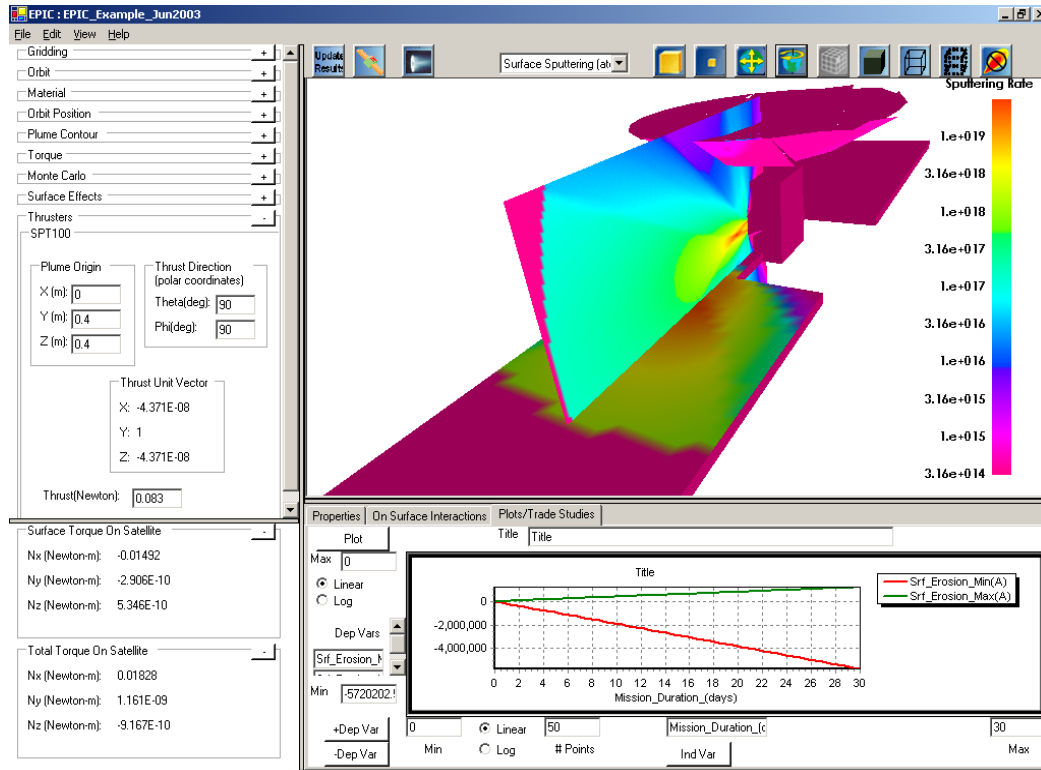

Figure 10. Additional calculations and display options in *EPIC*.

Summary

The near and long-term benefits of electric propulsion are now widely recognized and accepted by both the government and the private sector. Solar-powered EP systems have been used successfully in numerous missions, with many more readied for near-term applications. Through Project Prometheus NASA now also focuses on nuclear electric propulsion (NEP) as the "way to defeat distance and time in exploring the outer planets." However, integration of EP systems on spacecraft presents serious barriers to implementation. In the absence of accurate assessments, interactions between the propulsion system and the surrounding spacecraft components may threaten mission success. Quantifying such interactions within the design of specific spacecraft is a complex task with no comprehensive tools for the spacecraft engineer in existence. In response to the growing need by the electric propulsion community for a stand-alone design tool that addresses these issues, SAIC is developing the Electric Propulsion Interactions Code, *EPIC*. *EPIC* is a windows-based interactive, computer tool that allows the spacecraft designer to conduct the complete interactions process including geometry definition, EP plume generation, and interactions evaluation in 3-D. A fully functional beta version of the tool was delivered to the SEE Program on July, 2003.

Acknowledgments

References

1. Mikellides. I.G., Kuharski, R.A., Mandell, M.J., Gardner, B.M., "Assessment of Spacecraft Systems Integration Using The Electric Propulsion Interactions Code (EPIC)," AIAA Paper 2002-3667, July 2002.

2. Fife, J.M., et al., "The Development of a Flexible, Usable Plasma Interaction Modeling System," AIAA Paper 2002-4267, July 2002.

3. Purrin, V., Pogarieloff, D., Metois, P., and Brosse, S., "PPS Effects on Satellites Analyses and Tools in Alcatel Space Industries," IEPC Paper 01-262, Oct. 2001.

4. Davis, V.A., et al., "Ion Engine Generated Charge Exchange Environment: Comparison Between NSTAR Flight Data and Numerical Simulations," AIAA Paper 2000-3529, July 2000.

5. Gardner, B.M., Katz, I., Davis, A. and Mandell, M. "Hall Current Thruster (HCT) IR&D Plume Environment Characterization and Electrostatic Return Current Assessment" Final Report for Lockheed Martin Space Systems Company (MTSD-DPR-01-16648), Jan. 2001.

6. Mandell, M.J., et al., "Nascap-2k, A Spacecraft Charging Analyis Code for the 21st Century," AIAA Paper 2001-0957, Jan. 2001.

7. Mikellides. I.G., et al., "Assessment of High-Voltage Solar Array Concepts for a Direct Drive Hall Effect Thruster System," AIAA Paper 2003-4725, July 2003.

8. Mikellides, I.G., et al., "Plume Modeling of Stationary Plasma Thrusters and Interactions with the Express-A Spacecraft," J. of Spacecraft and Rockets, Vol. 39, No. 6, 2002, pp. 894-903.

9. Mikellides. I.G., et al., "The Electric Propulsion Interactions Code (EPIC): A Member of the NASA Space Environment and Effects Program Toolset," AIAA Paper 2003-4871, July 2003.

10. Gardner, B.M., et al., "Electric Propulsion Interactions Code, EPIC," Final Report (No. SAIC 02/2043) prepared under NASA Contract #NAS8 02028, Nov. 2002.

11. Child, M., Molecular Collision Theory, Academic Press, London, 1974, pp. 9-20.

12. Mott, N.F., and Massey, H.S.W., The Theory of Atomic Collisions, Ch. I,V and XII, Clarendon Press, Oxford, 1949.

13. Amarouche, M., Durand, G. and Marlieu, J.P., "Structure and Stability of Xe_n^+ Clusters," J. Chem. Physics, Vol. 88, 1988, pp. 1010-1018.

14. Katz, I., et al., "A Hall Effect Thruster Plume Model Including Large-Angle Elastic Scattering," AIAA Paper 2001-3355, July 2001.

15. Mikellides, I.G., Katz, I., Mandell, M.J., "Modeling the Exit Plane of a Hall Effect Thruster," AIAA Paper 01-3505, July 2001.

16. Mikellides, I.G., et al., "A Hall-Effect Thruster Plume and Spacecraft Interactions Modeling Package," IEPC Paper 01-251, Oct. 2001.

17. Roussel, J.F., Bernard, J., Garnier, Y., "Numerical Simulation of Induced Environment, Sputtering and Contamination of Satellite due to Electric Propulsion," ONERA-CERT/DERTS, Proc. Second European Spacecraft Propulsion Conference, May 1997.

EFFECTS OF LARGE-AMPLITUDE RF EMISSIONS ON OEDIPUS-C FLOATING VOLTAGES

J.G. Laframboise
Physics and Astronomy Department, York University
4700 Keele Street, Toronto, Canada M3J 1P3.
Phone: 416 736 5621
Fax: 416 736 5516
E-mail: laframboise@quasar.phys.yorku.ca

D.D. Wallis
Magnametrics, Canada

H.G. James
Communications Research Centre, Canada

Abstract

The TCM voltmeter experiment on the OEDIPUS-C tethered payload provided a unique opportunity to compare the charging of two geometrically similar spacecraft, one of which carried a high-voltage RF transmitter. The data from this experiment, together with measurements of ambient plasma parameters from other onboard instruments, have permitted stringent testing of available theories for electron collection by strongly driven antennas in the space plasma. Earlier simple theories have predicted that a transition occurs from rectification-dominated electron collection at low frequencies, causing the spacecraft's floating potential to be driven negative, to ponderomotive-dominated collection at higher frequencies, causing this potential to be driven positive. Our calculation incorporates a model of a transition between these two cases as the frequency increases.

Introduction

The OEDIPUS-C tethered payload (Fig. 1) was launched on 7 November 1995 from the Poker Flat Research Range, Alaska (Fig. 2) [*James and Calvert*, 1998, *James et al.*, 1999, *Prikryl et al.*, 2000, *James*, 2000]. The Tether Current Monitor (TCM) instrument operated the two subpayloads and the conducting tether as a double electrostatic probe. During the part of the experiment discussed here, the flight upleg, the angle between the tether and the geomagnetic-field direction was less than 5 degrees. The TCM configured the payload cyclically as a high-impedance voltage probe and as a low-impedance current probe.

OEDIPUS C also carried a pulsed high-frequency RF exciter (HEX) on its forward subpayload. HEX drove the forward subpayload's V-dipole stems symmetrically with respect to the central point of the RF feed, which was grounded to the spacecraft body.
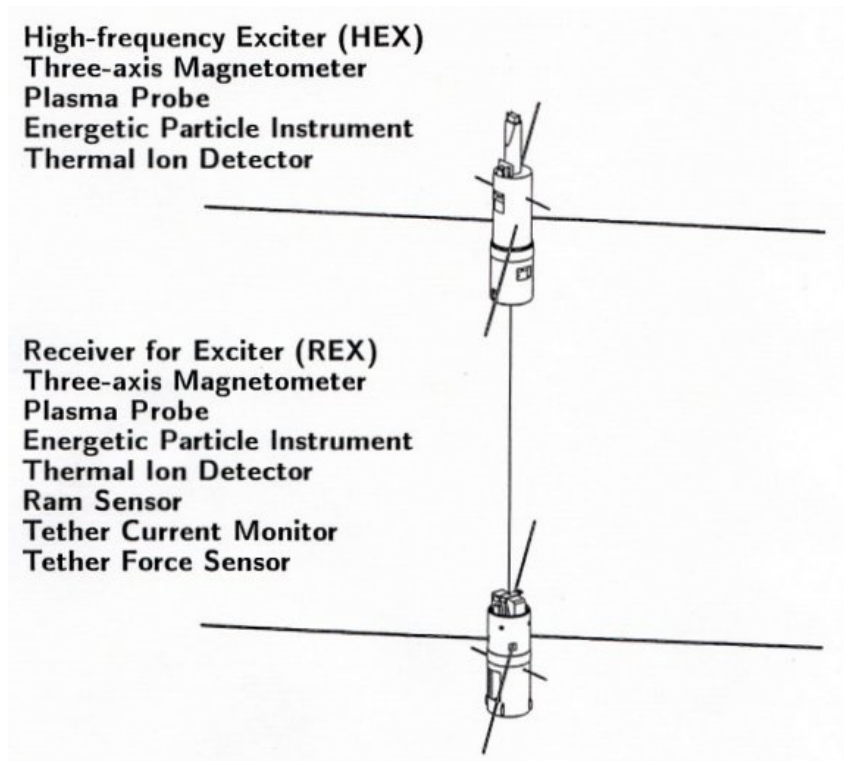
Figure 1. OEDIPUS-C tethered payload, two seconds after separation.
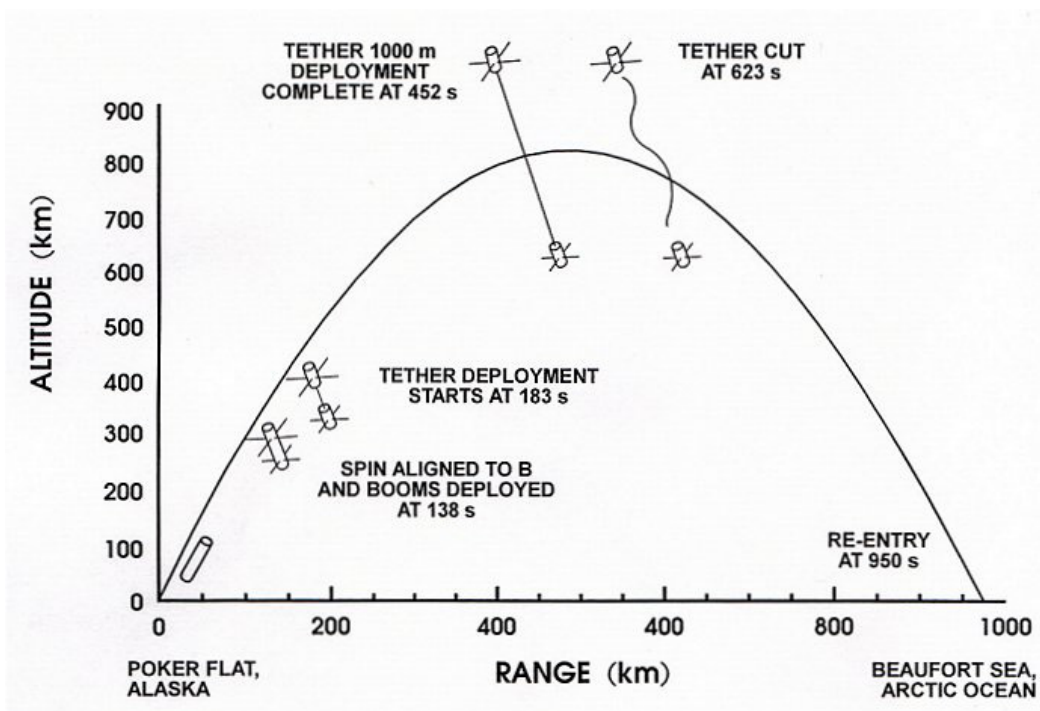

Figure 2. Trajectory of the OEDIPUS-C flight, with major payload events.

The stems of two onboard Langmuir probes were also grounded to the spacecraft body. With the HEX connected to the forward subpayload dipoles and with the frequency of the pulses swept progressively from 25 kHz to 4.1 MHz, the transient response of the TCM voltage showed a number of reproducible features. At the lowest frequencies of the sweep, the RF pulses drove the forward subpayload's potential negative with respect to that of the aft payload (REX) by several tens of volts. The time-constant of relaxation of the payload's potential between the HEX pulses increased as background density decreased.

The TCM voltmeter data (Figs. 3-8) showed a steady rise in the floating voltage of the forward subpayload as the HEX transmitter was swept from lower to higher frequencies. This is as expected when ponderomotive effects become relatively more important relative to rectification. Superposed on this was another feature in which the forward subpayload was driven increasingly negative as the frequency approached the electron gyrofrequency from below, and increasingly positive as it approached it from above. This feature became progressively more evident as background density decreased.

OEDIPUS C TETHER VOLTAGE MONITOR
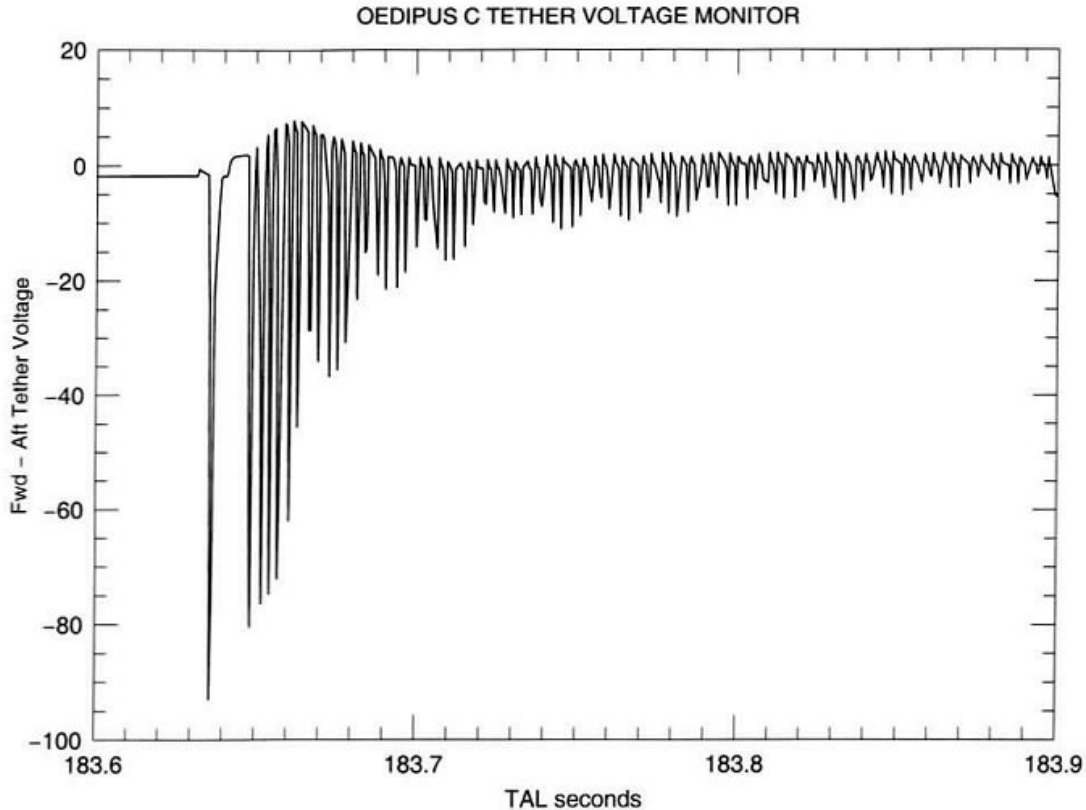
Figure 3. HEX spacecraft voltage relative to that of REX during a frequency sweep by the HEX transmitter. In this and other sweeps shown in subsequent Figures, an initial 600μsec pulse at 25 kHz is followed after 12.12 msec by a series of 300μsec pulses at intervals of 3.03 msec, having frequencies which begin at 100 kHz and increase by increments of 50 kHz up to 4.1 MHz. During this sweep, measured values of ambient parameters were: ne = 4.5 x 103 cm-3, kTe/e = 0.34V, and induced tether voltage v x B.L = 0, where v is the spacecraft's velocity and L is a separation vector directed upward from REX to HEX.
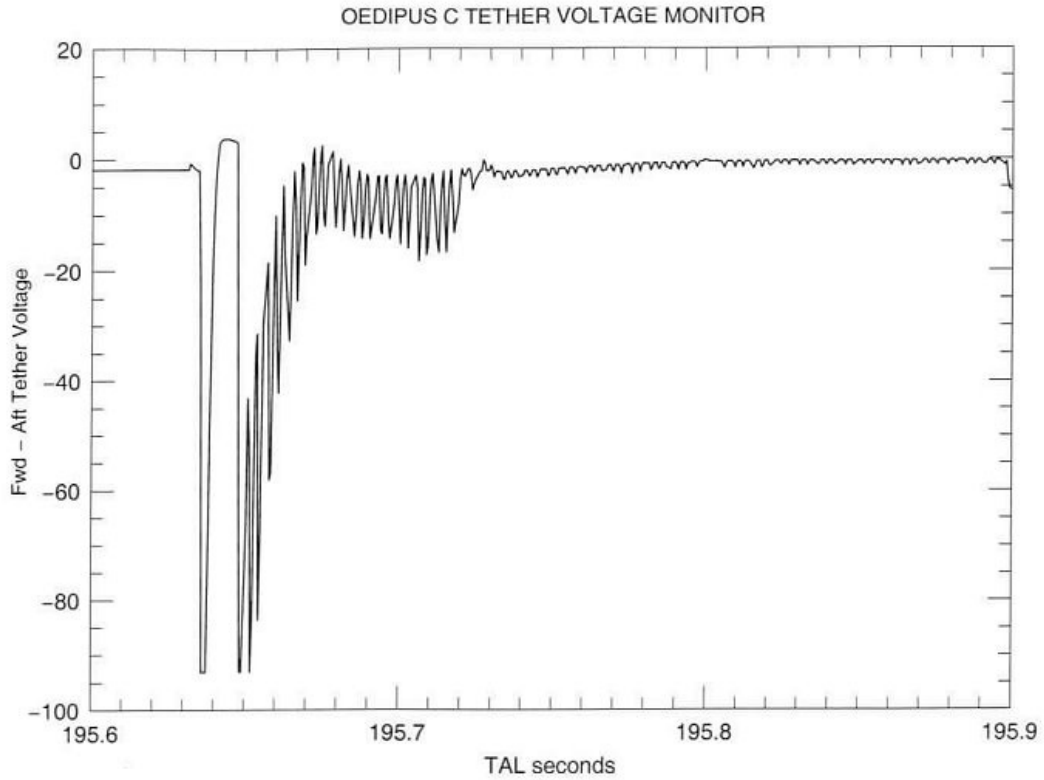
Figure 4. Same as Fig. 3 except that ne=6.1 x 103 cm-3, kTe/e=0.29V, and v x B.L=-0.05V.
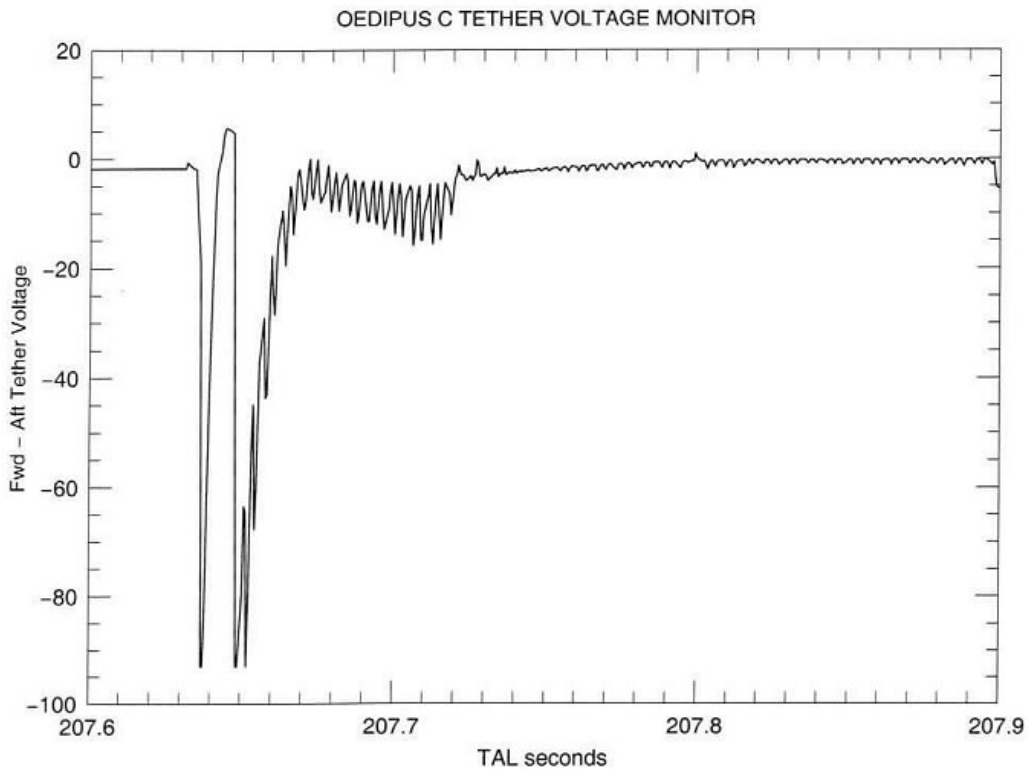
Figure 5. Same as Fig. 3 except that n_e = 4.1 x 10^3 cm^{-3}, kT_e/e = 0.30V, and v x B.L = -0.09V.

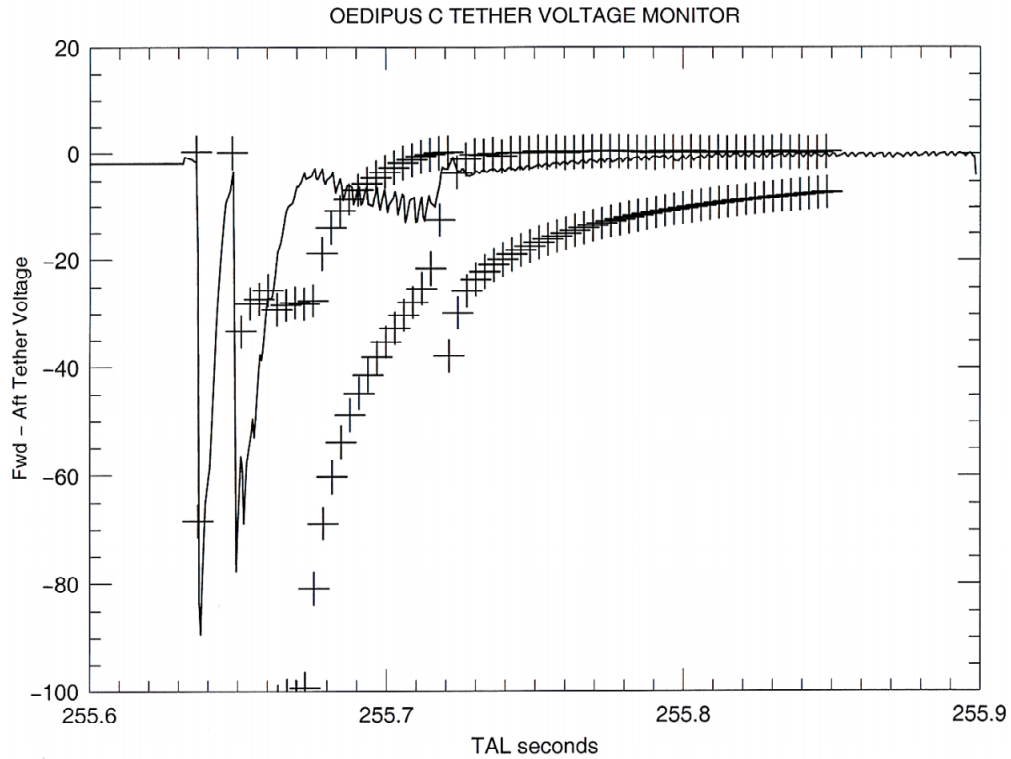**Figure 6.** Same as Fig. 3 except that $n_e = 2.5 \times 10^3$ cm^{-3}, $kT_e/e = 0.43$V, and v x B.L = -0.27V. In Figs. 6-8, preliminary results from our calculation are indicated by crosses, for times corresponding to the beginnings and ends of RF pulses.
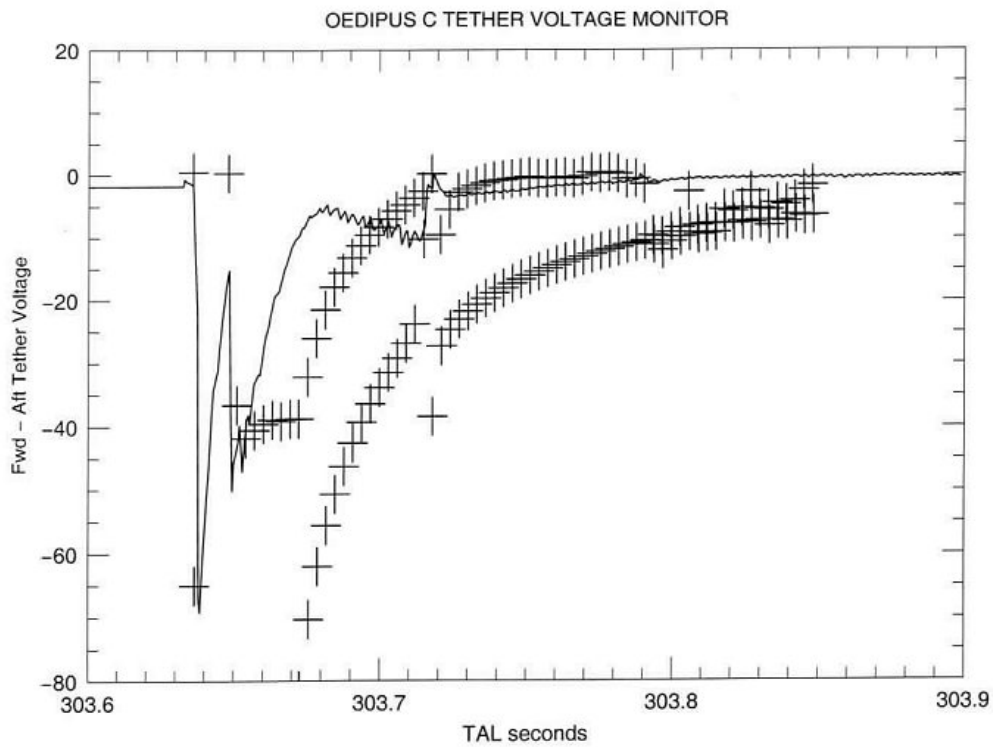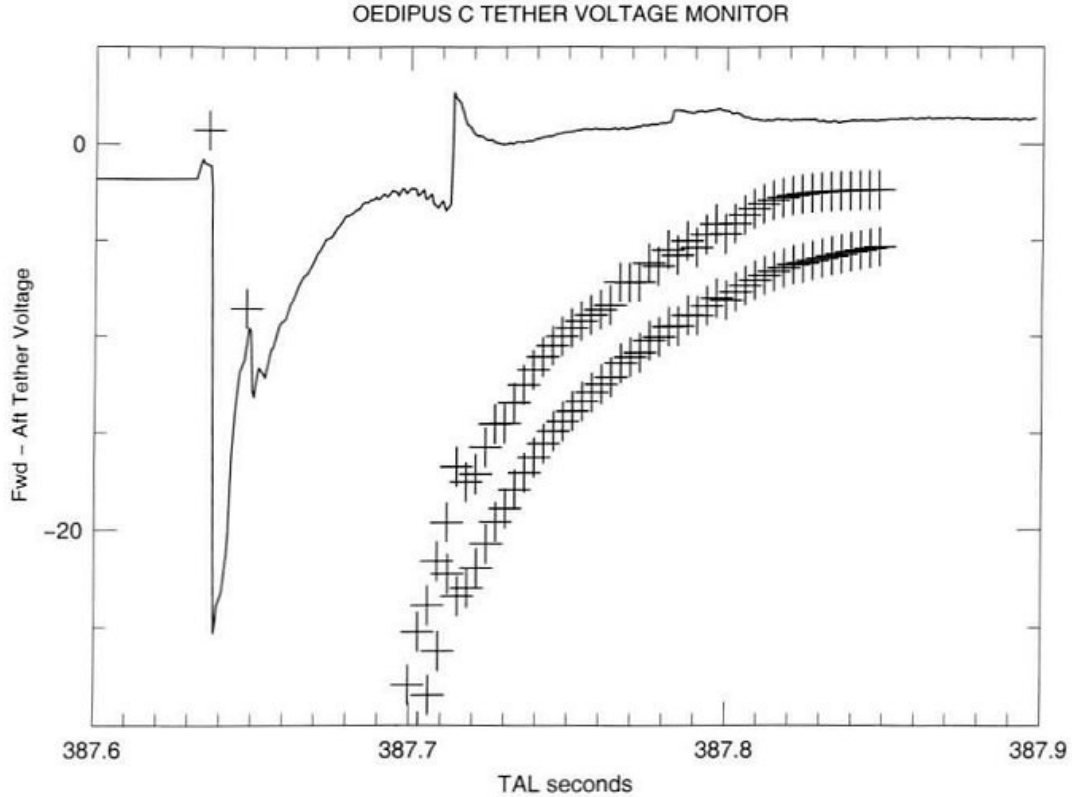

Figure 7. Same as Fig. 3 except that $n_e = 1.5 \times 10^3$ cm^{-3}, $kT_e/e = 0.74$V, and v x B.L = -0.45V.

OEDIPUS C TETHER VOLTAGE MONITOR

Figure 8. Same as Fig. 3 except that n_e = 0.3 x 10^3 cm^{-3}, kT_e/e = 1.25V, and v x B.L = -0.68V.

It corresponds to a feature which appears in the dependence of the applied RF voltage on frequency, through the dipole impedance theory assumed [Sec. 4, item (2)]. Another feature at twice the electron gyrofrequency also became more evident as background density decreased. Both features are most evident in Fig. 8, at times after launch (TAL) of about 387.713 and 387.783 seconds, respectively.

Also visible in Figs. 3-8 is a succession of positive overshoots in the same voltage following the first few RF pulses in each sweep. As the background density decreases, these overshoots become less evident. In Figs. 4 and 5, the overshoots following the first pulse have had time to reach maximum values and begin to decrease, at times after launch of about 195.645 and 207.645 seconds, respectively. Fitting exponential decay curves to the decreasing voltages following each maximum yields time-constants of approximately 17 and 15 milliseconds. If we assume that these decays are indications of the collapse of an enlarged disturbance-region produced by each RF pulse, and we also assume that this collapse progresses inward at the ion-acoustic-wave speed, then we obtain roughly 46 m and 39 m, respectively, for the characteristic scale of these disturbances. These distances are very large compared with known spatial scales of our situation, including the tip-to-tip length of the HEX V-dipoles (19 m) and the calculated source radius described in Section 3.1.2 (up to about 10 m at the lowest HEX frequencies). We are presently investigating whether these distances correspond to the characteristic scale of the "ponderomotive presheath" which extends beyond this source radius.

In order to investigate these features, we have performed a calculation of the charging and discharging behaviour of HEX relative to that of REX during and between RF pulses as their frequency was swept. Our strategy for these calculations is as follows. We have so far avoided three-dimensional particle-in-cell calculations, because the wide disparities among temporal and spatial scales in the OEDIPUS-C situation appear likely to result in unacceptably long computational times for such calculations. Instead, our approach has been to assume that charging and discharging times are long compared to other time-scales involved, and therefore to use or develop simple parameterizations, for steady-state currents, as functions of spacecraft voltage, collected by all spacecraft surfaces except the HEX dipoles during RF pulses, and for current collection, time-averaged over an RF cycle, by these dipoles during these pulses. Our charging and discharging calculations require us also to use or develop parameterizations for the electric fields, either steady-state or time-averaged over an RF cycle, outside all spacecraft surfaces. Our calculations include effects of time-dependent sheath expansion following the start of RF pulses, and of time-dependent sheath collapse following their end.

Theory

For completeness, we repeat briefly some of the ideas contained in **Rubinstein and Laframboise** [1970] and **Laframboise et al.** [1975]; see also **Laframboise et al.** [2001].

Low frequencies

If the RF field varies slowly enough, the plasma will have time to accommodate itself to the static configuration corresponding to the instantaneous potential of the antenna; "slowly enough" means that the driving frequency ω is small compared with the electron plasma frequency ω_{pe}. Each half of the dipole (each dipole element) then has the static current-voltage characteristic of a Langmuir probe.

With the transmitter off, the antenna is at the Langmuir floating potential, $V_{FL} \sim -kT_e/e$, which is much smaller than the amplitude $\tilde{V}$ of the RF voltage. Here, k is Boltzmann's constant, T_e is the electrons' temperature, and e is the magnitude of unit electronic charge. When the transmitter is switched on, each dipole element becomes positive half the time, with potential up to $+\tilde{V}$, and therefore electron-attracting; the opposite will happen during the next half-cycle, but because the ion saturation current is much smaller than the electron saturation current, the net result will be an increase of negative charge on the element, which will lower its DC potential.

This process will continue until the total (AC + DC) potential of each element is positive and negative during intervals τ_+ and τ_-, respectively, which satisfy:

$$\frac{\tau_-}{\tau_+} \simeq \frac{I_{e,saturation}}{I_{i,saturation}}$$

(1)

Under this condition, the net charge gain at the end of a cycle is zero. Since $I_{e,saturation} \gg I_{i,saturation}$, this will happen for

$$V_F \simeq -|\tilde{V}| \ll V_{FL}.$$

(2)

High frequencies

In the presence of intense RF emission from a spacecraft antenna, electrons near the antenna are strongly repelled from it due to a nonlinear effect of the emission. This repulsion arises because of the radial oscillations performed by the electrons in the near field of the antenna. At the innermost end-point of such an oscillation (the point nearest the antenna), the outward force due to the near field is stronger than it would be at the same instant at the central point of the oscillation. Conversely, at the outermost end-point, the inwardly directed force is weaker. Therefore, there is a net time-averaged force on the electrons, and to a much smaller extent on ions, directed away from the antenna. It has been shown by a small-amplitude perturbation analysis [***Boot et al.***, 1958] that this time-averaged "ponderomotive" force is equivalent to a static force:

$$-(q^2/4m\omega^2)\nabla(E_1^2)$$

(3)

where q and m are the electronic change and mass, ω is the angular frequency of the RF, and E_1 is the near-field RF electric-field amplitude. The implications of the ponderomotive force for radiating antennas in ionospheric plasmas have been discussed by ***Getmantsev and Denisov*** [1962], ***Whale*** [1964], ***Rubinstein and Laframboise*** [1970, 1972], ***Laframboise et al.*** [1975], and following Eq. (8) of ***Calder et al.*** [1993]. Because this force can be expressed as a gradient, its presence is equivalent to the existence of an additional term

$$\phi_a = (q/4m\omega^2)E_1^2$$

(4)

in the static potential as seen by electrons. Therefore it can be incorporated easily into the self-consistent numerical treatment of a cylindrical, perfectly absorbing electrode (Langmuir probe) in a collisionless plasma, already developed for the time-independent case [***Laframboise***, 1966]. Based on this formulation, an analysis of static sheath effects around such an antenna, due to intense RF emission by it, has been published [***Rubinstein and Laframboise***, 1970, ***Laframboise et al.***, 1975]. This analysis assumed that E_1 was just the vacuum near-field of the antenna, and hence the approximation $\omega \gg \omega_{pe}$ was implied. For ionospheric sounding antennas of the type carried by the Alouette and ISIS satellites, it predicted enlargement of these antennas' sheaths from a few cm to roughly 1 m radius. This prediction is consistent with ISIS I and II observations [***James***, 1980, Sec. IV].

A more refined analysis has also been published [***Rubinstein and Laframboise***, 1972], in which the restriction to a vacuum near-field was removed by calculating, at each step of the numerical iteration, the dielectric-constant profile implied by the static electron-density profile (the latter having itself been calculated during the previous iteration step), then using this dielectric-constant profile to calculate the modified radial dependence of E_1 for input to the next iteration step. In this manner, the calculation was extended to ω/ω_{pe} ratios down to 1.5. In all of these calculations, the time-averaged force on ions due to the RF was ignored, and we retain this approximation here also.

At cylindrical radii $r \ll$ wavelength λ, and over most of the antenna's length, the instantaneous near field of a cylindrical antenna has the same dependence on position as the static Coulomb field of an infinite cylinder. Hence, we assume that:

$$E_{rf} = n_r(c_1/r)\cos \omega t = E_1 \cos \omega t \tag{5}$$

Substitution into Eq. (4) then yields:

$$\phi_a = (qc_1^2/4m\omega^2)(1/r^2) \tag{6}$$

We introduce a dimensionless additional antenna potential G as follows:

$$G = \frac{q\phi_{aA}}{kT} = \frac{q^2 c_1^2}{4m\omega^2 r_A^2 kT} \tag{7}$$

where ϕ_{aA} and r_A represent additional potential and radius at the antenna's surface, and $q =$ -e. The input parameters for static sheath calculations are then three in number: the value of G, the value of the dimensionless antenna static potential $\psi_A = e\phi_A / kT$, and the antenna Debye ratio $r_A/\lambda_D = r_A/(e^2 n_\infty/\varepsilon_0 kT)^{1/2}$. Here, n_∞ is the electron or ion number density far from the antenna, and ε_0 is the permittivity of free space. We have eliminated the ion-to-electron temperature ratio T_i/T_e as a parameter by assuming that $T_i = T_e \equiv T$ throughout.

Intermediate frequencies

The preceding discussion implies that at low frequencies, we expect the rectification effect to predominate, and the spacecraft to be driven negative. Conversely, at high frequencies, we expect the ponderomotive effect to predominate, and the spacecraft to be driven positive. A central issue in modeling the TCM voltmeter results then is: how do we describe the transition from one to the other? We address this issue in Section 3.1.2.

Ion and Electron Collection by Spacecraft Surfaces

These surfaces include the HEX and REX spacecraft bodies, dipoles, and probe stems. We assume that collisionless theory applies throughout.

Electron collection

We ignore the spacecraft's speed compared with the electron (but not the ion) thermal speed. We ignore all end-effects and effects of interactions among spacecraft bodies, dipoles, and probe stems.

HEX and REX spacecraft bodies:

We ignore the misalignment of these bodies with the geomagnetic field **B**; this was less than 5° during the analyzed portion of the flight. For electron-attracting (positive) surface potentials, measured relative to space potential, we use the lesser of the canonical-upper-bound current prediction for a finite cylindrical probe aligned with **B** [*Rubinstein and Laframboise*, 1982, Eqs. (30), (33)-(35), and 1983, Sec. 2B], and the *Mott-Smith and Langmuir* [1926] orbital-motion-limited current prediction for a spherical probe; reasons for this choice are discussed in *Laframboise and Parker* [1973]. For electron-repelling (negative) surface potentials, we use the

lesser of the current given by **Rubinstein and Laframboise** [1982, Eqs. (30), (36), and (37)], and the Boltzmann factor.

HEX radiating dipoles:

We obtain sheath and presheath potential distributions using a two-region approximation of the theory of **Laframboise et al.** [1975, Figures 3-8]. In this approximation, the sheath region is assumed to contain a uniform density of ions only, and the presheath region is assumed quasineutral, with ponderomotive repulsion of electrons only. The potential and the electric field are assumed to be continuous at the sheath-edge. We calculate a "source radius" for electrons collected on the dipole elements, by using the lesser of: (a) the steady-state sheath-edge radius given by the two-region approximation, or (b) an expanding sheath-edge radius which is assumed to move outward at the ion-acoustic-wave speed, starting at the antenna radius r_A at the beginning of each RF pulse. The use of this expanding radius is suggested by the expanding ion-acoustic wavefronts seen in Fig. 13 of **Calder et al.** [1993]. We also assume that the alternating electric field is given by Eq. (5) between r_A and this source radius, and that the electron distribution at this source radius is a steady-state Maxwellian which includes a Boltzmann factor based on the combined electrostatic and ponderomotive potentials at this radius. These assumptions provide an electron-collection model which incorporates both the rectification effect described in Section 2.1 and the ponderomotive effect described in Section 2.2.

Probe stems, HEX dipoles between RF pulses, and REX nonradiating dipoles:

For positive surface potentials, we use the lesser of the canonical-upper-bound current prediction for infinite-cylindrical probes inclined to **B** [**Rubinstein and Laframboise**, 1978, Eq. (11)], and the orbital-motion-limited current prediction for infinite-cylindrical probes [**Mott-Smith and Langmuir**, 1926, Eq. (29)]. For negative surface potentials, we use the lesser of the currents given by the corresponding canonical-upper-bound prediction for repelling probes [**Rubinstein and Laframboise**, 1978, Eq. (13)], and the Boltzmann factor.

Ion collection

HEX and REX spacecraft bodies, REX nonradiating dipoles, and probe stems:

The ions' average gyroradius is much larger than the spacecraft dimensions, so magnetic-field effects on ion collection can be neglected. However, the spacecraft speed is comparable to the ion thermal speed, and therefore ion drift effects cannot be neglected. Available theory for this situation [**Godard and Laframboise**, 1983], combines ion drift with available self-consistent potentials for corresponding *nondrifting* cases. However, the results of this theory are in tabular form, which is inconvenient for our purposes, and may not cover the complete range of external parameters found in our situation.

Therefore, we approximate further as follows. Around each of the spacecraft bodies, dipole elements, and probe stems, we separately assume cylindrical symmetry of the sheath potential distribution. For negative (ion-attracting) surface potentials, we calculate the sheath potential distribution using a uniform-ion-density, zero-electron-density model. We then approximate the

more realistic drifting Maxwellian ion distribution by a monokinetic one whose total kinetic energy includes transverse drift and thermal energies. Specifically, if U_n is the component of ion drift speed transverse to the cylinder's axis, we assume that every ion has transverse kinetic energy $\frac{1}{2} m_i U_n^2 + \frac{1}{4} \pi kT$ far from the cylinder's surface; this choice gives the correct current for zero drift and zero surface-potential [***Laframboise***, 1966, Eq. (10.11)]. We assume that ion collection is limited by the least angular momentum of accelerated ions which can exist at any radius from the collector to the sheath-edge. The result is a simple numerical approximation for ion collection. For sufficiently positive (ion-repelling) surface potentials $q\phi_s > \frac{1}{2} m_i U_n^2$, we approximate the ion collection very crudely by a modified Boltzmann factor $\exp[(-q\phi_s + \frac{1}{2} m_i U_n^2) / kT_i]$ times the random ion current.

HEX radiating dipoles

For these, we use an ion-collection model similar to that described just above, but modified to include the ion-repelling potential peak predicted by the two-region model potential described earlier [Section 3.1.2 above].

Further Details of the Calculation

(1) Effects of finite HEX driving frequency (compared to the electron plasma frequency) on the ponderomotive presheath potential distribution are included. This permits our calculation to extend over the full range of HEX driving frequencies, both below and above ω_{pe}.

(2) Driving voltages across the HEX V-dipole terminals are used directly to provide electric-field amplitudes as functions of radius. The voltages are computed using an equivalent-circuit analysis of the HEX power amplifier and dipoles [James, 2003].

(3) The HEX dipole elements' finite lengths (9.28m) cause the ponderomotive repulsion to decrease more steeply at radii comparable to these lengths. We have included this effect, by approximating the alternating electric-field distribution outside each dipole element by that outside a prolate spheroid having the same length-to-diameter ratio.

(4) We have rederived the ponderomotive repulsion including the geomagnetic field B. Our results indicate that electrons are repelled only along B, not across B. Therefore the curvature of the alternating electric field E away from B diminishes this repulsion, especially near the dipole elements' roots where this curvature is largest. This situation suggests that electron collection at lowest frequencies may occur mostly near these roots. We have included this effect by approximating the electric-field lines connecting opposite dipole elements very crudely as semicircles centered on the central point of the antenna.

Acknowledgments

References

1. Boot, H.A.H., S.A. Self, and R.B.R. Shersby-Harvie, Containment of a fully-ionized plasma by radio-frequency fields, J. Electron. Control, 4(5), 434, 1958.

2. Calder, A.C., G.W. Hulbert, and J.G. Laframboise, Sheath dynamics of electrodes stepped to large negative potentials, Phys. Fluids B, 5(3), 674, 1993.

3. Getmantsev, C.G., and N.G. Denisov, Concerning an effect during measurement of electron concentration in the ionosphere by the antenna probe method, Geomagn. Aeronomy, 2, 575, 1962.

4. Godard, R., and J.G. Laframboise, Total current to cylindrical collectors in collisionless plasma flow, Planet. Space Sci. 31(3), 275, 1983.

5. James, H. Gordon, Tests of impedance theories for a transmitting dipole in an ionospheric plasma, IEEE Trans. Antennas Propagation, AP-28(5), 623, 1980.

6. James, H.G., Ionospheric duct parameters from a dual-payload radio-frequency sounder, J. Geophys. Res., 105(A9), 20,909, 2000.

7. James, H.G., Electromagnetic whistler-mode radiation from a dipole in the ionosphere, Radio Science 38(1), 1009, doi: 10.1029/2002RS 002609, 2003.

8. James, H.G., and W. Calvert, Interference fringes detected by OEDIPUS C, Radio Science, 33(3), 617, 1998.

9. James, H.G., V.I. Sotnikov, W.J. Burke, and C.Y. Huang, OEDIPUS-C observations of electrons accelerated by radio frequency fields at whistler-mode frequencies, Phys. Plasmas, 6(10), 4058, 1999.

10. Laframboise, J.G., Theory of spherical and cylindrical Langmuir probes in a collisionless, Maxwellian plasma at rest, Rep. 100, Institute for Aerospace Studies, University of Toronto, Toronto, Ontario, Canada, 1966.

11. Laframboise, J.G., and L.W. Parker, Probe design for orbit-limited current collection, Phys. Fluids, 16(5), 629, 1973.

12. Laframboise, J.G., J. Rubinstein, and F.H. Palmer, Theory of topside sounder transmission effects on antenna quasistatic sheath impedance, Radio Science, 10(8,9), 773, 1975.

13. Laframboise, J.G., D.D. Wallis, and H.G. James, RF effects on OEDIPUS-C floating voltages, in: Proceedings of the 7th Spacecraft Charging Technology Conference, edited by R.A. Harris, 23-27 April 2001, ESTEC, Noordwijk, The Netherlands, ESA SP-476, November 2001, pp. 309-314.
14. Mott-Smith, H.M., and I. Langmuir, The theory of collectors in gaseous discharges, Phys. Rev., 28(4), 727, 1926.

15. Prikryl, P., H.G. James, D.J. Knudsen, S.C. Franchuk, H.C. Stenbaek-Nielson, and D.D. Wallis, OEDIPUS-C topside sounding of a structured auroral E region, J. Geophys. Res. 105(A1), 193, 2000.

16. Rubinstein, J., and J.G. Laframboise, Plasma sheath around a floating cylindrical antenna at high power, Can. J. Phys., 48(16), 1882, 1970.

17. Rubinstein, J., and J.G. Laframboise, Ion temperature diagnostic using a high power alternating current probe, Phys. Fluids, 15(7), 1259, 1972.

18. Rubinstein, J., and J.G. Laframboise, Upper-bound current to a cylindrical probe in a collisionless magnetoplasma, Phys. Fluids, 21(9), 1655, 1978.

19. Rubinstein, J., and J.G. Laframboise, Theory of a spherical probe in a collisionless magnetoplasma, Phys. Fluids, 25(7), 1174, 1982.

20. Rubinstein, J., and J.G. Laframboise, Theory of axially symmetric probes in a collisionless magnetoplasma: aligned spheroids, finite cylinders, and disks, Phys. Fluids, 26(12), 3624, 1983.

21. Whale, H.A., Ion sheath effects near antennas radiating within the ionosphere, J. Geophys. Res., 69(3), 447, 1964.

SPARCS: AN ADVANCED SOFTWARE FOR SPACECRAFT CHARGING ANALYSES

S. Clerc
Alcatel Space
100 Bd du Midi
FR-06156 Cannes La Bocca Cedex
Phone: +33 4 92 92 64 83
Fax: +33 4 92 92 69 70
E-mail: sebastien.clerc@space.alcatel.fr

S. Brosse
Alcatel Space

M. Chane-Yook
INRIA, Sophia-Antipolis, France

Abstract

We report on the development of SPARCS (SPAcecRaft Charging Software), a simulation tool for spacecraft charging analyses. The code computes electron and ion currents from the magnetosphere on the surfaces of the satellite with a back-trajectories algorithm. Secondary emission and photo-emission currents are computed using standard models. Special care is given to the computation of recollected secondary electrons. The current balance is used to update the absolute and differential potentials.

The code also computes the potential around the spacecraft, which is in turn used to compute electrons and ions collection. In a geostationary environment, space charge can be neglected. The resulting Poisson equation is solved with a Finite Element method on an unstructured mesh, coupled with Infinite Elements to enforce the correct decay of the potential at infinity. Large time steps can be used thanks to a quasi-implicit method.

We describe our validation strategy and give some preliminary results of this work program.

Finally, optimization of the linear system solver with the HYPRE library and parallelization keep the run time low, making SPARCS a fast and accurate tool for spacecraft charging analyses.

Introduction

At Alcatel, numerical modeling plays a crucial role in the management of electrostatic risks arising from spatial charged particles. However, the old version of the reference code NASCAP/GEO currently in use has several limitations. We have therefore decided to develop a new computer code, SPARCS, to perform charging simulations with up-to-date numerical modeling. This effort started in 1998 with a Ph. D. work [1,2] and resulted this year in the first release of a 3D code for spacecraft charging computations in geostationary environment. The aim of this paper is to describe this code in terms of physical and numerical models and capabilities. We also provide some information on our validation strategy and on the parallelization of the code.

Physical Model

The current version of the code is specifically designed for low-density, collisionless, hot plasma found in geostationnary environment during substorms. In this situation, it is legitimate to neglect space charge effects. We thus solve the stationary Vlasov-Poisson equations for the plasma and electrical potential:

$$\begin{cases} mv \cdot \nabla_x f_\alpha + q\nabla_x \varphi \cdot \nabla_v f_\alpha = 0, \\ \qquad\qquad \Delta\varphi = 0, \end{cases}$$

with suitable boundary conditions.

Classical models are used for secondary electron emission, back-scattering, ion- and photon- induced emission, as well as conductivity of the materials (cf. [3]). Another important aspect of the model is the computation of recollected secondary electrons: this point will be described in more details below.

The differential charge of the dielectric materials and the absolute charge evolves according to the value of the local or global current balance respectively. The code can compute accurate transients or steady-state solutions through time-marching.

Numerical Model

A computational volume is defined around the spacecraft and discretized with elementary thetrahedra. The use of an unstructured mesh has several advantages over that of a structured mesh:

✓ Easy modeling of complex shapes (e.g. antennas, scientific instruments)

✓ Automatic meshing

✓ Easy local refinement.

The Laplace equation is solved on this domain by a P1 finite element method, coupled with an Infinite Element method on the outer artificial boundary to enforce the proper decay of the potential at infinity. The resulting linear system is solved by a conjugate gradient method.

The surface of the spacecraft is discretized in elementary triangles. On each of these triangles the distribution of incident ions and electrons is computed. The half-space of incoming velocity vectors is discretized on a regular grid. For each incident velocity of the grid, the particle is back-tracked to its starting point on the boundary of the computational domain (see Figure 1). By Liouville's principle, the value of the distribution function is constant along this trajectory, and this value is known on all boundary conditions for incoming particles. The case of secondary electrons emitted from satellite surfaces is treated likewise (see below).
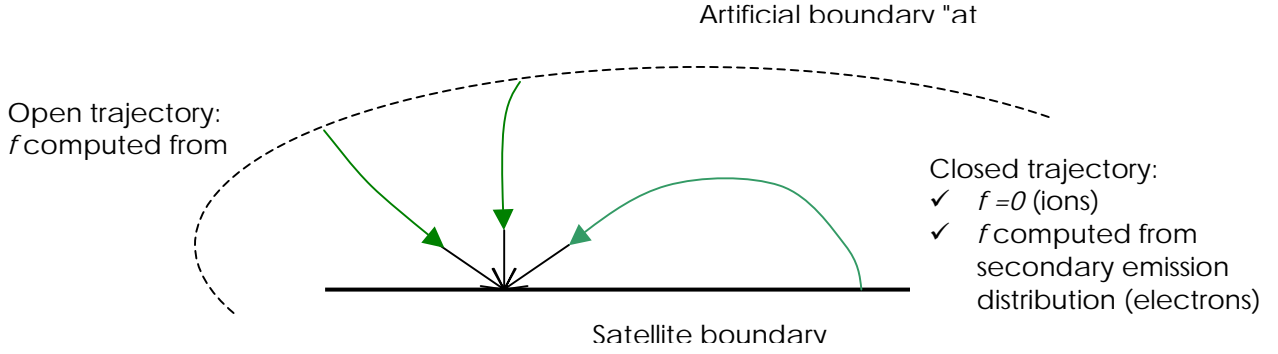
Figure 1. Computation of particle distribution by the back-trajectory algorithm.

Once the incident current of electrons and ions is known, secondary emission and bulk conduction current can be computed. To determine the value of photo-emission current, lighting of each surface (including cast shadows) is computed.

Current balance equations are then used to update the value of absolute and differential potentials. The evolution equation for the absolute potential reads

$$\varepsilon_0 C_{abs} \partial_t \varphi_{abs} = \int_\Gamma J \, ,$$

where C_{abs} is the absolute capacity and the right hand side is the integral of the total current on the spacecraft metallic structure. In order to stabilize the computation with relatively large time-steps, we use a quasi-implicit time-stepping procedure:

$$\varepsilon_0 C_{abs} \frac{\varphi_{abs}^{n+1} - \varphi_{abs}^n}{\delta t} \approx \int_\Gamma J^n + \tilde{J}' \cdot \left(\varphi_{abs}^{n+1} - \varphi_{abs}^n\right),$$

where $\tilde{J}'$ is an approximation of the differential of the total current. A suitable choice for the latter is the differential of the total current on a sphere, which can be computed analytically.

Finally, the value of the potential around the spacecraft is computed and a next time-step can be processed.

Recollection of Secondary Electrons

In geostationary environment, secondary (and photoelectric) emission is limited by the formation of local potential barriers. These barriers are created either by the space charge of the electron cloud or by the configuration of the electric field due to differential charging. Since space charge is not computed in SPARCS, only the second effect is currently modeled.

Also note that potential barrier is not the only phenomenon which leads to electron recollection: two surfaces facing each other will recollect all re-emitted electrons regardless of their energy (screening effect).

The recollection current is computed on satellite surfaces in much the same way as the incident current (see Figure 1). The velocity discretization takes into account the smaller value of the temperature of these electrons. In the absence of specific information on the distribution of secondary an photo-electrons, a Maxwellian distribution with temperature 2 eV is assumed. However, this is not a limitation of the code, and we plan to use better descriptions in the future.

Secondary electrons hitting satellite surfaces will in turn yield new secondarys, in an electron multiplying process. Ideally, this current should be computed and iterations performed until self-consistency is reached. For the sake of simplicity, we chose to neglect this effect.

Validation Strategy

Our validation strategy is composed of three steps:

✓ Analytic test cases (sphere)

✓ Cross-comparison with other codes

✓ Validation with experimental data (on ground and flight)

We have first validated the implementation of the physical models by computing the charging of a sphere and comparing with semi-analytic MATLAB results. Models for each of the secondary emission processes were validated independently. SPARCS calculations were shown to be accurate. As an example, we give the results of the charging of a sphere with magnetospheric currents, back-scattering of electrons, ion-induced secondary current and photo-emission.

Table 1. Example of analytic results on a conducting sphere

	Analytic results	SPARCS results
Potential (V)	-7098.2	-7014.6
Primary electrons (A/m^2)	$2.65 \ 10^{-6}$	$2.67 \ 10^{-6}$
Backscattered electrons (A/m^2)	$5.836 \ 10^{-7}$	$5.85 \ 10^{-7}$
Ration J_e^{back}/ J_e	0.22	0.219
Protons (A/m^2)	$1.196 \ 10^{-7}$	$1.19 \ 10^{-7}$
Secondary electrons due to protons	$1.448 \ 10^{-6}$	$1.47 \ 10^{-6}$
Ration J_e^{ions}/ J_e	12.11	12.38
Photo-emission (A/m^2)	$5 \ 10^{-7}$	$5 \ 10^{-7}$

In a second phase, we perform cross-comparisons with NASCAP/GEO [3] on a typical telecom spacecraft. This work is still under progress. We present below some preliminary results of the study. In Figure 2 we show the evolution of the absolute potential during an eclipse and in Figure 3 the differential potential after 10s. More results will be published elsewhere.
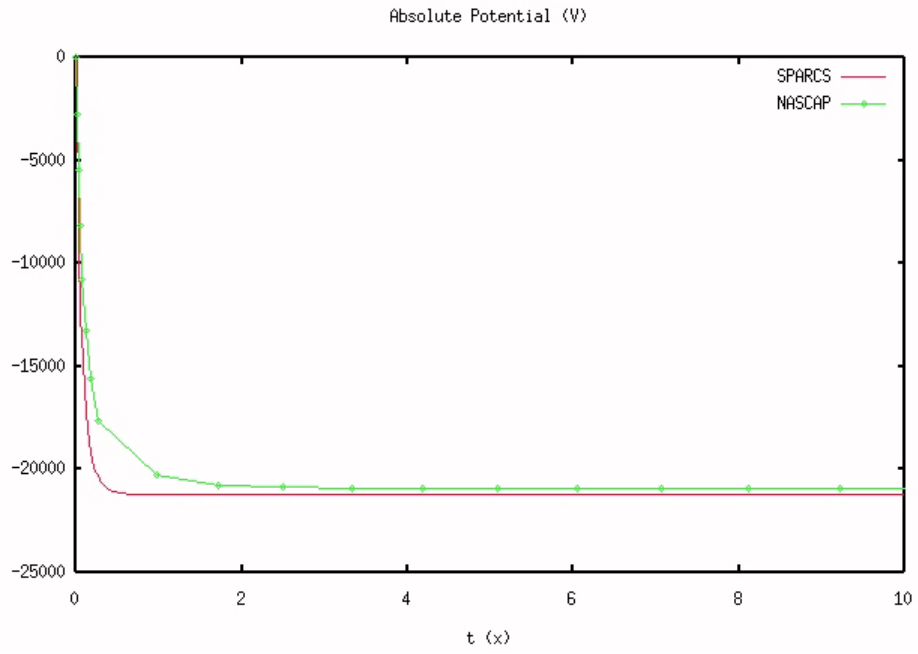
Figure 2. Charging of telecom spacecraft in eclipse.
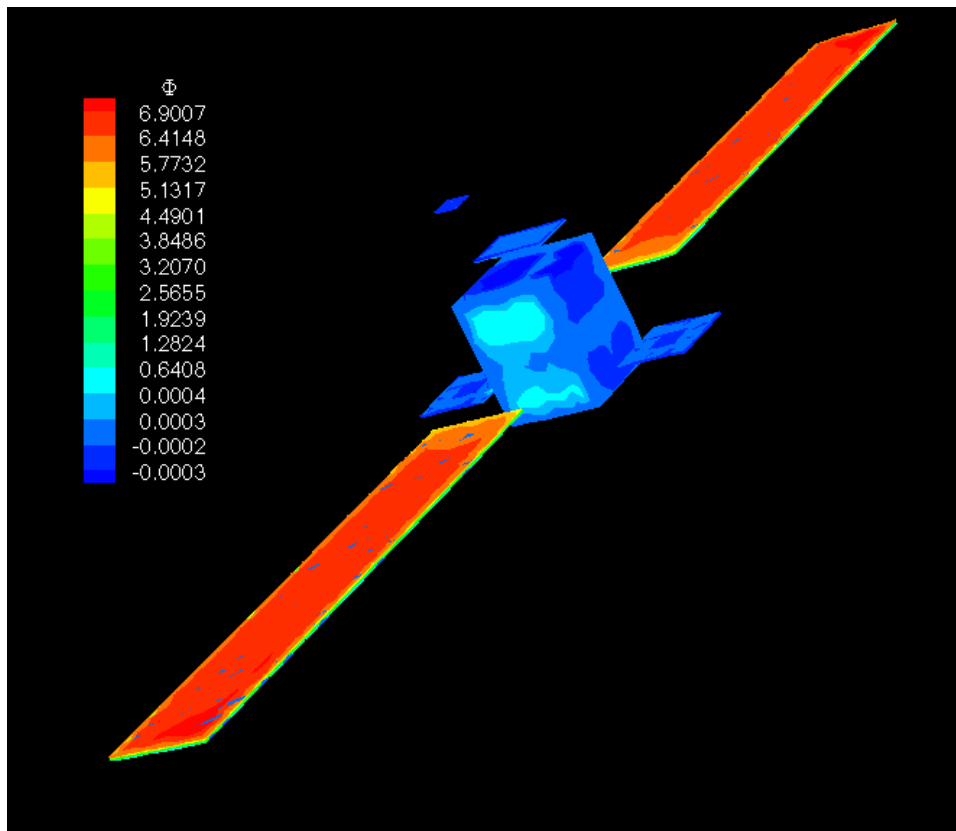
Figure 3. Differential potential on satellite surfaces after 10s.

The third phase will consist of comparisons with experimental ground and flight data. The tentative qualification program is the following:

✓ Charging of a material coupon in the SIRENE (large spectrum electron gun) facility at ONERA. The aim is the validation of secondary emission and conductivity models.

✓ Potential barrier build-up experiment. The future experimental set-up aims at validating models of secondary of photo- emission current limitation by potential barrier build-up mechanism. This project should be launched in year 2004.

✓ We are also thinking about investigating the charging of a complete satellite mock-up in a plasma chamber. This study should benefit from the output of the potential barrier build-up experiment, and would thus start in 2005 approximately.

✓ Finally, we are considering an in-flight experiment on a telecom satellite. Another benefit of this work would be to assess the representativity of experimental ground facilities.

Parallelization

It is well known that plasma simulation is very costly in terms of computational time, mainly because problems are set in a high dimensional space ($\mathbf{R}^7$ for time-dependent problems). Even with the important simplification of neglecting space-charge effects, it was found desirable to speed up computations by using parallelization techniques.

In view of this point, we have used two different parallelization paradigms. First, we have used the OpenMP library to distribute the computation of particle trajectories between processors. On the other hand, the HYPRE library [4] was used for the solution of the linear system arising from the Finite Element discretization of the Poisson problem. A state-of-the art Agglomeration Multigrid preconditioner was used to improve the convergence of the conjugate gradient iterative method. The parallelization relies on the MPI library and thus works on computers with distributed memory (e.g. PC clusters). While this dual, shared memory/distributed memory approach yields optimal performance for each task, it is quite cumbersome in terms of portability. This is why we will probably have to rethink the parallelization strategy in the future.

In the meantime, it is often sufficient to parallelize only the particle trajectories to ensure a significant speed up. On a HP GS320 computer, using 4 processors, we have observed a parallel efficiency ranging from 74 to 99 % depending on the cases.

Conclusion

The SPARCS project aims at providing an advanced spacecraft charging software for electrostatic discharge protection analyses. Thanks to innovative numerical treatment and parallelization, we are able to make accurate simulations within a reasonable run-time. In the future, we will concentrate on validation efforts and extensions to other plasma environments (LEO and artificial thruster plasma).

References

1. O. Chanrion, Simulation de l'influence de la propulsion plasmique sur la charge électrostatique d'un satellite en milieu magnétosphérique, Ph. D. thesis, École Nationale des Ponts et Chaussées, 2001.

2. O. Chanrion, Electrostatic charging simulation of spacecraft using a stationary plasma thruster in geostationary plasmic environment, 7th Spacecraft Charging Technology Conference, Noordwijk, The Netherlands, 2001

3. Stannard P.R., Katz I., Gedeon L., Roche J. C., Rubin A.G. and Tautz M.F., Validation of the NASCAP model using spaceflight data, 20th Aerospace Sciences Meeting, Orlando, Florirda, 1982.

4. Falgout, R. D., and Yang, U. M., **"**hypre: a Library of High Performance Preconditioners**,"** in Computational Science - ICCS 2002 Part III, P.M.A. Sloot, C.J.K. Tan. J.J. Dongarra, and A.G. Hoekstra, Eds., Lecture Notes in Computer Science, vol. 2331, pages 632-641, 2002, Springer-Verlag.

COMPUTER SIMULATION OF RADIATION CHARGING PROCESSES IN SPACECRAFT MATERIALS

Valery Mileev
D.V. Skobeltsyn Institute of Nuclear Physics
Moscow State University
Vorob'evy Gory, Moscow 119899
Russian Federation
Phone: +7 095 939-1007
Fax: +7 095 939-0896
E-mail: mileev@sinp.msu.ru

L.S. Novikov
Moscow State University, Russian Federation

Abstract

The problems of application of Monte-Carlo method to modeling of processes of internal charging of spacecrafts dielectric materials of under impact of electrons with energies 0.1 - 10 MeV, appropriate to range of energy spectrums of the Earth radiation belts electrons are considered. The dynamic model of internal charging including self-consistent calculation of internal electrical field and its influence to motion of primary and secondary charged particles is shown.

In terms of the simulation results, the differences between processes of internal charging of dielectrics in space conditions and in laboratory experiments in electron accelerators are explained.

Introduction

The radiation charging of spacecrafts is one of the most important factors resulting in to origin of failures in operation of the spacecraft onboard systems[1].

Last years, the increasing attention attracts the process of internal radiation charging of dielectric materials of spacecraft under impact of electrons with energies ~1–5 MeV, contained in the Earth's radiation belts. Earlier, it was considered on the basis of results of laboratory researches of accumulation internal charge in dielectrics at irradiation of ones by electron beams that this charging type is not implemented in space conditions[2]. However data of special experiments conducted onboard the CRRES spacecraft, crossing the Earth's radiation belts region, have shown convincingly that the origin of internal electric discharges in dielectric materials is possible in space conditions. For this purpose, the accumulation of electrons fluencies of ~10^{11} 1/cm^2 is necessary, and the value is less by order of 3 compared to the conditions of laboratory experiments[3].

The purpose of the paper is the computer simulation of the internal charging processes in spacecraft dielectric materials under impact of electrons with energies in an interval 0.1-10 MeV corresponding to range of the Earth's radiation belts electron energy spectra, and recognition on the basis of simulation distinctions in internal charging of dielectrics in space conditions and in laboratory experiments on electron accelerators.

Technique of Simulation of Dielectrics Internal Charging Dynamics

As the base of algorithms and programs package for simulation, the GEANT-3 software package developed initially for solution of fundamental problems in high-energy physics[4] was chosen. This package does not contain the utility to take into account the influence electrical field created by the absorbed internal charge on motion of the charged particles inside the dielectric. It is extremely important to take into account the influence in simulation procedures, because the electrical field mentioned substantially determines the depth distribution of the injected charge in dielectric. In this connection, the utility for simulation of influence of the internal electrical field on process of charged particles passing in substance was developed.

At the description of electron passing through the substance, the continuous energy losses on ionization in multiply scatterings with small energy transmissions in each collision and discrete processes with secondary electron and photon formation among which the dominating role is played by knockout of δ-electrons from energies above 10 keV were taken into account. At calculation of distribution of an accumulated charge in dielectric, it is necessary to take into account formation of an excess positive charge ("holes") after ionization of atoms also.

At simulation of process of dynamic accumulation of the internal charge in dielectric using the Monte-Carlo, approximation of "large" particles is used in fact. In the method, a set of N particles with a charge eZN and a given energy and incident angle distribution function of particles falling on the target in time Δt corresponds to each event. After modeling of one event and tracking of primary and secondary particles in the target, the increment of function of distribution of he internal charge $\Delta\rho(\mathbf{r})$ in given points is evaluated. In terms of the calculated distribution of the internal charge $\rho(\mathbf{r})$, electric field intensity E $(\mathbf{r})$ and potential U $(\mathbf{r})$ are calculated an the same points which will be used at simulation of following event. Thus, the series description of time development of the internal charging process, and also self-consistent calculation of the internal electrical field and its influence on motion of primary and secondary charged particles is carried out.

For estimation of probability of electrostatic breakdowns in dielectric and computation of the breakdown values, distributions of density of ponderomotive forces $\mathbf{F}(\mathbf{r}) = \rho(\mathbf{r})\,\mathbf{E}(\mathbf{r})$ and density of an internal energy of free charges $W(\mathbf{r}) = \rho(\mathbf{r})\,U(\mathbf{r})$ are evaluated too.

Calculation Results

On the basis of the technique developed, the computer simulation of the internal charge accumulation in the case of monochromatic beams of electrons and electrons with energy spectra typical for radiation belts of the Earth was done. Glass slab of width 0.5 cm was used as a sample. For modeling of laboratory conditions in accelerators, the energy of the collimated electron beam was 1.0-10.0 MeV. The energy spectrum of electrons of radiation belts of the Earth incident on the sample isotropically, was described by exponent with mean energy 0.5 MeV which is similar to models of conditions of "the worst case" for an internal charging developed in NASA[5] and DERA[6].

The depth distribution of the internal charge is one of the main characteristics determining the phenomenon of dielectric material charging under impact of the high energy

electrons and possible discharge processes in dielectrics. As it was already noted above, this distribution is determined by as distribution of stopped electrons in the target (i.e. having energy below threshold), and by distribution of the produced positively ionized atoms (holes). Let's consider a case of the collimated electron beam with energy 2 MeV.

In Fig. 1a, the distribution of the stopped electron number (both primary, and secondary, basically, δ-electrons) is presented. In Fig. 1b, the similar distribution of number of positive vacant electron sites is adduced. As it is seen on Fig. 1ae, the distribution of stopped electrons is practically homogeneous till the depth of 0.25 cm, that is in good agreement with empirical formulas[7] and results of other calculations[8]. However, as it is seen from matching Fig. 1a and Fig. 1b that maxima determined by knock-out of δ-electrons exist in both distributions on small depth (~0.025 cm).

Net distribution of the internal charge (Fig. 2a) shows that the two distributions above substantially compensate each other, which is connected to small values of energies and correspondingly small range of δ-electrons. The considerable role in formation of these distributions is played by the electrical field of the internal charge.

Qualitatively different distribution of the internal charge is obtained at irradiation of the target by an isotropic electron beam with spectrum typical for the Earth radiation belt (Fig. 2b). Almost all internal charge has appeared to be concentrated in the surface area with depth less than 0.01 cm. It is determined by three reasons: presence of low energy particles in the spectrum, significant fraction of particles with small incident angle in the case of isotropic distribution and retarding field of the internal charge. Thus, density of the absorbed internal charge for space radiation considerably exceeds density of charges for the case of the monoenergetic collimated electron beam at small depth.

Computations of the electric field strength in laboratory (Fig. 3a) and space (Fig. 3b) conditions yield depth distribution close to each other as in curve shape, as in absolute value. Significant difference in the electric field intensity magnitude arise at small depth (lower 0.01 cm) where the magnitude value in space increases the value in laboratory conditions by a factor of 2.

Conclusion

Thus, characteristics of the arising internal charge considerably differ in case of laboratory simulation experiments in accelerators and in space conditions of spacecraft charging of in the Earth radiation belts. The indicated differences allow to explain the origin of internal electric discharges in dielectrics in space conditions at considerably lower values electron fluencies as contrasted to the laboratory experiment condition.
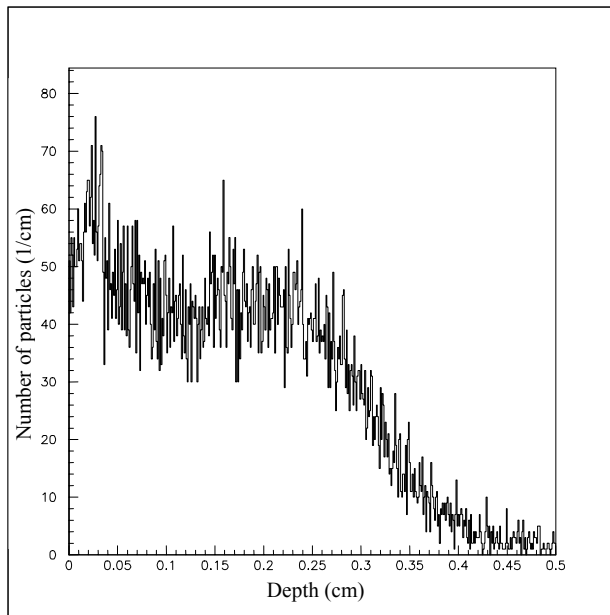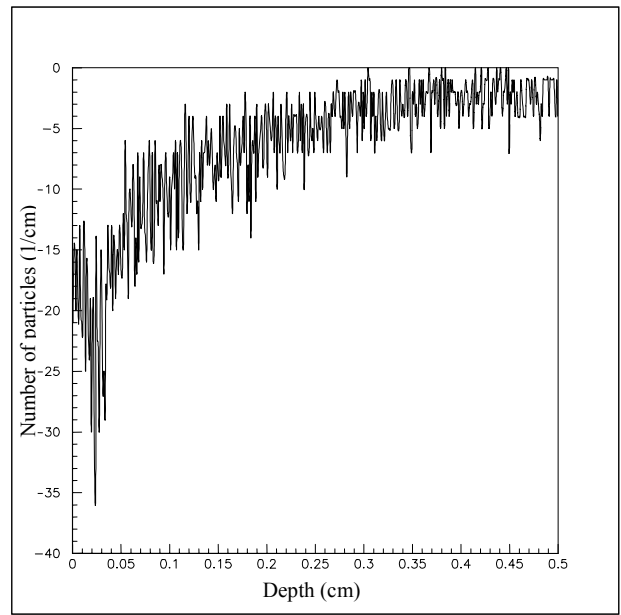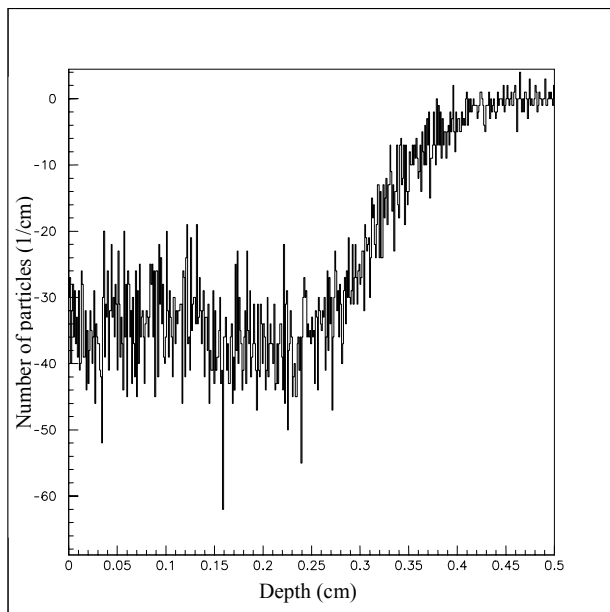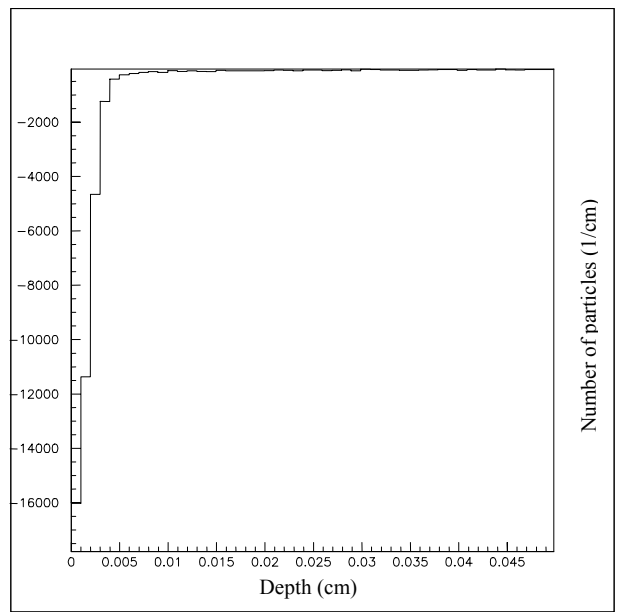
Figure 1. Distribution on depth of a sample of number of charged particles for a monochromatic beam with energy 2.0 MeV at normal incident angle.
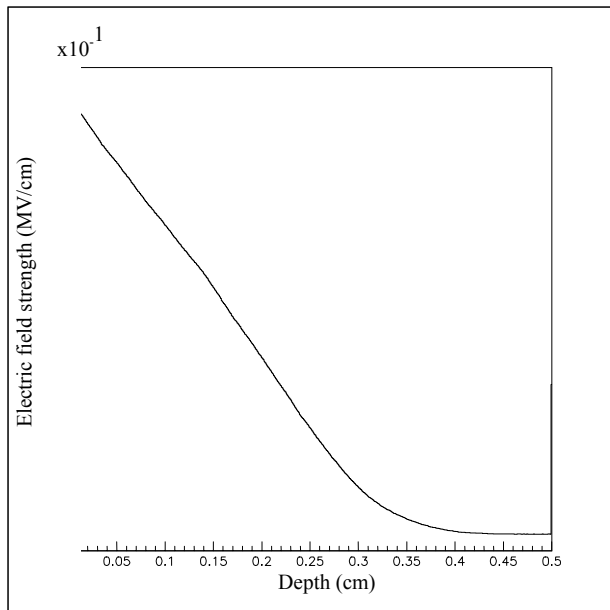**A. Distribution of stopped electrons; b - distribution of positively ionized atoms.**
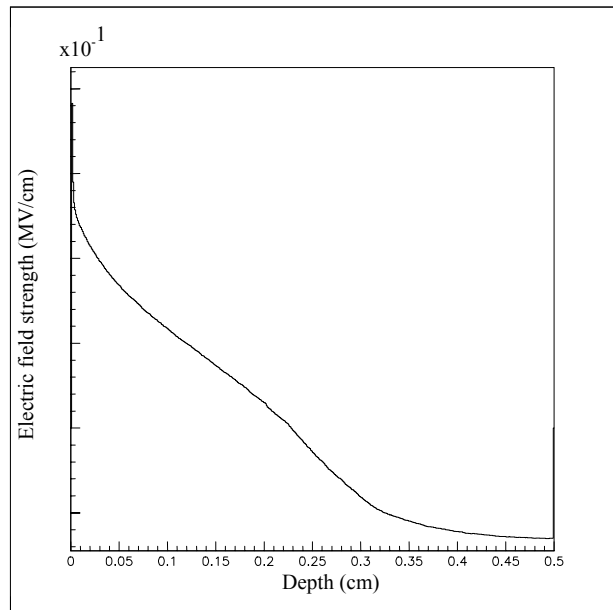

Figure 2. Internal charge distribution on depth of sample.
A. For a monochromatic beam of electrons with energy 2.0 MeV at normal incident angle;
B. For Earth radiation belt electrons spectrum with isotropic angular distribution.

Figure 3. Electric field strength distribution on depth of a sample.
A. For a monochromatic beam of electrons with energy 2.0 MeV at normal incident angle;
B. For Earth radiation belt electrons spectrum with isotropic angular distribution.

References

1. The encyclopedia " New high technologies in engineering ", vol. 16 " Effect of a space environment on materials and equipment of spacecrafts ", editors L.S. Novikov and M.I. Panasyuk, Moscow, 2000

2. A.L. Akishin, Yu. S. Goncharov, L.S. Novikov, Yu. L. Tyutrin, L.I. Tseplyaev. Discharge Phenomena in Electron Irradiated Glasses. Radiat. Phys. Chem. 1984, v. 23, no. 3, pp. 319-324

3.   A.R.Frederickson, E.G.Holeman, E.G.Mullen. Characteristics of spontaneous electrical discharging of various insulators in space radiations. IEEE Transactions on Nuclear Science, 1992, Vol.39, p.1773

4. R. Brun, et al. GEANT User's Guide, 1993

5. Avoiding problems caused by spacecraft on-orbit internal charging effects, NASA Technical Handbook, NASA-HDBK-4002, 1999

6. G.L. Wrenn, D.J. Rodgers and P. Buehler. Modeling the outer belt enhancements of MeV electrons, J. Spacecraft and Rockets, 2000, vol. 37, no. 3, pp. 408- 415

7. K.H. Weber, Nucl. Inst. Meth., 1964, 25, p. 261

8. C. Trenkel, Comparison of GEANT 3.15 and ITS 3.0 radiation transport codes, ESA working paper, EWP 1747, 1993

DESIGN OF A NEW MODULAR SPACECRAFT PLASMA INTERACTION MODELING SOFTWARE (SPIS)

J.-F. Roussel
ONERA, 2Av E Belin
31055 Toulouse cedex 4, France
Phone: +33 5 62 25 27 35
Fax: +33 5 62 25 25 69
E-mail: **Jean-Francois.Roussel@onecert.fr**

F. Rogier, M. Lemoine, D. Volpert
ONERA

G. Rousseau
University Paris 7

G. Sookahet, P. Sèng
Artenum

A. Hilgers
ESA

Abstract

The development of a new software for spacecraft plasma interactions modeling was started in Europe at the end of 2002. This Spacecraft Plasma Interaction Software (SPIS) is developed for and by SPINE community (Spacecraft Plasma Interaction Network in Europe) on an open source basis. The ESA contractors, ONERA, Artenum, and University Paris 7 are in charge of the development of SPIS framework and main numerical modules. SPINE community will be able to add extra modules and apply the code to its needs. The software framework is based on the integration or interfacing with available open source tools for CAD, 2D meshing, 3D meshing, GUI, post-processing and graphical display. The numerical routines will allow the modeling of plasma dynamics (kinetic or fluid, electrostatic with possible extension to electromagnetic) and its coupling with the spacecraft (equivalent circuit approach). The modeling of all types of environments and devices will be allowed (LEO/GEO/PEO…, EP/solar arrays…). The emphasis has been put on the code modularity to allow the interoperability of modules, through an object-oriented approach throughout the code. User requirements were defined in February 2003 (4th SPINE meeting), major technological choices and top level design were performed in June 2003 (unstructured mesh is the basics, Java language was selected for coding, pre-post/processing tools were chosen). The first release of the framework was in October 2003. The major features of the software framework and of the physical numerical routines are presented in this paper.

Introduction - SPIS Project Background

The interest in spacecraft plasma interaction modeling is almost as old as the discovery of the possibly detrimental effects of high energy plasma on satellites. The first concerns had to do with the integrity of the spacecraft platform, i.e. with its capability to operate normally. They are usually called "technological" (as in the name of this conference). The early issues were due to high level charging in Geostationary Earth Orbit (GEO), then in Polar low Earth Orbit (PEO), and the subsequent ElectroStatic Discharge risk (ESD). More recently extra concerns about plasma interactions with active devices, such as Photo Voltaic Arrays (PVA) and Electric Propulsion (EP), also became of prime importance. A second category of concerns are considered as pertaining to "science" rather than technology. Scientists study earth, planetary, interplanetary and solar environments, and their measurements can be spoiled by plasma effects. The most typical situation is the partial or total alteration of the low energy plasma measurements by even a small charging potential, at the Volt scale (to be compared to the hundreds or thousands of Volts scale of technological issues). Modeling the spacecraft and its local plasma environment may allow to predict and/or avoid detrimental charging as in the technological issues, but may also is some cases help the interpretation of the data by "subtracting" the charging effects from the data. Although the typical charging levels of "technological" and "scientific" issues are very different, many modeling techniques are common and a properly designed simulation code should be able to address both. The need to address both domains is also very clear in Europe where both commercial spacecraft and scientific missions are flown by prime companies and ESA.

Unfortunately there is no simulation code both able to answer these needs and available at Europe level or worldwide. Proprietary codes are by definition not available to any user and suffer from the high costs of development and maintenance by a single company (as e.g. ONERA SILECS code[1]). Commercial codes do exist, but they are either outdated (early NASCAP/GEO[2]) or not available in Europe due to US export control regulations (NASCAP-2K[3]).

These needs are at the origin of SPIS project (Spacecraft Plasma Interaction Software) presented here. Another element of great importance in SPIS project background is the existence of SPINE community. It stands for Spacecraft Plasma Interaction Network in Europe although it is not limited to Europe and involves a few Americans and Japanese. It has been set up in 2000 and has been meeting approximately twice a year since then (see http://www.spis.org). The origin of its members is quite diverse: spacecraft technology, space science, plasma science, computer science… First aiming at exchanging information about spacecraft-plasma interaction physics, flight observations, data, simulation methods and results, needs, etc. SPINE community now plays a central role in the development of SPIS software reported here. This development is both performed for the community and by the community on a collaborative basis.

Moreover, a prototype code, PicUp3D[4,5] (J. Forest Ph.D.), was already developed in the context of SPINE community. It first tested some technical tools which were chosen for SPIS (Java, VTK). The activity around PicUp3D (users, extra developers) also demonstrated the interest for such an open collaborative approach.

The first section of this article presents SPIS project objectives. The second section describes the project organization for a collaborative development. The project schedule, including past achievements and future plans, are presented next. Entering a little more into the technical details the last two section respectively deal with the global framework of the code and the object oriented design of the numerical solvers.

SPIS Project Objectives

Since the need of a spacecraft plasma interaction simulation code was clear, that none was available, and that a lively community existed, it appeared clear that a new code had to be developed in the framework of this SPINE community. SPINE members had the need for the code and could offer some development effort.

In that context, the first objective of the code was to answer the whole set of needs of the community. Beyond the large common basis, different needs were expressed in all domains, ranging from solvers to interactions, or plasma source libraries (environment, artificial sources such as EP…). So, the code had first to be *versatile*. If all the requirements could not be met in its first versions, its structure should allow the extension of the code to fulfill them later.

The *versatility* of the code, i.e. its offering different modeling capabilities, could only be achieved through a good *modularity*. Beyond answering this first requirement of versatility, modularity also offered other advantages. It is of course known to be a condition for an efficient code maintenance and evolution. But in the framework of SPINE, the major interest of building a modular code was to permit a collaborative development, i.e. allow community members to develop their own modules, to be shared with the whole community through neat imbedding in the global code.

The direct consequence of the modularity requirement was the choice of an open source policy. Although the interfacing of "black boxes" is possible when their inputs and outputs are well documented, module interfacing at source level is much more efficient and safe. Since no compatibility had to be insured with any inherited black box component, it was decided to enforce open source policy on all developed modules for this new code. It did not mean at all that it had to be developed from scratch since many modules are now available on an open source basis both for pre/post-processing and numerical libraries.

Organisation for a Collaborative Development

The organization of SPIS code development was thus optimized for a collaborative development within SPINE community. As depicted in figure 1, three major entities were set up to collaborate in the code development.

A contract was first attributed to a contractor consortium after an open competition bidding phase. The major roles of the contractor are to:

1- propose requirements in a first phase (Dec. 2002 through June 2003)

2- design a modular software architecture and develop its core modules (framework and basic solvers) in a second phase (June 2003 through June 2004)

3- support the community for an appropriation and testing of the code in a third phase (June 2004 through June 2005) including the use a of collaborative web platform LibreSource **http://www.libresource.org**.

The consortium is led by ONERA, the French aerospace research public company, in charge of project management and coordination, numerical architecture design and core numerical solvers development. Subcontractors are Artenum company, specialized in consulting and development in numerical engineering, in charge of SPIS framework development (pre/post-processing, solvers embedding) and open source consulting, and University Paris 7 for community related consulting.

A board was then set up to supervise the software development, the SDAB (Software Development Advisory Board). It is composed of 1 contractor member, 1 ESA member and 3 community members. It supervises and orients the code development in particular in emitting recommendations when tradeoffs are needed between different possible choices or requirements.

The third entity is SPINE community. For SPIS development, three Working Groups (WGs) have been set up. Each WG has been defined around a specific subject and a challenging test case related to that topic. In the first phase each WG emits requirements relevant to its domain, then requests specific developments and eventually participates in code validation and development in the third phase, where all resources will be devoted to running the test cases and check the capability of the code to model them, upgrading it if necessary. The three WGs were defined by the following topics and test cases:

- WG1: Sheaths, test case = Cluster spacecraft
- WG2: Artificial plasma (mostly EP), test case = SMART 1
- WG3: Material interaction, test cases = high level charging SC (Freja in PEO, Scatha in GEO)

More can be found on SPIS web site http://www.spis.org/spis. about SPIS project organization
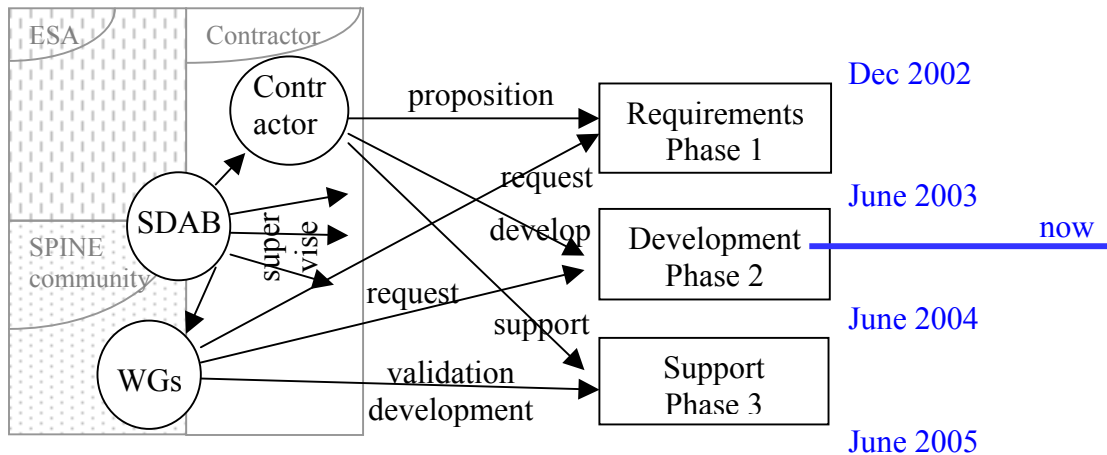
Figure 1. SPIS project organization

Schedule: First Achievements - Future

User requirements were first to be defined. A first version was written by the contractor. It was discussed within the community, in particular during 4th SPINE Meeting (Feb. 2003), and upgraded with community feed back (during and after the meeting). The User Requirement Document (URD) is accessible at http://www.spis.org/spis/docs/technical/SPIS_URD.pdf.

The major user requirements were the following:

- Solvers: Poisson, Vlasov (PIC), Poisson-Vlasov coupling, SC circuit, SC-Plasma coupling, possibility to include extra solvers (Maxwell, fluid models for matter…)
- Environment: LEO, GEO, flexible environment model...
- Interactions: photo-emission, secondary emission, induced conductivity… basic models provided, possibility to modify them and add extra models
- Sources: Maxwell distributions, electric propulsion… highly customisable
- Framework: GUI and command line / scripts, for pre/post-processing and computing
- Specific need to handle thin surfaces and wires (solar array, wire-like boom…)

In all of these subject, emphasis was put on modularity. If a capability may be needed but will not be implemented initially, compatibility of the code architecture with its future implementation must be insured.

The next trimester (March – June 2003) was devoted to Software Requirements (SRD) and top level design. They were finalized after the Preliminary Design Review (PDR) between the contractor and SDAB (June 2003). Major choices for languages and tool choices were performed:

- Java was chosen for numerical modules and part of the framework coding, because:

  - An Object Oriented (OO) language was needed for a better modularity
  - Java is a pure OO-language contrarily to C++

- Benchmark on PicUp modules in Java (Julien Forest) showed that C++/Java speed ratio is only on the order of 1 to 2, and even around 1 for compiled Java

- Jython, a python script language interpreter written in Java (homogeneous with solvers), was chosen for part of the framework
- Pre- and post-processing open source tools to be integrated were chosen.

The major choices for numerical modeling were the following:

- Primary mesh will be unstructured (it does not exclude future usage of structured meshes)
- Solvers: Poisson, Vlasov, (spacecraft circuit), etc. will be developed for unstructured mesh
- The need of a specific handling of 2D and 1D physical elements was identified as deriving from the thin surfaces and wires user requirements (not through 3D pizza-boxes or thin cylinders, but through actual 2D and 1D elements). The electric field singularity around a thin wire or a panel edge shall be extracted thanks to specific finite elements, allowing exact particle trajectory integration. This is the only way to properly model plasma dynamics around a singular geometry such as e.g. Cluster wire booms (40 m length versus diameter around 1 mm!)

With the third trimester (June-Sept 2003) started the development phase. A large part of SPIS framework was implemented:

- pre-processing
- some framework capabilities (group handling, scripting…)
- solver encapsulation: interfacing with PicUp3D prototype code was performed as a demonstration (interfacing with SPIS solvers cannot yet be demonstrated since most routines do not exist yet)

The full framework with post-processing capabilities will only be released in November 2003. Concerning the numerical routines, progress was:

- detail design of numerical routines architecture, emphasizing modularity and polymorphism
- prototype routines development.

The first SPIS release was presented during 5th SPINE meeting, on September 16-17, 2003. It is now available at http://www.spis.org/spis/download/software/software.html. It was released under the General Public License (GPL). It is a well known open source license (Linux license for instance) which essentially forces the users of the distributed source code to further distribute these source codes under the same GPL license.

The future milestones are the following:

- Release of full framework in November 2003 (post-processing added)
- Release of full SPIS software (framework + solvers) in March 2004, with course on SPIS (6th SPINE meeting)

- Release of extended SPIS in June 2004 (7th SPINE meeting): the major extension should be the specific handling of 2D and 1D elements (singularity extraction through specific finite elements close to edges or wires for Poisson, analytical particle trajectories close to singularities), although it still need to be confirmed at 6th SPINE meeting.

SPIS Framework

We just sketch here a few technical details of SPIS code framework. It has both a Graphical User Interface (GUI) and a command line interface with the capability to run scripts (Python script language). Commands can either handle high level objects (example: object = plasma, action = integrate over time t), or address low level objects, achieving a much more detailed tuning of the computation thanks to the perfect encapsulation of Java objects in the Java-coded Python script interpreter called Jython (example: object = Poisson boundary conditions on computation box boundary, action = set it as homogeneous Fourier conditions with local parameter defined so as to mimic a $1/r^2$ potential decay mimicking potential in a pre-sheath around a sphere).

SPIS architecture is depicted in Figure 2. The GUI in the two lower rows indeed generates commands (row above), which are transferred to the control center. The control center has its own data structure (row above) for geometry, meshes, physical data and visualization. It transfers them to and from the various modules (geometry and mesh generation, physical properties handling, numerical solvers, and post-processing).
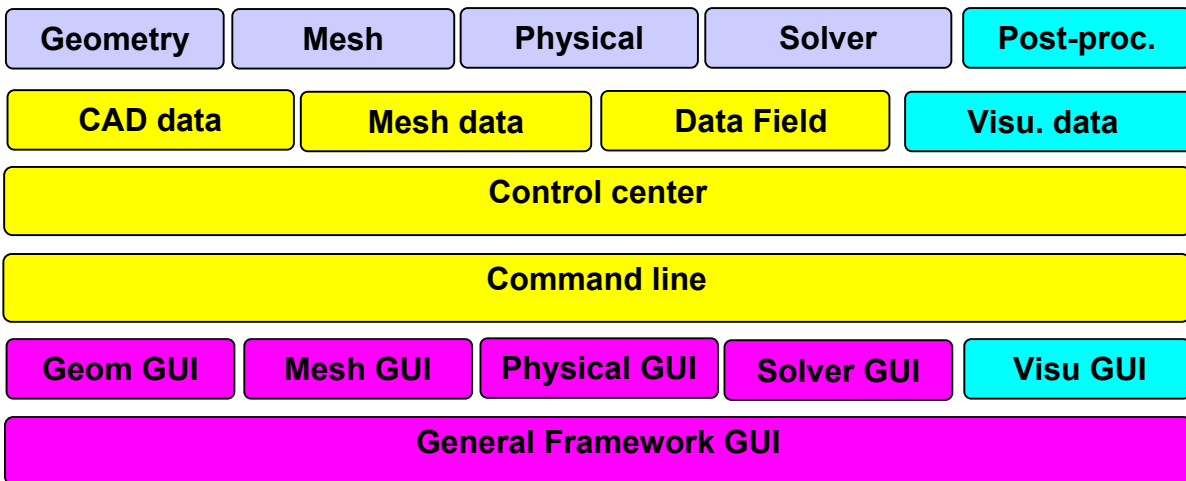
Figure 2. SPIS framework architecture

An example screenshot is then presented in Figure 3. This picture only shows a prototype which was written in wxPython when the C++/Python solution was investigated, whereas the final language choice of Java/Jython led us to consistently implemented the GUI in Java/Swing (the full GUI will only be released in November).

The main window...   and the VTK views
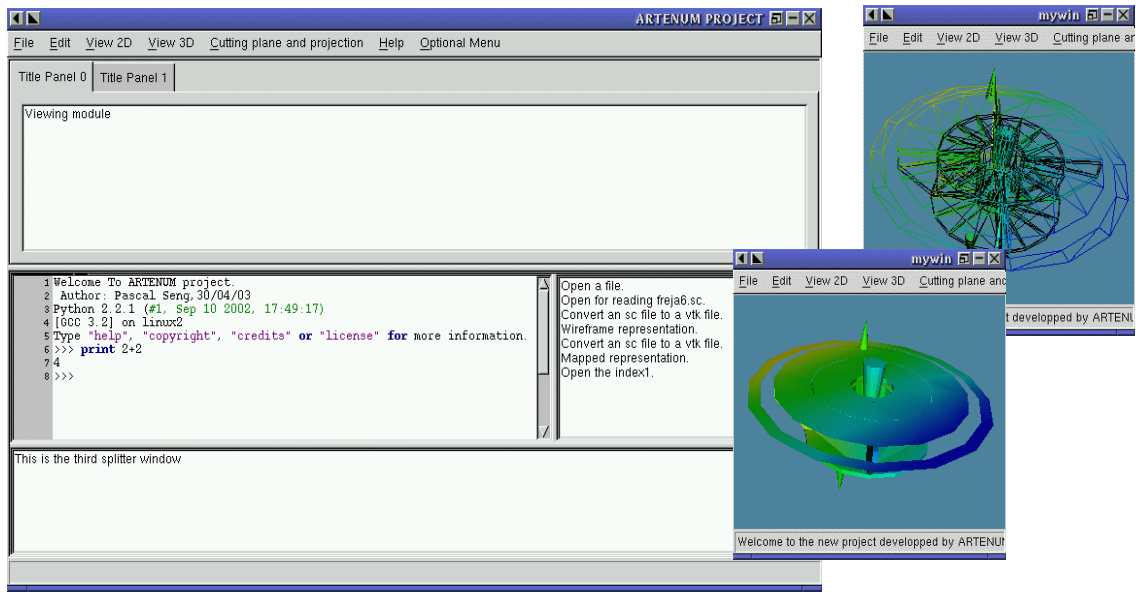
Figure 3. Prototype screenshot in wxPython and VTK pop up windows (post-procressing)

An example of volume meshing with one of the two interfaced mesh generators (Tetgen) is also reported in Figure 4. This second mesh generator offers volume meshing around 1D or 2D objects (infinitely thin arrays on the Fig. 4 plot) contrarily to the first interfaced mesh generator (GMSH).
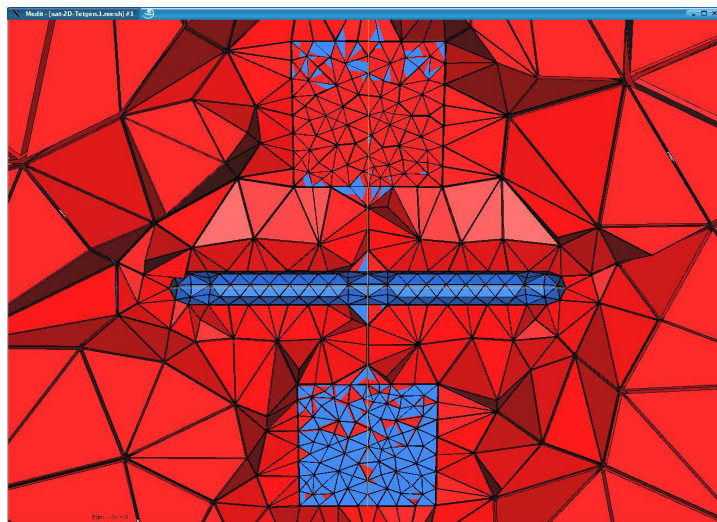
Figure 4. Example of volume meshing with Tetgen (supports thin objects, as the PVA here)

Modularity and Polymorphism of Numerical Routines

In their current development state, the main novelty in the numerical routines, as compared to existing codes, is their modularity. It can roughly be stated that we know how to do a software to

simulate plasma-spacecraft interactions. This statement is supported by the number of existing such codes, even though some solvers may of course be more or less efficient, accurate or stable. What we have to do here yet involves a significantly extra difficulty. We have to make it modular so as to incorporate very heterogeneous modules such as:

- Mesh: unstructured or structured
- Dimension: 3D, 2D, 1D (+ axysymetric…)
- Matter: kinetic (e.g. Particle-In-Cell, PIC), fluid, or global (Boltzman distribution)
- (Electric) Field: stored as a field, or stored as a potential
- Field or variable: centring (nodes/edges/surfaces/cells), scalar/vector…
- Solvers: different versions
- …

As briefly stated above, using OO languages greatly helps to reach that goal, hence the choice of Java. This is implemented through polymorphism, i.e. different versions of objects, which, although internally coded very differently, offer the same services to external requests. For example, a matter distribution object shall offer two basic services, "*move*" and "*get moment*," whatever their internal representation, either kinetic (PIC), fluid or global. So, the basic tool to implement modularity is available in an OO code. This is yet far from doing the job. The real difficulty indeed lies in the number of different polymorphisms to be implemented (list above). Straightforwardly implementing the polymorphism recipe just described leads to an horrific implementation, such as the examples depicted in Figure 5. A new branching of the derivation tree is defined to implement each polymorphism. The number of derived classes is multiplied at each step. The resulting enormous amount of classes is very difficult to handle, support and modify. Development costs rise, while modularity is largely lost. So, the right way to ensure a good modularity is by uncoupling the polymorphisms, replacing class number multiplications by additions, as will be explained next.
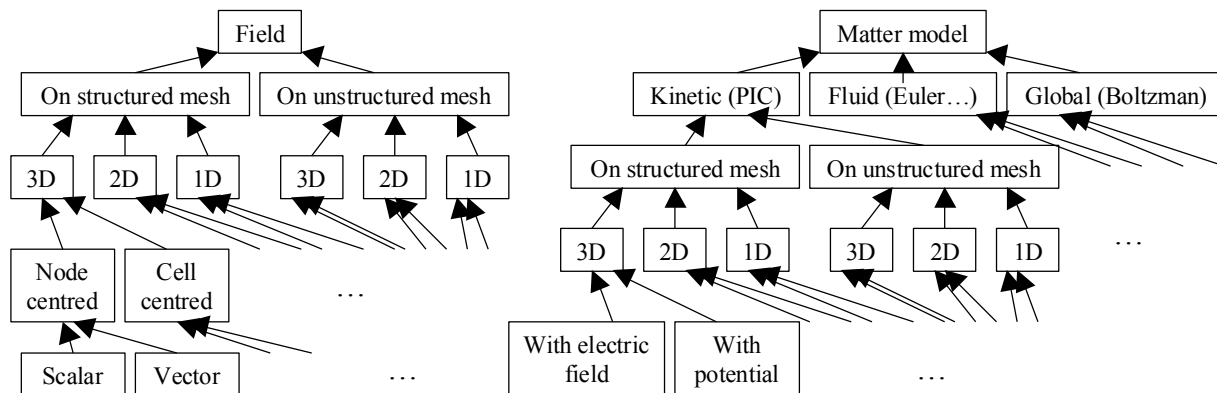
Figure 5. Two examples of horrific implementation of multiple polymorphism (triangle arrows represented different derived classes in these UML diagrams)

Before explaining this idea through a few examples, we present the overall SPIS conceptual class diagram in Figure 6. It will help understand the examples. In the UML graph of the figure

the arrows ended with a diamond represent the aggregation, or composition: the *Simulation* object on the right is composed of 1 *Plasma* object and 1 *Spacecraft* object, etc. The arrows ended with a triangle represent derivation or specialisation: a *VolDistribution* object can be either of a *FluidDistribution* version, a *KineticPICDistribution* or a *GlobalDistribution*. In the 1st case it will be composed of *VolField* objects (distribution moments), of 1 *ParticleList* object in the 2nd case, and simply a few global parameters in the 3rd case (not represented). The class names should be explicit enough for the reader to understand the chart.
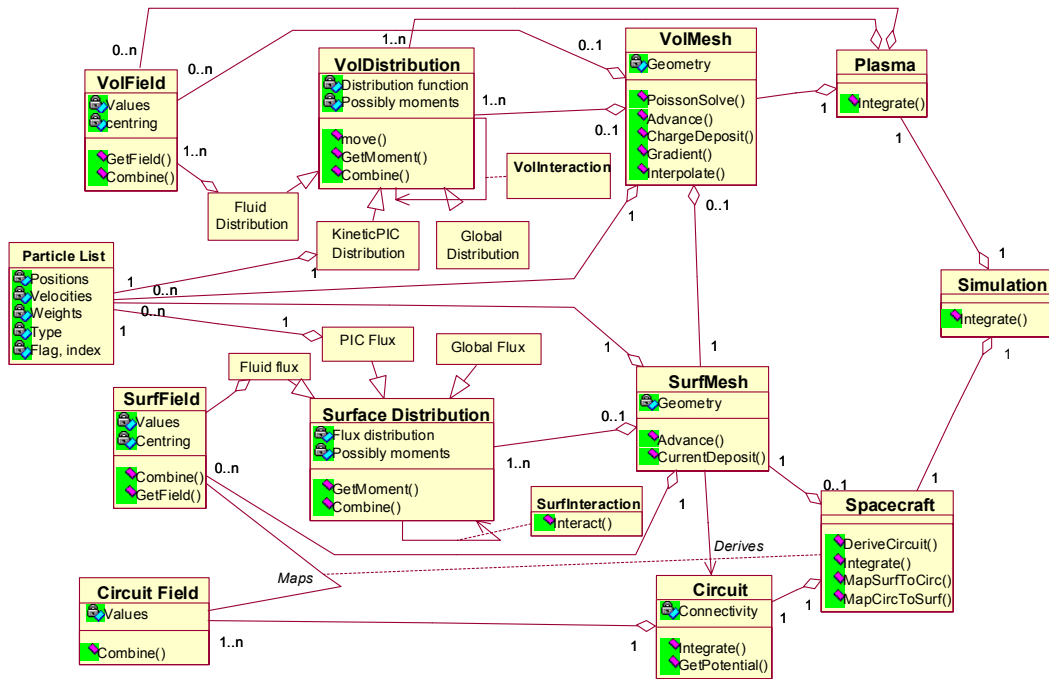
Figure 6. UML graph of SPIS conceptual class design. Each box is a class, the 2nd part of the box contains attributes (i.e. data), the 3rd part operations (i.e. methods). Diamond arrows indicate composition, triangle arrows indicate specialization (i.e. derivation).

Figure 7 represents a top level design of the *Volume Distribution* class, and in particular how its polymorphism can be uncoupled from others. As already written above, the three derived classes are *PIC Volume Distribution, Fluid Volume Distribution*, and *Global Volume Distribution* of Boltzmann type, one per column (class names are sometimes abbreviated but should remain explicit enough). The *Move* and *Get Moment* methods must be implemented for each of the classes derived from *Volume Distribution*. The coding of these methods is necessarily different for each derived type, kinetic, fluid, or global. The good design introduced above, i.e. the uncoupling of polymorphisms, consists in making the implementation of these methods independent of the other polymorphisms, e.g. the mesh type, space dimensionality, E field storage, etc. The arrows on the left hand side show how it works on some examples:

- The *E.GetField(pl, E_Val)* method of the *E field* object returns the electric field value at the particle list positions whatever the specialization of E is, either stored as a potential (usual in electrostatics) or as an actual vector field (more common in electromagnetism). The

polymorphism of the vector field potential/vector is uncoupled from the volume distribution one, it is transparent when integrating particle trajectories. This was a very simple case.

- The *pl.vm.Advance(pl,dx)* method is basically a computation of particle trajectories intersection with spacecraft and box boundaries. It is of course very dependant of the type of mesh (structured or unstructured…). But this is transparent for the particle method *Move*, which simply requires this computation from the generic *Advance* method of the volume mesh *vm* in which the particles are tracked, whatever the volume mesh type is.

There is indeed many more polymorphisms to uncouple in this routine than actually emphasized by the arrows. Space dimension does not show in this routine whereas it might be omnipresent, if coded without care. This is true for the *Advance* method already discussed, since its actual implementation is dependant on the mesh type but of course also on space dimension. It is also the case for the trajectory integration, which is the core of that routine. It is crudely symbolized in this figure by '*v = v + (E+vXB) dt; dx = v dt*', but the vectors (lists) *x*, *v*, etc. are dependant on space dimension. The relationship between *x* increment and *v* gets even more complex in case of non Cartesian geometry (e.g. axisymmetry). So, both the objects (*x*, *v*, etc.) and the operations between them must be invoked independently of their actual implementation (e.g. through a *position_increment_from_velocity* method here in Java (not represented in the figure), not by overloading the + operator as it could perhaps be done in C++ if sub-types are accurate enough).

Class: VolDistrib		
Attributes:		
Methods: **Move**(float dt,SurfDistrib[...] FluxIn, SurfDistrib[...] FluxOut,VolField E, VolField B...) **GetMoment**(VolField mom, int order)		
Derived Classes (non exhaustive):		
Class: **PICVolDistrib**	Class: ****FluidVolDistrib**	Class: **GlobalVolDistrib**
Data/Attributes: **PartList pl**: particle list	Data/Attributes: **ScalVolField dens**: density **VectVolField velo**: velocity	Data/Attributes: **Float n,v,T**: global density, velocity and temperature for Boltzman distribution

Operations/Methods:
Move(dt,FluxIn,FluxOut,E, B)
   E.**GetField**(pl,E_Val)
   B.GetField(pl,B_Val)
   v = v + (E+vXB) dt
   dx = v dt
pl.vm.**Advance**(pl,dx)
 	
If TypeOf(FluxOut) is PICSurfDistrib then
  pl.ExtractFlux(FluxOut, pl)
else
  pl.ExtractFlux(new Partlist FO)
  FluxOut.Add(FO)
GetMoment(mom,order)
Pl.vm.ChargeDeposit(pl, mom)
	Operations/Methods:
	Move(dt,FluxIn,FluxOut,E,B)
	   dens.vm.**EulerSolve**(dens,velo,E,B)
	GetMoment(mom,order)
	  Simply
	  Mom = dens, or = velo, etc.
		Operations/Methods:
		Move(dt,FluxIn,FluxOut, E,B)
		   No dynamics =>
		   nothing to do
		GetMoment(mom,order)
		  If E is a PotVectVolField (if not, impossible):
		   E.**GetPot**(pot)
		   dens = exp(e pot / k T)
		   mom.set(dens)

- Vector field
- Vector field stored as a potential
- Structured mesh
- Unstructured mesh
- Even no mesh (analytical field)

Figure 7. Example of polymorphism: Volume Distribution

Thanks to this uncoupling the *Move* method can perform its main job, i.e. particle trajectory integration[†], independently of the sub-types of the other objects. In the simple example of Figure 7, it is a basic first order scheme. If an improved scheme is to be implemented, as a leapfrog (magnetic force to be changed) or an higher order scheme, it can simply be done in the *Move* routine, independently of the mesh type, space dimension, E or B field storage, etc., which is very important to offer a good modularity.

As a final illustration of polymorphism uncoupling, let us list how different objects, which might a priori depend on space dimension (and symmetries), were made as much as possible independent of space dimension (object in bold font could not escape an explicit dimension-dependant implementation):

[†] Things are not as simple as in the simplified illustration of Figure 7, since for example the integration time step can depend on the mesh (CFL-type conditions), which forces to transmit such information from the mesh to the integration routine (simply as a global maximum time step, or better a particle-dependent time step for sub-cycling)

- ***Volume or surface mesh***:

  - ***Data structure***: explicit implementation
  - ***Solvers***: partially dimension-specific: e.g. Poisson equation matrix writing is dimension-specific, whereas its solving is not

- ***Vector table*** : explicit implementation, table of different dimension

- ***Particle list:*** transparent, handled at *vector table* level

- ***Volume or surface fields***: transparent (a vector field in 3D is <u>3D</u> table of <u>3</u> values):

  - stored in 1D tables (may be recast in 3D/2D tables for structured solvers, but this is handled at mesh/solver level)
  - Vector fields => handled at "vector table" level

- ***Volume or surface distributions***: transparent:

  - *data*: transparent, handled at *particle list* (*PIC Distribution*) or *field* level (*Fluid Distribution*)
  - *Solvers, main example of Move()* (cf. Figure 7):
    - if PIC transparent
    - if fluid => transferred to mesh solver.

A last remark about object design has to do with efficiency. OO programming is very interesting to design modular codes, but there is a cost associated with each object, a memory cost and certainly more important a computation time cost. In order to avoid these costs to impact significantly the overall performance, no "small objects" were defined, i.e. individual particles or mesh cells were not defined as objects. As visible on the examples above, only "large objects" were implemented, i.e. particle lists or cell lists. This allowed to maintain the extra computation load due to object handling to a very reasonable amount.

Conclusions

A new software dedicated to spacecraft plasma interaction modeling was presented. Its major originality is its openness. It is collaboratively developed within SPINE community, an open community of scientists and engineers studying spacecraft plasma interactions. In that purpose, the code is released under an open source form (sources distributed under GPL license). The code framework based on modern techniques (Java, Jython, Swing) and on open source pre-post/processing tools, and the object design of the solvers ensuring an efficient modularity were eventually presented.

The free access to this code should allow an important spreading in science and technology teams, leading to an extensive testing and validation. The principle of open source collaborative development is to use the code, enhance it by adding extra modules, improving the existing ones,

or simply testing them, and then let the community profit by these improvements as a return. As shown by the interest for the code in Europe and worldwide, this positive dynamics is likely to be significantly enhanced after SPIS full release in spring 2004.

References

1. Roussel, J.-F, "Spacecraft Plasma Environment and Contamination Simulation Code: Description and First Test," Journal of Spacecraft and Rockets, Vol.35, No.2, p.205-211, 1998.

2. Neergaard, L. et al., "Comparison of the NASCAP/GEO, SEE Interactive Charging Handbook and NASCAP-2K Spacecraft Charging Codes," 7th Spacecraft Charging Technology Conference,23-25 April 2001, ESTEC, The Netherlands, ESA SP-476, pp115-, 2001.

3. Mandell, M., "NASCAP-2K – An Overview," this conference.

4. Forest, J., "Feedbacks On the PicUp3D Experience and the Open Source Strategy Applied to a Spacecraft-Plasma Interaction Simulation Code," this conference.

5. Thiebault, B., "Modeling Of The Photoelectron Sheath Around An Active Magnetospheric Spacecraft With Picup3d," this conference.

DEVELOPMENT OF A VIRTUAL TESTING LABORATORY FOR SPACECRAFT-PLASMA INTERACTIONS

J. Wang
Department of Aerospace and Ocean Engineering
Virginia Polytechnic Institute and State University
Blacksburg, VA 24061-0203
Phone: 540-231-8114
E-mail: **jowang@vt.edu**

L. Brieda
R. Kafafy
J. Pierru
Virginia Polytechnic Institute and State University

Introduction

Modeling and simulation are playing an ever more important role in space environments and effects research activities. In recent years, the sophistication of the models and the capability of state-of-the-art supercomputers have reached such a level that in many cases one can produce simulation results that are in good quantitative agreement with experimental data. For example, the 3-D ion thruster plume model described in Wang et al.[2001] produced results that are in excellent agreement with data taken from Deep Space 1 in-flight measurements. The recent advance in simulation capabilities suggests that "virtual" experiments using first-principle based models may be used to replace real experiments to quantify spacecraft environment interactions for many applications.

This paper discusses a prototype virtual testing laboratory for spacecraft plasma interactions and electric propulsion. As illustrated in Fig. 1, this virtual laboratory consists of a simulation engine and a virtual testing environment. A user provides physical parameters and spacecraft configurations to the simulation engine. The virtual laboratory simulates the physical processes using a set of particle simulation codes and then displays the results in a virtual testing environment using immersed and/or collaborative visualization.

In order to develop a virtual laboratory based on first principle based simulations, one must overcome at least two major challenges. First, one needs to be able to build up a code that is sophisticated enough so the complex geometry associated with a satellite can be modeled properly and yet computationally efficient enough so large-scale 3-D particle simulations can be performed routinely. Second, one needs to be able to quickly transform "data rich" simulation results to "information rich" for engineering applications. Two research activities at Virginia Tech were carried out to address these two issues. First, a new particle simulation code, DRACO, was developed for plasma simulations involving complex boundary conditions. A unique feature of DRACO is that incorporates the recently developed immersed finite element particle-in-cell (IFE-PIC) algorithm. This method allows one to use a Cartesian mesh to handle complex geometric or time-varying interface between plasma and object without scarifying the accuracy in electric field solutions. The computational speed of an IFE-PIC simulation is about

the same as that of standard PIC simulation. Second, a new visualization and data analysis tool, capVTE, was developed for visualizations using both virtual reality environments and regular desktop/laptop machines. capVTE offers immersed visualization for users with access to virtual reality environments as well as a shared, collaborative environment that allows remotely connected users to interact with each other over the same data objects. Both DRACO and capVTE are cross platform. DRACO and capVTE form the foundation for a virtual testing laboratory.

This paper is organized as follows: section II discusses the development of DRACO; section III discusses the design of capVTE; section IV presents examples of spacecraft-electric propulsion plume interactions visualized through the desktop interface of capVTE (examples of immersed visualization are shown in the presentation); Section V contains a conclusion.

3-D Particle Simulation Engine: DRACO

Overview

The simulation engine of the virtual testing laboratory is a multi-purpose particle simulation software, DRACO. DRACO is designed to perform first-principle based, high fidelity simulations of spacecraft-plasma interactions. DRACO runs on UNIX, Linux, and Window. Many of DRACO's subroutines are based on 3-D plasma particle simulation codes previously developed by J. Wang to simulate ion thruster plume interactions [Wang et al., 2001] and ion optics plasma flow [Wang et al., 2003a]. The plume simulation model by Wang et al.[2001] produced results that are in excellent agreement with data from Deep Space 1 in-flight measurements and the ion optics model by Wang et al.[2003a] produced results that are in excellent agreement with data taken during the long duration tests of the NSTAR thruster. Additionally, DRACO also includes a new particle simulation algorithm based on the immersed finite element (IFE) formulation [Wang and Lin, 2003; Wang et al., 2003b], IFE-PIC.

As shown in Fig.1, DRACO allows a user to choose from three simulation modules. In the QN-PIC module, the plasma is assumed to be quasi-neutral and the electric field is obtained by assuming the electron density follows the Boltzmann distribution. The QN-PIC module is intended for quick calculations and cannot be used to resolve the plasma sheath. The DADI-PIC module is a standard PIC code using a finite-difference formulation to solve the electric field. DADI-PIC is designed for problems with relatively simple geometric conditions. Out of considerations for computational efficiency for large-scale simulations, DADI-PIC uses a Cartesian mesh. To resolve the geometry associated with a curved surface, a method of sub-grid scale placement of boundaries is used. This method explicitly includes the location of object surface in relation to the computational mesh so that the placement of the object boundary is not restricted to the mesh points. The electric field is obtained by solving the Poisson's equation using a dynamic alternating direction implicit (DADI) method [Doss et al.,1979; Hewett et al.,1992] with a defect correction using the Douglass-Gunn operator splitting [Douglas and Gunn, 1964]. This DADI method was chosen over other algorithms for its increased stability properties over fully explicit methods and its relatively simple tridiagonal system of equations produced by the partially implicit nature of the method. This DADI-PIC model was discussed in [Wang et al, 2001].

The IFE-PIC is DRACO's most sophisticated module. The IFE-PIC is based on a finite element formulation, and is designed to perform simulations accurately for problems involving complex geometric and material boundary conditions.   Instead of using a complex mesh to body-fit the body surface, the IFE method uses a structured mesh without consideration of the object surface location. Hence, one may use the standard, Cartesian mesh based method for particle-mesh interpolations and pushing particles even in simulations involving complex geometric boundaries. This allows IFE-PIC to retaining the computation speed of a standard particle-in-cell code [Wang et al., 2003b].   The next section presents a brief overview of he IFE-PIC model.

As the purpose of DRACO is to solve real engineering problems, DRACO reads in spacecraft configurations defined by commercial CAD tools. A Mesh Generator module is developed as the interface between CAD tools and the PIC code. The outputs from CAD tools are stored in an ANSYS file. The Mesh Generator then performs the "intersection" operation to identify the intersections by an object of arbitrary geometrical shape onto the computational mesh.

Immersed Finite Element Particle-in-Cell (IFE-PIC)

A PIC code typically spends a significant portion of its computing time performing particle-mesh interpolations and pushing particles. Out of consideration for speed, standard PIC codes are based on the use of structured, Cartesian mesh so the location of memory of quantities defined in neighboring cells can be found trivially via indexing. However, a Cartesian mesh based field solver is susceptible of losing accuracy when a irregular boundary is involved. To solve the electric field accurately for complex geometries, one would typically need to use an unstructured mesh to body-fit the boundary surface. However, an unstructured grid based PIC code can be significantly more expensive computationally because it requires additional memory references (e.g. lookups in a table) to find neighboring cells and a complex scheme to push particles [Westermann, 1992; Wang et al., 1999]. Hence, accuracy and computing speed often represent conflicting requirements for a PIC code.

We recently developed a new, 3-dimensional PIC algorithm using the recently developed immersed finite element (IFE) method [Ewing et al., 1999; Lin et al., 2000] to solve the electric field. Rather than treating the object surface as a boundary condition, this method includes the object material as part of the solution domain and solves the original boundary value problem as an "interface" problem. For instance, consider the electric field in a composite domain consisting of two sub-domains each occupied by a different type of material (Fig. 2). These two sub-domains are separated by a curved surface. The electric potential is described by a boundary value problem:

$$-\nabla \cdot (\sigma \nabla \Phi) = f(\Phi)$$

together with the boundary conditions and the jump conditions on the interface. The media property is described by a material dependent coefficient $\sigma(X)$ (i.e. permittivity). Mathematically, $\sigma(X)$ is a piecewise constant function defined by:

$$\sigma(X) = \begin{cases} \sigma^-, X \in \Omega^-, \\ \sigma^+, X \in \Omega^+. \end{cases}$$

To solve the interface problem above, one may treat Γ either as a boundary to the sub-domains Ω^+ and Ω^-, or as an interface inside the entire domain Ω. The IFE method treats Γ as an interface and uses the finite element formulation to solve $\Phi(X)$ over domain Ω.

The essence of the IFE method is that its mesh can be formed without consideration of the interface location. While this "interface" concept is the same as that used in the immersed/imbedded boundary techniques developed for CFD, the IFE method itself is significantly different because a) the IFE method is based on the finite element formulation and b) the trial functions used in the IFE method are constructed only using physics based jump conditions at the interface.

The IFE-PIC model uses a structured Cartesian-tetrahedral mesh. The Cartesian mesh is the primary mesh used by PIC. Each Cartesian cell is further divided into five tetrahedral elements as shown in Fig. 3. The tetrahedral mesh is the secondary mesh used only by the IFE field solver. When a curved object surface is present, the IFE mesh will include both interface cells (those cells that have at least one edge whose interior intersects with the interface) and non-interface cells. In a non-interface cell, the standard linear local nodal basis functions can be used to span the local finite element space. In an interface cell, the physical jump conditions at interface are used to determine the basis function. For instance, consider the interface cell shown Fig.3. The interface divides a typical interface tetrahedron T, with vertices $A_i, (i = 1,2,3,4)$, into T^+ and T^-. This partition of T can be used to introduce four piece-wise linear local nodal basis functions $\Psi_i(x)$:

$$\Psi_i(\vec{x}) = \begin{cases} \Psi_i^+(\vec{x}) = a_0 + a_1 x + a_2 y + a_3 z, \vec{x} \in T^+, \\ \Psi_i^-(\vec{x}) = b_0 + b_1 x + b_2 y + b_3 z, \vec{x} \in T^-. \end{cases}$$

The coefficients in the linear basis functions are determined by the following physical jump conditions to be satisfied by the solution:

1. Continuity on the plane *EFGH:*
$$\Psi_i^+(P_j) = \Psi_i^-(P_j), i = 1,2,3,4 \quad \text{and} \quad j = 1,2,3$$

2. Flux continuity across the plane *EFGH*:
$$\int_{EFG} (\sigma^+ \frac{\partial \Psi_i^+}{\partial n} - \sigma^- \frac{\partial \Psi_i^-}{\partial n}) dS = 0, i = 1,2,3,4$$

Satisfying these conditions provides eight equations for each local basis function which are enough to uniquely determine that basis function. Further details of the IFE method are discussed in [Wang and Lin, 2003; Wang et al., 2003b], where it is also shown that the IFE field solver possesses a second order convergence.

The Virtual Testing Environment: capVTE

Overview

Large-scale, 3-D simulation models generate a wealth of data output. However, in order to apply these models as engineering design tools, one must be able to quickly transform "data rich" simulation results to "information rich" results. To achieve this goal, one needs a data analysis environment which would satisfy at the minimum the following requirements: 1)allow easy visualization and interpretation of complex multi-dimensional data generated by particle or CFD codes; 2)enable interactive access to information from different geographic locations and online collaborations; and 3)be machine independent. A data analysis tool that satisfies these requirements in essence becomes a "virtual" testing environment.

The CAP Lab Virtual Testing Environment (capVTE) is a cross-platform visualization and data analysis tool [Brieda et al., 2003]. Visual analysis can be performed on a wide variety of hardware platforms, ranging from high-end PCs, through SUN and SGI workstations, to virtual reality facilities such as CAVE. In addition to standard graphics capability visualizing multi-dimensional data set, capVTE offers immersed visualization for users with access to virtual reality environments as well as a shared, collaborative environment which allows remotely connected users to interact with each other over the same data objects.

The source code of capVTE was designed to be machine independent so that it may be run from any computing platforms. The graphic engine used by capVTE is the open-source Visualization Toolkit (VTK) library by Kitware and QT by Trolltech. Both VTK and QT are platform independent. VTK interacts with the OpenGL package, and versions of VTK are available for Windows, UNIX/Linux and Mac OS X. QT is the basis of GUI, which is used as the user interface for capVTE. QT is used to handle issues associated with cross-platform development, such as interaction with windows, user input, and the creation of timers. Therefore, deployment of capVTE for a particular platform involves only linking the source code with the VTK and QT libraries made for that specific platform.

The user interface of capVTE, as shown in Fig. 4, is a multi-window GUI application. The user navigates through each data set in real-time using the mouse. Menus and toolbars are used to select the active tools and to change their properties. The data input consists of a single ASCII file which contains the appropriate header, followed by program commands and data blocks. However, a data set is allowed to span over several physical files, in a fashion similar to that of C/C++'s *#include* directive. The main input file can be a just a short collection of statements pointing at a geometry file created from an output generated by 3D object modeling tools, and the grid and particle files, generated by particle codes or CFD codes.

CapVTE allows a data export in three formats: JPEG, VRML (Virtual Reality Markup Language), and Inventor. JPEG is used to save images from static snapshots. Both VRML and Inventor are used for interactive visualization of 3-dimensional images. As VRML is commonly used to publish 3D data on the Internet and plugins are available for the popular browsers, capVTE uses the VRML format for online collaborative visualization through network. Inventor is compatible with DIVERSE (Device Independent Virtual Environment Reconfigurable

Scalable Extensible), a collection of Application Programming Interfaces (APIs) developed at Virginia Tech to run the virtual reality facility CAVE. CapVTE uses the Inventor format for immersive visualization.

Immersive visualization

Immersed visualization currently is performed using the DIVERSE software to drive a variety of immersed visualization equipment such as the CAVE (Cave Automatic Virtual Environment), Immersa Desk, Head Mounted Display (HMD), etc. DIVERSE can also be used to drive visualization on conventional desktop or laptop computers.

The CAVE is a multi-person, room-sized, high-resolution, 3D video and audio environment used as a "virtual reality theater". The CAVE facility at Virginia Tech, shown in Fig. 5, has a size of 73.5x84 inch footprint and a 104-inch high ceiling. The three side faces along with the floor act as screens, on which an image is projected from four Electrohome Marquis 8000 projectors. The false-color images are shifted such that, when viewed using the CrystalEyes goggles, they create a perception of the visualized object floating in the center of the cube.

Inside the CAVE, one "walks" into an image. Navigation is through a tracking headset. Its position and view angle is tracked by an array of sensors. The central computer then adjusts the projections to create a realistic image. Further control can be accomplished using a hand-held wand. Its translation and rotation are both tracked, and thus the wand can act as a virtual pointer. A small joystick located on the wand allows the user to travel greater distances than that allowed by the limited physical size of the CAVE.

Collaborative visualization

The real-time data immersion capability of capVTE allows the creation of a collaborative virtual environment on the internet. capVTE includes a network module, based on a client/server and TCP/IP architecture. The network module simplifies data sharing and allows interactive visualization by remotely connected users. The user specifies whether a new server should be established, or whether the program should connect as a client to an already running collaboration. Each user specifies an "avatar", a small graphical object, which is located and oriented according to that user's viewpoint. Thus, every member of the online collaboration can see what part of the dataset that the others are looking at, as illustrated in Figure 4. The network is also partially synchronized. When one client toggles cutting planes, for instance, cutting planes will be toggled for all other clients as well. Thus, all members share the same virtual space with the only difference being the position from which the view is made.

Simulation Examples

To demonstrate the capability of the virtual testing laboratory, this section shows one simulation example of ion thruster plume spacecraft plasma interaction. Other simulation examples are shown in the presentation. We consider a model spacecraft shown in Fig. 6. The spacecraft geometry is composed of a box bus, a thruster, an antenna dish, and a flat solar array orientated at an angle with respect to the thrust direction. Fig. 7 shows the primary Cartesian

mesh used by DRACO and the intersection of spacecraft with the computation mesh. The thruster is taken to be the 30cm NSTAR ion thruster used on Deep Space 1. Simulation setup and thruster operating conditions are the same as that discussed in Wang et al.[2001]. We assume that the solar array surface, spacecraft bus, and antenna are at the same potential.

Simulation results using the DADI-PIC and IFE-PIC module are shown in Figs 8 and 9, respectively. To further demonstrate the effect of solar array on charge-exchange ion backflow, the normal direction of the solar array in the DADI-PIC run is taken to be –45 degree with respect to z while that in the IFE-PIC run is taken to be +45 degree. The DADI-PIC run uses a computation mesh of 91x41x71 with a mesh resolution of 5cm. The number of micro-particles used is more than 5 million. The primary Cartesian mesh used in IFE-PIC run is 60x26x46 with a mesh resolution of 7.5cm. The number of micro-particles used is more than 2.3 million. Comparing Figures 8 and 9, one finds that both runs show similar results in the downstream region of the thruster. However, the upstream region shows significant difference due to the different solar array orientation angle. It is interesting to observe that, in the DADI-PIC run, the solar panel accelerates the backflow charge exchange ions and produces a significant plasma wake behind the antenna dish.

Summary and Conclusions

In conclusion, we have developed a prototype virtual testing laboratory for spacecraft plasma interactions. This virtual laboratory uses a simulation engine based on a set of plasma particle simulation codes, DRACO, and a virtual testing environment, capVTE. A major feature of DRACO is that it includes a new particle simulation algorithm IFE-PIC. The IFE-PIC allows one to use directly the standard Cartesian mesh based algorithms for particle push regardless of the geometry of object boundary. Hence, simulations involving complex boundary conditions can still be performed at a computational speed close to that of a standard PIC code. The interface formulation used by the IFE method to solve the electric field allows material properties to be included explicitly and maintains the desired physics at a given material interface. capVTE enables a quick transform of "data rich" simulation results to "information rich" ones through immersive and/or collaborative visualization. The immersed and shared visualization environment driven by capVTE also provides an virtual experimental platform. Both DRACO and capVTE are cross platform. Currently, the virtual laboratory only concerns spacecraft-plasma interactions. Future work will expand the virtual testing laboratory into other areas of spacecraft-environmental interactions.

Acknowledgments
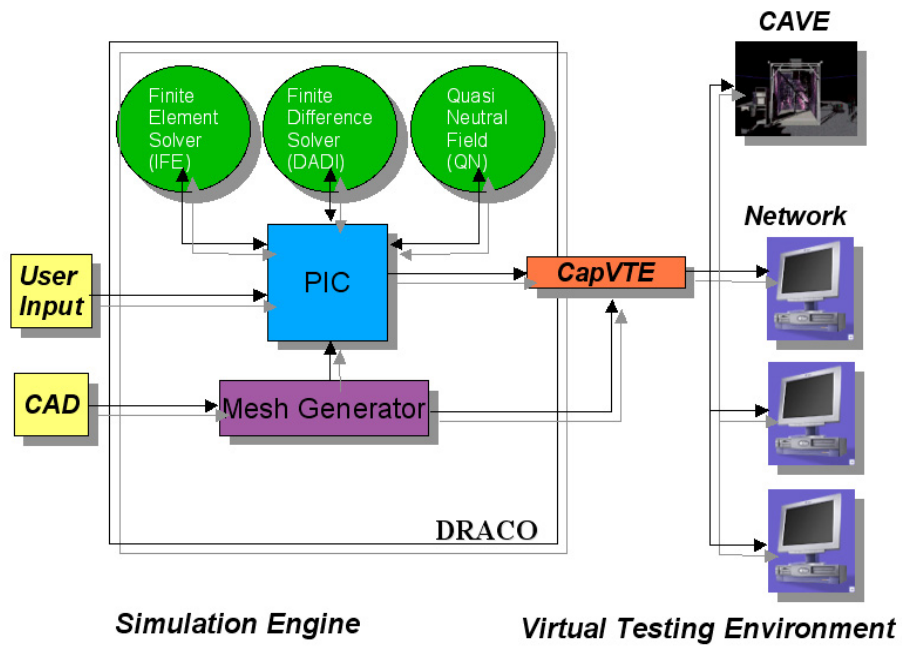
Figure 1. Virtual Testing Laboratory block diagram
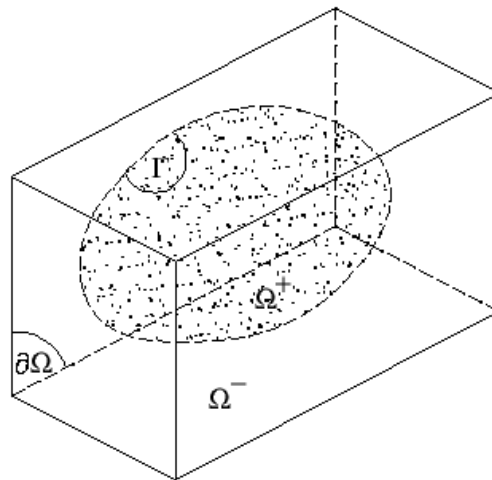
Figure 2. The 3-D interface problem domain
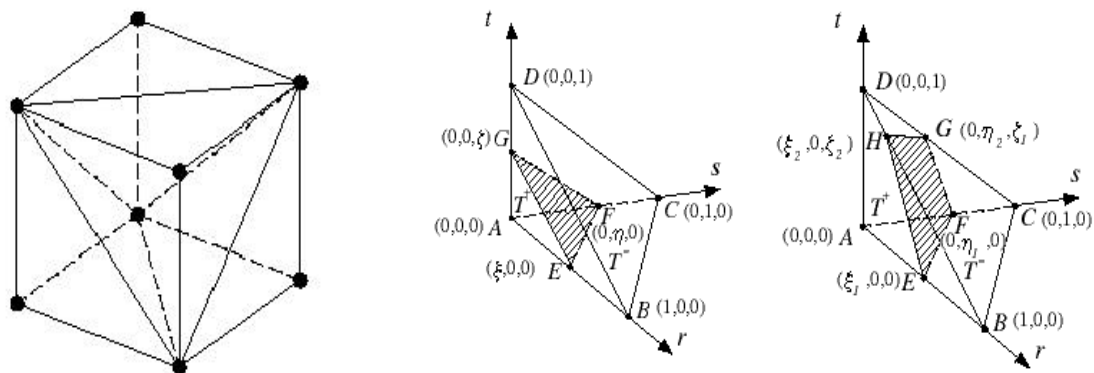
Figure 3. The Cartesian-tetrahedral cell used by IFE-PIC and intersection topologies of a tetrahedral element
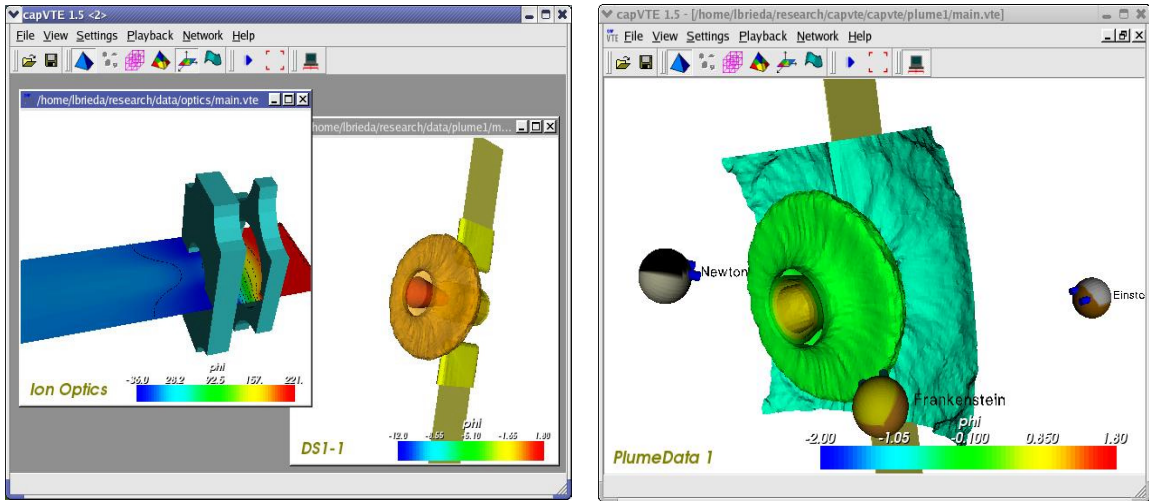
Figure 4. CapVTE desktop interface. Left: single user viewing multiple data objects. Right: multiple users connected through network viewing the same data object.
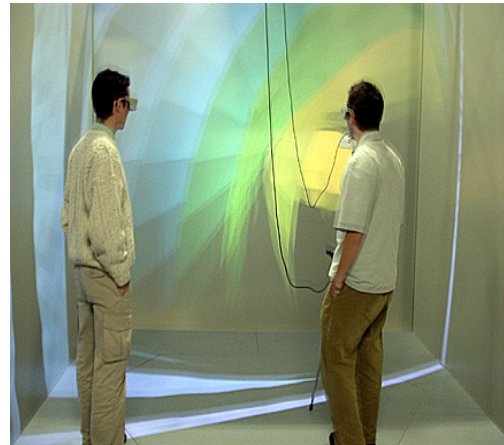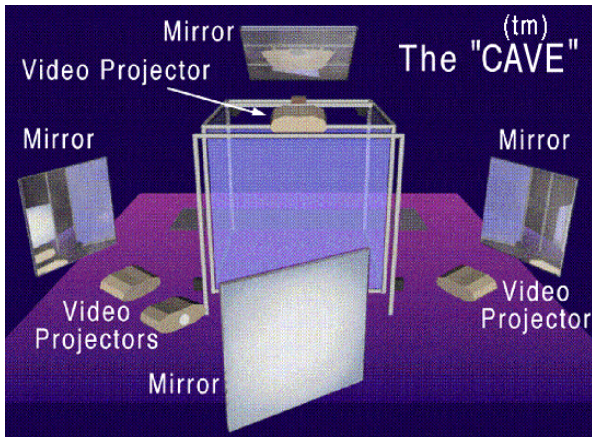

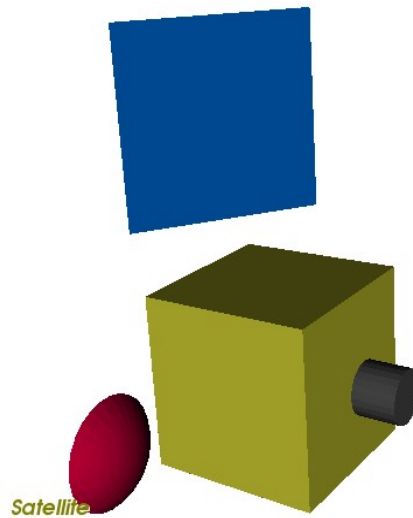**Figure 5. The Virginia Tech CAVE facility(left) and immersed visualization inside CAVE (right).**

Figure 6. A model satellite configuration generated by CAD as simulation input.
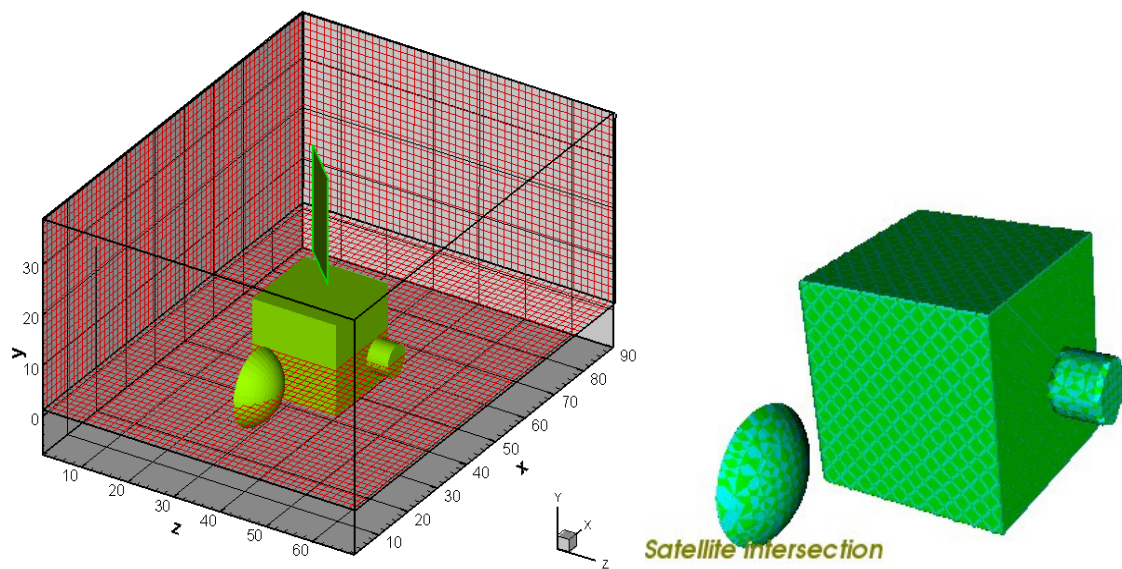
Figure 7. Left: simulation domain with Cartesian primary mesh. Right: interface cells from satellite surface intersection with the Cartesian mesh.
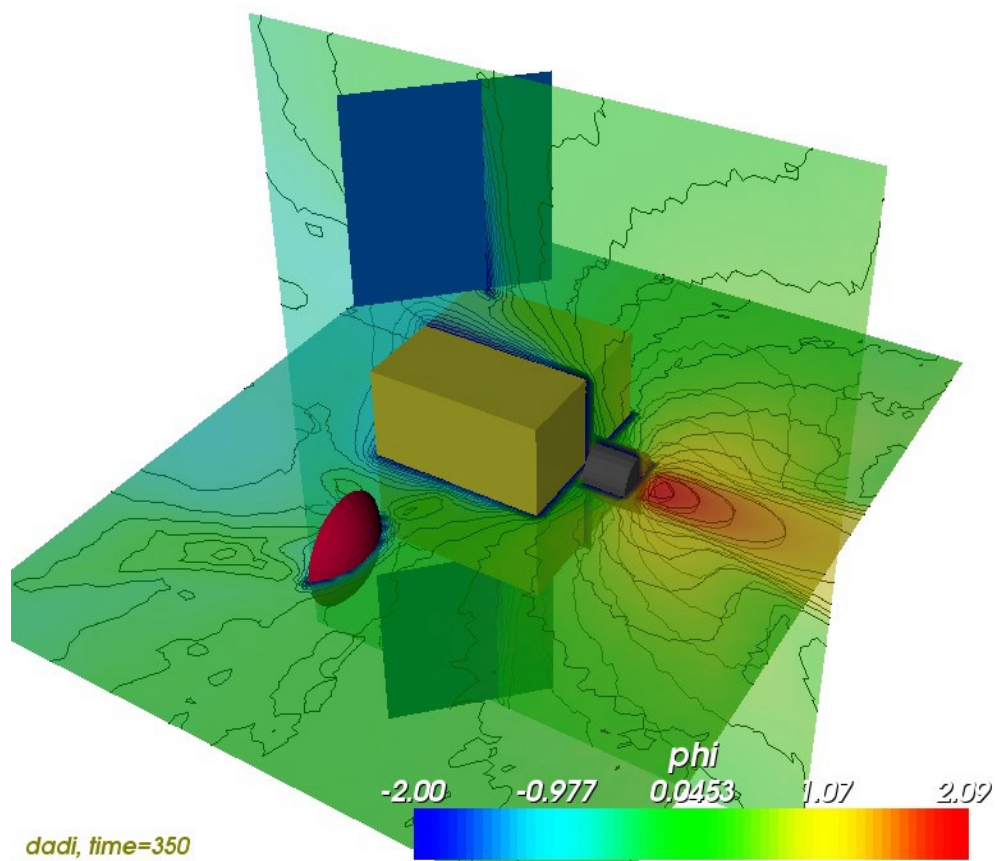
Figure 8. 3-D ion thruster plume simulation by the DADI-PIC module: potential contours
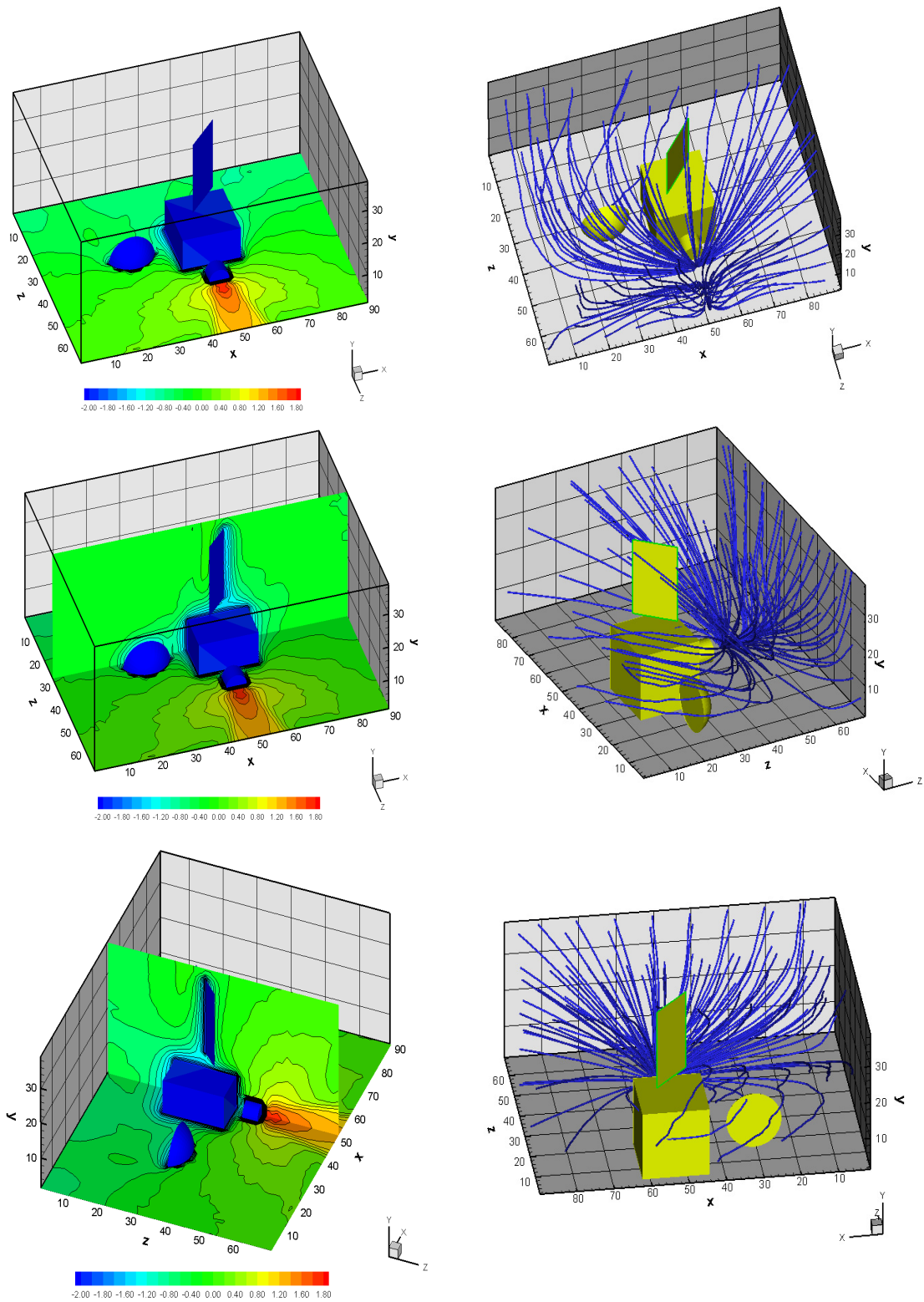
Figure 9. 3-D ion thruster plume simulation by the IFE-PIC module. Left: potential contours. Right: charge-exchange ion trajectories.

References

1. L. Brieda, J. Pierru, R. Stillwater, and J. Wang, "A Virtual Testing Environment for Electric Propulsion", AIAA 2003-5020, 2003.

2. S. Doss,S. and K. Miller, "Dynamic ADI Methods for Elliptic Equations", Siam J. Numer. Anal., 16(5), pp837-855, 1979.

3. J. Douglas and J. Gunn, "A General Formulation of Alternating Direction Methods: Part I. Parabolic and Hyperbolic Problems", Numerische Mathematik, 6, pp428-453, 1964.

4. R. Ewing, Z. Li, T. Lin, and Y. Lin, "The immersed finite volume element method for the elliptic interface problems", Mathematics and Computers in Simulation, 1999.

5. D. Hewett, W. Larson, and S. Doss, "Solution of Simultaneous Partial Differential Equations using Dynamic ADI: Solution of the Streamlined Darwin Field Equations", J. Computational Physics, 101, pp11-24, 1992.

6. T. Lin, Y. Lin, R.C. Rogers, and L.M. Ryan, "A rectangular immersed finite element method for interface problems", In Proceeding of the 2nd International Workshop on Scientific Computing and Applications, Kananaskis, Canada, May 28-June 1, 2000.

7. J. Wang, J., D. Kondrashov, P. Liewer, and S. Karmesin, "3-D Deformable Grid Electromagnetic Particle-in-Cell for Parallel Computers", J. Plasma Physics, 61(3), pp367-389, 1999.

8. J. Wang, D. Brinza, and M. Young, "Three-Dimensional Particle Simulation Modeling of Ion Propulsion Plasma Environment for Deep Space 1", J. Spacecraft & Rockets, 38(3), pp433-440, 2001

9. J. Wang, J. Polk, J. Brophy, and I. Katz, "3-D Particle Simulations of Ion Thruster Optics Plasma Flow and Grid Erosion", J. Propulsion & Power, 2003a (in press).

10. J. Wang and T. Lin, "The Immersed Finite Element Method for Plasma Particle Simulation", AIAA 2003-0842, 2003.

11. J. Wang, R. Kafafy, and L. Brieda, "An IFE-PIC Simulation Model for Plume-Spacecraft Interactions", AIAA 2003-4874, 2003b.

12. T. Westermann, "Localization schemes in 2D boundary-fitted grids", J. Computational Physics, 101, p307, 1992

FEATURES OF CHARGING OF COMPOSITE CONFIGURATION SPACECRAFT CHARGING IN HIGH ORBITS

Valery Mileev
D.V. Skobeltsyn Institute of Nuclear Physics
Moscow State University
Vorob'evy Gory, Moscow 119899
Russian Federation
Phone: +7 095 939-1007
Fax: +7 095 939-0896
E-mail: mileev@sinp.msu.ru

A.A.Makletsov
L.S.Novikov
Moscow State University

Abstract

Typical feature of spacecraft charging in geosynchronous and high-elliptical orbits in hot magnetosphere plasma is formation of electrostatic potential distribution on the spacecraft surface (differential charging) and complexity of the charging dynamics. For mathematical simulation of spacecraft charging in high orbits, the modified version of the COULOMB program tool was developed in D.V.Skobeltsyn Institute of Nuclear Physics of Moscow State University.

The program tool enables to study dynamics of the spacecraft charging processes in high orbits in various conditions of the spacecraft environment for the spacecraft models with large number of discretization elements.

In the report, the results of modeling of the composite configuration spacecraft charging taking into account the peculiarities of their design and charging conditions are presented.

Introduction

Typical feature of spacecraft charging in geosynchronous and high-elliptical orbits is differential charging of the spacecraft surface dielectric materials. Differential charging is determined by various of electric current on different elements of the spacecraft which has composite geometrical shape. The very important role in formation of the differential current picture of the spacecraft surface elements enlightened by the Sun is played by process of external photoelectric effect, as the initial photoelectric current is superior to all remaining component of the full current.

The modern model of the spacecrafts charging in high-altitude orbits should be are capable to reveal and to research the mentioned above typical features of the charging process, and to describe dynamics of potential and current distribution on the spacecraft surface correctly in various time scales, and to take into account composite structure of the electrical field near to inhomogeneous and geometrically composite spacecraft configuration elements.

Therefore, we have improved physical and mathematical model and the COULOMB program complex for description of spacecraft charging processes in geosynchronous and high-elliptical orbits, which were developed in D.V.Skobeltsyn Institute of Nuclear Physics of Moscow State University (SINP MSU) at the end of 80th – beginning of the 90th years[1, 2, 3, 4] and were based on big computers of the 3rd generation. Considerable progress in computer performance, development of interactive capabilities of PCs have allowed to achieve the qualitatively new level of physical and mathematical models and software for computer simulation of the spacecraft charging in high orbits.

In the paper, basic principles of physical and mathematical model of the spacecraft charging in high orbits are presented, computation results obtained for the model of typical composite shape spacecraft of the are submitted, and the analysis of main features of charging in various conditions of the spacecraft operation is done.

Physical and Mathematical Model of the Spacecraft Charging in High Orbits

The physical and mathematical model of the spacecraft charging in high orbits includes the description of the spacecraft geometrical model, electrophysical characteristics of construction materials of the spacecraft, properties and parameters of hot magnetosphere plasma.

Description of the Spacecraft Model

The model of spacecraft is constructed in terms of a set of basic geometric primitives, integrated in a hierarchic tree structure. Following simple geometrical surfaces and their fragments are used as basic primitives: plane, diaphragm, cylinder, sphere, cone, torus. For each elementary surface, type of material (dielectric or metal) and its electrophysical characteristics taken from appropriate base of the spacecraft construction materials (thickness, conductivity, properties of secondary emission arising at impact of hot space plasma components and of the Sun ultra-violet radiation) are set.

The base three-dimensional surface $F (x, y, z) = 0$ in local coordinate system is described parametrically using the two dimensional system of parametric coordinates: $x=x (t, v)$, $y=y (t, v)$, $z=z (t, v)$. Each surface is triangulated separately into elementary triangles by even grid in the a parametric coordinate system (t, v). The elements are grouped in units and are placed in global coordinate system with the help of translation and rotation of local coordinate system. Finally, the surface of the spacecraft model is described as a grid of large number of elementary triangles. Number of triangles in the each geometrical surface, the triangles sizes, and the total number of elementary triangles can vary in the wide range determined by the spacecraft design features and the computing problem peculiarities.

The system of computer visualization of the 3D spacecraft models and graphical presentation of the computation data on values describing the spacecraft charging (distribution of potential, electric charge, electric field intensity etc.) is closely connected to the program of the spacecraft model construction. As universal graphic interface, the free and commercial VRML browsers (FREEWRL, OpenVRML, Cortona, Cosmo Player etc) are used in the program complex.

Description of the Hot Space Olasma in High Orbits

The hot plasma power electron and ion energy spectra in the region of geosynchronous orbit occupy energy range from 0.05 up to 100 keV. It is shown in[5,6] that the distribution function of the hot magnetosphere plasma particles is correctly approximated by superposition of two Maxwell distributions with energies $kT_1 \cong 0.2\text{-}0.4$ keV and $kT_2 \cong 5\text{-}10$ keV

$$f_j\left(v_j\right) = n_{1j}\left(\frac{m_j}{2\pi kT_{1j}}\right)^{3/2}\exp\left(-\frac{m_j v_j^2}{2kT_{1j}}\right) + n_{2j}\left(\frac{m_j}{2\pi kT_{2j}}\right)^{3/2}\exp\left(-\frac{m_j v_j^2}{2kT_{2j}}\right),$$

where n_j - density j-th type of particles (electrons, protons or other heavier ions) for components with temperatures T_1 and T_2 accordingly; m_j, v_j - mass and velocity of particles, k - Boltzmann constant.

Program of Solution of the Spacecraft Charging Problem in High Orbits

The spacecraft charging process in high orbits is described by the following set of equations.

1. The potential $U(r)$ in a point r at time t in rare plasma satisfies the Laplace equation:
$$\Delta U(\mathbf{r},t) = -4\pi\rho(\mathbf{r},t).$$

2. The distribution function of primary and secondary particles on velocities $\mathbf{v}$, $f_\alpha(\mathbf{v},\mathbf{r},t)$, obey to the collisionless Vlasov equation:

$$\mathbf{v}\frac{\partial f_\alpha}{\partial \mathbf{r}} + \frac{q_\alpha}{m_\alpha}\frac{\partial U}{\partial \mathbf{r}}\frac{\partial f_\alpha}{\partial \mathbf{v}} = 0,$$

where index α corresponds to particles with mass m_α, charge q_α and velocity $\mathbf{v}$.

3. The description of processes of interaction of charged particles and solar radiation with the spacecraft surface is described by the set of coupling equations:

$$f_\alpha(\mathbf{v},\mathbf{r},t) = \int d\mathbf{x}(\mathbf{vn})\sum_{\alpha'} F^{\alpha\to\alpha'}(\mathbf{v},\mathbf{v}',\mathbf{n}) f_{\alpha'}(\mathbf{v},\mathbf{r},t),$$

where the factors $F^{\alpha\to\alpha'}(\mathbf{v},\mathbf{v}',\mathbf{n})$ are the probability characteristics of various processes (e.g. secondary emission process).

4. Local current density on the spacecraft surface taking into account the internal conduction currents:

$$j(\mathbf{r},t,U) = \sum_\alpha \int d\mathbf{v}q_\alpha(\mathbf{vn}) f_\alpha(\mathbf{v},\mathbf{r},t) + j_{cond}(\mathbf{r},t,U),$$

where $j_{cond}(\mathbf{r},t,U)$ – of conduction current density.

5. Full current on the spacecraft:

$$Q(t) = \int_S dS \int_{-\infty}^{t} J(\mathbf{r}, t') dt'$$

6. For thin dielectric coatings on the conductive spacecraft ground, the spacecraft boundary conditions for the Laplace equation differentiated in time in approximation of double electrical layer is following:

$$-\frac{\left(\dfrac{dU}{dn}\right)}{dt} + \frac{\varepsilon(\mathbf{r})}{d(\mathbf{r})}\left(\frac{d\,U(\mathbf{r},t)}{dt} - \frac{d\,U_c(t)}{dt}\right) = 4\pi j(\mathbf{r},t),$$

Here:

ε - dielectric permittivity of the material;

d - thickness of the material;

$U_c(t)$ - the potential of the metal ground under the dielectric.

For numerical solution of the electrostatic problem in 3D space instead of the differential problem, the method of integral equations is used in which the unknown value of the surface charge density is connected with the given value of the potential on the spacecraft surface:

$$U(\mathbf{r}) = \int_S \frac{\sigma(\mathbf{r}')}{|\mathbf{r} - \mathbf{r}'|} dS' + \int_S \frac{\mu(\mathbf{r}')((\mathbf{r} - \mathbf{r}')\mathbf{n})}{|\mathbf{r} - \mathbf{r}'|^3} dS' \quad ,$$

where $\mu(\mathbf{r})$ - density of electrical dipole moment of the double electric layer in the surface point $\mathbf{r}$.

For numerical solution of this integral equation, the method of boundary elements in which the considered values are decomposed in basic functions is used. As the result, the system of linear equations for the charge densities σ_i on discrete parametric elements of the spacecraft model is following:

$$\sum_j \mathbf{A}_{ij} \sigma_j = U_i^* \quad ,$$

where $\mathbf{A}_{ij}$ - matrix of Coulomb interaction of elements, U_i^* - "effective" surface potential of element describing contribution of space charge, and of electrical dipole moment to the potential.

Taking into account features of the considered problem, the inverse matrix of the Coulomb interaction is computed on preliminary step to rise efficiency of computation, and the charge density is evaluated on each time step not with the help of the equation set solution, but by multiplying of the matrix by vector, that considerably increases the computation rate.

$$\sum_j \mathbf{A}_{ij}^{-1} U_i = \sigma_j$$

Thus, the development of the spacecraft charging process in time is described by the system of coupled differential equations for potentials of elementary triangles of the spacecraft surface[7] :

$$\frac{\partial}{\partial t} U_k(t) = \mathbf{G}_{kl} j_{toatl,l}(t)$$

where $\mathbf{G}_{kl}$ - matrix, the elements which are calculated for the spacecraft surface configuration and for given properties of the dielectric coating materials.

Due to composite relation between the current density and the value of the potential, the solution of the set of equations above can be obtained only by numerical integration.

On each integration step the following calculations are carried out:

– in terms of values of potentials on elementary surfaces determined earlier (initial values or ones found on the previous integration step), the values of the electric field intensity on the spacecraft surface elements are calculated;

– in terms of the values of potentials and electric field intensities, the local primary currents for given elementary surfaces are calculated;

– in terms of the computed values of local primary currents and supplementary data on the secondary emission properties of materials of the surface, local secondary currents and photoelectric currents are evaluated taking into account the suppression of the secondary electron and photoelectron output by external electrical field;

– the currents between elementary surfaces and their fragments and spacecraft design elements are calculated in terms of the supplementary parameters on electrical conductivity of materials.

Thus, the iterative loop of the solution of the set of equations above is executed till condition of the current balance on each surface element is achieved, that allows to obtain the equilibrium distribution of the potential on the spacecraft surface.

It is necessary to underline, that rates of potential variations on various spacecraft surface elements and design of can be, generally speaking, significantly different, and may differ on the orders of magnitude. Therefore, Gear method with automatic selection of the integration order and integration step[8] specially developed for solution of "rigid" systems of differential equations was used for computer simulation of development of the spacecraft charging processes in time. The increase of modern PC performance has enabled to use this method for the spacecraft models with number of elements up to ~2000. The test calculations displayed high stability and accuracy of the methods used even at destabilizing influence of the spacecraft model discretization.

The technique developed is applied to the analysis of the spacecraft charging processes in high orbits under different conditions.

Computation Results

The technique above enables to find potentials of separate spacecraft surface elements as function of time, and to determine typical charging times required to achieve the steady state values. It enables also to calculate distribution of the electrical field on the spacecraft surface and in the spacecraft environment, to build 2D maps of the potential distribution in given cross-sections of space.

As an example, the results of computer simulation of the real spacecraft charging in geosynchronous orbit are presented in figs. 1-5. Special method of color code was developed for visualization of the potential distribution on the spacecraft surface. In the method, the spacecraft VRML-model elements of which are painted in colors (or using greyscale for black and white figures) corresponding to the potential values (see the scale in fig. 1). 2D maps of the potential distribution in the spacecraft environment at various moments of time t are shown in figs.1-4 (top) with potential values on lines. Corresponding screenshots of the painted spacecraft VRML-model is shown in the bottom of the figures. Arrows show direction of the Sun light. Computation parameters values corresponding to the charging conditions in geosynchronous orbit are following: hot plasma density 1.0 cm^{-3}, hot plasma temperature 10 keV, photoemission current $1.0 \cdot 10^{-8}$ A$\cdot$cm^{-2}.

Fig.1 shows the initial stage of the charging process when the potential is practically constant on the spacecraft (integral charging). Moving from fig. 1 to figs. 2, 3 and 4 (steady state), one can see the arising and development of the potential distribution distortion (differential charging) due to photoemission on the lightened side of the spacecraft. Distortion of the electric field in the vicinity of the spacecraft and variations of the electrostatic potentials of different spacecraft elements achieve maximal values in the steady state. At the same time, the potential of the metal spacecraft ground increases (in absolute value), and the potential difference between the metal ground and the dielectric surface elements increases too. It is important that the equipotential lines in fig.4 show typical electric field configuration ("saddle point") suppressing the secondary electron and photoelectron output from the spacecraft surface.

In fig. 5, potentials on the lighted spacecraft elements and on the dark ones, and the metal ground potential as function of time are shown. One can see that steady state is reached at $\sim 1.0 \cdot 10^{4}$ s in the charging conditions above. Note that the charging time in the given environment conditions depends on the electric properties of the spacecraft surface materials. The connection between the material parameters and the charging time value is rather difficult, e.g. decrease of conductivity of the surface materials in the range $10^{-15} - 10^{-19}$ (Ohm.cm)$^{-1}$ leads to increase of the charging time by a factor of ~ 5.

The computation results presented in figs. 1-5 demonstrate features which are typical for spacecraft charging process in hot magnetosphere plasma. We see that the problem is non-local: electric field on an element of the spacecraft surface influences the process of charging not only on this element but on the other elements of the spacecraft. As an example of the effect, we see that distribution of potential along the solar battery plane (fig. 4) is noticeable.

The modeling technique and the developed visualization tools enable to show the development of the "saddle point" configuration of the electric field (figs. 3, 4), and the effect of shielding of spacecraft design elements by the other ones. Influence of these features on the spacecraft charging depends significantly on the spacecraft design.

Note that the spacecraft charging time is rather high, and the steady state may be unreachable in the real space flight conditions (e.g. when the time of the spacecraft pass through the hot plasma region is short). The modeling technique enables to make prediction of the spacecraft charging in this case too, as far as in the case of rotating spacecrafts.
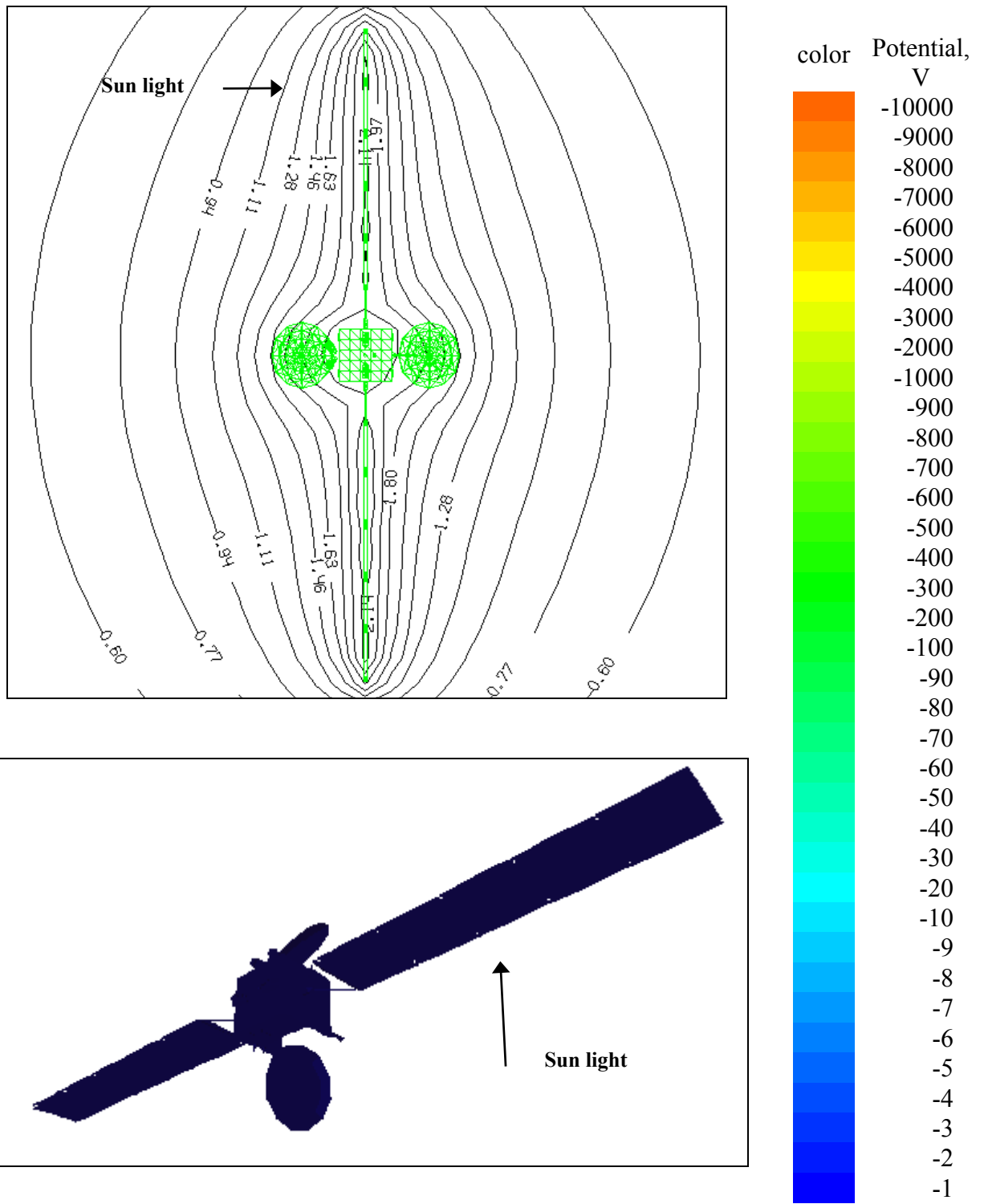
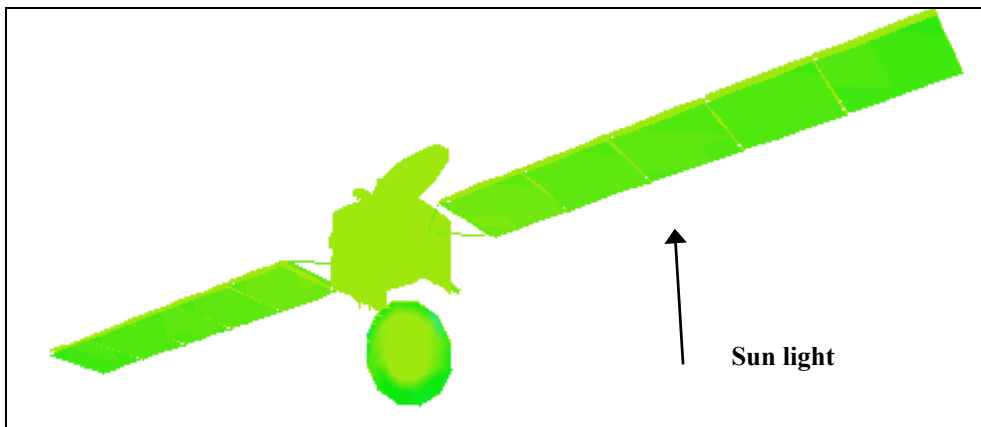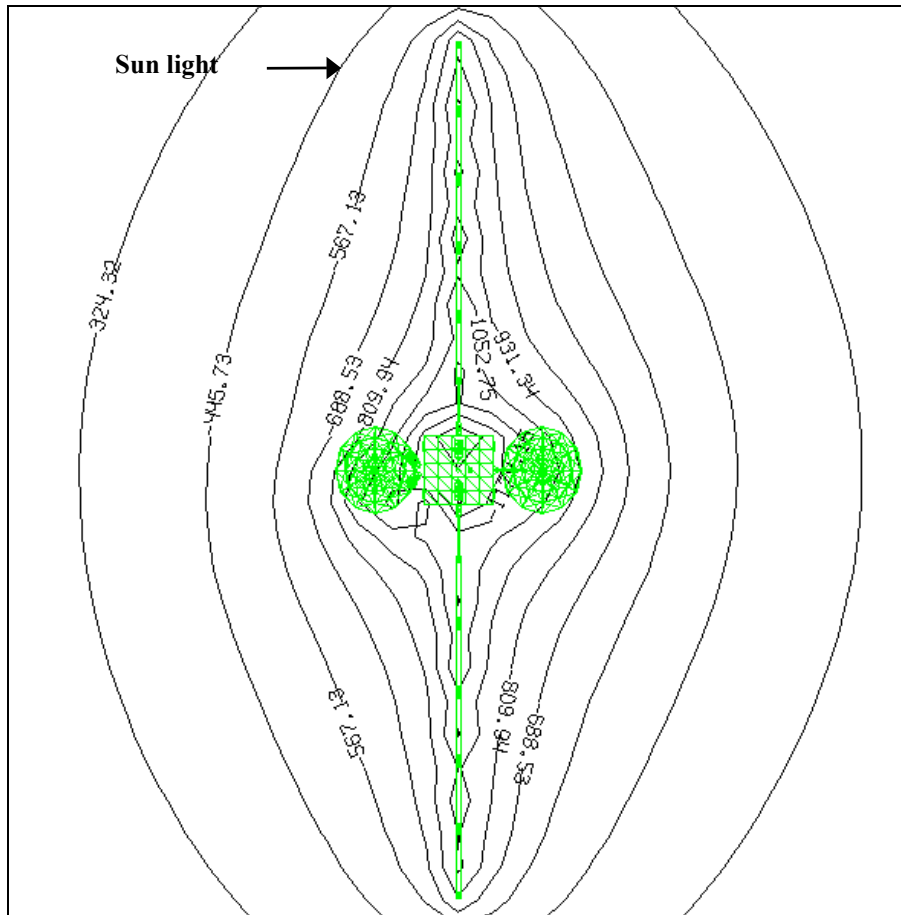**Figure 1. Spacecraft charging at t=1.3.10^{-3} s. Color code scale is on the right**
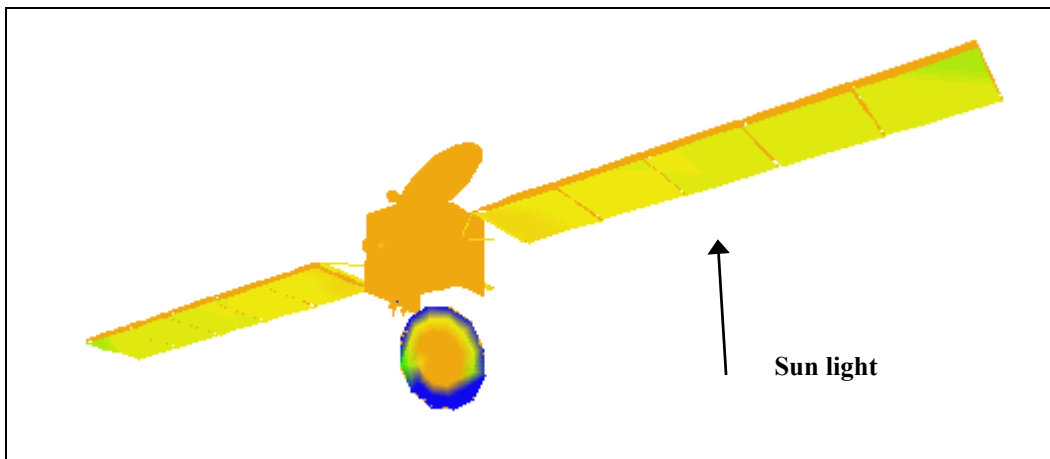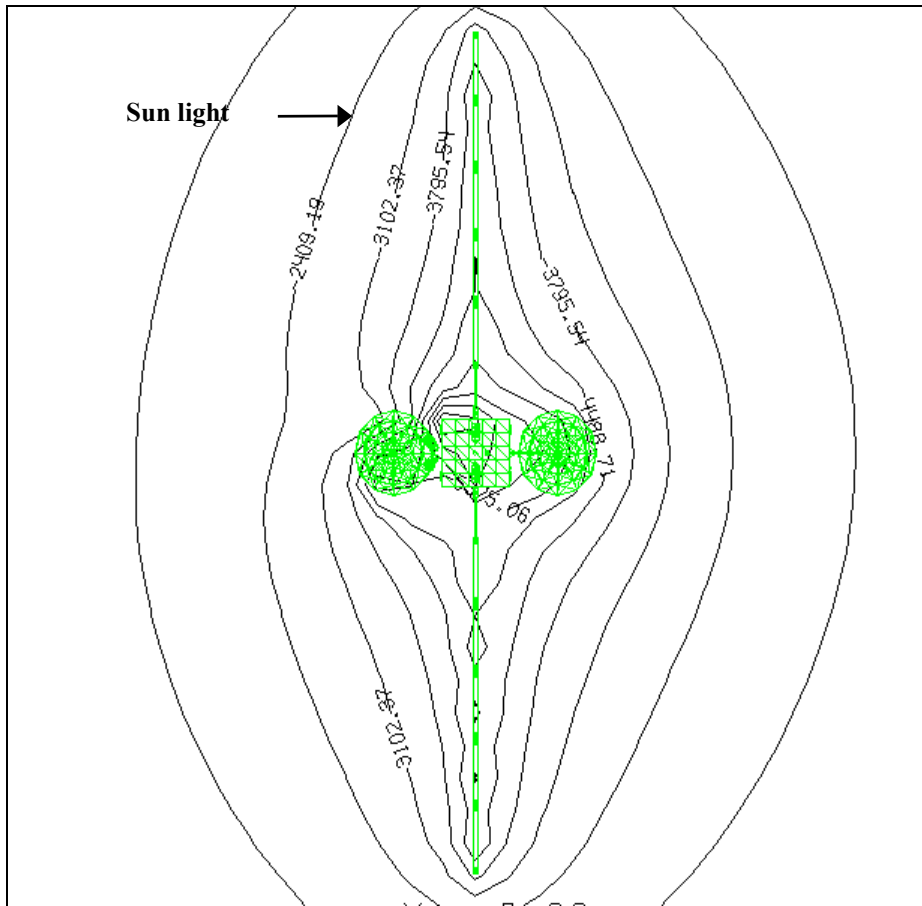
Figure 2. Spacecraft charging at t=3.0.10^2 s.

Figure 3. Spacecraft charging at t=2.9.10^3 s

Sun light

Sun light

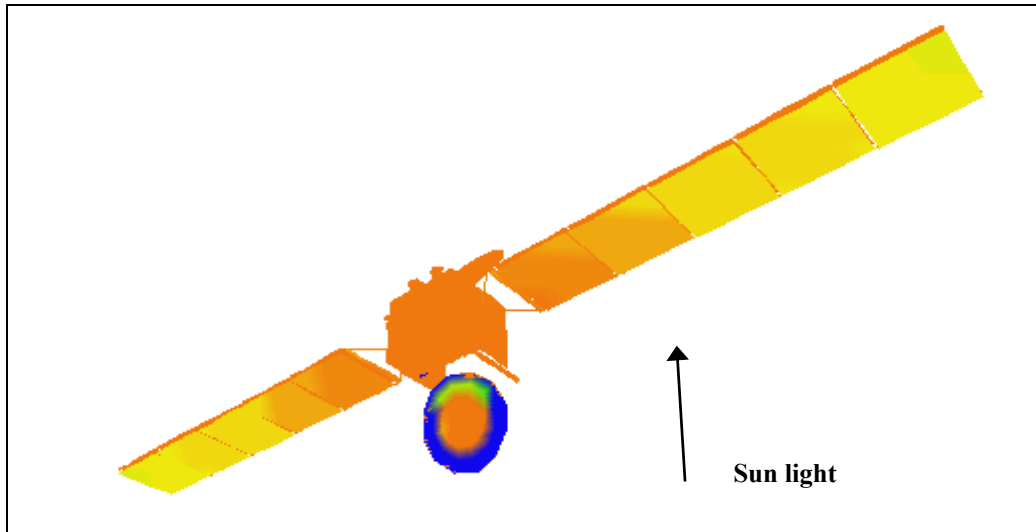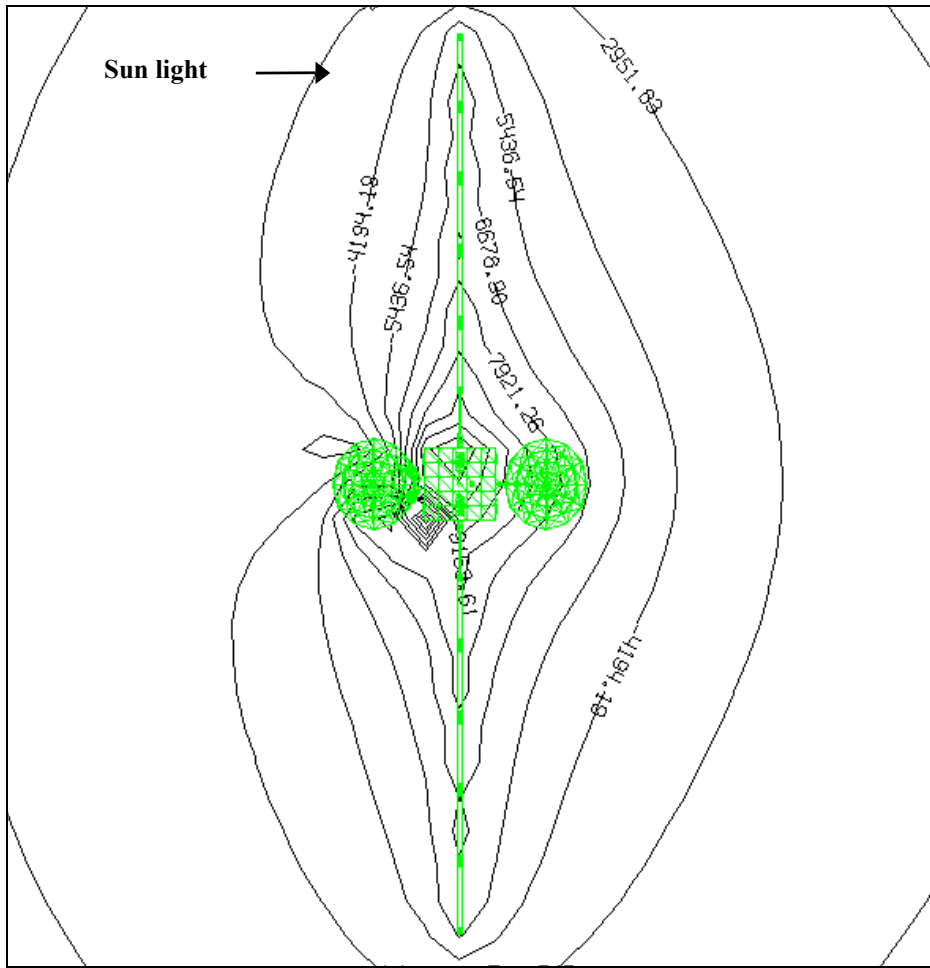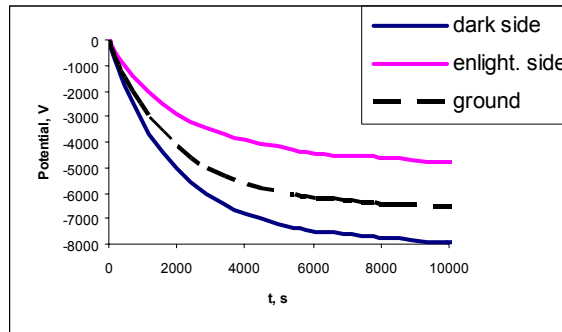**Figure 4. Spacecraft charging at t=2.0.10^4 s (steady state)**

Figure 5. Potential on various spacecraft surface elements as function of charging time

Conclusion

The modified version of the COULOMB tool developed in SINP MSU for modeling of spacecraft charging in high orbits enables to calculate the values of electrostatic potential on the spacecraft surface as the in case of integral charging, and in case of differential charging. Modeling of the dynamics of the spacecraft charging in the given irradiation conditions enables to obtain typical charging time of the spacecraft surface elements. The modern software is applied to the spacecraft model building and to the computer visualization of the modeling results.

References

1. Mileev, V.N., and L.S.Novikov (1989): "Physical and mathematical model of spacecraft charging in geosynchronous and high-elliptical," Research on Geomagnetism, Aeronomy and Physics of the Sun, No. 86, 64-98.

2. Krupnikov, K.K., V.N. Mileev, L.S. Novikov, and G.V. Babkin, "Mathematical Modeling of High Altitude Spacecraft Charging", International Conference on Problems of Space/Environment Interactions, Novosibirsk, Russia, 1992, 167-175

3. Krupnikov, K.K., V.N. Mileev, and L.S. Novikov (1996): "A Mathematical Model of Spacecraft Charging ('COULOMB' Tool). Radiation Measurements", Vol.26, No.3, 513-516.

4. Mileev V.N., K.K. Krupnikov, A.A. Makletsov, L.S. Novikov, and V.V. Sinolits, "The Description of Dynamic Spacecraft Charging using of Modern Computer Tools".7th Spacecraft Charging Technology Conference, Noordwijk, The Netherlands. April 23-27, 2001. ESTEC SP-476, 211-216.

5. Garret H.B., and S.E. De Forest (1979): "An analytical simulation of the geosynchronous plasma environment", Planet. Sp. Sci., No 8, 1101.

6. Garret H.B. (1979): "Review of quantitative models of the 0- to 100-keV near Earth plasma", Rev. Geophys. Space. Phys., vol. 17, No. 3, 397-417.

7. New high technologies in engineering, Vol. 17 "Effect of space environment on materials and spacecraft equipment". Ed. by L.S.Novikov and M.I.Panasyuk, Moscow, ENCITEH, 2000 (in Russian).

8. Gear C.W. (1971): "Numerical initial value problems in ordinary differential equations", Englewood Cliffs: Prentice Hall.

REPRESENTATION OF THE GEOSYNCHRONOUS PLASMA ENVIRONMENT FOR SPACECRAFT CHARGING CALCULATIONS

V. A. Davis
Science Applications International Corporation
10260 Campus Point Dr., M.S. A1
San Diego, CA, 92121
Phone: 858-826-1608
Fax: 858-826-1652
E-mail: victoria.a.davis@saic.com

M. J. Mandell
Science Applications International Corporation

M. F. Thomsen
Los Alamos National Laboratory

Historically, our ability to predict and "postdict" surface charging has suffered from both a lack of reliable secondary emission and backscattered electron yields and poor characterization of the plasma environment. One difficulty lies in the common practice of fitting the plasma data to a Maxwellian or Double Maxwellian distribution function, which may not represent the data well for charging purposes.

For 13 years Los Alamos National Laboratory (LANL) has been accumulating measurements of electron and proton spectra from Magnetospheric Plasma Analyzer (MPA) instruments aboard a series of geosynchronous satellites. These data provide both a plasma characterization and the potential of the instrument ground.

We use electron and ion flux spectra measured by the LANL MPA to examine how the use of different spectral representations of the charged particle environment in computations of spacecraft potentials during magnetospheric substorms affects the accuracy of the results. We calculate the spacecraft potential using both the measured fluxes and several different fits to these fluxes. These flux measurements and fits have been corrected for the difference between the measured and calculated potential. The potentials computed using the measured fluxes, the best available material properties of graphite carbon, and a secondary electron escape fraction of 81%, are within a factor of three of the measured potential for nearly all the data. Using a Kappa fit to the electron distribution function and a Maxwellian fit to the ion distribution function gives agreement similar to the calculations using the actual data. Alternative spectral representations, including Maxwellian and double Maxwellian for both species, lead to less satisfactory agreement between predicted and measured potentials.

Background

Historically, our ability to predict and "postdict" spacecraft surface charging has suffered from both a lack of reliable secondary emission and backscattered electron yields and poor characterization of the plasma environment. One difficulty lies in the common practice of fitting

the plasma data to a Maxwellian or Double Maxwellian distribution function, which may not represent the data well for charging purposes. We examine how the use of different spectral representations of the charged particle environment in computations of spacecraft potentials during magnetospheric substorms affects the accuracy of the calculations.

The approach is as follows:

1. Examine charging and non-charging, electron and ion fluxes to determine relevant spectral characteristics.
2. Compute net fluxes and correlate with potential.
3. Compare the measured potential with the potential computed from measured fluxes to validate the charging computation.
4. Determine the analytic representation that best preserves the charging characteristics.

Data

For 13 years Los Alamos National Laboratory (LANL) has been accumulating measurements of electron and proton spectra from Magnetospheric Plasma Analyzer (MPA) instruments aboard a series of geosynchronous satellites.[1] The MPA is a spherical section electrostatic analyzer. The MPA is mounted so that the spacecraft spin allows the instrument to view 360° in azimuth. These data provide both a plasma characterization and the potential of the instrument ground.[2] We use electron and ion spectra measured by the LANL MPA and compare predictions with observed charging potentials. We focus on data taken by one MPA during eclipse periods in September 2001. This dataset has 973 measurements of charging to potentials ranging from 3 V to nearly 10 kV negative.

Fluxes

In eclipse, the net charging flux to the spacecraft is the sum of the incident electron and ion fluxes and secondary and backscattered electron fluxes.[3] The integral of the incident spectrum against the area-averaged yield functions gives the secondary and backscattered fluxes. Steady-state is established when the net charging flux is zero.

For a spacecraft charged to a surface potential of ϕ, the net charging flux can be written as the difference between the net ion and electron fluxes, given by the following expressions:

$$\text{Flux}_{\text{net}}^{e} = \int_{0}^{\infty} F_e(E)\left[1 - \gamma Y_e(E) - B(E)\right]dE = \sum_{E > E_{\text{min}}} F_e(E)\left(1 - \gamma Y_e(E) - B(E)\right)\Delta E \quad (1)$$

$$\text{Flux}_{\text{net}}^{i} = \int_{-\phi}^{\infty} F_i(E)\left[1 + \gamma Y_i(E)\right]dE = \sum_{E} F_i(E)\left(1 + \gamma Y_i(E)\right)\Delta E$$

F_e and F_i are the measured electron and ion fluxes respectively, the Y_e and Y_i are the area-averaged secondary yields due to electron and ion flux respectively, B is the area-averaged backscattered yield, and γ is the fraction of low-energy electrons that escape. The electron

minimum energy, E_{min}, used is the minimum of -ϕ/2 and 30 eV. Many of the low-energy secondary electrons are trapped by electric fields due to differential potentials. The value of E_{min} is selected to remove these secondaries from the integral, while including some of the structure of the low energy portion of the spectrum in the non and low charging cases.

If we use graphite material properties to represent the area-averaged material and assume that all the secondary electrons escape, the measured potential as a function of the measured incident electron flux and the net electron flux, calculated according to Equation 1, appears as shown in Figure 1. This figure illustrates the difficulties of assuming that the potential is a function of either the incident electron flux or the net electron flux alone. While from the figure one could argue that there is a correlation between the potential and the average net electron flux, the net electron flux value does not provide a good prediction of the potential.
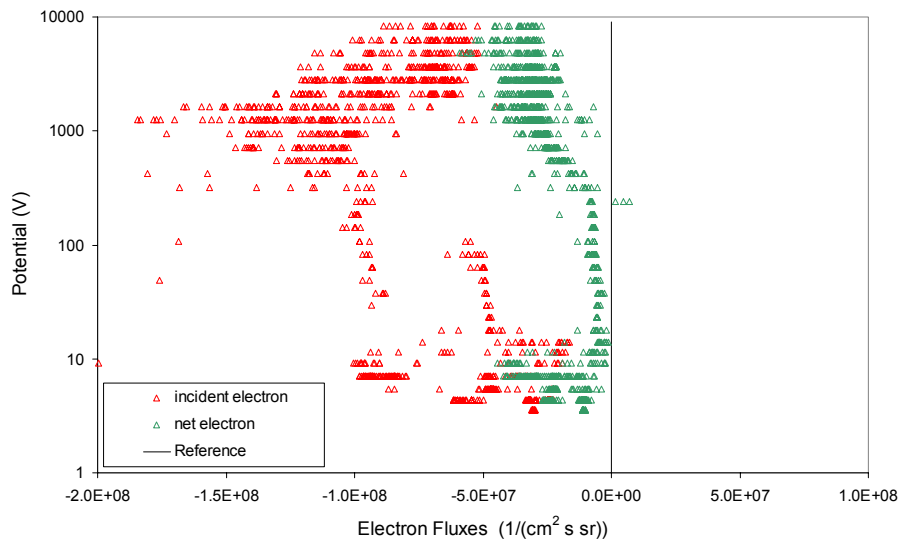
Figure 1. Incident and net electron fluxes at all potentials. The quantity plotted is minus the flux.

The net electron and ion fluxes, computed under the above assumptions, appear in Figure 2. If the material properties were perfectly known and the spectrum perfectly measured, the sum of the net electron and ion fluxes, the net charging flux, would be zero. As, on the average, the net charging flux is about 10% of the incident electron flux and greater than the incident ion flux, these properties provide poor potential estimates. We also computed the net charging flux using different techniques to compute the integral and different strategies to compute E_{min}. The results do not vary significantly. We computed the net charging flux using the material properties of gold, Kapton, solar cells, and optical solar reflectors for all of the materials and got much larger net charging fluxes. However, as shown in Figure 3, the net charging flux computed using the properties of graphite can be made to fall near zero for most of the data, if a value of 0.81 for γ is assumed.
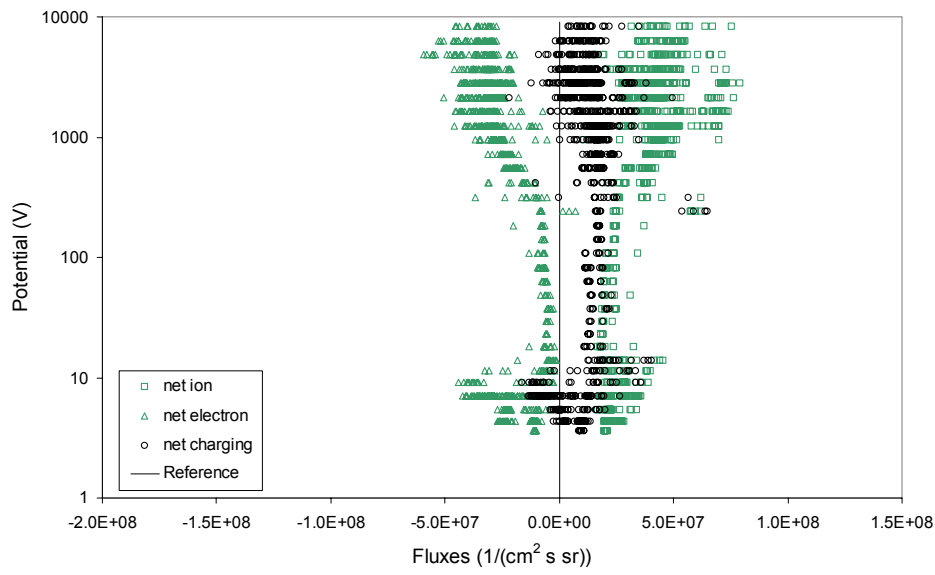
Figure 2. Net ion and electron fluxes and their difference, the net charging flux. For the net electron flux, the quantity plotted is minus the flux. A complete flux spectrum, correct yield function, and proper accounting for suppression of secondaries by barriers would give a value of zero for all potentials.
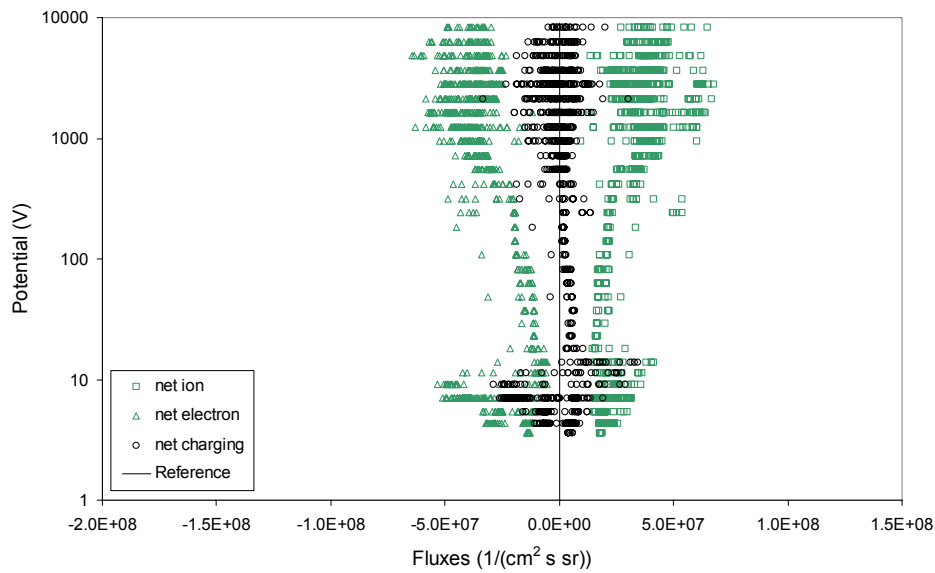
Figure 3. Net electron and ion fluxes and their sum, the net charging flux, assuming that only 81% of the electrons escape. For the net electron flux, the quantity plotted is minus the flux.

Potential Computation

The approach for the potential calculation using measured fluxes is as follows:

1. Given the measured potential, use the measured spectra and Liouville's theorem to compute the ion and electron spectra at infinity.

2. Using the computed ion and electron spectra at infinity, determine the net charging flux (incident, secondaries, and backscattered) to the spacecraft as a function of the spacecraft chassis potential.

3. Search for a unique chassis potential between -1 V and -10,000 V at which the net charging flux magnitude is zero, or a minimum.

4. If the computed and measured potential are within experimental error of each other, the potential prediction technique is good.

The net charging flux in terms of the measured fluxes, F_e and F_i, the proposed potential, ϕ', and the measured potential, ϕ_m, is given by

$$F_{net}(\phi') = -\int_{\max(0,\phi_m-\phi')}^{\infty} dE_m \left(1 - \frac{\phi_m - \phi'}{E_m}\right) F_e(E_m) \left[1 - \gamma(\phi') Y_e(E_m - \phi_m + \phi') - B(E_m - \phi_m + \phi')\right]$$

$$+ \int_{-\phi_m}^{\infty} dE_m \left(1 + \frac{\phi_m - \phi'}{E_m}\right) F_i(E_m) \left[1 + \gamma(\phi') Y_i(E_m + \phi_m - \phi')\right] \tag{2}$$

Figure 4 shows the potential computed using the measured fluxes and the best available material properties of graphite carbon, with a secondary electron escape fraction of 81%. The computed potential is within a factor of 1.5 of the measured potential for 66% of the data and within a factor of 3 for 87% of the data.
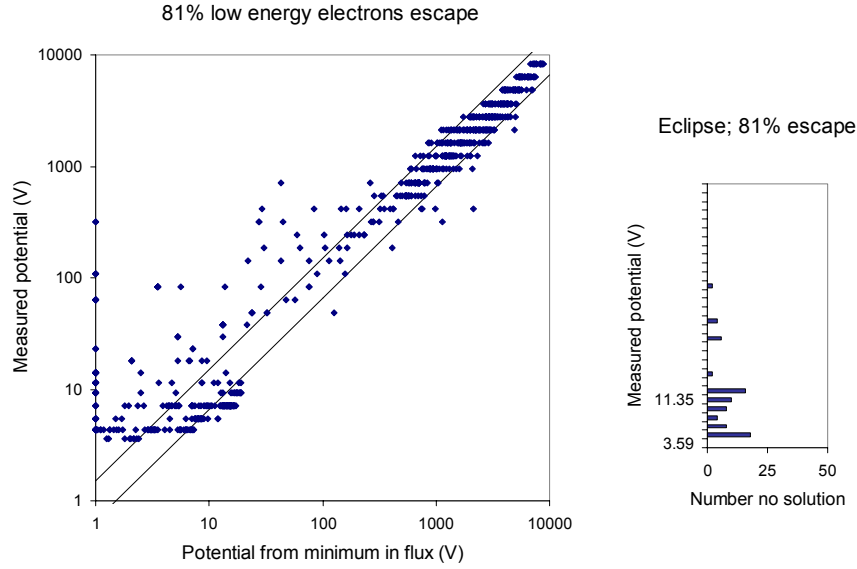
Figure 4. Meaured potential as a function of the potential computed from the minimum in the net charging flux with 81% escape fraction.

Potentials Using Fit Fluxes

The potentials can be computed using a fit to the measured fluxes as well as using the measured fluxes themselves. Several functions were tried. Those that work best are the traditional Maxwellian and double Maxwellian and the Kappa distribution. The Kappa distribution was selected for investigation as Christon, *et al*[4] have shown that it provides a good fit to the quiescent plasma sheet environment at greater than 12 R_E. (Geosynchronous is at 6.6 R_E.) The Kappa function has the shape of a Maxwellian at low energies and a power law at high energies, providing a high-energy tail to the distribution.

$$\text{Flux}^{\text{Maxwellian}}(E) = n\frac{e}{4\pi}\sqrt{\frac{1}{2\pi me\theta}}\frac{E}{\theta}\exp\left(-\frac{E}{\theta}\right)$$

$$\text{Flux}^{\text{DoubleMaxwellian}}(E) = en_1\sqrt{\frac{1}{2\pi me\theta_1}}\frac{E}{\theta_1}\exp\left(-\frac{E}{\theta_1}\right) + en_2\sqrt{\frac{1}{2\pi me\theta_2}}\frac{E}{\theta_2}\exp\left(-\frac{E}{\theta_2}\right) \quad (3)$$

$$\text{Flux}^{\text{Kappa}}(E) = A\,E\left(1+\frac{E}{\kappa E_o}\right)^{-\kappa-1}$$

The most accurate potential predictions, shown in Figure 5, were obtained using a Kappa function fit to the electron distribution and a Maxwellian function fit to the ion distribution. The potentials computed using the fit agree with the measured potentials about as well as the potentials computed using the measured fluxes directly. The computed potential is within a factor of 1.5 of the measured potential for 65% of the data and within a factor of 3 for 80% of the data. Alternative spectral representations, including Maxwellian or Kappa distributions for both species, led to less satisfactory agreement between predicted and measured potentials.

The Kappa-Maxwellian fits often generate no potential solution between 30 and 300 V and sometimes predict high potentials for low measured-potential cases. These high-predicted potentials were examined. The automated fitting of the low temperature ion spectrum gives a high temperature Maxwellian due to the high weight of the wider higher potential bins. A smarter fitting procedure would give more accurate potential predictions.
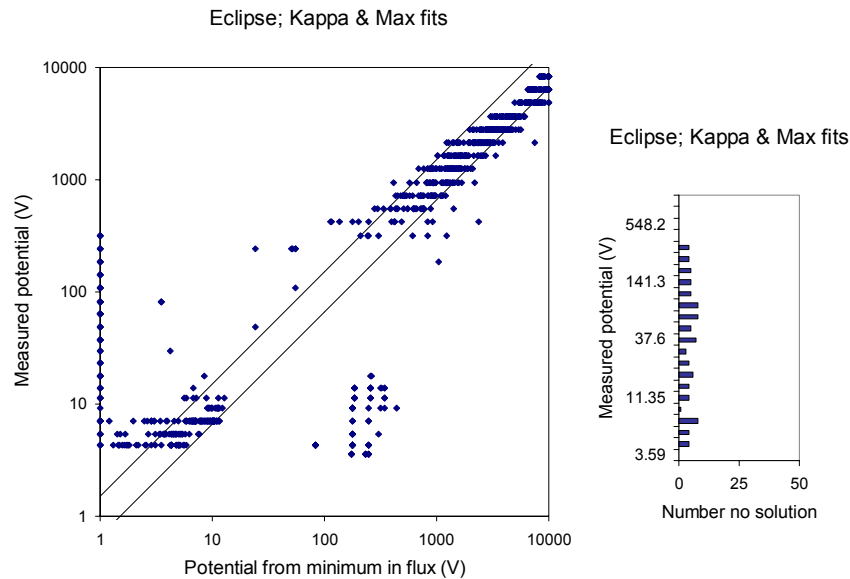
Figure 5. Measured potential computed from the minimum in the net charging flux, where the fluxes are computed from a Kappa fit to the electron flux and a Maxwellian fit to the ion flux.

Summary and Discussion

The LANL dataset has proven to be a powerful tool for the investigation of spacecraft surface charging. The flux spectra provide adequate resolution and accuracy for "postdiction" spacecraft surface charging calculations.

Using the measured flux spectra, we determined that for this spacecraft, computing the fluxes using a set of material properties for graphite carbon and a low-energy secondary electron escape fraction of 81%, gives computed potentials consistent with measured values. The estimated potential is within a factor of 1.5 of the measured potential for 66% of the data and within a factor of 3 for 87% of the data. While this approach is valid for any spacecraft in eclipse, where geometric effects are less important, the specific material properties and secondary electron escape fraction are spacecraft-specific quantities.

It is necessary to include all the current components–incident electrons and ions, secondary electrons, backscattered electrons, and (in sunlight) photoelectrons–to accurately "postdict" chassis potentials from measured flux spectra.

Potential "postdictions" using a Kappa distribution to fit the incident electron flux spectrum and a Maxwellian distribution to fit the incident ion flux spectrum give results similar to "post-

dictions" using the measured flux spectra directly. We expect better results would be obtained if additional intelligence in the low energy portion of the flux spectrum was added to the ion flux fitting procedure. While the specific material properties and secondary electron escape fraction are spacecraft-specific, the conclusion regarding the best functional forms to use for the environment are appropriate to all geosynchronous spacecraft.

The difference between a Maxwellian distribution and a Kappa distribution is in the tail of the distribution. The Kappa distribution falls off more slowly with energy. The difference between the accuracy of results computed using the two types of fits is consistent with earlier work by Katz et al.[5] in which it was shown that the form of the secondary yield in the high energy range is critical to the computation of spacecraft charging.

While this study has established that a Kappa distribution fit rather than a Maxwellian distribution fit to a known electron flux spectrum is preferred for spacecraft charging calculations, the question of the appropriate parameters to use for preflight predictions remains. A similar study using sunlit data and spacecraft geometric information would provide additional support for the results.

Acknowledgments

References

1. S.J. Bame, D.J. McComas, M.F. Thomsen, B.L. Barraclough, R.C. Elphic, J.P. Glore, and J.T. Gosling, Magnetospheric plasma analyzer for spacecraft with constrained resources, Rev Sci Instrum 64, p 1026, 1993.

2. M. F. Thomsen, D. J. McComas, G.D. Reeves, and L.A. Weiss, An observational test of the Tsyganenko (T89a) model of the magnetospheric field, JGR 101, p. 24827, 1996.

3. Purvis, C.K., H.B. Garrett, A.C. Whittlesey, and N.J. Stevens, Design Guidelines for Assessing and Controlling Spacecraft Charging Effects, NASA Technical Report Paper 2361, September 1984.

4. S.P. Christon, D.J. Williams, and D.G. Mitchell, L.A. Frank, C.Y. Huang, Spectral characteristics of plasma sheet ion and electron populations during undisturbed geomagnetic conditions, J. Geophys. Res. 94, A10, p 13,409, 1989.

5. I. Katz, M.J. Mandell, G.A. Jongeward, The importance of accurate secondary electron yields in modeling spacecraft charging, JGR, 91, p. 13739, 1986.

AN EMPIRICAL LOW-ENERGY ION MODEL OF THE INNER MAGNETOSPHERE

J. L. Roeder
The Aerospace Corporation
MS M2-260, P. O. Box 92957, Los Angeles, CA
310-336-7081
E-mail: James.Roeder@aero.org

M. W. Chen
J. F. Fennell
The Aerospace Corporation

R. Friedel
Los Alamos National Laboratory

Abstract

Ion flux measurements by the CAMMICE/MICS and Hydra instruments on the NASA Polar satellite have been used to build empirical models of the ion environment at low energies in the Earth's inner magnetosphere. These models may be used to develop design and test specifications for spacecraft surface materials, which are susceptible to damage by the ions. The combination of the CAMMICE/MICS and Hydra models provide the ion flux at energies in the range 20 eV–200 keV as a function of position in the magnetosphere. For the 1–200 keV energy range, the H^+ and O^+ ion flux is estimated separately using the CAMMICE/MICS data. Average environments have been calculated for several sample orbital trajectories: a geosynchronous orbit and the orbits of several satellites in the Global Positioning System (GPS) constellation. At high energies (~100 keV) the flux estimates agree with corresponding estimates from the NASA AP-8 model, but the fluxes at low energies are larger than those extrapolated simply from AP-8. The CAMMICE/MICS model shows that H^+ dominates the >2 keV ion populations, but that the O^+ flux becomes comparable to the H^+ flux at ~1 keV. The standard deviation of both the ion and electron flux was found to be 100–200% of the average value over the entire considered energy range. The average 1–200 keV O^+ flux estimates for GEO appear very similar to the averages for GPS orbit, so that any material damage due to O^+ ions in this energy range should be the same for the two orbits.

Introduction

The impact of charged particles from the space environment can have substantial effects on the parts and materials used in space systems. The most well known is the gradual degradation of microelectronic devices by relatively high-energy (>100 keV) particles in the Earth's radiation belts. But lower energy particles also significantly damage materials at their outer surfaces. The effects include the collisional ejection of atoms of the material (sputtering), implantation of incident ions in the material, and chemical changes in the material due to those implanted ions [Johnson, 1990; Nastasi, 1996]. These processes become especially important for the design of optical and thermal coatings for the satellite surface. Such coatings rely on precisely known properties of the material surface to remain within specification over the mission lifetime.

Effects such as sputtering occur very gradually over the space mission but the damage is cumulative, similar to the total dose radiation effects on microelectronics. Because of this, the relevant specification for the environment is the average flux of particles as a function of incident energy over the entire mission. This spectrum may then be converted to a profile of dose versus depth that is related to the damage of the material.

The charged particles in the space environment consist of electrons and ions of various masses and charge states. Higher mass particles tend to be more effective at a given energy for damaging the surface of materials, so the flux of ions of each species is important for estimating these effects. The range of ion energy that is important for material surface damage is quite uncertain. It depends on many factors including incident angle, material properties, and particle mass. In broad terms, ions of energy in the range from ~100 eV to ~100 keV are important for surface effects. The electrons in this energy range may cause little surface damage to materials but result in other important effects such as the surface charging of dielectric materials [Hastings and Garrett, 1996].

The NASA radiation belt models such as AE8 and AP8 are traditionally used to specify the average charged-particle flux for space missions [Vette, 1991]. But these models cover the energy range of 0.04–10 MeV for electrons and 0.1–10 MeV for protons. The particles in these ranges are too energetic to cause significant damage to the surface of spacecraft materials, and will instead burrow deep in to the spacecraft. Extrapolation of the NASA models to low energies is too uncertain for use as an environmental specification, and so a low-energy particle model is needed for space system design.

In this report we present a model of charged particles in the energy range 20 eV–200 keV that we have constructed using particle observations by the recent NASA Polar satellite. The model consists of the average flux for the major ion species as a function of the three-dimensional position in the Earth's magnetosphere. Similar to the NASA models, one can then "fly" a spacecraft through the model and determine the average environment along the trajectory. We use the model to determine the average particle environment for spacecraft in both geosynchronous orbit and a representative orbit of the Global Positioning System (GPS). The results are compared with the NASA AP8 and AE8 and other published models.

Instrumentation

Polar is a NASA satellite mission to investigate the Earth's magnetosphere [Acuna et al., 1995]. It is part of the Global Geospace Science program that is designed to improve understanding of the flow of energy, mass, and momentum in the solar-terrestrial environment. The Polar spacecraft was launched on February 26, 1996 into a 1.8 x 9 RE orbit with a 90° inclination and an 18-hour period. The spacecraft has both spinning and de-spun platforms for instruments. All the instrumentation described in this report were mounted on the spinning platform which has a spin period of ~6 s. The spin axis pointed nearly perpendicular to the orbit plane so that the satellite cartwheeled along the orbit.

Data from two instruments on the Polar satellite were used to construct a model of the charged particle environment. The Magnetospheric Ion Composition Spectrometer (MICS) was

part of the Charge and Mass Magnetospheric Ion Composition Experiment (CAMMICE) on the Polar satellite. MICS measured all positively charged ion species ranging in mass from hydrogen to iron in the energy-per-charge range 1–200 keV/q. This sensor was similar to an identically named instrument on the USAF/NASA CRRES mission [Wilken et al., 1992].

MICS determined the identity of each detected ion from three measurements: the energy-per-charge (E/q), the time-of-flight (TOF) for the ion to traverse a fixed distance, and a total energy (E). The detection events were then sorted by a data processing unit for accumulation into bins for the various ion mass species and charge states [Koga et al., 1992]. The major ion species (H, He, and O) in the magnetosphere each had a low and a high-energy channel. The high-energy channel required a valid energy measurement in addition to the TOF and E/q, and was able to unambiguously determine the ion charge state. The low energy channel required only TOF and E/q measurements and was thus insensitive to the ion charge state. Inside the Earth's magnetosphere the particle populations are heavily dominated by singly charged ions, so the low energy channels are assumed to represent ions of charge state one. The data from the low and high-energy channels may then be combined into a composite spectrum in the range 1–200 keV. The hydrogen and oxygen ion spectra in this report are all composite measurements constructed by this process. A total ion channel is also recorded which counts ions irrespective of mass or charge state. Data from this channel is assumed to be protons.

MICS measured the ion flux in 24 logarithmically-spaced steps over the range 1–200 keV/q. The instrument was programmed to provide a full-resolution energy spectrum every 202 s. The MICS sensor had a single field-of-view directed perpendicular to the spacecraft spin axis. Ion counts were accumulated in 32 equally-space sectors for each spacecraft spin period, which effectively limited the angular resolution to ~11.25°.

The CAMMICE/MICS data was supplemented by measurements from the Hydra instrument, also on the Polar mission. Hydra measured ion and electron flux in the energy-per-charge range 2 eV/q–35 keV/q [Scudder et al., 1995]. This instrument had multiple fields-of-view to effectively cover all possible angles of particle incidence. No information was analyzed on the ion mass or charge state composition, and so all ions detected by Hydra are assumed to be protons. The instrument had a routine time resolution of 0.5 s to achieve an angular resolution of ~16°.

Databases and Modeling

The particle environment model was constructed separately for CAMMICE/MICS data and the Hydra data. Because the multiple fields-of-view of the Hydra instrument result in nearly full coverage of all angles, the Hydra data may be easily averaged into a good representation of the omni directional flux. In contrast, the single field-of-view of the MICS sensor has good angular coverage for some intervals, but inadequate coverage at other times. This makes the construction and interpretation of the CAMMICE/MICS model more complex. The following sections describe the databases and models of the two data sets.
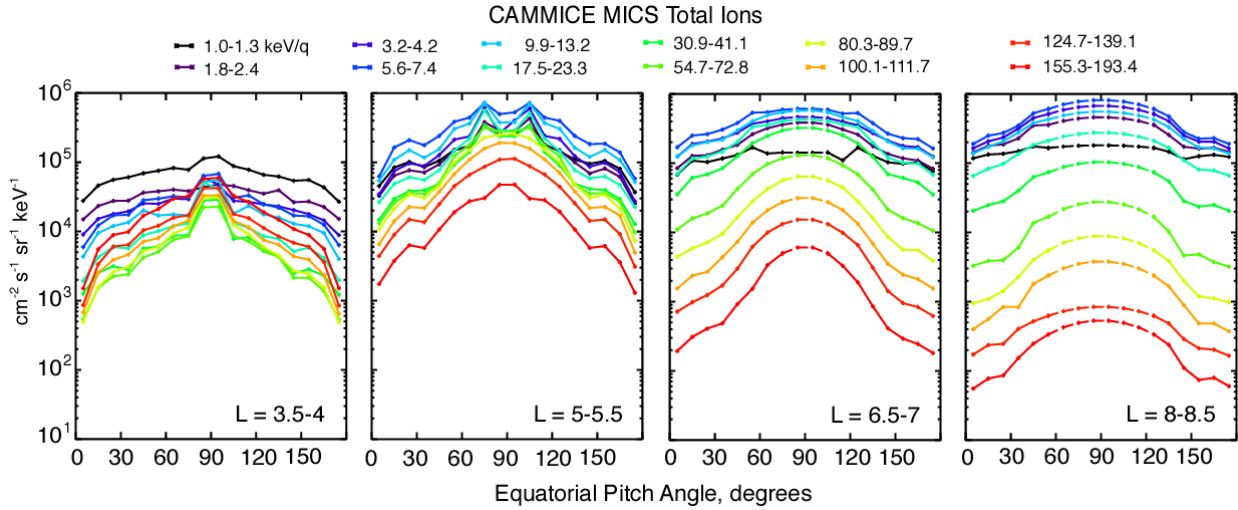
The NASA radiation belt models of high-energy particles are two-dimensional models, consisting of the average flux as a function of the radial magnetic coordinate L and the latitudinal coordinate B. The L coordinate is a constant for all positions along a magnetic field line and is

approximately equal to the geocentric radius of the field line where it intersects the magnetic equator. L is always given in units of Earth radii (RE). The B coordinate is the ratio of the magnetic field magnitude at the point of interest to the minimum field at the equatorial point mapped along the magnetic field line. High-energy particles such as those estimated by the NASA models form relatively symmetric azimuthal distributions. Particles of lower energy are sensitive to several effects that cause highly asymmetric populations, including electric fields and asymmetric magnetic fields. Therefore, any model of the low energy particles must be three-dimensional and use the magnetic local time as an azimuthal coordinate.

CAMMICS/MICS Model

Because of the intermittent lack of full angular coverage by MICS, the model for this data was organized by pitch angle, which is defined as the angle between the particle velocity and the local magnetic field vector. The ion flux distributions versus pitch angle were mapped to the equator and averaged into the spatial bins. Averaging over several years of the Polar mission achieved complete coverage of the equatorial pitch angle bins and provided a good representation of the average flux in most bins. Then, to obtain the omni directional flux at some latitude off the equator, the model pitch angle distributions were mapped from the equator to the latitude of interest and averaged over angle. This is equivalent to the mapping in B and L coordinates in the NASA AE8 and AP8 radiation belt models.

The raw CAMMICE/MICS data for 3.5 years were averaged into 5-minute distributions in energy and local pitch angle to build the database. The 24 energy steps from the MICS instrument were combined into 12 channels by averaging the fluxes for every other step to improve statistics. The local pitch angles for each measurement were computed using the simultaneous data from the Polar magnetic field experiment [Russell et al., 1995]. The local pitch angle distribution for each energy was averaged into 18 equally-spaced bins of 10° widths. Then the local pitch angles were converted into equatorial pitch angles using the ratio of the measured local magnetic field magnitude to the equatorial magnetic field magnitude [Schulz and Lanzerotti, 1974]. The equatorial magnetic field was calculated for this purpose using the IGRF model of the geomagnetic field. The equatorial pitch angle distribution at each energy was then averaged into spatial bins in equatorial magnetic coordinates. The magnetic equatorial plane was divided into a grid of 16 equally-spaced bins in L in the range 2–10, and 2-hour bins in magnetic local time.

CAMMICE MICS Total Ions

|					
1.0-1.3 keV/q	3.2-4.2	9.9-13.2	30.9-41.1	80.3-89.7	124.7-139.1
1.8-2.4	5.6-7.4	17.5-23.3	54.7-72.8	100.1-111.7	155.3-193.4

Figure 1. Average pitch angle distributions of the differential number flux of all ion species detected by the CAMMICE/MICS experiment on the Polar spacecraft. The four panels show distributions for different L bins in the 1800-2000 MLT sector.

Figure 1 shows the average pitch angle distributions of the total ion flux measured by MICS in several of the spatial bins. All twelve energy bins in the CAMMICE model are presented for each of four L bins in the dusk sector of magnetic local time. The ion energy spectrum at any given pitch angle tends to harden dramatically for the lower L bins, consistent with the adiabatic acceleration of particles. All the L bins exhibit fairly symmetric peaks at an equatorial pitch angle of 90°, which is characteristic of particles trapped in the radiation belts. The angular anisotropy, defined as the ratio of perpendicular particles to parallel particles, provides a measure of the variation of the ion flux with magnetic latitude. The anisotropy is low for the lower energy ions and increases significantly for the highest energies. This implies a substantial population of low energy ions away from the magnetic equator. The anisotropy at high L tends to be lower than that at low L for all energies. The MICS ion flux values are consistent with previously published measurements [Milillo et al., 2001].

Because of the high inclination of the Polar orbit, the coverage of the magnetic equator was lacking at high L. Polar crossed the equator at L ~ 3 just after launch, and the crossing point moved outward in L as the orbit precessed during the mission. At the end of 3.5 years, the magnetic equatorial crossing point had moved outward to L ~ 5. The ions trapped at the magnetic equator correspond in Figure 1 to the fluxes near 90°. The gap in coverage produces a corresponding gap centered at 90°, which widens in angle as L increases. Future work will include the processing of several more years of MICS data, which will increase the maximum L of the equatorial measurements.

A fitting procedure was devised to replace the missing equatorial data at high L. For each energy channel, the available data for a limited pitch angle range on either side of the gap were fitted to the standard model function A sinⁿ α where the parameters of the fit are A, designating the flux at 90°, and n, the anisotropy index. The missing data was then filled with the model distribution using the parameter values. The limited angular range of the fitting procedure tended
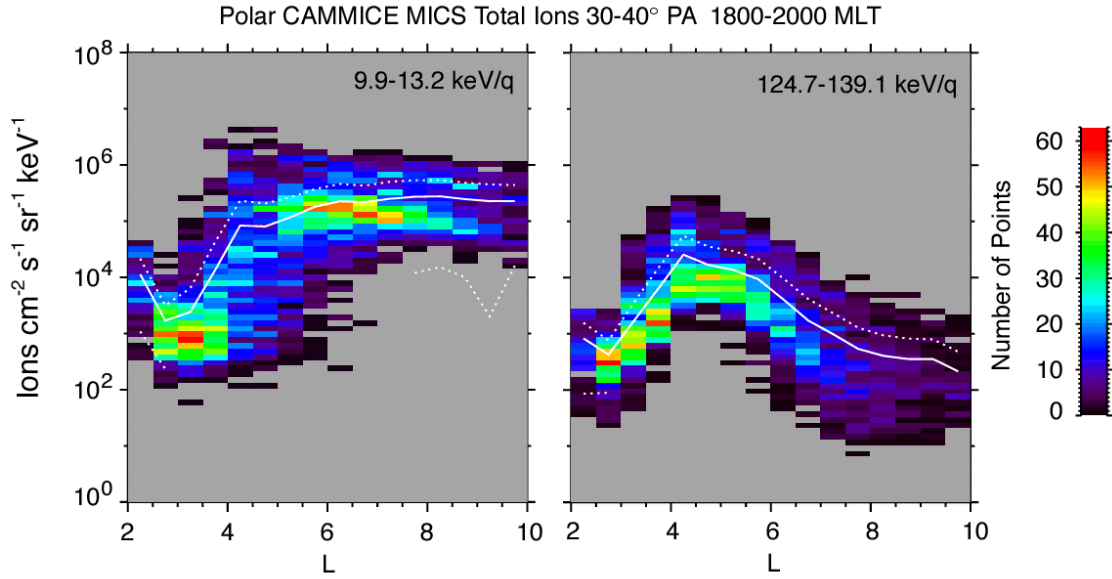
Figure 2. Statistical distribution of the total ion flux in two energy ranges for each of 16 equally-space L bins in the range 2-10. The ions shown are for the equatorial pitch angle range 30-40 in the 1800-2000 MLT sector. The solid line represents the average flux in each bin. The dotted lines mark the average flux plus and minus the standard deviation of the flux, respectively.

to preserve the character of the measured distribution. However, the fit could not compensate for the lack of measurements at the equator and so the model did not include any sharp features within the measurement gaps at 90°.

The particle flux in the Earth's magnetosphere in this interval underwent large variations. During intense geomagnetic storms the flux exceeded the quiet-time value by as much as three orders of magnitude. This is illustrated by the statistical distributions of flux shown in Figure 2. The color of each pixel in the images represents the number of MICS measurements recorded in the 3.5-year interval at a particular pitch angle for each level of flux and L. In some L bins the range of observed fluxes exceeded four orders of magnitude. To obtain a quantitative measure of this variability, standard deviations were computed for each bin of the MICS average model. The solid line in the figure represents the average flux in each bin. The dotted lines mark the average plus the standard deviation and the average minus the standard deviation of the flux, respectively. The standard deviation of the flux in each bin is typically in the range of 100–200% of the average value.

Maps of the average equatorially trapped H$^+$ flux are shown in Figure 3 as a function of position in the magnetic equatorial plane. These measurements correspond to the fluxes at pitch angles of 90° in the distributions shown in Figure 1. The four panels present different energy ranges of the total ion flux. The rectangular coordinates in units of Earth radii are the result of a standard polar-to-rectangular conversion of the magnetic coordinates of the bins in L and magnetic local time. The axes are oriented so that the sun is on the left side of the plot, midnight is on the right, dawn is at the top, and dusk is at the bottom, respectively. The sunlit Earth is drawn in the center of each panel for reference. The database was limited to L in the range 2–10 and so the areas outside this range were set to the color black to represent "no data."

Figure 3 displays the expected falling spectrum with increasing energy for almost all positions, with the highest flux values at 3–4 keV and the lowest values at 155–193 keV. The maps also show that the distribution of ions in the highest energy range is relatively symmetric in local time, but the lower energy ions exhibit a pronounced enhancement in the dusk to midnight sector. At the lowest energy (3–4 keV), this dusk side bulge extends over almost the full L range. This structure is consistent with the nominal drift trajectories of low energy ions in toward the Earth from the night side and then eastward as they become energized adiabatically.
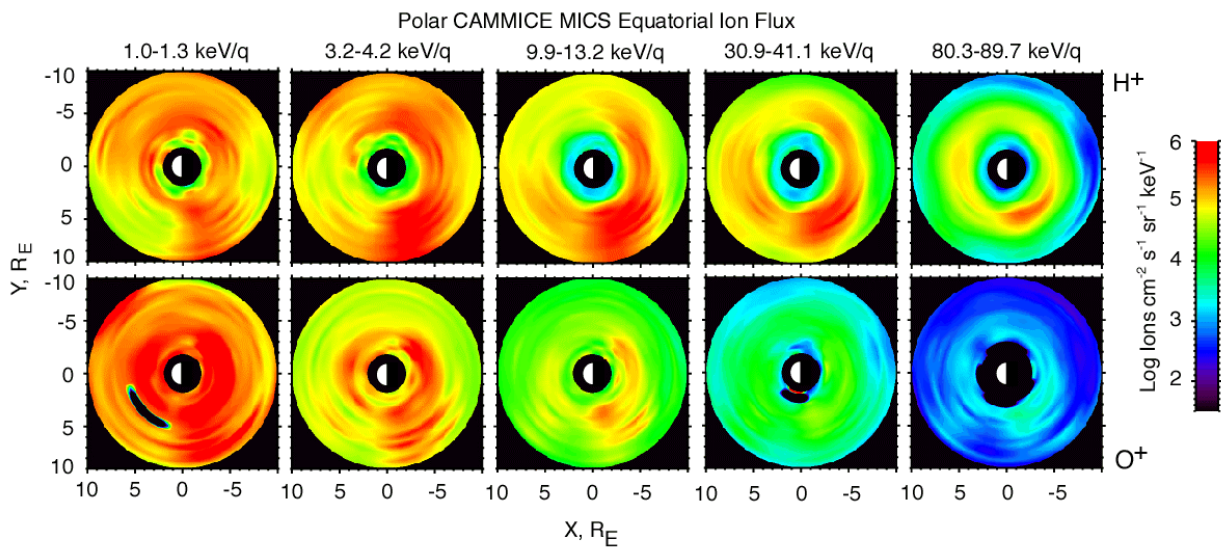
Figure 3. Average equatorially-trapped flux of H$^+$ and O$^+$ ions in five energy-per-charge ranges detected by CAMMICE/MICS plotted as a function of position in the magnetic equatorial plane.

The figure also shows maps of the equatorially-trapped O$^+$ ion flux as a function of position in the equatorial plane. The O$^+$ ions have the same spatial structures as the H$^+$ ions, but the energy spectrum at all locations is much softer. In the lowest energy range, the O$^+$ flux becomes comparable to the H$^+$ flux, or even dominant in some spatial bins. This figure illustrates the substantial low energy (1-5 keV) populations at L ~ 3.5-6 f for all local time sectors except dawn. In the midnight local time sectors these low energy components appear to extend to the outer boundary of the model at L ~ 10.
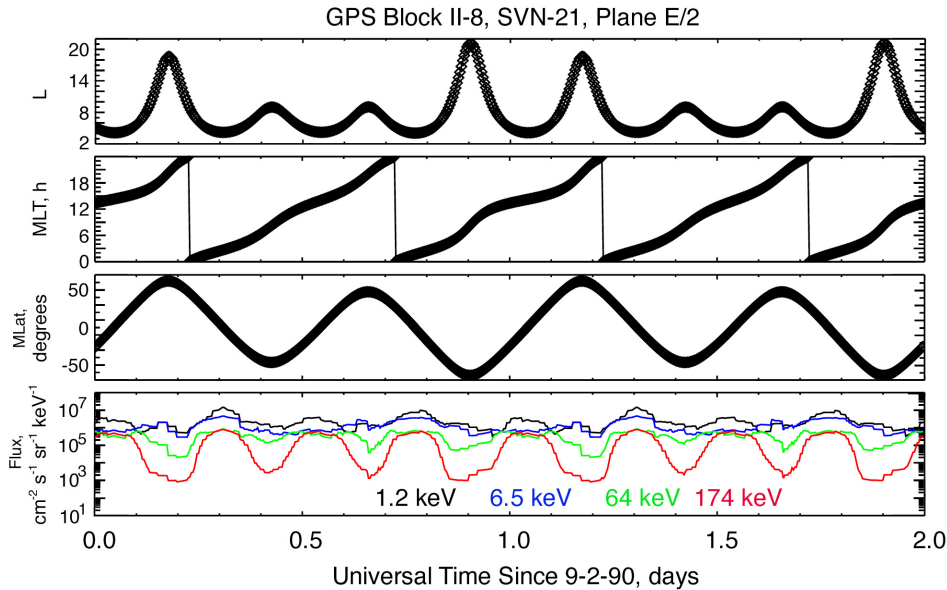
Figure 4. GPS satellite position and model H$^+$ flux variations for a representative two-day interval. The top three panels show the GPS satellite position in magnetic coordinates as L, magnetic local time in hours, and magnetic latitude in degrees. The bottom panel presents the average total ion flux for the GPS trajectory for four energy channels.

Hydra Model

The multiple detectors of the Hydra instrument provide full coverage of the all angles during each 6-s spacecraft spin period. So, a good estimate of the omni directional flux can be constructed by averaging the data from all detectors over any time interval longer than the spin period. The averages of the Hydra omni directional flux were averaged in a spatial grid of bins in the magnetic coordinates of L, magnetic local time, and magnetic latitude. The range and resolution of the grid are as follows: every 0.2 in L in the range 3.5–15; every 5º in magnetic latitude from –75º to 75º; and every hour in magnetic local time in the range 0000–2400. The energy resolution and range of the Hydra instrument vary with operating mode. To aid in interpretation, the model flux spectrum in each spatial bin was interpolated to a constant set of 10 logarithmically-spaced energy channels over the range 20 eV–15 keV.

Model Average Spectra

Using the CAMMICE/MICS and Hydra models, the average environment and its variation may be estimated for a satellite in any orbit that is sufficiently covered by the model range of L and magnetic latitude. We have computed the average particle spectra for several orbits in the GPS constellation and also for a geosynchronous orbit (GEO).

To compute the average flux spectrum for a given orbit we used the following procedure. The orbital elements were used to compute the evolution of the spacecraft position in Earth Centered Inertial (ECI) coordinates. The length of the time interval was chosen to assure unbiased coverage of local time and latitude. The time resolution of the position was selected to provide
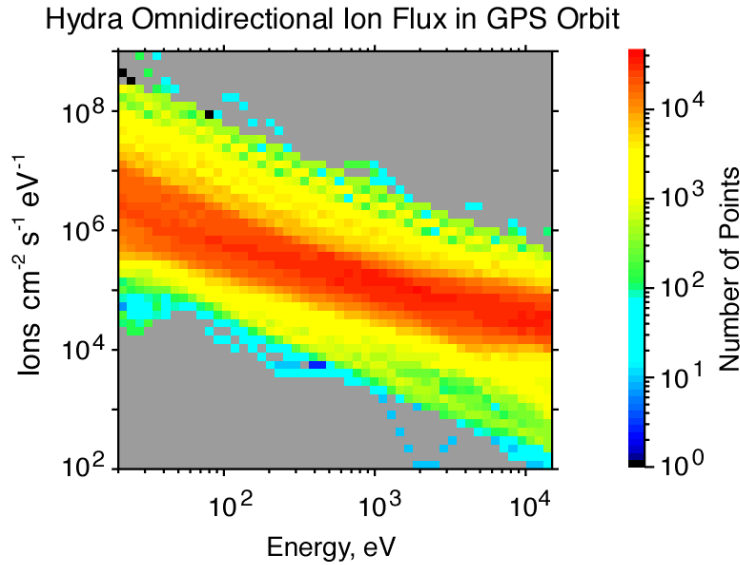
Figure 5. Ion flux measurements by the Hydra instrument on the Polar satellite averaged over the trajectory of a GPS satellite for a one-year interval.

spatial resolution comparable to, or finer than the particle models. For the GPS and GEO cases, we used 1-year intervals with the satellite position computed each minute.

The spacecraft ECI position and the Universal Time were used to compute the satellite position in the magnetic coordinates of L, magnetic latitude, and magnetic local time. These coordinates are then used to determine the model bin specifying the flux at that position. The omni directional flux spectrum at each position of the satellite was then obtained by a query to the Hydra model. The average spectrum over the orbit is the mean of these spectra at all the positions over the 1-year interval.

The CAMMICE/MICS model, in contrast to the Hydra model, is specified at the magnetic equator and these fluxes must be mapped to the satellite latitude to estimate the local environment. Such a mapping along the magnetic field line may be performed using only the ratio of the magnetic field magnitudes at the two locations. The IGRF empirical geomagnetic field model was employed to calculate the magnetic field magnitude at the satellite to the field magnitude at magnetic equator along the same field line. With the ratio of these two field magnitudes, we converted the average equatorial pitch angle distribution at each energy in the specified bin to the pitch angle distribution locally at the satellite latitude. The omni directional flux spectrum was then calculated by integrating the distributions over all local pitch angles for each energy channel. The omnidirectional spectrum was then averaged over all positions of the satellite, similar to the Hydra data.
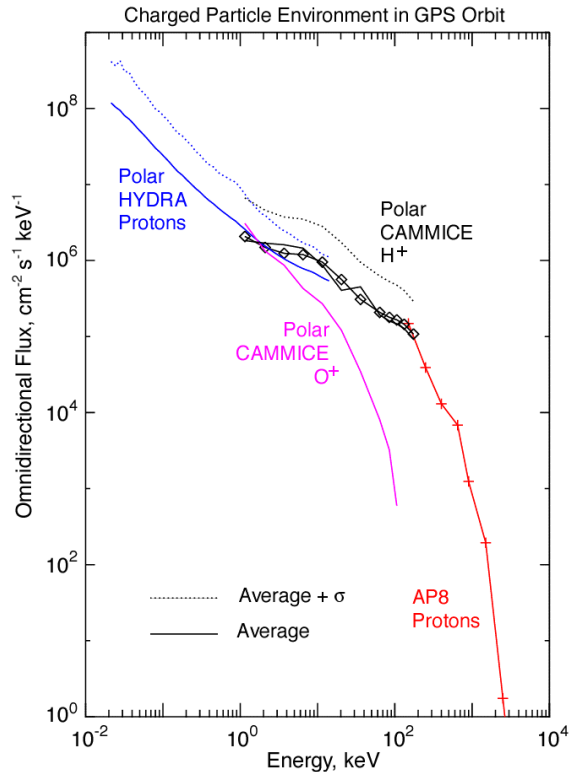
Figure 6. Average model omnidirectional differential number flux spectra of several species of ions experienced by a GPS spacecraft. Solid lines mark the average flux and dotted lines represent the average plus the standard deviation of the flux, respectively.

Figure 4 shows a portion of the data from the calculation of the orbital-averaged environment for the case of the GPS mission. This particular case is for the trajectory of the GPS Block II-8, SVN-21 in orbital plane E/2. The top three panels present the position of a GPS satellite in the magnetic coordinates of L, magnetic local time in hours, and magnetic latitude in degrees for an arbitrary 2-day interval. The satellite trajectory covered a range of ±70º in magnetic latitude and L ~ 3–21. All local times are covered and the magnetic equatorial crossings occur near the times of the minimums in L. The bottom panel shows the average total ion fluxes at four energies given by the CAMMICE/MICS model for these positions. At all energies the flux tended to maximize during the equatorial crossings and decreased at times when the satellite is at high values of L. The CAMMICE/MICS model covered the range L ~ 2–10 and we have chosen to set the flux for all positions for L > 10 to the model flux value at the outer boundary of L ~ 10. The flux at the outer boundary tended to be low and so this approximation does not affect significantly the orbital average. The orbital variation was almost three orders of magnitude at high energies and much less at the low energy channels.

The results of the Hydra orbital average calculation are shown in Figure 5. The plot displays the statistical variation of the ion spectrum as a function of energy in the range 20 eV–14 keV. The color of each pixel in the images represents the number of Hydra measurements recorded for each level of flux and energy. Due to the high time resolution of the Hydra instrument, the number of points for each energy is quite high. The relative standard deviation of the flux are in the range of ~100–200%, similar to the statistics of the CAMMICE/MICS data.
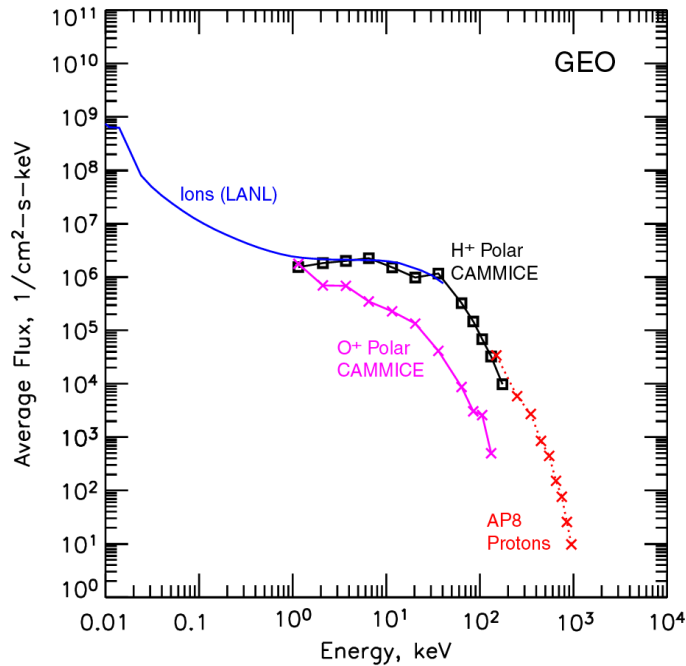
Figure 7. Average model omnidirectional differential number flux spectra of ions and electrons experienced by a spacecraft in geosynchronous orbit.

Figure 6 presents a summary of the model results for the particle environment in GPS orbit. The average omni directional flux spectra from the CAMMICE/MICS and Hydra models are compared with the output of the NASA radiation belt models. The solid lines represent the average flux and the dotted lines mark the sum of the average plus the standard deviation of the flux for each species. The color of the plotted lines identify the measured particle species: Hydra protons as a blue line, CAMMICE/MICS total ions as a black diamonds, CAMMICE/MICS H^+ as a black line, and CAMMICE/MICS O^+ as a magenta line. The protons from the NASA AP8 model averaged over the same orbit are plotted as a red line with crosses.

The plotted CAMMICE/MICS model spectrum for H^+ ions overlays the total ion spectrum within the limitations of statistics. This demonstrates that H^+ is the dominant ion species excepting energies of ~1 keV. The average ion flux spectrum measured by Hydra agrees with the CAMMICE/MICS result within a factor of two in the overlapping energy range of 1–14 keV. The NASA AP8 model provided an average spectrum of protons for energies of 100–3000 keV which is plotted as red crosses in the figure. It fits smoothly with the CAMMICE/MICS spectrum of H^+ ions at 100 keV. So we have constructed a reasonable estimate of the average ion proton flux spectrum in the GPS orbit over six orders of magnitude in energy. The dotted lines mark the sum of the average and the standard deviation of the flux from the CAMMICE/MICS and Hydra instruments. This provides an estimate of the flux variation averaged over the GPS trajectory.
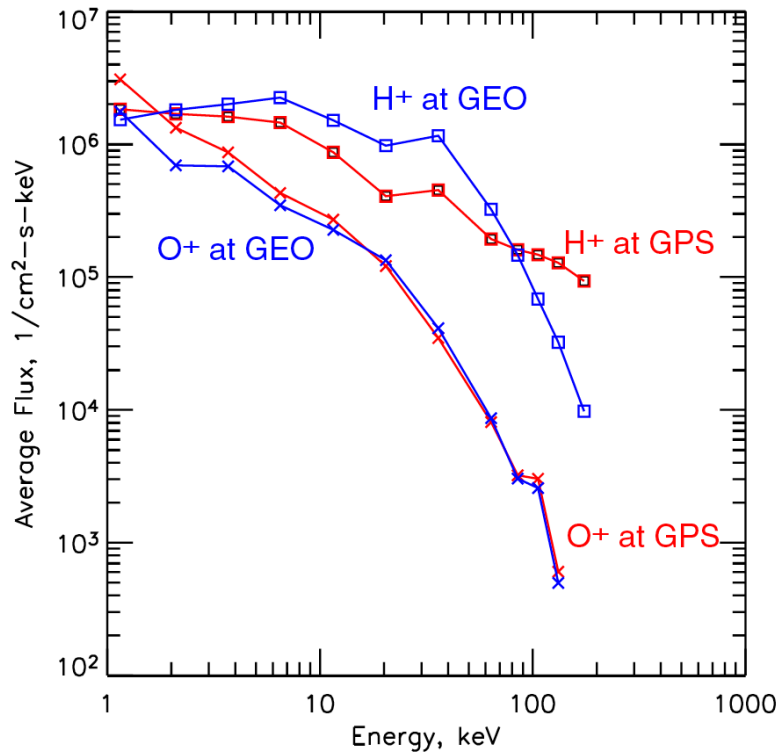
Figure 8. Average model omnidirectional differential number flux spectra of ions and electrons experienced by a spacecraft in geosynchronous and GPS orbit.

Figure 6 also shows that O^+ flux plotted in magenta becomes comparable to the H^+ flux at energy of 1–2 keV. At energy below 1 keV the oxygen ion flux is uncertain because the Hydra measurements cannot distinguish between different ion species. Similar calculations for other GPS orbital planes and phases exhibit differences of ~2% from these results.

The CAMMICE/MICS model has also been used to estimate the average particle environment of spacecraft in geosynchronous orbit (GEO). Figure 7 shows a summary of the average particle spectrum for GEO. The CAMMICE/MICS spectra are compared with the low energy ions and electrons from the LANL empirical model [Korth et al., 1999]. The LANL model was constructed using the data from the Magnetospheric Plasma Analyzer (MPA) on several geosynchronous spacecraft. The LANL model provides the ion flux at energies in the range 10 eV–31 keV as a function of the planetary magnetic index K_p, but with no mass or charge state information. The average ion spectrum at GEO was computed from the LANL model using the statistical distribution of Kp during 1996. Figure 7 shows that the LANL average ion spectrum matches the CAMMICE/MICS H^+ spectrum to within 50%. The CAMMICE/MICS H^+ spectrum also coincides very well with the proton estimate from AP8. The electron flux at from the LANL model matches the AE8 flux at 40 keV within a factor of two, but the slope of the spectrum is discontinuous at that energy.

Figure 7 also presents the CAMMICE/MICS average flux of O^+ ions for GEO as red crosses. It is not very different from the average O^+ spectrum in GPS orbit. This point is illustrated by

Figure 8, which compares the CAMMICE/MICS H^+ and O^+ average flux spectra for the two orbits. The GPS averages are plotted in red and the GEO averages are shown in blue.

Summary

A three-dimensional model of the average ion environment in the energy range 1–200 keV was constructed from 3.5 years of data from the CAMMICE/MICS instrument on the NASA Polar satellite. The model provides the average H^+ and O^+ ion flux as a function of energy and pitch angle for any equatorial spatial position in the range $L \sim 2$–10 and all magnetic local times. Using a magnetic field model, the angular distributions may be mapped to any magnetic latitude in the range $\pm 70º$. The mapped fluxes can then be integrated over all angles to obtain the omni directional ion flux spectrum as a function of the three-dimensional position in space. We have averaged the ion flux over GPS and geosynchronous orbits resulting in an estimate of the average ion environment for a satellite in those orbits.

For the case of the GPS orbit, the CAMMICE/MICS model has been compared to a similar model of six years of Hydra ion measurements in the energy range 0.02–14 keV. The Hydra model provides the average total omni directional ion flux as a function of energy for spatial position. The Hydra ion spectra were averaged over the GPS orbit for comparison to the CAMMICE/MICS model. Excellent agreement between the two models was achieved in the overlap energy range 1–14 keV. The average ion spectra in GEO estimated from the CAMMICE/MICS model also compared favorably with the average ion flux derived from the model of Korth et al. [1999].

At high energies the CAMMICE/MICS average ion spectra in GEO and GPS orbits was compared with estimates of the proton flux from the NASA AP-8 model. Good agreement was achieved between the models in the energy range 100–200 keV. Combining all the above models made possible an unprecedented estimate of the ion environment from 20 eV to 3 MeV.

At high energies (~100 keV) the flux estimates agree with corresponding estimates from the NASA AP-8 model, but the fluxes at low energies are larger than those extrapolated simply from AP-8. The CAMMICE/MICS model shows that H^+ dominates the >2 keV ion populations, but that the O^+ flux becomes comparable to the H^+ flux at ~1 keV. The standard deviation of both the ion and electron flux was found to be 100–200% of the average value over the entire considered energy range. The average 1–200 keV O^+ flux estimates for GEO appear very similar to the averages for GPS orbit, so that any material damage due to O^+ ions should be the same for the two orbits.

Acknowledgements

References

1. Acuna, M. H., K. W. Ogilvie, D. N. Baker, S. A. Curtis, D. H. Fairfield, and W. H. Mish, The global geospace science program and its investigations, Space Sci. Rev. 71, 5-21, 1995.

2. Blake, J. B., J. F. Fennell, L. M. Friesen, B. M. Johnson, W. A. Kolasinski, D. J. Mabry, J. V. Osborn, S. H. Penzin, E. R. Schnauss, H. E. Spence, D. N. Baker, R. Belian, T. A. Fritz, W. Ford, B. Laubscher, R. Stiglich, R. A. Baraze, M. F. Hilsenrath, W. L. Imhof, J. R. Kilner, J. Mobilia, D. H. Voss, A. Korth, M. Gull, K. Fisher, M. Grande, D. Hall, CEPPAD, Space Sci. Rev., 71, 531-562, 1995.

3. Hastings, D., and H. Garrett, Spacecraft-Environment Interactions, Cambridge University Press, Cambridge, United Kingdom, 1996.

4. Johnson, R. E., Energetic Charged-Particle Interactions with Atmospheres and Surfaces, Springer-Verlag, Berlin, Germany, 1990.

5. Kistler, L. M., F. M. Ipavich, D. C. Hamilton, G. Gloeckler, B. Wilken, G. Kremser, and W. Studemann, Energy spectra of the major ion species in the ring current during geomagnetic storms, J. Geophys. Res., 94, 3579-3599, 1989.

6. Koga, R., S. S. Imamoto, N. Katz, S. D. Pinkerton, Data processing units for eight magnetospheric particle and field sensors, J. Spacecraft and Rockets, 29, 574-579, 1992.

7. Korth, H., M. F. Thomsen, J. E. Borovsky, and D. J. McComas, Plasma sheet access to geosynchronous orbit, J. Geophys. Res., 104, 25047-25061, 1999.

8. Milillo et al., An empirical model of the ion distributions in the equatorial inner magnetosphere, Phys. Chem. Earth, 24, 209-214, 1999.

9. Milillo et al., Empirical model of proton fluxes in the equatorial inner magnetosphere: development, J. Geophys. Res., 106, 25713-5729, 2001.

10. Nastasi, M., J. W. Mayer, and J. K. Hirvonen, Ion-solid interactions: fundamentals and applications, Cambridge University Press, Cambridge, United Kingdom, 1996.

11. Russell, C. T., R. C. Snare, J. D. Means, D. Pierce, D. Dearborn, M. Larson, G. Barr, and G. Le, The GGS/Polar magnetic fields investigation, Space Sci. Rev., 71, 563-582, 1995.

12. Schulz, M., and L. J. Lanzerotti, Particle Diffusion in the Radiation Belts, Springer-Verlag, Berlin, Germany, 1974.

13. Scudder, J., F. Hunsacker, G. Miller, J. Lobell, T. Zawistowski, K. Ogilvie, J. Keller, D. Chornay, F. Herrero, R. Fitzenreiter, D. Fairfield, J. Needell, D. Bodet, J. Googins, C. Kletzing, R. Torbert, J. Vandiver, R. Bentley, W. Fillius, C. McIlwain, E. Whipple, and A. Korth, Hydra-a 3-dimensional electron and ion hot plasma instrument for the polar spacecraft of the GGS mission, Space Sci. Rev., 71, 459-495, 1995.

14. Vette, J. J., The NASA/National Space Science Data Center Trapped Radiation Model Program (1964-1991), NSSDC World Data Center A for Rockets and Satellites, Report Number 91-29, November 1991.

15. Wilken, B., W. Weiss, D. Hall, M. Grande, F. Sorass, J. F. Fennell, Magnetospheric ion composition spectrometer onboard the CRRES spacecraft. J. Spacecraft and Rockets, 29 585-591, 1992.

INNER RADIATION BELT REPRESENTATION OF THE ENERGETIC ELECTRON ENVIRONMENT: MODEL AND DATA SYNTHESIS USING THE SALAMMBO RADIATION BELT TRANSPORT CODE AND LOS ALAMOS GEOSYNCHRONOUS AND GPS ENERGETIC PARTICLE DATA

R. H. W. Friedel
Los Alamos National Laboratory, Los Alamos, NM, USA

S. Bourdarie
ONERA/DESP, Toulouse, France

J. Fennell
The Aerospace Corporation

S. Kanekal
Catholic University of America

T. E. Cayton
Los Alamos National Laboratory

Abstract

The highly energetic electron environment in the inner magnetosphere (GEO inward) has received a lot of research attention in resent years, as the dynamics of relativistic electron acceleration and transport are not yet fully understood. These electrons can cause deep dielectric charging in any space hardware in the MEO to GEO region. We use a new and novel approach to obtain a global representation of the inner magnetospheric energetic electron environment, which can reproduce the absolute environment (flux) for any spacecraft orbit in that region to within a factor of 2 for the energy range of 100 KeV to 5 MeV electrons, for any levels of magnetospheric activity. We combine the extensive set of inner magnetospheric energetic electron observations available at Los Alamos with the physics based Salammbo transport code, using the data assimilation technique of "nudging". This in effect input in-situ data into the code and allows the diffusion mechanisms in the code to interpolate the data into regions and times of no data availability. We present here details of the methods used, both in the data assimilation process and in the necessary inter-calibration of the input data used. We will present sample runs of the model/data code and compare the results to test spacecraft data not used in the data assimilation process.

Introduction

The natural energetic electron environment in the Earth's radiation belts is of general importance as dynamic variations in this environment can impact space hardware in those regions and contribute significantly to background signals in a range of other instruments flown in that region.

The interest in these events arises in part because of the increasing evidence of the

correlation between the occurrence of these fluxes and of subsequent spacecraft operating anomalies or failures, especially at geosynchronous altitude. The prediction and mitigation of these effects should be possible when the causes of the flux buildups are under-stood [*Baker*, 1996]. In addition, because of the apparent complexity of these mechanisms, their understanding will contribute significantly to the general knowledge of transport and heating processes in the magnetosphere.

There is intense interest in isolating and understanding the mechanisms that contribute to the frequently observed MeV electron flux buildups in the outer magnetosphere, which is frequently observed during the recovery phase of geomagnetic storms.

While this is not a new topic, the unprecedented density of observations of relativistic electrons in the inner magnetosphere in the modern era has led to new questions and unsolved problems. In a recent review, *Friedel et al.* [2002] covers in detail the current state of research into this topic.

The scientific community is engaged in understanding the underlying physics to the observed dynamics; however, the question that is of most importance to spacecraft operators that are faced with an anomaly on a spacecraft is: "Was my anomaly due to the environment?" To answer this question one needs to be able to accurately describe the environment at any point in the inner region, *even in the absence of in-situ measurements*.
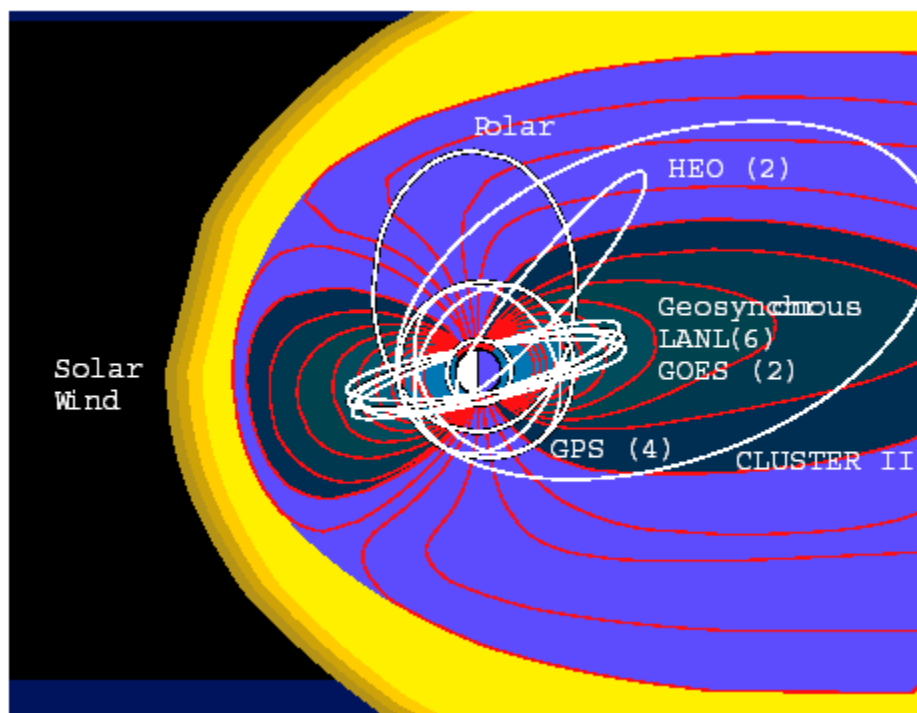
Figure 1. Schematic of current inner magnetosphere missions.

Data from any single point measurement in space has traditionally been used to derive information about the local environment at that satellite. There have been some earlier attempts of obtaining a dynamic global state of the inner magnetospheric electron populations based on single spacecraft observations *Friedel and Korth* [1995], based on the CRRES data, our community's last mission dedicated to the radiation belts. CRRES alone, on a 5.5 hour resolution, was able to provide a basically complete description of the inner region, across a wide eenergy range - due to it's ideally suited geosynchronous transfer orbit. However, CRRES flew in 1990/1991, and one has to look to other resources for such information today. *Friedel et al.* [1998] used a multi-spacecraft synthesis using simple interpolation techinque with data from up to 11 spacecraft to assemble a "map" of the inner radiation belt energetic electron population. This simple approach led to radiation belt maps that could represent the dynamics of the inner region on around a 3 hour time scale, but the simplistic interpolation and intercalibration scheme employed led to many unrealistic local time and radial variations which were clearly not physical but rather a reflection of insufficient instrument characterization.

In order to characterize this environment energetic particle detectors have routinely been flow on a range of DOE, NOAA and DOD spacecraft in geosynchronous, GPS and Moulniya orbits. Beyond these programmatic missions, this region has also been the subject of purely scientific investigations with current missions such as CLUSTER (ESA), POLAR (NASA). A schematic of the orbits of these missions available today is shown in Figure 1.

While the scientific measurements can provide the full three-dimensional particle distribution function and local magnetic field data (allowing data to be determined at constant adiabatic invariants, which are the coordinates that allow data to be inter-compared throughout the inner magnetosphere), these data are not available on long time scales or on a reliable basis into the future, and, when present, have a limited spatial coverage by themselves.

Data from the programmatic missions provides excellent time coverage, longevity and spatial coverage, but with particle instrumentation that provides omni-directional data and no magnetic field information.

The challenge is thus to utilize the available data in a framework that still allows us to retrieve high fidelity global maps of the inner radiation belts. Our approach here is a synthesis between multiple point space measurements and a physics based radiation belt model that makes full use of all the data from our current constellation of energetic electron measurements in space (up to 6 simultaneous geosynchronous and 4 simultaneous GPS orbit measurements) and uses the model to provide a physical interpolation between the data. The end result is a dynamic and global model of the energetic electron radiation environment at all points in space, which can provide reliable environmental data for locations of satellites that do not carry any energetic particle instrumentation.

Data for our assimilation at this point comes primarily from the LANL Geosynchronous ESP instrument [*Reeves et al.*, 1997]; the LANL GPS energetic particle sensors [*Feldman et al.*, 1985]. For testing purposes we also use data from the HEO energetic particle instruments [*Blake et al.*, 1997].

The Model

We use here a custom version of the SALAMMBO radiation belt code developed by our collaborators at ONERA in Toulouse, France [*Beutier and Boscher*, 1995; *Bourdarieet al.*, 1996b; *Boscher et al.*, 2000]. This is a diffusion code that models physical processes in the inner magnetosphere by their respective diffusion coefficients (radial and pitch angle diffusion). A schematic of this code is shown in Figure 2.

This code used the planetary disturbance index Kp to parameterize radial diffusion and the position of the plasmapause which controls wave activity and thus pitch angle diffusion. The code is symmetrical in local time since on a given drift orbit particle fluxes are the same at all local times on timescales on the order of the drift time, which is typically around 10 minutes for the highly energetic electrons. The code traces the full particle distribution function in the coordinate space of L* (magnetic coordinate of the drift shell), B/Bo (the ratio of the local magnetic field strength to the equatorial magnetic field strength on a given magnetic field line) pitch angle and energy.

The code has successfully been used to model the response of the inner magnetospheric energetic electron population to geomagnetic storms [*Bourdarie et al.*, 1996a]. Recent work by *Summers et al.* [1998] pointed out the importance of energy diffusion by whistler mode waves for relativistic electrons as being an important energization source, and *Meredith et al.* [2002] have shown a direct relation- ship between relativistic electron acceleration and substormenhanced whistler mode chorus. This physics is currently not included in the Salammbo code. As it turns out, our data assimilation can compensate for this: inclusion of relevant amounts of data "pulls" the code in the right direction, even in the absence of this missing physics.

Data preparation

In response to the lessons learned by *Friedel et al.* [1998] a large amount of effort was devoted processing our data to a level that made inclusion into a model feasible. Models in general have no way of distinguishing between "good" and "bad" data - garbage in simply leads to garbage out. early assimilation runs suffered from stability problems arising from importing data that was wildly different from the model representation. It was necessary to interpolate and clean up the data to a high degree of fidelity before any import of the data into the model was attempted. This effort alone took almost 4 Friedel et al. 2 years. Here we present a brief outline of the procedures adopted.

Inter-calibration

It was decided to boot-strap out data to the last high- fidelity energetic particle instrument flown in the inner magnetosphere, the MEA instrument [*Vampola et al.*, 1992] on board CRRES. This was a magnetic spectrometer with full anti-coincidence electronics that does not suffer some of the background and noise problem encountered on the LANL GEO, GPS and HEO instruments. Using the overlapping time periods between CRRES and LANL GEO and GPS missions, we could inter-calibrate those missions to agree with the CRRES measurements. This

required the definition of conjunctions between two spacecraft. In order to obtain a sufficient number of conjunctions, we used the following set of conditions (see Figure 3).

- $L < 6$ and $\Delta L < 0.1$
- $\Delta B / D_{EQ} < 0.1$
- Magnetic local time (MLT) within 2 hours of 06:00 and 18:00 and $\Delta MLT < 0.15$
- Magnetospheric activity quiet ($Kp < 2$ for two days before conjunction
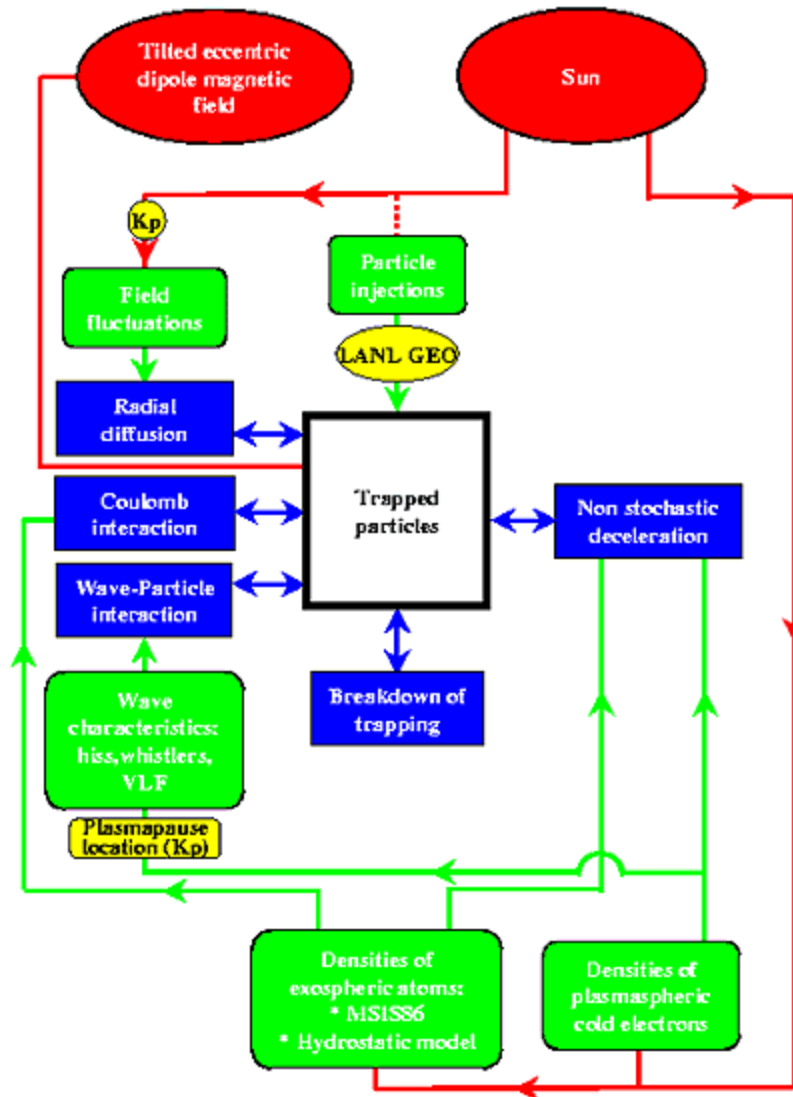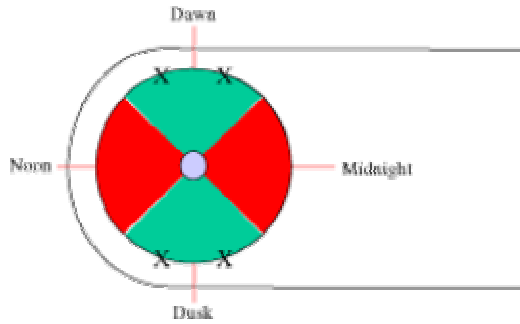- $\Delta t < 3$ hours

Figure 2. Schematic the Salammbo radiation belt code for Electrons

Figure 3. Schematic showing the green region of "allowed" Conjunctions

The restriction in local time is due to the use of model magnetic fields in obtaining the required model coordinates (L*), which are best in these regions. The low activity requirement allows us to relax the time constraint on conjunctions; this allows us to obtain more conjunction points.

Since GEO and GPS can never fulfill the conjunction requirements used here, they were both independently calibrated against CRRES, which has conjunctions with both.

Figure 4 shows our resulting inter-calibration between LANL geosynchronous and CRRES data, showing an excellent match. Figure 5 shows the result of inter-calibrating CRRES with GPS ns18. For the GPS spacecraft, the energy thresholds are gain dependent; the red triangles show the raw, uncorrected data and the black crosses the new spectra after adjusting the energy thresholds to match the CRRES spectra.
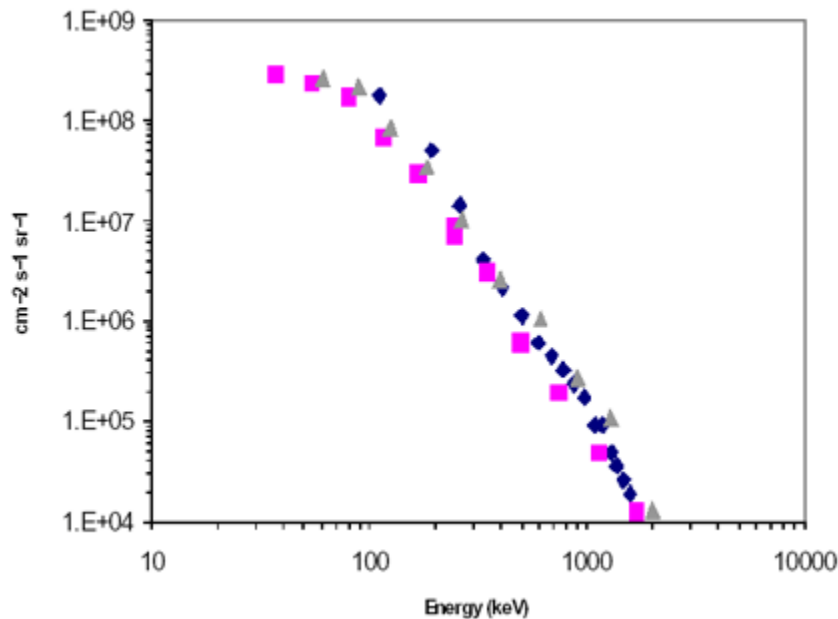
Figure 4. Matching spectra between CRRES and two LANL GEO spacecraft in September 1990

Once these calibrations had been done the calibrations were propagated forward in time by matching overlapping Data assimilation with the Salammbo code 5 GEO and GPS data. In this way a consistent set of intercalibration data for all GPS and GEO spacecraft could be found to the present. Our best estimate of the accuracy of this intercalibration is that on average the calibration is good to within a factor of 2.

The details of this calibration procedure can be found in a 60-page document available at http://nis-www.lanl.gov/friedel/lws_proj/GPS_calibration_2002.doc.
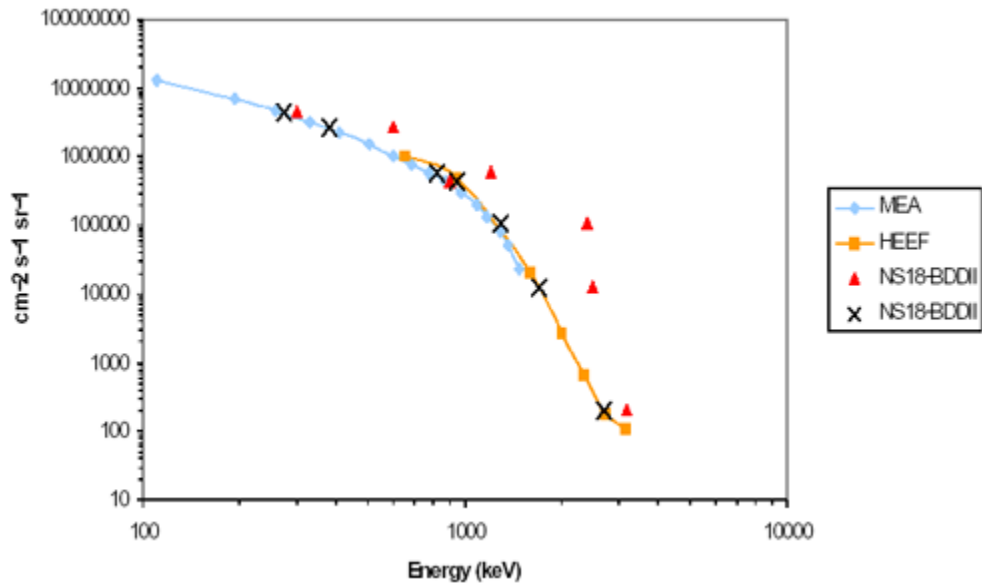
Figure 5. Matching spectra between CRRES and GPS ns18 spacecraft in September 1991

Data contamination

It is well known that during times of solar energetic proton events (SEPs) many of the detectors used here are contaminated with strong background counts. We use the NOAA GOES energetic proton data to mask out our data during such active times, by monitoring a threshold flux of $10^{-5}cm^{-1}s^{-1}sr^{-1}keV^{-1}$ on the 39–65 MeV proton channel. During times when this threshold is exceeded we to not assimilate any data into out model but allow the model to run freely.

Saturation / background

Data saturation occurs in some instruments as a limit of counting speed during high count intervals, leading to an artificial plateau in observed counts. These levels are statistically observable and we can ensure that only those data below saturation levels are used in the assimilation process.

Background levels due to thermal noise or other contamination such as cosmic rays are present in all particle instruments. These levels can be detected by examining data during intervals when the spacecraft are outside the trapping region for energetic electrons, this occurs over the polar cap on open field lines for GPS and during extreme magnetospheric compression

events for the geosynchronous regions. We detect and track these background counts over time and subtract these counts before using the data in our assimilation.

Data Assimilation Techniques

This model has been tightly integrated into our data system at LANL, and allows us to input data from various spacecraft sources directly into the model grid. The difference here is that the model no longer uses a simple boundary condition, but allows direct input into the code grid at any location for which data is available. This corresponds to the data assimilation method of "nudging".

Data input

In order to seed the code with real data the data has to be transformed into the model coordinate space. The Salammbo code internally uses a custom spaced grid in energy, pitch angle and L*. L* here corresponds to the third adiabatic invariant and is closely related to a particle's drift shell. For energetic particles for which electric field drifts can be ignored, L* almost exactly labels the drift shell a real particle follows.

Due to the nature and limitations of the data used the determination of this mapping requires some assumptions:

- L* depends on a magnetic field model. At this stage of our assimilation work we use the same model for all data - the static Olson Pfizer 1977 model. Extensions to more complex and dynamic models are planned.
- Current data sources provide omni-directional data and no magnetic field information. We thus use a statistical representation of pitch angle distributions as a function of L* derived from CRRES data. This is overwritten at times when we are able to determine the pitch angle distribution directly from data (see Figure 6): whenever there are "conjunctions" in the input data (satellites at the same L* but at different magnetic latitudes) we use a fitting procedure to derive the best fit to a pitch angle distribution that yields the observed omni-direction data at the two latitudes. Such "measured" pitch angle distributions override the statistical distributions with a persistence of one hour.
- Energy channels are interpolated to the required grid energy values. Measurements are assigned to the two closest grid points in L weighted according to their distance from the grid point, to ensure smooth data insertion.
- The outer boundary of the simulation is at L*=9. The value of this boundary is either set the AE8 model 6 Friedel et al. value at L=9 [*Vette*, 1991] or when GEO data is available to the geosynchronous data values adiabatically shifted to L*=9.
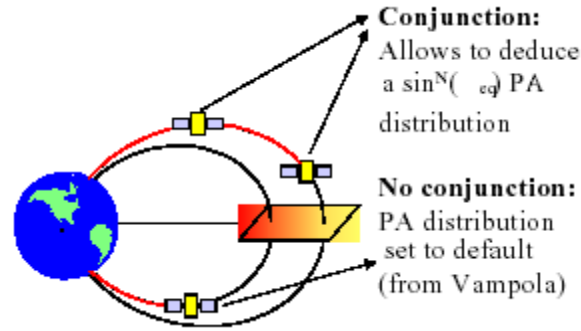
Figure 6. Schematic of model "conjunctions" allowing determination of pitch angle distribution from omni-directional data.

We need to point out here that the methods described here represent out first approach and are constantly being re-fined. As the model evolves (finer grid spacing) and our data evolves (inclusion of pitch angle sorted data from LANL GEO, POLAR and CLUSTER) our assimilation techniques will become more complex.

In a general run input data thus transformed is entered into the grid for the locations and times available, and the model is allowed to act for all other periods and locations.

Model output

The output of the Salammbo code is a time series of states in model coordinates that define the global inner radiation belt for energetic electrons in L* (1.1 to 8). The time resolution currently is 10 seconds.

Once a model run for a given set of input data for a given period has been performed, we can "fly" any required spacecraft orbit through the model grid. All we need to do is to transform any satellite ephemeris to the required magnetic coordinates of the model grid and specify which energy we want. The model can return data either in differential or integral energy flux, either pitch angle resolved or summed to give an omni-directional equivalent.

First Results

An initial run was performed for the period of one of the NSF GEM storm of September 1 - October 10, 1998. The model was run with the correct Kp values for this period, and data was assimilated into the model from one geosynchronous satellite (LANL-GEO 1994 084) and one GPS satellite (ns33). The model output at one time step is shown in Figure 7.

In order to assess model performance we used several test satellites that were "flown" through the model results. We then compared the model fluxes versus the actually measured fluxes on the test satellites.

Model + LANL GEO, HEO as test

Here we performed ouR model run using ONLY the LANL GEO data as input. The results are shown in Figure 8. The model is initialized with a default state at the beginning of the run representing an average quiet magnetosphere, taken from CRRES measurements.

HEO data is used as a test: At this point HEO HAS NOT been fully inter-calibrated with GEO and GPS. Initial com- parisons however show that for the energy range chosen in our comparisons here, agreement between HEO, GPS and GEO is generally good.
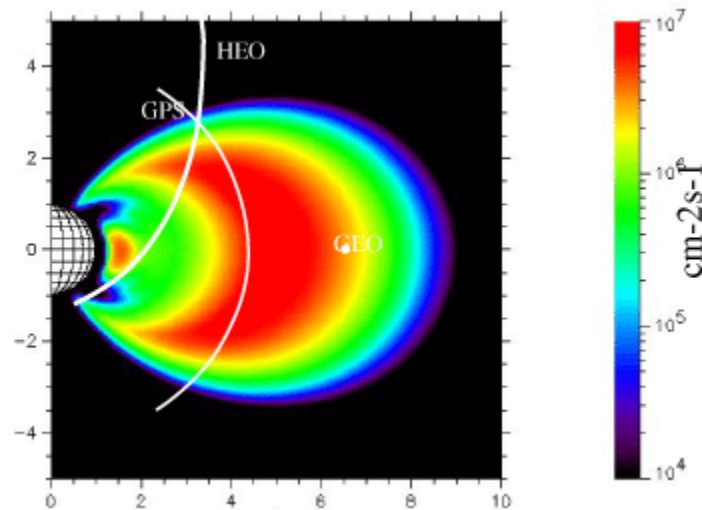
Figure 7. A graphical representation of the model fluxes at one time step in the simulation. Shown superimposed are the orbits of lANL GEO and GPS and HEO (used for testing output only)

The description of Figure 8 also applies to Figures 9 and 10. The top three panel show data in the L* versus time format, where each color coded vertical bar in the plot represents the flux along the satellites cut through L at this time. The top panel shows the actual HEO-2 satellite data for the ¿0.63 MeV channel. The next panel shows the model output along the orbit on HE0-2; both these panels share the same color bar. The third panel shows the ratio model divided by data, and the color bar represents ratios up to 10 in yellow/ red graduations and ratios down to 0.1 in blue/dark blue graduations. The bottom panel shows the Dst storm index for reference.

Ideally, if model and data agree 100 %, this ratio should be 1 (black). Here we see large deviations from 1 in two areas: the outer belts near GEO and the inner region near the slot. The first discrepancy can be explained in terms of the missing model physics as described earlier: whistler chorus interactions are not yet modeled, and in the absence of any assimilation data inside of geosynchronous that helps define the GEO pitch angle distributions. HEO has a highly elliptical orbit and cuts through GEO at high latitude – obviously the statistical pitch angle representation is not a good one for this time period. The discrepancy at low L is simply due to wrong initial state and short model run: diffusion is extremely slow in this region and we simply observe a persistence of the initial state.
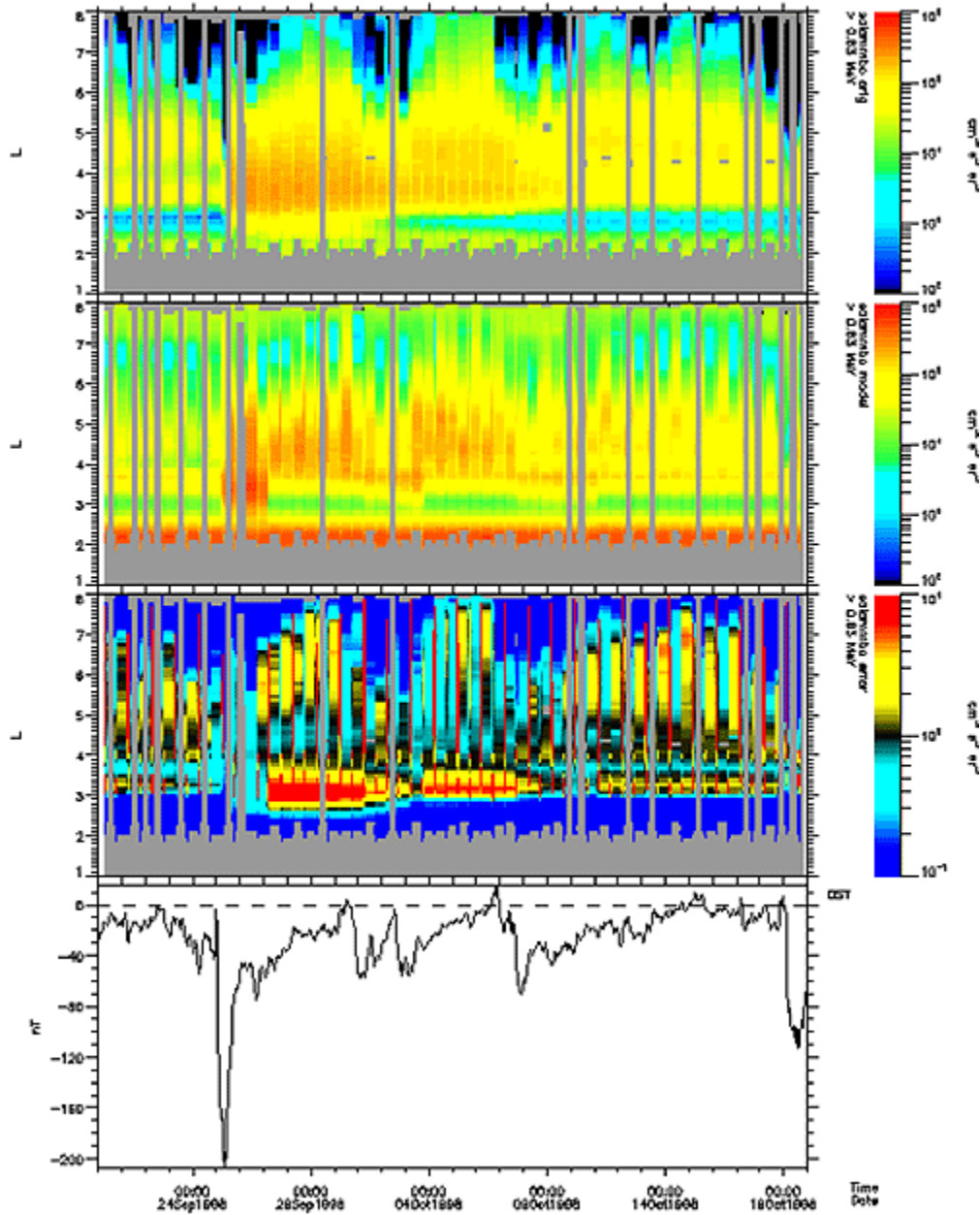
Data assimilation with the Salammbo code
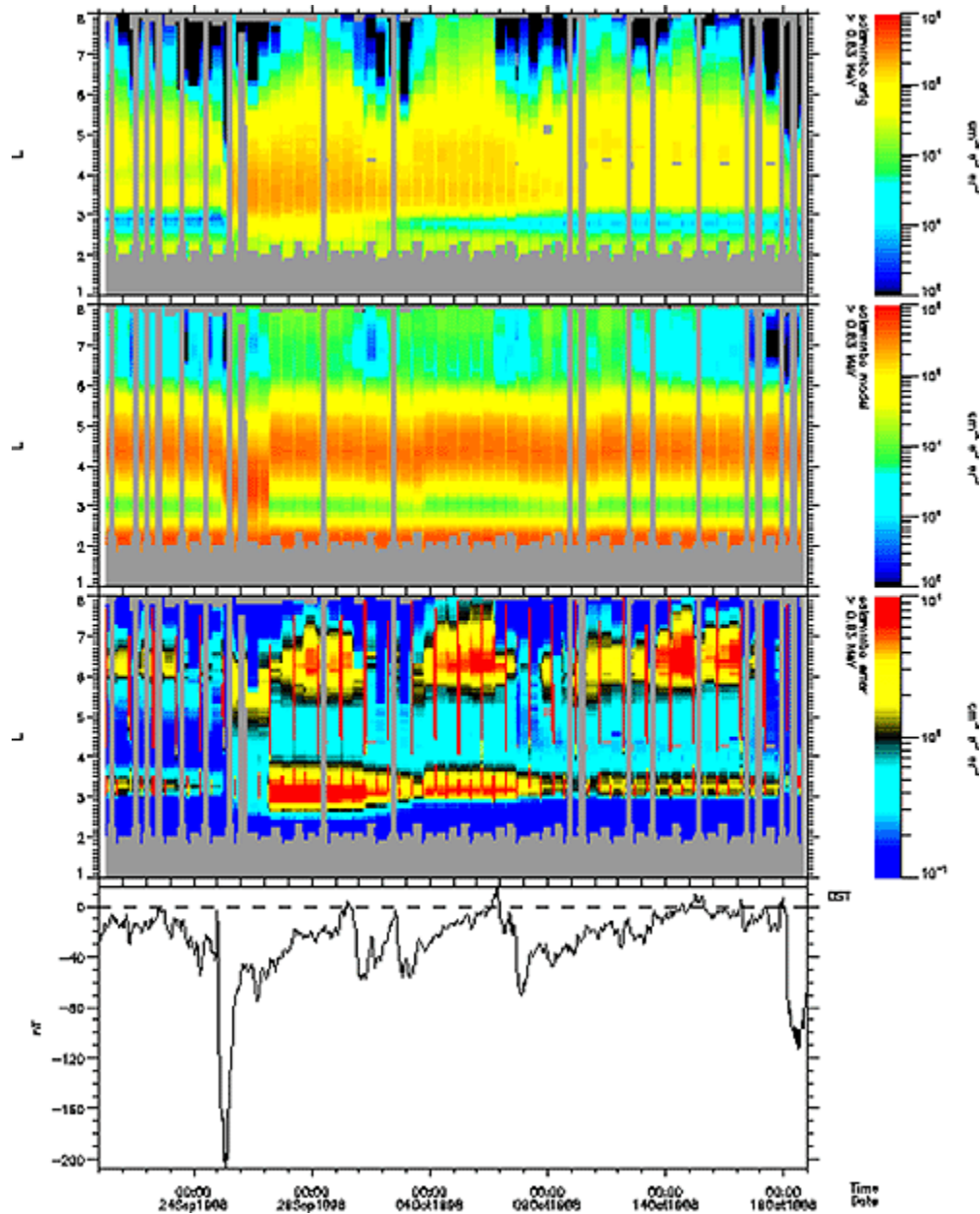
Figure 8. Data, model and comparison outputs. See text for details.

Model + LANL GEO + GPS, HEO as test

This model run uses both the LANL GEO and GPS data as input, which assimilates data into the region down to L=4. The results are shown in Figure 9.

As a quick visual comparison between Figures 8 and 9 easily shows the model performance is much improved by the inclusion of just one additional satellite in the assimilation process. This

is particularly true for the region which is now covered by data input - GPS data is available from L=4 outward, and in that region the model /data comparison shown mainly black and light yellow indicating performance of model to within a factor of 2-3 of the data. Inclusion of GPS around L=4 to 5 compensates for the missing physcis in the region, while near geo it helps to properly define the pitch angle distribution which is needed to correctly estimate the fluxes at the high latitudes of HEO. The inner region remains badly represented here since no additional satellite data was used there. The addition of low altitude data from SAMPEX will help out in this region.

Figure 9. Data, model and comparison outputs. See text for details.

Model + LANL GEO + GPS, another GPS as test

This model run uses both the LANL GEO and GPS ns33 data as input, but uses another GPS satellite, ns24 as the test satellite. The results are shown in Figure 10.
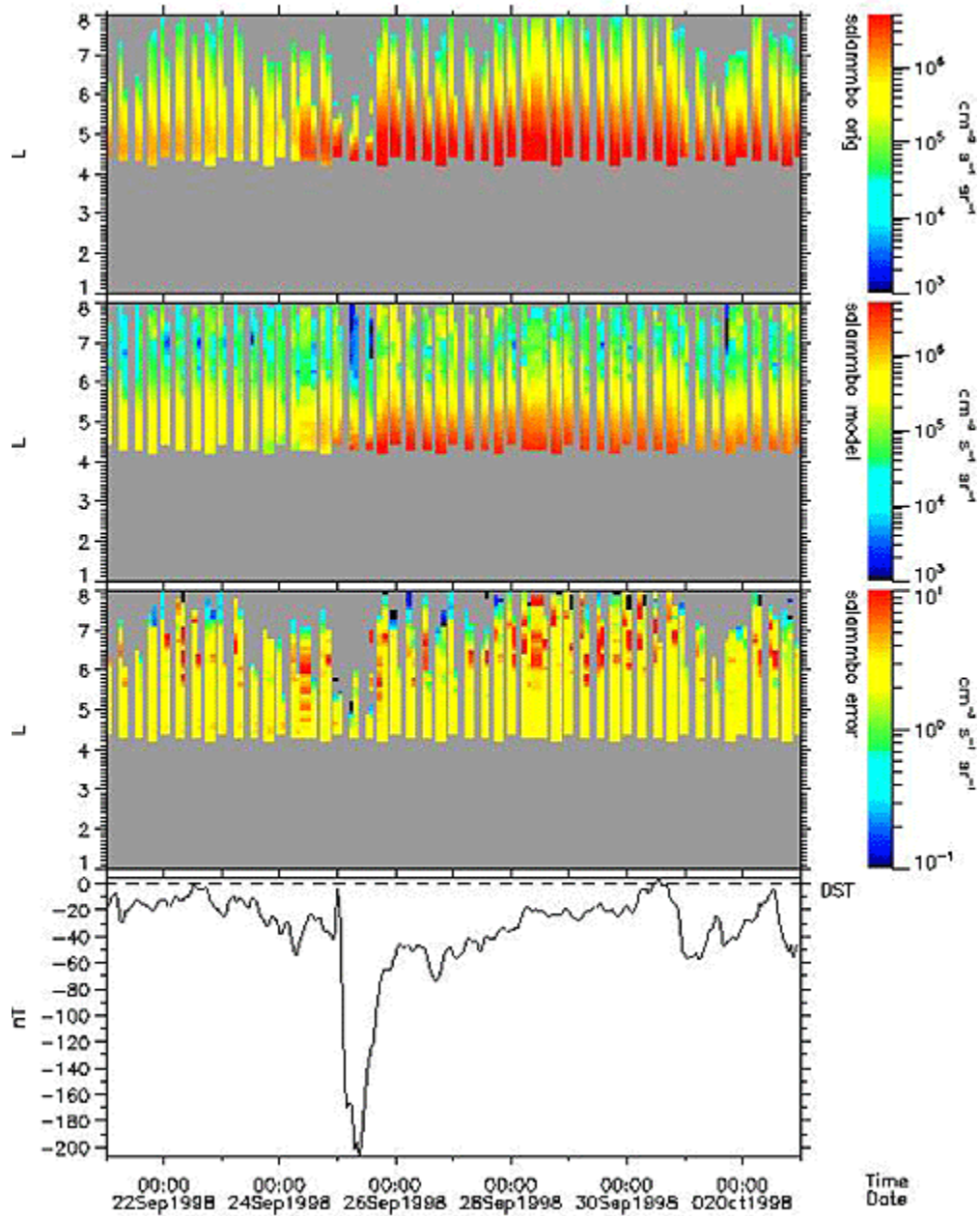
Figure 10. Data, model and comparison outputs. See text for details.

Not surprisingly the model data comparison shows consistent ratios of 2-3 throughout the whole period, regardless of activity levels. This is expected as the region tested is also the region seeded with assimilation data. What the residual ratios of 2-3 however indicate is that this is about as good as we can hope to get with this method. Factors of 2-3 represent the fidelity of our original data intercalibration.

Summary

This project is in its initial stages and a lot of further fine tuning of the assimilation method and input data is needed. First results however are promising. We are confident that for spacecraft orbits in the MEO to GEO orbital range we can reproduce the real environment with this method to 10 Friedel et al. within factors of 2-3.

We will extend our model further to include as many data sources as possible, especially at lower altitudes. It must be noted that before further data can be incorporated a similar intercalibration effort as done fro GEO and GPS needs to be undertaken for HEO, POLAR, SAMPEX and CLUSTER. Further, once pitch angle resolved input data is being used from GEO, POLAR and Cluster our data assimilation methods need to be upgraded to correctly map the data into the model, as shell splitting effects in real magnetic fields need to be taken into account.

We anticipate using this model/data synthesis both for research and for Space Weather now-casting (limited by realtime data availability, currently not possible for GPS). For research, having this model "specify" the real environment we can then run the model in a not assimilative mode to see what physics is missing/under-represented. For Space Weather, we can specify the environment for any past time time going back approximately one solar cycle, which is required for any post-event anomaly analysis.

Further, we can use this model to explore exactly what kinds of data and data locations are needed for optimal input that would increase the fidelity of the model.

Acknowledgments.

References

1. Baker, D. N., Solar wind-magnetosphere drivers of space weather, J. Atmos. Terr. Phys., 58, 1509–1525, 1996.

2. Beutier, T., and D. Boscher, A three-dimensional analysis of the electron radiation belt by the salammbˆo code, J. Geophys. Res., 100, 14,853–14,861, 1995.

3. Blake, J. B., D. N. Baker, N. Turner, K. W. Ogilvie, and R. P. Lepping, Correlation of changes in the outer-zone relativisticelectron population with upstream solar wind and magnetic field measurements, Geophys. Res. Lett., 24, 927–929, 1997.

4. Boscher, D., S. Bourdarie, R. M. Thorne, and B. Abel, Influence of the wave characteristics on the electron radiation belt distribution, Adv. Space Res., 26 (#1), 163–166, 2000.

5. Bourdarie, S., D. Boscher, T. Beutier, J. A. Sauvaud, and M. Blanc, Magnetic storm modeling in the Earth's electron belt by the salammbo code, J. Geophys. Res., 101, 27,171–27,176, 1996a.

6. Bourdarie, S., D. Bosher, T. Beutier, J. A. Sauvaud, M. Blanc, and R. H. W. Friedel, A physics based model of the radiation belt flux at the day timescale, in Proceedings of the Symposium on Environment Modelling for Space-Based Applications, SP-392, pp. 159–163, ESA, ESA Publications Division, ESTEC, Noordwijk, The Netherlands, 1996b.

7. Feldman, W.,W. Aiello, D. Drake, and M. Herrin, The BDD II: An improved electron dosimeter for the global positioning system, Tech. Rep. LA-10453-MS, Los Alamos Natl. Lab., Los Alamos, N. M., 1985.

8. Friedel, R. H.W., and A. Korth, Long-term observations of keV ion and electron variability in the outer radiation belt from CRRES, Geophys. Res. Lett., 22, 1853–1856, 1995.

9. Friedel, R. H. W., G. D. Reeves, and T. Obara, Relativistic electron dynamics in the inner magnetosphere – a review (online pdf version), J. Atmos. Terr. Phys., 64, 2002.

10. Friedel, R. H. W., et al., A multi-spacecraft synthesis of relativistic electrons in the inner magnetosphere using LANL, GOES, GPS, SAMPEX, HEO and POLAR, Adv. in Space Res., 1998.

11. Meredith, N., R. B. Horne, R. Iles, R. M. Thorne, D. Heyndericks, and R. A. Anderson, Outer zone relativistic electron acceleration associated with substorm-enhanced whistler mode chorus, J. Geophys. Res., 107, 1144–1144, 2002.

12. Reeves, G. D., R. D. Belian, T. C. Cayton, M. G. Henderson, R. A. Christensen, P. S. McLachlan, and J. C. Ingraham, Using Los Alamos geosynchronous energetic particle data in support of other missions, in Satellite-Ground Based Coordination SourceBook, edited by M. M.Lockwood and H.J.Opgenoorth, pp. 263–272, ESA Publications, ESTEC, Noordwijk, The

Netherlands,1997.

13. Summers, D., R. M. Thorne, and F. Xiao, Relativistic theory of wave-particle resonant diffusion with application to electron acceleration in the magnetosphere, J. Geophys. Res., 103, 20,487– 20,500, 1998.

14. Vampola, A. L., J. V. Osborne, and B. M. Johnson, CRRES magnetic electron spectrometer AFGL-701-5A (MEA), J. Spacecr.Rockets, 29, 592–594, 1992.

15. Vette, J. I., The NASA/National Space Science Data Center Trapped Radiation Environment Model Program (1964–1991), Tech. Rep. NSSDC/WDC-A-R & 91-26, Goddard Space Flight Center, NASA/GSFC, Greenbelt, USA, 1991.

16. R. H. W. Friedel, T. E. Cayton Los Alamos National Laboratory, P.O. Box 1663, Los Alamos, NM 87545 (tcayton@lanl.gov; rfriedel@lanl.gov) This preprint was prepared with AGU's LATEX macros v5.01, with the extension package 'AGU__' by P.W. Daly, version 1.6b from 1999/08/19.

ASSIMILATIVE FORECASTING OF THE ENERGETIC PARTICLE ENVIRONMENT

S. Naehr
Department of Physics and Astronomy
Rice University
6100 Main Street, Mail Stop 108
Houston, TX 77005
Phone: (713) 348-2408
E-mail: **naehr@rice.edu**

F. Toffoletto
Rice University

Abstract

We present a computational approach to specifying and forecasting the outer radiation belt particle distribution, by incorporating data from space-based measurements. In this approach, a Kalman-Bucy filter is designed to assimilate particle flux data from a spacecraft spanning a broad range of particle drift paths. A spatial analysis algorithm is used to incorporate this data into the framework of a physics-based forecast model, using the statistical error structures of the model and data to produce an optimal estimate. The assimilation algorithm is validated in a set of experiments simulating a magnetic storm, using artificial magnetic field and particle flux data fabricated by an independent model. The simulated data is compared to the model over the entire modeling region at each time step, providing a global assessment of the model's accuracy over the course of dynamically active period.

Introduction

Our ability to forecast the environment of energetic particles trapped within the Earth's magnetosphere is limited by our incomplete understanding of the physical processes involved, and by our inability to accurately represent the dynamic behavior of the magnetic field. This paper describes an approach to overcoming these limitations, by incorporating real-time *in situ* data into a physics-based dynamic model. Techniques in spatial analysis and data assimilation, widely used in atmospheric weather modeling, are adapted to the problem of modeling the trapped radiation environment with a limited number of space-based observations.

The greatest difficulty in applying these techniques to the modeling of magnetospheric phenomena is the sparseness of real-time data. In the case of the radiation belts, for example, there are seldom more than two or three satellites providing simultaneous measurements of particle flux at points throughout the magnetosphere, and these measurements tend to be largely concentrated in geosynchronous orbit. However this situation is likely to change in the near future, as the number of spacecraft put into orbit for scientific, military, and commercial purposes continues to increase.

In anticipation of increasing data availability, we have begun to develop the theory and computational tools needed to incorporate data into a variety of magnetospheric models, such as

the radiation belt model described in this paper. While the full benefits of this approach may not become clear until the observing system becomes more complete, the results presented below suggest that the assimilation of even a few observations may significantly improved the accuracy of specification and forecast models.

The next section provides a brief overview of the data assimilation techniques employed in this study, with emphasis on the terminology and mathematical formalism guiding our approach. Section 3 describes the application of this formalism to a simple model of radiation belt particle dynamics. In section 4, we describe a simulated magnetic storm scenario that is used to test the data assimilation algorithm. The results of these tests are presented in section 5, and in section 6 we assess the viability of our approach and consider its extension to more complicated and realistic situations.

Data Assimilation

The data assimilation approach used in this paper is known as the Kalman-Bucy filter, originally devised for linear systems of ordinary differential equations [*Kalman*, 1960, *Kalman and Bucy*, 1961]. The Kalman-Bucy (KB) filter has two main components: spatial analysis and prediction. The spatial analysis algorithm combines localized observations with a model-computed background configuration to estimate the most probable state of the entire model system at a particular time. The prediction algorithm propagates the configuration forward in time, using the physical rules of the forecast model to govern the evolution of the system. In the KB filter, the output of the prediction algorithm forms the background configuration for subsequent spatial analysis.

In the spatial analysis portion of the KB-filter, observations are incorporated into the background configuration of the system by a process known as statistical interpolation, originally devised by *Kolmogorov* [1941] and *Wiener* [1949]. Statistical interpolation is essentially a weighted least-squares fit between observed and background values, in which the statistical weights are functions of the errors and correlations (known or estimated) associated with each value.

The formalism of statistical interpolation can be defined as follows. Suppose at a time t_n the configuration or state of a system is defined by a set of quantities $\underline{s}_n$, where $\underline{s}_n$ is a vector of length L (hereafter a single underline denotes a column vector, and double underlines a rank-2 array). The state vector might represent, for example, the value of some physical quantity on a regular grid of locations $\mathbf{r}_1, \mathbf{r}_2, \mathrm{K}, \mathbf{r}_L$. An empirical model or a previous forecast provides a background estimate of the state $\underline{s}_n^{\mathrm{F}}$. Further suppose that at t_n there exists K observations $\underline{d}_n$ of a physical quantity d, which is related to the global state $\underline{s}_n$ by

$$d_n = H_n(\underline{s}_n) \tag{1}$$

For example, d might be the value of s at an observing location $\mathbf{r}_o$, which does not (in general) coincide with a point on the model grid. In this case $H(\underline{s})$ is simply an interpolation of the state variables onto the point $\mathbf{r}_o$. More generally H can be any linear or non-linear transformation or

interpolation of the state vector $\underline{s}_n$. If H is a linear function of the state variables, then it may be written as a $K \times L$ array defined by

$$\underline{d}_n = \underline{\underline{H}}_n \, \underline{s}_n \qquad (2)$$

The background, observations, and transformation function may all contain errors, and in general these errors may be correlated to one another. The expected covariances among the errors are assumed to be known, unbiased, and normally distributed. They are expressed in the statistical interpolation formalism by *error covariance matrices*. The background error covariance matrix is defined in terms of the errors $\varepsilon_n^F = s_n^F - s_n^{true}$ at each grid point by

$$\left[\underline{\underline{P}}_n^F \right]_{ij} = \left\langle \varepsilon_n^F(\mathbf{r}_i) \varepsilon_n^F(\mathbf{r}_j) \right\rangle \qquad (3)$$

where the angle brackets denote the expectation operator. The observation error covariance $\underline{\underline{R}}_n$ matrix is similarly defined, but includes errors and correlations associated with the function $H(\underline{s})$ as well as the observations themselves.

With these definitions, the statistical interpolation procedure is [*Daley, 1991*]

$$\underline{s}_n^A - \underline{s}_n^F = \underline{\underline{K}}_n \left[\underline{d}_n - \underline{\underline{H}}_n \underline{s}_n^F \right] \qquad (4)$$

$$\underline{\underline{K}}_n = \underline{\underline{P}}_n^F \underline{\underline{H}}_n^T \left[\underline{\underline{R}}_n + \underline{\underline{H}}_n \underline{\underline{P}}_n^F \underline{\underline{H}}_n^T \right]^{-1} \qquad (5)$$

$$\underline{\underline{P}}_n^A = \left[\underline{\underline{I}} - \underline{\underline{K}}_n \underline{\underline{H}}_n \right] \underline{\underline{P}}_n^F \qquad (6)$$

The vector $\underline{s}_n^A$ is the analyzed state of the system—that is, the most probable set of values given the background $\underline{s}_n^F$, observations $\underline{d}_n$, and the corresponding error covariance matrices. The matrix $\underline{\underline{K}}_n$ is a set of weighting coefficients, which essentially determines the statistical significance of each observation in $\underline{d}_n$ to the analysis. The matrix $\underline{\underline{P}}_n^A$ is the analysis error covariance matrix; it contains the expected errors and correlations associated with $\underline{s}_n^A$.

The prediction part of the KB-filter is defined by the forecast model. In the following we assume that the evolution of the system from time t_n to t_{n+1} can be represented by a linear matrix operator $\underline{\underline{M}}_n$ acting on the state vector at t_n. The forecast is assumed to be imperfect, with a known error covariance matrix $\underline{\underline{Q}}_n$. Given the analyzed state vector and its error covariance matrix, the forecast state and error covariance matrix are given by

$$\underline{s}_{n+1}^F = \underline{\underline{M}}_n \underline{s}_n^A \qquad (7)$$

$$\underline{\underline{P}}_{n+1}^F = \underline{\underline{M}}_n \underline{\underline{P}}_n^A \underline{\underline{M}}_n^T + \underline{\underline{Q}}_n \qquad (8)$$

Equations (4)-(8) provide the governing equations of the data assimilation algorithm in a general form. The next section describes the application of this algorithm to the specific problem of modeling radiation belt dynamics.

Model

The Kalman-Bucy filter can be applied to a variety of dynamic systems. In this section we describe the application of a KB-filter to a simple model of radiation belt dynamics. The physical basis of the forecast model is briefly outlined, and cast into a computational form consistent with the KB-filter equations (4)-(8). We next discuss the transformation/interpolation of observed fluxes onto the model grid, using an estimate of the magnetic field configuration computed by an independent model.

Forecast model

The forecast model used in this study considers the phase space density of relativistic (MeV-range) electrons stably trapped in the radiation belts. For these particles we assume that the adiabatic invariants J_1, J_2, J_3 associated with the particle gyration, bounce, and drift motions are approximately conserved, except for small stochastic fluctuations. Under this assumption the evolution of the particle distribution can be represented by diffusion in the adiabatic invariants, of the form

$$\frac{\partial f\left(J_1, J_2, J_3; t\right)}{\partial t} = \sum_i \sum_j \frac{\partial}{\partial J_i}\left[D_{ij} \frac{\partial f\left(J_1, J_2, J_3; t\right)}{\partial J_j}\right] \quad (9)$$

Here D_{ij} are diffusion coefficients, related to the expected rate of change in each adiabatic invariant. For simplicity we limit our investigation to equatorially mirroring particles—that is, particles with zero second adiabatic invariant, in a magnetic field configuration where the minimum field strength along each field line lies in the equatorial plane. Such particles are entirely confined to the equatorial plane, and drift along paths of constant field strength. We further assume that diffusion in the first adiabatic invariant and losses (due to collisions with the Earth's atmosphere, e.g.) are negligible, so that the governing equation becomes a simple 1D diffusion equation in the third adiabatic invariant. Using μ for the first adiabatic invariant and the Roederer L parameter $L \propto J_3^{-1}$ in place of the third, the radial diffusion equation is

$$\frac{\partial f\left(\mu, L, t\right)}{\partial t} = L^2 \frac{\partial}{\partial L}\left[\frac{D_{LL}}{L^2} \frac{\partial f\left(\mu, L, t\right)}{\partial L}\right] \quad (10)$$

We assume a time-independent diffusion coefficient of the form

$$D_{LL} = D_0 L^n \quad (11)$$

with quiet-time values $D_0 = 7.905 \times 10^{-12}$ hrs^{-1} and $n = 11.7$ adopted from the study of *Selesnick et al.* [1997].

Computationally, the diffusion equation is solved in discretized form by the Crank-Nicholson numerical method – a semi-implicit approach with second-order accuracy in both space and time. For the interior grid points ($l = 2, 3, \ldots, N$-1), the distribution at $t = t_{n+1}$ is defined by

$$[-\alpha(1-\beta)]f_{l-1}^{n+1} + (1+2\alpha)f_l^{n+1} + [-\alpha(1+\beta)]f_{l+1}^{n+1} = \alpha(1-\beta)f_{l-1}^n + (1-2\alpha)f_l^n + \alpha(1+\beta)f_{l+1}^n \quad (12)$$

$$\alpha = \frac{1}{2}\frac{D_0 L^n \Delta t}{(\Delta L)^2}, \quad \beta = \frac{(n-2)\Delta L}{2L} \qquad (13)$$

The end-point values are determined by the boundary conditions. At the inner boundary of the modeling region where $L \sim 1$, the diffusion coefficient D_{LL} becomes vanishingly small; hence f is very nearly constant at the inner boundary, so $f_{l=1}^{n+1} = f_{l=1}^n$. Since the outer boundary distribution is unknown (unless an observation happens to be available), a Neumann-type (zero slope in f) outer boundary condition is applied at $l = N$. To second order accuracy in space, the discrete outer boundary condition is thus

$$3f_N^{n+1} - 4f_{N-1}^{n+1} + f_{N-2}^{n+1} = 0 \qquad (14)$$

The discretized governing equations and boundary conditions can be conveniently summarized in matrix form. Writing the set of value $[f_l^n, l = 1,2, \ldots]$ as the column vector $\underline{s}_n$, we have

$$\underline{\underline{A}}\,\underline{s}_{n+1} = \underline{\underline{B}}\,\underline{s}_n \qquad (15)$$

or, equivalently,

$$\underline{s}_{n+1} = \underline{\underline{M}}\,\underline{s}_n$$
$$\underline{\underline{M}} = \underline{\underline{A}}^{-1}\underline{\underline{B}} \qquad (16)$$

The square matrices $\underline{A}$ and $\underline{B}$ are nearly tridiagonal, with interior elements defined by equation (12), and first and last rows defined by the boundary conditions.

The set of phase space densities f, defined on a grid of discrete values of μ and L, represents the state-vector characterizing the configuration of the system. The discretized radial diffusion operator and boundary conditions of equations (12)-(16) form the forecast matrix $\underline{M}_n$ in equation (7). This matrix completely describes the evolution of the phase space density distribution over time, given an initial state.

The KB-filter additionally requires an initial estimate of the state at $t_{n=0}$, and error covariance matrices associated with both the initial state and the forecast model. In the test simulations described below, the initial distribution function is specified arbitrarily, and the errors associated with it are assumed to be large and uncorrelated. Since the forecast error covariance matrix is continuously modified with each data assimilation cycle (equations (6) and (8)), the algorithm is not especially sensitive to its initial value. The forecast error covariance matrix $\underline{Q}$ is somewhat more complicated: it represents both errors in the discretization of the forecast equation (10), and variations in the true system that are not represented by the forecast equation. These errors of representativeness are difficult to quantify. In the present study we make the simplest possible approximation, in which the expected forecast errors are uncorrelated and equal to a constant.

Spatial analysis

The analysis portion of the KB-filter requires a set of observations $\underline{d}_n$ and a transformation function $H_n(\underline{s}_n)$ for each time t_n For our model system the observations are taken to be measurements of differential directional flux at discrete energy levels, obtained at regular intervals along the orbit of a spacecraft confined to the equatorial plane. The differential directional flux j of particles with momentum p is simply related to the phase space density by

$$j = p^2 f \tag{17}$$

Since the forecast model operates in an adiabatic invariant coordinate system rather than physical space, it is necessary to determine the adiabatic invariants associated with each observation. These quantities depend on the configuration of the magnetospheric magnetic field. For a given observation position $\mathbf{r}$ and kinetic energy E (or corresponding momentum p), they are given by

$$\mu = \frac{p^2}{2mB(\mathbf{r})} \tag{18}$$

$$L = 2\pi B_0 R_E^2 \Phi^{-1}, \quad \text{where} \quad \Phi = \oiint_{\text{drift path}} B(\mathbf{r})\, dA \tag{19}$$

The magnetic field configuration must be supplied by another model, and is considered an input to the assimilation model. In principle, any magnetic field model, whether empirical, theoretical, or even a simple dipole field, can be used. However the likely error (and error correlations) associated with the model must be estimable, as these are also input to the spatial analysis algorithm. In this study we presuppose a magnetic field model that provides the magnetic field strength B, the L parameter, and the associated error covariances for any input set of positions $\mathbf{r}$ in the equatorial plane

Given estimates of μ and L corresponding to the observation, the function H becomes a two-dimensional interpolation onto the model grid. For simplicity we use a bilinear interpolation of the form

$$H_{ml}(\mathbf{r}, E) = p(E)^2 c_m(\mathbf{r}, E) d_l(\mathbf{r}) \tag{20}$$

The coefficients c and d are given by

$$c_m(\mathbf{r}, E) = \begin{cases} \frac{\mu_{m+1} - \mu(\mathbf{r}, E)}{\mu_{m+1} - \mu_m}, & \mu_m \le \mu(\mathbf{r}, E) < \mu_{m+1} \\ \frac{\mu(\mathbf{r}, E) - \mu_{m-1}}{\mu_m - \mu_{m-1}}, & \mu_{m-1} \le \mu(\mathbf{r}, E) < \mu_m \\ 0 & \text{, all other } m \end{cases} \qquad d_l(\mathbf{r}) = \begin{cases} \frac{L(\mathbf{r}) - L_l}{L_{l+1} - L_l}, & L_l \le L(\mathbf{r}) < L_{l+1} \\ \frac{L_{l-1} - L(\mathbf{r})}{L_l - L_{l-1}}, & L_{l-1} \le L(\mathbf{r}) < L_l \\ 0 & \text{, all other } l \end{cases} \tag{21}$$

The final element needed for the KB-filter is the observation error covariance matrix. This matrix has two components: covariances associated with the instrument error of the observing

satellite, and error covariances produced by the transformation function H. In the following we assume that instrument errors are known and uncorrelated. The errors associated with the transformation function are assumed to be dominated by errors in the values of μ and L computed by the magnetic field model. The error ε_H in H is related to the errors ε_μ and ε_L to first order by

$$\varepsilon_H(\mathbf{r},E) \approx p(E)^2 \left| \frac{\partial f}{\partial \mu}\bigg|_{\mu(\mathbf{r},E)} \varepsilon_\mu(\mathbf{r},E) + \frac{\partial f}{\partial L}\bigg|_{L(\mathbf{r})} \varepsilon_L(\mathbf{r}) \right| \tag{22}$$

The observation error covariance matrix is then constructed from the covariances among the ε_H for each energy channel and position of the observation set, together with the expected error variance of the observed fluxes.

Simulated Storm

In order to test the data assimilation algorithm, a simple scenario was constructed, in which a storm-time enhancement of the outer radiation belts is observed by a single spacecraft traversing the radiation belts. While not necessarily realistic, the use of fabricated data in this testing procedure allows us to control and simplify the behavior of the system, to more easily identify the response of the assimilation algorithm to various factors. Furthermore the simulated system provides a global picture of the "true" evolution of the system, against which the assimilation algorithm can easily be compared.

The observing system in this simulation is a single satellite measuring differential directional flux in ten channels of kinetic energy $E = 1, 2, 3, \ldots, 10$ MeV. The satellite lies in the equatorial plane, on an elliptical orbit with 24-hour period. The satellite's orbit crosses a wide range of L shells, from $L \sim 1.2$ to beyond the outer modeling boundary $L = 10$, as shown in figure 1. Satellite measurements are computed and delivered to the assimilation algorithm once per hour; measurements beyond the modeling boundary are simply ignored. The fluxes measured by the satellite are computed from the true phase space density distribution and magnetic field configuration described below.
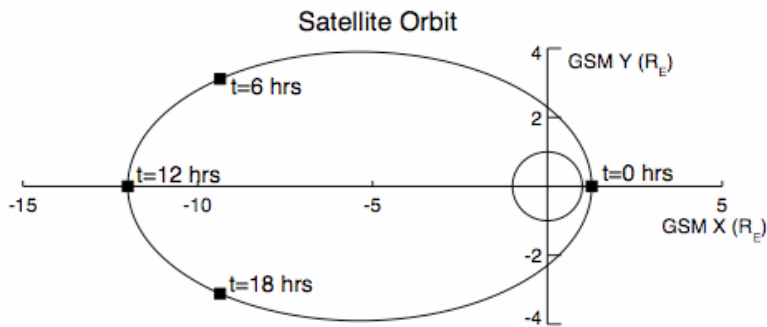
Figure 3. Orbital path (in magnetic equatorial plane) of satellite providing data during the simulated storm. Black squares indicate the spacecraft's position at 6, 12, and 18 hours from perigee. The orbital period is 24 hours.

The simulated environment consists of a simple magnetic field model, and a time-dependent phase space density distribution. The initial phase space density was chosen to be constant in L, with a simple power-law dependence in μ given by $f \propto \mu^{-5}$. The magnetic field model consists of the Earth's dipole field B_D (with zero tilt) and a time-dependent symmetric ring current B_{RC}, parameterized by the field depression Dst at the equator:

$$B(r,t) = B_D(r) + Dst(t)\, B_{RC}(r) \tag{23}$$

$$B_D = \frac{B_0 R_E^3}{r^3}, \quad B_{RC} = \frac{r - r_0}{1 - r_0} \tag{24}$$

Over the course of the 10-day simulation period, the system underwent a "storm" in which the ring current became stronger, and phase space densities at the outer boundary of the modeling region at $L = 10$ were enhanced by an order of magnitude for all values of μ. The time variation of the ring current parameter and outer boundary condition over the course of the simulation are shown in figure 2.
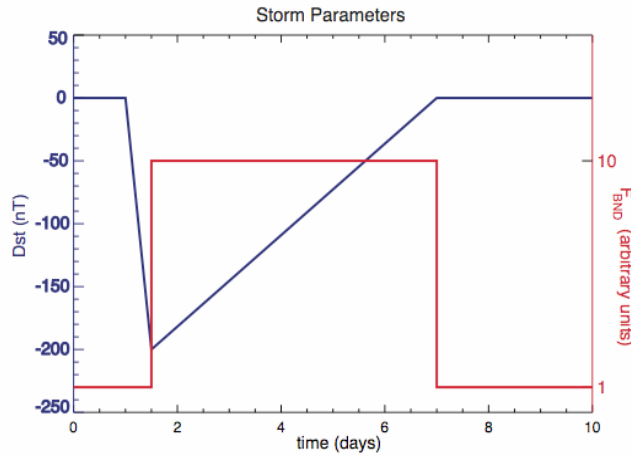
Figure 2. Time-variation of the simulated storm parameters Dst and F$_{BND}$, as described in the text.

The enhancement of phase space density at $L = 10$ was propagated inward to low L by the radial diffusion defined in equations (10) and (11), with Dirichlet rather than Neumann outer boundary conditions. Figure 3 depicts the evolution of the phase space density at $\mu = 5623$ MeV/G as a function of L and time over the course of the simulation. In this simulation the evolution at other values of μ is identical.
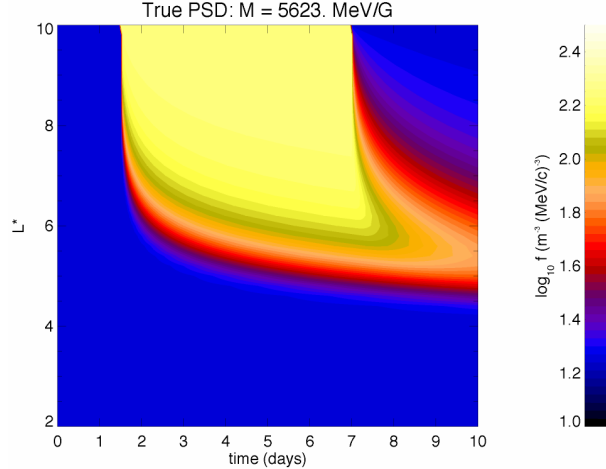
Figure 3. Contours of phase space density at $\mu = 5623$ MeV/G vs. L and time, for the true (simulated) electron population.

Results

The data assimilation algorithm described in sections 2 and 3 was used to model the response of the radiation belt electrons to the simulated storm described above. The correct initial distribution at the beginning of the event was supplied to the assimilation model, in order to better illustrate the model's ability to capture dynamic changes to the system.

The model computes changes in phase space density at each time step by solving the radial diffusion equation with Neumann boundary conditions. Since the initial distribution is constant in L and therefore a steady state solution to equation (10), the forecast model predicts absolutely no change in the phase space density over the course of the simulation, in the absence of assimilated data.

We first consider an idealized case in which perfect data is supplied to the assimilation algorithm. That is, the fluxes measured by the satellite each hour correspond exactly to the correct phase space density distribution, and the magnetic field model provides a perfect transformation from spatial to adiabatic invariant coordinates. In this case the observation error covariance matrix $\underline{\underline{R}}_n$ in equation (5) is a null matrix. The assimilation model is not without error, however, because the satellite provides the correct phase space density only for a few values of μ at a single value of L at each time step. The spatial analysis must spread these discrete points of data over the entire (μ, L) grid, and it does so with errors given by equation (6).

Figure 4 shows the predicted phase space density at $\mu = 5623$ MeV/G over the course of the storm, in the same format as that of figure 3. At this value of μ the assimilation does an admirable job of reproducing the correct behavior of the system. The discontinuous changes in f that appear periodically reflect the assimilation of new measurements from the satellite. The cadence is approximately 12 hours because the value of μ corresponding to a given energy channel depends strongly on the magnetic field strength, and therefore on the position of the satellite. Thus the phase space density at $\mu = 5623$ MeV/G, which corresponds to ~ 2 MeV at $L \sim 6.6$, is sampled by the satellite in tightly clustered groups around $L \sim 5$-7 on each inbound and

outbound pass. Results similar to those in figure 4 are obtained over a wide range of μ, from ~ 10^3 to 10^5 MeV/G.
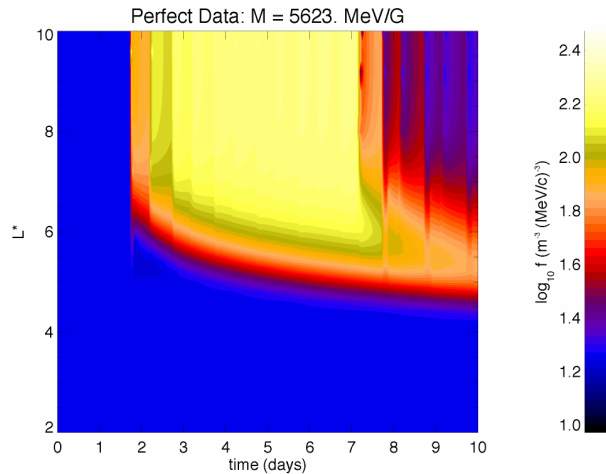
Figure 4. Assimilation model results with perfect observations, in the same format as figure 2.

The spatial analysis algorithm can be quite effective in inferring the complete distribution in L from only a few well-placed measurements. However the success of the assimilation algorithm depends strongly on the location of those measurements. Since the observed μ is largely a function of observing position, the model is much less successful at reproducing the phase space density at extreme μ values. Figure 5a shows the predicted phase space density at μ = 177.8 MeV/G (the true distribution is nearly identical to figure 3, with the values corresponding to each color offset). The satellite's 1-10 MeV energy channels sample this low μ only at large values of B corresponding to positions Earthward of $L \sim 3$, where the true distribution remains virtually constant over time. The storm-time ring current exacerbates this problem by decreasing the field strength in the inner magnetosphere, pushing the sampling range even closer to the Earth. Thus the assimilation fails to capture most of the dynamic changes to the system. Only late in the event, when the ring current has largely subsided, does the satellite begin to sample this value of μ. A similar behavior is seen at very large μ, as shown in figure 5b. The spacecraft samples μ = 10^6 only when B is less than ~30 nT. Again the satellite encounters this range of B only after the ring current (which increases the field strength in the outer magnetosphere) has subsided.
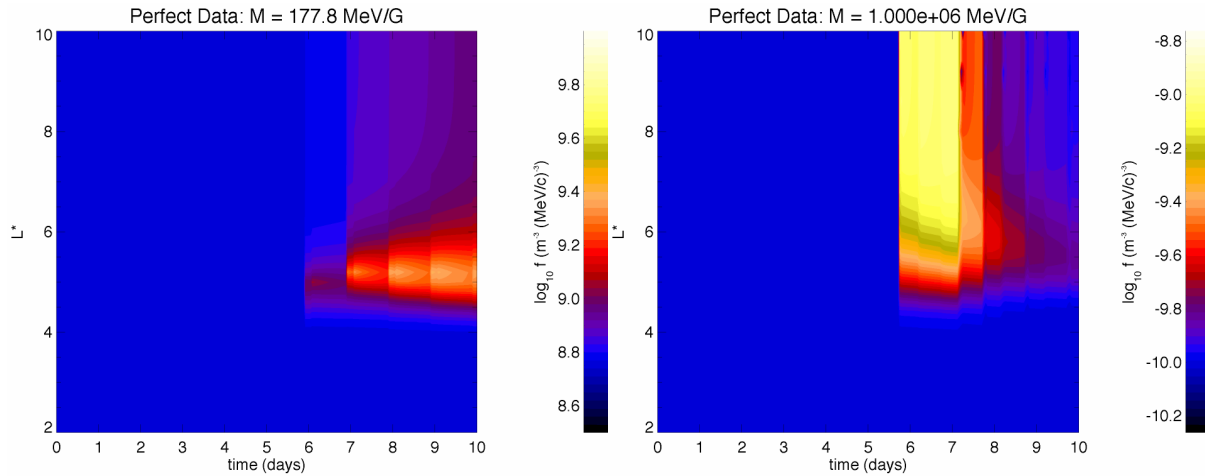
Figure 5. Same as figure 4, at (a) $\mu = 177.8$ MeV/G, and (b) $\mu = 10^6$ MeV/G.

We next consider the effects of various kinds of error on the assimilation results. Figure 6 displays the predicted phase space density at $\mu = 5623$ MeV/G, for an assimilation in which two types of observational error are simulated. The first is an error in the measured flux, simulated by randomly perturbing the correct value. The second is an error in the magnetic field model used to calculate the μ and L values corresponding each observation's position and energy channel. The magnetic field errors are generated by randomly perturbing the value of Dst in equation (23), and by adding random, spatially uncorrelated field fluctuations with a spatial scale of 1 R_E. The random variations added to the flux, Dst, and the perturbation field are all normally distributed, with standard deviations of 10%, 10 nT, and 5 nT, respectively. These expected errors are considered known in the assimilation algorithm, and contribute to the observation error covariance matrix $\underline{\underline{R}}_n$.
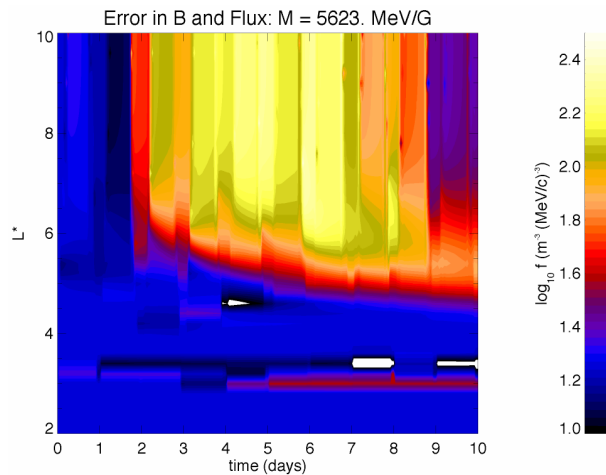
Figure 6. Same as figure 4, with errors in the observed fluxes and magnetic field.

The effect of these errors is evident in the noisy, patchy distribution shown figure 6 (compared to figure 4, for which no errors were included), but the overall picture remains reasonably faithful to the true distribution (figure 3). Errors at low L are especially noticeable for two reasons. First, the magnetic field strength is large at low L, so only measurements in the

highest energy channels sample $\mu = 5623$ MeV/G. Thus there are fewer total observations at low L. Second, diffusion is very slow in this region, so errors introduced at a particular (μ, L) tend to persist until repeated measurements at the same values become available. Random fluctuations in the magnetic field make repeated sampling of the same (μ, L) an unlikely event.

In figure 7, the effects of errors in the forecast model are shown. Here there are no errors associated with the observations or the magnetic field, but the diffusion coefficient defined by equation (11) is made to be artificially large, scaling as L^{13} rather than $L^{11.7}$. In this model the diffusion coefficient is not modified in the data assimilation cycle, so the forecast consistently overestimates the rate at which enhancements in the phase space density propagate to lower L. The observations, however, continually correct this error, creating a sawtooth pattern in the evolution of the enhancement's leading edge over time. The resulting distribution is still reasonable, but by the end of the simulation the enhancement has moved too far Earthward by a margin $\Delta L \sim 1.0$.
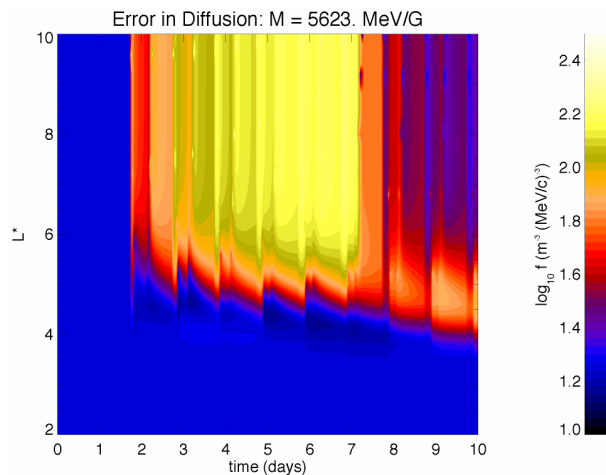
Figure 7. Assimilation results at $\mu = 5623$ MeV/G, with errors in the forecast model diffusion coefficient.

Conclusions

This paper illustrates the application of data assimilation techniques —specifically the Kalman-Bucy filter—to a physics-based model of radiation belt dynamics. A rudimentary assimilation consisting of a single observing spacecraft and a simple forecast model was compared to the prescribed evolution of the radiation belts during a simulated magnetic storm, with encouraging results. The assimilation of even small amounts of data can markedly improve a forecast model, if the observations are fortuitously placed in regions of high uncertainty. When the physics underlying the forecast model is sufficiently realistic, and the errors well known, the spatial analysis algorithm is able to infer the global distribution of the phase space density from these sparse observations with remarkable accuracy. The assimilation model is fairly robust, in that random errors in the observations, magnetic field model, and/or forecast models do not drastically degrade the predicted distribution —provided that the expected errors are accurately represented in the KB-filter formalism.

The development of a realistic radiation belt forecast model will require further research on a number of different fronts. First, the 1D forecast model described above is far too simplistic. It neglects much of the known physics governing the radiation belts, such as losses due to pitch-angle scattering into the loss cone, acceleration mechanisms such as ULF-drift resonance, and variations in the radial diffusion coefficient with time and μ. The application of the KB-filter to a more realistic dynamic model will require careful assessment of the errors and correlations associated with each facet of the model.

A realistic assimilation model will also require a far more sophisticated representation of the magnetic field. The one-parameter, azimuthally symmetric field model used above is clearly a poor representation of the magnetosphere. Fortunately there already exist advanced, data-based models of the magnetospheric magnetic field (e.g., *Tsyganenko*, 2002), which can be readily adapted to the assimilation model described here. However, as with the forecast model, the errors and correlations associated with the selected magnetic field model must be reliably estimated.

Finally, the assimilation model must be tested will actual data. This will require realistic estimation of the instrument error and background noise level associated with each measurement, and a careful selection of events based on data availability. In particular, the assimilation must be tested on events in which at least two independent sets of observations are available, so that the accuracy of the model can be assessed.

The work presented here represents a preliminary step toward assimilative modeling of the radiation belts. While the development of a fully realistic assimilation model faces a considerable number of challenges, the results presented here demonstrate the potential of the assimilation techniques employed here to significantly improve the specification and forecasting capabilities of dynamic models.

References

1. Daley, R., Atmospheric data analysis, Cambridge University Press, New York, 1991.

2. Kolmogorov, A., Interpolated and extrapolated stationary random sequences, Isvestia an SSSR, seriya mathematicheskaya, 5, p. 85, 1941.

3. Selesnick, R. S., et al., A quiescent state of 3 to 8 MeV radiation belt electrons, Geophys. Res. Lett., 24, p. 1343, 1997.

4. Tysganenko, N. A., A model of the near magnetosphere with a dawn-dusk asymmetry—1. Mathematical structure, J. Geophys. Res. 107, A8, SMP-12, 2002.

5. Wiener, N., Extrapolation, interpolation, and smoothing of stationary time series, John Wiley, New York, 1949.

OPERATIONAL PREDICTION AND SPECIFICATION OF THE SPACECRAFT CHARGING ENVIRONMENT

Terrance Onsager
National Oceanic and Atmospheric Adminstration (NOAA)
NOAA Space Environment Center
325 Broadway
Boulder, CO 80305
Phone: 303-497-5713
E-mail: terry.onsager@noaa.gov

Introduction

Fluxes of outer radiation belt electrons change dramatically over a broad range of time scales, ultimately driven by the solar wind, but controlled within the magnetosphere by the action of numerous acceleration and loss mechanisms. The particle dynamics are influenced by both adiabatic and non-adiabatic processes, involving in-situ acceleration or loss as well as diffusion either into or out of the radiation belt across its inner and outer boundaries. (see recent review by Friedel et al. [2002]). Although many different processes have been shown to cause either acceleration or loss of radiation belt particles under different circumstances, there currently is not a quantitative understanding of which processes dominate under any specific conditions. Without this quantitative understanding of the competing source and loss mechanisms, accurate physics-based modeling of the time-dependent radiation belts is not possible.

The processes that either accelerate or deplete the radiation belt electrons do not operate uniformly throughout the magnetosphere, and therefore gradients will develop in the radial distribution of electrons. These gradients could be created, for example, through enhanced wave energization or scattering into the loss cone within the radiation belts in the inner magnetosphere [e.g. Horne and Thorne, 1998; Elkington et al., 2003], or through increases or decreases in the electron phase space density in the outer magnetosphere, at the outer boundary of the trapped radiation belts [e.g., Brautigam and Albert, 2000]. Radial diffusion, which is a primary mechanism for radial transport, will then act to reduce the gradient, transporting plasma from locations of high phase space density to low. Because the various source and loss processes may operate at different times and locations within or outside the radiation belts, the continuous measurement of the radial profile of phase space density is one important way of identifying which processes are acting at which times.

One of the most significant impediments to identifying peaks or gradients in phase space density is that our in-situ satellite measurements are not available in terms of the adiabatic invariants. When expressed in terms of parameters other than the adiabatic invariants, such as fixed energy, the electron flux can undergo huge variability due entirely to adiabatic (i.e., reversible) processes [e.g., Li et al., 1997; Kim and Chan, 1997]. Only when the adiabatic behavior of the electrons is known can the important non-adiabatic source and loss processes be quantified and understood. From knowledge of phase space density in terms of the adiabatic invariants, key quantities for understanding radiation belt dynamics, such as its radial gradient, can be calculated and analyzed.

Although we have extensive data sets acquired by a large number of satellites over decades, no long-term characterization of the radiation belts in terms of adiabatic invariants exists today. Calculations of phase space density in terms of adiabatic invariants have been done on short, isolated intervals of data, in most cases concentrating on dynamic geomagnetic storm intervals [Selesnick and Blake, 1997a; 1997b; 1998; 2000; Hilmer et al., 2000; McAdams et al., 2001]. Estimates of the radial gradient of phase space density have been made in two ways. One technique has been to use satellites whose orbits cross a large range of L-shells, such as CRRES and Polar, to calculate phase space density for fixed values of the first two adiabatic invariants over individual orbits or consecutive orbits [e.g., Brautigam and Albert, 2000; Selesnick and Blake, 2000]. The other technique utilizes simultaneous measurements from satellites widely separated in radial distance, such as GPS measurements at L = 4.2 and geosynchronous measurements at L = 6.6 to estimate the radial profile of phase space density [e.g., Hilmer et al., 2000; McAdams et al., 2001].

The CRRES and Polar results suggest that a peak in phase space density occurs inside geosynchronous orbit associated with radiation belt enhancements, but that phase space density generally increases with increasing radial distance from inside to outside geosynchronous orbit during quiet times. Through the GPS and LANL comparisons, phase space density has been consistently found to be higher at L = 6.6 than at L = 4.2; however, measurement of the local gradient at geosynchronous orbit or additional observations inside or outside geosynchronous orbit would be required to further constrain the location of the peak. These studies have also highlighted the large uncertainty in calculations of phase space density in terms of adiabatic invariants, and the ambiguity of the location of its peak due to uncertainties in the global field model and the details of the electron distribution function.

The focus of this effort will be to develop a new technique for determining the radial gradient of phase space density at geostationary orbit, and to apply this technique under a wide variety of solar wind and geomagnetic conditions. The primary data we will use are from the GOES 8, 9, 10, 11, and 12 satellites, which measure energetic particle flux and magnetic field. Although the GOES satellites are three-axis stabilized while in operational use, a number of the GOES satellites acquired data while spinning during on-orbit storage. Data from the spinning satellites allow us to calculate electron pitch angle distributions, which are key to accurately estimating phase space density. These data are available over years of geosynchronous measurements, allowing us also to characterize the pitch angle distributions as a function of local time and geomagnetic activity. These data will be augmented during selected time periods with data from the LANL geosynchronous satellites and from the POLAR satellite to further constrain the global magnetic field and to provide valuable inter-calibration of flux levels, energy spectra, and pitch angle information obtained from the different instruments to more accurately determine phase space density and its gradient.

Our research will answer the following questions: What is the radial gradient of phase space density at geosynchronous orbit? How does the direction of the gradient vary from quiet to active times? How does the direction of the gradient vary between key phases of the solar cycle, such as during storms driven by solar wind transients versus radiation belt enhancements driven by high-speed streams? How sensitive is the calculation of phase space density in adiabatic invariant space to uncertainties in the electron pitch angle distribution, energy spectrum, and to

inaccuracies in the global magnetic field models? How do the electron pitch angle distributions vary with local time, geomagnetic activity, and magnetic field inclination?

In addition to determining the local gradient of phase space density, we will provide a long-term reference for phase space density in terms of adiabatic invariants at multiple locations in geostationary orbit over years of data that can be used by other researchers for comparison with data from other satellites. We will make the databases of phase space density mapped to adiabatic-invariant space and our computer codes available to the research community. The database will include the raw measurements of integral flux, magnetic field, and the calculated phase space density mapped to adiabatic invariant space. The computer codes will enable the calculation of the adiabatic invariants (*M, K*, and *L**) using a set of publicly available magnetic field models.

The results of this research will have direct relevance to four of the five NASA Strategic Enterprises. This research will quantify the dynamics of an important aspect of the Sun-Earth system over a large fraction of a solar cycle (a goal of the Space Science Enterprise), and improve our understanding of the radiation environment that is important both for human activities in space (Biological and Physical Research Enterprise and Human Exploration and Development of Space Enterprise) and for space system design (Aerospace Technology Enterprise). This research will provide critical new information on the location of the source and loss processes affecting the radiation belt electrons, and therefore contribute directly to our ability to predict changes in Earth's radiation belt environment through internal processes and through solar wind driving, which is directly relevant to Strategic Goal 1, Sun-Earth Connection Theme, RFA 1(b) and Strategic Goal 2, Sun-Earth Connection Theme, RFA 1(c). From the error analyses we conduct, we will help to define the requirements for future Living With a Star missions, such as the Radiation Belt Storm Probe mission.

Calculating Phase Space Density and its Radial Gradient

The GOES data provide the opportunity to calculate radiation belt electron phase space density in adiabatic-invariant space at multiple locations in geostationary orbit over a solar cycle. However, as mentioned above, there are numerous difficulties associated with making these calculations. In the following example, we describe the technique we will use to make these calculations, and we illustrate the sensitivity of our results to uncertainties in the energy spectrum and the pitch angle distributions. A potentially important source of error is introduced by the necessity of using a magnetic field model to characterize the global azimuthal drift of the electrons. For the example given here, we have chosen to analyze a geomagnetically quiet time, when the magnetic field models are likely to be the most accurate. An important part of this research will be to investigate in detail the consistency of simultaneous phase space density calculations at a large number of local times (using GOES and LANL geosynchronous satellites and Polar during crossings of the equatorial plane near geosynchronous orbit) during active as well as quiet times, and to determine if the agreement can be improved by utilizing the most recent magnetic field models that include azimuthal variations in the field.

A key application of our calculations of phase space density will be to determine its local radial gradient at geosynchronous orbit. As demonstrated below, the east and west GOES

satellites are located at different geomagnetic latitudes due to the tilt of Earth's dipole magnetic field. Therefore, these spacecraft provide simultaneous measurements in different L-shells. If phase space density and the adiabatic invariants can be determined with sufficient accuracy, these calculations will give a continuous measure of the local radial gradient of phase space density. Quantifying the accuracy of these calculations is an important part of this research. In addition, these calculations will give a valuable reference value for phase space density at geostationary orbit to allow comparison with other spacecraft in more largely separated L-shells, either inside geosynchronous orbit, such as GPS, or outside, such as POLAR or CLUSTER.

For the example we describe here, measurements of the GOES >2 MeV electron flux at geostationary orbit and Dst index on February 1-8, 1996 are shown in Figure 1. The top panel contains the electron flux at GOES-8 (solid) and GOES-9 (dashed), and the bottom panel contains the Dst index, courtesy of the World Data Center, Kyoto, Japan.

The electron flux was moderately high, with some periods of relatively little variability (Feb. 3-6) and some instances of fairly abrupt changes in the flux levels (e.g., Feb. 2 and Feb. 7), with no significant activity seen in Dst. An obvious feature of the electron flux at geostationary orbit is the consistent diurnal variation, with higher fluxes observed near noon and lower fluxes observed near midnight. This variation in the fluxes is due to the local-time asymmetry of the magnetic field and the fact that in the outer magnetosphere, particle flux at constant energy decreases with increasing distance from Earth. Other noticeable features in the electron data are that the fluxes measured by GOES 9 (dashed curve) appear to be offset in time relative to GOES 8 and have consistently higher values.
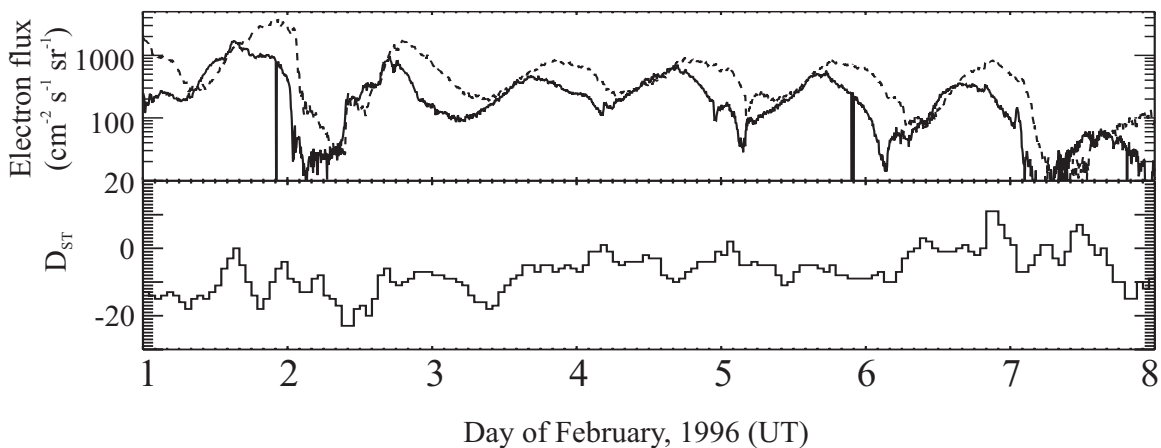
Figure 1. (Top) geosynchronous electron flux, and (bottom) Dst during an extended period with elevated >2 MeV electron flux and quiet geomagnetic conditions.

The difference in flux levels at the two spacecraft is due to the different longitudinal locations of the two spacecraft. Diagrams illustrating the locations of GOES 8 and 9 are shown in Figure 2. The right panel in Figure 2 contains a view of the geographic equatorial plane from above, and the left panel contains an illustration of the locations of the two spacecraft relative to the geomagnetic equator. Note that the field lines that pass through the two spacecraft do not

actually lie in the same plane, as shown in the left panel, but are drawn coplanar only to indicate the approximate geomagnetic latitudes of the two satellites.

The local-time separation in the GOES spacecraft has two effects. First, because GOES 9 lags GOES 8 in its orbit, it observes the spatial, diurnal variation in the particle flux with an offset corresponding to the separation in local time. Another important difference in the measured fluxes occurs because the spacecraft are located at different geomagnetic latitudes. Although both spacecraft are located at the geographic equator, Earth's magnetic dipole is tilted toward the geomagnetic equator in approximately the longitude of GOES 8. As a result of the dipole tilt, GOES 8 is at a geomagnetic latitude of about 11°. The dipole tilt has a much smaller effect on the geomagnetic latitude of GOES-9, which is about 4°. Although GOES 8 and 9 are both located at the geographic equator, GOES 8 is at a higher geomagnetic latitude and, therefore, under most circumstances will be measuring particles in larger L shells.
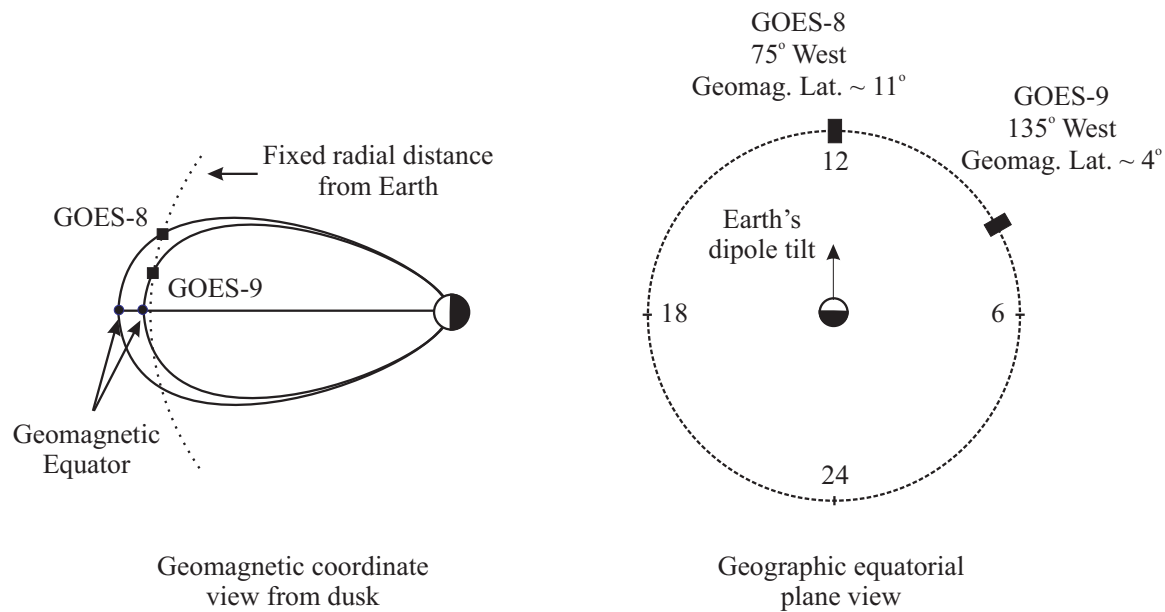
Figure 2. The geomagnetic latitudes of GOES 8 and GOES 9 (left) and their locations in the geographic equatorial plane (right). Note that although the east and west GOES satellites are both located in the geographic equatorial plane, the tilt of Earth's dipole results in a geomagnetic latitude difference of about 7°.

In order to establish that the electron detectors are accurately inter-calibrated and that the flux difference is in fact due to the longitudinal separation of the spacecraft, we have analyzed data from time intervals when GOES 9 was located close to GOES 8, prior to arriving at it operational location. Shortly after launch in May 1995, GOES 9 was located at about 90° west Longitude, about one hour in local time from GOES 8. It remained there until December 1995, when it was moved to 135° west Longitude.

A comparison of flux measurements from these times with different longitudinal separations is shown in Figure 3. This figure contains scatter-plots of the >2 MeV integral flux measured at GOES 8 versus the flux measured at GOES 9. The measurements in Figure 3a are from the three-

day period from Feb. 3-6, 1996 (from the middle of the interval shown in Figure 1). The GOES 9 measurements have been shifted four hours later in time so that each point represents the flux measured at the same local time by the two spacecraft. Some scatter occurs due to the temporal variations in the flux over the four hours between the GOES 8 and 9 measurements.

It is clear in Figure 3a that there is an offset in the measurements, with GOES 9 (at a lower geomagnetic latitude) measuring higher fluxes than GOES 8. This is consistent with the fact that at constant energy, radiation belt flux in the vicinity of geostationary orbit decreases with increasing radial distance from Earth.

Measurements made when the two spacecraft were at nearly equal geomagnetic latitudes are shown in Figure 3b. These data were obtained over the three-day period from July 3-5, 1995,
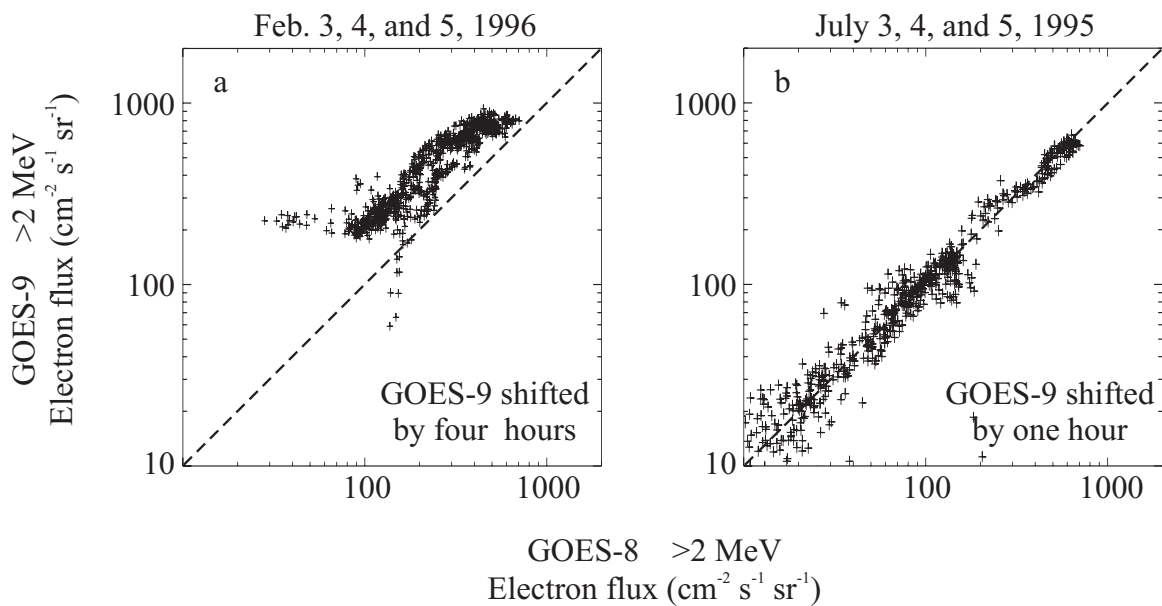
Figure 3. (Left) comparison of GOES 8 and 9 measurements obtained when the spacecraft were separated by four hours of local time and roughly 7° in geomagnetic latitude, and (right) when the spacecraft were separated by only one hour of local time and at approximately equal geomagnetic latitudes.

when GOES 9 was located one hour to the west of GOES 8. At this longitude, the geomagnetic latitude of GOES 9 was about 10.5°, within about 0.5° of the latitude of GOES 8. For this plot, the GOES 9 data were shifted in time by one hour, so that the values represent the flux measured at the same local time.

The close agreement between the GOES 8 and 9 measurements when the two spacecraft were at nearly equal geomagnetic latitudes indicates that the electron detectors are well inter-calibrated, and that the systematic difference seen in Figure 3a is due mainly to the geomagnetic latitude difference. Another factor that could contribute to the difference in flux measured at GOES 8 and 9 is the slightly different inclination of the magnetic field at the two spacecraft and any anisotropy in the pitch angle distributions. This, however, is not likely to cause a large effect,

given the broad field of view of the detectors and their westward look direction. Since the magnetic field inclination at geostationary orbit is primarily either toward or away from Earth, the westward-pointing detectors will always measure a broad range of pitch angles including 90°, even in the extreme cases of purely vertical or purely horizontal fields.

The GOES satellites, with their well inter-calibrated detectors and their simultaneous measurements in slightly separated L-shells, provide measurements that can be used to estimate the radial gradient of phase space density. The radial gradient, or $\partial f/\partial L$, is estimated by calculating phase space density at fixed values of the first two adiabatic invariants, M and K, and then comparing these values at different locations in L.

Two main assumptions are made to allow the calculation of phase space density at fixed M and K from the measured integral fluxes at fixed energies. The first assumption is that electron phase space density can be approximated with an exponential distribution:

$$f(E) = f_o e^{-E/E_o} \qquad (1)$$

which is related to the differential directional number flux, $j(E)$, and the particle momentum, p, by:

$$f(E) = \frac{j(E)}{p^2}. \qquad (2)$$

The integral flux is related to the differential flux by

$$J(>E) = \int_E^\infty dE' \, j(E') \qquad (3)$$

or,

$$J(>E) = \int_E^\infty dE' \, f(E')p^2. \qquad (4)$$

With the assumed functional form of phase space density, (1), we can integrate (4) directly and solve for $f(E)$ in terms of the measured integral flux, $J(>E)$,

$$f(E) = \frac{c^2 J(>E)}{(E_0^{\ 2} + EE_0)\,2mc^2 + 2E_0^3 + 2EE_0^2 + E^2 E_0}. \qquad (5)$$

The second main assumption used in this analysis is that the pitch angle distribution at the equator can be described by:

$$f_{eq}(E,\alpha_{eq}) = f_{eq}(E)\sin^m \alpha_{eq}. \qquad (6)$$

The phase space density at a given pitch angle and energy at any latitude, λ, along a field line is equal to the phase space density at the same energy and its corresponding pitch angle at the equator (from Liouville's Theorem):

$$f_\lambda(E,\alpha_\lambda) = f_\lambda(E)g(\alpha_\lambda) = f_{eq}(E,\alpha_{eq}) = f_{eq}(E)\sin^m \alpha_{eq}. \qquad (7)$$

From conservation of the first adiabatic invariant, M,

$$M = \frac{p_\perp^2}{2mB} = \frac{p^2 \sin^2 \alpha}{2mB}, \qquad (8)$$

$$\sin\alpha_{eq} = \left(\frac{B_{eq}}{B_\lambda}\right)^{\frac{1}{2}} \sin\alpha_\lambda, \qquad (9)$$

so that,

$$f_\lambda(E,\alpha_\lambda) = f_\lambda(E)\sin^m \alpha_\lambda = f_{eq}(E)\left(\frac{B_{eq}}{B_\lambda}\right)^{\frac{m}{2}} \sin^m \alpha_\lambda. \qquad (10)$$

Therefore, the pitch angle dependence will have the same functional form everywhere along the field line. The peak amplitude of the phase space density (at 90° pitch angle) at latitude λ on the field line will be related to the peak amplitude at the equator by:

$$f_\lambda(E) = f_{eq}(E)\left(\frac{B_{eq}}{B_\lambda}\right)^{\frac{m}{2}}. \qquad (11)$$

Combining (5) and (11), we obtain the phase space density at 90° pitch angle at the magnetic equator as a function of the measured integral flux at latitude λ at 90° pitch angle,

$$f_{eq}(E) = \frac{c^2 J_\lambda(>E)}{(E_0^2 + EE_0)2mc^2 + 2E_0^3 + 2EE_0^2 + E^2 E_0}\left(\frac{B_{eq}}{B_\lambda}\right)^{\frac{m}{2}}. \qquad (12)$$

Using (12), phase space density is calculated for equatorially mirroring particles ($K = 0$), with magnetic moment $M = 6000$ MeV/G. A magnetic moment of 6000 MeV/G corresponds roughly to 2 MeV electrons in a 100 nT magnetic field, which is a typical field strength at geosynchronous orbit. The phase space density is first determined for 2 MeV particles from the measured integral flux, and then calculated for the appropriate energy for the selected value of M using (1).

A magnetic field model is used to calculate the ratio of the local and equatorial fields used in (12) and the $L*$ parameter [Roederer, 1970], which is related to the third adiabatic invariant,

$$L = L* = \frac{2\pi k_0}{a\Phi},$$ (13)

where k_0 is Earth's magnetic dipole moment, a is the radius of Earth, and Φ is the magnetic flux enclosed in the particle drift. For this example, we have done the calculations using the Tsyganenko 1989 and the Tsyganenko 2001 and verified that for these quiet conditions, our results do not depend on this choice of field model.

The results of the L-shell calculations for the two spacecraft and the energy of the particles corresponding to $M = 6000$ MeV/G are shown in Figure 4. The upper panel (a) contains the measured >2 MeV electron flux, which is also shown in Figure 1. Panel (b) contains the calculated L values, and panel (c) contains the particle energies, which vary to maintain constant magnetic moment as the magnetic field varies. In panels (a)-(c), the GOES 8 values are shown with a solid line and the GOES 9 values with a dashed line. As seen in panel (c), the choice of $M = 6000$ MeV/G insures that the energies used in our analysis are near the measured energy, which minimized the dependence of our results on E_0 (through Equation (1)). Panel (d) contains the difference in the L values at the two spacecraft, $\Delta L = L_9 - L_8$.

Note that although GOES 8 is always at a higher geomagnetic latitude than GOES 9, GOES 8 is sometimes at lower L-shells. This is due to the asymmetric magnetic field, which is more compressed (resulting in lower L-shells) near noon than near midnight.
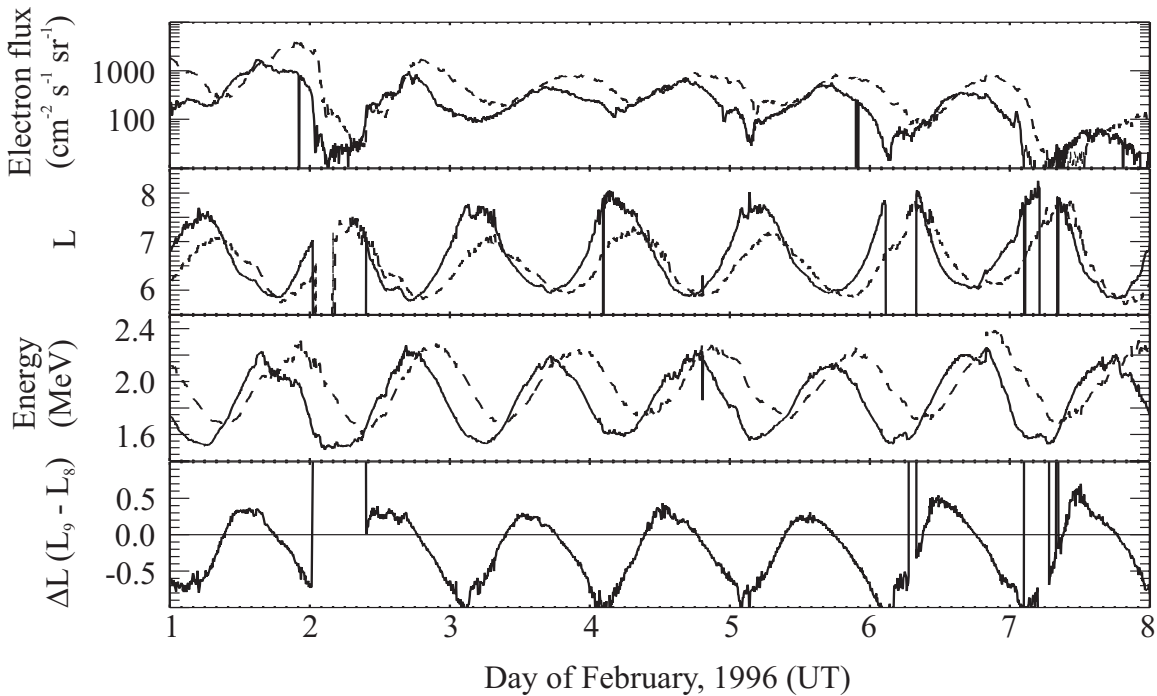
Figure 4. Electron flux, L-shell, particle energy for constant magnetic moment, and the L-shell difference of the GOES 8 and 9 measurements. Note that twice per day the two spacecraft are simultaneously measuring electrons in the same L-shell.

Consequently in the dawn magnetosphere, the increased compression in the magnetic field experienced by GOES 8 relative to GOES 9 as GOES 8 leads in local time by four hours causes the GOES 8 L-shells in this region to be lower than those of GOES 9. There are two L-shell crossings each day, one post midnight and one near noon, which correspond to times when the two spacecraft are simultaneously in the same L-shell.

These measurements made by the two satellites in the same L-shell give us the opportunity to test our assumptions about the particle distributions and to investigate uncertainties in the magnetic field models. As outlined above, the two parameters that need to be estimated to calculate phase space density from the measured integral fluxes are the index, m, in the pitch angle distribution (10) and the characteristic energy, E_0, in the energy distribution (1). The pitch angle index is estimated by considering the measurements at the locations where the two spacecraft are simultaneously in the same L-shell. At these locations, the calculated phase space density should be equal.

For the example presented here, we have only considered equatorially mirroring electrons $(K = 0)$. Therefore, the calculations of L depend only on the equatorial magnetic field strength. Times when the L values for the two spacecraft are equal correspond to times when the equatorial magnetic field strengths are equal. At these times, the energies of the particles being considered are also equal, for a fixed magnetic moment. The ratio of the phase space densities at these locations reduces to:

$$\frac{f_8(E)}{f_9(E)} = \frac{J_8(>2)}{J_9(>2)} \left(\frac{B_{8\lambda}}{B_{9\lambda}} \right)^{\frac{m}{2}} = 1 . \qquad (14)$$

Therefore, from the measured integral flux and the model magnetic field, (14) can be used to estimate the pitch angle index in the vicinity of the L-shell crossings.

Calculations of phase space density in the vicinity of the L-shell crossing $(\Delta L = 0)$ that occurred at 0930 UT on February 4 are shown in Figure 5. The left panel illustrates the dependence of the difference in phase space density measured at the two spacecraft, $\Delta f = f_9 - f_8$, on the assumed value of m. This analysis indicates that phase space density is equal at the L-shell crossing when a weak pitch angle dependence ($m \sim 0.25$) is assumed. At this time (0930 UT), GOES 8 was located at 0430 LT and GOES 9 was located at 0030 LT. This result is reasonable, given that the electron distributions can range from being highly peaked at 90° near local noon (large values of m) to having a local minimum at 90° near midnight [e.g., West et al., 1973a,b; Selesnick and Blake, 2002].

Calculations of the difference in phase space density measured at the two spacecraft, $\Delta f = f_9 - f_8$, versus the difference in L-shells, $\Delta L = L_9 - L_8$ in the vicinity of this L-shell crossing are shown in the middle panel Figure 5. These results are from the time interval 0800 − 1100 UT, a three-hour interval centered on the L-shell crossing. The values of Δf and ΔL shown in Figure 5 indicate that phase space density had a positive radial gradient ($\partial f / \partial L > 0$) at this time. On either side of the L-shell crossing, the spacecraft at the large L measured a larger phase space density. The magnitude of $\partial f / \partial L$ is estimated by the slope of the least-squares fit to the calculations. For

$E_0 = 250$ keV (used for the calculations shown in the middle panel), the slope is approximately 1.3, corresponding to $\partial f/\partial L \sim 1.3 \times 10^{23}$ (MeV s L)$^{-1}$. The dependence of $\partial f/\partial L$ on the characteristic energy, E_0, is shown in the right panel of Figure 5. It is found that the value of $\partial f/\partial L$ is maximum and positive for low values of E_0, and decreases as E_0 increases. Over the full range of expected E_0 values [e.g., Cayton et al., 1989; McAdams et al., 2001], $\partial f/\partial L$ remains positive in the vicinity of this L-shell crossing.

A similar analysis has been performed for the L-shell crossing that occurred near local noon, at about 18 UT on February 4 (not shown). Near local noon, the pitch angle index required to have equal values of phase space density at the calculated L-shell crossing was $m \sim 12$. Although this value of m is quite large, it is consistent with observations of pitch angle distributions that are strongly peaked at 90° near local noon [e.g., Selesnick and Blake, 2002]. We have independently inspected pitch angle distribution using Polar data near noon and found examples where this value of m is reasonable. The calculated slope of the Δf versus ΔL values shows a positive radial gradient of phase space density, consistent with the results obtained from the earlier L-shell crossing.

The results presented here demonstrate that the well inter-calibrated electron detectors on the GOES satellites can be used to calculate the local radial gradient of phase space density at geosynchronous orbit due their separation in geomagnetic latitude. This example also indicates

February 4, 1996   08 - 11 UT
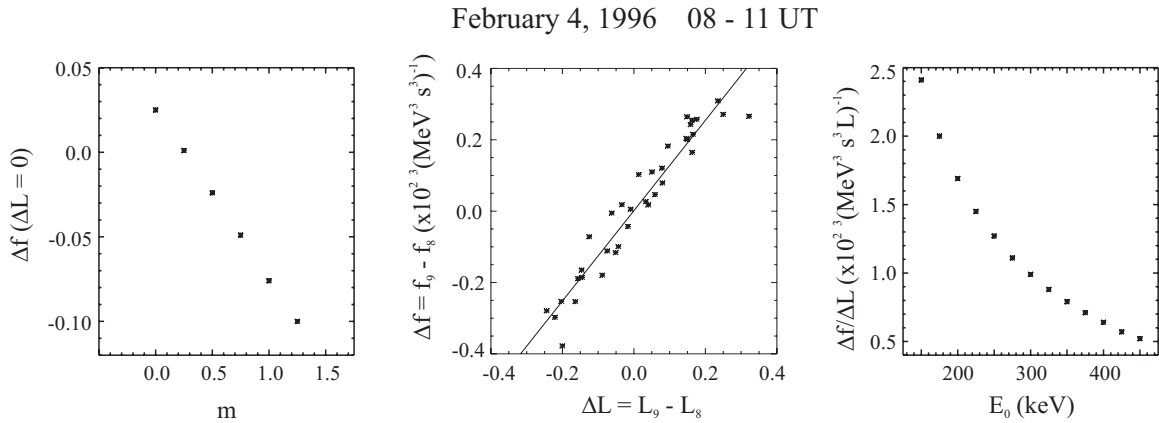
Figure 5: (Left) dependence of the value of df at the night-side L-shell crossing, (middle) phase space density difference versus separation in L-shell in the vicinity of the L-shell crossing, and (right) dependence of $\partial f/\partial L$ on the assumed value of E_0.

the importance of the pitch angle distribution in the calculations, and our ability to use the times when the spacecraft are simultaneously located in the same L-shell (based on the model magnetic field) to estimate the index of the pitch angle distribution (independent of the characteristic energy of the distribution function). Following the research plan described below, this technique will be further tested and applied to years of geosynchronous measurements, utilizing simultaneous pitch angle measurements from spinning GOES satellites (described below), and using additional data for the LANL geosynchronous satellites and from the Polar satellite during selected times to further constrain the global magnetic field model, the energy spectra, and the pitch angle distributions.

Research Plan

This research will be conducted over a three-year period and will quantify the phase space density of radiation belt electrons and its radial gradient at geostationary orbit. These results will establish a reference for the direction of radial diffusion and the variability of phase space density under a wide range of solar wind and geomagnetic activity conditions.

Our first task will be to calculate phase space density and its radial gradient over long time periods, including quiet and active conditions, using pitch angle measurement obtained from a third GOES satellite when one was in on-orbit storage and spinning. Over nearly two years from August 1998 to May 2000, GOES 9 was spinning and acquiring data at approximately 100º west Longitude, between GOES 8 and GOES 10 at the east and west operational locations (75º west and 135º west, respectively). For about one year from December 2001 until January 2003, GOES 12 was spinning and acquiring data at approximately 90º west Longitude, and GOES 11 began transmitting data while spinning in July 2003 and will continue to transmit data as long as GOES 12 (east) and GOES 10 (west) remain operational. These data are available with up to 10.24-second resolution. The first calculations will be done for a single magnetic moment, $M = 6000$ MeV/G, and for equatorially mirroring particles, $K = 0$. We will initially use the Tsyganenko 1989 field model, which can be parameterized with the Kp index only. We will then compare our results using other magnetic field models, such as Tsyganenko 2001, to investigate the dependence of our results on the field model.

Over these time periods, which include the approach to solar maximum and now the declining phase of Solar Cycle 23, pitch angle measurements were made continuously by the spinning spacecraft. We will use the simultaneously measured pitch angle distributions to calculate phase space density and its radial gradient using the technique described above. With these long periods of pitch angle measurements, we will characterize statistically the functional forms of the pitch angle distributions as a function of local time, geomagnetic activity, and local magnetic field inclination. Assuming a consistent statistical relationship for pitch angle distributions emerges, this result can be applied to the full GOES data set, including those time for which direct pitch angle measurements are not available.

In the example described above, the pitch angle index was determined at the L-shell crossings under the assumption that the magnetic field model was correct. During the extended times when pitch angle measurements are available, we will be able to use the measured pitch angle distributions to investigate the accuracy of various magnetic field models in determining the locations of the L-shell crossings. This will provide an additional consistency check on our results, which will be particularly valuable during active times when the magnetic field may be changing rapidly.

Our second task will be to use Polar and LANL geosynchronous data to further refine and validate our calculations during selected time intervals of interest. The Polar spacecraft made a large number of equatorial crossings near geosynchronous orbit, covering nearly all local times (see Figure 6 of Selesnick and Blake [2002]). These crossings provide electron energy spectra, electron pitch angle, and magnetic field measurements that can be compared with the GOES

measurements and with the magnetic field model. The LANL data will provide dense coverage at geosynchronous orbit of the electron energy spectra, magnetic field inclination, and pitch angle distributions, using techniques recently developed for identifying preferred directions in the electron flux measurements. These measurements will be used to validate, and if necessary, to modify our specifications of the electron distributions used in our calculations. In addition, the magnetic field measurements from GOES and Polar and the determination of the magnetic field inclination made by LANL will provide strong constraints on the magnetic field model used for our calculations of the adiabatic invariants. We are particularly interested in determining if the most recent magnetic field model by K. Tsyganenko, which includes azimuthally asymmetric fields in the magnetosphere, can be used to find an optimal fit to our multi-point determination of the magnetic field and phase space density.

Our third task will be to extend our calculations of adiabatic invariants to include off-equatorially mirroring particles. These calculations will be limited to time periods when we have sufficient confidence in the measured energy spectra, pitch angle distributions, and magnetic field model. We anticipate that we will utilize the most recent magnetic field model available, using the full constellation of satellites to determine the optimal model inputs. From our investigations of the pitch angle distributions, energy distributions, and sensitivity of the phase space density calculations on these parameters and on the parameterized magnetic field, we will know the level of confidence we can have in processing the GOES data over a full solar cycle (1995 – 2006), which would include the time periods for which we do not have simultaneous GOES pitch angle measurements. If the electron distributions can be parameterized sufficiently accurately by geomagnetic activity or magnetic field inclination, then this extension of our processing of the data will yield a full solar cycle of radiation belt electron phase space density mapped to adiabatic invariant space.

In addition to publications of our research, this effort will result in a number of deliverables to the LWS program. First, the dataset of phase space density mapped to adiabatic invariant space will be made available, together with the raw satellite measurements. And second, the source code used to calculate the adiabatic invariants will be made available with sufficient documentation that researchers will be able to reproduce and to extend our results. We feel it is critical for the progress of radiation belt research that measurements mapped to adiabatic invariant space and the tools needed to perform this mapping are made broadly available. Our documented source code will allow researchers to calculate the adiabatic invariants, M, K, and $L*$, with the magnetic field models that we will use (T89, T2001, and others that include azimuthal asymmetry) and will give people the flexibility to modify and recompile the source code and take advantage of other magnetic field models as they desire.

At the end of this research, we will have determined the variability of phase space density and its radial gradient at geosynchronous orbit in terms of the adiabatic invariants over a minimum of many years, including the approach to solar maximum, near solar maximum, and now during the declining phase of Solar Cycle 23, and perhaps over the full solar cycle. This research includes the development and application of a new technique for calculating the radial gradient of phase space density, which exploits the separation in L-shell of longitudinally separated geostationary satellites. From years of direct pitch angle measurements made by

spinning GOES satellites, we will characterize the pitch angle distributions as functions of local time and geomagnetic activity.

The results of this research will provide critical new information for determining the source and loss processes operating in the radiation belts. In addition, our calculated values of phase space density in adiabatic-invariant space and the source code used to make these calculations will be made available through LWS-supported data and model centers for other researchers to use and extend. This effort contributes directly one of the specific research topics of high current interest in the TR&T program (the generation and decay of the Earth's radiation belts as a function of geomagnetic and solar wind conditions), and is relevant to four of the five NASA Strategic Enterprises. This research will improve our understanding of the basic response of magnetospheric electrons to solar variability and internal source and loss processes, and provide valuable information for the planning of future Living With a Star missions, such as the Radiation Belt Storm Probes, and the interpretation of their data.

Data Availability

For this research we will utilize data from the NOAA and LANL geosynchronous satellites, the ISTP Wind, and ACE satellites. Beginning early 1995, nearly continuous solar wind data are available from Wind and later from ACE. Periodic data outages during times such Wind perigee passes are not critical for this analysis. These data are available through CDAWeb and the NSSDC, and the real-time quick-look ACE data are available at NOAA/SEC.

Continuous geosynchronous energetic particle and magnetic field measurements are available from the NOAA GOES spacecraft: GOES-8 (launched May, 1994 and currently operating), GOES-9 (launched May, 1995 and removed from operation in 1998), and GOES –10 (launched in April, 1997 and currently operating). These data are all readily available at NOAA SEC. Energetic particle data are available from up to four simultaneously operating LANL spacecraft over the time period from 1995 to the present and these data are readily available at LANL. Data from the Polar spacecraft are available through Aerospace Corp. (see attached letter).

Project Management and Schedule

The Principal Investigator, T. Onsager, will have overall responsibility for establishing goals and milestones for this research. T. Onsager will be responsible for processing the NOAA data, including calculations of the pitch angle distributions and phase space density. J. Green and S. Elkington will be responsible for calculating the adiabatic invariants using their current software and for extending this software to allow the calculation of adiabatic invariants for off-equatorially mirroring particles. They will also provide the code documentation for when the software is delivered to the LWS program. J. Green will be responsible for processing the Polar data. G. Reeves will be responsible for collecting and verifying the LANL data, and providing magnetic field inclination and pitch angle distributions. All investigators will collaboratively conduct the research tasks described above. In addition, Dr. Anthony Chan of Rice University, who has been involved in the initial calculations of phase space density described here, will also participate as an unfunded collaborator (see attached letter). Although the order of the tasks may

vary slightly as the research develops, it is anticipated that the first tasks will be accomplished during Year 1 of this effort, the second task will be accomplished during Year 2, and the third task will be accomplished during Year 3.

Facilities and Equipment

All required facilities and equipment to conduct this research are currently available at the NOAA Space Environment Center, University of Colorado, Boulder, and at Los Alamos National Laboratory.

References

1. Brautigam, D. H., and J. M. Albert, Radial diffusion analysis of outer radiation belt electrons during the October 9, 1990 magnetic storm, J. Geophys. Res., 105, 291, 2000.

2. Elkington, S. R., M. K Hudson, and A. A. Chan, Resonant acceleration and diffusion of outer zone electrons in an asymmetric geomagnetic field, J. Geophys. Res., 108, 1116, doi:10.1029/2001JA009202, 2003.

3. Friedel, R. H. W., G. D. Reeves, and T. Obara, Relativistic Electron Dynamics in the Inner Magnetosphere - a Review, JASTP, (64) 265-282, 2002.

4. Hilmer, R. V., and G. P. Ginet, Enhancement of equatorial energetic electron fluxes near L=4.2 as a result of high speed solar wind streams, J. Geophys. Res., 105, 23,311, 2000.

5. Horne, R. B., and R. M. Thorne, Potential waves for relativistic electron scattering and stochastic acceleration during magnetic storms, Geophys. Res. Lett., 25, 3011, 1998.

6. Kim, H.-J., and A. A. Chan, Fully adiabatic changes in storm-time relativistic electron fluxes, J. Geophys. Res., 102, 22,107, 1997.

7. Li, X., D. N. Baker, M. Temerin, T. E. Cayton, G. D. Reeves, R. A. Christensen, J. B. Blake, M. D. Looper, R. Nakamura, and S. G. Kanekal, Multisatellite observations of the outer zone electron variation during the November 3-4, 1993 magnetic storm, J. Geophys. Res., 102, 14,123, 1997.

8. McAdams, K. L., G. D. Reeves, R. H. W. Friedel, T. E. Cayton, Multisatellite comparisons of the radiation belt response to the Geospace Environment Modeling (GEM) magnetic storms, J. Geophys. Res., 106, 10,869, 2001.

9. Roederer, J. G., Dynamics of Geomagnetically Trapped Radiation, 166 pp., Springer-Verlag, New York, 1970.

10. Selesnick, R. S., and J. B. Blake, A quiescent state of 3 to 8 MeV radiation belt electrons, Geophys. Res. Lett., 24, 1343, 1997a.

11. Selesnick, R. S., and J. B. Blake, Dynamics of the outer radiation belt, Geophys. Res. Lett., 24, 1347, 1997b.

12. Selesnick, R. S., and J. B. Blake, Radiation belt electron observations following the January 1997 magnetic cloud event, Geophys. Res. Lett., 25, 2553, 1998.

13. Selesnick, R. S., and J. B. Blake, On the source location of radiation belt relativistic electrons, J. Geophys. Res., 105, 2607, 2000.

14. West, H. I. Jr., R. M. Buck, and J. R. Walton, Electron pitch angle distributions throughout the magnetosphere as observed on Ogo 5, J. Geophys. Res., 78, 1064, 1973a.

15. West, H. I. Jr., R. M. Buck, and J. R. Walton, Satellite studies of magnetospheric substorms on August 15, 1968, 6, Ogo 5 energetic electron observations – Pitch angle distributions in the nighttime magnetosphere, J. Geophys. Res., 78, 3093, 1973b.

THE FLUMIC ELECTRON ENVIRONMENT MODEL

D.J. Rodgers
Space Department, QinetiQ
Farnborough, GU14 0LX, UK
Phone: +44-1252-394297
Fax: +44-1252-396330
E-mail: djrodgers@space.qinetiq.com

K.A. Hunter
QinetiQ

G.L. Wrenn
Retired from Space Department, DERA

Abstract

Assessments of the vulnerability of spacecraft materials to internal charging need a good electron environment model. Since the threat from electrostatic discharges is related to the occurrence of flux enhancements, the standard mean flux models are not appropriate. The requirement is for a model of enhanced flux conditions. These tend to occur mainly during the declining phase of the solar cycle.

FLUMIC (Flux Model for Internal Charging) was written to address this requirement. The model was originally developed as a simple engineering tool. Although simplicity of use is still the philosophy behind FLUMIC, it has undergone improvements to its accuracy and scope, mainly through the inclusion of better data sets and more sophisticated empirical modelling techniques. The latest version, FLUMIC3, has been developed in a new ESA study and relies heavily on data from the GOES/SEM and STRV-1b/REM instruments.

Although the outer belt, including geostationary orbit, is the region most at risk from internal charging effects, charging currents in the inner belt are not insignificant behind thin shields. The model now extends to the inner belt so that the current contributions from both inner and outer belts can be considered for satellites in eccentric orbits.

FLUMIC can be used as a tool in its own right but is also incorporated in the DICTAT internal charging tool. FLUMIC3 will be included in a new version of DICTAT to be released shortly.

Introduction

Internal charging is a well-established hazard that spacecraft designers must protect against and numerous design guidelines have been established, e.g. [1] for its mitigation. Energetic electrons that penetrate into dielectric materials lead to a build-up of charge. Grounded conductive components immediately leak away any deposited charge and so are safe from this process. However, ungrounded conductors collect charging in the same way as dielectrics and will be susceptible to ESD through intermediate insulators.

Although the fluxes of penetrating electrons are small, enhancements are long-lasting. In geostationary orbit outer belt enhancements may persist for several days. This is long enough

for strong electric fields to develop within dielectrics and between ungrounded conductors and other materials. As a result, there is the possibility of electrostatic discharge, which causes damage to sensitive electronics. There is clear evidence to indicate that many satellite systems have been degraded or destroyed by this process [2].

Protection by means of circuit desensitisation, careful component placement and shielding is possible but its implementation and validation can be time consuming and it adds cost to a mission. It is therefore important that unnecessary caution is avoided. There are long-established 'AE' and 'AP' series of electron and proton environment models for use in radiation calculations, of which AE-8 is the most recent electron model. This is a model of mean fluxes as a function of location, defined by B and L.. While this is useful for total dose calculations, it is inappropriate for the calculation of internal charging risk which is a function of temporary enhancements. Figure 1 shows the variability of daily averages of geostationary >2MeV electron flux in 1994, compared to the flux expected from the AE8 model.
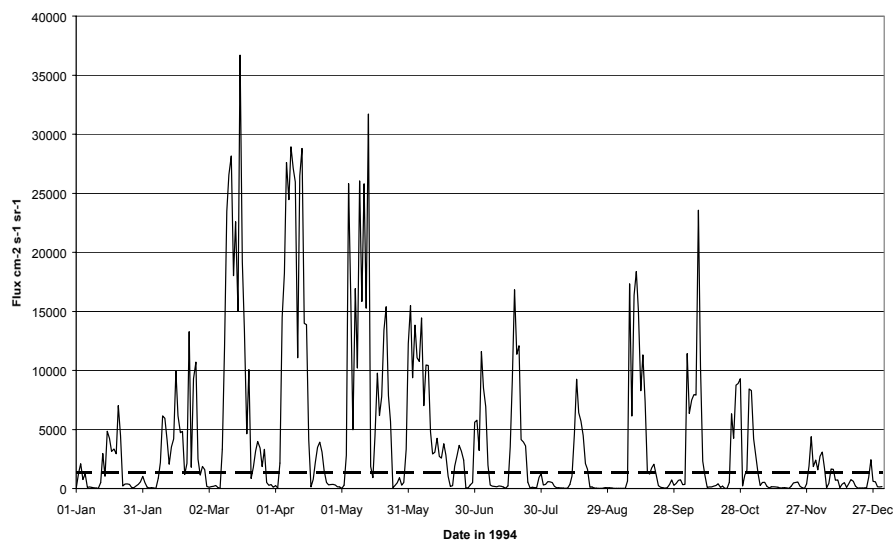
Figure 1. Daily-averaged >2MeV electron flux in geostationary orbit for 1994 as seen by GOES-7 compared to the AE-8 MIN model (dashed line).

A suitable severe case is needed by designers to use in risk assessment. Such a severe case is provided by FLUMIC (Flux Model for Internal Charging) described in this paper.

The 'Worst Case' Environment

It is common practice for designers to work to worst case specifications. However, this concept is often hard to define in practice. For internal charging, higher fluxes with energy sufficient to pass through spacecraft shielding lead to greater current deposited in internal dielectrics. However, such enhancements may be accompanied by a hardening of the electron energy spectrum which causes increased dose-rate, increase radiation-induced conductivity and a tendency to reduce charging. The balance between these competing effects depends on the properties of the material concerned. Also, a high flux for a brief period may be less hazardous than a lower flux for a longer period. Again this is material dependent. Hence there is no environment that is a worst case for all materials.

Characteristics of the FLUMIC Model

The characteristics of the model are defined to make it a severe environment generally applicable to all materials. These characteristics are:

- based on daily averages of flux – because only materials with a charging time-scale of 1 day or more are capable of charging to high levels.
- based on extreme flux levels at >2MeV – because high flux at this energy is most specifically associated with known spacecraft anomalies.
- based on the mean spectrum for the extreme flux level – because this leads to the most general severe case.

Other characteristics:

- conservative i.e. observed fluxes will virtually always be below that of the model.
- based on physical quantities, L and B/B0.
- most accurate where this is warranted. This means accurate at geostationary orbit where most spacecraft reside. For other orbits, it is most accurate near the magnetic equator, where fluxes are most intense. Accurate modelling of low-flux regions, e.g. near the atmospheric cut-off, is unnecessary.
- reflecting seasonal and solar cycle variations.

The Series of FLUMIC Models

FLUMIC was first created in 1998 [3] and was updated to FLUMIC2 in 2000 [4]. Both these versions of the code modelled the outer electron belt only. This latest version, FLUMIC3, updates the outer belt electron model and also models electron fluxes in the inner belt. Whilst internal charging has not been observed to be a problem for spacecraft confined to the inner belt, the extension of the model is to permit better assessment of eccentric orbits which encounter both inner and outer belt fluxes. All of the versions of FLUMIC have been designed to be used within the DICTAT [5] internal charging tool. However, FLUMIC can be used to provide input to other types of analysis and DICTAT can take other environment specifications as input. FLUMIC3 will be included in a new version of DICTAT to be released in 2004.

Data sources

FLUMIC3 is based heavily on data from the GOES/SEM [6] and STRV-1b/REM [7] instruments. This has is augmented in the inner belt by the short-lived STRV-1d/SURF [8] instrument because of its resistance to proton contamination.

GOES/SEM – Long-term seasonal and solar cycle behaviour of geostationary fluxes

STRV-1b/REM – Outer belt profiles and seasonal variation
STRV-1d/SURF & STRV-1b/REM – Inner belt profiles

The characteristics of these three databases are summarised in Table 1.

Other data sources have been used to provide confirmation of the these data sets. None of the data sets provided sufficient information away from the geomagnetic equator for this

variation to be explicitly modelled. Instead, the flux attenuation away from the equator was based on theoretical extrapolations.

Table 1. Summary of databases used for FLUMIC

REM	Orbit	GTO with inclination of 7˚
	Data duration	1994 to 1998.
	Data	Electron flux in three channels, 1-2.2 MeV, 2.2-4.6 MeV and 4.6-10 MeV
GOES	Orbit	Geostationary, with longitude around 75W and 135W.
	Data duration	More than a solar cycle
	Data	Electron flux in two channels, >0.6MeV and >2MeV.
SURF	Orbit	GTO, with inclination of 7˚
	Data duration	12 days, after which communication with the spacecraft was lost.
	Data	Electron current behind two levels of shielding, corresponding approximately to 1MeV and 1.7MeV

Cross- Calibration Issues

Effect of magnetic field co-ordinates

Cross calibration between different data sources can only be done at the same value of L and B/B0. In geostationary orbit, the gradient of flux in L is very steep and hence a spacecraft sees a significant variation in flux, due to the variation in L (typically L=6.6 to 7.5) caused by the pressure of the solar wind. The diurnal variation in L varies strongly with geomagnetic activity, as is exhibited by the Tsyganenko 1989 [9] model. An example of the effect on a typical geostationary satellite is plotted in Figure 2 below.

Variation of L value at GEO: 200 deg longitude, equinox
[Tsyganenko 1989]
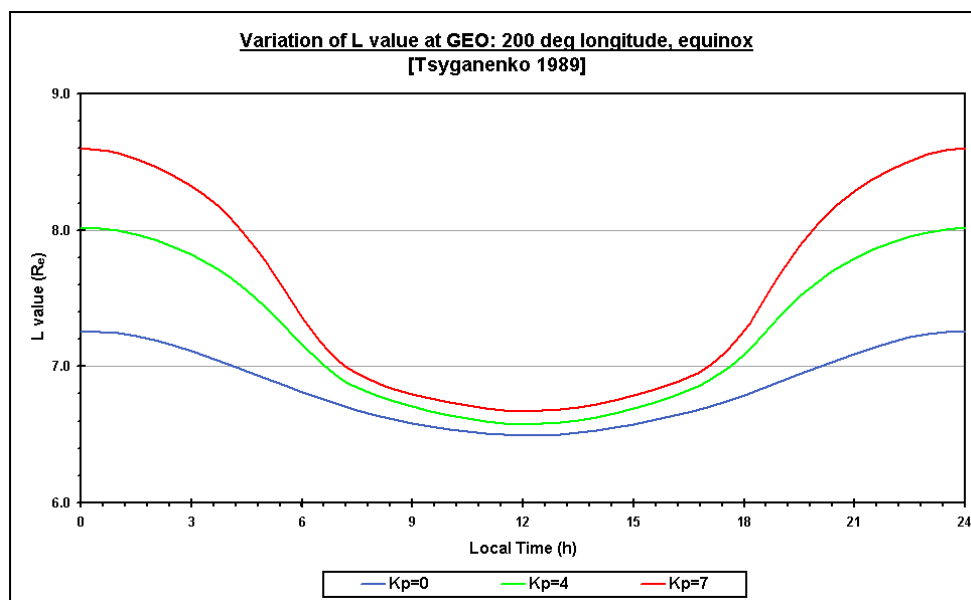
Figure 2. Diurnal variation of L value, as modelled by the Tsyganenko 1989 [9] model.

Figure 2 shows that L is least affected by changes in the shape of the magnetosphere around local noon. At this location, it makes little difference which level of geomagnetic activity is assumed. In the construction of FLUMIC3, a quiet-time (Kp=0) has been adopted.

This can be justified because it will lead to a safe over-estimation of flux and its effects will be limited because the intervals of substorm field distortion are generally short compared to the charge build-up times required to produce hazardous discharge. Very large, long-lasting geomagnetic storms can be considered separately.

GOES/GOES cross-calibration

Although GOES instrumentation is similar on the different satellites in the series, observed fluxes are significantly different. For example, GOES-8 values are significantly lower than GOES-7 values. If these data sets are to be used together we need to examine whether these differences can be explained solely by the difference in L arising from the longitude displacement between the spacecraft.

For each day in march 1994 and 1995, GOES-7 mean flux for the 3-hour interval closest to noon local time was extracted (or the maximum of the fluxes in the two nearest intervals). Data during solar proton events were removed because of potential contamination. In addition, data for electron enhancements immediately following Solar Proton Events were removed because the characteristics of these enhancements may differ from typical enhancements. Local noon L-values were computed as a function of spacecraft longitude using the Tsyganenko 1989 model. To retain the best accuracy, the observed Kp values were used in the magnetic field model. The results, shown in Figure 3, demonstrated that there was a significant variation in peak flux with L.
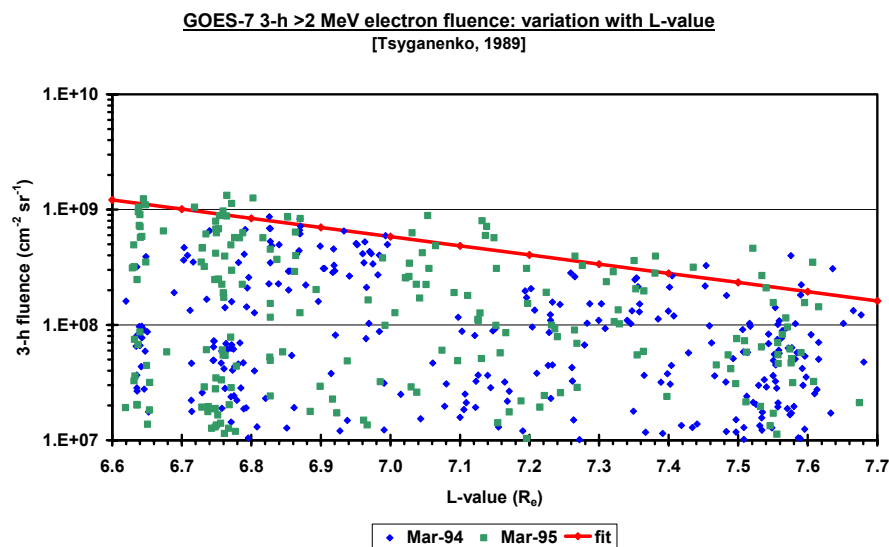
Figure 3. GOES-7 noon fluxes for March 1994 and 1995. A fit to the maximum fluxes is shown.

A straight line fit to the envelope of the GOES-7 data gives a suitable expression to translate all flux measurements to L= 6.6 equivalents: -

$$F_{6.6} = F_L \, 10^{(0.7955 \, L \, -5.25)}$$

There were good data simultaneously from both GOES-7 and GOES-8 spacecraft between 1 June 1995 and 30 April 1996. Using the above equation, these data were translated to L=6.6. The results, shown in Figure 4, indicate that GOES-8 measurements can be normalised to GOES-7 equivalents by application of the following expression:-

$$F_{G7} \text{ equivalent} = 10^{(1.22 \log [FG8] - 1.463)}$$

REM/GOES cross-calibration

The STRV-1b and GOES spacecraft inhabit similar L and B/B_0 locations when STRV-1b is near to apogee. Hence a comparison between the fluxes at these times is possible if one uses a realistic magnetic field model to remove local time effects. Using REM data that had been processed to include the detector response for an exponential spectrum [private communication, Buehler], the >2MeV flux can be inferred. A comparison for one day of a long-lived enhancement is shown in Figure 5. This shows good agreement between GOES-7 and REM. Over a longer period there are some differences but overall the two data sets are comparable (see Figure 6)
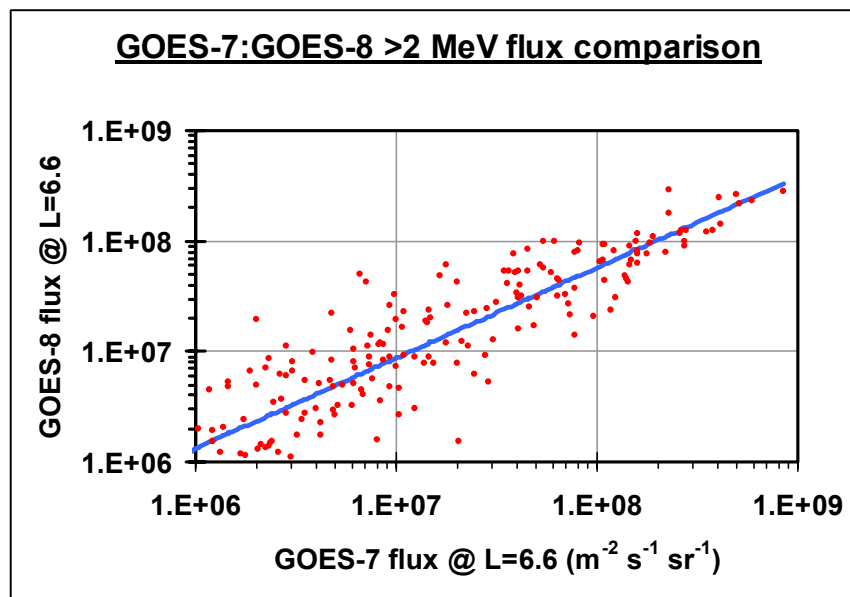
Figure 4. Comparison of GOES-7 and GOES-8 fluxes transformed to L=6.6.
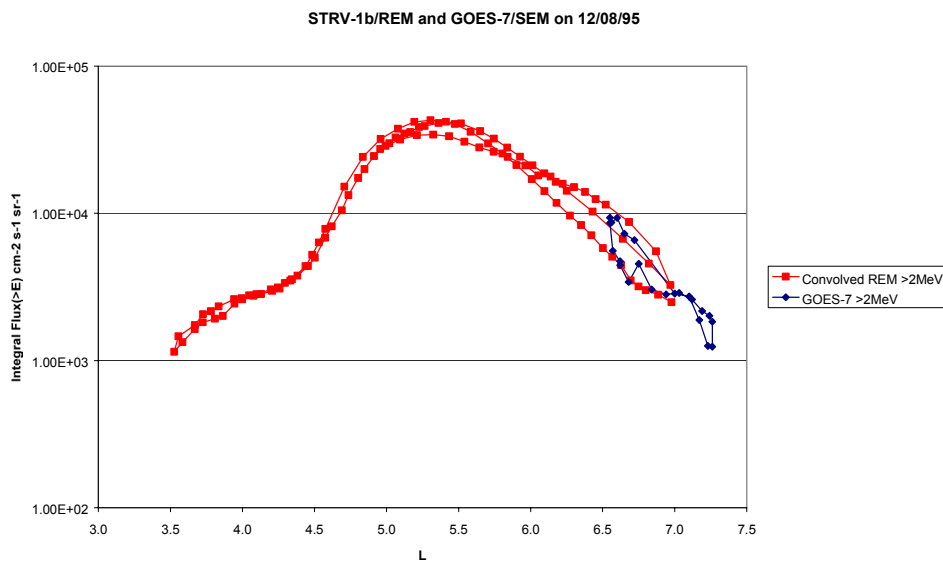
Figure 5. Comparison of convolved REM data and GOES L-profiles for a single day.
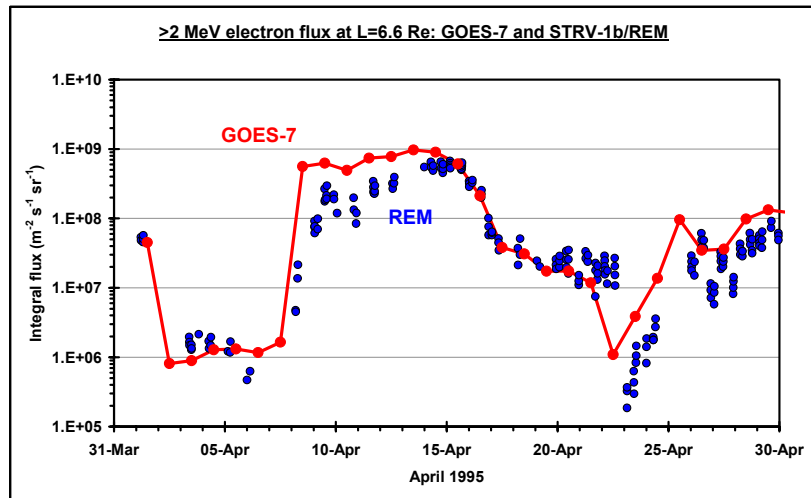
Figure 6. REM >2 MeV flux compared to GOES measurements at L=6.6 for April 1995

Modelling approach

Using magnetic field models to remove field-associated dependencies

Variations in the solar wind (i.e. speed, density and magnetic field) cause two separate effects that control observed energetic electron flux in the outer belt:

1. As a direct consequence of the field line motion, a spacecraft will sample different L shells; e.g. dropouts appear in flux in GEO as the field becomes more tail-like and the satellite effectively moves to higher L values.
2. The solar wind causes depletion and regeneration of the outer belt by whatever, poorly understood, processes occur – perhaps by injection, radial diffusion and acceleration, or wave particle interactions.

The first factor can be taken into account by a flux model in B/B0-L space if the adopted magnetic field model reliably reflects the existing level of geomagnetic activity. Models such as Olson-Pfitzer [10], Tsyganenko 1989 [9], and Tsyganenko 1996 [11], attempt to do this. The second factor must be modelled explicitly in the environment model. Using an activity-dependent model to determine L, might seem to negate the advantage of adopting the B/B0-L space framework, since geomagnetic activity cannot be an input when the model is used to estimate fluxes at future times. However, the long time-scales associated with internal charging help. The flux averaged over a day or more are heavily weighted by those intervals when the geomagnetic field was not greatly distorted, except for some periods with exceptional activity and then the intensities are normally low. Using a quiet-time (Kp=0) model errs on the conservative side. Modelling with a realistic magnetic field model therefore takes account of the asymmetry of the geomagnetic field involving orbit plane, longitude, local time and season.

Flux Envelopes

Because of the dynamically changing nature of the outer belt, a single B/B0-L co-ordinate may have widely differing flux at different times. Even during a single enhancement, the position of peak flux moves significantly, generally starting at high L and moving to lower L as the enhancement evolves [13]. An example is shown in Figure 7 for an enhancement in April 1995. This means that it is not sensible to select an outer belt profile from a single severe case but it is better to choose a flux profile that encompasses the range of outer belt profiles. This produces a conservative model that is applicable to all enhancements.

The occurrence rate of different flux levels is shown in Figure 8, for one channel of the REM data. This distribution has a steep upper boundary. Since FLUMIC seeks to give severe fluxes, it is this upper boundary that is modelled.

Spectrum

A convenient spectral shape for the outer belt is given by an exponential function, i.e.:

Flux $\propto \exp(-E/E_0)$ where E is energy and E_0 is the e-folding energy

The small number of energy channels in the GOES/SEM and REM instruments does not justify a more complicated expression than this. It has been observed in geostationary orbit [10], that there is a link between flux enhancements at >2MeV and a hardening of the spectrum. However, REM data show that E_0 has no clear dependence on >1MeV flux. These two results are not necessarily contradictory but this issue warrants further investigation. REM data show that E_0 is quite constant in the outer belt, if one selects only >1MeV fluxes close around the flux 'envelope'. This is shown in Figure 9.
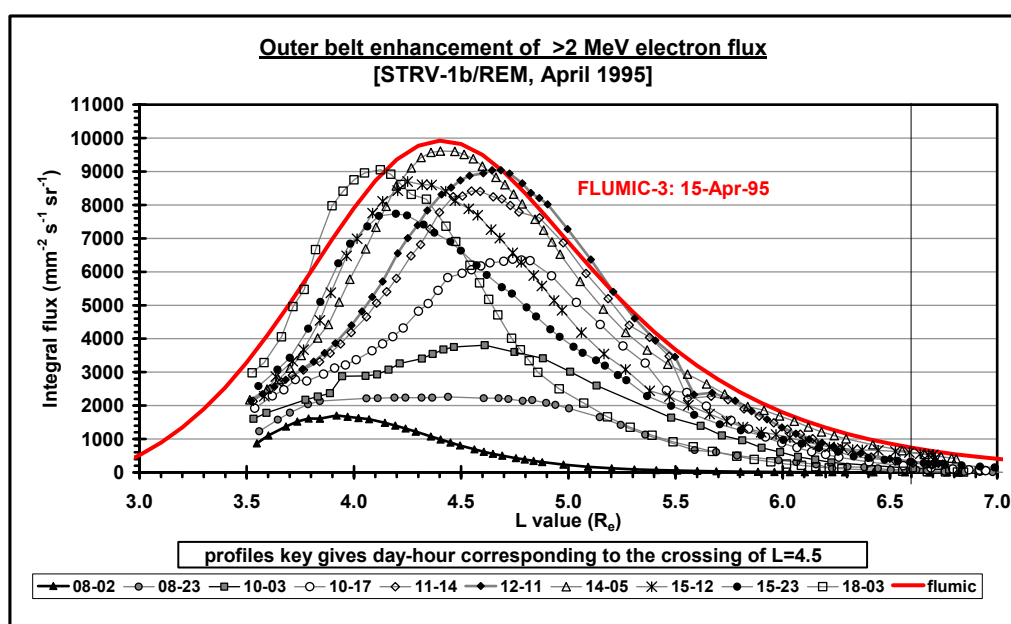
Figure 7. REM outer belt flux profiles over a 10-day period from 8th to 18th April 1995. Geostationary fluxes (marked by a line at L=6.6) are only weakly indicative of the behaviour of the belt as a whole. The FLUMIC3 'envelope' is shown.
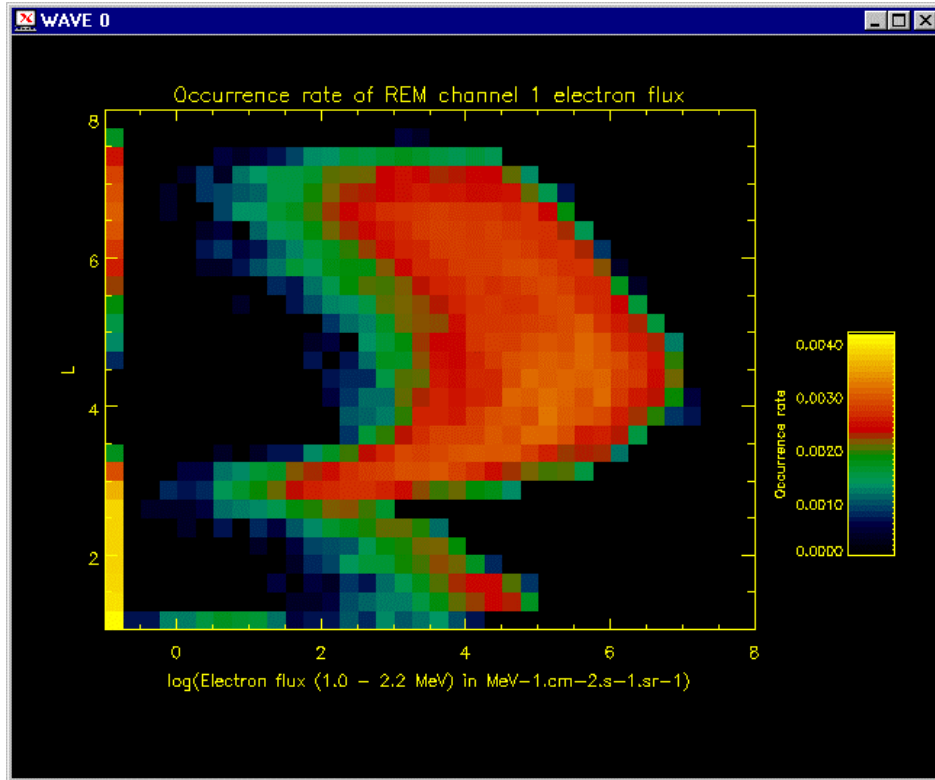
Figure 8. Distribution of flux values in the REM 1 to 2.2MeV channel.
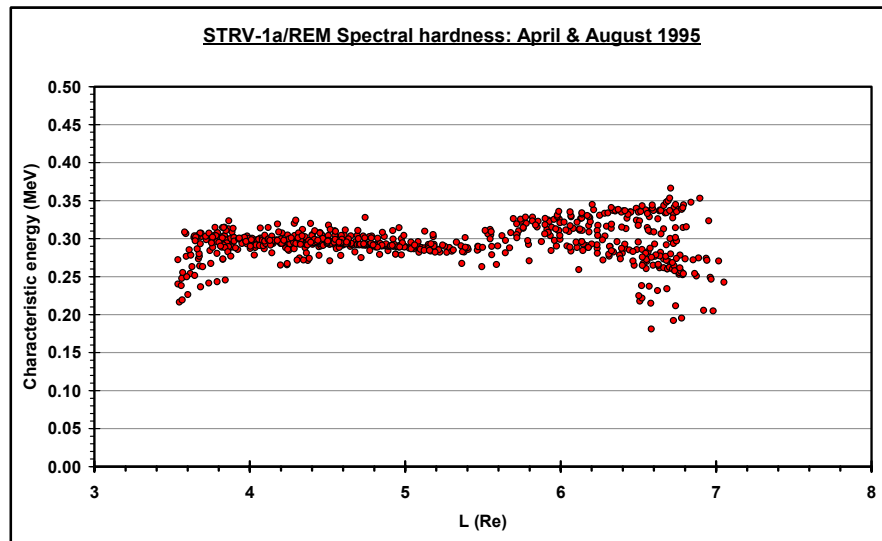
Figure 9. E_0 calculated from REM data, for times when >1MeV flux is more than 50% of the maximum for that L. L bins of width 0.2 were used.

In the inner belt, REM data in higher energy channels suffer some contamination from protons and so SURF data are used as the primary source of E_0. This is possible, despite the short time span of data from this instrument, because REM data show the inner belt fluxes to be very stable over long periods. SURF data show that E_0 is almost constant where fluxes are high and so a constant value of E_0 is a reasonable approximation.
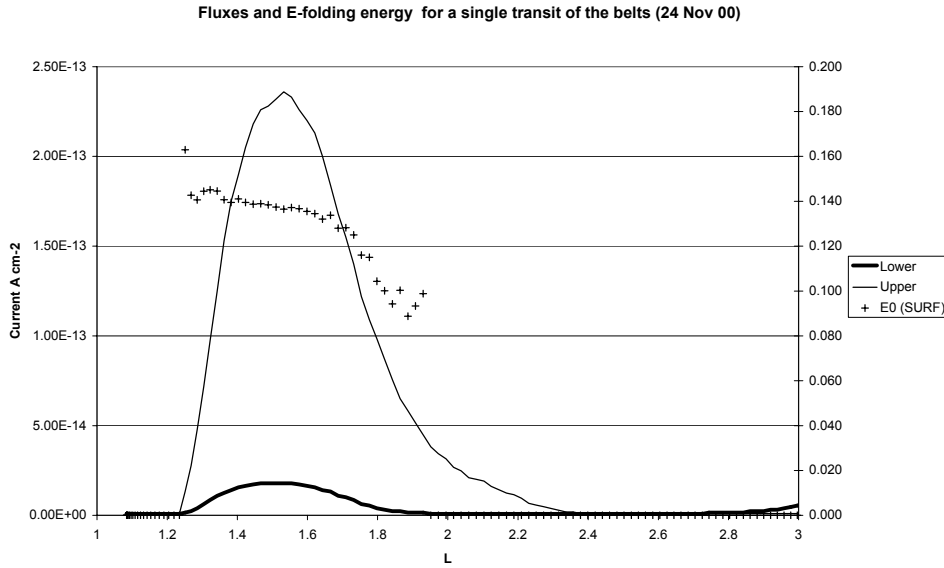
Figure 10. Current density measured in the SURF upper and lower plates for a
crossing of the inner belt. The calculated value of E_0 is also shown.

Solar Cycle variation

The outer belt exhibits a strong solar cycle variation, with a peak in the declining phase of
the sunspot cycle. Monthly maximum GOES >2MeV fluxes are shown in Figure 11 below. A
curve approximately encompassing the peak fluxes is shown.

Seasonal variation

The seasonal variation of flux may be examined with the same GOES >2MeV data. As is
shown in Figure 12 there are minima near the start and middle of the year, in agreement with
previous observations of enhancements near the equinoxes. A simple curve is used to
describe the variation in peak fluxes.
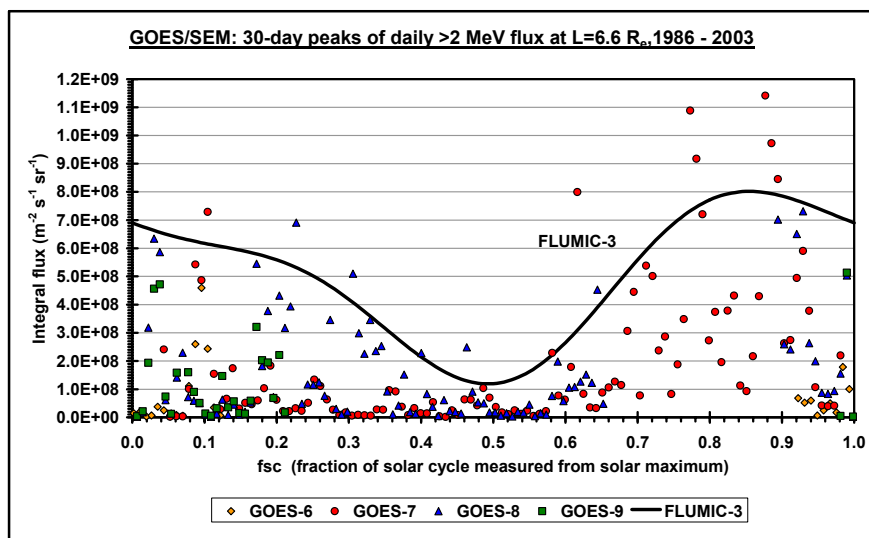
Figure 11. Solar Cycle variation of >2MeV electron flux for 1986-2003, normalised to
GOES-7 fluxes at L=6.6, plotted against solar cycle phase (fsc). A curve encompasses
almost all the enhancements.
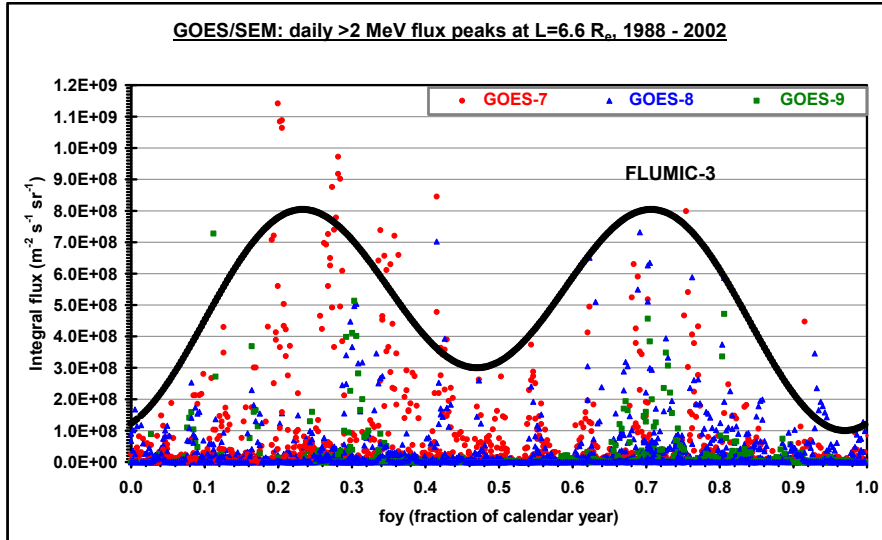
Figure 12. Daily >2MeV flux, plotted against fraction of calendar year (foy).

FLUMIC3 Equations Summary

The equations that comprise FLUMIC3 are shown below. These are currently in draft form.

OUTER BELT (L>2.5 R_e)

>2MeV Flux at L=6.6 R_e

The peak integral flux above 2 MeV at L= 6.6 is taken to be 8×10^8 m^{-2} s^{-1} sr^{-1}.

Solar Cycle
$F(fsc)= 8 \times 10^8 \{0.625+0.375\sin[2\pi*(fsc-0.7)]+0.125\sin[4\pi*(fsc-0.15)]\}$
      where *fsc* is the solar cycle phase starting at solar minimum.

Season
$F(foy,fsc)=F(fsc)\{0.625-0.375\cos[4\pi(foy+0.03)]-0.125\cos[2\pi(foy+0.03)]\}$
      where *foy* is the fraction of year starting from 1st January.

Spectrum
$F(>E)=F(>2MeV) \times \exp[(2-E)/E_0]$ where
      $E_0 = 0.25$ for $F(>2MeV) < 10^7$ m^{-2} s^{-1} sr^{-1}.
      $E_0 = 0.25+0.11((\log[F(>2MeV)] -7)^{1.3})$ for $F(>2MeV) > 10^7$ m^{-2} s^{-1} sr^{-1}.

E_0 in the outer belt is the subject of ongoing study and so this aspect of the model may be updated before the model is finalised.

Flux versus L profile
$F(>E,L) = F(>E,6.6) \times 16\tanh[0.6(L-2.5)]/\cosh[1.5(L-4.3)]$ m^{-2} s^{-1} sr^{-1}
      where $F(>E,6.6) = F(foy,fsc) \times \exp[(2-E)/E_0]$.

INNER BELT (L<2.5 R_e)

>1MeV Flux versus L profile

$$F(>1MeV,L) = 4.0 \times 10^{\{2.12+45.4/(L+0.05)^2 - 45.6/(L+0.05)^3\}} \qquad m^{-2} \, s^{-1} \, sr^{-1}$$

Spectrum

$$F(>E)=F(>1MeV) \times \exp[(1-E)/E_0]$$
$$\text{where} \quad E_0 = 0.14 \text{ MeV}$$

B/B0

For L < 3   Flux = Flux(equatorial)x10$^{(-a((B/B0)-1))}$
   where $a = -0.4559L+1.4385$ $L \geq 1.75$
   and $a = 36.(1/\sinh((L-1)x10.)+0.7)$ $L<1.75$
For $L \geq 3$ the formula of Vette [14] is used, as in AE8

Acknowledgments

References

1. Whittlesey, A. Ed., NASA Technical Handbook, "Avoiding Problems Caused by Spacecraft On-Orbit Internal Charging Effects", NASA-HDBK-4002, Feb. 1999.

2. Wrenn, G.L., D.J.Rodgers & K.A.Ryden, "A solar cycle of spacecraft anomalies due to internal charging", Ann. Geophys. 20, 953-956, 2002.

3. Rodgers D.J., K.A.Ryden, P.M.Latham, L.Levy, 'Engineering Tools for Internal Charging: Final Report', ESA contract 12115/96/NL/JG(SC), Aug. 1998

4. Rodgers D.J., K.A.Ryden, P.M.Latham, G.L.Wrenn (T.S.Space Systems), L.Lévy, B.Dirassen , Engineering Tools for Internal Charging: Final Report', ESA contract 12115/96/NL/JG(SC) WO.1, CCN1, March 2000

5. Rodgers D.J, K.A.Ryden, G.L.Wrenn, P.M.Latham, J. Sørensen and L.Levy 'An Engineering Tool for the Prediction of Internal Dielectric Charging', Proceedings 6th Spacecraft Charging Technology Conference, 1998.

6. GOES I-M Databook, 19 November 2001 edition, http://rsd.gsfc.nasa.gov/goes/text/goes.databook.html

7. P.Buehler, S.Ljungfelt, A.Mchedlishvili, N.Schlumpf, A.Zehnder, L.Adams, E.Daly and R.Nickson; Radiation environment monitor, Nucl. Instr. and Meth. in Phys. Res. A,368, pp. 825-831, 1996.

8. Ryden,K.A., P.A.Morris, A.D.Fydland, H.S.Jolly, D.J.Rodgers, C.S.Dyer, "Profiles of inner- and outer- belt internal charging currents against geomagnetic parameter 'L': results from the first SURF experiment", Proc. 7th Spacecraft Charging Technology Conf., ESA-ESTEC, Noordwijk, April 2001.

9. Tsyganenko, N. A., A magnetospheric magnetic field model with a wrapped tail current sheet, Planet. Space Sci., 37, 5-20, 1989.

10. Olson, W. P., and K. A. Pfitzer, Magnetospheric magnetic field modeling, Annual Scientific Report, AFOSR Contract No. F44620-75-C-0033, 1977.

11. Tsyganenko, N. A., and D. P. Stern, Modeling the global magnetic field the large-scale Birkeland current systems, J. Geophys. Res., 101, 27187-27198, 1996.

12. Desorgher, L., P.Bühler, A. Zehnder, E.Daly, L.Adams, Variations of the outer radiation belt during the last two years, SP-392, p137,1996.

13. Wrenn, G.L., Rodgers, D.J., and Buehler, P.: "Modeling the outer belt enhancements of penetrating electrons", J. Spacecraft and Rockets 37, 408-415, 2000.

14. Vette, J.I., The AE-8 Trapped Electron Model Environment, NSSDC report 91-24, November 1991.

NEW NASA SEE LEO SPACECRAFT CHARGING DESIGN GUIDELINES – HOW TO SURVIVE IN LEO RATHER THAN GEO

Dale C. Ferguson
Photovoltaics and Environmental Effects Branch
John H. Glenn Research Center at Lewis Field
21000 Brookpark Road, Mail Stop: 302-1
Cleveland, Ohio 44135-3191
Phone: (216) 433-2298
Fax: (216) 433-6106
E-mail: dale.c.ferguson@nasa.gov

G. Barry Hillard
John H. Glenn Research Center at Lewis Field

Abstract

It has been almost two solar cycles since the GEO Guidelines of Purvis *et al* (1984) were published. In that time, interest in high voltage LEO systems has increased. The correct and conventional wisdom has been that LEO conditions are sufficiently different from GEO that the GEO Guidelines (and other GEO and POLAR documents produced since then) should not be used for LEO spacecraft. Because of significant recent GEO spacecraft failures that have been shown in ground testing to be likely to also occur on LEO spacecraft, the SEE program commissioned the production of the new LEO Spacecraft Charging Design Guidelines (hereafter referred to as the LEO Guidleines). Now available in CD-ROM form, the LEO Guidelines highlight mitigation techniques to prevent spacecraft arcing on LEO solar arrays and other systems. We compare and contrast the mitigation techniques for LEO and GEO in this paper. We also discuss the extensive bibliography included in the LEO Guidelines, so results can be found in their primary sources.

Background

Historically, power systems on many space vehicles have operated at a nominal 28 V dc. At such low voltages, plasma interactions in LEO are negligible and have not been a consideration in spacecraft design. High power systems now being deployed for space applications operate at higher voltages in order to reduce power loss and system mass. The emergence of such systems is motivated primarily by a desire to save weight. Since the resistance of the necessary cabling is a decreasing function of mass per unit length and cable losses are proportional to current squared, it is desirable to furnish power at higher voltages and lower currents. A further consideration is the reduced effect of magnetic interactions (torque and drag) that will follow from low current operation.

While high voltage systems are clearly desirable to the power system designer, they suffer the drawback of interacting with the ionospheric plasma in several different ways. First, conducting surfaces whose electrical potential is highly negative with respect to the plasma can

undergo arcing. Such arcing not only damages the material but results in current disruptions, significant EMI, and large discontinuous changes in the array potential.

One of the difficulties in predicting the onset of arcing has been the realization that the threshold potential for arcing depends critically not only on the design of the solar cells, but also in the manner cells are laid down and connected. In the early 1990's traditional wisdom focused on the observation that silicon cells using traditional silver coated interconnects exhibited a threshold potential for arcing of about -230 volts relative to the plasma (Ferguson, 1986). Yet, since that time, it has been shown that catastrophic failures can occur on operating solar arrays at much lower voltages. For example, the TEMPO-2 and PAS-6 solar array failures in 1997 (Snyder *et al*, 2000) were on solar arrays that operated at string voltages of 100 volts or less, and ground-tests showed that the Terra solar arrays (operating at 120 V) were liable to the same type of failure in LEO.

An additional effect that plagues surfaces at high negative potential lies in the fact that inbound ions, accelerated by the high fields, cause sputtering from surfaces with which they impact.

For solar arrays or other surfaces that are biased positively with respect to the plasma, a second effect occurs. Such surfaces collect electrons from the plasma, resulting in a parasitic loss to the power system. Since the mass of an electron is much less than an ion, the magnitude of current density is much greater for surfaces with positive bias. At bias potentials greater than about 150 volts, sheath formation and secondary electron emission from the surface causes the entire surrounding surface, normally an insulator, to behave as if it were a conductor. This effect, often referred to as "snapover" (Stevens, 1982), results in large current collection from even a very small exposed area.

Besides producing a power loss, currents collected by biased surfaces significantly affect the potentials at which different parts of the spacecraft "float." Because of their large mass and low mobility, ions collected by negatively biased surfaces result in a relatively small plasma current density. The lightweight electrons, on the other hand, are readily collected by positively biased surfaces. Ram and wake effects further complicate the picture. Ram energy is considerably higher than ambient thermal energy so ram flow enhances ion collection relative to surfaces that are oblique to the plasma flow.

A spacecraft, reacting to these various current sources, must necessarily reach equilibrium at whatever potential results in a net collected current of zero. The worst situations occur when the spacecraft power system uses a negative ground. In such a configuration, large surfaces are negative and must collect slow moving ions to balance the current from electron collection that now occurs only from relatively small areas of positive surface. In the worst case, parts of the spacecraft will be biased with respect to the ionosphere to a level very near the maximum voltage used on the solar arrays.

As experience has accumulated within industry and government, the need to capture the state of understanding has become pressing. Recognizing this, the Space Environments and Effects (SEE) program, managed by the Marshall Spaceflight Center, has commissioned and funded a

series of software design tools and guidelines documents to aid the spacecraft community. The latest of these efforts is the document reported here, which focuses on high voltage interactions in Low Earth Orbit (LEO), the LEO Spacecraft Charging Design Guidelines.

LEO vs. GEO

As most of the spacecraft design community is aware, charging conditions in Geosynchronous Earth Orbit (GEO) are severe, and are caused mainly by high energy electrons impinging on spacecraft surfaces during geomagnetic substorms (Rosen, 1975). In such events, spacecraft surfaces can charge differentially by as much as the energies of the incoming electrons, which may be as high as several kilovolts. Because spacecraft surfaces may have differing capacitances due to differing materials and grounding, and because differing materials may have differing secondary electron emission coefficients and other charging properties, a high degree of differential charging can occur that can lead to arcing conditions. On the other hand, the thermal plasma in GEO is so tenuous that the times required for the thermal plasma to discharge spacecraft surfaces can be many minutes. Under such conditions, the only way to prevent differential charging of spacecraft surface materials is to coat all exterior surfaces with conductive coatings, and connect them all to spacecraft ground. Then, although the spacecraft as a whole can charge several thousand volts negative, differential charging is eliminated, and the high electric field strengths necessary for surface plasma arcing are thereby eliminated.

The basic tenets for preventing arcing from GEO spacecraft charging were presented by Purvis, *et al* (1984). Over the years, these "Design Guidelines for Assessing and Controlling Spacecraft Charging Effects," have become the spacecraft designers' charging bible, sometimes to the extent that spacecraft designers have attempted to apply them in LEO conditions. This is a gross mistake. For example, some designers have attempted to make their solar array coverslides conductive enough to prevent differential charging in LEO by using poorly conductive coatings. These satisfy the GEO Guidelines but that fall many orders of magnitude below the conductivity that will bleed off the currents collected in the dense LEO plasma. In addition, these coatings can contribute to perpetually having snapover currents collected even on surfaces at low positive potentials. In other words, there is a big difference between charging in LEO and GEO and spacecraft designers should take this into account. Up until now, however, recommendations for designing for LEO charging have been scattered throughout the literature. This was one rationale for producing the LEO Spacecraft Charging Guidelines.

In the following, we will point out differences between recommendations for spacecraft charging in GEO, as taken from the Purvis *et al* (1984) technical paper and recommendations for spacecraft charging in LEO, as taken from the LEO Guidelines. For designing specific spacecraft, designers should read the LEO Guidelines in their entirety.

Surface materials and grounding

GEO – "For differential charging control, all spacecraft exterior surfaces shall be at least partially conductive. All conducting elements, surface and exterior, should be tied to a common electrical ground, either directly or through a charge bleedoff resistor."

LEO – "Avoiding snapover has become a major design issue. Strategies include insulating all surfaces, where practical, and choosing insulators with low secondary electron emission yields. A thin insulator may undergo dielectric breakdown under the high electric field developed across it. Until the theoretical situation is better understood, plasma testing must be used to determine the dielectric strength of insulators." If conducting surfaces are exposed, care must be taken to prevent them from arcing at conductor-insulator junctions.

Enclosures and shielding

GEO – "The primary spacecraft structure, electronic component enclosures, and electrical cable shields shall provide a physically and electrically continuous shielded surface around all electronics and wiring (Faraday cage)."

LEO – "If all high voltage components are inside a sealed pressure vessel, they cannot collect current from the ambient plasma (and LEO charging cannot occur). Encapsulation (or grouting with RTV) of solar arrays has been shown to be an effective method to prevent electron collection and charging (Reed *et al*, 2001). One must be careful with the use of encapsulants, however, when the possibility exists of outgassing in the presence of high voltage components. When encapsulating....no air must be entrained anywhere. The trapped air will present the danger of Paschen breakdown under high voltage. Also, to avoid plasma interactions, care must be taken that plasma does not enter the enclosure and react with exposed conductors inside. The key requirement on such systems is that all openings must be smaller than the plasma Debye length."

Solar Arrays

GEO – "Solar panel back surfaces, edges, and honeycomb should be grounded conductors. The front surfaces of coverslides may be coated with a conductive, transparent coating of grounded tin oxide...." (Since 1997, when sustained arcing was discovered, some manufacturers have put restrictions on the spacing, string layout, and voltages of adjacent high voltage strings.)

LEO – "If possible, use array string voltages of less than 55 V. No trigger arcs have been seen on LEO arrays of less than about 55 V string voltage even under simulated micrometeoroid bombardment. Solar arrays coming out of eclipse will generate more voltage than when they operate at their max power point. If solar array cell edges or interconnects are exposed to the LEO plasma and string voltages are greater than 55 V, the strings should be laid out on the substrate such that no two adjacent cells have a voltage difference of greater than 40 V..." (to prevent sustained arcs).

Testing

GEO – Testing GEO spacecraft is mainly concerned with determining current paths when arcs occur, to prevent electronic upsets (ie "Internal (general) units must survive, without damage or disruption, the MIL-STD-1541 arc source test," etc.). More recently, some testing has been done to determine the extent of charging, should it occur, and the likelihood of arcing due to the charging from a worst-case environment.

LEO – LEO testing is mainly concerned with trigger and sustained arc thresholds and arc-current waveforms. "If one is interested in investigating transient arcs, one must decouple the DC power supply from the arc current during an arc. This means the bias supply circuit must have a time constant greater than a few hundred microseconds, so the arc can build up and dissipate without being powered by the bias supply. This can be done by putting a large resistance in the arc circuit, and incorporating a capacitor to simulate the array or structure capacitance that would be discharged in the arc."

Plasma contactors and other charge control devices

GEO – "Devices that emit neural plasmas or neutralized beams (e.g., hollow cathode plasma sources or ion engines) can maintain spacecraft potentials near plasma ground and suppress differential charging. These are therefore the recommended type of charge control devices."

LEO – "Electron guns were used on PIX-II (Purvis, 1985) and PASP Plus (Guidice and Severance, 1998) to emit the electrons being collected by high voltage solar arrays and thus prevent charging, but such devices are limited by space charge considerations to low emitted electron currents. A better solution is a device that is not limited by space charge considerations, i.e. a plasma contactor." "(The plasma contactor) current can be very large. For instance, the ISS PCU device has a hollow cathode element smaller than a little finger, but can emit up to 10 Amps of continuous electron current."

In addition to the above topics and several others not listed here, the LEO Guidelines contains a special section on mitigation techniques for solar array arcing in LEO. Please see the LEO Guidelines for complete advice on all the topics listed above and more.

The LEO Guidelines Searchable Bibliography

An attempt was made to pull together all published sources of information about designing for the LEO plasma environment. In order to do this, the CASI database (Center for Aerospace Information) was searched for authors, keywords, and subjects related to LEO spacecraft charging. Over 300 abstracts were obtained, and are listed in chronological order in the LEO Guidelines Searchable Bibliography, located at the end of the same .pdf file as contains the LEO Guidelines. Because of the multiplicity of papers by the same authors in any one year, the CASI Document ID is used as a reference (i.e. Guidice *et al*, **19980017264** instead of 1998). While every attempt has been made for completeness through the end of 2002, we are aware that we may have missed some references and are going to revise the Bibliography, if not the entire LEO Guidelines, every year to try to keep current and correct accidental omissions. To check the searchability of the Bibliography for this paper, I searched within Adobe Acrobat Reader for the name Guidice, and obtained fourteen references in the Bibliography within a few seconds.

Including the Bibliography, the LEO Guidelines comes to over 360 pages. It is recommended that the Guidelines be kept as a computer file reference book, or on CD-ROM, not as a printed reference. This will preserve the searchability feature, save trees, and make the LEO Guidelines completely portable, whereas a 360 page book is cumbersome, not searchable, and wasteful of natural resources. It is not believed that the LEO Guidelines contain any

copyrighted, classified or ITAR restricted material, and may therefore be shared with anyone. The authors respectfully request that when material from it is used, we be given the proper credit (Ferguson, D.C. and Hillard, G.B., 2003, "Low Earth Orbit Spacecraft Charging Design Guidelines," NASA/TP-2003-21228, National Aeronautics and Space Administration Marshall Space Flight Center, MSFC, Alabama 35812, February 2003.) The LEO Guidelines has been proposed as a NASA standard. If that status is achieved, it may then be proposed as a world standard under ISO 9001.

Availability

The Low Earth Orbit Spacecraft Charging Design Guidelines is available from the NASA MSFC SEE website (http://see.msfc.nasa.gov) as part of the Charge Collector CD-ROM (version 2.0) or as a separate CD-ROM, or on CD-ROM directly from the authors at the address given for them in this paper. All authentic versions are in .pdf format. Neither the authors, the SEE program, or NASA are responsible for incorrect conclusions drawn from it by any party. It is intended solely as an aid for spacecraft designers to prevent harmful effects of LEO plasma interactions. The authors welcome comments and suggestions for improvements.

References

1. Ferguson, D.C., 1986, "The voltage threshold for arcing for solar cells in LEO: Flight and ground test results," NASA TM-87259, presented at the24th AIAA Aerospace Sciences Mtg. and Exhibit, Reno, Nevada, Jan. 6-9, 1986.

2. Guidice, D.A. and Severance, P.S., 1998, "Chapter 3, Instrumentation," in Photovoltaic Array Space Power Plus Diagnostics (PASP Plus) Experiment, PL-TR-97-1013, by Guidice et al, the Air Force Research Laboratory, Kirtland AFB, March, 1997, p. 3-1 to 3-10.

3. Purvis, C.K., Garrett, H.B., Whittlesey, A.C., and Stevens, N.J., 1984, "Design Guidelines for Assessing and Controlling Spacecraft Charging Effects," NASA TP-2361, September, 1984.

4. Purvis, C.K., 1985, "The PIX-2 experiment: An overview", in Spacecraft Environmental Interactions Technology-1983, NASA CP-2359, AFGL-TR-85-0018, p. 321-332, NASA Lewis Research Center, March, 1985.

5. Reed, B.J., Harden, D.E., Ferguson, D.C., and Snyder, D.B., 2001. "Boeing's High Voltage Solar Tile Test Results, 17th Space Photovoltaic Research and Technology Conference, Ohio Aerospace Institute, September 11-13.

6. Rosen, A., 1975, "Large discharges and arcs on spacecraft," Astronautics and Aeronautics, vol. 13, June 1975, p. 36-44.

7. Snyder, D.B., Ferguson, D.C., Vayner, B.V., and Galofaro, J.T., 2000, "New Spacecraft-Charging Solar Array Failure Mechanism," 6th Spacecraft Charging Technology Conference, AFRL-VS-TR-20001578, pp. 297-301.

8. Stevens, N.J., 1982, "Review of biased solar array - Plasma interaction studies," AIAA PAPER 81-0738, AIAA, Japan Society for Aeronautical and Space Sciences, and DGLR, International Electric Propulsion Conference, 15th, Las Vegas, NV, Apr. 21-23, 1981, AIAA 16 p., International Electric Propulsion Conference Las Vegas, NV Apr. 21-23, 1981.

EMBEDDED-PROBE FLOATING POTENTIAL CHARGE-DISCHARGE MONITOR

Keith G. Balmain
University of Toronto
Department of Electrical and Computer Engineering
10 King's College Rd
Toronto, Ontario M5S 3G4, Canada
Phone: (416) 978-3127
Fax: (416) 971-3020
E-mail: Balmain@waves.utoronto.ca

P.C. Kremer
G.R. Dubois
A.A.E. Lüttgen
University of Toronto
Department of Electrical and Computer Engineering

Abstract

Described is a device that responds to the floating potential of an electrically isolated (or "floating") metal probe embedded in a dielectric slab and exposed to a source of energetic electrons. With the passage of time, the probe potential becomes increasingly negative due to the accumulation of electric charge both on it and nearby it in the surrounding dielectric, until equilibrium is reached between charge influx and charge conduction or emission.

The device ultimately would be mounted on a spacecraft positioned in an energetic-electron environment, typically in geo-synchronous orbit or geo-transfer orbit. The probe-plus-dielectric configuration would be designed to represent a relevant possible site for electrical breakdown, for example with the metal probe representing the inner conductor of a coaxial cable or a metallic trace on a printed-circuit board. A high probe floating potential or an abrupt change in potential would serve as advance warning of a charge accumulation threat or an electrical breakdown threat in the vicinity of the monitor. Multiple units with probes at different depths would respond preferentially to electrons with different penetration depths (i.e. different energies), thus conceivably providing data for correlation with energetic-particle spectra from other instruments on the same satellite or ones nearby.

Two designs are described, one motor-driven and one piezo-vibrator-driven, so that the mechanical movement can generate an electrical signal suitable for processing because it is proportional to the floating potential. Under high-vacuum exposure to Strontium-90 electrons up to 2 MeV, floating potentials to 12 kV have been measured, with breakdown and breakdown recovery detected. Various laboratory measurement examples will be presented.

Introduction

This paper describes two versions of a charge monitor. The main difference between the two versions are the means by which an AC signal that is proportional to the probe floating potential is generated. The first version involves a motor-driven perforated drum as a field interruptor and the other one involves a modulated high-voltage capacitor.

Figure 1. Motor-driven monitor: dielectric samples and embedded probes in the motor-driven monitor.

The first two sections of this paper describe the motor-driven and the piezo-driven versions, respectively. This is followed by one section each on the experimental results from each monitor.
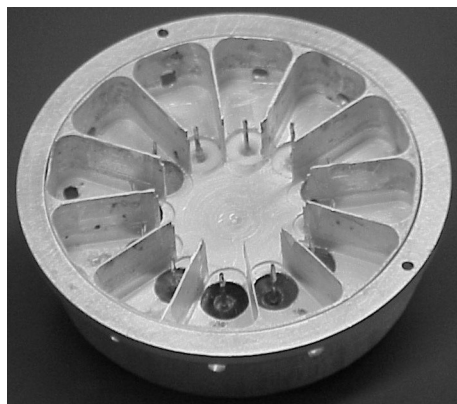
Figure 2. Motor-driven monitor: probes from dielectric samples, adjacent to perforated drum (not shown).

Motor-Driven Charge Monitor

This monitor includes an aluminum housing which is divided into twelve triangular sections, each separated by aluminum partitions which are part of the housing. These triangular sections each hold a dielectric sample such that the sample exactly fits into the space between the partitions. Each sample has a wire embedded in it which can be at three different depths in the dielectric – on its surface, or in the interior at depths of 2 mm or 4 mm. Figure 1 shows the top

view of the setup, which is the side which is exposed to highly energetic particles. Some of the embedded wires are clearly visible in Figure 1.
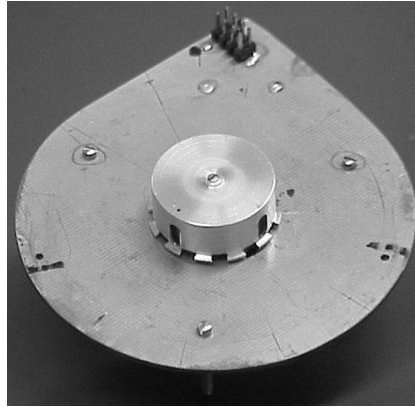
Figure 3. Motor-driven monitor: perforated-drum field interruptor.

The embedded wires are connected to one probe each, protruding from the bottom of the housing. Note that the wires are not in electrical contact with the housing and therefore can be considered as floating. Figure 2 shows the bottom of the setup with the twelve probes arranged in a circle. Partitions exist there as well to suppress crosstalk from the probes.
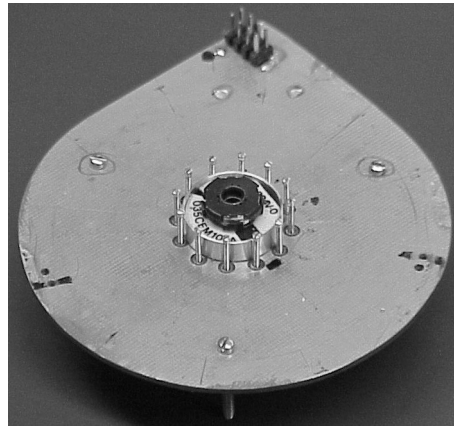
Figure 4. Motor-driven monitor: drive motor and probes to electronics.

Figure 3 shows the base of the setup which has a rotating drum that fits into the circle in which the probes are arranged in Figure 2 and is adjacent to the probes. A motor drives the drum which has a periodically perforated wall which is between the probes and a separate set of probes, which we may call sensing posts. The motor and the sensing posts are shown in Figure 4. Each sensing post is connected to an operational amplifier which provides an amplified signal proportional to the voltage on the probe. The electronics board is shown in Figure 5.

The rotation of the perforated drum opens and closes the windows, thus periodically turning on and off the weak electric field between each probe and its corresponding sensing post. Therefore the DC voltage on the probes is converted to an AC voltage on the sensing post.

The rim of the drum is notched to form tabs which extend outwardly from the drum wall (Figure 3) and a hole is located in the base positioned such that the tabs periodically over it so that a light beam emerging from a light source below the base is reflected back to an optical reader. This is used to synchronize the system.
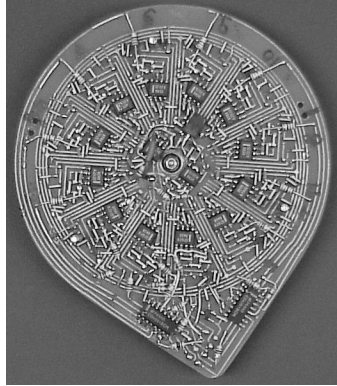
Figure 5. Motor-driven monitor: electronics board.

Piezo-Driven Charge Monitor

A cut-away drawing of another type of charge monitor is shown in Figure 6. This monitor can be operated mounted on a satellite or in a laboratory vacuum chamber. One main difference compared to the monitor described in the previous section is that no moving parts are needed to generate the AC signal. This entire charge monitor is contained within a cylindrical aluminum housing. A cylindrical aluminum screw holds in place a dielectric sample with an embedded metallic probe. The probe is connected to a metal disk which is electrically floating and is parallel to and spaced from a grounded metal disk on which a piezoelectric ceramic driver is mounted to vibrate it at a selected frequency. In order to make electrical contact between the embedded probe and the floating metal disk a pressure contact is maintained via a metal spring that presses directly against the probe. The spring is mounted over a conducting rod threaded into an insulating Teflon web. To avoid residual-gas breakdown, an elastomer O-ring seals a potential breakdown path through the channel that carries the spring and the rod. The floating metal disk is also connected to three identical 80 pF high-voltage capacitors C_3, C_4, and C_5. Since the probe can charge up to a floating potential of 15 kV, everything connected to the probe, including the floating metal disk, has to be contained in a Teflon insulating chamber.

The grounded metal disk and the floating disk which is at the probe potential form a parallel-plate capacitor and, due to the grounded disk driven by the piezoelectric vibrator, its capacitance oscillates. In the equivalent circuit of Figure 7, which also includes the high-voltage capacitors C_3, C_4, and C_5, this oscillating capacitance is labelled as C_1 and the probe voltage is denoted as "test voltage V". The oscillating capacitance produces an oscillating capacitor plate charge and therefore an oscillating current and AC voltage picked up by the signal processor at point A in Figure 6. This corresponds to voltage V across R in the circuit in Figure 7.
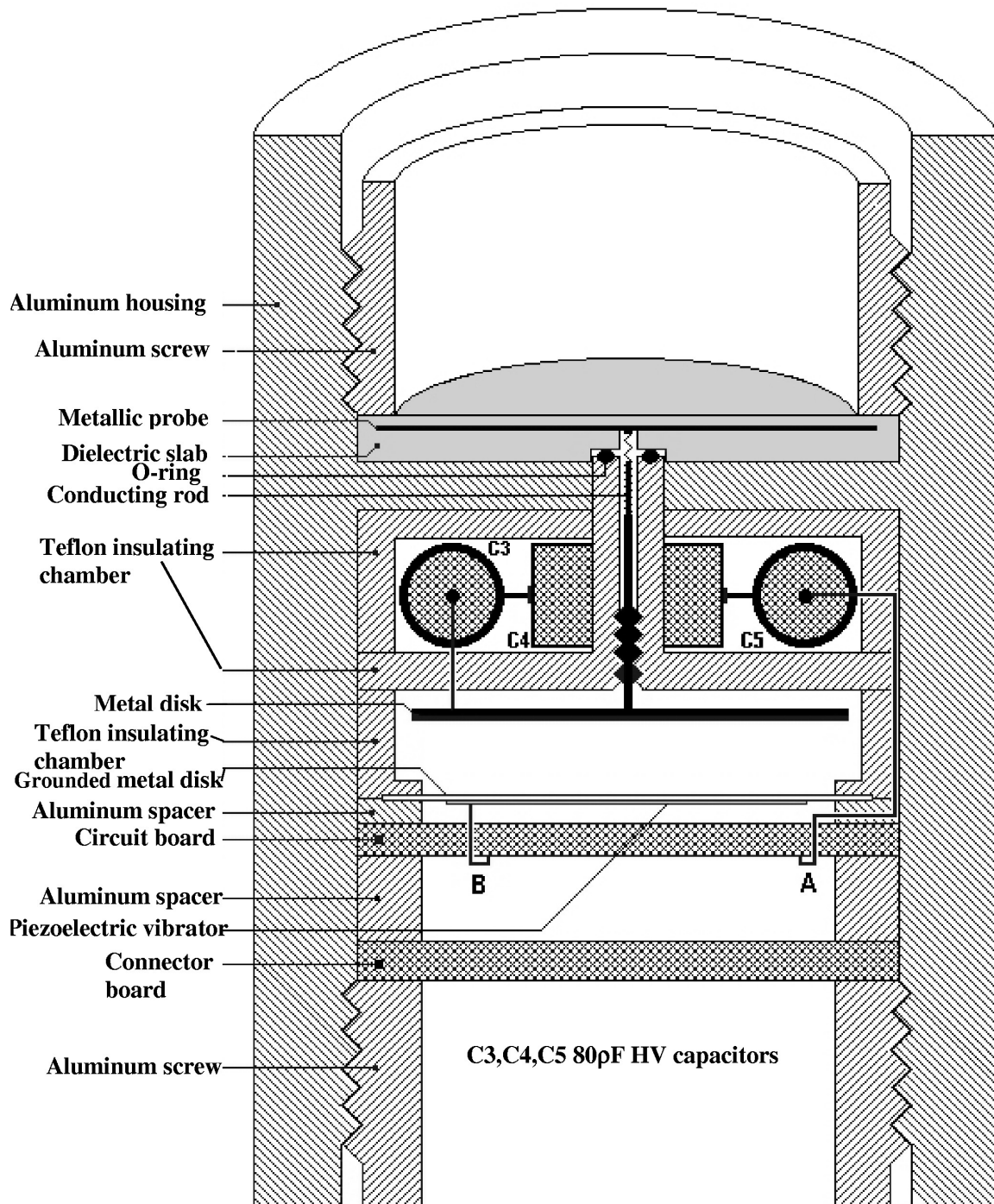
Figure 6. Piezo-driven monitor: cut-away drawing.

Labels (left side, top to bottom):
- Aluminum housing
- Aluminum screw
- Metallic probe
- Dielectric slab
- O-ring
- Conducting rod
- Teflon insulating chamber
- Metal disk
- Teflon insulating chamber
- Grounded metal disk
- Aluminum spacer
- Circuit board
- Aluminum spacer
- Piezoelectric vibrator
- Connector board
- Aluminum screw

Internal labels: C3, C4, C5, B, A

C3,C4,C5 80ρF HV capacitors

Figure 7. **Piezo-driven monitor: circuit showing piezo-driven capacitor C_1 and high-voltage fixed capacitor C_3, C_4, C_5, connected in series for a sufficient high-voltage rating. R is the input impedance of the signal processor.**

Figure 8 is the top view of the monitor with dielectric slab removed showing the container well and the probe contact. Figure 9 displays its connector end displaying the view of the connector board. In Figure 10 the connector board has been lifted up to show the electronic circuit board.
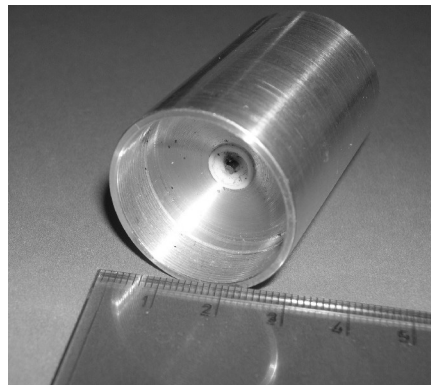
Figure 8. **Piezo-driven monitor: container well for dielectric sample showing probe contact.**
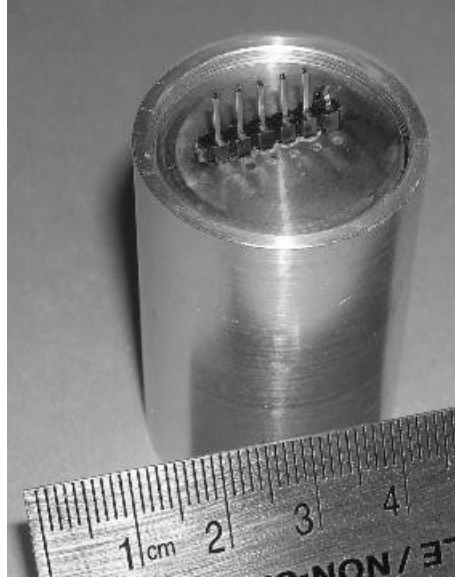
Figure 9. Piezo-driven monitor: connector end.
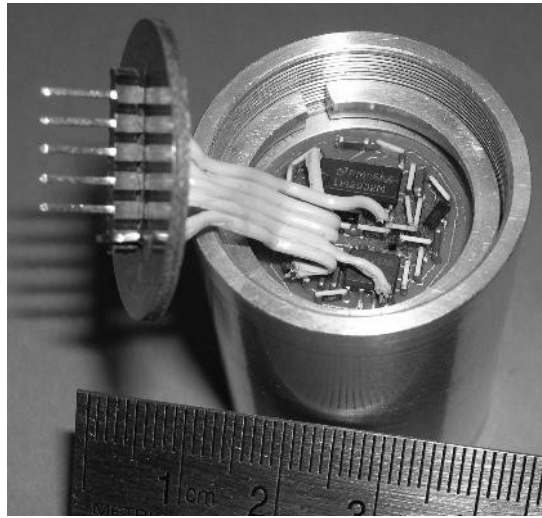
Figure 10. Piezo-driven monitor: connector and electronics.

Experimental Results for the Motor-Driven Monitor

Experiments using a Sr^{90} source emitting electrons with energies up to 2 MeV have been carried out using the motor-driven monitor. Results for samples of Rexolite, Acrylic, and Teflon are shown in Figure 11.
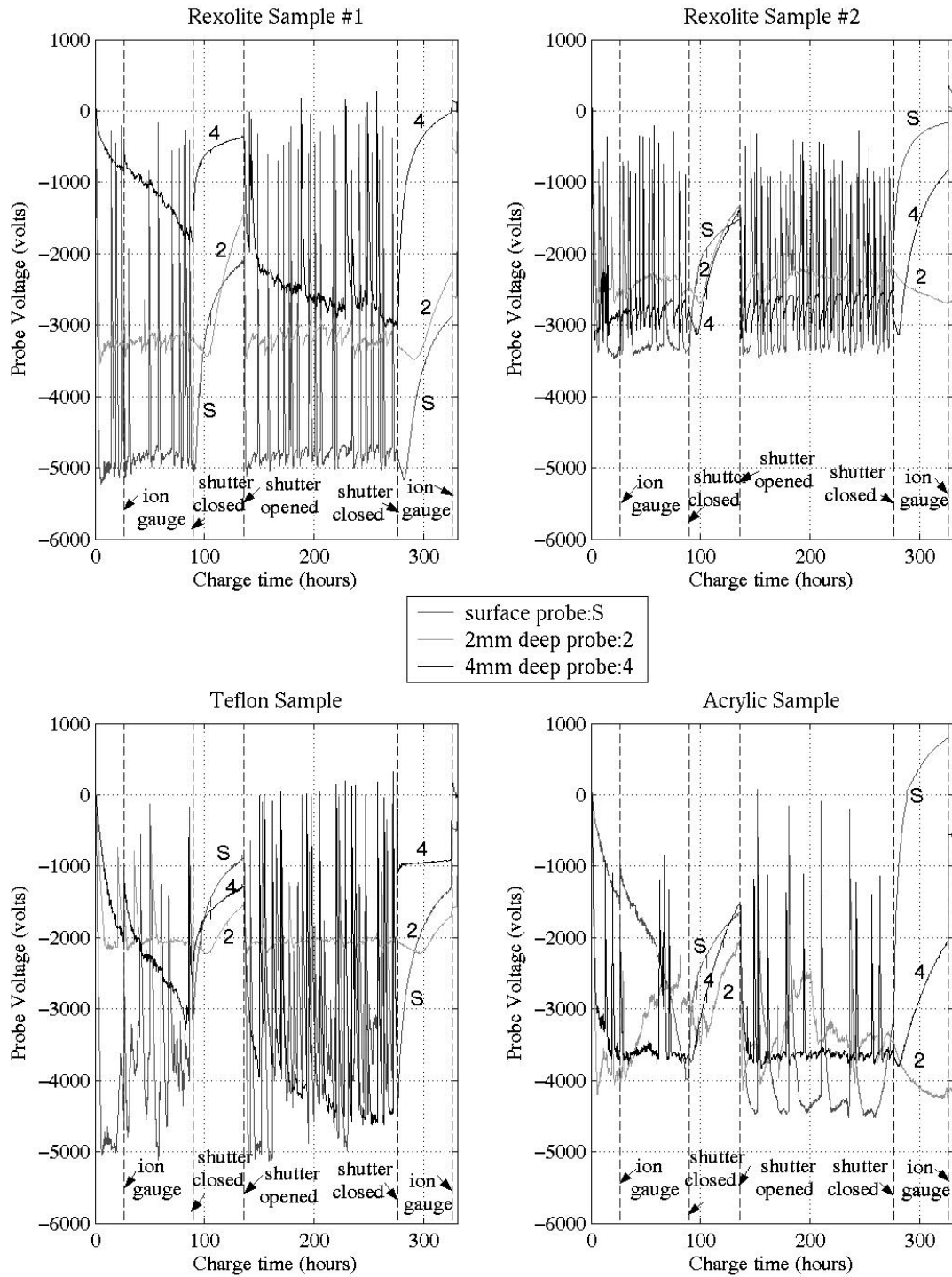
Figure 11. Motor-driven monitor: results for two Rexolite samples (top), a Teflon sample (bottom left) and an Acrylic sample (bottom right).

The various samples exhibit similar phenomena. Turning on the ion gauge produces enough ions to partly neutralize the surface. Closing the shutter starts a decay lasting about two days. The probes exhibit greater charging and more discharges as the probe locations become closer to the surfaces. However the sample to sample variations are significant but as yet unexplained.

Experimental Results for the Piezo-Driven Monitor

Initial measurements using the Sr^{90} source were carried out with the piezo-driven monitor with a Teflon sample. The results are shown in Figure 12. Qualitatively the sample results are similar to the motor-driven case.
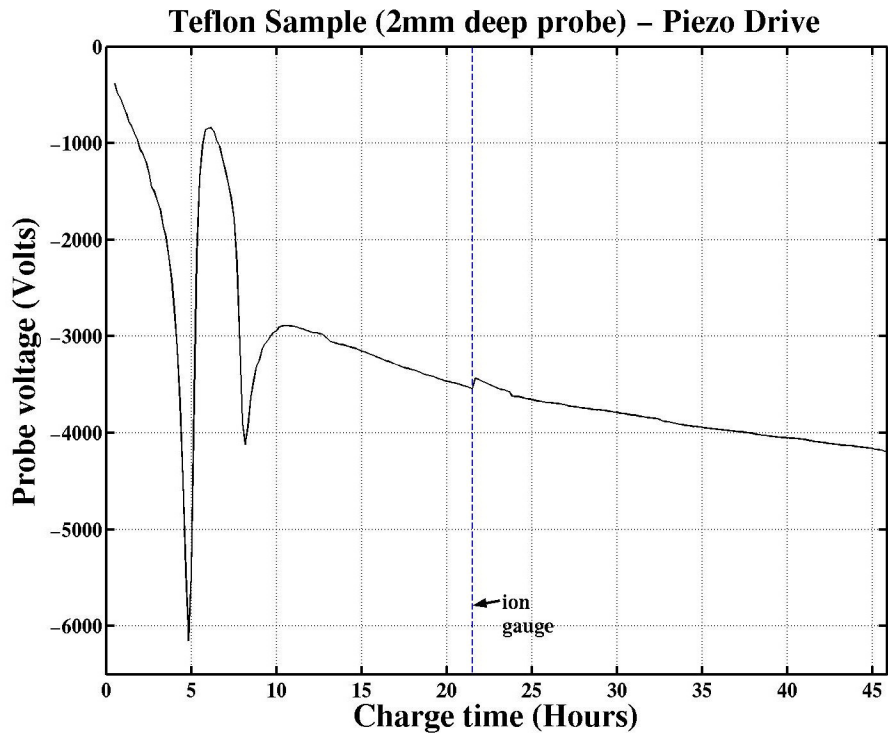
Figure 12. Piezo-driven monitor: initial results for Teflon.

WAKE EFFECTS ON POSITIVELY CHARGED SPACECRAFT IN FLOWING TENUOUS PLASMAS: CLUSTER OBSERVATIONS AND MODELING

Erik Engwall
Swedish Institute of Space Physics
Box 537, SE-751 21 Uppsala, Sweden
E-mail: **Anders.Eriksson@irfu.se**

Anders Eriksson
Swedish Institute of Space Physics

Arne Pedersen
Department of Physics, Oslo University, Norway

Julien Forest
Swedish Institute of Space Physics

Goetz Paschmann
Max-Planck-Institut für Extraterrestrische Physik, Germany

Jack Quinn
Roy Torbert
Space Science Center, University of New Hampshire, USA

Klaus Torkar
Space Research Institute, Austrian Academy of Sciences, Austria

Abstract

Comparison between electric field measurements made by the double-probe and electron drift instruments on the Cluster satellites have revealed significant perturbations in the signals from the electrostatic probes when Cluster is on magnetic field lines above the Earth's polar cap. In this region, there is a tenuous upflowing plasma known as the polar wind. The polar wind flow is supersonic, so a wake may form behind spacecraft structures. Usually, one expects wakes to be a problem mostly in denser plasmas. However, in this very tenuous environment, the spacecraft potential exceeds the kinetic energy of the ions (flow and thermal), so that the effective size of the wake is determined not by the spacecraft structures themselves, but by the potential distribution around them. As the plasma is tenuous, this is essentially the vacuum potential, which can extend very far from spacecraft structures. In particular, wire booms increase their effective size from the order of millimetres to the order of meters when the electrostatic effect is taken into account. We show the data to be qualitatively consistent with this interpretation. In particular, an observed alleviation of the effect when artificial potential control is applied lends strong support. Preliminary results of quantitative modeling and simulations provide additional insight.

Introduction

Spacecraft-plasma interaction studies usually focus on spacecraft charging to levels of kilovolts, as such potentials are an obvious source of technical problems for any spacecraft, particularly if different parts of the spacecraft charge to different voltages. In this study, we

will be concerned with much lower voltages, on the order of volts rather than kilovolts, occurring on conductive spacecraft where differential charging is not an issue. While this level of potential poses no danger to the physical health of a spacecraft, it can be a source of problems for scientific instruments intended for the study of plasmas in this energy range. Our particular concern in this paper will be a wake effect observed in cold tenuous plasmas by the electric field instruments on the Cluster spacecraft.

Each of the four Cluster spacecraft carries two instruments designed for measuring the electric field using different techniques, the double-probe Electric Fields and Waves instrument (EFW) (Gustafsson et al., 1997; Gustafsson et al., 2001) and the Electron Drift Instrument (EDI) (Paschmann et al., 1998; Paschmann et al., 2001). The performance of these two instruments have recently been compared by Eriksson et al. (2003). An interesting finding is that if a tenuous plasma (where the spacecraft potential V_s is positive due to photoemission) is so cool that the ions do not have sufficient energy to reach the spacecraft, the double-probe instrument EFW indicates apparent electric fields not seen by EDI. The observations were qualitatively understood in terms of a wake forming in the cold plasma, with a size determined not directly by the physical structure of the spacecraft but by the positive potential distribution around it.

In order to make this qualitative understanding a quantitative foundation, we need simulations of the plasma flow close to the spacecraft. The present paper is a report of initial results from such a simulation effort, using the open source particle-in-cell code package PicUp3D (Forest et al., 2001). This software is intended for workstations rather than supercomputers, and is excellently portable thanks to being written in Java. While this does not maximize the computational power, it simplifies the use of the code for engineers and scientists being able to run it on their own PCs. The primary aim of this study is to understand the EFW-EDI discrepancy, but a secondary goal is to verify that PicUp3D is useful for this kind of investigations. In Section 2, we show some Cluster data illustrating the problem, and introduce the qualitative model. The code and the simulations are presented in Section 3, with a concluding discussion in Section 4.

Enhanced Electrostatic Wakes in Cluster Data

Cluster is a mission designed for four-point measurements in key regions of the terrestrial magnetosphere and its adjacent environment in the solar wind (Escoubet et al., 2001), in particular boundary layers like the bow shock and the magnetopause. Thanks to its polar orbit with perigee at 4 RE and apogee at 19.6 RE, Cluster samples a broad range of plasma regions, from the cold and dense plasmasphere to the hot and tenuos plasma sheet. The four spacecraft were designed with identical payloads, each carrying a complete instrumentation for the study of particles and fields. For electric field measurements, Cluster includes two instruments using different techniques. The Electric Fields and Waves instrument (EFW) (Gustafsson et al., 2001) uses the well-known technique of measuring the voltage between spherical electrostatic probes at the ends of wire booms in the spacecraft spin plane (Pedersen et al., 1997). The technique allows sampling to essentially unlimited frequencies and can operate under widely varying plasma conditions, though great care is needed in the design in order to minimize disturbances from the spacecraft and the probe supports. EFW has two pairs of wire booms (2.2 mm diameter), with a distance of 88 m between opposite spherical probes (8 cm diameter). The Electron Drift Instrument (EDI) (Paschmann et al., 2001) uses a completely different technique (Paschmann et al., 1998), relying on observing the drift of electron beams emitted from the spacecraft and returned by the ambient magnetic field,

which thus has to be sufficiently strong for the method to work. Using electrons in the keV range, this technique is quite immune to any effects of spacecraft-plasma interactions in the eV range of energies. The Cluster spacecraft themselves are cylindrical, with radius 1.5 m and height 1.1 m.

The limitations of the two techniques for E-field measurements are quite different, and so they complement each other well. The EDI-EFW comparisons by Eriksson et al. (2003) showed the expected merits and weaknesses of each technique. To cite some examples, dynamic regions like the auroral zone are usually better covered by EFW because of its high sampling frequency and insensitivity to rapid variations of the background fields, while EDI often produces better data for small-amplitude electric fields in regions with cold plasma that perturb the EFW measurements. This happens particularly when the plasma is so cool that the ions cannot reach the spacecraft, which always is at a positive potential in the case of Cluster.
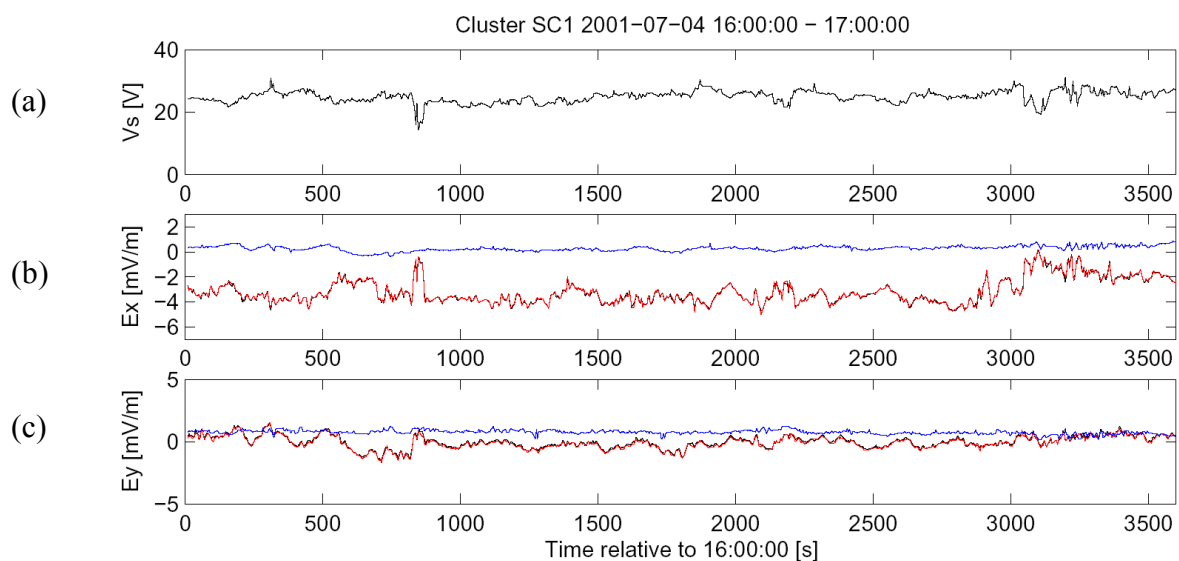
Figure 1. **Example plot of an interval where measurements of the electric field from the EFW (double-probe) and EDI (electron drift) instruments on Cluster differ. (a) Spacecraft potential V_s. (b) Electric field in the GSE X (sunward) direction from EFW (red and black) and EDI (blue). (c) Electric field in the GSE Y (duskward) direction in the same format.**

An example is shown in Figure 1. The data are from a position (1.6, -3.2, 7.9) R_E in GSE coordinates, which means Cluster is in the polar cap at a geocentric distance of 8.6 R_E, on magnetic field lines reaching into the northern geomagnetic tail lobe as illustrated in Figure 2. Panel (a) of Figure 1 shows the spacecraft potential V_s, estimated from the average voltage V_{ps} between the four EFW spherical probes and the spacecraft. As the application of a bias current ensures that the probes stays within one or two volts from the local plasma, the spacecraft potential $V_s \approx -V_{ps}$, where V_{ps} is the difference in potential between probes and spacecraft. The spacecraft potential depends strongly on the plasma density (Pedersen, 1995). For Cluster, the spacecraft potentials of 20 V to 30 V indicated here translates to approximate plasma densities between 1 cm^{-3} and 0.2 cm^{-3} (Pedersen et al., 2001). However, ion data from the Cluster Ion Spectrometer (CIS) (Rème et al., 2001) indicate much lower densities, well below 0.1 cm^{-3} throughout this interval (Eriksson et al., 2003). This can be explained by the presence of a cold plasma, with ion energies below eV_s, so that the ions cannot reach the

spacecraft. Such a plasma is indeed expected in this part of the magnetosphere, as this is the region of the cold plasma outflow known as the polar wind, studied by numerous spacecraft below a few Earth radii. Observations at higher altitudes are rare, as the low densities here give rise to high spacecraft potentials complicating direct observation of ions. However, by using artificial potential control of the POLAR satellite, Su et al. (1998) were able to study its properties at 8 R_E. Typical parameters for the proton component were found to be 0.3 cm^{-3} density, 45 km/s flow speed, and temperature 1 - 2 eV, resulting in a mean Mach number of 4.55. Oxygen and helium densities were lower by factors of around 6 and 38, respectively.

Panels (b) and (c) of Figure 1 show the GSE *X* and *Y* components of the electric field as derived from the EDI drift observations (blue) and from the EFW probe-to-probe voltages. The EFW data are plotted as two curves (black and red), derived by fitting a sinusoid to the signals observed in the rotating (4 second period) spacecraft frame by the two pairs of probes in the spin plane, P12 (black) and P34 (red). As the spacecraft spin axis is a few degrees from the GSE *Z* axis, the *X* and *Y* components actually are a few degrees off the corresponding GSE coordinate axes. The difference between EFW and EDI data in this time interval is apparent, reaching up to 5 mV/m. Comparisons to ion flow measurements show that in this case, the EDI data provide a good measurement of the natural electric field in the plasma, while EFW data are contaminated by potentials induced by the presence of the spacecraft (Eriksson et al., 2003). We may note that the source of this field is very stable in the sense that both EFW probe pairs provide essentially identical field estimates, as evidenced by the black and red lines in panels (b) and (c) lying on top of each other. It can be seen that in this case, the additional electric field points mainly in the -*X* direction, with a component in -*Y*. From the left panel in Figure 2, it is clear that a polar wind outflow along the magnetic field should be essentially in this direction in the spin plane, which is almost identical to the GSE *XY* plane. The direction is thus consistent with a wake-generated field.

Cluster1, 2001-07-04 15:00:00 - 18:00:00

Cluster1, 2001-07-04 15:00:00 - 18:00:00
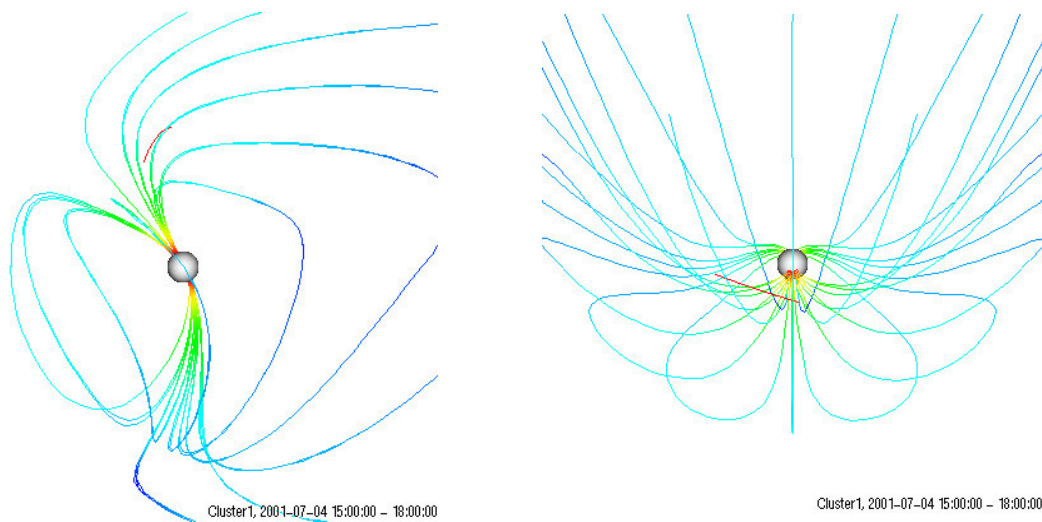
Figure 2. The red line marks the position of Cluster in the magnetosphere in the time interval 15:00 - 18:00 on July 4, 2001, as viewed from the GSE *Y* (left) and *Z* (right) directions. Some geomagnetic field lines are shown, colour coded for magnetic field intensity. Image produced using the orbit visualization tool, OVT (http://ovt.irfu.se), using IGRF and Tsyganenko-87 models for the magnetic field.

Perturbation potentials of this kind are commonly found to contaminate EFW data in the polar wind region and can sometimes be found also in other magnetospheric regions with a

cold tenuous plasma, but are rare in denser regions like the solar wind. In the solar wind, a wake may indeed form behind the spacecraft, but it is small and shows up as a pulse-like distortion of the EFW data when the probe passes through the wake. Such a wake poses no problem, while data like those shown in Figure 1 are not easily cleaned. Why is the wake problem so different in the two regions? The explanation lies in the relation between ion flow energy, $m_i v^2/2$, ion thermal energy KT_i, and spacecraft potential, V_s. In the solar wind, we certainly have $m_i v^2/2 > KT_i$ so that a wake is formed, but the plasma is sufficiently dense to ensure a low spacecraft potential, i.e. $eV_s < m_i v^2/2$. The ions can reach the spacecraft, and the transverse size of the wake is determined by the spacecraft geometry. In particular, the wire booms of 2.2 mm diameter cause a negligible wake. Now consider the case

$$eV_s > m_i v^2/2 > KT_i \qquad\qquad (1)$$

which is appropriate for the tenuous plasmas encountered by Cluster in the polar wind. The flow is supersonic and so a wake will form, but the size of this wake will now not be determined directly by the spacecraft mechanical structure but by the electrostatic equipotential $\Phi \approx m_i v^2/(2e)$ which no ions can climb. If we assume vacuum conditions, a spherical spacecraft of radius r at 20 V in a plasma with flow energy 5 V increases its effective size transverse to the ion flow from πr^2 to $16\,\pi r^2$, because the 5 V equipotential is at a distance of $4\,r$ from the centre of the spacecraft. This 16-fold increase in obstacle area may seem dramatic, but even more so is the effect on the wire booms. Assuming they behave like infinite cylinders of radius a in vacuum except for the potential going to exactly zero at a distance of $g\lambda_D$, where $g > 1$ is some real number, the potential field at radial distance r from a wire boom at potential V is

$$\Phi(r) = V\frac{\ln(r) - \ln(g\lambda_D)}{\ln(a) - \ln(g\lambda_D)} \qquad\qquad (2)$$

From this, we get the radial distance r_b at which $\Phi(r_b) = bV$, where $0 < b < 1$, as

$$r_b = a^b (g\lambda_D)^{(1-b)}. \qquad\qquad (3)$$

For the Cluster wire booms with $a = 1.1$ mm, a Debye length of 15 m, and an arbitrary but reasonable choice of $g = 2$, we get $r = 2.3$ m for the 5 V equipotential around a wire boom at 20 V. The effective size of the booms transverse to the flow therefore increases from 2.2 mm to 4.6 m, i.e. by three orders of magnitude. This increase depends to some extent on the arbitrary choice of g, but the effect is certainly significant for all realistic g. It is therefore possible that the normally neglegible wire booms supporting the EFW probes can become significant obstacles to the plasma flow in the conditions (1), as illustrated in Figure 3.

How large effects could such a wake have on double-probe electric field measurments? Considering a wake of slab-like geometry with thickness $d \ll \lambda_D$, we may assume perfect exclusion of ions and no impact on the electrons. Solving Poisson's equation gives a maximum potential in such a wake $\Phi_{wake} = (d/\lambda_D)^2\, KT_e/e$. For a wake of size $d \sim \lambda_D$ or larger, the potential saturates at $\Phi_{wake} \sim KT_e/e$, as further accumulation of electrons is inhibited. The
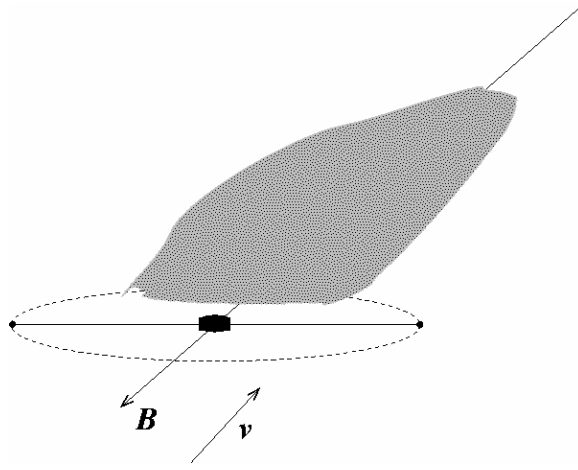
Figure 3. Sketch of a large scale wake forming behind the potential structure around a spacecraft equipped with wire booms at the same potential as the spacecraft, in the case of a plasma $eV_s > mv^2/2 > KT_i$ flowing along the magnetic field. The dashed line indicates the equipotential equivalent to the ion flow energy.

small wake with d on the order of millimeters found behind the booms in for example the solar wind thus cannot give rise to appreciable potentials, while it should be possible to get significant wake charging in the polar wind case of $eV_s > m_i v^2/2 > KT_i$. This wake field may impact on the measurements by a double-probe instrument in the way we have seen in the data presented above. An upper bound on the magnitude of this effect on the double-probe measurments can be obtained by assuming that one probe experiences the full wake potential while the other sees nothing, which would give a wake-induced electric field signal in the double-probe instrument of up to $KT_e/(2\,l\,e)$, where $2\,l$ is the separation between the two probes, i.e. 88 m for Cluster EFW. Assuming polar wind KT_e values of the order of a few tenths of eV, we find that wake-induced fields up to a few tens of mV/m could indeed be possible, which would explain the observations. However, to provide some more stable foundations to these estimates, we must go to simulations. This is the topic of Section 3 below.

We get evidence for the enhanced enhanced wake mechanism outlined above by studying intervals when the artificial potential control instrument ASPOC (Torkar et al., 2001) is operating. By emitting a current typically around 10 μA of keV ions, ASPOC stabilizes the spacecraft potential at around 8 V. Figure 4 shows data from two of the Cluster satelites, Cluster 1 (Rumba) in the top two panels and Cluster 3 (Samba) in the lower two. At the time shown, Cluster was above the northern polar cap at (-2.5, 1.4, 4.9) R_E in GSE coordinates. The environment is similar to that of Figure 1, though the peak V_s values of 40 V indicate densities down to 0.1 cm^{-3}. ASPOC is not operational on Cluster 1, but on Cluster 3, ASPOC is turned on close to 3250 s into the plot, resulting in an immediate and clearly visible stabilization of V_s. In the Cluster 1 data, EFW and EDI are seen to differ by up to 10 mV/m from 3000 s onwards. Only E_X is shown, as almost all the wake induced field turns up in this component because the magnetic field Y component is very small. The same EDI-EFW discrepancy initially occurs also on Cluster 3, but at the ASPOC turnon, the difference essentially vanishes. This is exactly the behaviour we should expect from a wake created by the spacecraft potential distribution as discussed above: when V_s decreases, so does the size of the wake and hence the perturbation it causes to the potential field around the spacecraft. The clear relation between the natural variations in spacecraft potential and the wake-induced field that can be seen in the Cluster 1 data shows that it really is V_s which is the controlling parameter, regardless of whether it is regulated by the plasma environment or by ASPOC.
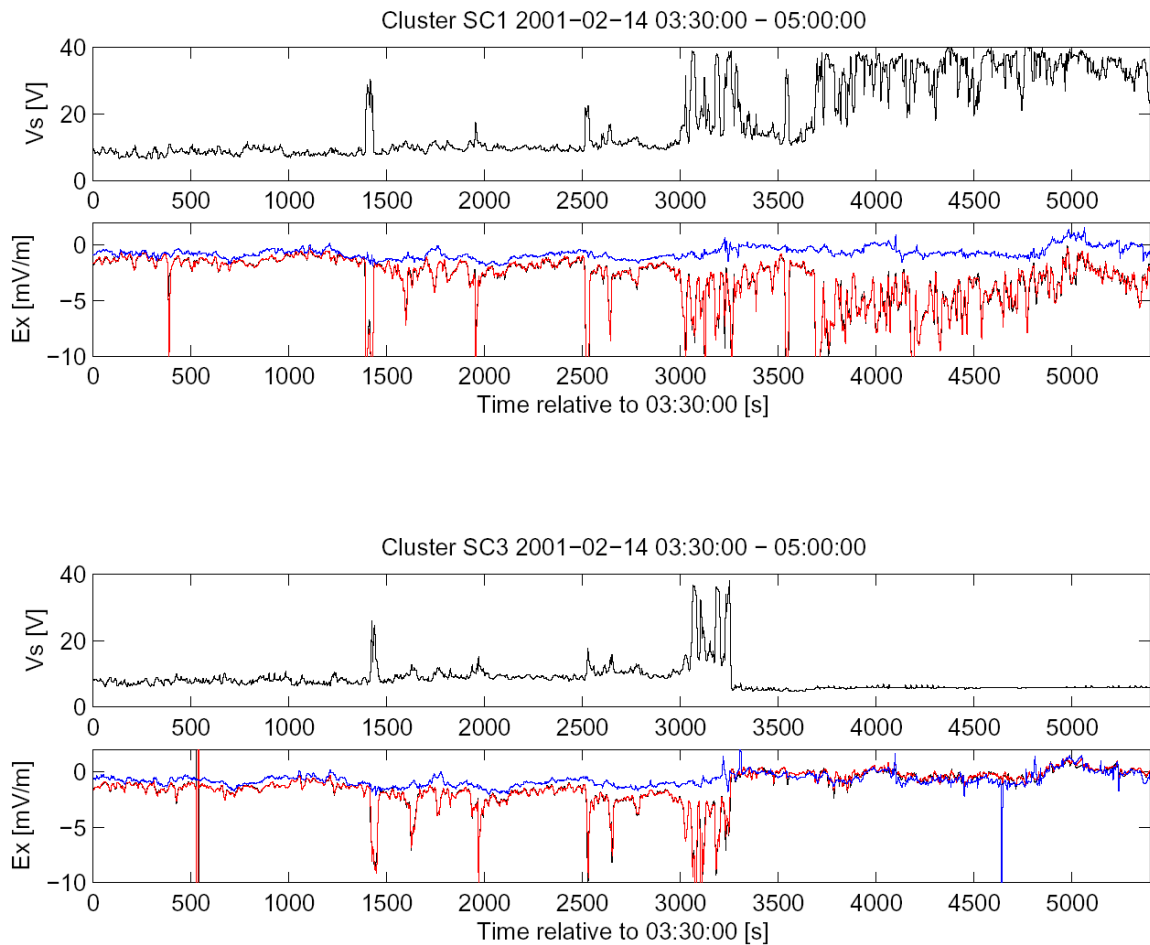
Figure 4. **EFW and EDI electric field data from Cluster 1 (top two panels) and Cluster 3 (lower two). For each s/c, the top panel shows the spacecraft potential V_s, while the lower panel displays the EDI (blue) and EFW (red, black) estimates of the GSE X component of the electric field. The jump in V_s for Cluster 3 at 3250 s into the plot is due to ASPOC turning on. Strong discrepancies between the EDI and EFW electric field estimates can be seen from around 04:20. For Cluster 1, they continue throughout the interval, while they almost disappear in Cluster 3 data when ASPOC is turned on.**

Simulations

We have used the simulation code package PicUp3D (Forest et al., 2001) to model the Cluster phenomena. This is a particle-in-cell code using a fixed homogeneous grid, assuming Dirichlet boundary conditions for the potential. PicUp3D does not self-consistently determine the potential of the spacecraft, but this is of no concern to us here as the density-potential relation is known (Pedersen et al., 2001). We have used common PCs (2.6 GHz AMD) with at most 0.5 GB of RAM allocated to the simulation. On these machines, the presented runs have typically taken around four days to complete.

In the simulation presented here the spacecraft is modelled as a single boom, neglecting the effects of the spacecraft body (Figure 5), in accordance with the discussion in Section 2 which suggested that the booms themselves may become significant obstacles to a cold flowing plasma. For this simulation we use the following plasma parameters:

- Plasma density, $n_0 = 0.15$ cm^{-3}
- Electron temperature, $KT_e = 1.8$ eV
- Ion temperature, $KT_i = 1.8$ eV
- Ion drift kinetic energy, $m_i v^2/2 = 9$ eV

These properties are consistent with the POLAR results (Su et al., 1998) cited above as well as with the Cluster observations in Figures 1 and 4. The Debye length becomes $\lambda_D \approx 26$ m and the electron plasma frequency $\omega_{pe}/(2\pi) \approx 4$ kHz. The ion drift kinetic energy corresponds to a flow velocity of $u = v_{th}^i \sqrt{10}$, which is taken to be in the y-direction. The magnetic field is neglected in the simulations, as the ion gyroradii are 1 km for protons and 5 km for O$^+$, both significantly larger than the scale of the problem and the simulation boxes. The electron gyroradius (30 m) is closer to the scale of the problem but has also been neglected, which possibly may cause some overestimation of the electron densities in the wake. We model only one ion species, with a mass ratio $m_i/m_e = 100$.

In general for these types of simulations, the size of the computational box is chosen as a compromise between the theoretical requirement that the boundary conditions for the potential should not affect the overall potential structure, and the practical desire to complete a normal simulation in less than a week. The boundary conditions are of Dirichlet type ($\Phi_b = 0$), which means that the walls of the computational box have to be sufficiently far away from the spacecraft. At a distance of $2\lambda_D$ the Debye shielding is supposed to have decreased the potential to a satisfactorily low level, why this is chosen to be the smallest distance from the spacecraft to any of the walls. Since the wake will be behind the spacecraft, the distance from the spacecraft to the far wall has to be much larger than this smallest distance. We will return to these limitations and their effect on the simulations below.
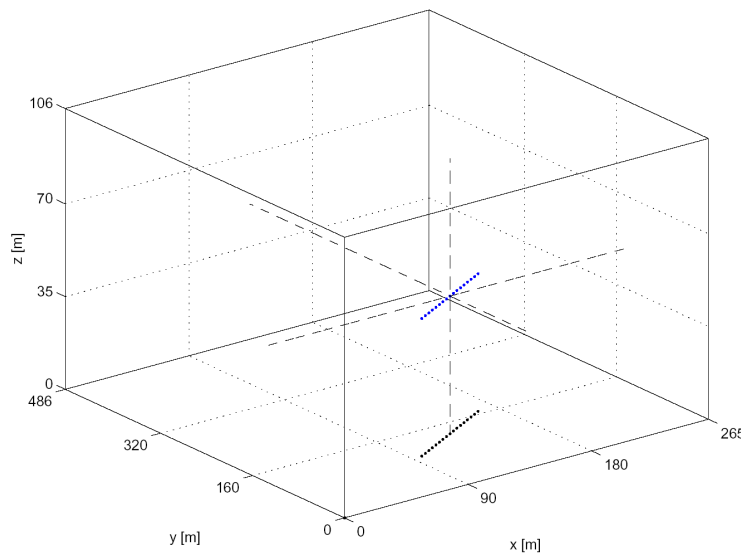
Figure 5. The boom in the computational box, which with the grid resolution of 4.4 m has the dimensions $x = 265$ m, $y = 486$ m, $z = 106$ m. The length of the boom is 100 m and is constituted of 17 discrete grid points (blue). The black dotted line is the projection of the boom on to the plane $z=0$.

For this specific run, the grid-size is approximately 4.4 x 4.4 x 4.4 m^3 and the number of grid-steps in each direction is $N_x=60$, $N_y=110$, $N_z= 24$ (Figure 5). Thus, the dimensions of the computational box is $x = 265$ m, $y = 486$ m, $z = 106$ m, which all may be compared to $\lambda_D = 26$

m. To achieve a satisfactory accuracy in the simulations, the number of particles is adjusted so that there are in average 8 particles per box. The integration time step for the motion of the particles is set to $0.034/\omega_{pe}$. It is chosen in such a way that no particle cross a cell in less than a few time steps.

The boom is placed in the *xy*-plane with $z = 53$ m at an angle of 45° relative to the positive *x*-axis, which means that it has the same angle to the flow. This angle has been chosen as typical. As PicUp3D includes no explicit provisions for modelling booms, we have instead fixed the potential of 17 discrete grid points, extending from (x=97, y=97) to (x=168, y=168). This means that the boom in the simulations obtains a length of 100 m, close to the actual length 88 m. Each grid point on the boom is set to the potential +36 V, which is consistent with the situations in Figures 1 and 4, and with a plasma density of approximately 0.15 cm^{-3} (Pedersen et al., 2001). However, due to the grid resolution of 4.4 m, the decrease of the potential close to the boom is slower than expected from a real wire boom of 2.2 mm diameter, and we will show later in this paper that the choice of 36 V for the grid points modelling the boom actually may correspond to a thin wire boom as high as 50 V. Further simulations are needed to take this under estimation of the potential into account.

Results from the boom simulations are shown in Figures 6 and 7. The output data is averaged over the time period from $30/\omega_{pe}$ to the end of the simulation at $60/\omega_{pe}$ in order to obtain smoother plots. Figures 6 a-c show the potential around the boom in the planes z=53, x=133 and y=243 respectively. As can be seen most clearly in Figure 6a, the dominating structure is the decaying potential around the boom, giving essentially elliptic equipotentials down to 1 V. As expected, a negatively charged wake forms behind the boom, reaching a minimum potential of -0.69 V. The ion density in Figure 7a shows the same wake structure, while the effect most apparent in the density of electrons in Figure 7b is their agglomeration around the positive boom. A small depletion in the region of the wake can also be seen, as is expected for a wake approaching Debye length scale. It should be noted that the ions, whose energy is around 9 eV, do not care about the details of a wake potential at a few tenths of volts. This means that the ion density in Figure 7a results essentially from the potential from the booms, so that the ion density is only marginally affected by any possible influence from the Dirichlet boundary conditions on the potential. With a Mach number of √10, few ions can leak into the central wake from the boundaries aligned with the flow, so the effect of this boundary should also be small. However, it is clear that the Dirichlet conditions on the potential do to some extent influence the potential and the electron density, as the ion wake seen in Figure 7a extends out through the boundary. A run with half the simulation box size in the *z*-direction resulted in a potential minimum of only -0.24 V, verifying that we are at least close to the limit where the boundary conditions influence the result. Further simulations with larger grid will be needed to resolve this issue. We thus consider the -0.69 V wake potential observed in this simulation to be a lower bound rather than a true estimate. The influence of the far wake boundary conditions on the wake does not seem to be significant. This has been verified by a simulation with a much more elongated computational box in the flow direction (900 m). The dimensions in the other directions and the simulation parameters remained the same, but the grid size was increased to 8.8 m in each direction to obtain reasonable convergence times.
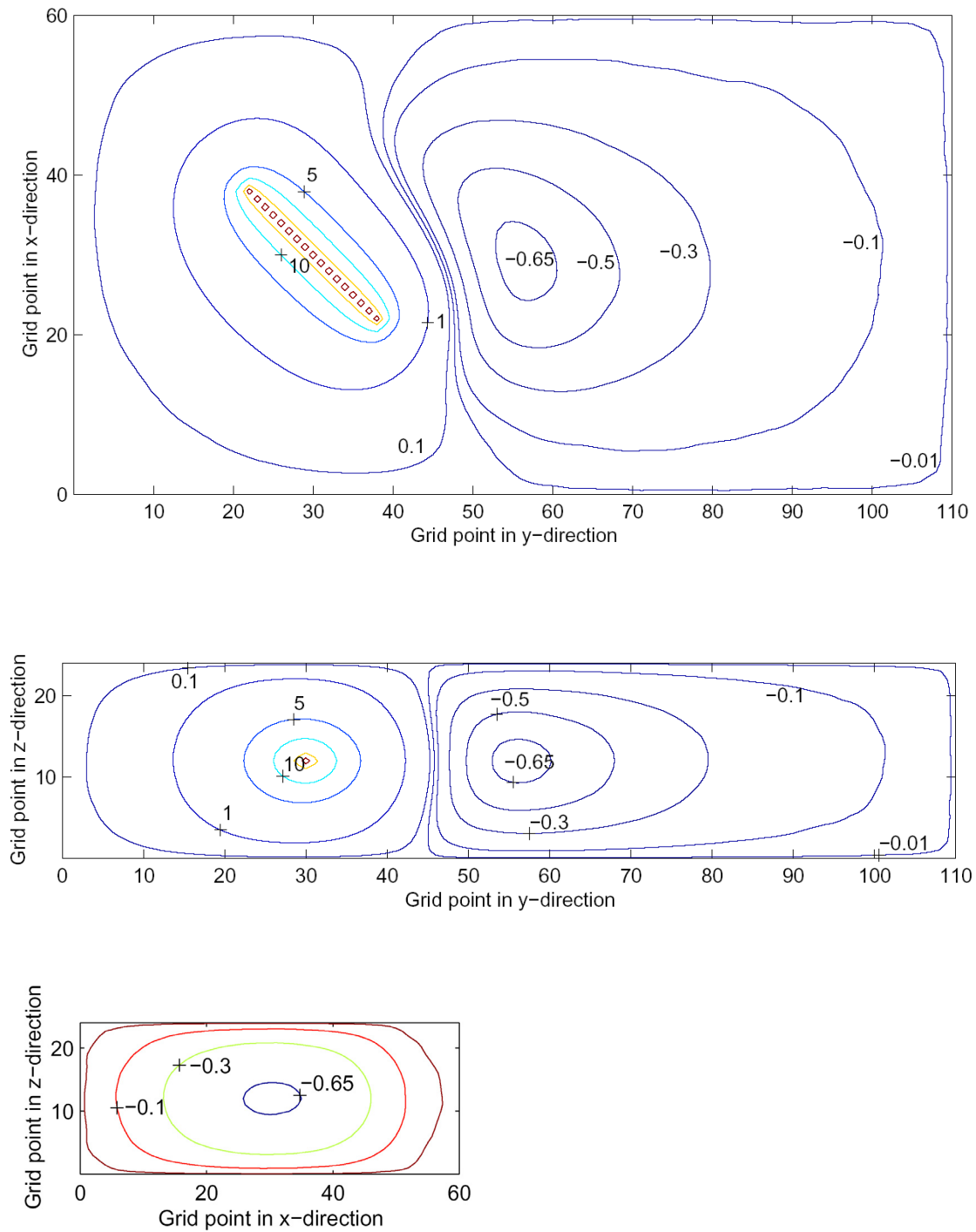
Figure 6. Contour plots of the potential for the boom simulations. The minimum value of the potential in the wake is -0.69 V. (a) Potential in the xy-plane with *z*=53. (b) Potential in the yz-plane with *x*=133. (c) Potential in the xz-plane with *y*=243. The grid spacing is 4.4 m.
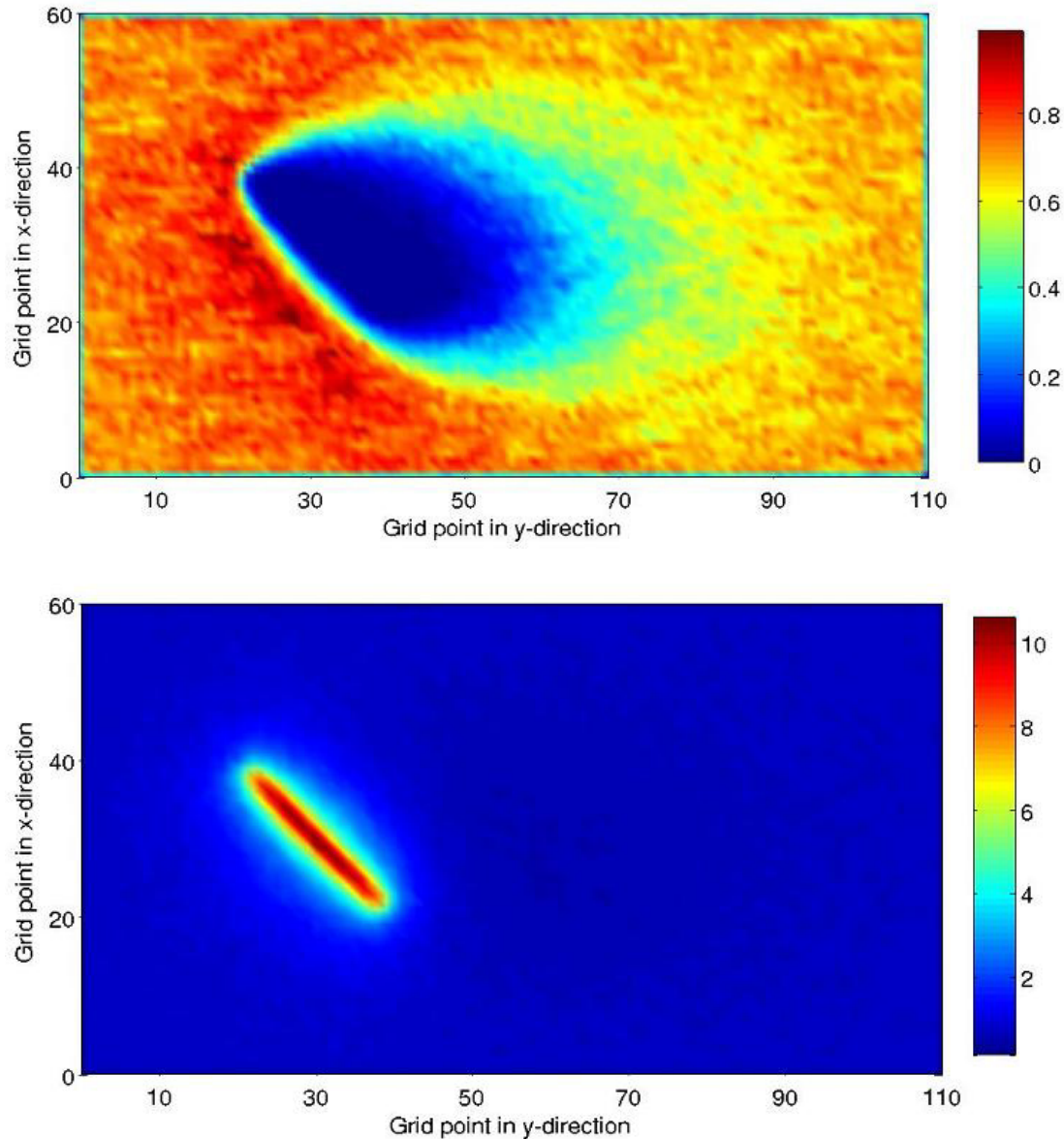
Figure 7. Densities of ions and electrons from the boom simulations. (a) Density of ions. (b) Density of electrons. The grid spacing is 4.4 m.

We will now use the simulation result to quantify the impact of the wake field on a double-probe electric field instrument. Such an instrument has one probe at each end of the boom, with bootstrapped elements in between to shield away the direct influence of the boom potential (Gustafsson et al., 2001). For Cluster EFW, the probes are 3 m outside the part of the wire booms which are at spacecraft potential. In Figure 8, we plot the difference in potential between two probes which are at the same distance from the opposite ends of the wire boom, as a function of this distance. The maximum potential difference is approximately 630 mV. One grid spacing distance (4.4 m) out from the boom on each side, which is close to the 3 m relevant for Cluster EFW, the observed potential difference between the probes is 490 mV. Dividing this by 100 m, we find that EFW could be expected to suggest an apparent electric field of 5 mV/m because of the wake. This is for the simulated boom angle with respect to the flow of 45°, but as the amplitude of the perturbation should vary with this angle, reaching a maximum at 0° and 180°, the wake induced field in spin fitted data like in Figures 1 and 4 could be expected to be somewhat larger, around 6 or 7 mV/m. This is close to the observed EFW-EDI discrepancies in Figure 1, though we should remember that the

plot in Figure 8 is based on a simulation with 4.4 m grid resolution. This cannot possibly catch all detail a few meters from the ends of the wire booms, but in as far as the difference results from the large scale properties of the wake, not from the details close to the probe positions, we may expect the result to be correct at least as an order of magnitude estimate.

(a)

(b)
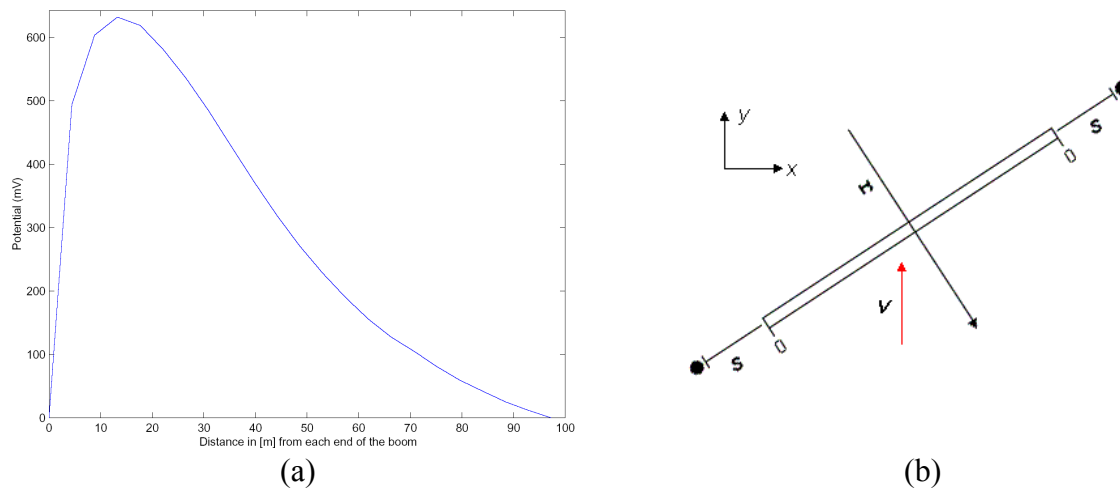
Figure 8. (a) Difference in potential between the ends of the boom. The maximum potential difference is 630 mV. (b) Schematic picture of the boom explaining the horizontal axis of (a): *s* is the distance from the boom end to the probe. The coordinate *r* is the radial distance from the midpoint of the boom used in Figure 9.

As have been mentioned above, the grid spacing of 4.4 m will result in the potential close to the boom attaining larger values than would have been the case for a real wire boom (2.2 mm diameter for Cluster EFW) at 36 V. At a distance of several Debye lengths from the boom, we may expect the simulation result to be the true potential, but not close to the boom. To compensate for this discrepancy, an effective boom potential is calculated by comparison with analytical models. At high potentials close to the boom the Debye shielding has only small effects and the boom potential can be compared with the vacuum potential of a thin cylinder. According to Hallén (1929), the vacuum potential of a thin cylinder at potential V is

$$\Phi(x',y',z') = \frac{V}{2\ln\left(\dfrac{l}{a}\right)} \ln\left(\frac{d-x'+r_1}{-d-x'+r_2}\right), \qquad (4)$$

where l is the length of the cylinder which is aligned with the x axis and centred on the origin, a is its radius, $d = l/2$, $r_1 = [(x'-d)^2 + y'^2 + z'^2]^{1/2}$ and $r_2 = [(x'+d)^2 + y'^2 + z'^2]^{1/2}$. We now look for a value of V in this expression that result in a potential approximately like the simulation result around 9 V and a few volts below, as this should be the most sensitive region for the dynamics of the ions, whose drift energy is 9 eV. Figure 9 shows a plot of the simulated potential (dashed blue) together with the analytic model for a thin boom potential of 52 V (black), with radial distance from the midpoint of the boom on the horizontal axis. It can be seen that this indeed approximates the simulated potential field around and below 9 V, and it may therefore be that the potential of 36 V applied to the point cluster simulating the booms corresponds to an actual potential as high as 50 V for a real wire boom.

Further away from the boom, (4) does not give a correct picture, because of the Debye shielding in the plasma. Therefore it is adequate to also compare the simulated boom potential to that of a Debye shielded infinite cylinder, which takes the form

$$\Phi(r) = V \frac{K_0\left(\dfrac{r}{\lambda_D}\right)}{K_0\left(\dfrac{a}{\lambda_D}\right)}, \tag{5}$$

where r is the perpendicular distance from the boom, a is the radius of the boom and K_0 a modified Bessel function of the second kind. Figure 9 shows the potential as a function of the perpendicular distance from the middle of the boom for the simulated boom potential, the Hallén potential and the Debye shielded potential. As expected, the Hallén model and the shielded cylinder approach each other far from the boom. Closer to the boom, the Debye shielding expression (5) breaks down because of violation of the assumption $e\Phi << KT_e$ inherent in the linear Debye shielding law. The influence of the wake on the potential can clearly be seen in the asymmetry of the simulation data.
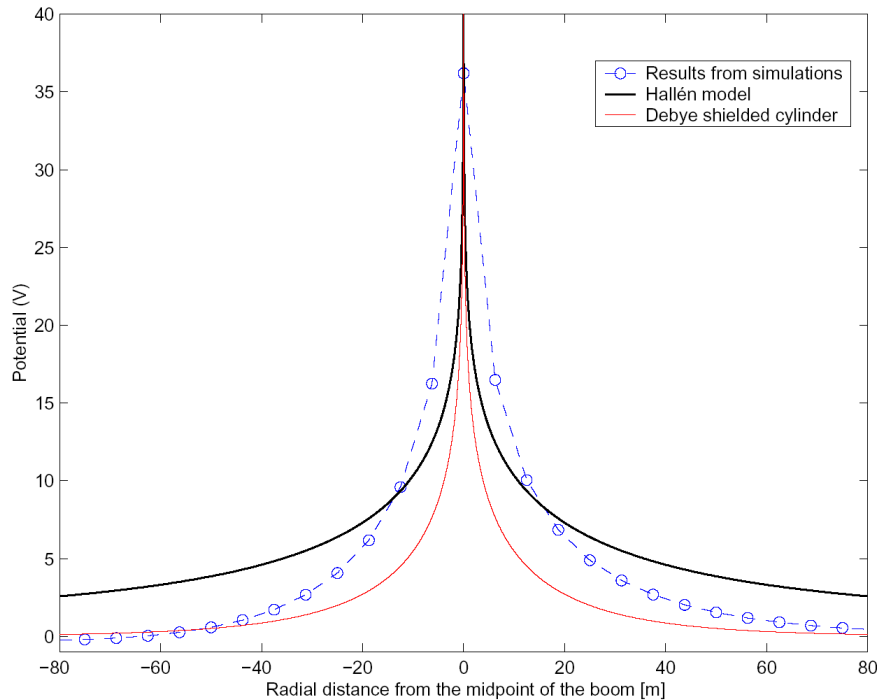
Figure 9. Comparison between the potential obtained from the simulation (dashed blue) and analytical models. The red line corresponds to an infinite Debye shielded cylinder and the black line to the model introduced by Hallén. The horizontal axis gives the radial distance from the center of the boom in the boom-flow plane (r in Figure 8b).

Discussion and Conclusion

In this paper, we have presented experimental data from the EFW and EDI electric field instruments on Cluster, showing some examples where EFW observes an electric field which to a large extent, or even dominantly, is not of geophysical origin. As such phenomena are not uncommon in the EFW data set in some regions of the magnetosphere, they are important

to understand to ensure maximal scientific return from the instrument. A model where the additional electric field seen by EFW is explained in terms of an electrostatic wake of enhanced size forming behind the wire booms when $eV_s > m_i v^2/2 > KT_i$ was introduced and found to be consistent with a number of features in the data, including the direction of the non-geophysical field, its dependence on spacecraft potential including its decay when this potential is controlled by the ASPOC instrument, and its presence in a region known to contain the cold and tenuous supersonic plasma flow of the polar wind. More detailed investigations of the experimental data is provided by Eriksson et al. (2003). We derived some analytical estimates of the magnitude of the effect at the end of Section 2, and went on to numerical simulations in Section 3. The simulations indeed verified the qualitative hypothesis, showing the generation of a negatively charged wake behind the spacecraft.

An attempt to derive the non-geophysical field observed by EFW resulted in 5-7 mV/m, which is close to observed magnitudes. Future work should include the effect of biasing and bootstrapping of the mechanical elements between the probe and the boom tip, which may have some impact on this value. However, for detailed studies of the influence of the near-probe environment, a more flexible grid is necessary. Potentially important factors not included in the present simulation also include the emission and exchange of photoelectrons by different electrical elements on the spacecraft. It is for example possible that the wake to a large extent is filled by photoelectrons emitted from the probes rather than by natural plasma electrons.

The simulations presented here leave several issues to be settled, and further work is necessary. Nevertheless, we have been able to verify the qualitative idea of an enhanced electrostatic wake, and got reliable results at least for the ion densities around the spacecraft. Our main conclusions from this work can be stated as follows:

1. The qualitative hypothesis of an electrostatic wake with dimensions determined by the spacecraft potential field forming in situations with $eV_s > m_i v^2/2 > KT_i$ is consistent with data.

2. Numerical simulations verify the qualitative picture, and have produced lower bounds on the induced wake potentials.

3. We consider the results from the simulations reliable in the entire simulation region for the ion density, but not for the potential, mainly because of influence from the boundary conditions. However, our main interest is the region close to the spacecraft, where impact of the boundaries should be smaller. Further simulations with varying grid size are needed to verify this. The main limitation of the used grid is its extension out of the plane containing the booms and the flow, which is the principal direction in which the ions are deflected by a quasi-cylindrical potential distribution around the boom.

4. The PicUp3D code proved very handy for this type of study. It is unlikely that we would have undertaken this venture without a code we can run on our workstations, and the open source is a major advantage for scientific use.

5. For this kind of problem, we consider the main technical limitation of PicUp3D to be that it only handles Dirichlet conditions on the potential. For a wake extending far from the spacecraft, Neumann conditions on all sides except the inflowing boundaries would be more suitable.

6. The inability of a fixed grid code to model thin booms leads to an under estimation of the simulated boom potential. This issue can in future simulations to some extent be circumvented by introducing an effective potential, using comparison to analytical expressions. The validity of the method using effective potentials should be verified by comparison to adaptive-grid codes.

7. From the simulation results, we have extracted an estimate of the wake-induced electric field signal observed from a pair of probes outside the ends of the modelled booms, assuming the probes perfectly couple to the plasma.

Acknowledgements

References

1. Eriksson, A., M. André, B. Klecker, H. Laakso, P.-A. Lindqvist, F. Mozer, G. Paschmann, A. Pedersen, J. Quinn, R. Torbert, K. Torkar, and H. Vaith, Cluster comparison of the double-probe and electron drift techniques for measuring the electric field, manuscript in preparation, 2003.

2. Escoubet, C. P., M. Fehringer, and M. Goldstein, The Cluster mission. *Annales Geophysicae, 19,* 1197 - 1200, 2001.

3. Forest, J., Eliasson, L., and Hilgers., A., A New Spacecraft Plasma Simulation Software, PicUp3D/Spis, in *Proceedings of the 7th Spacecraft Charging and Technology Conference,* ESA/SP-476, 515-520, 2001.

4. Gustafsson, G., et al., The Electric Field and Wave Experiment for the Cluster Mission. *Space Science Reviews, 79,* 137 - 156, 1997.

5. Gustafsson, G., et al., First results of electric field and density observations by Cluster EFW based on initial months of operation. *Annales Geophysicae, 19,* 1219 - 1240, 2001.

6. Hallén, E., Lösung zweier Potentialprobleme der Elektrostatik*, Arkiv för matematik, astronomi och fysik, 21A*, 22, 1929.

7. Paschmann, G., C. E. McIlwain, J. M. Quinn, R. B. Torbert, and E. C. Whipple, The Electron Drift Technique for Measuring Electric and Magnetic Fields. *Measurement Techniques in Space Plasmas: Fields*, AGU Geophysical Monograph 103, 1998.

8. Paschmann, G., et al., The Electron Drift Instrument on Cluster: overview of first results. *Annales Geophysicae, 19,* 1273 - 1288, 2001.

9. Pedersen, A.: Solar wind and magnetosphere plasma diagnostics by spacecraft electrostatic potential measurements, *Annales Geophysicae*, 13, 118–121, 1995.

10. Pedersen, A., F. Mozer, and G. Gustafsson: Electric Field Measurements in a Tenuous Plasma with Spherical Double Probes. *Measurement Techniques in Space Plasmas: Fields*, AGU Geophysical Monograph 103, 1-12, 1998.

11. Pedersen, A., et al., Four-point high time resolution information on electron densities by the electric field experiments (EFW) on Cluster, *Annales Geophysicae,* 19, 1483-1489, 2001.

12. Rème, H., et al., First multispacecraft ion measurements in and near the Earth's magnetosphere with the identical Cluster ion spectrometry (CIS) experiment, *Annales Geophysicae, 19,* 1303, 2001

13. Su, Y.-J.; Horwitz, J.L.; Moore, T.E.; Giles, B.L.; Chandler, M.O.; Craven, P.D.; Hirahara, M.; Pollock, C.J., Polar wind survey with the Thermal Ion Dynamics Experiment/Plasma Source Instrument suite aboard POLAR, *Journal of Geophysical Research, 103*, 29305-29337, 1998.

14. Torkar, K., et al., Active spacecraft potential control for Cluster - implementation and first results, *Annales Geophysicae, 19,* 1289, 2001

MODELING OF THE PLASMA ENVIRONMENT OF A FEEP MICRO THRUSTER WITH PICUP3D SIMULATION CODE: SAMPLE RESULTS

J. Forest
European Space Research and Technology Centre (ESA-ESTEC)
Also at Swedish Institute of Space Physics (IRF-K), Kiruna, Sweden and Planetary and
Terrestrial Environment Study Centre (CNRS-UVSQ/CETP)
E-mail: julien@irf.se

A. Hilgers
B. Thiébault
A. Popescu
M. Fehringer
European Space Research and Technology Centre (ESA-ESTEC)

Abstract

Electric thrusters are planned to be used on a broad scale on new generation spacecraft as main propulsion engines or for attitude and orbit control. In parallel many theoretical and experimental works about their performances and functioning are still in progress. One of the issue is their interaction with the surrounding plasma environment. This paper presents a study performed at the European Space Agency (ESA) for modelling the interaction between a Field Emitter Electric Propulsion (FEEP) system and a surrounding ionospheric plasma. A detailed 3D PIC model of the FEEP system and of its environment has been performed, using the PicUp3D code, developed in the framework of the SPINE network (http://www.spis.org). The model takes into account a detailed geometrical model of the inner volume of the thruster, including all electrodes and the aperture geometry, and the surrounding ambient plasma in a large computational space. This study helps to validate acceptable design in order to reduce back-streaming electron currents from ionospheric type environment and to assess the FEEP engine plume neutralisation process.

Introduction and Objectives of the Study

There is a growing interest for the use of electric propulsion systems in space as main propulsion engine or for attitude and orbit control. Field Emitting Electric Propulsion (FEEP) micro-thruster engines are being considered for drag compensation for low altitude Earth observation satellites. Such devices are characterised by a low current of high energy ions emitted by a thin anode and may interact in several ways with the surrounding plasma environment [cf e.g., Tajmar and Wang, 2000]. Two types of interactions are considered in this paper: (1) the neutralisation process of the plume by the surrounding plasma and (2) the current collection of ambient plasma by the emitting electrode.

The FEEP engine considered in this study is constituted by a very narrow hollow needle mounted on a tank of liquid Indium and biased at a very high potential (a few kV) with respect to an extractor electrode which is a circular ring located at a very short distance from the needle's tip. Although such a design has a long in space experience as a charge alleviating device on magnetospheric spacecraft [cf e.g. Torkar et al., 2001] some uncertainties remain on its behaviour in an ionospheric type of environment, i.e. when the surrounding plasma density is high. In particular, the number of electrons which may propagate from the outside to the anode is an issue for the control of the engine thrust and for the survivability of the

needle which may be destroyed by the heat. Therefore, several tests and numerical modelling have been performed in order to model the interaction of the FEEP system with a surrounding ionospheric plasma. Some sample results of the numerical simulations are presented in the following while more detailed and quantitative results will be published in a forthcoming paper.

Modeling Approach

Three types of inputs are required for this study: (1) the environment data, (2) the geometry, (3) the numerical model of the interactions. They are discussed in the following.

On very low altitude orbits (a few hundred kilometers), the ambient plasma environment is of ionospheric type. The density may be of the order of 10^{11} m^{-3} in the day side F layer region to 10^9 m^{-3} in the night side one. The temperature is of the order of 0.1 eV. If the spacecraft is equipped with a main ion engine system of the SPT type the ambient environment may be dominated by the charge exchange plasma with a density of typically 10^{11} m^{-3} to 10^{12} m^{-3} and a temperature of a few eV [cf e.g., Tajmar, 2001; Tajmar and Wang 2001]. For the purpose of this study, one used a rather high density plasma environment with a density of 10^{12} m^{-3} and a temperature of 0.1 eV. This corresponds to a Debye length of the order of 10^{-3} m.

The basic geometry of the FEEP engine is shown on Figure 1. Indium ions are emitted from a needle at a potential which may vary from 6 to 10 kV with respect to the ring shaped accelerating cathode. The narrowest diameter of the aperture diameter is 15 mm. The needle diameter is 0.25 mm. A repelling ring with negative biased potential is foreseen to prevent electrons from outside the thruster to propagate to the needle.
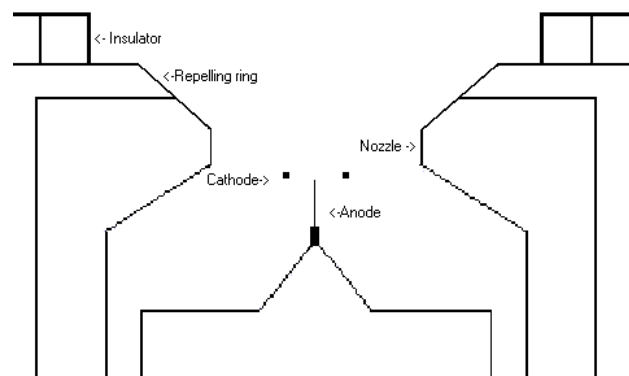
Figure 1. Sketch of the FEEP engine geometry (not on scale).
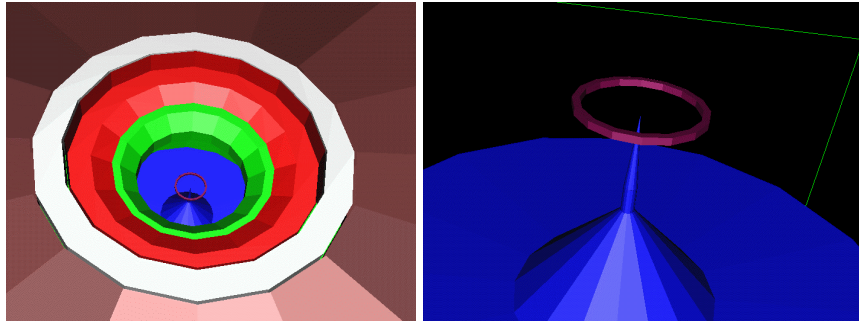
Figure 2. 3D views of the geometrical model of the FEEP thruster. One can see the anode (blue) constituted by the needle and the tank and the accelerating ring (pink). In addition a repelling ring can be used outside the aperture.

3D models of the complete system were generated with a CAD tool and described in VRML format. It allowed a description of the surface details as low as 0.25 mm. However, a coarser resolution had to be used for the potential solver (cf below). The FEEP micro-thruster environment is investigated as a stand alone body. The influence of any other part of the spacecraft is neglected. The ground potential of the thruster is kept fixed at 0V.

In this study only stationary regimes are investigated. The dynamics of the energetic ions emitted by the needle and accelerated by the anode is neglected. They are treated as an uniform static space charge in a cone of 15 degrees aperture angle. The ambient plasma environment in stationary regime is described by the set of the Poisson and Vlasov equations which are solved with the open source 3D PIC simulation code, PicUp3D, described in this spacecraft charging technology conference and the previous one [Forest et al., 2001]. The boundary equations are given by the potential on the material surfaces including the electrodes. The simulation box size is chosen such that it contains entirely the electrostatic sheath and therefore, the potential at the box boundary is set at 0V. Typically a 0.3 meter box size have been used for the simulations.

PicUp3D is solving the Poisson equation on a rectangular mesh. This imposed a severe constraint on the ratio of the spatial resolution to box size for a given memory size. The highest spatial resolution used in this study was a mesh size of 0.75 mm. While the largest computational grid used was constituted of 256x256x256 nodes. The needle itself was too thin to be accurately represented in the model and was treated as a one dimensional boundary condition for the potential solver.

Simulation were performed using a number of computer particles between 2.10^6 and 3.10^6 in order to have a good statistical basis for the estimate of particle density and collected currents. An ion to electron mass ratio equal to 100 was used to reduce the computation time. Nevertheless, the simulations took a long time before reaching a stationary regime. Typically, the runs had to last for more than 300 x $1/\omega_{pe}$ simulation time (where ω_{pe} is the plasma frequency). This corresponds to several days with a time resolution of dt=0.05 $1/\omega_{pe}$ on a PC with a processor at 1GHz.

Sample Results

A first series of computations was performed without repelling negative ring around the aperture and with a relatively thin spacecraft wall. It was found in this case that the potential

at the aperture was significantly positive (a few hundred volts) and the sheath extended by several centimeters away from the aperture. It would have resulted a backstreaming electron current to the anode above the acceptable level. On one hand it allowed to conclude that neutralisation of the FEEP plume space charge by the ambient ionospheric plasma was very efficient (neutralising device may still be needed to keep the spacecraft potential at moderate level). On the other hand, however, it indicated that a negative repelling ring is absolutely mandatory for preventing backstreaming electrons to the emitter. Another series of simulations was used to evaluate the required geometry and potential of this repelling ring. Sample results of this second series are presented in the following.

In Figure 3 the equipotential contours in the x-z plan are shown when computed in vacuum with an anode at +9 kV, a cathode at 0 V and a repelling ring at –2 kV. It can be seen that there is a negative barrier of about -450 V at the aperture of the thruster.
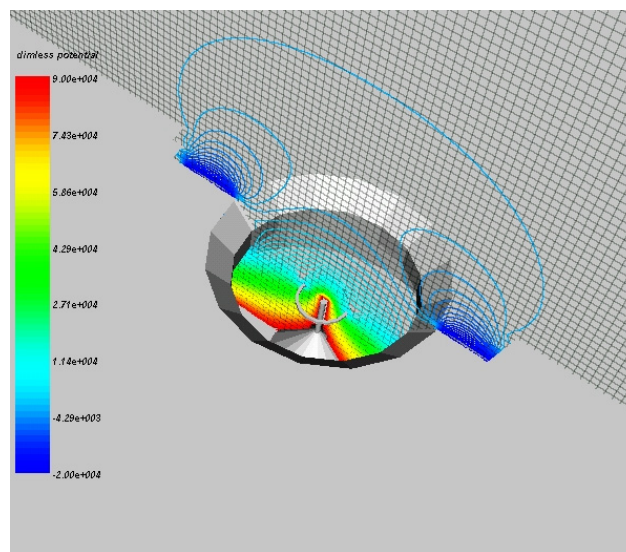
Figure 3: Equipotential in the x-z plan computed in vacuum of Vemitter= +9kV and Vrepel=-2kV. Potentials are expressed in $k_B Te/e$.

The effect of the ambient plasma and especially of the ion beam (with ion current, I_{beam}= 550 µA) space charge is shown on the equipotential contours of Figure 4. The barrier of potential is now of about –300 V. It is slightly decreased compared to the vacuum case but it is still strong enough to maintain the backstreaming current below an acceptable level. With the same configuration it was found that a repelling ring of –1 kV instead of –2 kV still lead to a potential barrier of –140 V. It must be noted that an unwanted consequence of the negatively biased rings is the creation of secondary electrons due to ion impacts which could in turn propagate to the anode. This phenomena had to be modelled as well but related results are not discussed here.
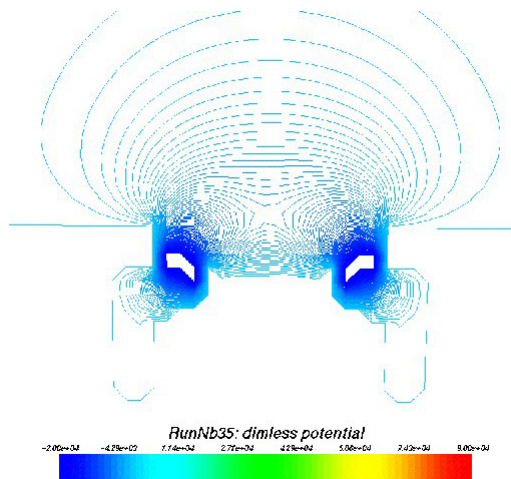
Figure 4. Equipotential in the x-z plan computed in an ionospheric plasma of Vemitter= +9kV and Vrepel=-2kV. Potentials are expressed in k_BTe/e.

Another design was investigated with a repelling ring located deeper inside the aperture. An example of the results for this new location and a bias potential of –1 kV is shown in Figure 5. In this case, no electrostatic barrier can be established along the direction of the ion beam and the number of backstreaming electron would have been critical.
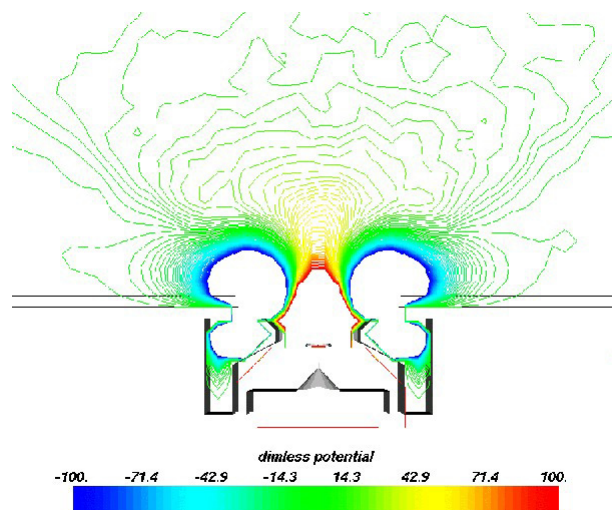
Figure 5. Same as Figure 4 but with the repelling ring at –1 kV and located closer to the anode. Potentials are expressed in k_BTe/e.

Finally, it must be noted that at low altitude, spacecraft are in a meso-thermal regime, meaning that the spacecraft velocity is lower than the electron thermal velocity and larger than the ion thermal velocity, therefore, in principle, the spacecraft velocity has to be taken into account in the ion dynamics. The effect on the ion plume when a FEEP thruster is emitting perpendicular to the ram direction is shown on Figure 6. Once can see that the equipotential contours are now asymmetric, however, it was found that the influence on the magnitude of the largely negative potential barriers was negligible.
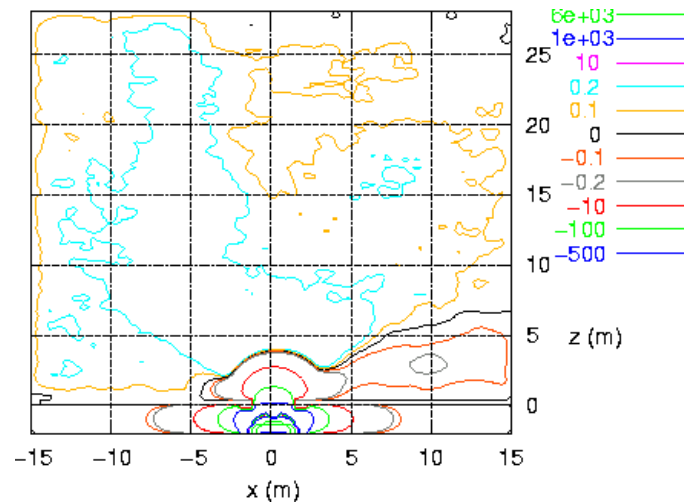
Figure 6: Ram effect on the electrostatic potential contours around a FEEP micro-thruster emitting perpendicular to the ram direction.

Conclusion

The PicUp3D code has been used to study various electrical configurations around a FEEP thruster aperture. It was observed that the effect of the beam space charge and the high potential electrodes of the FEEP engine is to expand the electrostatic sheath outside the aperture by about 0.2 m which is much more larger than the Debye length. The neutralisation of the plume space charge by ambient ionospheric plasma takes place within this distance. Potential barrier to prevent backstreaming electrons flux to the anode are mandatory but can be easily established with the help of a repelling ring-shaped electrode around the aperture. However, the magnitude of the barrier strongly depends on the detailed inner geometry and the setting of the various electrodes of control. Another effect which has to be taken into account is the current due to secondary electrons generated on the repelling electrode. This work confirms the capabilities of PicUp3D to model complex geometrical structures and plasma conditions, taking into account a very large range of ratio electrode potential to plasma thermal energy (10^4 in this study). A major limitation of this study results from neglecting the possibility of charge accumulation on insulators Another major limitation result from the poor spatial accuracy currently allowed by the use of the rectangular mesh for the Poisson solver. Improvements of the code foreseen in the coming few months would help to address this issue and allow accurate determination of the electrical current on each surfaces.

Acknowledgments

References

1. Forest J., L. Eliasson, and A. Hilgers, A new spacecraft plasma simulation software, PicUp3D/SPIS, 7th Spacecraft Charging Technology Conference, Proceedings pp.515-520, ESA/SP-476, ISBN No 92-9092-745-3, ESA-ESTEC, Noordwijk, The Netherlands, 23-27 April 2001.

2. Tajmar, M., Electric Propulsion Plasma Simulations and Influence on Spacecraft Charging, 7th Spacecraft Charging Technology Conference, Noordwijk, The Netherlands, pp. 545-553, 2001

3. Tajmar M. and J. Wang, 3D Numerical Simulation of Field-Emission-Electric-Propulsion Neutralization, Journal of Propulsion and Power, Vol. 16, No 3. , pp.536-544, 2000.

4. Tajmar M. and J. Wang, 3D Numerical Simulation of Field-Emission-Electric-Propulsion Backflow contamination, Journal of Spacecraft and rockets, 38(1), , pp. 69-78, 2001.

5. Torkar K., W. Riedler, M. Fehringer, C.P. Escoubet , K. Svenes, B.T. Narheim, A. Fazakerley, S. Szita, and M. André, Effect of active spacecraft potential control on Cluster plasma observations – first results, in proceedings of 7th Spacecraft Charging Technology Conference, pp.515-520, ESA/SP-476, ISBN No 92-9092-745-3, ESA-ESTEC, Noordwijk, The Netherlands, 23-27 April 2001.

CARBON NANOFIBER FILLED MATERIALS FOR CHARGE DISSIPATION

Ronald L. Jacobsen
Applied Sciences, Inc.
Box 579 Cedarville, OH 45314-0579
Phone: 937-766-2020 x137
Fax: 937-766-5886
E-mail: rljacobsen@apsci.com

Kent R. Walters
D. Gerald Glasgow
Applied Sciences, Inc.

Chyi-Shan Wang
University of Dayton Research Center

Abstract

This work explores the possibility of using carbon nanofibers to create improved versions of antistatic and conductive polyimide (e.g. Kapton™) for use in satellite charge control and dissipation. Carbon nanofibers have superior properties making them a candidate for this application, including very small diameter (to fit within a thin film), high aspect ratio (to form a network), moderate electrical conductivity, and excellent dimensional stability. Nanofibers in the diameter range from 60 – 200 nm (as distinct from smaller nanotubes) are now available relatively cheaply and in quantity. The primary challenge in making polyimide films is achieving adequate dispersion of nanofibers. This is complicated both by the fact that the nanofibers are entangled as produced, and that they are not naturally well wet by the polymer, causing them to agglomerate during processing prior to polyimide film casting. This paper describes methods for surface modification of nanofibers, as well as size separation of nanofiber agglomerates, to promote adequate dispersion in polyimide. Conductivity data on cast nanofiber filled polyimide films are also presented.

Introduction

In order to help mitigate differential charging on spacecraft and satellites, improved polymer materials are needed with electrical conductivity that is both sufficient to bleed charge and stable under temperature excursions typical to the orbital environment. The conductivity must be added without degradation of mechanical properties or increase in the material weight. Conductive versions of polyimide or teflon would be particularly useful.

Polyimide filled with carbon black is currently available. However, because carbon black is characterized by low aspect ratio particles, relatively high loadings are required to obtain a given level of conductivity, potentially compromising mechanical properties of the host polymer. Also, the materials are subject to electrical conductivity reduction or failure during relatively mild temperature excursions as thermal expansion of the matrix polymer pulls the conductive particles out of contact. Such failure may also occur under non thermally induced strains.

The work reported on here seeks to employ low cost carbon nanofibers to create improved forms of carbon filled polyimide. The high aspect ratio of the nanofibers is conducive to formation of a conductive network that both achieves a given level of conductivity at lower loading than is possible for low aspect ratio particles, and is less susceptible to disruption during thermal or mechanical expansion of the matrix. The primary challenges in crafting such a material include achievement of good dispersion of the nanofibers, and creation compatibility between the nanofiber surface chemistry and the polymer processing chemistry.

Carbon Nanofibers

The carbon nanofibers used in this work were Pyrograf®-III. The diameter of this nanofiber is typically in the range from 60 – 200 nm, with a length of 10 – 100 microns, and thus an aspect ratio in the range of 150 – 1500. The morphology of this nanofiber is that of stacked graphitic cones (as opposed to concentric graphitic cylinders, characteristic of multiwall nanotubes), as shown in Figure 1. Note that the graphitic planes do not run parallel to the fiber axis (indicated by a long white arrow), but are tilted at an angle. It is possible for the nanofiber to have a chemical vapor deposition (CVD) of carbon on the surface (as indicated in the figure). However the nanofibers used in the current effort typically do not. While the face of a graphitic plane can be a very inert surface that is difficult modify without damage to a nanofiber/nanotube, the exposed edges of these planes typical of Pyrograf®-III can allow more freedom for chemical modification to tailor the nanofiber for compatibility with specific polymers and polymer chemistries.
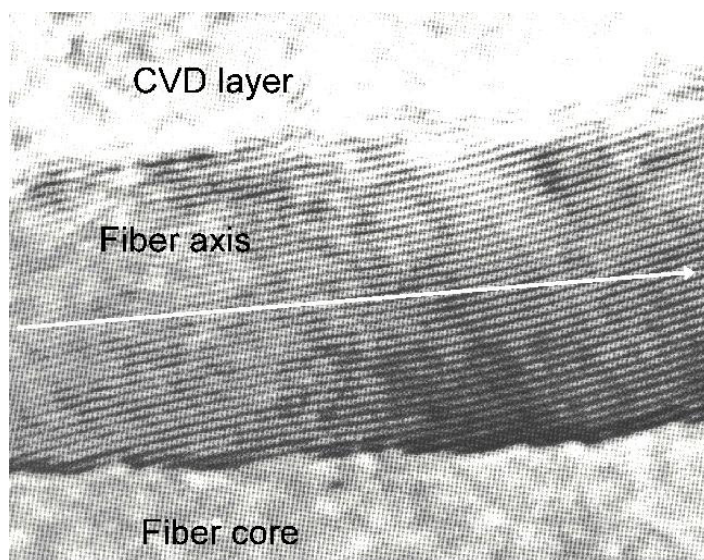
Figure 1. Morphology of Pyrograf®-III carbon nanofibers.

Nanofiber Dispersion

A key to achieving the best performing materials is to obtain the best possible dispersion of carbon nanofibers. This is a particular challenge for carbon nanofibers because they form entangled bundles during their growth process, and because the same property that allows them

to form a conductive network at low volume, their high aspect ratio, also makes it difficult for them to move past one another to become disentangled. (Indeed, some aggressive methods to achieve dispersion do so by reducing the aspect ratio, which is detrimental to the desired goal.) Truly monodisperse nanofibers may be extremely difficult to achieve, and often the best one can strive for is to minimize the size of entangled groups of nanofibers. Such minimization of bundle diameter is especially important for polyimide films, which are typically less than 4 mils (100 microns) thick. In these materials, a large nanofiber bundle is not just inefficiently dispersed, but actually represents a visible flaw in film, compromising its mechanical integrity.

Three methods have been used to minimize nanofiber bundle diameter and achieve better dispersion: ultrasonic agitation, a chemical method for sorting nanofiber bundles by size, and chemical modification of the nanofiber surface to promote solvent compatibility.

Ultrasonic agitation was somewhat effective improving nanofiber dispersion and reducing nanofiber bundle size. Table 1 shows an example of how the distribution of bundle diameters changes for nanofiber suspended in water as a function of sonication time. The "mean" column gives the bundle diameter, in microns, that represents the 50th percentile of those in suspension. The "d10" and "d90" columns given the diameter for the 10th and 90th percentiles, respectively. "d99.9" indicates the maximum observed bundle diameters. One can see that sonication reduces the bundle diameters at all percentiles. One also observes that the accessible surface area of the nanofiber increases as the nanofibers are dispersed. Importantly, the size of the largest bundles is greatly reduced. Ideally, the maximum bundle diameter should be below 20 μm for casting of high quality polyimide films. Sonication alone is not sufficient to achieve this goal.

Table 1. Example of nanofiber bundle diameter distribution vs. sonication time.

Sonication time (min)	d10 (μm)	Mean (μm)	d90 (μm)	d99.9 (μm)	Surface Area (cm^2/cm^3)
0	13.61	48.56	98.67	145.00	2,569
1	5.79	18.58	29.06	45.24	7,397
5	4.44	16.92	24.84	37.47	9,008
10	3.89	16.18	23.68	36.90	10,651
∞ (projected)	~3	~16	~23	~35	~12,000

A second method for reducing bundle diameter in the final material is to sort the larger bundles out of the mix at the start. This can be done by a chemical process in which the nanofiber is treated with starch. The starch attaches to the outside of the nanofiber bundles and facilitates their suspension in water. This sets up a competition between the starch working to hold the fiber bundles in suspension, and gravity. Only smaller bundles, with a higher surface to volume ratio, and therefore a larger proportion of starch, are able to stay in suspension. Large bundles precipitate and can be removed before further processing. The starch can then be easily removed from the nanofiber that is retained in suspension.

Table 2 shows an example of nanofiber bundle diameter distributions after a starch sorting procedure. Here we see that the diameter distribution is improved at all percentiles relative to unsonicated nanofiber, and in particular there the size of particles at and below the 10th percentile is much smaller than even for the most sonicated nanofiber. The accessible surface area is

concomitantly increased. There still remain a small percentage of larger diameter bundles, but these seem to be more readily broken up by sonication than those that have not received the starch treatment, as evidenced by the last line of the table. (Presumably, these are bundles of nanofibers that are less densely packed than others. Such bundles would allow starch to penetrate toward their center, giving them a high proportion of starch and better tendency toward suspension. Also, such loosely packed bundles would more easily fall apart during sonication.) The combination of the starch and sonication treatments appears to reduce all bundle diameters below the 20 μm limit for high quality films.

Table 2. Example of nanofiber bundle diameter distribution after starch treatment.

Sample Treatment	d10	mean	d90	d99.9	Surface Area
Starched	0.61	18.3	76.4	86.4	28,558
Starched and Sonicated	0.52	5.5	10.1	14.7	39,135

Finally, dispersion can be enhanced by treating the nanofiber for maximum compatibility with the solvent needed for casting the given polymer system. Polyimides, such as Kapton™, are typically cast from a chemistry that starts with the polymer dissolved in dimethylacetamide (DMAc) or similar solvent. The carbon nanofibers must also be suspended and dispersed in the solvent. As grown, the nanofibers are incompatible with DMAc and tend to precipitate out in larger agglomerates. To overcome this, the surface must be functionalized with carboxylic acid groups (COOH). This can be accomplished by wet treatment with sulfuric and nitric acid, which can put up to 20 atom % of oxygen, primarily in the form of carboxylic acid, on the nanofiber surface. Somewhat lesser, but still sufficient, amounts of oxygen can added by proprietary alkaline wet chemistry or *in situ* modification of the nanofiber growth process. The latter two methods are more amendable to large scale production than the acid based treatment. Nanofibers treated by the above methods were found to suspend readily in DMAc, and to disperse far better than untreated nanofiber.

Polyimide Film Casting and Properties

A 75 micron (3 mil) thick film cast in a Kapton™-like material with 16.7 % carbon nanofibers by weight was adequately strong (as determined by qualitative inspection), and had an electrical conductivity of 70 Ω/square (equivalent to a bulk resistivity of 0.5 Ω-cm). This material was cast from a solution in DMAc.

A similar effort in a polyamic acid derived polyimide resulted in a sample with resistivity of approximately 30 Ω/square. The mechanical properties of this specimen were also acceptable. This material, with a ketone linkage rather than the ether linkage typical of Kapton, was cast from a solution of n-methyl pyrrolidone (NMP).

The electrical performance of these films is superior as compared to Du Pont's current version of conductive polyimide, Kapton 275XC, which has a conductivity of 230 to 290 Ω/sq. It is apparent that there is latitude to work at lower nanofiber volume fraction (which could have mechanical benefits) and still obtain improved electrical performance over the state of the art. (It should be noted that the Kapton film was not cast with the best nanofiber dispersion so far

observed, and it is possible that further gains in performance will result when a more uniform film is cast from a suspension containing smaller nanofiber agglomerations.)

Additional casting efforts are underway to study higher and lower loadings of nanofibers, and to extend into other polyimide materials, such as bis analine M, and oxydianaline.

Conclusion

While this remains a work in progress, with much of the parameter space yet to be examined and some improvements in the degree of nanofiber dispersion desirable, it appears that carbon nanofibers can indeed be the basis for an improved family of conductive polyimide materials, giving specific levels of conductivity at lower loading fractions than carbon black based materials.

Acknowledgements

References

1. Produced by Pyrograf Products, Inc., Cedarville, OH.

COMPARISON OF CLASSICAL AND CHARGE STORAGE METHODS FOR DETERMINING CONDUCTIVITY OF THIN FILM INSULATORS

Prasanna Swaminathan
Physics Department, Utah State University
Logan, UT, USA 84322-4415
Phone: (435) 797-2936
Fax: (435) 797-2492
E-mail: JR.Dennison@usu.edu

J.R. Dennison
Alec Sim
Jerilyn Brunson
Eric Crapo
Physics Department, Utah State University

A. R. Frederickson
Caltech Jet Propulsion Laboratory

Abstract

Conductivity of insulating materials is a key parameter to determine how accumulated charge will distribute across the spacecraft and how rapidly charge imbalance will dissipate. Classical ASTM and IEC methods to measure thin film insulator conductivity apply a constant voltage to two electrodes around the sample and measure the resulting current for tens of minutes. However, conductivity is more appropriately measured for spacecraft charging applications as the "decay" of charge deposited on the surface of an insulator. Charge decay methods expose one side of the insulator in vacuum to sequences of charged particles, light, and plasma, with a metal electrode attached to the other side of the insulator. Data are obtained by capacitive coupling to measure both the resulting voltage on the open surface and emission of electrons from the exposed surface, as well monitoring currents to the electrode. Instrumentation for both classical and charge storage decay methods has been developed and tested at Jet Propulsion Laboratory (JPL) and at Utah State University (USU).   Details of the apparatus, test methods and data analysis are given here. The JPL charge storage decay chamber is a first-generation instrument, designed to make detailed measurements on only three to five samples at a time. Because samples must typically be tested for over a month, a second-generation high sample throughput charge storage decay chamber was developed at USU with the capability of testing up to 32 samples simultaneously. Details are provided about the instrumentation to measure surface charge and current; for charge deposition apparatus and control; the sample holders to properly isolate the mounted samples; the sample carousel to rotate samples into place; the control of the sample environment including sample vacuum, ambient gas, and sample temperature; and the computer control and data acquisition systems. Measurements are compared here for a number of thin film insulators using both methods at both facilities. We have found that conductivity determined from charge storage decay methods is 10^2 to 10^4 larger than values obtained from classical methods. Another Spacecraft Charging Conference presentation describes more extensive measurements made with these apparatus. This work is supported through funding from the NASA Space Environments and Effects Program and the USU Space Dynamics Laboratory Enabling Technologies Program.

Introduction

As interaction with the space environment builds up charge on spacecraft surfaces, the rate at which further charge accumulates will be affected. In the simplest scenario, for a fully conductive spacecraft the charge will readily redistribute over the entire satellite and will charge to the point where the incident currents from the environment fluxes are equal to emission currents. By contrast, as insulating spacecraft materials accumulate charge, their low charge mobility causes that charge to accumulate where deposited and local electric fields to rise until the leakage current from the insulators to conductors equals the accumulation current from the environment (or until the insulator actually breaks down and generates a charge pulse). Hence, conductivity of insulating materials is a key parameter to determine how accumulated charge will distribute across the spacecraft, how rapidly charge imbalance will dissipate, and what equilibrium potential an insulator will adopt under given environmental conditions [1].

Determination of values of resistivity for typical thin film insulating materials applicable to service in the space environment is problematic [1,2,3,4]. The bulk resistivity values of insulators used to model spacecraft charging have traditionally been obtained from the handbook [5] values found by the classical ASTM/IEC methods [6,7]. Classical methods use a parallel plate capacitor configuration to determine the conductivity of insulators by application of a constant voltage (E field) and the measurement of the resulting leakage current across the plates and through the insulator [6].

However, recent works have shown that these classical methods are often not applicable to situations encountered in spacecraft charging [1,2,3,4]. Conductivity is more appropriately measured for spacecraft charging applications as the "decay" of charge deposited on the surface of an insulator. Charge decay methods expose one side of the insulator in vacuum to sequences of charged particles, light, and plasma, with a metal electrode attached to the other side of the insulator. Data are obtained by capacitive coupling to measure both the resulting voltage on the open surface and emission of electrons from the exposed surface, as well monitoring currents to the electrode. When the resistivity data obtained were compared to existing ASTM data for some spacecraft insulators, the data calculated by the ASTM method was found to be higher by up to four orders of magnitude [1,2,3,4]. Results of the charge storage method have already been shown to correctly predict charging events observed in real satellite data, through modeling of pulses occurring aboard the CRESS satellite [4].

Given these results, we have concluded that classical resistivity methods are not the most appropriate methods for many spacecraft charging problems. Specifically,

1. The charge injection methods, and resulting internal charge profile and E field, are fundamentally different for the classical and charge storage methods. The voltages developed in space are generated by impressing charge into the insulation, not by the application of voltage from a power supply onto electrodes.

2. Conductors are placed on both surfaces of the insulators in ASTM tests, whereas the spacecraft most often has only one surface of the insulator in contact with a conductor.

3. The ASTM methods use classical ground conditions and are basically designed for the problems associated with power loss through the dielectric and not how long charge can be stored on an insulator surface or in the insulator interior [6].

4. The measurement of the leakage current is made only after few minutes of bias application in the classical methods. Initial measurements by Frederickson at the JPL indicate that the resistivity changes with time and that to adequately characterize the change of resistance with time, requires monitoring stored charge for up to 1 month [1,2,3,4]. The resistivity data in handbooks do not take into consideration the fact that the resistivity continues to increase even after the measurement is taken. But in spacecraft modeling we need to know the how the leakage decays for as long as year or more [1,2].

This paper describes the instrumentation and methods developed to implement the charge storage measurements and compares preliminary results of this effort with classical resistivity measurements. The work is a joint project by the Jet Propulsion Laboratory (JPL) and Utah State University (USU) sponsored through the NASA Space Environments and Effects (SEE) Program [8]. Preliminary studies using the charge storage method and further details of the methods and instrumentation are found elsewhere [1,2,3,4].

Classical Resistivity Method

The classical method for measuring the resistivity of thin film insulators is based upon measuring current flowing through a well-defined sample structure, for which the relationship

Figure 1. (a) Preferred sample design for classical resistivity method for thin insulators. (b) Experimental setup of classical method at JPL.

between the material's resistivity and the sample's resistance can be determined [6,7]. Figure 1(a) shows the preferred sample design for the ASTM-IEC or capacitor resistance method that is valid in the range of $10^7 < \rho < 10^{21}$ Ω·cm. An adjustable high voltage is applied to one sample electrode. Current flow to the sample electrode held at ground is measured by a picoammeter. A grounded guard ring serves to help establish approximately parallel electric field lines of uniform magnitude and to define the volume of material in which the measured current flows [6]. The resistance of the sample is then given by $R = \rho d / A_{eff}$, where ρ is the resistivity (ohm-cm), A_{eff} is the effective area (cm^2) slightly larger than the metal electrode, and d (cm) is the sample thickness. The resistance R is determined from an I-V curve using Ohm's law.

Classical resistivity measurements can vary appreciably—from factors of two to two orders of magnitude—due to variations in sample environments and test conditions [6]. Most reported ρ values are derived from measurements made at ambient temperature and relative humidity, which is not representative of the wide temperature range and vacuum conditions in which space hardware operates. Temperature variations can often be described as Arrhenius behavior of the form $\rho = \rho_o \exp[E_A / k_B T]$, where ρ_o is a material parameter and E_A is an activation energy

characteristic of a particular energy absorption process. Resistivity also changes appreciably—often orders of magnitude—with relative humidity or moisture content, particularly for thin film samples. Both ambient humidity and drying during sample conditioning need to be considered [6,9]. For example, resistivity has been shown to vary with time to the ½ power, as water diffused into or out of the sample [9]. Up to two orders of magnitude increase in ρ have been observed during vacuum pump down of polymer films [9] Further, dielectric resistivity often depends on duration and magnitude of the applied sample voltage. The observed decrease in current with time is due primarily to dielectric absorption (*e.g.,* interfacial polarization, volume charge, rearrangement of dipoles on the molecular level, *etc.*) and ion migration into the electrodes; it usually has the form $I(t)=A \cdot t^{-m}$, where $0<m<1$. Excessive voltage produces high internal electric fields, resulting in breakdown of the insulator when the dielectric strength is exceeded (typically, when the field exceeds 10^5 kV/cm) [2]. Sample impurities or surface contamination are known to substantially affect bulk resistivity and surface resistivity, respectively. Given the substantial variability in resistivity from these factors, it is essential that the sample preparation, conditioning history, and environment be well characterized and controlled for such measurements.

Classical method instrumentation at JPL

The classical method of measurement of resisitivity of thin film insulators at JPL follows the ASTM-257-99 guidelines [6], as shown in Figure 1(b). A damp cardboard is used to make more complete contact on the open face of the sample. A positive 64 V is applied for ten minutes at the end of which the current is recorded [2]. The bias polarity is then reversed and after 10 minutes the current is recorded. The resistance is defined as the ratio between the change in voltage (128 volts) and the change in current. Figure 3 shows the classical resistivity measurement from JPL as a function of time for 51 μm thick sample at 64 V [2].

Classical method instrumentation at USU

The capacitive resistance apparatus (CRA) at USU is designed as a more versatile instrument for classical resistance measurements under more tightly controlled conditions (see Fig. 2). The sample environment—including sample temperature, ambient vacuum or background gas, and humidity—can be strictly controlled. Computer automation of voltage and current measurements, together with environmental parameters, allow rapid and prolonged resistance measurements. Thus, the apparatus is capable of parametric studies of variables

(a)   (b)
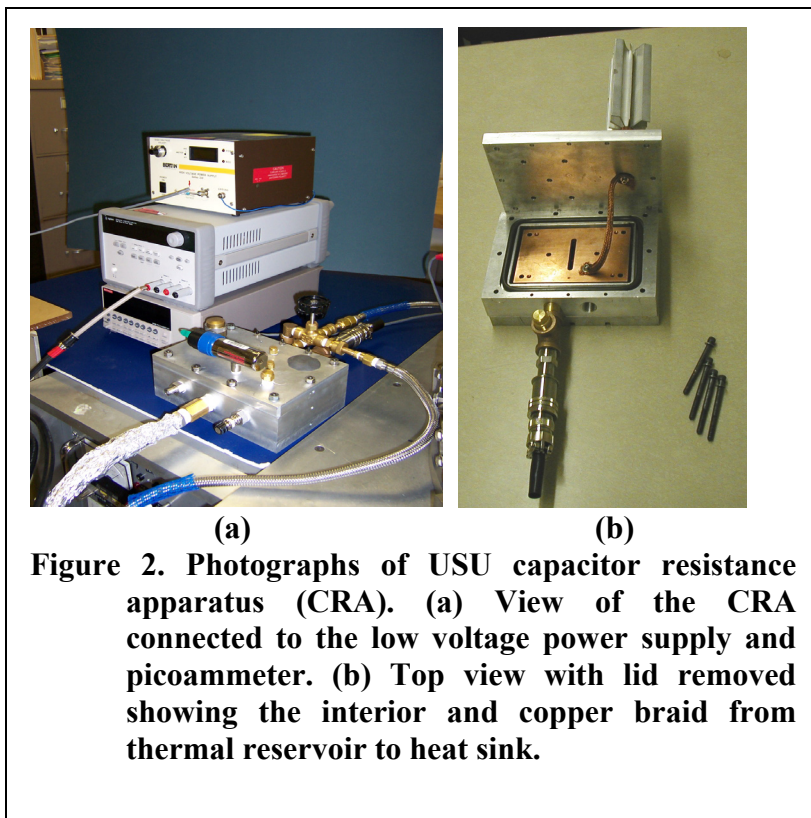
Figure 2. Photographs of USU capacitor resistance apparatus (CRA). (a) View of the CRA connected to the low voltage power supply and picoammeter. (b) Top view with lid removed showing the interior and copper braid from thermal reservoir to heat sink.

that influence the resistivity, including sample material and thickness, applied voltage magnitude and duration, sample temperature, ambient gas or vacuum, and humidity.

Two independent thin film insulator samples of up to ~1 mm thick can be mounted in the apparatus simultaneously; these are stretched over an electrically and thermally isolated Cu high voltage electrode and held smoothly in place with two polycarbonate sample clamps each. An adjustable voltage is applied using either a 0 to ±110 VDC, a 0 to 1 keV, or a 0 V to ±50 keV computer-controlled power supply, depending on the range required. Wiring to the high voltage electrode uses corona-free high voltage Teflon-insulated wire to a standard 15 kV coaxial SHV vacuum feedthrough. Current flow through the samples to two independent sample inner electrodes held at ground is measured by a dual channel picoammeter [2]. The unit is also designed to measure the punchthrough voltage of thin insulating films, by monitoring current across the sample while applying up to ±15 keV across the sample electrodes [10].

The unit is designed to control the temperature of the electrodes and the sandwiched samples to ~ ±2 °C using a standard PID temperature controller and platinum resistance thermometers. Two 70 W thermoelectric Peltier cooling units are mounted above the sample electrodes. In cooling mode, the Peltier coolers are designed to cool the sample to −100 °C and exhaust excess heat via a copper braid to an external heat sink through a O-ring-sealed compression port. In heating mode, the Peltier coolers are run with reverse voltage, drawing heat from the external heat sink. In this mode, the unit is designed to heat the electrodes up to +100°C.

The CRA aluminum-walled vacuum chamber is pumped with the same system used for the charge storage chamber (see details below). Ultimate pressure of the CRA system is 10^{-5} Torr, limited by pumping speed and O-ring seals. Vacuum connections between to the CRA chamber are made using standard Quick Connect and Conflat^{TM} fittings. The CRA vacuum chamber is also connected to a stainless steel gas handling system to allow control of the ambient gas environment composition and pressure; pressure is monitored by a standard vacuum thermocouple gauge (1 atm to 1 mTorr), a capacitance manometer (100 to 0.1 Torr), and a high pressure Si strain gauge transducer [10^{+6} to 10^{0} Torr].

Results of classical resistivity methods

Figure 3 shows data obtained using the classical ASTM resistance method shown in Fig.1(b). The JPL data are for a 51 μm thick Kapton H sample from Dupont taken at room temperature and high humidity with 64 V. The USU data were obtained for Sheldahl thermal control blanket material (51 μm and 130 μm thick Kapton H with 0.1 μm vapor deposited Al) at 26±2 °C in ambient room light at 30±5% ambient relative humidity with wet electrodes for a range of voltages from 300 V to 900 V. The samples were cleaned with isopropyl alcohol.

The curves showed linear behavior on a log-log plot with a slope of ~½ and converged to ~$(3\pm1) \cdot 10^{+16}$ Ω·cm at ~½ hr. The published resistivity value for Dupont Kapton HN is $1 \cdot 10^{17}$ Ω·cm [11]. There is no clear dependence of the data on applied voltage or sample thickness at 1 hr. Possible sources of deviation between samples include temperature, effectiveness of the voltage contacts, and drying time of the contact.
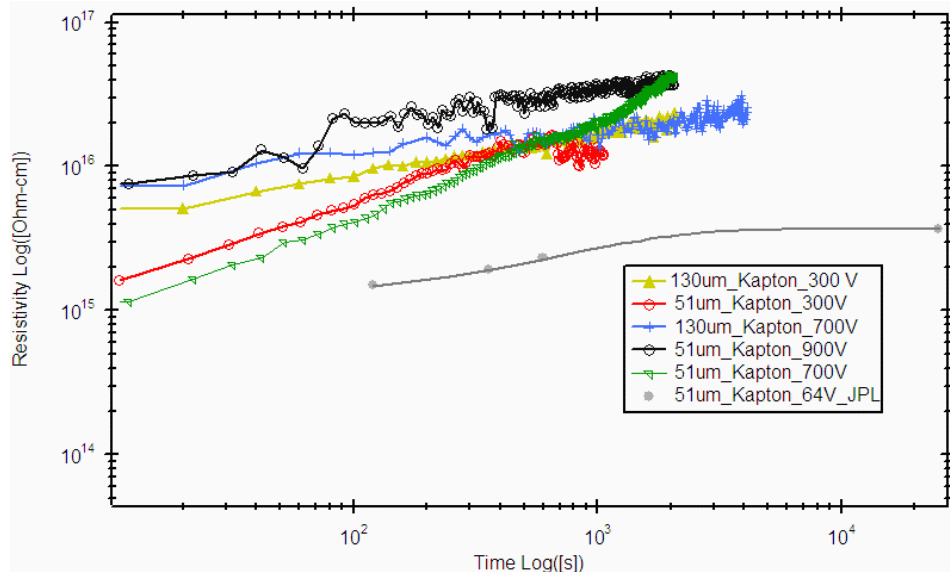
Figure 3. Classical resistivity measurements versus time for Kapton samples. Data shown are from USU for 51 μm and 128 μm thick samples at 300 V, 700 V and 900 V and from JPL for 51 μm thick sample at 64 V.

Charge Storage Method

As design criteria, fourteen key *Performance Requirements* (*PR*) required for our charge storage instrumentation were enumerated. Details of the design of two test chambers at JPL and USU are provided below, with an emphasis placed on how well the chambers meet the *PR* shown in Table I.

Table I. List of Performance Requirements for Charge Storage Decay Test Apparatus

1. *Sample Quantity*--Multiple samples in the chamber to enable high sample throughput
2. *Sample Monitoring*
   a. Monitor one sample at a time
   b. Isolate samples from one another during all treatments and monitoring
   c. Measure the current that charged the sample
   d. Require about 1-volt resolution for the charge probe
3. *Sample Treatment*--Apply special treatment to each sample
   a. Charge one sample at a time
   b. Charge the sample surface uniformly
   c. Charge samples using slow electrons and sample bias
   d. Charge or discharge samples using sample bias and plasma source
   e. Charge or discharge samples using fast electron beam
   f. Discharge samples using light for amenable samples
4. *Sample Environment*
   a. Avoid placing objects in the chamber (other than samples) that might accidentally charge up
   b. Maintain vacuum and instrument functions for at least one month
   c. Temperature control of sample over life of experiments

Experimental setup of charge storage method at JPL

The charge storage chamber at JPL is a sample handing system integrated into an existing vacuum chamber. At JPL the chamber provides the surface voltage measurements (*PR 2*), and, in addition, provides energetic electron irradiations to samples that are large enough to simulate pulsed discharges by materials flown on spacecraft (*PR 3*). This extra constraint causes the JPL chamber to differ from that at Utah State. The JPL samples will sometimes be as wide as 10 cm. Also, the vacuum space in front of the sample must be large enough to simulate the pulsed discharge phenomena that occur near insulator surfaces on spacecraft, constraining us to provide at least 10 cm of empty vacuum in front of the sample for pulsed discharges to propagate.

Figure 4 gives the detail of the entire charge storage set up at JPL with the sample environment and the chamber configuration; related photographs are found in Fig. 5. As shown schematically in Fig. 4(a), the chamber contains a broad-beam electron gun with accelerating potentials from 0 to 75 keV, a plasma source with bias capability, an electron-emitting filament, a light source, a sample surface voltage-sensing device, and temperature probes. The sample electrode can be attached to an oscilloscope, a current monitor, a voltage source or a voltmeter. The grounded grid across the center of the chamber prevents electric fields developed by the electron gun and the plasma source from affecting the sample.

Sample carousel and sample holder design

To partially meet *PR 1*, there can be three to five samples in the JPL chamber. The fifth object is a Faraday plate in a can to measure beam current (*PR 2c*) [2]. A cross-sectional view of the

Figure 4. JPL charge storage chamber design (a) Schematic of the sample environments and electrical measurements. (b) Chamber configuration for open and sealed sample mounts. (c) Detail of sample mount for sample open to vacuum (d) Detail of the "tin can" sealed sample mount [3].
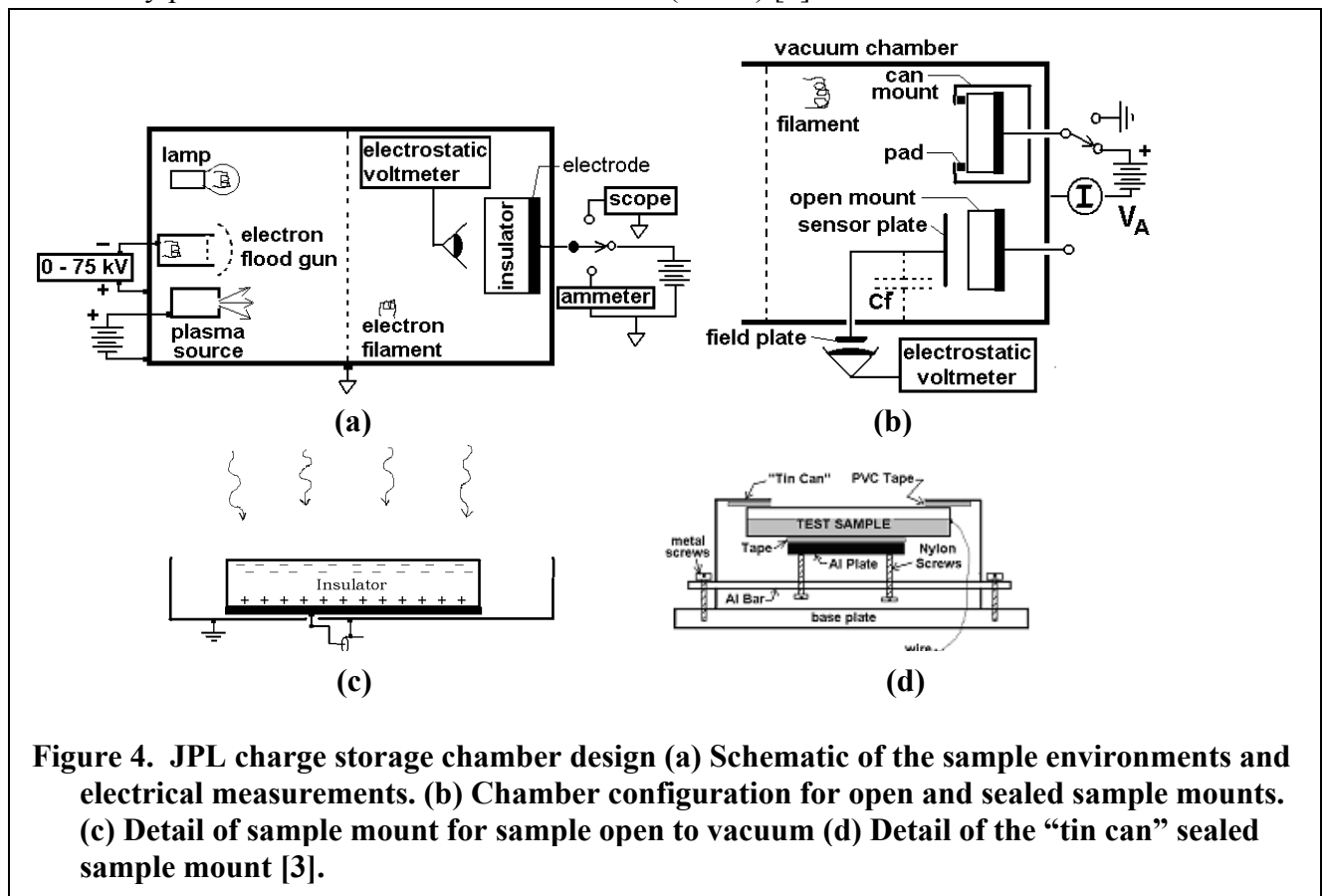
sample holder is shown in the Figure 4(d). Different sensor plates, carousels and sample plates can be configured for different samples in the JPL design [see Fig. 5(c)]. The sample mount assembly and the sample carousel are intended to avoid things that will charge up and try to provide electrical shielding for the probes and current sources as well as each sample. Note that electrons in the vacuum chamber can access only the exposed portion of the insulator surface (*PR 2b and 4a*) and cannot get to the rear sample electrode at all. There are no insulating surfaces visible by line-of-sight from the sample surface that can accumulate charge and produce perturbing electric fields. Charge accumulation on the sample electrode can create a tangential field adjacent to the front insulator surface, making characterization of the surface voltage difficult. Stray charge accumulation on the sample electrode also interferes with measurement of the current to the front of the sample surface during sample charging. Further, the design allows for no sources of light visible from the sample surface that could charge or discharge the sample surface; this requires a nearly light tight seal for each sample (*PR 2b*). Finally, RF signals emanating from the sample surface can get to the outside world only by coupling to the wire from the back of the sample [4]. If such a path exists, then the DC sample bias during charging will also cause charging on the polycarbonate and distort later field measurements.

The tin can, the base plate and the PVC tape provide an "air-tight" enclosure protecting the sides and back of the sample from electrons in the vacuum. Additionally, the wire can be brought through the base plate as a shielded coaxial cable so that electrons in the vacuum cannot "connect" to the wire. Alternatively, the region below the base plate may be free of electrons. The PVC tape provides a soft surface for the insulator under test to press against. The Nylon screws compress the Al Plate and its insulating tape against the electrode of the sample, and press the sample against the PVC Tape [2]. When using this sample holder, one must be aware of the effects of the PVC tape and the close vicinity of the tin can to the charged sample surface. Specifically, one must consider: (a) the insulating strength of the PVC tape and the insulator sample, together, must withstand the voltage applied to the sample electrode at the rear of the sample; (b) the PVC tape must be thin enough that, even if it is charged, it does not contribute charging signal to the TreK^{TM} probe; and (c) when the insulator is highly charged, the close proximity of the tin can may induce pulsed breakdowns at the edges of the sample.
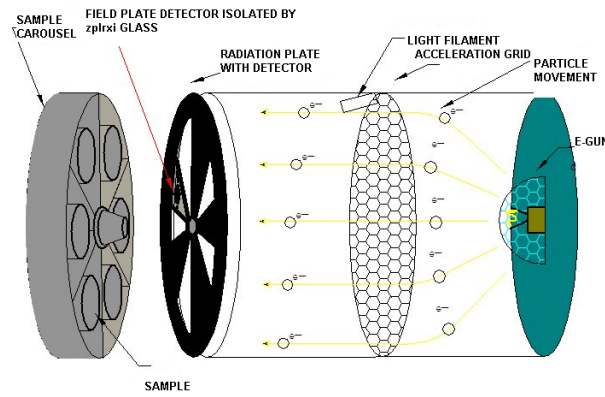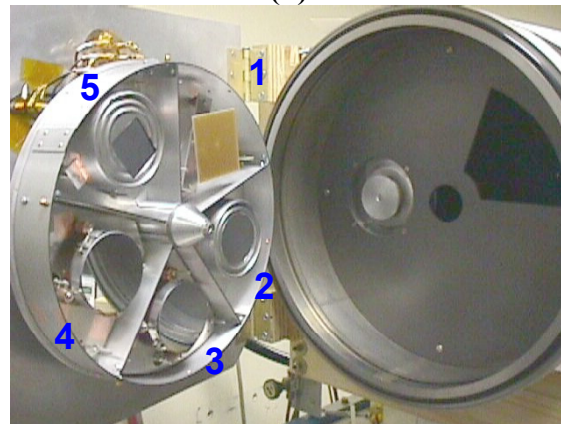
Figure 5. (a) Internal design of JPL charge storage chamber. (b) Photograph showing JPL chamber with door closed. (c) Carousel mounted to the door of the vacuum chamber on left half; the body of the vacuum chamber on right. Five samples are on this carousel: clockwise from 1-O'clock: (1) a square sample of circuit board material in the fully open mounting; (2) the mirror in the "air-tight" can; (3) and (4) two mirrors in an open configuration; and last (5) a carbon-coated metal in a can acting as a beam current monitor. When the door is closed, the carousel extends about 8 cm into the vacuum chamber and rubs against a carbon-coated aluminum plate called the shutter. The shutter is tightly affixed to the walls of the chamber.
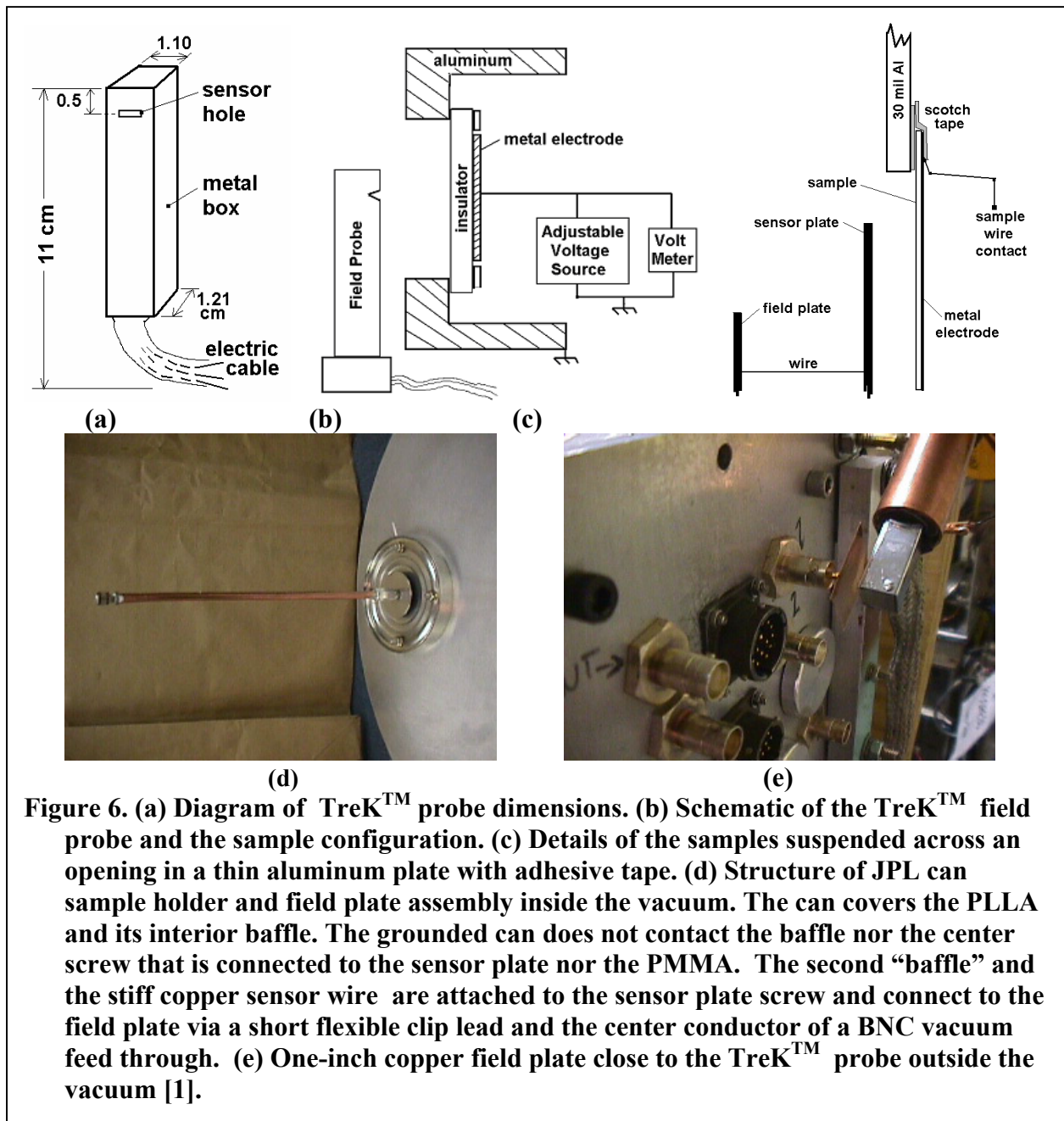
Figure 6. (a) Diagram of TreK^{TM} probe dimensions. (b) Schematic of the TreK^{TM} field probe and the sample configuration. (c) Details of the samples suspended across an opening in a thin aluminum plate with adhesive tape. (d) Structure of JPL can sample holder and field plate assembly inside the vacuum. The can covers the PLLA and its interior baffle. The grounded can does not contact the baffle nor the center screw that is connected to the sensor plate nor the PMMA. The second "baffle" and the stiff copper sensor wire are attached to the sensor plate screw and connect to the field plate via a short flexible clip lead and the center conductor of a BNC vacuum feed through. (e) One-inch copper field plate close to the TreK^{TM} probe outside the vacuum [1].

TreK^{TM} Probe Assembly

An electrostatic voltmeter [12] is used at both JPL and USU, that can sense surface voltages from –20 kV to +20 kV relative to local "ground," and from this infer local surface charge distributions [51 (*PR 2c*). The TreK^{TM} probe arrangement, its dimensions and the chamber photographs at JPL are shown in Fig. 6. The TreK^{TM} voltmeter is actually composed of an electric field sensor and an adjustable voltage source. An internal sensor monitors the electric field that penetrates into the hole in the face of the TreK^{TM} probe's metal box. The circuits adjust the potential of the metal box until it attains nearly the potential of the nearby high voltage (HV) surface, at which condition there is zero field penetrating into the small hole. A standard voltmeter is used to measure the potential of the box, and the sample surface potential is proportional to the box potential. No electrical contact is made to the nearby HV surface. In addition, as the box

voltage approaches the nearby HV surface voltage, the effective capacitance of the box to that surface approaches zero.

The electron beam, low-energy electron treatments, light photon treatments, thermal treatments, or other treatments of the samples must not affect the capacitor sensing circuit that brings the sample surface voltages out of the vacuum chamber. At JPL a custom capacitance transfer probe was constructed to make electric field measurements at sample surfaces *in situ* in the vacuum chamber, using a TreK^{TM} probe external to the chamber; this isolates the sensitive TreK^{TM} probe from the sample treatments.

Figures 6(c), (d) and (e) shows the JPL sample arrangement, TreK^{TM} probe structure and the probe outside the vacuum. Key aspects of our design are the geometry, construction and materials of the field probe, voltage sensor plate, connecting wire, and wire vacuum feedthrough. In addition, the coupling to the charge probe assembly—particularly the voltage sensor plate—to the sample and sample electrode are important. Both the mountings and the samples themselves must be coordinated so that the measurement technique corresponds to the physical and mathematical modeling. The spacing between the biased field-generating plate and the field probe is much smaller than the extent of the probe. Therefore, between the flat surface of the probe and the flat plate the electric field is plane-parallel. Note that surfaces at other voltages must be relatively far from the flat plate so as not to alter the field between the plate and the probe. We determined that a 12 mm x 12 mm flat plate spaced 3 mm from the probe satisfied this condition, even with most of the probe surrounded with protective copper pipe.

Sample treatment

The arrangement for charging and measuring the voltage on an insulated surface at JPL is defined in Figure 9(a). The insulated surface of the sample faces the electron source and/or the field probe. The other surface of the sample is metalized and connected to wiring so that it can be biased relative to ground, and relative to the electron source, or monitored for currents. The diameter of the center electrode on the sample is 4.6 cm and its area is 16.6 cm^2. The diameter of the opening on the aluminum mount is 5.08 cm. A grounded reference sample is used to establish the zero of the field probe.

An electron-emitting filament is used to provide uniform surface charge that does not penetrate far into the sample [*PR 3(b)*]. A positive bias is applied to the rear sample electrode. The filament source is used to inject electrons into the vacuum; slowly raising the sample electrode voltage to, say, 1 kV, one gently charges the sample with electrons that impact the sample with less than 25 eV and develops 1 kV across the sample. The filament source is then turned off, the rear sample electrode grounded, and a 1 kV voltage is measured on the front surface of the insulator sample with the capacitance transfer probe and TReK^{TM} probe. This method places the electrons gently onto the front surface, not deeper into the bulk of the insulator. The field in the sample is therefore ideal for our measurements. Measurement of total current flow with an electrometer as the sample electrode is changed from 1 kV to ground, as well as the sample electrode voltage, can be used to determine the current required to charge the sample [*PR 2(c)*] and to estimate the sample dielectric constant.

Alternately, a broad-beam electron gun with accelerating potentials from 0 to 75 keVA is available on the JPL chamber for uniform, stable charge deposition at energies in the few keV

regimes near the second crossover energy and at higher energies for study of internal sample charging [see Fig. 5(a)]. Charging induced by electron irradiation is strongly modified by the electron-hole pairs that the irradiation generates in the insulator. High field effects at 10^6 V/cm act strongly on the electron-hole pairs and on electrons in shallow traps to provide extended conductivity. Visible light can be used to investigate conduction by electrons (or holes) emitted from shallow trapping levels. The qualitative physics of such processes in solid dielectrics has long been known, and some instrumentation is developed here for measuring the effects in practical spacecraft charging applications.

As shown schematically in Fig. 4(a), the JPL chamber also has an integral plasma source with bias capabilities, plus W-filament and UV light sources. *PR 3(d)* requires the capability to charge or discharge of samples using sample bias with the sample electrode and a plasma source. Charging with electrons from the plasma can, in general, be accomplished more effectively with the low energy flood gun described above. But charging with positive ions is best accomplished with a plasma source. The plasma source is used while rear sample electrode is biased negative in order to get ions onto the surface. This is useful, for example, to see if ions chemically diffuse and produce conduction in insulating polymers when electrons do not, or to study about atomic diffusion in dielectrics. Further details of the use of the various sources is provided in Frederickson [2]. Specifically, this reference describes calibration of the TreK^{TM} probe and charge transfer probe, measurement of sample capacitance and leakage currents, investigations of the electric field (or charge) profile developed by charge injection with high energy electrons (up to 75 keV), studies of light-induced conductivity and emission, investigations of electric field enhanced conductivity, and surface emission occurring after irradiation (Malter Effect) related to negative electron affinity.

Experimental setup of charge storage method at USU

The USU charge storage chamber is a second-generation system designed such that up to 32 samples can be tested simultaneously in a controlled, stable vacuum environment for the duration of month-long experiments.

Chamber design and capabilities

Figure 7(a) shows the vacuum chamber with the sample carousel and 32 sample holders, the TreK^{TM} probe assembly, and the sample cover manipulator. The vacuum chamber is a 61 cm inner diameter stainless steel bell jar collar with ten Conflat^{TM} flange ports and six O-ring sealed ports. Two cm thick aluminum plates form the chamber walls above and below the collar.

PR 1 requires that the USU chamber allow many samples be tested simultaneously. To meet *PR 3*, the sample carousel has all samples at the same height on the circumference of a sample carousel that can be rotated to move each sample in front of stationary electron, ion or photon sources, charge probes, or the wobble stick of the sample cover manipulator to allow sample manipulation and inspection, charge deposition, sample treatments, or measurements. The sample holders form a 58 cm diameter, 32-sided right cylinder, ~7 cm high. Top and bottom Al plates attached to this right cylinder provide a light-tight conducting seal for the sample carousel enclosure to minimize electrical charging (*PR 4a*). The carousel is mounted on a ~43 cm diameter aluminum alloy lazy Susan bearing.
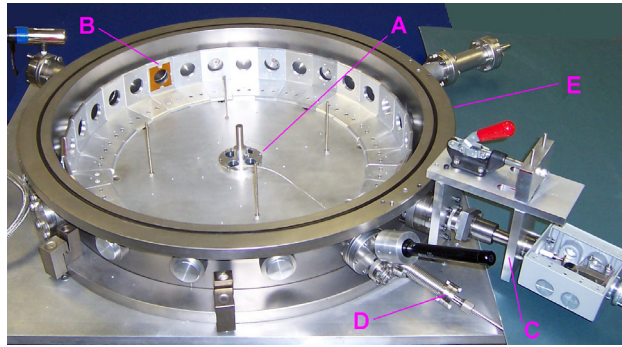
Figure 7 (a) Interior view of the USU charge storage chamber showing the (A) sample carousel, (B) sample holders, (C) charge probe assembly, (D) sample cover manipulator, and (E) electron gun port. (b) Detail of vacuum rotary feedthrough that allows the sample on the carousel to be moved in front of the electron gun, TreK^{TM} probe, *etc*.

Each sample can be positioned in front of a single field probe using a rotary feedthrough to facilitate the very large number of precise field measurements required in the long-term studies. Rotation is accomplished with a standard vacuum rotary feedthough mounted below the carousel, shown in the Figure 7(b). The rotary shaft flange is attached to the center of the sample carousel base plate; this couples the base plate to the rotary feedthough shaft. The angular position of the sample carousel is set by fitting a pin into one of 32 holes on a rotary motion positioning plate attached to the rotating exterior of the rotary feedthrough. The four holes visible in the rotary shaft flange [see Fig. 7(a)] provide access for coaxial electrical cables and cryogen lines from the feedthroughs below into the sample carousel enclosure. Two 20-pin electrical feedthroughs, mounted on a six-way cross, provide access for the coaxial leads to each sample electrode. A four-lead MHV electrical connector is attached to another port of the six-way cross; lead connections are made to a Faraday cup and other diagnostics on the sample carousel. A solenoid vacuum valve is connected to the six-way cross; this provides a connection from the turbo pump vacuum system to the charge storage chamber. All electrical connections are made inside the sample carousel enclosure to minimize electrical noise and to prevent extraneous sample charging. The cryogen feedthrough is also attached to the six-way cross. One sample position on the sample carousel has a flat metal sample to serve as both field probe calibrator and as the zero-set sample. Other positions will have a Faraday cup and UV sensitive photodiode to calibrate the flux of the charged particle and photon radiation, respectively (*PR 2c and 3f*).

Sample holder design

To meet *PR 2(b) and 4(a)*, the sample mount assembly and the sample carousel are designed to avoid things that will charge up and to provide electrical shielding for the probes and current sources and well as each isolated sample. Figure 8 shows details of the USU sample holder. While the basic sample mount configuration is similar to the JPL "tin can" sealed sample mount [see Figs. 4(d) and 6(b)], details differ. Access to the front surface of the thin film insulator sample is provided through a 1.25" hole in the Al sample holder. A stainless steel metal disk normally covers this opening [see Figure 8(a)], but can be rotated out of the way with a wobble stick on the sample cover manipulator [**D** in Fig. 7(a)] to expose the sample for charge deposition, sample treatments, or measurements. The back of the sample/electrode/PC sample mount assembly is enclosed in a solid Al can to provide complete electrical and light shielding [see Fig. 8(b)].

The sample mounting configuration to the Al sample holder is functionally equivalent to that used in the JPL design [see Fig. 6(c)]. A ~250 μm Kapton tape on the inner surface of the sample holder isolates it from the front surface of the sample. Each insulating sample is mounted with UHV compatible glue on its own ~50 mm diameter polycarbonate sample mount [see Fig. 8(c)]. A thin back electrode made of ~125 μm thick Cu foil, ~3.8 cm in diameter, with no guard electrode, is glued to the polycarbonate sample mount. An electrical connection to the back electrode is made via a phosphor bronze spring held in place with a Be-Cu clip and screw on the polycarbonate sample mount using UHV compatible Kapton[TM]-coated coaxial ground-shielded cable leading out the back. The sample/electrode/PC sample mount assembly is then mounted (using two Nylon screws) to one of the 32 sample holders on the sample carousel. Stainless steel set screws are inserted into the front of the two through-tapped holes to prevent the insulating surface of these nylon screws from being visible to incident electrons. A Be-Cu tension relief clamp visible on the bottom of the sample holder provides strain relief for the coaxial cable.

TreK[TM] Probe Details

The USU chamber uses the same basic concepts as the JPL chamber for the field probe. Figure 9(a) illustrates the basic components of this capacitance transfer probe assembly, including the field plate and adjacent grounded copper guard tube and TreK[TM] probe (at right), the connecting wire and associated insulation and vacuum feedthroughs (center), and. the voltage sensor plate and interface to the sample and sample electrode (at left). The capacitance transfer probe uses a voltage sensor plate that truly integrates over the sample surface to obtain some measure of the average potential of its surface. The voltage sensor plate is made of OFHC Cu with Au plating to minimize stray electric fields and charging that would be a result of oxidation of the plates [see Fig. 9(b)].

The vacuum end of the capacitance transfer probe is mounted on a UHV manipulator to allow measurements to be compatible with the USU sample carousel. A ~2.5 cm diameter voltage sensor plate is housed in a Au plated metal housing [see Fig. 9(b)]. With the sample cover disk fully opened on a sample holder, the voltage sensor plate housing will fit snuggly into the 1¼" diameter hole in the sample holder to provide reproducible positioning relative to the sample surface and tight shielding during charge measurements. Precise positioning of the voltage sensor plate ~2 mm above the sample results from alignment of a chamfer in the voltage sensor plate housing with the outer surface of the sample holder. When the housing is retracted, the sample carousel can be rotated to align another sample with the housing. The TreK[TM] probe and field plate are mounted in a probe box

(a)

(b)

(c)
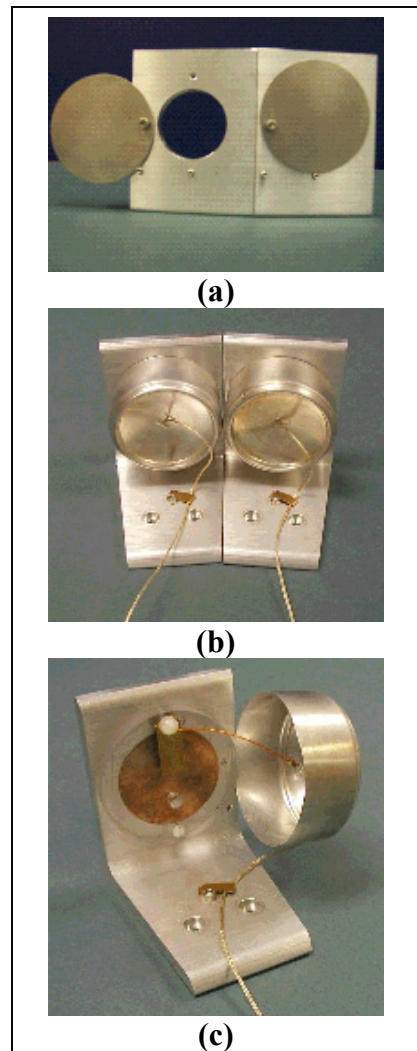
Figure 8. Photographs of the USU sample mount. (a) Front view showing one open and one closed sample mount. (b) Rear view of the sample mounts showing the sample can and the sample electrode wire. (c) Rear view of with sample can removed.

[see Fig. 9(2)], that move with the voltage sensor plate maintaining the precise 3 mm gap between the TreK[TM] probe and field plate.

Sample Treatment

A custom designed miniature W-filament low energy flood gun, described in more detail in Thomson [13,14], is a source of monochromatic low energy electrons required to meet *PR 3(c)*. To meet *PR 3(e)*, a medium energy electron flood gun will be installed for uniform, stable charge deposition at energies in the few keV regime near the second crossover energy for the insulators to be studied. The gun will be mounted on an available Conflat[TM] flange on the vacuum chamber to allow charging of one sample at a time [*PR 3(a)*]. Beam currents and beam profiles will be monitored with a standard Faraday cup mounted on the sample carousel.

To provide optical access to the samples to treat samples with UV/VIS light and to discharge samples using light [*PR 3(f)*], a standard UV-grade sapphire viewport mounted on a Conflat flange is attached to the chamber bell jar collar [see Fig. 7(a)]. Broadband W-filament and Dueterium or Hg discharge sources and IR/VIS/UV quasi-monochromatic LED external light sources can be mounted on the viewport flange as required. An additional quartz viewport is available for visual inspection of the samples. Both viewports are equipped with external covers to block light from entering the chamber, light that might result in sample charging through the photoelectric effect, except when desired.

Sample environment-vacuum system and temperature

In order to measure long charge decay time constants, one must provide continuous high vacuum testing, without exposure to even partial vacuum, with approximately one measurement per sample per day for about a month (*PR 4b*). Gas conduction activated by background radiation is a limitation for our methods. It will slowly discharge samples, or bring charge from one sample to another. The vacuum system

(a)

(b)   **(c)**
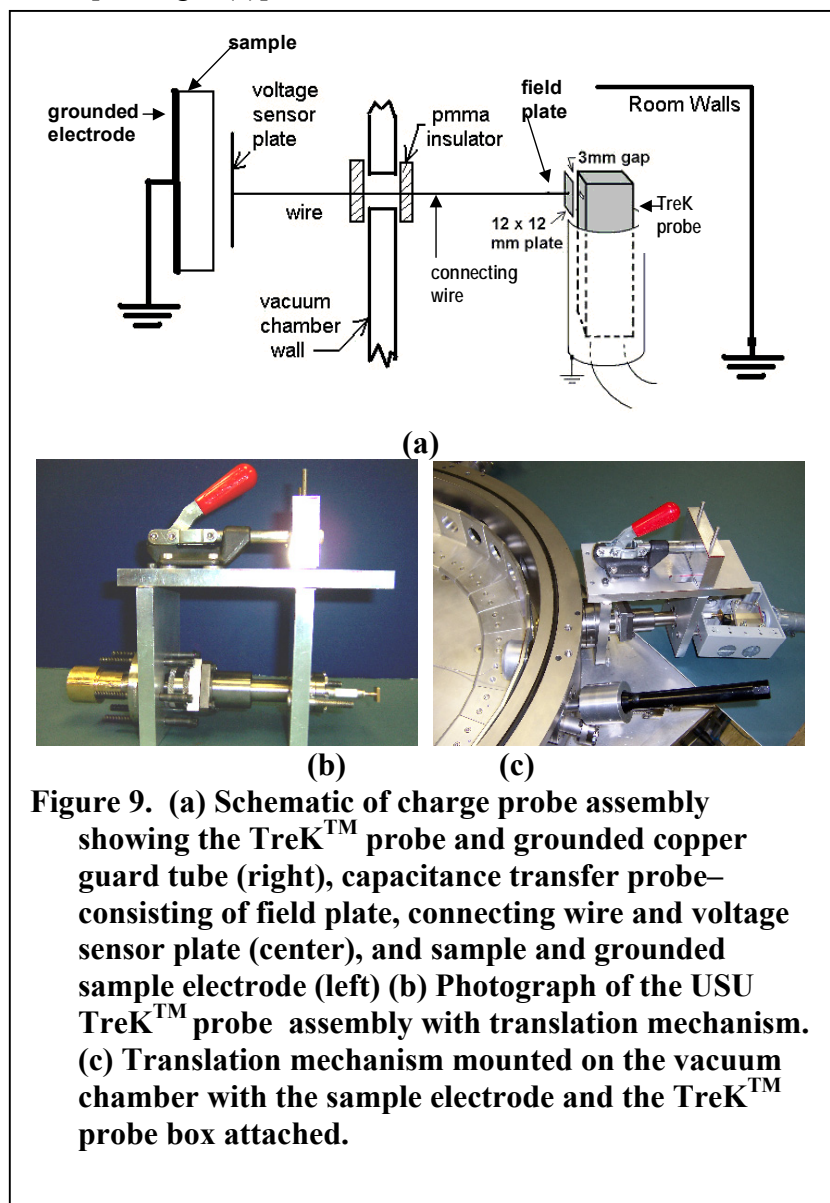
Figure 9. (a) Schematic of charge probe assembly showing the TreK[TM] probe and grounded copper guard tube (right), capacitance transfer probe–consisting of field plate, connecting wire and voltage sensor plate (center), and sample and grounded sample electrode (left) (b) Photograph of the USU TreK[TM] probe assembly with translation mechanism. (c) Translation mechanism mounted on the vacuum chamber with the sample electrode and the TreK[TM] probe box attached.

must therefore work steadily at an operating pressure of ~10^{-7} Torr. Figure 10 gives the details of the vacuum system used at USU. The vacuum chamber uses a 55 liter/sec turbomolecular pump backed by a ~150 liter/s, two-stage, direct-drive, rotary-vane mechanical vacuum pump with a bakeable molecular sieve trap to minimize contamination due to backstreaming. Pressure is measured by a low-pressure nude UHV ion gauge (10^{-5} to 10^{-10} Torr), an intermediate pressure Convectron gauge (10^{-4} to 10^{+3} Torr), and a high pressure Si strain gauge transducer (10^{0} to 10^{+6} Torr). Relative humidity is monitored over a 0% to 100% range with a 2% accuracy using a standard gauge.

The experiment environment requires temperature control of the samples over the lifetime of the experiments, on the order of a month (*PR 4c*). Typical experiments to compare temperature dependence with theory for polymer insulator resistivity require ~±50 °C about room temperature [2]. Temperature control of the entire sample carousel is provided by two heat reservoirs attached to the carousel base plate. The unit is designed to control the temperature of the samples and entire sample carousel to ~±5 °C using a standard PID temperature controller and platinum resistance thermometers. Thermal isolation of the sample carousel from the rest of the chamber results from the weak thermal link across the lazy Susan bearing. The heat reservoirs can be filled with cooled or heated water from a closed loop system in contact with an external temperature bath, or with liquid nitrogen or other cryogens; they can also be heated with resistance heaters. Alternately, the heat reservoirs can act as thermal reservoirs to dissipate excess heat, via a heat transfer fluid, from four 70 W thermoelectric Peltier cooling units. The Peltier coolers, situated below the heat reservoirs in thermal contact with the carousel base plate, are designed to control the sample to ±100 °C.

Computer interface

To meet *PR 4(a)* to maintain vacuum and instrument functions for the life of the experiments (on the order of one month), a PC computer has been assembled with extensive hardware and software interface capabilities.

Figure 11. Assembly of the charge storage chamber vacuum system

A—Turbo pump controller
B— Nude UHV ion gauge
C— Automatic solenoid valve
D— Gas handling system valve
E— Solenoid valve
F— Bakeable molecular sieve trap
G— Exhaust oil mist filter
H—Vacuum gauge controller
I— ~150 litre/s mech. vacuum pump
J— High pressure Si strain gauge transducer
K— Turbo molecular pump
L— Convectron gauge

Instrumentation control is implemented using Labview^{TM} to automate the data collection and sample manipulation, to facilitate rapid surface charge measurements thereby minimizing the likelihood of disturbing charge on the samples. Analog inputs on the standard data acquisition card (DAC) are used to monitor various voltage signals including: output from the high voltage supply; temperature controller signals; beam voltage, filament current, and extractor voltage from the electron flood gun power supply and medium energy electron gun controller; and the electrostatic field strength from the TreK^{TM} probe controller. Digital outputs from the DAC card are used to enable the output of the low voltage and high voltage power supplies, to trigger a
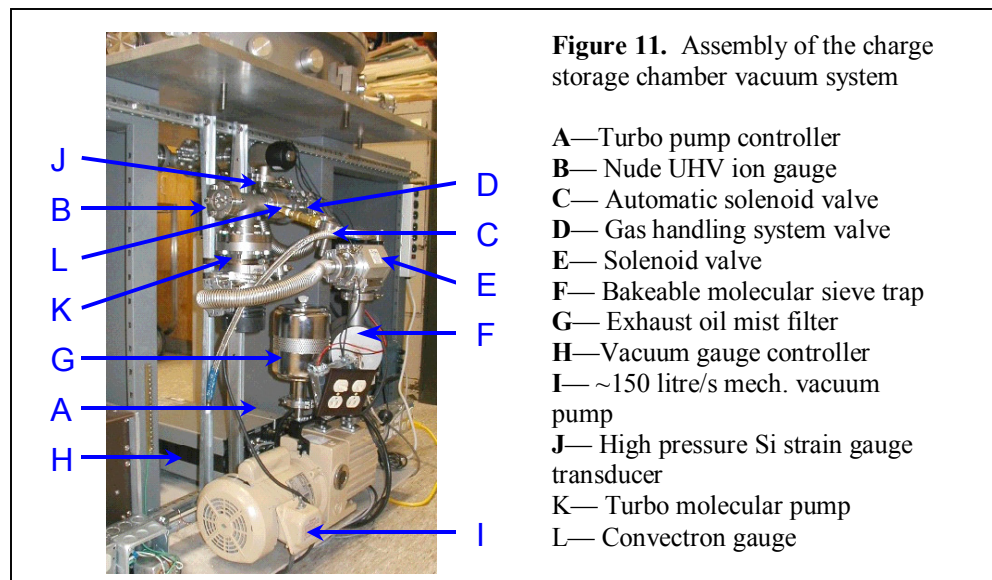
reading of the TreK^{TM} probe controller, and to provide beam blanking signals to the electron gun controllers. In addition, a GPIB interface card and USB ports are used to control instruments including power supplies, multimeters, and electrometers.
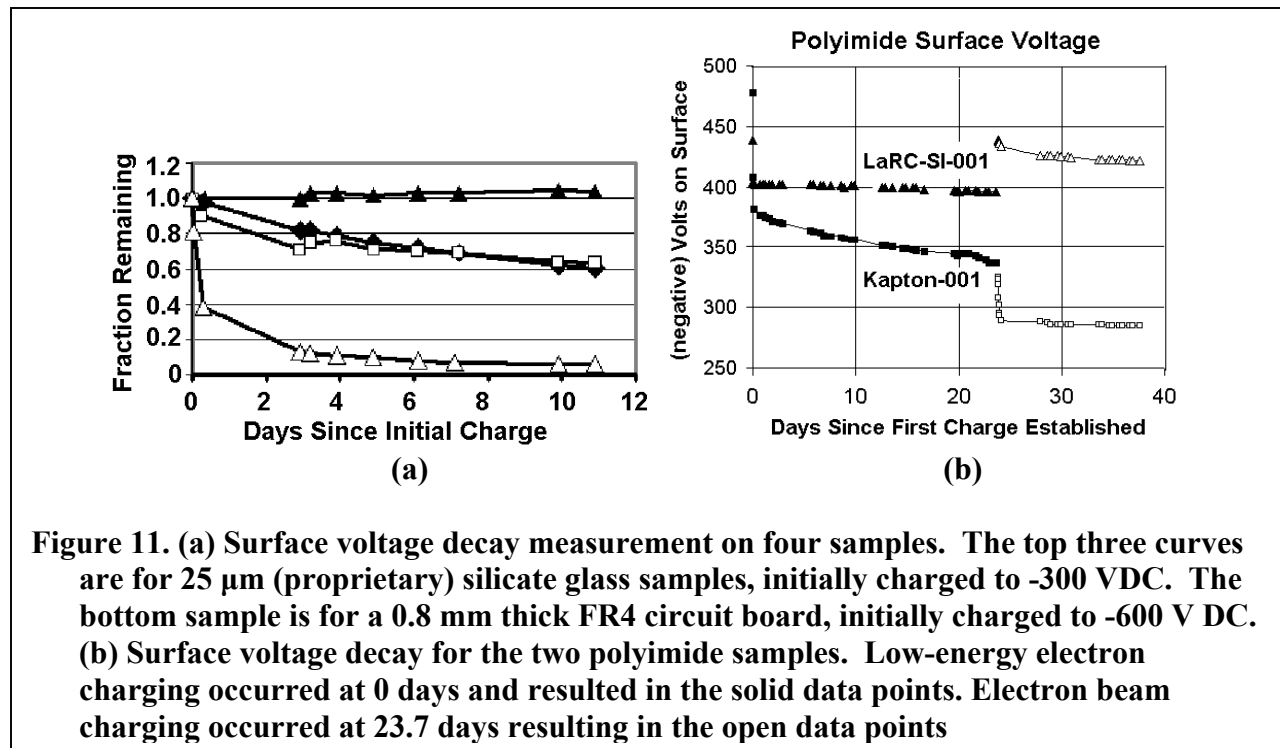
Figure 11. (a) Surface voltage decay measurement on four samples. The top three curves are for 25 μm (proprietary) silicate glass samples, initially charged to -300 VDC. The bottom sample is for a 0.8 mm thick FR4 circuit board, initially charged to -600 V DC. (b) Surface voltage decay for the two polyimide samples. Low-energy electron charging occurred at 0 days and resulted in the solid data points. Electron beam charging occurred at 23.7 days resulting in the open data points

A serial port-interfaced vacuum gauge controller is used monitor and control all vacuum gauges and vacuum processes for the charge storage chamber, the capacitance resistance apparatus, the gas handling system, and the turbo pumped vacuum system. The vacuum gauge controller reads signals from two UHV nude ion gauges, two low vacuum Convectron gauges, a low vacuum thermocouple gauge, an intermediate pressure capacitance manometer, a high pressure Si strain gauge, and a relative humidity gauge. The vacuum gauge controller also monitors digital input from the turbo pump controller and sentry valve and uses internal relays to open and close the Varian solenoid-controlled valve, the turbo vent valve, and small solenoid valves to the capacitance resistance apparatus and the gas handling system. The correct order of valve operation and pump restart in the event of a power failure or vacuum interrupt is controlled by the vacuum controller. Power to the vacuum controller, computer, valves and turbo pump controller are provided by an uninterruptible power supply in the event of power failure or surges.

Results of charge storage method

Figures 11(a) [1] and 11(b) [2] show charge storage decay curves for six different materials. In each case, the resistivity is two to four orders of magnitude larger than that obtained with classical methods. For example, the charge storage value of resistivity for aluminum-backed 51 μm Kapton H samples [11] was >5·10^{+19} Ω·cm [see Fig. 11(b)], compared to a value of ~(3±1) ·10^{+16} Ω·cm measured with classical methods (see Fig. 3).

Acknowledgments

References

1. A.R. Frederickson, C. E. Benson and J. F. Bockman, "Measurement of Charge Storage and Leakage in Polyimides," Nuclear Instruments and Methods in Physics Research B, 454-60, 2003.

2. A.R. Frederickson and J. R. Dennison, "Measurement of Conductivity and Charge Storage in Insulators Related to Spacecraft Charging," accepted for publication in IEEE Trans. Nuc. Sci., Dec. 2003.

3. J.R. Dennison, C.D. Thomson, J. Kite, V. Zavyalov, Jodie Corbridge, "Materials Characterization At Utah State University: Facilities And Knowledgebase Of Electronic Properties Of Materials Applicable To Spacecraft Charging," Proceedings of the 8th Spacecraft Charging Technology Conference, October 20-24, 2003, Huntsville, Alabama.

4. A.Robb Frederickson and Donald H. Brautigam, "Mining CRRES IDM Pulse Data and CRRES Environmental Data to Improve Spacecraft Charging/Discharging Models and Guidelines," Final Report: NASA SEE Program Contract No. NAS7-1407, Task Order 10676, 2003; to be published.

5. W. Tillar Shugg, Handbook of Electrical and Electronic Insulating Materials, 2nd Ed; The Guide to Plastics by the Editors of Modern Plastics Encyclopedia, McGraw Hill, Inc., N.Y., 1970.

6. ASTM D 257-99, "Standard Test Methods for DC Resistance or Conductance of Insulating Materials" (American Society for Testing and   Materials, 100 Barr Harbor drive, West Conshohocken, PA 19428, 1999).

7. IEC 93, International Electrotechnical Commission Publication 93, Methods of Test for Volume Resistivity and Surface Resistivity of Solid Electrical Insulating Materials, Second Edition, 1980.

8. J.R.Dennison and A.R.Frederickson,   "Electronic properties of materials with application to spacecraft charging", NASA Space Environments and Effects (SEE) Program Grant NAS8- 02031,.2002-2004.

9. J. M. Bodeau, private communications, 2003.

10. J.R. Dennison, A. R. Frederickson, Prasanna Swaminathan, "Charge Storage, Conductivity And Charge Profiles Of Insulators As Related To Spacecraft Charging," Proceedings of the 8th Spacecraft Charging Technology Conference, October 20-24, 2003, Huntsville, Alabama.

11. Kapton polyimide film product information: Physical Properties, Report H-38492-1, (Dupont, Wilmington, DE, February, 1997); http://www.dupontteijinfilms.com/ , June 20, 2002; The Red Book, RB 1, (Sheldahl Technical Materials, Northfield MN, 1995); http://www.sheldahl.com/Product/TechMaterials.htm , June 20, 2002.

12. Operators Manual, Model 341A, High Voltage Electrostatic Voltmeter, Trek, Inc., 11601 Maple Ridge Road, Medina, New York 14103, USA. Telephone: 1 (800) 367-8735 or 1 (585) 798-3140, http://www.trekinc.com/ .

13. C.D. Thomson, Measurements of the Secondary Electron Emission Properties of Insulators, Ph.D. dissertation, Utah State University, 2004.

14. C.D. Thomson, V. Zavyalov, J.R. Dennison, Jodie Corbridge, "Electron Emission Properties Of Insulator Materials Pertinent To The International Space Station," Proceedings of the 8th Spacecraft Charging Technology Conference, October 20-24, 2003, Huntsville, Alabama.

15. J.R. Dennison, W.Y. Chang, N. Nickles, J. Kite, C.D. Thomson, Jodie Corbridge, and Carl Ellsworth, "Final Report Part III: Materials Reports," NASA Space Environments and Effects Program Grant, "Electronic Properties of Materials with Application to Spacecraft Charging," September 2002; Available in electronic format through NASA SEE as part of the SEE Charge Collector Knowledgebase.

PARTICLE-IN-CELL SIMULATIONS ON ANTENNA CHARACTERISTICS IN MAGNETIZED PLASMA

Hideyuki Usui
Radio Science Center for Space and Atmosphere, Kyoto University
Gokasho Uji, Kyoto 611-0011, Japan
Phone: +81-774-38-3817
Fax: +81-774-38-3817
E-mail: usui@kurasc.kyoto-u.ac.jp

N. Nakamura
H. Kojima
H. Matsumoto
Y. Omura
Radio Science Center for Space and Atmosphere, Kyoto University

Abstract

We for the first time applied electromagnetic PIC (Particle-In-Cell) computer simulations to analyze the antenna characteristics in magnetized plasma. In a three-dimensional simulation space, we placed a dipole antenna which is a conducting current line in a magnetized plasma. By providing a Gaussian pulse as an input power to the center of the antenna and observing the current induced at the power feeding point, we obtain the input impedance of the antenna as a function of frequency. We particularly examined the electron kinetic effects on the antenna impedance such as electron temperature and electron evacuated region (ion sheath) formed around the antenna. It is confirmed that the most obvious resonance point is the local Upper Hybrid Resonance frequency. As the electron temperature increases, the resonance frequency also increases in accordance with the modification of dispersion relation for the UHR branch. We also examined the antenna impedance variation by changing the size of the electron evacuated region or ion sheath created around the antenna. We could confirm that the antenna resonance near the local UHR frequency is sharp for the small sheath while the profiles of the impedance approach to those of vacuum case as the sheath becomes large. The resonance frequency also decreases because the plasma density also decreases in the vicinity of the antenna.

Introduction

Antenna characteristics in plasma have been investigated by many scientists (e. g. Balmain, 1964, Adachi et al., 1977, Sawaya et al., 1976). However, the analysis of the antenna characteristics such input impedance is very complex because plasma is dispersive and anisotropic medium. In the previous theories with an assumption of cold plasma, approximations in the current distribution along the antenna or the sheath structure around the antenna were hired. Antenna analysis with warm plasma approximation was also done for some limited models (e.g. Kuehl, 1966). Meanwhile, recent progress of computer facilities enables us to analyze the antenna properties in vacuum with the FDTD (Finite Difference Time Domain) method which solves the Maxwell equations with spatial and temporal grid points. By using the FDTD method with a dielectric tensor obtained under the cold plasma approximation, we can basically analyze the antenna impedance in plasmas. However, in order to include the plasma kinetic effects in the antenna impedance such as electron

temperature and sheath around the antenna, we need to treat the plasma as particles in the simulations. To treat the plasma dynamics, we apply the PIC (Particle-In-Cell) method to the conventional FDTD field solving simulations. In the PIC method, we solve the equation of motion for each particle with the field components obtained at grid points with the FDTD method. To obtain the plasma density and current at each grid point, we use the area sharing method. In the present paper, we will report preliminary results of the antenna impedance obtained in the PIC simulations. We particularly focus on the dependence of antenna resonance on the electron temperature and sheath size around the antenna.

Simulation Model

In the current simulation studies, we use a three-dimensional full electromagnetic particle code called KEMPO (Matsumoto and Omura, 1985). In KEMPO, we solve Maxwell's equations and equations of motion of electrons and ions. To advance the electromagnetic field with Maxwell's equations in the simulation space, we adopted the FDTD (Finite-Difference Time-Domain) method. Plasma dynamics and the associated plasma current are solved by adopting the PIC (Particle-In-Cell) method (Birdsall and Langdon, 1985).

Three-dimensional simulation model is shown in Figure 1. In the simulation space with $64 \times 64 \times 64$ grid points a number of electrons is uniformly distributed. In the center, a dipole antenna with the length of 32 grid points is set. We assume that the antenna is a pure conductor, which implies that the electric field inside the antenna is assumed to be zero. To feed the power to the antenna, we adopted the delta gap feeding method. At one grid point located in the middle of the antenna, we provide voltage as a function of time. To obtain the wide-band characteristics of frequency with one simulation run, we utilize a Gaussian-type pulse for the voltage at the feed point. The induced current is obtained with the rotational field around the feed point. The antenna impedance is calculated as the ratio of the voltage to
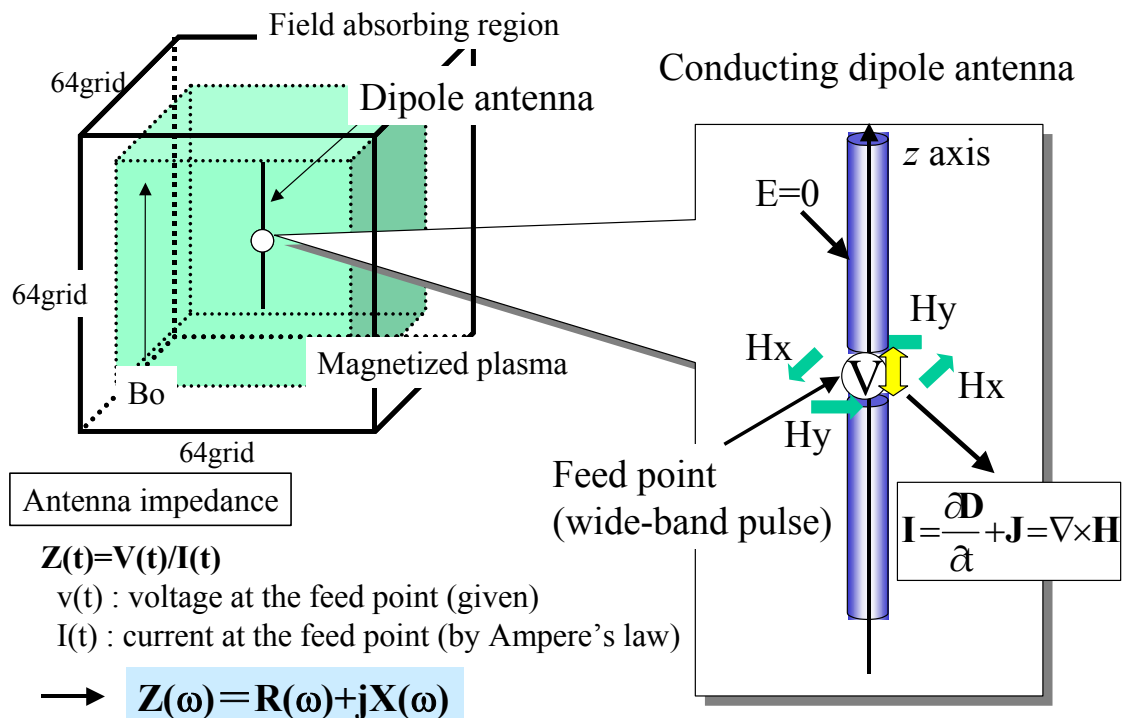
Figure 1. Simulation model

the current. By taking its Fourier transformation, we obtain the antenna impedance in frequency domain.

Dependence of Antenna Impedance on Plasma Temperature

Figure 2 shows the antenna impedance obtained in the simulations with different plasma temperature. The upper and lower panels indicate the real and imaginary parts of the impedance, respectively. The dashed lines correspond to the impedance for the vacuum case. As clearly shown, there is a large change of impedance at the Upper-Hybrid Resonance frequency ω_{UHR}. The real part of the impedance takes large values at peaks in comparison with the vacuum case, which implies that the minimum power is radiated in plasma from the antenna at ω_{UHR}. The interesting feature we should mention is that the peaks found in the real part of the impedance shift toward higher frequency as the plasma temperature increases. This tendency is not observed when no external magnetic field is included in the simulation model. Therefore, we speculate that specific plasma wave mode is closely related to the shift of the impedance resonance.

Figure 3 shows the dispersion curves of the slow-X mode with different temperature. At the wavenumber corresponding to the wave length which resonates with the present antenna, we can find the resonance frequency for each wave branch. As easily found, the resonance frequency on the slow-X mode also increases as the plasma temperature becomes high. This can explain the shift of the resonance frequency as shown in Figure 2.
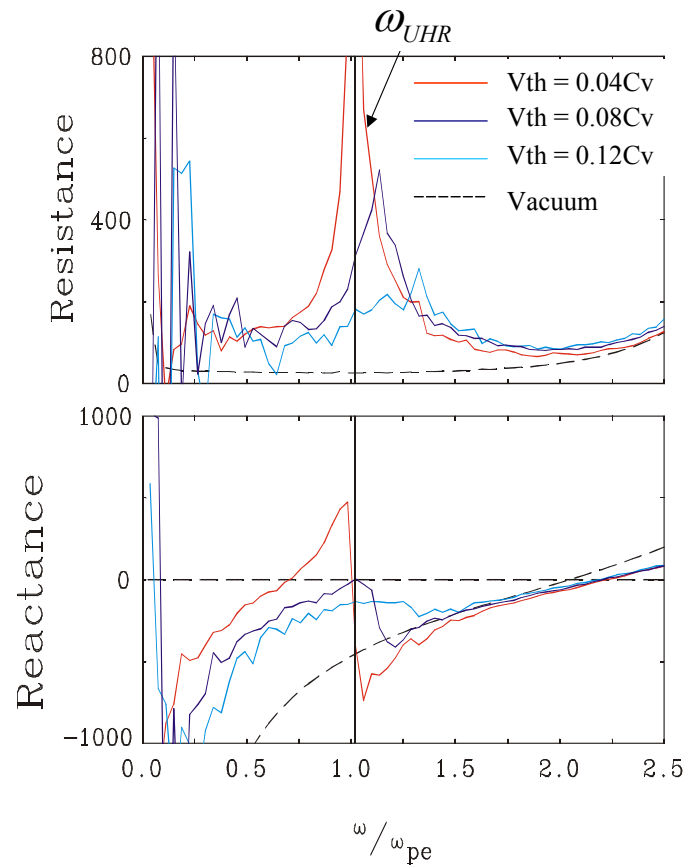
Figure 2. Antenna impedance with different plasma temperature.
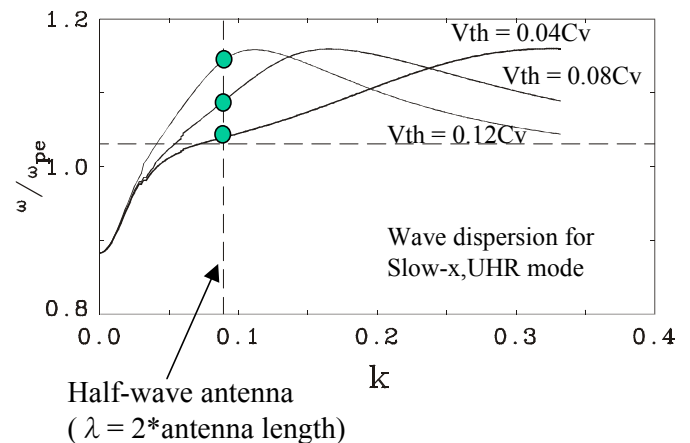
Figure 3. Slow-x mode with different temperature and the corresponding resonance frequencies.

Sheath Effect on the Antenna Impedance

Figure 4 shows the dependence of the antenna impedance at frequency around ω_{UHR} on the sheath size created around the antenna. The right panels depict the profiles of the sheath around the antenna. By changing the simulation parameters, we varied the size of the region where electrons are evacuated around the antenna. We regard the electron evacuated region as sheath. At each case, we examined the antenna impedance as shown in the left panels. It is obviously shown that the resonance at ω_{UHR} is sharp for the small sheath while the profiles of the impedance approach to those of vacuum case as the sheath becomes large. It is because the vacuum region around the antenna expands for the larger sheath. The resonance frequency also decreases because the plasma density also decreases in the vicinity of the antenna. It is theoretically examined that the impedance will be affected by the sheath resonance, which we could not confirm in the present simulations. It is also reported that sheath waves which propagate along the antenna surface may affect the antenna impedance. Currently we have been working on the properties of the sheath waves. We will examine the effect of the sheath waves on the antenna impedance with the larger scale of simulation model, which is left as a future work.
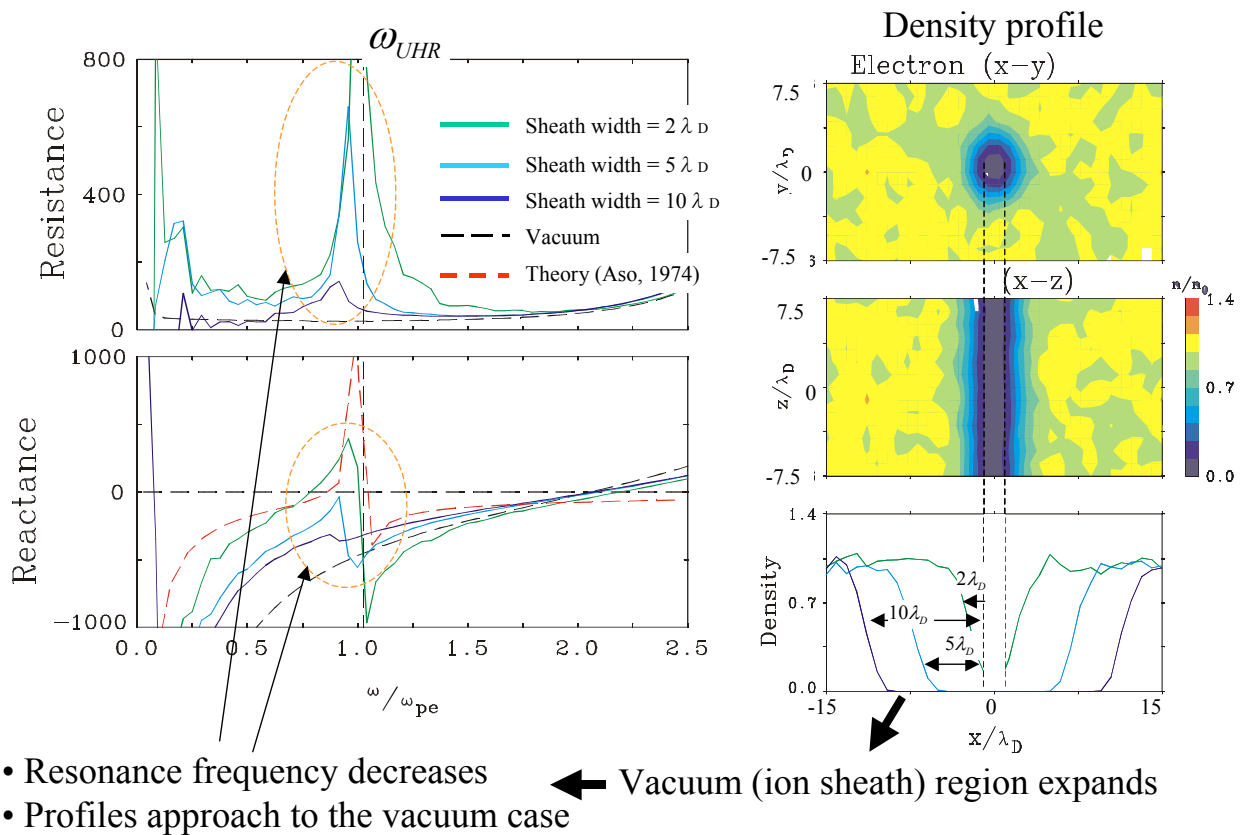
Figure 4.   Sheath profiles (right panels) and corresponding antenna impedance (left panels).

Conclusions

We for the first time applied three-dimensional electromagnetic PIC computer simulations to study the antenna impedance characteristics. We particularly focused on the electron kinetic effects on the antenna impedance such as electron temperature and electron evacuated region (ion sheath) formed around the antenna. We confirmed that a dipole antenna immersed in magnetized plasma has a resonance at the local Upper Hybrid Resonance frequency. As the electron temperature increases, the resonance frequency also increases in accordance with the modification of dispersion relation of the UHR branch. We also examined the antenna impedance variation by changing the size of sheath where electrons are evacuated around the antenna. We could confirm that the resonance at ω_{UHR} is sharp for the small sheath while the profiles of the impedance approach to those of vacuum case as the sheath becomes large. The resonance frequency also decreases because the plasma density also decreases in the vicinity of the antenna. Although the simulations performed in the current study are preliminary and the simulation results are rather conventional, it should be noted that antenna analysis by performing electromagnetic PIC simulations basically works and we will be able to apply this method to examine the antenna characteristics in various plasma situations such as the existence of photo-electrons, which is left as a future work.

Acknowledgments

References

1. Adachi, S., T. Ishizone, and Y. Mushiake, Transmission line theory of antenna impedance in a magnetoplasma, Radio. Science, 12-1, 23-31, 1977.

2. Balmain, K. G.,The Imedance of a Short Dipole Antenna, IEEE. Trans. Antennas Propag., AP-12, 605, 1964.

3. Birdsall, C.K. and A.B. Langdon, Plasma Physics via Computer Simulation, McGraw-Hill Inc., New-York, 1985.

4. Kuehl, H. H., Resistance of a Short Antenna in a Warm Plasma, Radio Science, 1-8, 971-976, 1966.

5. Matsumoto, H. and Y. Omura, Particle simulation of electromagnetic waves and its application to space plasmas, Computer simulation of space plasma, ed. By H. Matsumoto and T. Sato, Terra Sci. Pub., 43, 1985.

6. Sawaya, K., H. Mizuno, T. Isizone, and Y. Mushiake, Characteristics of a Linear Antenna in a Uniaxially Anisotropic Plasma, Trans. Inst. Electron. Commun. Eng. Jpn., 59, 254, 1976.

AN EDUCATIONAL MULTIMEDIA PRESENTATION ON THE INTRODUCTION TO SPACECRAFT CHARGING

E. Lin
DPL Science Inc.
2388 Tally Ho
St. Lazare, Quebec, Canada J7T 2B1
Phone: (450)458-0852
Fax: (450)458-2151
E-mail: info@dplscience.com

M. de Payrebrune
DPL Science Inc.

Background

Over the last few decades, significant knowledge has been gained in how to protect spacecraft from charging; however, the continuing technical advancement in the design and build of satellites requires on-going effort in the study of spacecraft charging.

A situation that we have encountered is that not all satellite designers and builders are familiar with the problem of spacecraft charging. The design of a satellite involves many talented people with diverse backgrounds, ranging from manufacturing and assembly to engineering and program management. The complex design and build of a satellite system requires people with highly specialized skills such that cross-specialization is often not achievable. As a result, designers and builders of satellites are not usually familiar with the problems outside their specialization. This is also true for spacecraft charging. Not everyone is familiar with the definition of spacecraft charging and the damage that spacecraft charging can cause. Understanding the problem is an important first step in getting everyone involved in addressing the appropriate spacecraft charging issues during the satellite design and build phases.

To address this important first step, an educational multimedia presentation has been created to inform the general engineering community about the basics of spacecraft charging. The content of this educational presentation is based on relevant published technical papers. The presentation was developed using Macromedia Flash. This software produces a more dynamic learning environment than a typical 'slide show', resulting in a more effective learning experience. The end result is that the viewer will have learned about the basics of spacecraft charging.

This presentation is available to the public through our website, *www.dplscience.com*, free of charge. Viewers are encouraged to pass this presentation to colleagues within their own work environment.

This paper describes the content of the multimedia presentation.

Description of the Presentation

Macromedia Flash was selected as the software tool for this presentation due to its powerful animation capability and its ability to support different media (CD, DVD, Video and Internet). The software allowed us to create the presentation as a stand-alone unit by combining text, pictures, video and audio tracks. We were able to successfully illustrate key points by maximizing the visual content and synchronizing the visual images with the audio track, resulting in an effective learning experience.

The information presented was gathered from various technical sources. A listing of these sources is provided at the end of this paper and includes the Canadian Space Agency, the European Space Agency, and NASA. Technical reviewers included Mr. Richard Adamo (SRI International), Dr. Keith Balmain (University of Toronto), and Mr. Jody Minor (NASA SEE Program). We are grateful for their comments.

The presentation is divided into six major sections. Figure 1 is a snapshot taken from the presentation, identifying the six sections.

Figure 1. The six major sections of the presentation.

Section 1: The sun and spacecraft charging

The presentation begins with a description of the sun and its role in spacecraft charging. We introduce the concepts of sunspot cycle, flares and eruptions, coronal mass ejection, solar wind and high-energy particles. Figure 2 is a snapshot taken from this section, comparing the size of the earth to that of a typical solar flare. The objective of this section is to explain to the viewer that the sun is the main contributing factor to the existence of high-energy particles and that the

presence of these high-energy particles is one of two primary reasons why spacecraft charging occurs.

Figure 2. A snapshot from Section 1 of the presentation, showing the size of a typical solar flare compared to the earth. (Photo credit NASA)

Section 2: Scope of the Problem

The second section focuses on the scope of the spacecraft charging problem. By 'scope of the problem', we aim to define the causes of spacecraft charging and hence explain why charging occurs. Spacecraft charging can exist because of the following situations:

- high-energy particles found in the natural space environment plus the existence of ungrounded metal, or

- high-energy particles found in the natural space environment plus the use of dielectric material.

The three components (high-energy particles, ungrounded metal and dielectric material) are then discussed.

The discussion on high-energy particles was presented in Section 1 so that only a brief summary is made here.

The discussion on ungrounded metal essentially advises the viewer that floating metal should be avoided. We emphasize that discharges from a floating metal can be more powerful than a

discharge from a dielectric because more electrons are involved in the discharging process, due to the high mobility of electrons in a conductor.

The discussion on dielectric material is the heart of this section. We explain that dielectric materials are abundantly used in spacecraft design and that their use cannot be avoided. The viewer learns that the unavoidable use of dielectric materials in spacecraft design is the other primary reason why spacecraft charging exists. Since it is necessary to use these materials, we need to understand their properties and behaviour. We introduce the concepts of resistivity and dielectric strength. Figure 3 is a snapshot taken from this section, illustrating the concepts of resistivity and dielectric strength. We explain that the continuing technical advancement in the design and build of satellites means that we cannot take previously used materials for granted. This includes commonly used materials such as Second Surface Mirrors, Sunshields and Thermal Blankets. We emphasize that the constant evolution in spacecraft design and technology implies that spacecraft designers must always be mindful about what dielectric materials are being used and where.

Figure 3. A snapshot from Section 2 of the presentation, illustrating the concepts of resistivity and dielectric strength.

Discharge effects are described briefly and include physical damage to the material and electromagnetic effects.

The section ends with a positive note: reference is made to the role of the Spacecraft Charging Specialist and how this technical authority can help in the mitigation and prevention of spacecraft charging and its effects.

Section 3: The Two Types of Charging

The third section describes the two types of charging: surface charging and internal charging. The objective is to differentiate the two and to explore ways in which the charging can be minimized.

We begin with the definition of surface charging and proceed to the design techniques to prevent surface charging. A simplified summary of some of the design guidelines found in NASA Technical Paper 2361 (Ref [11]) is presented to the viewer.

Next, we present the definition of internal charging and the design techniques to prevent internal charging. Figure 4 is a snapshot taken from this section, illustrating the meaning of internal charging. A simplified summary of the design guidelines found in NASA Handbook 4002 (Ref [9]) is presented to the viewer.

Figure 4. A snapshot from Section 3 of the presentation, illustrating the meaning of internal charging.

Since the selection of dielectric material will not always conform to the guidelines, we also look at the use of tests and analyses as methods of validating the choice of a dielectric material. Spacecraft charging tests and analyses are rarely straightforward and we identify some of the difficulties that are frequently encountered: lack of proper information on dielectric material properties (resistivity values over temperature, dielectric strength values), inaccuracies in the characterization of the space environment, limitations of a test set-up, uncertainty in the sensitivity of the victim circuit, etc.

Section 4: Test Facilities

The fourth section includes photographs of two spacecraft charging test facilities: SRI International in Palo Alto, California and the University of Toronto in Canada. The authors had the opportunity to work with Mr. Adamo and Dr. Balmain in past projects and were pleased to be able to include descriptions of their facilities in this presentation. Figure 5 is a snapshot taken from this section, showing Dr. Balmain's internal charging test set-up at the University of Toronto. This section gives the viewer a look at the practical aspects of spacecraft charging work, complementing the previous theoretical sections.

Figure 5. A snapshot from Section 4 of the presentation, with a look at Dr. Balmain's internal charging test set-up.

Section 5: Publications

The fifth section directs the viewer to some excellent publications available for further study. Figure 6 is a snapshot taken from this section, showing some of the suggested publications. We wished to emphasize to the viewer that this presentation is only a general introduction to the topic of spacecraft charging and that there are many articles and documents available for further reading.

Figure 6. A snapshot from Section 5 of the presentation, with a look at some of the suggested publications.

Section 6: Conclusions

The conclusion re-iterates the need for some of the on-going work in the field of spacecraft charging, namely: studies on the changing space environment and the characterization of dielectric material properties. Figure 7 is a snapshot taken from this section, reviewing the need to have more information on dielectric material properties. We wished to make this emphasis since the definition of the space environment and the identification of dielectric material properties have immediate impact on the ability to accurately assess spacecraft charging effects for any satellite program.

Figure 7. A snapshot from Section 6 of the presentation, emphasizing once again the need to have more information on dielectric material properties.

When played from start to end, the entire presentation will last approximately fifty (50) minutes. The viewer can pause the presentation at any time then resume playing when desired. Re-plays are also possible by using the 'play back' button. The viewer can also directly access a specific part of the presentation by using the Table of Contents feature. Figure 8 is a snapshot of the Table of Contents taken from the presentation.

Figure 8: The 'Table of Contents' in the presentation.

Conclusion

An educational multimedia presentation has been created to inform the general engineering community about the basics of spacecraft charging. The presentation is a general introduction to the topic and is intended for spacecraft designers, builders and project managers of all disciplines within the satellite industry. Topics covered in the presentation include the Sun and its role in spacecraft charging, the use of dielectric materials in spacecraft design, surface charging, internal charging, basic design guidelines to minimize charging, and spacecraft charging test facilities.

The presentation may be downloaded from our website *www.dplscience.com*, free of charge. We would appreciate feedback from the engineering community as to the effectiveness of this presentation as an educational tool.

Acknowledgements

We would like to thank the following organizations and individuals for their valuable support and assistance:

Canadian Space Agency   Mr. Richard Adamo
ESA   Dr. Keith Balmain
NASA   Mr. Larry Harding
SRI International   Mr. Jody Minor
University of Toronto

References

Technical information for the presentation was obtained from the following sources:

1.   Balmain K.G., "Surface Discharge Effects", American Institute of Aeronautics and Astronautics 1979.

2.   Czepiela S.A., Hastings D., McManus H., "Charging of Composites in the Space Environment", American Institute of Aeronautics and Astronautics 1997.

3.   Fennell J.F., Koons H.C., Roeden J.L., Blake J.B., "Spacecraft Charging: Observations and Relationship to Satellite Anomalies", The Aerospace Corporation, Los Angeles, CA 90009, USA.

4.   Garrett H.B., "The Charging of Spacecraft Surfaces", Reviews of Geophysics and Space Physics, Vol. 19, No. 4, Pages 577-616, November 1981.

5.   Herr J.L., McCollum M.B., "Spacecraft Environments Interactions: Protecting Against the Effects of Spacecraft Charging", NASA Reference Publication 1354, November 1994.

6.   Inouye G.T., Sanders N.L., Komatsu, G.K., Valles J.R., Sellen Jr. J.M., "Thermal Blanket Metallic Film Grounstrap and Second Surface Mirror Vulnerability to Arc Discharges", Spacecraft Charging Technology 1978.

7.   Joselyn J.A., Whipple E.C., "Effects of the Space Environment on Space Science", American Scientist, Volume 78.

8.   Leach R.D., "Failures and Anomalies Attributed to Spacecraft Charging", NASA Reference Publication 1375, August 1995.

9.   Mulville D.R., "Avoiding Problems Caused by Spacecraft On-Orbit Internal Charging Effects", NASA-HDBK-4002, February 1999.

10.   Nanevicz J.E., Adamo R.C., "Occurrence of Arcing and its Effects on Space Systems", American Institute of Aeronautics and Astronautics, 1980.

11.   Purvis C.K., Garrett H.B., Whittlesey A.C., Stevens N.J., "Design Guidelines for Assessing and Controlling Spacecraft Charging Effects", NASA Technical Paper 2361, 1984.

12.   "Environment Spatial Prevention des Risques Lies aux Phenomenes de Charge", CNES, Cepadues-Editions, 1996.

13.   "Proceedings of the 7th Spacecraft Charging Technology Conference, ESA Publication Number SP-476, November 2001.

14.   "Surface Charging / ESD Analysis", NASA Preferred Reliability Practices PD-AP-1301.

15.   "Thick Dielectric Charging / Internal Electrostatic Discharge", NASA Preferred Reliability Practices PD-AP-1316.

16.   www.spacedaily.com/news/eo-01r.htmp

17.   www.estec.esa.nl/conferences/98c05

CURRENT COLLECTION BY A SEGMENTED LANGMUIR PROBE IN THE IONOSPHERIC PLASMA

E. Séran
CETP, 4 Avenue de Neptune
94100 Saint-Maur, France

J.-J. Berthelier
CETP, France

J.-P. Lebreton
ESA/ESTEC, The Netherlands

Abstract

The segmented Langmuir probe (SLP) has been recently proposed by one of the authors (Lebreton, 2002) as an instrument for the newly prepared ionospheric mission DEMETER to determine the plasma bulk velocity in addition to the electron density and the temperature that are routinely deduced from the Langmuir probe data. The basic idea of the SLP concept is to measure the current distribution on the probe surface by means of the individual segments and then to use the current anisotropy to estimate the amplitude and the direction of the plasma bulk speed in the probe frame. With the aim to evaluate the performances of such a probe we have developed a numerical particle in cell (PIC) model which provides a tool to calculate the current collection by spherical probe and its segments. This model is based on the simultaneous determination of the charge densities in the near-probe sheath and on the surface of the probe which are then used to compute the potential distribution in the sheath region. This scheme is well adapted to the SLP problem and has an advantage with respect to other classical probe models, i.e. it provides a natural control of the charge neutrality inside of simulation box. Comparison of the results of our model with the exact solution given by Laframboise for the spherical probe in thermal non-flowing plasma demonstrates an excellent agreement. Here we present the results for the bulk thermal plasma in the case when Debye length and sphere radius have approximately the same values, i.e. few cm. These conditions are expected to be observed in the ionosphere at the altitude of ~700 km and therefore our model may be directly applied for the interpretation of the current measurements on the board the DEMETER satellite.

Introduction

Since the advent of the space era, the Langmuir probe is proven to be very efficient tool to study space plasmas by measuring two fundamental parameters, i.e. the electron density and the temperature, which are the key parameters that control the production and dynamics of the ionised environments of the Earth and planets. This instrument is one of the most used in the space missions because of its relative simplicity, light weight, easiness of operation and data reduction. Numerous papers have been published in the course of the last decades on theoretical studies and experimental validation of the operation of Langmuir probes in laboratory, ionospheric and magnetospheric plasmas. More generally, the problem of the spacecraft interaction with the ambient plasma has also attracted much attention (Al'pert, 1974 and references therein) because the charging processes and the electrical equilibrium of spacecraft are vitally important for the onboard observations. If analytical models have been used in initial studies (Laframboise, 1966; Sanmartin, 1970; Laframboise and Sonmor, 1993),

a number of numerical models have been developed since then (see, for example, Jolivet and Roussel, 2001; Roussel and Berthelier, 2003) because they are the only way to cope with complex geometries and variety of physical processes that must be taken into account.

The objective of our work is to study the operation and performances of a new concept of the segmented Langmuir probe in order to take benefit of the above mentioned advantages of conventional Langmuir probes while extending their capabilities by accessing to plasma bulk velocity. Since the first flight of the SLP will be onboard the DEMETER CNES micro-satellite we have concentrated our study on plasma conditions typical for the ionosphere at the altitude of ~700 km, where the Debye length and probe radius have approximately the same values, i.e. few cm, thermal ion velocity, plasma bulk velocity in the probe frame and thermal electron speed are related as $V_{Ti} \leq V_0 << V_{Te}$. In such conditions the plasma flow mainly modifies the ion current, the collection and the distribution of which on the probe surface is controlled by the ratio of the bulk velocity to the thermal ion velocity and also by the potential that applied to the probe. In the present configuration the SLP contains 7 circular caps which are electrically insulated from the rest probe surface and therefore may be considered as individual collectors, which allow to measure the angular anisotropy of the collected current. With the aim to simulate the current collection by the SLP in the flowing ionospheric plasma we have developed an electrostatic model of the particle in cell (PIC) type. Our model is based on the method which was proposed by one of the authors (Kolesnikova, 1997; Béghin and Kolesnikova, 1998) to determine the frequency response of electrostatic HF probes in plasmas. This method differs from the commonly adopted numerical scheme to solve the Poisson equation, i.e. the electrical potential is directly evaluated from the ensemble of charges in the near-probe sheath and on the probe surface, and has the advantage, i.e. it allows a natural control of the total charge neutrality of the system probe-sheath.

In the chapter 2 we describe the method and illustrate it for the case of spherical probe, in chapter 3 present numerical solution for non-flowing thermal plasma and compare it with exact solution of Laframboise, in the chapter 4 give results for the bulk thermal plasma and examine a possibility to use segmented probe for the flow diagnostics in the ionospheric conditions. Future development of our model is discussed in the conclusion.

Description of the model

We first wish to review very briefly the main principles of our model. The SLP is located in a centre of the simulation box divided into elementary cells by a 3D mesh. Ions and electrons are injected from the sides of the box and subsequently move under the action of electric field in the near-probe sheath (and possibly of a static magnetic field). After each computation step, the charge density deposited in each cell by electrons and ions is computed. Similarly, the surface charge density on each element of the probe surface is calculated to satisfy the condition that all contributing charges, i.e. in the sheath and on the probe surface, sum up to create the desired polarization potential on the probe surface. The newly computed space and surface charges are then used to iterate the electric field for the next computation step. The particles that hit the probe surface are lost from the system and contribute to the collected current. After a number of computation steps, the system converges towards a stationary state which provides the solution we are looking for. In the following paragraphs we expose in more details the main features and parameters of our model.

Size of the simulation box

Conditions of the charge neutrality and the density continuity at the box boundary presume that the boundary has to be placed at least outside of the sheath region, dimensions of each are determined by a variety of parameters, i.e. size and form of obstacle, applied potential (in the case of the conducting surface), ratio of the bulk and thermal velocities, characteristic plasma lengths, magnitude of the magnetic field, etc. Basic ideas of the cavity size around the charged obstacle in plasma may be borrowed from the estimations of its size in the case of non-charged body. For example, in a motionless plasma the variation of the density n as a function of distance r from the centre of the sphere can be written as

$$n/n_0 = 0.5 \left(1 + \sqrt{1 - [r_s/r]^2}\right), \tag{1}$$

where n_0 is the undisturbed density and r_s is the probe radius. By this way, the density differs by 2% from the undisturbed value at a distance $\sim 4\, r_s$. The corresponding formula for the density variation in the wake behind a probe in a flowing thermal plasma is

$$n/n_0 = 0.5 \left(1 - \Phi(\chi) + \cos\theta \exp(-\chi^2 \sin^2\theta)(1 + \Phi(\chi\cos\theta))\right), \tag{2}$$

where $\chi = V_0/V_T$ is the ratio between the bulk and thermal velocity, $\theta = arctg(r_s/r)$ and Φ is the error function. Therefore the disturbed region in the wake extends till $\sim 9\, r_s$ for $\chi = 1$ and $\sim 28\, r_s$ for $\chi = 4$. Polarised probe totally modifies the structure and the size of the sheath region. According to Laframboise (1966) the disturbed region around a spherical probe of the radius $1\lambda_D$ and of the potential $25\, kT/e$ increases to $\sim 13\, r_s$ in the case of non flowing plasma, here λ_D is the Debye length, T is the temperature which is supposed to be the same for electrons and ions, k is the Boltzman constant and e is the absolute value of the elementary charge.

The correct choice of the simulation box size might be proven numerically by looking at the variation of the collected currents for the different box sizes with the aim to ensure the inaccuracy on the currents less than 2%.

Cell size and time step

Size of the integration cell is determined by the minimal characteristic length of the system plasma-obstacle. In particular case of the observations in the ionosphere at the altitude of ~ 700 km the Debye length, the typical linear dimension of electrostatic probes and the Larmor radius are related as $\lambda_D \leq r_s < r_L$. Therefore the characteristic cell size in such conditions is chosen to be equal $1\lambda_D$. In the non-magnetised plasma there exist two types of the particles motion, i.e. thermal and bulk. Thermal speed of the electrons is much larger than that of the ions, the last may have the same order of magnitude as the bulk velocity of plasma with respect to the probe in the conditions of the ionospheric satellite observations. Thermal electrons (hereafter we define the thermal velocity as $V_T = \sqrt{2kT/m}$, m is the mass of a particle) pass the distance of $1\lambda_D$ during the time $\omega_{pe}^{-1}/\sqrt{2}$ (here ω_{pe} is the angular electron

plasma frequency). To avoid the fluctuations of the density inside of the simulation box the characteristic time has to be small enough to integrate even minor energetic population, such as suprathermal electrons with the speed of $2V_T$, which consist of ~2% of the total population (assuming the last to be Maxwellien with $T = 0.2\text{eV}$). Taking into account these considerations the characteristic time for the electrons is chosen to be $0.25\omega_{pe}^{-1}$. However this time is extremely small for the ions which have the thermal speed in $\sqrt{m_i/m_e}$ times less than that of the electrons (hereafter we assume that all populations have the same temperature). Using the fact that we are interesting in a stationary solution, the characteristic time for each species is chosen by analogy with the considerations which were undertaken for the electrons and is defined to be equal $0.25\omega_{pe}^{-1}\gamma$, here $\gamma=\sqrt{m_i/m_e}/(1+V_0/V_{Ti})$. Similar techniques of the "numerical time step" was used by Jolivet and Roussel (2001) and Roussel and Berthelier (2003). Total time of the integration is the time when the computed parameters reach a stationary solution and the total charge of the system sheath-probe attains zero. Naturally, this time has to be superior the particle travel time through the simulation box.

To illustrate the above discussion we present in the Fig. 1 time variation of (a) the total current collected by spherical probe and (b) the total space and surface charges, which are computed for the case of the negatively polarised probe with $\varphi=-20\ kT/e$ in the thermal bulk plasma with $\lambda_D=2\text{cm}$, $T = 0.2\text{eV}$. Upper, middle and lower curves in the Fig. 1a correspond to the H^+ plasma with $V_0 =V_{Tp}$, $V_0 =2V_{Tp}$ and to the O^+ plasma with $V_0 =4V_{TO}$, respectively. Blue lines represent calculated values of the ion current and red lines stand for their averages over a period $5\omega_{pe}^{-1}\gamma$. In all presented cases the computed currents are converged to their limit values at the end of the integration time. Correctness of the obtained solution is ensured by the charge neutrality of the system sheath-probe. Time variations of the total space (red line) and surface (blue line) charges are shown in the Fig. 1b for the case $V_0 =V_{Tp}$. Charges are normalised by the surface charge in the vacuum, i.e. $4\pi\varepsilon_0 r_s\,\varphi$. At the end of the integration time the space and surface charges have opposite signs and converge to the same absolute value.

Particles injection

To reproduce the conditions of the non-disturbed plasma at the boundary of the simulation box 5 rules have to be fulfilled, i.e.

- velocity distribution has to be that in the infinity;
- space distribution has to be uniform;
- plasma has to be neutral;
- potential has to be zero (in absence of external electric field);
- number of macro-particles has to be sufficiently high to provide a good statistics.

In our model we generate the macro-particles with the Maxwellien velocity distribution which are uniformly distributed in the pre-box region of the width $\lambda_D/\sqrt{2}$ on each side of the

simulation box. The number of the generated macro-particles depends on the box volume and is chosen to provide ~180 particles of each species per cell at the box boundary. This number produces the dispersion of the collected current of ~5% from the average value (see Fig. 1a). Injection of the different plasma species is controlled by the imposing the potential value on the boundary of the simulation box to be equal 0. In the case of non-isotrope plasma (for example, flowing or magnetised) the condition of the "free boundary" (when the potential on the boundary is not fixed, but calculated at the same manner as in the internal points), might lead to the accumulation of the charge (positive or negative) inside of the simulation box and therefore might produce a violation of the total charge neutrality. An example of the potential distribution along the probe axis parallel to the vector of the bulk velocity in the H^+ plasma with $V_0 = V_{Tp}$ is shown in the Fig. 2. Plasma parameters and probe potential are the same as in the Fig. 1.

Surface and space charges

After each time step the charges deposited by ions and electrons in the cells are determined by a classical method. Each macro-particle is considered as a cube of dimension λ_D (this length corresponds to the undisturbed plasma) with a uniformly distributed charge inside of it. The macro-particle gives to each of the 8 adjacent cells a contribution equal to the common volume of this cube with the cell itself. The potential at the centre of any element k (either a cell in the volume surrounding the probe or a surface element of the probe) can be expressed as the sum of the individual contributions due (i) to the surface charges on the elements of the probe surface $i \neq k$, (ii) to the volume charges in the cells $j \neq k$, and (iii) to the charges of the element k itself, i.e.

$$\varphi_k = \sum_{i \neq k} \frac{q_{si}}{4\pi\varepsilon_0 r_{ik}} + \sum_{j \neq k} \frac{q_{vj}}{4\pi\varepsilon_0 r_{jk}} + \frac{q_k}{4\pi\varepsilon_0}\phi_{kk} \quad , \tag{3}$$

here charge q of any element is supposed to be located at the centre of mass of the element, r_{lm} is the distance between the centres of the elements l and m and s_k (v_k) is the surface (volume) of element. The last term expresses the contribution of the charge of the element k itself which may be written (see Kolesnikova, 1997) as $\phi_{kk} = \frac{1}{s_k}\iint_{s_k} \frac{ds}{\rho_k}$ for surface element and

$\phi_{kk} = \frac{1}{v_k}\iiint_{v_k} \frac{dv}{\rho_k}$ for space element, here ρ_k is the distance between the centre of mass and another point inside of the element. Once the volume charges in the cells are determined the surface charges on the sphere are computed by using equation (3) for each surface element k to express that the potential on the surface is equal to the desired value φ. This comes down to solving a linear system to get the surface charges. The complete set of volume and surface charges is then used to compute the electric field which will control the particles motion during the next time step.

The sphere is represented by an assembly of pentagons and hexagons each of them might be cut into the smaller elements. For the simple case of a sphere in vacuum, the approximation of the sphere by an assembly of planar elements results in an underestimate of the total charge by about 5% compared to the true value $4\pi\varepsilon_0 r_s$. The same ratio between true and computed charges must also globally hold in the presence of a sheath since this is only a

geometrical effect. We can take this into account by multiplying the contributions of the surface charges by 1.05 in expression (3).

Particles hitting the surface of the probe are lost from the system, but give a contribution to the current, j, which is collected by a surface element. This current is calculated as $j = -\sum_i e_i N_i / \tau$, where e_i is the species charge (negative for electrons and positive for ions) and N_i is the number of particles of i-species collected by a surface element during the time step τ. Particles hitting the side of the box are lost. Photoelectrons that are emitted by the probe under solar UV radiation have not been taken into account in this version of the code.

Probe Response in Non-Flowing Thermal Plasma

In order to validate our model we have compared the results with the exact solution provided by Laframboise (1966) for an attractive probe in a non-flowing thermal plasma. This comparison was made for a probe with radius $r_s = 2$ cm, similar to the SLP which will be flown on DEMETER, and for plasma conditions close to those anticipated along the orbit, i.e. density $\sim 2.8 \cdot 10^4$ cm^{-3}, equal ion and electron temperatures $T_e = T_p = 0.2$eV, that correspond to $\lambda_D = 2$cm and $r_s/\lambda_D = 1$. Displayed in Fig. 3 are the theoretical values of the current of attracted particles for several potentials shown by blue dots and our model results represented by red dots. Potential is normalized by the plasma temperature and collected current by its value at $0V$ which is $j_0 = 2\sqrt{\pi} e r_s^2 n V_T$. The current-voltage characteristics, shown as solid lines, has been fitted by the analytical law

$$ j/j_0 \approx \alpha \left[1 - \frac{e_i \varphi}{kT} \right]^{\kappa}, \; e_i \varphi \leq 0, \tag{4a} $$

with $\alpha = 1$, $\kappa = 0.95$.

Fig. 4 displays the model currents for protons (blue dots) and for electron (red dots) in the probe potential range from $-6\,kT/e$ to $6\,kT/e$. The total current, sum of the ion and electron currents, is shown by solid line for the H$^+$ plasma and by dashed line for the O$^+$ plasma. Currents for repelling particles are fitted by the analytical law

$$ j/j_0 \approx \alpha b^{-\frac{e_i \varphi}{kT}}, \; e_i \varphi \geq 0, \tag{4b} $$

with $\alpha = 1$, $b = 2.25$. Floating potentials are $\approx -3kT/e$ for H$^+$ plasma and $-4.5kT/e$ for O$^+$.

Presented in Fig. 5 are (a) the density distribution for attracted (blue) and repelling (red) particles, (b) the potential profile in the sheath. Analytical solution is shown by solid line and model results by dots. The nearly perfect agreement between theoretical and model results, with maximum differences less than $\sim 3\%$, convincingly proves the validity and good accuracy of our code.

Probe Response in Bulk Thermal Plasma

Bulk velocity of plasma with respect to the probe produces an asymmetry of the charge distribution in the sheath region and therefore modifies the current collection and leads to an asymmetry of the current distribution on the probe surface. In case of on-board satellite observations in the ionosphere the bulk velocity mainly arises from the satellite movement (~7 km s^{-1}), proper plasma velocity might consist up to ~10% of the satellite speed. Most adapted instrument to measure the ion flows in such conditions is the retarding analyser (see, for example, Hanson, 1970; Séran, 2003). Segmented spherical probe was proposed as an alternative technique to resolve the bulk velocity. Here we examine this possibility, by analysing (i) current which is collected by entire probe and (ii) angular distribution of the currents which are measured by individual segments placed on the probe surface.

(i) In the conditions of ionospheric observations bulk speed of plasma with respect to the probe is much less than electron thermal velocity, but has the same order of magnitude as ion thermal speed. Therefore plasma flow will mainly modify the ion branch of the collected current. In Fig. 6 collected currents versus potential which is applied to the probe are presented for the cases of H$^+$ plasma in the conditions $V_0 = 0$ (black), $V_0 = V_{Tp}$ (blue), $V_0 = 2V_{Tp}$ (green) and of O$^+$ plasma with $V_0 = 4V_{To}$ (red). Dots are used to indicate computed values, lines stand for their fittings by the law (4). Plasma characteristics are chosen the same as in the Fig. 1. The presented solutions demonstrate that decrease of the ion current might be caused by two effects, i.e. increase of the bulk velocity and presence of the heavy ions. Therefore the proper plasma speed (which consists only some percents of the total bulk speed) may be resolved from the Langmuir probe measurements only if the exact ion composition is known. An additional complexity in the interpretation of the negatively polarised probe measurements arises from the photoelectron emission from the probe surface. Under the action of the sun ultra-violate radiation the photoelectron current may attain amplitude of the ion current in the oxygen-dominated plasma. In such circumstances the possibility of the velocity determination from the probe measurements in the dayside ionosphere commences to be doubtable.

(ii) Currents, which are collected by the individual segments placed on the probe surface, maintain information about plasma anisotropy related to the flow. Under the action of electric field in the sheath region, the ions will be speed up in the lobe part and slow down in the wake. En consequence, the lobe part of the probe sheath will have luck of the positive charge and the wake will be overloaded with ions. The distribution of the ions in the sheath is controlled by the probe potential, or more precisely by the ratio of the ion energy to the attractive energy which is created by the polarised probe. Because we are interesting in the ion branch of the collected current, the range of the probe potentials under consideration is limited and sets between the lower value of the polarised potential, which is ~-40 kT/e, and the floating potential φ_f, which is ~ -6 kT/e for the O+ plasma (see Fig. 6). Therefore, in the considered range the attracted probe energy is higher than proton energy and has the same order of magnitude as the kinetic energy of the oxygen. This is why the highest density of the positive charge in the wake region is expected to be found in the vicinity of the probe. In the Fig.7 density distribution of the electrons (red line) and ions (blue line) along the probe axis parallel to the bulk velocity are presented in the case of the $\varphi = -20$ kT/e for (a) the H$^+$ plasma with $V_0 = V_{Tp}$ and (b) the O$^+$ plasma with $V_0 = 4V_{TO}$. Plasma parameters are chosen the same as in the Fig. 1. Charge densities are normalised to their values in the non-disturbed

plasma and averaged over the time period $5\omega_{pe}^{-1}$. It worth to note that in the O$^+$ plasma the region of the charge separation in the wake is increased twice with respect to the H$^+$ plasma.

Charge anisotropy in the sheath leads to the current anisotropy on the probe surface. In the Fig. 8 the current distributions versus angle between the bulk velocity vector and the external normal to the probe surface are shown for three cases, i.e. $V_0=V_{Tp}$ (in blue) , $V_0 =2V_{Tp}$ (in green) in the H$^+$ plasma and $V_0=4V_{To}$ (in red) in the O$^+$ plasma in the same conditions as in the Fig.7. Dots stand for the numerical solutions and lines for their fit by exponential law. Current is normalized to its value at the angle 0°. The presented solutions demonstrate that current distribution versus angle is almost uniformly distributed on the upstream part of the probe (similar to the case of non flowing plasma), contrary to the distribution on the downstream side which adequately reacts on the wake overloading with the positive charge. Wake side distribution is narrower in the plasma with higher bulk speed or lower ion thermal velocity. This feature together with the ratio of the currents measured at 0° and 180° can provide a tool to deduce the bulk velocity in the ionospheric plasma. Here again we have to mention that photoelectron emission will add an additional asymmetry and in such case the interpretation of the current angular measurements might be problematical.

Conclusions

We propose numerical model of the PIC type which allows to solve the problem of the current collection on the surface of segmented probe. This model was applied for the case of bulk thermal plasma with the characteristics that are expected to be observed in the ionosphere at the altitude of ~700 km. We conclude that currents, which are simultaneously measured by the spherical probe and its segments, might provide a possibility to resolve the flow velocity. To use this model for the interpretation of the Langmuir probe measurements in the ionosphere two additional effects have to be considered, i.e. magnetic field and sun ultra-violet radiation. Each effect will introduce its own asymmetry in the system probe-sheath. First effect will modify the electron branch and second the ion branch of the collected current. These topics will be considered in the following papers.

Acknowledgements
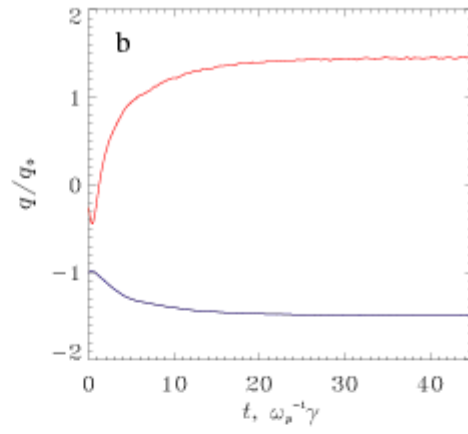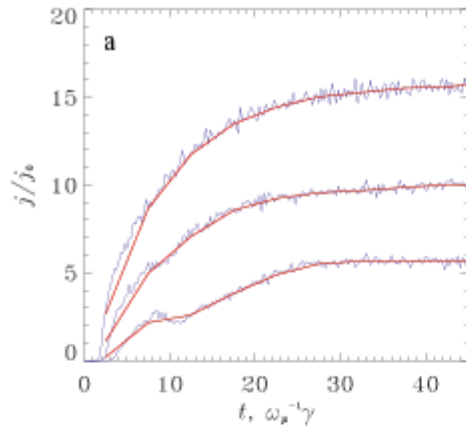
Fig. 1
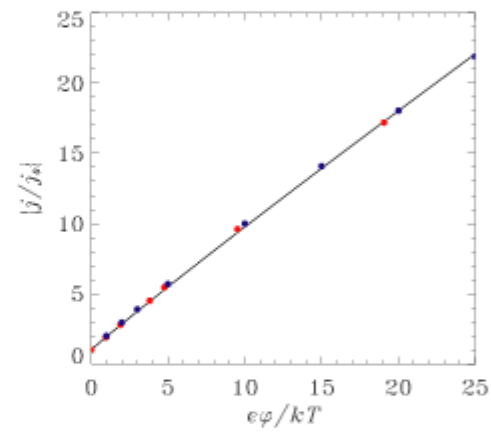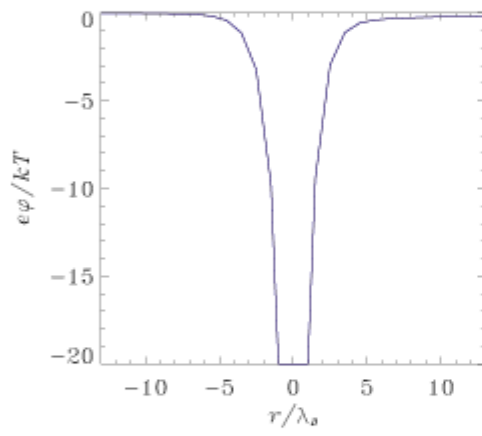
Fig. 2

Fig. 3
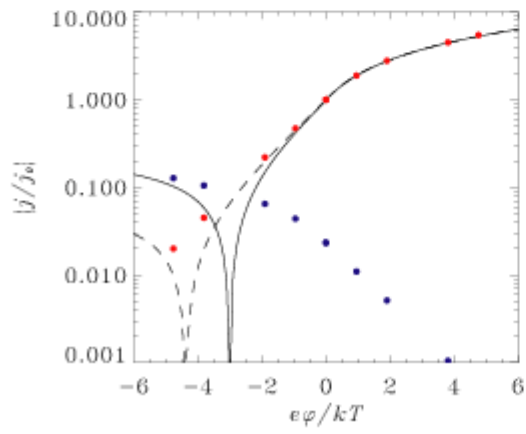
Fig. 4
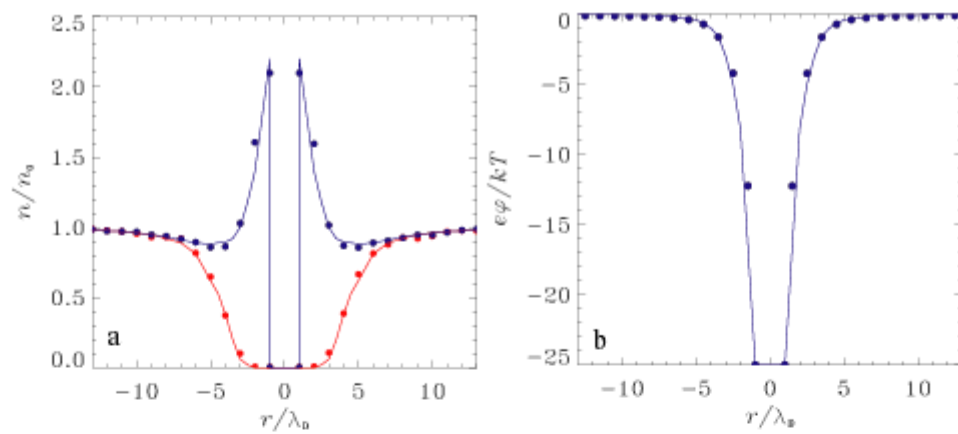
Fig. 5
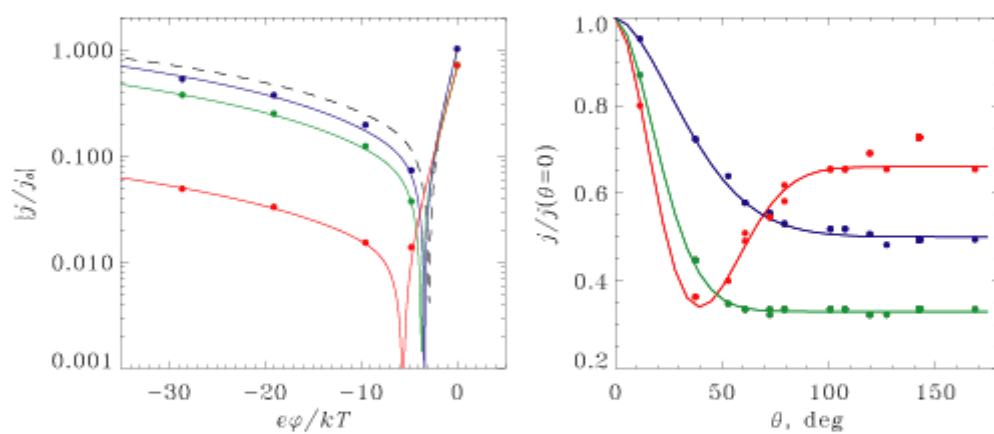
Fig. 6

Fig. 8
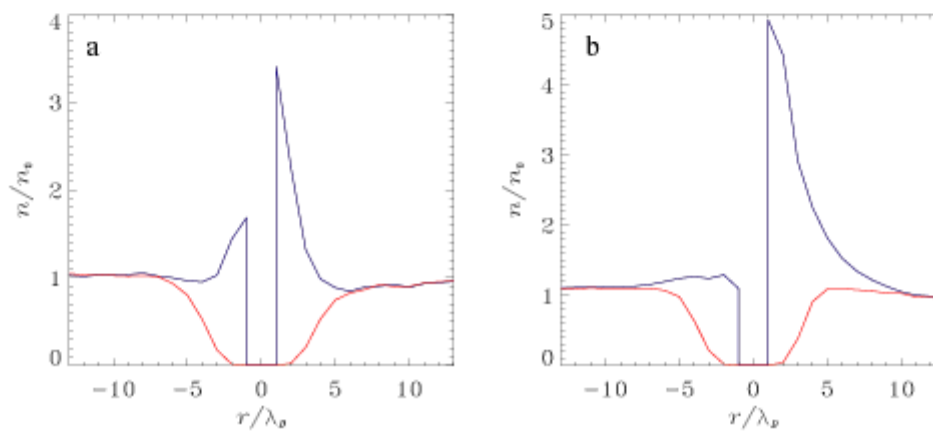
Fig. 7

<u>Figures captures</u>

Figure 1. (a): total current collected by spherical probe in the case $\varphi=-20\ kT/e$, $\lambda_D=2\mathrm{cm}$, $T=0.2\mathrm{eV}$. Upper, middle and lower curves correspond to the H$^+$ plasma with $V_0=V_{Tp}$, $V_0=2V_{Tp}$ and the O$^+$ plasma with $V_0=4V_{TO}$, respectively. Blue lines represent calculated values of the ion current and red lines stand for their averaging over the period $5\omega_{pe}^{-1}\gamma$. (b): variation of the total space (red line) and surface (blue line) charges for the case $V_0=V_{Tp}$. Charges are normalised by the surface charge in the vacuum.

Figure 2. Potential distribution along the probe axis parallel to the bulk velocity in the H$^+$ plasma with $V_0=V_{Tp}$. Plasma parameters and probe potential are the same as in the Fig.1, potential is normalised by the plasma temperature.

Figure 3. Normalised current as a function of the normalised attractive potential of the spherical probe of radius 2cm in the non-flowing plasma with $\lambda_D=2\mathrm{cm}$ and $T_e=T_p=0.2\mathrm{eV}$. Blue dots show the exact solution of Laframboise, red dots represent the numerical solution, solid line stands for the fitting of the analytical solution.

Figure 4. Normalised current as a function of the normalised potential (attractive and repelling) of the spherical probe in the same plasma conditions as in the Fig. 3. Red and blue points represent the numerical solution for electron and proton currents, respectively, and solid line stands for the total current. Dashed line represents the collected current in the case of the O$^+$ plasma.

Figure 5. (a) Density distribution for attracted (blue) and repelling (red) particles, (b) the potential profile in the sheath in the case of non-flowing plasma with $\lambda_D=r_s=2\mathrm{cm}$, probe potential is fixed at $\varphi=-25\ kT/e$. Analytical solution is shown by the solid lines and model results by dots.

Figure 6. Normalised current versus normalised potential in the H$^+$ plasma with $V_0=0$ (black), $V_0=V_{Tp}$ (blue), $V_0=2V_{Tp}$ (green) and in the O$^+$ plasma with $V_0=4V_{TO}$. Dots indicate computed values, solid lines stand for their fittings. Plasma characteristics are chosen the same as in the Fig. 1.

Figure 7. Positive (in blue) and negative (in red) charge density along the probe axis parallel to the bulk velocity (a) in the H$^+$ plasma with $V_0=V_{Tp}$ and (b) in the O$^+$ plasma with $V_0=4V_{TO}$. Plasma parameters and probe potential are the same as in the Fig.1. Charges are normalised by their values in the non-disturbed plasma, distance is normalized by the Debye length.

Figure 8. Current distribution as a function of angle between the vector of plasma bulk velocity and the external normal to the probe surface in the H$^+$ plasma with $V_0=V_{Tp}$ (in blue), $V_0=2V_{Tp}$ (in green) and in the O$^+$ plasma with $V_0=4V_{TO}$ (in red). Dots indicate computed values, lines stand for their fits. Plasma characteristics are chosen the same as in the Fig. 1. Current is normalized to its value at the angle 0°.

References

1. Al'pert Ya. L., Waves and artificial bodies in near-Earth plasma, in Russian, Nauka, Moscow, 1974.

2. Béghin, C. and E. Kolesnikova, The Surface-Charge Distribution approach for modellization of quasistatic electric antennas in isotropic thermal plasma, Radio Sci., 33, 503, 1998.

3. Jolivet L. and J. F. Roussel, Numerical simulation of plasma sheath phenomenon in the presence of secondary electronic emission, submitted to IEEE Trans. Plasma Sci., 2001.

4. Hanson, W. B., S. Sanatani, D. Zuccaro, T. W. Flowerday, Plasma measurements with the retarding potential analyser on OGO 6, J. Geophys. Res., 75, 5483-5501, 1970.

5. Kolesnikova, E., Méthode des distributions superficielles de charges pour la modélisation des antennes électriques en plasma homogène, isotrope et Maxwellien, Thèse de Doctorat, Univ. Orléans, 1997.

6. Laframboise, J. G., Theory of spherical and cylindrical Langmuir probes in a collisionless, Maxwellian plasma at rest, UTIAS report N 100, Institute for aerospace studies, University of Toronto, 1966.

7. Laframboise, J. G. and L. J. Sonmor, Current collection by probes and electrodes in space magnetoplasma : a reveiw, J. Geophys. Res., 98, 337-357, 1993.

8. Lebreton, J.-P., Micro-satellite DEMETER, DCI-ISL, Technical note, ESTEC SCI-SO, 2002.

9. Roussel, J. F. and J. J. Berthelier, A study of the electrical charging of the ROSETA Orbiter, I-Numerical Model, J. Geophys. Res.-Planets, accepted for publication, 2003.

10. Sanmartin, J. R., Theory of a probe in a strong magnetic field, Phys. Fluids, 13, 1970.

11. Séran, E., Reconstruction of the ion plasma parameters from the current measurements: Mathematical tool, Annales Geophysicae, 21, 1159-1166, 2003.

CALIBRATING THE FLOATING POTENTIAL MEASUREMENT UNIT

Dr. Charles M. Swenson
Electrical and Computer Engineering
Utah State University, Logan, UT 84322
Phone: (435) 797-2958
Fax: (435) 797-3054
E-mail: charles.swenson@usu.edu

Chad Fish
Space Dynamics Laboratory
Utah State University

Dr. Don Thompson
Center for Atmospheric and Space Sciences
Utah State University

Abstract

The Floating Potential Measurement Unit (FPMU) is an instrument being developed to study the spacecraft surface charging of the International Space Station (ISS). Charging on the ISS is unique because of the station's size and the high voltage solar arrays with exposed interconnects. The FPMU consists of four instruments: a floating potential probe, two Langmuir probes, and a plasma impedance probe. These probes will measure the floating potential of the ISS, electron density, and electron temperature with redundancy. The instruments were calibrated using test loads over a range of temperatures. The FPMU is being integrated into the ISS at one of the existing external camera locations that places it in clear ram flow of the space plasma. Operational constraints of the ISS will result in the FPMU being used to obtain snapshots of data and not as a continuous monitor of the ISS charging and environment. The FPMU is awaiting launch to the ISS on the first flight of the Space Shuttle when it returns to service. This paper presents an overview of the FPMU instruments and calibration results.

Introduction and Background

The Floating Potential Measurement Unit (FPMU), shown in Figure 1, has been created to aid in the understanding of the complex surface charging physics of the International Space Station (ISS). The instrument was originally to be deployed on the ULF-1 mission in March of 2003 but was delayed by the Space Shuttle Columbia accident that occurred in February of 2003. A single FPMU is currently scheduled to be deployed when the Space Shuttle returns to flight and construction missions for the ISS resume. This will be no earlier than March of 2004. When deployed the FPMU will be used to characterize the charging physics and validate charging models after each stage of ISS assembly. Changes to ISS charging physics are expected as additional solar arrays are added to the structure due to their enhanced ability to collect electrons from the surrounding ionospheric plasma (1, 2). An overview of the FPMU and its mission has been previously presented by Swenson et al (3).
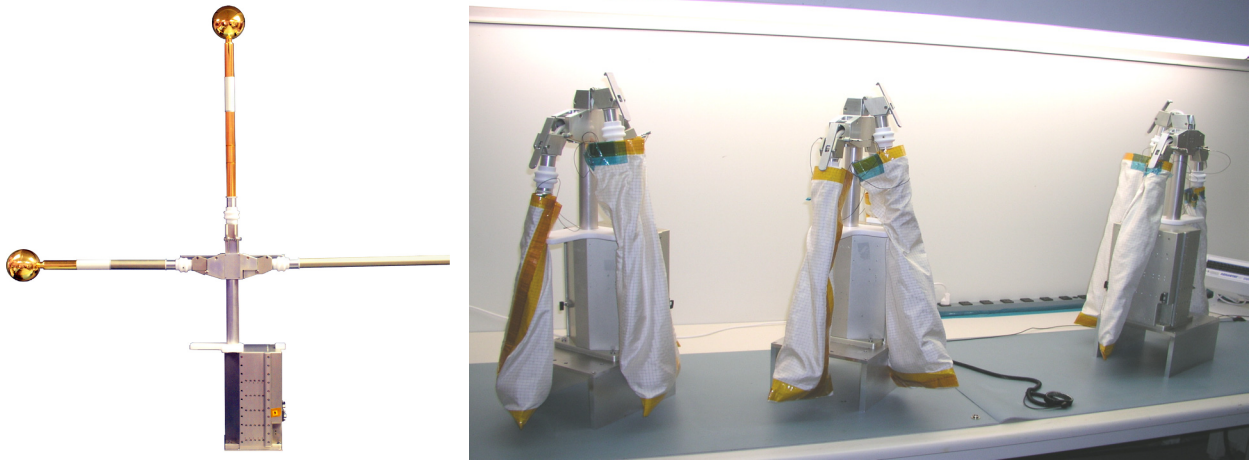
Figure 1. Photographs of the Floating Potential Measurement Unit (FPMU). (Left) Flight unit with sensors deployed. (Right) One flight unit and two flight-spares in protective covers with sensor booms stowed, October 2003.

Excessive charging of the ISS has been identified as a potential shock hazard to astronauts on Extra Vehicular Activity (EVA) due to the nature of the US space suit design. Industrial safety standards for workers around high voltage would indicate that this hazard exists when the floating potential of the ISS exceeds 40 Volts (4). There is also a concern for the long term stability of the anodized aluminum surfaces on the exterior of ISS modules. Charging greater than 80 Volts relative to the space environment causes electrical breakdown of the capacitive layer on the anodized aluminum due to its relatively weak dielectric nature (5). The dielectric breakdown results in arcs, sputtering, pitting and contamination of the surface properties. Over long periods of time this can change the surface temperature of ISS modules, creating a touch temperature concern for astronauts on EVA. These concerns prompted the construction of the FPMU and it predecessor, the Floating Potential Probe (6, 7, 8).

The FPMU development team was challenged at both systems and instrument levels primarily due to the short ten-month development requirement compounded by NASA's safety, testing, and documentation requirements. The FPMU is to be operational for a period of at least three years to cover the construction phase of the ISS and to provide measurements of vehicle floating potential, local plasma density, and electron temperature. To achieve these requirements commercial parts were used in radiation tolerant designs and multiple FPMUs were fabricated as replacement units. It was critical that there be evidence to indicate when, or if, FPMU data was erroneous. This was achieved by including significant internal system monitoring and by using multiple instrument and measurement techniques (floating probes, Langmuir probes, radio frequency probes). At the current stage of assembly, shown in Figure 2, there are no sites for external mounting of generic instruments on the ISS structure. The FPMU, therefore, masquerades as an external TV camera in order to receive power and transmit data encoded in TV images though the ISS video systems.

Instrumentation

The FPMU is comprised of four instruments to measure floating potential, plasma density and temperature. The instruments use different techniques or geometries to provide redundancy

and cross-validation of the final data products. The instruments are the Floating Potential Probe (FPP), the Wide-sweeping Langmuir Probe (WLP), the Narrow-sweeping Langmuir Probe (NLP), and a Plasma Impedance Probe (PIP) as illustrated in Figure 2 (right). The FPMU is planned to be initially installed at camera port 2 on the end of the S1 truss of the ISS. This location will be out of the plasma wake for nominal ISS flight orientation. Interference or cross-talk between the individual instruments of the FPMU was a concern. The probe surfaces have been set at least two Debye lengths apart for a worst-case rarified and cold ionospheric plasma. The tip-to-tip distance from WLP to the PIP is 130 cm, and the whole instrument stands 150 cm tall. We briefly present an overview of each instrument.
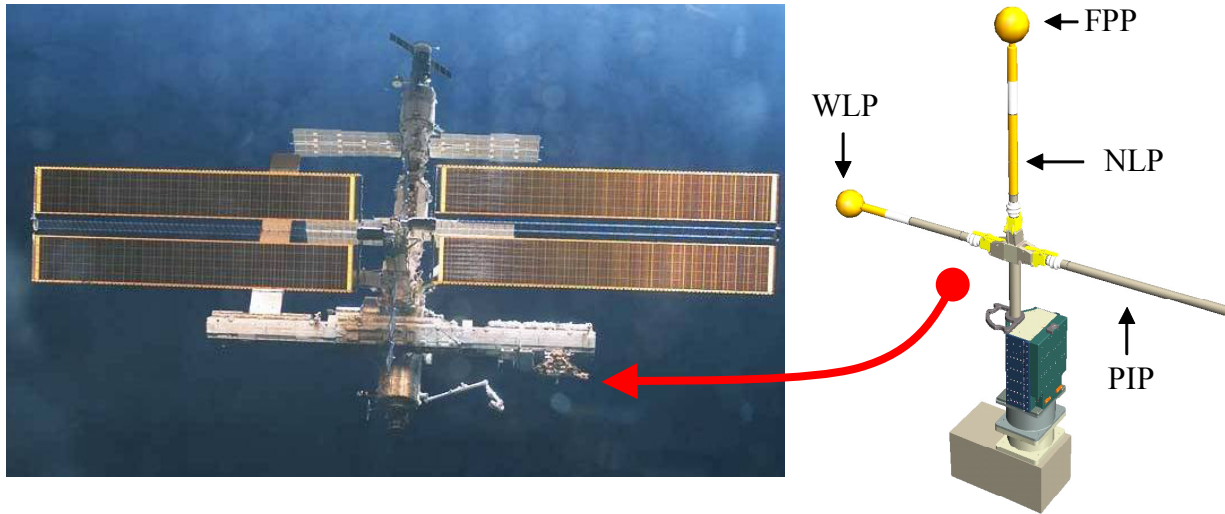
Figure 2. (Left) Photograph of the ISS December 2002. (Right) The FPMU showing the locations of the four instruments; Floating Potential Probe (FPP), Wide-Sweep Langmuir Probe (WLP), Narrow-Sweep Langmuir Probe (NLP), and the Plasma Impedance Probe (PIP).

The Floating Potential Probe (FPP) is a gold plated sphere of radius 5.08cm. The sphere is isolated from chassis ground by a high impedance circuit, approximately $10^{11}\Omega$. The sphere "floats" at a floating potential determined by local plasma conditions, which is within a few k_BT_e of the plasma potential, and provides a good reference for measuring the potential of the ISS. Data is sampled as a 12-bit word with 100mV resolution.

The Wide-Sweep Langmuir Probe (WLP) is a gold plated sphere of radius 5.08cm. A voltage sweep from –20V to 80V relative to chassis ground, the ISS structure, is applied to the probe, and the resulting currents to the probe are measured. Sweeps are accomplished each second, with the potential sweeping from low to high voltage one second and back down from high to low the next. The sweep is comprised of three parts: steps of ~250mV from –20V to 0V, steps of ~25mV from 0V to 50V, and steps of ~250mV from 50V to 80V. This pattern was chosen as a balance between available telemetry space and the amount of data necessary to derive the required parameters. The small step size from 0V to 50V provides sufficient resolution for a determination of Temperature, T_e (which requires several samples in the electron retarding portion of the sweep). The floating potential can be obtained over the full –20V to 80V range, within the uncertainty requirement of ±2V. The current resulting from the applied voltage sweep

is measured on two different 12-bit channels. The low-gain channel has a resolution of 700 nA/count and the high gain channel has a resolution of 3.5 nA/count. The high-gain channel has sufficient sensitivity to observe both photo emission and ion collection currents, whereas the low-gain channel is suited for observing ambient electron currents.

Measurement of ionospheric electron temperature by Langmuir probes is subject to significant error if the probe surface material does not have a uniform work function, or if the probe is not clean (10). Gold was chosen as the surface coating for the Langmuir probes owing to its nearly uniform work function when properly applied and cleaned (12) and its stability in the atomic oxygen environment of low earth orbit. The WLP can be cleaned on orbit by heating the probe surface to approximately 350 C. This is accomplished via a small halogen lamp inside the hollow sensor sphere that can be powered on and off. Cleaning Langmuir probes in this fashion has been shown to be effective by W.E. Amatucci et al (9).

The Narrow-Sweep Langmuir Probe (NLP) is a gold plated cylinder of radius 1.43cm and length 5.08cm. The NLP is placed mid-way on the boom supporting the FPP. The probe surface of the NLP is surrounded on each side by a gold-plated guard cylinder of radius 1.43cm and length 10.2cm, which are swept in synchrony with the NLP. A sweep from –4.9V to +4.9V, in steps of ~12mV, is applied to the NLP during one second, followed by a sweep down from 4.9V to –4.9V the next second. This sweep voltage is referenced to the floating potential measured by the FPP. Hence, even though the sweep range of the NLP is small compared to the possible range of ISS potentials, the electron and ion retarding regions of the plasma current-voltage profile will be seen, as the region sampled will move through the –180V to +180V range of the FPP to match the current conditions. This configuration will allow N_e (the local plasma density) and T_e to be determined at 1Hz. In addition, the ISS potential measured by the FPP will be verified, since if it is incorrect, the NLP will not be referenced to the proper potential and the transition from electron collection to ion collection will not be seen in the ±4.9V sweep.

The current resulting from the applied voltage sweep is measured on two different 12-bit channels. The low-gain channel has a resolution of 87.5 nA/count and the high gain channel has a resolution of 0.44 nA/count. Like the WLP the high gain channel has sufficient sensitivity to observe both photo emission and ion collection currents, whereas the low-gain channel is suited for observing electron currents. The surfaces of the NLP and WLP are both gold for the same reason: the desire for a uniform work function and stability in atomic oxygen. However, there is no heating lamp within the NLP, so there is no active cleaning mode for this probe.

The Plasma Impedance Probe (PIP) consists of an electrically short dipole antenna electrically isolated from the ISS. The dipole is normally oriented perpendicular to the ram flow direction and away from the ISS wake. The PIP measures the electrical impedance (magnitude and phase) of the antenna at 256 frequencies over a 100 KHz to 20 MHz range. Electron density, electron-neutral collision frequency, temperature and magnetic field strength can potentially be deduced from these impedance measurements (11). The PIP will also track the frequency at which an electrical resonance associated with the upper-hybrid frequency occurs using a technique known as the Plasma Frequency Probe (PFP). From this resonance the absolute plasma density will be determined at a 512 Hz rate with great accuracy. The PIP is considered an experimental instrument and has no formal NASA requirements for operation.

The performance of the FPMU instruments to measure the ISS floating potential, V_{ISS}, the local plasma density, Ne, and Temperature, Te are summarized in Table 1.

Table 1. The measured parameters, rates, and effective ranges for the FPMU instrumentation.

Instrument	Parameter	Rate	Effective Range
FPP	V_{ISS}	128Hz	-180V – +180V
WLP	Ne	1Hz	$10^9 m^{-3} – 5 \times 10^{12} m^{-3}$
	Te	1Hz	500K – 3000K
	V_{ISS}	1Hz	-50V – 20V
NLP	Ne	1Hz	$10^9 m^{-3} – 5 \times 10^{12} m^{-3}$
	Te	1Hz	500K – 3000K
	V_{ISS}	1Hz	-180V – +180V
PIP	Ne	512Hz	$10^8 m^{-3} – 10^{13} m^{-3}$

Calibration

The FPMU was calibrated by examining the response of the instruments to known loads or test conditions. These measurements were performed both under bench-top conditions and while the FPMU was undergoing thermal vacuum testing. Efforts were made to minimize noise during this process although this was not completely possible. When the FPMU was undergoing thermal vacuum testing long leads were run from the probe surfaces, through vacuum feed through connecters, and then to test equipment and loads external to the chamber. These long leads were a source of white noise that was detectable on the high gain channels of the WLP and the NLP but was largely below the detectable threshold of the low gain channels.

The calibration data has been reduced to a set of polynomial coefficients that are applied to the telemetered values (12-bit integers). The actual calibrations are stored in a file for use by the FPMU ground station software. The file contains blocks composed of one or more comments, followed by a line of polynomial coefficients of the form:

$$y = A_0 + A_1 x + A_2 x^2 + ...$$

where y is the calibrated quantity (volts, amperes, centigrade, etc) and x is the telemetered integer quantity. Each of the FPMU flight units has its own calibration file, with its own unique set of coefficients. The WLP and NLP are found to have calibrations that vary with the temperature of the electronics. Hence, the calibration coefficients, A_0 and A_1 are functions of temperature. The calibration file contains 4 coefficients for each of Langmuir probe channels. These four coefficients, called m_0, b_0, m_1, and b_1, respectively, are the coefficients that can be used to calculate A_0 and A_1 according to:

$$A_0 = b_0 + m_0 T_{12}$$
$$A_1 = b_1 + m_1 T_{12}$$

where T_{12} is the uncalibrated value (counts) of the FPMU Sensor Board Top Temperature Sensor (housekeeping measurement T_{12}). The corrected values for A_0 and A_1 are used to produce engineering values for the Langmuir probe channels. We now present a brief overview of the major calibration and test results for each of the FPMU instruments.

The FPP testing and calibration results are summarized in Figure 3. For FPMU serial number 4, A_0 and A_1 were found to be $A_0 = -194.6$ and $A_1 = 0.095$. The input resistance of the FPP must be sufficiently high such that the measurement current will be a small fraction of either the ambient ion or electron collection currents. This required that the input resistance of the FPP be greater than 10^9 Ohms and preferably as high as possible. This was tested by applying a capacitor in parallel with the probe, charging it to 3 Volts, and observing the resulting discharge curve, Figure 3 (right). This data was consistent with a leakage current dominated by discharge through the relatively dry air around the probe and the change of stray capacitance due to the motion of technicians near the probe conducting the test. The FPP testing and calibration results for each of the flight units showed similar results.
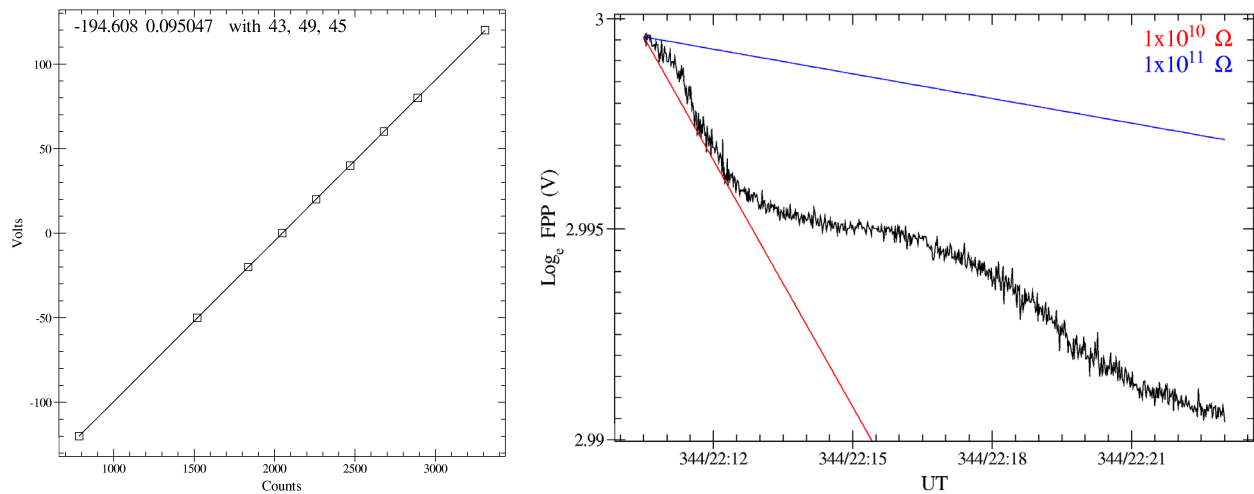
Figure 3. (Left) Calibration results of the FPP showing a linear response of instrument with applied voltage. (Right) Input resistance test of the FPP by capacitive discharge.

The WLP and NLP temperature dependent calibrations for the high gain channel are shown in Figure 4. The probes were calibrated over the range of 17 to 59 C while the expected operating range is 25 to 40 C and is thermostatically controlled. Several thousand IV curves were analyzed and the resulting calibrations for A_0 and A_1 are displayed as points. The trend lines are the resulting temperature dependent calibrations b_1 and m_1. The gain coefficient, A_1, is relatively insensitive to temperature for both probes and very near the desired values of 3.5 nA/count and 0.44 nA/count with a fraction of a count of drift with temperature. The noise or distribution of gain observed in Figure 4 is not expected for on orbit operation.
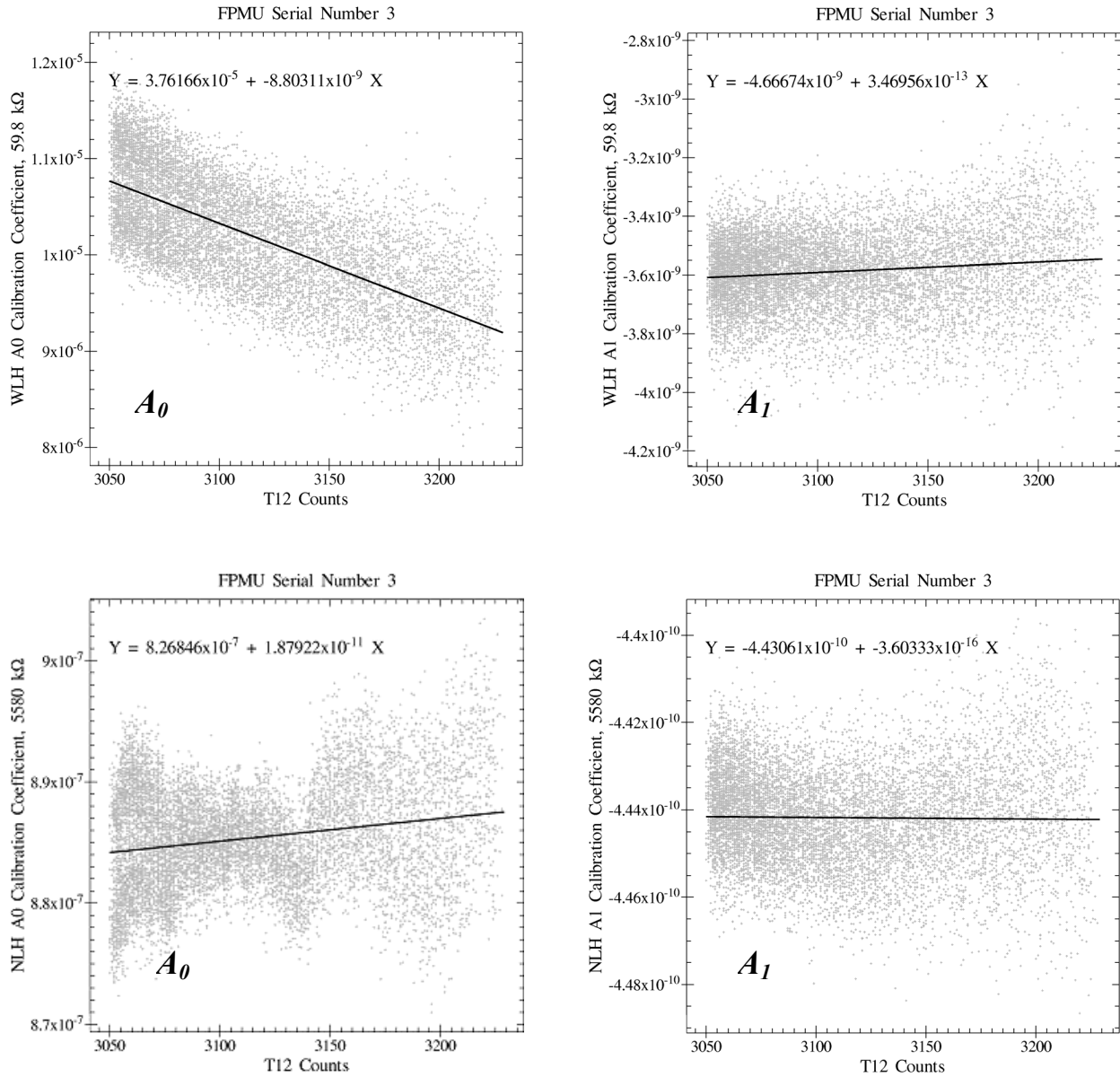
Figure 4. Temperature dependent calibration for the high gain channels of the Langmuir probes on FPMU serial number 3. The graphs are for the A_0 coefficient for the WLP (top left), A_1 coefficient for the WLP (top right), A_0 coefficient for the NLP (top left), A_1 coefficient for the NLP (top right). T_{12} counts are converted to centigrade by A_0=689.9 and A_1=-0.2068 giving a temperature range of 60 to 17 C for these plots.

The offset coefficient, A_0, that can be thought of as the zero reference level, shows considerable drift over the temperature range that corresponds to 350 counts for the WLP and 25 counts for the NLP. Neither of these drifts significantly change the range of currents that can be observed for normal ionospheric operations. The corrections for these drifts are critical to observing Ion currents as they are on the order of the expected photo emission currents.

Figure 5 presents the temperature dependent calibrations for the low-gain channels. They reflect that design goals have been achieved and show expected measurement quantization noise effects reflecting the technical simplicity of these channels relative to the high gain channels. The two lines for the WLP calibration result from the difference of one count of the measurement of the calibration load. The NLP similarly shows a faint bi-modal distribution resulting from one count of difference over the measurement range.
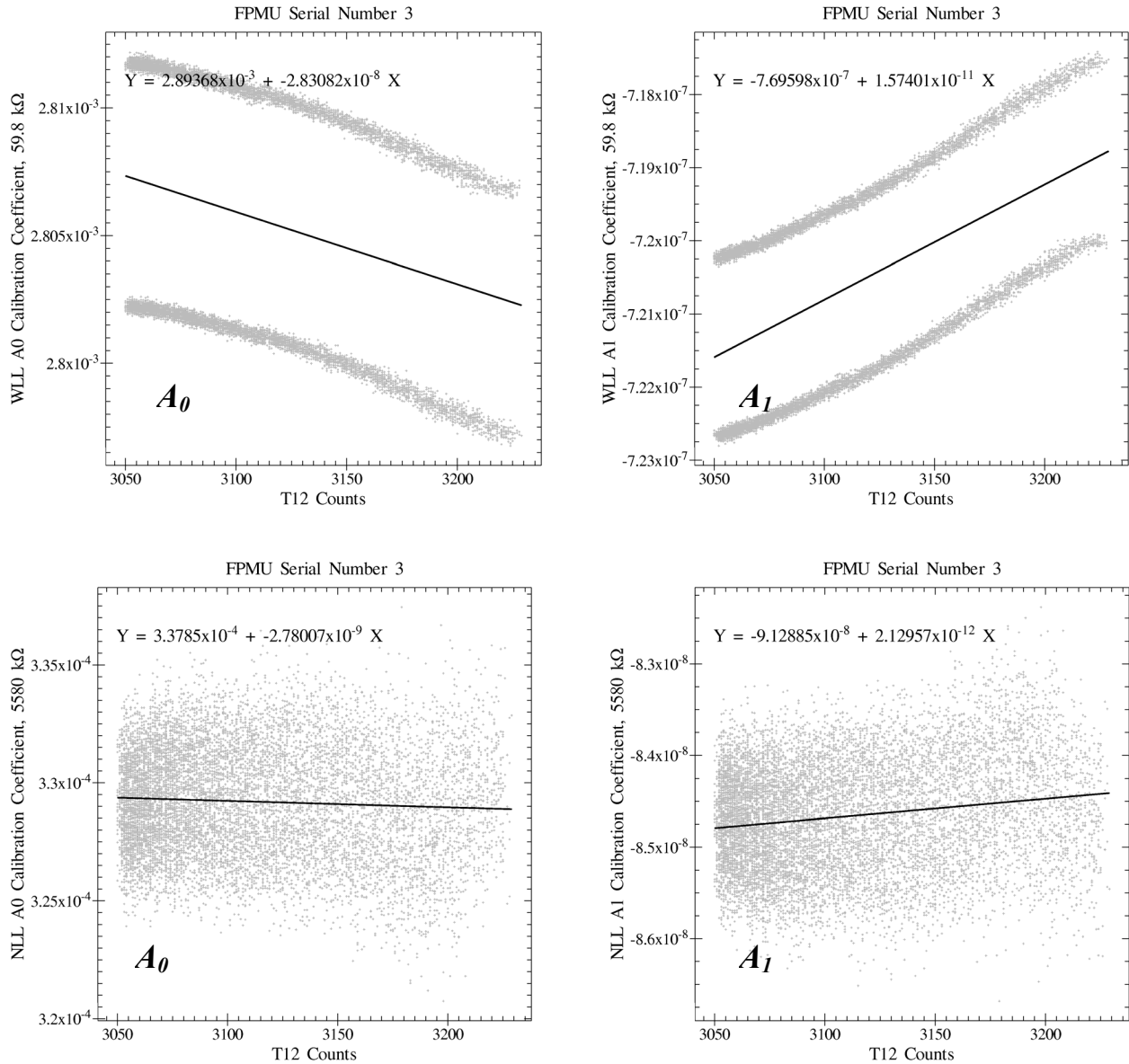
Figure 5. Temperature dependent calibration for the Low gain channels of the Langmuir probes on FPMU serial number 3. The graphs are for the A_0 coefficient for the WLP (top left), A_1 coefficient for the WLP (top right), A_0 coefficient for the NLP (top left), A_1 coefficient for the NLP (top right). T_{12} counts are converted to centigrade by A_0=689.9 and A_1=-0.2068 giving a temperature range of 60 to 17 C for these plots.

The PIP is a more complex instrument than the other FPMU instruments, and testing and calibration is problematic due to its RF operating range. The probe is calibrated before final assembly of the FPMU when the antenna components are not attached. A set of test loads consisting of resistors, capacitors, and inductors are placed at the antenna feed. The output of the magnitude and phase channels are then compared to the impedance of the loads as measured on a network analyzer (Figure 6, left). The resonance tracking PFP is tested with a R-L-C network that simulates the resonance observed at the upper-hybrid frequency. The results of this testing are shown in Figure 6 (right) where a 7.21 MHz resonance frequency calibrator is tracked with an accuracy of better than 0.1%.
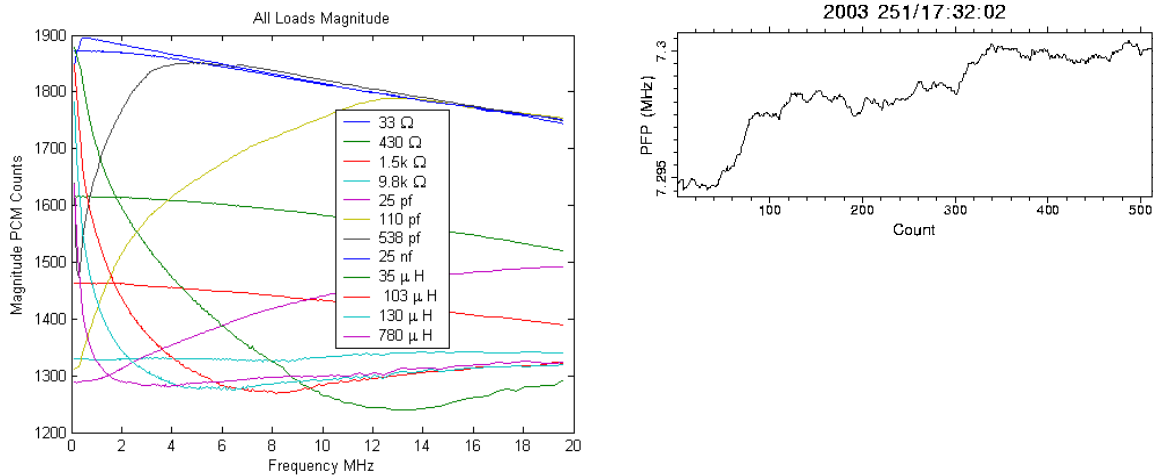
Figure 6. (Left) The magnitude channel of the PIP sweeps data for different calibration loads. (Right) The frequency tracked, or measured, by the PFP of a 7.21 MHz resonant network versus time or sample count.

The calibration of the PIP sweeps channels, magnitude and phase, are not completed at this time. The response of the instrument to a given load antenna load, Z_a, is given by:

$$\text{Magnitude} = K_1 + K_2 \, \text{Log}_{10}(\,|\,\alpha + Z_f/Z_a\,|\,)$$

$$\text{Phase} = K_3 + K_4 \, \text{Arg}(\,\alpha + Z_f/Z_a\,)$$

where K_1, K_2, K_3, K_4 are gain or offset coefficients for each of the channels and Z_f is the known feedback impedance of the preamplifier of the instrument. The constant α has a value from 0 to 1 and results from the subtracting of the RF drive signal from the measurement signal. Ideally α would be 0, resulting in the magnitude channel being a simple admittance measurement of the antenna, but α has a value of $1/11^{th}$ resulting in a coupling between the admittance magnitude and phase of the load for each of the measurement channels. The calibration of the PIP sweeps amounts to determine the value of the constants K_1, K_2, K_3, and K_4 at each of the 256 measurement frequencies. The calibration of the PIP sweep data to date has shown an absolute accuracy of only about 20% for the instrument, which is considerably off the 1% goal for the instrument. We are unsure whether this is a result of discrepancy of the applied loads due to the difference of measurement fixtures between the FPMU and the network analyzer used to determine the calibrators, or whether there is an additional oversight in our determinations of the

calibration constants. Investigation and calibration are continuing and we are optimistic that a 1% to 5% absolute impedance measurement can be demonstrated.

Summary and Conclusions

The FPMU was produced under an extremely tight 10-month development schedule but was then placed under a one-year delay for deployment due to the Columbia accident. The calibration of FPP, WLP, and NLP show that these instruments have sufficient sensitivity to achieve NASA's mission of understanding the charging physics of the ISS. The sweep (magnitude and phase) of the PIP data stream has not been successfully calibrated at this time due to instrumentation issues. The instrument could not be corrected during development due to schedule constraints when the problem was identified. A correction is expected to be possible through the calibration and data analysis software.

The video interface for data transmission is both a boon and a bane for science uses of FPMU data. The large bandwidth available allows an unprecedented amount of raw instrument data to be transmitted to the ground. The direct comparison of so many different probe types simultaneously measuring the same space plasma is a first and is sure to lend insight into both Langmuir and RF probe theory. The WLP is a unique instrument in that it is the first Langmuir probe to be flown with such a large bias sweep (100 Volts) where all of the data is being transmitted to the ground. The ability to clean the surface of WLP may make it useful for studying the contamination environment of the ISS. The video system is a bane in that the FPMU will be operated largely as a snapshot instrument. There is no way to store FPMU data onboard the ISS and then later send it down at a higher data rate. This severely limits the usefulness of the FPMU as an ionospheric diagnostic instrument. A large dataset covering years of operation will not be produced as this would require a continuous, real-time ISS video link dedicated to the FPMU.

References

1. D.E. Hastings, *A Review of Plasma Interactions with Spacecraft in Low Earth Orbit,* Journal of Geophysical Research, Journal of Geophysical Research, Vol. 100, No. A8, pages 14,457-14,483, Aug. 1, 1995.

2. Dale C. Ferguson, David B. Snyder, Ralph Carruth, *Report of the Joint Workshop of the Space Station Freedom Plasma Interactions and Effects Working Group, the Space Station Freedom Plasma Working Group, and the Space Station Freedom EMI/EMC and Electromagnetic Effects Working Group,* 1990.

3. C. Swenson, D. Thompson , C. Fish, *The Floating Potential Measurement Unit,* number AIAA-2003-1081 in 41st Aerospace Sciences Meeting and Exhibit, January 2003.

4. Steve Koontz, Marybeth Edeen, William Spetch, Thomas Keeping, Penni Dalton, *Assessment and Control of Spacecraft Charging Risks on the International Space Station,* 8th Spacecraft charging Technology Conference, Hunsvile, Alabama, October, 2003.

5. M.R. Carruth, Todd Schneider, Matt McCollum, Miria Finckenor, and Rob Suggs and Dale Ferguson and Ira Katz and Room Mikatarian, John Alred, and Courtney Pankop, *ISS and Space Environment Interactions Without Operating Plasma Contactor,* AIAA Paper #2001-0401, 2001.

6. T. Adams, D. Down, G. Murphy, K. Neal, *The Little Probe that Could! (A Story of Mission Impossible Engineering) or How to Design, Build, and Deploy Small Spacecraft in Four Months,* 15th AIAA/USU Conference on Small Satellites, Paper SSC01-IV-7, 2001.

7. T.L. Morton, J.I. Minow, *Floating Potential Probe Langmuir Probe Data Reduction Results,* AIAA Paper 2002-0936, 2002.

8. R. Mikatarian, H. Barsamian, J. Kern, S. Koontz , J.F. Roussel, *Plasma Charging of the International Space Station,* IAS paper IAC-02-T.2.05, 2002.

9. W.E. Amatucci, P.W. Schuck, D.N. Walker, P.M. Kintner, S. Powell, B. Holback, D. Leonhardt, *Contamination-free sounding rocket Langmuir Probe,* Review of Scientific Instruments, Vol. 72, No. 4, April 2001.

10. Larry H. Brace, *Langmuir Probe Measurements in the Ionosphere,* Measurement Techniques in Space Plasma: Particles, Geophysical Monograph 102, 1998.

11. Pavel Nikitin and Charles Swenson, *Impedance of a Short Dipole Antenna in a Cold Plasma,* IEEE Transactions of Antennas and Propagation, Vol. 49, No. 10, October 2001.

12. J.B. Camp, T.W. Darling, Ronald E. Brown, *Macroscopic variations of surface potentials of conductors,* American Institute of Physics, 1991.

THE DEFLECTION PLATE ANALYZER: A TECHNIQUE FOR SPACE PLASMA MEASUREMENTS UNDER HIGHLY DISTURBED CONDITIONS

Kenneth H. Wright, Jr.
NASA/MSFC, Mail Stop: SD50
National Space Science Technology Center
320 Sparkman Dr., Huntsville, AL 35805
Phone: 256-961-7648
Fax: 256-961-7216
E-mail: Kenneth.H.Wright@nasa.gov

Ken Dutton
Madison Research Corporation

Nelson Martinez
Dennis Smith
NASA/MSFC

Nobie H. Stone
SRS System Technology Group

Abstract

A technique has been developed to measure the characteristics of space plasmas under highly disturbed conditions; e.g., non-Maxwellian plasmas with strong drifting populations and plasmas contaminated by spacecraft outgassing. The present method is an extension of the capabilities of the Differential Ion Flux Probe (DIFP) to include a mass measurement that does not include either high voltage or contamination sensitive devices such as channeltron electron multipliers or microchannel plates. This reduces the complexity and expense of instrument fabrication, testing, and integration of flight hardware as compared to classical mass analyzers. The new instrument design is called the Deflection Plate Analyzer (DPA) and can deconvolve multiple ion streams and analyze each stream for ion flux intensity (density), velocity (including direction of motion), mass, and temperature (or energy distribution). The basic functionality of the DPA is discussed. The performance characteristics of a flight instrument as built for an electrodynamic tether mission, the Propulsive Small Expendable Deployer System (ProSEDS), and the instrument's role in measuring key experimental conditions are also discussed.

Introduction

The technique described in this paper is derived from the basic Differential Ion Flux Probe (DIFP) instrument. The DIFP is a scientific instrument capable of deconvolving several coincident ion streams, differing in flow direction and/or energy, and independently determining the flow direction, current density, and energy distribution of each stream.[1] The DIFP was developed for laboratory investigations in the area of plasma-body interactions [2,3,4] and later upgraded for flight on the STS-3 and Spacelab-2 shuttle missions and for flight aboard the CENTAUR-I and -II sounding rockets.[5] On the Spacelab-2 mission, the DIFP performed the

first in situ differential, vector measurements of ion streams in the disturbed, non-parallel flow produced in the wake of an ionospheric satellite.[6] A similar instrument was used to diagnose the highly disturbed plasma, such as ion reflection from a positive sheath, surrounding the tether satellite during the TSS-1 and TSS-1R missions. [7,8,9]

With our improved comprehension of the complexity of plasma processes involved in the earth's magnetosphere and the local, perturbed environment of a spacecraft, the need for sophisticated measurements and a more careful assessment of spacecraft environmental effects has become apparent. For example, it appears that spacecraft charging effects were erroneously interpreted as either a wake traversal of the satellite Ganymede or a "bubbling" state of the Jovian magnetospheric plasma.[10]   The effect of spacecraft-space plasma interactions was further emphasized by the results of the STS-3 and Spacelab-2 missions, where outgassed contaminants produced a co-orbiting neutral gas cloud that surrounded the space shuttle and significantly modified the physics of its interaction with the ionosphere.[11,12] In addition, active experiments that involve perturbing influences, such as charge particle beam injection, high power rf wave injections, and electrodynamic tethers that use plasma contactors must deal with situations that represent strong departures from the ambient conditions for which the typical plasma instrumentation is designed.

In the geophysical context, strong evidence has been presented in recent years that the "core plasma" population in the terrestrial magnetosphere results from the plasma outflows that occur in the high-latitude polar ionosphere.[13]   Spacecraft that are positioned to study these processes pass through highly disturbed, non-equilibrium plasmas and require the type of instrumentation examined herein. For example, this instrument can provide measurements of the early development of ion conics in the ionospheric plasma and is able to deconvolve these effects from those effects associated with spacecraft charging.[14,15]

Measurement Concept

The original DIFP sensor head consisted of an electrostatic deflection and collimation system mounted in front of a planar, gridded retarding potential analyzer (RPA). As shown in Figure 1, a stream of ions arriving at the entrance slit with some angle of attack, Θ, which lies in a plane perpendicular to the collimation slits (the "analysis plane"), and with some energy, E, will be deflected through the exit slit by applying a specific potential, Φ_d, of opposite polarity to the deflection plates. Note that in the original design, only the components of the ion velocity vector lying in the analysis plane could be analyzed.

At any given deflection potential, the instantaneous field of view in the analysis plane is limited by the geometry of the deflection and collimation system to approximately $\Delta\Theta$ (there is a second-order increase with Φ_d). Therefore, by sweeping Φ_d, the DIFP can differentially scan over the angular range of +/- Ω. If the ion energy is increased, a higher potential must be applied to the plates to deflect the ions the same amount for any value of Θ. Therefore, the electrostatic deflection and collimation system can be viewed as an energy-angle filter which operates such that at any given deflection potential, Φ_d, the energy and angle of the admissible ion must satisfy a known relation, $f(\Theta, E) = \Phi_d$, where the function f is a characteristic of the deflection and collimation system design.

After passing through the deflection and collimation system, the ions enter the Retarding Potential Analyzer (RPA) section at an angle α, which is much smaller than Θ. Their energy, due to the velocity component normal to the grids, is proportional to the potential at which the ions are retarded and can, therefore, be determined by sweeping the retarding potential, Φ_r. The measured values of Φ_d and Φ_r then provide two known variables that can be used to determine the two unknown characteristics of the ions, Θ and E.

Functional Description of the New Technique

The new method is basically a modified and enhanced version of the previous DIFP. The measurement capabilities are expanded to include (1) all three components of the ion velocity vector and (2) ion mass analysis. Figure 2 shows a functional schematic of the new design, the Deflection Plate Analyzer (DPA).

The ion optics from the earlier design remain divided into an angle selection system and an energy (plus mass) system. However, to resolve all three velocity components, the angle selection system has been modified to include of two pairs of orthogonal deflection plates beneath the entrance aperture. The lower panel in Figure 2 shows the angle selection system as viewed from the top along the instrument axis. By sweeping an applied voltage to the pair of deflection plates labeled 1, with polarity indicated, the ion stream moves along the X-direction until the ion stream hits the angle locator bar. At this point the voltage on deflection pair 1 is held constant (Φ_X) while the voltage applied to deflection pair 2 is swept, with the indicated polarity. The ion stream moves along the locator bar in the Y-direction until the hole is encountered, thereby deflecting the ion stream down the sensor axis. At this point, the voltage on deflection pair 2 is held constant (Φ_Y).

In the energy/mass analysis section, the grids from the earlier design have been replaced by a series of four deflection plates. For a unique voltage $\Phi_{E,M}$ and polarity between the plates, as shown in the top panel of Figure 2, the ion stream will execute a "dog-leg" path. Because the ions, in this section, travel parallel to the instrument axis (i.e., there is no angular variation), the voltage required to deflect the ions, $\Phi_{E,M}$, is directly proportional to the ion drift energy, E; i.e. $\Phi_{E,M} = \beta E$, where β is proportional to the deflection angle. For a typical design, the deflection angle is approximately 15° and $\beta \approx 0.2 - 0.3$. For the RPA design of the DIFP, $\beta = 1$ since the ions had to be completed retarded at some point. In the Deflection Plate Analyzer, ions are merely deflected through a curved path, therefore, requiring less voltage, which increases the energy range for a given voltage.

If the bias voltage $\Phi_{E,M}$ is modulated, the ion stream can be "gated" between the plates to provide a time-of-flight measurement for ion velocity and, therefore, mass. The modulation will cause the stream to execute either of the two trajectories shown in the top panel of Figure 2. Summing the two alternating paths increases the instrument's throughput. A unique frequency can be found that allows the ion stream to pass through the instrument and reach the collector. Time-of-flight (and, therefore, ionic mass) is inversely proportion to this frequency.

The operation of the DPA provides the following six known measurement values: collected ion current, angle deflection voltage Φ_X, angle deflection voltage Φ_Y, energy deflection voltage

Φ_E, width of energy response curve, and modulation frequency. These values can be used to solve for the six unknown properties of each ion component of the plasma: ion stream density, angles-of-incidence (azimuth θ_X and pitch θ_Y relative to the instrument normal) and ionic drift energy, temperature, and mass.

An early flight version of the DPA was built and tested as part of the Plasma Experiment Satellite Test that was flown as part of the Joint Air Force Weber State Satellite in January 2000. A malfunction on the satellite prevented the power up of the experiment. However, the information gained in development of a flight version of the instrument lead to design changes for an improved flight instrument described below.

Flight Instrument Development

A potential opportunity for flight validation of the DPA technique arose on the Propulsive Small Expendable Deployer System (ProSEDS) mission. ProSEDS is designed to provide an on-orbit demonstration of the propulsion capabilities of electrodynamic tethers in space.[16] The motion of the 5-km conducting bare tether through the magnetized ionospheric plasma will transform orbital kinetic energy into electrical power resulting in the collection of multi-Amp currents. This loss of orbital energy, due to the decelerating force produced by the interaction of the tether current with the Earth's magnetic field, will lower the orbit much faster than what results from aerodynamic drag alone. ProSEDS is a secondary payload on a Delta-II expendable rocket.

The DPA provides three critical measurements of the experimental conditions during various tether circuit operational sequences. (1) It will provide a measurement of the background ionospheric plasma density. (2) It will provide a reliable measure of the potential between the Delta stage and the surrounding ionospheric plasma. This plasma sheath results from the operation of a hollow cathode plasma contactor as it returns the tether current to the ionosphere. Determination of the sheath potential is accomplished by measuring the energy of the ions accelerated into the sensor by this potential. The geometry and size of the Delta stage's plasma sheath, therefore, do not effect the measurement. (3) The emission of ionized Xenon gas by the plasma contactor will contaminate the local ionospheric plasma. The DPA, with its mass analysis capability, will measure the composition of the environmental plasma. The presence or absence of Xenon ions will be determined and used to access the quality of the ambient plasma measurements.

Note: In published ProSEDS papers and internal documentation, this instrument is denoted as the Differential Ion Flux Probe w/Mass analysis (DIFPM). Our preferred name for the instrument is the DPA, as used in this paper.

Ion optics

Figure 3 illustrates the packaging of the DPA ion optics stack. The housing consists of three parts that contain the five deflection plates necessary for control of the ion trajectory through the stack. Each deflection plate is fabricated from a ceramic. A gold paste is "fired" onto the surface to provide the necessary conductive areas; i.e., ground planes, signal traces, and

electrodes. The dimension of the entrance aperture is 0.050 in by 0.050 in. The overall dimensions of the cylindrical ion optics stack are roughly 1.5 in diameter by 2.5 in long. Attached to the bottom of the stack (not shown) is a housing containing two electrometer circuits (including pre-amps) that serve the collector plate and the angle locator bar. Each electrometer is sensitive down to the pico-Amp current range and has two gain ranges. The throughput for the ion optics stack is 18%. The ion optics stack and the electrometer package constitute the DPA sensor. For comparison, the throughput value for the DIFP sensor used on the Spacelab-2 and TSS missions was 35%. The increased functionality of the DPA was achieved at a decrease by a factor of 2 in throughput.

Operational control

A separate electronics box provides the sweep voltages and electrometer control signals to the sensor. The sensor(s) plus the electronics box comprise the instrument package. The power and data interface is also through this electronics box. The operational control of the different measurement sequences of the sensor is accomplished through the use of two micro-controller integrated circuit chips. These chips have the capability to be reprogrammed in real-time which allows for a drastically easier effort in fine-tuning the control software during vacuum plasma tests of the instrument.

The operation of the DPA is a specific application of the measurement sequence described in the previous section. Initially, a 128-point bi-polar voltage sweep in X is performed. The voltage locations (Φ_X) for up to 10 current peaks are stored. These are ordered with respect to decreasing current (high to low). The number ten is chosen to accommodate for noise, i.e., false positives. The current measured for the X-voltage sweep is the sum of the collector and locator bar responses. Current peak detection is performed via software. After the X-sweep and current peak ordering is completed, further analysis is performed on the three highest current peaks. For each current peak, a 128-point bi-polar voltage sweep in Y is performed. The current monitored in this case is only from the collector. The voltage location (Φ_Y) at the current peak is stored. The voltage pair (Φ_X,Φ_Y) is applied to the entrance deflection plates and held constant while a 99-point bi-polar voltage is swept for the energy analysis (E-sweep). The voltage location (Φ_E) for the current peak is stored and used for the mass analysis. The Φ_E voltage serves as the amplitude of a square wave for a 99-point frequency sweep from 100kHz to 2 MHz (M-sweep). The frequency values (F_M) for up to four current peaks are stored. Figure 4 shows the response for each of the four operations described above.

To minimize the size of the telemetry, the voltage-current (V,I) response for each operation is not stored. The nominal telemetry frame consists of (Φ_X,I) for each peak in the X-sweep; (Φ_Y,I) for the peak in the Y-sweep; all 99 I-values for the E-sweep; and (F_M,I) for the peaks in the M-sweep. At regular intervals, a "calibration" telemetry frame is returned. This frame consists of the information in the nominal telemetry frame plus the (V,I) values for the X-sweep, Y-sweep, and M-sweep.

The DPA instrument can operate in a single, automated analysis mode that will determine all of the plasma properties for several ion streams. The time for analysis of a single ion stream is about one second. Obviously, if a faster response is needed the number of points in the various

sweeps can be reduced. Depending on the science objective, the proper trade can be made between speed and resolution (voltage range and voltage step size).

Calibration data

Functional testing and calibration of the DPA was performed in the Space Plasma Physics Laboratory of the Space Science Department at the National Space Science and Technology Center. The test facility is comprised of a Kaufman ion thruster attached to a 4 ft x 8 ft vacuum chamber that is evacuated with an oil-free pumping system (both roughing and high-vacuum). The system operating pressure during plasma testing was $7\text{-}8 \times 10^{-6}$ Torr. A mounting table attached to a mechanical, rotating feed through allowed for the angular characteristics of the DPA to be determined. The ion component of the plasma stream has typical properties of 10s of eV drift energy with a temperature in the drift direction of 300 K – 500 K.

Figure 5 shows the calibration data for the angle, energy, and mass (velocity) operations. The equations used to derive the various plasma quantities are given by:

(1) Angle: θ_X, θ_Y (deg) $= 30\Phi + 0.48\sin^{-1}(0.8\Phi)$, where $\Phi \equiv \varphi_{X,Y}/E$

(2) Angular sensitivity: for $\theta_{X,Y}$ (deg) $<= 17°$: $g = \exp(-2.63\times10^{-3}\theta^2 + 1.0\times10^{-6}\theta^4)$
    for θ (deg) $> 17°$: $g = 0.0441\cos^2\theta + 0.565\cos^4\theta$

(3) Energy: $E(eV) = 4.0\varphi_E(V)$

(4) Velocity: $V(km/s) = [F(kHz) +10.5]/51.7$, where $F \equiv$ frequency @ peak

(5) Mass: $M(amu) = 193[E(eV)/V^2 (km/s)]$

(6) Density: $N(\#/cm^{-3}) = 2.04\times10^{16} [I_0(Amps) / V(km/s)]$, where
    $I_0(Amps) = I_Y(Amps) /[g\,(\theta_X)*g\,(\theta_Y)]$

Using the above equations and other instrument parameters, the performance characteristics for the present DPA instrument can be stated as - ambient ionospheric density: 4.4×10^3 - 3.9×10^6 cm^{-3}; energy range: up to 100 eV; ion flow direction: +/- 60 deg for both X- and Y-directions; and deconvolve multiple streams at normal incidence with 3 deg resolution. For Xenon neutrals from the hollow cathode that ionize via the pick-up process, the DPA can diagnose them over the velocity range $0.35V_{orb} – 1.55V_{orb}$ where $V_{orb} = 7.8$ km/s. Recall the pick-up process produces ions with velocities ranging from 0 to $2V_{orb}$.

Two-stream data

To illustrate the multiple stream diagnosis capability of the DPA, data from a test set-up where a biased cylinder was placed in front of the sensor was obtained. This is shown in Figure 6. The cylinder was biased to ~ -18V. The X-sweep clearly identifies two streams. For each of these streams the Y-, E-, and M-Sweep data is shown. Since the energy and mass of each stream are equal by definition, the curves from each of these sweeps overlay each other. Differences are

due to differing trajectory paths through the ion optics. The asymmetry of the current in the Y-sweep is due to the physical details of the aperture in the angle locator bar (see Figure 2). Also of note is that sometimes the peak value of current in the Y-sweep does not equal the peak current value of the middle peak in the E-sweep. This effect can introduce second order corrections to the density. The reasons for the difference lies in the Φ_Y sweep and the dwell time for the voltage step versus the fixed Φ_Y and dwell time for the Φ_E voltage step.

ProSEDS system test

The DPA participated in a system test under vacuum to verify proper functioning of the complete system to the fullest extent possible. A simulated emf could be imposed on the system resulting in current flow in the circuit. The hollow cathode was operated thereby emitting a Xenon plasma. The vacuum chamber had no background plasma so closure of the hollow cathode current was accomplished via an anode plate located near the orifice of the hollow cathode. The DPA sensors were located approximately a meter away from the plasma column and oriented such that any Xe^+ ions emitted perpendicular to the column could be detected. Figure 7a shows the three sensors mounted for the test. The various operational sequences of the tether circuit were exercised which resulted in various levels of Xe^+ ion flux emitted from the plasma column. Data from the middle sensor in Figure 7a of the Xe^+ ions for two circuit configuration are shown in Figure 7b. In the shunt mode, a 15-ohm resistor is placed in the circuit. In the second mode, a load resistor of 2200-ohm is placed in the circuit while the emf remains constant. More of the emf is used to support the voltage drop across the load resistor resulting in less current and hence, less ionization in the plasma column between the hollow cathode and the anode plate.

Summary

A new technique for measuring disturbed plasmas has been discussed. The technique is an extension of a method began by our group in the 1970's to diagnose the complex plasma behavior of the wakes of bodies in flowing plasmas. A new flight instrument has been developed and is quite rugged, judged by the fact that it has survived severe environmental testing – random vibration levels of 27.5 g rms and a temperature range of –40C to 85C. The capabilities of the instrument are well suited to active spacecraft experiments and electrodynamic tethers (such as ProSEDS) – in particular its ability to distinguish between the ambient ionospheric plasma and the spacecraft generated plasma. The DPA angle discrimination ability makes it a good candidate instrument for use both in the high latitude ionosphere and for inferring **ExB** drifts from ram deviated flows (in the case of high angular resolution). Future enhancements to the instrument involve (1) miniaturizing the control electronics packaging such that it can be contained in a small volume at the end of ion optics stack; and (2) improving the resolution at low energy by removing the central peak in the energy sweep response.

Figure 1. DIFP functional schematic showing a cut through the instrument in a plane normal to the deflection system entrance aperture. [1]
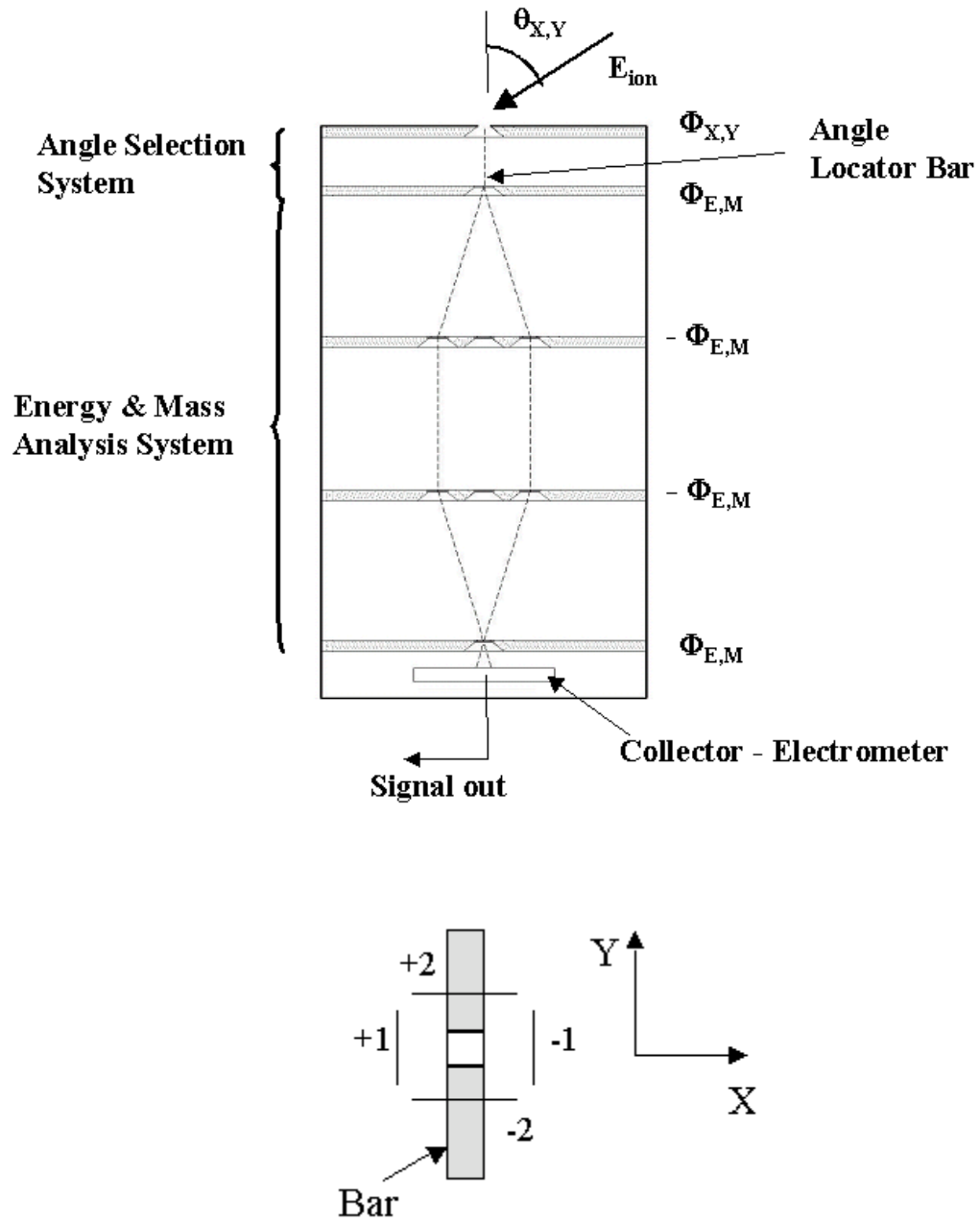
Figure 2. DPA functional schematic. The upper panel shows a cut through the instrument in a plane normal to the entrance aperture. The lower panel shows an exaggerated view of the angle locator bar and the projection of the deflection plates of the entrance aperture.
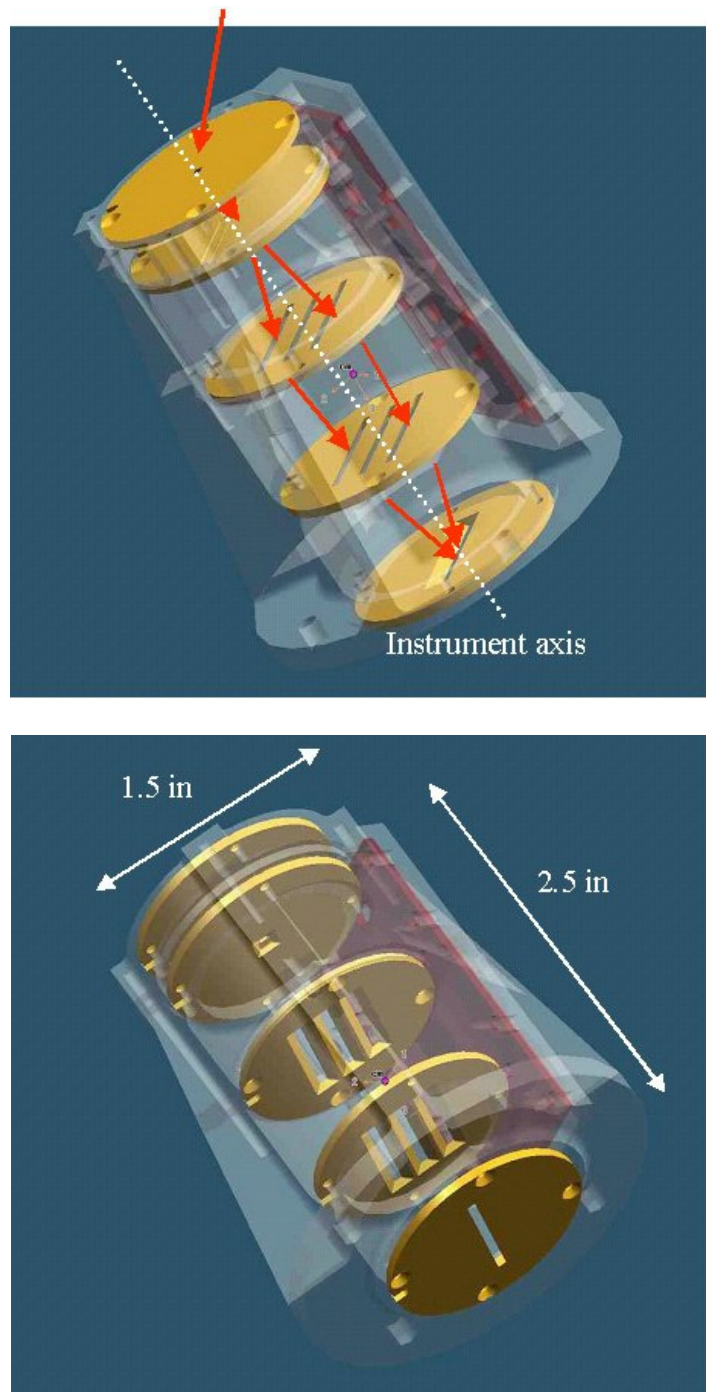
Figure 3. DPA ion optics stack. Upper panel: ion trajectory into and through instrument. Lower panel: view illustrating the various apertures, biased surfaces and overall dimensions.
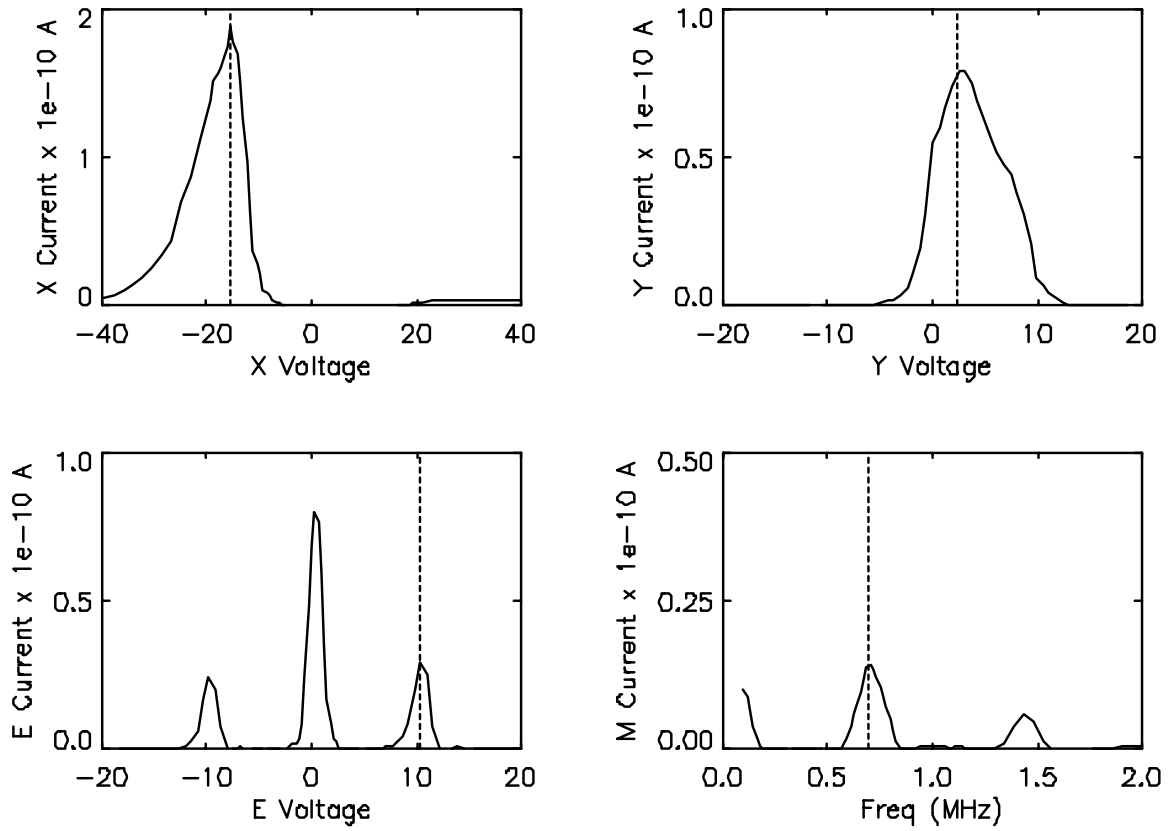
Figure 4. Instrument response for the X-, Y-, E-, and M-sweeps. For the X-sweep, the current plotted is the sum of both the bar and the collector current. For the other sweeps, only the collector current is analyzed. The vertical dashed line in each panel indicates where the embedded software has determined the current peak location.
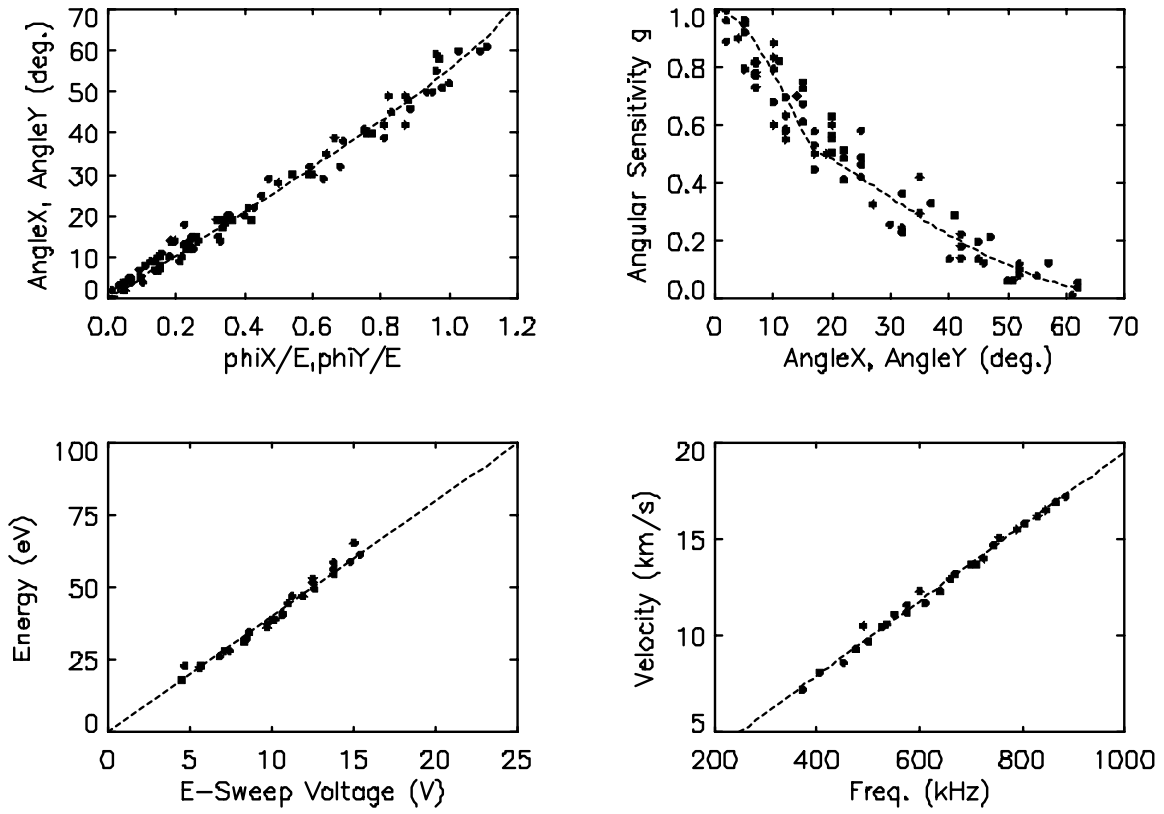
Figure 5. Calibration data for angle, energy and velocity from the DPA instrument. Dashed lines are equations (1) – (4).
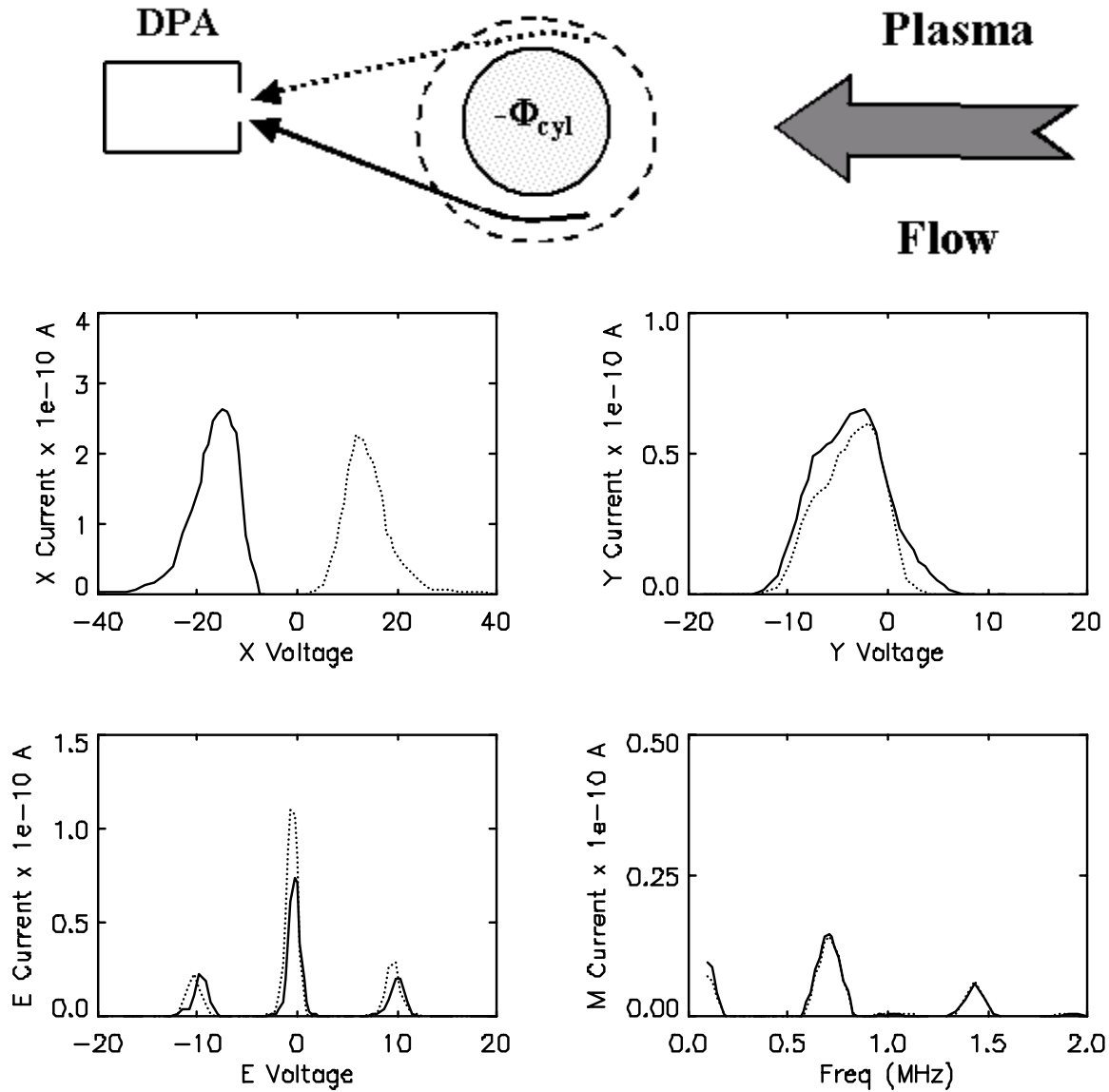
Figure 6. Two stream data. Upper panel shows the experiment setup with plasma impinging on a negatively biased cylinder and deflection of the ion stream by the sheath around the cylinder. The plots in the lower part of the figure show the X-, Y-, E-, and M-sweep analysis of the two streams.
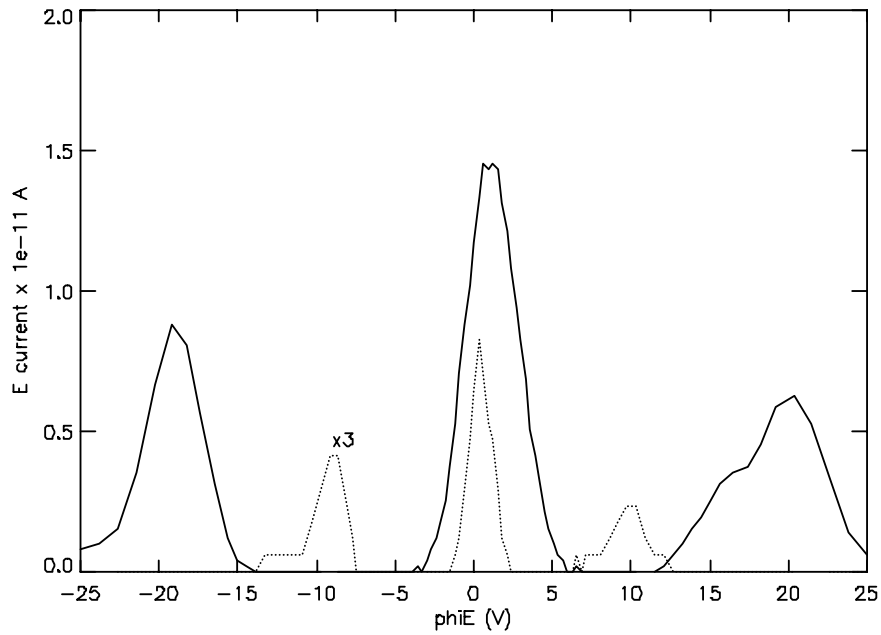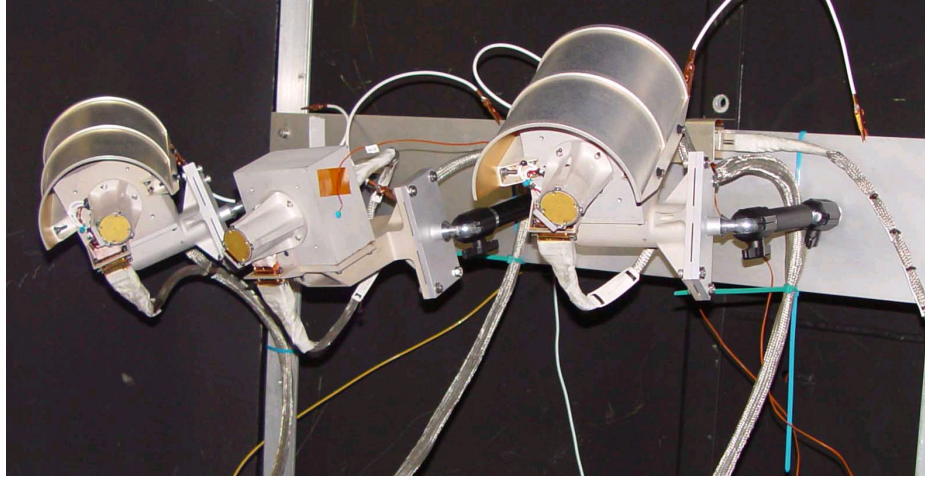
Figure 7. Top panel: view of sensor set-up for system test. Bottom panel: response of DPA energy analysis for two system operating modes. Solid line is for shunt mode and dashed line for load resistor mode. In the shunt mode, a stream of Xe^+ ions at density 2×10^5 cm^{-3} and energy 77 eV were observed. In the load resistor mode, a stream of Xe^+ ions at density 1×10^5 cm^{-3} and energy 37 eV were observed.

References

1. Stone, N. H., Technique for measuring the differential ion flux vector, Rev. Sci. Instru., 48, 1458, 1977.

2. Stone, N. H., The plasma wake of mesosonic conducting bodies. Part 1. An experimental parametric study of ion focusing by the plasma sheath, J. Plasma Phys., 25, 351, 1981.

3. Wright, K. H., Jr., N. H. Stone, and U. Samir, A study of plasma expansion phenomena in laboratory generated plasma wakes: Preliminary results, J. Plasma Phys., 33, 71, 1985.

4. Wright, K. H., Jr., A study of single and binary ion plasma expansion into laboratory generated plasma wakes, NASA Contractor Report 4125, February, 1988.

5. Stone, N. H., B. J. Lewter, W. L. Chisholm, and K. H. Wright, Jr., Instrument for differential ion flux vector measurements on Spacelab 2, Rev. Sci. Instrum., 56, 1897, 1985.

6. Stone, N. H., K. H. Wright, Jr., U. Samir, and K. S. Hwang, On the expansion of ionospheric plasma into the near wake of the space shuttle Orbiter, Geophys. Res. Lett., 15, 1169, 1988.

7. Stone, N. H., K. H. Wright, Jr., J. D. Winningham, J. Biard, C. Gurgiolo, A technical description of the TSS-1 ROPE investigation, Il Nuovo Cimento, 17C, 85, 1994.

8. Wright, K. H., Jr., N. H. Stone, J. Sorensen, J. D. Winningham, C. Gurgiolo, Observations of reflected ions and plasma turbulence for satellite potentials greater than the ion ram energy, Geophys. Res. Lett., 25, 417, 1998.

9. Stone, N. H., W. J. Raitt, and K. H. Wright, Jr., The TSS-1R electrodynamic tether experiment: Scientific and technological results, Adv. Space Res., 24, 1037, 1999.

10. Khurana, K. K., M. G. Kivelson, T. P. Armstrong, and R. J. Walker, Voids in Jovian magnetosphere revisited: Evidence of spacecraft charging, J. Geophys. Res., 92, 13399, 1987.

11. Pickett, J. S., G. B. Murphy, W. S. Kurth, C. K. Goertz, and S. D. Shawhan, Effects of chemical releases by the STS-3 Orbiter on the ionosphere, J. Geophys. Res., 90, 3487, 1985.

12. Paterson, W. R. and L. A. Frank, Hot ion plasmas from the cloud of neutral gases surrounding the space shuttle, J. Geophys. Res., 94, 3721, 1989.

13. Moore, T .E, Origins of magnetospheric plasma, U. S. Natl. Rep. Int. Union Geod. Geophys. 1987-1990, Rev. Geophys., 29, 1039, 1991.

14. Stone, N. H., U. Samir, K. H. Wright, Jr., and K. S. Hwang, Comment on "Ram ion scattering by space shuttle VxB induced differential charging" by I. Katz and V. A. Davis, J. Geophys. Res., 93, 4143, 1988.

15. Katz, I. and V. A. Davis, Reply, J. Geophys. Res., 93, 4149, 1988.

16. Johnson, L., R. D. Estes, E. Lorenzini, M. Martinez-Sanchez, and J. Sanmartin, Propulsive Small Expendable Deployer System Experiment, J. Spacecr. Rockets, 37, 173, 2000.

NEARLY EIGHT YEARS OF SOHO OBSERVATIONS – SOME HIGHLIGHTS

P. Brekke
RSSD, European Space Agency
NASA GSFC, Greenbelt, MD 20771, USA
Phone: (301) 286-6983
Fax: (216) 286-0264
E-mail: pbrekke@esa.nascom.nasa.gov

B. Fleck
RSSD, European Space Agency

Abstract

Since its launch on 2 December 1995, the Solar and Heliospheric Observatory (SOHO) has provided an unparalleled breadth and depth of information about the Sun, from its interior, through the hot and dynamic atmosphere, and out to the solar wind. SOHO has continued to revolutionize our understanding of the Sun with its 24 hour per day observations of our daylight star. The main objectives of the SOHO mission was to study the structure and dynamics of the solar interior, the heating of the solar corona, and the acceleration of the solar wind. Five years later, science teams from around the world have made great strides toward answering these "big three" questions. At the same time, SOHO's easily accessible, spectacular data and basic science results have captured the imagination of the space science community and the general public alike. This presentation will summarize some of the scientific highlights and illustrate how SOHO is monitoring the energy output from the Sun and how it acts as s watchdog for solar storms. It will also summarize some of the space weather effects on the SOHO spacecraft itself.

The SOHO Spacecraft

The SOHO mission (Domingo, Fleck & Poland, 1995) is a major element of the International Solar Terrestrial Programme (ISTP), and, together with Cluster, forms the Solar Terrestrial Science Programme (STSP), the first cornerstone in ESA's long-term science programme 'Horizons 2000'. ESA was responsible for the spacecraft's procurement, integration and testing. It was built in Europe by an industry team led by Matra Marconi Space (now called Astrium). Weighing in at 1,850 kg, the SOHO spacecraft measures about 9.5 m across with its solar panels extended and is 4.3 m high. NASA provided the launcher, launch services and ground-segment system and is responsible for in-flight operations. Mission operations are conducted from NASA/Goddard Space Flight Center (GSFC).

SOHO was launched by an Atlas II-AS from Cape Canaveral on 2 December 1995 and was inserted into its halo orbit around the L1 Lagrangian point on 14 February 1996, six weeks ahead of schedule. Commissioning of the spacecraft and the scientific payload was completed by the end of March 1996. The launch was so accurate and the orbital manoeuvres were so efficient that enough fuel remains on board to maintain the halo orbit for several decades, many times the lifetime originally foreseen. An extension of the SOHO mission for a period of five years beyond its nominal mission duration (2 years), i.e. until March 2003, was approved in 1997 by ESA's

Science Programme Committee (SPC). A second extension of another four years, i.e. until March 2007, was granted by the SPC in 2002. This will allow SOHO to cover a complete 11-year solar cycle.

SOHO has a unique mode of operations, with a "live" display of data on the scientists' workstations at the SOHO Experimenters' Operations Facility (EOF) at NASA/Goddard Space Flight Center, where the scientists can command their instruments in real-time, directly from their workstations.

The Solar Interior

Just as seismology reveals the Earth's interior by studying earthquake waves, solar physicists probe inside the Sun using a technique called "helioseismology" (e.g. Christensen-Dalsgaard, 2002). The oscillations detectable at the visible surface are due to sound waves reverberating through the Sun's interior, providing information about the structure and dynamics of the regions they pass through.

Data obtained with the Michelson Doppler Imager (MDI) revealed "zonal bands" in the northern and southern hemispheres where currents flow at different speeds (~ 5 m/s) relative to each other (Schou et al., 1998, Schou, 1999). The zonal bands were found to migrate towards the equator with time, and there are indications that they penetrate down to the bottom of the convection zone (Vorontsov et al., 2002).
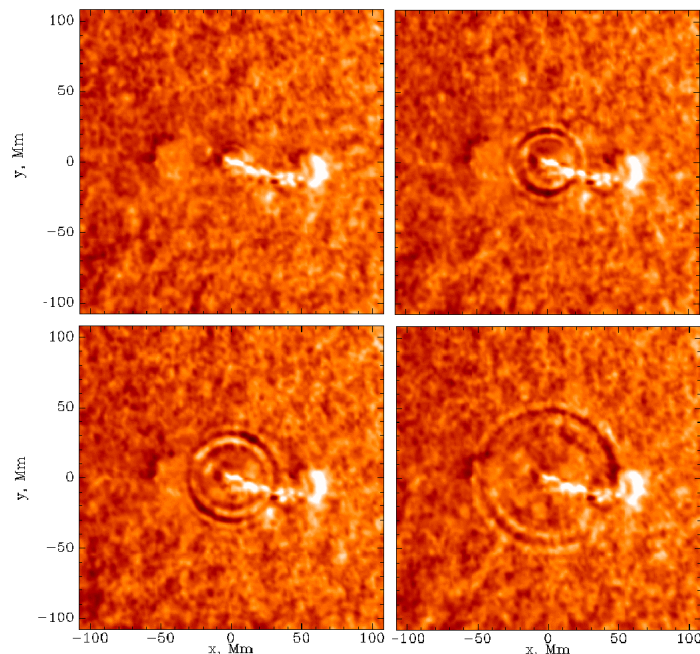
Figure 1. Seismic waves ('sun quake') produced by a solar flare on 9 July 1996. (From Kosovichev & Zharkova, 1998)

MDI has also made the first observations of seismic waves from a solar flare (Kosovichev & Zharkova, 1998), opening up possibilities of studying both flares and the solar interior. During

the impulsive phase of the X2.6 class flare of 9 July 1996 a high-energy electron beam caused an explosive evaporation of chromospheric plasma at supersonic velocities. The upward motion was balanced by a downward recoil in the lower chromosphere which excited propagating waves in the solar interior. On the surface the outgoing circular flare waves resembled ripples from a pebble thrown into a pond (Figure 1). The seismic wave propagated to at least 120,000 km from the flare epicenter with an average speed of about 50 km/s on the solar surface.

Currents of gas deep inside the Sun appear to pulsate like the blood in human arteries, speeding and slackening every 16 months (Howe et al., 2000). This result comes from combined observations by MDI and GONG (Global Oscillations Network Group), a worldwide chain of ground stations. The observed variations in the flows of gas occur about 220,000 km beneath the visible surface - almost a third of the way down to the centre of the Sun. Here is the supposed dynamo region, where the turbulent outer region, the convection zone, meets the more orderly interior, the radiative zone. In this region, called the tachocline, the rotation speed of the gas changes abruptly from differential rotation to uniform rotation in the radiation interior. Near the equator the outer layers rotate faster than the inner layers. At mid-latitudes and near the poles, the situation is reversed (Figure 2).
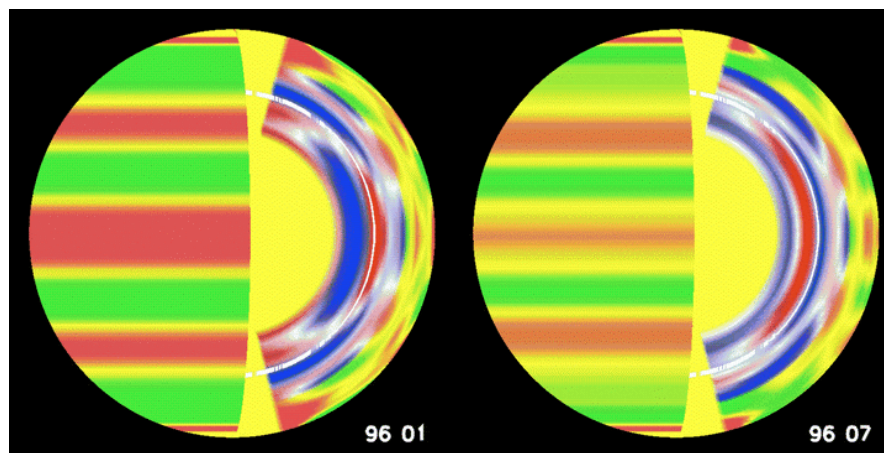
Figure 2. Currents of gas deep inside the Sun pulsate like the blood in human arteries, speeding and slackening every 16 months. Rotation rates near the bottom of the convection zone (white line), the level of the suspected dynamo, change markedly over six months. Faster/slower rates are shown in red/blue. Meanwhile near the surface (seen plainly on the left of each cutaway) bands of faster (red) and slower (green) rotation move towards the equator.

The new results show that the contrast in speed between layers above and below the supposed dynamo region can change by 20 per cent in six months. When the lower gas speeds up, the upper gas slows down, and vice versa. The observations indicate a heartbeat of the Sun at one pulse per 15-16 months in equatorial regions, and perhaps faster at higher latitudes (Figure 3). This result is quite surprising, considering the much longer 11-year period observed in the sunspot cycle, thought to be governed by the same dynamo region. The amplitude of this tachocline oscillation has been greatly reduced since the Sun approached its maximum activity around 2000 (Howe, 2003) and it will be interesting to see if and when it will appear again.
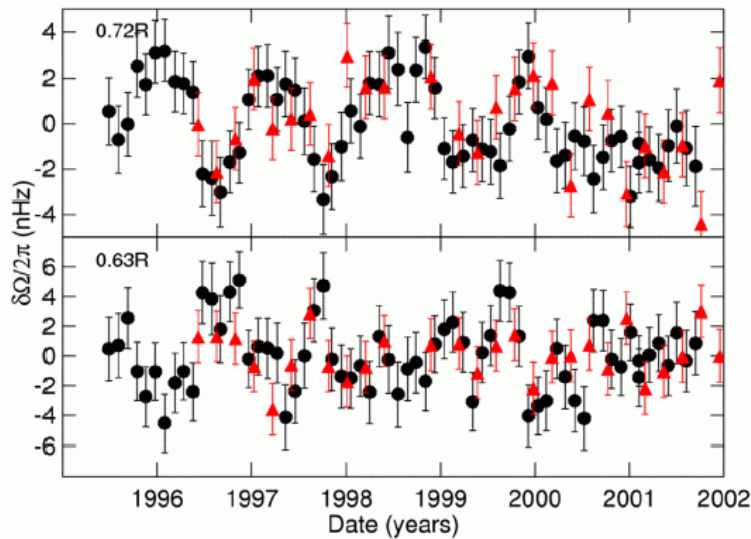
Figure 3. Variation with time of the difference of the rotation rate from the temporal mean at 0.72 R located above the tachocline and at 0.63 R below it, both sampling speeding up and slowing down in the equatorial region. Results obtained from MDI data for two different inversions are shown with red symbols, those from GONG with black symbols (Howe 2003).

The availability of high spatial resolution data from MDI opened a new window to look inside and even right through the Sun. "Time distance helioseismology" or "solar tomography" (Duvall et al., 1993), is a new field in solar research which is developing primarily with MDI data. It is one of the most exciting and most promising techniques for probing the 3-D structure and flows beneath the solar surface and offers the possibility of studying the birth and evolution of active regions below the Sun's surface and the detection of sunspots on the invisible far side of the Sun. Since spring 2001 the SOHO/MDI team has been making images from the far side of the Sun available routinely to everyone, including the forecasters of space weather. Speeded up by the intense magnetic fields associated with sunspot regions, sound waves reflected from far-side sunspots arrive a few seconds early at he Sun's near-side face, compared with sound waves from sunspot-free regions (Lindsey & Braun, 2000).

A longstanding problem in solar physics has been to explain how sunspots can last for several weeks without flying apart. Theories have been developed that require inward flows of material that stabilise the structure. The problem: Material often appears to be flowing out of sunspots! 'Time distance helioseismology' has helped shed light on this problem: Just below the surface, the required inward flows are present. We now have the first clear picture of what lies beneath sunspots, the enigmatic, planet-sized dark areas on the surface of the Sun; and have peered inside the Sun to see swirling flows of plasma that create a self-reinforcing cycle which holds a sunspot together (Zhao et al., 2001; Figure 4).
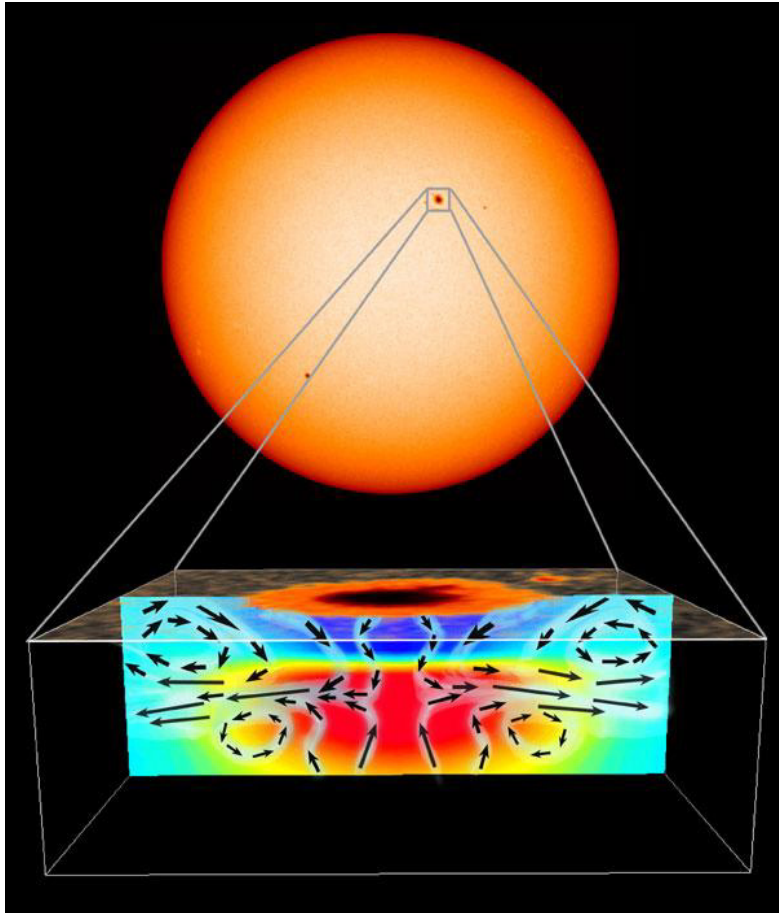
Figure 4. SOHO's MDI reveals subsurface inflows beneath a sunspot. A cross-section going down 12000 kilometres below the surface of the Sun in the vicinity of a sunspot shows a convergence of cool gas (blue) near the surface. This inflow concentrates the magnetic field and suppresses hot gas (red) trying to rise from below. The analysis also revealed that sunspots are surprisingly shallow, changing from cooler to hotter than the surroundings only 5000 km below the surface.

Another SOHO instrument, called SWAN (short for Solar Wind Anisotropies), is also capable of detecting active regions on the far side of the Sun (Bertaux et al., 2000). Mapping the whole sky in ultraviolet light, it sees a huge cloud of interstellar hydrogen that bathes the entire Solar System and interacts with the solar wind (Figure 5). Bertaux et al. (2000) have found that the hydrogen cloud beyond the Sunglows more strongly in the presence of active regions on the far side of the Sun compared to when there are no active regions. The enhanced emission from an active region on the far side of the Sun moves across the sky like a lighthouse beam as the Sun rotates.
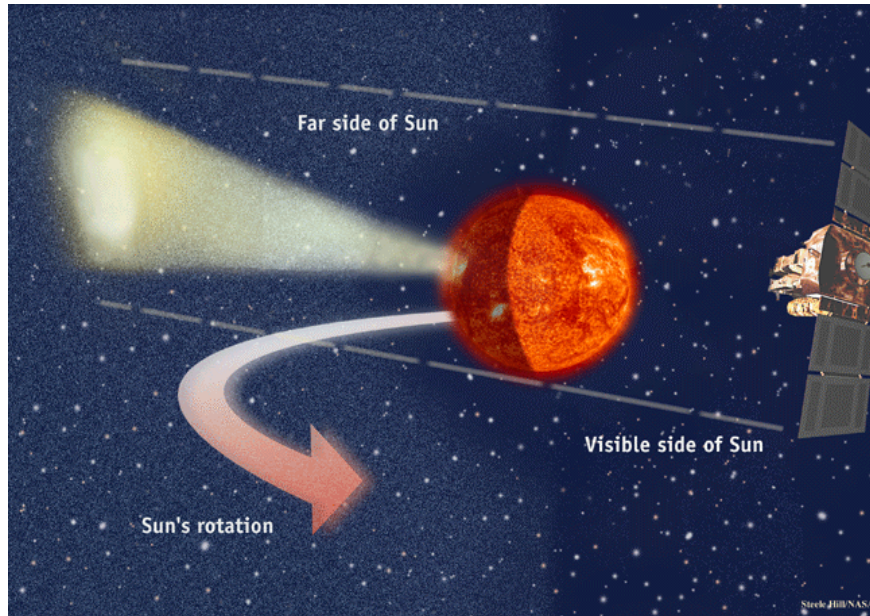
Figure 5. Schematic illustrating SWAN's capabilities of detecting active regions on the far side of the Sun.

The Dynamic Solar Atmosphere

Observations from SOHO and TRACE have replaced the previous view of a quiescent solar atmosphere with a new, extremely dynamic picture. The solar atmosphere undergoes continuouschange on every scale from structures that affects the entire Sun down to tiny loops at the instrument resolution limits. The combination of high spatial, spectral and temporal observations has made it possible to derive three dimensional images of the emission and velocity structures of solar features. These new observations have significantly contributed to a better understanding of the structure of the solar atmosphere. However, at the same time new and interesting challenges arise to interpret and model this highly dynamic and time variable atmosphere.

One of the most puzzling problems in solar physics is the average net redshift of emission lines in the solar transition region. During the last decades, this phenomenon has been observed with several UV instruments with different spatial resolution. Several investigations using precise observations from SUMER have revisited this problem and extended this work to include lines formed at higher temperatures. Peter and Judge (1999) found that the hotter lines show blueshifts.

These recent results suggest that the upper transition region and lower corona appear blueshifted in the quiet Sun, with a steep transition from red- to blue-shifts above $5 \ 10^5$ K. This transition from net redshifts to blueshifts is significant because it has major implications for the transition region and solar wind modeling as well as for our understanding of the structure of the solar atmosphere. The results also motivate new laboratory measurements of the wavelengths of hotter lines since the choice of rest wavelengths used to derive these results are crucial for the interpretation of the data.

Active regions have been extensively observed with the EUV instruments on SOHO and recently also by TRACE. In particular, observations of active regions on the solar limb have revealed that loops emitting at transition region temperatures are highly dynamic (e.g. Kjeldseth-Moe and Brekke 1998). Furthermore, large Doppler shifts in active region cool loops (i.e. T ≤ 0.5 MK) have been reported with line-of-sight velocities reaching ±100 km s^{-1}. This is a result that challenges existing loop models. In some active regions plasma has been observed to be ejected from the surface. Spike-like jets of material have been observed as well as larger extended ejections of plasma.

Acceleration of the Solar Wind

Coronal hole outflow velocity maps obtained with the SUMER instrument in the Ne VIII emission line at 770Å show a clear relationship between coronal hole outflow velocity and the chromospheric network structure (Figure 6), with the largest outflow velocities occurring along network boundaries and at the intersection of network boundaries (Hassler et al., 1999). This can be considered the first direct spectroscopic determination of the source regions of the fast solar wind in coronal holes.
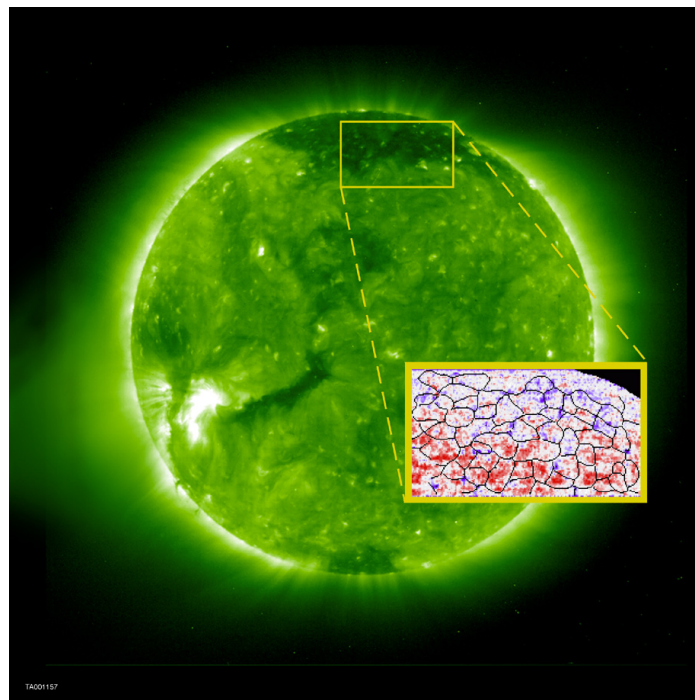
Figure 6. EIT full sun image taken in the emission line of Fe XII 195A, revealing gas at 1.5 million degrees. The "zoomed-in" or "close-up" region shows a Doppler velocity map of plasma at about 630,000 K at the base of the corona, as recorded by SUMER in the Ne VIII emission line at 770Ă. Blue represents blue shifts or outflows and red represents red shifts or downflows. The blue regions are inside a coronal hole, or open magnetic field region, where the high speed solar wind is accelerated. Superposed are the edges of "honey-comb" shaped patterns of magnetic fields at the surface of the Sun, where the strongest flows (dark blue) occur.

Proton and O VI outflow velocities in coronal holes have been measured by UVCS using the Doppler dimming method (Kohl et al., 1997; Cranmer et al., 1999). The OVI outflow velocity was found to be significantly higher than the proton velocity, with a very steep increase between 1.5 and 2.5 $R_\odot$, reaching outflow velocities of 300 km/s at around 2 $R_\odot$. While the hydrogen outflow velocities are still consistent with some conventional theoretical models for polar wind acceleration, the higher oxygen flow speeds cannot be explained by these models. A possible explanation is offered by the dissipation of high-frequency Alfvén waves via gyroresonance with ion cyclotron Larmor motions, which can heat and accelerate ions differently depending on their charge and mass.

Comet Observations

Other instruments on SOHO have proved to be the most prolific comet finders in the history of astronomy. Most of the more than 660 SOHO comet discoveries were made with the Large Angle Spectrometric Coronograph (LASCO) instrument, a set of coronagraphs that view the space around the Sun out to 20 million kilometers (30 $R_\odot$), while blotting out the bright solar disk with occulting disks.
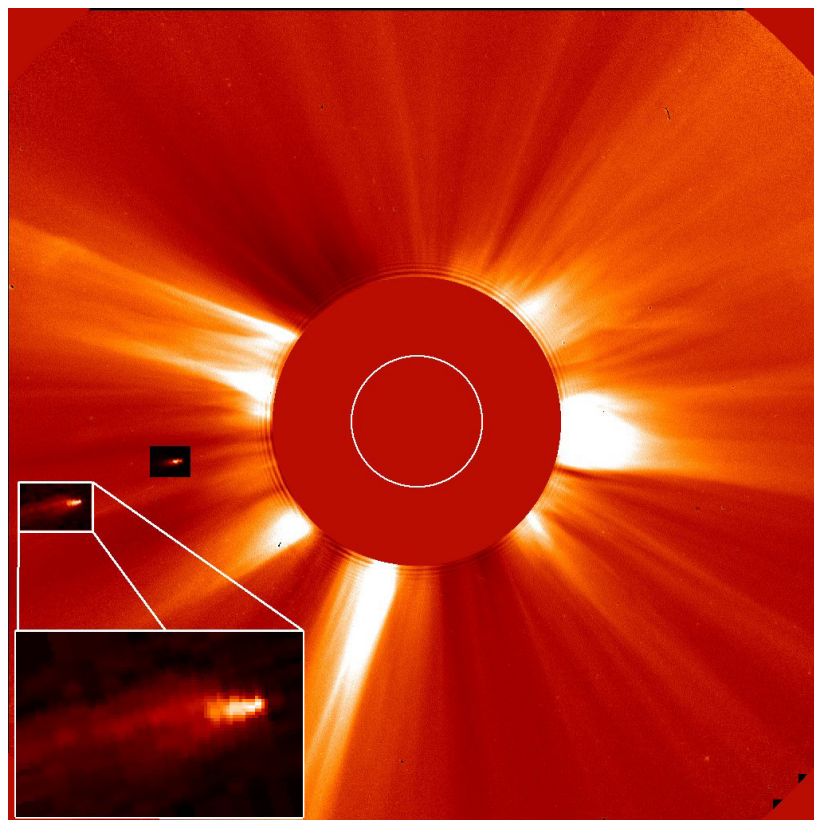
Figure 7. Composite of a LASCO C2 white light image and two UVCS Lyman α images, showing Comet C/2001 C2 (also known as SOHO-294) as it approaches the Sun on 6-7 February 2001. These observations enabled estimates of the outgassing rate and the size of the comet as well as the local density of the solar wind.

Until a few years ago, most of the comets had been discovered by SOHO scientists, but since the images have been freely available on the Internet in almost real-time, the majority of the comets discovered so far have been found by amateur astronomers.

Most comets observed by LASCO are "Kreutz" sungrazers which do not survive their close encounter with the Sun. They are quite small, typically only about 10 m in diameter. They all come from the same direction in space. They are fragments of a huge comet, probably more than 100 km in diameter and well visible even during daylight. Big fragments of this comet were seen by the ancient Greeks, more than 2000 years ago.

Thanks to the near real time operation capabilities of SOHO, UVCS (short for Ultraviolet Coronagraph Spectrometer) has been able to capture the first ever space-based UV spectrometric observations of a comet's tail (Figure 7). SOHO Comet 104 was discovered by LASCO on 9 February 2000 and observed by UVCS at four different heights above the limb the following day. These observations were used to gauge the density of the corona at the position of the comet (Raymond et al., 1998).

When comet Hale-Bopp flew near the Sun in 1997, parading its 100 million kilometres-long tail, it was also observed by the SWAN instrument. The scientists spotted a remarkable feature - never before seen by astronomers - the elongated shadow of a comet tail, more than 150 million kilometers long (Lallement et al., 2002). Water-ice in the comet's nucleus began to vaporise as Hale-Bopp approached the Sun. As expected, the Sun's ultraviolet radiation split the water molecules, liberating a cloud of hydrogen atoms that glow in the ultraviolet light. As the distance between the comet and the Sun quickly decreased, the release of vapour from the nucleus and the consequent production of hydrogen increased. As a result, in a huge, 10 million kilometre-wide region around the nucleus, the comet absorbed most of the ultraviolet light coming from the Sun. Thus, the comet projected a distinct shadow on the hydrogen haze of the Solar System. For an imaginary ultraviolet-eyed onlooker situated on the side of the comet opposite the Sun, it would have been a perfect opportunity to observe a total solar eclipse by a comet!

When Comet Wirtanen, made its most recent periodic visit to the Sun, it pumped out water vapour at a rate of 20,000 tons a day, according to the SWAN data. For the great Comet Hale-Bopp the rate reached 200 million tons a day, and SWAN watched its hydrogen cloud grow to 100 million kilometres - by far the largest object ever seen in the Solar System (Combi et al., 2000).

The SWAN instrument also observed the break-up of Comet LINEAR (Mäkinen et al., 2001). The total amount of water vapour observed by SWAN from 25 May to 12 August 2000 was estimated at 3.3 million tons. Only about 1% of this was left on 6 August, when observations by the Hubble Space Telescope of the dying comet's fragments gave an estimate of the total volume of the fragments. Combining the two numbers give a remarkably low value for the density - about 15 kg/m^3, compared with 917 kg/m^3 for familiar non-porous ice. Even allowing for an equal amount of dust grains, 30 kg/m^3 is far less than the 500 kg/m^3 often assumed by comet scientists.

Such observations illustrate how SOHO, in addition to giving us new information about the Sun, is expanding our knowledge about the inner solar system and the physics of comets.

Coronal Mass Ejections

The Large Angle Spectrometric Coronagraph (LASCO) takes images of the solar corona by blocking the light coming directly from the Sun itself with an occulter disk, creating an artificial eclipse within the instrument. LASCO best observes limb CMEs, but its excellent sensitivity also allows unprecedented detection of halo CMEs.

LASCO has been collecting an extensive database for establishing the best statistics ever on CMEs and their geomagnetic effects. By June 2003 more than 6000 CMEs have been recorded[*]. CME's are vast structures of plasma and magnetic fields that are expelled from the Sun. CMEs moving outward from the Sun along the Sun-Earth line can, in principle, be detected when they have expanded to a size that exceeds the diameter of the coronagraphs occulting disk. CME's directed toward or away from the Earth should appear as expanding halo-like brightenings surrounding the occulter.

Although halo CMEs were discovered by the SOLWIND coronagraph two solar cycles ago (Howard et al., 1982) the LASCO experiment is the first to observe a significant number of these events, thanks to its extended field of view and its improved sensitivity compared with earlier coronagraphs.

An extensive survey of CME observations from SOHO shows that the CME rate increases by an order of magnitude from 0.5/day at solar minimum to 6/day at solar maximum (Gopalswamy et al, 2003). This rate is almost twice the rates estimated from previous cycles. Another interesting feature is that the maximum CME rate peaked about 2 years after the peak of the sunspot number as can be seen in Figure 8.

---

[*] A complete list of all detected CMEs with LASCO can be found at: http://lasco-www.nrl.navy.mil/cmelist.html
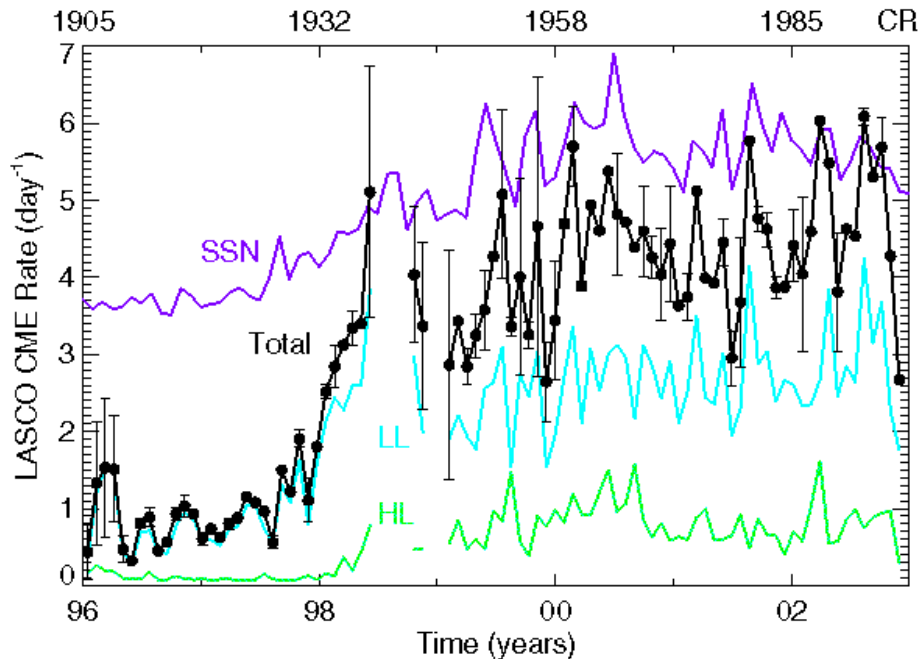
Figure 8. Comparison between low-latitude (LL), high-latitude (HL) and total (black) rates of CME's as a function of time. The sunspot number (SSN) is also shown (from Gopalswamy et al 2003).

Space weather forecasting

The response of the space environment to the constantly changing Sun is known as "space weather". Most of the time space weather is of little concern in our everyday lives. However, when the space environment around the Earth is disturbed by the variable outputs of the Sun, technologies that we depend on can be affected.

Our society is much more sensitive to space weather activity today than was the case during the last solar maximum in 1991. An example is the possible disruption of satellites. We depend on satellites for weather information, communications, navigation, exploration, search and rescue, research, and defense systems. Thus, the impact of satellite system failures is more far-reaching than ever before, and the trend will almost certainly continue at an increasing rate. Furthermore, safe operation of the International Space Station depends on timely warnings of eruptions on the Sun.

Two instruments on SOHO have proved to be especially valuable for continuous real-time monitoring of solar storms that affect space weather. One is the Extreme Ultraviolet Imaging Telescope (EIT) that provides images of the solar atmosphere at four wavelengths, revealing flares and other stormy events in the atmosphere.

The other is LASCO (see section on comets above), which was designed to detect and study coronal mass ejections (CMEs). CMEs that are heading towards Earth are causing some of the most dramatic space weather effects. Figure 9 shows one of the most dramatic eruptions

recorded by SOHO. As this event was directed towards the side and not towards Earth, it had no effect in geospace.
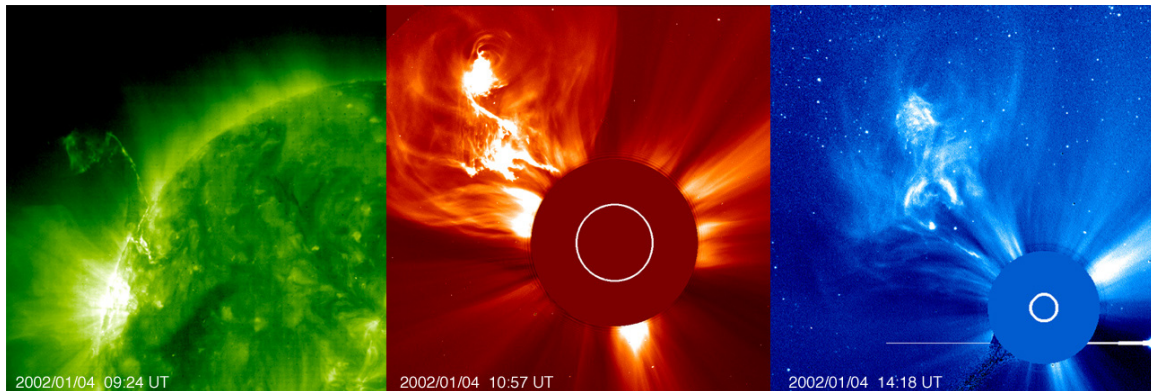
Figure 9. A spectacular Coronal Mass Ejection (CME) taking off from the Sun on 4 January 2002, starting off as a filament eruption seen by EIT in Fe XII 195 Å. The complexity and structure of the CME as it passed through the LASCO C2 and C3 fields of view amazed even experienced solar physicists at the SOHO operations center.

SOHO has proved to be an important tool in monitoring eruptions from the Sun that causes effects on the Earth. Before SOHO was operational the accuracy in forecasting geomagnetic disturbances was fairly poor. The Space Weather Operations Center at the Space Environment Center (SEC) in Boulder uses SOHO images daily. The forecast operations have become to rely on SOHO on a routine basis as a key input to solar observing and geomagnetic forecasting. LASCO provides the only direct observation of coronal mass ejections. Prior to LASCO they had to rely on activity they knew to be well associated with CMEs, but none of these associations are 100% reliable. They use direction, size, and velocity information in LASCO images to help determine the arrival time and effectiveness of the disturbance.

EIT also plays an important role at SEC to pin down the source of any eruption. In addition EIT is a very good source for identifying erupting prominences and to identify coronal hole locations. Coronal holes have become an increasingly important part of the geomagnetic forecasting process. In fact at this point in the solar cycle coronal hole activity has become the predominant driver of geomagnetic activity.

Total Solar Irradiance Variations

The VIRGO instrument on SOHO extends the record of total solar irradiance (TSI) measurements into cycle 23 (Quinn & Fröhlich, 1999). In Figure 10 measurements from six independent space-based radiometers since 1978 (top) have been combined to produce the composite TSI over two decades (bottom). They show that the Sun's output fluctuates during each 11-year sunspot cycle, changing by about 0.1% between maxima (1980 and 1990) and minima (1987 and 1997) of solar activity. Temporary dips of up to 0.3% and a few days duration are the result of large sunspots passing over the visible hemisphere. The larger number of sunspots near the peak in the 11-year cycle is accompanied by a general rise in magnetic activity that creates an increase in the luminous output that exceeds the cooling effects of sunspots.

Offsets among the various data sets are the direct result of uncertainties in the absolute radiometer scale of the radiometers (±0.3%). Despite these biases, each data set clearly shows varying radiation levels that track the overall 11-year solar activity cycle.
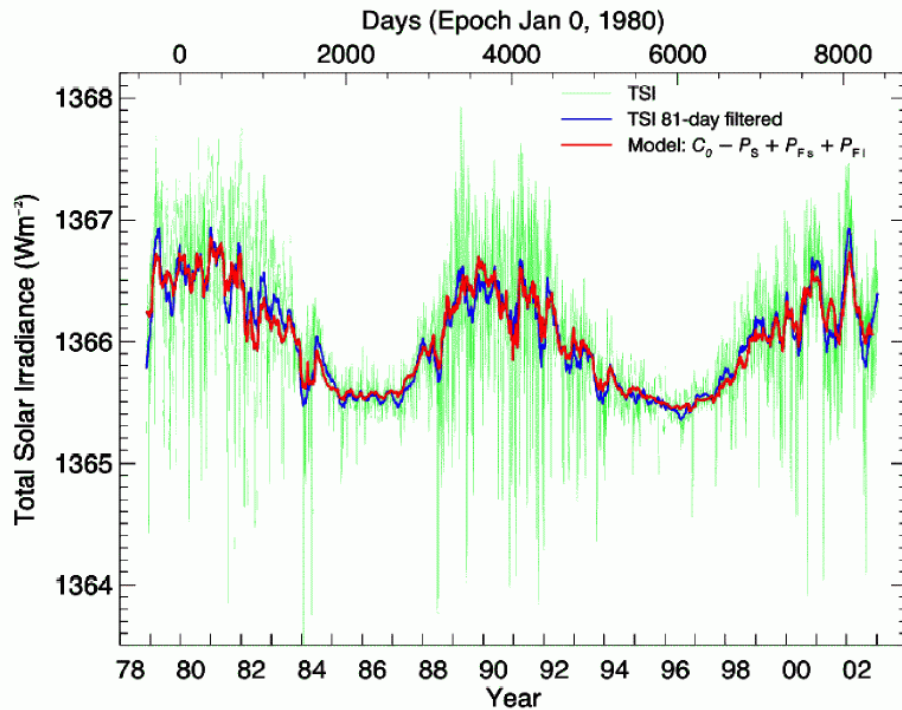
Figure 10. Daily values of total solar irradiance from 1978 to present. The data labeled TSO are a composite of observations from HF on NIMBUS-7, ACRIM-I on SMM, ACRIM-II on UARS and from VIRGO radiometers on SOHO. The blue line shows the 81-day smooted values. For comparison, the 81-day filtered proxy model (red curve) from Fröhlich and Lean (2002).

Conclusions

SOHO was set out to tackle three broad topics in solar and heliospheric physics: the structure and dynamics of the solar interior, the heating and dynamics of the solar corona, and the acceleration and composition of the solar wind. In all three areas, observations from SOHO have caused great strides in our understanding of the diverse physical processes at work in our Sun. This has been made possible by the comprehensive suite of state of the art instruments mounted on the superb and stable platform of the SOHO spacecraft, placed in the unique vantage point of the L1 halo orbit.

In complex areas of research such as solar physics, progress is not made by just a few people acting in a vacuum. The scientific achievements of the SOHO mission are the results of a concerted, multi-disciplinary effort by a large international community of solar scientists, involving sound investment in space hardware coupled with a vigorous and well-coordinated scientific operation and interpretation effort. The interplay between theory and observations has given many new insights and will continue to do so for many years. With the treasure of SOHO data already in the SOHO archive (and many more data yet to come), we should be able to unravel even more mysteries of the closest star.

References

1. Bertaux, J.L., et al.: 2000, GRL 27, 1331

2. Christensen-Dalsgaard, J.: 2002, Rev. Mod. Phys. 74, 1073

3. Combi, M.R., et al.: 2000, Icarus 144, 191

4. Cranmer, S.R., et al.: 1999, ApJ 511, 481

5. Domingo, V., Fleck, B., Poland, A.I.: 1995, Solar Phys. 162, 1

6. Duvall, R.L., Jr., et al.: 1993, Nature 379, 235

7. Fröhlich, C., Lean J.: 2002, Astron. Nachr. 323, 203

8. Gopalswamy, N., et al.: 2003, ApJ, in press

9. Hassler, D.M. et al.: 1999, Science 283, 810

10. Howard, R. A., Michels, D. J., Sheeley, N. R., Jr., and Koomen, M. J.: 1982, ApJ, 263, L101

11. Howe, R., et al.: 2000, Science 287, 2456

12. Howe, R.: 2003, in Proc. of SOHO 12/GONG+ 2002 Workshop, ESA SP-517, 81

13. Kjeldseth-Moe, O., Brekke, P.: 1999, Solar Phys. 182,73

14. Kohl, J.L., et al.: 1997, Solar Phys. 175, 613

15. Kosovichev, A.G., Zharkova, V.V.: 1998, Nature 393, 317

16. Lallement, R., et al.: 2002, Earth Moon Planets 90, 67

17. Lindsey, C., Braun, D.C.: 2000, Science 287, 1799

18. Mäkinen, T., Bertaux, J.-L., Combi, M.R., Quemerais, E.: 2001, Science 292, 1326

19. Peter, H., Judge, P.G.: 1999, ApJ 522, 1148

20. Quinn, T.J., Fröhlich, C.: 1999, Nature 401, 841

21. Raymond, J.C., et al.: 1998, ApJ 508, 410

22. Schou, J.: 1999, ApJ 523, L181

23. Schou, J., Antia, H.M., Basu, S., et al.: 1998, ApJ 505, 390

24. Vorontsov, S.V., Christensen-Dalsgaard, J., Schou, J., et al.: 2003, Science 296, 101

25. Zhao, J., Kosovichev, A.G., Duvall, T.L., Jr.: 2001, ApJ 557, 384

SPACE WEATHER EFFECTS ON SOHO AND ITS ROLE AS A SPACE WEATHER WATCHDOG

P. Brekke
RSSD, European Space Agency
NASA GSFC, Greenbelt, MD 20771, USA
Phone: (301) 286-6983
Fax: (216) 286-0264
E-mail: pbrekke@esa.nascom.nasa.gov

B. Fleck
S.V. Haugan
RSSD, European Space Agency

T. van Overbeek
H. Schweitzer
SCI-P, European Space Agency, GSFC

M. Chaloupy
Astrium, GSFC

Abstract

Since its launch on 2 December 1995, the Solar and Heliospheric Observatory (SOHO) has provided an unparalleled breadth and depth of information about the Sun, from its interior, through the hot and dynamic atmosphere, and out to the solar wind. In addition SOHO has several times demonstrated its leading role in the early-warning system for space weather. SOHO is in a halo orbit around L1 Lagrangian point where it views the Sun 24 hours a day. Thus, it is situated outside the Earth's protective magnetosphere which shields other satellites from high energy particles and the solar wind. We present a summary of the observed effects on the instruments and electronics on SOHO throughout the mission. In particular we focus on a number of large particle events during the recent years while the Sun was approaching maximum activity, and how they affected both the scientific data as well as hardware components.

The SOHO Spacecraft

The SOHO mission is a major element of the International Solar Terrestrial Programme (ISTP), and, together with Cluster, forms the Solar Terrestrial Science Programme (STSP), the first cornerstone in ESA's long-term science programme 'Horizons 2000' [1]. ESA was responsible for the spacecraft's procurement, integration and testing. It was built in Europe by an industry team lead by Matra Marconi Space (now called Astrium). Weighing in at 1,850 kg, the SOHO spacecraft measures about 9.5 m across with its solar panels extended and is 4.3 m high. Figure 1 provides a schematic view of the SOHO spacecraft. NASA provided the launcher, launch services and ground-segment system and is responsible for in-flight operations. Mission operations are conducted from NASA/Goddard Space Flight Center (GSFC).

SOHO was launched by an Atlas II-AS from Cape Canaveral on 2 December 1995 and was inserted into its halo orbit around the L1 Lagrangian point on 14 February 1996, six weeks ahead of schedule. Commissioning of the spacecraft and the scientific payload was completed by the end of March 1996. The launch was so accurate and the orbital maneuvers were so efficient that enough fuel remains on board to maintain the halo orbit for several decades, many times the lifetime originally foreseen. An extension of the SOHO mission for a period of five years beyond its nominal mission duration (2 years), i.e. until March 2003, was approved in 1997 by ESA's Science Programme Committee (SPC). A second extension of another four years, i.e. until March 2007, was granted by the SPC in 2002. This will allow SOHO to cover a complete 11-year solar cycle.
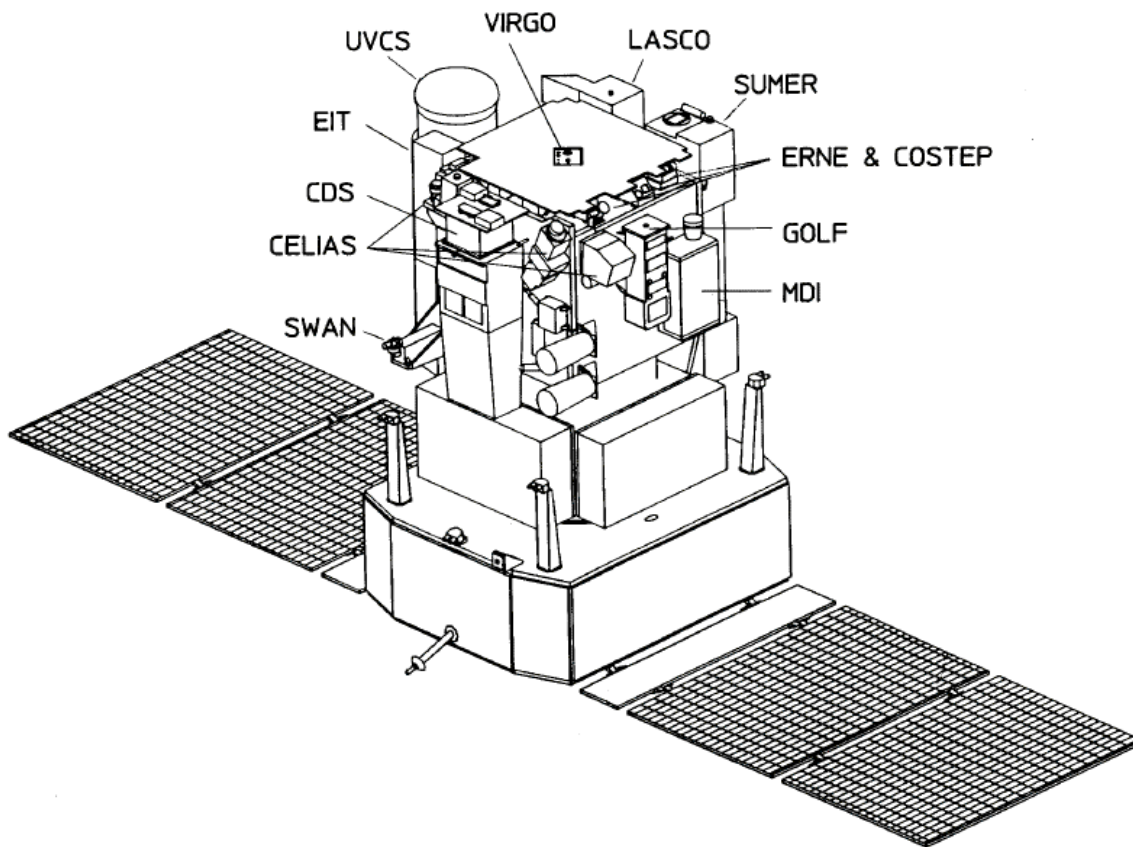
Figure 1. SOHO spacecraft schematic view.

SOHO has a unique mode of operations, with a "live" display of data on the scientists' workstations at the SOHO Experimenters' Operations Facility (EOF) at NASA/Goddard Space Flight Center, where the scientists can command their instruments in real-time, directly from their workstations.

SOHO enjoys a remarkable "market share" in the worldwide solar physics community: over 1500 papers in refereed journals and over 1500 papers in conference proceedings and other publications, representing the work of over 1500 scientists.

SOHO - A Space Weather Watchdog

Observations of the solar corona with the Large Angle Spectrometric Coronagraph (LASCO) and the Extreme ultraviolet Imaging Telescope (EIT) instruments on SOHO provide an unprecedented opportunity for continuous real-time monitoring of solar eruptions that affect space weather. LASCO takes images of the solar corona by blocking the light coming directly from the Sun itself with an occulter disk, creating an artificial eclipse within the instrument. LASCO best observes limb CMEs, but its extreme sensitivity even allows unprecedented detection of halo CMEs. EIT provides images of the solar atmosphere at four extreme ultraviolet wavelengths and reveals flares and other associated events in the atmosphere. EIT can usually determine whether CMEs seen by LASCO originated on the near or far side of the Sun, based on the presence or absence of corresponding events on the near side.

LASCO has been collecting an extensive database for establishing the best statistics ever on CMEs and their geomagnetic effects. By June 2003 more than 6000 CMEs have been recorded[*]. CME's are vast structures of plasma and magnetic fields that are expelled from the Sun. CMEs moving outward from the Sun along the Sun-Earth line can, in principle, be detected when they have expanded to a size that exceeds the diameter of the coronagraphs occulting disk. CME's directed toward or away from the Earth should appear as expanding halo-like brightenings surrounding the occulter. An example of a halo-CME is shown in Figure 2 as recorded by the LASCO C3 detector on 6 June 2000. Although halo CMEs were discovered by the SOLWIND coronagraph two solar cycles ago[2] the LASCO experiment is the first to observe a significant number of these events, thanks to its extended field of view and its improved sensitivity compared with earlier coronagraphs.

The properties of all the 841 CMEs observed by the LASCO C2 and C3 white-light coronagraphs from January 1996 through the SOHO mission interruption in June 1998 were studied and compared those properties to previous observations by other instruments[3]. The CME rate for solar minimum conditions was slightly higher than had been reported for previous solar cycles, but both the rate and the distribution of apparent locations of CMEs varied during this period as expected. While the pointing stability provided by the SOHO platform in its L1 orbit and the use of CCD detectors have resulted in superior brightness sensitivity for LASCO over earlier coronagraphs, they have not detected a significant population of fainter CMEs. The general shape of the distribution of apparent sizes for LASCO CMEs is similar to those of earlier reports, but the average and median apparent size of 72° (50°) is significantly larger.

The statistics of halo CMEs have also been studied in detail[3]. Using full disk EIT images they found that 40 out of 92 of these events might have been directed toward the Earth. A comparison of the timing of those events with the Kp geomagnetic storm index in the days following the CME yielded that 15 out of 21 (71%) of the Kp > 6 storms could be accounted for as SOHO LASCO/EIT frontside halo CMEs. An additional three Kp storms may have been

---

[*] A complete list of all detected CMEs with LASCO can be found at: http://lasco-www.nrl.navy.mil/cmelist.html

missed during LASCO/EIT data gaps, bringing the possible association rate to 18 out of 21 (86%).

More recently it was found that 22 out of 27 (81%) major geomagnetic storms occurring between 1996-2000 were identified with front side halo (FSH) CMEs[4]. Of these 16 (59%) were associated with unique FSH CMEs while 6 (22%) where related to multiple FSH CMEs. They also find that while these geoeffective CMEs are either full-halo CMEs (67%) or partial-halo CMEs (30%), there is no preference for them to be fast CMEs or to be associated with major flares and erupting filaments. Again, this illustrates that SOHO has been providing new valuable information to better understand CMEs as well as being the only monitoring system for Earth directed CMEs until more ideal missions are launched (e.g. STEREO).
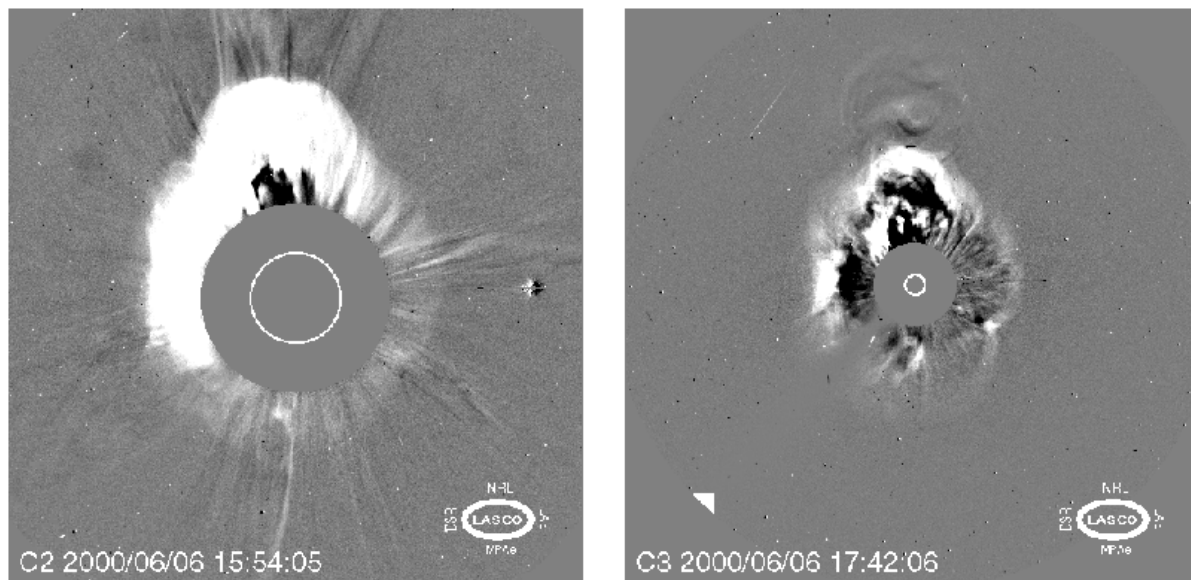
Figure 2. Example of a full halo CME observed by LASCO C2 (left panel) and C3 (right panel) coronagraphs. The field of view of the images are 2-6 and 3.5-30 solar radii.

SOHO's role at the Space Environment Center

The Space Weather Operations Center at the Space Environment Center (SEC) in Boulder uses SOHO images daily. The forecast operations have become to rely on SOHO on a routine basis as a key input to solar observing and geomagnetic forecasting. LASCO is the only direct observation of coronal mass ejections. Prior to LASCO they had to rely on activity they knew to be well associated with CMEs, but none of these associations are 100% reliable. They use direction, size, and velocity information in LASCO images to help determine the arrival time and effectiveness of the disturbance.

EIT also plays an important role at SEC to pin down the source of any eruption. In addition EIT is a very good source for identifying erupting prominences and to identify coronal hole

locations. Coronal holes have become an increasingly important part of the geomagnetic forecasting process. In fact at this point in the solar cycle coronal hole activity has become the predominant driver of geomagnetic activity.

Finally, forecasters use the MDI data on SOHO in order to track sunspot growth and decay and the magnetograms are used to track magnetic field strengths and complexity, a valuable input for flare forecasting.

Automated Detection of CMEs

The visual detection of CMEs in the flood of incoming LASCO data is a labour-intensive task. Until today it is essentially the human eye that detects a CME occurrence and a scientist that collects all the CME parameters. An automated detection system called "Computer Aided CME Tracking (CACTus) has been developed for the LASCO images[5]. The software detects bright ridges in [height, time] maps using the Hough transform and creates a list of events with principle angle, angular width and velocity estimation for each CME. In contrast to lists assembled by human operators, these CME detections by software can be faster and possibly also more objective. The first version CACTus has been evaluated and it obtained a success rate of about 75%. This number is expected to improve in later versions. The software also detected some CMEs that were not reported in the official human created catalogs.

Solar Wind Shockspotter

The CELIAS/MTOF/PM instrument on SOHO measures the solar wind speed, density and temperature. A group at the University of Maryland recently implemented a "Shockspotter" program to identify interplanetary shocks in near-real time using proton monitor data. The program is based on semi-empirical algorithms using only solar wind proton data (since no magnetometer data is available on SOHO). Shock candidates are classified into 4 distinct zones, with confidence levels ranging from about 40% to 99%. Results have been used to study the frequency distribution of interplanetary shocks over the solar cycle. The Shockspotter program is now part of the proton monitor real time data page at http://umtof.umd.edu/pm. The program can alert users (via eMail, upon request) whenever a shock front passes the SOHO spacecraft approximately 30-60 minutes prior to the arrival at Earth. A catalog of interplanetary shocks is also maintained at http://umtof.umd.edu/pm/figs.html . The Maryland CELIAS group has also developed Web pages that show the solar energetic particle flux deduced from proton monitor background levels (http://umtof.umd.edu/pm/flare) and the solar soft X-ray flux from SEM measurements (http://umtof.umd.edu/sem/).

Space Weather Effects on Service Module

SOHO is designed to withstand the effects of the varying flux of high energy particles encountered in its L1 Halo orbit. These effects can be separated at least into three classes. First we will discuss the effects on the spacecraft (service module and solar panels) and then the effects on the different scientific instruments. A brief summary of efforts to prevent interruptions to the daily operation of the spacecraft is also discussed.

During its lifetime the spacecraft components receive an integrated radiation dose that degrade their performance and can cause the following failures:

A) Solar Arrays

The only permanent effect so far is the degradation of the solar arrays due to high energetic protons from solar eruptions. This degradation is due to "displacement damage": energetic particles interact with the solar cell lattice producing defects which enhance electron and hole recombination thus reducing the solar cell's output voltage and current. The actual degradation of the solar array is given in Figure 3. The degradation due to proton events is evident with significant drops during the July 14, 2000 and November 4 & 23, 2001 events. The degradation after 80 months in space is 13.8%. This is an annual average degradation of 2.01%, well within the 4% per year requirement. SOHO can operate down to 70% sensitivity without taking any energy saving action.
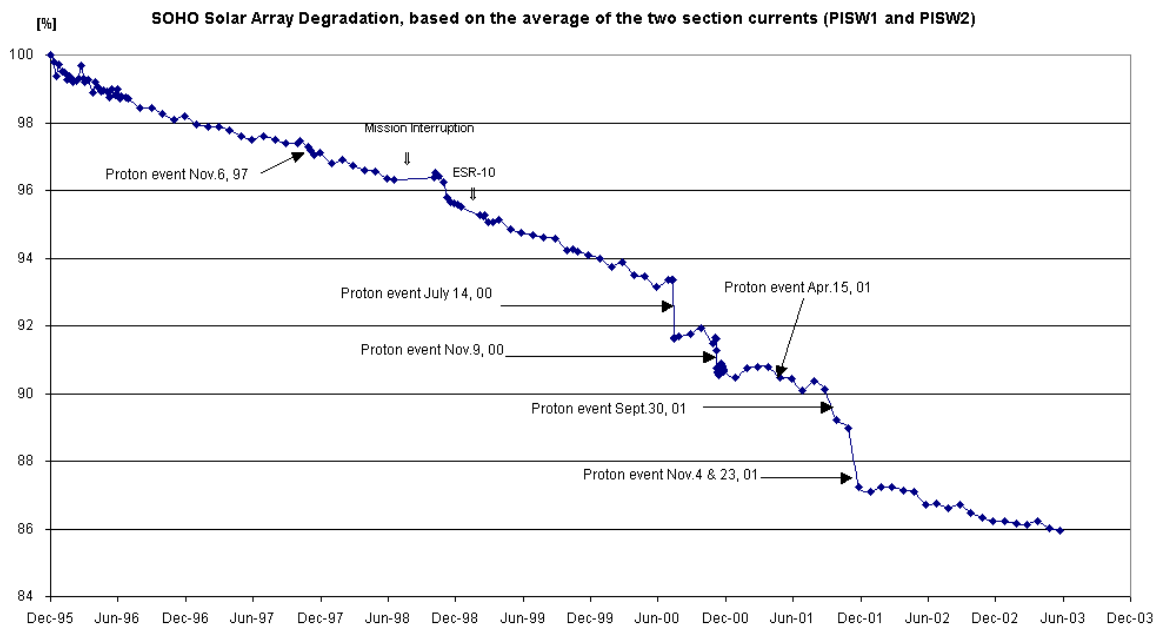
Figure 3. SOHO solar array degradation since the launch in 1995. The drop in sensitivity due to individual proton events is evident.

B) Sensitivity of the Fine Pointing Sun Sensor

The Fine Pointing Sun Sensor (FPSS), together with the Star Sensor Unit (SSU), is part of SOHOs Attitude and Orbit Control System (AOCS).
Similar to the solar array, the FPSS sensitivity is gradually decreasing due to the impinging radiation over several years. The present performance is still sufficient, but in the long run, we might eventually require a new calibration of the output level of the FPSS. This is a simple on-board parameter change.

Radiation induced background

Radiation impinging on detectors or associated electronics can produce an increase of the background noise. The Star Sensor Unit consist of an optical system with thermal sensors for calibration of the focal length of the optics and a CCD detector (377 x 283 pixels), mounted on a Peltier cooler with thermal control for the CCD temperature (– 40°C) and for the electronics of the detector drivers and data pre-processing. The background noise of the Star Sensor Unit so far is very stable since the beginning of the mission

Single event upsets (SEUs)

Cosmic rays or heavy ion impact can provoke single event upsets, which may disrupt the operation of sensitive electronics.

A) Electronic units self switch-off

A fair number of self switch-off events occurred, which are attributed to Single Event Upsets (SEUs). Three of them caused transitions to the spacecraft safe mode (Emergency Sun Reacquisition – ESR), causing major disruptions of science operations. Five times the battery discharge regulators switched themselves off and there were about 7 occurrences, where instrument boxes were switched off or required rebooting. Many of the self switch-offs are probably caused by false triggering of internal protection circuits, which are designed to protect against over-voltage or over-current. In all cases, no permanent damage occurred and the systems could be re-activated successfully.

B) Solid State Recorder

A major temporary radiation effect is the SEUs in the Solid State Recorder (SSR), resulting in bit flips in the memory. The EDAC (Error Detection And Correction) detects and corrects these single errors (in the same word). Double errors are detected but not corrected.

Single errors are very common for the SSR 2Gbit memory:

- at solar min: 1 SEUs/minute
- at solar max: 0.5 SEUs /minute
- during proton events: up to 76 SEUs /minute (July 14, 2000 event)

So far there has only been 1 double error since launch, which was corrected as soon as the effected memory location was overwritten with new data. A plot of the SEU's/ minute/2GB over the entire mission is given in Figure 4.

SOHO SSR Single Event Upsets, parameter DKSSCSEF (events/minutes/2G-bit)
Note: since Sept.13, 00, the MU 15 is OFF (corrected for in the plot)
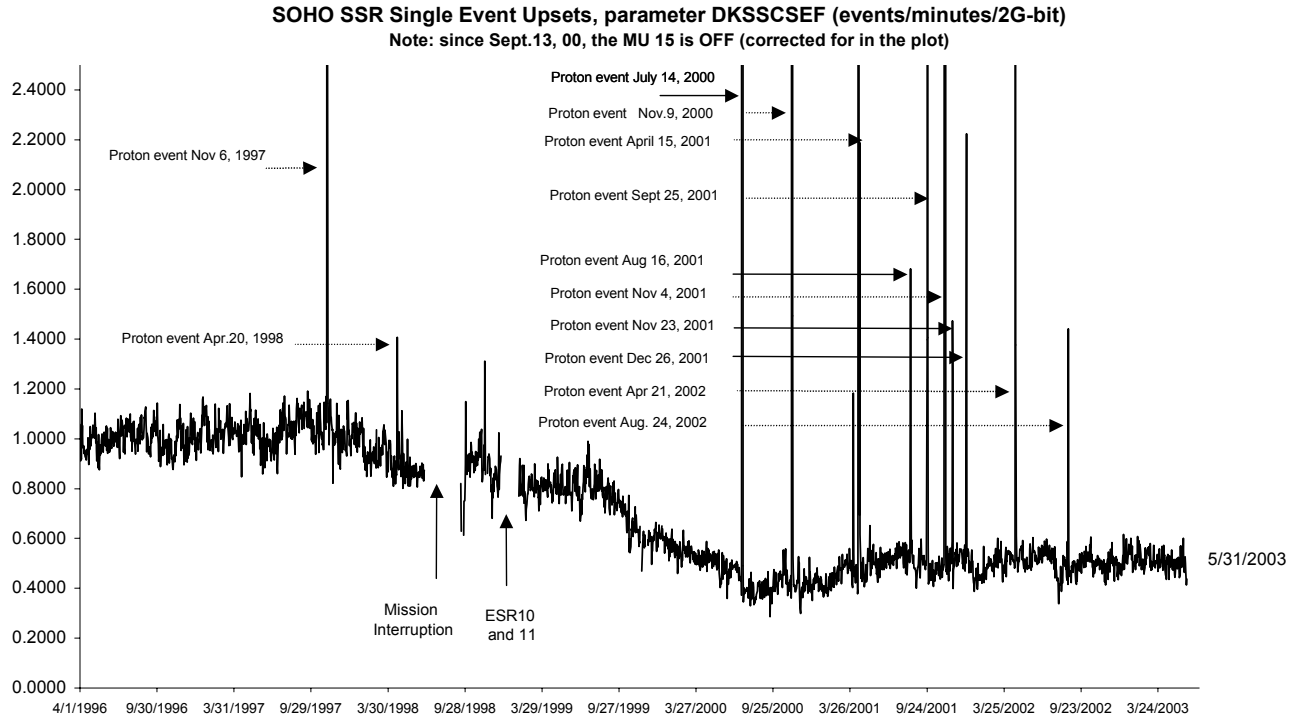
Figure 4. Number of SEU's per minute per 2GB over the entire mission. The solar cycle effect can be clearly seen with more SEU's during solar minimum (weaker solar magnetic field). Overlayed are the proton events during the SOHO mission.

C) Star Sensor Unit

Another temporary radiation effect is observed on Star Sensor Unit (SSU). When particles hit the CCD (Charge Coupled Device) of the SSU, they generate electrons, which charge up the pixels just like the regular photons, producing bright star-like signatures.

The SOHO star tracker tracks five stars in small tracking windows. If a particle hits the tracking window it can result in a wrong assessment of the tracked star's barycenter and/or magnitude.

The SSU interprets this as a movement of the star it was tracking thus providing wrong information to the attitude control software, resulting in turn in wrongful attitude correction orders to the wheels. Furthermore, the Star Tracker itself is moving its tracking window to the new wrong barycenter, and sometimes loses the true star in doing so.

The star tracker had lost the guide star 54 times the first 3 years. Most of these resulted in loss of nominal attitude (fall back into Roll Maneuver Weels mode/gyro mode), with the consequence of reduced science during the special operation to recover to nominal configuration.

Improvements to onboard software

The onboard software was designed to be upgraded and a series of improvements have taken place throughout the mission. Two improvements to increase the robustness to SEUs have been implemented:

The star tracker's internal software was modified:

- to filter out transient changes in the star barycenter (Position Jump Filter).
- to filter out transient changes in the star's magnitude

The result is that for both transient changes no false event report is sent to the AOCS software.

The AOCS overall task is to provide the spacecraft with the requisite pointing performance during the various spacecraft activities. The AOCS software was modified to delay the effect of false event reports of the SSU to the attitude control computer (Staircase Filter). This filter was first implemented as a patch, but was later included in the gyroless software.

Automatic "star swap" capability

An automatic "star swap" capability was added to the attitude control computer gyroless software. Before 1998, the control mode was automatically changed from Normal Mode to Roll Maneuver Wheels mode, where the roll control was switched from the star tracker to the gyros, when the guide star was lost or simply flagged invalid due to a SEU.

We no longer have gyros for backup, but the new software can now automatically use one of the 4 other stars that it is tracking as new guide star. Thanks to this, SOHO was able to remain in normal mode during the Bastille Day (July 14, 2000; 3 star swaps) and the Nov 9, 2000 event (also 3 star swaps). There have been 11 star swaps in all, since October 1999.

Since the new gyroless software with the star swap feature was uploaded, we had not a single loss of nominal attitude (i.e. fall back into the new gyroless Coarse Roll Pointing mode). SEUs can still cause the stars to be flagged "invalid" for a while, but they have always returned to valid on their own. With these new upgrades SOHO is now extremely stable!

Effects on the Scientific Instruments and Operation

As with spacecraft electronics and detectors, several instruments are also subject to effects from energetic particle events. For some *in situ* sensor instruments, the particles are the main subject matter; for some, the particles are mostly a nuisance causing image degradation, but some instruments have health and safety concerns, due to e.g. high voltages on their detectors, the potential for arcing and permanent damage.

Image degradation

As can be seen in Figures 5, 6 and 7, the image degradation experienced during energetic particle evens can be quite severe. Not only does the (relatively short-lived) degradation render images nearly useless for scientific analysis and space weather purposes – they also cause them to be much less compressible by the on-board software, in the case of EIT and LASCO. With a limited amount of telemetry and on-board storage, this results in the instrument getting "backed up", with a shifting of scheduled observations to a later time. While not necessarily critical under regular circumstances, certain joint observing programs rely on a closely coordinated timeline between a number of instruments both on board SOHO and on other spacecraft, as well as ground based observations. This can only be corrected by intervention from the ground, using near-real-time (NRT) commanding to flush queues, skip observations, or upload new plans.
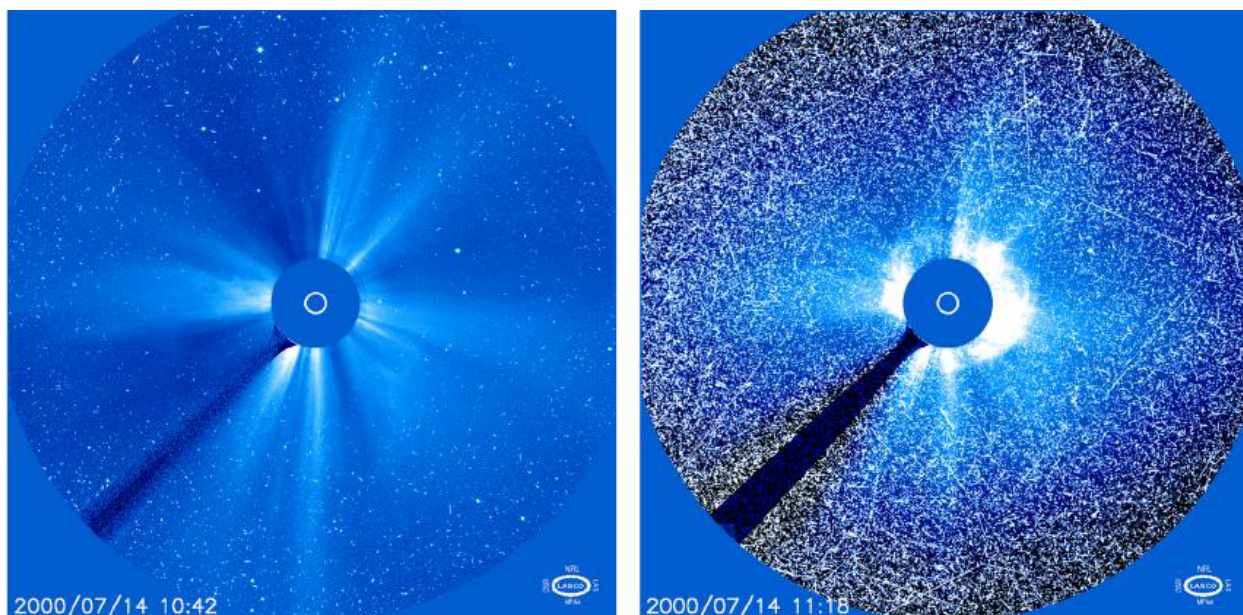
Figure 5. Images taken by the LASCO C3 coronagraph during the July 2000 solar energetic particle event showing severe effects on the detector from radiation background. Note that even though the images appear to be totally swamped during a proton storm, we are scaling the images to show the subtle coronal changes so that the particles are enhanced. They really don't saturate the detectors.

Health and safety effects

With several types of instruments operating detectors that have high voltage "image intensifiers" of different types, energetic particle showers are not purely an inconvenience. Although no incident has yet damaged any of the SOHO instruments, precautions have been put in place to ensure that the likelihood of damage is being kept as low as possible. Since, in general, the image-intensified instruments' data during particle events are not very useful

anyhow, the loss of science data is not of concern; health and safety takes priority for those that feel a "better safe than sorry" approach is appropriate. The instruments that do take precautions of various kinds are: Coronal Diagnostic Spectrometer - CDS (continuous detector readouts to prevent charge build-up), Ultraviolet Coronagraph Spectrometer - UVCS and Solar Ultraviolet Measurements of Emitted Radiation - SUMER (high voltages turned down).
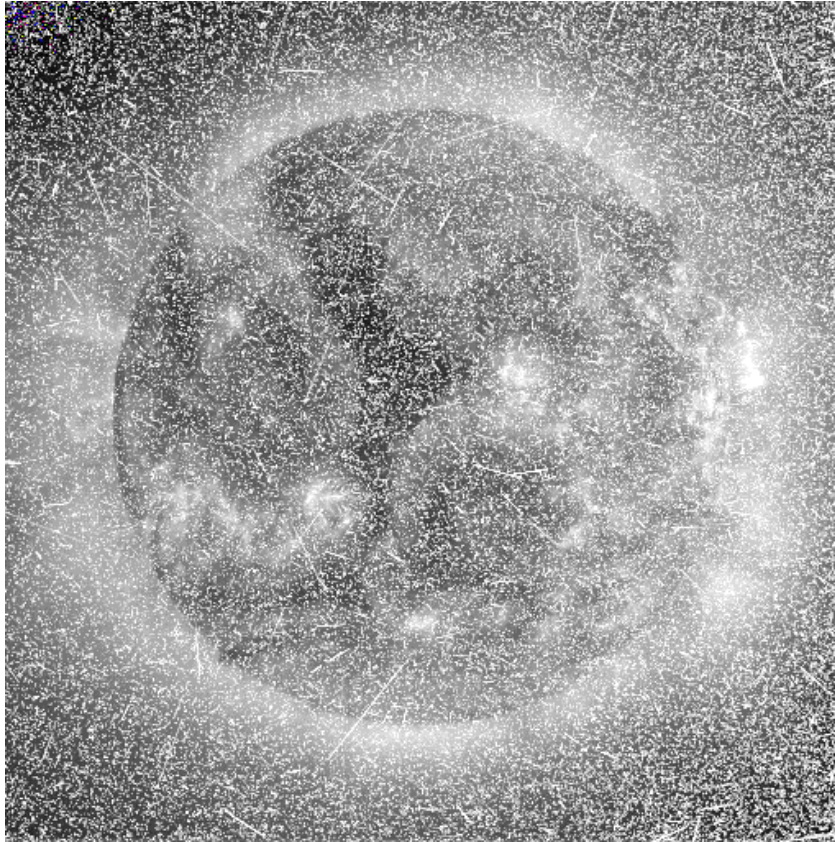
Figure 6. The Extreme Ultraviolet Imaging Telescope (EIT) observing during a proton event.
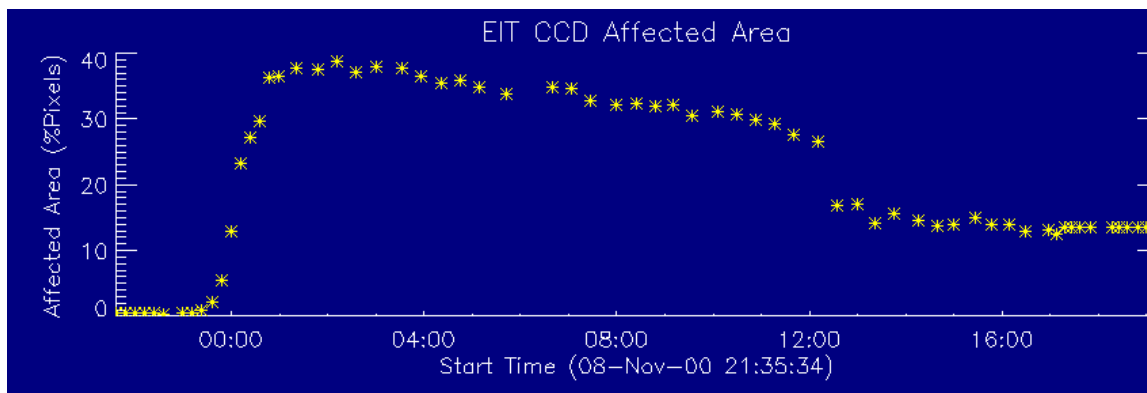
Figure 7. During a strong proton storm about 40% of the EIT detector is affected. The effect of the protons can be seen for a few.

Operational implications

The main operational "warning system" is the spacecraft solid state recorder. Since the SSR SEU counter is being monitored on the ground while the spacecraft is in contact (to prevent the SEU counter from overflowing), the impacts to normal operations are minimal when there is no particle event. If the SEU counter needs to be reset more often than once per hour, the Science Operations Coordinators are contacted, alerting instrument teams about the situation according to their own criteria.

For times when the spacecraft is not in contact, the warning system is based on NOAA GOES data from the web. Of course, with no spacecraft contact, nothing can be done about the instruments, so the status is only checked some time in advance of station passes with commanding ability. In addition, a 24/7 system based on automatic paging of the SOCs is in place, using NOAA GOES data from the web.

Long-term effects

No serious long-term adverse effects have yet been noted, although the high energy particle environment does contribute to the gradual degradation of instruments. In particular, contaminant "doping" of refractive optics changes the absorption coefficients (impacting the optics temperatures), and the indices of refraction (focus changes). In addition, parts of the gradual sensitivity losses experience by many instruments can be attributed to contamination of detector electronics.

Mission Status and Future Plans

Although long past the design lifetime of 2 years, SOHO is doing remarkably well. Fuel reserves of 123 kg should last 10 more years according to conservative estimates, and the solar array degradation is at only 10%, with a remaining margin of 25% before conservation measures must be applied. The gradual degradation of instruments and multi-layer insulation due to EUV exposure and high-energy particles is as expected, and not a cause of concern. Barring unexpected events, there seems to be no technical reason why SOHO and its instruments should not be able to complete observations of a full solar cycle. With several years until heirs to the throne can be expected, we hope that SOHO will continue its hegemony in the field of solar and heliospheric observations for years to come.

Acknowledgements

References

1. Domingo, V., Fleck, B., and Poland, A.I. 1995, Solar Physics, 162, 1.

2. Howard, R. A., Michels, D. J., Sheeley, N.R., Jr., and Koomen, M. J. ApJL, 263, 101.

3. St.Cyr, C., Howard, R.A., Sheeley, N.R. 2000, J. of Geophys. Res., 105, 185.

4. Zhang, J., Dere, K.P., Howard, R. A., Bothmer, V. 2002, ApJ, 582, 520

5. Berghmans, D., Clette, F., Cugnon, P., Gabryl, J.-R., Hochedez, J.-F., Van der Linden, R., A.M., Verwichte, E., 2002, JASPT, 64, 757

IN-FLIGHT ANOMALIES ATTRIBUTED TO ESD'S.
RECENT CASES AND TRENDS

Jean-Pierre Catani
Centre National d'Etudes Spatiales
18, avenue Edouard-Belin
31401 Toulouse cedex 9

Abstract

The general problem of charging is usually shared out four domains of physics or technology: astrophysics for the knowledge of environment, materials technology for understanding and prediction of charge build-up, plasma physics for predicting thermal or electromagnetic effects of discharges, and space engineering for assessing effects of transients on the space system.

The environment monitoring at the geosynchronous altitude has been carried out for years beginning with the first launches of NOAA GOES satellites. Their drawback is they provide only local data. The development of Space Weather activities let foresee the possibility of deriving the charging particles content in the immediate vicinity of the space vehicle from a limited set of flight-monitored data. Today, anomalies attributed to charging are fortunately infrequent, making unreliable statistical correlation between environmental data and event occurrence. It can be conclusive only in some cases of surface charging.

The understanding of interaction of materials with a well-representative simulation of environment is a priority in Europe, especially at CNES, the French Space Agency. In a CNES/ONERA test facility in Toulouse the main features leading to both surface and internal charging are simulated for all altitudes. An aim is the characterization of new technologies and new materials: electrical thrusters, active antennas, conductive coatings. Another aim is the issuing of design rules in the frame of the European Space Standardization. The plasma discharge is the source of an electromagnetic field transient. At equipment level an ESD immunity test has been used for now fifteen years. A system level test remains to be defined.

General

The spacecraft anomaly is at the end of a long chain of causes and consequences. At the origin we find the Sun, it is the source of plasma ejected in the zone of space called heliosphere comprising all planets of the solar system and extending much farther. This plasma interacts with the Earth magnetic field and can partially diffuse into the magnetosphere, the zone of space governed by the terrestrial magnetic field. The solar plasma is not emitted uniformly inducing large instabilities of the magnetosphere; it results heating of magnetosphere plasma at hundreds of kiloelectronvolts at the altitude of geostationary spacecraft and megaelectronvolts by orbits of positioning system satellites. The interaction of the satellite body with this hot plasma is frame charging at high negative potentials, also differential charging between insulated parts resulting in electrostatic discharges. The fast release of charges creates high-amplitude electromagnetic fields, then current and voltage transients onto box interconnecting cables. The pulses penetrate inside boxes, propagate along printed-circuit-board tracks, reaching active devices, toggling flip-flops, saturating amplifiers, or fusing lanes inside integrated circuits.

Each step of the process is highly random. Even if we are able to analyze each one, we have no mean to derive the behavior of the system from Sun observation or magnetosphere radiations monitoring, even not from electrical measurement on the spacecraft. On the opposite side, once an anomaly has occurred, it is possible (and useful) to assess the probability of a charging cause. It is the aim of on-orbit investigations.

Investigation

Main steps of investigation

How to know what happens in flight? A Ground Control Center dedicated to a Space System is permanently checking the spacecraft configuration. An alarm or warning is triggered when the spacecraft is getting out of its nominal working state. An electrostatic discharge is not observed itself but only when it has permanent consequences. Telemetry data is never designed for surveying unforeseen events; it is defined for command control and good-health diagnosis. Probes are exceptionally implemented on commercial spacecraft to determine the state of environment at the location of the spacecraft, at the time of the anomaly.

Spacecraft event understanding is the conclusion of three convergent ways of analysis: environmental data monitoring, vacuum charging tests, and electromagnetic immunity tests. Only one criterion is rarely convincing enough.

First step: Use of environmental monitors

What is the electronic content at time and location of the satellite? Charging fluxes are varying very rapidly, the duration of a charging event is only a few minutes. Since there is no on-board sensor, we can only lean on environmental plots issued by the Space Environment Center of Boulder, CO, USA (0). It is only informative because measurements are not made at the same location of the orbit as the concerned spacecraft. A proton analyzer provides proton flux data from solar flares in three spectral bands: E>10 MeV, E>50 MeV and E>100 MeV. By experience, only the upper band is correlated with upsets (which are not charging effects). Electron fluxes are plotted for two bands: E>600 keV and E>2 MeV. The collapse of high-energy electrons is an effect of substorm mid-energy electron fluxes, an indication of possible surface charging. On the third panel, the H_p magnetic component at GOES location is plotted. The plot would be a clean sine curve in absence of geomagnetic activity. Magnetic noise on this curve witnesses to substorm fluxes of precipitating mid-energy particles. On the lowest panel, planetary K-indices bar-plots confirm occurrence of substorms (when K_p is above 3).
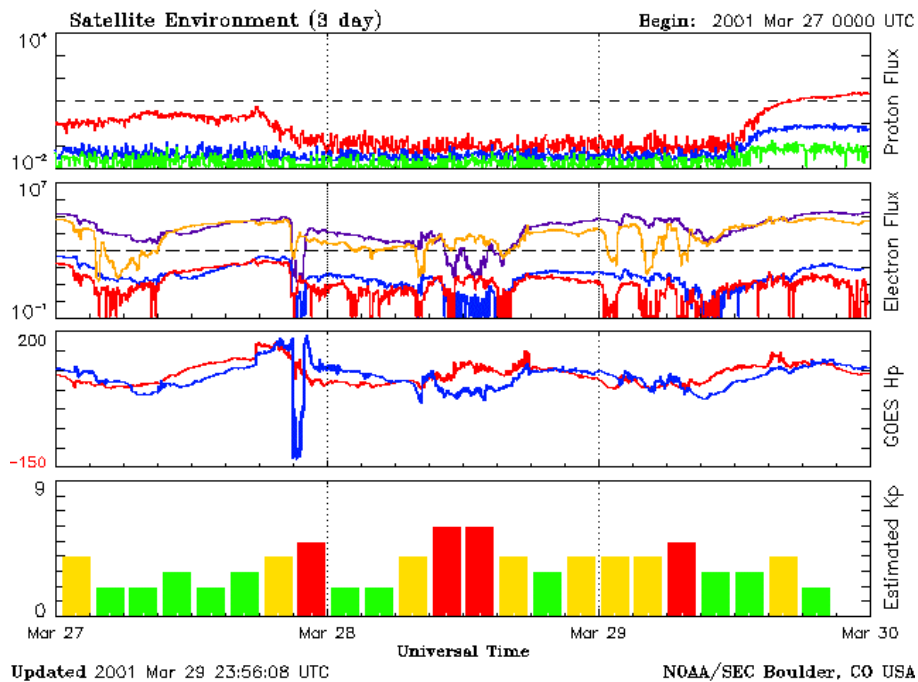
Figure 1. Example of data used for determination of solar and geomagnetic environment. Information from the Space Environment Center, Boulder, CO, National Oceanic and Atmospheric Administration (NOAA), US Dept. of Commerce.

During active periods, during the existence of a magnetic storm, the probability is high for the spacecraft to be impacted by energetic electrons. However even during very quiet periods, charging fluxes are still possible. Moreover we have to take into account a "memory effect". Impinging electrons during active periods become embedded inside dielectric material and can be free some hours, maybe some days, later, resulting into an electrostatic discharge. Electrons of moderate energy (a few 10keV's), buried in surface materials can be responsible of this effect. The discharge triggering may have several causes; for example a local dissymmetry of charge induced by lighting, creates a voltage difference where the voltage was uniform in darkness.

MultiMeV electron fluxes may vary through several decades at different space-time locations. Moreover the charging effect is highly dependent on the spectral signature. They can have a beneficial effect by keeping surface-voltage building-up (radiation-induced conductivity). On the opposite side they are cause of hazardous internal charging.

Second step: Use of environment simulators

Charging properties of rough materials are more or less known. Bulk and surface resistivity, secondary emission yield to electrons and ions, photoemission efficiency are documented during the spacecraft development for charging assessment. Actually, materials are used in complex assemblies; possible interactions between adjacent materials have an influence on charging balance and discharge processes. Testing flight-representative items in a vacuum facility with a representative charging ambiance is a way for assessing the discharge risk. It provides information on discharge characteristics: duration of the discharge, current amplitude, and associated electromagnetic field. It will also provide information for the design of an electromagnetic simulator.

A set of electron guns generates an electron beam in broad range of energy from 10 keV to 200 keV or more. The item under test is polarized with respect to the chamber walls for simulating the absolute voltage of the spacecraft. UV-light or a proton source simulates locally the positive charging effect of sunlight.
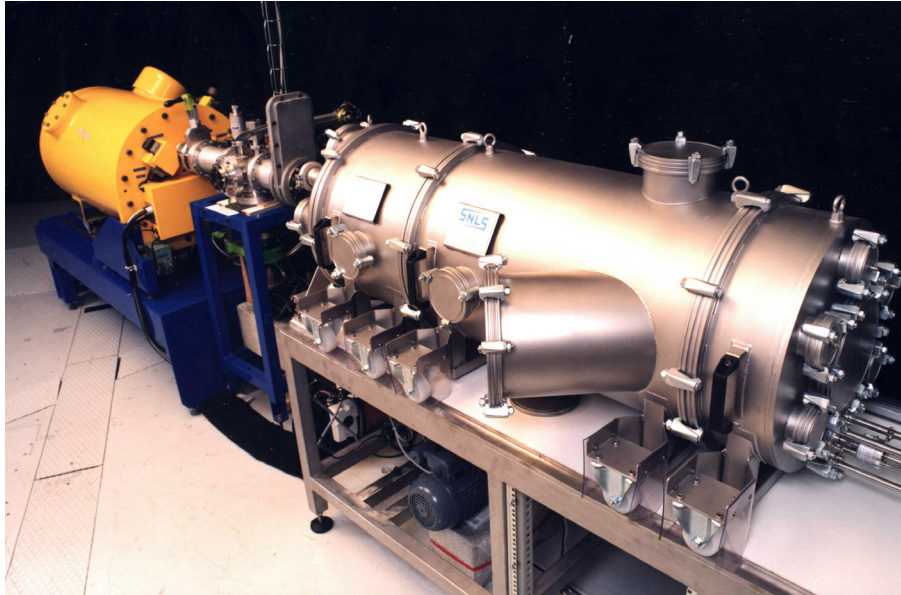
Figure 2. Wide-spectrum charging environment facility SIRENE (photo ONERA)

A NASCAP simulation is useful for preparing the test and defining the voltage configuration (polarization) of the specimen under test and the electron flux.

Third step: Use of ESD simulators

The plasma created by the electrostatic discharge can have primary effects; for example, to trigger a cold arc discharge between cells of the solar generator. However, in most cases electromagnetic effects of electrostatic discharges are preponderant. Two types of electromagnetic sources have been identified.

The discharge process is a transition from a charged state to a discharged one; it is seen as an electric-field transient step. During the transition, a replacement current is flowing in the spacecraft frame; this is one of electromagnetic sources. At the same time, electrons are blown off from the site of discharge, repelled by the negative potential. The charge present at a given time in free space before being recollected (or lost in space) generates an electric field pulse of several tens of kilovolts per meter in the immediate vicinity of the site of discharge, inducing current or voltage pulses onto close wires or bundles.

What is the response of a box to an electrostatic discharge, in other terms is the anomaly a possible response of the box to an electrostatic discharge? Analyzing the electrical schemes or drawings is not conclusive. Immunity or susceptibility is affair of details; it is the consequence of parasitic elements, stray capacitances, bonding inductances, nonlinear effects in active devices, a lot of unspecified parameters. A susceptibility test is the only mean to know the equipment behavior to electrostatic discharges. A numerical analysis is useful to understand the susceptibility mechanism inside the box.

At equipment level a susceptibility test has been developed at CNES and used for fifteen years. This is a recommended test of the standard "ISO-14302, EMC for Space Systems. It can be performed by a coupling method using a wire adjacent to the bundle (0). A 100pF capacitor charged at 6kV is discharged through a fast spark gap. The discharge current is electromagnetically coupled to the bundle. This test has been designed to replace the radiated field test from a sparking device and the conducted test by discharging an arc onto the structure, tests defined by the older MIL-STD-1541 standard.

In most cases ESD events and electronic upsets have no consequence at system level due to internal redundancy or logical filtering. A system level test remains to be defined.
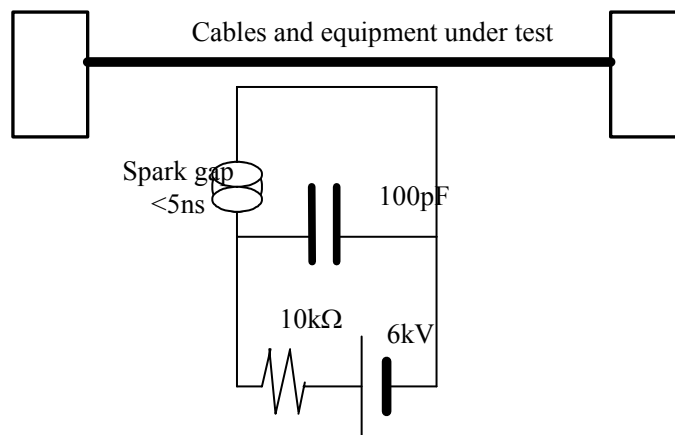
Figure 3. Recommended spacecraft charging ESD immunity test at unit level

Flight Experiences

All anomalies experienced in flight have not the same weight. We used to distinguish at least two kinds of anomalous behavior:

- Major anomalies: malfunctioning (temporary or permanent) with operational consequences (failure, automatic recovery, loss of control, loss of performances)
- Minor anomalies: anomalous functioning without operational consequence.

We give the example of a European program of several satellites, totalizing 22 temporary major anomalies for 38 years of cumulated time in orbit, about one event per satellite every two years. It seems to be a normal rate for the current generation of satellites. The associated outages are well inside the standard requirement and far from hundreds of events experienced in the 70's or 80's which have initiated research programs about charging.

However the fact that anomalies consecutive to charging events are still experienced from time to time is the indication we are at the border-line between safe and weak systems. Most of anomalies occur on subsystems connected to an external equipment, sensor or actuator; this is a noticeable point which helps us to define mitigation techniques and prepare test plans.

First example: Unlocking of a phase-locked loop

The described anomaly is unlocking of a receiver phase-locked loop. Applying the normal procedure of investigation when an environmental induced discharge is suspected, we plot events on a time-date diagram (Figure 4).
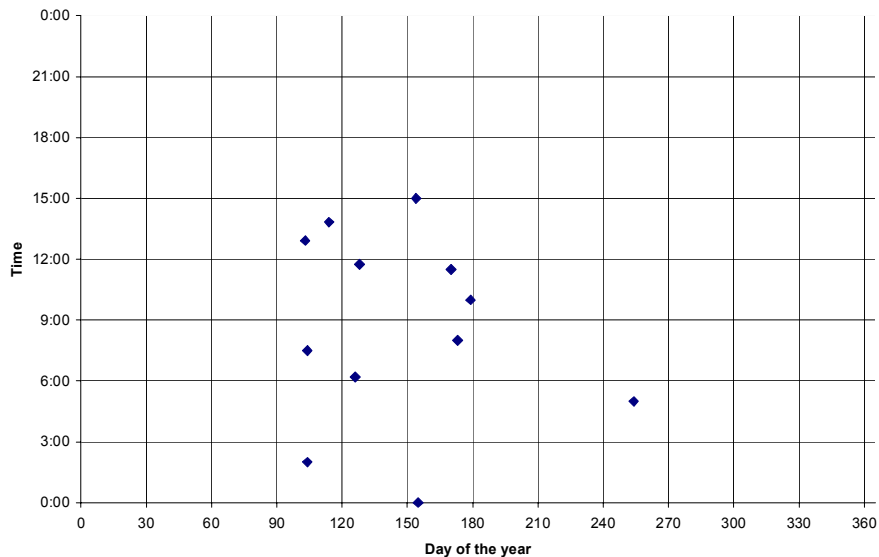
Figure 4. Time-date distribution: seasonal and time dependence (from 12 events in 5 years)

Though the small numbers of events, the dots do not seem randomly distributed, a seasonal and time dependence is visible. Mainly, a majority of events has occurred in the morning where surface charging is more frequent. Views of NOAA diagrams (Fig. 5) sometimes show a correlation between the geomagnetic activity and occurrence of anomalies. The charging event is guessed from ripples on the magnetic field amplitude at the altitude of geostationary satellites. It was true for 11 events not for the twelfth one, on June 28th, 2002. This kind of exception is not infrequent, rendering difficult definite conclusions.

19 June 2001, 10am   22 June 1997, 8am   28 June 2002, 10am
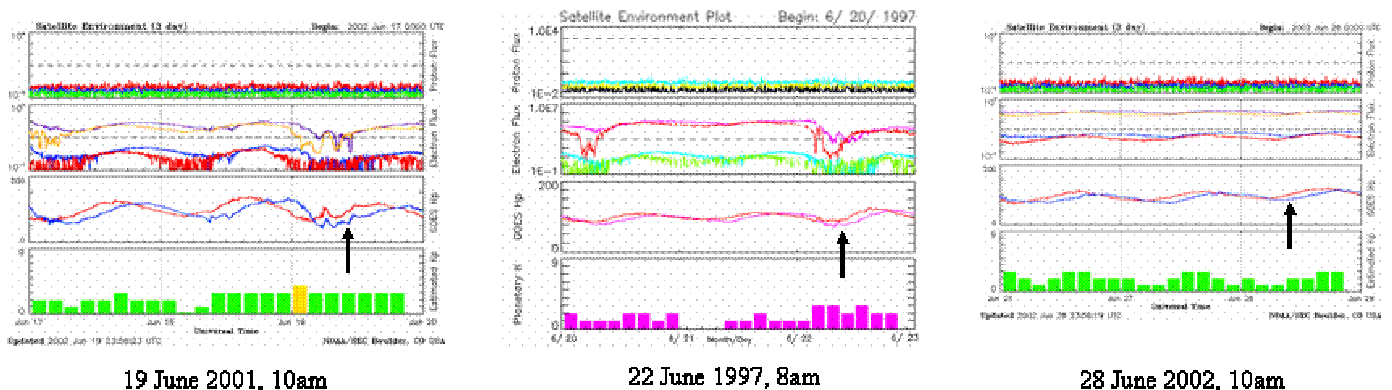
Figure 5. NOAA reports for three of the events

As the anomaly was of minor type, reproducing it in under an EMC test was not attempted. It was explained by a voltage spike induced by an electrostatic discharge.

Second example: saturation of an op-amp

The second example is concerning six events in seven years on different satellites using the same type of equipment. One event occurred some days after the coronal mass ejection of January 6th, 1997 when the level of multiMeV electron flux was largely increased. Four events took place in the morning quadrant of local time, two outside. From the environment monitoring it was seen that this anomaly always occurred following a storm when the high-energy content of the magnetosphere had become maximal. Environmental induced discharges were supposed to be the cause of anomalies.

The anomaly is seen as the saturation of an operational amplifier (0) masking the nominal low-level signal (0). It was a temporary malfunction the consequence of which was an outage of the whole subsystem. The electronic anomaly was well-explained by a voltage spike in the vicinity of the op-amp input stage. It was reproduced by an ESD immunity test confirming the hypothesis.
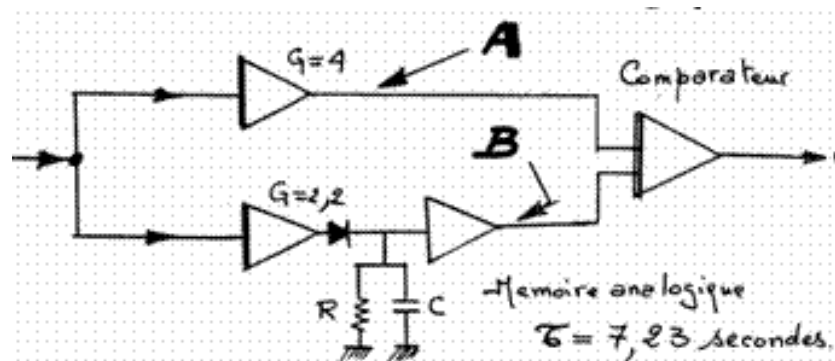
Figure 6. Simplified scheme of the comparator
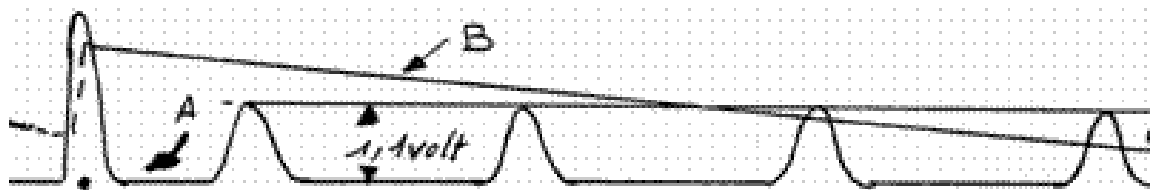
Figure 7. The recurrent pulse on channel A is masked by the low response to the transient on channel B

Towards an ESD-free program

A design and development objective would be a zero-failure mission. In most cases programs are not actually affected by environmental induced discharges. This is a pretext to decrease the costly effort of implementing mitigation techniques with respect to the charging risk. However, any manufacturer has been, is or will face major problems related to charging. The first effort consists of convincing management the risk is not overestimated. The spacecraft provider has to lean on experimented staff. It is not so easy since various domains of physics and technology are involved. The subject needs a continuous funding even when there is an apparent absence of risk in periods free of anomalies.

Mitigation techniques for lowering the charging risk follow two convergent ways. Everything is done for decreasing the number of discharge sources, in the same time, any

equipment potentially exposed to charging has to be submitted to an electromagnetic immunity test. Visual inspection and knowledge of materials is primarily used for identifying possible discharge sites.

Design rules have not to be too numerous if we want their strict implementation. Main rules are zero floating-conductor (disregarding the size), the main frame must be a screen to electromagnetic interference and to high-energy electrons, external cables (in the sense they are submitted to electric transients) will be shielded. Any external equipment (equipment outside the shielded main frame) is supposed to be exposed to EMI, so an immunity test will be applied to it.

At a higher level of technical management, continuous Research & Technology activities will be carried out for characterizing new technologies (concerning charging), and possible evolution of older technologies. A systematic investigation of every in-flight anomaly (major or minor) is necessary.

Problems of Qualification and Verification

Qualification at equipment and subsystem level is possible and actually carried out. However representative tests at equipment level are always difficult to achieve. It is never ensured that cables are similar to the flight model, or that same controls are used during the test as on flight telemetry. We know equipment passing successfully ground tests, experiencing charging anomalies in flight.

At system level, no verification test is sure enough to prove the ability of a given S/C to sustain a charging environment. Often we are relying on methods and procedures, and visual inspection.

Trends

Charging and consequences at the altitude of geostationary satellites are well understood; mitigation techniques are known and generally applied. Standardized guidelines will be issued at end of 2004 in Europe (ECSS-E20-07).

Though the number of events becomes low, manufacturing processes are in permanent evolution, causing bad surprises: components supposed to be safe become dangerous.

New technologies (electrical propulsion, high-voltage bus bars, very low-voltage logics, active antennas) are causes of unexpected problems.

A NOVEL SPACECRAFT CHARGE MONITOR FOR LEO

Luke Goembel
Goembel Instruments
1020 Regester Avenue, Baltimore, MD 21239
Phone: 410-377-6828
E-mail: luke@goembel.biz, www.goembel.biz

Introduction

Five years ago we introduced a new method for measuring spacecraft chassis floating potential relative to the space plasma ("absolute" spacecraft potential) in low Earth orbit. The method, based on a straightforward interpretation of photoelectron spectra, shows promise for numerous applications, but has not yet been tried. In the interest of testing the method, and ultimately supplying another tool for measuring absolute spacecraft charge, we are producing a flight prototype Spacecraft Charge Monitor (SCM) with support from NASA's Small Business Innovation Research (SBIR) program. Although insight into the technique came from data collected in space over two decades ago, very little data are available. The data indicate that it may be possible to determine spacecraft floating potential to within 0.1 volt each with the SCM second under certain conditions. It is debatable that spacecraft floating potential has ever been measured with such accuracy. The compact, easily deployed SCM also offers the advantage of long-term stability in calibration. Accurate floating potential determinations from the SCM could be used to correct biases in space plasma measurements and evaluate charge mitigation and/or sensing devices. Although this paper focuses on the device's use in low Earth orbit (LEO), the device may also be able to measure spacecraft charge at higher altitudes, in the solar wind, and in orbits around other planets. The flight prototype SCM we are producing for delivery to NASA in the third quarter of 2004 will measure floating potential from 0 to -150 volts with 0.1 volt precision, weigh approximately 600-700 grams, consume approximately 2 watts, and will measure approximately 8 x 10 x 17cm.

Spacecraft Charge Sensing

The phenomenon of spacecraft charging is of concern to those who maintain platforms in space. Spacecraft charge collection can take place in a variety of ways, including photo ionization of spacecraft surfaces by solar radiation and by interactions between the spacecraft and charged particles in space (free electrons and ions – space plasma).

There is a distinction made between "absolute" and "differential" spacecraft charging. Absolute spacecraft charging is the charging of the spacecraft chassis relative to the surrounding space plasma. Differential spacecraft charging is charging between electrically isolated parts of a spacecraft. Large differential charging is thought to be a cause of spacecraft system failures or, in extreme cases, entire spacecraft failures. Differential charging is generally though to be more of a hazard to spacecraft than absolute charging. Spacecraft designers try to avoid differential charging by providing electrical contact between parts. Sometimes this is done with an electrically conductive coating. Although steps can be taken to limit differential charging on spacecraft, absolute charging is less readily avoided. Since the SCM is designed to measure

absolute spacecraft charge, all of the discussion of "spacecraft charge" or "spacecraft floating potential" that follows will be in reference to the charge of the spacecraft chassis relative to the space plasma.

Since a spacecraft chassis is not normally "grounded" to the surrounding space plasma, it is free to collect charge and reach a floating potential relative to the space plasma. Although the absolute charge on a spacecraft should theoretically be very small (a few volts) under "normal" conditions, geomagnetic-activity-induced and spacecraft-power-system-induced charging can charge spacecraft to tens, hundreds, or even thousands of volts. Although geomagnetic-activity-induced charging might be rare (or mild) for some orbits, spacecraft-power-system-induced charging of nearly the voltage of the power system (e.g., about a hundred volts for the International Space Station) may take place every time a satellite's solar arrays are illuminated.

Spacecraft designers are concerned about absolute charge collection because it can affect the operation of the spacecraft. Even relatively mild (less than 100 volts) absolute spacecraft charge can disrupt the operation of electrically biased instruments, bias the data collected by scientific instruments, attract contaminants to sensitive instrument surfaces, and ultimately cause arc discharges and sputtering that deteriorate spacecraft surfaces or even cause electronics components to fail.

Charge mitigation schemes have been proposed to avoid the problems associated with absolute spacecraft charging. For example, the International Space Station is expected to be prone to significant charging due to its high-voltage (160-volt) DC power system and its orbit in a plasma-rich region of space. Designers predict that constant arc discharges will deteriorate surfaces of the station unless charge collection is mitigated. Therefore, the Plasma Contactor Unit has been designed to harmlessly dissipate charge from the International Space Station.

We believe efforts to study the spacecraft-charging phenomenon and efforts to successfully mitigate spacecraft charging will be advanced by the instrument we are now developing. Although the hazards of spacecraft charging are well known, the actual measurement of spacecraft floating potential has proven difficult. In cases where it is thought spacecraft systems have failed due to problems associated with spacecraft charging, the conclusion has usually been arrived at by very careful deduction rather than by direct measurements of spacecraft charge at the time of failure. Methods now used to measure spacecraft potential depend on relatively bulky, expensive instrumentation and/or complicated data analysis.

The instruments listed in the following table are used to measure spacecraft potential in low Earth orbit. The table lists the instrument, the method used, and some of the factors that limit the effectiveness of the method. Our comparison of the various methods available today is not made in an attempt to discount the careful work that has been done in the past by specialists in the field of spacecraft charging. By all accounts it has proved difficult to measure spacecraft charge by any method. In fact, the closest we have found to a published comparison of multiple methods of spacecraft floating potential measurement used on a single flight is the following: "the various methods [used to measure spacecraft charge] yielded very different results" [*Myers et al.,* 1990]. Clear statements of accuracy may be rare because it is difficult, if not impossible, to estimate the accuracy of current techniques (there are many factors that must be considered to make such

estimates). It may also be difficult to find statements of accuracy simply because there has not been a demand for reliable spacecraft potential measurements until recently.

Methods Now Used to Measure Spacecraft Potential

Instrument	Method	Major Limitations
Double Probe	SpacecraftÕs Electric field measured by potential difference between two probes mounted on booms.	Biases due to changes in probe work function, probe photoemission, etc. Booms needed. [Maynard, 1998]
Langmuir Probe	Volt-ampere characteristic of probe immersed in space plasma is measured.	Biases due to changes in probe work function, magnetically induced probe potentials, and so on. [Brace, 1998]
Retarding Potential Analyzer (RPA)	A current-voltage curve from the instrument is analyzed to determine ion drift velocity.	Biases due to uncertainty in expected ion drift for spacecraft at 0 potential. [Anderson, 1994]
Ion Energy Analyzers	Ion spectra of space plasma are analyzed for Ņlow energy cutoff.Ó	Biases due to uncertainty in the Ņlow energy cutoffÓ from such measurements. [Moore, 1996]

Methods now used to measure spacecraft (chassis) floating potential

Electron-Spectroscopic Charge Sensing

While examining high energy-resolution electron spectra for another purpose, an unexpected shift in the energy location of sharp electron spectroscopic peaks was observed. What was an annoyance in that study (the peak shift had to be compensated for) led the way to a novel method for determining absolute spacecraft floating potential. The data examined were from the Photoelectron Spectrometer Experiment (PES) of Atmosphere Explorer E (AE-E)[*Doering, Bostrom, and Armstrong,* 1973].

The peak shift, illustrated in the following diagram, was due to the ~0.5 volt change in spacecraft chassis floating potential as the satellite changed in altitude from 250 to 150 km.
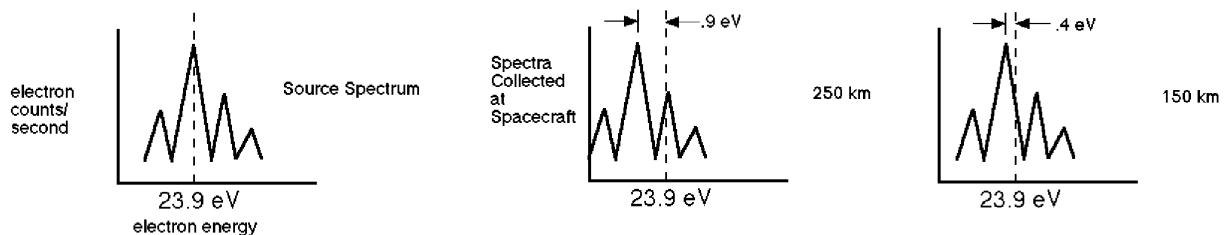
Electron-spectroscopic peak shift due to change in satellite floating potential.

The electron-spectroscopic technique of charge sensing is possible because 22.2, 23.9, 25.2, and 27.2 eV electrons are produced by the photoionization of oxygen and nitrogen at 150-300

km altitude by 304Å solar radiation. Simply put, the energy location of the four photoionization peaks (source spectrum) is well defined; therefore, an apparent shift in their energy location is due to deceleration or acceleration of the source electrons by the spacecraft's floating potential. Although the phenomenon was first observed due to a 0.5-volt change in spacecraft floating potential, the phenomenon can be used to determine floating potential of any magnitude.

Spacecraft floating potential can be determined from any electron spectra that contain the characteristic peaks that are produced by the 304Å photoionization of the atmosphere. Such spectra can be collected from all locations in the sunlit atmosphere at low altitudes (from 150-250 km, the "production region" for photoelectrons). In the production region photoelectrons are produced and lost locally and the distribution is isotropic. However, not many spacecraft fly at 150-250 km altitude. Fortunately, the electron spectroscopic method can be extended to higher altitudes, as will be described below.

An upper boundary of 250 km has arbitrarily been chosen for the photoelectron production region. It can extend to 300 km if the density of neutrals (mostly atomic oxygen at those altitudes) is great enough. Above 250-300 km the density of neutrals is so low that the photoelectrons observed at those altitudes are almost exclusively escaped photoelectrons from the top of the production region (from 250-300 depending on atmospheric density). The photoelectrons travel from the region of production to higher altitudes along geomagnetic field lines. Fluxes of photoelectrons to higher altitudes are great enough that spectra that contain the characteristic peaks due to 304Å photoionization of the atmosphere can readily be obtained with the SCM. If the photoelectrons pass through a region of low thermal plasma density, the spectra will be little changed from spectra collected at lower altitudes [*Lee et al.*, 1980b], and it will be possible to make very accurate spacecraft potential determinations at that location. Spectra collected by PES exhibit the 304Å photoionization peaks at all altitudes for which data is available (PES collected no data above 1000 km). However, there is evidence that the electron-spectroscopic method could be used to determine spacecraft floating potential at very high altitudes. Research indicates that conjugate photoelectron spectra (spectra of photoelectrons that have traveled along geomagnetic field lines to the nighttime ionosphere) might contain the peaks needed to determine floating potential. Studies of satellite data show that conjugate photoelectrons, even after travelling great distances along field lines, do not change significantly in energy (they had no discernable change in energy within the limits of the experiment) [*Peterson et al.,* 1977a and b].

Data from PES of AE-E indicate that it should be possible to make spacecraft potential determinations that are accurate to 0.1 eV at local times from 6 to 9 at altitudes to 1000 km without the use of correction factors, since spectra from those local times will resemble those collected in the production region. Thermal plasma densities are too low at early local times to degrade the spectral peaks through coulomb scattering. At other local times, where the photoelectrons from the production region may need to pass through a region of high thermal plasma density before detection by the SCM, the photoelectron peaks will be broadened and somewhat lowered in energy due to coulomb scattering. It may be possible to use a correction factor in the analysis of spectra that exhibit peak broadening (and the coinciding lowering in peak energy) in order to preserve the 0.1 volt accuracy of the electron spectroscopic method.

Such a factor could be derived from electron transport theory (e.g., as exemplified in the work of Jaspers and Smith [1978] and Link [1992]).

A noteworthy advantage of the electron-spectroscopic method of charge sensing is the promise of an accurate measure of spacecraft charge with few effects that will reduce the reliability of the measurement over time. A predominant method now used (i.e., the use of Langmuir probes) suffers from calibration drift due to a change in probe surface work function with exposure to atomic oxygen. Since the electron-spectroscopic method is based on the determination of the energy location of electron-spectral peaks, drift in the floating potential measurement over time can only be due to a drift in the energy calibration of the electron spectrometer. With careful electronics design, such drift for even a space flight electron spectrometer can be made negligible.

Although this paper focuses on the use of the SCM in low Earth orbit (where all of the PES data was gathered), it may be possible to extend the technique not only to higher orbits (as was just described) but to orbits around other planets as well. The same technique that the SCM will use to determine floating potential above the Earth's atmosphere could be used to determine floating potential above other planets since the dominant 304Å ionizing solar radiation will produce peaks in photoelectron spectra from other atmospheres.

A somewhat different phenomenon will enable the SCM to determine spacecraft charge in the solar wind. There is a distinct peak in electron abundance in the solar wind at about 10 eV. By measuring how much the 10 eV electrons have been accelerated or decelerated by the spacecraft, the floating potential can be measured. In fact, the method is already used, as will be described in detail below.
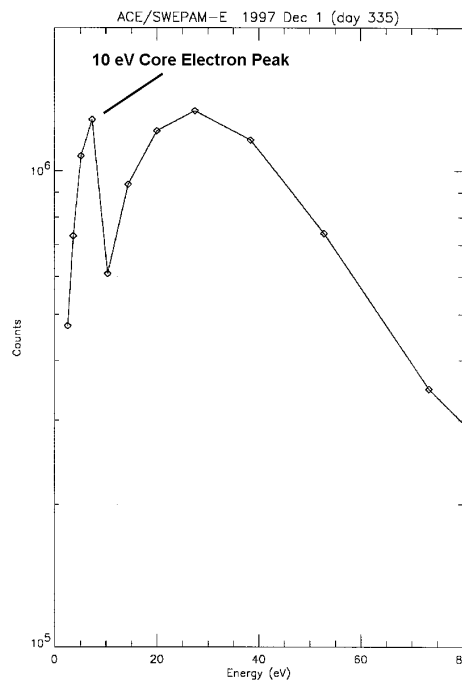
Energy spectrum of solar wind electrons from ACE. Courtesy of Ruth Skoug.

The spectrum shown above is typical of the data now used to determine spacecraft floating potential in the solar wind. It is data from the SWEPAM instrument on the ACE spacecraft. Curve fitting is used to determine where the 10 eV "solar core electron" peak appears. Note that the peak of interest, at about 10 eV, consists entirely of 5 data points, over a range of about 10 eV. The SCM, with twenty-fold the geometric factor of the SWEPAM instrument at 10 eV, would have much greater sensitivity to the signal used to determine floating potential. Given the same amount of time, the SCM would be able to collect much more data in the critical 0-20 eV range. The quality of the data the SCM would collect would enable a more accurate and/or higher frequency determination of the spacecraft floating potential. The same performance characteristics that enable the SCM to measure floating potential from atmospheric photoelectrons (i.e., energy resolution and data gathering rate) will allow the SCM to excel at measuring floating potential in the solar wind. However, at this time our efforts are primarily focused on flying the SCM in low Earth orbit, where the need for the device is immediate and chances of obtaining a timely first flight are better.

The Spacecraft Charge Monitor

Although the electron spectroscopic method of spacecraft charge sensing shows great promise, its feasibility has only been demonstrated through theory and a single, relatively small data set - the photoelectron spectra from PES. Although the PES instrument gave us the first clues to the method, PES collected data that is difficult to interpret for our purposes (more about this appears in Goembel and Doering [1998]). This is understandable because the method was not published until 22 years after the last PES instrument was launched. The PES instrument was designed to make a broad survey of photoelectrons over a large energy range (0-500 eV). The next step in learning how to best exploit the method is to collect electron spectra from various orbits with an instrument designed specifically for electron-spectroscopic charge sensing.

To that end, Goembel Instruments has been developing a device that will use high energy-resolution electron spectroscopy to determine spacecraft charge. To the best of our knowledge, PES has been the only satellite instrument able to collect data with sufficient energy resolution in the energy range needed to determine spacecraft charge. Its energy resolution (2.5% $\Delta E/E$) was unusually high: most charged-particle spectrometers flown have energy resolution that is far worse (typically 10%, 15% or even 30%). Those instruments would not be able to produce spectra that exhibit the well-defined peaks needed to determine spacecraft charge. The primary reason only low-energy-resolution charged-particle spectrometers are now flown is that there is a trade-off between instrument resolution and data gathering rate for instruments of traditional design. If one wanted to improve the data gathering rate of a traditional concentric-hemispherical-analyzer (e.g., PES), one could simply increase the size of the device. Doubling the size (diameter) of the PES concentric-hemispherical-analyzer, and scaling up all other dimensions (such as aperture diameter) would increase the data-gathering rate of PES 8-fold while retaining its 2.5% energy resolution. Of course, doubling the size of the concentric-hemispherical-analyzer would add a great deal to the bulk of the device, an action to be avoided in space flight instrument design.

The SCM contains a charged-particle spectrometer of distinctly non-traditional design. In fact, the SCM includes a unique, patent-pending collimator/aperture arrangement that will for the

first time allow the collection of high energy-resolution charged-particle spectra at a high rate with a small diameter concentric-hemispherical-analyzer. The unique collimator/aperture arrangement will enable the SCM to collect the data needed to determine spacecraft floating potential in about one-sixtieth the time it would take PES to collect the same data. Whereas PES weighed 3,160 grams [*Doering, Bostrom, and Armstrong,* 1973], the flight prototype SCM will weigh approximately 600-700 grams. The flight prototype SCM will have a data-gathering rate per gram two orders of magnitude greater than that of PES even though it will have the same extraordinary energy resolution of PES.

The following photograph is of the flight prototype SCM in its current state, 13 months into its 24-month development through Phase II SBIR funding. All that remains to complete the device is the fabrication of the electronics and electronics housing, which are represented by clear plastic in the photograph.
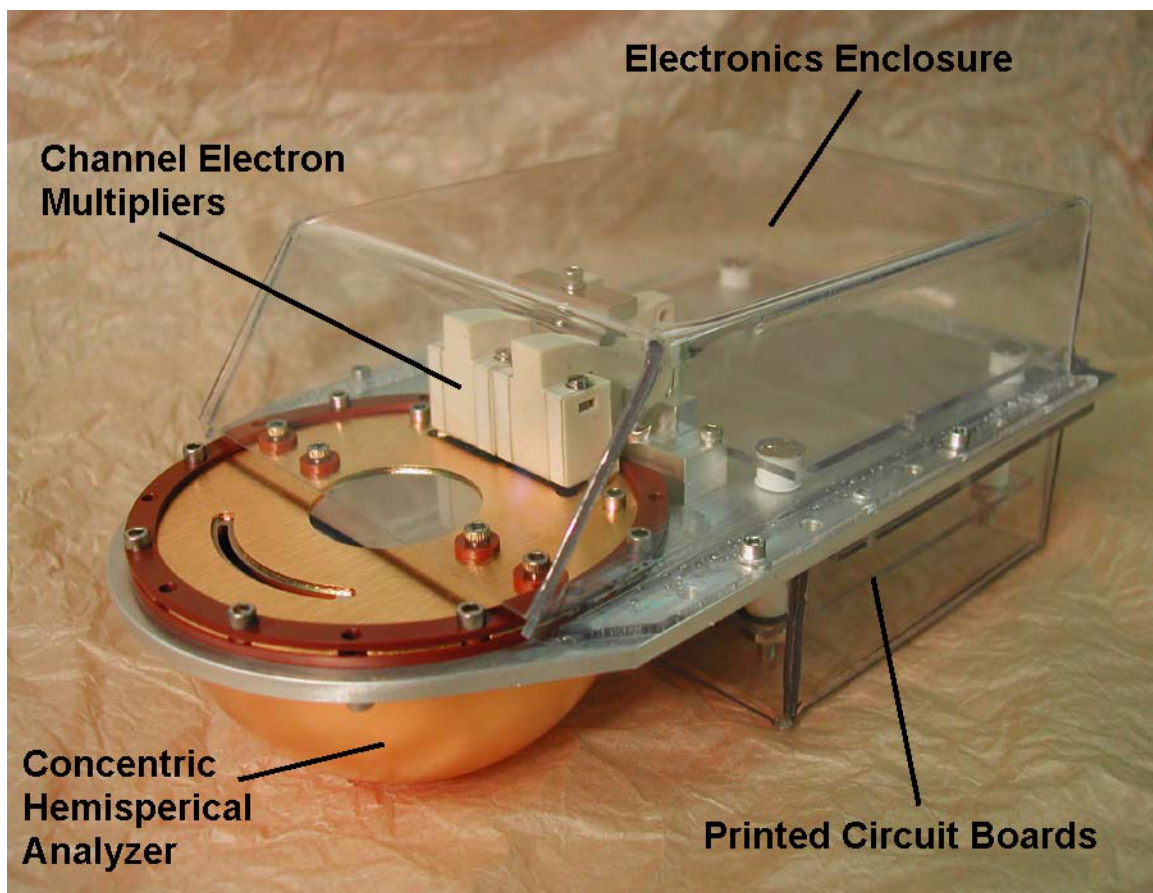
The Goembel Instruments Spacecraft Charge Monitor (incomplete assembly).

The function of the SCM is now described with reference to the following numbered diagram. The SCM consists of a concentric-hemispherical electrostatic charged-particle energy analyzer, two large aperture channel electron multipliers, instrument electronics, and supporting structure. The concentric-hemispherical-analyzer contains three electrostatic surfaces: the inner hemisphere, the outer hemisphere, and the aperture/collimator. Electrons (1) enter the SCM

through the ~60° x ~20° fan-shaped field-of-view of the entrance aperture/collimator (2) and enter the hemispherical shell-shaped space (3) defined by the inner and outer hemispheres. Electrons with kinetic energy in the narrow range allowed to pass through the exit aperture (4) strike the CEMs (5) and are "multiplied" into detectable pulses at the output anode of the CEM. The SCM electronics (6) control the electrostatic surfaces of the concentric-hemispherical analyzer, process the pulses from the electron multipliers, receive commands from the spacecraft, and output data to the spacecraft. The pulses are counted at each energy and, thus, an electron energy spectrum is produced. The SCMs field-potential-gate-array processor (FPGA) will receive commands from the spacecraft to set the data-gathering mode of the device and will output data to the spacecraft. All of the device's electronics will reside on three printed circuit boards within a 1.5 mm-walled aluminum enclosure. The complete flight prototype SCM fits within a volume of 8 x 10 x 17cm. The device requires approximately 2 watts (28 volts, unregulated) to power, will communicate with the spacecraft through a standard RS 422 interface, and is designed to operate over a -24°C to +61°C temperature range.
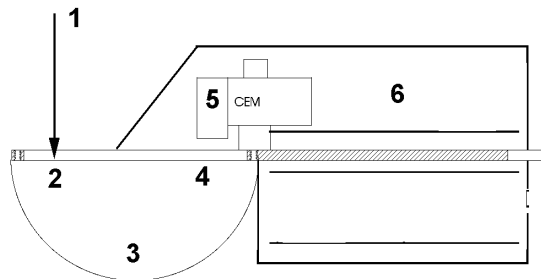
Functional diagram of the SCM

<u>Laboratory Tests of the SCM</u>

The Goembel Instruments electron spectroscopy laboratory is equipped with a high vacuum chamber, precision electron monochromator, and all of the apparatus needed to performance test the SCM. A hybrid turbomolecular/molecular drag pump and an oil-free rough pump evacuate the vacuum chamber. Custom-built electronics control the electron monochromator. The vacuum chamber and electron monochromator control electronics are shown in the following photograph.

SCM test and calibration apparatus

The following photograph illustrates the arrangement of the electron source (electron monochromator) and laboratory prototype SCM in the vacuum chamber (top section of chamber removed).
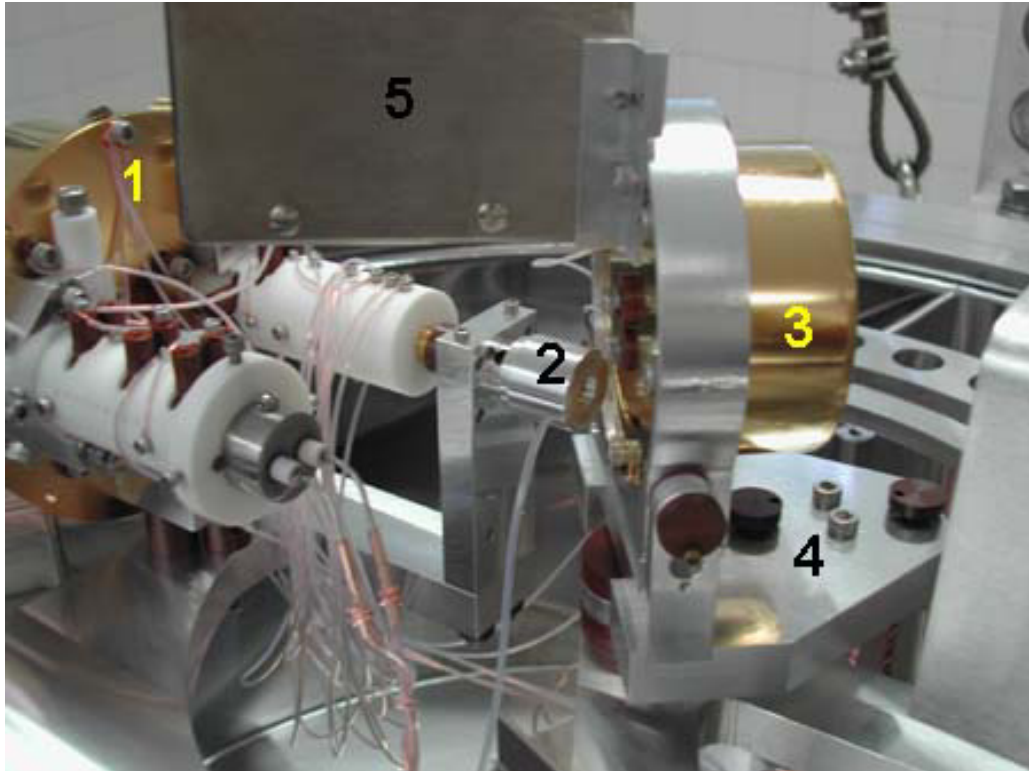
Photograph of the electron monochromator and laboratory prototype SCM

The numbers that appear in the photograph will aid the reader in the description. Keep in mind that the laboratory prototype SCM concentric-hemispherical-analyzer (3) has the identical electron-optical design of the flight SCM and is being used in laboratory tests of the SCM until the completed flight prototype electronics are delivered. The electron monochromator (1) produces a well-collimated beam of electrons with an energy spread of less than 0.1 eV. The electron monochromator is described in detail in Goembel and Doering [1995]. The electron beam passes through a gas cell (2), where gas is admitted so that electron scattering spectra of the gas can be gathered by the SCM. The laboratory prototype SCM concentric hemispherical analyzer (3) is held in an angular-controlled mount (4). The mount includes an angular control so that we can measure the SCM field-of-view. An AMPTEK MD-501 electron detector module (5) is mounted at the exit aperture of the SCM hemispherical analyzer. The electron detector module (5) and the FPGA-based laboratory prototype control electronics (not shown) serve the same purpose as the integral CEMs/electronics of the flight prototype SCM.

The following spectrum was gathered with the laboratory prototype SCM.
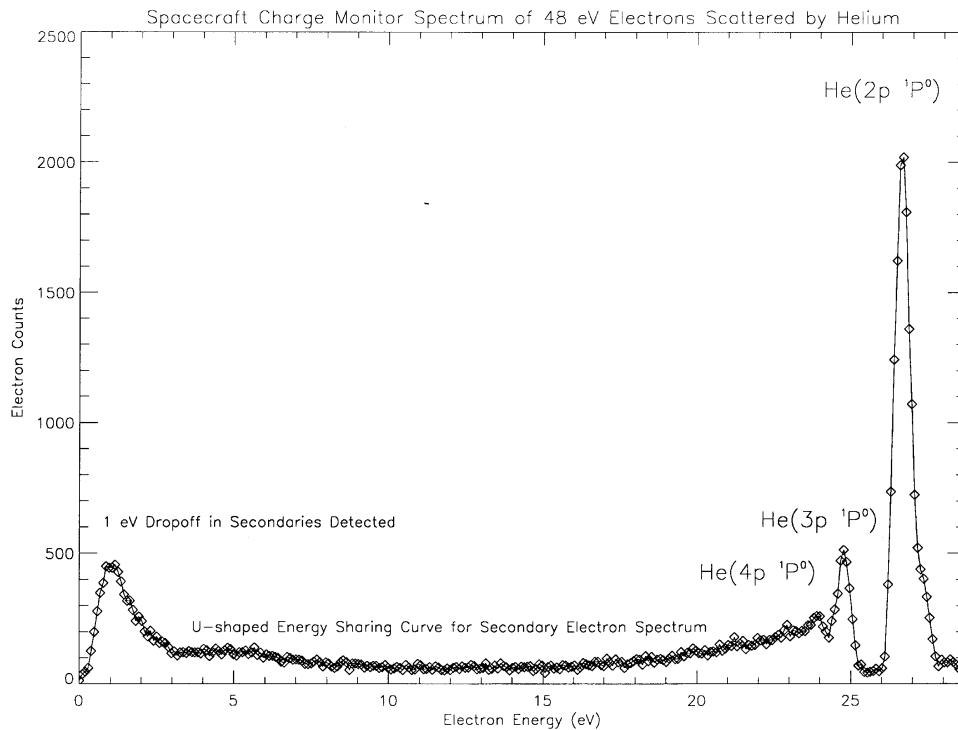
SCM Electron Impact Spectrum of Helium

The spectrum covers an energy range of 0-30 eV in 0.1 eV steps. The electrons detected by the SCM are those that result from the scattering 48 eV source electrons (from the electron monochromator) by helium. The peaks that appear at energies greater than 23 eV are due to the electron impact excitation of helium to various electronic (quantum) states above the ground state. The electrons that have been detected by the SCM have lost some of their 48 eV of kinetic energy in collisions with the helium atoms. The final state of the electrically excited helium atoms produced is labeled above each of the peaks in the spectrum. The tallest peak in the spectrum (at about 27 eV) is the first in the Rydberg series. The Rydberg series converges to a continuum to the left of the peaks at ~23.4 eV: 48 eV minus the ionization potential of helium

(I.P.$_{\cdot He}$ = 24.58 eV). The table, below, gives the final state of the He produced, and the energy lost by the 48 eV electrons in the inelastic collision with the gas.

The ionization of helium to certain final electronic states produces the peaks in the spectra.

He$^+$ Electronic State Produced by Collision	Energy Lost by Primary (48 eV) Electron
4p ^{1}P^0	23.73 eV
3p ^{1}P^0	23.08 eV
2p ^{1}P^0	21.21 eV
2s ^{1}S	20.61 eV
2s ^{3}S	19.81 eV

At energies less than 23 eV the spectrum exhibits the u-shaped "energy-sharing curve" expected for secondary electron production through the collision of the 48eV electrons with a gas. The sudden reduction in intensity that appears at 0-1 eV in the spectrum is also expected. It is due to the inability of concentric-hemispherical-analyzers configured as this one is to pass electrons with less than ~1 eV energy. The spectrum collected with the SCM laboratory prototype confirms that the patent-pending design of the SCM retains the 2.5% energy resolution of the PES device in precisely the energy range needed to determine spacecraft floating potential. This and other spectra collected from the SCM demonstrate that the SCM has the high energy resolution and excellent internally-produced-secondary-electron (noise) suppression needed to collect spectra for the determination of spacecraft floating potential.

Tests of the complete flight prototype SCM are planned to commence after the delivery and integration of the flight electronics. Instrument field-of-view, energy calibration, temperature stability, etc. will be determined. Vibration and thermal vacuum tests will also be performed.

Integration of the SCM onto a Spacecraft

Experience gained from the deployment of the six PES instruments on three Atmosphere Explorers (AE-C, -D, and -E) will guide us in the deployment of the SCM. As the following photographs illustrate, the PES instruments were mounted on the AE satellite so that the entrance aperture/collimator of the device protruded slightly from the satellite's outer surface.
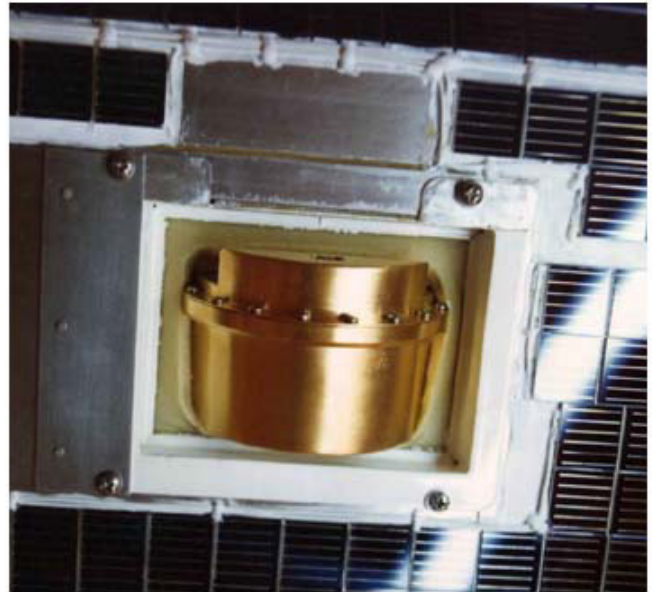
PES sensor 1 (left) and sensor 2 (right) mounted on AE-E, circa 1976.

It is desirable to orient the look direction of the SCM so that it points to within 55˚ of geomagnetic field lines that pass through the photoelectron production region. The "55˚" guideline results from the experience gained from the orientation of PES sensor 1 of the AE-E satellite. PES sensor 1 was mounted on the ram side of the despun spacecraft looking along the spin axis (AE-E orbited at an inclination of ~20˚). Interested readers can learn more about how to best mount the SCM on a spacecraft by referring to Goembel and Doering [1998] and Appendix 1 and 2 of Lee et al., [1980a]. One of the great advantages offered by the electron spectroscopic method of charge sensing is that regardless of the vagaries of the orientation of the sensor, if a signal is recieved (peaks in the photoelectron spectrum), the floating potential can be determined. Misalignments from an ideal orientation will not bias the measurement.
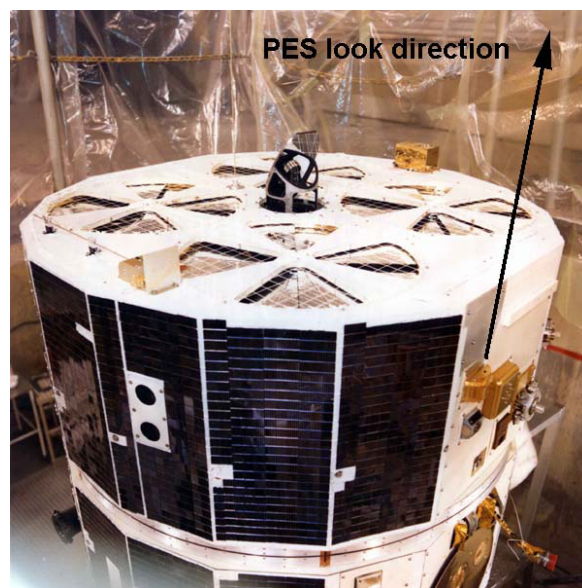
The look direction of PES sensor 1 on AE-E, circa 1976.

Whereas PES has a field of view of approximately 20˚ x 9˚, the SCM has a field of view of approximately 60˚ x 20˚, as illustrated by the following diagram.
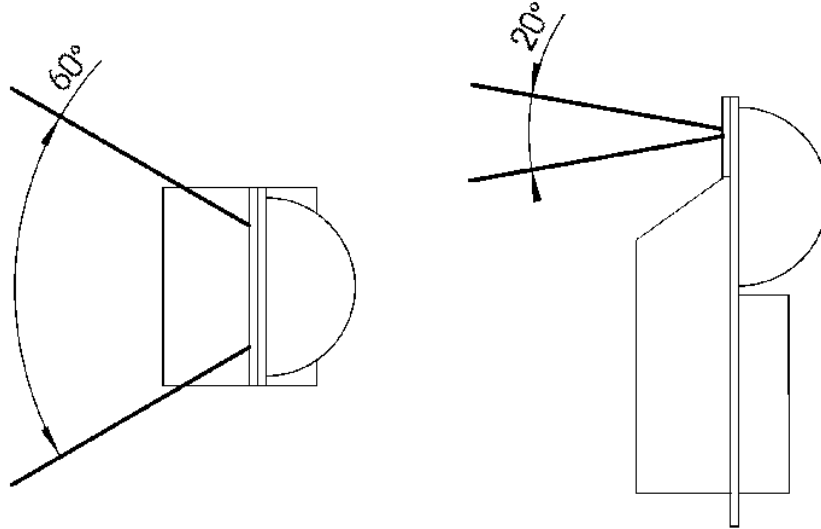
60˚ x 20˚ field of view of the SCM

The field of view is actually a more complex shape than that shown due to the patent-pending electron optical design of the SCM, but for spacecraft integration purposes the 60˚ x 20˚ approximation suffices. The larger field of view contributes to the greater data-gathering rate (larger geometric factor) of the SCM. It also allows more flexibility to mount the device in an orientation that maximizes the portion of an orbit that photoelectron spectra can be gathered.

To recap what was said in section in 4 of this paper: the flight prototype SCM will measure floating potential from 0 to -150 volts with 0.1-volt precision, weigh approximately 600-700 grams, require approximately 2 watts (28 volts, unregulated) to power, and have the dimensions of approximately 8 x 10 x 17cm. The SCM will communicate with the spacecraft through a standard RS 422 interface, and is designed to operate over a -24˚C to +61˚C temperature range. The flight prototype we are developing will be delivered to NASA in the third quarter of 2004. We are looking forward to retrieving data from the flight of the prototype and are already considering options for subsequent versions of the SCM.

Acknowledgements

References

1. Anderson, P. C., Hanson, W. B., Coley, W. R., and Hoegy, W. R., Spacecraft potential effects on the Dynamics Explorer 2 satellite, J. Geophys. Res., 99, A3, 3985-3997, 1994.

2. Brace, L. H., Langmuir probe measurements in the ionosphere, <u>Measurement technologies in space plasmas: particles</u>, Robert F. Pfaff, Joseph E. Berovsky, and David T. Young, editors, Geophysical Monograph 102, AGU press, 1998.

3. Doering, J. P., Bostrom, C. O., and Armstrong, J. C., The Photoelectron-Spectrometer Experiment on Atmosphere Explorer, Radio Science, 8, 387-392, 1973.

4. Goembel, L., Measuring spacecraft potential with an electron spectrometer, Proceedings of the 6th Spacecraft Charging Technology Conference, AFRL-VS-TR-20001578, 287-290, 2000.

5. Goembel, L., and Doering, J. P., A compact, light weight, high resolution electron monochromator, Rev. Sci. Instr., 66, 6, 3472-3474, 1995.

6. Goembel, L., and Doering, J. P., Instrument for measuring spacecraft potential, J. Spacecraft and Rockets, 35, 66-72, 1998.

7. Jasperse, J. R., and Smith, E. R., The photoelectron flux in the earth's ionosphere at energies in the vicinity of photoionization peaks, Geophysical Res. Lett., 5, 10, 843-846, 1978.

8. Lee, J. S., Doering, J. P., Potemra, T. A., and Brace, L. H., Measurements of the ambient photoelectron spectrum from Atmosphere Explorer: II. AE-E measurements below 300km during solar minimum conditions, Planet. Space Sci., 28, 947-971, 1980a.

9. Lee, J. S., Doering, J. P., Potemra, T. A., and Brace, L. H., Measurements of the ambient photoelectron spectrum from Atmosphere Explorer: II. AE-E measurements from 300 to 1000 km during solar minimum conditions, Planet. Space Sci., 28, 973-996, 1980b.

10. Link, R., Feautrier solution of the electron transport equation, J. Geophys. Res., 97, A1, 159-169, 1992.

11. Maynard, Nelson C., Electric field measurements in moderate to high density space plasmas with passive double probes, <u>Measurement technologies in space plasmas: fields</u>, Robert F. Pfaff, Joseph E. Berovsky, and David T. Young, editors, Geophysical Monograph 103, AGU press, 1998.

12. Meyers, N. B., Raitt, W. J., White, A. B., Banks, P. M., Gilchrist, B. E., and Sasaki, S., Vehicle charging effects during electron beam emission from the CHARGE-2 experiment, Journal of Spacecraft and Rockets, 27, 1, 25-37, 1990.

13. Moore, T. E., Chandler, M. O., Pollack, C. J., Reasoner, D. L., Arnoldy, R. L., Austin, B., Kintner, P. M., and Bonnell, J., Plasma heating and flow in an auroral arc, J. Geophys. Res., 101, A3, 5279-5297, 1996.

14. Peterson, W.K, Doering, J. P., Potemra, T. A., McEntire, R. W., and Bostrom, C. O., Conjugate photoelectron fluxes observed on Atmosphere Explorer C, Geophysical Res. Lett., 4, 3, 109-112, 1977a.

15. Peterson, W.K, Doering, J. P., Potemra, T. A., Bostrom, C. O., Brace, L. H., Heelis, R. A., and Hanson, W. B., Measurement of magnetic field aligned potential differences using high resolution conjugate photoelectron energy spectra, Geophysical Res. Lett., 4, 9, 373-376, 1977b.

ACTIVE SPACECRAFT POTENTIAL CONTROL FOR CLUSTER RESULTS FROM THREE YEARS IN ORBIT

Klaus Torkar
Space Research Institute, Austrian Academy of Sciences
Schmiedlstrasse 6
8042 Graz, Austria
Phone: +43 316 4120 531
Fax: +43 316 4120 99531
E-mail: klaus.torkar@oeaw.ac.at

Mats André
Swedish Institute of Space Physics, Sweden

Andrew Fazakerley
MSSL, UCL, UK

Michael Fehringer
ESA/ESTEC, The Netherlands

Henri Rème
CESR, France

Wolfgang Steiger
Austrian Research Centers, Austria

Knut Svenes
Norwegian Defence Research Establishment, Norway

Abstract

The technique chosen to control the potential of the Cluster spacecraft is based on liquid metal ion sources generating an energetic ion beam. The ion current counteracts the photo-electron current and thereby clamps the spacecraft potential to few volts positive even in a very tenuous plasma environment where few other charge carriers exist. This principle and its implementation on the Cluster spacecraft is reviewed from both technical and scientific perspectives. The ion sources are light and require very moderate power resources. Initial results reported earlier have already proven the efficiency of the method and the absence of any interference with field, wave, and plasma measurements. After three years in space further conclusions can be drawn with respect to charging and the efficiency of the control. An overview of the performance of the ion emitters is given, and examples demonstrating the helpful effect on low energy plasma measurements - both electrons and ions - are presented. Finally, the possible application of this technique in future missions is addressed.

Introduction

Active spacecraft potential control has been recognized as a suitable means to ensure accurate plasma measurements on board a spacecraft.

First instruments serving this purpose were designed in the 1980's and flown in the 1990's. The technique which was applied in most cases was the one also used on Cluster: the emission of an ion beam with an energy of several kiloelectronvolt moves the equilibrium potential of the spacecraft into the desired range. Another principle using a plasma source instrument (PSI, Moore et al., 1995[1]) was applied on the Polar spacecraft. This technique brought about quite different results, some of them undesirable.

Two other instruments relied on energetic ion beams:

- Instrument RON on board of the Russian Interball Auroral Probe (Torkar et al., 1998[2]) launched in 1995 into a high inclination Earth orbit

- The Potential Control Device on board of Equator-S (Torkar et al., 1999[3]) launched in 1998 into an eccentric, equatorial Earth orbit

Both instruments can be considered as direct predecessors of the instruments flown in the Cluster mission. The Cluster example provides us with the first long-term data set for studying the effects of active spacecraft potential control. The satellites were launched in July and August, 2000, respectively.

Principle of Operation

Let us review the principle of operation applied for active spacecraft potential control on Cluster. The spacecraft have polar orbits around the Earth with 4 x 19.6 R_E and lead regularly into the polar regions and in the lobes of the magnetosphere, where plasma density may be very low ($<<1$ cm^{-3}). Under these conditions the plasma electron current to the spacecraft surface is small compared to the current of photo-electrons generated at the surface. Therefore the high-energy tail of the photo-electrons suffices to compensate the plasma current, resulting in a highly positive equilibrium potential which allows only these high-energy electrons to escape. By artificially adding another current of the order of the one carried by the bulk of the photo-electrons to this system, one can achieve a significant reduction of the equilibrium potential and a stabilization to values of a couple of volts. The sheath around the spacecraft shrinks due to the reduced spacecraft potential, improving not only the particle measurements, but very often also the electric field measurements by double-probes.

The instruments onboard Cluster are known as ASPOC. The acronym stands for Active Spacecraft Potential Control. A description can be found in Torkar et al. (2001)[4]. The instruments emit an Indium ion beam of 5 to 50 µA, and 5 to 9 keV into the direction of the spin axis. The ion sources are of the Liquid Metal Ion Sources type, where liquid Indium at T≈200 C covering a needle is ionized in strong E-field. The beam consists of >90% singly charged In$^+$>90% single charged In$^+$, and minor contributions of other charge states and clusters. The isotopic composition is dominated by the isotope 115 amu (95.7%), followed by 113 amu (4.3%).

These sources require little electric power: just about 0.5 W for a small heater element and the energy needed in the high voltage system to accelerate the ions into a beam. The mass of the charge material is negligible. One gram of Indium is sufficient for about 4000 hours of operation at 10 µA. The instruments on Cluster contain several emitters in order to increase the total operating time and to have some redundancy, but only one emitter is operated at one time.

Operations on Cluster

After many tests in the commissioning phase of the Cluster, the routine operation of the ASPOC instruments started with the beginning of the nominal mission on February 1st, 2001. Spacecraft potential control on Cluster is still active to date, although the nominal mission has ended on February 1st, 2003, and we are already half a year into the extended mission phase. Active operations is not continuous, but concentrates on key regions:

- the high latitude magnetosphere, with dynamic boundaries, presence of low plasma density regions, occasionally together with the presence of very cold plasma component.

- the lobes of the magnetosphere, in particular the boundaries to the tail plasma sheet.

While the Cluster orbits have their apogee in the tail region of the magnetosphere, the scientific objectives are fulfilled by operating the instruments over

- 7 hours around outbound cusp crossing

- 7 hours centered at neutral sheet

- 7 hours around inbound auroral zone crossing

Seven hours are not a limitation by the technique, but have been chosen as a compromise to allow coverage far into the extended mission. The instruments had also been operated throughout complete Cluster orbits (57 hours).

Table 1 shows a summary of ASPOC operations onboard Cluster, as of August 21st, 2003.

Table 1. Summary of ASPOC/Cluster operations

	Spacecraft			
	Salsa	Samba	Tango	Total
Total operation time (hours)	234	2543	2115	4892
Maximum total operation time of a single emitter (hours)	128	2525	1468	
Number of operations	107	450	373	930
Average duration of single operation (hours)	2.4	5.9	5.8	5.5
Maximum duration of single operation (hours)	7.8	36.4	35.8	

Beam Current and Energy

Figure 1 shows the spacecraft potential of the Cluster spacecraft number 1 and 2, both encountering almost the same plasma conditions. The magenta line indicates the time interval when the ASPOC ion beam was active on Cluster 2, with a beam current of 10 µA. It should be mentioned that this and some following figures show the voltage measured between double probes and spacecraft body as approximation to the real spacecraft potential. The measurements of the spacecraft potential are provided by the double probe instrument (EFW) described in Gustafsson et al. (2001)[5]. The figure shows:

- The potential of Cluster 1 (black) varies strongly, following the variations of density and temperature of the plasma in the changing environment.

- Without potential control at the beginning and the end of the time interval shown, the potentials of the two spacecraft follow each other closely, demonstrating that the conditions were similar on both spacecraft.

- A constant ion beam current is applied on spacecraft 2 between 05:15 and 09:30. It results in a compression of the variations of the spacecraft potential into a narrow band between 6 and 9 V. Some spikes in the raw potential data shown are caused by the operation of the active sounder and should be ignored in this context.
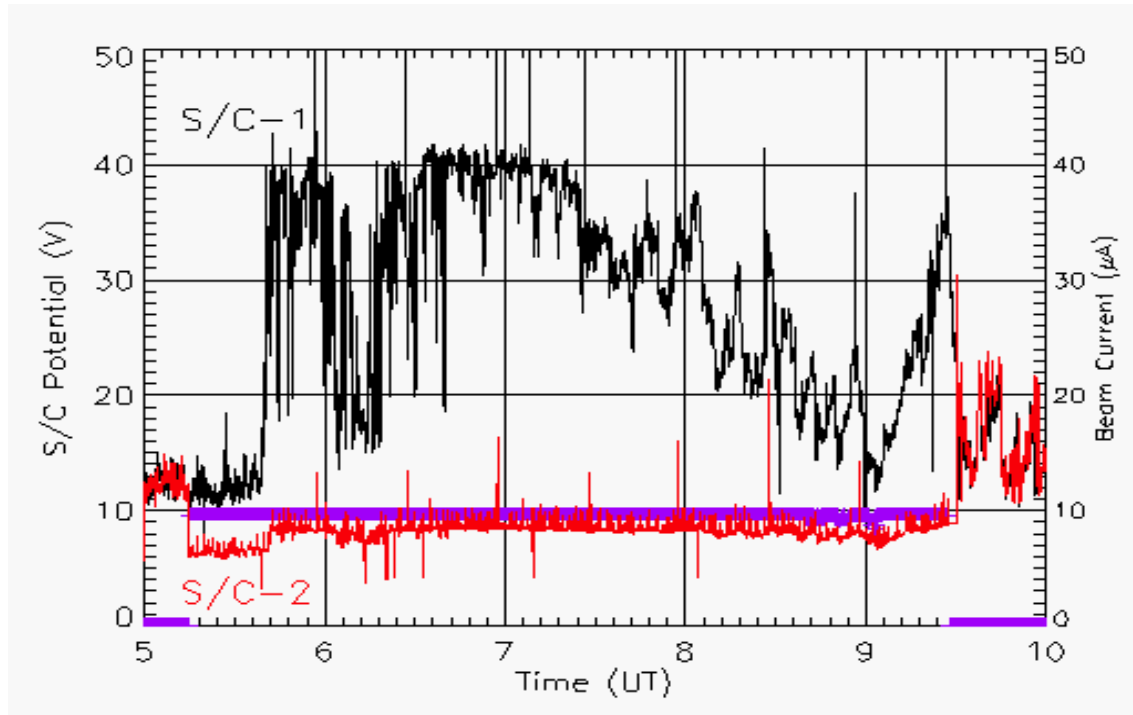
Figure 1. Spacecraft potential on Cluster 1 (black) and Cluster 2 (red), and ion beam current applied on Cluster 2 (magenta).

In summary, the spacecraft potential is very stable during ASPOC operation with constant beam current regardless of how the changing ambient plasma population, enabling better plasma measurements, as will be shown later.

By operating the ion sources in constant current mode, the extraction voltage varies according to the flow conditions of the liquid indium. Furthermore, the typical operating voltage varies between individual emitters due to small mechanical variations. The resulting voltages throughout the first years of the Cluster mission are shown in Figure 2. The horizontal axis refers to operational cycles of an instrument, which implies a typical operating time of 7 hours per cycle.
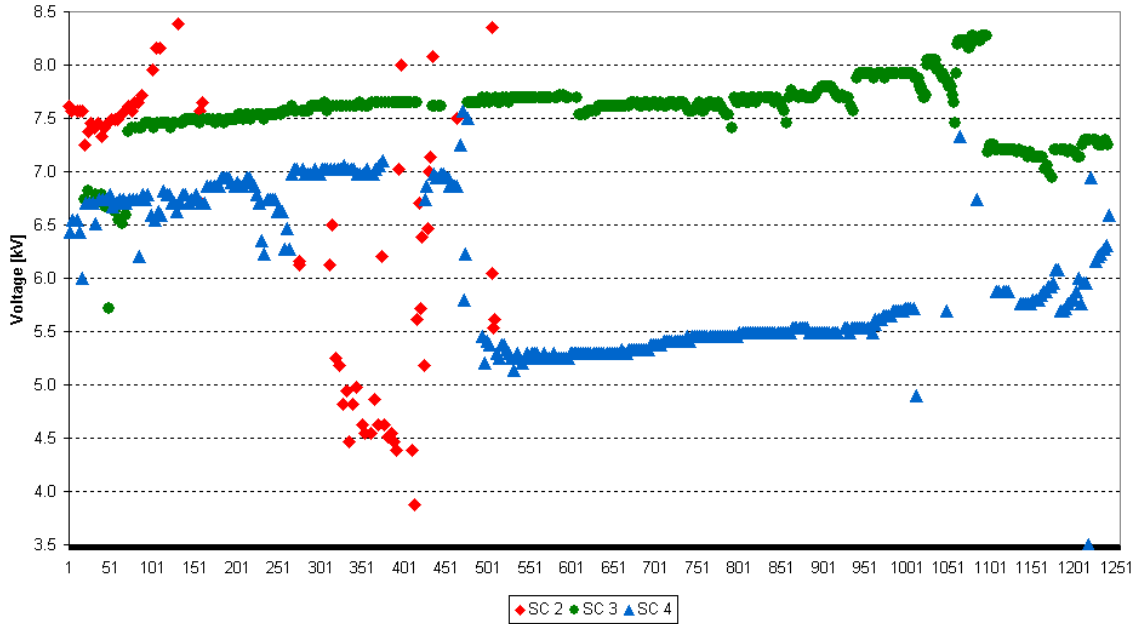
Figure 2. Development of beam energy. Horizontal axis refers to operational cycles of the instruments.

Spacecraft Potential Results

The correlation between the spacecraft potential on the Cluster spacecraft with and without spacecraft potential control has been analyzed on a statistical basis. The following figures display some results for the year 2001. Figure 3 shows a histogram of the spacecraft potential for Cluster 1 and 2, for all times without active spacecraft potential control, confirming that both spacecraft saw similar plasma conditions, and hence both spacecraft have almost identical potentials.

Figure 4 shows histograms, again for Cluster 1 and 2, for all times when the potential control was active, but only on Cluster 2. The peaks around 5 V in the Cluster 1 distribution can be associated to the solar wind and magnetosheath regions. Their position is only slightly shifted to lower voltage when the ion beam is turned on on Cluster 2. However, the range of potentials between 7 V and 45 V measured on Cluster 1 in low density regions in the magnetosphere is converted to a single peak at about 8 V on Cluster 2 due to the ion beam.
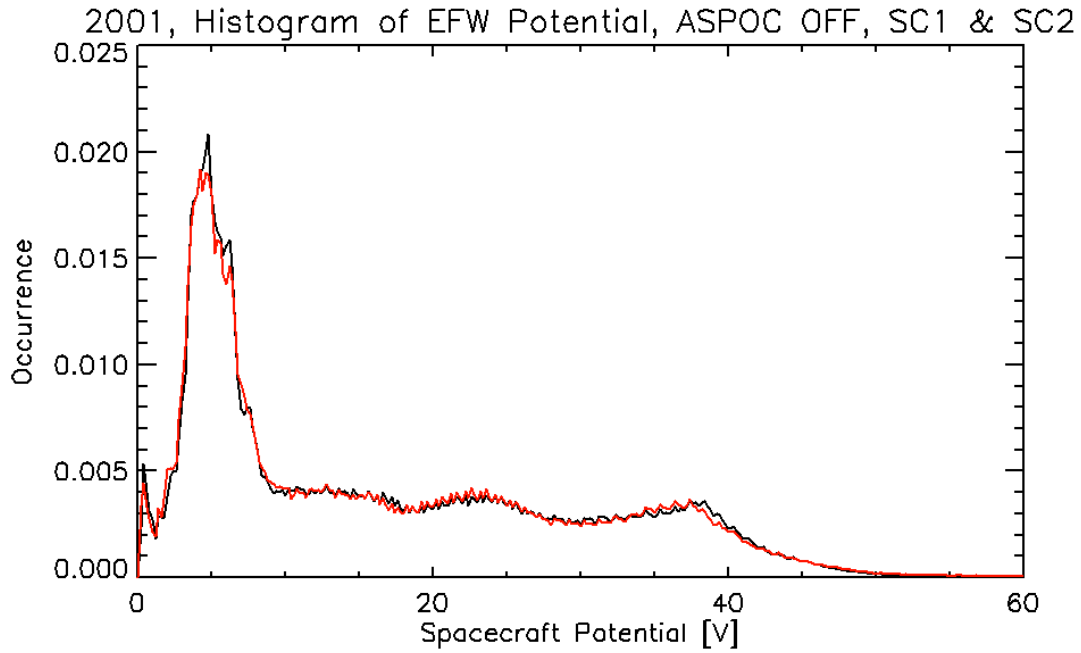
Figure 3. Histogram of spacecraft potential on Cluster 1 and 2 in 2001, for periods without spacecraft potential control
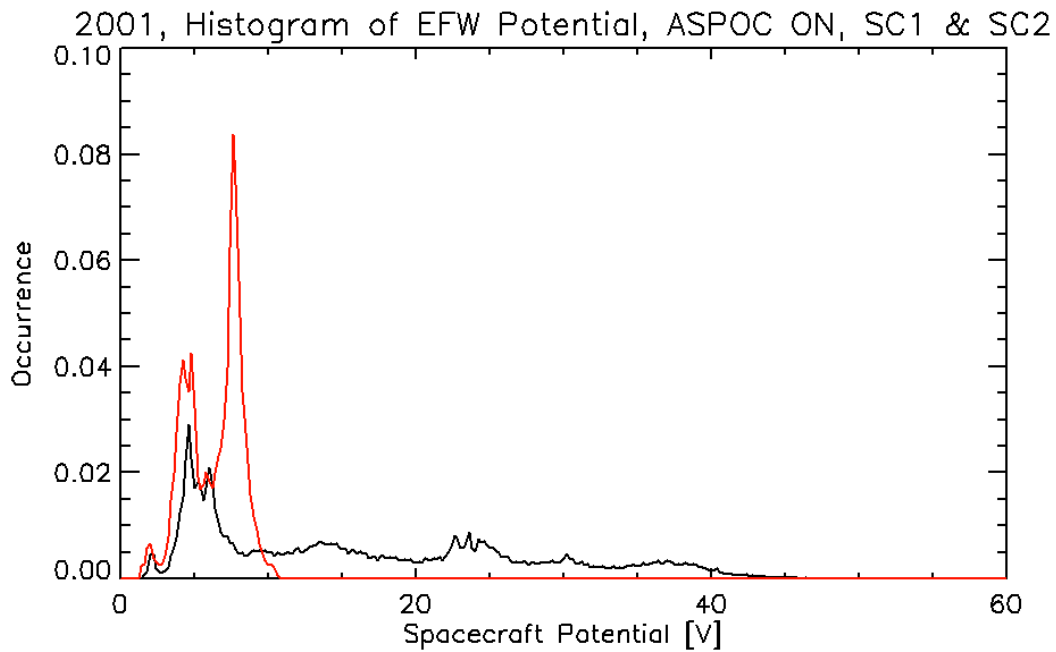
Figure 4. Histogram of spacecraft potential on Cluster 1 and 2 in 2001, for periods with spacecraft potential control

Plasma Electron Measurements

Why is spacecraft potential control so important for a payload dedicated to plasma and field studies in near Earth space? It is shown by examples in this paper that a complete plasma and fields data set is important for many studies. If spacecraft potential reaches several tens of volts positive, which is a common situation in the regions mentioned above, the modifications of the ambient plasma before it eventually can reach a sensor on the spacecraft may introduce severe errors or uncertainties in the measurements and derived quantities.

An essential quantity is plasma density. It can be measured by several techniques which are complementary to each other. Density measurements inferred from particle detectors are necessarily inaccurate if low energies are included in the integration, and if the trajectories and energies of these particles have been severely modified by the spacecraft sheath. Alternatively, if the lower energy limit for the calculation is set to higher energies, then the cold plasma is excluded from the calculation, and a major contribution to the total density is missed.

If the structure of the sheath is known, the modifications of the ambient electrons in the sheath could in theory be calculated and the measurements be corrected. There are, however, major practical limitations. It is difficult to model a sheath around a highly structured spacecraft and its booms, and it is even more difficult if the model has to include plasma density in a self-consistent way. Moreover, the higher the spacecraft potential, the more photo-electrons generated at the spacecraft surface cannot escape into space, and some of them enter the sensors and flood the detectors up to energies comparable to the spacecraft potential.

The abundance of photo-electrons in the sensor data when the spacecraft potential is high makes it difficult to identify ambient electrons: If the spacecraft crosses a boundary from low to higher plasma density, the corresponding sudden lowering of the spacecraft potential has the effect that at energies, where previously photo-electrons were observed, now plasma electrons enter the sensor.

The energy resolution of particle detectors is proportional to energy. Therefore a high potential dramatically lowers the capability to resolve the distribution of the ambient cold electrons. Whereas a typical plasma electron instrument may resolve energies below 10 eV in several bins, these electrons, having been accelerated to 50-60 eV in the electric field of the sheath, would fall into one or two bins only, resulting in a very poor measurement of this component.

Some of the problems with high spacecraft potential are illustrated by Figure 5. Figure 5a shows an electron spectrogram measured by the LEEA sensor of the PEACE instrument (Szita et al., 2001)[6] onboard Cluster 1 in one particular viewing direction (zone 11). One can see the red band of photo-electrons, and the difficulty to distinguish between photo-electrons and plasma electrons in the time interval before 04:30 UT is obvious.

Figure 5b shows the situation onboard Cluster 2, where the ASPOC ion beam was active after 02:20 UT. The distortion of the distribution function f(v) is reduced, and the calculation of moments on-board will be reliable.
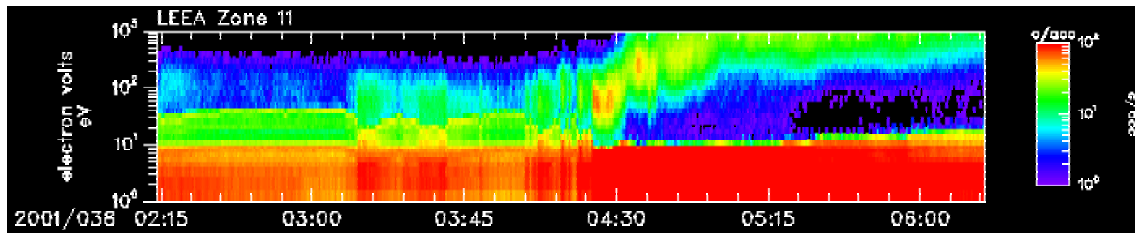
Figure 5a. Electron spectra measured by LEEA/PEACE onboard Cluster 1 without spacecraft potential control.
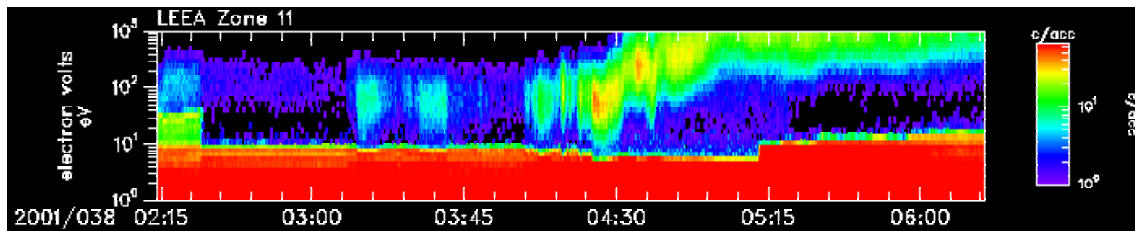
Figure 5b. Electron spectra measured by LEEA/PEACE onboard Cluster 2. Spacecraft potential control sets in at 02:20 UT.

The bottom panel of Figure 6 shows a typical example of Cluster/PEACE electron measurements with active spacecraft potential control. The data are from March 21st, 2001 (AE<50 nT, K_p=1-). Cluster was located in the polar cap (X=-1R_E, Y=2.6 R_E, Z=5 R_E in GSE coordinates). The geomagnetic conditions are quiet.

The top panel shows the (negative of the) spacecraft potential. Before 21:10 UT it fluctuates between 20 and 30 V, which is indicative of low densities in the polar cap. The ASPOC ion beam is turned on at 21:10 UT to a value of 10 µA and clamps the potential to about 7 V. At around 21:53 UT, the ion beam current of ASPOC was increased to 25 µA and then to 30 µA for one minute, and the potential is further reduced to less than 5 V.

Field aligned electrons are present in several bursts until 21:30. When the ASPOC ion beam is turned on at 21:10 UT it permits the measurement of these beams, which otherwise would have partly disappeared in the photo-electrons and shifted to higher energies and to lower resolution. With ASPOC, the features sticking out of the photo-electron baseline are resolved down to about 2 eV, whereas without ASPOC the best resolution is only 10 eV. The features at 21:15 and 21:28 are clearly field-aligned. At around 21:53 UT, when the ion beam current of ASPOC was increased to 25 µA and then to 30 µA for one minute, it removed most of the remaining photo-electrons from the spectrum. There are just a few ambient electrons present at that time, but they remain undisturbed by the beam.
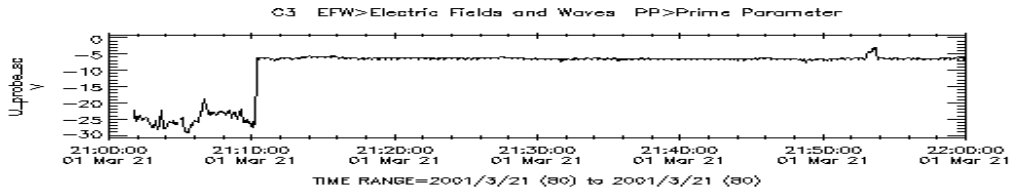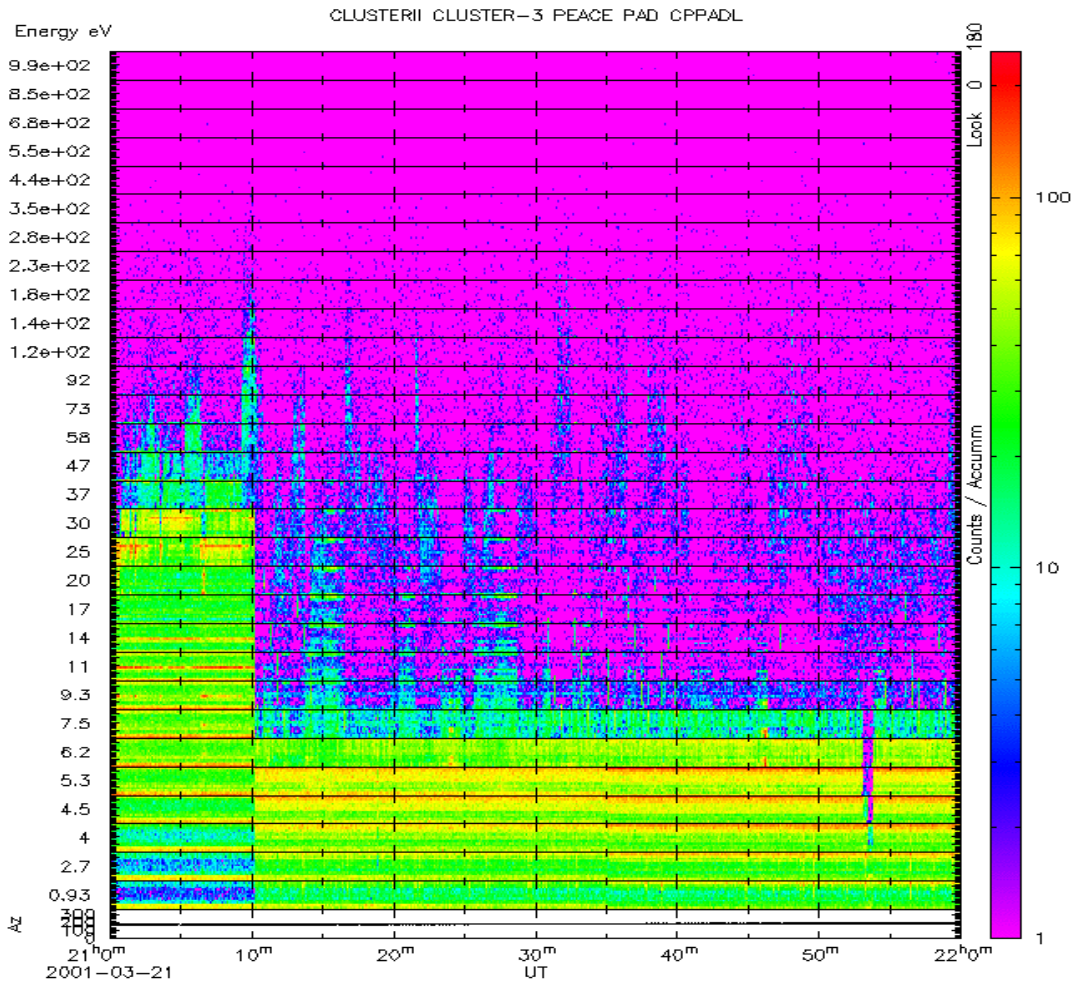
Figure 6. Electrons from Cluster 3 plotted as function of time and pitch angle on March 21st, 2002, from 21 to 22 UT. Individual panels show look angles increasing in upward direction from 0 to 180° (electron pitch angles from 180 to 0°) for each energy band of the LEEA sensor.

Ion Measurements

For positive ions encountering a positively charged spacecraft, the thermal component is repelled or deflected from the sensors and cannot be measured. This is particularly problematic if the cold component are a major constituent, such as for example in the tenuous plasma of the polar cap region, where cold ion beams occur as a regular feature.
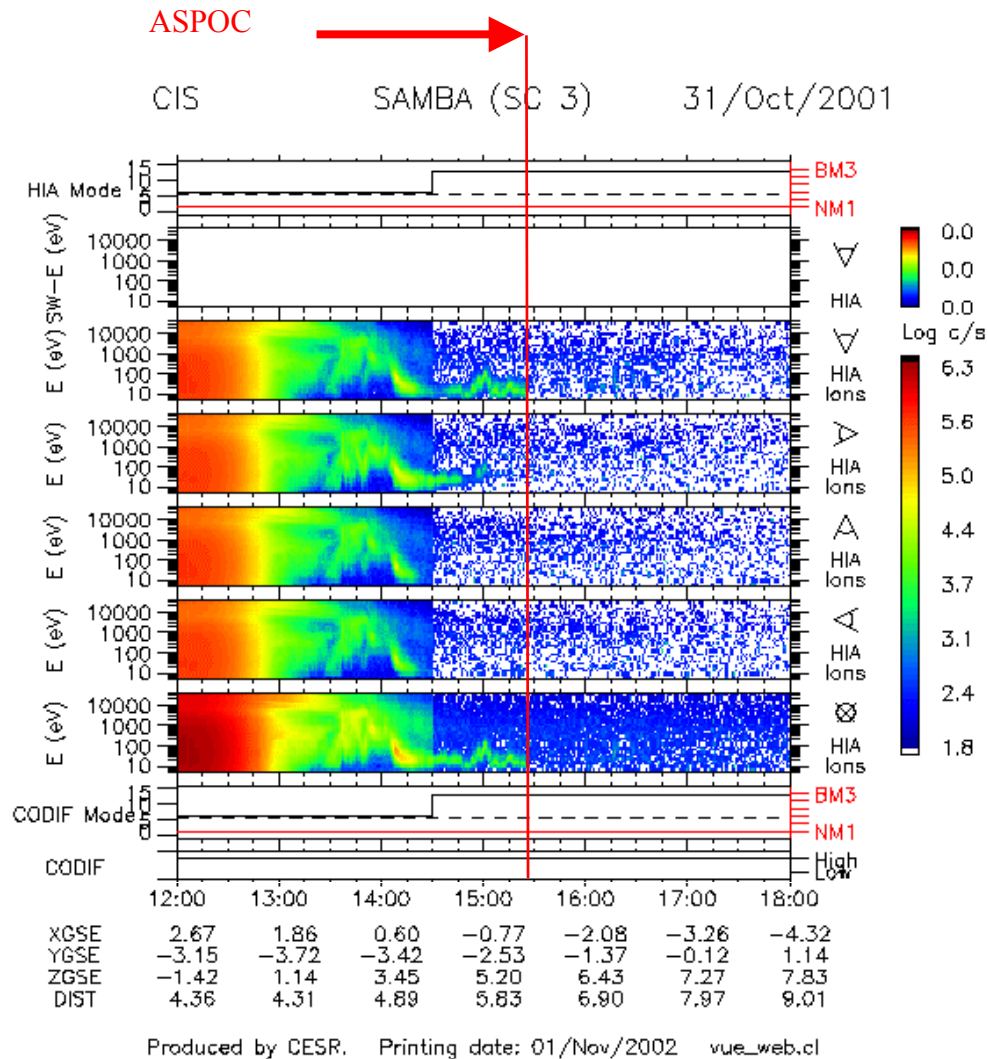
Figure 7. CIS/Cluster data from Cluster spacecraft 3, 31st October 2001. The spectrograms contain from top to bottom: tailward, dawnward, sunward, duskward flowing ions and the total.

Figure 7 shows a measurement of the Hot Ion Analyzer (HIA) as part of the CIS instrument on Cluster (Rème et al., 2001)[7], taken on Cluster 3 on 31st October 2001, between 12 and 18 UT. The five spectrograms show ions in four azimuthal sectors, the uppermost panel showing tailward flowing ions, and the total in the lowest panel. Before 15:25 UT the ASPOC ion beam is active and limits the spacecraft potential to 6.6 V. This allows the measurement of a tailward flowing, cold ion beam. When ASPOC is turned off at 15:25 UT, the potential increases to ≈27

V, and these ions can no longer enter the sensor and disappear from the data. Similar effects can also be seen in H^+, He^+ and O^+ data. A lowering of the spacecraft potential to <10 V clearly helps the measurement of cold ions. By support of ASPOC it could be shown that such beams exist.

Concluding from both electron and ion measurements it becomes clear that only on board of a spacecraft with a low potential the undisturbed measurements of both electrons and ions range down to almost zero energy and thus ensure that (almost) complete distribution functions are measured. This fact is the more important for multi-spacecraft missions such as Cluster or the future Magnetospheric Multiscale mission, where much emphasis is being laid on measuring differences between spacecraft to infer the structure of plasma boundaries and measure currents.

Electric Field Data

So far we have not yet mentioned electric field measurements employing double probes. They have to use long wire booms in order to keep the probes outside the sheath even if the Debye length is large. The high potential region near the spacecraft body and also extending along the wire booms may create a barrier for cold ions, In any case, the further outward any given equipotential surface is located, the more likely it affects the E-field measurement by disturbing the natural plasma flow. On an actively controlled spacecraft the equipotential surfaces move inward and thus reduce any problems the double probes might have to measure in a low density environment. The photo-electrons, however, also encounter a weaker electric field in the sheath if the potential control is working. The size of the photo-sheath grows accordingly. Already simple models show that also any spatial asymmetries of the photo-electron distribution between the sunlit and dark hemispheres grow in size, i.e. the center of their space charge slightly moves in sunward direction, thereby changing the spurious electric field created by them in the double probe measurement.

Side Effects

Is there any undesirable effect of active spacecraft potential control using an energetic ion beam? Absolutely no artificial plasma waves have ever been observed on Cluster, which were related to the ion beam emission. The Cluster wave instruments are very sensitive and cover frequencies from DC to 500 kHz. It had been expected out of theoretical considerations that a beam of heavy ions at the energies and currents applied on Cluster would have negligible growth rates for waves, including electrostatic ion cyclotron waves.

There are two possible effects which deserve some attention in future modeling work, although it must be mentioned beforehand that neither effect could yet be verified by data.

- The cone-shaped plume generated by the ions is readily neutralized at some distance from the spacecraft, which varies with ambient plasma conditions. Certainly at some tens of meters distance the beam charge is neutralized. Close to the spacecraft, however, the ion density in the beam can reach a few 100 ions cm^{-3} at 3 m distance. One should keep in mind that the photo-electron density near the surface reaches comparable values, and an efficient neutralization of the ion beam even at short distances may be possible, but must be studied and modeled in detail.

- Without active spacecraft potential control the negative space charge of the photo-electrons is not important for the overall potential distribution in the sheath, as it will at most create a small sunward-antisunward asymmetry in the potential map of less than one volt. If active spacecraft potential control is applied, the potential of the spacecraft is much smaller, and the space charge of the photo-electrons may drive the potential into negative territories, resulting in a potential barrier. The height of this barrier is difficult to assess numerically. Models range from small fractions of a volt to two volts.

Data from the electron and ion spectrometers on board of Cluster did not show any signature of non-gyrotropy or other effects which might be related to the beam space charge or a potential barrier.

Outlook and Conclusion

Active Spacecraft Potential Control using liquid metal ion sources significantly improves the measurements of low energy electrons and ions onboard Cluster, without compromising wave and electric field measurements. By lowering of the spacecraft potential the characterization of the ambient plasma by on-board sensors becomes more accurate. A low potential also allows the escape of a larger fraction of photo-electrons into space, whereby the wear of micro-channel plates in the electron detectors due to high count rates is reduced. Changes of the s/c potential between <10V and >20V clearly influence the measurements of cold ions. Also the electric field measurements on Cluster, after some initial doubts, have been shown to benefit from spacecraft potential control.

For Cluster operations, there are still on-board resources to continue spacecraft potential control well into the extended mission phase.

While ASPOC is emitting 10 µA ion current, the spacecraft potential does not exceed 8 to 9 V, with 12 to 15 µA => 6 to 7 V. Histograms peak at ≈7 V when ASPOC is active.

Work has to continue on analyzing particle data and modeling the details of the sheath structure when the energetic ion beam is emitted. Up to now, nothing has been found in the electron and ion data which would indicate the presence of any other effects but the desired reduction of sheath effects to all ambient particles. Initial efforts undertaken by some research groups suggest that only minor deviations from an ideal, reduced sheath are present.

Accurate plasma measurements are highly desirable for any spacecraft with plasma physical objectives, but they are particularly essential for multi-spacecraft missions which require reliable data on differences between quantities measured on several spacecraft. The absence of any disturbances from the ion beams applied on Cluster and the moderate resource requirements make this technique a promising candidate for future missions.

References

1. Moore, T.E., C.R. Chappell, M.O. Chandler, S.A. Fields, C.J. Pollock, D.L. Reasoner, D.T. Young, J.L. Burch, N. Eaker, J.H. Waite, Jr., D.J. McComas, J.E. Nordholdt, M.F. Thomsen, J.J. Berthelier, and R. Robson, The thermal ion dynamics experiment and plasma source instrument, Space Sci. Rev., 71, 409–458, 1995.

2. Torkar, K., M.V. Veselov, V.V. Afonin, H. Arends, M. Fehringer, G. Fremuth, K. Fritzenwallner, Y.I. Galperin, A.I. Kozlev, A. Pedersen, S. Perraut, F. Rüdenauer, A. Smit, N. Valavanoglou, L.V. Zinin, An experiment to study and control the Langmuir sheath around INTERBALL-2, Ann. Geophys., 16, 1086-1096, 1998.

3. Torkar, K., W. Riedler, M. Fehringer, F. Rüdenauer, C.P. Escoubet, H. Arends, B.T. Narheim, K. Svenes, M.P. McCarthy, K. Parks, R.P. Lin, H. Reme, Spacecraft potential control aboard Equator-S as a test for Cluster-II, Ann. Geophys., 17, 1582-1591, 1999.

4. Torkar, K., W. Riedler, C.P. Escoubet, M. Fehringer, R. Schmidt, R.J.L. Grard, H. Arends, F. Rüdenauer, W. Steiger, B.T. Narheim, K. Svenes, R. Torbert, M. André, A. Fazakerley, R. Goldstein, R.C. Olsen, A. Pedersen, E. Whipple, H. Zhao, Active spacecraft potential control for Cluster - implementation and first results, Ann. Geophys., 19, 1289-1302, 2001.

5. Gustafsson, G., M. André, T. Carozzi, et al., First results of electric field and density observations by Cluster EFW based on initial months of operation, Ann. Geophys., 19, 1219-1240, 2001.

6. Szita, S., A. N. Fazakerley, P. J. Carter, A. M. James, P. Trávnícek, G. Watson, M. André, A. Eriksson, K. Torkar, Cluster PEACE observations of electrons of spacecraft origin, Ann. Geophys., 19, 1721-1730, 2001.

7. Rème, H., C. Aoustin, J.M. Bosqued, et al., First multispacecraft ion measurements in and near the Earth's magnetosphere with the identical Cluster ion spectrometry (CIS) experiment, Ann. Geophys., 19, 1303-1354, 2001.

ON-ORBIT EXPERIMENTS AND RESEARCH ON MEASURING THE SPACECRAFT CHARGING

Nikolski Evgeny
EMC and ESD division
Russian Aviation-Space Agency, Lavochkin Association
Russia, 141400, Moscow region, Khimki-2, Leningradskaya st., 24
Phone: 07-095575-57-95
Fax: 007-095573-22-42
E-mail: nikolski@laspace.ru

Sokolov Arcady
Russian Aviation-Space Agency, Lavochkin Association

Introduction

Lavochkin Association is one of the leading enterprises in Russia for about forty years, having specialized in the field of design and manufacturing of tools for orbital injection of payloads and automatic vehicles to further study the solar-earth relationships, the Moon, small heavenly bodies and planets of the solar system.

A long-term experience of the Association in the field of space engineering also includes the development of anti-charging protection tools for s/c. This protection is achieved by means of bonding and screening. Originally, two flight experiments on measuring the surface of the s/c charging have been initiated in 2002 and thereafter continued.

The purpose of these experiments is as follows:

- Receiving the data on relationship between s/c charging and operational capability of its systems;
- Obtaining the experimental data about specific parameters of the charging;
- Study of the regularities of the charging process.

Onboard Measurement Equipment.

"Zond-Zaryad" equipment, which is analogous to the one that has been installed on "Mir" station (1), has been used for these experiments. The characteristic feature of this equipment and the experiment in general is the capability to monitor continuously the s/c parameters in orbit. Such capability is reached through the presence of the monitoring equipment that continuously accumulates and stores the information and, then, transmits it to the Earth during communication sessions. The information entry phase is approximately 40 seconds. There is also a capability for data direct transmission into the telemetry system. In this case, the frequency of the sensors inquiry is up to 200 Hz.

The following parameters have been measured:

- electrostatic field;
- Variable electric field;
- Current on a sensor.

The quasistatic electric field is measured by the sensors of vibrational type (electric field frequency modification is up to 10 Hz). The principle of sensors' operation is similar to the one described in (2). The measurement range is approximately:

- ±350 kV/m – in case of direct data transmission into the telemetry system of the s/c;
- ±6 kV/m – in case when the values are entered into sensor's own storage device (the variance in measurement ranges is connected with potential of the memory storage device and limitations to the volume of the information that can be transmitted).

A variable electrostatic field is measured over the frequency range up to 2000 Hz. The amplitude of the variable field is up to 1.5 kV/min. This parameter is recorded only onto the own memory device. It is the maximum value, which occurs during the measurement (period), that is measured in the course of experiment.

The current on a sensor is in the range of ±1.5 nA/sm^2.

Orbit Parameters and S/C Attitude Control Modes.

The s/c for optic-electronic observation "ARCON-1" (international label -2002-037A) has been launched into orbit on July 25, 2003 with the following parameters:

Perigee altitude – 1513.8 km;
Apogee altitude – 1841.7 km;
Obliquity – 63.46º;
Orbit time – 119.89 min.
Later, the orbit of the space craft did not undergo any considerable modifications (3).
The exterior of this s/c is pictured on fig. 1.
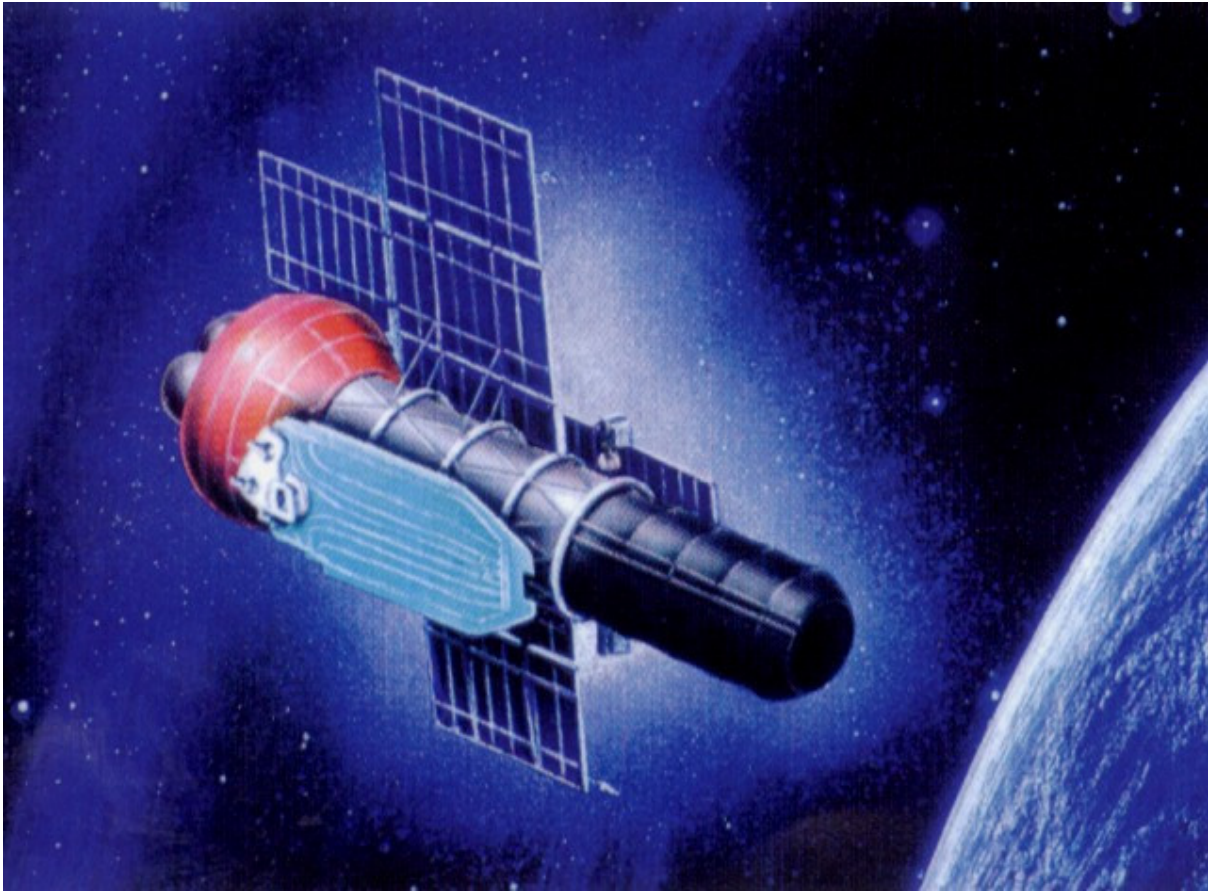
Figure 1.

The s/c "Cosmos - 2393" (international label - 2002-059A) has been launched into orbit on December, 24, 2002 in the interests of the Ministry of Defense of the Russian Federation with the following parameters:

Perigee altitude - 523 km;
Apogee altitude - 39067 km;
Obliquity – 62.83º;
Orbit time – 702.34 min (4)
The exterior of this s/c is pictures on fig. 2.
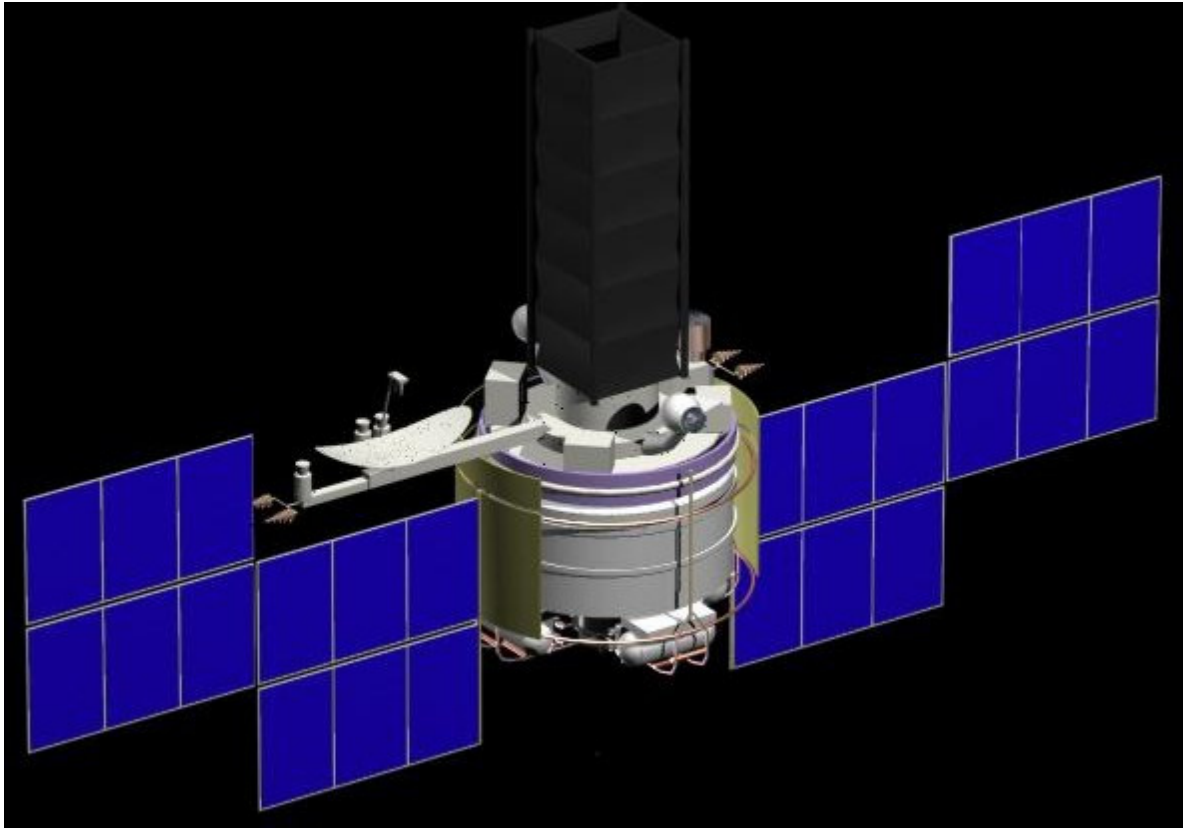
Figure 2.

<u>Installation of the Measuring Equipment on the S/C</u>

The following criteria were considered for selecting of the installation points for the sensors on the surface of the space craft:

- Lack of small parts of the s/c located near the sensors;
- Sensors should be located at the spots that differ from each other in the view of the exterior factors effecting these placement spots;
- Devices that could be potential subjects to the charging effect should preferably be located near the sensors.

The fulfillment of these requirements at installating the sensors should enable to use the data received in the process of measuring both directly – by estimating the relationship between the s/c charging and the malfunctions of the certain airborne systems, and indirectly - by estimating the s/c charging in general (including the use of mathematical modeling).

"ARCON-1" is the s/c operating on LEO and equipped with five sensors, thus measuring all three parameters listed above (part 1). The setting spots of the sensors on the s/c surface are indicated on Scheme 1.

Sensor #2 is placed under the back panel of the solar battery at the distance of about 100 mm from its edge. The axes of sensitivity of all sensors are directed by a normal line from the body of the s/c.

Such placement of the sensors allows measuring the following characteristics of the s/c charging:

Scheme 1
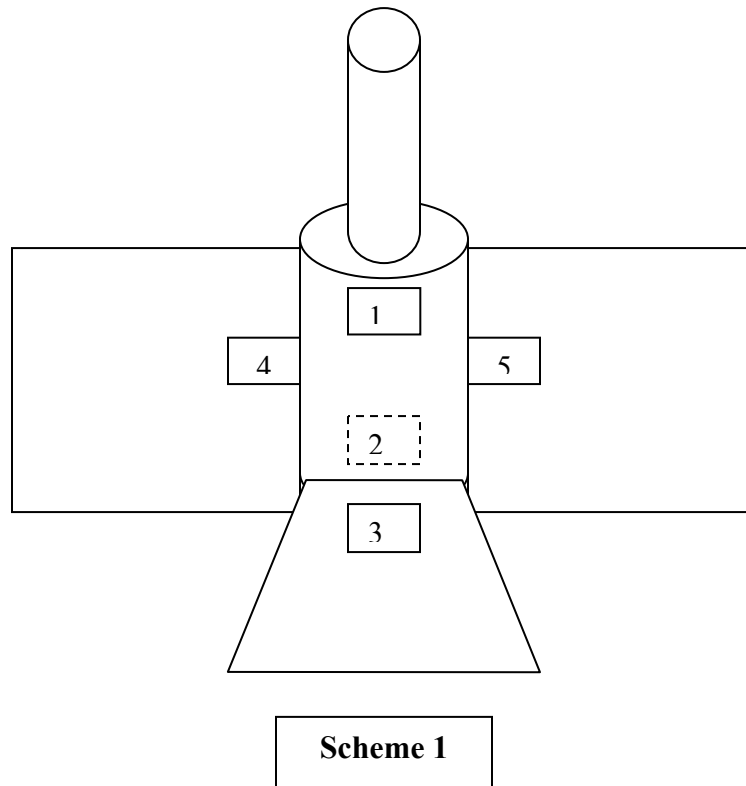
- Difference in charging characteristics of the diametrically opposite panels of the s/c body through indications of sensors #4 and #5 (that is similar to the "Kvant" module of "Mir" station);
- Currents on a sensors from three different directions (sensors #4, #5 and #1);
- Effect of the s/c structural elements on the measured parameters under the condition of equal orientation of the sensors axes (sensors #1 and #3);
- Charging of the solar battery back panel.
- Operating in high-elliptical orbit "Molniya" s/c is equipped with two sensors (setting points for the sensors are indicated on Scheme 2).

Scheme 2
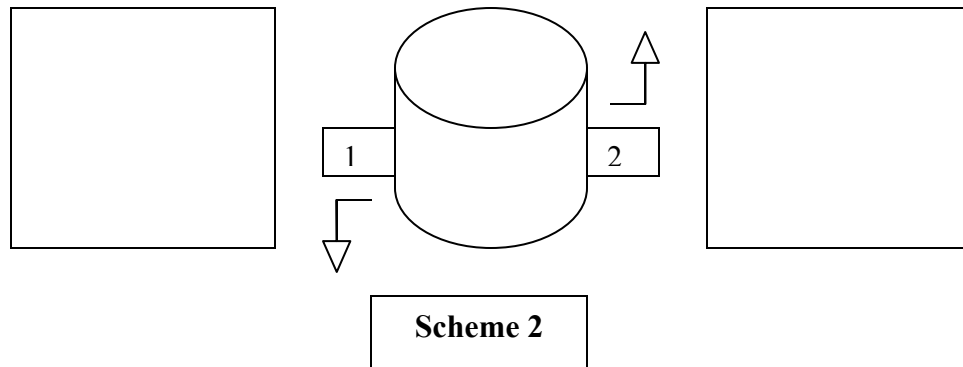
A diametrically opposite placement of sensors allows measuring of specific characteristics of the s/c charging connected with the following factors effects:

- Level of illuminance of the s/c opposite panels;
- Vector of the s/c linear velocity.

Findings

At present, connection between the measured parameters and malfunctions in operation of airborne systems is not detected.

Data was obtained during one year of measurement in LEO and approximately 6 months of measurement experiments in "Molnya" orbit.

As the result of this measurement, we determined the following:

- Regular changes of electrostatic fields has the average range of ±3 kV/m;
- Maximum values of stationary values of electrostatic fields range from -14 kV/m up to 4.3 kV/m for "Cosmos-2393" space craft and from -5.9 kV/m up to 4 kV/m for "ARCON-1" space craft;
- Tension of the electrostatic field measured by sensors located under the solar battery of s/c "ARCON-1" has predominately a positive polarity;
- On "ARCON-1" s/c, the maximum values are observed both on separate sensors and on several sensors simultaneously. These values have equal polarity;
- Variable electric fields are within the limits of 1.5 kV/m (measuring limit of sensors);
- Currents on sensor are ±1.5 nA/sm2 (measuring limit of sensors). For "ARCON-1" space craft, a period of time during which these values were fixed, is, as a rule, no more than tens seconds. For "Cosmos-2393" s/c, this time can reach several hours.

Due to the great volume of data, on analysis of the relationship between measured parameters of the s/c charging and exterior conditions has been performed mostly for "ARCON-1" s/c.

In the observed time periods, we found the following regularities:

For "ARCON-1" s/c:

- Variable electric fields have major intensity on the irradiated segments of the s/c orbit and are observed at the entrance/exit of the s/c from the shadow of the Earth. In the shadow of the Earth, the intensity of variable electric fields is rather insignificant (fig.3);
- Maximums of the constant electric field fall in the auroral areas of the magnetosphere. In some cases, the values of up to -5.9 kV/m (the measuring limit of the sensors) were observed. During the period of time from May 07, 2003 till May 09, 2003, in all six cases, the maximum values have been registered when the s/c was in auroral areas of the magnetosphere of the Earth. At the same time, the maximum values have not been registered at each and every time when the s/c was located in these areas (fig. 4).
- There is a relationship between the intensity of variable electric fields (frequency of ignition and amplitude) and the attitude control mode of the space craft. Curve 1, depicted on fig.5, reflects the mean value of the variable electric field registered during one orbit by five sensors; Curve 2 reflects an approximate time unit when the s/c changed its orientation.
- In order to estimate the geomagnetic activity, we have used index Kp and index of avroral activity, obtained through analyzing the data received by one of the "POES" s/c. These data have been retrieved from http://www.sec.noaa.gov. Fig.3 and Fig. 4 shows these values for the time period from May 7, 2003 to May 9, 2003. It allows us to draw a conclusion, that these indices do not directly influence the parameters
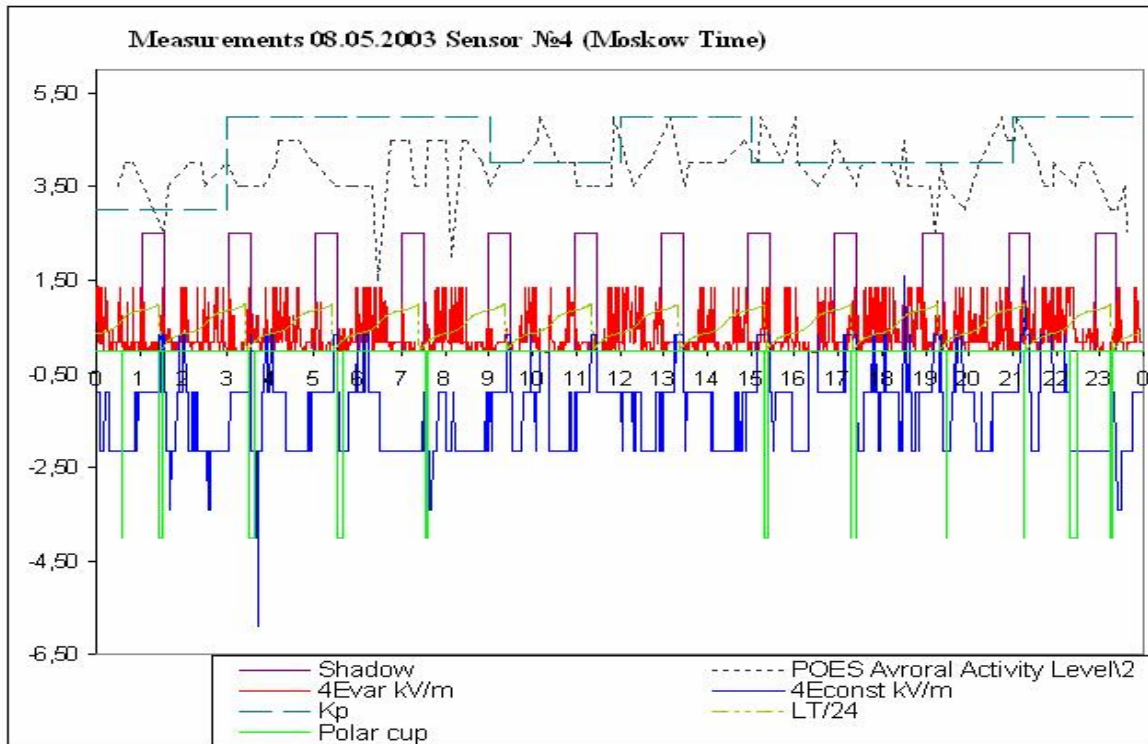
Figure 3.
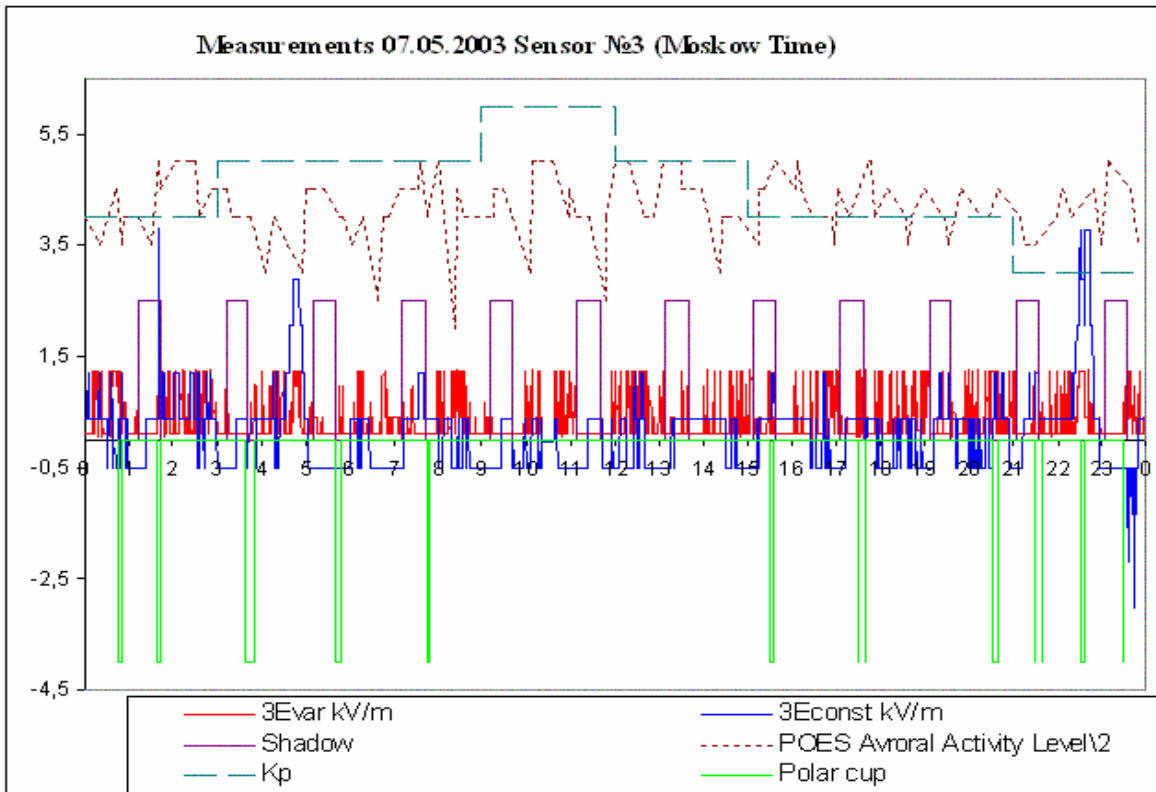
Figure 4.

of the s/c charging. It might be necessary to consider a hypothesis, offered in the paper cited as (2), that there is a time detrusion between the disturbances of the magnetosphere and the s/c charging.

- A sensor that has been covered by the bonding part of the s/c for several weeks did not show any fluctuations of any of the measured parameters during all this time. It proves both that the protective quality of the s/c construction elements is really high and the parameters measured are indeed bound up with the environmental effects.

The very first estimates for the "Cosmos-2393" s/c are as follows:

- There is an essential difference in the values of all three measured parameters, indicated by the sensors that were installed on the irradiated and the shadow panels of the s/c (Fig. 6). In particular, the current on a sensor was about -1.5 nA/sm2 when the sensor was installed on the irradiated panel of the s/c, while the electrostatic field of -3.5 kV/m (a measuring limit of sensors) has been registered by the sensor installed in the shadow panel of the s/c during several consecutive hours;

- There is a relationship between measured parameters of the s/c charging and the s/c position in orbit from perigee to apogee. On Fig. 6, the perigee values are 9.00 and 21.00 and apogee value is 15.00 (Moscow time);
- The maximum value of electrostatic field (-14 kV/m) has been registered in the period of low geomagnetic activity (Kp=3).
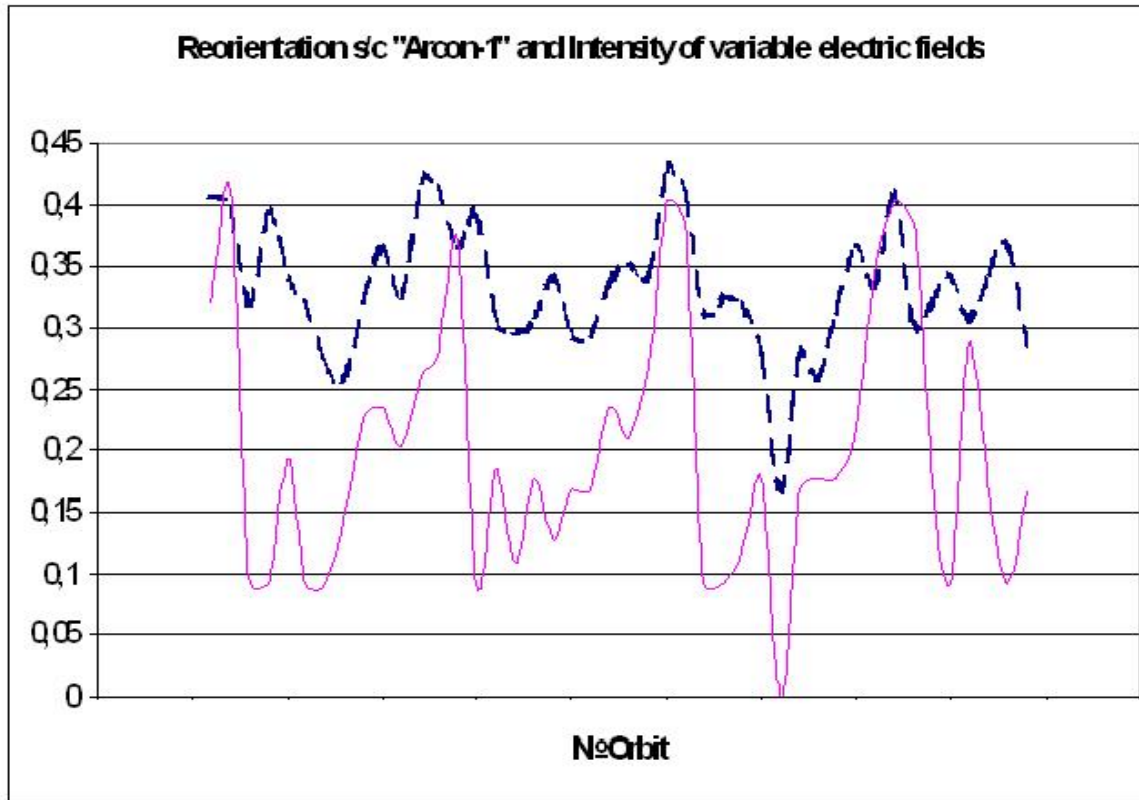
Figure 5.
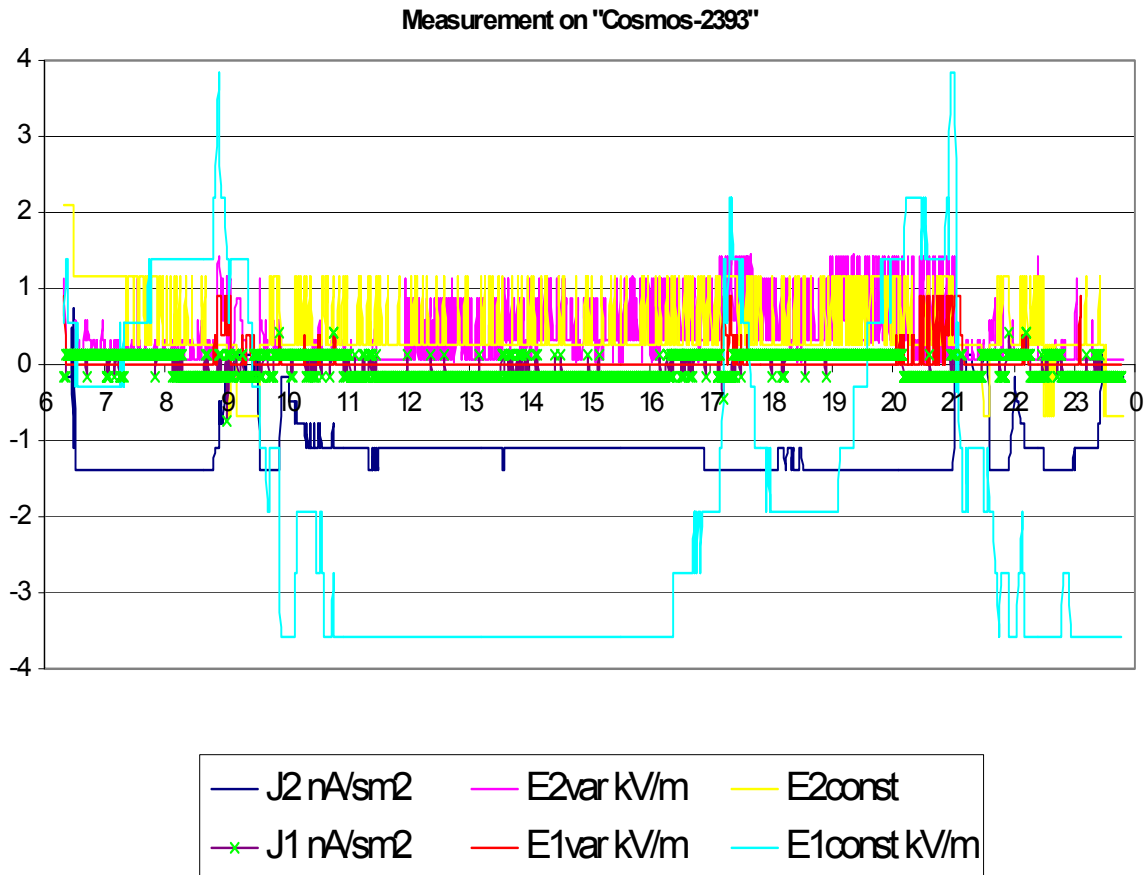
Figure 6.

Conclusion

In general, the experimental data obtained at the present stage of research corresponds with the basic theoretical knowledge about the s/c charging in the Earth orbit. In particular, it is true for the orbit with an altitude of 1500-1800 km and an obliquity of 63°:

- S/c absolute and differential charging up to potential values of several kV is observed;
- Intensity of variable electric fields is influenced by the s/c rotation (the difference is roughly two times) and by the illuminance level of the s/c surface;
- Maximum values of electrostatic field (up to-5.9 кB) are observed in the auroral areas of Earth magnetosphere.

Lack of connection between parameters of the s/c charging and the malfunctions of airborne systems that is currently observed, most likely, indicates the effectiveness of today's anti-charging protection measures.

In order to obtain more statistically reliable experimental data and discover new regularities in s/c charging, we will continue our analysis of the available and new information.

Lavochkin Association is open for cooperation with all organizations interested in any aspects ofthe s/c charging problem (i.e. simulation, protect, ground tests, flight experiments, etc.). Thus, Lavochkin Association has great capabilities to conduct flight experiments of different degrees of complexity and develop and manufacture special experimental s/c that can use the equipment provided by the customer.

References

1. In Flight Measurement of the Outside Surface Potential of "Mir" Orbital Station Klimov, S.I. et al. SP-476 7th Spacecraft Charging Technology Conference p.303, 2001

2. In Flight Results of Spacecraft Charging Investigation for Russian High AltitudeSatellites, by V. I. Guselnikov, A. A. Kocheev, Yu. M. Prokopiev, O.S. Grafodatsky, 1998 Proceedings from 6th Spacecraft Charging Technology Conference p.21.

3. Novosti Kosmonavtiki #10(237), 2002, Events of August, 2002, p.25

4. Novosti Kosmonavtiki #2(241), 2003, Events of December, 2002, p.38

8th Spacecraft Charging Technology Conference - Hunstsville, Alabama

October 20-24, 2003
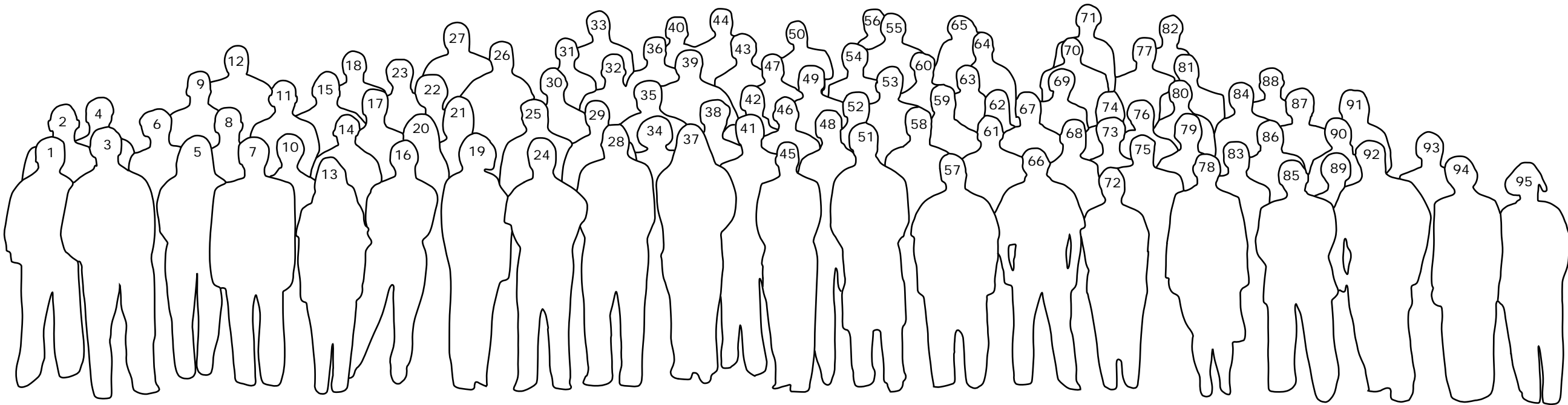
1 - Richard Briet, The Aerospace Corporation, USA

2 - James Laframboise, York University, Canada

3 - Jody Minor, NASA Marshall, USA

4 - Hideyuki Usui, Kyoto University, Japan

5 - Sopo Yung, CSC, USA

6 - Masao Nakamura, JAXA, Japan

7 - Shu Lai, AFRL, USA

8 - Kai Hwang, CSC, USA

9 - Billy Kauffman, NASA Marshall, USA

10 - Claude Berthou, ALCATEL Space, France

11 - Ed Heise, Eastman Kodak Company, USA

12 - Bob Wood, BWACS, USA

13 - Lisa Putt, ASRI, USA

14 - Alain Hilgers, ESA/TOS-EES, The Netherlands

15 - Tony Clark, NASA Marshall, USA

16 - Ioannis Mikellides, SAIC, USA

17 - Micheal Bodeau, Boeing Satellite Systems, USA

18 - Klaus Torkar, IWF/OAW, Austria

19 - Barbara Gardner, SAIC, USA

20 - Karen Stephens, NASA Marshall, USA

21 - Miria Finckenor, NASA Marshall, USA

22 - Elizabeth Berman, AFRL, USA

23 - Paal Brekke, ESA, USA

24 - Dong-Shiun Lin, Swales Aerospace, USA

25 - Gary Pippin, Boeing, USA

26 - James Roeder, The Aerospace Corporation, USA

27 - Steven D. Pearson, NASA Marshall, USA

28 - Mike Lassise, Raytheon, USA

29 - Marc Van Eesbeek, ESA, The Netherlands

30 - David Rodgers, QuinetiQ, UK

31 - Aroh Barjatya, Utah State University, USA

32 - Bob Hilmer, AFRL, USA

33 - Keith Ryden, QuinetiQ, UK

34 - Barbara Stone-Towns, NASA Marshall, USA

35 - Mukund Deshpande, AMSE, USA

36 - Charles Swenson, Utah State University, USA

37 - Nicola Burgess, Raytheon, USA

38 - Erik Engwall, Swedish Institute of Space Physics, Sweden

39 - James Howard, Jackson & Tull, USA

40 - Yusuke Usui, Musashi Institute of Technology, Japan

41 - Eloy Sasot Samplon, ESA, The Netherlands

42 - Kent Watson, National Institute of Aerospace, USA

43 - Haruhisa Fujii, Nara National College of Technology, Japan

44 - Satoshi Hosoda, Kyushu Institute of Technology, Japan

45 - Veronica Ekstrand, Kongsvberg Satellite Services, Norway

46 - Joe Bonometti, NASA Marshall, USA

47 - Joel Galofaro, NASA Glenn, USA

48 - Benoit Thiebault, ESA, The Netherlands

49 - Boris Vayner, Ohio Aerospace Institute, USA

50 - Hiraki Miyake, Musashi Institute of Technology, Japan

51 - Sieu Viet Nguyen, Raytheon, USA

52 - Karl Jurisson, Northrop Grumman, USA

53 - Keith Balmain, University of Toronto, Canada

54 - Yasuhiro Tanaka, Musashi Institute of Technology, Japan

55 - Noriyuki Osawa, Musashi Institute of Technology, Japan

56 - Michael Godefroy, CETP, France

57 - Clint Thomson, Utah State University, USA

58 - Luke Goembel, Goembel Instruments, USA

59 - Alec Sim, Utah State University, USA

60 - Fuyuko Fukuyoshi, Musashi Institute, Japan

61 - Prasanna Swaminathan, Utah State University, USA

62 - Elise Lin, DPL Science Inc., Canada

63 - Mark de Payrebrune, DPL Science Inc., Canada

64 - George Wertz, NASA Marshall, USA

65 - Elena Séran, CETP, France

66 - Glenn Berg, Boeing, USA

67 - Neal Foushee, Spectrum Astro Inc., USA

68 - Richard C. Adamo, SRI International, USA

69 - Takahisa Masuyama, Osaka University, Japan

70 - Jean-Pierre Catani, CNES, France

71 - Jean-Francois Roussel, ONERA, France

72 - Linda Neergaard, Jacobs Sverdrup, USA

73 - Hideaki Koakutsu, Mitsubishi Electric, Japan

74 - Sizuka Nagaya, USA

75 - Henry Garrett, JPL, USA

76 - J.R. Dennison, Utah State University, USA

77 - Tetsuo Sato, JAXA, Japan

78 - Victoria Davis, SAIC, USA

79 - Mengu Cho, Kyushu Institute, Japan

80 - Terrance Onsager, NOAA, USA

81 - David Cooke, ARFL/VSBX - Hanscom AFB

82 - Joseph Wang, Virginia Polytechnic, USA

83 - Leon Levy, ONERA, France

84 - Myron Mandell, SAIC, USA

85 - Thomas Jordan, EMP Consultants, USA

86 - Joseph Minow, Jacobs Sverdrup, USA

87 - Yoshio Shikata, Kyushu Institute, Japan

88 - Kazuhiro Toyoda, Chiba University, Japan

89 - Teppei Okumura, Kyushu Institute, Japan

90 - Ron Elsen, Boeing, USA

91 - Gayle Brown, USRA, USA

92 - Barry Willits, Spectrum Astro Inc., USA

93 - Julien Forest, IRF-K/CETP, France

94 - Janet Barth, NASA Goddard, USA

95 - Donna Hardage, NASA Marshall, USA

8th Spacecraft Charging Technology Conference - 2003 - Huntsville, Alabama

STS-85 CREW
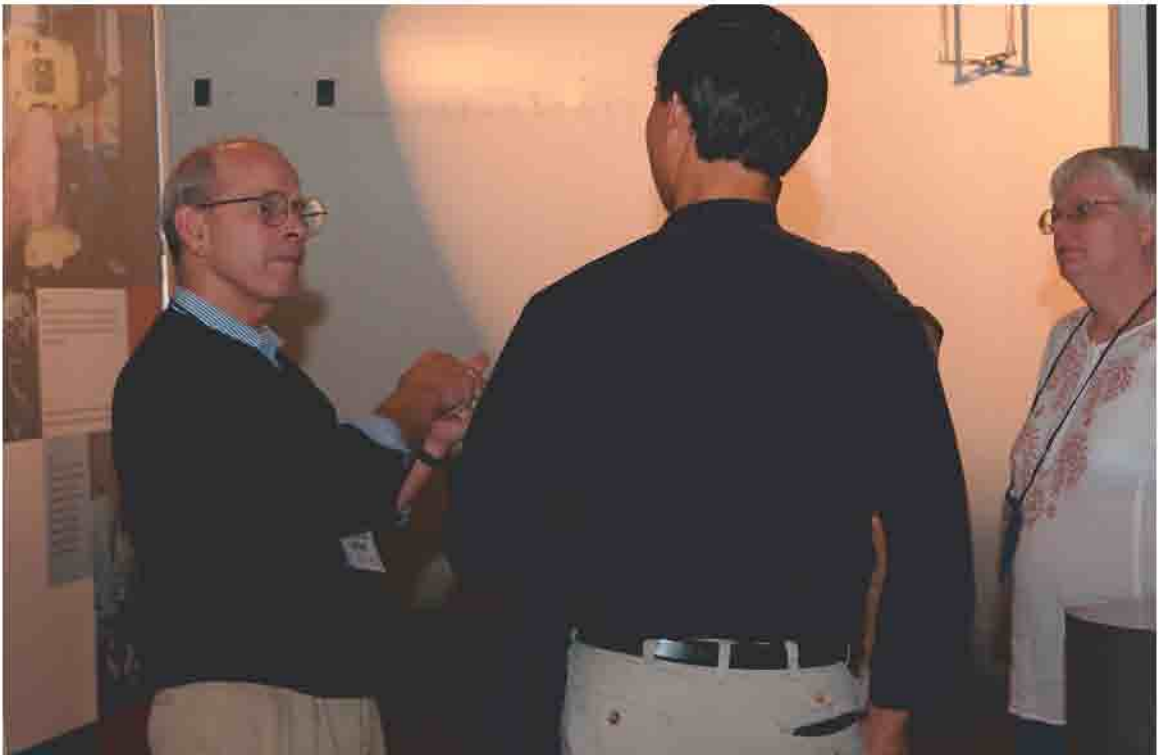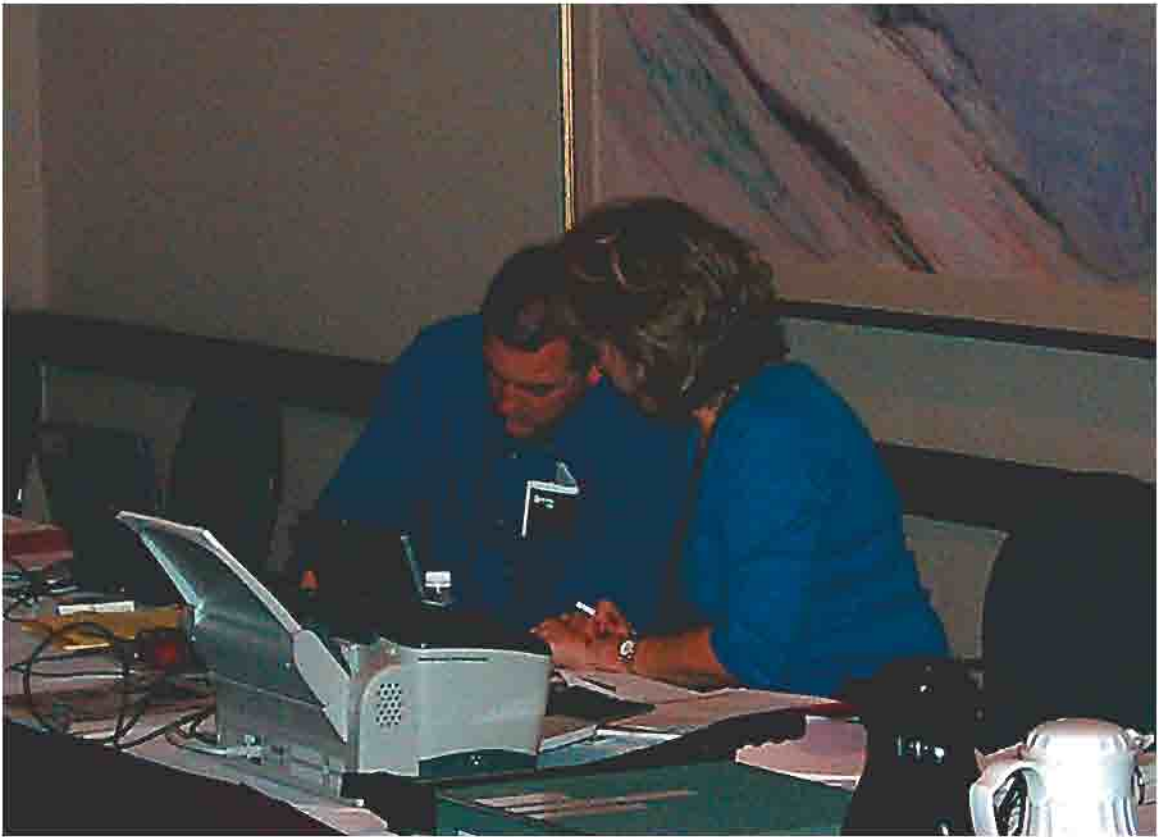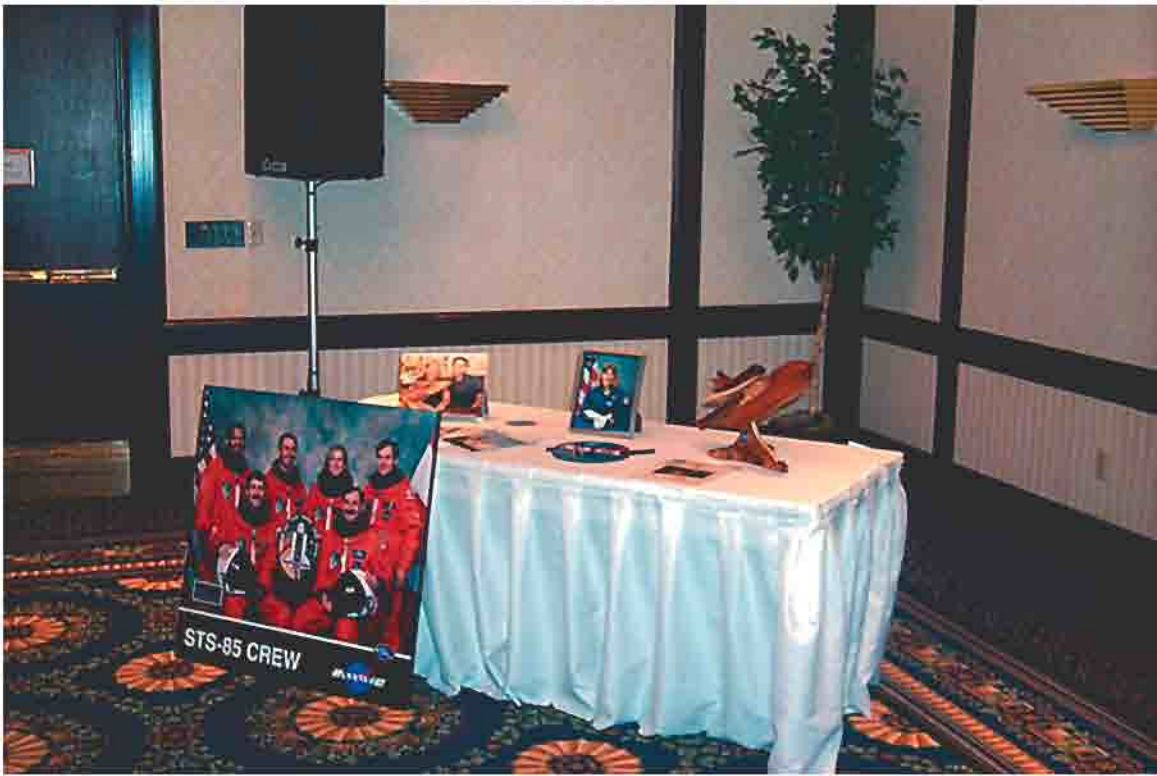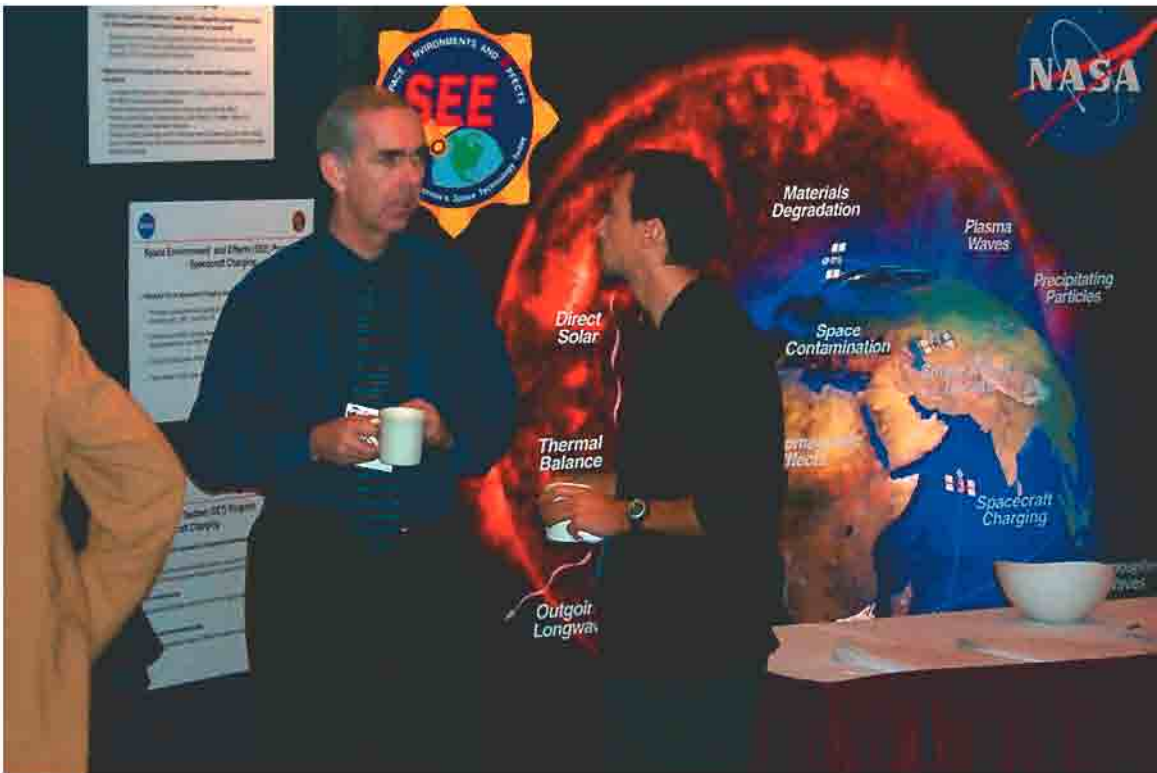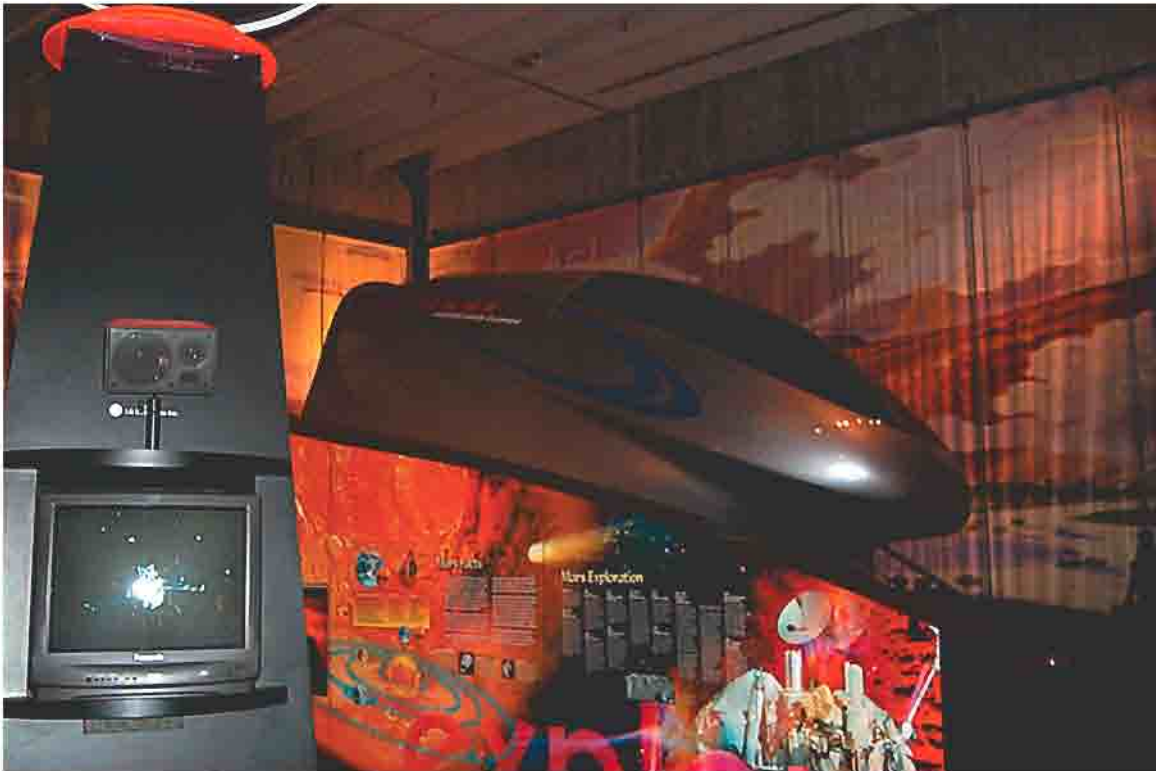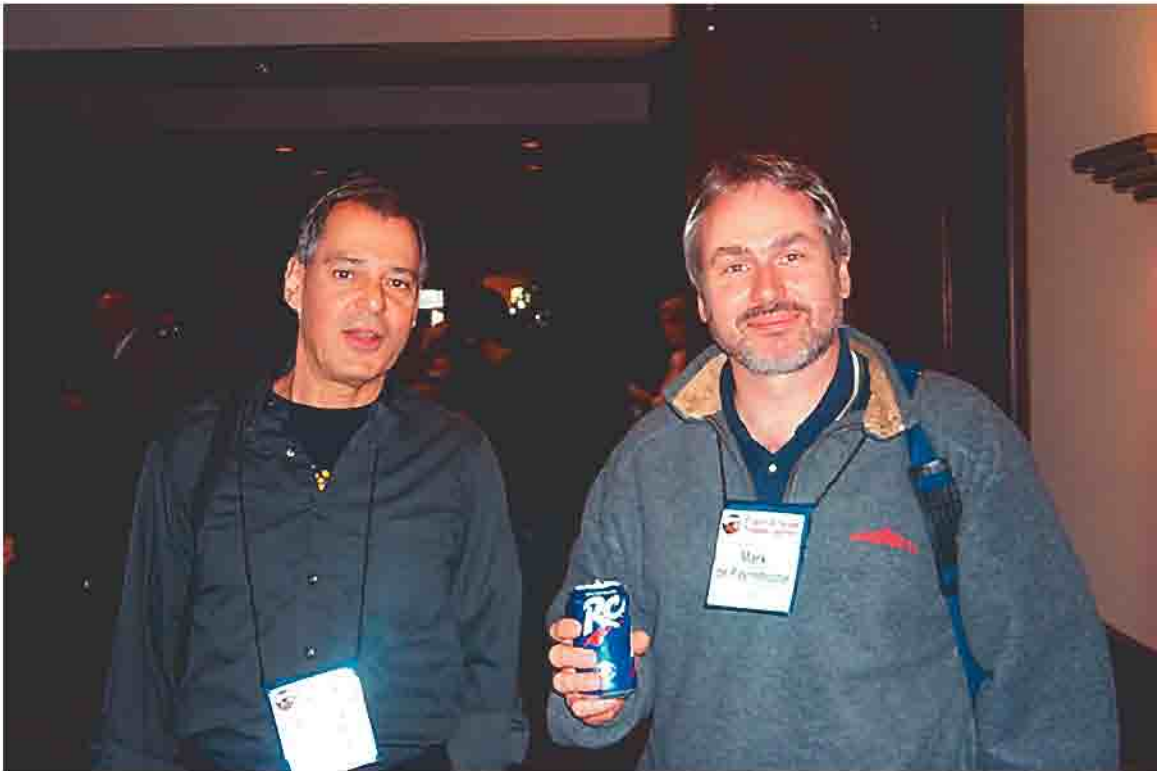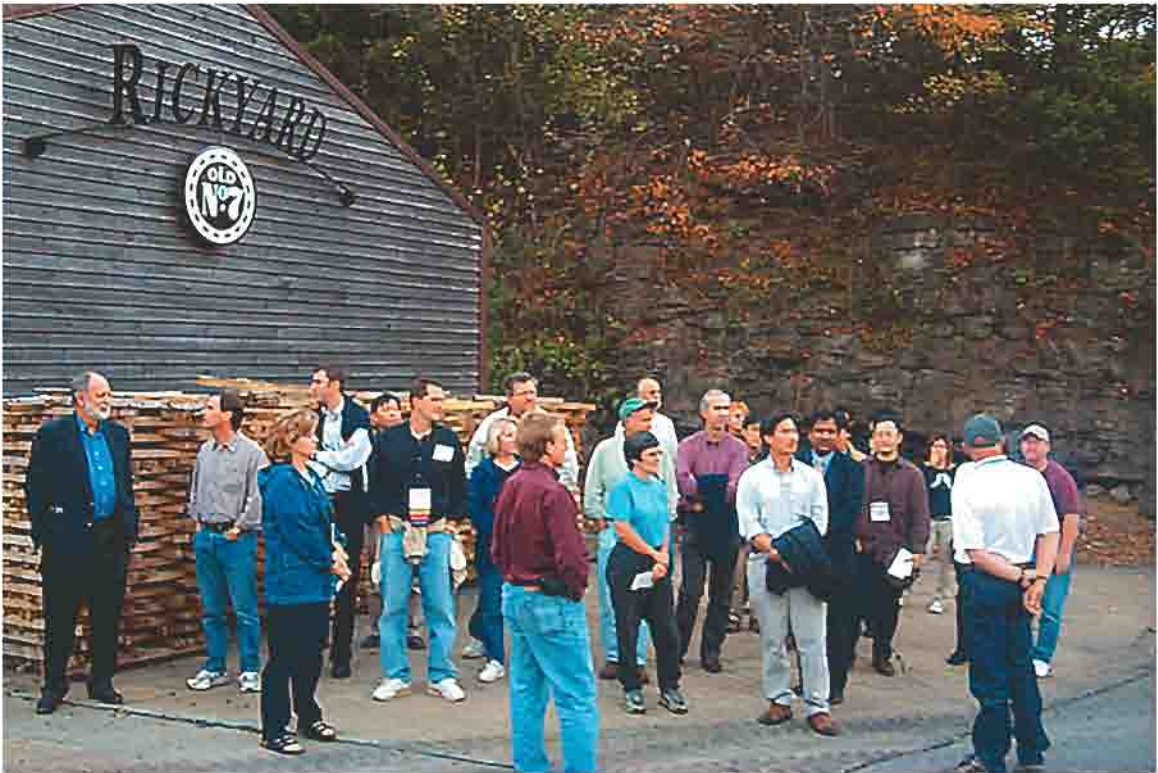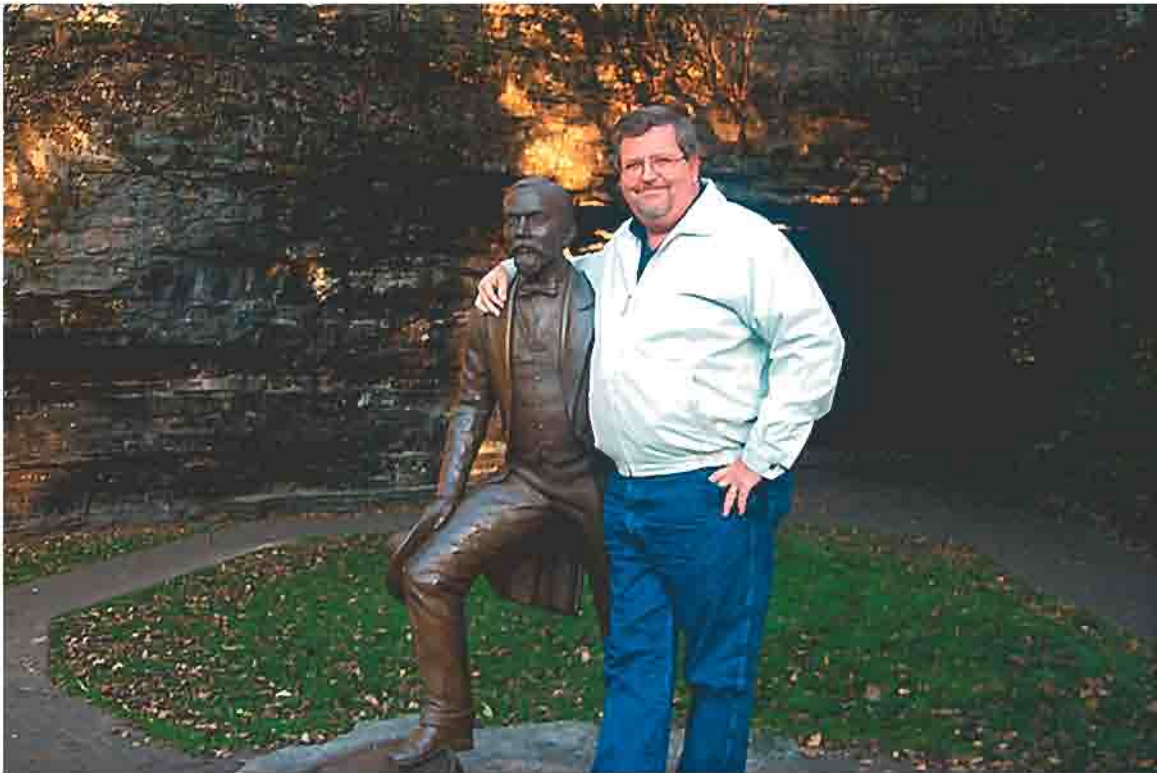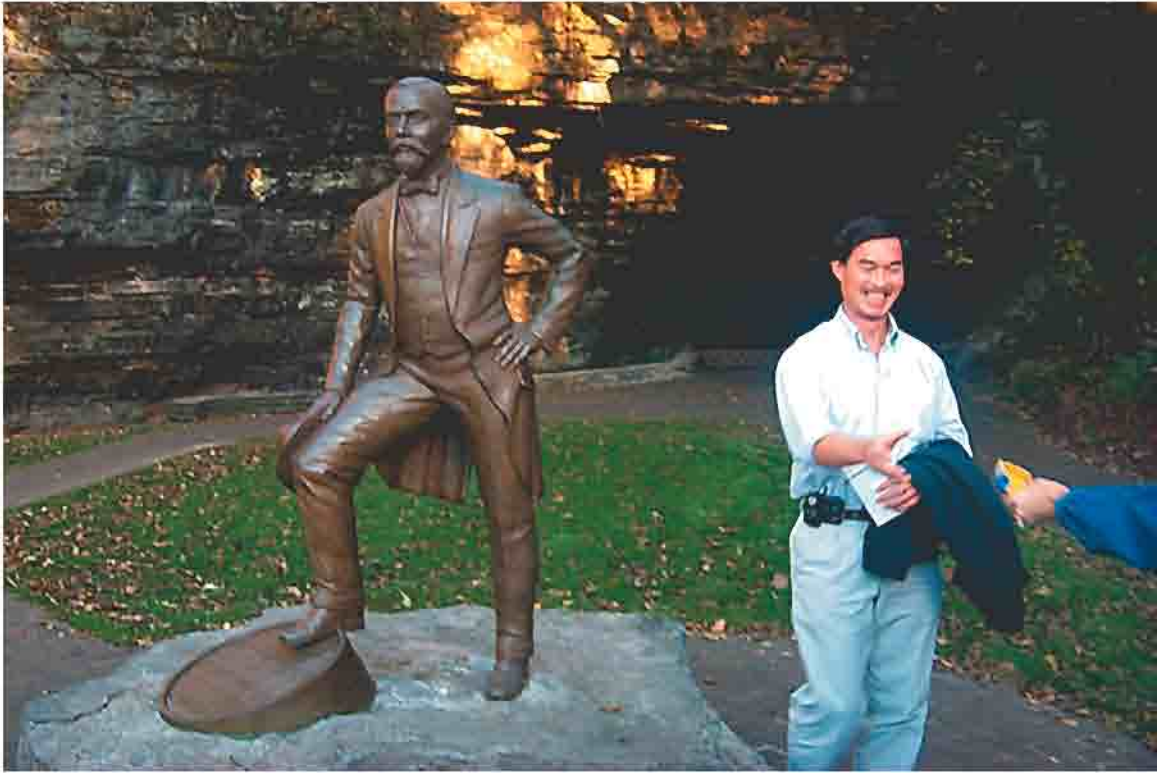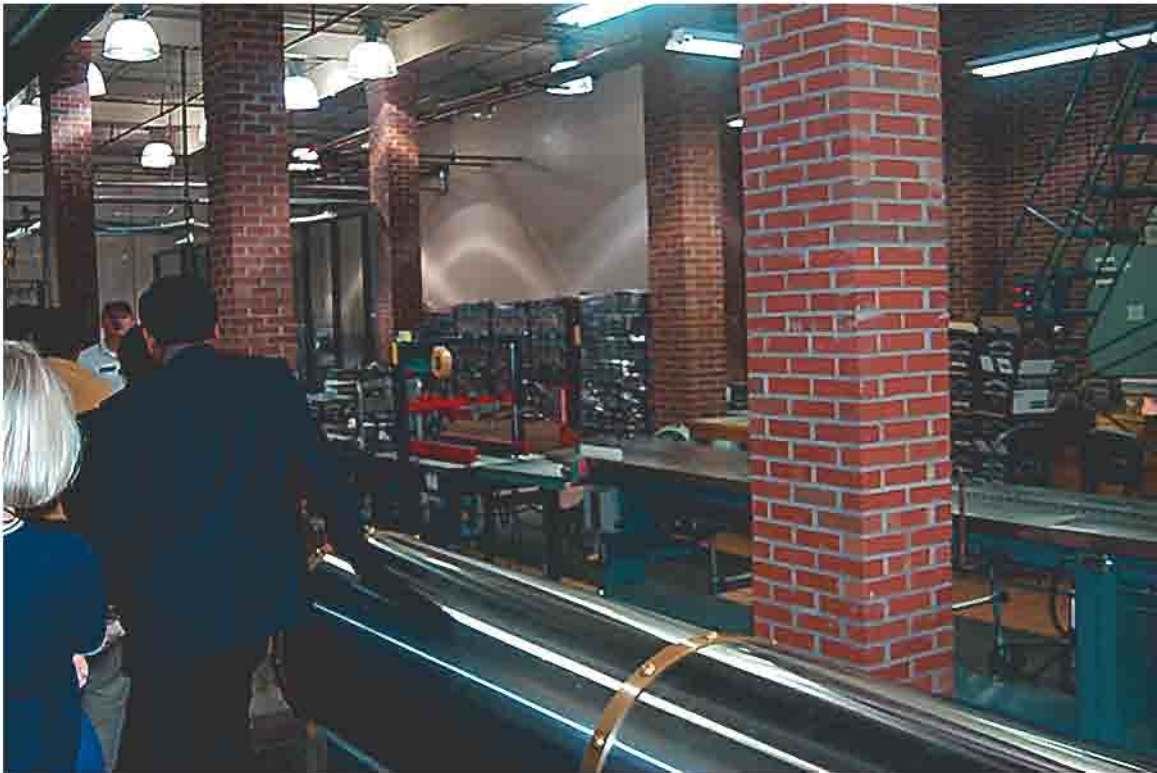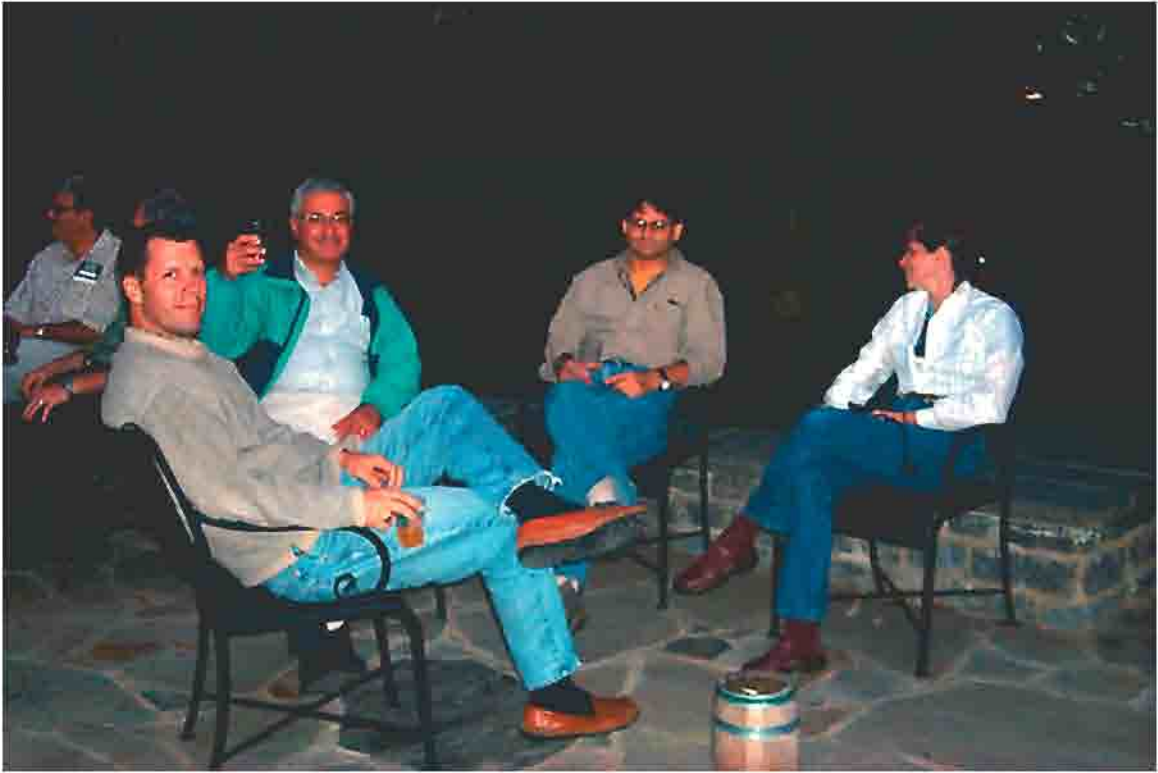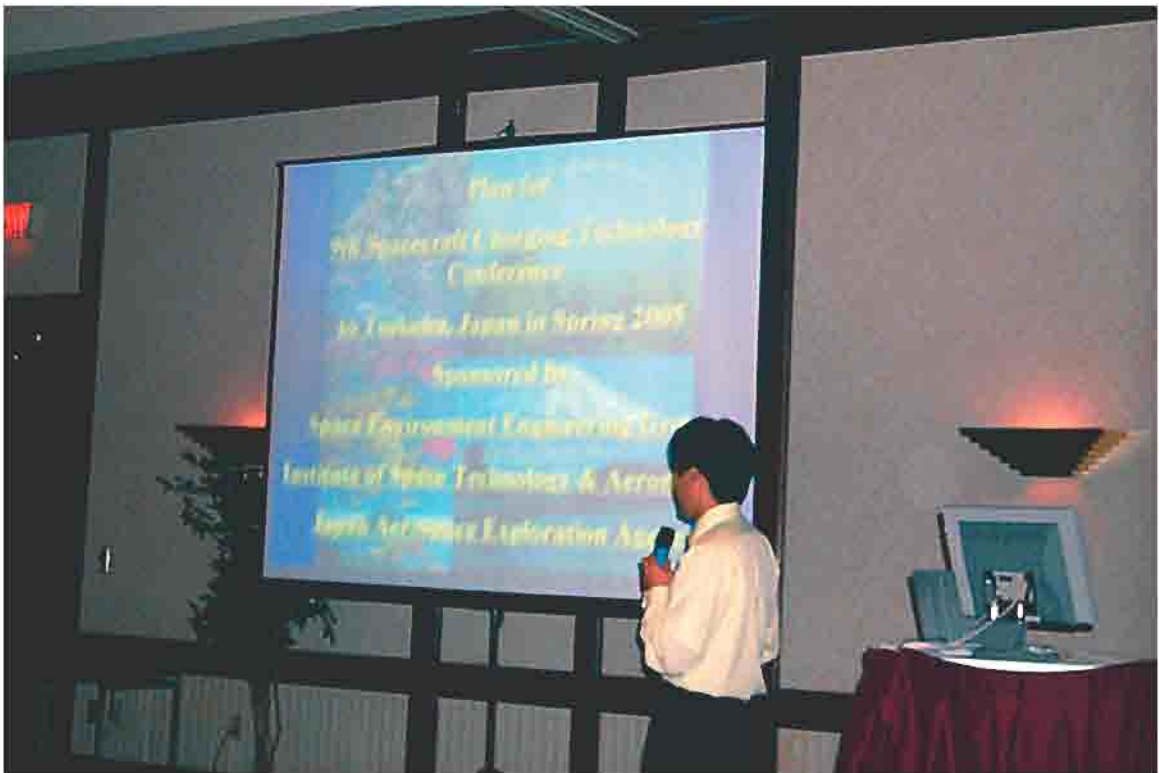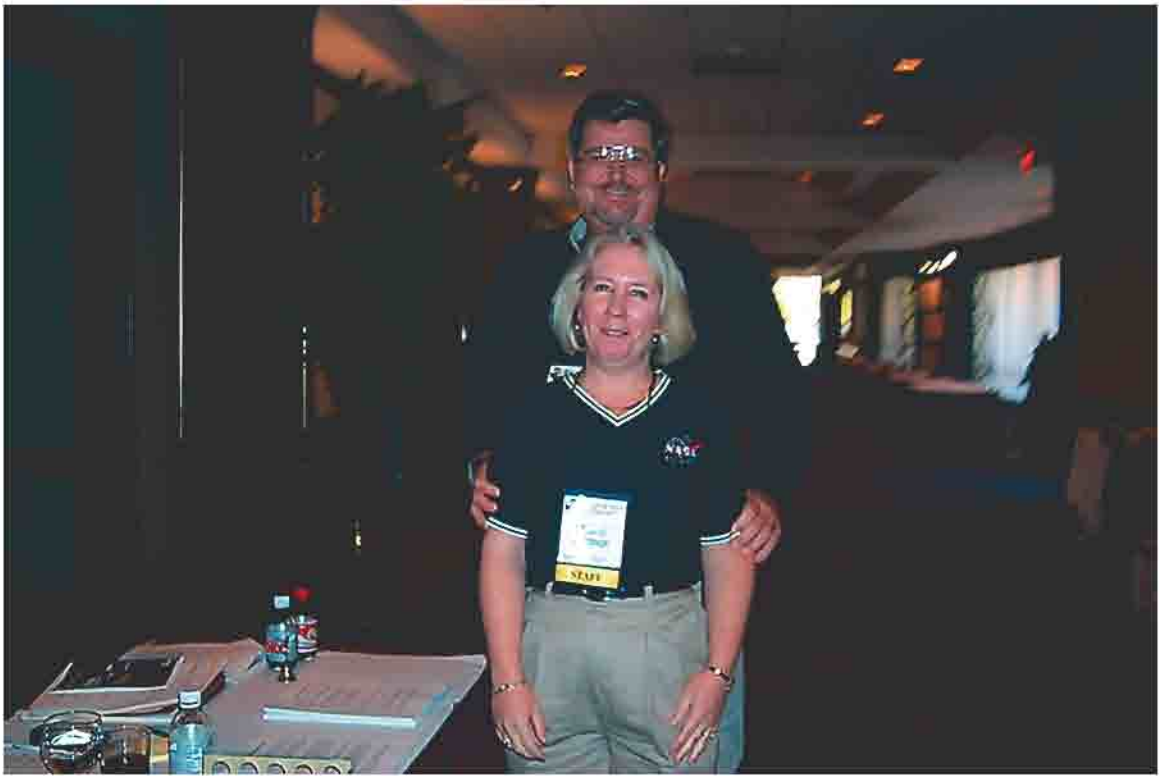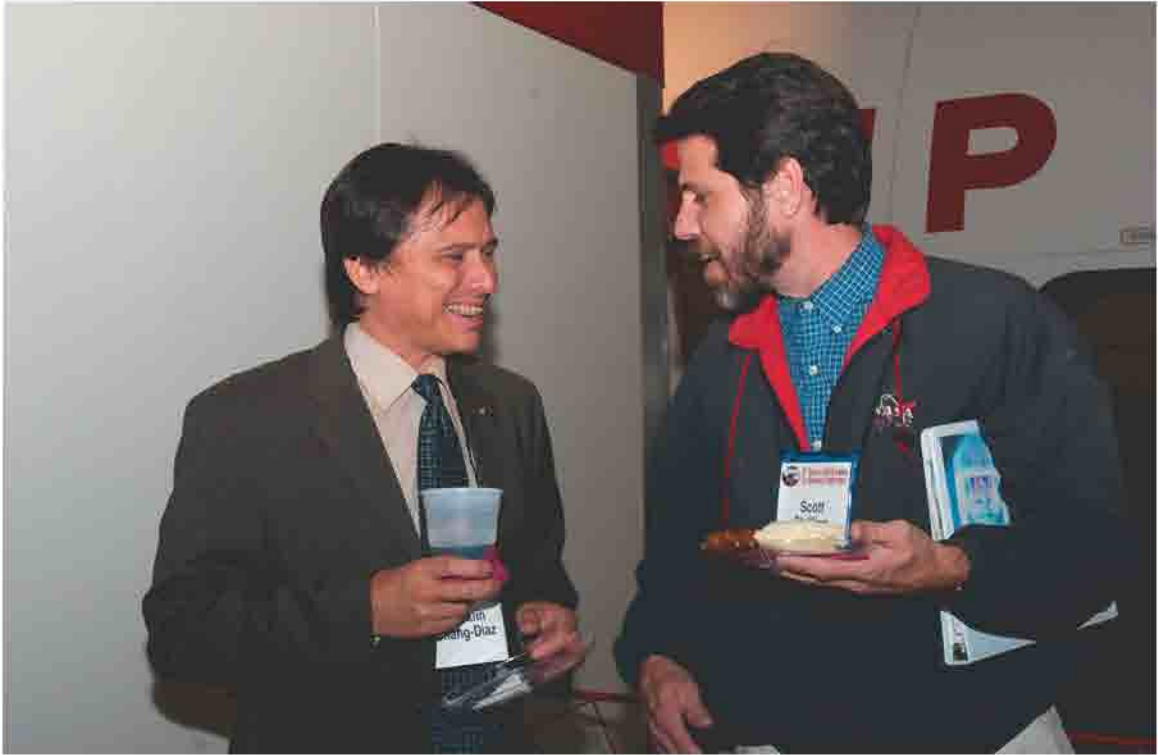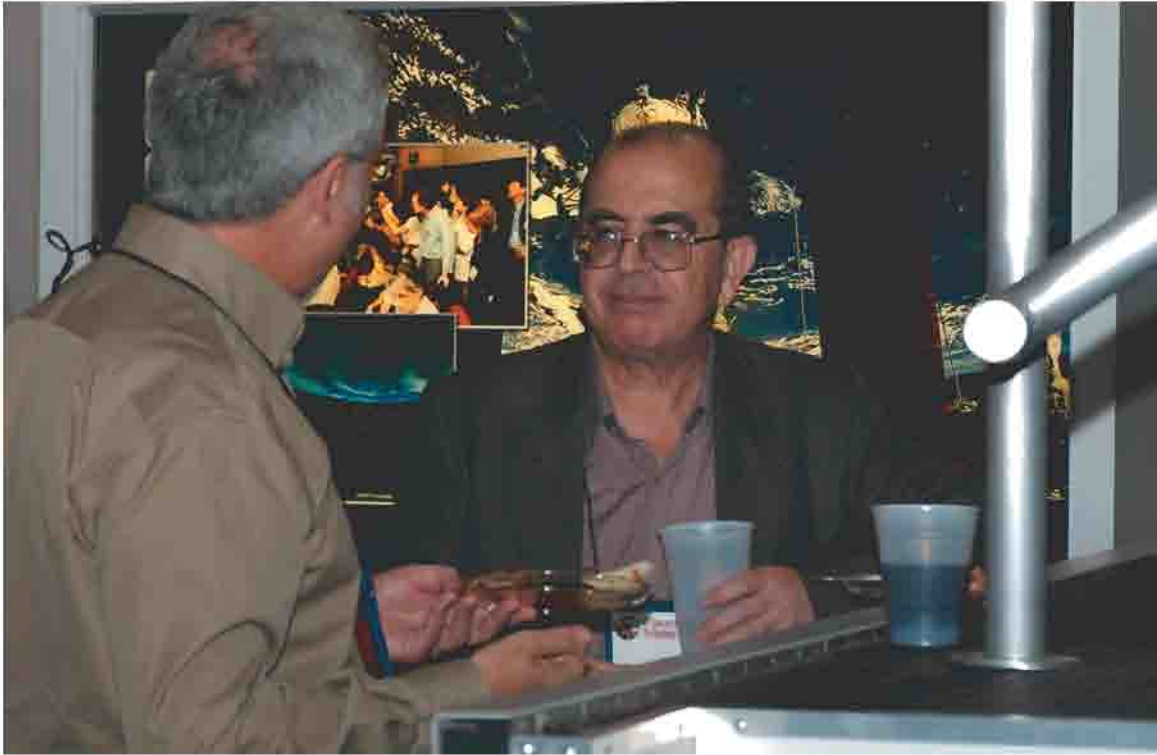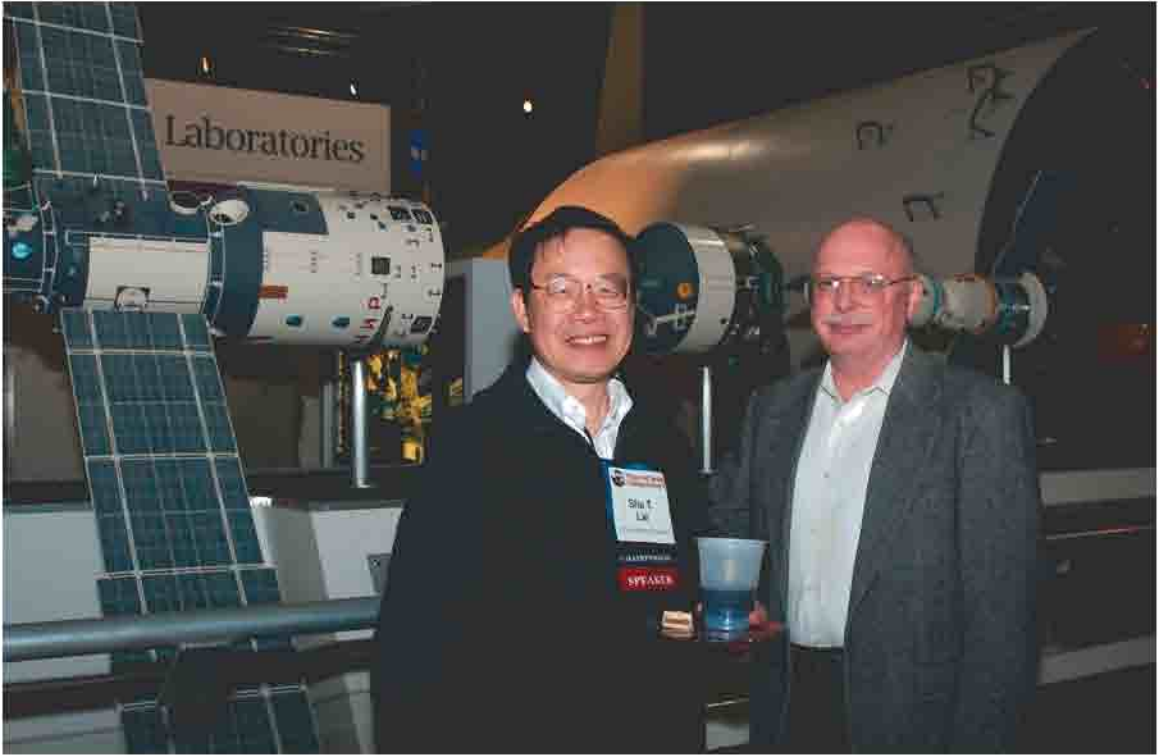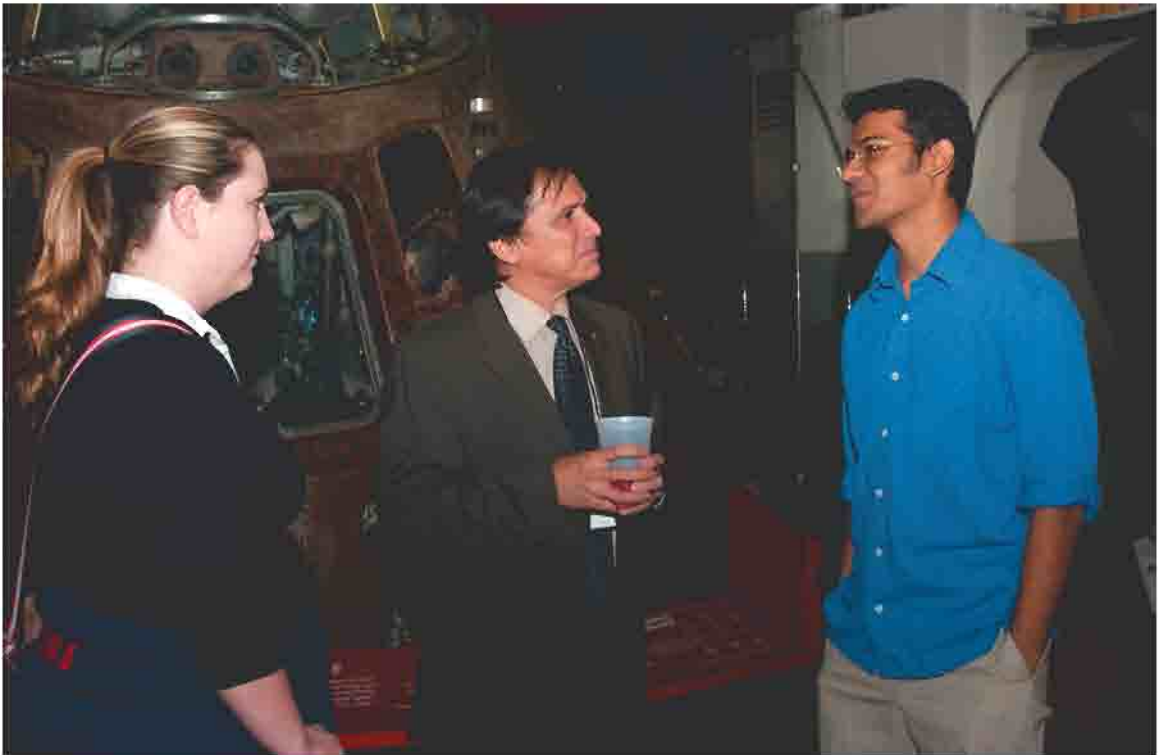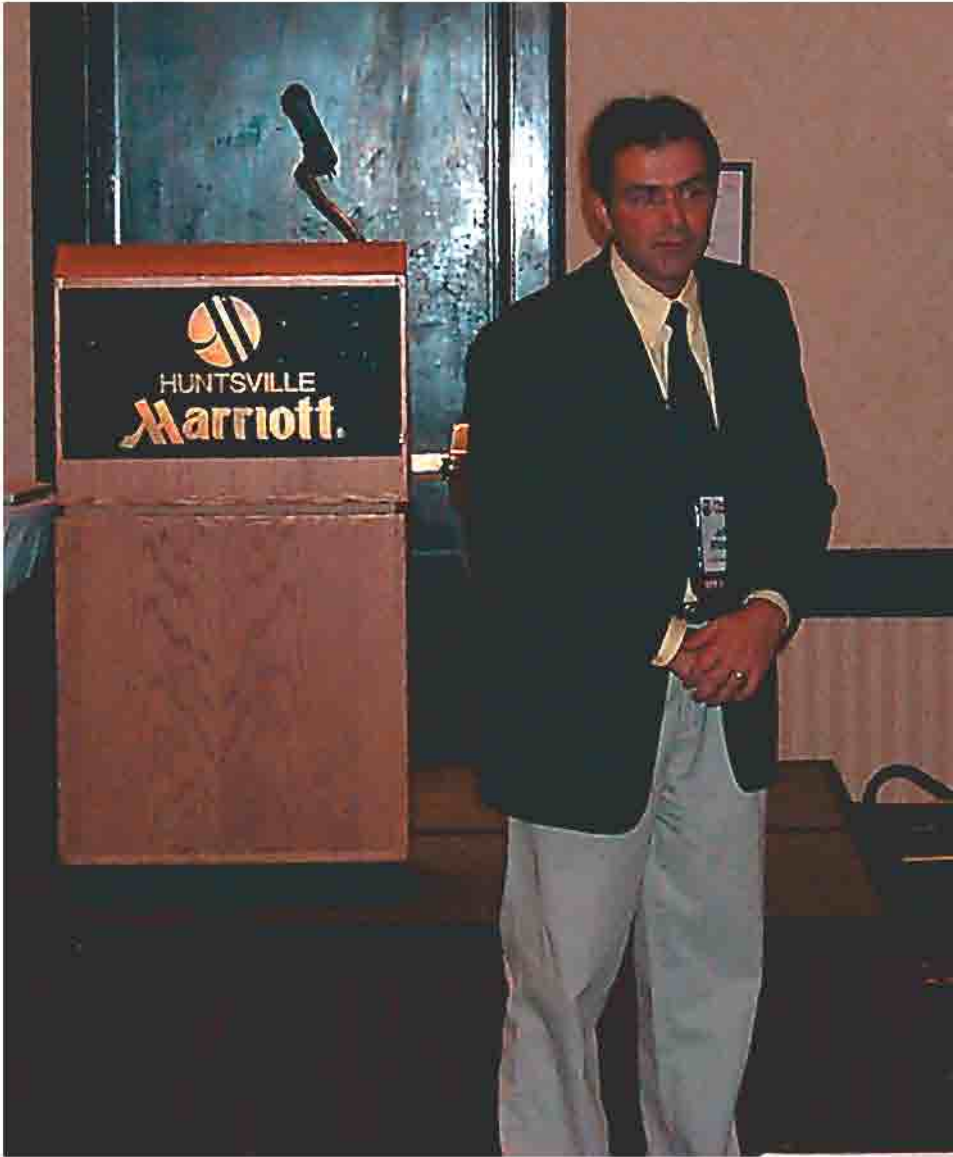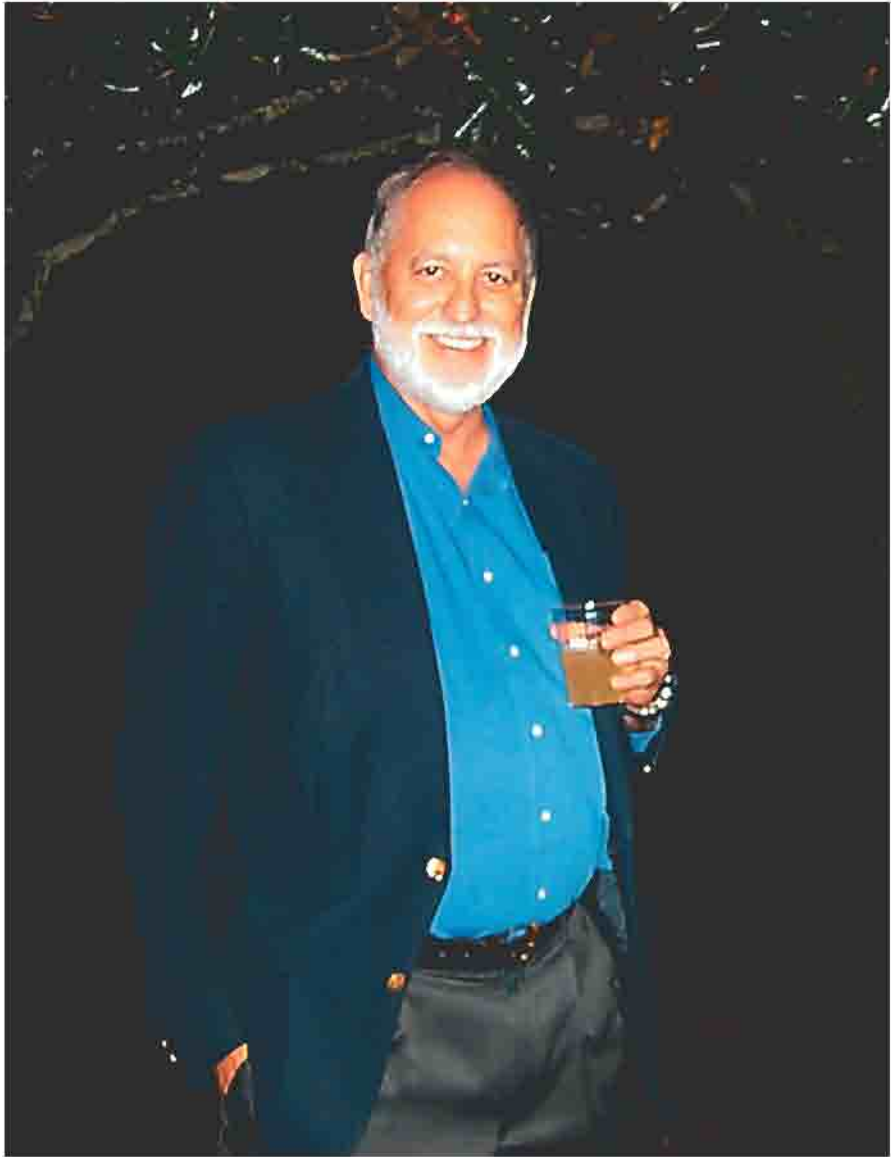
Plan for

9th Spacecraft Charging Technology Conference

to Tsukuba, Japan in Spring 2005

Sponsored by

Space Environment Engineering Group

Institute of Space Technology & Aeronautics

Japan Aerospace Exploration Agency

LOCATION OF JAPAN

Noshiro Testing Center (NTC)

Sanriku Ballon Center (SBC)

Kakuda Space Propulsion Center (KSPC)

Sagamihara Campus

Tsukuba Space Center (TKSC)

Earth Observation Center (EOC)

Usuda Deep Space Center

Katsuura Tracking and Communication Station

Aerospace Research Center (ARC)

Earth Observation Research and Application Center (EORC)

Tokyo Office

Headquaters Office

Nagoya Office

Industrial Collaboration Department

Uchinoura Space Center (USC)

Masuda Tracking and Communication Station

Tanegashima Space Center (TNSC)

Okinawa Tracking and Communication Station

Ogasawara Downrange Station

TSUKUBA SCIENCE CITY

The 46 national and other experimental research and educational facilities in the City.
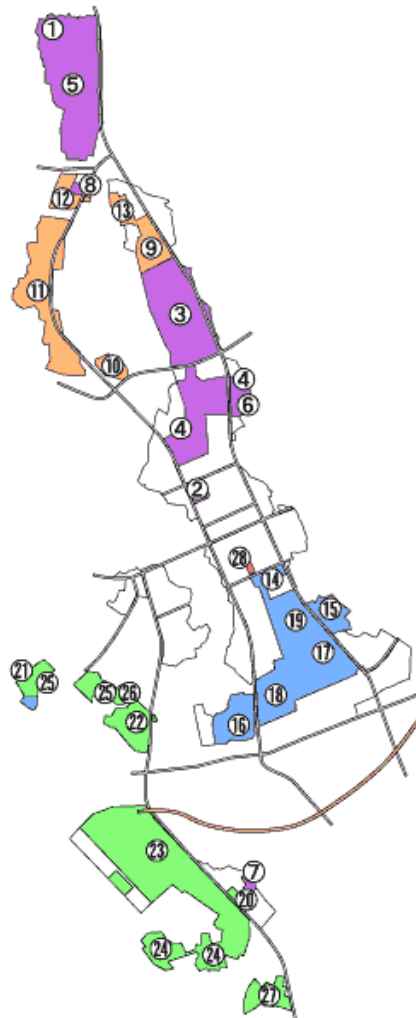
	Name of Institution
1	National Archives of Japan Tsukuba Annex
2	University of Library and Information Science
3	University of Tsukuba
4	Tsukuba College of Technology
5	High Energy Accelerator Research Organization (KEK)
6	Tsukuba Research & Material Center, National Science Museum
7	Tsukuba International Center, JICA Tsukuba International Agricultural Training Center(JICA)
8	National Education Center Institute for Educational Research and In-service Training
9	National Research Institute for Earth Science and Disaster Prevention
10	Geographical Survey Institute
11	Public Works Research Institute
12	Building Research Institute
13	NTT Access Network Service Systems Laboratories
14	National Institute for Materials Science (Old:National Research Institute for Metals,Tsukuba Laboratories)
15	National Institute for Materials Science (Old:National Institute for Research in Inorganic Materials)
16	National Institute for Environmental Studies
17	National Institute of Advanced Industrial Science and Technology(AIST) Tsukuba Research Administration Office National Institute for Advanced Interdisciplinary Research (NAIR)

ACCESS TO TSUKUBA

Narita Airport ⬄ Tsukuba Center

Limousine Bus: 100 min. (about 2 hours interval)

Tokyo Station ⬄ Tsukuba Center

Express Bus: 70 – 90 min. (about 12-min. interval)
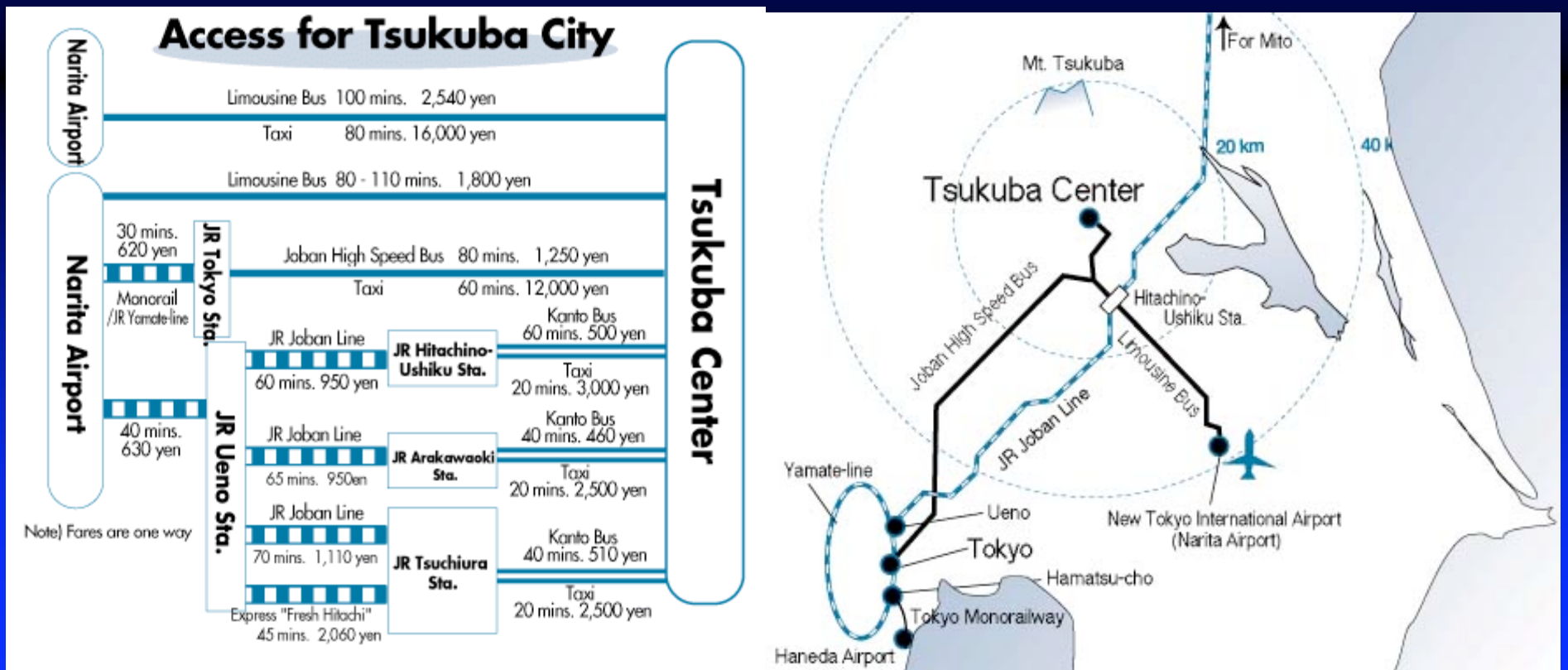
EPOCHAL TSUKUBA (OKURA HOTEL)
International Congress Center

http://www.epochal.or.jp/english/index.html

EPOCHAL TSUKUBA (OKURA HOTEL)
International Congress Center

Spacecraft Charging study of recent Japanese high voltage satellites

Muses-C (2003) ISAS
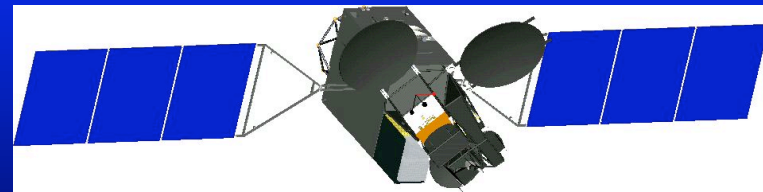
WINDS (2005) NASDA

ETS-VIII (2004) NASDA
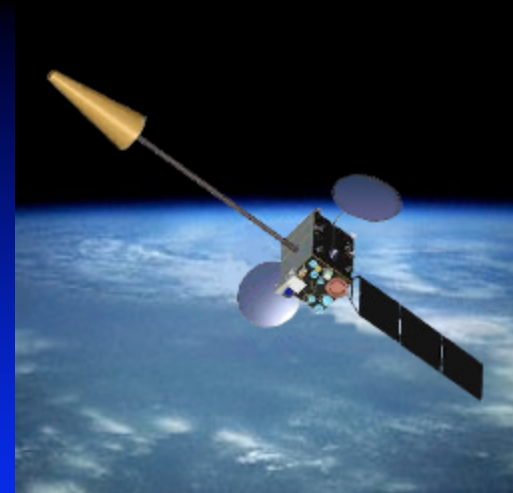
MTSAT-2 (2004) Ministry of Land, Infrastructure and Transport

SCIENTIFIC & TECHNOLOGICAL HIGHLIGHTS : 1. GROUND TEST

SFU
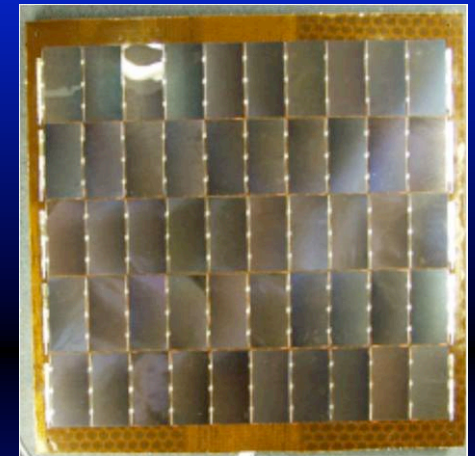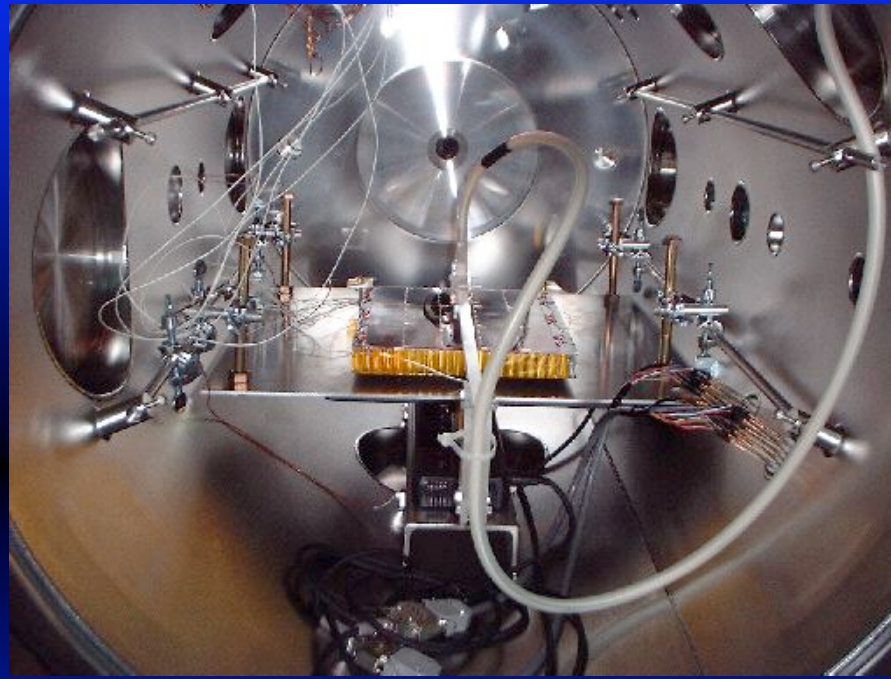
Large coupon
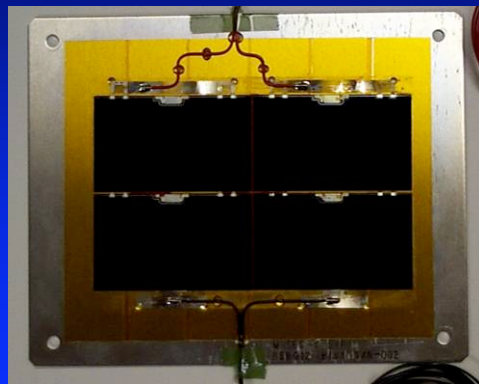
Muses-C
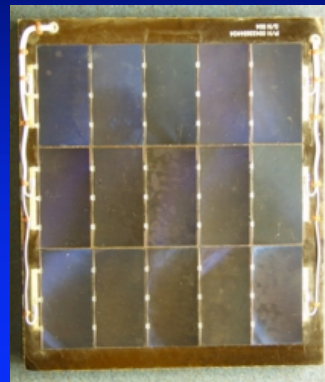
ETS-VIII
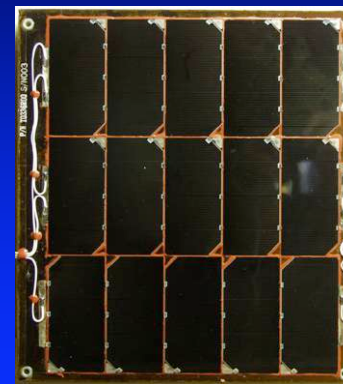
WINDS
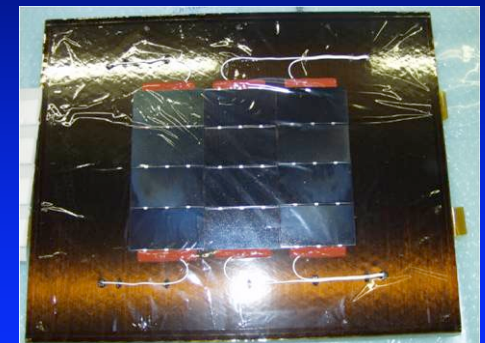
400V array

SCIENTIFIC & TECHNOLOGICAL HIGHLIGHTS : 2. SATELLITE OBSERVATION

Potential Monitor

Figure 1. ETS-VIII In-orbit Image
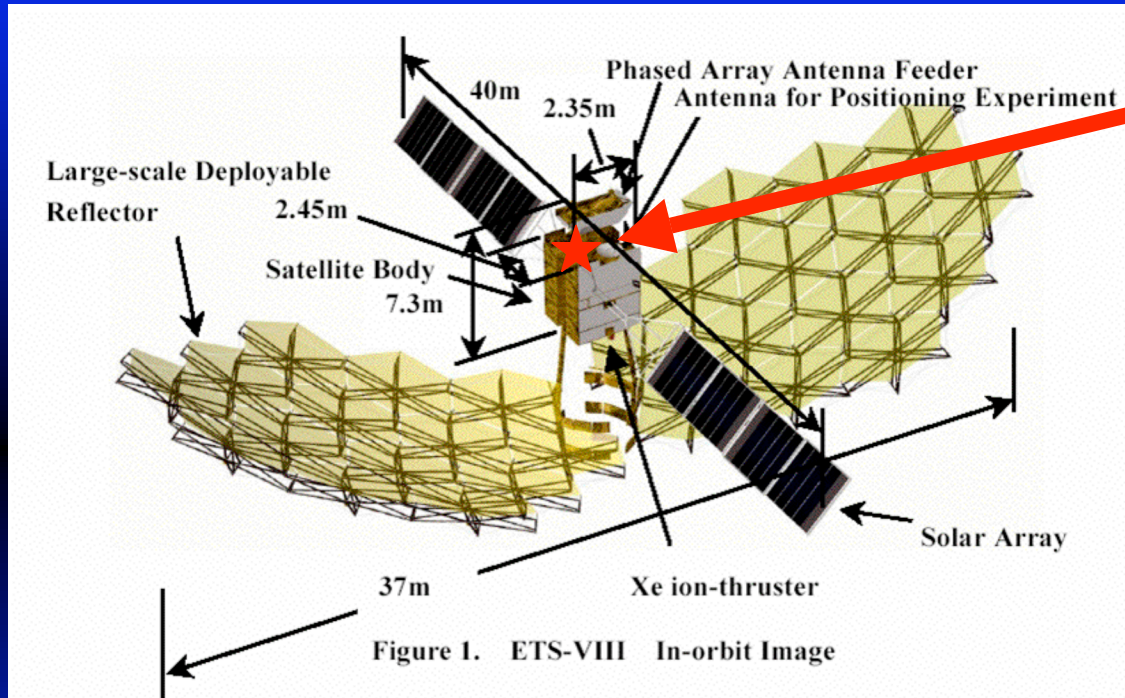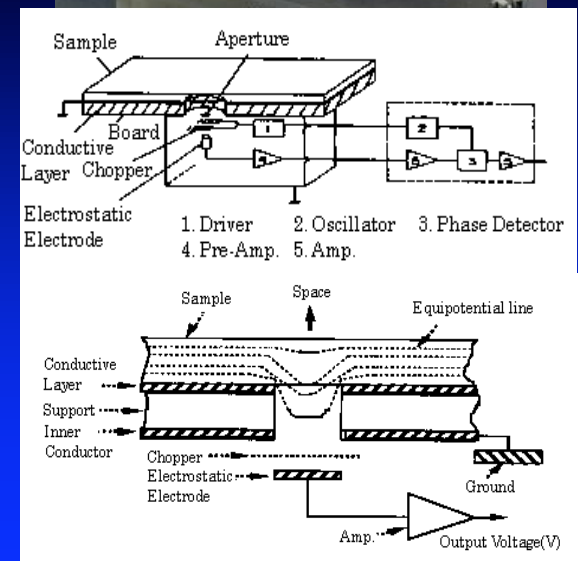
- To be launched in 2004
- 100V bus for 7.5kW
- 105V V_{oc} with NRS IBF Si cells
- Ion thruster for NS keeping
- Mission duration 3 years

SCIENTIFIC & TECHNOLOGICAL HIGHLIGHTS : 3. MODELING & SIMULATION

NASCAP Simulation of ETS-VIII

SPIS Simulation (ESTEC)

Microwave-plasma interactions

ISS

Ion engine

Large scale space structure

Space solar power system (SSPS)

Magnetosphere

Science satellite

Bow shock

Satellite environment (charging, antenna characteristics)

Plasma around antenna

Gespace Environment Simulator with Earth Simulator
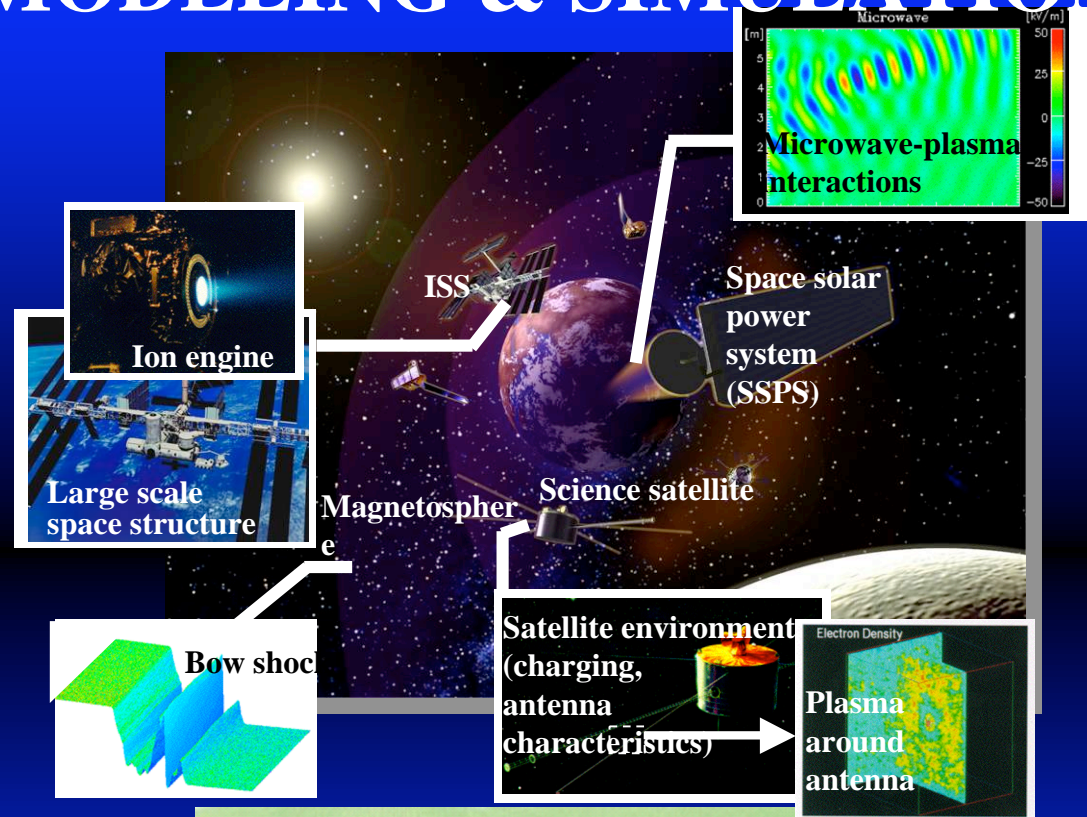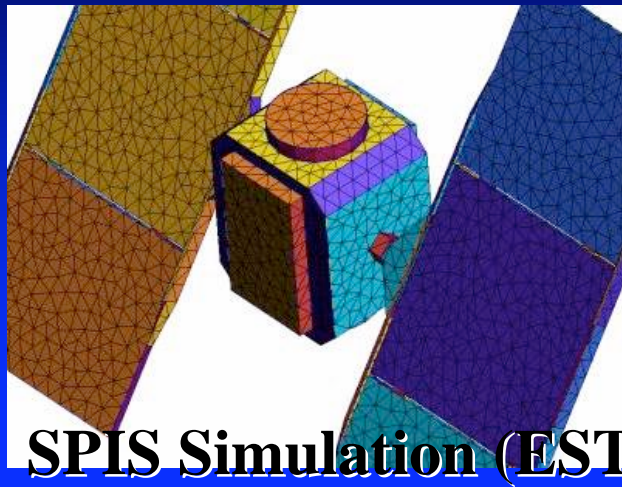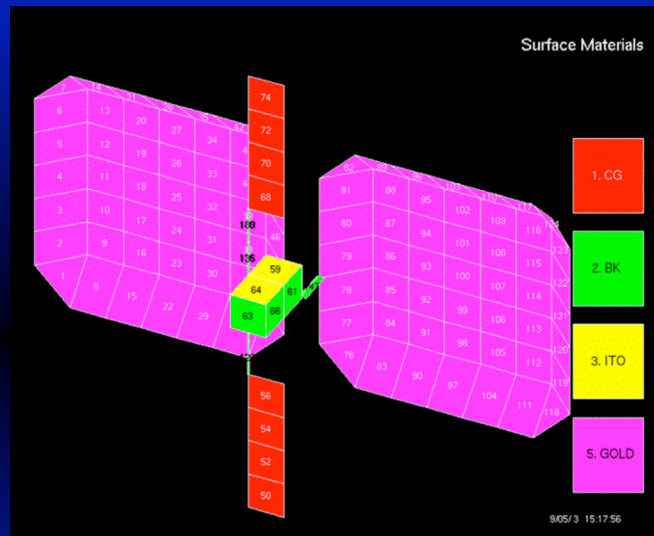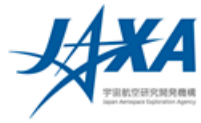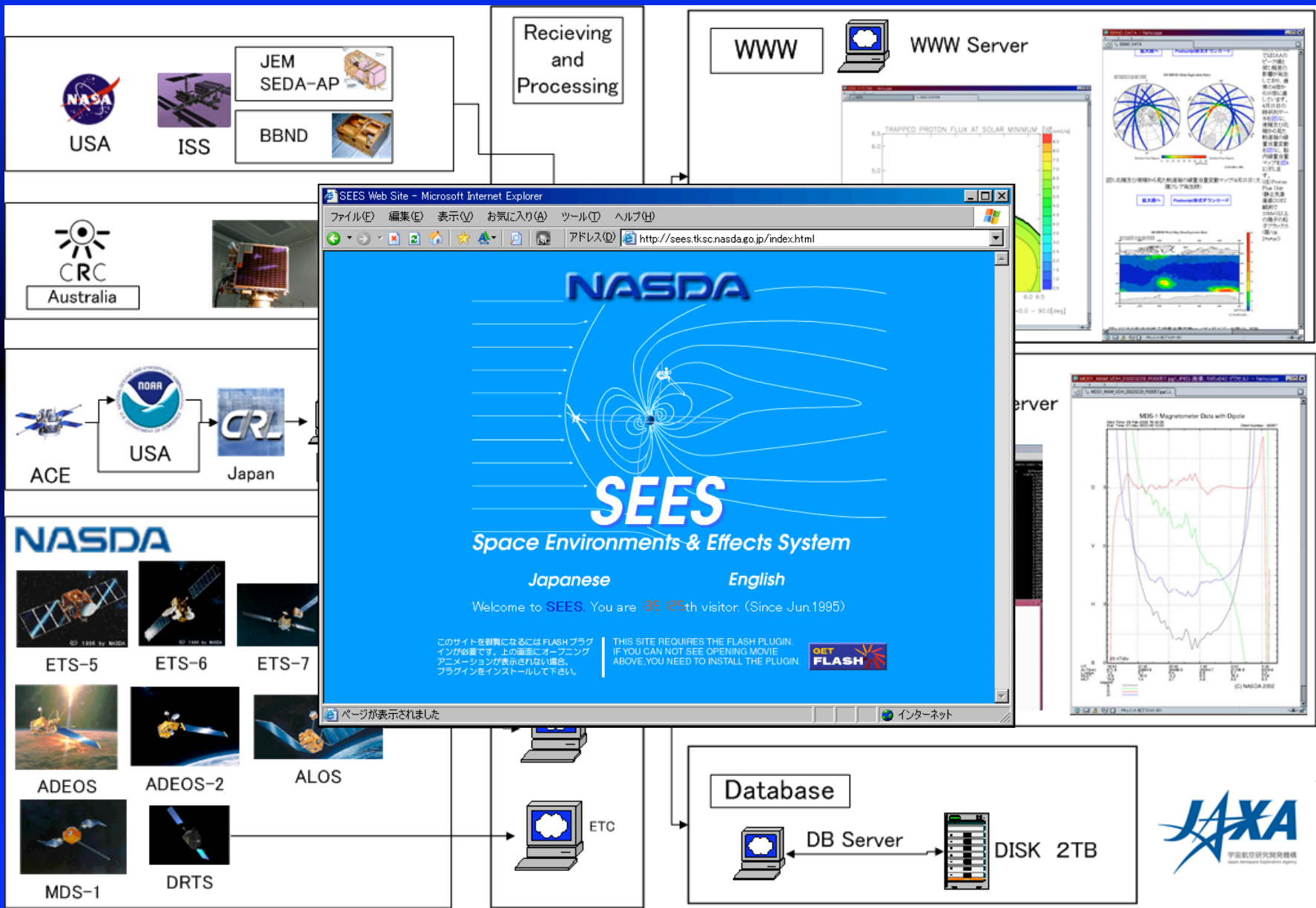
TENTATIVE EXCURSION PLAN ASAKUSA & DOWNTOWN OLD TOKYO

Dr. Tateo Goka
Director of Space Environment Engineering Group,
Institute of Space Technology and Aeronautics,
Japan Aerospace Exploration Agency (JAXA)
Tsukuba Space Center
2-1-1, Sengen, Tsukuba, Ibaraki, 305-8505, Japan
goka.tateo@jaxa.jp

Would you like to come to Tsukuba, Japan?

Thank you for your attention.

2003 8th Spacecraft Charging Technology Conference Attendee List

Adamo, Richard C.
SRI International
Bldg 408/70
333 Ravenswood Ave.
Menlo Park, CA 94025
USA
650-859-2370
richard.adamo@sri.com

Balmain, Keith
University of Toronto
10 King's College Rd., Dept. ECE
Toronto, Ontario M5S 3G4
Canada
1-416-978-3127
balmain@waves.utoronto.ca

Barjatya, Aroh
Utah State University
UMC 4120
Logan, UT 84322
USA
435-881-1616
arohb@cc.usu.edu

Barsamian, Hagop
The Boeing Company
13100 Space Center Blvd
MC HB3-20
Houston, TX 77058
USA
281-226-6734
Hagop.R.Barsamian@boeing.com

Barth, Janet
NASA Goddard Space Flight Center
Code 561.4
Greenbelt, MD 20771
USA
301-286-8046
Janet.L.Barth@nasa.gov

Berg, Glenn
The Boeing Company
3800 Lewiston Street
Suite 100
Aurora, CO 80011
USA
303-677-2045
glenn.a.berg@boeing.com

Berman, Elizabeth
Air Force Research Laboratory
2941 Hobson Way, Rm. 136
WPAFB, Ohio 45433
USA
937-255-2465
elizabeth.berman@wpafb.af.mil

Berthou, Claude
ALCATEL Space
100, Boulevard du Midi
Cannes La Bocca, France 06150
33 (0) 4-92-92-65-01
claude.berthou@space.alcatel.fr

Bodeau, Michael
Boeing Satellite Systems
2060 E. Imperial Hwy
EL Segundo, CA 90009
310-416-6928
michael.bodeau@boeing.com

Bonometti, Joel
NASA Marshall Space Flight Center
Mail Code TD05
Building 4203, Room 6104
Huntsville, AL 35812
256-544-4019
Joseph.A.Bonometti@nasa.gov

Brekke, Paal
European Space Agency
NASA/GSFC Mailcode 682.3
Bldg 26, Room G-1
Greenbelt, MD 20817
USA
301-286-6983
pbrekke@esa.nascom.nasa.gov

Brickhouse, Kyle
Universities Space Research Association
108 Gray Run
Huntsville, AL 35824
USA
256-544-4193
kyle.brickhouse@msfc.nasa.gov

Briet, Richard
The Aerospace Corporation
2350 E El Segundo Blvd
El Segundo, CA 90245-4691
USA
310-366-1912
Richard.Briet@aero.org

Brown, Gayle
Universities Space Research Association
108 Gray Run
Huntsville, AL 35824
USA
256-544-2104
gayle.brown@msfc.nasa.gov

Burch, Jackie
Teledyne Solutions, Inc.
5000 Bradford Drive, Suite 200
Huntsville, AL 35805
USA
256-726-3505
jackie.burch@tdytsi.com

Burgess, Nicola
Raytheon
7401 E. Speedway, #12206
Tuscon, AZ 85710
USA
520-794-0845
nicola_burgess@raytheon.com

Catani, Jean-Pierre
Centre National d'Etudes Spatiales
(CNES)
18, Avenue Edouard-Belin – 31401
Toulouse Cedex 9
France
05.61.27.36.77
jean-pierre.catani@cnes.fr

Cho, Mengu
Kyushu Institute of Technology
1-1 Sensui Tobata-ku
Kitakyushu, Fukuoka 8048550
Japan
+81-93-884-3228
cho@ele.kyutech.ac.jp

Clark, Tony
NASA Marshall Space Flight Center
Mail Code ED44/4708
Huntsville, AL 35812
USA
256-544-2394
tony.clark@nasa.gov

Cooke, David
AFRL/VSBX – Hanscom AFB
Bedford, MA 01731-3010
USA
781-377-2931
david.cooke@hanscom.af.mil

Davis, Victoria
Science Applications International
Corporation (SAIC)
10260 Campus Point Drive
Mailstop A1
San Diego, CA 92121
USA
858-826-1608
victoria.a.davis@saic.com

de Payrebrune, Mark
DPL Science
2388 Tally Ho
St. Lazare, Quebec J7T2B1
Canada
450-458-0852
mark@dplscience.com

Dennison, JR
Utah State University Physics
Department
4415 Old Main Hill
Logan, UT 84322-4415
USA
435-797-2936
JR.Dennison@usu.edu

Deshpande, Mukund
Applied Material Systems Engineering
Inc./AMSENG
2309 Pennsbury Court
Schaumburg, IL 60194
USA
630-372-9650
m.deshpande@comcast.net

Edwards, Dave
NASA Marshall Space Flight Center
ED31 Bldg 4711, Rm. W110A
256-544-4081
USA
David.L.Edwards@nasa.gov

Ekstrand, Veronika
Kongsberg Satellite Services AS SvalSat
P.O. 242
Longyearbyen, 9171
Norway
+47 79023771
veronika@ksat.no

Elsen, Ron
The Boeing Company
3800 Lewiston Street
Suite 100
Aurora, CO 80011
USA
303-677-2046
ronald.k.elsen@boeing.com

Engwall, Erik
Swedish Institute of Space Physics
Box 537
Uppsala, 75121
Sweden
+46184715930
eren7803@student.uu.se

Ferguson, Dale
NASA Glenn Research Center
MS 302-1
21000 Brookpark Road
Cleveland, OH 44135
USA
216-433-2298
dale.c.ferguson@nasa.gov

Finckenor, Miria
NASA Marshall Space Flight Center
Mail Code ED31
Bldg. 4711/Room W100B
Huntsville, AL 35812
USA
256-544-9244
miria.finckenor@nasa.gov

Forest, Julien
IRF-K/CETP
50 rue de la Republique
Montreuil, 93100
France
+33148570152
julien@irf.se

Foushee, Neal
Spectrum Astro
1440 N Fiesta Blvd
Gilbert, AZ 85233
USA
480-892-8200
neal.foushee@specastro.com

Friedel, Reiner
Los Alamos National Laboratory
MS D436
Los Alamos, NM 87545
USA
505-665-1936
friedel@lanl.gov

Fujii, Haruhisa
Nara National College of Technology
22, Yata-Cho
Yamatokoriyama, Nara 639-1080
Japan
+81-743-55-6091
fujii@elec.nara-k.ac.jp

Fukuyoshi, Fuyuko
Musashi Institute of Technology
1-28-1
Tamazutumi
Setagaya-ku, Tokyo 158-8557
Japan
81-3-5707-2156
fukuyoshi@me.musashi-tech.ac.jp

Gaillot, Ludovic
EADS-ASTRIUM
37 Av des Cosmonautes
31402 Toulouse
Cedex 4, France
France
0033 5 62 43 38 63
ludovic.gaillot@astrium.eads.net

Galofaro, Joel T.
John H. Glenn Research Center
21000 Brookpark Road, Mail Stop 302-1
Cleveland, OH 44135
USA
216-433-2294
Joel.T.Galofaro@grc.nasa.gov

Gardner, Barbara
Science Applications International
Corporation
10260 Campus Point Drive
Mailstop A3
San Diego, CA 92121
USA
858-826-1614
barbara.m.gardner@saic.com

Garrett, Henry
Jet Propulsion Laboratory
JPL (122-107)
4800 Oak Grove Drive
Pasadena, CA 91109
USA
818-354-2644
henry.garrett@jpl.nasa.gov

Godefroy, Michel
CETP
4 Avenue de Neptune
Saint-Maur, 94100
France
33 1 45 11 42 91
godefroy@cetp.ipsl.fr

Goembel, Luke
Goembel Instruments
1020 Regester Avenue
Baltimore, MD 21239
USA
410-377-6828
luke@goembel.biz

Gordon, Mike
Lockheed Martin
P.O. Box 179
Denver, CO 80201
USA
303-971-4310
Michael.j.Gordon@lmco.com

Hardage, Donna
NASA Marshall Space Flight Center
ED03
Huntsville, AL 35812
USA
256-544-2342
donna.hardage@nasa.gov

Hartman, Fred
Sandia National Labs
MS1167
PO Box 5800
Albuquerque, NM 87185
USA
505-845-3473
efhart@sandia.gov

Heise, Ed
Eastman Kodak Company
867 Rush Road
Rush NY 14543-9780
USA
585-588-3649
edward.heise@kodak.com

Hilgers, Alain
European Space Agency/TOS-EES
Keplerlaan 1
Noordwijk, 2200AZ
The Netherlands
+31 71 565 5836
Alain.Hilgers@esa.int

Hilmer, Robert
AFRL/VSBXR
29 Randolph Road
Hanscom AFB, MA 01731
USA
781-377-3211
Robert.Hilmer@Hanscom.af.mil

Hosoda, Satoshi
Kyushu Institute of Technology
1-1 Sensui-cho, Tobata-Ku
Kitakyushu, Fukuoka 804-8550
Japan
81-93-884-3228
hosada@ele.kyutech.ac.jp

Hovater, Mary
NASA Marshall Space Flight Center
Mail Code ED31
Huntsville, AL 35812
USA
256-961-0309
mary.a.hovater@nasa.gov

Howard, James
Jackson & Tull
GSFC Code 561.4
Bldg. 22, Room 056
Greenbelt, MD 20771
USA
301-286-1023
jim.howard@gsfc.nasa.gov

Hubbs, Whitney
NASA Marshall Space Flight Center
Huntsville, AL 35812
USA
256-544-0615
whitney.hubbs@nasa.gov

Hunt, Charles
NASA Marshall Space Flight Center
Mail Code VS20
Huntsville, AL 35812
USA
256-544-6706
charles.d.hunt@nasa.gov

Hwang, Kai
Computer Sciences Corporation
P.O. Box 240005
Huntsville, AL 35812
USA
256-544-6080
kai.shen.hwang@msfc.nasa.gov

Jacobsen, Ronald
Applied Sciences, Inc.
P.O. Box 579
141 W. Xenia Ave.
Cedarville, OH 45314-0579
USA
937-766-2020 x137
rljacobsen@apsci.com

Jordan, Thomas M.
E.M.P. Consultants
P.O. Box 3191
Gaithersburg, MD 20885
USA
301-869-2317
tj@empc.com

Jurisson, Karl R.
Northrop Grumman Co.
R4/1166A, One Space Park
Redondo Beach, CA 90278
USA
310-812-1151
karl.jurisson@ngc.com

Kauffman, Billy
NASA Marshall Space Flight Center
Mail Code ED03
Huntsville, AL 35812
USA
256-544-1418
billy.kauffman@nasa.gov

Koakutsu, Hideaki
Mitsubishi Electric Corporation
Kamakura Works, Sagami Factory
1-1-57, Miyashimo
Sagamihara, Kanagawa 229-1195
Japan
+81-42-775-1209
hideaki.koakutsu@kama.melco.co.jp

Koontz, Steven L.
NASA Johnson Space Center
2101 NASA Road 1
Houston, TX 77058
USA
Steven.l.koontz@nasa.gov

Laframboise, James
York University
Physics & Astronomy Department
4700 Keele Street
Toronto, Ontario M3J1P3
Canada
416-736-5621
laframboise@quasar.phys.yorku.ca

Lai, Shu T.
Air Force Research Laboratory
Mailing Stop: VSBXT
29 Randolph Road
Hanscom, AFB, MA 01731-3010
USA
Shu.Lai@hanscom.af.mil

Lassise, Mike
Raytheon
7640 N. Becky Jo Lane
Tuscon, AZ 85741
USA
520-794-5851
rmlassie@raytheon.com

Leung, Philip
Boeing Satellite System
P.O. Box 92919 MC W-S25-C372
Los Angeles, CA 90009
USA
310-364-8567
Philip.l.leung@boeing.com

Levy, Leon
ONERA
BP4025, 2Av. Edouard Belin
31055 Toulouse Cedex
France
33-562 25 2740
levy@onecert.fr

Lin, Elise
DPL Science
2388 Tally Ho, J7T2B1
St. Lazare, Quebec
Canada
450-458-0852
elise@dplscience.com

Lin, Dong-Shiun
Swales Aerospace
5050 Power Mill Road
Beltsville, MD 20705
USA
301-286-5798
dong.lin@gsfc.nasa.gov

Mandell, Myron
Science Applications International Corp.
10260 Campus Point Drive
Mail Stop A3
San Diego, CA 92121
USA
858-826-1622
myron.j.mandell@saic.com

Masuyama, Takahisa
Osaka University
1-3, Machikaneyama
Toyonaka, Osaka 560-8531
Japan
+81-6-6850-6178
masuyama@yoshikawa.me.es.osaka-u.ac.jp

McCollum, Matthew
NASA Marshall Space Flight Center
Mail Code ED44
Huntsville, AL 35812
USA
256-544-2351
matt.mccollum@nasa.gov

Mendonca, J. T.
GoLP – Instituto Superior Tecnico
Av. Rovisco Pais 1
Lisbon 1049-001
Portgual
351-21-841-9324
titomend@ist.utl.pt

Mikellides, Ioannis
Science Applications International Corp.
10260 Campus Point Drive
Mailstop A3
San Diego, CA 92121
USA
858-826-1649
ioannis.g.mikellides@saic.com

Miller, Nikki
NASA Marshall Space Flight Center
RS30
Huntsville, AL 35812
USA
256-544-8955
nikki.miller@nasa.gov

Minor, Jody
NASA Marshall Space Flight Center
Bldg.4487, MC ED03
Huntsville, AL 35812
USA
256-544-4041
jody.minor@nasa.gov

Minow, Joseph
Jacobs Sverdrup
Mail Code ED44
Huntsville, AL 35812
USA
256-544-2850
joseph.minow@msfc.nasa.gov

Miyake, Hiroaki
Musashi Institute of Technology
1-28-1 Tamazutumi
Setagaya-ku, Tokyo 158-8557
Japan
81-3-5707-2156
miyake@me.musashi-tech.ac.jp

Naehr, Steve
Rice University
6100 Main Street, MS 108
Houston, TX 77005
USA
713-348-2408
naehr@rice.edu

Nagaya, Shizuka
22-68 27th Street #1A
Astoria, NY 11105
USA
718-726-0540
bra_sn@hotmail.com

Nakamura, Masao
Japan Aerospace Exploration Agency
2-1-1 Sengen
Tsukuba, Ibaraki
305-6505
Japan
+81-29-868-4177
nakamura.masao@jaxa.jp

Neergaard, Linda
Jacobs Sverdrup
P.O. Box 9030
Huntsville, AL 35812
USA
256-544-5313
Linda.neergaard@msfc.nasa.gov

Nguyen, Sieu Viet
Raytheon Electronic Systems
1810 W. Moore Ave.
Santa Ana, CA 92704
USA
svnguyen@raytheon.com

Okumura, Teppei
Kyusyu Institute of Technology
1-1 Sensui Tobata-ku
Kitakyusyu 804-8550
Japan
+81-93-884-3228
c346406t@tobata.isc.kyutech.ac.jp

Onsager, Terrance
NOAA Space Environment Center
325 Broadway
Boulder, CO 80305
USA
303-497-5713
terry.onsager@noaa..gov

Osawa, Noriyuki
Musashi Institute of Technology
1-28-1 Tamazuyumi
Setagaya-ku, Tokyo
158-8557
Japan
81-3-5707-2156
osawa@me.musashi-tech.ac.jp

Pearson, Steven D.
NASA Marshall Space Flight Center
Mail Code ED03
Huntsville, AL 35812
USA
Steven.pearson@nasa.gov

Pippin, Gary
Boeing Phantom Works
P.O. Box 3707, Mailstop 73-09
Seattle, WA 98124-2207
USA
425-234-7959
Harold.g.pippin@boeing.com

Putt, Lisa
ASRI
Mail Code CD20
Huntsville, AL 35812
USA
256-544-1030
Lisa.putt@msfc.nasa.gov

Rodgers, David
QinetiQ
Cody Technology Park
Farnborough, Hampshire GU14OLX
UK
+44-1252-394297
djrodgers@space.qinetiq.com

Roeder, James
Aerospace Corporation
Mail Stop M2-260
P.O. Box 92957
Los Angeles, CA 90009
USA
310-336-7081
james.roeder@aero.org

Roussel, J.-F.
ONERA
2   Av. Edouard Belin
Toulouse 31055
France
+33-5-62-25-27-35
roussel@onecert.fr

Ryden, Keith
Qinetiq
Cody Technology Park
Farnborough, Hamshire GU14OLX
UK
+44-1252-393057
karyden@space.qinetiq.com

Sanmartin, Juan R.
ETSI Aeronauticos – Universidad
Politecnica de Madrid
Pza. C. Cisneros, 3
Madrid, Madrid 28040
Spain
34-91-336-6302
jrs@faia.upm.es

Sasot Samplon, Eloy
European Space Agency/TOS-EES
Keplerlaan 1
Noordwijk, 2200AZ
+31-71-565-6448
Eloy.Sasot@esa.int

Sato, Tetsuo
NASDA
2-1-1 Sengen
Tsukuba, Ibaraki 305-8505
Japan
+81-29-868-4058
satoh.tetsuo@nasda.jo.jp

Schneider, Todd
NASA Marshall Space Flight Center
Mail Stop ED31A
Huntsville, AL 35812
USA
256-544-2595
todd.a.schneider@nasa.gov

Segraves, Nicholas
Universities Space Research Association
NASA Marshall Space Flight Center
Mail Code ED03
Huntsville, AL 35812
USA
256-544-4115
Nicholas.segraves@msfc.nasa.gov

Seran, Elena
CETP/CNRS
4 avenue de Neptune
Saint Maur 94100
France
33 6 84 88 40 17
Elena.Seran@cetp.ipsl.fr

Shikata, Yoshio
Kyushu Institute of Technology
1-1, Sensui-cho, Tobata-ku
Kitakyushu, Fukuoka 804-8550
Japan
+81-93-884-3228
c346414y@tobata.isc.kyutech.ac.jp

Sim, Alec
Utah State University
Physics Department UMC 4415
Logan, UT 84322-4415
USA
435-797-2936
alecmsim@cc.usu.edu

Stephens, Karen
NASA Marshall Space Flight Center
Mail Code ED03
Huntsville, AL 35812
USA
256-544-3414
Karen.l.stephens@nasa.gov

Stone-Towns, Barbara
NASA Marshall Space Flight Center
Engineering Cost Office
Huntsville, AL 35812
USA
256-544-3050
Barbara.Stone-Towns@nasa.gov

Suggs, Robert M.
NASA Marshall Space Flight Center
Mail Code ED44
Huntsville, AL 35812
USA
256-544-2704
rob.suggs@nasa.gov

Swaminathan, Prasanna
Utah State University
Physics Department
4415 Old Main Hill
Logan, UT 84322-4415
USA
435-797-2936
prasanna@cc.usu.edu

Swenson, Charles
USU Space Dynamics Laboratory
1695 N. Research Parkway
Logan, UT 84341
USA
Charles.Swenson@usu.edu

Tanaka, Yasuhiro
Musashi Institute of Technology
1-28-1 Tamazutsumi
Setagaya-ku, Tokyo 158-8557
Japan
+81-3-3707-3111
tanaka@me.musashi-tech.ac.jp

Thiebault, Benoit
ESTEC/ESA –TOS/EES
Keplerlaan 1
Noordwijk 2201 ZH
The Netherlands
+31715656361
benoit.thiebault@esa.int

Thomson, Clint
Utah State University
Physics Department
4415 Old Main Hill
Logan, UT
84322-4415
USA
435-797-2936
slphb@cc.usu.edu

Torkar, Klaus
IWF/OAW
Institut fuer Weltraumforschung
Schmiedlstrasse 6
Graz 8010
Austria
+433164120531
Klaus.torkar@oeaw.ac.at

Toyoda, Kazuhiro
Chiba University
1-33 Yayoi Inage-ku
Chiba 263-8522
Japan
+81-43-290-3221
toyoda@tu.chiba-u.ac.jp

Usui, Hideyuki
Radio Science Center for Space and
Atmosphere, Gokasho
Kyoto University
Uji, Kyoto 611-0011
Japan
+81-774-38-3817
usui@kurasc.kyoto-u.ac.jp

Usui, Yusuke
Musashi Institute of Technology
1-28-1 Tamazutsumi
Setagaya-ku, Tokyo 158-8557
Japan
81 3-5707-2156
usui@me.musashi-tech.ac.jp

Van Eesbeek, Marc Robert Julien
ESA/ESTEC The Netherlands
Kepleraan 1
2200 AG Noordwijk
Zuid Holland
The Netherlands
+31-71-565-3896
marc.van.eesbeek@esa.int

Vaughn, Jason
NASA Marshall Space Flight Center
MS ED31
Huntsville, AL 35812
USA
256-544-9347
Jason.a.Vaughan@nasa.gov

Vayner, Boris
NASA Glenn Research Center
MS 302-1
Cleveland, OH 44135
USA
216-433-8058
vayner@grc.nasa.gov

Wang, Joseph
Virginia Polytechnic Institute & State Univ.
Dept. of Aerospace & Ocean Engin.
Blacksburg, VA 24061-0203
USA
jowang@vt.edu

Watson, Kent
National Institute of Aerospace
NASA Langley Research Center
MS 226
Hampton, VA 23681-2199
USA
757-864-4287
k.a.Watson@larc.nasa.gov

Wertz, George
NASA Marshall Space Flight Center
MS ED31
Huntsville, AL 35812
256-544-2663
USA
George.wertz@nasa.gov

Williams, Desiree D.
Colorado State University
1320 Campus Delivery
Ft. Collins, CO 80523
USA
970-491-8564
daisyw@engr.colostate.edu

Williams, John D.
Colorado State University
1320 Campus Delivery
Ft. Collins, CO 80523
USA
970-207-1692
johnw@engr.colostate.edu

Willits, Barry
Spectrum Astro, Inc.
1440 N. Fiesta Blvd.
Gilbert, AZ 85233
USA
480-892-8200
barry.willits@specastro.com

Wood, Bobby
BWACS, Inc.
402 Lannom Circle
Tullahoma, TN 37388-2464
USA
931-455-0375
bwacs@charter.net

Wright, Ken
CSPAAR/UAH
301 Sparkman Dr.
Huntsville, AL 35899
USA
256-961-7648
Kenneth.H.Wright@nasa.gov

Yung, Sopo
Computer Sciences Corporation
Mail Code ED03
Building 4487, Room B278
Huntsville, AL 35812
USA
256-544-9511
sopo.yung@msfc.nasa.gov

Summary of International ESD Round-Table Discussion at 8th Spacecraft Charging Technology Conference

Compiled By:
Mengu Cho
Kyushu Institute of Technology (KIT)
cho@ele.kyutech.ac.jp

Below, you will find the text version of the minutes of the round table discussion held at the end of the 8th SCTC. Any comments to the following discussion items will be highly appreciated. Last week, I had a chance to talk with the convener of ISO SC14 WG1, Mr. Keiichiro Eishima of Mitsubishi Electric Corp. ISO SC14 deals with space systems and has six working groups. Working Group 1 (WG1) deals with Design Engineering and is the most appropriate WG to discuss the issue of ESD ground tests for solar arrays.

In the next ISO meeting in Moscow, May 2004, the ESD test standard will be proposed as a new work item. Once it is approved we have to make the standard within three years.

I think three years is appropriate considering the fact that we will have two SCTCs (April 2004 Japan and 2006 France) by then. To meet that goal, I would like to proceed until 9th SCTC as following:

(1)   Define basic items such as the definition of ESD ground test to be covered by the ISO standard or basic terminologies.

(2)   Sort out what we agree and what we disagree.

(3)   Identify action items to be done to resolve the disagreement

(4)   Work on the action items by 9th SCTC, April 2004.

(5)   Present the result at 9th SCTC.

(6)   Next Round Table discussion at 9th SCTC.

Return to Title Page

The following minutes were made by listening to the recorded conversation. Not everything is recovered here because of the poor recording quality. I didn't reconstruct statements word-by-word. I suggest you listen to the recording and confirm what you said. The number in the bracket corresponds to the time marker of the recording. If any mistakes have been made, please accept my apology in advance. If you want to make any corrections, please don't hesitate to contact me. I will be happy to make a new version and think the correction process serves as the starting point of our further discussion.

Minutes of the Round Table discussion: International Standard of ESD Testing at the 8th Spacecraft Charging Technology, Huntsville, Alabama, USA, October 20-24, 2003.

Number of participants: 44

Mengu Cho described the nature of the round table discussion and explained the procedure of meeting.

Leon Levy (ONERA)(07:35)
*   Secondary arc is triggered by a primary arc.

*   Primary arc is one kind of vacuum arc that have been studied extensively in other fields.

*   Test should be carried out so that primary arc occurs between solar array adjacent cells.

*   Minimum voltage for secondary arc is not more than 20V.

*   Solar array simulator is important. The use of classical power supply gives too much output capacitance.

*   Test should be based on the worst case, not on the nominal case.

*   Whether the test is carried out in plasma or electron environments, the difference is small.

*   For a large dummy coupon, we saw only local neutralization of insulator charge and no global neutralization like reported by P. Leung.

*   For a large solar array coupon, so far we have not seen the global neutralization.

*   There is no need for a large differential capacitance to trigger secondary arc.

*   Even small coupon can have secondary arc.

*   Remaining issues are what should be the value of absolute capacitance and what is the practical size of coupon.

Comments on the statement of Leon Levy by Boris Vayner (NASA GRC)(20:00)
*   We should compare the results of plasma environment and electron environment.

*   Each coupon is different.

*   Size of coupon doesn't matter.

*   We start the test from low conditions and move to high condition (higher voltage, higher current).

Comments by Leon Levy (23:18)
*   It is difficult to trigger discharge in electron environment. Therefore, we use plasma environment while GEO is concerned.

Michael Bodeau (Boeing)(24:20)
*   We need to show a safe operation region and to show the design has a margin because the results depend on workmanship.

*   To explain that the test is adequate, we need to prepare for the worst case.

*   External capacitance should represent the remainder of full panel.

*   Propagation speed of plasma over the surface is important because it determines the current waveform. For inverted gradient it is 10^6 cm/s or less. For normal gradient is faster.

*   Need to put a current limiting resistance so that the time constant of the current corresponds to (scale of array)/(plasma speed).

*   Without the current limiting resistance, the peak current is too high leading to unrealistic extensive damage.

*   Normal gradient occurs on a high power satellite as a big antenna dish makes shadow on solar array.

*   Normal gradient test should be included because of faster pulse and larger current peak, i.e. higher likelihood of sustained arc.

Dale Ferguson (NASA GRC)(36:00)

*   To determine threshold, we draw a plot of arc rate versuss bias voltage like below.

*   Test a panel from a low voltage to a high voltage to avoid destroying or conditioning.

*   Need to do the test long enough to get some statistics.

*   Extrapolate the data points to the lower value and carry out the test just below the lowest data point long enough to be sure that the probability of arc is 3-sigma below.

*   Some kind of statistics is necessary to determine threshold.

*   We need to show threshold for a given solar array is well over the operation voltage we use. To do so, some set of margin is important. What is the reasonable margin?

*   Outgassing is extremely important for threshold of arc rate. Arc rate goes down 30 times after baking array for 1 week. RTV grouting absorbs a lot of water and this leads to lower threshold for primary arc.

*   Operationally, by not turning solar array on before outgassing, we can avoid arcing.

*   In LEO plasma condition, every bit of capacitance connected to the arc site is discharged whether or not the arc plasma reaches there because the ambient plasma conductivity is high. The situation is probably different in GEO.

*   We don't see any dependence of arc rate on the area of test panel.

Claude Berthou (Alcatel)(48:50)

*   Even a GEO satellite goes through LEO anyway. So we carry out test only in LEO-like plasma to save the money.

Ferguson (49:40)

*   If anybody can show testing in plasma environment and electron environment are essentially the same, it should be possible to test in LEO even though the satelilte is for GEO.

Hideaki Koatkutsu (Mitsubishi Electric)(51:00)

*   It is very surprising to see not only secondary arc but also primary arc causes solar cell degradation. But this is probably caused by too severe condition , such as a large capacitance.

*   I agree that establishing the international standard of ESD is important.

*   We should include the ESD test method into the solar array qualification
        international standard that is currently discussed in ISO. Ms. Bailey of NASA
        Glenn leads the discussion.

Ferguson (54:00)
*   Ms. Bailey is in my branch. We should ask her. She would be very interested in
        doing this with us.

Bodeau (54:20)
*   I agree that we give a presentation to space power workshop in probably 2 years
        from now.

*   GaAs has less junction capacitance. We found that if we give a large pulse, it will
        damage the solar cell. This is the second reason why we need a current limiting
        resistance in front of the external capacitance to stretch the current pulse. If the
        current is too fast and too big, it leads to the power loss that would not be
        observed in space.

Ferguson (55:50)
*   To make sure the test-setup is working, we should reproduce sustained arc at least
        once.

Todd Schneider (NASA MSFC)(57:25)
*   Do we have to include statistics of different sample?

*   Do we have to illuminate the cells during test?

Ferguson (59:50)
*   Solar cell resistance is dynamic. Probably arc rate doesn't matter even if we
        illuminate the cell. But the current waveform will be affected.

Bodeau (1:01:50)
*   Outgassing of molecules other than water continues for long time even though it
        is small. There is always material that feeds trigger arc. The idea of not operating
        solar array for a while is a loosing proposition because the battery is not big
        enough.

Fergsuon (1:04)
*   We know the water is important for trigger arc, but not for other molecules.

Bodeau (1:04:55)
*   We saw spectra of CH and Si in arc plasma.

Vayner (1:05)
*   We also saw the spectrum of CH, but it comes from the background plasma. If we outgass a little in orbit, we can shift the threshold higher.

Jean-Pierre Catani (CNES)(1:06)
*   I agree that we need to see at least one sustained arc to validate the test facility.

*   We are building a satellite before fully understanding the mechanism of primary and secondary arcs.

*   I am not sure whether the plasma diffuses along the panel. Maybe we have stepping from interconnector to interconnector.

*   We have to use knowledge of vacuum arc, e.g., movement of cathode spot and positive column.

Tetsuo Satoh (JAXA)(1:11:10)
*   If international standard of ESD test is made, it will contribute a lot to space activity.

*   The standard should include a method to evaluate the test result.

David Cooke (AFRL)(1:12:50)
*   We should adapt a challenge for next charging conference that laboratories develop candidate for standard arc sample for calibration. In the next SCTC (Tsukuba) we decide 3 or 4 different standard arc calibrator. Then in the subsequent conference (Toulouse) we show how various facilities respond to the standard samples.

Bodeau (1:14:00)
*   By testing different coupons, we can show by side-by-side comparison that one design is defective and the others not. But I don't know how many times we need to test a defective coupon. Once we agree that a design is defective, we don't use it anymore.

Cooke (1:15:30)
*   We don't have to use a solar cell coupon as the standard arc sample. It can be something we can build by ourselves, such as glass and aluminum.
.
Bodeau (1:15:40)
*   High voltage power supply for thruster or ion engine is probably not built with the same standard as other high voltage devices. Deep charging in orbit might release plasma and gas leading to breakdown in power supply. An easy way to test is to power up the circuit in a vacuum chamber and reintroduce atmosphere. If there is defect we see Paschen breakdown. It is overtest, but if we really want to test

workmanship, it is necessary.

Ferguson (1:17:30)
* We can turn on the circuit in the atmosphere and go down to the lower pressure.

Hilgers (ESA)(1:18:00)
* We encourage identifying international standard for testing.

Ferguson (1:19:50)
* We have made a good start today.

* The standard is useful for commercial purpose.

Bodeau (1:21:52)
* Eighteen months is too long to resume the conversation and organizing a conference is a big deal. Is there a semi-official way to structure a committee, international working group to set the standard, via teleconference or video-conference?

Catani (1:23:05)
* One possible way is to propose to ISO standard.

Ferguson (1:24:07)
* Why don't we set up an ad-hoc committee to study the test standard?

Henry Garrett (NASA JPL)(1:24:30)
* There is an official ISO panel to study regularly all of these aspects including space environment. We should work with ISO. All of people here should be involved in the panel.

Cho (1:24:54)
* Today we have agreed on having some kind of standard.

* We should go to ISO and talk to key persons in ISO nearby about the importance of the standard.

* Mailing list will be set up and the record of this discussion will be sent.

The following list contains the initial discussion items that will be discussed in the ESD mailing list. This is a running conversation and so some items already have responses. If you would like to provide comments or join the mailing list, please contact Mengu Cho.

(1)   Definition of basic items
(1-1)   Definition of ESD ground test to be covered by the ISO standard
(1-2)   Terminology of ESD phenomena

(1-2-1)	Primary arc, trigger arc, primary ESD
(1-2-2)	Secondary arc, sustained arc, continuous arc
(1-3)	Items to be specified by the standard
(1-3-1)	Test environment
(1-3-2)	Power supply
(1-3-3)	Test duration
(1-3-4)	External capacitance
(1-3-5)	Others

(2) Points of agreement

(2-1) International standard is useful. We should try to make the standard an ISO standard.

(2-2) We should continue discussion until 9th SCTC via e-mails.

(2-3) We need to simulate the worst case to verify the immunity against sustained arc.

(2-4) A satellite opens solar panels in LEO. Therefore, a test under LEO-plasma like condition is necessary.

(2-5) Only Minimum amount of external capacitance is necessary to produce secondary arc.

(2-6) The test result should reflect statistical error. We need to show that there is sufficient margin from the threshold of sustained arc inception.

(2-6-1) In order to verify the test set-up, we should produce sustained arc at least once.

(2-6-2) We must distinguish the set of parameters that causes sustained arc from the set of parameters that doesn't cause sustained arc.

(2-6-3) The standard should include how we evaluate the test results.

(3) Points of disagreement

(3-1) Secondary arc occurrence is the same between LEO-plasma environment and GEO-plasma environment (electron beam charging).

(3-1-1) We need to carry out the same experiment with the same test sample both in LEO environment and GEO environment and verify that the occurrence probability of secondary arcs and the duration of secondary arcs are the same in both the environment. (Action item)

(3-1-2) If the results are the same, we can substitute a test in LEO environment for a test in GEO environment.

(3-2) The current waveform supplied by an external capacitance must simulate the expansion of plasma cloud over solar array panel. Especially the current peak value must be adjusted to a realistic value.

(3-2-1) We need to investigate the process of coverglass charge neutralization via the expanding plasma.(Action item)

(3-2-2) The effect of current supplied by the external capacitance on the duration of secondaryarc and the probability of transition to permanent sustained arc must be investigated. (Action item)

(3-3) Size of test solar array coupon is not important.

(3-3-1) We need to determine appropriate (minimum) size and number of solar array coupon by taking into account statistical error.(Action item)

(3-4)   To simulate the solar array string circuit, a solar array simulator with a small output capacitance should be used.

(3-4-1)   Solar array simulator (commonly Agilent E4351B) simulates solar array output only electronically. If possible, a power supply that is robust enough against instantaneous voltage change like ESD tests. (Action item)

(3-5)   The external circuit must include a proper amount of inductance that represents the real solar array circuit.

(3-5-1)   We need to investigate the effect of circuit inductance on the secondary arc occurrence. (Action item)

(3-6)   We must make an appropriate number of primary arcs occur on a solar array test coupon to verify that sustained arc will not occur.

(3-6-1)   We need to estimate an expected number of primary arcs that would occur during satellite lifetime. (Action item)

(3-7)   We should illuminate a solar array test coupon.

(3-7-1)   We need to investigate whether illuminating a coupon makes any difference in the secondary arc occurrence. (Action item)

REPORT DOCUMENTATION PAGE

Form Approved
OMB No. 0704-0188

Public reporting burden for this collection of information is estimated to average 1 hour per response, including the time for reviewing instructions, searching existing data sources, gathering and maintaining the data needed, and completing and reviewing the collection of information. Send comments regarding this burden estimate or any other aspect of this collection of information, including suggestions for reducing this burden, to Washington Headquarters Services, Directorate for Information Operation and Reports, 1215 Jefferson Davis Highway, Suite 1204, Arlington, VA 22202-4302, and to the Office of Management and Budget, Paperwork Reduction Project (0704-0188), Washington, DC 20503

1. AGENCY USE ONLY *(Leave Blank)*	2. REPORT DATE	3. REPORT TYPE AND DATES COVERED
	March 2004	Conference Publication

4. TITLE AND SUBTITLE

8th Spacecraft Charging Technology Conference

5. FUNDING NUMBERS

6. AUTHORS

J.L. Minor, Compiler

7. PERFORMING ORGANIZATION NAMES(S) AND ADDRESS(ES)

NASA Space Environments and Effects (SEE) Program
George C. Marshall Space Flight Center
Marshall Space Flight Center, AL 35812

8. PERFORMING ORGANIZATION REPORT NUMBER

M–1102

9. SPONSORING/MONITORING AGENCY NAME(S) AND ADDRESS(ES)

NASA Space Environments and Effects (SEE) Program
George C. Marshall Space Flight Center
Marshall Space Flight Center, AL 35812

10. SPONSORING/MONITORING AGENCY REPORT NUMBER

NASA/CP—2004–213091

11. SUPPLEMENTARY NOTES

Prepared by NASA's Space Environments and Effects (SEE) Program
Technical Monitor: Jody Minor, NASA Marshall Space Flight Center, 256-544-4041

12a. DISTRIBUTION/AVAILABILITY STATEMENT

Unclassified-Unlimited
Subject Category 18
Availability: NASA CASI (301) 621–0390

12b. DISTRIBUTION CODE

13. ABSTRACT *(Maximum 200 words)*

The 8th Spacecraft Charging Technology Conference was held in Huntsville, Alabama, October 20–24, 2003. Hosted by NASA's Space Environments and Effects (SEE) Program and co-sponsored by the Air Force Research Laboratory (AFRL) and the European Space Agency (ESA), the 2003 conference saw attendance from eleven countries with over 65 oral papers and 18 poster papers in the areas of Plasma Propulsion and Tethers, Ground Testing Techniques, Interactions of Spacecraft and Systems With the Natural and Induced Plasma Environment, Materials Characterizations, Models and Computer Simulation, Environment Specifications, Current Collection and Plasma Probes in Space Plasmas, and On-Orbit Investigations. A round-table discussion of international standards regarding electrostatic discharge (ESD) testing was also held with the promise of continued discussions in the off years and an official continuation at the next conference.

14. SUBJECT TERMS

spacecraft, charging, plasma, electro-static, discharge, voltage, charge, differential, material, simulation, test, tether, induced, interactions, environment, current, LEO, GEO

15. NUMBER OF PAGES

1158

16. PRICE CODE

17. SECURITY CLASSIFICATION OF REPORT	18. SECURITY CLASSIFICATION OF THIS PAGE	19. SECURITY CLASSIFICATION OF ABSTRACT	20. LIMITATION OF ABSTRACT
Unclassified	Unclassified	Unclassified	Unlimited

NSN 7540-01-280-5500

Standard Form 298 (Rev. 2-89)
Prescribed by ANSI Std. 239-18
298-102